MEGAGAUSS MAGNETIC FIELD GENERATION, ITS APPLICATION TO SCIENCE AND ULTRA-HIGH PULSED-POWER TECHNOLOGY

Proceedings of the VIIIth International Conference on Megagauss Magnetic Field Generation and Related Topics

Tallahassee, Florida, USA
18-23 October 1998

Edited by
Hans J. Schneider-Muntau

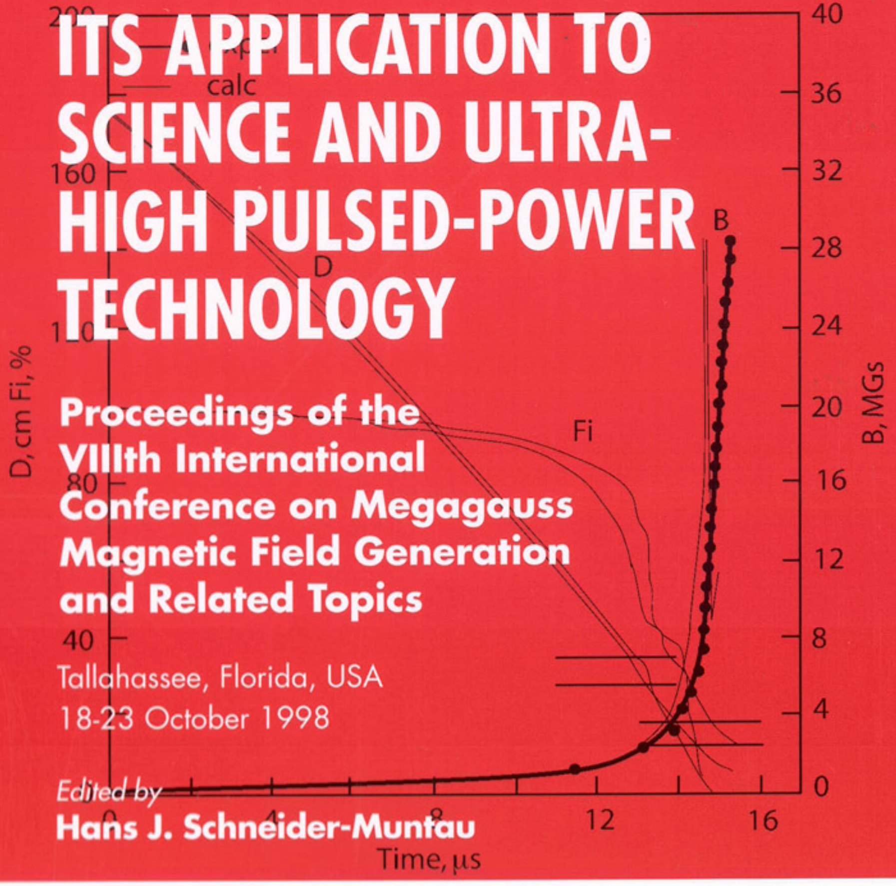

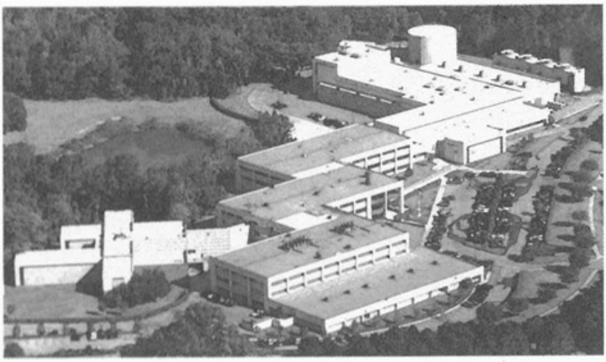

World Scientific

MEGAGAUSS MAGNETIC FIELD GENERATION, ITS APPLICATION TO SCIENCE AND ULTRA-HIGH PULSED-POWER TECHNOLOGY

MEGAGAUSS MAGNETIC FIELD GENERATION, ITS APPLICATION TO SCIENCE AND ULTRA-HIGH PULSED-POWER TECHNOLOGY

Proceedings of the VIIIth International Conference on Megagauss Magnetic Field Generation and Related Topics

Tallahassee, Florida, USA
18-23 October 1998

Edited by

Hans J. Schneider-Muntau
National High Magnetic Field Laboratory
Florida State University, USA

World Scientific

NEW JERSEY • LONDON • SINGAPORE • BEIJING • SHANGHAI • HONG KONG • TAIPEI • CHENNAI

Published by

World Scientific Publishing Co. Pte. Ltd.
5 Toh Tuck Link, Singapore 596224
USA office: 27 Warren Street, Suite 401–402, Hackensack, NJ 07601
UK office: 57 Shelton Street, Covent Garden, London WC2H 9HE

British Library Cataloguing-in-Publication Data
A catalogue record for this book is available from the British Library.

The editor of this book wishes to thank those who worked so hard to make the conference such a success. A greater challenge turned out to be the peer review of all the articles and the editing of the book. The untiring efforts of Ms. Pam Houmere for the technical editing of the papers are especially recognized. Without her help this book would not have been possible. Many thanks also go to the people who helped over the years with the follow-up on the collection of the original and reviewed papers: Ms. Terry Pace, Janet Neff-Shampine, again Pam Houmere, and others.

The peer review of the papers and the book was produced with ultimate care. Nevertheless, we cannot warrant the information contained in this book to be free of errors. The quality of the pictures, figures, and equations stems from the originals we received from the authors.

Particular thanks go to Mr. Walter Thorner for the design and lay-out of the book.

On the Cover: The National High Magnetic Field Laboratory in Tallahassee, Florida with a reproduction of the 2800 T (28 MGauss) field pulse obtained in Sarov in 1998.

MEGAGAUSS VIII
Proceedings of the VIII International Conference on Megaguass Magnetic Field Generation and Related Topics

ISBN 982-256-016-5

This book is printed on acid-free paper.

Printed in Singapore by Mainland Press


game

DEDICATED TO THE 80th BIRTHDAY OF MAX FOWLER

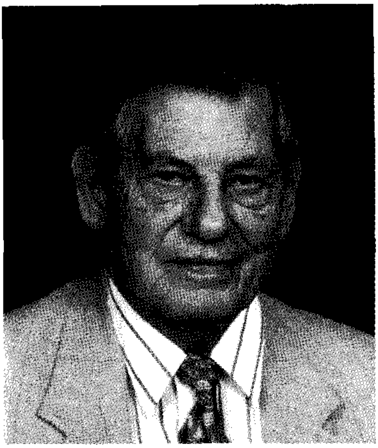

Max Fowler, 1998

During the "Megagauss VII" Conference in Sarov, the International Steering Committee voted to ask the National High Magnetic Field Laboratory to host the next "Megagauss-VIII" Conference in Tallahassee, Florida, U.S.A. and to dedicate it to the 80th birthday of Dr. Clarence M. Fowler, known simply as "Max" to his many friends and colleagues. By this decision, the International Steering Committee emphasized not only the outstanding contribution of Max Fowler as a pioneer in the field of megagauss magnetic field generation, design of generators of magnetic fields and electromagnetic energy, and the application of the generators to various problems of experimental physics, but especially his outstanding contribution to the creation of the International Megagauss Community.

It is a great honor for us to write this short article about Max, our wonderful colleague and friend. To write about Max is simultaneously easy and difficult. There are two attributes which we find remarkable; his outstanding scientific success, because many of his papers became classical and well known to the scientific community, and his scientific drive infecting everyone he met with his enthusiasm and passion for research.

Max Fowler was born in November 26, 1918, in the small town of Centralia, Illinois, U.S.A. He obtained a B.S. degree in Chemical Engineering from the University of Illinois in 1940. After graduation, he worked at the American Steel and Wire Company in Cleveland, Ohio. There, he met his future wife, Janet Brown. Max and Janet will soon celebrate their 60th wedding anniversary. Following the outbreak of WWII, he enlisted in the Navy. Upon his discharge in mid 1946, he enrolled as a graduate student in Physics at the University of Michigan. After completing his graduate work in late 1949, Max accepted an appointment at Kansas State University (KSU) as Assistant Professor. He set up a laboratory at KSU dedicated mainly to the beta and gamma ray spectroscopy of neutron induced radioactive rare-earth elements. In the early 1950's, he started at the Los Alamos Scientific Laboratory as a summer Visiting Scientist. It was during these visits that Max fired his first flux compression shots. He eventually resigned from his position as Full Professor of Physics at KSU in 1957 to devote all of his time to a broad program in Magnetic Flux Compression at Los Alamos.

A pioneer himself, Max is linked to early pioneers such as Peter Kapitza and Francis Bitter. Bitter worked as a consultant during many summers in Los Alamos developing new designs of pulse magnets to increase the seed field of flux compression devices. Max is also connected to another pioneer, Heinz Knoepfel, who developed a flux compression facility with Fritz Herlach in Frascati, Italy.

Dr. Fowler is the author or coauthor of nearly 200 open-literature publications on such different subjects as difference equation stability, diffusion, nuclear spectroscopy, shock wave induced phase transitions and other effects in metals, and most predominantly in explosive flux compression. Over the years, he and his colleagues have utilized explosive flux compression to produce very large magnetic fields and to generate large electromagnetic pulses. They have used both techniques in many applications, including megagauss field generators for solid state research, pulsed power supplies for a number of devices including theta pinches, plasma guns, plasma focuses, lasers, imploding foils for soft X-ray production, e-beam accelerators, rail guns and, more recently, as magnetic field generators to study high-temperature superconductors in megagauss fields.

We mention here explicitly three of Max's especially worthy publications. His very first paper was titled "Analysis of Numerical Solutions of Transient Heat Flow Problems" [1]. Max is very proud of this paper. He told us that he has received the most reprint requests for this paper. His contribution was awarded the Miller Prize in mathematics at the University of Michigan. Max's most significant and well-known paper is the "Production of very high magnetic fields by implosion" [2]. It was the first report of magnetic field generation above 10 MG and up to 14 MG. It stimulated much work in liner implosion of plasmas, material research in megagauss fields and ultimately, the Megagauss Conferences. Let us note that it took almost 40 years to double the field value to 28 MG as reported at this conference [3]. As the third paper, we wish to cite the review paper at this conference [4] where Max gives a thorough overview of his work in flux compression.

Max's earlier work had a strong influence on subsequent megagauss-field solid-state research, liner implosion of plasmas, and on the initiation of the International Conferences on Explosive Generation of Megagauss Fields and Related Topics, now known as the Megagauss (MG) Conferences. Dr. Fowler chaired the MG Conference held in Santa Fe, NM in 1986 and, as a member of the International Steering Committee, assisted in organizing most of the other Megagauss Conferences. Relations with Russian colleagues, within limitations imposed by the political climate of those times, were greatly stimulated by the relationship that developed between Fowler and Gennady Shvetsov, of the Lavrentyev Institute of Hydrodynamics in Novosibirsk. This collegial relationship then led to one with the late Academician Alexander Pavlovski, who directed a similar flux compression effort at Sarov, a complex similar to Los Alamos and now Los Alamos' "sister city". The existence of the subsequent, unclassified scientific programs carried out jointly between these two "weapons" laboratories, was due in considerable part to the Pavlovski-Fowler relationship. It was their profound friendship and the peaceful scientific cooperation that helped to break the ice between the U.S. and Russia at the end of the cold war. Max was also instrumental in helping the Florida State University/University of Florida/Los Alamos Proposal to develop the National High Magnetic Field Laboratory partly due to the high magnetic field research done at Los Alamos by the Explosive Flux Compression Team.

Dr. Fowler has served on a number of panels and committees including the National Science Foundation Panel on High Magnetic Fields, the Defense Science Board, NATO, DOE, DoD, and has directed a number of programs for some of these organizations. He is a long-time Fellow of the American Physical Society (1964) and was one of the early Los Alamos National Laboratory Fellow Appointees (1982). Dr. Fowler was awarded an Honorary Doctorate from Novosibirsk State University for his work in high energy density physics and for furthering scientific relations between the United States and Russia. He was honored in a special session of the MG VIII Conference held in Tallahassee in 1998. Although retired for several years, he has remained active in both publishing and lecturing. In the last two years, besides lectures in the U.S., he has presented lecture series in Korea, Russia and Germany.

At the special session of the MG-VIII Conference at which friends and colleagues congratulated Dr. Max Fowler on his anniversary, conference participants of the Lavrtentyev Institute of Hydrodynamics read out the following congratulation:

> *"Dear Max,*
>
> *In everyone's life there happen events that can be considered the most important and years later the person realizes better and better how many things in his personal life would be different if this event did not occur. For us, such an event was the acquaintance and cooperation with you. In your person we have an outstanding scientist, a reliable friend, and a wonderful man. Today, many-many years after our first meetings in Los Alamos and Novosibirsk, we thank our lucky stars that we have the good fortune to know and love you and work together with you.*
>
> *Our hearts are with you and your incomparable Janet. On the occasion of your 80th birthday we wish you good health and great success."*
>
> *We would like to conclude this dedication by joining in the above wishes from the depth of our hearts.*
>
> *Gennady A. Shvetsov*
> *Hans J. Schneider-Muntau*

References

1. Fowler, C. M., Analysis of Numerical Solutions of Transient Heat Flow Problems, *Quart. Appl. Math.* **3** (1946) p. 361.
2. Fowler, C. M., Garn, W. B., Caird, R. S., Production of Very High Magnetic Fields by Implosion, *J. Appl. Phys.* **31** (1960) p. 588. Also, *Bull. Am. Phys. Soc.*, **4** (1959) p. 96.
3. Boyko, B. A., Bykov, A. I., Dolotenko, M. I., Kolokol'chikov, N. P., Markevtsev, I. M., Tatsenko, O. M., Shulvalov, A. M., Generation of Magnetic Fields Above 2000T with the Cascade Magneto-Cumulative Generator MC-1, this conference.
4. Fowler, C. M., Explosive Flux Compression: a Review of 50 Years of Los Alamos National Laboratory Activities, this conference.

EDITOR'S PREFACE

The generation of megagauss fields for science and technology is an exciting area where new physical phenomena, technological challenges, and the selection and development of materials together create a unique potential and synergy resulting in fascinating discoveries and achievements. The controlled handling and applications of extremely high power and energy densities in small volumes and on short time scales is the common theme of this collection of contributions. All papers have been peer-reviewed and carefully edited.

The VIIIth International Conference on Megagauss Magnetic Field Generation and Related Topics (MG-VIII) united more than 200 participants from over 14 countries, with 87 delegates from the U.S. and 30 from Russia. These Proceedings provide the latest research results on the generation of very high magnetic fields up to and well above the megagauss level. One of the highlights is the report on the highest magnetic field ever generated, 2800 T (28 MG), using explosive flux compression technology. An entire session is devoted to the Dirac series of scientific experiments in fields up to 1000 T. Contributions about the generation of fields in the millisecond pulse range, fields in small volumes, and material developments in this area, conclude the first section of the Proceedings.

Megagauss VIII was held in connection with the conference "Physical Phenomena at High Magnetic Fields - III" (PPHMF-III) in order to encourage and facilitate cross-links between the two scientific communities. This was highly successful since 26 PPHMF participants also registered at MG-VIII. The chapter "Science in Megagauss Magnetic Fields" reflects these contributions.

The following section of the Proceedings is devoted to new results in the more traditional fields of the Megagauss conference: generation of plasmas, magnetized plasma, imploding liners, and fusion. Two major chapters describe progress with generators that use explosives to create ultra-high pulsed power for different applications, and other activities such as rail guns and launchers, codes and modeling. All of these contributions underline the ever-growing importance of advancing ultra-high power density technologies. The Proceedings close with descriptions of magnetic field facilities that are open to users who wish to do experiments in high and ultra-high magnetic fields.

The conference organizers want to thank the members of the International Steering Committee, the Program Committee, and the Local Organizing Committee. Help and assistance by the Megagauss Institute Inc. is especially recognized. Our gratitude also goes to the numerous conference sponsors who helped to make the conference become such a congenial and successful meeting.

It is impossible to acknowledge all those who helped to organize the conference. Special thanks go to Ysonde Jensen, Joanne Palmer, and Brenda Cornett. These Proceedings would not have been possible without the guidance of the Board of Editors and the untiring help of Pam Houmere and Walter Thorner. Peer review, editing of the many foreign contributions and putting them into a coherent electronic format turned out to be a major effort.

Hans J. Schneider-Muntau

This page intentionally left blank

INTERNATIONAL STEERING COMMITTEE

Larry L. Altgilbers - Missile Defense Space Technology Center
William L. Baker - Phillips Laboratory
Evgenii I. Bichenkov - Lavrentyev Institute of Hydrodynamics/Russian Academy of Sciences
Jay B. Chase - Lawrence Livermore National Laboratory
Maynard (Bill) Cowan - Sandia National Laboratories
Dennis J. Erickson - Los Alamos National Laboratory
C. Max Fowler - Los Alamos National Laboratory
James H. Goforth - Los Alamos National Laboratory
F. Herlach - Catholic University, Leuven
Noboru Miura - Institute for Solid Physics/University of Tokyo
Bob Reinovsky - Los Alamos National Laboratory
Hans J. Schneider-Muntau - National High Magnetic Field Laboratory
Victor D. Selemir - All-Russian Scientific Research Institute of Experimental Physics
Gennady A. Shvetsov - Lavrentyev Institute of Hydrodynamics/Russian Academy of Sciences
Vladimir M. Titov - Lavrentyev Institute of Hydrodynamics/Russian Academy of Science
Peter J. Turchi - The Ohio State University
E. P. Velikhov - Kurchatov Institute for Atomic Energy

PROGRAM COMMITTEE

L. Campbell - Los Alamos National Laboratory
R. Clark - University of New South Wales
J. Degnan - Air Force Research Laboratory, Phillips Reseach Site, Kirtland AFB
P. Frings - Van Der Waals-Zeeman Institute
J. Goforth - Los Alamos National Laboratory
F. Herlach - Catholic University, Leuven
H. Jones - University of Oxford
W. Joss - Grenoble High Magnet Field Laboratory
K. Kindo - Osaka University
A. Lagutin - Kurchatov Institute of Atomic Energy
N. Miura - Institute for Solid State Physics
N. Popkov - Russian Federal Nuclear Center, All-Russian Scientific Research Institute of Experimential Physics
R. Reinovsky - Los Alamos National Laboratory
G.A. Shneerson - St. Petersburg Technical University
G. Shvetsov - Lavrentyev Institute of Hydrodynamics
R. Spielman - Sandia National Laboratories
M. Springford - H.H. Wills Physics Laboratory, University of Bristol
P. Turchi - The Ohio State University
M. von Ortenberg - Humboldt University, Berlin

LOCAL ORGANIZING COMMITTEE

Jim Brooks - National High Magnetic Field Laboratory
Jack E. Crow - National High Magnetic Field Laboratory
James H. Degnan - Phillips Laboratory
Lloyd Engel - National High Magnetic Field Laboratory
C. Max Fowler - Los Alamos National Laboratory
Jerry T. Jones - Air Force Wright Laboratory
Daniel A. Matuska - Orlando Technology, Inc.
Bob Reinovsky - Los Alamos National Laboratory
Dwight Rickel - Los Alamos National Laboratory
Alita Roach - Los Alamos National Laboratory
Hans J. Schneider-Muntau - National High Magnetic Field Laboratory
Rick B. Spielman - Sandia National Laboratories

SPONSORING ORGANIZATIONS

Los Alamos National Laboratory
Sandia National Laboratories
Air Force Research Laboratory, Phillips Site, Kirtland AFB
National High Magnetic Field Laboratory
Megagauss Institute
Russian Federal Nuclear Center, All-Russian Scientific Research Institute of Experimental Physics
Oxford Instruments
Keithley Instruments
F.W. Bell, Division of Bell Technologies
GMW Associates
Lakeshore Cryotronics
Janis Research Co.
Leon County Tourist Development Council

TABLE OF CONTENTS

GENERATION OF MEGAGAUSS MAGNETIC FIELDS

GENERATION OF MEGAGAUSS MAGNETIC FIELDS

ADVANCED HIGH EXPLOSIVE PULSED POWER TECHNOLOGY AT VNIIEF

V. K. CHERNYSHEV
All-Russian Research Institute of Experimental Physics, Sarov, Russia

The primary purpose of this presentation is to present the possibilities of super high power explosive magnetic energy sources and to demonstrate some of their applications where their use would be most impressive and beneficial.

1 Introduction

High-power sources storing 10 to 100 MJ, and capable of generating pulsed currents from 50 to 100 MA in different loads, are required to solve a number of important problems of modern science and technology. Large and costly stationary capacitor bank facilities have been created for these purposes and are being designed and built abroad. There exist the PEGASUS facility in LANL (5 MJ), Shiva star facility in the Phillips Laboratory (10 MJ), ATLAS facility in LANL (36 MJ), JUPITER facility in Sandia (100 MJ), and others. The energy carriers in these facilities are dielectrics in which energy storage is limited to about 100 J/l.

VNIIEF chose a unique path of experimentation [1-7]. In 1951, the academician A. D. Sakharov proposed using an explosive to carry energy, creating energy storage five orders of magnitude greater than previously available. To convert the chemical energy of the explosive into electromagnetic energy, Sakharov proposed using magnetic cumulation, an effect based on compression assisted by the explosion of a conducting contour with a magnetic flux introduced from an outside source. The results were very fruitful.

In the process of implementing magnetic cumulation, the MC-2 system design proposed by Dr. Sakharov was considerably improved, and the new generation of devices called helical EMGs. Principally new types of explosive systems were created [8-25] based on different operation principles. The research results follow:

1. The "Potok" family of EMGs with record performance were created.
2. New systems of power amplification were created: fast opening switches made possible the generation of a current pulse with 70-100 MA amplitude, a 1 μs front of increase and an output voltage of 500 kV.
3. Application of fast-operating superpower helical EMGs and opening switches, in particular, allowed formation of an ionized and magnetized plasma in a volume of 1000 cm^3 with a temperature of 0.2 to 1 keV and 2 μs lifetime. This plasma is suitable for additional adiabatic compression and achievement of thermonuclear ignition [26-28].

2 Quick-Operating Helical EMGs

The design simplicity and compactness of helical EMGs, as well as their high power and energy characteristics, attracted the attention of both development engineers and users. After the first open publications of papers [1,2] dozens of international investigators developed helical EMGs. However, not all were successful.

The helical EMG is a very complex 3-D system that seems initially simple. Such a 3-D problem has had neither solution nor expression, theoretically or computationally. Success in its solution depends on the skills of the scientists and development engineers.

Under rapid compression of the circuit, when the active resistance may be neglected and the magnetic flux may be considered to be constant, current and energy increase proportionally to the circuit compression ratio $K_L = L_f / L_o$.
$L_o I_o = \Phi_o = L_f I_f = Const,\ I_f = I_o = L_f \cdot K_L,\ Ef = (L_f \cdot I_f^2)/2 = \Phi_o^2/2L_f = Eo \cdot K_L$
Subscripts ‘o’ and ‘f’ mark the initial and final values of inductance, current, and energy, respectively.

It is difficult to conserve magnetic flux in the compression process. There are always flux losses in real constructions (only some part of initial flux may be conserved, $\eta=\Phi_f/\Phi_o$) because of the geometrical imperfection of the compression contour, the ohmic resistance of the conductor material and the high voltages leading to electrical breakdowns. The current and energy increase less $I_f = \eta \cdot I_o \cdot K_L$, $E_f = \eta^2 \cdot E_o \cdot K_L$; η, in its turn, largely depends on K_L, making it difficult to use this characteristic.

The best characteristic of coil operation during the process of magnetic cumulation was proposed by J. Shearer in 1968 [29]. It is the perfection index (“Figure of merit”), determined from the expression $F(t) = -(\dot{I}/I)(\dot{L}/L)$.

The high-power helical EMGs developed in the Electrophysical Department at VNIIEF are comparable in energy with the largest US capacitor bank facilities and have been used successfully in Russia, the USA and France to solve a variety of scientific problems.

3 Plasma Focus Powering By Helical EMG Raises Neutron Yield And Makes The Entire System Transportable

The chamber using plasma focus was suggested and developed by N. V. Filippov and T. I. Filippova in 1955 [30] and was later refined in many countries [31-40]. A French article published in 1971 noted that when an EMG with 0.7-1.0 MA current powered a plasma focus chamber (filled with D-D mixture), a yield of 1.5×10^9 neutrons/pulse at 2.5 MeV was recorded [35]. Later, information surfaced that research on PF type discharges using the EMG was done in the United States [34,37-39]. This research occurred simultaneously at VNIIEF.

In 1986, a Russian article was published announcing that a small EMG with an opening switch at a discharge current of ≈400 kA produced a neutron yield of $\approx 3 \cdot 10^{10}$ n/pls [36]. In that experiment, the influence of the rate of current increase on plasma shell dynamics and neutron pulse parameters was studied in the gas discharge chambers, which were analogous to the Filippovs’ chambers. These chambers were filled with a 1:1 mixture of deuterium and tritium within the pressure range of 5-20 tor.

The experiments showed that, in the plasma focus chambers, application of the EMG resulted in a neutron yield 3-4 times higher than the use of a capacitor source at approximately the same discharge current. This occurred because the current rise rate was increased by 2.5-3 times in the EMG compared to an ordinary energy source.

For the EMG experiment providing a 1 MA current with 0.5 μs duration of the increase front, in the chamber filled with D-T mixture up to 15 torr pressure, the neutron yield was ~$1.0 \cdot 10^{12}$ n/pls. We can conclude that using explosive magnetic energy sources produces a factor of 3-4 times higher neutron yield in comparison with capacitive energy sources, while preserving the same current pulse amplitude in the chamber, and rendering the entire system transportable.

4 Study of Instability Growth in High-Speed Implosion

When the liner is accelerated by a magnetic field [41-48], various phenomena may occur between the liner and the electrode walls. There can occur some advance or lag of the liner boundaries in a pre-wall region of the electrodes, melting or vaporization of the liner material, or a local distortion of the liner shape.

In [44,45], the aluminum liner interactions with the electrode walls are described and the choice made by which the liner and electrodes are attached to provide a continuous contact. To make the experiments more informative, a system consisting of two independent liners was used at strictly the same discharge current. To define the liner shape, a radiographic image of the walls-electrodes interaction was made.

The helical EMG-100, used as the energy source, had an inner helix turn diameter of 100 mm, length of 700 mm, effective current rise time of 15-17 μs, and it could provide currents of up to 5.8 MA in the liner system (LS). X-rays having pulse duration of ~50-70 ns and charging voltage ~700 kV recorded the liner motions.

A series of explosive experiments was performed and the results are described in detail in [44,45].

5 Helical EMG as Energy Preamplifier for High-Power Disk EMG

A schematic of a disk explosive magnetic generator (2) powered by a helical generator (1) is shown in Fig. 1.

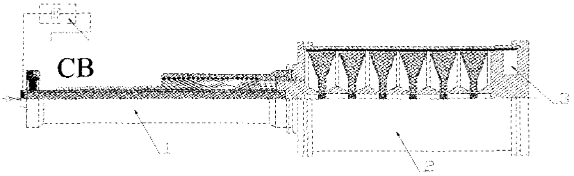

Figure 1. 1. Helical explosive magnetic generator (HEMG), 2. Disk explosive magnetic generator (DEMG), 3. Load

To power a large, multielement disk generator of 1 m in diameter, a helical generator of 240 mm was developed. [49,50]. When powering a 3-element generator, the following parameters were obtained:

Initial inductance of the helical generator	115 μH
Initial inductance of a 3-element disk generator	85 nH
Initial current of the helical generator powering	28 kA

Final current at the exit of the helical generator	13.7 MA
Initial energy in a 3-element disk generator of ∅ 1 m	8 MJ

6 Magnetized Plasma Preliminary Heating in MAGO Chamber

A device designed to power the plasma chamber is presented in Fig. 2. The helical explosive magnetic generator, II, provides preliminary powering of chamber I using magnetic flux. Upon completion of preliminary powering, a source of rapid powering, III, consisting of the helical explosive magnetic generator, A, and a fast opening switch, B, switches on. Gas discharge takes place in section 1 of the chamber resulting in "sticking" in the magnetic field plasma. Under the effects of the magnetic field, the formed plasma flows out of the first section to the second through nozzle 3. The plasma flow becomes supersonic at the nozzle exit due to the rapid increase in magnetic field. A high-temperature region is formed in the second section, in which deceleration and heating of plasma take place [27].

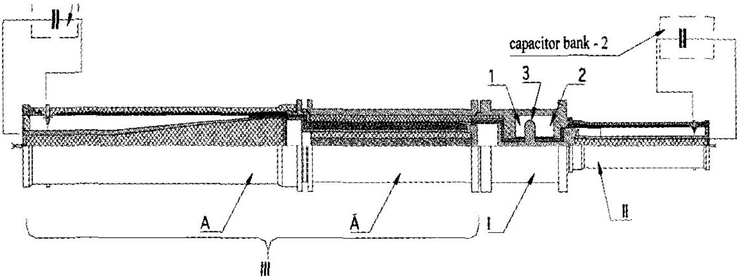

Figure 2. The schematic of MAGO chamber powered by two HEMGs.

Table 1 presents the results of chamber testing in which a 200 mm diameter helical generator with a fast opening switch served as a quick-operating source. A 160 mm diameter helical generator was used as a preliminary powering source.

Table 1

No.	$I_{prel.}$, MA	I_1 MA	i_1 A/s	$E_{EMG,}$ MJ	N neutrons
1	4	9.5	$3.1 \cdot 10^{12}$	6.9	$1.4 \cdot 10^{13}$
2	3	10.5	$3.9 \cdot 10^{12}$	10	$2.0 \cdot 10^{13}$
3	1.01	8	$4.0 \cdot 10^{12}$	6.8	$4.0 \cdot 10^{13}$

7 Quick-Operating Superpower Disk EMG

High-power, quick-operating sources of energy, able to provide current pulses of tens of megaamperes in the outer load for tens of microseconds (rate of rise is 10^{12} A/s and higher) are increasingly used in many world laboratories to solve both scientific and engineering problems.

Increasingly, in large facilities, the energy delivered to the load during a single experiment is higher and the cost of the parts destroyed in the shot (not only the load, but the facility parts around it, as well) becomes much higher. The protective measures to be taken must be great if the energy delivered to the load is, for example, 100 MJ (equivalent to 25 kg of trinitrotolluene (TNT)). VNIIEF presently possesses much experience in the development and application of EMGs [1,2,22-24].

There are advantages in using single-action EMGs at certain energies. Also, there are no stationary systems (e.g. for energy 200 MJ at currents of more than 200 MA) that could provide the output characteristics of EMGs. It is expedient to use helical EMGs for energy levels up to 50 MJ and currents up to 50 MA, while disk EMGs [22-25] become preferable for energy levels of 20-30 MJ at currents greater than 30 MA (up to 100 MJ at currents up to 300 MA, see Fig. 3, Table 2). Transition from helical to disk EMGs allows the speed of the current rise in the load to increase by an order of magnitude (up to 10^{13} A/s and higher) without using fast opening switches, although their use is very important in some cases.

Among the three types of disk EMGs, the one with disk modules of 400 mm diameter are most widely used. This is due to its modest dimensions, high specific characteristics and comparatively low cost. Several dozens of experiments have been performed with this EMG using between 5 to 25 disks. This EMG was used in the first joint VNIIEF/LANL experiment successfully performed at Sarov in 1993. A 1m diameter disk EMG has also been repeatedly and successfully tested.

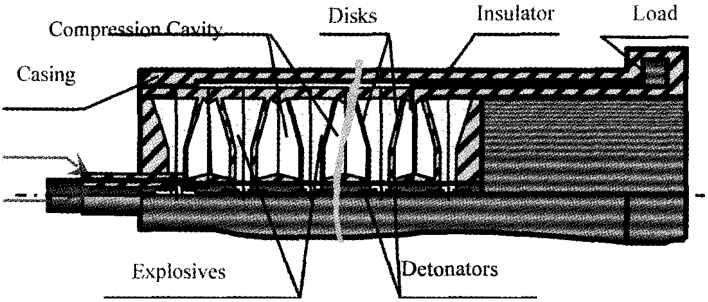

Figure 3. High-power quick-operating "POTOK" family disk generator.

Table 2. Characteristics of "POTOK" family Disk EMGs

EMG type	P1	P2	P3
Disks diameter, mm	250	400	1000
Load, nH	10	10 15	25
Energy amplification coefficient	10 15	10 15	10 15
Magnetic field specific energy, J/cm^3	250	300	250
Output energy, MJ	25	50 90	200
Current amplitude, MA	60	100	300
Characteristic time, μs	2 4	4 5	10 12

8 Implosion of 1.5 Kg Condensed Liner with 100 MA Current Pulse

One might hope for the creation of a stationary superpower facility in 10 or 20 years capable of accelerating 1 kg solid liners carrying a 100 MA current pulse, by transmitting 20 MJ or more energy to the liners. However, the technology of quick-operating superpower

"POTOK" family helical and disk EMGs, developed at the Electrophysical Department of VNIIEF, accomplished this 10 years ago. The experiments were performed in 1988 [19].

To demonstrate this technology potental, a joint VNIIEF/LANL experiment at Sarov, aimed at liner acceleration, was planned two years ago. The initial mass of the accelerated part would be more than 1600 grams, the current pulse no less that 100 MA [20]. Fig. 4 shows the schematic of the device. The current pulse shape from that experiment is shown in Fig. 5.

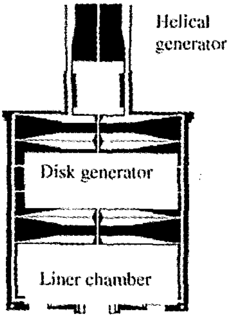

Figure 4. Experimental device schematic.

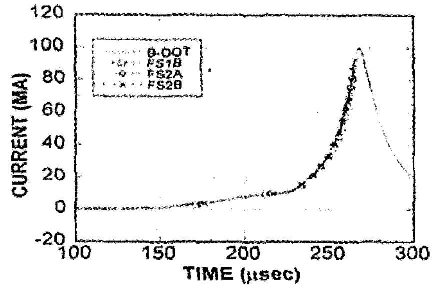

Figure 5. Current through the liner pulse shape.

Solid, high-velocity liners can be applied to:

1. Generate superhigh pressures of tens of megabars
2. Generate superhigh magnetic fields of 50 MG and more
3. Magnetize plasma compression until thermonuclear ignition is achieved

Magnetic compression of the preliminary heated magnetized plasma is the shortest and the most economical way to achieve ignition

9 MAGO Position

Two principle ways to achieve thermonuclear ignition have already become classical: magnetic confinement and inertial confinement.

The drawbacks of magnetic confinement are the "cyclopean" dimensions of the facility, high cost and long construction time. The drawbacks of inertial fusion are a very high ratio of the target compression, difficulty in achieving the required compression symmetry and high cost. The drawbacks of magnetic compression (MAGO) are its novelty and singularity.

The advantages of MAGO are:

1. Pre-heating and magnetizing the plasma considerably simplify the gas compression ratio requirements (compared to ICF, the requirements are 10 times lower) and ensure necessary symmetry (the requirements become 100 times lower).
2. Bulky and high-cost facilities are unnecessary. Ignition becomes possible with the help of the existing superpowered EMGs.

3. The cost can be reduced significantly and the ignition occurs much faster.

10 Principle Tenets of MAGO

Superhigh magnetic fields formed by explosive magnetic generators are used to:

- Pre-heat (up to several hundred electron-volts) DT-gas (plasma)
- provide the required thermal insulation of the fuel
- confine the charged reaction products within the chamber volume.

Subsequent adiabatic compression of the volume occurs with a pre-heated DT-gas by the chamber wall, set in motion by a quick-increasing magnetic field from a superpower EMG having 100-500 MJ of energy storage.

The proposed solution of a controlled thermonuclear fusion problem based on thermonuclear target compression by magnetic field, i.e MAGO in Russian, was first presented in 1976 in a very detailed report by Yu. B. Khariton, V. N. Mokhov, V. K. Chernyshev and others at one of the sessions of the USSR Academy of Sciences [18]. A short version was published in 1979 in the Reports of the Academy of Sciences (DAN) [26].

The MAGO chamber schematic is presented in Fig. 6.

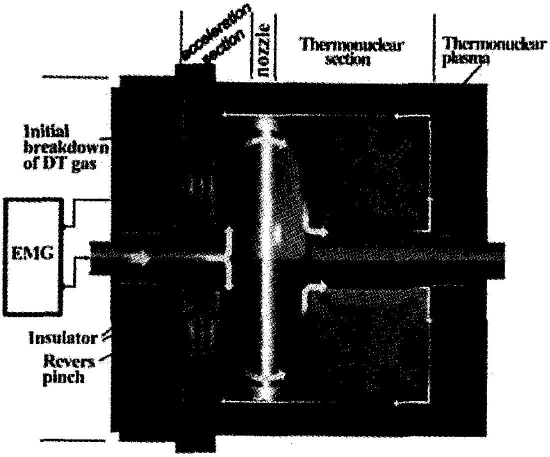

Figure 6. MAGO Chamber Schematic

Table 3 describes the parameters of the required energy sources and the sequence and conditions of operations.

Table 3

Sequence of operations	Conditions
1. Introduction into DT-gas of magnetic field generated by a source with energy storage	0.1-0.2 MOe 1...2 MJ
2. *Ionization and supermagnetosonic flow of ionized gas through the annular nozzle by introduction of electromagnetic energy from a quick-operating source with energy storage*	10...20 MJ
3. Plasma preheating in a shock wave at the nozzle exit up to temperature	0.2...0.5 keV
4. Additional adiabatic compression of preheated magnetized plasma (with a lifetime of microseconds) by a semispherical (or cylindrical) pusher accelerated by a quick-increasing magnetic field generated by a high-power EMG with energy storage	100...500 MJ

VNIIEF specialists succeeded in photographing a hot zone in self-neutrons (Fig. 7) with a pinhole camera. They have also achieved good repeatability of the results. The following plasma parameters were obtained:

Current, generating magnetic field in the chamber	2 MA
Main current pulse with the amplitude of	7 MA
Main current risetime	1.5-2.0 μs
Number of thermonuclear reactions	5 x 10^{13}
Neutron radiation duration	2 μs
Electron temperature	0.2-0.5 keV

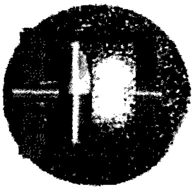

Fig. 7 Camera image.

Conclusion

New types of powerful, fast operating explosive magnetic generators for different thermonuclear and physical applications were invented and then widely successfully used in a large number of experiments. They allowed handling of multi-megampere (up to several hundreds of MA) current sources and made it possible to study many interesting physical phenomena in such fields as high energy density, plasma physics and liner implosions, among others.

References

1. Sakharov, A. D., Ludayev, R. Z., Smirnov, E. N., et al., *Magnitnaya kumulatsia*. DAN USSR **196** No. 1 (1965) pp. 65-68.
2. Sakharov, A. D. Vzryvomagnitnie generatory. *U.F.N.* **88** No. 4 (1966) p. 725.
3. Sakharov, A. D. *Vospominaniya*, **1** (Prava cheloveka, Moscow, 1996).
4. Terletskii, Ya. P., Poluchenie sverkhsilnykh magnitnykh polei putem bystrogo szhatiya provodiashchikh obolochek. In ZhETF, **32** No.2 (1957).
5. Fowler, C. H., Garn, W. B., Caird, R. S., Production of very high magnetic fields by implosion. *J. Appl. Phys.* **31** No. 3 (1960) pp. 588-592.

6. Shearer, J. W., Abraham, F. F., Alpin, C. M. et al., Explosive- Driven Magnetic- Field Compression Generators. *J. Appl. Phys.* **39** No. 4 (1968) pp. 2102-2116.
7. Knoepfel, H., Sverkhsilnie magnitnie polya. Moscow, *Mir* (1972) p. 221.
8. Chernyshev, V. K., Zhariniov, E. I., Kazakov, S. A., et al., Magnetic Flux Cutoffs in Helical Explosive Magnetic Generators. In *Proceedings of the fourth International Conference on Megagauss Magnetic Field Generation and Related Topics*, pp. 455-469.
9. Ultrahigh Magnetic Fields. Physics. Techniques. Applications. *Proceedings of the Third International Conference on Megagauss Magnetic Field Generation and Related Topics.* Novosibirsk, June 13-17, 1983, Ed. by V. M. Titov, G. A. Shvetsov (Moscow, Nauka, 1984).
10. Demidov, V. A., Zharinov, E. I, Kazakov, S. A., Chernyshev, V. K., Visokoinduktivnie vzryvomagnitnie generatory s bol'shim koeffitsientom usileniya energii. *PMTF*, No. 6, (1981) pp.106-111.
11. Chernyshev, V. K., Zhariniov, E. I., Kazakov, S. A., et al., I.,Magnetic Flux Cutoffs in Helical Explosive Magnetic Generators. In *Proceedings of the fourth International Conference on Megagauss Magnetic Field Generation and Related Topics*, pp. 455-469.
12. Megagauss Physics and Technology. *Proceedings of the Second International Conference on Megagauss Magnetic Field Generation and Related Topics*, Washington, D.C., May 30-June 1, 1979, Ed. by P. J. Turchi (Plenum Press, New York and London).
13. Megagauss Technology and Pulsed Power Applications. *Proceedings of the Fourth International Conference on Megagauss Magnetic Field Generation and Related Topics*, Santa Fe, July 14-17, 1986, ed. by C. M. Fowler, R. S. Caird, D. J. Erickson (Plenum Press, New York and London).
14. Megagauss Fields and Pulsed Power Systems. *Proceedings of the Fifth International Conference on Megagauss Magnetic Field Generation and Related Topics*, Novosibirsk, July 3-7, 1989, ed. by V. M. Titov and G. A. Shvetsov (Nova Science Publishers).
15. Megagauss Magnetic Field Generation and Pulsed Power applications. *Proceedings of the 6th International Conference on Megagauss Magnetic Field Generation and Pulsed Power Applications*, New York. Ed. by M. Cowan and R. B. Spielman (Nova Science Publishers).
16. Digest of Technical Papers of the Ninth IEEE International Pulsed Power Conference. Albuquerque, New Mexico, June 21-23, 1993, ed. by K. R. Prestwich and W. L. Baker (Institute of Electrical and Electronics Engineers).
17. Digest of Technical Papers of the Tenth IEEE International Pulsed Power Conference. Albuquerque, New Mexico, 1995, ed. by W. Baker and G. Cooperstein.
18. Khariton, Yu. B., Mokhov, V. N., Chernyshev, V. K., Yakubov, V. B., O rabote termoyadernykh mishenei s magnitnym obzhatiem. *U.F.N.,* **120** (1976) p. 706.
19. Chernyshev, V. K., Mokhov, V. N., Protasov, M. S., et al., Investigation of Liner Ponderomotor Units, Used as Drivers on Magnetic Implosion System. In: *Proc. VIII IEEE International Pulsed Power Conference.* San Diego, 1991, ed. by R. While and K. Prestiwich (Institute of Electrical and Electronics Engineering, New York, 1991) pp. 438-456.
20. Reinovsky, R. E., Anderson, B. G., Clark, D. A., et al., HEL-1: a DEMG Based Demonstration of Solid Liner Implosion at 100 MA., *11th IEEE International Pulsed Power Conference*, Baltimore, Maryland, 1997.
21. Chernyshev, V. K., Protasov, M. S., Shevtsov, V. A., Pervye diskovye vzrivomagnitnye generatory. Protasov, M. S., Arkhipov, B. V., Petrukhin, A. A., Prokopov, V. A., Chernyshev, V.K., Shvetsov, V. A., Bystrokhodnyi diskovyi vzryvomagnitnyi generator. Sverkhsylnye magnitnye polya., Fizika. Tekhnika. Primenenie. Trudy 3 Mezhdunarodnoi konferentsii. Moscow, Nauka (1983) p. 23,26.
22. Chernyshev V. K., Mohov, V. N., On the progress in the creation of powerful explosive magnetic energy Sources for thermonuclear target implosion. *Proceedings of 8th Pulsed Power Conf.,* San Diego (1991) p. 395.

23. Chernyshev, V. K., Protasov, M. S., Shvetsov, V. A., et al., Explosive magnetic generators of "Potok" family. *Proceedings of 8th Pulsed Power Conf.*, San Diego (1991) p. 419.
24. Chernyshev, V. K., Grinevich, B. E., Vakhrushev, V.V., Mamyshev, V. I., Scaling Image of 90 MJ Explosive Magnetic Generators. In *Proceedings of Fifth International Conference on Megagauss Magnetic Field Generation and Related Topics*, p. 347.
25. Chernyshev, V. K., Demidov, V. A., Kazakov, S. A., et al., Multielement Disk EMG powering, Using High-Inductive Helical Generators. In: Megagauss Magnetic Generation and Pulsed Power Applications, Ed. by M. Cowan and R. B. Spielman. (Part I., Nova Science Publishers, Inc., N.Y., 1994) pp. 519-524.
26. Mokhov, V. N., Chernyshev, V. K., Yakubov, V. B., et al., O vozmozhnosti resheniya problemy upravlyaemogo termoyadernogo sinteza na osnove magnitogazodynamicheskoi kumulatsii energii. DAN USSR, **247** No. 1, (1979).
27. Buyko, A. M., Volkov, G. I., Garanin, S. F. et al., Issledovanie vozmozhnosti polucheniya termoyadernoi zamagnichennoi plasmy v sisteme s magnitnym obzhatiem - MAGO. 3 Zababakhinskie nauchnye chteniya, January 1992 , Kyshtym, Russia.
28. A.Buyko,, G.Volkov,, S.Garanin,, et al., Investigation of Possibility of Thermonuclear Magnetized Plasma in the System with Magnetic Implosion-MAGO. *Proceedings of the 9th International Pulsed Power Conference*, Albuquerque (1993).
29. Shearer, J. W., Abraham, F. F., Alpin, C. M., et al., Explosive-Driven Magnetic Field Compression Generators. *Journal of Applied Physics*, **39** No. 4 (1968) pp. 2102-2116.
30. Filippov, N. V., Obzor eksperimental'nykh rabot vypolnennykh v IAE im. Kurchatova I.V., po issledovaniyu plasmennogo focusa. *Fizika plasmy*, **9** No. 1 (1983) pp. 25-44.
31. Ware, K. D., Williams, A. H., Clark, R. W., Operation of a 720 kJ, 60 kV, Dense Plasma Focus. *Bull. Amer. Phys. Soc.*, **18** No. 10 (1973) p. 1363.
32. Haines, M. G., Dense Plasma in Z-pinches and the Plasma Focus. *Phil. Trans. Roy. Soc. Lond. A300* (1981) pp. 649-663.
33. Gribkov, V. A., Filippov, N. V., Istoriya razvitiya i poslednie dostizheniya v issledovaniyakh po plsmennomu focusu. Preprint *FIAN* No. 94, Moscow (1979) p. 49.
34. Getes, D. C., Demeter, L. I., Production of 14 MeV Neutrons with a 500 kJ Coaxial Plasma Gun. *Bull. Amer. Phys. Soc.* **15** No. 11 (1970) p. 1464.
35. Bernard, J., Boussinesq, J., Morin, J. et al., An Explosive Generator - powered plasma focus, *Phys. Lett.* **35 A** No.4 (1971) pp. 288-289.
36. Chernyshev, V. K., Tsukerman, V. A., Gerasimov, V. M., et al., Vliyanie zameny kondensatornogo istochnika energii induktivnym na parametry plasmennogo focusa. *ZhTF* **56** No. 5 (1986).
37. Freeman, B. L., Caird, R. S., Erickson, D. J. et al., Plasma Focus Experiments Powered by Explosive Generators. LA-UR-83-1083.
38. Caird, R. S., Erickson, D. J., Freeman, B. L. et al., Neutron Yields from an Explosive Generator Powered Plasma Focus. *IEEE Int. Conf. on Plasma Science*, (Madison, 1980. Conf. Rec.) pp. 40-41.
39. Freeman, B. L., Caird, R. S., Erickson, D. J. et al., Plasma Focus Experiments Powered by Explosive Generators. *Third Int. Conf. on Megagauss Magnetic Field Generation and Related Topics. Book of Abstracts.* Novosibirsk, (1983) p. 17.
40. Azarkh, Z. M., Makeyev, N. G., Tsukerman, V. A. et al., Primenenie kamer s plasmennym focusom dlya rentgenostrukturnykh issledovanii polikristallicheskykh obraztsov s nanosecundnymy ekspozitsiyami. DAN USSR **232** No. 5 (1977) pp. 1049-1051.
41. Pavlovskii, A. I., Ultrahigh Magnetic Fields Cumulation. *Megagauss Fields and Pulsed Power Systems. MG-V*, ed. by V. M. Titov and G. A. Shvetsov (Nova Science Publishers, New York) pp. 1-13.
42. Degnan, J. H., Baker, W. L., Beason, J. D., et al., Multi-Megajoule Shaped Solid Liner Implosions. Ibid, pp. 623-630.

43. Degnan, J. H., Alme, M. L., Baker, W. L., Buff, J. S. et al., *Megagauss Technology and Pulsed Power Applications. MG-IV*, ed. by C. M. Fowler, R. S. Caird and D. J. Erickson. (Plenum Press. New York and London, 1987) pp. 699-706.
44. Chernyshev, V. K., Zharinov, Ye. I., Kudelkin, I. D., et al., Cylindrical Liner: Implosion Dynamics Under EMG Magnetic Pressure. *Book of abstracts. MG-VI*, Albuquerque, New Mexico (1992) p. 92.
45. Chernyshev, V. K., Zharinov, Ye. I., Mokhov, V. N., et al., Study of Imploding Liner-Electrode Wall Interaction. BEAMs '96. Proceedings **1**, *1st International Conference of High Power Particle Beams* (Prague, Czech Republic June 10-11, 1996) p. 558.
46. Bujko, A. M., Garanin, S. F., Demidov, V. A., et al., Investigation of the Dynamic of a Cylindrical Exploding Liner Accelerated by a Magnetic Field in the Megagauss Range. *Megagauss Fields and Pulsed Power Systems*, Ed. by V. M. Titov and G. A. Shvetsov. MG-V, (Nova Science Publishers) p. 743.
47. Megagauss and Megaampere Pulse Technology and Applications. Ed. by V. K. Chernyshev, V. D. Selemir, L. N. Plyashkevich. *Proceedings of 7th International Conference on Megagauss Magnetic Field Generation and Related Topics,* (Sarov, VNIIEF, 1997).
48. Chernyshev, V. K., Zharinov, E. I., Grinevich, B. E., et al., Uskorenie ploskikh metallicheskikh i dielektricheskikh lainerov magnitnym polem. Zababakhinskie nauchnye chteniya, 14-17 January 1992 (tezisy dokladov), Kyshtym, Dal'nya Dacha.
49. Chernyshev, V. K., Volkov, G. I., Ivanov, et al., Explosive Magnetic Source, Storing 30 MJ of Energy to Power Gaseous Ponderomotor Unit. In *Proceedings of the 6th International Conference on Megagauss Magnetic Field Generation and Pulsed Power Applications*, p. 557.
50. Chernyshev, V. K., Grinevich, B. E., Vakhrushev, V. V., Mamyshev, V. I., Scaling Image of 90 MJ Explosive Magnetic Generators. In *Proceedings of the Fifth International Conference on Megagauss Magnetic Field Generation and Related Topics*, p. 347.

THE DIRAC EXPERIMENTS - RESULTS AND CHALLENGES

R. G. CLARK, J. L. O'BRIEN, A. S. DZURAK, B. E. KANE, N. E. LUMPKIN, D. J. REILLEY, R. P. STARRETT
National Pulsed Magnet Laboratory and Semiconductor Nanofabrication Facility, University of New South Wales, Sydney, Australia

D. G. RICKEL, J. D. GOETTEE, L. J. CAMPBELL, C. M. FOWLER, C. MIELKE, N. HARRISON, W. D. ZERWEKH, D. CLARK, B. D. BARTRAM, J. C. KING, D. PARKIN
Los Alamos National Laboratory, New Mexico, USA

H. NAKAGAWA, N. MIURA
Institute for Solid State Physics, University of Tokyo, Japan

The 1997 international Dirac II Series held at Los Alamos National Laboratory involved low temperature electrical transport and optical experiments in magnetic fields exceeding 800 T, produced by explosive flux compression using Russian MC-1 generators. An overview of the scientific and technical advances achieved in this Series is given, together with a strategy for future work in this challenging experimental environment. A significant outcome was achieved in transport studies of microfabricated thin-film YBCO structures with the magnetic field in the CuO plane. Using a GHz transmission line technique at an ambient temperature of 1.6 K, an onset of dissipation was observed at 150 T (a new upper bound for superconductivity in any material), with a saturation of resistivity at 240 T. Comparison with the Pauli limit expected at B = 155 T in this material suggests that the critical field in this geometry is limited by spin paramagnetism. In preparation for a Dirac III series, a systematic temperature-dependent transport study of YBCO using in-plane magnetic fields of 150 T generated by single-turn coils, at temperatures over the range 10-100 K, has been undertaken in collaboration with the Japanese Megagauss Laboratory. The objective is to map out the phase diagram for this geometry, which is expected to be significantly different than the Werthamer-Helfand-Hohenberg model due to the presence of paramagnetic limiting. Nanofabricated magnetometers have also been developed in a UNSW-LANL collaboration for use in Dirac III for Fermi surface measurements of YBCO in megagauss fields, which are described.

1 Introduction

The Dirac Series of experiments was instituted in 1996 at Los Alamos National Laboratory so that a variety of experimental projects could access fields approaching 1000 T to study new physical phenomena in condensed matter systems. The second Series was undertaken in 1997 and a third Series is planned for 1999, with the overall program including groups from six nations. Central to this has been a US-Russia collaboration in which Russian-developed MC1-class [1] flux-compression generators have been provided for the experiments. The Series has included studies of magneto-optics in magnetic materials [2] and semiconductors [3], quantum limit effects in organic metals [4] and chemical bond strengths in organic materials [5].

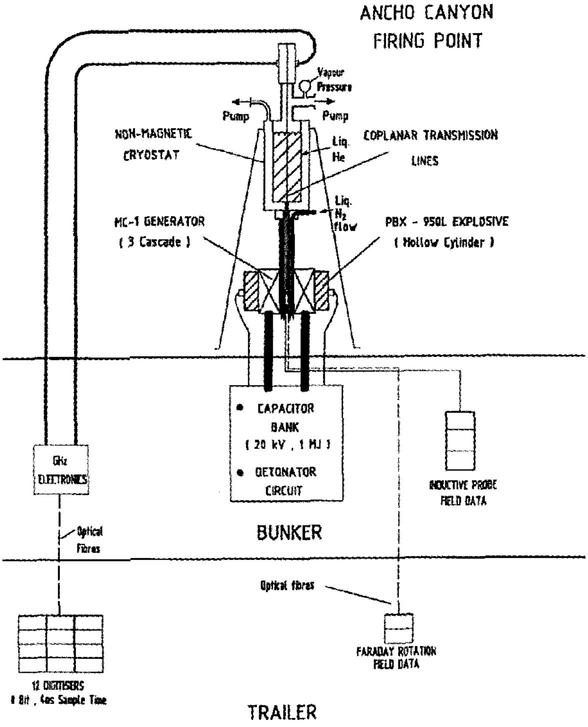

Figure 1. Configuration for implosive flux compression experiments at Los Alamos National Laboratory, USA. The thick lines at top-left represent low-loss cables for the GHz transport measurements.

One of the most ambitious experiments within the Dirac Series has been the attempt to obtain reliable transport data on both semiconductor and high-T_c superconductor materials by an Australia-Japan-US team. The experiments required a number of innovations for the elimination of Faraday pick-up [6]. Measurements during Dirac I [6,7] on semiconductor heterostructures demonstrated the success of the technique, paving the way for a fruitful and detailed investigation of the high-T_c superconductor, $YBa_2Cu_3O_{7-\delta}$ (YBCO) during Dirac II. Here we discuss the measurements on YBCO in detail, which have provided the first evidence of paramagnetic limiting in the high-T_c cuprates [8,9], as well as previewing planned experiments for Dirac III in 1999.

2 Experimental Innovations for μs Transport Measurements

The conditions during an MC1 generator pulse are extreme, with the generator, cryostat and samples all destroyed after the pulse. Fig. 1 shows the experimental arrangement for the low temperature measurements. During the pulse, dB/dt can reach 10^9 T/s, creating voltage up to1 kV in a conducting loop of area 1 mm^2. Minimization of Faraday pick-up was therefore critical and specially designed [6] coplanar transmission lines (CTLs) patterned on a printed circuit board (PCB) substrate were used to achieve this. Eddy current heating of the CTL connections represented a potential problem, since Cu of thickness 9 μm can heat above 10 K during the field pulse [6]. Thermal isolation of the samples was achieved by patterning thin (80 nm) Au CTLs directly onto the samples, bridging a 2 mm gap in the *thick* CTLs on the PCB (see Fig. 2). To avoid the problem of erratic ohmic contacts at large B, a layer of Si_3N_4 dielectric was sandwiched between the YBCO and the metal CTLs [10], to achieve a capacitive coupling to the sample.

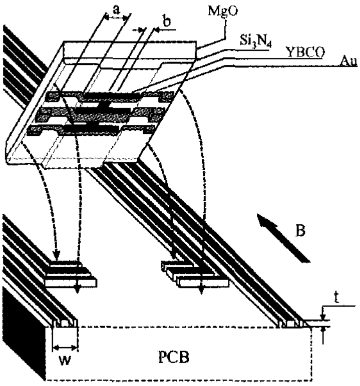

Figure 2. Flip-chip sample mounting. Thin Au transmission lines (80 nm) bridge gaps in the thicker lines on the PCB. Six Au pads (300 nm) provided contacts and the chips were held in place using a heat curable epoxy. Here a = 150 μm, b = 10 μm, t = 9 μm and w = 410 μm.

3 Transport Measurements of YBCO to 300 T

We first discuss results obtained during the Dirac-II Series in 1997, which suggest that critical fields in YBCO for $B \perp c$-axis are determined by paramagnetic limiting. The experimental configuration shown in Fig. 2 probes the in-plane resistivity ρ_{ab} of YBCO through its modulation of the transmission S of GHz radiation. If the sample is superconducting, the inner and outer conductors of the CTL triplet are shorted so that S is zero, except for a small contribution from cross-talk, whereas a perfect insulator has no effect on transmission. Although the sample impedance at 1 GHz is a complex quantity the measurement provides no phase information, so for simplicity, we assume that the impedance corresponds to a scalar resistivity ρ.

Figure 3 shows results for T = 1.6 K, i.e. $T/T_c \sim 0.02$, in an 850 T MC1 field pulse. Only data to 320 T are plotted, since results above this field were obscured by noise, discussed below.

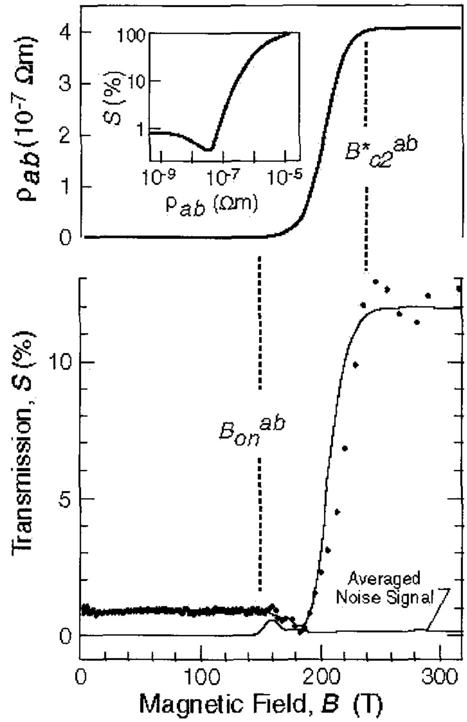

Figure 3. Measured normalised transmission S data (•) for YBCO with $B\perp c$ obtained in an MC1 pulse with $T = 1.6$ K, $\nu = 0.9$ GHz and a power ~1 mW at the sample. The bold line is a fit to this S data. A small averaged noise background (fine line) has been subtracted from the data. The upper curve is the calculated resistivity, assuming the transmission function $S(\rho_{ab})$ shown in the inset. The dip in S at $\rho \sim 5\text{x}10^{-8}$ Ωm is well understood and results from interference between ingoing and reflected signals on the CTLs. Taken from Ref. [8].

We observe the onset of a dissipative ($\rho > 0$) state at $B_{on}^{ab} = (150 \pm 20)$ T and define $B^*{}_{c2}^{ab} = (240 \pm 30)$ T as the field at which S, and therefore ρ, saturates, using an asterix to indicate that the transition may result from paramagnetic limiting. The uncertainties in B reflect the noise-limited accuracy with which we can define inflection points in the S data, together with an estimate of timing accuracy.

To our knowledge $B_{on}^{ab} \sim 150$ T is the largest field in which a superconducting phase has been observed. A broader superconductor-normal (S-N) transition than observed here, spanning 75 T - 340 T, has been observed in previous measurements [11,12], possibly due to the high frequency (94 GHz) used. We also note that the strongest saturation feature present in this data [11,12] is near our critical field of 240 T.

To determine the response in Fig. 3 accurately it was necessary to subtract from the raw data a noise background (as shown). Below 300 T the noise is small and occurred in the interval 150 T - 180 T [8], due to the fusion of metal wires comprising the second of the three generator liners. Above 300 T wire fusion proceeded in the third liner with the noise creating severe problems for transport measurements. To avoid this problem during Dirac III in 1999, one or two of the inner liners will be removed from the MC-1 generators. Thus configured, the generators are still capable of reaching 400 T, which exceeds the critical field in these samples and offers the opportunity of observing any possible reentrant states above $B^*{}_{c2}^{ab}$.

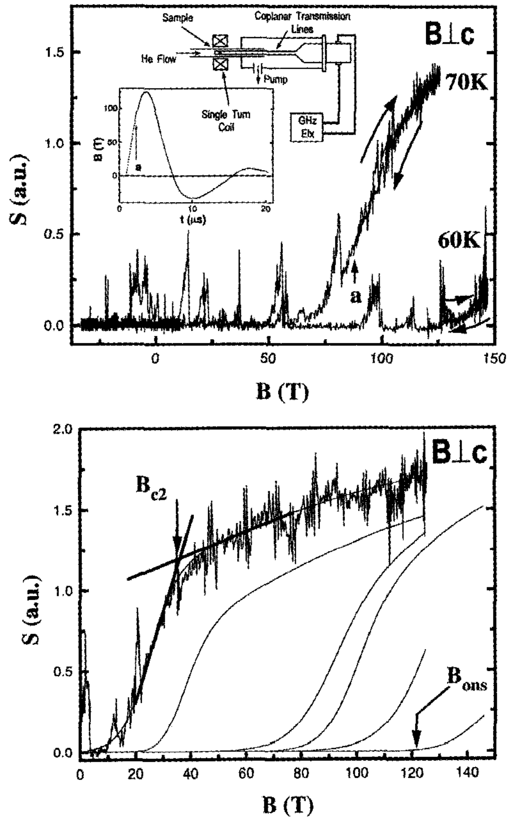

Figure 4. GHz transport data on YBCO obtained in *destructive* single-turn coil pulses to 150 T. (Top) Raw transmission S data at T = 60 K and 70 K. The inset shows the experimental arrangement and the field profile $B(t)$. Data is shown for times after the arrow marked **a** in the inset. (Bottom) Magnetoresponse $S(B)$ at T = 80 K, 77 K, 70 K, 66 K, 65 K and 60 K, in order of increasing B_{ons}. The curves are fits to the data, with the raw data at 80 K shown for comparison. Also shown are the definitions used for B_{c2} and the onset field, B_{ons}.

4 Single Turn Coil Measurements of YBCO to 150 T

For Dirac II and the coming Dirac III Series, complementary measurements have been made at the Japanese Megagauss Laboratory using single-turn coil pulsed field systems [13] to collect systematic data sets and study dynamic effects through an examination of any hysteresis present. For bore sizes ~10 mm these systems produce ~30 T non-destructively, or ~150 T in pulses which destroy the generator but leave the sample unperturbed. The rise time is ~3 μs (see inset to Fig. 4, Top), giving a peak $dB/dt \sim 10^8$ T/s which, while around an order of magnitude smaller than the MC1 generators, provides indicative information about dynamic effects.

Results obtained prior to Dirac II using non-destructive pulses to 30 T showed that dynamic effects on a μs timescale are negligible in YBCO with $B \perp c$ [8]. This conclusion has been reinforced in recent measurements using destructive shots to 150 T [14]. Fig. 4 shows GHz transmission S data obtained at a variety of temperatures below T_c. For these measurements it was possible to tune the frequency so that $S = 0$ when the film was superconducting. Transmission increased monotonically with ρ as B drove the sample into the normal state. The raw data in Fig. 4 show a number of positive-going perturbations to S corresponding to GHz noise, probably associated with RF emissions from the vaporizing coil. The underlying sample response $S(B)$ is clear, however, and has been fitted for a series of temperatures in Fig. 4(Bottom).

As the inset to Fig. 4(Top) shows, the coil generates a damped oscillating B that produces a number of cycles before destruction. The raw data in Fig. 4(Top) show S over this full period except for the first 2 μs, where large electrical noise obscures the data. Note that there is *no measurable hysteresis* in S between B increasing and decreasing throughout the resistive transition. This is significant, since it implies that the S-N transition is a quasi-equilibrium process, even in μs pulses to 150 T. Dynamic effects associated with flux motion or heating caused by the large dB/dt are clearly not as important as one might suspect, providing confidence in interpretation of the data from Dirac flux-compression measurements.

The critical fields B_{c2} and resistive onsets B_{ons} as defined in Fig. 4(Bottom) are plotted for a detailed data set on a single YBCO sample to create a B-T phase diagram (Fig. 5). B_{c2} varies linearly with T up to ~100 T, with a slope close to the often quoted value $dB_{c2}/dT = -10.5$ T/K obtained by Welp *et al.* [15] from magnetization measurements in magnetic fields up to 6 T.

5 Discussion and Strategy for Dirac III

It is clear from our data that the low-T S-N transition for YBCO is very different for the two orientations $B \perp c$ and $B // c$. The phase diagram for $B // c$ (inset to Fig. 5a), from Ref. [16], is in good agreement with the BCS model of Werthamer-Helfand-Hohenberg (WHH) which, neglecting contributions from the Zeeman energy of the electron spins, gives $B^0{}_{c2}(T = 0) = 0.70\, T_c(\partial B_{c2}/\partial T)|_{T_c}$ [17]. Inserting the slope $\alpha = -2.0$ T/K gives $B^0{}_{c2}(T = 0) = 120$ T which

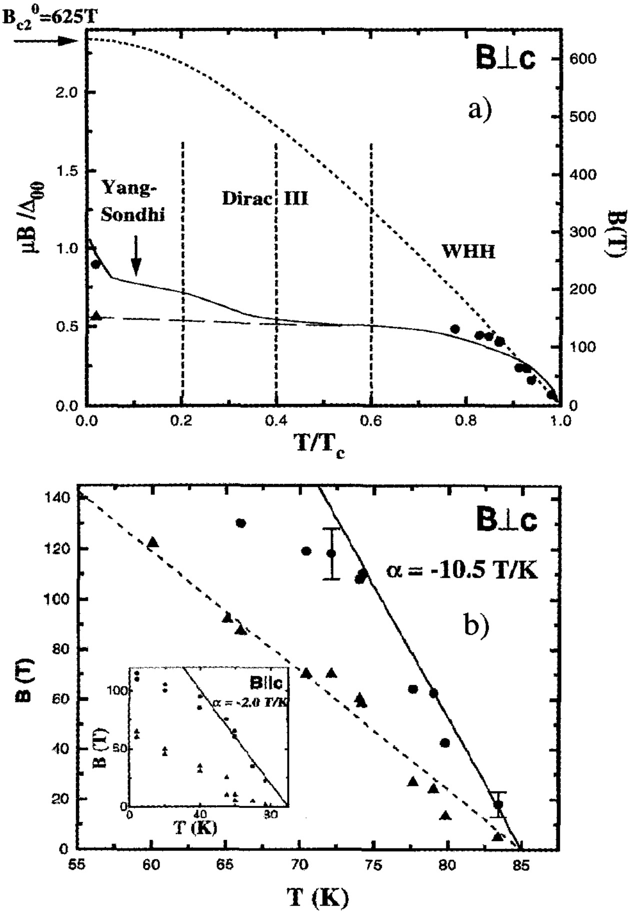

Figure 5. (a) YBCO phase diagram for $B \perp c$ determined from GHz measurements using single-turn coils. The symbols marked ● (▲) represent B_{c2} (B_{ons}) values as defined in Fig. 4(b). The dashed line corresponds to $dB_{c2}/dT = -10.5$ T/K, determined from magnetisation measurements by Welp et al. [15]. Inset: Phase diagram for $B // c$ determined from transport measurements using single-turn coils [taken from Ref. 16]. (b) Full YBCO phase diagram for $B \perp c$. The symbols ● (▲) represent B_{c2} (B_{ons}) values obtained from MC-1 and single-turn coil data in Figs. 3 and 4. The solid line represents B_{c2} calculated for a $d_{x^2-y^2}$ superconductor while the dashed line depicts a first order transition from a BCS state to a Fulde-Ferrell state [taken from Ref. 20]. The dotted function is the WHH prediction assuming no spin paramagnetism. The vertical lines show planned temperatures for MC-1 shots during Dirac III.

is consistent with that observed experimentally. Using the same model for $B\perp c$, however, predicts $B^0_{c2}(T = 0) = 625$ T which is almost a factor of three greater than the measured value (see Fig. 5b). One explanation is that a misalignment of B could probe properties in the ***a-b*** planes, which would reduce the observed B_{c2}. This effect can be dramatic for highly anisotropic materials such as organic superconductors [18] but should be small for YBCO that has much smaller anisotropy. A more probable explanation is that for $B\perp c$ the Zeeman energy associated with maintaining the singlet state exceeds the superconductor energy gap well before B^0_{c2} is reached. The field B_p at which this occurs is referred to as the paramagnetic (or Clogston) limit which, from BCS theory, is given by $B_p = \gamma T_c$ with $\gamma = 1.84$ T/K [19]. For our samples we have $B_p \sim 155$ T, which is above B^0_{c2} for $B//c$ but well below it for $B\perp c$. Our data may therefore represent the first observation of paramagnetic limiting for a cuprate superconductor, providing additional experimental information relevant to current models of high-T_c superconductivity. Recent interpretations in terms of a $d_{x^2-y^2}$ state have motivated a number of new models. The phase diagram predicted by one model [20], which considers the coupling of B only to the spins of the electrons, is plotted in Fig. 5(b). The agreement with our low-T data is remarkably good. In this model a first order phase transition (dashed line) occurs for $T/T_c < 0.5$ between a zero momentum pairing state at low B and a finite momentum, or Fulde-Ferrel (FF), state at higher B. We note that our low-T B_{ons} coincides with this transition, although ρ would be expected to remain at zero throughout the FF phase. Our data provide a useful preliminary picture of the YBCO phase diagram with strong paramagnetic effects and the primary aim for Dirac III is to complete this diagram, with shots at several temperatures as shown in Fig. 5(b).

6 Development of de Haas-van Alphen Coils for Dirac III

For the 1999 Dirac III series it is also planned to extend a previous measurement of the de Haas-van Alphen (dHvA) effect and Fermi surface of YBCO in a 100 T flux compression system [21] to higher magnetic fields. To achieve this aim, it is necessary to develop sensitive, perfectly compensated dHvA coils using electron beam lithography, for use with small samples, which can be connected to the coplanar transmission line geometry that minimizes dB/dt pickup in the MC-1 generator environment.

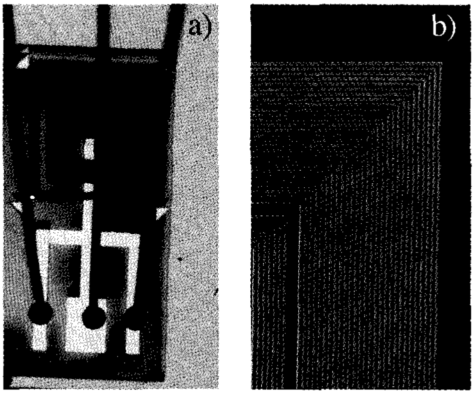

Figure 6. dHvA coil magnetometers used in pulsed fields and fabricated at UNSW. a) Optical micrograph showing full device with bond wires attached. The outermost coil is 450 μm on a side. (b) SEM image showing the individual windings of the coil, fabricated by electron-beam lithography. This coil has 250 nm metal wires with 250 nm spacing.

As a first step in this direction, dHvA coils of this design have been fabricated for tests in ms pulsed fields (see Fig. 6). The coil geometry and data taken for a LaB_6 single crystal test sample in a 50 T pulse at 4 K are shown in Fig. 7. For the orientation of this crystal, the three branches of the α frequency (α_1, α_2, α_3) [22,23] are clearly observed at 4 K (together with the second harmonic $2\alpha_3$) on a small sample with a coil comprised of only 46 inner and 16 outer windings of 0.5 μm width and 1.5 μm spacing, using a preamplifier gain of only 5000.

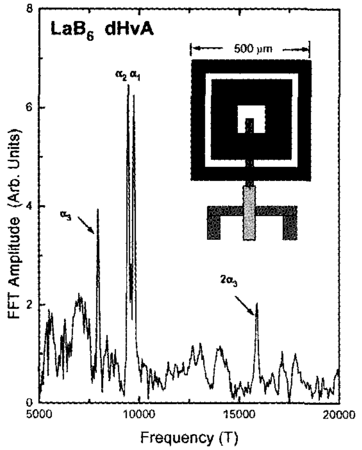

Figure 7. Fourier transform of the dHvA signal measured in LaB_6 at 4 K on the falling magnetic field, analyzed over the range 30-50 T in a ms pulse. The single crystal sample with linear dimensions ~200 μm was orientated with the [001] axis at an angle of ~15° to the pulsed field (towards [101]). The inset shows the nanofabricated dHvA coil geometry. Compensated coils with both 0.5 μm and 0.25 μm wide gold lines on a GaAs substrate have been developed, comprised of 46 (181) inner turns and 16 (60) counterwound outer turns, respectively. The coils are designed for connection to coplanar transmission lines developed for the Dirac Series transport measurements.

A number of technical difficulties remain to be solved for the more stringent environment of the MC-1 shots, associated with details of the connection of the magnetometer coil to the CTLs and screening of the CTLs for dHvA measurements. The ms pulsed field test results are nevertheless encouraging and highlight the importance of nanofabrication technology to advances in megagauss magnetic field measurements.

7 Conclusions

The Dirac Series has motivated significant innovations for electrical transport measurements in megagauss magnetic fields, allowing a detailed study of the phase diagram of $YBa_2Cu_3O_{7-\delta}$. Our data suggests that with B directed along the CuO planes, paramagnetic limiting determines the upper critical field, the first evidence of this effect in an optimally doped high-T_c material. Additional developments in nanofabricated dHvA coils provide an opportunity to study the Fermi surface of this important cuprate superconductor above 100 T.

References

1. Pavlovskii, A.I., et al., in *Megagauss Physics and Technology*, Ed by P.J. Turchi, Plenum, New York, (1980) p. 627.
2. O.M. Tatsenko, et al., *Physica B* **246-247**, (1998) p. 315; and these proceedings.
3. Brooks, J. S., et al., *Physica B* **246-247**, p. 50 (1998); and these proceedings.
4. Brooks, J. S., et al., Los Alamos Preprint Report LA-UR 96-3472; J. S. Brooks, J. S. et al., *Proc. Megagauss VII,* Sarov - Russia, (1996).
5. Maverick, A. S., Butler, L. G., *Int. J. Quant. Chem.* **64**, (1997) p. 607.
6. Kane, B. E., et al., *Rev. Sci. Instr.* **68**, (1997) p. 3843.
7. Kane, B.E., et al., *Proc. Megagauss VII,* Sarov - Russia, 1996.
8. Dzurak, A. S. et al., *Phys. Rev. B* **57**, R14084 (1998).
9. Dzurak, A. S., et al., *Physica B* **246-247**, (1998) p. 40.
10. For fabrication details see: Lumpkin, N. E., et al., *Physica B* **246-247**, (1998) p. 395.
11. Goettee, J. D., et al., *Physica C* **235-240**, (1994) p. 2090.
12. Bykov, A. I., et al., *Physica B* **211**, (1995) p. 248.
13. Nakao, K., et al., *J. Phys. E* **18**, (1985) p. 1018.
14. O'Brien, J. L. et al., to be published.
15. Welp, U., et al., *Phys. Rev. Lett.* **62**, (1989) p. 1908.
16. Nakagawa, H., et al., *Physica B* **246-247**, (1998) p. 429.
17. Werthamer, N. R., Helfand, E., Hohenberg, P. C. *Phys. Rev.* **147**, (1966) p. 295.
18. Wanka, S., et al., *Phys. Rev. B* **53**, (1996) p. 9301.
19. Clogston, A. M., *Phys. Rev. Lett.* **9**, (1962) p. 266.
20. Kun Yang and Sondhi, S. L., cond-mat/9706148 **2** (1998).
21. Fowler, C. M., et al., *Phys. Rev. Lett.* **68**, (1992) p. 534; and Comment by Springford, M., Meeson, P., Probst, P-A., *Phys. Rev. Lett.* **69**, (1992) p. 2453.
22. Ishizawa, Y., et al., *J. Phys. Soc. Jap.* **42**, (1997) p. 112.
23. Harrison, N., et al., *Phys. Rev. Lett.* **80**, (1998) p. 4498.

EXPLOSIVE FLUX COMPRESSION: 50 YEARS OF LOS ALAMOS ACTIVITIES

C. FOWLER, D. THOMSON, W. GARN
Los Alamos National Laboratory, Los Alamos, NM, USA

Los Alamos flux compression activities are surveyed, mainly through references in view of space limitations. However, two plasma physics programs done with Sandia National Laboratory are discussed in more detail.

1 Introduction

In this section, we briefly outline major Los Alamos (LANL) flux compression activities. More detailed discussions are given of two programs done with Sandia National Laboratories, (SNL) intermittently from 1966 to 1973. Use of flux compression generators (FCGs) to power θ-pinches is discussed below. The "Birdseed" program, in which 150-200 kJ of neon plasma was injected into the ionosphere, is discussed later in this paper, together with plans for a more energetic system. The first open description of the Los Alamos objectives was published in [1], which featured the use of high magnetic fields made at Los Alamos to compress D-T plasmas to make large neutron bursts, for solid-state investigations, and to accelerate matter. These are all topics that remain relevant today. Later, unclassified Los Alamos activities were surveyed at the first Megagauss Conference (1965), [2]. The next Megagauss Conference took place in 1979 [3]. Other activities between these conferences included high field solid-state and isentropic compression experiments. Component development included construction of megavolt transformers and FCG improvements, as with the plate generator. FCG uses as power supplies for railguns, the plasma focus, laser generation, e-beam machines and soft X-ray generators are described in later Megagauss Conference Proceedings, as is the development of high current opening switches. A collaborative flux compression program with Los Alamos and Russian scientists from Arzamas-16 began in 1993, and included Magnetized Target Fusion and high field experiments [4], also reported at MG VII. Little of our solid-state work has appeared in the Megagauss Proceedings. However, surveys appear in [5,6,7]. More recent work has been done in the "Dirac" shot series where scientists from the USA and several other countries have collaborated on high field experiments using Russian MC-1 high field generators and Los Alamos strip generators. Various aspects of this program are treated at this conference and at the preceding MG VII Conference.

2 Explosive-Driven Θ-Pinch Experiments

2.1 Θ-Pinch Liner Implosion Experiments

Early experiments [2a,c, 8] at Los Alamos to apply explosively driven flux compression (MG fields) to high temperature plasmas were exploratory, and involved creating a fast theta pinch inside a thin, implodable cylindrical θ-coil. Parameters were chosen to achieve MG fields with systems then available at Los Alamos, and used early θ-pinch data (Scylla I, Scylla III) [9,10]. Implosion of the plasma/magnetic system was started using high T high β plasma confined by the axial magnetic field.

In these experiments, a good diagnostic neutron signal verified that the initial plasma was in place as expected, and gave a measure of the plasma behavior *vs* time during the explosive driven phase. Fundamental problems existed. Plasma confinement in the short coil (~25 cm) θ-pinches available for the firing point was limited to 2-3 μsec due to end-loss, flute instabilities [8,10,11] and to field asymmetries [2c]. In 1966, a new θ-pinch (Scyllacita) with a faster capacitor bank was used to create the initial plasma [8]. A new side-fed coil implosion system eliminated field asymmetries. Since the basic plasma confinement time limitation with the short θ-coil (~3 μs) remained, as did the quenching effect of the imploding discharge tube, we did not pursue this approach beyond one Scyllacita shot at the firing site. However, the goal of achieving fusion with MG fields in imploding liners remains valid today. We suggest developing a technique, such as an FRC [12], to inject an initial, high-beta plasma axially into a clean, resistive liner implosion system at the proper time [2c] for explosive compression to 4 MG or greater. For good confinement, the implosion system length should be increased to one half meter or more. Parameter studies of FRC transport and injection characteristics at high densities ($>10^{17}/\text{cm}^3$) would be needed to fully explore the feasibility of this approach, since only plasmas of substantially lower densities have been so transported to date.

2.2 *The Explosive Generator Powered θ-Pinch*

In 1967, Los Alamos and Sandia Laboratories collaborated in a series of generator powered θ-pinch experiments using Sandia generators [13-16]. Two sizes of helical generators were used: the Model 106 generator (5# of PBX 9404 explosive) and the larger Model 169 (17# of PBX 9404 explosive). Exploding wire fuses were used to sharpen the pulses to drive the θ-pinch coils. The θ-coils were switched in when the voltage across the fuses reached preselected voltages. The initial plasma was created by first putting a few kG bias field B_z in the coil, then passing a linear z-current through the deuterium to preionize it, and finally applying the main drive field to heat and compress the plasma.

Nine shots were fired, five with the Model 106 generator and four with the Model 169. Table I of [16] lists conditions for each shot. The pre-ionized plasma was created inside a 2 mm wall Pyrex or quartz discharge tube with a 40 kA linear current discharge (from a 7.5 μF, 15 kV bank), which was shorted out after a half-cycle to eliminate axial current before switching in the generator.

Discharge tube conditioning for each shot involved warm-up θ-pinch shots with an auxiliary capacitor bank [14-16]. The generator-powered θ-pinch shot was then fired, complete with preionization, bias field and diagnostics, within 30-60 minutes of the last warm-up shot. Results of the nine generator driven pinch shots are also given in Table I [16]. Time resolved neutron yields, measuring plasma behavior, have been reported [14-17]. The shot series demonstrated the importance of reverse bias field, tube conditioning, preionization, and particularly the initial voltage, V_θ, applied to the preionized plasma. Good diagnostic neutron yields were obtained on 7 of the 9 shots. Results for shots 8 and 9 are shown in Fig. 1, which gives the time history of the applied magnetic field (B_z) and the resulting neutron yield rate for each shot. The highest neutron yield ($1.4\text{x}10^8$) occurred when all drive parameters were optimized. The maximum neutron yield rate per unit coil length was comparable to or better than those for laboratory theta pinches worldwide [18]. In 1968, the Frascati group conducted five generator-driven θ-pinch shots with at least one neutron yield ($5x10^7$) [19], supporting our demonstration of the feasibility [14,15,16] of generator-driven θ-pinches.

2.3 *Predictions With A θ-Pinch Scaling Model*

A θ-pinch scaling model was developed [20] using a simple computer code and used to calculate plasma radius, temperature, density, neutron yields and radiation rates for a large variety of short-coil (~25 cm) Los Alamos θ-pinches (1963-1978). The one-dimensional model assumes that V_θ drive voltage, reverse field cancellation, and adiabatic compression may be separated. End-losses are neglected for 2 μs. A $\beta = 1$ plasma and perfect conductivity are assumed during compression. The code assumes adiabatic compression ($T \sim B^{4/5}$) and used a radiation loss rate $\sim n_e n_i T_e^{1/2}$ during the compression phase. The code contained a single scaling constant, K, which successfully correlated results from Scylla III, Scyllacita and Scylla IA and then the results of the 1967 explosive generator shot series.

In the 1970s, a dedicated theta pinch, Scyllar, was used at Los Alamos to study plasma radiation, opacities, and atomic properties in high temperature plasmas [21,22]. The code [20] was used to compare Scyllar results at higher densities ($>10^{17}$/ec) than used previously ($\sim 10^{16}$/cc). Comparisons with experiment were generally good [20].

In the mid 1970s, high-current plate generators were developed extensively at Los Alamos [17,23]. These generators are fast and can generate multi- MA currents at terawatt levels. Using a typical plate generator performance [17], a calculated [20] field vs. time dependence for a θ-coil (25.4 cm long, 7.6 cm i.d.) is shown in Fig. 2. V_θ is about 50 kV, and B_z rises from 0 to 900 kG in 2 μs. With a 50 mT D_2 fill, the code predicts a fusion (10 keV) neutron yield of $\sim 3x10^{11}$ which could be increased to $\sim 3x10^{15}$ by using a DT mixture and extending the coil length to one meter. With a fill of 1.0 torr D_2, seeded with a high Z species, a final temperature is predicted of 1.0 keV (Fig.2) at a density of $10^{19}/cm^3$. If seeded with selected high-Z elements, as with Scyllar [21,22], these plasmas would allow studies of atomic processes and opacities at temperatures and densities much higher than those obtained in the laboratory, making possible unique regimes for accurate comparison of spectral observations with theory.

3 The Birdseed Program

The initial goal of the Birdseed Program was to inject neon plasma into the ionosphere to study its interaction with ionospheric matter and magnetic fields. It was hoped that at least 100 kJ of plasma could be injected, with average directed velocity of 100 km/s or greater. Program planning began in 1967. A Marshall plasma gun would produce the plasma [24] and the system would be launched in a Sandia Laboratory STRYPI rocket. The gun would be fired when the rocket reached the ionosphere (approximately 220-240 km altitude). The STRYPI payload was of order 500 kg. of which somewhat more than 200 kg were available for the power supply. An FCG system was selected to power the plasma gun to meet weight and volume restrictions. All system components were designed to be compatible with the

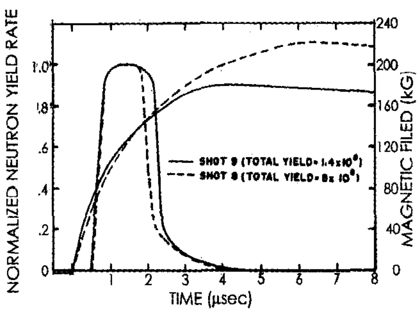

Figure 1. Magnetic field and relative neutron yield rate vs. time for two Θ-pinch shots using Model 169 generator.

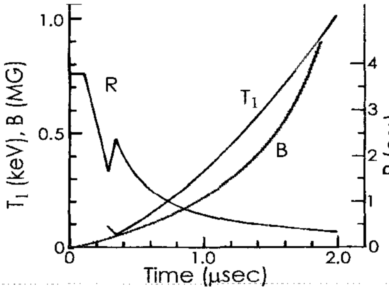

Figure 2. B vs. time in θ-coil (L=25 cm, i.d.=7.6 cm) calculated from plate generator data. Plasma temperature and radius vs. t are predicted from scaling code. D_2 fill is 1.0 torr; bias field is 2 kG.

planned payload layout and to meet the STRYPI acceleration demands. Figure 3 shows the placement of the major components. These consisted of a capacitor bank, the initial energy source; a Mark V booster generator; the Model 169 output generator; a ballast load and the plasma gun. Components would be switched into the system with detonator closing switches. Neon gas was first injected into the plasma gun from a storage plenum through a detonator-actuated valve. The capacitor bank (~15 kJ, charged mainly during flight by a battery powered DC-DC converter) was then fired to energize the Mark V generator (~400 μH), which delivered 60 to 75 kJ to the Model 169 generator. This generator was then fired, first into the ballast load B, and subsequently into the plasma gun. Tests at the Los Alamos Firing Site showed that this system delivered 300-350 kJ to the gun with about 60 % of the energy going into the directed plasma. Diagnostics showed that, for a typical shot, plasma velocities varied from 50 to 250 km/s, with mean velocities of 90-110 km/s. The program culminated in three successful shots at the Barking Sands Facility in Kauai, Hawaii, two in 1970 (Birdseed I), the third in 1971 (Birdseed II). A summary of the generator-gun development program through Birdseed I can be found in [25], while discussions of the diagnostics employed are available in [26,27]. The system engineering development is treated in [28], and a general description of the STRYPI rocket is given in [29].

Planning for Birdseed III began in late 1970. The system was to be launched in a STRYPI rocket, but was to deliver ten times the plasma energy of Birdseed II, thus calling for major changes in the plasma gun and the power supply.

3.1 Plasma Gun

Birdseed plasma spectra showed appreciable contaminants from gun components that did not appear in lower energy laboratory tests. Consequently, a new gun was designed [30], but not tested, which was expected to generate the required plasma and to withstand the substantially larger required currents. The inner electrode diameter was increased from 6.35 to 30 cm, the outer electrode diameter from 15.24 to 50 cm., the length from 100 to 150 cm.

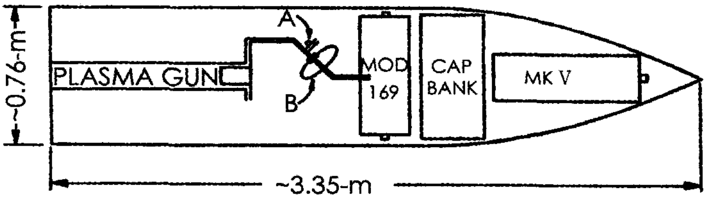

Figure 3. Location of major system components in STRYPI payload. Ballast load B carries all the current until plasma gun is switched into circuit by detonator switch A.

1.2 Power Supply

The power supply, a single, helical generator, was required to deliver a total of about 5 MJ, of which 3.5 MJ would go to the gun. A superconducting coil would supply the initial flux. A full-scale helical generator was built and tested with satisfactory results, as were acceleration test results on the stator. A NbTi superconducting, scaled-down coil was built. Acceleration tests [31] showed that it would withstand the rocket accelerations without going normal. The coil was then tested in an explosive shot, where it supplied the initial flux for a scaled down helical generator with satisfactory result [32]. There was also some concern that the coil might go normal during launch as the system swept by the steel rocket launch structure. Calculation [33] indicated that a few sheets of magnetic shielding around the coil would solve this problem if it indeed existed.

4 Summary

These experiments demonstrated the feasibility of using FCGs to power θ-pinches and plasma guns for physics, fusion and space applications.

Acknowledgment

This work was supported by the US Department of Energy.

Dedication

The authors dedicate this paper to the memory of their colleague and friend, Robert S. (Bob) Caird who passed away on March 27, 1997. Bob was a pioneer in magnetic flux compression, and shared co-authorship with us on the first paper published in the Megagauss Conference series.

References *

1. *Atomic Energy Research in the Life and Physical Sciences.* Available from US Government Printing Office, Washington 25, DC, (1960) p. 104.
2. *Megagauss Magnetic Field Generation by Explosives and Related Experiments*, Ed. by H. Knoepfel, F. Herlach, Euratom, (1966) a: p. 1; b: p. 101; c: p. 491.
3. *Megagauss Physics and Technology*, ed. by P.Turchi, Plenum, NY (1980).
4. Lindemuth, I., Ekdahl, C., Fowler, C., Reinovsky, R., Younger, S., Chernyshev, V., Mokhov, V., Pavlovskii, A., *IEEE Trans. Plasma Sci.*, **25** (6) (1997) pp. 1357-1372.
5. Fowler, C. M., *Science* **180** (1973) p. 261.
6. Fowler, C., Caird, R., Erickson, D., Freeman, B., Garn, W. in *Physics in High Magnetic Fields*, Ed. by S. Chikazumi, N. Muira (Springer-Verlag, New York, 1981) pp. 54-63.
7. Fowler, C., Freeman, B., Brooks, J., Goettee, J., Hults, W., King, J., Mueller, F., Rickel, D., Smith, J., *Physica B* **201** (1994) pp. 33-39.
8. Thomson, D., Caird, R., Ewing, K., Finlayson, V., Fowler, C., Garn, W., Kemp, E., Kewish, R., Sawyer, G., Tuck, J., LANL Report LA-3863-MS (1968), (Scyllacita).
9. Boyer, K., Elmore, W., Little, E., Quinn, W., Tuck, J., *Phys. Rev.*, **119** (1960) (Scylla I) p. 831.
10. Little, E. M., Quinn, W. E. *Phys. Fluids* **6** (1963) (Scylla III) p. 875.
11. Sawyer, G., Finlayson, V., Jahoda, F., Thomas, K., *Phys. Fluids* **10** (1967) Finlayson, V. A., LANL Report, LA-4042 (1968) (Scylla IA) p. 1564.
12. Rej, D., Taggart, D., Baron, M., Chrien, R., Gribble, R., Tuszewski, M., Waganaar, M., Wright, B., *Phys. Fluids B* **4** (7) 1909 (1992); Alikhanov, S., Bakhtin, V., Es'kov, A., Kurtmullaev, R., Semenov, V., Strizhov, E., Kozlov, N., Khvesyuk, V., Yaminskij, V., in *Plasma Phys. and Controlled Nucl. Fus. Research, 1982*, IAEA, Vienna, Vol III, pp. 319-327, (1983); Armstrong, W., Linford, R., Lipson, J., Platts, D., Sherwood, E., *Phys. Fluids.* **24** (1981) p. 2068.
13. Crawford, J. C., Damerow, R. A., *JAP* **39** (1968) p.5224.
14. Thomson, D., Caird, R., Ewing, K., Fowler, C., Garn, W., Crawford, J., Damerow, R., *Proc. of Conf. on Pulsed High Density Plasma*, LANL Report, LA-3770 (1967) Paper H3.
15. Damerow, R., Crawford, J., Fowler, C., Caird, R., Ewing, K., Gam, W., Thomson, D., *SNL Report.* SCRR 69-51 (1969).
16. Damerow, R., Crawford, J., Thomson, D., Caird, R., Ewing, K., Garn, W., Fowler, C., in *Proc. of Symp. on Engin. Problems of Fusion Research*, LANL Report LA-4250 (1969) Dl-8.
17. Fowler, C., Caird, R., Erickson, D., Freeman, B., Thomson, D., Garn W., in *Energy Storage, Compr. and Switching, Vol. 2*, Ed. by V. Nardi, H. Sahlin, W.Bostick, Plenum Press (1983) p. 19.
18. See Table II, Ref [16] and Table I, Ref [15].
19. Hamm, J., Knoepfel, H., Krogler, H., Linhart, J., Verbeek, R., in *Proc. Third Conf. on Plasma Phy. and Controlled Nuclear Fusion Research, Vol. Il*, (IAEA, Vienna, 1969) p. 629.
20. Ewing K.J., Thomson, D.B., LANL Report, LA-9074 MS (1982).
21. Thomson, D., Jones, L., Bailey, A., Engleman, Jr., R., in *Pulsed High Beta Plasmas*, ed. by D. E. Evans (Pergamon Press, New York, 1976).
22. Thomson, D. B., LANL Report, LA-7684-MS (1980).
23. Caird, R., Erickson, D., Garn, W., Fowler, C., *Proc. IEEE Int. Pulsed Power Conf., 1976* (IEEE, N.Y. 1976) Paper III, D-3.

24. Marshall, J., Henins, I. in *Plasma Physics and Controlled Fusion Research*, (IAEA, Vienna, 1966) Vol II, pp. 449-461.
25. Fowler, C., Thomson, D., Garn, W., Caird, R., LANL Report, LA 5141-MS (1973).
26. Caird, R., Fowler, C., Garn, W., Henins, I., Ingraham, J., Jeffries, R., Kerr, D., Marshall, J., Thomson, D., LANL Report, LA-4302-MS (1970).
27. Kerr, D.M., Hansen, H.E., LANL Report, LA-4741-MS (1971).
28. Adams, F., Corn, R., May, J., Price W., Seyler, R., SNL Report, SC-DR-70-741 (1971).
29. "STRYPI Rocket Systems" SNL Report, SLA-73-0213, (1973).
30. Marshall, J., LANL Progress Report, Group P-17, Jan. 1971, pp. 2-5.
31. Rogers, J. D., LANL Report, LA-DC-72-724 (1972).
32. Fowler, C., Caird, R., Garn, W. LANL Report, LA-5890-MS, (1975), pp. 13-14.
33. Private communication, J. D. Rogers, LANL, June 1998.

* We note with sadness the loss of our colleague in the Birdseed program, John Marshall, who passed away on October 21, 1997.

A REVIEW OF U. S. HIGH EXPLOSIVE PULSED POWER SYSTEMS

J. H. GOFORTH

University of California, Los Alamos National Laboratory, USA

This paper summarizes current high explosive pulsed power (HEPP) work in the U.S. Three categories are listed in the following text: computational, experimental, and university programs. The focus is on the type of work being done rather than the goals of each program. Most of the work mentioned is also represented elsewhere in the conference, and specific program goals are described in those papers. The programs are treated individually within each category. In reviewing the work, many papers are referenced *in this conference* (ITC) by principle author, but will not be compiled in a reference list due to space. The reader can find the author, hence the paper, in the index.

1 Introduction

High explosive pulsed power (HEPP) is a specialized subset among pulsed power endeavors that takes advantage of the very high energy density available in both magnetic fields and high explosives (HE). To introduce basic concepts, I will divide HEPP components into generators (magnetic field (B) or current (I)) and switches. Magnetic field and current generators start with magnetic field trapped in a conducting volume. Magnetic flux can be expressed as either LI or BA, where L and A (inductance and cross sectional area) are both geometry dependent circuit properties. In a purely inductive circuit, flux is conserved, so $L_1I_1 = L_2I_2$ or $B_1A_1 = B_2A_2$. In our technique, HE is used to propel circuit elements that perform work against the trapped magnetic field as L or A is reduced, yielding increased I or B. Here, I will use the term flux compression generator (FCG) for these devices although the reader will find a variety of acronyms in the literature. Fowler et al. [1] gives a good primer on FCGs.

HE is also used to provide opening and closing switches for HEPP circuits. Closing switches do not require great sophistication and will not be discussed. Opening switches typically use the energy of HE to rapidly reduce the current- carrying cross section of a particular circuit element, and often require sophisticated detonation systems to match the contour of that element (e.g. cylindrical). This may either cause a direct increase in resistance or create the circumstance in which the remainder of the material fuses due to ohmic effects. Many good papers on explosive-driven opening switches can be found in previous Megagauss conference proceedings, and these are also a good source for information regarding HEPP endeavors outside the U.S.

At this conference, Max Fowler discusses the history of HEPP at Los Alamos. Here, I will summarize current HEPP work in the U.S. From the perspective of the U.S. at large, HEPP activities began at Los Alamos in the mid-'50s. The field became very active during the '60s and early '70s, with efforts at Los Alamos, Lawrence Livermore National Laboratory (LLNL), and Sandia National Laboratory (SNL), and considerable interest from Air Force Research Laboratory (ARFL) and other DoD laboratories. Interest in HEPP waned in the '70s and '80s, and LLNL and SNL effectively ceased HEPP activities by the end of the '80s. Among the reasons for the decline was the fact that large energies could be generated using HEPP, but we lacked power-conditioning tools and did not have sophisticated techniques for delivering the large currents to loads of interest. FRL, with its Shiva Star facility, maintained a continuing interest in low-voltage long pulse techniques, including HEPP, but for a short time in the early '90s only Los Alamos maintained an active HEPP effort in the US. There is renewed interest in HEPP. Among the reasons are that HEPP devices are being rediscovered as compact and flexible sources of pulsed power, and that we have developed some of the necessary tools and sophistication that were lacking in the '80s. HEPP technology attained a high degree of maturity in the U. S. with the advent of the Los Alamos Procyon system in the early '90s. During the '80s a great deal of technology for delivering microsecond scale current pulses to interesting loads was developed at the AFRL Shiva facility [2]. Simultaneously, at Los Alamos, we were making good progress in pulse conditioning using HE driven opening switches. The combined knowledge of these two efforts were merged in the Procyon HEPP system and in 1994 we achieved our long-term goal of producing over 1 MJ radiation from a microsecond scale plasma z-pinch [3]. Today there are efforts in both government laboratories and the private sector involving HEPP, which will be described here.

2 Computational Work

One of the fastest growing areas for HEPP is in component modeling and associated tools. Modeling efforts cover the spectrum from empirical models for circuit codes to sophisticated 1-D and 2-D MHD calculations. Represented in these efforts are both government laboratories and the private sector, typically under government sponsorship. Several modeling efforts are currently supporting the AFRL Phillips Site (PS). Among the private sector endeavors is the modeling work done by CARE'N Company using their CAGEN code. This work is described by Chase, ITC, and has enjoyed considerable success in modeling helical FCGs for the AFRL/PS. In calculations performed either by AFRL/PS personnel or Numerex Inc., the MACH II 2-D MHD code is also seeing considerable use for modeling HEPP components. Noteworthy are recent predictions by MACH II that the magnetic force acting on the surface of wires in helical FCGs causes wire flattening resulting in sideways expansion. This expansion may lead to insulation failure if wires are too closely packed and may explain certain failures that seem inexplicable. Ruden, ITC, describes further AFRL/PS work in assessing the material state of FCG armatures. Those calculations are focused on loss mechanisms. In addition to these FCG efforts, MACH II is now being used to model explosively formed fuse (EFF) opening switches as part of the AFRL/PS program. Numerex Inc. recently put an explosive burn routine into MACH II to support Los Alamos programs [4], paving the way for the EFF work. Dennis Keefer presents some of these calculations ITC, and it is interesting to compare them with the experimental work that Tasker, at Los Alamos, presents here.

For other work sponsored by AFRL at Eglin AFB, SAIC has developed the FCGSCA code for modeling FCGs. The code is programmed in Visual Basic, is very graphic, and is set up for performing parametric studies easily. It has met with some successes in matching results from both MK-IX and Ranchito helical FCGs from Los Alamos, and is the subject of a paper ITC by Cornette.

At Los Alamos, we continue to use the Scat95 code to perform HEPP circuit simulation. The main strength of this code is the coupling of a variety of HEPP component models ranging from helical to coaxial FCGs, with a circuit code for system simulation. Tabular values for inductance and resistance can be inserted as inductors or resistors, allowing use of experimental curves as circuit elements. Scat95 also provides a data analysis package that allows quick comparison of experimental data with circuit predictions. Another effort at Los Alamos has been development of a first principles model of helical generators. This analytical model defines inductance using the magnetic vector potential, and is discussed by Fortgang, ITC. Another noteworthy modeling effort is a disk FCG model by Reinovsky at Los Alamos [5]. This model uses Gurney theory; with modifications to account for ring-up effects to drive plates at a prescribed burn velocity along a 2-D contour. It includes field diffusion into conductors and magnetic pressure, allowing prediction of flux pocketing. We have used this model with our CONFUSE code [6] as one of our principle analysis tools in collaborative work with VNIIEF (Lindemuth, ITC) and to analyze results from the few disk FCG tests performed. Finally, at Los Alamos, we are using one and two-dimensional MHD codes to model various aspects of our high current Ranchero generators. Recent 1-D calculations show that the use of SF_6 gas in our Ranchero FCG accounts for a considerable retardation of the armature as it approaches the stator, and that the generator exhibits largely 1-D behavior with that factor included.

3 Experimental Programs

Both government laboratories and the private sector are involved in HEPP experimental programs. Although most work involves government projects, that done by Schlumberger in the oil service industry is an exception. Schlumberger has proposed using small CMF devices (patent # 5505134) to fire slapper detonators down a hole to perforate well casings. This and other options are currently being considered for future development.

The U.S. Army Space and Missile Defense Command presently sponsors an experimental technology evaluation program. A paper presented by Altgilbers, ITC, describes this effort and includes work performed by Explosive Pulsed Power Industries, Inc., a new, private sector company involved in experimental HEPP work. U.S. tests in this program are conducted at the Energetic Materials Research and Technology Center located at New Mexico Technological University.

The Naval Surface Warfare Center (NSWC) has also sponsored HEPP work. In one effort, they investigated the effects of driving current through a detonation front to enhance the explosive performance. This resulted in a demonstration that measurable increase in metal plate acceleration could be detected using a Los Alamos HEPP system. NSWC has also fielded FCG tests with Enig and Associates to demonstrate metal plate acceleration capability.

In one of the largest experimental efforts in the U. S., the AFRL/PS is working on helical FCGs and first stage pulse compression. The helical FCG effort is aimed at a system that will deliver ~1 W at ~2 MA, and is the subject of a paper by LEHR, ITC that presents experimental results. The AFRL/PS is also sponsoring explosive-driven opening switch work at Los Alamos to perform pulse conditioning on the waveform produced by their helical generator. Los Alamos has developed the sophisticated detonation systems required for this work and has experience with large, high-energy systems. The major challenges are to reduce size and manage larger voltages in smaller packages. This work is meeting with some success and is the subject of papers ITC by Kiuttu, Keefer, Degnan, and Tasker.

At Los Alamos, we continue to pursue a wide variety of HEPP endeavors as well as the work for AFRL/PS just noted. Our current thrusts are in three principle directions. The first is the continued development of HEPP components. We are currently working on Ranchero FCGs as a 30-80 MA current source to drive hydrodynamic liner loads. Goforth and Tasker, ITC, report this work. Additionally, we have dedicated experiments to the development of the Ranchito generator. This is a mid-sized helical FCG designed to allow operation of high-energy generators in remote locations without a large capacitor bank to provide the several MA initial current required. Our second thrust is to continue to apply HEPP techniques to a variety of systems. We expect the development of a system to be more difficult than that of any individual component. We have previously mentioned Procyon as an example of a very mature system, and are conducting experiments that couple Ranchero generators to imploding liner loads with fuse opening switches (Goforth, ITC). Another system aspect addressed at Los Alamos is use of transformers to provide impedance matching for high impedance loads (Fortgang, ITC). In our third thrust, we maintain an active effort in generating high magnetic fields for their own sake. ITC, we have reports by Brooks and Clark on recent Dirac series experiments in which we used either Los Alamos 1-2 MG systems or VNIIEF MC-1 10 MG systems to perform high field physics experiments. More Dirac experiments are being planned, and experiments and magnetic field requirements are being defined.

4 University Programs

Because of the renewed interest in HEPP, some work is now being sponsored at universities. All of these efforts are just beginning and we are looking forward to the availability of information they will provide. For instance, the Aeronautics and Astronautics Department at the University of Washington is performing helical FCG modeling for the Air Force Office of Scientific Research [5].

We have also instituted a considerable effort in the form of a Multidisciplinary University Research Initiative (MURI) on “Explosive-Driven Pulsed Power Generation”. This is a joint effort between Texas Tech University and The University of Missouri at Rolla. Kristiansen, ITC, describes one project. The major research objectives are to gain improved understanding of FCG issues and develop methods for efficient conversion of FCG outputs to forms suitable for directed energy systems.

Finally, Freeman, ITC describes a proposed facility for performing HEPP experiments at Texas A&M University.

5 Conclusion

A relatively large fraction of our total effort is now being applied to modeling helical FCGs. Although these are among the oldest types of FCGs in use, they are among the most difficult to model. In the meantime, codes like CAGEN, FCGSCA, and Scat95 provide convenient PC based platforms for system or component modeling. 1-D and 2-D calculations are performed at Los Alamos using resident MHD codes, and MACH II is being used by a variety of institutions for 2-D MHD component modeling. This is also being applied to EFF opening switches. Experimentally, there are significant efforts to develop helical FCGs at Los Alamos and AFRL. Los Alamos continues to work on high energy FCGs, with most work done on Ranchero systems at this time. In spite of the relative importance of pulse conditioning, the only active efforts are in developing pulse transformers at Los Alamos, and EFFs at Los Alamos for both Los Alamos and AFRL programs. Finally, high magnetic field work continues at Los Alamos.

References

1. Fowler, C. M., Caird, R. S., Garn, W. B., An Introduction to Explosive Magnetic Flux Compression Generators, Los Alamos internal report LA-5890-MS, February 1975.
2. Baker, W. L., et al., Plasma Flow Switch Driven Implosions, Megagauss Fields and Pulsed Power Systems, Proceedings of the Megagauss Fifth Conference, Ed. by Titov and Shvetsov, Nova Science Publishers, Inc. (1990) p.615.
3. Goforth, et al., Procyon: 18 MJ, 2-μs Pulsed Power System, Proceedings of the Tenth IEEE International Pulsed Power Conference, Albuquerque, New Mexico, Ed. by Baker and Cooperstein (1995) p. 478.
4. Frese, M., Numerex Inc., private communication.
5. Buyko, A. M., et al., Results Of Russian/US High Performance DEMG Experiment, Proceedings of the Tenth IEEE International Pulsed Power Conference, Albuquerque, New Mexico Ed. by Baker and Cooperstein (1995) p.269.
6. Lindemuth, I. R., Reinovsky, R. E., Goforth, J. H., Exploding Metallic Foil Fuse Modeling at Los Alamos, Proceedings of the Megagauss Fifth Conference, Ed. by Titov and Shvetsov, Nova Science Publishers, Inc., (1990) p. 269.
7. Udrea, B., Shumlak, U., Numerical Study of a Magnetic Cumulative Generator, Conference Record – Abstracts, of the 1998 IEEE International Conference of Plasma Science, June 1998, Raleigh, North Carolina.

MEGAGAUSS FIELDS FROM FORTY YEARS AGO INTO THE NEXT CENTURY

F. HERLACH
Laboratorium voor Vaste-Stoffysica en Magnetisme, Katholieke Universiteit Leuven, Leuven, Belgium

The development of the megagauss conferences is traced from their origin. The development of techniques for generating megagauss fields is reviewed, and an outlook to future developments is given.

1 Origin and Development of the Megagauss Conferences

Fowler et al. published the first paper on explosive-driven flux compression in 1960 [1]. This inspired J.G. Linhart to propose a nuclear fusion experiment making use of megagauss fields. He persuaded H. Knoepfel and F. Herlach to join his EURATOM research group at Frascati, in order to develop an experimental facility for explosive-driven flux compression. At that time, special techniques of manufacturing and using high explosives with the required precision were classified and only available at military laboratories. In co-operation with private industry, the Frascati group engaged in a research program for developing the necessary techniques. As a first step, a small bunker was built as a pilot facility where a capacitor bank and equipment for high-speed photography were installed. After developing the essential techniques for generating cylindrically converging detonation waves and accelerating metal liners to high speed, the first flux compression devices were built and tested, with disappointing results. At that point, Max Fowler was invited to come for two months to Frascati as a consultant. Following his advice, about 2 megagauss were obtained almost immediately with one of the Frascati devices, and another result of this visit was a lasting friendship between the families of the researchers who participated in these early experiments.

The Frascati group then developed a number of flux compression devices with cylindrical as well as plane geometry. In particular, the simple "top hat" and "bellows" devices gave very reproducible performances, and the compressed field could be measured well beyond the maximum ("turnaround"). However, despite very substantial efforts, peak fields in excess of 400 T (we used to call it 4 mega-Oersted) could not be achieved. We suspected that in several countries there were research groups engaged in classified work on the generation of megagauss fields. So one day Heinz Knoepfel suggested that we call a "megagauss conference" in order to "beat them out of the bush". In many discussions between the two of us – some of them in our rowing boat on beautiful Lago Albano – the idea of the megagauss conference gradually took shape. When we finally sent out the first announcement after some informal inquiries, it was still a shot in the dark; the outcome was fairly unpredictable. The result was a pleasant surprise, abstracts and registrations came in from all over the world, including a large number of abstracts from the USSR – this was the first time we heard of A.D. Sacharov and his group.

None of us had been involved in the organisation of a conference before, so this was quite an adventure. A secretary was hired, preparations went ahead on a shoestring budget, and we were looking forward to meeting many new colleagues. The first (and luckily, last) emergency occurred on the first day of the conference: everybody had arrived except the entire Russian delegation! The Russian embassy kept assuring us that the delegation was on its way, they were just temporarily held up at Moscow. As a replacement, they sent us a few other Russian scientists who just happened to be in Brussels, among them the son of P. Kapitza. One of them dutifully took photographs of every slide that was shown, but the speakers for the 8 announced lectures never arrived and we had to improvise on the program. Nevertheless, all went smoothly including the successful demonstration shot with a 220 T bellows device at our new bunker to which all participants were invited. This flux compression experiment in public certainly was unique at that time; the next comparable event took place at the occasion of the first DIRAC series in 1996, with a much more restricted audience.

In all, 27 papers were presented and resulted in lively discussions. We were reassured that we were not alone in trying to generate megagauss fields, and that others also found it difficult to get beyond the apparent 500 T barrier with reproducibly working devices. Some research groups did not yet bring out their work into the open at that time, but it can be assumed that the megagauss conference was a catalyst that resulted in later publications in the open literature.

Around the time of the megagauss conference, the first signs of trouble emerged that led to the eventual demise of the Frascati group. The plasma compression experiments for which the installation had been built turned out to be non-feasible by a large margin. This not only created some friction but the support for this research was finally withdrawn, although the generation of megagauss fields had been a great technical success. The group slowly dispersed, and the bunker with its complete and well-designed instrumentation was finally reclaimed by weeds and mice. However, the experience was not lost. It resulted in books and review articles, and similar flux compression devices were later built at the Illinois Institute of Technology.

To establish a series of conferences, the second may be as important as the first. This is certainly true for the megagauss conferences, and it is the merit of Peter Turchi to have revived it 14 years later - an essential event that resulted in the series of conferences that now has become a tradition:

I. 1965 Frascati, Sept. 21-32, Heinz Knoepfel and Fritz Herlach [2]
II. 1979 Washington D.C., May 29-June 1, P. J. Turchi [3]
III. 1983 Novosibirsk, June 13-17, V. M. Titov, G. A. Shetsov [4]
IV. 1986 Santa Fe, July 14-17, C. M. Fowler, R. S. Caird, D. J. Erickson [5]
V. 1989 Novosibirsk, July 3-7, V. M. Titov, G. A. Shetsov [6]
VI. 1992 Albuquerque, Nov. 8-11, M. Cowan, R. B. Spielman [7]
VII. 1996 Sarov (Arzamas-16) August 5-10, V. K. Chernyshev, V. D. Selemir

At MG-II, high velocity launchers appeared among the applications. Pulsed power from explosive-driven generators, as well as imploding liners for nuclear fusion, were principal topics at all subsequent conferences. The single turn coil made its appearance and was thereafter regularly represented by an average of 3 papers. MG-III was the first conference in the USSR; together with the conference excursions, a memorable experience for all participants. Nondestructive submegagauss fields were included at MG-IV with a presentation by S. Foner, as these were approaching 70 T due to the use of high-tech materials. This was the first conference to include a substantial amount of experimental applications. At MG-V, the Pavlovskii group announced the reproducible generation of 15 MG, and H.-J. Schneider-Muntau suggested that fields up to 100 T could eventually be generated non-destructively or even in a quasi-stationary way. MG-VI had papers on megagauss generators driven by lasers and even by nuclear explosives.

Papers in MG -	**I**	**II**	**III**	**IV**	**V**	**VI**	**VII**
Total	27	61	65	98	101	127	168
Pulsed Power	5	22	25	35	27	48	53
Exp. applications	2	5	10	19	10	17	22
Launchers		2	5	10	9	13	9
Implosion/fusion	2	11	9	11	15	20	27
Sub-megagauss				2	1	9	5

2 40 (or 70?) Years of Megagauss Fields

If "half a megagauss" would qualify, then Kapitza's 1927 paper could be taken as the first milestone in the development of megagauss fields. P. Kapitza (1894-1984) was indeed aiming at fields up into the range of 200-300 tesla, and he lived to witness the first report on the generation of 160 T by Furth et al [8] with remarkably simple equipment, discharging a fast capacitor bank into a single turn coil. It was the 1960 paper by Fowler et al, which started the ball rolling, and the first megagauss conference then resulted in bringing the work from other research groups into the open. Shortly afterwards, the Sacharov group reported on the generation of very high fields [9]. Since the generation of megagauss fields is closely related to military applications, much of the work had been classified and was published long after it had been accomplished. Therefore, it is difficult to establish priorities and describe the development in real chronological order. In any case, at MG-I a consensus was reached that not more than 500 T could be generated reproducibly at that time. Some researchers even believed that there was an absolute limit, but this was refuted by later results (Besançon, AWRE, Hawke), in particular from the Pavlovskii group that introduced the method of "cascades" [3] for obtaining a high initial field and stabilising the implosion. This method was reported at MG-II and up to now it yields the highest fields for use in experiments; at the present conference, it was reported that the level of 2000 T (sometimes written 2 kT) has been reached.

In parallel to the explosive-driven experiments, Linhart had also run the first experiment with flux compression in a metal cylinder imploded by magnetic forces in z-pinch geometry. This was not much of a success, perhaps because too much emphasis was placed on the detection of fusion neutrons. The first successful electromagnetic flux compression experiment in theta-pinch geometry was reported by Cnare [10], and an excellent z-pinch experiment was reported by Alikhanov et al [11]. At the University of Tokyo (Institute for Solid State Physics), the theta-pinch technique was developed on a large scale for use in experiments [12]. In this geometry, the driving field is generated by a single turn coil, which surrounds the cylinder. A problem is given by the irregularity in the driving field at the feed gap of this coil, which results in a dent in the imploding cylinder.

This grows during the implosion and severely disturbs the regularity in the critical end phase of the compression. The z-pinch (where the driving field is generated by a current passed through the cylinder in axial direction) does not suffer from this problem, but the requirements for the capacitor bank are even more severe than with the theta-pinch. The researchers at ISSP have recently committed themselves to further development of the theta-pinch technique with very heavy equipment [12]. It can be expected that this will make fields up to 1000 T available in a laboratory environment. Experiments at cryogenic temperatures are now successfully conducted at ISSP.

The single turn coil technique was revived by Forster and Martin [13], who demonstrated that high fields could be obtained with a relatively small but very fast capacitor bank driving a lightweight coil. Herlach and McBroom [14] developed this technique into a research instrument, and the 100 kJ, 40 kV instrument built in 1983 at ISSP has been in continuous, trouble-free operation since then, yielding a wealth of experimental results. Recently, an installation with 200 kJ at 60 kV has become operational at the Humboldt Magnetic Field Center at Berlin [15], yielding peak fields up to 300 T.

3 Where Do We Go From Here?

Making predictions or suggestions for future development is a matter of personal judgement. For sure, the rate of progress has been very slow - it is measured in decades rather than in years. This is a clear indication of the extreme difficulties that are encountered in the generation of megagauss fields.

The single turn technique will certainly be further developed and more widely used as an efficient workhorse for research in megagauss fields. At ISSP, two new single turn coil generators will be installed. It is not so certain whether the prediction of Forster and Martin to eventually obtain peak fields up to 700 T with a 1 MJ capacitor bank can be fulfilled, but of course, it may be worth a try.

With the large investments made at ISSP, the continuing development of the electromagnetic implosion technique is assured. In principle, this technique is open-ended because the transfer of energy to the imploding liner is not limited by the speed of sound, as is the case for explosives. However, extremely high energy at high power is required to obtain a sufficiently high implosion speed. For ultimate performance, it may be possible to derive this from an explosive-driven generator with power conditioning by an opening switch. There are very large and fast capacitor banks available or under construction for other purposes, at some of these it is considered to implement an electromagnetic implosion experiment. This makes much sense for exploring the limits but may not directly result in a useful research instrument as the operation of these large, advanced capacitor banks is costly and inconvenient, and the repetition rate is very low.

For some time to come, explosive-driven flux compression devices will provide the highest fields available for research, although it is unlikely that fields much in excess of 2000 T can be conveniently obtained with this method. All facilities outside the military domain (except a small one at Tsukuba) were closed down for one reason or another, but fortunately the facilities at Los Alamos and Sarov (Arzamas-16) were recently opened for series of experiments with wide international participation, the DIRAC and KAPITSA series. The key to more efficient use of explosive-driven experiments would be more emphasis on simplicity at all levels: implosion devices, experiments and diagnostic instrumentation. It should be quite feasible to design simple devices of the type developed by the Frascati group [2] for experiments up into the 1000 T range.

Finally, there is the old dream of generating fields up to 100 T with non-destructive coils, dating back to the ambitions of Kapitza. This is now getting a step closer to reality through the combined effort of several European laboratories with a similar, parallel development at the NHMFL. This will eventually succeed but perhaps not as fast as it is now optimistically assumed. The first such magnet is likely have a small bore (~ 1 cm) and a short pulse duration (~ 1 ms). Therefore, potential users of these magnets are encouraged to miniaturize their experiments by using the modern technology that is now available. Pioneering work in this direction is done in experiments with the single turn coil. Eventually, miniaturization will lead to the design and use of "micro-magnets" as discussed for the first time at this conference in a dedicated session.

Acknowledgements

The preparation and presentation of this paper was supported by the NHMFL, by the Flemish F.W.O. and by the European Union under the TMR program.

References

1. Fowler, C. M., Garn, W. B., Caird, R. S., *J. Appl. Phys.* **31** (1960) pp. 588-594.
2. *Proc. Conf. on Megagauss Magnetic Field Generation and Related Experiments,* Ed. by H. Knoepfel and F. Herlach, (Euratom, Bruxelles 1966) p. 537.
3. Megagauss Physics and Technology, Ed by Peter J. Turchi, (Plenum Press New York 1980) pp. 683.
4. Ultrahigh Magnetic Fields: Physics. Technics. Applications, Ed. by V. M. Titov and G. A. Shvetsov, (NAUKA, Moscow 1984) pp. 415.
5. Megagauss Technology and Pulsed Power Applications, Ed. by C. M. Fowler, R. S. Caird, D. J. Erickson (Plenum Press New York 1987) p. 875.
6. Megagauss Fields and Pulsed Power Systems, Ed. by V. M. Titov and G. A. Shvetsov, (Nova Science Publishers New York 1990) p. 859.
7. Megagauss Magnetic Field Generation and Pulsed Power Applications, Ed. by M. Cowan and R. B. Spielman, (Nova Science Publishers, New York 1994).
8. Furth, H. P., et al., *Rev. Sci. Instrum.* **28** (1957) pp. 949-58.
9. Sacharov, A.D., *Usp. Fiz. Nauk.* **88** (1966) pp. 725-34.
10. Cnare, E. C., *J. Appl. Phys.* **37** (1966) pp. 3812-6.
11. Alikhanov, S. G., et al., *J. Phys. E: Sci. Instrum.* **1** (1968) pp. 543-5.
12. Miura, N., in these proceedings.
13. Forster, D. W., Martin, J. C., in *Proc. Int. Conf.* Les champs magnétiques intenses, leur production et leurs applications (CNRS Paris 1967) pp. 361-70.
14. Herlach, F., McBroom, R., *J. Phys. E: Sci. Instrum.* **6** (1973) pp. 652-4.
15. von Ortenberg, M., et al., in these proceedings.

THEORIES OF HIGH TEMPERATURE SUPERCONDUCTIVITY

J. R. SCHRIEFFER
Florida State University Department of Physics, and National High Magnetic Field Laboratory, Tallahassee, FL, USA

While the theory of low temperature superconductors has been well established for more than two decades, the theory of the high temperature cuprates has yet to be agreed upon. Several of the leading proposals will be discussed, including spin fluctuations, interlayer tunneling, phase fluctuations of the order parameter, and excitations in short coherence length materials. The essential physical ideas will be stressed. These materials will depend upon high and ultra high magnetic fields to judge which theory is correct.

1 Introduction

There have been many theoretical approaches to high temperature superconductivity since the discovery of this phenomenon in 1987. The schemes include weak coupling theories in which the Coulomb interaction is taken as the perturbation, and extended Bloch waves are used as a basis. In the strong coupling regime, the kinetic energy of the electrons is taken as the perturbation, with localized states being taken as the basis. Since the actual physical situation lies between these limits, presumably either approach should be able to describe the correct physics.

An important fact is that in these materials antiferromagnetism is close to superconductivity in the phase diagram. For example, in $La_{2-x}Sr_xCuO_4$ for x up to 3%, the material is an antiferromagnet (AF) while for x ~ 5% the system becomes superconducting (SC). Short-range AF spin fluctuations extend into the SC phase.

2 Spin Fluctuations

In the weak coupling approach [1] one assumes that the phonon interaction between quasi-particles in the normal phase of the low temperature superconductors is replaced by exchanging AF spin fluctuations. As shown in Fig. 1, the spin susceptibility χ leads to an oscillatory interaction in real space due to a peak of χ_q in momentum space, as shown in Fig. 2. This peak is a consequence of nesting properties of the Fermi surface, as illustrated in Fig. 3.

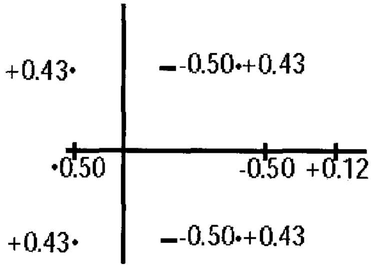

Figure 1. Pairing interactions in real space.

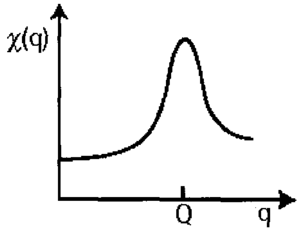

Figure 2. Spin susceptibility showing a peak at the spin fluctuation wave vector.

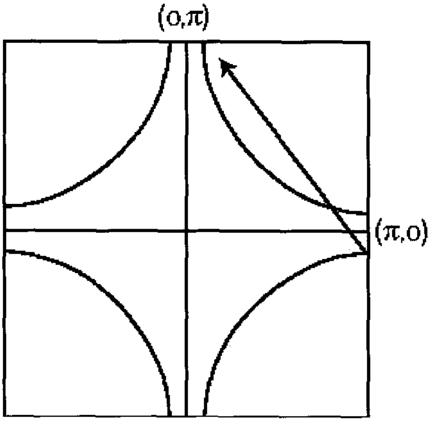

Figure 3. Fermi surface of Bi2212.

A key feature of the AF interaction is that it leads to a gap parameter Δ_k that varies in k space as a d-wave, i.e.,

$$\Delta_k=\Delta_0\,(\cos k_x a - \cos k_y b).$$

This form of Δ allows the positive interaction $V_q = g^2\chi_q$ to be attractive since V_q connects primarily states of opposite sign of Δ_k. Thus the gap equation

$$\Delta_k = -\sum_k \frac{\Delta_{k'}}{2E_{k'}} \tanh \beta E_{k'}$$

can be satisfied, where $E_k = (\varepsilon_k^2+\Delta_k^2)^{1/2}$ and $\beta = 1/k_BT$. The form of χ_q is

$$\chi_q = \frac{\chi_Q}{1+(q-Q)^2\xi^2 + \frac{i\omega}{\omega_{sf}}}$$

where Q is the wave vector of the AF state in the undoped system, ξ is the spin-spin correlation length and ω_{sf} is the characteristic spin fluctuation frequency. ξ and ω_{sf} are related by

$$\omega_{\mathrm{sf}}\ \mu\ \xi^{-2} \cong \boldsymbol{a} + \boldsymbol{bT}$$

in an overdoped regime, as shown in Fig. 4.

For optimally and underdoped material:

$$\omega_{\mathrm{sf}} \sim \xi^{-1} \cong \boldsymbol{c} + \boldsymbol{dT}$$

In this regime, angle-resolved photoemission shows that a pseudo-gap exists between the SC transition temperature T_c and a temperature T_* such that long-range order of Δ is lost while short-range order persists.

This phenomenological model can account for a broad range of experimental facts, including NMR, transport, and aspects of neutron scattering. One shortcoming of this scheme is that it treats the spin fluctuations as bosons, where each state q can be occupied by 0, 1, 2, …∞ bosons. In fact, since the Cu^{++} ion has spin 1/2, only two states are allowed, $m_s = \pm\frac{1}{2}$. This imposes a restriction on $\chi_q(\omega)$, $\Sigma_{q\omega}\ \chi_q \propto <s^2> \leq 3/4$. For χ near the AF boundary, this condition is not satisfied.

A second shortcoming is that high order corrections in the coupling of a spin fluctuation and an electron (hole) must be included for a small x near AF phase boundary [2,3]. This leads to $g_q \rightarrow \Gamma_{-q} \sim |q-Q|\ \Gamma_0$, so that the coupling vanishes as χ_q diverges, leading to a limit for $\Gamma_q^{\,2}\chi_q$ which is finite as $q \rightarrow Q$.

3 Strong Coupling

Anderson [4] and coworkers have proposed that the breakdown of Fermi liquid theory in one dimension to form a Luttinger liquid that extends to two dimensions. In a Luttinger liquid, the excitations are holons that carry charge but no spin and spinons that carry spin and no charge, in contrast to electron and hole quasi-particles for a Fermi liquid.

Anderson proposed that the holons and spinons hop coherently between planes in the normal phase while two pairs of holons and spinons hop coherently between planes in the SC phase, thereby lowering the energy. In this scheme the gap equation becomes,

$$\Delta_k = \frac{1}{\dfrac{1-|\boldsymbol{T_k}|^2\ \boldsymbol{tanh\beta E}}{2\omega_c \boldsymbol{E_k}}} \sum_{\boldsymbol{k}} \frac{V\theta(\omega_c - |E_{k'}|)\Delta_{k'}\ \boldsymbol{tanh}\dfrac{\beta \boldsymbol{E_k}}{2}}{2\boldsymbol{E_{k'}}}$$

where $\theta(x) = 1, x > 0$ and zero for $x < 0$. T_k is the single particle hopping matrix element between planes.

4 Quasi Particle Pockets

The phase diagram shown in Fig. 4 exhibits a peak of T_c, from which three phases emerge. Below T_c a pairing gap exists, while for $T_c < T < T_*$ a pseudogap exists and above T_* the gap vanishes. To account for the low values of T_c for small x, Lee and Wen [5] have assumed that the gap is

$$\Delta_{k=}\Delta_0 (\cos k_x a - \cos k_y a)$$

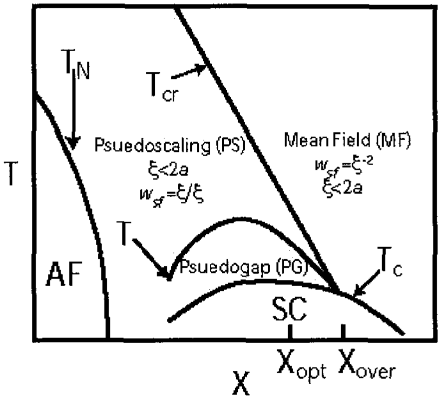

Figure 4. Generic phase diagram showing the relation of the spin fluctuation frequency and the spin correlation length.

In the vicinity of the nodes of the gap near ($\pi/2a$, $\pi/2a$) the quasi-particle has an energy $Ek^2 = (v_1^2 k_1^2 + v_2^2 k_2^2)$ where $k_l = (k_x + k_y, \pi/a)/(2)^{1/2}$ and $k_2 = (k_x - k_y)/(2)^{1/2}$, with $v_1 = 2(2)^{1/2} t_1 a$ and $v_2 = \Delta_0\, a/(2)^{1/2}$, where t_1 is the hopping matrix element. In addition they assume that in the presence of a vector potential A, the quasi-particle energy shifts to

$$E_k(A) = E_k + \frac{e}{c} \vec{v}_k \cdot \vec{A}$$

to first order in A. Thus, the current carried by a quasi particle is $-c\partial E/\partial A = -e v_k$, where $v_a = d\varepsilon_k/dk$. This result is in agreement with conventional pairing theory. They further propose that the superfluid density is given by

$$\rho_S(T) = \rho_S(0) - \rho_n(T)$$

where ρ_n is the normal fluid density. They assume that

$$\rho_S(T = 0) = x/a^2$$

with x being the doping concentration. This assumes a small Fermi surface whose area scales with x. The free energy of the quasi particle is

Thus, $$F(A,T) = -k_B T \sum_{k,\sigma} log\left(1 + e^{-\beta E_k(A)}\right)$$

so that $$\rho_n = -2m \sum_k (\partial E/\partial A)^2 \frac{\partial f}{\partial E} = -2m \sum_k v_k^2 \frac{\partial f_k}{\partial E_k}$$

$$\rho_s(T) = x/a^2 - \alpha m T$$

where $\alpha = (8\mathit{In}2\pi)t_1/\Delta_0$. Therefore T_c is given by

$$k_B T_c \cong 2x\Delta_0$$

Assuming that Δ_0 is independent of x for $x << 1$, the linear variation of Δ with x agrees with muon spin resonance measurements. [6]

5 Phase Fluctuations

In conventional pairing theory, the gap goes to zero at T_c. In HTS materials in the underdoped regime, the gap persists above T_c, presumable due to long wavelength fluctuations of the phase θ of the gap, where $\Delta = \Delta_0 e^{i\theta}$. Thus the short-range order of $|\Delta| = \Delta_0$ remains unaffected by the phase fluctuations. Emery and Kivelson [7] proposed such a model based on the Ginsburg-Landau free energy,

$$E = \frac{1}{2} m^* n_s \int v_s^2 dr$$

where $v_s = \hbar \nabla\theta / 2m^*$. Ignoring all fluctuations other than that of the phase, they define T_θ^{max} as that temperature at which long range phase ordering disappears. Then if $T_\theta^{max} >> T_{c,}$ phase fluctuations are unimportant while if $T_\theta^{max} \cong T_{c,}$ they are important. These authors only consider classical phase fluctuations neglecting quantum fluctuations and quasi-particle excitations, taking $n_s(T{=}0) = n_s$. As in the x-y model, θ is defined on the interval $0 < \theta < 2\pi$. The characteristic energy scale is then defined as the phase stiffness $V_0 = \hbar^2 n_s A / 4m^*$, where a as a cutoff length below which the gradient expansion is invalid. Using the relation $4\pi\, n_s(0)/m^* = (c/e\lambda)^2$, where λ is the penetration depth, V_0 becomes

$$V_0 = \frac{a}{16\pi}\left(\frac{\hbar c}{e\lambda}\right)^2$$

The length a is chosen to be $a^2 = \pi\xi^2$. Since V_0 is the energy scale for the problem,

$$k_B\, T_\theta^{\max} = A V_0$$

where $A = 0.9$ for uncoupled planes and 2.2 for an isotropic solid. In Table 1, $T_\theta^{\max}/T_c$ is listed for a number of materials. One sees that $T_\theta^{\max} \sim T_c$ for HTS materials, while $T_\theta^{\max} >> T_c$ for low T_c materials. Thus, phase fluctuations are important for HTS systems.

6 High Magnetic Fields

At low fields, the elastic interactions between vortices govern their structure in a solid phase. Weak pinning sites usually destroy long-range order. At higher fields, disorder dominates and vortex-defect interactions result in an entangled glassy solid. At high fields and high temperature, a liquid phase exists. A first order transition exists between the quasi-lattice and the liquid phase, which likely ends in a critical point.

Table 1.

	$T_\theta^{\max} / T_c$
Pb	2×10^5
Nb3Sn	2×10^3
K3C60	50
Tl2Ba2CuO6+δ	2
Bi2Sr2CaCuO4+δ	1
Yba2Cu3O7-δ	1.4

While complex behavior is observed in these materials, many of the effects that occur can be described in terms of a Ginsburg-Landau approach, while the Ginsburg-Landau approach is insensitive to the details of the microscopic theory. There are, however, quasi-particle states, for example in the vortex cores, which are more sensitive to the microscopic theory.

The effects of high T_c short coherence length and anisotropic crystal structure introduce a rich variety of new phenomena in HTS materials. The very high value of H_{c2} requires high magnetic fields to study these systems. A crude phase diagram is shown in Fig. 5 for $Bi_2Sr_2CaCu_2O_8$ (BSCCO) with weak disorder.

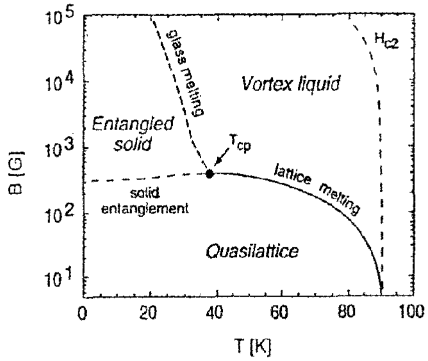

Figure 5. Schematic phase diagram of high T_c material.

7 Conclusions

A number of theoretical schemes continue to exist for HTS materials. A broad range of experimental techniques is being used to clarify the fundamental properties of those systems. High magnetic fields play an essential role in this process, both in revealing the properties of the normal phase below T_c and understanding the magnetic phase diagrams in the Type II regime.

Acknowledgment

This work was supported by NSF grant 9629987.

References

1. Pines, D. *Physica C* **282-287**, (1997) p. 273: *Physica C* **282-287**, (1997) p. 282.
2. Schrieffer, J. R., *J. Low Temp. Phys.* **99**, (1995) p. 397.
3. Chubukov, D. R., Morr D. R., Shalnovich, K. A., *Phil. Mag.* **74**, (1996) p. 563.
4. Chakravarty, S., Sudbö, A., Anderson, P. W., Strong, S., *Science* **261**, (1993) p. 337.
5. Lee, P. A. and Wen, X.-G., *PRL* **48**, (1997) p. 4111.
6. Uemura, Y. *et al., PRL* **62**, (1989) p. 2317; *PRL* **66**, (1991) p. 2665.
7. Emery, V. J., Kivelson, S., *Nature* **374**, (1995) p. 434.

INVESTIGATIONS OF FLUX COMPRESSION ENERGY SOURCES AND ULTRA-HIGH MAGNETIC FIELD GENERATORS IN VNIIEF

V. D. SELEMIR, V. A. DEMIDOV
VNIIEF, Sarov, Russia

Results of VNIIEF investigations in the creation of flux compression energy generators (FCG) with different geometry are considered. Calculations and experimental data are analyzed on application of these devices for pulsed formation of high voltages, generation of high-power electron beams and of ultra-high magnetic fields. Perspectives on the development of explosive generators are connected with the creation of the “Sprut” energy system and complex EMIR, intended for investigations in high-energy density physics. Experiments using ultra-high magnetic field generators created, for the first time in the world, a magnetic field of 28 MG.

1 Introduction

One of the activities of the Science and Technology Center of High-Energy Density Physics and Directed Radiation Fluxes is to create flux compression power sources and ultra-high magnetic fields. The variety of uses for these sources, despite unified operation principles based on magnetic flux compression, predetermines the different geometries and output characteristics of the devices developed. Helical flux compression generators with current opening switches and transformers are being developed to form high-voltage pulses with fronts of 0.1-0.7 μs on high-inductance loads. Progress in high-energy density physics is connected with the development of fast disk generators, non-traditional energy pulse transformation systems and creation of energy complexes > 1 GJ. The issue of ultra-high magnetic field generation in MC-1 generators has a singular place in our investigations.

2 High-Voltage Pulse Formation

We used two schemes for short, high-voltage pulse formation: a helical FCG with a two-stage current opening switch; and a helical FCG, transformer and current opening switch.

A 100 mm diameter helical FCG was used in the first scheme. An explosive opening switch [1] was used in the initial current pulse-sharpening cascade, and a fuse was used in the second cascade. A junction diode with 90 mm diameter graphite cathode and ~20 mm cathode-anode gap was used as a load. The diode was connected to the FCG with a cable, which made it possible to save the load at the experiment. Investigations showed that 40 wires 0.12 mm in diameter and 420 mm long, connected in parallel, provide an output voltage of more than 500 kV on an equivalent resistive load.

Results of the diode powered with this generator are shown in Figure 1. Diode current is 27 kA with a rise time of ~80 ns. Maximum voltage is ~380 kV.

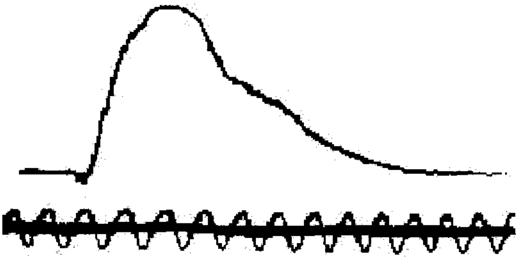

Figure 1. Diode current. Maximum value 27 kA, time marks at 0.04 μs.

The flux compression power source of the diode is autonomous. An initial energy pulse of 6-8 J is produced by an explosive piezo generator. Energy is then amplified to kilojoule levels with a small-scale helical FCG and sent to a transformer and to a 100 mm diameter MCG, which amplifies it to ~500 kJ [2]. The autonomous source without opening switches is shown in Figure 2.

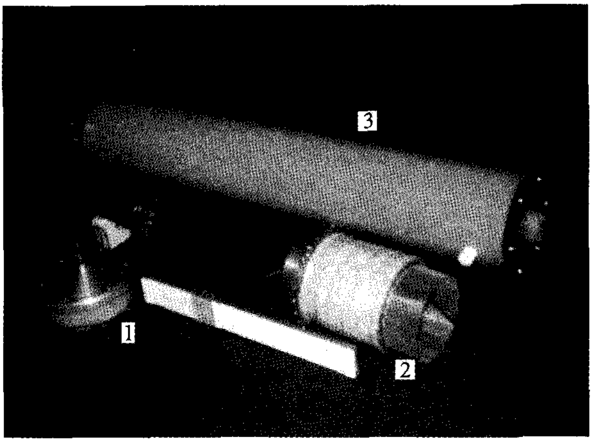

Figure 2. The cascade FCG. 1 – explosive piezogenerator, 2 – FCG-50 with transformer, 3 – FCG-100.

FCG-160 with a transformer energy output (Figure 3) and an opening switch made of fuses was used to form voltage pulses greater than 1 MV. Voltage pulses of 1.3 MV with a ~0.75 μs front were obtained by the liquid resistor experiments having an active resistance of ~13 Ω.

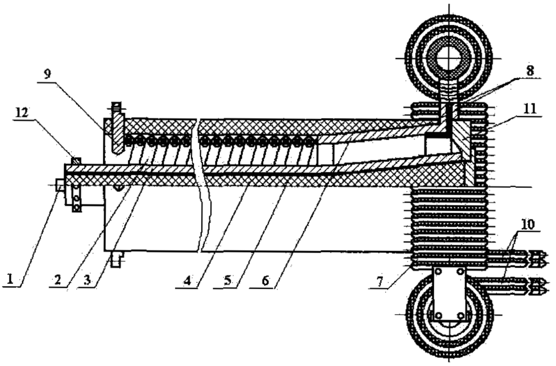

Figure 3. FCG-160 with transformer energy output. 1 – detonator, 2 – multi-sectional helix (stator), 3 – metal tube (armature), 4 – HE-charge, 5 – plexiglass tube, 6 – tapered coaxial area, 7 – transformer unit, 8 – generator output, 9 – closing switch, 10 – transformer unit output, 11 – tapered flange, 12 – fastening clamp.

To obtain short voltage pulses with amplitudes of several megavolts, we also consider high-inductance, fast helical FCGs (Figure 4) and voltage-multiplication switching schemes (Figure 5) powered from FCG.

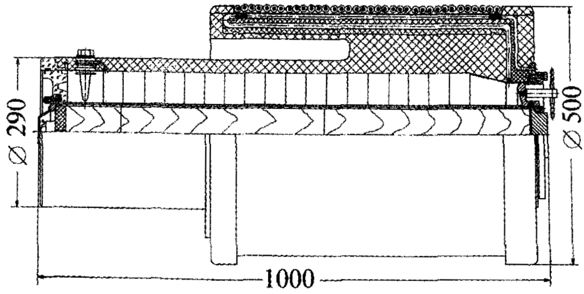

Figure 4. High inductance, fast helical FCG with transformer output.

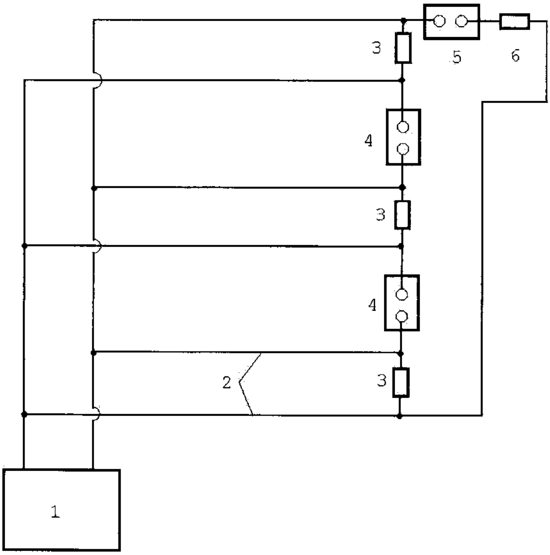

Figure 5. Source circuit with voltage multiplication. 1 – FCG, 2 – transmitting line, 3 – fuse, 4 – commutator, 5 – discharger-sharpener, 6 – load.

3 High Current Flux Compression Generators and their Use

To obtain a current pulse of tens and hundreds of megamperes we developed a fast disk FCG (DFCG) with 240 mm and 480 mm diameter HE charges (DFCG-240 and DFCG-480). The ratio of the main linear dimensions of the generators is 1:2. The sketch of the FCG with cable energy output is shown in Figure 6. Figure 7 shows half of the DFCG element, which was used to calculate the generator parameters.

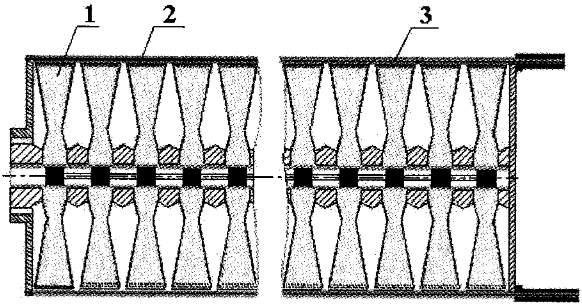

Figure 6. Disk FCG with cable energy output. 1 – HE-charge, 2 – copper shell, 3 – cable.

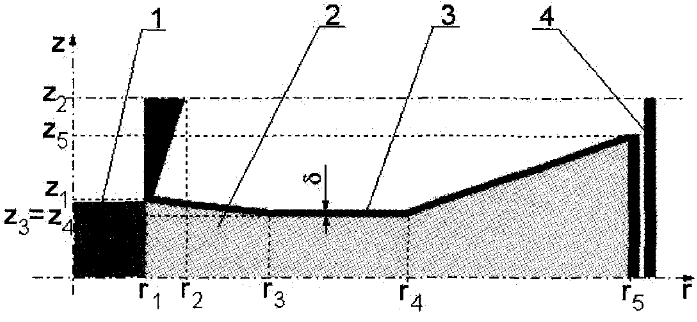

Figure 7. Half of the DFCG element. 1 – initiation system, 2 – HE-charge, 3 – armature, 4 – reverse current conductor.

Calculations show that a 20-element DFCG-240 with a HE-charge density of 1.82 g-cm^{-3} and 7 MA initial current provides a current of ~70 MA for a 10 nH load, with a characteristic rise time of τ~3.5 μs. For a 20 nH load, it provides a ~45 MA current with τ~4.5 μs (Figure 8). The output energy is ~20 MJ. According to the calculations, maximum DFCG-480 current is ~150 MA and magnetic energy is ~200 MJ.

We have performed the first experiments with DFCG-240. Powering the 3-element generator with a 5 MA current from the FCG-100 helical generator, we obtained a current of ~50 MA. This corresponds well to the calculations.

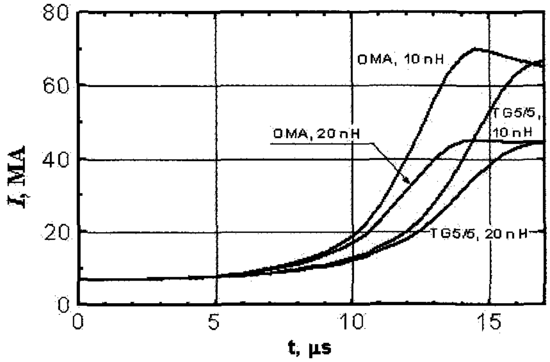

Figure 8. Time dependence of current for DFCG-240 at I_0 = 7 MA.

To power real loads with high currents, it is useful to create batteries made of multi-element DFCG of relatively small diameter and connected in parallel. In the modular power source, "Sprut" [3], the connection of disk generators to the load is made with high-voltage, low-inductance cables (Figure 9). This scheme provides a symmetrical current supply to a load having any number of modules.

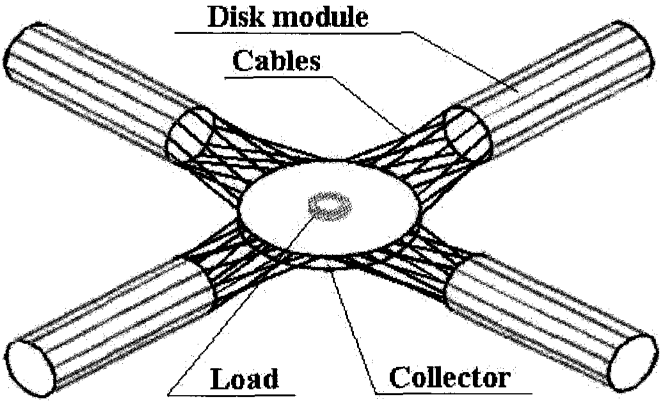

Figure 9. Scheme of modular power source "Sprut"

"Sprut" is intended for investigations of magneto-gasdynamical energy cumulation, megabar pressure generation and for other high energy density physics experiments, where sources with energy capacity of 500-1000 MJ are required. "Sprut" can provide this energy by parallel connection of 3-6 DFCG-480 modules. Characteristic current rise time will be under 10 μs.

We proposed the idea and principles of project realization of explosive electrophysical complex EMIR [4] for generating pulsed fluxes of soft x-ray radiation (SXR). The EMIR device is based on high-power, fast disk FCG technologies developed in VNIIEF, and transforming systems based on lines with distributed parameters and opening switches. Vacuum lines with magnetic insulation or water coaxial lines are considered to transmit energy pulses to the load. Transformation of magnetic to kinetic energy, thermalization and SXR generation are performed in z-pinch with a double liner system.

The complex EMIR is designed on the module principle. A 20-element DFCG-240 is the power base of the complex. Radial water lines with 3 m external diameter and 1 m internal diameter are used in the transformer (Figure 10). The key element of the transformer is an opening switch with an operation time less than the electromagnetic wave running time on a short-circuit line. The final resistance of the opening switch should be higher than the line wave resistance. According to the estimations, a five-element transformer module powered from DFCG-240 provides 10 MV at 120 ns pulse length on a 5 Ω load. Energy pulses, formed by the base modules, are transmitted to the radial (biconical) line by the vacuum or water coaxial line. The load is located at the center of the radial (biconical) line. In particular, realization of ~0.1 Ω wave resistance in the summator radial line requires parallel operation of 48 modules.

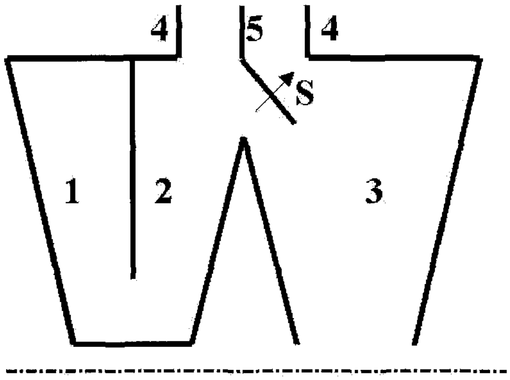

Figure 10. EMIR base module transformation circuit. 1, 2 – short-circuit line, 3 – transmitting line, 4, 5 – coaxial line providing energy supply from external source, S – opening switch.

The principle scheme of the device to generate SXR is presented in Figure 11. As a result of a shock, kinetic energy of the external liner is transmitted to the internal liner 4. SXR, which appears at the internal liner collapse, travels through window 5 to the spherical cavity with thermonuclear target.

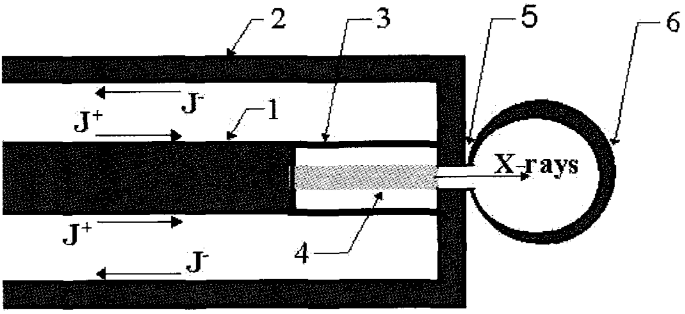

Figure 11. Scheme of the plasma element to generate SXR. 1 – supplying current conductor, 2 – reverse current conductor, 3 – external liner, 4 – internal liner, 5 – radiation output window, 6 – spherical cavity with thermonuclear target.

To determine the SXR parameters, we solved hydrodynamic equations together with the radiation transmission equation in 2-D geometry. We used the state equations in approximation of Thomas-Fermi, considered braking absorption, photoionization, and absorption in the lines. Calculations showed that maximum intensity of the outgoing to the cavity SXR is obtained at a liner velocity of $\sim 7 \cdot 10^7$ cm/s. The calculated energy balance is: supplied electromagnetic energy of ~85 MJ; kinetic liner energy of ~17 MJ, energy of incoming to the cavity radiation of ~1.7 MJ. Maximum radiation intensity is ~0.5 MJ/ns, maximum temperature in the cavity of ~1 cm^3 volume is ~0.3 keV.

One method to obtain ultra-high magnetic fields is magnetic flux compression with electrodynamical liner acceleration. Projects generating fields of 10-20 MG using z-pinch based devices are powered from the "Pegasus" and "Atlas" capacitor banks at Los Alamos National Laboratory, USA [5].

We have proposed a scheme (Figure 12) of obtaining fields greater than 10 MG. MC-1 generator and fast DFCG are used jointly in this scheme. It is expected that liner 5 moves under both the influence of current I of DFCG and that of HE-charge explosion products 1. Liner 5 and reverse current conductor 3 are fabricated using the technology of MC-1 cascade generators.

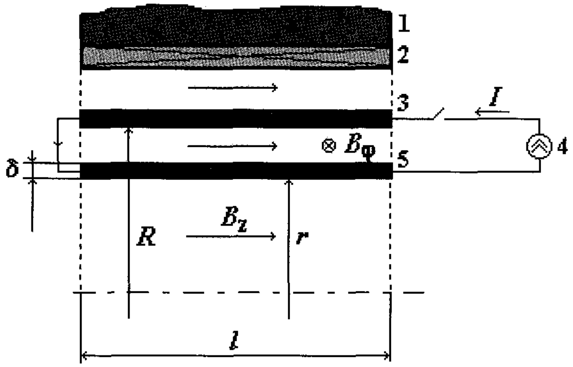

Figure 12. Scheme of obtaining ultra-high magnetic fields using DFCG and MC-1. 1 – MC-1 HE-charge, 2 – MC-1 generator solenoid, 3 – reverse current conductor, 4 – power source (DFCG), 5 – liner, B_z – MC-1 generator axial magnetic field, B_φ - azimuthal magnetic field of the source, I – source current, R – internal radius of the reverse current conductor, r – internal liner radius, δ - liner thickness, l – liner length.

We solved a one-dimensional equation of the system of magnetic hydrodynamics jointly with the electrotechnical circuit equation. A 20-element DFCG-240 and an aluminum liner 10 cm long, 5 cm internal radius and 3 mm thick were used. Through calculations, without considering the energy taken by the liner from the HE-charge, we obtained a magnetic field of 18 MG in the 3 mm cavity at 50 MA DFCG current. Calculation results are presented in Figure 13. The distinctive feature of this scheme is a low (~0.5 μs) characteristic magnetic field time. This is important for application of such a device to obtain high temperature plasmas.

Calculations certify that the magnetic field reaches ~30 MG in a cavity of more than 2 mm radius and 5 cm in length at ~90 MA current (for example, using DFCG-480).

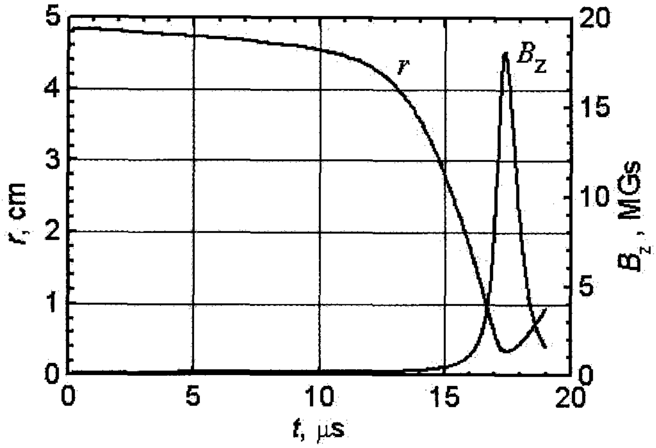

Figure 13. Calculation results of flux compression generated by the DFCG current profile.

References

1. Selemir, V. D., Demidov, V. A., et al., High-Current (30 MA and More) Energy Pulses for Powering Inductive and Active Loads. In *Megagauss and Megaampere Pulse Technology and Applications*, ed. by V. K. Chernyshev, V. D. Selemir, and L. N. Plyashkevich (Sarov, VNIIEF, 1997) pp. 241-247.
2. Demidov, V. A., Sadunov, V. D., et al., Helical Cascade FCG Powered by Piezogenerator. In *Digest of Technical Papers 11th IEEE International Pulsed Power Conference*, ed. by G. Cooperstein and I. Vitkovitsky (Baltimore, Maryland, 1997) pp. 1476-1481.
3. Demidov, V. A., Kazakov, S. A., et al., High-Power Energy Sources Based on the FCG Parallel and Serial Connection. In *Digest of Technical Papers 11th IEEE International Pulsed Power Conference*, ed. by G. Cooperstein and I. Vitkovitsky (Baltimore, Maryland, 1997) pp. 1459-1464.
4. Selemir, V. D., Demidov, V. A., et al., Explosive Complex for Generation of Soft X-ray Radiation Pulsed Fluxes. In *12th International Conference on High Power Particle Beams BEAMS '98*. Program and Abstracts (Haifa, Israel, June 7-12, 1998) p. 21.
5. Sheppard, M. G. et al., Multi-Megagauss Field Generation Using Capacitor Banks. In *Megagauss and Megaampere Pulse Technology and Applications*, ed. by V. K. Chernyshev, V. D Selemir and L. N. Plyashkevich (Sarov, VNIIEF, 1997) pp. 205-212.

ELECTROMAGNETIC LAUNCH - STATE OF THE ART AND OPPORTUNITIES

G. A. SHVETSOV

Lavrentyev Institute of Hydrodynamics, Novosibirsk, Russia

One of the most interesting applications of high magnetic fields is related to projectile acceleration to high velocities. This problem is traditionally considered at conferences on megagauss magnetic field generation and related topics. The applied significance of this problem has stimulated worldwide large-scale laboratory research and has led to the organization of regular, international conferences on electromagnetic launch problems. Here, the present state of the art of this research area is analyzed, the most significant (in the author's opinion) advances are outlined, and problems and prospects of electromagnetic launching of solids are discussed.

1 Introduction

The possibility of using electric energy to accelerate solids have aroused considerable interest of researchers engaged in the area of pulsed-power, high magnetic fields and high-velocity impact phenomena. This problem is traditionally considered at conferences on megagauss magnetic field generation and related topics. The applied significance of this problem has stimulated large-scale research at many laboratories all over the world.

However, electromagnetic launchers that out-perform other types of high-velocity accelerators of solids cannot be designed without comprehensive basic research of physical processes and phenomena that prevent attainment of high velocities and acceptable efficiency of EM launchers. This affects the direction of most of the studies presently performed at various laboratories in Russia. These studies are carried out in two directions. The first is in developing the potential for conducting experiments on projectile acceleration over a wide range of electric pulse parameters at various projectile masses and velocities. This line of research is primarily related to the work on designing and improving high-power pulsed energy sources and high-current switching devices.

The second is to search for new possibilities of increasing the velocity level and efficiency of EM launchers. This approach is concerned with studying physical processes and phenomena in rail gun channels; electric and heat processes in the chambers of electric discharge launchers; design of new materials; search for new schemes of projectile acceleration and new possibilities of using electric energy for this purpose.

Here, primary emphasis is given to the most significant advances attained in Russia. The most interesting and record values obtained at various laboratories of the world will be mentioned. The most important advances in the first line of research attained recently in Russia are discussed in [1] from results obtained in the second line of research.

Before proceeding to the results, a few preliminary remarks should be made. In the USSR, as in other countries, the idea of electromagnetic launching of solids has a long history. Without discussing the historical aspect of the problem, we shall dwell on studies that had the greatest impact on this line of investigation.

In 1957, L. A. Artsimovich and his co-workers published the results of theoretical and experimental studies on plasma acceleration between two parallel plane electrodes, also known as rails. This method showed promise for accelerating plasma and solids [2]. At the beginning of the 1960s, A. M. Stolov performed a comprehensive study of projectile acceleration in rail guns. For a 2 g mass, velocities of 5.5-6.0 km/s were obtained. However, many of his attempts to reach velocities higher than 6.0 km/s were not successful. The main difficulties were due to erosion of the launcher channel materials [3].

In 1978, S. C. Rashleigh and R. A. Marshall published a paper [4] in which they proposed to accelerate dielectric solids in railguns with a plasma armature. It was expected that this method would decrease the thermal loads on the accelerated projectile and electrodes and yield velocities exceeding those attained on light-gas guns and explosive launchers of solids. Projects to reach velocities of 12 km/s, 15 km/s, and 50 km/s with a projectile mass of the order of one gram have evolved. Sakharov's experiments [5], in which a 2 g aluminum ring, although evaporating, was accelerated to 100 km/s in a rail gun powered by an explosive MC-generator, were widely cited in many papers.

The paper by Rashleigh and Marshall [4], and subsequent projects to reach velocities of 12 km/s, 15 km/s, 25 km/s and higher for a mass of about 1 g, have attracted the attention of many scientists in Russia. However, scientists that were aware of the results reached by Stolov's group were reserved in their estimates for the prospects of reaching the indicated velocities [6,7].

The research program in the USSR and then in Russia included investigation of the potentials of a variety of electromagnetic launchers of solids: rail guns, ET guns, and ETC guns. In this review, we shall briefly mention the most significant advances in the study of these electromagnetic launchers.

Traditionally, two aspects of the potentials of electromagnetic launchers of solids have been studied: basic research and applied (military) research. This paper reports results of basic research and outlines the plans of some research teams for the nearest years.

2 Projectile Acceleration in Rail Guns

The main projects and farthest advances in the attainment of high velocities of solids in rail guns are summarized in a paper [8] that was presented at the previous Megagauss conference, so I shall not dwell on them. However, in the last two years there have been essentially no new results in the attainment of high velocities in acceleration of small masses (~1-10 g) in plasma armature rail guns. The highest velocities are, with small fluctuations, in the range of 6.0 -7.0 km/s.

The main line of investigations involves analysis of physical processes and phenomena that hinder the attainment of high velocities in rail guns, and searches for new ideas and possibilities.

It is shown [9] that the use of composite materials can considerably increase the critical current density. Experiments on erosion of Mo/Cu and W/Cu electrodes produced by explosive compaction of powders showed that, under certain conditions, erosion of these materials can be one third the erosion of pure Mo and W and one tenth the erosion of pure Cu electrodes, and this is not the limit. However, the question of whether use of these materials in rail guns can lead to velocities much higher than those presently attained remains open until experiments are performed.

Poltanov [10], who proposed and developed a number of new framework-matrix type composites, obtained similar results. These materials show increased (by 4 or 5 times) erosion resistivity in tests compared to the traditional materials used in electromagnetic accelerators.

Important results were obtained at the Institute of High Temperatures [11]. It was shown that the regime of EM launching in a plasma armature rail gun is absolutely unstable due to the restricted ability of the barrel to transfer electromagnetic energy to the projectile through the tail of the RG armature.

Presently, several groups of researchers are discussing prospects of multistage rail guns (see [1]) but, as far as I know, there have been no experimental results that deserve consideration.

In the second scientific trend, acceleration of large bodies having a mass of several hundreds of grams to several kilograms, a number of outstanding results were obtained. Projectiles of mass 1-2 kg were accelerated to velocities of 2.5-4.0 km/s [12]. Acceleration of a 3.5 kg projectile to a velocity of 1700 m/s, and of a 0.35 kg mass to a velocity of 2230 m/s has been reported [13].

Considerable attention has been given to the experimental and theoretical study of processes in sliding metal contact and to the search for methods of increasing the critical velocity. Several significant results obtained in the solution of this problem should be mentioned.

A qualitative theory of a failure wave for metal contact has been developed and tested experimentally [14,15]. Some methods of stabilizing metallic contact have been analyzed. These methods include the application of highly resistive layers, such as graphite layers, on rails, and reinforcement using materials with a special spatial orientation of binary electroconducting structures [15].

In a rail gun with a metal armature, a critical velocity $V_{cr} > 2.5$ km/s of metal contact was obtained in a channel made of common electrical materials. The channel caliber was 10 mm, the current was 300 kA, and the preliminary acceleration of a 2 g body was 500 m/s. An increase in V_{cr} was achieved by improving the channel design.

The most important advances of the group of Yu. A. Kareev from TRINITI were attained in studies of solid state electric contact in a rail gun with rails covered by a graphite layer [16]. An aluminum armature with a mass of 2.6 g was accelerated by a sinusoidal current of 390 kA up to a velocity of 4.6 km/s with retention of solid-state contact.

This group also proposed and studied experimentally a new technique for increasing the critical velocity. The technique was called the method of Dynamic Current Distribution (DCD) over the entire contact surface of a projectile [17]. This method is as follows: during projectile acceleration, a narrow localized region of current is moved along the contact surface of the body in the direction opposite to the velocity. This method uses special rails, and a body moving along these rails can be in contact alternatively with one or two teeth through which the current flows.

This group plans to continue the work using the DCD method. Investigations will emphasize a further increase in V_{cr}. Thus, it is necessary to examine in detail the electrodynamics of an elasto-plastic armature in the channel (in a 3-D field and current pattern).

In my opinion, mention should be made of the investigation of multi-rail launchers with series connection of their rails, having an increased linear inductance of 6 to 20 μH/m [17,18]. The working current of this multi-turn rail gun is significantly lower than that of traditional rail guns with the same accelerating force. This decreases heat losses in energy supply lines and erosion of the rail gun channel.

Two variants of such rail guns were designed and tested [17]: RBM-3, which has three pairs of rails, channel cross section of 40x30 mm^2, length 1 m, $L' = 6$ μH, for launching 0.1-0.3 kg projectiles at velocities of 1500-900 m/s; and RBM-5, which has five pairs of rails, channel cross section 80x70 mm^2, length 0.5 m, $L' = 19$ μH/m, in which a 1.3-kg projectile is accelerated to a velocity of 710 m/s. Future experiments will show whether it is possible to obtain record velocities on this railgun.

3 ET and ETC Launchers

The problem of acceleration of large bodies to high velocities is primarily related to the study of the potentials of using launchers for military purposes. Investigations performed theoretically and with model-caliber systems indicate the existence of optimal penetration velocities that are considerably higher than those achievable by conventional gun technologies. To attain these velocity levels, it is necessary to improve the existing gun technologies and develop new technologies (electric or electromagnetic guns). Among the results obtained recently for ET - launchers, the following deserve attention.

A paper [19] describes experiments in which 1.9 kg projectiles have been accelerated to muzzle velocities of 2400 m/s. Recently, ET launchers were employed in an investigation of the interaction of a multibar projectile with various types of targets over a velocity range of 1.8–2.2 km/s. These investigations solved problems of the stability of multi-component projectiles in a launcher and the aerodynamic stabilization of the projectile in free flight. Projectiles of this configuration with a total mass of about 160 g are accelerated to velocities of ~2000 m/s [20]. The high level of required energy is a main drawback that limits the use of EM launchers.

In recent years, electrothermal-chemical launchers have attracted considerable interest. It is expected that the use of small amounts of electric energy would make it possible to efficiently control propellant combustion and to increase the projectile velocity [21]. Furthermore, ETC launchers can diminish the spread of the final projectile velocity [22] and decrease (in essence, eliminate) the dependence of the projectile velocity on the ambient and cold temperature [23]. Among recent studies, mention should be made of papers [24, 25]. Experiments on model ETC launchers in which the projectile velocity was increased by 19% (819 m/s for conventional ignition and 976 m/s for ETC ignition) are described in [24]. The increase in the kinetic energy was 35%.

Similar results have been reported in [1,25]; approximately a 15% increase in the velocity is obtained (796 m/s and 917 m/s, respectively). The increase in kinetic energy was 33%. Obviously, the ETC concept assumes even higher integration of knowledge than in studies of conventional guns. Therefore, comprehensive basic research in this case is very important.

4 Conclusion

Analysis of the modern state of research in the electromagnetic acceleration of solids show that significant advances have been achieved in all of the critical elements of electromagnetic launch technology. No physics show stoppers have emerged; however, important physics and engineering challenges remain. Previously, research programs have been substantially redirected to better understand the fundamental properties of physical processes that hinder the attainment of high velocities, high performance, and high efficiency for EM guns.

References

1. Shvetsov, G. A., Rutberg, Ph. G., Kolikov, V. A., Electric launch in Russia. A Review of Recent Results, Proc. of the 9th EML Symposium, Edinburgh (1998) (in press).
2. Artsimovich, L. A., Luk'yanov, et al., Electrodynamic acceleration of plasmoids, *Zh. Tekh. Fiz.*, **33**, No. 1 (7), (1957) pp. 3-8.
3. Stolov, A. M., Report of Efremov Research Institute of Electrophysical Apparatus (1964).
4. Rashleigh, S. C., Marshall, R. A., *J. Appl. Phys.*, **49** (1978) p. 2540.
5. Sakharov, A. D., Explosive magnetic generators, *Usp. Fiz. Nauk.*, **88**, No. 4, (1966) pp. 725-734.
6. Shvetsov, G. A., Titov, V. M., Anisimov, A. G., et al., Rail gun accelerators of macroparticles, Proc. of the 4th Int. Conf. on Megagauss Magnetic Field Generation and Related Topics, Santa Fe, (1986), pp. 775-794.
7. Shvetsov, G. A., Titov, V. M., Anisimov, A. G., et al., Rai gun accelerators of macroparticles: hopes and reality, Proc. of the 5th Int. Conf. on Megagauss Magnetic Field Generation and Related Topics, Novosibirsk (1989), pp. 767-772.
8. Shvetsov, G. A., Titov, V. M., Electromagnetic launchers. Achievements. Problems. Perspectives, Proc. of the 7th Int. Conf. on Generation of Megagauss Magnetic Fields and Related Topics, Sarov (1996). (in press).
9. Shvetsov, G. A., Maly, V. J., Anisimov, A. G., et al., Erosion of explosively compacted Mo/Cu and W/Cu electrodes in high-current arc discharges, Proc. of the 7th Int. Conf. on Generation of Megagauss Magnetic Fields and Related Topics, Sarov (1996). (in press).
10. Poltanov, A. E., Dgidailo, N. A., et al., Study of new materials for rail gun launchers, *IEEE Trans. on Magnetics*, **33**, No. 1, (1997) pp 406-409.
11. Ostashev, V. E. Fortov, V. E., Summary of HEDRC - IVTAN rail gun investigations, *IEEE Trans. on Magnetics*, **33**, No. 1, (1997) pp. 589-593.
12. Fair, H. D., Electromagnetic Launch, A review of the US National Program, ibid., pp. 11-16.
13. Haugh, D., An update on the UK electric gun research program, ibid., pp. 17-20.
14. Glinov, A. P., Farkova, N. A., About influence of contact resistance on current skin in rail gun, Proc. of the 5th European EML Conf., Toulouse, paper No. 14 (1995).

15. Glinov, A. P., Kotova, L. G., Halimullin, Yu. A., About crisis of high-speed metal contact in rail gun, ibid., paper No. 6.
16. Yu. A. Kareev, L. G. Kotova, A. T. Kucharenko, and Yu. A. Halimullin, "Investigation of the metal contact crisis in railguns with resistive rails," ibid., paper No. 22.
17. Kondratenko, A. K., Poltanov, A. E., et al., Analysis of some variants of multirail systems with close magnetic coupling, Proc. of the 9th EML Symposium, Edinburgh (1998), (in press).
18. Poltanov, A. E., Kondratenko, A. K., et al., Experimental; study of multirail launchers with high inductance gradient, Proc. of the 9th EML Symposium, Edinburgh (1998), (in press).
19. Weise, Th. H. G. G., Electrothermal Gun Research in Europe. Summary of major activities and results obtained from German and Franco-German R&D Programs, *IEEE Trans on Magnetics*, **33**. No. 1, (1997) pp. 21-25.
20. Savvateev, A. F., Budin, A. V., Kolikov, V. A., Rutberg, Ph. G., Launch Package for Multiple-Rod Hypervelocity Impact Investigation, (to be published).
21. Oberle, W. F., Wren, G. P., An analysis of ballistic parameters/mechanisms affecting efficiency in electrothermal-chemical (ETC) guns, *IEEE Trans. on Magnetics*, **33**, No. 1, (1997) pp. 310-315.
22. Kaplan, Z., Melnik, D., et al., A fluid study of a hypervelocity solid propellant electrothermal 105-mm launcher, *IEEE Trans. on Magnetics*, **31**, No. 1, (1995) pp. 425-430.
23. Chaboki, A., Zelenak, S., Isle, B., Recent Advances in Electrothermal-Chemical Gun Propulsion at United Defense, L. P. *IEEE Trans. on Magnetics*, **33**, No. 1, (1997) pp. 284-288.
24. Goodell, B., Staierr, D., Dyvik, J., Chaboki, A., Potential Army Applications of Electrothermal-Chemical (ETC) Gun Propulsion. Proc. of the 9th EML Symposium, Edinburgh, 1998 (in press).
25. Shvetsov, G. A., Luk'yanchikov, L. A., Bashkatov, Yu. L., Grigor'ev, V. V., Search for the methods of controlling the regression of energetic materials and high-velocity acceleration of solid bodies, to be published.

MORE THAN 20 MG MAGNETIC FIELD GENERATION IN THE CASCADE MAGNETOCUMULATIVE MC-1 GENERATOR

B. A. BOYKO, A. I. BYKOV, M. I. DOLOTENKO,
N. P. KOLOKOL'CHIKOV, I. M. MARKEVTSEV,
O. M. TATSENKO, A. M. SHUVALOV
RFNC-VNIIEF, Sarov, Russia

Design of the MC-1 cascade generator with a cascade system of liner acceleration was predicted by calculations and proven experimentally. The most important components of the explosive liner compression system were modified and their main characteristics measured. The initial parameters of the final variant of the cascade MC-1 generator are: external diameter of the main HE-charge is 650 mm, HE-charge total weight is about 170 kg, initial internal diameter of the first cascade is 175 mm, length is 500 mm, and internal diameters of the second and the third cascades are 28 and 12 mm, respectively. In its two final tests the generator, whose initial magnetic field was about 120 kG, had a final magnetic field reaching >20 MG in the first experiment and more than 28 MG in the second, measured with optical diagnostics. This is the maximum value of magnetic fields measured directly on Earth. The volume diameter of the maximum magnetic field is ~4 mm.

1 Introduction

The interest in ultra-high magnetic fields is created by the ability to accumulate high energy densities in a magnetic field. The transition from a range of 10 MG fields to those having a factor of 2 to 3 times higher field strength was mastered through the cascade magnetocumulative generator (MCG) developed by the authors [1,2]. The MCG significantly increases experimental capabilities for studying material properties under extreme conditions. As a result of long-term work at VNIIEF on developing magnetic cumulation, a MC-1 cascade generator producing a magnetic field greater than 20 MG was created. Following is a brief description of the MCG design, experimental set-up and test results.

2 Cascade Generator Design

Developed at VNIIEF, the cascade MCG can reach record reproducible magnetic fields of ~10 MG. It is now a serial production device used in various studies in ultra-high magnetic fields. However, the power of the magnetic flux compression system of this generator cannot obtain fields significantly higher than 10 MG. To overcome this limitation, it was proposed to increase the amount of explosive by a factor of two for the outer diameter and about a factor of 10 in mass. Fig. 1 shows cross sections of both small and large MCGs, their main units and radial sizes. The large MC-1 generator is supplemented by the cascade gas-dynamic compression unit containing the main HE charge, impactor and internal HE charge.

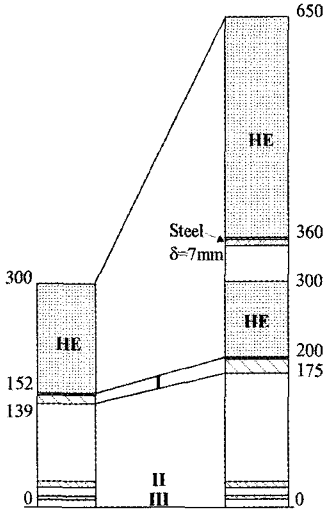

Figure 1. Cross-section of three cascade generators. 10 MG range MC-1 generator (left); 20 MG range MC-1 generator (right). Diameters are given in mm.

The first experiments with the new MCG design proved that we chose the right approach in order to double the final value of obtained magnetic fields [3,4]. We then modernized the HE initiation system, aiming to improve the detonation wave shape. We proposed and tested a new material for generator inner cascades, and evaluated and modified methods of diagnostics and measuring. We performed two full-scale experiments using a model of a large generator with a modified system of initiating a cylindrical detonation wave. The experiments aimed to determine the shock symmetry at the impactor and the first generator cascade diameters. During these experiments, contact probes measured the time at which the liner impacted the probe. The probes were located at 356 mm and 175 mm diameters, in four opposite directions, pitched along the axis at 20 mm and 15 mm. There were a total of 100 probes. The experimental results show that the time difference at the first diameter in the 200 mm long central region is < 0.1±0.12 μsec in the first experiment and 0.09±0.13μsec in the second; the time difference at the second diameter at the 150 mm length is 0.08±0.15μsec in the first experiment and 0.11±0.2μsec in the second.

The MCG liner is compressed by a simple, one-cascade system of gas dynamic cumulation, consisting of a large HE charge with a mass of about 170 kg, a steel impactor with a 7 mm thickness optimized by numerical calculations and a dielectric pad as an internal HE charge with a mass of about 15 kg. In both cases the explosive is TG 50/50. The velocity of the MCG first cascade liner is about 6 km/s, a factor of 1.5 higher than that of the small generator and a little higher than if a total volume of HE charges, impactor and gap were filled with HE.

The first cascade of a large MCG is similar to a solenoid-liner of a small MCG, made of close packed copper insulated wires having an insulating layer and a back output [5] with an increased cavity area and mass of about a factor of 1.5. The proposal was to use a composite material based on the powder of a heavy metal (Tungsten), and a polymeric binding (polypropylene or Teflon), as a material for the inner second and third cascades instead of a composite of close-packed insulated copper wires [6]. This material allows the initial density of the liner kinetic energy to be increased twice, resulting in a higher value of the final field. However, experiments with large and small MCGs, based on various material combinations for inner cascades, showed that the material conductivity appeared to be lower than that of the wire composite, while large-sized imploding liners used the advantages of the powder composite only if the final liner diameter was large enough [7]. In the final version of a large MCG the final magnetic field has small dimensions; the MCG has inner cascades made of wire composite with diameters of 28x35 mm and 12x17.5 mm.

Many efforts were made to develop reliable optical methods to measure magnetic field, digitize the field and analyze the data. Efforts to create a small, multi-channel measuring unit less than 5 mm in diameter with inductive probes and fiber input-output of a probing light failed due to inexplicable interruption of the light that passed through the fibers. A measuring unit consisting of a ceramic tube with an outer diameter of ~3.5 mm, containing an optical probe inside and inductive probes of varying sensitivities outside worked well. The light to and from the probe was delivered by air, then split into two beams and delivered to two photo receivers by polarizers-analyzers having polarization axes turned relative to each other. The measuring unit had an overall diameter of less than or equal to 4.5 mm.

3 Experimental Set-up

The shot with a big MC-1 generator has the following configuration (see Fig. 2): A unit with a HE charge is installed on the platform provided by aligning units. Other MC-1 components such as a steel impactor, inner HE charge, or solenoid-liner are individually fixed to the main unit. A solenoid is then connected to a power source (helical MCG of HMC-320 type) by 72 coaxial cables 8 m in length. The component containing inner cascades and a measuring unit is placed into a solenoid. Probes are connected to measuring cables. The optical measurement system is aligned. Then the control equipment, synchronization, diagnostics and measuring equipment are checked. Finally, the HMC-320 charge and the main MC-1 charge are detonated.

In the first experiment, the second MC-1 cascade was made of a powder composite with an initial density of 10 g/cm^3; the third cascade was of a wire composite. The measuring unit has three channels: two fiber and one air. Optical probes in the ceramic tubes are made of heavy flint glass of different lengths. Probe signals describe all three stages of the experiment in details when the voltage across even the smallest probe is higher than 1 kV: powering of HMC-320 generator, powering of MC-1 generator solenoid by HMC-320, magnetic field increase up to >6 MG by MC-1 generator. The data from various methods and probes agree well and complement each other. However, the signal stopped passing along fiber lines before the field reached its maximum. The optical signal in the air channel appeared to be very noisy, which made it difficult to acquire information on the increase of the amplified field. However, the results of the signal analysis by several independent operators agreed, which allowed us to consider that the maximum magnetic field measured in the shot was higher than 20 MG.

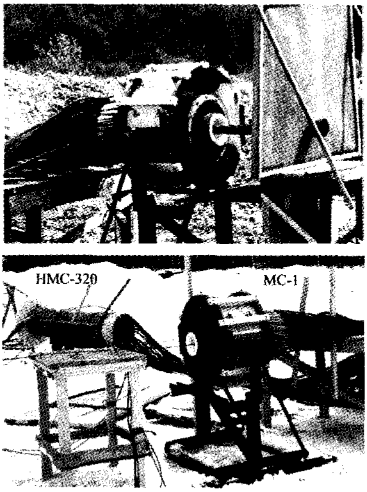

Figure 2. The upper picture shows the MC-1 generator ready to work. The lower picture shows the entire experiment with the initial field power source HMC-320 and the MC-1 generator with measuring cables.

In the second experiment both cascades were made of wire composite. The measuring unit had one air channel. We measured the signals of all the probes and methods and determined the time dependencies of the magnetic field and its derivative. A complete set of MC-1 characteristics also includes the trajectory of imploding liner D(t) and the curve of the magnetic flux conservation coefficient Fi(t). To construct the curve D(t) we used moments of impact between the cascades visible on dB/dt oscillograms, the measured time when the field amplification stopped and the reasonable connection of these points on the r-t plane. After that, we determined the curve of the magnetic flux conservation coefficient Fi(t) and checked whether it is monotonously decreasing. Finally, we checked the reliability of the experimental data by comparing them with the calculations. As a result, we got a set of calculated curves and experimental dependencies B(t), D(t) and Fi(t), presented in Fig. 3. All three parameters measured in the experiment agree well with each other and with the calculations, which is especially valuable. A little discrepancy in the curves at the end of the process may be explained by some insignificant violation of the cascade symmetry, which is not taken into account by the 1-D numerical model. Thus, we can say that we got a complete picture of phenomena in the cascade MC-1 generator at the field level of more than 20 MG.

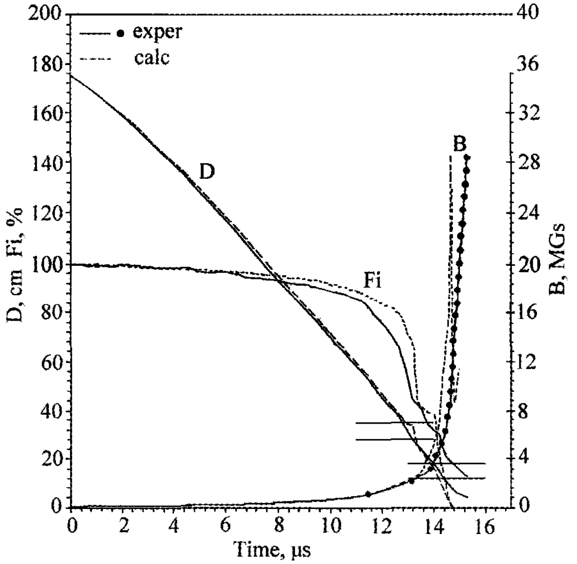

Figure 3. Main parameter curves of the ultra-high magnetic field generator of 20 MG range: inner liner diameter D(t), magnetic field B(t) magnetic flux conservation coefficient Fi(t). Experimental data and calculation results are shown.

4 Conclusions

The data of the last shot with a cascade MC-1 generator allows us to discuss magnetic fields higher than 28 MG measured for the first time in the world under terrestrial conditions. In a volume of about 3 cm^3, we reached an energy >3.1 MJ/cm^3, which is a factor of 370 higher than the density of the HE chemical energy. The flux density of the energy generated the cumulation volume reached a value of ~5 TW/cm^2, the current amplitude was >500 MA.

The cost, complexity, volume of equipment, and level of participation in experimental procedures for an experiment with a MCG in the 20 MG range of ultra-high magnetic fields far exceeds that for an experiment with an MCG in the 10 MG range. Therefore, the especially rigid requirements concerning the reliability of equipment and diagnostics were presented. This unique experiment, due to its complexity and cost, first requires the development of well thought-out goals and problems posed before its undertaking. The authors call on the international scientific community to advance proposals and to participate in joint experiments for the application of the developed generator of pulsed ultra-high magnetic fields for research or other purposes.

Acknowledgments

All activity was performed under ISTC project #237-95. The authors cordially thank the large team that had an essential role in the development of the generator: the project participants, the VNIIEF firing point team and the foreign project collaborators M. Sheppard and F. Herlach.

References

1. Pavlovskii, A. I., et al., Reproducible Generation of Multimegagauss Magnetic Fields. In: *Megagauss Physics and Technology*, Ed by P.J.Turchi, Plenum Press, NY and London (1980) pp. 627-639.
2. Pavlovskii, A. I., et al., Kaskadny magnitokumulyativny generator sverkhsil'nykh magnitnykh poley. In: *Sverkhsil'nye magnitnye polya. Fizika. Tekhnika. Primenenie.* Ed by V.M.Titov and G.A.Shvetsov, Moscow:Nauka, (1984) pp. 19-22.
3. Pavlovskii, A. I., et al., Generatsiya vosproizvodimykh impul'snykh magnitnykh poley do 20 MGs. *Sov. Doklady AN SSSR*, **334** 3 (1994) pp. 300-303.
4. Pavlovskii, A. I., et al., Cascade Magnetocumulative Generator of 20 MG Range Magnetic Fields. In: *Megagauss Magnetic Fields Generation and Pulsed Power Applications*. p. 1. Ed. by M.Cowan and R.B.Spielman, Nova Science Publishers, Inc., New York (1994) pp. 141-148.
5. Pavlovskii, A. I., et al., Solenoid nachal'nogo magnitnogo potoka vzryvomagnitnogo generatora MK-1. *Sov. PTE*, **5** (1979) pp. 195-197.
6. Bykov, A. I., et al., MK-1-generator sverkhsil'nykh magnitnykh poley s kaskadami iz poroshkovogo kompozitnogo materiala. In: *Megagauss and Megaamper Pulsed Technology and Applications*, Ed by V.K.Chernyshev, V.D.Selemir and L.N.Plyashkevitch, Sarov, VNIIEF, (1997) pp.133-136.
7. Aseeva, V. V., et al., Investigation of Conducting Properties of MC-1 Generator Cascades Material from Powder Composite. This conference report.

ULTRA-HIGH MAGNETIC FIELDS GENERATION USING A DISK FLUX COMPRESSION GENERATOR OF ENERGY

V. D. SELEMIR, V. A. DEMIDOV, A. A. KARPIKOV,
YU. V. VLASOV, S. A. KAZAKOV, N. P. KOLOKOLCHIKOV
VNIIEF, Sarov, Russia

We propose to generate an ultra-high magnetic field greater than 10 MG on the basis of a z-pinch liner powered with a fast disk flux compression generator (DFCG) and a MC-1 generator. A mathematical model of the electromagnetic liner acceleration and the magnetic flux compression when DFCG current passes through the liner in z-pinch geometry is formulated. The DFCG was simulated magnetohydrodynamically as a variable inductance with set time dependence according to calculated and experimental results. Numerical simulations were made on the basis of a system of one-dimensional equations of MHD in Lagrange variables together with differential circuit equations for the DFCG and liner. DFCG and liner parameters were determined by calculations, allowing us to obtain a magnetic field greater than 10 MG in a cylindrical volume of 5-10 cm length and 3-5 mm radius.

1 Introduction

Magnetic fields of 10 MG and more are necessary to obtain high-temperature plasmas, study material properties under extreme conditions and for other investigations. Ultra-high magnetic fields are currently generated by magnetic flux compression in a cavity confined by a cylindrical conducting shell, accelerated either by a charge of high explosives (MC-1 generator [1]) or electro-dynamical forces (θ-pinch [2], Z-pinch [3]).

Relatively low velocity of the shell compressing the magnetic flux is one of the factors limiting the magnetic field in a MC-1 generator. Higher velocities can be achieved using the electrodynamic method of liner acceleration. There are some projects to produce 10-20 MG magnetic fields with devices based on Z-pinch and powered by the capacitor banks "Pegasus" and "Atlas" in Los Alamos National Laboratory, USA [4].

The scheme for generating a magnetic field pulse greater than 10 MGs in a cylindrical volume of 5-10 cm length and 3-5 mm radius, jointly using MC-1 and DFCG generators, is proposed in this paper.

2 The Scheme of Obtaining Ultra-High Magnetic Fields with DFCG and MC-1

The liner (5) and reverse current conductor (3) move under the influence of azimuthal magnetic field B_φ, created with the DFCG current I (4), and compress the external axial magnetic field B_z. Field B_z is created by the MC-1 generator solenoid (2) and accelerated by the HE-charge (1). The liner (5) and reverse current conductor (3) will be created similar to [1], which will provide their conductivity in the azimuthal direction at a set time.

We propose using a 240 mm diameter multi-element DFCG (DFCG-240) [5] as a power source. DFCG-240 will provide a current of ~70 MA with a load of 10 nH having a characteristic rise time of ~3 μs, i.e. the power of this device will be on the same order as the projected "Atlas" device [4]. A 20-element DFCG with a 480 mm diameter (DFCG-480) [5] would provide a current of ~140 MA with a load of 20 nH having a characteristic rise time of ~7 μs. The power of this DFCG significantly exceeds the power of the "Atlas" device.

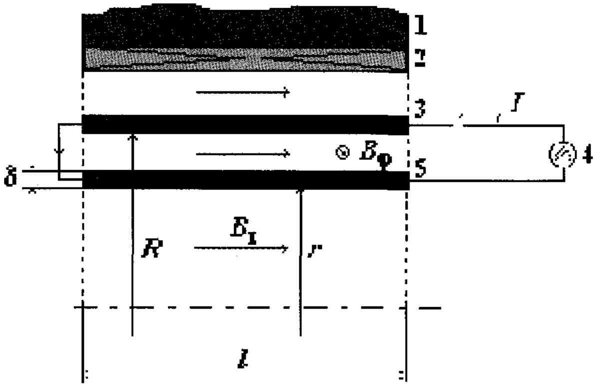

Figure 1. The scheme to obtain ultra-high magnetic fields using DFCG and MC-1. 1-MC-1 generator HE charge, 2-MC-1 solenoid, 3-reverse current conductor, 4-current source (DFCG), 5-liner, B_z -axial magnetic field of MC-1 generator, B_φ -azimuthal magnetic field of the source, I -current of the source, R -internal radius of the reverse current conductor, r -liner internal radius, δ -liner thickness, l -liner length.

As is mentioned in [4], the liner should collapse without total evaporation, significant development of instabilities or destruction during power source operation. By using DFCG current sharpening utilizing an explosive opening switch [6], it could be possible to decrease instabilities and accelerate thinner liners to higher velocities. To suppress instabilities, it is also possible to use a multi-cascade liner system similar to [1].

3 Mathematical Model

Numerical simulations were performed by the solution of a one-dimensional MHD equation system in Lagrange variables for two components of the magnetic field B_z and B_φ, material density, specific internal energy, and material velocity in the cylindrical coordinate system [7]. The motion of the MC-1 generator solenoid was not considered in our former calculations. The value of the radius of the reverse current conductor R was not changed during the calculation. The DFCG was simulated with variable inductance, connected in series with the liner. The time dependence of the inductance was known from the calculated and experimental data. The equation of state and conductivity of copper was determined from reference [8], and for aluminum from [9].

4 Calculating Results and their Analysis

Calculations for several proposed liner designs in a circuit were performed. The quantity of generator elements, liner material and length, its internal radius and thickness, and the initial value of the magnetic field were varied. Results of a calculation are presented in Figure 2.

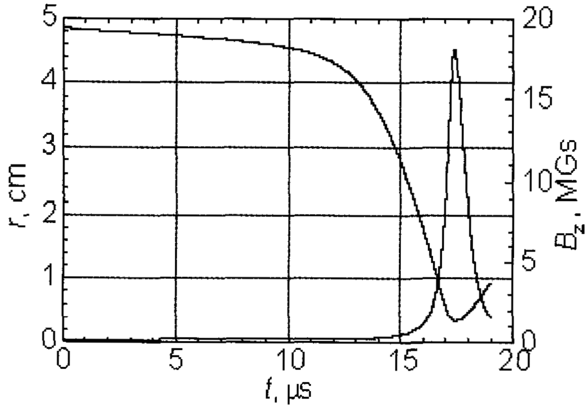

Figure 2. Calculated results of the flux compression under the influence of DFCG current.

In this calculation we considered a 20-element DFCG-240 and an aluminum liner 10 cm in length, having a 5 cm internal radius and 3 mm thickness. In a cavity of 3 mm final radius, we obtained magnetic field of 18 MG having a full width at half maximum of 0.9 μs. These characteristics are realized at a DFCG current of 50 MA. Calculations show that the magnetic field in a cylindrical cavity with a radius not less than 2 mm and a length of 5 cm is ~30 MG at a current of ~ 90 MA. An important feature is the low characteristic rise time of the magnetic field (~0.5 μs), which is necessary for producing high-temperature plasma. Liner designs considered here are feasible.

5 Conclusions

We propose to generate an ultra-high magnetic field greater than 10 MG on the basis of a z-pinch liner powered with a fast DFCG. Numerical simulation was made on the basis of a system of 1-D MHD equations in Lagrange variables together with differential circuit equations for the DFCG and liner. We considered a 20-element DFCG-240 and aluminum liner 10 cm in length, having a 5 cm internal radius and 3 mm thickness. We obtained an 18 MG magnetic field having a full width at half maximum of 0.9 μs in the cavity having a 3 mm final radius. These characteristics are realized at a 50 MA DFCG current. An important feature is the low characteristic rise time of the magnetic field (~0.5 μs), which is necessary for producing high-temperature plasma.

References

1. Pavlovsky, A. I., et al., Cascade Magnetocumulative Generator of Ultra-high Magnetic Fields. In. *Ultra-high Magnetic Fields. Physics. Technique. Application.* Ed. by V. M. Titov , G. A. Shvetsov, M. Nauka. (1984) pp. 19-22.

2. Miura, N., Chikazumi, S., Computer Simulation of Megagauss Field Generation by Electromagnetic Flux-Compression. *Japanese J. Appl. Phys.* **18** v.3. (1979) pp. 53-564.
3. Alikhanov, S. G., et al., The Production of Pulsed Megagauss Fields by Compression of the Metallic Cylinder in Z-Pinch Configuration. *J. Phys. E.* **1** No. 2. (1968) pp. 543-545.
4. Sheppard, M.G., et al. Multu-Megagauss Field Generation Using Capacitor Banks. In. *Megagauss and Megaampere Pulse Technology and Applications.* Ed by V. K. Chernyshev, V. D. Selemir, L. N. Plyashkevich. Sarov. VNIIEF. (1997) pp. 205-212.
5. Demidov, V. A., Kazakov, S. A., Kravchenko, A. S. et al., High-Power Energy Sources Based on the FCG Parallel and Serial Connection. In: *Digest of Technical Papers 11th IEEE International Pulsed Power Conference*. Ed. by G. Cooperstein, I. Vitkovitsky. Baltimore, Maryland. (1997) pp. 1459-1464.
6. Vlasov, Y. V., Demidov, V. A., Demin, A. N. et al., Explosive Magnetic Energy Sources to Generate Low Energy X-Rays Using Liner Implosion. Ed. by M. Cowan, R. B. Spielman. N.Y.: Nova Science Publishers. Inc. (1994) pp. 913-920.
7. Gavrilov, N. F. et al., UP-OK Software for Solution of One-dimensional Tasks of Continuous Medium Mechanics in One-dimensional Complex. VANT. Series: *Methods and Programs of Numerical Solution of Mathematical Physics Tasks*. Iss. 3-11 (1982) pp. 11-14.
8. Bakulin, Yu. D., Kuropatenko, V. F., Luchinsky, A. V. Magneto-hydro-dynamical Calculation of Explosive Conductors. *JTP*. **46** No. 9 (1976) pp. 1963-1969.
9. Bujko, A. M. et al., Investigation of the Dynamics of a Cylindrical Exploding Liner Accelerated by a Magnetic Field in Megagauss Range. In *Megagauss Fields and Pulsed Power Systems*. Ed. by V. M. Titov, G. A. Shvetsov. N.Y. (1990) pp. 743-748.

MULTIPLE-TURN MAGNETOCUMULATIVE GENERATOR

A. J. KARTELEV, V. K. CHERNYSHEV

All-Russian Scientific Research Institute of Experimental Physics, Russia

The description and operating principle of multiple-turn magnetocumulative generators (MCG) are presented here. These generators agree well with a capacitor type source and operate within the same range of magnetic field intensities as a helical or a bar magnetocumulative generator.

1 Introduction

Magnetic fields of the order of 100 T or more are necessary to study superconductors and magnetic materials. A single turn solenoid is very suitable for these studies, but such a system requires a special and expensive capacitor bank having very low inductance and resistance [1].

Foner and Kolm [2] have successfully used a solenoid coil to obtain magnetic fields with an intensity of up to 700 T. Relatively large values of coil inductance allows a reduction of the feed current and the use of technically simple capacitor banks. Furthermore, such a coil has a high mechanical strength.

Another method to obtain magnetic fields of 75–110 T is to apply MCG of a helical [3] or a bar [4] type. The advantages of these MCGs are their simplicity and efficiency; their disadvantages are their low inductance and the need for high feeding current and energy. Thus, it is necessary to use a large number of power cables and a capacitor bank with capacitance 5–10 times exceeding the generator feeding energy to feed these generators.

This report presents the description and operation principle of the two versions of the new multiple turn MCG proposed by the authors in 1988 [5].

2 Multiple Turn MCG Design

1.1 Cylindrical Multiple-turn Generator

The generator contains the external and internal current conducting circuits, a load and a power source (Fig. 1). The external circuit is formed by a multiple-turn cylindrical helix with the load section connected in each turn. The helix and the load are wound with wire having a rectangular cross-section or made of thick metal tubing. The helix turns are enclosed by epoxy compound. There are 6-10 helix turns. The width of the helix turn and load is 2-3 cm.

The internal circuit is shaped like a tube and is filled with explosive. The tube is mounted eccentrically in relation to the helix. HE charge initiation is conducted with a chain of radial electric detonators.

The dimensions of the external helix, the internal tube and the load (serving as an installation for solid body samples and magnetic field probes) are the same as in the known single-turn MCGs.

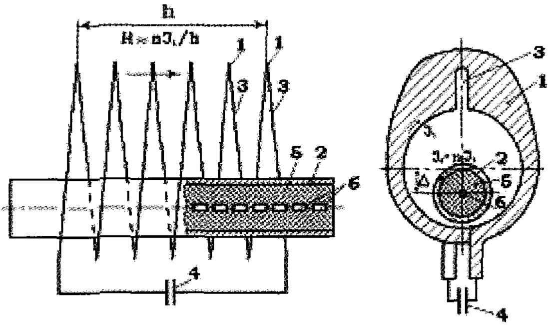

Figure 1. Scheme of a cylindrical multi-turn generator: 1-outer cylindrical coil; 2-inner copper armature; 3-load sections (continuation of HE coil turns); 4-power source; 5-explosive charge; 6-chain of electro-detonators.

2.2 *Toroidal Multiple-turn Generator*

In this generator (Fig. 2) the external current-conducting circuit and the load have the form of toroidal coils and are made of sheet copper 2-5 mm thick.

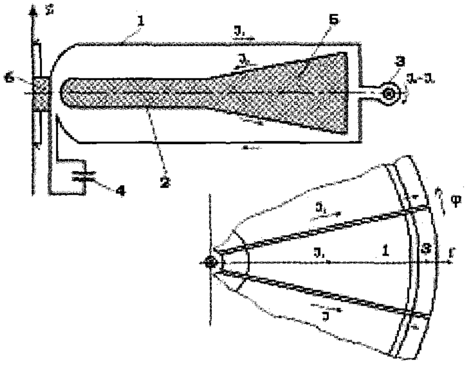

Figure 2. Scheme of a toroidal multi-turn generator: 1-outer toroidal coil; 2-inner copper cassette; 3-load sections; 4-capacitor power source; 5-disk explosive charge; 6-explosives cartridge with two electro-detonators.

The outer diameter of the toroidal coil (without load) is 420 mm, the inner diameter is 40 mm and the thickness is 60 mm. The number of the coil turns and the load is 6 to 12. The coil turns increase in width toward the periphery load sections. The beginning and the end of the toroidal coil are run to the axis and are connected to a capacitor bank.

The internal current conducting circuit resembles a profiled cassette with a 60 mm inner diameter, 114 mm outer diameter and an 18 mm thick center and 54 mm peripheral thickness. The cassette walls are made of 1mm thick sheet copper. The inner cassette space is filled with a trinitrotoluene type high explosive. HE charge initiation system uses two electric detonators and the 40 mm diameter intermediate HE blasting cartridge, installed on the generator axis.

Load sections (turns) are made of the same copper sheet as the toroidal coil turns.

3 Multiple-turn Generator Operation Principle

When connecting the external helix to a capacitor bank, the electric current $I_1 = (u/\omega L_1)\sin(\omega t)$ flows along the helix and load turns, and along the internal tube surface. The current $I_2 = -(L_1 M_{12})I_1 = -nI_1$ flows along the secondary winding of a transformer, where U and C are the voltage and capacitance of the bank; n and L_1 are the number of turns and the external multiple turn coil inductance; $\omega = 1/\sqrt{L_1 C}$ is the primary loop frequency; M_{12} and $K_{cpl} = S_2/S_1$ are mutual inductance and magnetic coupling factor between the external coil and internal tube, S_2 and S_1 are cross-sectional areas of the internal tube and external coil. The initial magnetic flux $\Phi_0 = I_1 L_1$ is introduced into the compression volume (the air space between the external coil and internal tube).

At the moment of maximum feeding current I_1, the electric detonators actuate and initiate the high explosive charge. Under the effect of explosion products the internal tube starts to expand and first touches the section of the coil turns that is opposite the load turns. The power supply is switched off the generator and the ampere-turns nL1 of the external coil are re-switched to the current $I_2 = -nI_1$ of the internal tube. Then the expanding tube slides simultaneously along the insulated, parallel turns of the external coil and presses magnet flux out of the compression volume into the load. In the load, an exponential increase in magnetic field is observed which is proportional to the ratio of cross-sections of the compression-intercircuit space and the load.

4 Conclusions

The division of the external current conducting circuit and the generator load by the slots transverse to the axis into several n>2 switched sections (turns) leads to the fact that during generator initial powering, the current flows n times over compression and load volumes. As a result, the initial generator inductance increases some ten times. Therefore, it is possible to decrease the energy capacity and the cost of the capacitor bank – the souce of the initial feeding – by a factor of about 20.

At the magnet flux cumulation stage, the external coil system consisting of n parallel and insulated current fibers without any physical limitations re-switches to the uniform current sheet – the internal tube or cassette. For a multiple-turn MCG the conductor usage factors, electrical current amplification and energy at the magnetic flux cumulation stage are the same as those for bar, turn, and disk MCGs.

The additional advantage of multiple-turn MCGs is the absence of edge effects and a uniform distribution of current and magnetic field through the load width and perimeter.

References

1. Karasik, V. R., Physics and technology of high magnetic fields. *M. Nauka,* (1964) p. 347.
2. Foner, S., Kolm, H. H., Coils for the production of High-Intensity Pulsed Magnetic Fields, *Rev. Sci. Instr.*, **28**, (1957) p. 799.
3. Pavlovski, A. I., Lyudayev, R. Z., Vasyukoiv, V. A., Ruskov, A. S., Katayev, V. N., Makartsev, G. F., Bukharov, V. F., Magnetocumulative turn generators of fast growing current pulses., Ultrahigh Magnetic Fields., Physics, techniques, application, *M. Nauka*, (1984) pp. 292-297.
4. Knoepfel, H., Ultrahigh pulsed magnetic fields, *M. Mir*, (1972) p. 391.
5. Kartelev, A. Ja., Chernyshev, V. K., Explosive magnetic generator A.s. No. 1588244 (USSR).

GENERATION OF MEGAGAUSS MAGNETIC FIELDS BY INITIATION AND GROWTH OF MHD INSTABILITIES

P. I. ZUBKOV AND K. A. TEN
Lavrentyev Institute of Hydrodynamics, Sibirian Branch of the Russian Academy of Sciences, Novosibirsk, Russia

Estimates of magnetic fields generated by initiating and development MHD-instabilities (m = 0;1) are presented. It is demonstrated that the development of the cylindrical Z-pinch and spiral instabilities produces magnetic fields many times larger than those without instabilities. For a non-cylindrical Z-pinch within the framework of MHD approximation, the magnetic fields generated are formally infinite. Some experimental results are presented.

1 Introduction

Plasma is unstable in electromagnetic fields. In particular, magnetohydrodynamic (MHD), or force, instabilities such as pinches and kinks can evolve. Excitation and growth of these instabilities leads to the increase in inductance of the current-carrying plasma column. The emf of the electromagnetic induction is generated on the increasing inductance. The redistribution of current results in the redistribution switching of magnetic fields. This can be used for the generation of megagauss magnetic fields.

Since our principal aim is to show the possibility of generating strong magnetic fields by the purposeful excitation and development of force plasma instabilities, estimates were made considering the plasma to be ideally conducting. The plasma is also considered as ideal gas. As for the instabilities, they can be induced by the initial boundary conditions or external magnetic fields in a pre-assigned place and at a prescribed time.

2 Generation of Magnetic Field in Z-Pinch

When kinks form in a non-cylindrical Z-pinch [1,2] we simplify the calculation of the inductance L of the plasma column by assuming that it is a step function. We consider a plasma column of length λ equal to the wavelength of the perturbation. The radius of the kink at a distance $\lambda/2$ from the top of the column is equal to r-δ, where r is the equilibrium radius, and δ is a perturbation. In the lower half of the column the radius of the kink is r+δ. In this approximation the external inductance of a plasma column of length λ is

$$L = \lambda \bullet ln \frac{R^2}{r^2 - \delta^2}$$

where R is the radius of the outer current conductor. We obtain the following equation for the induction of the magnetic field in the kink:

$$B = \frac{2 \cdot I}{c \cdot (r - \delta)} = \frac{2 \cdot L_0 I_0}{c \cdot (r - \delta)} \cdot \left(L_0 + \lambda \cdot ln \frac{R^2}{r^2 - \delta^2} \right)^{-1}$$

The constriction in the kink is unbounded in the MHD approximation [1,2], therefore, the above equation has the formal implication that $B \to \infty$ in the limit $\delta \to r$. Consequently, the magnetic induction can be unbounded in the kink. In regard to the space in which a strong magnetic field is generated, we have shown [2] that it can be fixed by the initial and boundary conditions.

For the cylindrical Z-pinch, when it is possible for a train of heteropolar, high-intensity electrical pulses to be generated [2], a train of magnetic field pulses can be generated as well. In this case

$$B_{max} = B_0 \cdot \frac{R \cdot L_0}{r_0 \cdot (L_0 + l \cdot ln(R/r_o))} \approx B_0 \cdot \frac{R}{r_0} ,$$

where r_0 is the stopping radius of the cylindrical Z-pinch. For $R >> r_0$ the maximum induction B_{max} can be much higher than B_0.

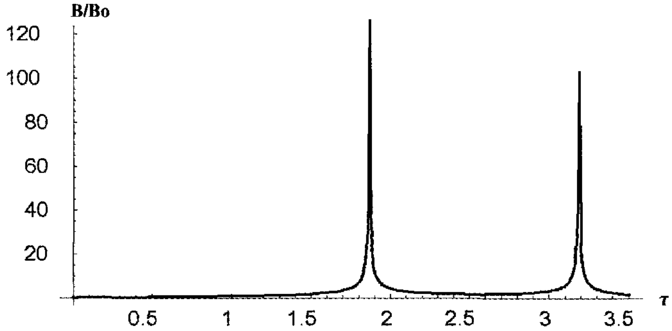

Figure 1.Numerical computation of magnetic field on cylindrical path boundary.

Figure 1 shows the characteristic numerical computation of the magnetic field on the boundary of a cylindrical pinch. A compression of the pinch was computed by the "snowplough" model combined with circuit equations. Results of numerical experiments show that, depending on the initial conditions, magnetic fields can be amplified by several orders of magnitude in comparison with fields without pinch compression.

3 Generation of Magnetic Field by Helical Instabilities

Figure 2 shows an experimental arrangement in which the excitation and development of the helical instability has resulted in the formation of a plasma solenoid. A helical filament 2 is formed from the inner surface of the plastic cylinder 1. A solid fluoroplast (Teflon-like) rod 3, with aluminum foil 4 deposited on it, is tightly fitted into this cylinder. The whole unit is placed in a conducting cylinder 5, which serves as reverse-current conductor. The cylinder 5 is split lengthwise to prevent azimuthal currents from being generated in it. Sensor 6, placed on the axis of the fluoroplast rod, measures the current in the circuit and the derivative of the magnetic field induction.

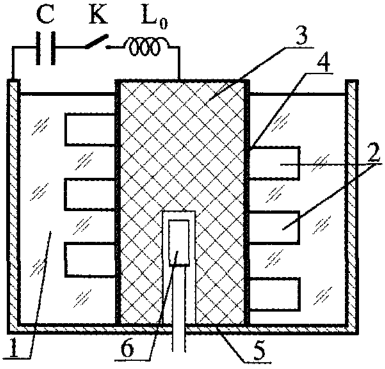

Figure 2. Experiment forming plasma solenoid.

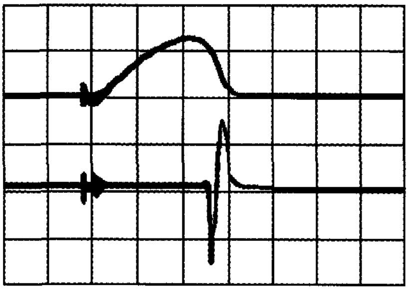

Figure 3. Oscillogram of discharge

Figure 3 shows an oscillogram of discharge, where the upper trace represents the current in the circuit (amplitude 180 kA, sweep rate 10 μs/interval), and the lower trace represents the derivative of the magnetic induction in the center of the rod. The discharge is initially cylindrically symmetric and no axial magnetic field exists on the discharge axis. When the foil explodes under the influence of the flowing current, a plasma channel is formed. It is unstable against an increase in the inductance, and a helical instability develops in it, inducing an axial magnetic field that shows up on the lower trace. The current and the magnetic field change form, and plasma solenoid is formed with an axial magnetic field generated along its axis. The wavelength λ of the helical instability can be predetermined by the boundary conditions. In the reported experiments λ was specified by the pitch of the helical channel.

We consider the plasma to be ideally conducting. This assumption is valid when the characteristic time of evolution of the instabilities is much shorter than the discharge period, as is generally the case. Here, the circuit current I at the instant when the inductance of the plasma channel becomes equal to L owing to the development of the force instabilities, can be determined from the conservation of magnetic flux:

$$L_0 \cdot I_0 = (L_0 + L)I \ ,$$

where L_0 and I_0 are the inductance and maximum current in the unformed loop. The initial inductance of the plasma column is much lower than L_0 so it can be disregarded. It is always possible to achieve the onset of instabilities at near-maximum current, by trial and error, as observed experimentally (Fig. 3).

When a plasma solenoid is formed, the induction of the axial magnetic field B at a helical-instability wavelength λ much shorter than the distance l between electrodes is given by the expression

$$B \approx \frac{4\pi}{c} \cdot \frac{I}{\lambda} \cdot$$

The inductance L in this approximation is

$$L \approx \frac{4\pi^2 r^2 l}{\lambda^2} \ ,$$

where r is the initial radius of the discharge channel. For the magnetic induction B we then obtain the expression

$$B \approx \frac{4\pi}{c} \cdot L_0 I_0 \cdot \frac{\lambda}{L_0 \cdot \lambda^2 + 4\pi^2 r^2 l} \ ,$$

which has a maximum at $\lambda = \left({4\pi^2 r^2 l}/{L_0} \right)^{1/2}$. The channel inductance in this case is $L = L_0$.

The maximum induction B_{max} can be written in the form

$$B_{max} = \frac{1}{2} B_0 \sqrt{{L_0}/{l}} = {B_0 \cdot \pi r}/{\lambda} \ ,$$

where B_0 is the induction of the azimuthal magnetic field on the surface of the cylinder before the onset of the helical instability at the maximum current. If $L_0 >> l$ or $r >> \lambda$, we have $B_{max} >> B_0$.

4 Conclusion

These estimates and experimental results show that force instabilities can be used to generate strong and ultra-strong magnetic fields; in other words they are not always harmful and can even be useful. Nature, if we would promote rather than hinder it, give us powerful methods for the generation of strong magnetic fields, high-strength electrical pulses and the commutation of currents.

Acknowledgments

This work was partly supported by the Russian Fund for Basic Research, Grant No. 95-02-04411.

References

1. Aleksandrov, A. F., Rukhadze, A. A., Physics of High-Current Electrical-Discharge Light Sources [in Russian] (Atomizdat, Moscow, 1976).
2. Zubkov, P. I., Ishchenko, S. M., Ten, K. A., in Proceedings of the Seventh International Conference on the Generation of Megagauss Magnetic Fields and Related Experiments [in Russian] (Sarov, Arzamas Province, 1996), pp. 41-42.
3. Vikhrev, V. V., Braginskii, S. I., in Reviews of Plasma Physics, Vol. 10, Ed. by M. A. Leontovich (Consultant Bureau, New York, 1986) [Russ. original, Atomizdat, Moscow, 1980], pp. 243-248.

INVESTIGATION OF EFFECTIVENESS OF MC-1 GENERATOR CASCADES MATERIAL MADE FROM POWDER COMPOSITE

V. V. ASEEVA, B. A. BOYKO, A. I. BYKOV, M. I. DOLOTENKO,
N. P. KOLOKOL'CHIKOV, O. M. TATSENKO, V. I. TIMAREVA
RFNC-VNIIEF, Sarov, Russia

Results are presented of experimental investigations of composite material properties, based on metal powder and polymeric binding, and offered as MC-1 generator cascade material. The possibility of direct comparison of wire and powder composite properties is realized in specially performed experiments with the cascade MC-1 generator. Along with the earlier mentioned composite properties of higher initial substance density and the possibility of its control within wide limits, composite conductivity greatly depends on the condition of further liner compression after the shock wave passage. If the diameter of a composite liner is so large that the composite compression at the liner implosion is one-dimensional at first approximation, the composite conductivity is small in comparison with the wire composite. This leads to significantly greater losses of magnetic flux. This effect disappears when the cascade radius is small, when its cylindrical shape is noticeable and two-dimensional substance compression occurs.

1 Introduction

The efficiency of the magnetic cumulative generator MC-1 (i.e., final magnetic field value and its volume) is determined by the amount of the liner kinetic energy and its density taken from HE. There exists an optimal liner for each specific HE charge of a definite size and type. Among the variety of liners of differing thickness and material densities, the optimal liner is the thinnest one with the maximum material density. MC-1 cascade material must be non-conducting to allow free diffusion of the magnetic flux inside; at some point it must become conducting to trap the magnetic flux and compress it [1]. In a cascade MCG the cascades are made of densely packed copper insulated wires placed along a cylinder surface. It is a challenge to fabricate such a cascade, and it is difficult to change its initial sizes and impossible to change the initial material density.

Below are results of the conductivity study for another composite material made from metal powder and polymeric binding, whose electric conductivity in the initial state is very low but increases significantly when a shock wave passes.

2 Experiment and Results

We have proposed [2] to use as a cascade material a composite of a heavy metal (Tungsten) powder and a polymeric binder, uniformly and homogeneously mixed and compressed up to a required density. Varying the component ratio can easily change the initial powder density. Machining of the composite is very simple. Its initial electric conductivity, depending on the amount of metal in a mixture, changes from dielectric to metal. When the composite density is high enough, i.e., a factor of 1.5 or 2 higher than wire composite density, its conductivity is still low and the magnetic flux passes through freely.

In all experiments where MCG inner cascades were made of powder, the resulting maximum magnetic field was about 1 MG higher than in similar experiments where wire composite [2] cascades are used. However, how conductive is a composite when a liner compresses a magnetic flux? To find out, we have performed two experiments with a three-cascade MCG. The experimental results and numerical model allowed estimation of the composite conductivity.

In the first experiment we studied the possibility of increasing the weight of the first MCG cascade by a layer of a powder composite on the inside. By sacrificing velocity, this increases kinetic energy concentration at the inner liner layer and increases the efficiency of the energy transfer from the first cascade to the inner cascade, which is also made from the powder composite.

The following is one design of a three-cascade MCG. First, we have a standard solenoid liner with 139 mm inner diameter. Then comes a 0.5 mm air gap with a Tungsten-Teflon composite cylinder with a density of 10 g/cm^3, a 2 mm wall thickness and a linear mass of ~85 g/cm (a bit less than the mass of the first cascade). Then there are the second and the third cascades made of a Tungsten -Teflon composite having a density of 8 g/cm^3 and diameters of 30.7x36.7 and 12x17 mm. When the inner boundary of the first cascade starts its motion, the initial magnetic field is 170 kG. By the time the inner boundary of the heavy layer starts moving, the field is about 190 kG. The final magnetic field measured by induction and optical methods is <6.5 MG.

Fig. 1 shows the magnetic field and its derivative curves at the MCG axis at various scales from the beginning of the flux compression process. The picture shows the beginning of the first cascade implosion, its impact with the heavy layer, layer closure and acceleration. For the remaining phase of MCG operation the picture shows a generalized liner trajectory and the magnetic flux conservation curve inside the powder cylinder.

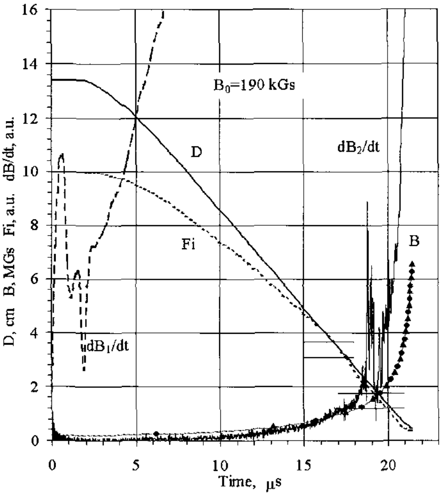

Figure 1. Liner inner diameter D(t), magnetic field B(t), its derivative dB/dt and flux conservation coefficient Fi(t) from the shot with a cylinder of powder composite. Points on B(t) are optical data.

In the second experiment with a three-cascade MCG having wire composite cascades, the initial magnetic field was the same, 190 kG. The inner cascade sizes are standard: 28x35 mm and 12x18 mm. Here, the maximum magnetic field is a little bit less than 6.2 MG, but the field has been measured for more than 1.5 μsec after maximum, the impact over the third cascade is not discovered, i.e. the volume of the maximum field is more than 12 mm.

The results of both shots allow the direct comparison of conducting properties between wire and powder composites for a liner of a large diameter, and (using the experimental result with two-cascade MCG having the second cascade of a powder composite [2]) for small diameter liners. This is shown in Fig. 2, where one can see dependencies of the relative magnetic field $b(d) = B/B_0$ and the magnetic flux conservation coefficient Fi(d) on relative diameter $d = D/D_0$. Fig. 2 also shows a large loss of magnetic flux in a large diameter powder liner as compared to wire composite, and approximately equal loss in small (about the size of the second cascade and less) diameter liners.

3 Discussion

The experimentally discovered poor conductivity of a powder composite in large diameter liners becomes clear if the cross section of both composites is observed. When the wire composite is compressed, in order to compact the wires the wire layer must be moved in a radial direction relative to the adjacent layer by the distance equal to the thickness of the enamel wire insulation. This can be easily accomplished with liners of different sizes, if even a weak shock wave passes. To provide good compaction of metal particles in a powder composite, the compression must develop in two directions: radial and azimuthal. Such 2-D composite compression takes place at small liner radii only under highly cylindrical conditions.

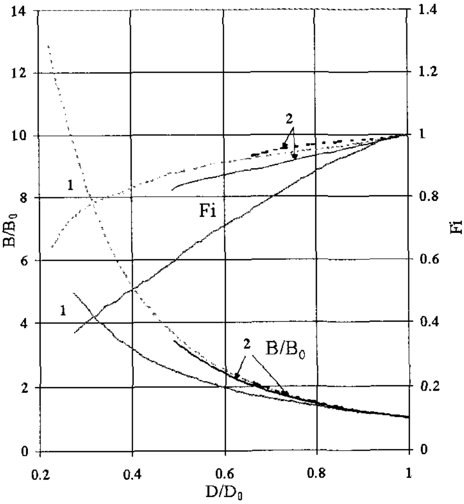

Figure 2. Plots of relative magnetic fields $b=B/B_0$ and magnetic flux conservation coefficient Fi as a function of a relative liner diameter $d=D/D_0$. The numbers indicate:

1 – in the 1st cascade, B_0 =190 kGs, D_{0w}=139 mm, D_{0W}=134 mm;

2 – in the 2nd cascade, B_{0w} =2.94 MGs, B_{0W}=2.31 MGs, D_0=28 mm.

Thus, a composite based on a metal powder can be effectively used as a liner material for MC-1 generators only for cascades of a small (2-4 cm) diameter, and increasing the first cascade weight may be done by producing it from, for example, isolated tungsten wires.

References

1. Pavlovskii, A. I. et al., Kaskadnyi magnitocumulativnyi generator sverkhcilnykh magnitnykh polei. *Sverkhcilnyie magnitnyie polya. Fizika. Tekhnika. Primeneniye.* Ed. by V. M. Titov and G. A. Shvetzov, M: Nauka, (1984) pp. 19-22.
2. Bykov, A. I. et al., MC-generator of ultra-high magnetic fields with cascades of powder composite material. *Megagaussnaya i impulsnaya tekhnologiya i primeneniya.* Ed. by V. K. Chernyshev, V. D. Selemir, L. N. Plyashkevich, Sarov, VNIIEF, (1997) pp. 133-136.

MEGAGAUSS FIELDS DURING MILLISECONDS

L. J. CAMPBELL, D. EMBURY, K. HAN, D. M. PARKIN
Center for Material Sciences, Los Alamos National Laboratory, NM, USA

A. G. BACA, K. H. KIHARA, J. R. SIMS
ESA-DE, Los Alamos National Laboratory, NM, USA

**G. BOEBINGER, Y. EYSSA, B. LESCH, L. LI, J. SCHILLIG,
H. SCHNEIDER-MUNTAU, R. WALSH**
NHMFL, Tallahassee, FL, USA

A non-destructive, one megagauss magnet is now being designed in cooperation between the Los Alamos National Laboratory and the National High Magnetic Field Laboratory (NHMFL) through joint funding by the US Department of Energy and the US National Science Foundation. The design combines two types of pulsed magnet now in use at the NHMFL: a capacitor-driven 'insert' magnet with a total pulse width of order 10 ms and a much larger 'outsert' magnet with a total pulse width of order 2 seconds that is driven by a controlled power source. The insert and outsert produce approximately 1/2 megagauss each. Although the design uses CuAg as the principal conductor, further design efforts and materials development involve exploring CuNb and stainless steel-clad copper as possible future alternatives. A crucial innovation employed wound steel strip (sheet) as reinforcement in both insert and outsert coils. This gives extra strength due to the higher degree of cold-work possible in strip materials. A key role is played by materials development for this leading edge magnet. A major component, the 7-module, 560 MVA controlled dc power supply required for the outsert has been installed and commissioned.

1 Introduction

The promise and possibility of non-destructive 100 tesla (one megagauss) research magnets have been discussed for several years [1,2].

Here, we present progress on the NHMFL/DoE design proposed in 1995 that combines two distinct types of pulsed magnets: a small capacitor driven magnet that requires high power, and a large controlled power magnet that requires high energy [3].

The yield strength of known conductors is much less than the magnetic pressure associated with the energy density of a 100 T field region, $B^2/2\mu_0 = 3.98$ GPa. This pressure can be related to the hoop stress on a wire element at radius r carrying current I in a field B, which is proportional to rIB. Therefore, the hoop stress (or differential magnetic pressure) can be reduced by using a small r or small I, implying a small bore or a large magnet, respectively. However, bore size has a lower limit for experimental usefulness and magnet size has an upper limit for a practical power supply. Existing energy sources and available materials permit a solution to these problems for 100 T in a bore of 15 mm.

2 Design

Many aspects of the NHMFL/DoE design have been considered since 1995 [4]. Not only was the original concept confirmed but the availability of better materials and the use of more accurate design tools have increased the level of safety and design confidence.

The 100 T insert produces 53 T and is similar to high field pulsed magnets commonly found in research laboratories in the pulse length, the bore size, the reinforcement tailored for each layer, the liquid nitrogen (LN) pre-cooling, the weight, and the limited lifetime. The principal difference is the magnetic stress, which is more uniformly distributed over the volume of the insert due to the high background field from the outsert. The high level of this stress calls for greater innovation, design optimization, material strength, and fabrication quality, which will also benefit conventional pulsed magnets. The insert design will continue to evolve.

The mechanical data for the first insert are given in Table I.

Table I
Mechanical Data for Insert Magnet

Layer	Conductor Size (mm)	Turns per layer (mm)	Cond. Layer ID (mm) (mm)	Reinforcement (mm)
1	3.4 x 6.0[a]	31	15	3.5[c]
2	3.5 x 6.6[b]	28	28.8	3.8[c]
3	“	“	43.4	5.6[c]
4	“	“	61.6	7.5[c]
5	“	“	83.6	9.3[c]
6	“	“	109.2	11.0[c]
7	“	“	138.2	12.0[c]
8	“	“	169.2	14.5[d]

[a]GlidCop Al-15™; [b]CuAg; [c]MP35N strip and Zylon; [d]MP35N strip.

Table II
Mechanical Data for Outsert Magnet

Coil	Conductor Size (mm)	Turns per layer/layers	Coil ID/OD (mm)	Shell Thickness
1	5.2 x 7.2[a]	58/4	210/258	27.7[d]
2	“	“	320/368	29.3[d]
3	5.5 x 10.5[b]	“	432/483	35.8[d]
4	“	“	562/613	31.9[d]
5	8.5 x 11.4[b]	66/4	685/759	36.0[d]
6	“	“	841/916	24.9[d]
7	8.5 x 11.4[c]	66/6	976/1087	38.1[e]

[a]CuAg, [b]GlidCop Al-15™, [c]hard Cu, [d]301HYSS strip, [e]304SS

The outsert magnet produces 47 T and has many similarities to the NHMFL 60 T quasi-continuous magnet that was recently commissioned.[5] The outsert's salient features are seven free-standing, mechanically independent coils, divided into three electrical circuits that are sequentially energized. The coils are cooled in LN before a pulse and are predicted to reach LN temperature again in less than one hour following a pulse.

The mechanical data for the outsert are given in Table II. The cross-section for the full magnet is shown in Fig. 1 and the stress distribution in Fig. 2.

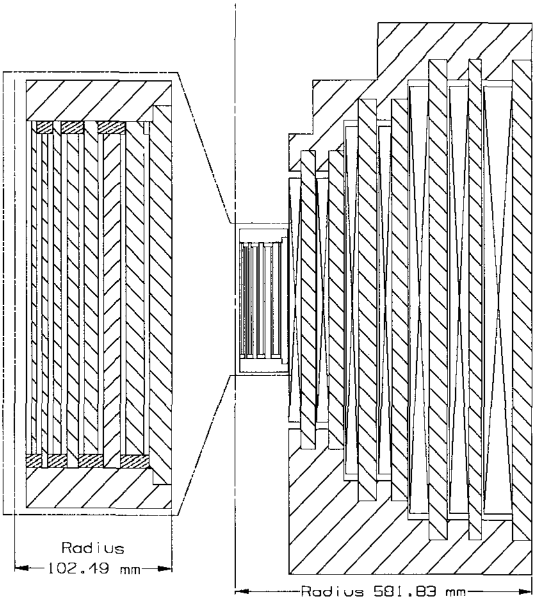

Figure 1. Cross-section of 100 T magnet, with expansion of insert.

3 Materials

The materials properties needed for a 100 T magnet are unprecedented, and achieving these has consumed a large fraction of the effort to date. The conductor wire posed the greatest challenge, and required a joint collaboration between staff metallurgists and manufacturers to achieve a product that permitted a feasible design. Suitable wires must have high strength and high electrical conductivity, sufficient dimensions (up to 5 mm x 8 mm cross-section and 120 m length), and acceptable fabricability, joinability and service life. Possible conductors include Cu-Ag, Cu-Nb, and stainless steel clad Cu (Cu-SS). The fabrication and properties of such wires are discussed in these proceedings (see J. D. Embury and K. Han) and elsewhere [6,7].

The principal wire of choice now for both the insert and outsert is a cold-drawn, co-deformed Cu-(16 at.%)Ag composite, although both Cu-Nb and Cu-SS remain important candidates for upgrades and new insert designs.

As a result of employing strip winding for the reinforcement shells, mentioned earlier, it became possible to employ the 'super alloy,' MP35N, as a reinforcement material in the insert (YS=2.5 GPa, UTS=2.7 GPa, at LN temp.). Likewise, strip winding takes advantage of the cold-worked strength of 304SS for outsert reinforcements. Zylon fiber is also used in the insert because it is strong, stiff, and an insulator.

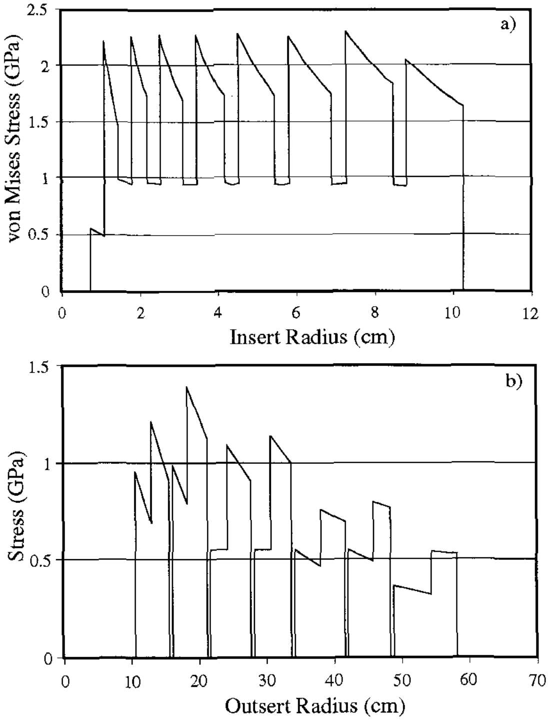

Figure 2. Stress distribution a) in the insert and b) in the outsert.

4 Power Supplies

The capacitors and switches for the insert's power supply are ready for assembly. For flexibility in accommodating future inserts this bank is configured into four independent 6 kV units that can be connected to give either 6, 12, 18, or 24 kV with a maximum energy of 2.4 MJ. The bank can be divided to power duplex coils, if necessary, but the present insert only requires a single 12 kV source.

The outsert will use 7 ac-dc power converters and controllers that have individual full-load ratings of 3.2 kV, 20 kA, and 64 MW. These are powered by a 1.4 GVA motor-generator that can deliver 600 MJ from stored inertial energy. The outsert coils are grouped into 3 independent, series-connected circuits (coils 1&2, 3&4, 5-7). Correspondingly, the 7 converters are grouped into 3 circuits: 2, 2, and 3 series-connected converters, respectively. The outsert contains 140 MJ of magnetic energy at peak field.

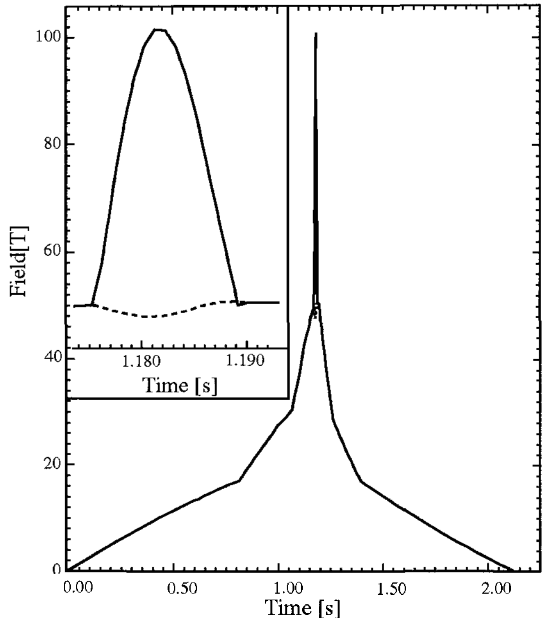

Figure 3. Reference pulse shape of combined insert and outsert.

5 Fabrication

For both the insert and outsert a different approach to reinforcement was taken with the use of wrapped metal strip. The advantages of wrapped strip include: a wider range of materials and processing are available; greatest cold working strength is parallel to the greatest stress; fabrication is facilitated by winding strip as needed; eddy currents can be reduced if the strip layers are insulated; transfer of axial forces to the reinforcement occurs; crack propagation is interrupted; uniform loading is improved; it is easier to place multiple metal reinforcements in one magnet; thickness of strip can be chosen for various purposes (ease of winding, cold work strength, precision of overall thickness, etc.).

In particular, the insert reinforcement for each layer is a combination of Zylon fiber and wound MP35N strip 0.125 mm thick. The outsert reinforcing shells will be produced by winding highly cold worked, extremely high strength, 304 stainless steel sheet onto a less strong but very tough Nitronic 40™ bobbin.

The method of 'autofrettage' will be utilized in the more highly stressed outsert coils to achieve reduction of conductor stress during routine magnet operation. This is achieved by allowing the conductor to strain soften as required during routine magnet operation or by a subjecting the coils to a deliberate one-time overstressing pulse to produce permanent plastic deformation in the conductor and the accompanying beneficial state of compressive pre-stress. Improved articulation and adjustablity of connections between coil leads and busbar, and within the busbar, will be obtained by incorporating and fingerstock fittings

(Multilam™) These changes will provide relief to the coil and busbar manufacturing tolerances and will speed assembly and disassembly by reducing the amount of manual fitting required. The use of double wrapped Kapton LT tape in place of half-lapped and staggered Kapton and e-glass fabric tape is being investigated.

6 Conclusion

A non-destructive 100 T research magnet has been designed and funded, and is now following a well defined engineering plan to completion. Within the next year an insert prototype will be built and tested, a prototype of the smallest outsert coil will be built, and delivery will be taken on the final CuAg wire. The insert's capacitor power supply is on hand and the huge 560 MVA dc supply for the outsert has been commissioned.

The next millennium will begin with a research tool that seemed a dream only a decade ago.

References

1. Challis, L., Franse, J., Herlach, F., Wyder, P., *European Workshop on Science in 100 T,* [KUL, Leuven, Belgium], **1** (May 15-17, 1992), **2** (September 30 - October 1, 1994).
2. Boebinger, G. S., Brazovskii, S., Campbell, L. J., Condensed Matter Physics for Non-Destructive 100 T Magnets, *Physica B* **246-247** (1998) pp. 61-66.
3. Campbell, L. J., Eyssa, Y., Gilmore, P., Pernambuco-Wise, P. Parkin, D. M., Rickel, D. G., Schillig, J. B., Schneider-Muntau, H. J., The US 100 T Magnet Project, *Physica B* **211** (1995) pp. 52-55.
4. Boenig, H., Campbell, L. J., Eberl, K. R., Eyssa, Y., Schillig, J., Sims, J. R., Parkin, D. M., Schneider-Muntau, H. J., Pernambuco-Wise, P., Design Approach of the US 100 Tesla Nondestructive Magnet System, Proceedings of MegaGauss VII, Sarov, Russia, (August 4-9, 1996) to be published.
5. Sims, J. R., Boenig, H. J., Campbell, L. J., Rickel, D. G., Rogers, J. D., Schillig, J. B., Schneider-Muntau, H. J., Completion of the US NHMFL 60 T Quasi-Continuous Magnet, Proceedings of 15th Intl. Conf. on Magnet Technology, Beijing, China, (October 20-24, 1997).
6. Han, K., Embury, J. D., Sims, J. R., et al., The Fabrication, Properties and Microstructure of Cu-Ag and Cu-Nb Composite Conductors, submitted to *MaterialsScience & Engineering.*
7. Embury, J. D., Han, K., Conductor Materials for High Field Magnets, *Current Opinion in Solid State & Materials Science* **3** (1998) pp 304-308.

PULSED POWER SUPPLY BASED ON MAGNETIC ENERGY STORAGE FOR NON-DESTRUCTIVE HIGH FIELD MAGNETS

G. AUBERT, S. DEFOUG, W. JOSS, P. SALA
Grenoble High Magnetic Field Laboratory, Max-Planck-Institut für Festkörperforschung and Centre National de la Recherche Scientifique, Grenoble, France

M. DUBOIS
Schneider Electric SA, Centre de Recherches A2, Grenoble, France

V. KUCHINSK
D. V. Efremov Scientific Research Institute of Electrophysical Apparatus, St. Petersburg, Russia

The first test results of a recently built pulsed power supply based on magnetic energy storage will be described. The system consists of the 16 kV shock alternator with a short-circuit power of 3600 MVA of the VOLTA Testing Center of the Schneider Electric SA company, a step-down transformer with a ratio of 1/24, a three-phase diode bridge designed for a current rising exponentially to 120 kA, and a big, 10 ton, heavy, 10 mH aluminum storage coil. The system is designed to store 72 MJ, normal operation will be at 50 MJ, and will work with voltages up to 20 kV. A transfer of 20% of the stored energy into the high field coil should be possible. Special making switches and interrupters have been developed to switch the high currents in a very short time. For safety and redundancy two independent monitoring systems control the energy transfer. A sequencing control system operates the switches on the ac side and protective switches on the dc side, a specially developed real-time control-monitoring system checks several currents and voltages and commands the dc circuit breakers and making switches.

1 Introduction

For resistive magnets, the maximum field is proportional to the square root of the electric power. Therefore, no theoretical limitation for the generation of high magnetic fields exists; only the costs are becoming prohibitive. For higher fields (the aim being 100 T) the solution is to generate quasi-stationary fields with energy provided indirectly. In a first stage, electrical energy from the network is stored in a few seconds (or minutes) and then discharged into the magnet in a short time, e.g. a few tenths of a second.

Energy storage devices can be classified in four main types: mechanical, chemical, capacitive and magnetic. Batteries are expensive, as special designs with low internal resistance are required. Alternators used in the short-circuit mode need to be over-dimensioned. Capacitive energy storage is applied in several laboratories but the shape of the field is sinusoidal. For large stored energies, inductive storage seems a competitive alternative [1 and References therein], but involves the development of high-current circuit breakers. The project presented below is a feasibility study for the generation of quasi-stationary magnetic fields using magnetic energy storage.

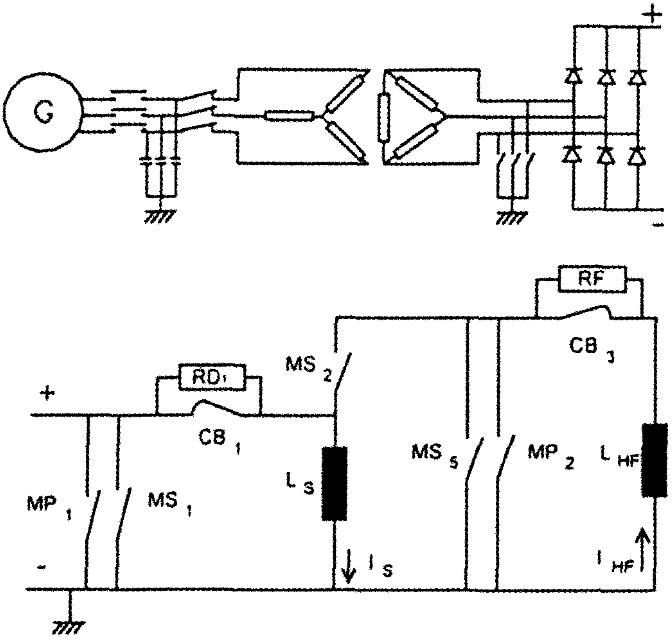

Figure 1. Circuit diagram of the pulsed power supply based on magnetic energy storage.

2 Set-up of the Pulsed Power Supply

The circuit diagram of the power supply system is shown Figure 1. The process is composed of three stages. In the first stage, the storage coil L_s is charged from the ac supply through a rectifier bridge. In the second stage, the switches MS1 and MS2 are closed and the circuit breaker CB1 is opened. The energy in the storage coil is quickly transferred to the high field magnet L_{HF}. In the last stage, a fast discharge of the high field magnet is made by closing MS5 and opening CB3.

Our installation is located in a rented cell of the VOLTA testing center of the Schneider Electric Company. The VOLTA testing center operates a 16 kV alternator with a short circuit power of 3600 MVA and a step-down transformer with a ratio of 1/24.25. The rectifier is a three-phase diode bridge designed for a current rising exponentially in three seconds up to the maximum current of 120 kA. The storage coil has a time constant of three seconds and is able to store 72 MJ of magnetic energy. Both the making switches and the breaker operating within 1 ms, can afford high voltages and carry high currents during a few seconds. The making switches are based on electrodynamical forces generated by eddy currents: these forces push up a closing contact which tears an insulation film between two fixed contacts and closes the main circuit. For reliability a Master Pack, a commercial

Schneider Electric switch, is placed in parallel with our making switch. The breaker consists of a current-carrying aluminum cylinder, which is destroyed by an explosive wire driven by a capacitor bank. The breaker is associated with a high voltage fuse to increase its lifetime and with a non-linear resistance in order to limit over-voltages and to control the shape of the pulse passively.

The sequencing control system of the VOLTA testing center drives only the switches on the ac side and the protective Master Pack switches on the dc side of the power supply. Our specially developed real-time control-monitoring system located 15 m from the cell is designed to check several currents and voltages before sending commands to the circuit breaker and making switches. The voltage sensors are capacitive dividers. The currents are measured by Rogowski coils, where the output is a voltage proportional to the derivative of the current and connected to integrators with a large time constant. The main advantage of such sensors is their insensitivity to magnetic stray fields. For a reliable data transfer all signals are transmitted over optical fibers.

3 Results

The rectifier manufactured by Westinghouse and tested at the VOLTA testing center has fulfilled its short circuit (180 kA) and endurance requirements. The real-time control-monitoring system and the communication with Schneider Electric's sequencing control system has been successfully tested. Currents on both systems were measured with a

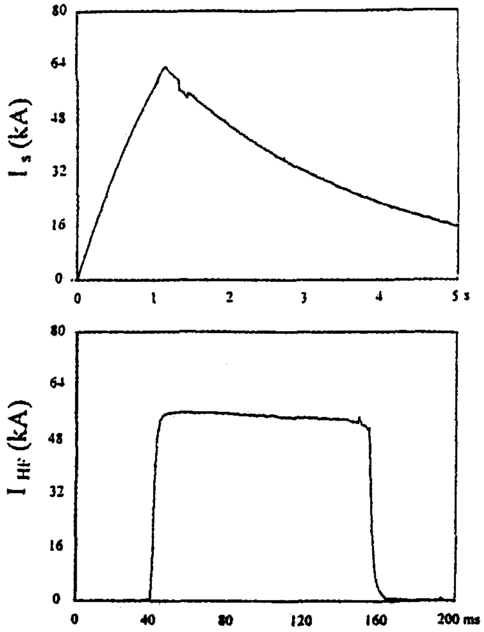

Figure 2. Commutation test. Current in storage (S) and dummy (HF) coil.

precision of 1%. The storage coil has been pretested with high voltages (up to 50 kV) at Haefely Trench's factory before delivery. The storage phase was tested up to 108 kA, which corresponds to a stored energy of 58 MJ. This is the maximum current the generator can deliver. In this test 150 MJ were extracted from the generator, far more than in usual tests at the VOLTA testing center. So far the commutation phase has been successfully tested with a dummy load with an inductance of 0.2 mH and a time constant of 0.3 s. Figure 2 shows the results of such a test. The upper curve shows the current in the storage coil during the charging and discharging phase in a 5 s interval, whereas the lower curve represents the 54 kA-100 ms current pulse in the dummy load.

4 Conclusion

A pulsed power supply based on magnetic energy storage has been developed for the generation of quasi-stationary magnetic fields. The storage phase has been tested up to 108 kA and 59 MJ stored energy. Commutation tests with a dummy load up to 63 kA have been performed successfully. The power supply is now ready to be used with a high-field magnet. It is planned to increase the efficiency of the energy transfer by charging two identical subsections of the storage coil in series and discharging them in parallel. The long-term goal is to charge the storage coil directly from the electrical utility network.

Acknowledgement

This work was financially supported by the European Community, the German Ministry of Education and Research and the Rhône-Alpes Region.

References

1 Aubert, G. et al., Proc. Megagauss and Megaampere Pulse Technology, Sarov, Russia, 1996 (Megagauss VII), Ed. by V. K. Chernyshev, *et al.*

HIGH FIELD PULSED MAGNETS FOR CHARACTERISATION OF TECHNICAL HIGH TEMPERATURE SUPERCONDUCTORS

P. M. SALEH, D. T. RYAN, H. JONES

University of Oxford, Clarendon Laboratory, Oxford, U.K.

Industry is currently producing High Tc superconducting tapes of such lengths and quality that they are beginning to be used in experimental coil winding programs. It is thought that these materials will play a very important part in superconducting coils of the future because of their superior Bc_2 characteristics. However, little is known about the behaviour of practical conductors, such as powder-in-tube and dip-coat tapes, in very high magnetic fields (>20 T). Characterization of these conductors in pulsed magnetic fields is therefore desirable, although problematic. The pulsed coils used in these experiments must therefore be designed with their task in mind. Two designs will be presented in this paper, a long pulse solenoid and a split pair arrangement. The benefit of these designs and the challenges involved will be discussed.

1 Introduction

Although critical current measurements in pulsed fields have been successfully performed in the past by Hole [1], the quality of results and types of samples tested were limited by the design of the pulsed magnet used. The need was identified for future coils to be designed specifically for the purpose of high T_c tape characterization rather than the general user who, generally, simply requires the highest possible field. Two designs will be presented in this paper: a long pulse magnet, designed to reduce inductive signal and investigate effects of eddy currents on silver sheathed tapes, and a split pair pulsed magnet which enables us to characterise materials that cannot be tested in traditional solenoids due to geometric constraints.

2 Long Pulse Solenoid

Traditional solenoids used at the Oxford pulsed fields facility [2] have a standard design [3]. They generally consist of 10 layers of copper-stainless steel macro composite wire, internal and external reinforcement using carbon fiber, a 20 mm or 12 mm bore, a pulse length of about 15 ms, and they can generate fields in excess of 50 T. However, this configuration is not ideal when testing superconducting tapes. The pulsed nature of the field means that the sample experiences huge inductive effects. This not only affects measurements by swamping the small voltage signal from the sample, but also raises the prospect of eddy currents being induced in the sample. Certainly excessive eddy currents in the metallic substrate/sheath of these conductors are undesirable, as any temperature fluctuations would cast uncertainty on the validity of critical current measurements. For these reasons, a magnet with a longer pulse is desirable if only to examine the effects of varying pulse length.

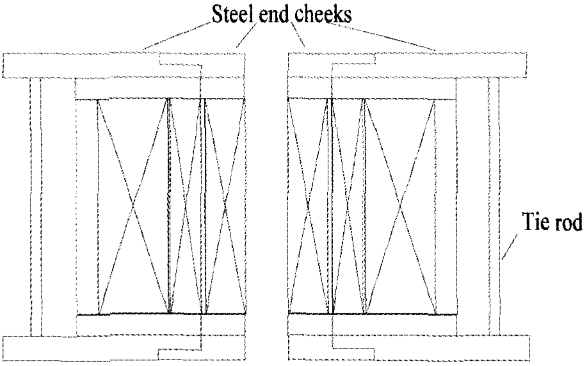

Figure 1. 110 ms pulsed magnet schematic.

The coil in Figure 1 is was designed using software developed by Eyssa [4] at the NHMFL in Florida. The design incorporates as many elements as possible from current coil design in Oxford in order to reduce risk of failure. This includes using as many tried and tested materials and techniques as possible. The reason for this conservative approach is that, as a long pulse and therefore high alpha coil, it will involve many more man-hours and materials to construct. For example, 200 meters of wire is used as opposed to around 30 meters for a standard 15 ms pulse coil.

Another precautionary measure incorporated into the design of the magnet is the inclusion of a demountable insert. The highest stresses in solenoids are to be found on the inner windings, thus failure in many pulsed magnets can be traced to an insulation breakdown in this region. By making the first eight layers of this magnet a separate, removable section that can be replaced in case of failure, the larger inconvenience of constructing a new magnet may be avoided for the sake of a few layers of windings. As well as re-enforcing the insert with carbon fiber, the outer coil also contains a layer of internal reinforcement and a thick outer shell of carbon fiber as is commonly used in Oxford coils.

Because of this reinforcement and the inherent strength of the copper-stainless steel conductor, the coil is predicted to reach fields to 50 T. Indeed, due to the energies involved, we are reaching a point where the capacitor bank of the Oxford pulsed facility may be more of a limiting factor.

3 Split Pulsed Magnet

In order to simulate the configuration of windings in a solenoid, critical current measurements are performed with the applied field perpendicular to the direction of transport current. When testing in a solenoid bore, the geometry of the sample is constrained by the need for this field perpendicular to current arrangement. For instance, dip-coated tapes must be mechanically manipulated to form a meander pattern as shown in Figure 2. This manipulation tends to damage the sample thus reducing performance, which is undesirable. More importantly, perhaps, is the fact that materials such as BSSCO 2223 powder in tube tapes cannot be used in this configuration, as any mechanical deformation would cause serious damage to these tapes. As this type of superconductor is being produced by industry to a very high standard and shows a lot of potential for future applications, it was thought necessary that any characterization program on technological high Tc superconductors should include BSSCO 2223 tapes. It is for this reason that a split pulsed magnet has been designed.

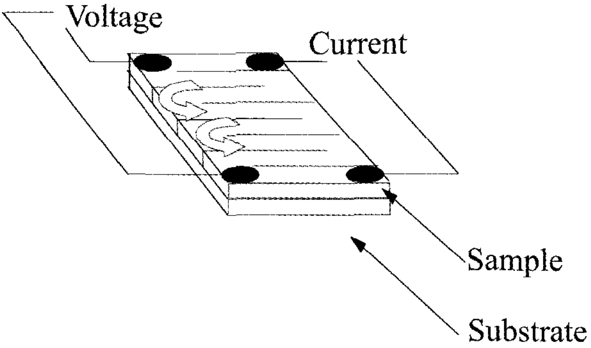

Figure 2. Meander pattern arrangement of dip coat samples.

Once again, a fairly conservative approach has been taken for this design. A field of around 30 T is adequate for proof of principle. Limiting the field to this lower value also means that the design can be simplified. For example, internal reinforcement of the coils is unnecessary due to lower stresses. Also, the compressive force between the coils can be kept to such a level that the mid-section can be fabricated from a material such as Tufnol 10G/40, an epoxy inpreganated glass cloth, rather than steel. This is desirable, as it reduces the risk of electrical short circuiting.

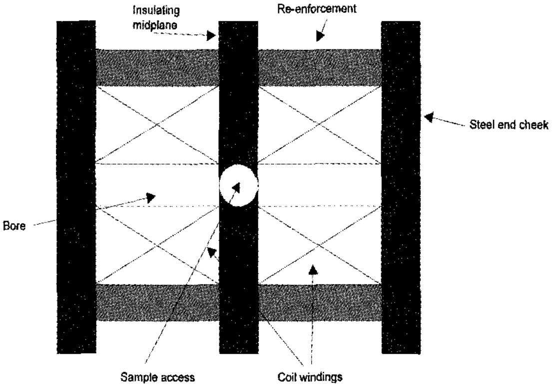

Figure 3. Schematic of split pulsed magnet.

The pulse length is limited to around 15 ms due to energy limitations, however, this should be adequate for initial investigations, and acts as a stepping stone for future split pulsed magnet development in Oxford. The coils contain 10 layers of copper/stainless steel wire, have a 12 mm bore and are seperated by a 12 mm thick disk of 10G/40. Neither coil contains any internal reinforcement, but they are strengthened externally by a 1 cm shell of carbon fiber.

4 Conclusion

Two designs have been briefly presented, a 110 ms pulse solenoid capable of ~50 T and a 15 ms pulse split magnet capable of ~30 T. Both magnets have been designed to improve and expand the technique of characterizing technological superconducting tapes in pulsed fields. These magnets, when built and tested, will also enhance the Oxford pulsed magnet facility's range of service and expertise. Test results of these magnets will be found in future publications.

References

1. Hole, C., Jones, H., and Goringe, M., A Technique for DC Transport Critical Current Measurements on High-Temperature Superconductors in Pulsed Magnetic Fields *Meas. Sci. Technol.* **5** (1994) p. 1173.
2. Siertsema, W., and Jones, H., The Oxford Pulsed Facility *IEEE Transactions on Magnetics* **30**, No. **4** (1994) p. 1809.
3. Jones, H., Van Cleemput, M., Hickman, A. L., Ryan, D. T., and Saleh, P. M., Progress in High-Field Pulsed Magnets and Conductor Development in Oxford *Physica B* **246-248** (1998) p. 337.
4. Eyssa, Y., and Pernambuco-Wise, P., Electrical, Thermal and Mechanical Modeling of Pulsed Magnets *NHMFL Internal Report* (1995)

GENERATION OF MEGAGAUSS FIELDS IN INDESTRUCTIBLE SOLENOIDS WITH QUASI-FORCE-FREE WINDINGS

G. A. SHNEERSON, E. L. AMROMIN, V. Y. KHOZIKOV
Electromechanics Department, St.Petersburg State Technical University, Russia

A. I. BOROVKOV
Physics and Mechanics Department, St.Petersburg State Technical University, Russia

The application of solenoids with force-free windings and uniformly loaded back current zones allows the avoidance of the exponential rise of radial coil size in fields higher than one megagauss that is distinctive for uniformly loaded solenoids with azimuthal current. Considered here is the possibility of a real quasi-force-free magnet system analogous to a force-free one. The coil consists of N current layers. For two types of windings the opportunity of decreasing static stresses N or N^2 times, respectively, is shown compared to magnetic field pressure at the coil axis is shown. An estimate of coil geometric sizes satisfying the mechanical strength and heating conditions in fields higher than one megagauss is presented. The possibility of voltage decrease between coil layers is considered, an estimate of energy is presented and the problem of the geometric shape of quasi-force-free magnets is discussed.

1 Introduction

Despite many years of research and development in long duration, extra-high magnetic field generation (10^{-3}-10^{-2} s) the obtained amplitude does not exceed 100 T. In the pioneering works of Kapitsa during the 1920s, a field with induction of about 30 T was obtained [1]. Such slow progress is due to extreme difficulties associated mainly with providing mechanical strength to the winding. The use of radially equally loaded windings [2,3,4] allows solution of the problem, in principle. However, substantial decrease in the mechanical stresses in the winding compared to its ultimate strength (maximum admissible azimuthal stress σ_0) is only possible by exponentially increasing the ratio of the outer radius to the inner one: $R_2/R_1 \approx \exp(B_0/B_m)^2$, where $B_m = (2\mu_0\sigma_0)^{1/2}$ is "magnetic strength limit", B_0 is the induction at the solenoid axis. For a material with $\sigma_0 = 10^9$ Pa ($B_m = 50$ T) this ratio is 55 if $B_0 = 100$ T, and increases to 8×10^3 for $B_0 = 150$ T. It follows that fields with inductions of 150 - 200 T and greater should be produced by other means. Here, force-free fields are very attractive. Their properties are quite well studied. Nevertheless, they cannot be created in a real magnet with azimuthal current for two reasons: the winding has finite dimensions and its current distribution has discrete character. However, it is possible to create a system in which the equally loaded back current region [5,6] complements a winding with the current distribution close to the force-free one. This paper examines the possibility of producing such a system. The estimates of its characteristic dimensions are given, and the problem of designing the solenoid end regions is considered. These issues are examined in the approximation of the continuous current distribution. Further, we examine the possibility of approximating a force-free current distribution by a real system of discrete currents, and give examples of strength calculation results for concrete systems.

The problem of developing quasi-force-free magnets remains to be solved, and the aim of the paper is to draw expert attention to this promising avenue of megagauss technology development.

2 The General Arrangement of a Magnet with a Force-Free Winding and Equally Loaded Back (Poloidal) Current Region

The system of currents distributed in a finite region cannot be force-free [7]. However, a configuration is possible in which the force-free field exists in the part of the finite region where axial and azimuthal currents are distributed [5] (Fig. 1).

Axial and azimuthal currents situated in Zone 1 produce an exactly force-free field with continuous or nearly continuous current distribution, produced by discrete current layers.

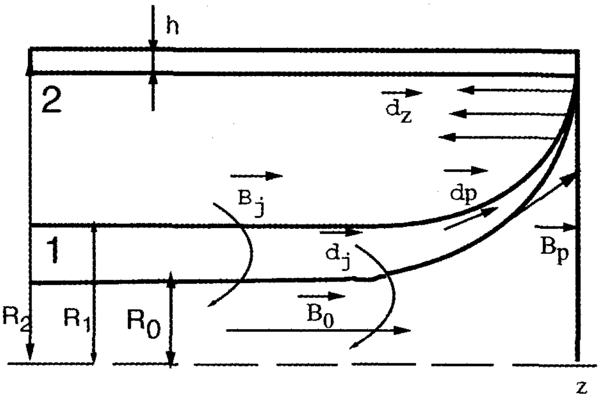

Figure 1. The cross-section of force-free winding for a solenoid. 1 - force-free area, 2 - equally loaded area.

An outer, equally loaded region 2 where the field is not force-free encloses the latter. In Zone 2 the induction has only an azimuthal component and the current distribution satisfies the uniform loading condition

$$\sigma_\varphi = -r\delta_z B_\varphi = -\frac{1}{\mu_0} B_\varphi \frac{d}{dr}(rB_\varphi) = const \tag{1}$$

In the general case when the thin-walled band h with allowable stress σ_l remains on the outer radius the following expressions for the induction and ratio of radii hold true

$$B_\varphi(r) = B_\varphi(R_1)\cdot\frac{R_1\sqrt{\alpha^2 - r^2/R_1^2}}{r\sqrt{\alpha^2 - 1}} \tag{2}$$

$$R_2 = R_1\sqrt{\frac{1 + 2B(R_1)/B_M^2}{1 + 2h\sigma_1/(R_2\sigma_0)}} \tag{3}$$

where $\alpha = (R_2/R_1)\,(1+2\sigma_1 h/\,(\sigma_0 R_2))$. It follows from formula (3) that in the medium with $\sigma_0 = 10^9$ Pa (B_m=50 T) $R_2/R_1 = 5.74$ in the field with the 200 T induction, if h=0. The given relationships show that the combination of the force-free and equally loaded winding removes the problem of catastrophic rise in magnet dimensions for the generation of ultra-high fields. However, the realization of such a winding requires solving some theoretical and practical problems. The first of them is the choice of the solenoid end regions.

3 The Choice of the End Region in the Model of the Thin Force-Free Winding

The problems arising in the calculation of the end region geometry of the solenoid are very complex, even in the simplest case of the thin force-free winding [8,6]. In the model, the winding thickness may be assumed to be equal to zero. The force-free region degenerating into the surface should satisfy the following conditions: it should be the boundary of two regions, in one of which the magnetic field is poloidal (axial zone) (Fig. 1). The poloidal field induction B_p is then tangent to the boundary, and the condition $|B_p| = |B_\varphi(r)| = f(r)$ is satisfied at each point of the boundary S. The law of axial current distribution determines the shape of the function $f(r)$. This condition requires the equality of magnetic pressures at both sides of the force-free layer. The solution of the problem presents large difficulties, as the boundary shape is not known in advance and should be found from the iteration procedure. A similar problem is solved in finding the equilibrium shape of a theta-pinch [9]. Certain forms of S corresponding to solutions of examined problems are shown in Fig. 2.

These solutions were obtained for long and very thin windings. The increase in the ratio R_2/R_1 leads rapidly to the transformation of all shapes to a limited one. The problem becomes substantially more complicated in the case of a winding of finite thickness. Presently, we can only state the problem of such a calculation. In approximating the continuous current distribution, we should find a shape of the force-free field domain such that the condition $B_\varphi = 0$, $(\mathbf{B}_p, \mathbf{n}) = 0$ be satisfied at the boundary S. Here $\mathbf{B}_p$ is the poloidal field induction, $\mathbf{n}$ is the normal to the boundary $S1$, $B_p = 0$, $B_\varphi = f(r(s_2))$ at the boundary S_2. In a real solenoid the poloidal current should be divided between several conductive layers. Therefore, the system of thin current layers seems to be a reasonable approximation to a real one.

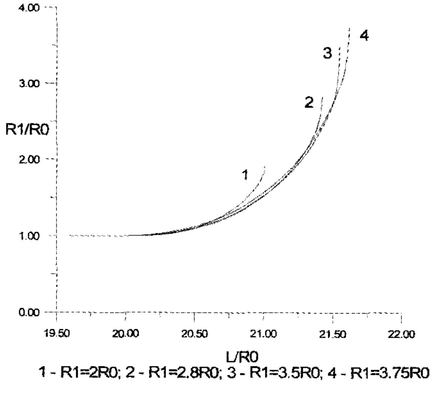

Figure 2. Examples of possible butt-ends of force-free winding.

The configuration of each layer can be found by the method similar to that described above for a single layer. The mutual influence of current loops should be taken into consideration in this procedure. The condition of force compensation remains valid for each loop: $B_p^2\ (1) - B_p^2\ (2) = 2\mu_0 j_p\ B_\varphi(s)$, where $B_p\ (1)$, $B_p\ (2)$ are the magnetic poloidal field induction at both sides of the layer at the point s, j_p is the linear poloidal current density and B_φ is the azimuthal field induction at this point. The calculation according to this scheme involves substantial computational difficulties due to the necessity of simultaneously varying several current loops in the iteration process.

One alternative to construct the force-free distribution in the winding in the continuous current distribution is as follows. The poloidal current distribution is constructed for the given region configuration from the solution of the Laplace equation for the potential whose gradient is the poloidal current density δ_p. This equation is solved with the following boundary conditions: $(\delta_p, \boldsymbol{n}) = 0$ at S_1, $(\delta_p, \boldsymbol{n}) = (\delta_z(s), \boldsymbol{n})$ at S_2. The latter condition describes the continuity of the current density normal component at the boundary S_2. The calculated distribution $\delta_p\ (r, z)$ allows us to find the field, B_φ, and the ratio $\alpha = \delta_z / \delta_r$. In the force-free field, $\alpha = B_z / B_r$. This yields the following equation for the azimuthal vector potential component: $(1/r)\ \partial\ (rA_\varphi)/\partial\ r = -\alpha\partial A_\varphi/\partial r$. Its solution allows us to find further B_z and B_r and to calculate the azimuthal current density $\delta_\varphi = (1/\mu_0)\ (\partial\ B_r/\partial\ z - \partial\ B_z/\partial\ r)$. The boundary shape should be varied until the value found will satisfy the force compensation condition: $\delta_\varphi = B_\varphi\ \delta_z/B_z = B_\varphi\ \delta_r/B_r$.

According to formula (3), the ratio $R_2\ /R_1$ should be sufficiently large (of the order of several units). The poloidal field beyond the boundary S_2 is then greatly reduced. Therefore, it can be expected that the azimuthal forces acting in region 2 near the ends will be fairly small and will not act as an important factor in the solenoid construction.

4 Quasi-Force-Free Winding

This section presents an estimate of parameters for a real magnet system consisting of current layers approximating the force-free current distribution. This winding may be naturally termed as a quasi-force-free one. For simplicity, the end effects are not considered here. The field is examined in the middle part of the long solenoid, far from its ends.

The current density vector in the force-free field changes its direction with radius. In practice, such a distribution may be approximated by a discrete one in two ways: alternating the layers with axial and azimuthal currents or alternating layers in which the current density vector is directed at its own angle to the z-axis (Fig. 3). Although the second scheme, as shown below, has better strength characteristics, we will deal mainly with the first, as it is easier in practice.

We consider a winding having conductor thickness much larger than that of the insulation gaps between them. It consists of N pairs of alternating layers with orthogonal currents in each pair (Fig.3a). The distribution of axial and azimuthal currents approximating the force-free distribution is effected so that the compressive stress acting upon the external layer with the axial current compensates the tensile stress in each pair that acts upon the annular turn. Each pair is in equilibrium and the insulation gasket is subject to compression.

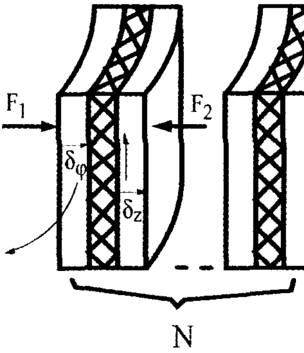

Figure 3a. Paired current layers.

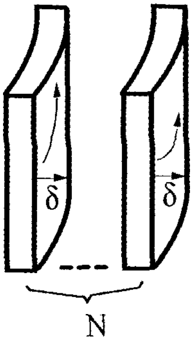

Figure 3b. Current layers with variable current density vector.

We assume that the thickness of both layers in the n-th pair is equal, and the number of pairs $n >> 1$. The tensile stress acting upon layer 1 with the azimuthal current per unit surface is then equal to:

$$F_{r1} = \frac{B_z^2(r_n) - B_z^2(r_{n+1})}{2\mu_0} \tag{4}$$

where B_z is the axial induction component. Then

$$B_z(r_{n+1}) = B_z(r_n) - \mu_0 \int_{r_n}^{r_{n+\Delta}} \delta_\varphi dr \approx B_z(r_n) - \mu_0\delta_\varphi(\Delta - \frac{\Delta^2}{2r_n^2}) \tag{5}$$

In this formula $\delta_{\varphi n}=\delta_\varphi(r_n)$, in its development the dependence $\delta_\varphi = \delta_{\varphi n} r/r_n$ was assumed.

Without the terms of the order of $(\Delta/r_n)^3$ the force F_{r1} is expressed as follows:

$$F_{r1} = B_z(r_n)\delta_{\varphi n}\Delta - B_z(r_n)\delta_{\varphi n}\frac{\Delta^2}{2r_n} - \mu_0\delta_{\varphi n}^2\frac{\Delta^2}{2} \tag{6}$$

The compressive force acting upon layer 2 is expressed in the same approximation by the formula:

$$F_{r2} = B_\varphi(r_n')\delta_{zn}\Delta - \frac{\mu_0\delta_{zn}^2\Delta^2}{2} \tag{7}$$

where $r_n' = r_n + h + \Delta$. The equilibrium equation $F_{r1}+F_{r2} = 0$ should be satisfied for each pair of the layers. This yields the following system of equations allowing us to find the distribution of azimuthal currents in layers for a given distribution of axial currents or to solve the inverse problem:

$$B_z(r_n)\delta_{\varphi n}\Delta - B_\varphi(r_n')\delta_{zn} - B_z(r_n)\delta_{\varphi n}\frac{\Delta}{2r_n} - \frac{\mu_0(\delta_{\varphi n}^2 + \delta_{zn}^2)}{2} = 0 \tag{8}$$

The induction components B_φ and B_z in these equations are determined from the following approximate formulas:

$$B_{zn} = B_0 - \Delta \cdot \mu_0 \sum_{1}^{n-1} \delta_{\varphi n}(1 - \frac{\Delta}{2r_n}) \tag{9}$$

$$B_\varphi(r'_n) \approx \frac{(r'_{n-1} + \Delta)}{r'_n}\left(B_\varphi(r'_{n-1}) + \mu_0 \Delta \cdot \delta_{z,n-1}\right) \tag{10}$$

The modulus of compressive stress σ_r acting upon insulation gasket 3 may be approximately calculated from the formula:

$$\sigma_r = F_{r1} = F_{r2} = B_\varphi(r'_n) + \frac{\mu_0 \Delta \cdot \delta_z^2}{2} \ . \tag{11}$$

The first term in this formula is the most significant. It has the order of $B_0^2/(2\mu_0 N)$, as B_φ has the order of B_0, and δ_φ is of the order of $B_0/(\mu d)$, where $d = 2N\Delta$ is the winding thickness. So one can consider that the compressive stresses in the system with orthogonal currents are approximately N times less than the magnetic pressure corresponding to the field B_0.

Solving the axi-symmetric problem of elasticity theory for a heterogeneous body allows for the final checking of calculations and correction of the current distribution by the finite element method and program system of finite element analysis FEA [10]. The finite element model includes from 950 to 1004 square eight-point elements with numbers of degrees of freedom from 6122 to 10046. Table 1 and Fig. 4 show the results of such calculations for particular cases. They confirm the possibility of realizing a winding whose insulation layers are loaded by compressive stresses on the order $B_0^2/(2\mu_0 N)$. Table 1 also lists the residual values of azimuthal stresses σ_φ that are considerably less than the compressive ones.

Table 1

B, T	$\lvert\sigma_\varphi\rvert^{\max}$, MPa	$\lvert\sigma_r\rvert^{\max}$, MPa
100*	229	330
100**	78	61
150*	286	630
150**	206	100

* - The value of induction for winding with pair current layers.

** - The value of induction for winding with variable vector of current in each layer.

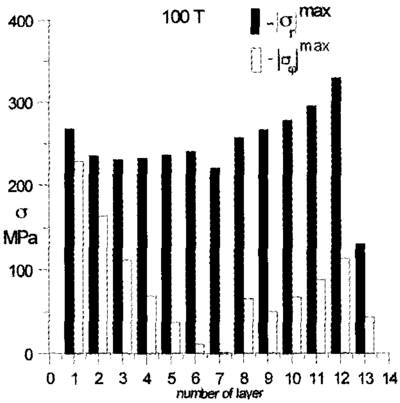

Figure 4a. Azimuthal σ_φ and radial σ_r stress components of a 100 T model coil with a pair of current layers.

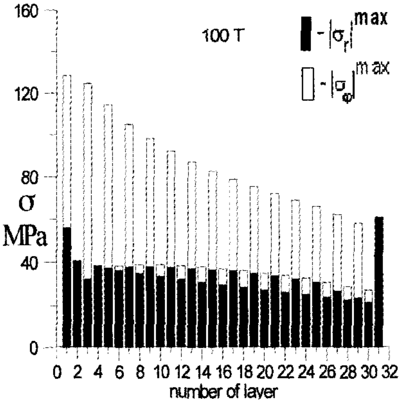

Figure 4b. Azimuthal σ_φ and radial σ_r stress components of a 100 T model coil with variable current vector.

We give a stress estimate in the system of current layers with alternating current direction. The possibility of decreasing electromagnetic force in the multi-layered system with tilted currents approximating the force-free system was shown in [11-13,15]. The proposed method of current distribution in layers is an advancement of the method in [15]. The current density components δ_z and δ_φ in each of N layers may be calculated from equating to zero the total radial force

$$F_r = \int_{r_n}^{r_n+\Delta} f_r dr \tag{12a}$$

where r_n is the inner radius of the n-th layer, Δ is the layer thickness, $f_r = \delta_\varphi B_z - \delta_z B_\varphi$ is the volume electromagnetic force. Such a simplified calculation without using the equations of elasticity theory allows us to estimate the stress σ_r and provides initial data to construct the current distribution among the layers. It can be refined in the following approximation and corrected according to results of rigorous computer calculation, just as in the case of the system with orthogonal currents. The expression for the total force at the point with coordinate x (Fig. 3b) including principal expansion terms with respect to coordinate x has the form:

$$F_r(x) = \int_{r_n}^{r_n+x} f_r dx = (\delta_\varphi B_z - \delta_z B_\varphi)x - \frac{\mu_0}{2}(\delta_\varphi^2 + \delta_z^2) - \delta_\varphi B_z \frac{x^2}{2r_n} \tag{12b}$$

where $\delta_\varphi \equiv \delta_\varphi(r_n)$; $B_z \equiv B_z(r_n)$; $B_\varphi \equiv B_\varphi(r_n)$, δ_z is the azimuthal current density in the n-th layer. It was assumed in the calculation that $\delta_\varphi = \delta_\varphi r_n /(r_n+x)$. From the equilibrium condition of the layer $F_r(\Delta) = 0$ we obtain:

$$\Delta = \frac{2 \cdot (\delta_\varphi B_Z - \delta_z B_\varphi)}{\mu_0(\delta_\varphi^2 + \delta_z^2) + \delta_\varphi B_z} \tag{13}$$

Equation (13) may be used to calculate the axial current in each layer for prescribed axial distribution of azimuthal currents. Induction $B_\varphi(r_n)$ and $B_z(r_n)$ at the inner boundary of each layer is determined by formulas (9,10). The volume force is alternating in sign within the layer $0 < x < \Delta$ and equals zero at the point $x_m = \Delta/2$, where F_r has maximum. The value of that maximum may be used as the estimate of the stress σ_r:

$$\sigma_r = (\delta_\varphi B_z - \delta_z B_\varphi)\frac{\Delta}{4} = \frac{\mu_0 \Delta^2}{8}(\delta_z^2 + \delta_\varphi^2 + \frac{\delta_\varphi B_z}{\mu_0 r_n}) \tag{14}$$

The current density in all layers has the order of $B_0/(\mu_0 \Delta N)$, hence σ_r is of the order of $B_0^2/(\mu_0 N^2)$.

The example of the computer calculation given in Fig. 4 and Table 1 confirms that a sharp decrease in residual stresses takes place in the system with tilted currents.

5 Calculation Examples and Scaling Relationships

Data given in Table 1 show the results of strength calculations of quasi-force-free windings for several magnets with arbitrarily chosen parameters. These examples confirm the possibility of sharply decreasing mechanical stresses for given cross-sections of the windings by increasing the number of conductive layers. Maximum allowable current density is determined by heating conditions if the winding is not superconducting. In other words, the radius R_1 (for given R_0) is determined by heating conditions rather than by material strength. Strength considerations may become decisive in the determination of radius R_2. Presently, there is no experience in designing quasi-force-free magnets. The data given below are the results of pilot studies. One example of such a study is a magnet with inner radius of 5 cm intended to generate a 100 T field. The winding is cooled to 77 K and the pulse duration is 25 ms. The current density of copper is 5×10^9 A/m^2. A composite material consisting of niobium-titanium wires of 5.0×2.7 mm^2 cross section in the copper matrix used in superconductive magnets is employed for the winding. The allowable stress for that material is 900-1000 MPa. The following conditions are satisfied in the quasi-force-free winding: $\delta_\varphi \leq 3.6 \times10^9$A/m^2, $\delta_z \leq 4.7\times10^9$A/m^2, $\sigma_r < 540$ MPa. The latter stress is admissible for the insulation gasket made of SPPEP-type glass-plastic. In the back current region, the conductors are distributed in discrete current layers. As the calculations show, the conditions $\delta_z \leq 1.5 \times 10^8$ A/m^2, $396 < \sigma_\varphi < 403$ MPa are satisfied in the real, discrete system. The conductors are connected in parallel groups of 6 pieces each, and these groups are connected in series. The total current in the group with azimuthal current is 48 kA, and 61 kA in the group with axial current. The supply voltage is 60 kV and the pulse shape is close to a half sine wave. As follows from the listed data, the back current region mainly determines the magnet dimensions.

We may attempt to estimate the dimensions and magnetic energy of solenoids versus the generated field if we adopt that, due to the increase in the number of layers, the mechanical stresses in the winding will be less than the ultimate ones, regardless of its thickness and induction value. To simplify the problem, consider the case when $R_1 >> R_0$. The solenoid radial dimensions will be determined by two parameters: the radius R_1 depending on the allowable current density and the radius R_2, determined by material strength according to (3). Since one half of the winding carries axial current and the other carries azimuthal current, the radius R_1 is determined as $R_1=2B_0/(\mu_0\delta_\varphi)$. In the case $R_2>>R_1$ $B_0 \approx B_m R_2/(2^{1/2} R_1)$. This yields

$$R_2 = \frac{2\sqrt{2}B_0^2}{B_m \mu_0 \delta_\varphi} \tag{15}$$

The maximum allowable current density determined by heating conditions $\delta_\varphi = \delta_{lim} = (S/\tau)^{1/2}$, where S is the allowable value of the action integral, may be used for the estimate. For copper, with initial temperature 77 K and allowable overheating 576 K, we get $S = 5.6\cdot10^{17}$ A^{2}s / m^4. In the case of $\tau = 25$ ms, $\delta_{lim} = 4.72\cdot10^9$A/m^2. This yields $R_2 = 0.45$ m at $B_0 = 200$T. To estimate the magnet volume we represent it in the form of a cylinder of radius R_2 and length $l = 2\alpha R_0$:

$$V = 2\alpha\pi R_2^3 = \frac{32\cdot\sqrt{2}\pi\alpha B_0^6}{(B_m\mu_0\delta_{lim})^3} \tag{16}$$

The field energy may be estimated as follows:

$$W \approx \frac{B_0^2 V}{2\mu_0} = \frac{32\cdot\sqrt{2}\pi\alpha B_0^8}{2\mu_0^4(B_m\delta_{lim})^3} \tag{17}$$

In the examined case at $\alpha = 1$ $V = 0.57$ m^3, $W = 9$ GJ. The dimensions and energy of the magnet with 200 T field are fairly large. They may be lowered to the values $V = 0.05$ m^3 and $W = 0.8$ GJ by shortening the pulse duration to 5 ms. For this duration, the 400 T field may be produced in the magnet with $R_2 = 0.8$ m that corresponds to $V = 3.2$ m^3 and $W = 200$ GJ.

References

1. Kapitza, P. L., *Proc. Phys. Soc.*, **A42**, 5 (1930) p. 425.
2. Ignatchenko, W. A., Karpenko, M.M., *Journ. Tech. Phys.*, **38** (1968) p. 200.
3. Schneider-Muntau, H. J., Rub, P., “The Helix Project”, *Colloques internatiaux C.N.R.S.*, No. 242 – Physique Sous Champes Intenses (1974) p. 161.
4. Campbell, L. J., Boenig, H. J., Schneider-Muntau. H. J., *Physica B.* **216** (1996) p. 218.
5. Shneerson, G. A., *Journ. Techn. Phys.*, **56**, 1 (1986) p. 36.
6. Shneerson, G. A., *IEEE Trans. on Magnetics*, **28**, 1 (1992) p. 505.
7. Parker, E. N., *Phys. Rev.*, **109** (1958) p. 1440.
8. Hang, G. L., Levine, M. A., *Phys. Rev.*, **127**, 6 (1962) p. 1856.
9. Amromin, E. L., *Sov. Phys. Tech. Phys.*, **37**, 2 (1992) p. 232.
10. Borovkov. A. I., et al. Finite Element Modelling in Mechanics of Solids and Structures, Program System FEA, Int. Workshop. Tools for Mathematical Modeling, St. Petersburg, Russia, (1997) p. 11.
11. Wells, D. R., Miells, R. G., In *High Magn. Fields*, N.J.-London, John Wiley & Sons Inc., Cambrige, Mass., “Techn. Press” (1962) p. 44.
12. Claude, M. L., Mailfert, A., *Bull. Frans. Electriciens,* **4** (1963) p. 37.
13. Kuznetsov, A. A., *Journ. Techn. Phys.*, **31**, 6 (1961) p. 650.
14. Levine, M. A. In *High Magn. Fields*, N.J.-London, John Wiley & Sons Inc., Cambrige, Mass., “Techn. Press” (1962) p. 227.
15. Bodrov, S. G., Shneerson, G. A., *Tech. Phys. Lett.*, **20**, 5 (1994) p. 361.

SPATIAL MULTI-TURN STRUCTURE OF FLAT SHEETS FOR MEGAGAUSS MAGNETIC FIELD GENERATION

I. P. EFIMOV, S. I. KRIVOSHEYEV, G. A. SHNEERSON
St. Petersburg State Technical University, St. Petersburg, Russia

A system of flat busses with slits and radial openings can be used as a multi-turn solenoid for small duration megagauss magnetic field generation. The simplicity and cheapness of manufacturing are the advantages of this system. The design of a magnet providing high power efficiency at work with large condenser bank is described in the report. The concept of geometrical factor account is also described in the report. The results of a magnetic field configuration and an estimate of its heterogeneity are described, and the methods of field correction are considered. The possibility of creating a convenient magnet with a large aperture for accommodating a vacuum chamber is demonstrated.

1 Introduction

Semi-destructive single-turn solenoids may be efficiently used in laboratory conditions for magnetic field generation of the megagauss range. Their characteristic is relatively low inductance (on the order of 10^{-9} H). Therefore, to provide high efficiency of the energy transfer from the capacitor bank source to the magnetic field, its own inductance should have the same order. The efficiency of the energy transfer can be increased and higher field in the solenoid reached if its turn number is increased to two or more. A system of flat buses with slits and openings may be used as the magnetic system. They form the working volume occupied by the magnetic field [1].

2 Research Results

The busses are folded in such a way that the axes of openings in each layer coincide, and the slits are made in opposite directions. The example of the simplest two-layered system is shown in Fig. 1.

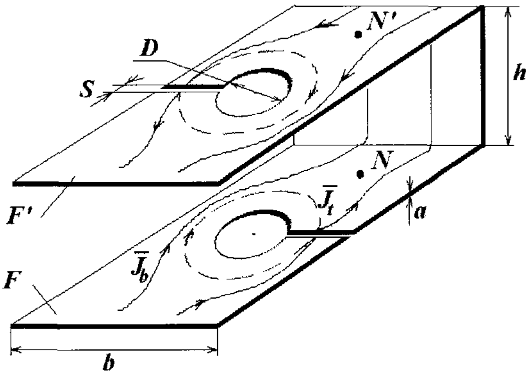

Figure 1. Two-layered magnetic system. See text for details.

It is known [2] that the field in the gap between two flat parallel sheets does not depend on the coordinate perpendicular to the bus plane. The deviations from such a distribution may occur only in the narrow zone (on the order of h) near the bus boundary. The vector of surface current density on the sheets F and F' at the points N and N' differs only in sign

$$J(N) = -J(N') = \frac{2\nabla_F \varphi(N)}{\mu_0 h}$$

where $\nabla_F \varphi(N)$ is the scalar potential gradient satisfying the Laplace equation. In other words, the current distribution is a bifilar one.

If openings and slit systems at the sheets F and F' are different, the condition of bifilarity remains valid, as the current distribution on both sheets remains identical except for the sign of the vector $\boldsymbol{J}$. For example, the slit in the sheet F' (Fig. 1) causes the current at that sheet to flow arround it. At the same time, the similar current distribution emerges on another sheet although there is no slit there.

Bifilarity (antisymmetry) of current distribution on closely spaced sheets is partly broken if the slits on both sheets overlap or, in other words, if they have such a form that in their superposition in one plane a common slit is formed oriented across the current lines that bisects the busses. This case is examined in [2]. The current across the slit boundaries comes to the outer sheet surface and forms a closed loop.

In this case, the bifilarity of the current distribution is retained at the inner surface of the sheets facing the insulation gasket between them. However, the bifilarity is broken for that part of the current that is distributed at the other surface of the sheets. Such a configuration may be used as a solenoid (Fig. 1).

The current distribution in this system may be represented as the superposition of two currents: a bifilar one J_b and the outer one J_t (Fig. 1). If the slit width s and the spacing between the buses h are much less than the characteristic dimension of the magnetic system D, one may assume that the bifilar current J_b flows at the inner bus surface, and its distribution corresponds to the current distribution in the system with openings but without any slits. The current J_t makes up half of the current J_b, rounding the slit at the outer side. The current distribution J_t is close to that of the disc solenoid. Then the magnetic field is formed in the opening D just due to the current J_t, similarly as in the case of a single-turn solenoid.

To augment the effective turn number one may use additional slits or increase the number of parallel sheets folding them into a "pile" (Fig. 2). In the limit, the latter configuration differs from Bitter's solenoids only by the presence of the system of bifilar currents having no effect on the field in the opening.

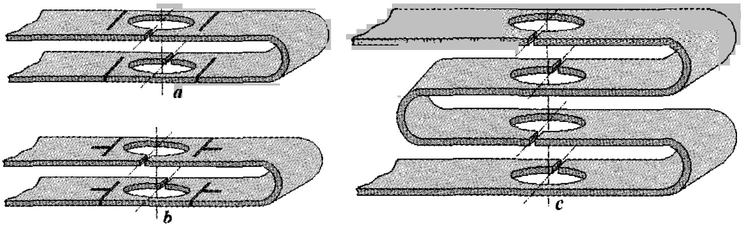

Figure 2. Methods to increase the geometric factor.

It is possible to use additional slits in the current carrying busses to increase the part of the current participating in forming the solenoid magnetic field. The current distribution for this case, with additional slits overlapping in the plane, is shown in Fig. 3.

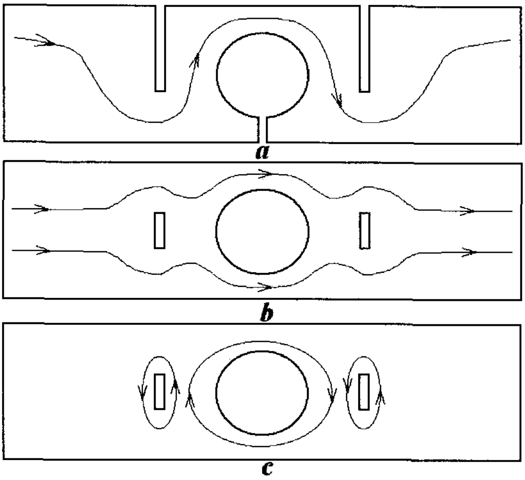

Figure 3. Current distribution in a two-layered system with additional slits. a) the resulting current distribution, b) bifilar current component, c) outer current component.

The systems presented in Fig. 2 were studied in model experiments. The measurements were made at a frequency of 200 kHz. The conditions are $\delta << a$, $\delta << h << D$, where δ is the skin layer depth, a and h are the bus thickness and that of the insulation gasket, respectively, and D is the diameter of the opening of the solenoid. Results of the measurements are presented in the table, where the significances of the geometrical factor $g = B/i$, and where B is the induction at the center of a hole and i is the current. We compare the results with the geometrical factor of a solenoid with the same radius as opening in an unlimited, ideally conducting thin sheet. The value of the geometric factor of the 9.5 mm diameter ideal disc solenoid was determined by the formula [2]:$g_d = \mu_0/\pi R$, where R is the radius of the solenoid. It equals 0.842 MGs/MA. It follows from the data listed in Table 1 that the system described allows one to obtain a fairly large geometric factor.

Table 1. Geometric Factors of Various Magnetic Systems.

magnetic system	***Fig. #***	***g*** MGs/MA	***g/g$_d$***
two-layered system	1	0.9	1.07
two-layered system with a single slit	2a	1.01	1.19
two-layered system with two slits	2b	1.13	1.34
four-layered system	2c	2.07	2.46

It is obvious that:

- The system with openings and slits is equivalent to a single-turn solenoid.
- Additional transversal slits allow increase of the geometric factor.
- In passing to the four-layered system, the geometric factor increases more than twice compared to a single-turn solenoid with an ideal slit.

3 Conclusions

This solenoid design is simple to manufacture and may be easily connected to flat busses of low-inductance capacitive storage. A similar design principle may be used not only for solenoids made of thin sheets, as in the model experiments described, but also in solenoids having axial dimensions commensurate with the opening radius.

References

1. Botcharov, Yu. N., Krivosheyev, S. I., Kruchinin, A. I., Churayev, V. A. Multiturn solenoid for the production of strong magnetic fields. Patent USSR 1349578, 1985.
2. Shneerson, G. A. Fields and Transients in Superhigh Pulse Current Device. (Nova Science Publishers, Inc., New York, 1997) p. 560.

OPTIMAL USE OF MAGNETIC ENERGY IN A MAGNET

R. KRATZ
Max-Planck-Institut für Physik komplexer Systeme, Dresden, Germany
and Forschungszentrum Rossendorf, Dresden, Germany

Y. M. EYSSA, L. LI, H.J. SCHNEIDER-MUNTAU, M. R. VAGHAR,
S. W. VAN SCIVER
National High Magnetic Field Laboratory, Tallahassee, USA

We report on calculations concerning the optimization of solenoid coils. The task was to find the best radial current density distribution producing the highest possible field in the center. Constraints consisted of a finite mechanical strength of the coil and an upper limit for the current density. An ideal polyhelix coil approximated the coil, and the material properties were assumed to be isotropic.

1 Introduction

The most expensive component in a pulsed magnetic field facility consists of the energy source. Greatest savings can therefore be achieved if the stored energy can be reduced to its minimal necessary value. The necessary energy is determined by the desired magnetic field, the geometric dimensions of the coil, the current density distribution within the magnet, and the mechanical strength of the magnet structure.

2 Magnet Model

As a magnet model we use a coil with a rectangular cross section. The material properties (yield strength, specific heat, specific resistivity) are assumed to be homogeneous and isotropic, and the current density distribution is taken as a continuous function of the radial position, $j = j(r)$.

To estimate the magnet heating, the coil material is assumed to be copper, which is reinforced on a microscopic scale to achieve a specific yield strength. Since the current is allowed to flow only in the copper, the ratio of copper to reinforcement also determines the amount of adiabatically heated copper.

Lorentz forces in the radial as well as axial direction are taken into account. The mechanical stresses in the coil are calculated for the case of an idealized polyhelix coil, i.e. there is no transmission of mechanical forces in the radial direction.

3 Algorithm

The numerical problem to be solved is: Find for a coil of the above mentioned type and with a given cross section the optimal current density distribution j(r) which gives the highest field in the center under the following conditions:

1. The von Mises stress should stay below some given value.
2. There is an upper limit for the current density j_{max}.

The second condition assures that there is a lower limit for the pulse length, since $j^2_{max} \times t_{pulse}$ = const. = F, where F depends only on the material properties and the initial and final temperature of the coil [1].

We use the code 'SolvOpt' (Solver for local optimization problems), which is concerned with minimization or maximization of nonlinear problems and accounts for constraints by the method of exact penalization [2]. An overview of available algorithms and techniques can be found in [3].

4 Example

In a series of calculations, we vary the outer radius of the coil and the strength of the material. The height of the coil is always taken equal to its outer diameter. Then the maximal magnetic energy is calculated, which complies with the two boundary conditions thus giving the maximum possible field. The fixed parameters of the coil are:

inner radius	5 mm	
initial temperature	77 K	
final temperature	400 K	
Conductor	320 MPa	copper
max. current density	10^9 Am^{-2}	

The outer diameters are 100, 150, 200, 250, 300, 350 and 400 mm. The strength of the bulk material ranges from 1.00 GPa to 2.25 GPa in steps of 0.25 GPa. The strength of the (microscopic) reinforcement is 2.7 GPa.

The results of the calculations are shown in Fig. 1. The upper graph gives the central field as a function of the magnetic energy, with the strength of the bulk material as a parameter. For the same amount of magnetic energy, the stronger materials produce more field. All curves show the same tendency; they increase strongly for low values of the magnetic energy, and then they flatten out.

For the designer of a magnet system, this means that one should avoid the 'flat' region because the magnetic energy is used very inefficiently there. For a given strength of the material, there exists a useful size, field, and magnetic energy. The designer is responsible for giving a good definition of 'useful' here. Furthermore, one can trade the conductor strength against magnetic energy. The same field can be generated either by a strong material with a few megajoules or by a weak wire with many megajoules of magnetic energy.

The lower graph of Fig. 1 shows the thermal energy Q_{th}, given in units of the magnetic energy, as a function of the magnetic energy. With thermal energy we mean the energy that heats the copper in the coil adiabatically from the initially 77 K to the final temperature of 400 K. For very small magnetic energies, hence also small coils, this ratio can be as large as 1.5. The ratios then descend rather quickly, and for magnetic energies above 10 MJ they lie below 0.5. In terms of energy, thermal energy defines small coils and magnetic energy defines large coils.

For a first rough estimate of the necessary total energy for a magnet system, one can add the values of the magnetic energy and the thermal energy. This is an overestimation as ultimately the magnetic energy is transferred into heat. For large coils, where the magnetic energy exceeds the thermal energy, this means that a considerable part of the coil's energy must be dumped outside of the coil. Otherwise, one would overheat the coil.

5 What About 100 T?

Our estimations indicate a possible path to a nondestructive, pulsed coil producing 100 T with a pulse length of several milliseconds. We would suggest a 10 mm bore size. For a not-too-exotic strength of the coil material, as for instance 1.5 GPa, the coil must have a diameter and a height of 300 mm. The magnetic energy would be 4.2 MJ and the thermal energy 1.1 MJ so that a capacitor bank of 5.3 MJ would be necessary. The pulse length of a sinus half wave would be 8.5 ms.

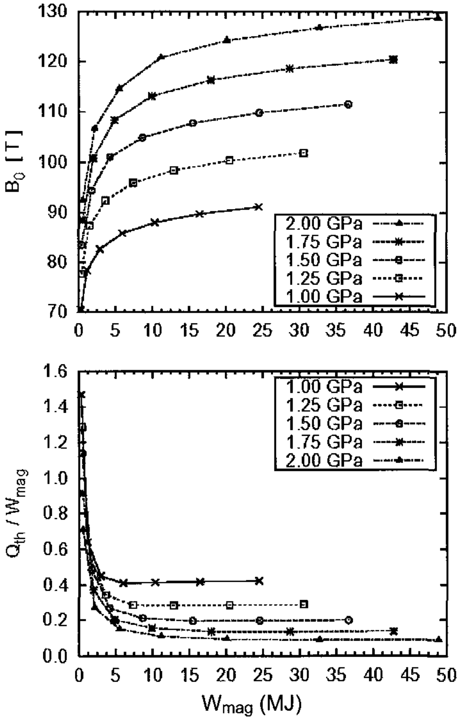

Figure 1: Coils with a bore of 10 mm and various sizes were energized to their limits, i.e. the indicated strength and a maximal current density. The upper graph shows the central field, the lower one the thermal energy as a function of the magnetic energy. For further details see text.

6 Estimations and Reality

Several assumptions have been made for the calculations performed here. First, the coil was treated as an ideal polyhelix, which causes decoupling of the radial and azimuthal component of the stress tensor. This allows for a fast computation of the stresses, hence for an efficient numerical search for the optimized coil.

The coil is operated in the elastic regime. In this respect the calculated coils have some safety margin built in. The material properties in a real coil are not isotropic; instead the coil is separated into conductor, insulation, and reinforcement. Additionally the material properties of these components are a function of temperature, field and history (plastic deformation!). For comparison, a coil with a more realistic model has been calculated. The differences give an indication of the error [4]: The field and the magnetic energy are about ten percent off and the pulse length is overestimated by a factor of about two. These elaborate coil models are the result of another optimization process that is quite time consuming. Therefore, the combination of both methods requires excessive computer times. Insulation, magnetoresistance and eddy currents were also neglected here. The main effect would be a reduction of the pulse length.

An exact calculation of the necessary energy of a capacitor bank would sum up the magnetic energy at the field maximum, the thermal energy in the coil at this time, and additional losses in the current leads and the surrounding circuit.

7 Conclusion

The optimization performed here gives the designer of a magnet system information about the expected field, the necessary magnetic and thermal energy, the current density distribution and the pulse length. Though the coil model used (polyhelix coil with isotropic material properties) seems very simple, a comparison with more elaborate models shows that the field and the magnetic energy are about ten percent off and the pulse length is overestimated by a factor of about two.

Acknowledgement

This work was done during a research stay of R.K. at the NHMFL in Tallahassee. Special thanks go to all who helped with fruitful discussions and encouragement. Thanks also to the staff at the NHMFL, their southern hospitality will always be remembered.

References

1. De Klerk, D., 'The Construction of High Field Electromagnets', Newport Instruments Ltd., 1965.
2. The homepage of 'SolvOpt' with manual and sources is *http://bedvgm.kfunigraz.ac.at:8001/alex/solvopt/slvmain.html.*
3. The Nonlinear Programming FAQ can be found on the web at *http://www.mcs.anl.gov/home/otc/Guide/faq/nonlinearprogrammingfaq.html.*
4. Calculations performed by Y.M.Eyssa and M.R. Vaghar, Magnet Science and Technology group, NHMFL, Tallahassee.

1-, 2- AND N-COIL SYSTEMS

R. KRATZ
Max-Planck-Institut für Physik komplexer Systeme, Dresden, Germany
and Forschungszentrum Rossendorf, Dresden, Germany

Y. M. EYSSA, L. LI, H. J. SCHNEIDER-MUNTAU, M. R. VAGHAR,
S. W. VAN SCIVER
National High Magnetic Field Laboratory, Tallahassee, USA

Various coil designs consisting of 1, 2 and n coils are compared with each other. Furthermore, each coil type was calculated for the real case with finite height and the case of an infinite long coil system. In the investigated parameter space the estimation with infinitely long magnets gives about 5 to 10% higher fields. For the same geometric dimensions the generated field increases with the number n of coils.

1 Introduction

A principal question in the generation of high magnetic fields is how to find the best magnet design. The comparison of the various coil designs is hindered by the fact that the magnetic field and the mechanical stresses in a solenoid cannot be calculated analytically but only by numerical methods. An elaborate analysis is, therefore, at least time consuming and mountains of numerical results may hide the underlying basics.

Making the coil infinitely long circumvents this obstacle and allows for an analytical calculation of the magnetic fields and the mechanical stresses. The stress calculation can be carried out for a massive coil as well as a coil without radial transmission of forces [1,2]. The latter one represents an ideal polyhelix coil, the first one a wire wound coil.

This analytical treatment allows for easy comparisons of the various coil designs and also gives expressions for important quantities like the magnetic energy. Of course the situation in a real coil with finite length is different. A few examples will illustrate how close the estimation with infinite long coils will come to calculations of real coils.

2 Setup, Infinite Long Coils

We regard only cylindrical, infinitely long coils with a constant current density distribution and filling factor = 1. The inner radius is generally taken as $a_1 = 1$ cm, all geometric dimensions are normalized to a_1. The magnetic field then has only an axial component. It is constant in regions outside of the coil; within the coil it is a linear function of the radial position. For the general calculation of the stress tensor σ one has to solve the equilibrium condition $\nabla \sigma + \mathbf{f} = 0$ where $\mathbf{f}$ is the density of the Lorentz forces, in conjunction with the so-called stress-strain-relations [3]. For the mechanical properties of the used materials (Young's modulus, Poisson ratio, etc.) we assume the isotropic, elastic case. The von Mises stress is used to determine the yield stress of the material.

Three types of coils are investigated:

1. A single coil: The coil extends radially from 1 to $\alpha = a_2/a_1$. Mechanical forces are transmitted radially. This is the model of a wire wound coil.
2. Two nested coils: The inner coil stretches from 1 to α_1 and the outer coil from $\alpha_1 + \delta$ to α, where the gap δ is taken as infinitely small. The maximal possible yield strengths in the inner and outer coil are σ_1 and σ_2, respectively. Mechanical forces are transmitted radially except at the gap at α_1. The current density in each coil should be constant but may differ for the inner and outer coil. For any given set of α, α_1, σ_1 and σ_2 there exists one intersection radius α_1 that results in the highest central field under the boundary condition that the stress limits of both coils are not exceeded.
3. Polyhelix coil: The coil extends radially from 1 to α. Each helix is operated at the same current density. Mechanical forces are <u>not</u> transmitted radially. The mechanical stress tensor σ has only one non-vanishing component $\sigma_{\varphi\varphi} = j \times r \times B(r)$.

3 Setup, Real Coils

Calculations of real coils corresponding to the above three cases were performed with a finite element program [4]. The height of these coils was usually chosen to be equal to the outer diameter. Again the isotropic, elastic case for the mechanical properties was assumed. As coil material we used copper, with data taken from [5].

4 Results, Infinitely Long Coils

*4.*1 Single coil: The central field is a function of the yield strength σ_0 of the coil material and the outer radius α. In the limit of $\alpha \to \infty$ the field converges to $B_0 = \sqrt{\mu_0 \sigma_0} \times 1.177$, so that the maximal achievable field is only a function of the materials yield strength.

For an outer radius of $\alpha = 20$ one gets $B_0 = \sqrt{\mu_0 \sigma_0} \times 1.170$, and using a yield strength of 1 GPa results in $B_0 = 41.5$ T.

4.2 Two nested coils: We fix the outer radius of the outer coil to $\alpha = 20$ and the yield strength of the outer coil to $\sigma_2 = 1$ GPa. Central fields B_0 and separation radius α_1 for a few representative values of the inner coil's yield strength σ_1 are shown in Table 1:

σ_1 [GPa]	α_1	B_0 [T] =	B_1 [T] +	B_2 [T]
1.0	4.3	55.4	15.6	39.8
1.5	4.9	61.9	22.5	39.4
2.0	5.4	67.9	22.8	39.1

Table 1: Central fields for two nested infinitely long coils.

By increasing the inner coil's yield strength σ_1 the two-coil system responds with an increase of the separation radius α_1, an increase of the field B_1 from the inner coil and an increase of the total field B_0. The field B_2 from the outer coil decreases slightly.

4.3 Polyhelix coil: For an outer radius of $\alpha = 20$ and a yield strength of 1 GPa one gets $B_0 = 67.4$ T.

5 Results, Real Coils

5.1 Single coil: As already mentioned, we took the coil's height equal to its diameter, i.e. here $\alpha = \beta = 20$. This coil generates a central field of 40.4 T.

5.2 Two nested coils: The outer radius of the outer coil is fixed to $\alpha = 20$, the yield strength to $\sigma_2 = 1$ GPa. The height of the outer coil was again $2\times\beta_2 = 40$, the height of the inner coil was taken to be $2\times\beta_1 = 20$. This somehow reflects the ideal Kelvin current density distribution. One can also say that those current elements far from the coil's midplane and close to its axis give only minor contributions to the central field. The gap at the separation radius α_1 was assumed to be symmetrical around α_1 with a width of 0.5. For the same representative values of the inner coil's yield strength σ_1 we get for the central field B_0:

σ_1 [GPa]	α_1	B0 [T]	B0,∞ [T]	Error
1.0	4.3	53.1	55.4	4 %
1.5	4.9	59.4	61.9	4 %
2.0	5.4	64.8	67.9	5 %

Table 2: Finite element calculations for two nested coils and comparison with the estimation for infinitely long coil system.

With $B_{0,\infty}$ [T] we mean the field from the infinitely long coil. Also indicated is the error of the calculation of the infinite long coil with respect to the real coil.

5.3 Polyhelix coil: The stresses in a polyhelix coil are easier to calculate. Because of the missing radial transmission of forces the differential equation $\nabla\,\sigma + \mathbf{f} = 0$ gets decoupled, the azimuthal component is $\sigma_{\varphi\varphi}(r,z) = j \times r \times B_z(r)$ and the axial component can be found with the vector potential method, $\sigma_{zz}(r,z) = j \times (\,A_\varphi(r,\beta) - A_\varphi(r,z)\,)$. A polyhelix coil with $\alpha = \beta = 20$ and a yield strength of 1 GPa generates a central field of $B_0 = 60.6$ T.

6 Comparison

For a quick overview we repeat the results for the central fields in Table 3. Fixed values are a yield strength of the material of $\sigma = 1$ GPa, an inner radius of $a_1 = 1$ cm and an outer radius of $\alpha = 20$. The real coils had $\beta = 20$.

Infinitely long coil	Real coil	
41.5 T	40.4 T	Single coil
55.4 T	53.1 T	Two nested coils, $\sigma_1 = \sigma_2$
67.9 T	60.6 T	Polyhelix coil

Table 3: Comparison of coil types and calculation methods.

7 Conclusion

The approximation with infinitely long coils overestimates the fields between five and ten percent. For a given yield strength, inner radius a_1, and coil parameters α and β and constant current density distribution the single coil produces the lowest fields. The design is the simplest one, however. The highest fields are generated with the polyhelix design that may be difficult to manufacture. The method with two nested coils may be the best solution regarding achievable field and ease of manufacture.

In the framework of these simple models discussed here, one can treat an internal or external reinforcement as increasing the yield strength of the coil structure.

References

1 Montgomery, D. B., 'Solenoid magnet design', Wiley-Interscience, 1969.
2 Wilson, M. N., 'Superconducting magnets', Clarendon Press, Oxford, 1983.
3 Sommerfeld, A., 'Mechanik der deformierbaren Medien', 1978.
4 PDEase™ syma Inc., 20 Academy Street, Arlington, MA 02174, USA, *http://www.macsyma.com*
5 NIST Monograph 177, Properties of Copper and Copper Alloys at Cryogenic Temperatures.

THE CONSTRUCTION OF HIGH PERFORMANCE PULSE MAGNETS AT NHMFL

B. LESCH, V. COCHRAN, L. LI, P. PERNAMBUCO WISE, S. TOZER,
H. SCHNEIDER-MUNTAU, S. VAN SCIVER
NHMFL, Tallahassee, Fl., USA

The construction techniques for High Performance Pulse Magnets produced at the NHMFL pulse coil winding facility in Tallahassee are described. The mechanical design, parts fabrication and manufacturing of these magnets are discussed. In conclusion, proposed changes made in the construction of the coils after analyzing failure tests carried out at the NHMFL pulsed field facility in Los Alamos are noted.

1 Introduction

Throughout 1998, the NHMFL Pulse Magnet Winding Facility has designed, built and tested numerous high performance pulsed magnets using *CuNb* conductor and *Zylon* fiber composite reinforcement. Recently three of these magnets with bore sizes of 24 mm, 15 mm and 10 mm were tested to failure at the Los Alamos National Laboratory (LANL) Pulse Magnet User Facility. These magnets failed at peak fields of 65 T, 74.2 T and 80.1 T respectively (Figure 1). Lessons learned from the failure tests have resulted in an upgraded design for future high performance magnets. All aspects of manufacturing these magnets are performed in house at the NHMFL facility.

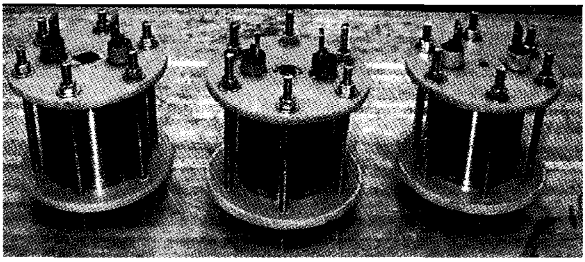

Figure 1. Three high performance pulse magnets with 10, 15 and 24 mm bore sizes

2 Construction Design

Once the final conceptual design of the high performance pulse magnet has been calculated, the first step necessary to realize this is to make a series of computer aided design (CAD) drawings. These drawings detail each part needed to build the magnet, the dimensions and type of material to be used, and how the parts will fit together. The drawings are then taken to the machine shop to be fabricated.

3 Parts Fabrication

The machine shop at NHMFL plays a very valuable role in the process of constructing high performance magnet parts. The majority of all magnet parts are fabricated in house. The following is a list of materials used in the manufacturing of high performance magnet parts:

A286 Stainless Steel - an iron based super alloy useful for applications that require high strength and high elongation. The reinforcing steel shell of the magnet is made from A286 Stainless Steel.

Beryllium Copper - a compound of Cu and Be which drastically increases the tensile strength of copper, making its properties very close to that of high strength steel. The pressure plate assembly tie rods are made from CuBe.

G10 - a glass fiber material that retains its strength at very low temperatures. The cartwheels, transition ramps, pickup probes and other smaller magnet pieces are made from G10.

MP35N - a nickel-cobalt based alloy that has a unique combination of properties: ultra high strength, toughness, ductility and outstanding corrosion resistance. MP35N is used for the pressure plate assembly in the magnet.

Stress Proof Steel - a tool steel that can be taken to very high temperatures, allowing Teflon© to be applied without distortion. The winding mandrel is made of stress proof steel.

4 Magnet Manufacturing

The G10 end flanges, or *cartwheels*, are connected to the winding mandrel. A mounting rod, or arbor, is fixed to each end of the cartwheels so that it can be held while the whole apparatus is secured inside the chuck of the winding machine. A spool of CuNb wire is placed on the wire tensioner. This device allows the tension of the wire to be kept constant during the winding process so that the magnet does not unwind. The tensioner is movable so that the angle or pitch of the wire into the winding machine can be changed. The CuNb conductor is then fed from the tensioner through a channel in the cartwheel. The first layer of the conductor is then wound onto the mandrel.

Once the first conductor layer is in place, zylon fiber is distributed over the CuNb using a fiber-winding machine. A different thickness of zylon fiber is applied between each layer of conductor. This provides reinforcement for the magnet against the very large forces that try to deform the conductor outwards during magnet operation. Multiple passes are necessary to obtain the pre-calculated thickness of zylon between each layer. While each layer of zylon fiber is being applied, epoxy resin is brushed on simultaneously. This technique is known as *wet winding.*

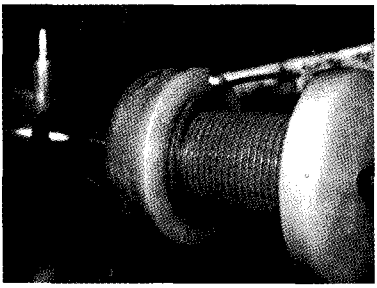

Figure 2. Transition point of conductor.

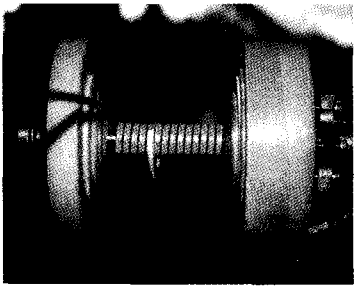

Figure 3. Ramps fitted into the transition.

The end of each conductor layer lies against the cartwheel or transition point (Figure 2). This provides a particular difficulty as the conductor must be lifted from the previous layer up to the new layer and it must also reverse pitch to transverse the mandrel towards the other end. Specially designed G10 pieces called *ramps* are machined to guide the wire and support it at these transition points (Figure 3).

When the last layer of CuNb has been wound onto the coil, the wire is cut and bent upwards through a pre-cut groove in the cartwheel. The groove is filled with a designated G10 piece and then the last layers of zylon are wound onto the magnet. Once the zylon has been applied, the magnet is then overbanded with S glass fiber. This allows the surface to be machined after impregnation. The supporting arbors are then unscrewed and the magnet is removed from the winding machine. The two wire ends are stripped of insulation and later bolted to copper bus bars that will form the electrical connections to the outside world.

As soon as the magnet is pulled from the winding machine, it is put into an *epoxy impregnation bath* in a special steel cylinder. Epoxy is then poured into the cylinder around the magnet. The cylinder is then sealed and put into the oven for curing. A head of pressure is introduced into the cylinder; this will reduce any voided areas. The oven is then brought up to temperature and the magnet cured for a predetermined amount of time (Figure 4).

After cooling, the magnet is pushed out of the cylinder and the excess epoxy is machined away so that the last layer of zylon can just be seen. A large, round G10 plate or support flange is then fixed to the top of the magnet. An A286 stainless steel shell is machined so that it is about 0.1 mm smaller than the outside diameter of the magnet. The steel shell is used to further the magnet reinforcement. The shell is heated to about 100 C so that it expands slightly and the magnet is dropped into the shell. As the shell cools it shrinks to make a tight fit with the magnet. Once the magnet is in the shell it is overwound with zylon to increase the radial strength of the steel. The bottom end flange is then attached to the magnet. The support flanges and pressure plates are bolted to the base. The manufacturing process is then complete. As a final step before training and commissioning, the resistance of the coil is determined (Figure 4).

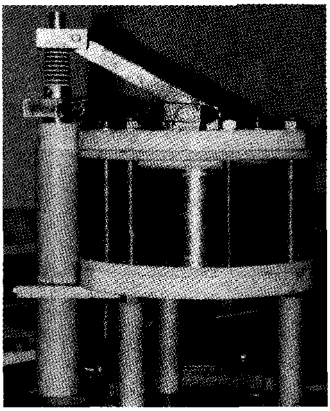

Figure 4. A High Performance magnet ready to be tested.

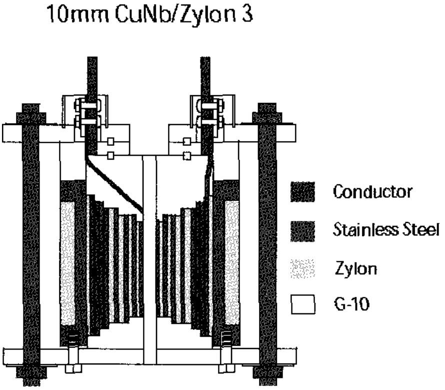

Figure 5. Revision 3 cross section view detailing internal mechanical design.

5 Conclusion

It was found that the radial containment of the wire transition from layer to layer required additional reinforcement. Revision 3 (Figure 5) shows one approach to this problem by lengthening each layer axially to support these transitions, and may be used in future tests.

References

1. P. Pernambuco-Wise, Hans Schneider-Muntau, "Design, Construction and Testing of Pulse Magnets at the National High Magnetic Field Laboratory", MT13, Oct. 1997.
2. L. Li, "High performance pulsed magnets: Theory, Design and Construction", Ph.D. thesis, K. U. Leuven 1998.

DESIGN OF A 90 T PULSE MAGNET

M. R. VAGHAR, L. LI, Y. EYSSA, H. J. SCHNEIDER-MUNTAU
National High Magnetic Field Laboratory (NHMFL), Florida State University, Tallahassee, FL

R. KRATZ
Forschungszentrum Rossendorf E. V., Germany

The primary reasons for pulse magnet failures are excess heating and stresses due to the Lorentz forces. Uniform heating and constant stress through all layers will improve the performance of a magnet. A computer code is introduced to optimize the magnetic field of a pulse magnet based on the type and dimensions of the conductor layers, and thickness of the reinforcement layers. Dimensions of each conductor layer are computed to achieve uniform final maximum temperature for all layers. Internal reinforcement thickness, along with the type of each conductor, is calculated based on the maximum stress in the reinforcement and the maximum elongation in the conductor. The program uses the Newton's finite difference method to find the optimum solution. This program was applied for the design of a 10-layer pulse magnet with an 11 mm bore diameter. Copper-stainless steel wires were used for the conductors (with different percentage of steel resulting from the optimization) and MP35N was utilized for the internal layer reinforcement. Optimized solutions were found for the maximum final temperature of 320 K, maximum von Mises stress of 2.0 GPa in the reinforcement (77% of the yield stress of MP35N), and maximum elongation of 3% in the conductor. With an energy of 0.72 MJ and a voltage bank of 12 kV, a field of 89 T can be reached, and with 24 kV and 1.9 MJ the achievable field may be increased to 93 T. The results show that a 100 T field can be attained (with an energy of 1.9 MJ) by permitting a maximum final temperature of 400 K and maximum von Mises stress of 2.60 GPa (100% of the yield stress of MP35N). Therefore, future research activities should focus on the development of stronger reinforcement materials.

1 Introduction

In the design of pulse magnets, there are a number of parameters that affect the magnetic field. Among these parameters are bore diameter, number of layers, energy supply, bank voltage, conductor dimensions and material, reinforcement thickness and material. In this paper, the magnetic field is optimized for a magnet with a certain bore size and number of layers. The reinforcement thickness, the type of wire used for making the conductor and the dimensions of the wire are used as parameters of the optimization. Calculations are performed for different energy levels and different bank voltages. The maximum stress in the reinforcement, the maximum elongation in the conductor and the final maximum temperature in the conductor layers are used as constraints of the optimization.

2 Optimization

The Lorentz forces result in very high stresses in a pulse magnet. All known conductors fail at much lower stresses. To compensate for the lack of strength in conductor materials, a reinforcement of high strength is introduced after each conductor layer so that the stresses are passed from the conductor to the reinforcement. The existence of these reinforcements lowers the overall current density, resulting in a lower field. Thus, the thickness of a reinforcement layer must be kept to a minimum such that both the reinforcement and the conductor reach their failure criteria simultaneously. Another method to compensate for the lack of strength in the conductor is to combine the conductor and a reinforcement to increase the strength of the overall conductor. Copper-stainless conductor is an example of the application of this method. Both methods have advantages and disadvantages; therefore for best results the combination of both methods is applied. To reach the optimum field, copper-stainless steel wires are used for the conductor layers, and high strength MP35N is utilized for the reinforcement layers. The thickness of the reinforcement layers and the percentage of the steel in the wires are computed for maximum allowable effective stress in the reinforcement and maximum allowable elongation in the conductor. The dimensions of each wire are calculated to reach the same final maximum temperature for all conductor layers. The temperature in a conductor layer and also the stresses decrease by increasing the cross section of the wire. Computing the wire dimensions is not independent of calculating the reinforcement thickness and percentage of steel in the wire. The variance in thickness of reinforcement will alter the magnetic field, which changes both the temperature and stresses in the magnet. Also changing the percentage of steel in the wire has a direct effect on the temperature in the conductor.

3 Computer Code

A computer code has been written to optimize the field. This code applies the Newton's finite difference method [1] (for a system of nonlinear equations) for optimization. The code utilizes two major subroutines for calculating thermal, electrical and mechanical properties of a pulse magnet. Both subroutines have been written at the National High Magnetic Field Laboratory [2,3]. The first subroutine is a thermal code and circuit solver that solves multiple circuits powered by different power supplies. It also solves for temperature distribution in each conductor turn. It uses a finite difference technique to calculate all variables (temperature, current, voltage, resistance, field and field derivative) as a function of time. The second subroutine is a stress analysis code. It computes stresses, strains and displacement at the mid-plane (where the effective stress is maximum) of both conductor and reinforcement regions. The stress analysis is based on the generalized plane strain condition for a multilayer solenoid magnet with orthotropic material properties.

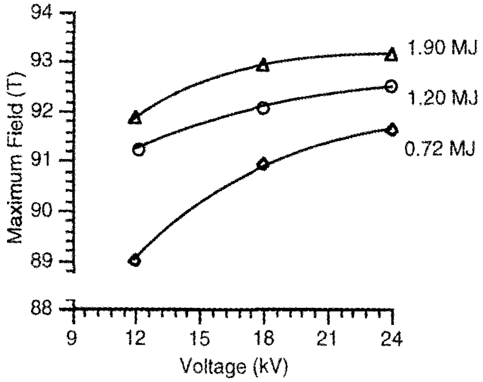

Figure 1. Optimized field vs. voltage for different energy supplies

4 Results and Discussions

Series of optimized solutions were found for a 10-layer pulse magnet with 11 mm bore diameter.

Fig. 1 shows the optimized field as a function of voltage for different energy supplies. For this calculation, a maximum von Mises stress in the reinforcement of 2.0 GPa (77% of the yield stress of MP35N), a maximum elongation in the conductor of 3%, and a final maximum temperature in the conductors of 320 K are assumed. The magnetic field improves by about 1.6% or 1.5 T by increasing the bank voltage from 12 kV to 24 kV. This increase is not significant and results from reduced eddy current losses due to smaller wire cross sections at the expense of a lower space factor. The more important beneficial effect of higher voltages comes from the fact that smaller cross sections are helpful in terms of manufacturing and winding the conductors. Increasing the energy supply will improve the field by utmost 3 T or 3.3% (for a bank voltage of 12 kV) (Fig. 1). Note that in all of the optimization calculations a moderate crow bar of 0.25 Ω and zero lead resistance or inductance are assumed. The same optimization (for an energy supply of 1.9 MJ) has been performed with the assumption of maximum von Mises stress of 2.60 GPa (100% of the yield stress of MP35N) in the reinforcement.

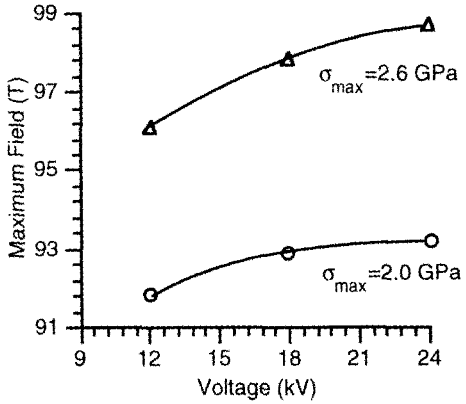

Figure 2. Optimized field vs. voltage for maximum von Mises stress of 2.60 GPa and 2.0 GPa in the reinforcement.

Fig. 2 shows results of these calculations. The magnetic field now improves by an average of 5% or 5 T by admitting the von Mises stress in the reinforcement to increase from 2.0 GPa to 2.6 GPa. The growth in field by increasing the bank voltage from 12 kV to 24 kV is about 2.5 T. Permitting the maximum final temperature to increase from 320 K to 400 K will also improve the field.

Fig. 3 shows this improvement for maximum effective stress of 2.6 GPa (in reinforcement) and energy supply of 1.9 MJ. The field grows about 1 T or 1.1% when a maximum final temperature of 400 K is assumed. It is evident from above that the magnetic field improves the most with stronger reinforcement.

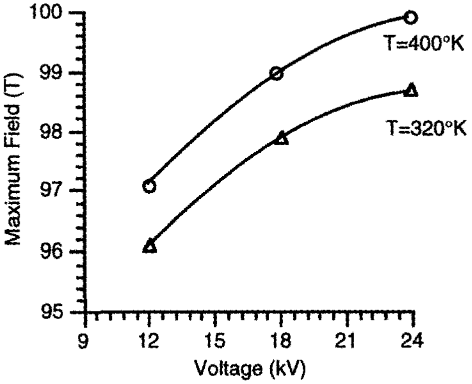

Figure 3. Optimized field vs. voltage for a maximum final temperature of 320 K and 400K in conductors.

5 Conclusion

A computer code was introduced to optimize the design of a pulse magnet. Maximum achievable magnetic fields are computed under the condition of uniform heating in the conductors and constant effective stress in the reinforcement layers. The results show fields of 80 - 90 T may be generated for a 10-layer pulse magnet and 11 mm bore diameter. An energy of 0.72 MJ and voltages of 12 kV to 24 kV are required to attain these fields. Reinforcement layers will be stressed up to 2.0 GPa and the final temperature in the conductors will rise to 320 K. The conductor layers will deform plastically, but their elongation will be less than 3%. Operating with higher voltages does not improve the field as much as it helps in terms of winding the conductor layers. To achieve higher fields more energy is required, nevertheless, the improvement in field by increasing the energy tends to decline. Increasing the final temperature limit also improves the field although this improvement is not substantial. Stronger reinforcement materials improve the magnetic field significantly. A field of 100 T is achievable with reinforcement layers that can be stressed up to 2.6 GPa. Therefore, to improve the magnetic field, future research activities should be focused on the development of stronger reinforcement materials. Note that here the failure criterion for the conductor is based on maximum elongation, and fatigue of the conductors is not considered. Thus, if high longevity is required, i.e., the conductor layers remain in the elastic region (like the reinforcement layers) then development of stronger conductors is also imperative.

6 References

1. Dennis, J. E., Schnabel, R. B., *Numerical Methods for Unconstrained Optimization and Nonlinear Equations*, Prentice-Hall, Englewood Cliffs, 1983.
2. Eyssa, Y. M., Pernambuco-Wise, P., *Electrical, Thermal and Mechanical Modeling of Pulsed magnets*, Internal Report, National High Magnetic Field Laboratory, Tallahassee, FL, 1995.
3. Markiewicz, W. D., Vaghar, M. R., Dixon, I. R., Garmestani, H., Jimeian, J., *Generalized Plane Strain Analysis of Solenoid Magnets: Formulation and Examples*, Internal Report, National High Magnetic Field Laboratory, Tallahassee, FL, 1993.

HIGH FIELD PULSE MAGNETS WITH NEW MATERIALS

L. LI, B. LESCH, V. G. COCHRAN, Y. EYSSA, S. TOZER, C. H. MIELKE*,
D. RICKEL*, S. W. VAN SCIVER, H. J. SCHNEIDER-MUNTAU

National High Magnetic Field Laboratory, Tallahassee, USA
**National High Magnetic Field Laboratory, Los Alamos National Laboratory, USA*

High performance pulse magnets using the combination of CuNb conductor and Zylon fiber composite reinforcement with bore sizes of 24, 15 and 10 mm have been designed, manufactured and tested to destruction. The magnets successfully reached the peak fields of 64, 70 and 77.8 T respectively with no destruction. Failures occurred near the end flanges at the layer. The magnet design, manufacturing and testing, and the mode of the failure are described and analyzed.

1 Introduction

Pulsed magnets presently used at the Pulsed field facility of the National High Magnetic Field Laboratory at Los Alamos National are operated at 50 T and 60 T with bore sizes of 24 mm and 15 mm. With the increased experience of using pulse magnets in experiments, the pulse magnetic field users are becoming interested in higher fields even at the expense of bore size. Three pulsed magnets were designed and manufactured by the pulsed magnet group of the National High Magnetic Field Laboratory at Tallahassee and tested at the Los Alamos National Laboratory. The primary objective was to obtain user magnets that can generate 70, 65 and 55 T regularly, with bore sizes of 10, 15 and 24 mm, respectively.

2 Materials

The 15 and 24 mm bore pulse magnets were made from Glidcop wire with S2-glass fiber as internal reinforcement. Because of the low strength of 540 MPa, the conductor suffers plastic deformation during both up-sweep and down-sweep of a high field pulse. The fatigue life of such magnets is normally 500-600 full field shots. The requirement for longer life expectancy calls for a design where the strain cycle of the conductor is kept as small as possible compared with its elastic strain range to avoid fatigue. The best way to do so is by using high strength conductors in combination with high modulus reinforcing materials. High modulus materials such as steel, carbon and boron cause insulation problems when used as internal reinforcements. A good combination did not exist until Dr. S. Tozer introduced us to Zylon fiber for pulsed magnet construction. The three test magnets reported here are made of CuNb wire with Zylon fiber as internal and external reinforcements.

2.1 CuNb Conductor

The CuNb conductor was developed by Supercon. Inc. It offers a good combination of conductivity and strength. It has a tensile strength of 0.99 GPa at room temperature and 1.24 GPa at 77 K. The elongation of the wire at 77 K is 5.4%. At room temperature, the conductivity is 72% and the resistivity ratio between 300 K and 77 K is approximately 4.3. The wire has a rectangular cross section of 3 mm by 4 mm and is insulated by Al-polyimide 32LQI-2 film from Fraivillig Materials Company. The wire shows a good windability and can be wound onto a 10 mm bore. The double wrapping of the Al-polyimide 32LQI-2 film gives it good turn-to-turn voltage insulation.

2.2 *Zylon Fiber*

The use of HM (high modulus) Zylon fiber as internal reinforcement was studied to further increase the performance of the user magnets. This Zylon fiber will be beneficial for longer life magnets because it reduces the strain cycle of the conductor during the pulse. The Zylon fiber is commercially available from TOYOBO CO., LTD. The fiber has a modulus of 280 GPa with a tensile strength of 5.8 GPa and an elongation at break of 2.5%. As the CuNb conductor reaches 95% of its UTS at the same elongation, the combination of these two materials uses the full potential of both the conductor and the reinforcement at high magnetic fields. The packing factor of the Zylon fiber was measured to be above 80% [1]. It is difficult to vacuum-impregnate windings with such a high packing factor so both the internal and external reinforcements were applied using wet winding.

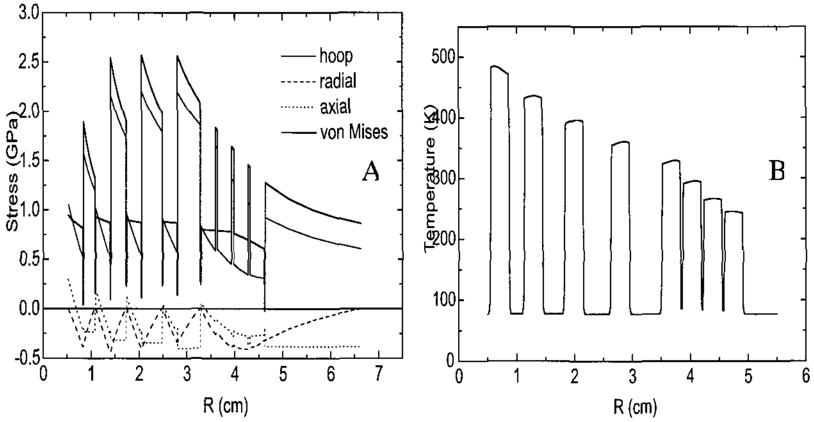

Figure 1. A: Stress in the mid-plane of the magnet at the peak of an 80 T pulse; B: temperature distribution in the mid-plane of the magnet at the end of the pulse. Bars on top mark the positions of the conductor layers.

3 Design and Manufacturing

3.1 *Magnet Design*

The key to the successful design of a pulsed magnet is the optimization of the electric, thermal and mechanical performance of the magnet and the electric circuit. These are strongly interrelated, therefore coil design is an iterative process done by computer codes [2,3]. The dimensions of the magnets and the distribution of the internal and external reinforcement are given in Table 1. The determination of the appropriate amounts of reinforcement to be applied after each layer is based on the iteration process where stresses and the stress cycle amplitudes in the magnets are calculated and subsequently adjusted.

Table 1. Details of the geometry of the CuNb magnets reinforced with zylon

Name	Bore	Height	Layers	Thickness of the int. reinf. (Zylon)					Ext. reinf
	(mm)			#1	#2	#3	#4	#5-#8	Zy+SS+Zy
Zy10	10	87	8	2.3	3.2	4.2	4.7	0.25	4.2+7.5+11.5
Zy15	15	92	8	2.5	3.6	4.4	4.4	0.25	5.3+7.5+7.5
Zy24	24	95	8	3.5	4.3	4.9	2.2	0.25	5.7+10+5

Figure 1 shows the stresses (left) in the mid-plane of magnet Zy10 at the peak field of 80 T and the temperature distribution (right) after the pulse. The inner four layers are supported by the internal reinforcement and are mechanically independent, while the outer four layers are compressed radially and transfer part of the load to the outer shell. The inhomogeneous temperature distribution with the peak at the innermost conductor layer results from the magnetoresistance and the skin effect.

3.2 Manufacturing

The magnets were wound on the winding machine at the NHMFL, which is equipped with an in situ fiber wrapping mechanism to apply the fiber reinforcement after every layer of conductor. At the layer-to-layer transitions, specially designed G10 ramps were made to guide the wire. After impregnation the magnets were machined to the correct dimensions for the A286 stainless steel cylinder to be shrink fitted to the magnet to provide extra axial reinforcement. The external reinforcement (on top of the cylinder) was applied afterwards using wet winding.

4 Testing Results and Analysis

The magnets were tested at the NHMFL pulsed field facility at the Los Alamos National Laboratory by a series of pulses with successively higher fields. Fields up to 63.5, 70 and 77.8 T were obtained with magnets of 24, 15 and 10 mm respectively, without destruction. The typical pulse shapes of these magnets are shown in Fig. 2. All magnets failed after

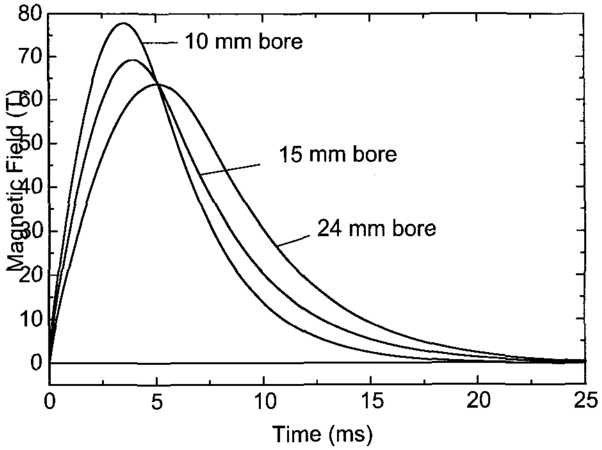

Figure 2. Measured wave forms of the tested magnets.

reaching the peak fields of 65, 75 and 80 T, respectively. Investigation of the damaged magnets showed that the failures occur near the end flanges at the layer transitions. The transition G10 ramps were glued with epoxy to the surroundings. It is likely that the ramps became loose or were damaged at high fields and cannot provide any reinforcement in the hoop direction. The coil windings were still in one compact piece with no damage seen in the midplane of the magnets. This indicates that higher fields can be obtained if the design of the transition is improved.

5 Conclusion

Design of magnets with a CuNb conductor and Zylon fiber reinforcement showed capability of producing fields reliably up to 55, 65 and 70 T in bore sizes of 24, 15 and 10 mm. Use of Zylon fiber as internal reinforcement was successfully addressed, yielding magnets reaching fields of up to 77.8 T. Efforts will be made to improve the design of the transitions to obtain higher fields.

References

1. Pernambuco-Wise, P., "Report of magnet testing at the NHMFL pulse magnet user facility, LANL" internal report of NHMFL, August 1997.
2. Li, L., "High performance pulsed magnets: Theory, Design and Construction" Ph. D. thesis, K. U. Leuven (1998).
3. Eyssa, Y. M., Pernambuco-Wise, P., "Electrical, thermal and mechanical modelling of pulsed magnets" internal report of NHMFL, (1995).

NEW CONDUCTORS FOR MAGNETS

S. ASKÉNAZY[1], F. LECOUTURIER[1], L. THILLY[1,2], G. COFFE[1]
[1] *Service National des Champs Magnétiques Pulsés*
118, Route de Narbonne, 31062 Toulouse Cedex, France
[2] *Laboratoire de Physique de la Matière Condensée*
Complexe Scientifique de Rangueil, 31077 Toulouse Cedex, France

Pure copper has the highest metallic Action Integral $AI = \int_{63K}^{250K} C_V/\rho . dT$. *AI* determines the pulse duration of the magnetic field. The Von Mises stress ($\sigma_{V.M}$) in the winding achieves $0.6P_{mag}$, i.e. $\sigma_{V.M.} = 2400$ MPa for a 100 Tesla field. High yield strength, i.e., $\sigma_{0.2\%} > \sigma_{V.M}$, is required for the reliability of the winding. The ideal conductor for long pulse duration and non-destructive magnetic fields should have its *AI* as close as possible to that of copper and exhibit extremely high elastic limit. Thus alloys cannot be used, while the copper-based macrocomposites cannot offer the best mechanical properties. The ultimate performances are achieved with new nanocomposites reinforced with continuous nanowhiskers, made of a metal non-miscible with copper, distributed on an Abrikosov lattice. The ultimate tensile strength of the nanowhiskers tends to the theoretical value for perfect crystals, $\mu/2\pi$ (15 GPa for Nb and 30 GPa for Ta), where μ is the shear modulus. This paper presents the characteristics of these structures and their latest developments.

1 Introduction

The duration of the magnetic field pulse is $\Delta t = T \cdot W_{mag}^{2/3} \cdot B_0^{-10/3} \cdot AI$. T is a geometrical factor linked to the coil structure. W_{mag} is the magnetic energy and B_0 is the field amplitude at the center of the coil. Through the action integral, it is obvious that high heat capacity and high conductivity material will give long Δt.

Among all the possible magnet structures [1], the conventional coil having uniform current distribution gives the longest pulse duration because its geometrical factor T is maximum. The stress distribution is proportional to the magnetic pressure $P_{mag} = B_0^2/2\mu_0$. The maximum value of the Von Mises stress ($\sigma_{V.M.,max}$) which takes into account the tangential and the longitudinal component of stresses is 0.6 P_{mag}. Thus, the solution to obtain non-destructive high-pulsed magnetic fields is to use insulated conductors with an elastic limit higher than $\sigma_{V.M.,max}$ (for 100 T, $\sigma_{V.M.,max} = 2400$ MPa). To improve the magnetic field pulse characteristics, the conducting materials used for the winding must possess the highest *AI* value and the best mechanical properties. Pure copper is the conducting material that exhibits the greatest *AI*, $\left\{[AI]^{250K}\right\}_{Cu} = 8.5 \cdot 10^{16} A^2 \cdot s \cdot m^{-4}$ [2]. Copper is ideal for the conducting characteristics but its mechanical properties are weak. It cannot be used to obtain magnetic fields much higher than 45 T in a conventional coil maintained by a reinforcing cylinder. To solve this problem, other materials must be chosen with conducting properties close to those of copper, and they must have extremely high mechanical properties. The criterion of selection can be simplified to $[AI] \approx \left\{[AI]_{77K}^{250K}\right\}_{Cu}$ and $\sigma_{UTS} \geq \sigma_{V.M.,max}$ [a].

2 Materials For High Pulsed Magnet Windings

The mechanical properties of materials are linked to their plasticity, ruled by the dislocation motion. They can be enhanced by the introduction of obstacles to the dislocation motion such as crystal defects (dislocations) and impurities. Nevertheless, the effects of such obstacles on resistivity, which are temperature independent, remain important at the working temperature during the magnetic field pulse. In this paper, we will only focus on the cost effective macrocomposite wires reinforced by stainless steel and on the sophisticated, continuous nanofilamentary nanocomposite wires developed by the Service National des Champs Magnétiques Pulsés (SNCMP) in order to satisfy condition [a].

2.1 The Macrocomposite Materials

This family of conductors has been developed under a simple concept; the conducting matrix is reinforced with a material chosen for good mechanical properties, both materials having a macroscopic size (>100 μm). Since the distance between dislocations is negligible compared to the size of the materials, each component can be considered as bulk material. The mechanical properties of the macrocomposites are then defined by the Rule of Mixtures. The electrical conductivity is ruled by the parallel conduction. *AI* is proportional to the square of V_{Cu}, the volumic fraction of copper. $[AI]_{comp} = V_{Cu}^2 [AI]_{Cu}$, assuming the Joule energy produced during the current pulse is dissipated only in copper.

The SNCMP develops its own macrocomposites [3], shown in Fig. 1, with a volumetric fraction of copper ranging from 40 to 80%. Electrolytic (ETP) and Oxygen Free High Conductivity (OFHC) copper are used, while the jacket is made of austenitic Stainless Steel (SS304L). Although ETP and OFHC copper give the same mechanical and electrical properties, only OFHC copper is now used to avoid the formation of oxides during annealing and the embrittlement of the interface. At 77 K, the 60% SS wire has σ_{uts}=1550 MPa, its resistivity is 0.59 μΩ/cm and RR = 6.4. An attempt was also made by the SNCMP to develop a copper conductor reinforced with macroscopic stainless steel fibers to increase the Action Integral by heat exchange [4]. To avoid the diffusion of iron, chromium and nickel in copper, a niobium barrier has been inserted between the copper matrix and the fibers, however the formation of hard and brittle intermetallic compounds between Nb, Fe, Cr, Ni weakens the interface. We have therefore orientated our production exclusively on jacketed wires that improve mechanical and electrical properties in the same level as similar systems developed elsewhere [5,6]. The production capability of our wire drawing shop depends on the human potential. One technician can produce much more than 500 Kg/year of jacketed wires. These jacketed wires will guarantee the longevity of conventional coils of 60 Tesla.

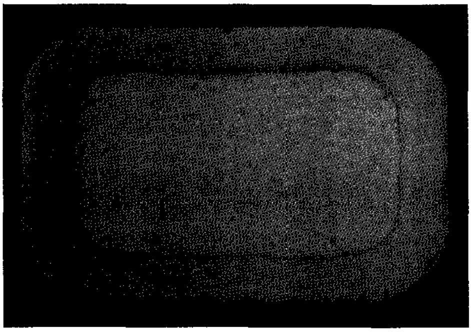

Figure 1: Cross section of Cu/SS jacketed wire.

2.2 *The Continuous Nanocomposite Materials*

The SNCMP has recently elaborated a new generation of continuous nanocomposite Cu/Nb wires. The elaboration of these nanocomposite wires reinforced with continuous whiskers is based on the restacking process used in manufacturing superconducting multifilamentary wires. We should remember that ten years ago the SNCMP obtained a 61 Tesla impulsion of 200 ms duration in a 1.25 MJ coil having a Cu/NbTi wire winding developed in collaboration with the Alsthom Company [7].

2.2.1 *Elaboration And Physical Properties*

Our strategy was to develop a process based on the cold-drawing and restacking of a niobium rod inserted in a copper jacket. This billet is co-extruded and cold-drawn to a hexagonal shape. 55 hexagons are stacked and inserted in a copper jacket. This process is repeated 3 times, and the final Cu-30%vol Nb conductor is a copper matrix reinforced with 55^4 (i.e. $9 \cdot 10^6$) continuous niobium fibers, shown in Fig. 2, with a 40 nm diameter, distributed on an Abrikosov lattice. These wires exhibit a UTS of 1950 MPa at 77 K. Itsresistivity at 77 K is 0.6 μΩ·cm with a resistivity ratio of RR = 4.7. The metallic Action Integral has been calculated to be $[AI]_{63K}^{250K} \approx 3{,}8.10^{16}\ A^2.s.m^{-4} = 0.45\,[AI]_{Cu}$. It clearly appears that the continuous nanocomposites have better electrical properties than the in-situ nanocomposites for the same strength level [2]. The origin of this high conductivity is the size of the copper channels, which is almost everywhere greater than the mean free path of electrons (250 nm at 77 K). IT should be possible to manufacture conventional coils of 75 Tesla with these wires.

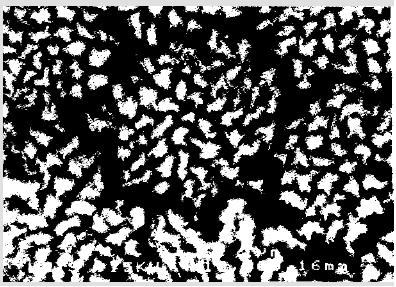

Figure 2: Cross section of the Nb fibers in a continuous nanofilamentary wire.

2.2.2 Fine Structure of the Continuous Nanocomposites

The study of the structure of the Cu/Nb nanofilamentary conductors showed that high texturing of copper and niobium appeared during the cold drawing process. The niobium developed a <110> texture parallel to the wire axis while copper exhibited a <111> texture. TEM observations of the niobium nanofibers showed that they are single crystals over a long range (>5 μm) with a low density of dislocations. This was confirmed by measurements that showed no effect of the strain rate on the UTS during tensile tests. In a first step, the UTS of the Nb fibers has been extrapolated without taking into account the effect of highly cold worked copper; their UTS is inversely proportional to their diameter and tends to the theoretical value for perfect crystal $\mu/2\pi$ [8] as it is presented in Fig. 3. μ is calculated for a <110> orientation. At 77 K, the whiskers properties are enhanced by the Peierls effect that is only present in bcc structures. All these features lead to conclude that the niobium fibers can be considered as nanowhiskers.

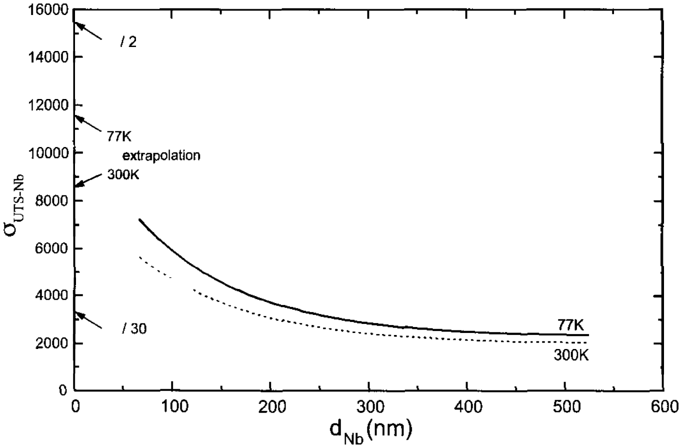

Figure 3: σ_{UTS-Nb} versus d_{Nb} for Cu/Nb continuous nanofilamentary wire.

HREM observations (Fig. 4) show semi-coherent interfaces between the (111) planes of Cu and the (110) planes of Nb, perpendicular to the drawing axis. After Fourier filtering, misfit dislocations appeared at the interface, with a mean distance equal to 8 planes, which is the theoretical value for a complete relaxation of the interface. The cold drawing process performed a quasi-epitaxy between the inter-filamentary copper and the niobium nanowhiskers. This epitaxy first observed on our continuous nanocomposites [9] has been observed later on in-situ Cu/Nb wires [2, 10] and on Cu/Ag multilayers [11]. This epitaxy seems to be a specific feature of the heavily cold-deformed composite metals.

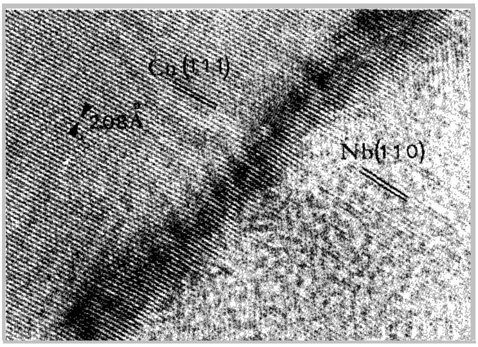

Figure 4:HREM micrograph of Cu/Nb interfaces.

2.2.1.1 Future Continuous Cu/Nb Nanocomposites

The challenge is to improve the already extraordinary properties of the continuous Cu/Nb nanocomposites. From the electrical point of view, the best way to reduce the resistivity is to maintain large copper channels in the conductor. This will be realized by inserting pure copper cores, the size of which is greater than the mean free path of electrons. The mechanical properties can be improved in two ways: reducing the fiber diameter (it will enhance the whisker effect and the fiber's UTS will more greatly approximate the $\mu/2\pi$ value); and increasing the Cu/Nb interfacial surface, which is a strong obstacle to the dislocation motion (this is possible by inserting a greater amount of fibers). Our solution is to stack 85 hexagons instead of 55, and iterate the restacking and cold drawing process 5 times instead of 4. The result will be a copper conductor reinforced with 85^5 (i.e. $4 \cdot 10^9$) continuous Nb fibers, with a diameter down to 10 nm. For a section of 10 mm^2, the UTS should approximate 3000 MPa, with improved conductivity. These new Cu/Nb conductors are being elaborated and should be obtained rapidly in their final state. They should allow the construction of a conventional, non-destructive coil of 100 T.

3 Future Materials For High Pulsed Magnet Windings

The results obtained with the first continuous Cu/Nb nanocomposites proved that the whisker properties of the fibers are responsible for the extreme mechanical properties. The selecting criterion for the strengthening material is a shear modulus higher than the one of Nb ($\mu_{\mathrm{Nb}} = 40$ GPa), the bcc structure and the immiscibility with Cu. Only Ta, Fe (for T

< 300°C) and W possess these characteristics. Their shear moduli are respectively 69 GPa, 80 GPa and 160 GPa. In the first step, the Cu/Ta system is being investigated. One can then expect to obtain wires exhibiting a UTS close to 4000 MPa.

3.1 The Cu/Ta System

For the elaboration of new composite wires, a Ta (99.97%) rod was inserted in a CuOFHC (99.99%) jacket with a volumetric fraction of 18%. The billet was then cold drawn to a Reduction in Area (RA) of 60%. For RA = 60%, the CuOFHC jacket has been etched to release the Ta rod and examine its surface. A first observation revealed the presence of a macroscopic roughness of the Ta surface. In Fig. 5, one can clearly see the wavy shape of the Ta surface. It is then possible to define two sets of oscillations:

- The first set is characterized by oscillations along the Ta rod perimeter with a crest line parallel to the drawing axis. The spacing between two neighbouring crest lines can be considered as a wavelength ($\lambda_{//}$) and the average wavelength is 110 μm ($\lambda_{//}$ varies between 50 and 200 μm).
- The second oscillation set is perpendicular to the previous one: the waves are located along the drawing axis with a crest line parallel to the Ta diameter. The wavelength ($\lambda_{\perp}$) varies between 200 and 800 μm.

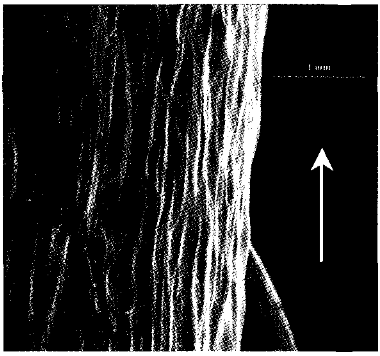

Figure 5: SEM observations of the oscillations on Ta surface

The presence of the two perpendicular sets led to the development of oscillation segments parallel to the drawing axis. This can be explained considering that the second set annihilated the first set when they had opposite amplitude. This would imply that the second system of oscillations appeared after the formation of the first one. This phenomenon did not appear during the elaboration of the Cu/Nb composite wires, even though Nb and Ta have the same lattice structure. The major difference between the two systems is the shear modulus of Ta that has twice the value of that of Nb.

To our knowledge, such roughness development has never been reported for three-dimensional bulk materials. We then focused on the surface instabilities appearing on one- or two-dimensional systems under stress. In 1985, M. A. Grinfeld elaborated a theory on the instabilities created by a non-hydrostatic stress field at the boundary between an elastic body and its melt [12], and extrapolated this theory to a solid with free surfaces and to a boundary between two solids. First, the instabilities of free surfaces of stressed solids were investigated [13,14,15]: a sinusoidal perturbation $z_A = e_A \cos(2\pi x/\lambda)$ has been introduced on a planar surface of a solid under homogeneous tensile stress $\sigma_{xx}=\sigma_0$. The surface energy is thus increased and the equilibrium conditions of the free surface are no longer verified. Elastic relaxation takes place because of the created stresses. The resulting energy variation ΔW was calculated to the second order in e: $\Delta W = \pi\gamma e^2[(1-\lambda/\lambda_c)]/\lambda^2$ with $\lambda_c = 2\pi\mu\gamma/(1-\nu)\sigma_0{}^2$, where ν and γ are respectively the Poisson's ratio and the surface energy per unit area. For wavelengths larger than λ_c , ΔW becomes negative and the instability develops. The energy variation is minimum for $dW/d\lambda = 0$ that is for $2\lambda_c$. Thus, a surface fluctuation with $\lambda > \lambda_c$ will develop into oscillations with a $2\lambda_c$ periodicity. The next step concerned planar interfaces between two stressed semi-finite solids, A and B, limited by surfaces $z_A = e_A \cos(2\pi x/\lambda)$ and $z_B = e_B \cos(2\pi x/\lambda)$ joined together after elastic displacements [16]. The conditions at the interface are the displacement continuity, and the force acting on the interface must be zero. The energy variation of the solids reduced to the unit area is calculated to be $\Delta W = \gamma\ \Delta S + \Delta W_{elas}$, where ΔS and ΔW_{elas} are respectively the surface variation and the elastic energy variation. ΔW_{elas} can be calculated using the surface dislocation model [17]. If one considers a shear stress discontinuity $\tau^0 = \tau_B^0 - \tau_A^0$, for example in the case of epitaxy between bcc and fcc crystals along (110) and (111) planes. Respectively, the critical wavelength is [16]: $\lambda_c^* = 2\pi\gamma(\mu_A+\mu_B)/(\tau^0)^2$. For $\lambda > \lambda_c^*$, ΔW becomes negative: the roughness develops and the equilibrium is obtained for $2\lambda_c^*$.

The previous presentation of the characteristics of the Cu/Nb nanofilamentary wires showed that high texture in the <111> direction for copper and <110> for niobium appeared during the cold drawing process and can reasonably be extrapolated to the Cu/Ta system. It is known that fcc and bcc materials have different slip systems with different orientations. Thus, in the case of the Cu/Ta and Cu/Nb systems, there is a shear stress discontinuity $\tau^0 = \sigma_0(m_{bcc} - m_{fcc})$ at the interface, since σ_0 is applied in the drawing axis direction, parallel to $<110>_{\text{Ta or Nb}}$ and $<111>_{Cu}$. m_{bcc} and m_{fcc} are the Schmid factor for bcc and fcc metals. This stress discontinuity creates a non-hydrostatic stress field at the boundary that can be responsible for the interface perturbation initiation, which is assumed to develop under the applied stress field. For the Cu/Nb system, since both materials have the same shear stress the instabilities are expected to develop for small thickness. It could then explain why no roughness was observed on Nb. However, for the Cu/Ta system where $\mu_A >> \mu_B$, the instabilities are expected to develop sooner in the elaboration process and can be observed for smaller RA values [18].

During the cold-drawing process, stresses are applied on materials during two different phases:

- The first step is the section reduction occurring at the entrance of the die: at this stage, the stress field is mainly radial. It could explain the generation of the first set of fluctuations, along the Ta diameter (Fig. 11).
- In the second step, the wire undergoes tensile stress along the drawing axis. This would explain the generation of the second set of oscillations that are along the Ta rod axis.

Thus, two perpendicular stress fields are applied successively. This could explain the presence of the oscillations segments described previously.

To compare theory and experimental observations we can use the formula $\lambda_p=2\lambda_c^*$, given in the case of shear stress discontinuity. The applied stress during the cold-drawing process is of the order of 300 MPa. Thus, $\tau^0=\sigma_0\left(m_{bcc}-m_{fcc}\right)=41$ MPa. We used μ_{Ta} = 69 GPa and μ_{Cu} = 45 GPa, while γ was approximated to 0.5 N/m (measured for Cu/Nb multilayers [19]). The resulting value for λ_p is 430 μm, which is of the same order of magnitude as the observed wavelengths of the second set in the drawing axis direction. Concerning the first set of oscillations, the stress field is more complex than the tensile stress. An expression for λ_p has not yet been calculated.

Since the energy variation increases with the applied stress, a solution for controlling the fluctuations' development could be to perform smaller Area Reduction during the elaboration process in order to reduce the stress level. Another way could be to reduce the internal stresses, responsible for the elastic relaxation, by frequent annealing. The best solution is currently defined to continue with the development of new Cu/Ta nanocomposites.

3.2 The Cu/Fe And Cu/W Systems

These two systems should allow optimization of the strength of nanocomposite wires. Nevertheless, several conditions must be considered during the elaboration of these very high strength conductors. Concerning the Cu/Fe system, the use of high temperature (T > 300°C) during the process must be avoided because the diffusion of iron in the copper matrix will induce an important loss in conductivity. For the Cu/W system, we have to remember that tungsten presents a ductile behaviour only at high temperature or under high pressure. It means that tungsten cannot be drawn in the classical conditions (room temperature and atmospheric pressure). We have chosen to work in high-pressure conditions. The preliminary study of this very high strength Cu/W system is performed in collaboration with the Laboratoire de Physico-Chimie des Matériaux (CNRS, Meudon, France) where a great knowledge in deformation under high pressure had been developed over many years. The purpose of the actual collaboration is the construction of a high-pressure cell that will be used on our 30 ton draw-bench.

4 Conclusion

In late 1999, we plan to obtain a Cu-20% vol Nb conductor with a strength of 3000 MPa and an Action Integral of the order of $[AI]_{Cu}/2.2$. These wires will be used to build a 100 T non-destructive conventional coil.

If we reduce the total Nb fraction to 12%, the strength level will be reduced to 2000 MPa and *AI* will increase to $[AI]_{Cu}/1.5$. This less reinforced Cu/Nb nanofilamentary wire will allow us to reach 80 T during 400 ms in a conventional coil with $2a_1 = 15$mm, powered by our 14 MJ capacitor bank [20]. For such a strength level, the Cu/Ta system can be used with a reduced amount of Ta. Consequently, *AI* will approach that of copper and the pulse duration of the 80 T field will be longer than 400 ms.

5 References

1. Askénazy, S., *Physica B*, **211** (1995) p. 56.
2. Snoeck, E., Lecouturier, F., Thilly, L., Casanove, M. J., Rakoto, H., Coffe, G., Askénazy, S., Peyrade, J. P., Roucau, C., Pantsyrny, V., Shikov, A., Nikulin, A., *Scripta. Mat*, **38**,11 (1998) p. 1643.
3. Dupouy, F., Askénazy, S., Peyrade, J. P., Legat, D., *Physica B* **211** (1995) p. 43.
4. Dupouy, F., Doctoral Thesis, n°367, INSA, Toulouse (1995).
5. Dew-Hughes, D., *Mat. Sci. Eng.*, A168, (1993) p. 35.
6. Shikov, A., Pantsyrny, V., Vedernikov, G., Gubkin, I., Salunin, N., Private report, March 1998.
7. Askénazy, S., Marquez, J., Ricart, D., *Physica B* **155** (1989) p. 55.
8. Frenkel, J., *Z. Physik* **37** (1926), p. 572.
9. Dupouy, F., Snoeck, E., Casanove, M. J., Roucau, C., Peyrade, J. P., Askénazy, S., *Scripta. Mat*, **34**, 7 (1996) p. 1067.
10. Wood, J. T., Griffin, A. J., Embury, J. D., Zhou, R., Nastasi, M., Veron, M., *J. Mech. Phys. Solids*, **44**, 5 (1996) p. 737.
11. Yasuna, K., Terauchi, M., Otsuki, A., Ishihara, K. N., Shingu, P. H., *J. Appl. Phys.*, **82** (5) (1997).
12. Grinfeld, M. A., *Sov. Phys. Dokl*, **31** (10), (1996) p. 831.
13. Srolovitz, D. J., *Acta. Metall. Mat*, **37** (2) (1989) p. 621.
14. Grilhé, J., *Acta. Metall. Mat*, **41**(3) (1993) p. 909.
15. Grilhé, J., *Europhys. Lett.*, **23** (2) (1993) p. 141.
16. Junqua, N., Grilhé, J., *Phil. Mag. Lett.*, **69** (2) (1994) p. 61.
17. Jagannadham, K., Marcinkowski, M. J., *Phys. Stat. Sol* (a), **50** (1978) p. 293.
18. Thilly, L., Colin, J., Lecouturier, F., Peyrade, J. P., Grilhé, J., Askénazy, S., to be published in *Acta. Met.*
19. Mitchell, T. E., Lu, Y. C., Griffin, A. J., Nastasi, M., Kung, H., *J. Am. Ceram. Soc.*, **80** (7) (1997) p. 1673.
20. Askénazy, S., Bendichou, L., Coffe, G., Lagarrigue, J. M., Laurent, J. P., Lecouturier, F., Marquez, J., Marquez, S.,Ricart, D., to be published in these proceedings.

INVESTIGATION, DEVELOPMENT AND MANUFACTURE OF HIGH STRENGTH, HIGH CONDUCTIVITY CU/SS WIRE FOR LARGE SCALE MAGNETS

V. PANTSYRNYI, A. SHIKOV, A. NIKULIN, G. VEDERNIKOV, I. GUBKIN, N. SALUNIN
Bochvar All-Russia Research Institute of Inorganic Materials, Moscow, Russia

Macrocomposite wire, comprised of a Cu core with a stainless steel (SS) jacket, is a promising material for application in outer windings of high field pulsed magnets. Different types of SS have been reviewed. Commonly available Cr-Ni stainless steel 12X18H10T, which has good workability, was chosen to initiate work on Cu/SS wires. Avoiding martensitic transformation by replacing carbon with nitrogen looks promising in developing stronger Cr-Ni stainless steels. The manufacturing process of macrocomposite Cu/SS wires was investigated and developed. Several long length (>50 m each) 3x5 mm^2 experimental Cu/SS wires were fabricated. The Cu/SS wires have exhibited ultimate tensile strength (UTS) values exceeding 1300 MPa at 77 K and conductivities higher than 50% IACS at room temperature.

1 Introduction

Pulse magnets provide the only economically acceptable way to generate magnetic fields 50-70 T and higher [1]. Huge Lorenz forces exerted on winding wires could damage the magnet. Therefore, the wires to be designed must perform at appropriately high strengths (≥1000 MPa). One of the promising materials for use in pulsed magnet windings is the wire consisting of a Cu core in a SS jacket [2,3]. High conductivity reduces the Joule heating during the current pulse. The Cu content of this wire should be 50-60% as its conductivity is determined mainly by volume fraction of Cu. The cross section of wire must be rectangular, with surface area ranging from 6-100 mm^2. The unit length should attain ≥100 m [4]. Objectives of the present work were to choose the proper materials for Cu/SS wire and to develop the design and appropriate manufacturing process.

2 Macrocomposite Cu/SS Conductors Design

Ultimate tensile strength (UTS) of high purity annealed Cu only equals 200-230 MPa. Thus, the necessary strength must be attained almost entirely by SS. Taking into account that the characteristic dimensions of SS and Cu components in cross sections of this wire are ≥1 μm, the well known Rule Of Mixtures (ROM) can be applied to calculate the composite conductor's strength and conductivity. Results of the calculations show that to attain necessary values of wire strength (1100-1350 MPa) at 50-60% IACS conductivity, the UTS of SS component should range from 2000-3000 MPa.

Using pearlitic steels could attain maximum wire strength. Pearlitic steel wires that have undergone heavy deformation and are characterized by an ultradispersive microstructure have extremely high UTS values up to 4.0-5.0 GPa. However, these steels have a strong tendency to become brittle at cryogenic temperature (77 K).

The highest values of UTS (up to 3.4 GPa) among the stainless steels are achieved in austenite-martensite steels in wire form. The disadvantage of these steels is nonuniformity of their chemical composition and structure. Therefore, its properties differ not only from batch to batch but sometimes within a batch delivered by one supplier. Usually, steels belonging to this group contain structural inclusions of α-ferrite. The presence of these inclusions leads to increased brittleness during cold deformation.

Among the steels designed for application at cryogenic temperatures, the most promising types for achieving the highest strength are Cr - Ni austenitic steels, so-called 18-10 steels with unstable austenite. Chemical compositions in accordance with RF standard GOST 5632-72 are presented in Table 1.

The strength of 18-10 type steels, after undergoing heavy deformation, depends primarily on structural hardening due to γ-α transformation. Strengthening is connected to the presence of C and N. Both of these elements stabilize the γ-phase. Higher Ni and Cr content reduce the rate of deformation strengthening.

Table 1. Composition of Different Types of Steels

Type of steel	Chemical composition (Fe-base), wt%							
	C	*Si*	*Mn*	*Cr*	*Ni*	*Ti*	*S*	*P*
12X18H9	<0.12	<0.8	2	17-19	8-10	<0.5	<0.02	<0.035
08X18H10	<0.08	<0.8	2	17-19	9-11	<0.5	<0.02	<0.035
12X18H9T	<0.12	<0.8	2	17-19	8-9.5	0.5-0.7	<0.02	<0.035
08X18H10T	<0.08	<0.8	2	17-19	9-11	0.5-0.8	<0.02	<0.035
12X18H10T	<0.12	<0.8	2	17-19	9-11	0.5-0.8	<0.02	<0.035
12X18H12T	<0.12	<0.8	2	17-19	11-13	0.5-0.7	<0.02	<0.035
S30400 (304)US	<0.08 N≤0.1	<0.75	<2	18-20	8-12		<0.03	<0.045
S30453 (304LN)US	<0.03 N=0.1-0.16	<0.75	<2	18-20	8-12		<0.03	<0.045

The increase in strain results in the increase in the amount of martensite type α-phase. Ti, Nb and Si provoke the formation of α-phase. Ni and Cr in the presence of Ni stabilize γ-phase and prevent γ-α transformation.

Steel 12X18H9 (USA analogue steel 302) when produced in wire form (∅ 0.3 mm) has UTS=2.5-2.8 GPa. During the heat treatments for 12X18H9, 08X18H10 steels at 700-750°C, carbide $Cr_{23}C_6$ formation takes place, leading to strong embrittlement. All of these alloys are produced as cold, deformed tubes in accordance with RF standard GOST 9941-81 and could be used for Cu/SS wire manufacture.

During heat treatments for 12X18H9T, 08X18H10T and 12X18H10T steels at 500-800°C, carbides $Cr_{23}C_6$ and TiC are formed. The majority of C in these steels is present as very stable primary Ti carbide (carbide-nitride) with inclusions formed during the solidification of the molten steel. The formation of additional (secondary) inclusions does not significantly influence the workability of these steels.

The stainless steels 12X18H9T and 08X18H10T are also used to manufacture high strength wires with UTS up to 2.5 GPa. These steels, particularly 08X18H10T, are similar to USA steel 321.

To a large extent, replacement of C by N diminishes the tendency for embrittlement in the deformation process. The presence of rather large amounts of N in austenite does not lead to deterioration of fatigue properties at cryogenic temperatures, which is related primarily to the higher solubility of chromium nitrides in austenite in comparison with chromium carbides.

In almost all N-doped steels, the C content is reduced to 0.02-0.03% to avoid embrittlement at cryogenic temperatures. These Cr-Ni steels with low C content are equivalent to USA steels 304LN(S30453) and 304N(S30454). The maximum C content is limited to 0.03%, Cr content is in the 18-20% range and Ni is in the 8-12% range. The N content is 0.1-0.16% for 304LN steel and 0.16-0.3% for 304N.

As previously mentioned, the wide range of Cr and Ni contents could lead to instability of mechanical strength attained after cold deformation. It would be beneficial to diminish the width of these ranges. The desirable contents of Ni and Cr could be 8-8.5% and 17-18%, respectively. Cr-Mn and Cr-Mn-Ni steels are also promising because of their higher rates of deformation hardening. The achievable level of UTS is equal to 2.0-2.5 GPa.

3 Macrocomposite Cu/SS Conductor Fabrication

We have investigated the processing of Cu/SS wires with a rectangular cross section of 3x5 mm^2. The data on mechanical and electrophysical properties for these 50-70 m long wires are presented in Table 2.

The most promising method used to attain high wire strength seems to be cold deformation with intermediate and final heat treatments. Deformation hardening depends on several factors - the total amount of cold deformation, the amount of deformation at each step of a drawing process, the subtotal amount of cold deformation between intermediate heat treatments, and regimes of intermediate and final heat treatments. Lubricants and toolings used in deformation also influence the resulting strength. The fabrication of composite wire can be influenced by more factors. The main additional factor is the quality of metallurgical bonding between soft Cu and hard SS. This factor becomes decisive if complicated Cu/SS wire with additional internal fibrous reinforcement is produced.

As the first stage, the simplest Cu/SS wire design with a single Cu core inside a SS jacket was chosen (Fig.1a). Two more complicated Cu/SS wire designs were also fabricated (Fig.1b). High purity Cu in rod form and 12X18H10T steel in tubular form were used as raw materials. The initial SS tubes were quenched at 950-1150°C. The higher temperatures led to undesirable increase in grain size and formation of coarse, needle-like inclusions of martensite during the following cold deformation, making it impossible to attain high wire strength. Acceptable uniformity of the microstructure in the initial tube precursor was not achieved at lower temperatures. After quenching the SS tubes, the Cu rods were inserted inside and the resulting billets were cold drawn with one or two intermediate heat treatments. The number of heat treatments and their regimes is determined by the chosen dimensions of the initial billet and required dimensions of the final wire, and by the necessity to achieve good metallurgical bonding between copper and

SS. The amount of final cold deformation was equal to 70-90%. A further increase in the degree of deformation led to the creation of transverse cracks in the SS cladding. In the cold-deformed condition, a high level of strength could already be attained, but the level of Cu core conductivity was not at its maximum.

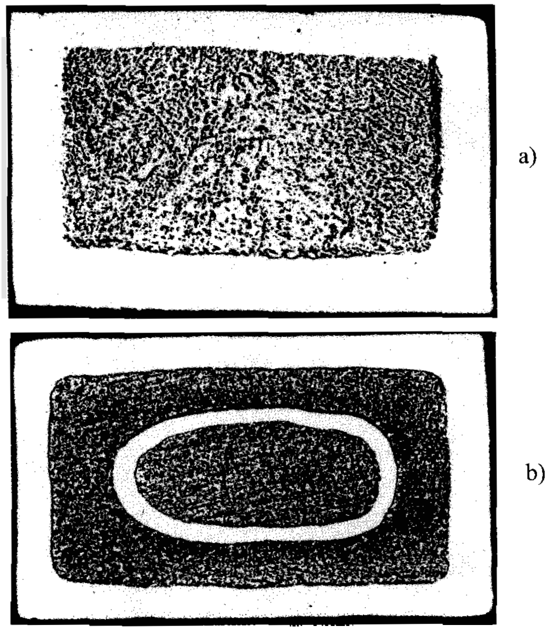

Figure 1 Cross section of 3x5 mm^2 Cu/SS wire: a) with single SS jacket; b) with separated "tube in tube" SS reinforcement.

Application of final heat treatment at 375-510°C leads to increased strengthening due to the process of SS aging. The strength of Cu/SS wire also increased in spite of Cu softening. The final heat treatment resulted in increased Cu/SS wire conductivity.

Table 2 Characteristics of 3x5 mm^2 Cu/SS Macrocomposite Wires.

Composite	State	V.f. Cu, %	IACS, %	RRR 300/77	293 K $\sigma_{\_}$, MPa	293 K $\sigma_{0,2}$, MPa	293 K δ, %	77 K σ_B, MPa	77 K $\sigma_{0,2}$, MPa
12X18H10T/Cu	CW	50.5	48.6	6.92	990	921	2.4	>1300	
12X18H10T/Cu	CW	54.3	50.3	6.7	970	882	3.4	>1340	
12X18H10T/Cu	HT	53	51	8.0	1120	1110	2.1	>1200	
12X18H10T/Cu	HT	55	53.8	8.13	>1050	870	2.8	>1290	
12X18H10T/Cu	HT	58	50.5	8.09	>1000	580			
12X18H10T/Cu (tube in tube)					>1000	630			
12X18H10T/Cu	HT	58	51.9	8.38	910	630	2.2		
12X18H10T/Cu (tube in tube)					915	630	2.2	>1250	930
12X18H10T/]3172 -	CW	50			930	710	-		
Cu					920	680	4.4	>1235	980
12X18H10T/]3172 -	HT	50	49.8	7.22	850	700	3.4		
Cu					850	700	3.4	>1030	970
03X17H12M3/Cu	CW	54.1	51.5	6.03	970	670	4.2	>1330	1000
03X17H12M3/Cu	HT	54.1	51.8	6.42	1000	735	3.2	>1330	990
03X17H12M3/Cu	HT	54.4	51.9	6.93				1225	960

It should be noted that technical grade Cu was used to fabricate another experimental Cu/SS wire, with the application of N-doped steel. Ingots of this steel (03X17H12M3), which is analogous to US steel 316L, were prepared for the fabrication of tubes. In this case, low conductivity values in the final wires could be explained by the possible deterioration of Cu conductivity due to the reaction with SS. Experiments showed that the same level of strength in 03X17H12M3 steel (compared with 12X18H10T) could be attained at the significantly lower temperatures of intermediate heat treatments. The values of strength were rather high, both in cold deformed (CW) condition [UTS (77K)>1330 MPa] and in the heat-treated (HT) state [UTS (77K)>1200-1250 MPa]. Investigating the strengthening mechanism in this type of steel has revealed that strengthening is determined mainly by deformation hardening confirmed by X-ray analysis. No martensitic γ-α transformation was detected. The structure was purely austenitic, which provided higher plasticity of these wires (up to 11% at 77K). The high level of strength was determined by N-doping. In the experimental ingot the N content was 0.08%, which seems to be lower than optimum. Thus, there is expectation that increasing N content to 0.1-0.16% will lead to appropriate enhancement of Cu/SS wire strength.

4 Conclusion

The manufacturing process of macrocomposite Cu/SS wires has been investigated and developed. The Cu/SS wires (cross section 3x5 mm^2, length >50 m) which have been produced using readily available 12X18H10T stainless steel and doped by nitrogen 03X17H12M3 steel have exhibited UTS (77K) values in excess of 1300 MPa. In both cases the conductivity was higher than 50% IACS. The possibility to further enhance Cu/SS wire strength and conductivity using steels with increased nitrogen content is suggested on the basis of these investigations.

References

1 Campbell, L. J., et al., *Physica B*, **211** (1995) pp. 52-55.

2 Cleemput, M. V., Jones, H., Van der Bergt, M., Eyssa, Y. M., Schneider-Muntau, H. J., *IEEE Trans. on Magn.* **32** No. 4, (1996).

3 Pantsyrnyi, V., et al., (MT-15 Proceedings, Science Press, (1998) pp. 1198-1201.

4 Pernambuco-Wise, P., NHMFL Workshop, August 18-19 (1994).

A SURVEY OF PROCESSING METHODS FOR HIGH STRENGTH-HIGH CONDUCTIVITY WIRES FOR HIGH FIELD MAGNET APPLICATIONS

J. D. EMBURY, K. HAN

Center for Materials Science, Los Alamos National Laboratory, Los Alamos, NM

This paper deals with the basic concepts of attaining an optimum combination of high strength and high conductivity in pure materials, *in-situ* composites and macrocomposites. It surveys current achievements and outlines where some future developments may lie in developing wire products that are close to the theoretical strength of future magnet applications.

1 Introduction

Processing appropriate conductor wires for winding coils of high field magnets is an important aspect of the construction process. This is a difficult task requiring attainment of the *reproducible* combination of extremely high mechanical strength and adequate electrical conductivity in *large cross sections and long lengths*. Thus, we must deal with basic considerations of how to attain the required combination of properties and produce flow charts of feasible manufacturing routes.

We can consider three routes to attain the goal of combined high strength and high electrical conductivity:

1. Increase the strength of pure copper either by adding second phase particles or by work hardening to increase the dislocation density of pure copper to very high levels.
2. Produce ultra-fine, scale drawn composites with extremely high amounts of internal interphase interfaces.
3. Produce macroscopic composites consisting of Cu, which provides the conductivity, and a second component which either has a very high strength or work hardens rapidly and provides the strength.

The approaches are described in separate sections below.

2 Strengthening of Copper

There are two basic problems that must be solved in adding dislocation barriers to copper to raise the yield strength. The dislocation barriers should not significantly increase resistivity, which rules out methods that add substutional solute elements to the copper. The obstacles must be stable during the temperature cycle 77 K to 393 K in order to be suitable for service in the magnet.

The traditional approach has been to use oxide dispersions in the copper. The materials are fabricated by internal oxidization of Cu-Al powder and the final product is oxide dispersion strengthened copper. The Al_2O_3 particle size is about 10 nm. The strength achieved in a commercially available wire (GlidCop) is about 600 MPa with 80% IACS conductivity. Previous experimental results revealed that GlidCop possesses a good resistance to thermal and mechanical fatigue, in addition to its moderate strength and high conductivity. However, quality control of the wire is crucial and difficult to achieve in a powder-processed material. We have occasionally found large aluminum oxide particles (about 1 μm) in these materials. These large oxides lead to the deterioration of the drawability and ductility of the materials, especially in GlidCop-15 + Nb (Cu -10 wt% Nb - 0.3 wt% Al_2O_3).

In conventional oxide dispersion strengthened materials such as GlidCop, the strengthening phase is equal across axes and provides an obstacle to dislocation motion. However, by changing the morphology of the strengthening phase, strength can be achieved by load transfer at the particle interface. 3M Inc. has recently developed aluminum based materials containing continuous fibers of Al_2O_3 [1] which can be produced economically in tape form and which have potential application as high strength, high conductivity materials.

It may also be possible to develop tape technologies based on functional graded materials in which gradients of strength can be produced by using internal oxidation of a copper based tape having a composition gradient on one side prior to internal oxidation.

A new, alternative approach to copper strengthening was recently suggested by Embury et al. in a research proposal to NHFML. In this method, it was proposed that a wire drawing facility would be developed to operate at 77 K and a pure copper conductor could be fabricated by cryogenic drawing. The liquid nitrogen used for cooling may serve as a lubricant, but alternative solid lubricants such as lead or graphite may also be required. The conductors fabricated in this way have the potential advantage of having strength levels on the order of 1 GPa and conductivity of order 85% IACS. Using pure Cu would initially seem out of the question because, when drawn at room temperature, Cu develops a maximum strength level of order of 450 MPa. However, based on the earlier work of Blewitt et al. [2], the deformation group at McMaster has studied the deformation of both Cu single crystals and polycrystals at 4.2 K. They found that even in uni-axial tension, strength levels of the order 850 - 950 MPa could be developed. If larger strains can be imposed, as in wire drawing, it should be possible to develop these strength levels at 77 K. The work hardening rate of polycrystal Cu is about 0.8 GPa at 77 K (calculated from $M^2\mu/200$, where $\mu = 33$ GPa and $M = 2.5$). Therefore, in order to achieve the strength level of 1 GPa, a true strain of only 1.5 is needed. An important observation in the 4.2 K deformation studies is that the strength developed at 4.2 K is stable after allowing the sample to heat to 298 K. It should also be noted that the scattering due to dislocations is weak compared to solute atoms. Thus, if the contribution to the resistance of the dislocations is of the order of 10^{-19} Ωcm per cm of dislocation line and at large strain the dislocation density is 10^{12} to 10^{13} cm/cm^3, the total resistivity change is of order 10^{-7} Ωcm. This can be compared with the scattering due to solutes, which is of order 10^{-6} Ωcm per atomic % solute. Heavily cold drawn pure copper should, therefore, retain a high percentage of IACS. The exploration of cryogenic working processes for pure Cu may be valuable in providing a new approach to high strength - high conductivity wires.

It is important to recognize that some basic physical phenomena remain to be explored in regard to materials deformed to large strain at low temperature. This includes the dynamic recovering mechanism when operated between 77 K and 293 K, and the role of alternative deformation modes such as twinning and the stability of the dislocation structures produced by cryogenic deformation. The very high densities of dislocations that can be accumulated by cryogenic deformation clearly represent a metastable state but may nonetheless provide a valuable mechanism for producing appropriate conductors.

3 Microscopic Composites

Different fabrication routes to produce Cu-Ag *in situ* composites of the required properties and sizes have been developed and are summarized in [3]. The total drawing strain necessary to achieve the 1 GPa strength level was estimated by assuming a linear work hardening rate (about 130 MPa), deduced from previous work [4] and verified for producing large cross-section wire [5]. A Cu-25 wt% Ag billet of large diameter was hot forged below 625 °C. The temperature of the hot forging operation was chosen to decrease dendrite size of the cast materials, avoid excessive grain growth, and allow adequate ductility for forging. After forging, the material was cold drawn to 5.2 mm x 8.6 mm with 1.6 mm corner radius, with or without intermediate heat treatment. A total drawing strain of 5 was needed in order to achieve the 1 GPa strength level.

Cu-Nb wires were fabricated by two methods at Bochvar in Russia. *In situ* composites were fabricated by a similar method to that used for Cu-Ag materials. Cu-Nb wires were also fabricated by bundling and deformation, using high purity Cu (99.99%) and Nb as summarized in [3]. A Nb ingot was re-crystallized at about 1200 °C and extruded to a 60 mm diameter rod at 700 – 800 °C. A composite billet made by inserting a Nb rod in a Cu can was evacuated and extruded to a 20 - 30 mm diameter rod with Nb of 40 vol%. The composite rod was cold-drawn to a hexagonal cross-section with deformation steps approximately 10 - 15% of the reduction area. Hundreds of composite rods were then assembled in a Cu can. The bundled composite was evacuated, welded, extruded at a temperature below 700 °C and cold drawn to a hexagonal rod. This procedure was repeated with different numbers of rods for bundling. The final products were composed of millions of Nb fibers embedded in Cu. In principle, this method can also be used to fabricate Cu-X materials, where X is Ag, Cr, Mo, Ta or Fe.

Many groups have studied the detailed structure of heavily drawn *in situ* composites. The seminal work of a number of French researches [6-8] clearly indicates the importance of both the scale and the detailed crystallographic relationship between the phases after deformation. In essence, the deformed embedded phases become nanoscale fibers after deformation. The detailed properties, both in terms of plasticity and electrical resistances, are determined by the detailed interfaces between the phases and the complex morphology. It is clear that new fabrication methods can be developed which combine rapid or directional solidification and wire drawing to produce a variety of ultrafine scale structures in which the volume fraction, scale, spatial distribution and interface geometry of the embedded phase can be tailored. Thus, there is potential to develop new families of high strength, high conductivity conductors by processing of *in situ* composites.

4 Macroscopic Composites

Macroscopic composite conductors can be fabricated using copper swaged or drawn in steel tubes. Such materials may have advantages in terms of their thermal properties and the lower temperatures reached during the pulses involved in energizing the magnet. Some previous research has utilized macroscopic composites based on copper and stainless steels [7]. It is also possible to develop strengths up to 1.6 GPa using macroscopic composites of copper and eutectic steel [8]. To date, neither the selection of the strengthening component or the hardening phase (e.g. the composition of the stainless steels) nor the geometric arrangement of the phase has been optimized. The development of new macroscopic composites remains a fruitful area for development. For instance choosing the optimum the stainless steel will give the required mechanical properties. An example shown in Fig.1 indicates that stainless steels that form martensite on deformation and contain sufficient levels of interstitials such as C and N can attain very high strengths at 58% reduction in area [11]. Using the data from different stainless steels, we can calculate the final strength obtained after a certain amount of deformation (58% cold deformation of Cu+40 vol% SS), as shown in Table 2.

Table 2. Strength of Cu+40vol%SS after 58% cold work

Steel	304/310/316	302	301
Strength of the cold deformed steel (MPa)	1112	1313	2008
Strength of Cu + 40 vol%SS (MPa)	625	705	983

The conductivity of stainless steel plus copper should be on the order of 60% IACS at room temperature. If the stainless steel has a very high work hardening rate, high strength can be achieved with a relatively small amount of cold work (e.g. 60 - 70% reduction in area). The high work hardening rate in stainless steels is complex because it involves four factors: (a) the extent of the transformation to martensite (b) the storage of the dislocation in the parent austenite (c) the transformation of the dislocation structure by the martensite transformation and (d) the influence of interstitials on the stability of the dislocation structure.

The detailed crystallography of the transformation of dislocations by twinning has been discussed by Basinski et al. [9,10]. They indicate that some sessile dislocations are formed from the glide dislocations in the parent phase.

The detailed understanding of austenite-martensite mixture hardening will require extensive high-resolution TEM studies in order to establish the details of the structure. The martensite transformation depends on both the degree of deformation and hardening. Further hardening may be achieved by quenching the materials in liquid nitrogen to increase the amount of martensite at an intermediate drawing stage. Quenching the

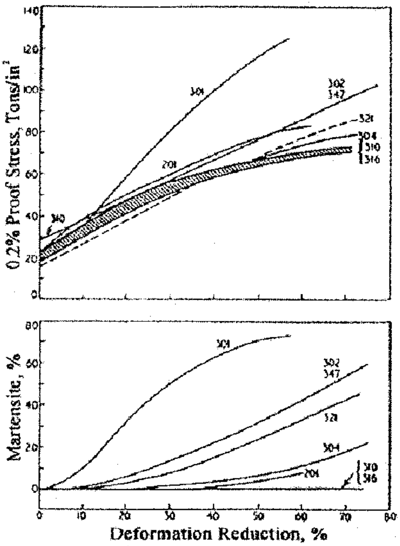

Figure 1. Effect of cold rolling on the 0.2% proof stress and martensite content of austenitic stainless steels [11].

materials also increases the stability of the materials in liquid nitrogen so that no phase transformation occurs during the service. It is important to realize that the methodology of combining deformation and phase transitions represents a very fruitful area for further development. Materials such as MP35N, having the composition of 35 wt%Co, 20 wt%Cr, 10 wt%Mo and 35 wt%Ni, possess attractive elastic properties with a Youngs modulus of 240 GPa. These materials are cold rolled to 85% and aged at 482 °C to develop very high strength levels. They are an example of achieving strength by a combination of extensive cold work and precipitation and represent a potentially useful strengthening phase for macroscopic composites.

The law of mixtures can predict properties such as elastic modulus, strength or conductivity of macroscopic composite, and this provides a valuable range of accessible properties. The elastic modulus along the wire axis of the macroscopic composite will be given by $E_{Comp} = E_{Cu}V_{fCu} + E_R(1-V_{fCu})$, where E_R is the modulus of the rapidly work hardening phase and E_{cu} is the elastic modulus of Cu and V_{fCu} is the volume fraction of Cu. For example, if we have a composite with 25% stainless steel as the rapidly hardening phase, the elastic modulus will be: $E_{Comp} = 124 \times 0.60 + 210 \times 0.40 = 158$ GPa. This can be compared with a value of $E = 115$ for currently available Cu-Ag wires.

5 Geometric Arrangement of Phases in Mesoscopic Composite

The geometric arrangement of copper and steel can be optimized so that composites can be produced with strength levels *in excess of* that estimated from a simple law of mixtures. The basic concept is to combine copper with materials which have a very high strain hardening rate and co-deform the materials so that the copper is *geometrically constrained* by the highly work hardening material.

An essential feature of such a macroscopic composite is the utilization of plastic constraints. A simple analogy is a soldered joint where a thin layer of Pb constrained between two layers of copper yields at the yield stress of the Cu, not of the softer Pb, due to the constraints exerted at the Cu-Pb interface. This concept can be applied to the case of macroscopic composites based on Cu plus a rapid work hardening phase.

If configurations such as those illustrated schematically in Fig. 2 are deformed to a strain of order 3, and the scale of the copper rod is reduced to a scale of 1 - 5 μm in a diameter, then the overall strength level will be governed by the strength level of the rapidly hardening phase and the distance between the copper fibers. The plastic constraint leverages the strength level attained in the hard phase so that it is this that controls the strength of the composite, not simply the volume fraction of the rapidly hardening phase. High strength levels can be attained if the reinforcing phase is only 20 - 25 vol% provided the geometries of the composite results in constrained flow.

Finally, the Jellyroll technique, currently used in the manufacture of superconductors [12], may also be used to fabricate high strength, high conductivity materials.

6 Testing the Properties of the Conductors

A systematic testing method has to be established to assess the merit of conductors fabricated by different methods. This should be connected to the magnet design. The principle properties that need to be assessed are stress-strain curves at room temperature and –196 °C, the elongation at room temperature and –196 °C, the reduction in area at room temperature and –196 °C and the conductivity. Thermal expansion coefficients in

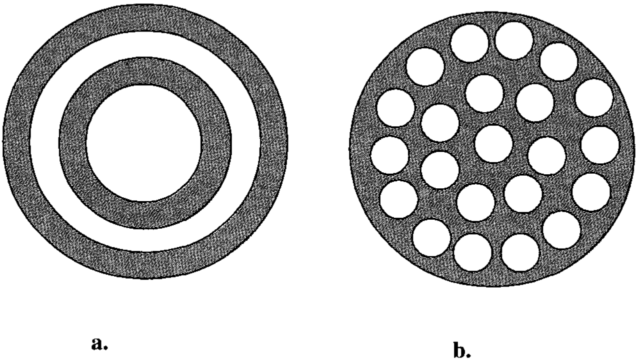

Fig 2. Schematic diagram showing the configuration of the composite made of Cu ○ and rapid work hardening phase ● .

the ranges from room temperature to 200 °C and from –196 °C to room temperature should also be determined.

The fatigue properties of the drawn material are important, both in terms of fatigue life and fatigue softening. Strain controlled fatigue tests can be performed using true plastic strain amplitudes of 0.001 - 0.01 up to 10,000 cycles to determine the fatigue behavior and test in tension after fatigue to determine the change in the true stress-true strain curve, elongation, and reduction in area. The stability of the materials should be assessed when they are cycled from –196 °C to 100 °C through 100 cycles.

For materials with mechanically or thermally bounded interfaces, we can perform compression tests along the drawing axes to determine the point of de-cohesion of the bonds. After samples are compressed to reduce height (e.g., 20, 30, 40 and 50%), a cross section should be cut and examined to determine the integrity of the bonding between different components.

We need to make a series of combined mechanical and electrical joints and test the mechanical properties and electrical conductivity of the material sections containing joints.

In addition to the examination of the compression test samples, the integrity of the interface should be determined by microscopy. The integrity of the bond between different components of a macrocomposite as a function of drawing strain should also be examined. This can be done by cutting metallographic sections so that we can examine the bonds along the drawing axis.

7 Fabrication of the Magnet

In addition to the tests described above, which can be made according to established standards, there are special requirements for magnet design. For instance, in addition to the joints mentioned above, bending must be considered for the conductor because of the magnet fabrication. The bending radius should be similar to the radius of the magnet coil. The surface coating of the insulation also must be investigated under various experimental conditions.

8 Conclusions

Various high strength, high conductivity materials were developed for high field magnet applications. Currently, the stresses generated by the magnetic field exceed the strength of most commercially available conductors and significant efforts are required in order to satisfy the design of high field magnets. The efforts include both the understanding of the strengthening mechanisms of the conductors and development of feasible techniques that can be used to fabricate conductors in large cross-section, long length and large quantities. Although nanostructure can provide high strength to the conductors, the scattering of the electrons by the interfaces cannot be ignored; it decreases the conductivities. It appears that such conductors are suitable to the magnet application that require ultra high strength but relatively lower conductivities. Increasing the dislocation density has negligible effect on the conductivity and rewarding influence on the strength. However, stabilization of metastable high-density dislocation at room temperature or higher remains an issue. Therefore, this approach is useful to the magnets that call for high conductivity but modest strength. The macrocomposite provides a feasible and economic high strength conductor suitable for applications with less rigorous requirements for strength and fatigue endurance.

Acknowledgement

This research is sponsored by the United States Department of Energy.

References

1. Deve, H. E., McCullough, C., *JOM*, **33** (1995).
2. Blewitt, et al., *Phys. Rev.*, **91** (1953) p. 1115.
3. Embury, J. D., Han, K., *Current Opinion in Solid State & Mater. Sci.* (1998) p. 304.
4. Frommeyer, G., Wassermann, G., *Acta Metall*, **23** (1975) p.1353.
5. Han, K., Embury, J. D., Sims, J. R., Campbell, L. J., Schneider-Muntau, H. J., Pantsyrnyi, V. I., Shikov, A., Nikulin, A., Vorobieva, A., "The Fabrication, Properties and Microstructure of Cu-Ag and Cu-Nb Composite Conductors", Submitted to Materials Science and Engineering (1998).
6. Snoeck, E., Lecouturier, F., Thilly L., Casanove, M. J., Rakoto, H., Coffe G., Askenazy, S., Peyrade, J. P., Roucau, C., Pantsyrny, V., Shikov, A., Nikulin, *Scripta Materialia*, **38**, No.11, (May 5, 1998) pp. 1643-1648.
7. Dupouy, F., Snoeck, E., Casanove, M. J, Roucau, C., Peyrade, J. P., Askenazy, S., *Scripta Materialia*, **34**, No.7, (Apr. 1, 1996) pp. 1067-1073.
8. Dupouy, F., Snoeck, E., Askenazy, S., Peyrade, J. P., Legat, D., *Physica B*, **211**, Nos.1-4, (May 1995) pp. 43-45.
9. Jones, H., van Cleemput, M., High Magnet Field: Application, Generation and Materials, Ed. by H. J. Schneider-Muntau, (1997) p. 499.
10. Zhou, R., Embury, J. D., Wood, J. T., Smith, J. L., High-Strength, High-Conductivity Copper-Steel Composite, *Materials Characterization*, **37**, No.5, (Nov. 1996) pp. 239-243.
11. Basinski, Z. S., Szczerba, M. S., Niewczas, M., Embury, J. D., Basinski, B. J., *Revue de Metallurgie*, (Sept., 1997) p. 1037.
12. Niewczas, M., Basinski, Z. S., Embury, J. D., *Mater. Sci. Eng.*, A234-236, (1997) p. 1030.
13 Llewellyn, D. T., Murray, J. D., in Metallurgical Developments in High Alloy Steel, Special Report No. 56, Iron and Steel Institute, U.K. (1964).
14 Kitai, T., Higuchi, M., Osamura, K.: Artificial Pinning Centers In Jelly-Roll Processed Nb/Cu Composites, *Cryogenics*, **37**, No.7, (Jul. 1997) pp.389-395.

INTERNAL STRESSES IN WIRES FOR HIGH FIELD MAGNETS

K. HAN
Los Alamos National Laboratory, Los Alamos, New Mexico, USA
Presently at: National High Magnetic Field Laboratory, Tallahassee, FL USA

J. D. EMBURY
Los Alamos National Laboratory, Los Alamos, New Mexico, USA
Presently at: McMaster University, Ontario, Canada

A. C. LAWSON, R. B. VON DREELE
Los Alamos National Laboratory, Los Alamos, New Mexico, USA

J. T. WOOD
Cymat Aluminum Corporation, Mississauga, Ontario, Canada
Presently at: University of Western Ontario, Ontario, Canada

J. W. RICHARDSON, JR.,
Argonne National Laboratory, Argonne, IL, USA

The codeformation of Cu-Ag or Cu-Nb composite wires used for high field magnets has important microstructural consequences including the production of very fine scale structures, the development of very high internal surface area to volume ratios during the drawing, and the storage of defects at interphase interfaces. In addition, the fabrication and codeformation of phases that differ in crystal structure, thermal expansion, elastic modulus and lattice parameter lead to the development of short wavelength internal stresses. These internal stresses are measured by neutron diffraction and transmission electron microscopy as a function of the imposed drawing strain. The internal stresses lead to important changes in elastic plastic response that is related to both magnet design and service life.

1 Introduction

The use of codeformation of in-situ composites such as those based on Cu-Ag or Cu-Nb is a very effective method of producing high-strength, high-conductivity wires for use in high field magnets [1-5]. The high strength of the materials is provided by very fine scale structures, very high internal surface area to volume ratios and the defects stored at interphase interfaces in the materials. Such structure can be produced by co-deformation of two-phase materials. The codeformation of two phases may also introduce short wavelength internal stresses, since two phases usually have a different crystal structure, elastic modulus and lattice parameter. Moreover, fabrication of two-phase composites, such as casting or hot extrusion, may also introduce internal stress, due to the difference in the lattice parameters and thermal expansions of the two phases. We have measured internal stresses by neutron diffraction and other methods as a function of the imposed drawing strain. We have related the internal stresses to the changes in elastic plastic response and to both magnet design and service life.

2 Experimental Methods

Fabrication methods for Cu-Ag and Cu-Nb can be found in [1]. Materials were examined using a variety of metallographic methods. First, scanning Electron Microscopy (SEM) samples were sectioned by a low speed saw and then cold-mounted, polished, and etched in a solution of 30% nitric acid in ethanol. Samples for neutron reflection examination were machined to rods that were 4 mm in diameter and 50 mm long to avoid absorption effects. For comparison, samples of cold work strain 0.71 were prepared with different diameters and with annealing. Tensile testing was done at 25 °C and –196 °C using an MTS machine at an initial strain rate of 10^{-4} $\sec^{-1}$.

3 Results and Discussions

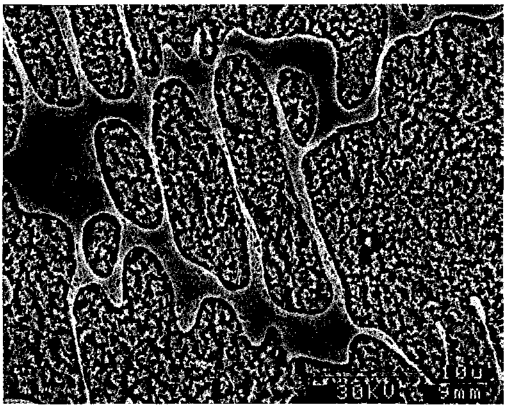

Figure 1. SEM second electron image (cross-section) showing the fine microstructure of the drawn Cu-25wt%Ag sample having a strain of 1.

The microstructure of Cu-Ag after drawing is shown in Fig. 1. The SEM image taken from a sample with a drawing strain of 1 (drawing strain $\varepsilon_d = 2 * \ln(D_0/D_\varepsilon)$, D_0 and D_ε are the original diameter of the wire and the diameter of the wire at strain of ε_d, respectively.) shows the combination of proeutectic Cu dendrites and the lamellar eutectic transformation product. As the drawing strain increases, both the dendrite spacing and the inter-lamellar spacing between Cu and Ag in the eutectic region decrease. The SEM images in a longitudinal direction (parallel to the drawing direction and not shown in this paper) demonstrate that the Cu and Ag phases were aligned along the drawing direction when the materials were strained further. Similar microstructure was observed in cold drawn Cu-Nb conductors.

The radial internal strains measured by neutron reflection of Cu-Ag after different drawing strains are shown in Fig. 2. The internal strains are different in different orientations in both phases. Fig. 2 also shows that the radial residual strains in Cu and Ag are in compression and tension, respectively.

In Cu-Nb samples, the radial internal strains, and therefore the internal stress, measured by neutron reflection are significantly higher than in Cu-Ag. Similar to the Cu-Ag system, internal strains differ in different orientations in both phases. However, the radial internal strain patterns in Cu-Nb are more complicated.

The internal strains or stresses resulted in the rounding of the stress-strain curves in both composite materials. The rounding of the stress-strain curve is more pronounced in Cu-Nb composites, since larger internal strains were observed. After fatigue tests, a sharper transition from elastic deformation to plastic deformation was observed. The change of the deformation behavior of the composites after fatigue can be related to the decrease of the internal stress in the composite. A shape transition from elastic deformation to plastic

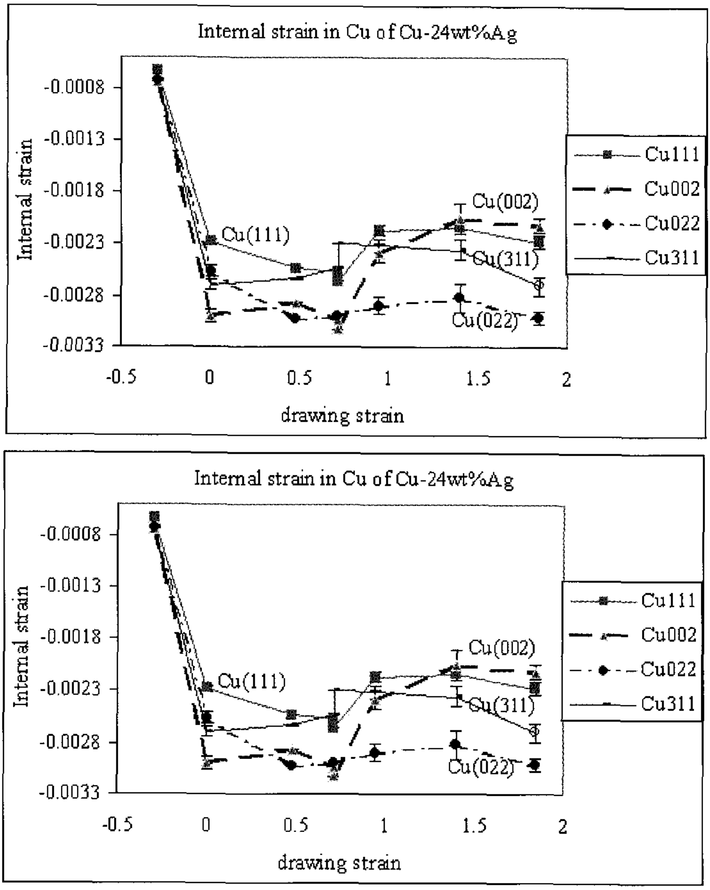

Figure 2. Radial internal strains of Cu and Ag in Cu-24wt%Ag at different drawing strains.

deformation makes determination of the yield strength more accurate and simplifies the design of the magnet.

4 Summary

The codeformation of Cu-Ag or Cu-Nb composite wires used for high field magnets produces very fine scale structures, very high internal surface area to volume ratios during the drawing and the storage of defects at interphase interfaces. The codeformation of Cu-Ag or Cu-Nb also leads to the development of short wavelength internal stresses and strains. Larger internal strains were observed in Cu-Nb composite than in Cu-Ag. The values of internal strains are different in different orientations. Therefore, the deformation of the composite is anisotropic. The internal stress leads to the rounding of the stress-strain curve, which is more pronounced in Cu-Nb composites.

Acknowledgement

This research is sponsored by the United States Department of Energy. The work has benefited from the use of the Intense Pulsed Neutron Source at Argonne National Laboratory and of the Los Alamos Neutron Scattering Center at Los Alamos National Laboratory. IPNS and LANSCE are funded by the U.S. Department of Energy, BES-Materials Science, under ContractW-31-109-ENG-38, and by US Department of Energy under Contract W-7405-ENG-36, respectively.

References

1. Wood, J. T., Embury, J. D., Ashby, M., *Acta Materialia*, **45** (3), (1997), pp. 1099-1104.
2. Embury, J. D.,Han, K., *Current Opinions in Solid State and Materials Science*, **3** (3), LANL, (1998), pp. 304-308.
3. Van Cleemput, M., Jones, H., Van der Burgt, M., Barrau, J-R., Lee, J. A., Eyssa, Y., Schneider-Muntau, H. –J., *Physica B*, **216** (1996) pp. 226-229.
4. Pernambuso-Wise, P. in High Magnetic Fields, Applications, Generation, Materials, Ed. by H. –J. Schneider-Muntau, World Scientific, NJ, USA, (1997) p. 371.
5. Frings, P. H., Vanbockstal, L., *Physica B*, **211** (1-4), (May, 1995), pp. 73-76.
6. Embury, J. D., Han, K., Sims, J. R., Pantsyrnyi, V. I., Shikov, A., Bochvar, A. A., Fabrication Routes for High Strength High Conductivity Wires, in this proceedings.

FABRICATION ROUTES FOR HIGH STRENGTH-HIGH CONDUCTIVITY WIRES

J. D. EMBURY, K. HAN, J. R. SIMS, J. Y. COULTER
Los Alamos National Laboratory, Los Alamos, USA

V. I. PANTSYRNYI, A. SHIKOV, A. A. BOCHVAR
All-Russia Scientific Research Institute of Inorganic Materials (ARSRIIM)
Moscow, Russia

The development of suitable wires for magnet windings requires both the attainment of suitable combinations of properties (electrical conductivity and strength), the development of a production route capable of fabricating suitable quantity of wire of required dimension (5.2 x 7.6 mm^2 cross-section and 120 m in length), and a product with acceptable fabricability, joinability and service life. In this survey, we will consider methods of producing suitable wire products by the co-deformation of *in-situ* composites. This will include the quality control of the processing of Cu-Ag and Cu-Nb and the assessment of their physical properties.

1 Introduction

The construction of a high field magnet is dictated by the available choice of conductor, insulation and reinforcement materials. The commercially available insulation and reinforcement materials currently appear to satisfy the design requirement of a 100 T quasi-continuous magnet. The conductor requires high mechanical strength (>1 GPa), high conductivity (>72% I.A.C.S (International Annealed Copper Standard, 100% IACS = 1.7241 μΩcm), good elongation, forgiving plastic behavior, long fatigue life (>10,000 discharges), high resistivity ratio (ratio of resistivity at room temperature and low temperature, e.g. –196 °C), suitable wire cross section (the largest one is 5.2 x 7.6 mm^2) and length (>120 m continuous length). No such conductor is currently commercially available. The work reported here encompasses choosing the elements to make a conductor, the selection of a suitable fabrication route, e.g. casting-forging-cold drawing or bundling-extruding-cold drawing, and the characterization of the mechanical properties and microstructure of the materials.

2 Materials Selection

In considering high strength conductors, attention has been paid to the metal matrix composite (MMC) conductors. The components of a MMC can be metal and metal or metal and ceramics. In metal-ceramic composites, the ceramic acts as a reinforcement component. The ceramics can be in the form of particles of fibers. The ceramic currently used is either Al_2O_3 or SiC. The matrix is usually Cu because of its high conductivity and reasonable cost.

In metal-ceramic composites, Cu-X systems have been studied. X can be an element or an alloy. In macroscopic MMC, X is usually the stainless steels. A co-deformation of two components at high temperature provides the interfacial bonding between the phases. Both the strength level and the conductivity are governed by the relative volume fraction of the Cu and steel. In microscopic MMC, the properties of a composite depend not only on the volume fraction of the components, but also on the scale and morphology of the microstructures, interface area to volume ratios, and the amount of defects stored at interphase interfaces. In order to obtain the required microstructure, significant amount of cold work has to be imposed. In the present paper, attention has been focused on co-deformation of composites, such as Cu-Ag and Cu-Nb, and development of fabrication routes for these materials.

3 Fabrication Routes

Different fabrication routes to produce Cu-Ag wires of the required properties and sizes have been developed and are summarized in Fig. 1. The total drawing strain, the ingot sizes and hot forging strain necessary to achieve the final strength level and cross-section should be estimated by assuming a linear work hardening rate which was deduced from previous work [1]. The cast Cu-Ag billet of large diameter was hot forged at a temperature below 625 °C to a smaller diameter. The temperature of the hot forging operation was chosen in order to decrease the dendrite size of the cast materials, avoid excessive grain growth, and to allow adequate ductility for forging. An annealing treatment may be introduced in order to homogenize the materials. After forging, the surface of the billets has to be cleaned in order to remove the oxidized layer and other defects. One of the surface defects we have found was the inverse segregation of Ag to the surface. The material was cold drawn in round cross-section, and finally to rectangular wires. In order to achieve the strength level of 1 GPa, the total drawing strain was higher than 4.8. Between the drawing, intermediate heat treatments between 300-400 °C may be introduced in order to remove the internal stress or possibly induce further precipitation.

Cu-Nb wires were fabricated by two methods. *In situ* composites were fabricated by a similar method to that used for Cu-Ag materials. Cu-Nb wires were also fabricated by bundling and deformation, using high purity Cu (99.99%) and Nb/Cu-Nb, as shown in Fig. 2. A Nb or Cu-Nb ingot was annealed at high temperature (e.g., 1200 °C for Nb) and extruded to a rod at 700-800 °C. A composite billet was made by inserting a Nb or Cu-Nb rod in a Cu can which was evacuated and extruded to a rod of 20-30 mm in diameter

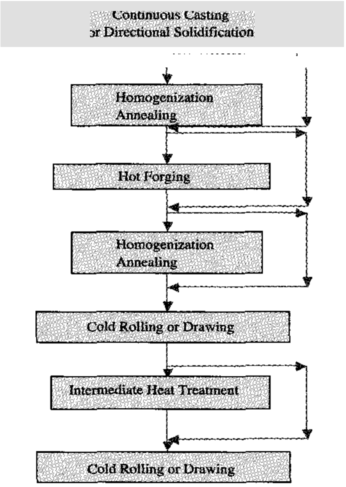

Figure 1. Fabrication flow chart of Cu-Ag

with Nb of 40 vol. %. The composite rod was cold-drawn to a hexagonal cross-section with the deformation steps approximately 10-15% of reduction area. n_1 (usually >100) composite rods were then assembled in a Cu can. The bundled composite was evacuated, welded, extruded at a temperature below 700 °C and cold drawn to a hexagonal rod. Such a procedure was repeated with n_1, n_2 ... n_i numbers of rods for bundling. The final product was composed of $n_1 \times n_2 \times \ldots n_i$ of Nb/Nb-Cu fibers embedded in Cu matrix.

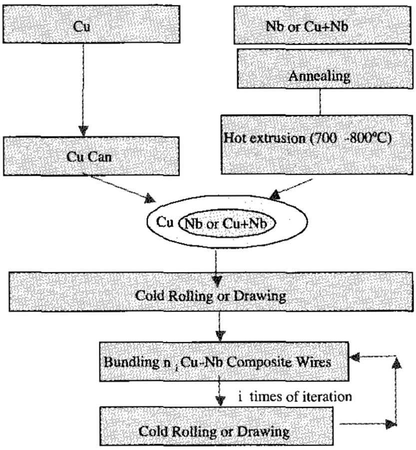

Figure 2. Fabrication flow chart of Cu-Nb composites.

4 Physical Properties

It is well known that cold-drawn wires may have different mechanical properties at the different positions of the wires because of the inhomogeneity of the deformation. The consistency of properties of different cross sectional sizes of the conductors was determined by comparison of the data taken from samples with various cross section sizes. We found that the properties were uniform. For 5.2 x 8.6 mm^2 cross-section Cu-Ag drawn to a strain of 5, the room temperature ultimate tensile stress, the 0.2% offset stress and the fracture stress are 890, 970 and 1350 MPa, respectively. The room temperature electrical conductivity for Cu-Ag is about 72 %IACS. The room temperature ultimate tensile stress and conductivity for 2 x 3 mm^2 cross-section Cu-Nb are 1050 and 68 %IACS.

5 Conclusions

Various routes were reviewed for fabrication of different metal-metal composite conductors. In order to achieve high strength, a significant amount of deformation is required which may introduce various defects in the materials. Therefore, careful assessment of the physical properties and microstructure of the drawn wires is important for application of the wires in fabrication of the high field magnet.

Reference

1. Frommeyer, G., and Wassermann, G., *Acta Metall*, **23**, (1975) p. 1353

GIGAGAUSS MAGNETIC FIELD GENERATION FROM HIGH INTENSITY LASER SOLID INTERACTIONS

J. SEFCIK, M. D. PERRY, B. F. LASINSKI, A. B. LANGDON, T. COWAN, J. HAMMER, S. HATCHETT, A. HUNT, M. H. KEY, M. MORAN, D. PENNINGTON, R. SNAVELY, J. TREBES, S. C. WILKS
Lawrence Livermore National Laboratory, Livermore, CA, USA

Intense laser (>10^{21} W/cm^2) sources using pulse compression techniques in the sub-picosecond time frame have been used to create dynamic electric field strengths in excess of 100 Megavolts/micron with associated magnetic field strengths in the gigagauss regime. We have begun a series of experiments using the Petawatt Laser system at LLNL to determine the potential of these sources for a variety of applications. Hot electron spectra from laser-target interactions in Au have been measured with energies up to 100 MeV. Hot x-ray production has been measured using filtered thermoluminescent dosimeters and threshold nuclear activation (γ,n) from giant resonance interactions. High-resolution radiographs through $\rho r \geq 165$ gm/cm^2 have been obtained. Dose levels in the x-ray band from 2–8 MeV have been measured at the level of several rads at one meter from the target for a single pulse. The physics of these sources and the scaling relationships and laser technology required to provide high magnetic fields are discussed. Results of preliminary magnetic field calculations are presented along with potential applications of this technology and estimates of the fundamental scaling limits for future development.

1 Introduction

The use of petawatt class lasers for the production of copious amounts of high energy x-rays has been discussed for over a decade [1,2]. Intermediate energy (0.1-1 MeV) x-ray production with table-top sized, terawatt class lasers is now a sub-field within the strong field interaction community. Numerous groups have observed electrons or bremsstrahlung spectra extending beyond 1 MeV [3,4,5,6].

Recent experiments on the petawatt laser at the NOVA laser facility at LLNL have demonstrated that short (<1 ps) laser pulses, when properly focussed on high-*z* targets, can produce hard, intense x-ray spectra that can be used for radiography. The outputs measured on these experiments imply very high electron current densities and current driven magnetic field strengths on the order of several gigagauss in extremely small volumes.

2 Experiments

Petawatt shots for the production of high energy x-rays for radiography have been performed at the Lawrence Livermore National Laboratory's NOVA laser facility since September 1997. Typical laser data implies a pulse duration of 460 ± 40 fs and a compressor throughput of 84%. Typical laser energy measured before compression was 450 J in a 46.3 cm diameter beam. The laser beam and diagnostic configuration for the shots is shown in Fig. 1. Due to the hole in the paraboloid, 7.4% of the incident energy is lost. The beam was focused using a Cassegrain telescope. The primary mirror was a paraboloid ($f = 180$ cm) overcoated with an HfO$_2$/SiO$_2$ multilayer designed for high reflectivity at normal incidence. The secondary mirror was a 5 cm diameter fused silica flat that was overcoated with a HfO_2/SiO_2 multilayer, highly reflective coating for 1054 nm and placed 10 cm from the target. The beam size on the secondary mirror is 2.6 cm corresponding to an irradiance of 1.67×10^{14} W/cm^2 for a nominal 400 J pulse incident on the mirror. At this irradiance, the top SiO_2 layer is converted to a critical density plasma within the first 50 fs of the pulse. As a result, the bulk of the laser pulse is reflected not by the multilayer structure of the mirror but rather by the sharp gradient plasma surface. Measurements of the reflectivity from this plasma surface suggest a reflectivity of greater than 85% for the petawatt pulse.

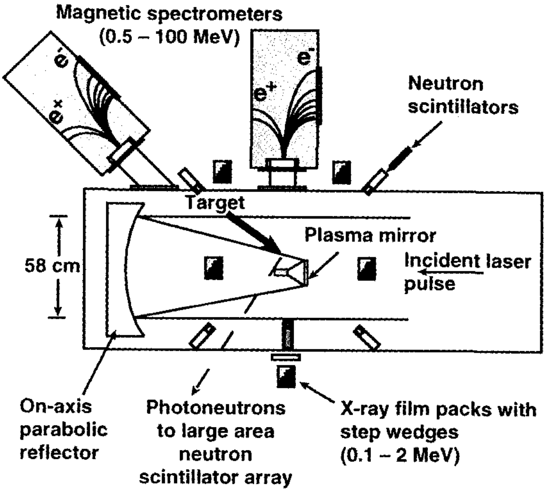

Figure 1. Diagnostic layout for Petawatt radiography experiments.

A typical target is shown in Fig. 2. The laser beam strikes the surface of the gold target at near normal (5°) incidence producing a strong relativistic electron current with a complicated angular distribution into the target. Electrons greater than approximately 2 MeV can escape the large space potential created within the target and penetrate the aluminum and CD_2 backing material. Electron spectrometers are placed in the plane of incidence at 30° from the laser axis and 95° from the axis. These electron spectrometers consist of a permanent dipole magnet with emulsion as the detector. The total electron energy range covered in the spectrometer is 0.2 - 130 MeV and the positron range is 0.2 - 40 MeV. The NASA/Marshall Space Flight Center group at Huntsville, Alabama analyzes the emulsion tracks.

An electron spectrum from a typical shot is shown in Fig. 3. This shot used a 0.5 mm thick gold target. Electrons were observed at energies extending above 90 MeV. However, the bulk of the distribution was in the range of ~2 – 15 MeV where the emission was found to be forward directed with about eight times more flux observed at 30°, with respect to the laser propagation direction, as compared to the flux at 95°. Integration of the electron spectrum convolved with the bremsstrahlung cross section does not accurately estimate the total photon yield or laser coupling efficiency since this electron spectrum is effected by the large space charge potential in the target and the energy loss (*dE/dx*) through the target assembly. The energy loss through the target for the electrons depicted in Fig. 3 is approximately 2.5 ± 0.5 MeV.

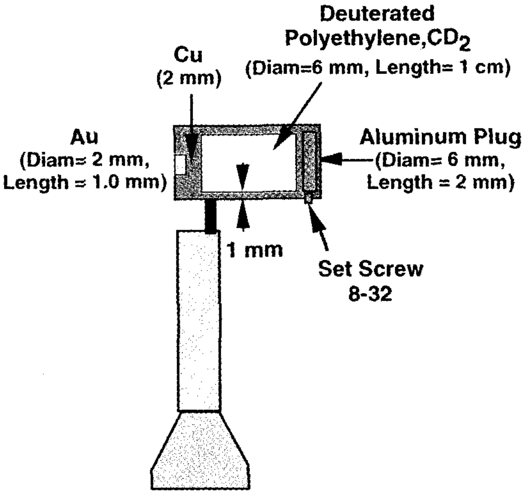

Figure 2. Petawatt radiography target.

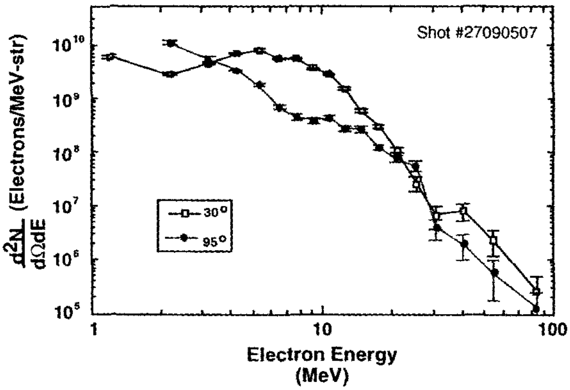

Figure 3. Electron spectra acquired at 30° and 95° with respect to the laser axis.

Aside from the suppressed region below ~5 MeV, the electron spectrum can be well fit by a "two temperature" distribution. The spectrum observed at 30 degrees to the laser is shown in Figure 4 along with two quasi-Maxwellian distributions given by

$$N(E)dE = C(E^{1/2}/E_e^{3/2})\exp[-E/E_e]dE, \qquad (1)$$

where C is the scaling parameter, and E_e is the characteristic electron energy. Detailed particle in cell (PIC) simulations suggest that this characteristic energy is well approximated by the cycle averaged quiver energy of a free electron within the intense field,

$$\langle E_e \rangle = m_e c^2(1 + 2U_p/m_e c^2]^{1/2}, \qquad (2)$$

where $U_p(eV) = 9.33\times10^{-14} I(\mathrm{W/cm^2})\lambda^2(\mu\mathrm{m})$. The laser conditions for the spectrum depicted in Figure 4 were such that ~50% of the 300 J incident on the target were focused within a 28×40 μm spot. This corresponds to an average irradiance of 8×10^{19} W/cm^2 for this shot. The average quiver energy for this irradiance [from Equation (2)] is 2.95 MeV in agreement with the characteristic electron energy for the bulk of the distribution of Fig. 4. The incident laser spot also contained substructure, which would have seeded self-focusing in the preformed plasma. This self-focusing is almost certainly responsible for the "hot tail" of the distribution characterized by a second Maxwellian with characteristic electron energy of 11.5 MeV. This is consistent with PIC simulations, which show the incident beam undergoing filamentation in the preformed plasma.

High-energy bremsstrahlung x-rays generated by these electrons in the gold target produced substantial radioactivity in the target assembly following the laser shot. This activity was from photonuclear reactions in both the gold and surrounding copper target-holder, producing transmutation to platinum and nickel daughter isotopes. Positron emission was determined by observation of 511 keV γ-rays resulting from annihilation radiation in the target assembly. Positive identification of both copper radioisotopes was established by fitting the decay curve with a two component decay with half-lives of 9.7 min and 12.7 min. The fit gives an identification probability of better than 99% for ^{62}Cu and ^{64}Cu, respectively. The threshold gamma-ray energy for photo-activation of the gold is 8.06 MeV, ^{65}Cu is 9.91 MeV and 10.85 MeV for ^{63}Cu, indicating a large flux of high-energy bremsstrahlung.

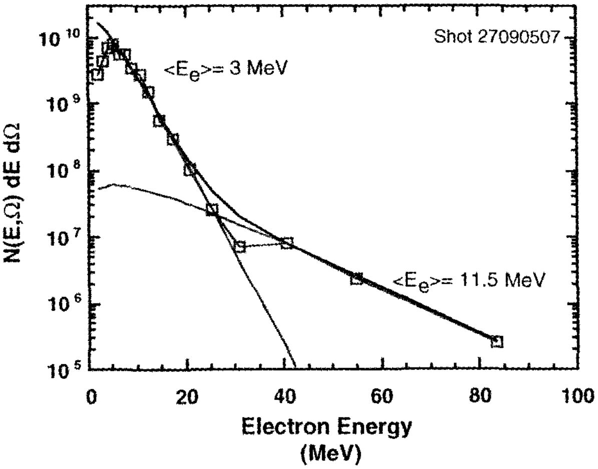

Figure 4. Electron spectrum and calculated Maxwellian distributions [Equation (2)]. The solid black curve is the sum of the two distributions.

High quality images of the far-field laser beam distribution are acquired on these shots. Beam distortion resulting from both pump-induced and thermal distortion in the Nova disk amplifiers has been corrected by the use of a deformable mirror. The system can produce a well-focused laser spot that is 9 μm in diameter (FWHM). As a result, in the absence of self-focusing, about 20% of the beam energy exceeds ~10^{20} W/cm^2. This suggests that most of the radiation is being produced by about 80 joules of the light incident on the target. Only the central spot would have had sufficient irradiance to produce the high-energy electrons necessary to produce the hard (>1 MeV) x-ray photons.

Multiple radiographs through varying thicknesses of lead are routinely acquired during shots. Their resolution suggests that the spot size for high-energy photon production from bremsstrahlung is less than 100 microns in diameter. These radiographs typically correspond to doses of >1 MeV photons as measured on thermoluminescent dosimeters of 0.1 - 2.0 Rads, depending on the parameters of the laser target interaction. Although the laser interaction is over within a few hundred femtoseconds, the electron beam produced in the target takes one or two picoseconds to complete its evolution and generate x-rays from bremsstrahlung interactions.

3 Calculations

Calculations of conditions within the electron beam generation region have been performed using the 2-D Particle in Cell code ZOHAR. The model provides a fully kinetic and non-linear description of the laser-plasma interaction that incorporates Ampere-Faraday-Maxwell fields, relativistic particle dynamics, and self-consistent particle-in-cell coupling to the field equations. These calculations have been performed for laser hole boring in plasma slabs with electron densities (n_e) that are 5 - 50 times the critical density (n_c). Individual particle orbits are tracked to study the evolution of the static magnetic and electric fields produced by the laser driven electrons.

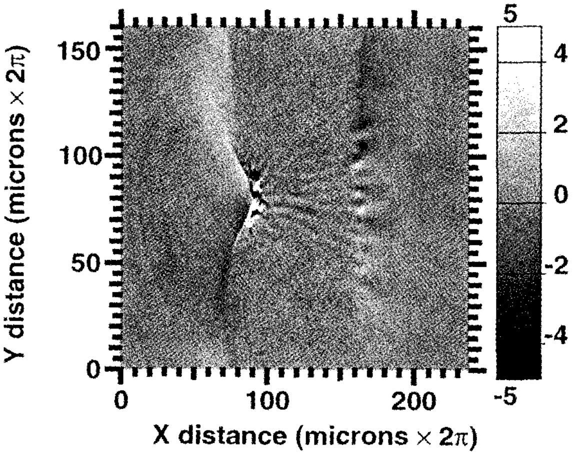

Figure 5. Magnetic field intensity produced by laser-plasma interaction. The vertical intensity scale is in gigagauss and is capped at 5 gigagauss.

A typical plot from a ZOHAR calculation of I = 10^{21} W/cm^2 laser pulse of 1 μm light interacting with a plasma slab at $n_e = 50\ n_c$ is shown in Fig. 5. These laser intensities are somewhat higher than those currently being achieved experimentally. The highest intensity magnetic fields are shown in this plot to exceed 5 gigagauss over a region of approximately

50 μm^{-3}. Fields in excess of 1 gigagauss span a region approximately 1000 μm^{-3}. Peak fields in this calculation reached approximately 15 gigagauss. Analysis of a number of calculations at laser intensities between 10^{20} W/cm^2 and 10^{21} W/cm^{2}suggest that the static magnetic field intensity generated by the electron beam formed by the laser reaches peak levels that are approximately 1/3 the dynamic magnetic field level in the incident laser beam. The duration of the magnetic field is on the order of picoseconds.

4 Future Work

Experiments with the Petawatt laser at the NOVA facility will continue to examine the optimization of the electron beam generated by the laser-plasma interaction for production of suitable x-ray sources for radiographic applications. Laser improvements will be incorporated to increase the fraction of the laser beam that is above the required intensity for the production of hot electrons. Grating development is underway to produce dielectric transmission gratings that will be capable of handling a 5 kJ pulse. Such a pulse, properly formatted, would increase the electron current by a factor of 50 over the present experiments. Further improvements using tailored target design might be possible. Measurements of the magnetic field intensity near the laser-plasma interaction region may be attempted.

5 Conclusions

High intensity laser sources using pulse compression techniques have been used to generate dynamic electric field strengths in excess of 100 Megavolts per micron. Experimental measurements have demonstrated hot electron production at energies as high as 100 MeV. Particle-in cell calculations of the magnetic fields associated with this experimental data suggest that the accompanying magnetic fields generated are on the order of a gigagauss in a volume of approximately 1000 cubic microns. The use of Petawatt level laser sources enables the accessibility of the gigagauss magnetic field regime for several picoseconds in experimental facilities.

Acknowledgement

This work was performed under the auspices of the Department of Energy by the Lawrence Livermore National Laboratory under Contract W-7405-Eng-48.

References

1. Priedhorsky, W., Lier, D., Day, R., Gerke, D., Hard x-ray measurements of 10.6 micron Laser Irradiated Targets, Phys. Rev. Lett. **47**, (1981) p.1661.
2. Perry, M. D., Keane, C., Campbell, E. M., Ultrahigh Brightness Lasers and their Applications, LLNL internal document (1987).
3. Kmetec, J. D., Gordon, C. L., Macklin, J. J., Lemoff, B. E., Harris, S. E., MeV X-ray Generation with Femtosecond Lasers, *Phys. Rev. Lett.* **68** (1992) p. 1527.
4. Malka, G., Miquel, J. L., Experimental Confirmation of Ponderomotive-Force Electrons Produced by an Ultrarelativistic Laser Pulse on a Solid Target, *Phys. Rev. Lett.* **77** (1996) p. 75.
5. Malka, G., Lefebvre, E., Miquel, J. L., Rousseaux, C., Observation of Relativistic Electrons Produced in the Interaction of 400 Fsec Laser Pulses with Solid Targets, Anomalous Absorption Conference, Fairbanks, Alaska, August 1996.
6. Gibbon, P., Efficient Production of Fast Electrons from Femtosecond Laser Interaction with Solid Targets, *Phys. Rev. Lett.* **73** (1994) p. 664

ELECTRICAL AND THERMAL PROPERTIES OF MICROELECTROMAGNETS FOR ATOM MANIPULATION

M. DRNDIC, K. S. JOHNSON, M. PRENTISS, R. M. WESTERVELT
Department of Physics, Harvard University, Cambridge, MA, USA

We have fabricated micro-electromagnets (μEMs) for atom manipulation consisting of micron-scale Au wire patterns on sapphire substrates. Micro electromagnets are able to support DC currents of several amperes with current density ~ 10^8A/cm^2, magnetic fields up to 0.3 T, and gradients to 10^3 T/cm. Electrical and thermal properties and possible improvements to achieve higher fields and gradients by these devices are discussed. Micro-electromagnets can create time-dependent magnetic fields and form adaptive atom optics elements such as mirrors, diffraction gratings, lenses and traps.

1 Introduction

Microfabrication, together with laser cooling of atoms, has led to a recent effort to design and construct optical elements for neutral atoms [1-10]. Atom-optical elements that are not based on light forces have been constructed using microfabricated, freestanding gratings [2] and permanent magnets [1,3,4,6,7,8]. We have fabricated a variety of micro-electromagnets (μEMs) for atom manipulation consisting of micron-scale Au wire patterns on sapphire substrates [9]. In this paper, we discuss electrical and thermal properties of μEMs and possible improvements to achieve higher fields and gradients. Fig. 1 shows several μEM devices. Microfabrication provides the possibility of making patterns for a variety of manipulations. The magnetic field profiles above the wires can be controlled by tailoring the wire patterns, allowing us to potentially influence atoms in novel ways and with greater control. Serpentine wire patterns (Fig. 1 (c)) have been used as atom mirrors [9,10], and circular wire patterns [9] (Figs. 1 (a) and (b)) suggested [11] as atom microtraps have been fabricated.

The manipulation of neutral atoms using μEMs is based on the Zeeman interaction between an inhomogeneous magnetic field and the atomic magnetic dipole moment [3,11]. Fig. 2 shows a computed magnetic field profile (contours of constant B-field amplitude) above a μEM mirror. The B-field magnitude decays exponentially in the direction perpendicular to the mirror plane, with the characteristic decaying length $k^{-1} = a/2\pi$, where a/2 is twice the separation between the wire centers.

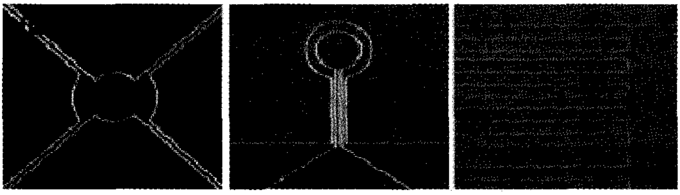

Figure 1. Micrographs of micro electromagnets: (a) and (b) geometries suggested [11] for trapping atoms, (c) serpentine wire geometry as atom mirrors

The details of fabrication and calibration of the magnetic fields of such devices have been published elsewhere [9]. We chose materials for their excellent electrical and thermal properties, cooled the devices to cryogenic temperatures, and typically operated the devices in a pulsed mode to reduce the average heat dissipation. Briefly, Au wires are fabricated on sapphire substrates in three steps: lithography, electroplating and thermal annealing (summarized in Fig. 3 (a-c)). Best results have been obtained with Au wires (DC current densities ~ 10^8 A/cm^2, magnetic fields ~ 0.3 T, and gradients ~10^3 T/cm [14]).

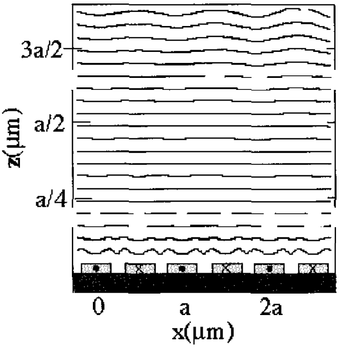

Figure 2. Computed contours of constant B-field magnitude above a μEM mirror with a = 48 μm, N = 83 lines with a rectangular cross-section 20 x 3 μm^2; z-axis is perpendicular to the mirror plane, x-axis is in the mirror plane and perpendicular to the wires. Infinitely long wires and uniform current density are assumed.

2 Electrical and Thermal Properties

Micro-electromagnets were tested in vacuum in a cryogenic apparatus [9]. The instantaneous device voltage V(t) and current I (t) were monitored; from these we find the device resistance R(t). The total lead and contact resistance is ~2 Ω. Fig. 4 (a) shows the measured DC current-voltage (I-V) curve for a μEM mirror at 100 K heat sink temperature. The mirror characteristics are total area 2 x 2mm^2, with N = 83 wires of width w = 20 μm and height h = 3 μm (Fig. 3 (d)). The resistance of this device is R(300 K) = 60 Ω, R(4 K) = 6 Ω; the measured inductance is L = 50 nH resulting in a L/R time constant of ~10 ns at low temperatures.

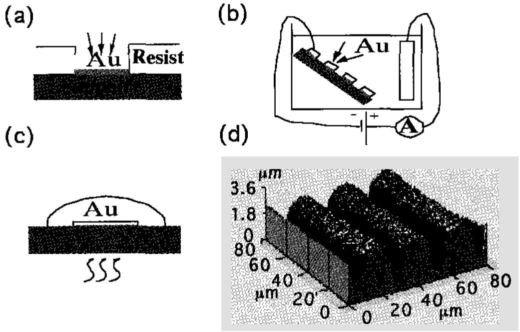

Figure 3. Schematic of μEM fabrication: a) lithography followed by metal evaporation, b) electroplating, c) thermal annealing; (d) atomic-force microscopic image of a fabricated μEM mirror.

To study the heating of μEMs, the wire temperature T_w (t) was found from the measured resistance R(t) using the known temperature dependence R(T). At I = 0.5 A (Fig. 4 (a)), T_w = 200 K still below room temperature. We operated the devices in a pulsed mode to reduce the average heat dissipation. Voltage pulses were applied at 300 K, 100 K and 20 K. Figures 4(b) and 4(c) show I(t) and T_w(t) for a mirror. As shown, mirror currents I ~ 3 A were achieved at 20 K using 1% duty cycle pulses. At 20 K heat sink temperature and 1% duty cycle, the wire quickly heats to 50 K (Fig. 4 (c)), and then increases more slowly to 80 K during the pulse. The instantaneous power dissipated by the mirror reaches large values up to ~10 kW/cm^2. From the measured wire heating we estimate the effective thermal conductance G ~ 4 W/K from the wire to the heat sink, and the thermal time constant C/G ~ 3 μs, where C = 1.3 x 10^{-5} J/K is the wire heat capacity. On the other hand, the thermal equilibration at DC current I = 0.5 A at a constant voltage V = 21 V takes ~10 min. This reflects the larger thermal time constant of the heat sink. At higher duty cycles (~20%) the maximum current supported by the wires is such that the time-averaged power dissipated is constant (~10 W) [13].

3 Conclusion

We have fabricated a variety of micro-electromagnets for atom manipulation. This work begins the experimental development of adaptive atom optical elements that exploit micro-fabrication and cryogenics. A possible way to achieve higher magnetic fields and gradients is fabricating devices such that R(300 K)/R(4 K) ~ 10 [3,4] using high purity wires. This could be done by etching through metal foils or by improving the purity of electroplated metals. Wires could be made from Au, or Cu and Ag with a layer of Au on top to prevent degradation. The current density potentially achieved in this way would be ~10^{10} A/cm^2, corresponding to constant surface fields of order B ~ 10 T and gradients of ~10^5 T/cm. With the present μEM mirrors, the maximum B-fields achievable could be estimated from a 'back of the envelope' calculation in the extreme limit of very short pulses Δt ~ L/R.

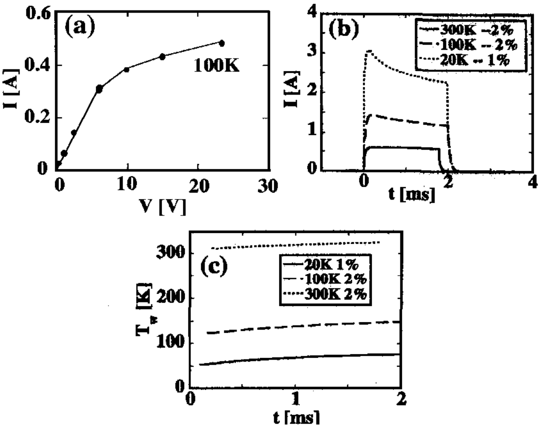

Figure 4. (a) Measured I-V characteristics for a μEM mirror at 100 K heat sink temperature for dc excitation. The surface B-field scales as B ~ 33 mT / A. (b) Mirror current I(t) during a voltage pulse V = 40 V at temperatures and duty cycles indicated. (c) Mirror temperature T_w(t) during a pulse V = 40 V, found using R (Ω) = 2.3 + 0.21 T_w(K).

Setting $I^2R\ \Delta t = C\ \Delta T$, where ΔT is the temperature rise in the wire during the pulse, and C is the wire heat capacity. For a mirror as discussed, taking $\Delta t \sim 10$ ns and $\Delta T = 500$ K, gives $I \sim 80$ A, which corresponds to a surface field $B \sim 3$ T. Higher fields could be achieved with more favorable μEM patterns.

References

1. Adams, C. S., Sigel, M., Mlynek, J., *Phys. Rep.* **240**, (1994) p. 143, and refs. therein.
2. Ekstrom, C. R., Keith, D. W., Pritchard, D. E., *Appl. Phys. B* **54**, (1992) p. 369.
3. Migdall, A. L., et al., *Phys. Rev. Lett.* **54**, (1985) p. 2596.
4. Kaenders W. G., et al., *Phys. Rev. A* **54**, (1996) p. 5067.
5. Opat, G. I, Wark, S. J., Cimmino, A., *Appl. Phys. B* **54**, (1992) p. 396.
6. Sidorov, A. I, et al., *Quant. Semi. Opt.* **8**, (1996) p. 713.
7. Roach, T. M., et al., *Phys. Rev. Lett.* **75**, (1995) p. 629.
8. Hughes, I. G., et al., *J. Phys. B* **30**, (1997) p. 2119.
9. Drndic, M., et al., *Appl. Phys. Lett.* **72**, (1998) p. 2906.
10. Johnson, K. S., et al., *Phys. Rev. Lett.* **81**, (1998) p. 1137.
11. Weinstein, J. D., Libbrecht, K. G., *Phys. Rev. A* **52**, (1995) p. 4004.
12. We have also made Cu and Ag wires. Au surface has the practical advantage of being chemically inert, which is necessary for a good heat transfer and electrical conductivity at interfaces.
13. For example, the measured peak current for a 1.5ms pulse and duty cycle ~15% was ~ 0.95A at 100K heat sink temperature.

NONDESTRUCTIVE MINI-COILS APPROACHING MEGAGAUSS FIELDS

M. VON ORTENBERG AND H.-U. MUELLER
Humboldt Universitaet zu Berlin, Germany

Monolithic mini-coils of the copper/(fiber/epoxy) type generate, in a 2 mm bore, magnetic fields up to 78.5 T and about 1 msec pulse length with a capacitor bank of 30 kJ. The coil is operated directly in liquid helium to take advantage of the increase of the action integral and provides a low-temperature environment in the bore without additional cryostat.

1 Introduction

Presently, the generation of nondestructive megagauss fields is one of the most ambitious projects worldwide [1,2]. Most of the concepts emphasize so-called "user-friendliness" both with respect to experimentally available space and pulse duration τ. The bore diameter, d, is essentially conditioned by the requirement of a low temperature, liquid Helium environment. Usually, this requires the use of an additional cryostat, so that the minimum bore diameter is about 10 mm. The limitations of the two parameters τ and d involve a considerably higher energy to drive the coil into the megagauss regime, so that the realization is only possible by national or even international projects [3,4]. In contrast to these programs we propose *Mini-Coils* of reduced bore diameter operated directly at Helium temperatures and with a pulse length of $\tau \cong 1$ msec.

2 Theoretical Aspects

The generation of megagauss fields with pulse durations on the order of 1 msec is an adiabatic process, so that the dissipated Joule energy is totally used for the temperature increase of the conducting windings [5]:

$$j(t)^2 {*} \rho(T[t], B[t])dt = \frac{c(T[t])}{D} {*} dT \qquad (1)$$

Here j(t) is the current density, ρ(T[t]) the resistivity, B[t] the magnetic field, c(T[t]) the specific heat and D the mass density of the wire material. Analytical integration of equation (1) is only possible for limiting conditions with respect to the field dependence of the resistivity. In a crude approximation, this dependence is neglected so that the integration directly yields:

$$\int_{T_i}^{T_f} \frac{c(T)}{\rho(T)}dt = \int_{0}^{\tau} \frac{j(t)^2}{D}dt = \tau {*} j_{max}^2/(2D) \qquad (2)$$

The right part of equation (2) is the result for a pulse of half-sinusoidal shape. The left part of the same equation is known as the *action integral* and is entirely a material property [5]. The integrand c(T)/ρ(T) of the *action integral* for copper of different purity is plotted in Fig. 1 as a function of the temperature T [6,7]. Usually, pulsed coils are operated at T = 77 K.

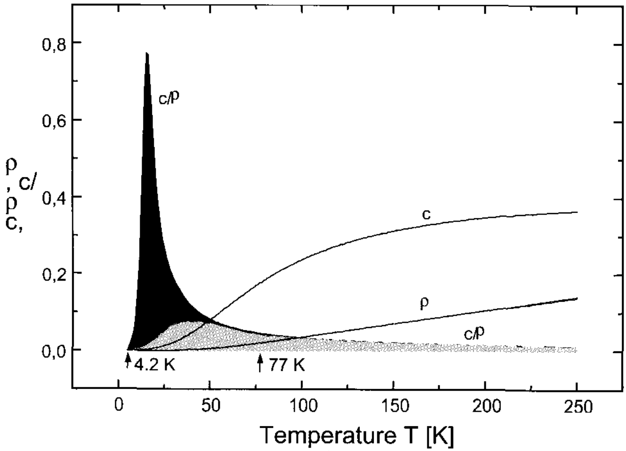

Figure 1. The integrand c/ρ of the *action integral* as a function of the temperature T for different purity of Cu [6,7].

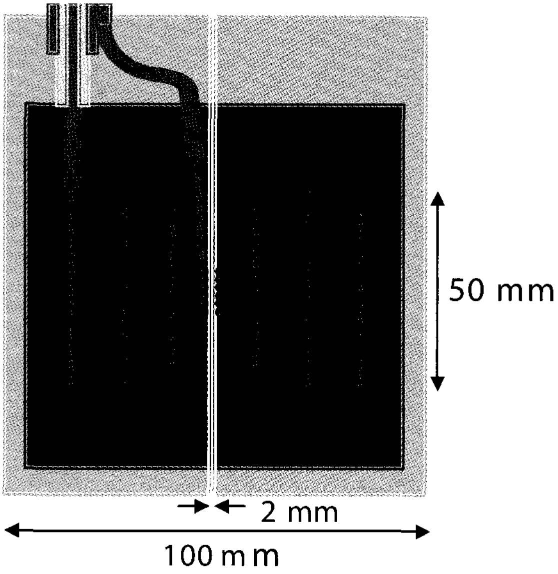

Figure 2. Schematic of the mini-coil.

For given pulse length τ, initial temperature T_i, and tolerable final temperature T_f of the windings directly follows the maximum current density j_{max} by integration over the temperature interval $<T_i,T_f>$. It should be noted that the *action integral* between 4.2 K and 77 K is up to three times larger than the integral between 77 K and 300 K. The decrease of the initial operating temperature of the coil to $T_i = 4.2$ K permits twice the current density with the same final temperature $T_f = 300$ K. Hence, the total number of windings can be reduced by a factor of 2, decreasing the inductance of the coil by a factor of 4.

The operation of the coil at Helium temperatures has the additional advantage that the usual requirement for solid-state experiments to be performed at low temperatures is possible without an additional cryostat, so that the bore diameter can be reduced to a minimum. This fact implies, however, smaller strain values in the coil so that the enforcement layers can be reduced. Our mini-coil has a d = 2 mm bore, allowing both optical and transport measurements using sophisticated experimental techniques.

3 Experimental Set-up

Our mini-coils consist of four protected layers of ordinary transformer Cu wire with 1.5 mm diameter as shown schematically in Fig. 2. Each winding layer is reinforced by a glass fiber/STYCAST 2855 compound, ensuring that the maximum tangential strain is less than 2.5 GPa. The inductance of the coil is about 100 μH so that a capacitor bank with C = 2.12 mF was suitable for pulse length $\tau \cong 1$ msec. An ordinary He-cryostat with stainless steel protection was used to avoid damage of the cryostat in case of coil explosion. The current connections of the coil were of the coaxial type and sealed by epoxy so that no gas discharge is possible even at reduced He-gas pressure. In the upper part of Fig. 3, the resulting field pulse is reproduced as obtained by the direct measurement of the pick-up voltage shown in the lower figure. A maximum field $B_{max} = 78.5$ T was obtained with a pulse length $\tau = 1.2$ msec. Further increase of the current density resulted in *axial* explosion of the coil.

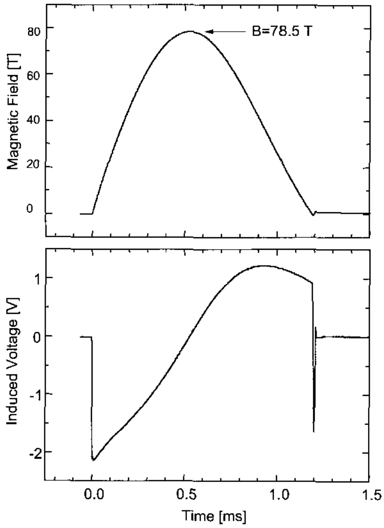

Figure 3. Field pulse and pick-up voltage for Mini-Coil 2.

4 Problems and Conclusions

More than ten mini-coils have been tested. All of them failed by axial disintegration, despite different methods of reinforcement in this direction. The coils exploded more-or-less smoothly, without harming the cryostat. We explain this failure, which emerges from the innermost windings, by the highly anisotropic properties of the glass fiber/epoxy compound. Due to the Lorentz force, the wire separates the protective fibers in the *axial* direction, affecting the low notch impact strength parallel to the fibers. A redesign using a multi-compound construction including the new material ZYLON [8] is in progress. We conclude that nondestructive Megagauss coils are possible.

References

1. Challis, L. J., *Physica B,* **211** (1995) p. 50.
2. Campbell, L., et al., *Physica B,* **211** (1995) p. 52.
3. Joss, W., this volume.
4. Campbell, L., this volume.
5. Herlach, L., *Physica B,* **246** (1998) p. 152.
6. Landolt Börnstein, **15** (1982) p. 31.
7. International Critical Tables of Numerical Data in Physics, *Chemistry and Technology*, **6** Mc Graw-Hill (1929) p. 124.
8. Toyobo Co., Ltd., Tokyo, Japan.

MAGNETO-OPTIC MEASUREMENTS UP TO 50 T USING MICRO-COILS

K. MACKAY, M. BONFIM, D. GIVORD, A. FONTAINE, J. C. PEUZIN
Laboratoire Louis Néel, CNRS, Grenoble, France

In this paper we present a system based on micro-coils capable of generating pulsed magnetic fields up to 50 T. We describe the magneto-optical measurement we have set up to study samples in these coils. We present our measured results of the Faraday rotation for a paramagnetic Praseodymium Gallium Garnet (PrGG) sample. We discuss the relative merits of such a system compared to conventional ones and the field characteristics obtained.

1 Introduction

Ever since the pulsed magnetic fields of Kapitza in 1924 [1], there has been continued effort to produce higher and higher magnetic fields. There exist world wide a number of large installations dedicated to producing fields in excess of 40 T using techniques ranging from capacitor discharge to implosive coils. Physicists who desire ever-greater magnetic fields to investigate fundamental physical properties of materials drive this effort. Most of the effort is oriented towards generating high, long pulse duration fields, requiring enormous energy consumption and capital investment.

However, an alternative approach to generating large magnetic fields is possible. The magnetostatic energy stored in a coil is proportional to its volume. By simply reducing the coil dimensions from the centimeter scale (the smallest currently used [2]) to the tens of micrometer scale (our coils), we can reduce the magnetostatic energy needed by a factor 10^9! The inductance of such small coils is also considerably reduced, allowing current pulses as short as 10^{-8} s to be used. Such short pulse durations are quite acceptable for many magnetic properties. Moreover, short pulses may open up the possibility of measuring real dynamic magnetization processes such as nucleation and domain wall propagation, in a very direct way [3].

Our aim is to produce high magnetic fields using micronic coils. Here, we report on results measured using pulse durations on the order of 10^{-8} s. We will discuss the advantages and disadvantages of this method.

2 Micro-coils: General Principle and Structure

Advances in modern micromachining techniques allow relatively easy fabrication of precise microscopic coils in large numbers and at low cost. We have chosen to demonstrate the principle using simple, single-turn coils made by such techniques. The feasibility of using such coils to generate high magnetic fields is illustrated by a simple, 50 μm diameter Cu coil. Production of 50 T requires a current on the order of 2500 A. The pulse duration must be sufficiently short to avoid melting the Cu. The coil inductance here is estimated to be <1 nH, but with connections the system inductance could be several nH. This allows pulse durations of 10^{-8} s. For such short pulses the current flows within the skin depth ($\delta \approx \sqrt{\rho/\pi\mu f}$ where ρ is the resistivity and f the frequency) which is around 12 μm in our case. The overall Joule heat generated in the skin depth is approximately 0.3 mJ. To melt this volume of Cu requires around 0.5 mJ, suggesting that such coils should not melt. The magnetic pressure acting on the coil is estimated from **B**xI/a to be around 3 GPa. However, the mechanical inertia of the system indicates that a small deformation is expected. These oversimplified considerations lead us to believe that such a system is feasible.

We have chosen Si as the substrate as most of the micromachining techniques have been developed around this material. Our chosen geometry is shown schematically in Figure 1. The fabrication was carried out by the LETI. A number of coil geometries were made; we will concentrate on those having an internal diameter of 50 μm and an external diameter of 150 μm and an electro-plated Cu thickness of 30 μm.

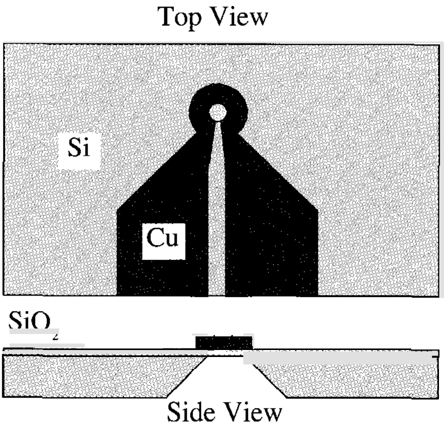

Figure 1. Schematic diagram of micro-coil structure

3 Current Generation

The current pulses were generated using the classical discharge technique across a spark gap. The capacitor bank used consists of 12, 1 nF ceramic type capacitors connected in parallel between two copper plates to reduce the overall circuit inductance. The spark gap is two small copper plates separated by 2.5 mm of air. The total size of the capacitor bank and spark gap is 75 mm x 25 mm x 5 mm. The discharge can be initiated either by charging up to the breakdown voltage or by focusing a pulsed laser beam between the two plates.

The capacitor bank can be recharged relatively quickly, giving us a pulse repetition rate of 1 Hz for peak current pulses of 3500 A and a maximum voltage of 5 kV. The current pulse was measured via a fixed coil placed next to the return current path, and its amplitude was deduced from circuit simulation and the discharge voltage. The discharge damage on the copper electrodes only changes their characteristics very slightly, as the total spark gap is large. There is a large pulse-to-pulse amplitude variation of around ± 10%. The results shown here represent the average pulse amplitude.

4 Measurement Techniques and Field Characterization

The use of such large dI/dt leads to the generation of considerable EM noise that is synchronous with the measurement. This makes normal inductive or transport measurements on a sample difficult. Optical measurements are very suitable for measurements in such small sample spaces. We have chosen to make magneto-optical measurements, which additionally allow us to physically separate the coil from the detector, thus reducing the EM pickup. The optical set-up is schematically shown in Figure 2.

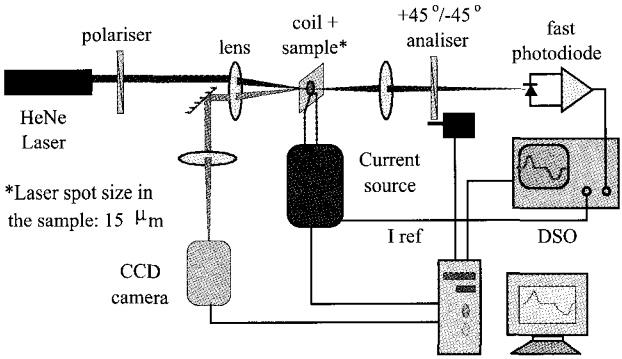

Figure 2. Schematic diagram of magneto-optical set-up and measurement system.

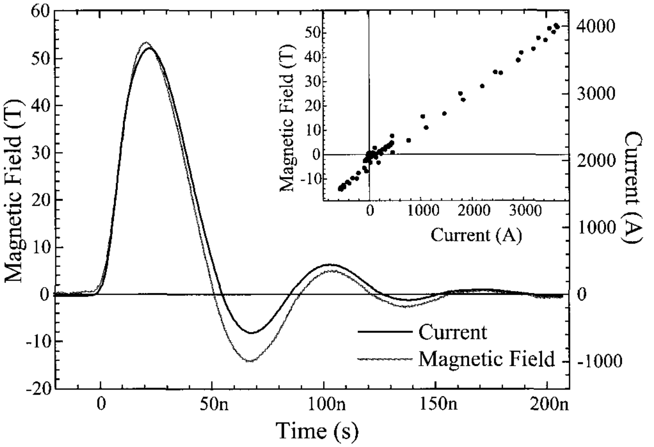

Figure 3. Measured Faraday rotation for Praseodymium Gallium Garnet (PrGG). Insert shows the variation of magnetic field (deduced from Faraday rotation) with respect to the current.

Polarized light from a 5mW HeNe laser is focused onto the sample in or on the micro-coil and the polarization of the reflected or transmitted light is then analyzed, and its intensity measured with a fast Si photodiode. In order to eliminate the EM noise, the analyzer is flipped from +45° to -45° (with respect to the incident polarization) between each field pulse. This technique is greatly superior to the more conventional technique using two detectors. The signals were measured and averaged using a fast digitizing oscilloscope (TEKTRONIX 640A) that has a bandwidth of 500 MHz and a digitizing rate of 2 GS/s. The polarization resolution achieved is estimated to be 10^{-5} rad.

5 Experimental Results

We have used these coils to make magneto-optical measurements for a number of transparent paramagnetic materials, with known Verdet's constants, at high magnetic fields. The measured Faraday rotations enable us to determine the maximum field achieved. The results for Praseodymium Gallium Garnet (PrGG) are shown in Fig. 3. The sample took the form of very thin slices (typically 50 μm thick) placed on top of the micro-coil. The current pulses are repeated at 1-2 Hz. The signals shown here result from an average of 5 minutes (300 pulses). The coils are not damaged at this field strength.

6 Discussion

The measurements shown here were made outside the coil; the field inside is roughly 15% higher. At higher fields of roughly 60 T outside the coil, the coils are destroyed after only some tens of pulses. The problem of the temperature is essentially equivalent to that of larger installations; the maximum field is limited by the melting point of the metal used. Here we have used Cu, allowing us to achieve 72 T in principle, while Tungsten coils would allow generation of 94 T [4].

The small sample volume available is not necessarily a disadvantage. Many materials currently studied are in the form of small crystals, thin films or even nanoparticles. The small sample size reduces the problems of eddy current shielding by metallic samples.

The current distribution within the coil is important. We have made simulations on idealized structures using FLUX2D. This showed clearly that the current passes mainly on the inside surfaces of the conductor but also on the outside, top and bottom surfaces. For certain geometries, this non-uniform current distribution changes the profile of B(t) compared to I(t). Thus, more current is needed to reach 50 T than would be required from a simple calculation for a single-turn coil.

The spark gap used here is rather primitive. The spark resistance is estimated to be 0.7 Ω, making it the major source of energy dissipation in the circuit. Use of a gas like SF_6 would allow the spark gap to be reduced while still retaining the ability to be charged to the same potential. Control of the gas pressure will allow the field amplitude to be managed via the breakdown voltage.

7 Conclusions

We have generated pulsed magnetic fields in excess of 50 T using capacitor discharge across a spark gap into a lithographically produced micro-coil. We have used this system to measure the Faraday rotation for a number of paramagnetic samples at 300 K. The magnetic field gradients associated with this system are very large; simulations give 104 T/m, and could be exploited to study some specific material properties. Field rise times up to 1010 T/s may be useful for studying magnetization dynamics in certain systems.

Acknowledgements

The authors would like to thank the Rhône Alpes Region and the CNRS, France for the funding of this research program. M.B. would like to thank the CAPES, Brazil, for their financial support.

References

1. Kapiza, *Proc. Roy. Soc.* **A105** (1924) p. 691.
2. Puhlmann, et al., *J. Phys. D: Appl. Phys.* **30** (1997) p. 1861.
3. Bonfim, et al., *J. Synchotron Rad.* **5** (1998) p. 750.
4. Furth, et al., *Rev. Sci. Instr.* **28** (1957) p. 949.

FEASIBILITY OF MICRO-COILS

M. R. VAGHAR
Benedict Engineering Company, Tallahassee, FL, USA

L. LI, H. J. SCHNEIDER-MUNTAU
National High Magnetic Field Laboratory (NHMFL), Florida State University, Tallahassee, FL, USA

S. WIRTH, V. NEU, P. XIONG, S. VON MOLNAR,
Center for Material Research and Technology (MARTECH), Florida State University, Tallahassee, FL, USA

The feasibility of micro-coils of the so-called pancake geometry is investigated. Different materials are being compared for optimum conductor choice, including electrical conductivity, specific heat, magneto-resistance and mechanical properties. The modalities of operation are presented. The feasibility of manufacturing such coils is examined. Planar coils consisting of about 100 turns with conductor widths as small as 3 μm are being fabricated. The turns will be deposited either directly onto Si or onto SiO_x/Si. All patterns will be defined by photolithography. The results show that the maximum stress is very high for such micro-coils. The maximum stress may be reduced by adjusting the current density.

1 Introduction

Inner bores of research magnets have been standardized to reduce the number of required cryostats. At the NHMFL, standard bore sizes are 15 and 24 mm for pulse magnets, and 32 mm for continuous and quasi-continuous magnets. The cryostats allow for thermal, electrical and mechanical decoupling of the sample from the magnet. The samples typically have a volume of only 1 to 10 mm^3. It has, therefore, been proposed to integrate sample and magnet with the advantage that the magnet volume and energy requirements could be decreased considerably. Nano- and micro-fabrication techniques could help reduce dimensions even further. Micro-coils have generated considerable interest [1] and it has been shown that HTS micro-coils can be made [2]. In this paper we investigate the feasibility and limitations of pancake micro-coils, as shown in Fig. 2. We also examine the feasibility of manufacturing of such coils.

2 Fabrication

There are two main challenges in making a functional micro-coil based magnet that is capable of generating high fields. The first is the difficulty in making electrical contact to the center of the planar coils because of the tiny bore size; the second is to increase the packing density of the coils (both the in-plane density and the stacking density in the z-direction). We attempt to solve these problems by using micrometer scale photolithography and an ultra-thin Si membrane as the substrate. The fabrication process is based on a set of mature technologies developed in microelectronics research. It involves Si processing, thin film metalization, and lithographic patterning and etching. A schematic illustration of the process is shown in Fig. 1.

To increase the packing density in the z-direction and solve the problem of making electrical connection to the center of the coils, we take advantage of a commercially available ultra-thin Si membrane (Virginia Semiconductors). The Si membrane is thinned down by a chemical-mechanical polish on both sides. As delivered by the manufacturer, the membranes have a thickness of ~ 4 μm, which can be further reduced with a CP4 etch (5 HNO3 : 3 HF : 3 CH3COOH). A dilute CP4 etch also serves to enhance the surface smoothness of the membrane. The 2" wafer is cleaved into 1 cm x 1.5 cm rectangles. An 8 μm x 8 μm hole is created in the substrate with high energy focused ion beam (FIB) milling. The 25 keV Ga ion beam at 0.5 nA is rastered over the 10 mm x 10 mm area, resulting in an etch rate of ~ 3 Å/s. To avoid charging during the milling, we first coated the substrate with a thin layer of copper. Alternatively, the hole can be created with a hot KOH etch. Since the conventional positive photoresist is not compatible with KOH, a thin gold film can be substituted as the etching mask. The hole in the gold film can be generated with photolithography and a compatible acid etch. The substrate is stripped clean of any metal film after the hole is created. Then a 5000-Å thick copper film is deposited onto both sides of the substrate via RF magnetron sputtering. Special care is taken to ensure that the copper film covers the inside wall of the hole. Finally, the copper coil is patterned with photolithography and a wet chemical etch. The second lithography is carefully aligned with the hole to ensure that the copper film around and inside the hole is preserved. Fig. 2 shows two micrographs of Cr coils, which will be used as the mask for making the copper coils. The dark areas are Cr films and the white areas are etched clean. The Cr lines are 4 μm in width and the separation is 2 μm. The dashed square indicates the location of the hole in the Si membrane. The etchant for copper, acquired from the Transene Company, has an etch rate of ~ 50 Å/s at 300 C. Once the feasibility study of this process is complete, we will explore reactive ion etching of the copper film to obtain better line width definition and preservation of the cross-sectional area of the copper wire.

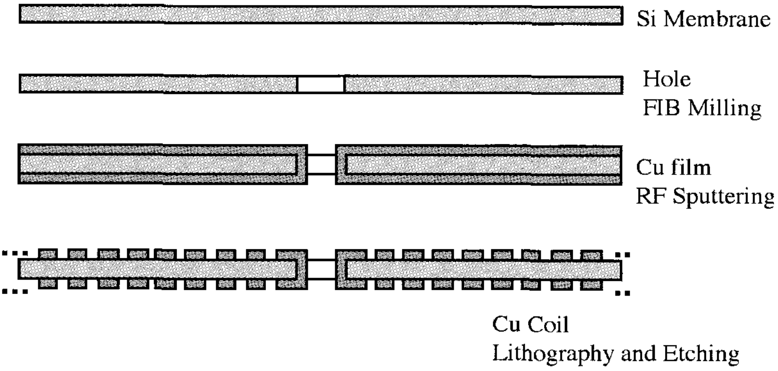

Figure 1. Schematic illustration of the fabrication process.

The resulting device is a copper coil on both sides of the Si membrane, electrically connected through the center hole. This winding geometry is known as "double pancake." The external electrical connections to the coil can then be made outside the activearea of the coil on patterned contact pads. There is no longer a need to make any electrical contact to the inner most layer of the coil. The thinness and the flexibility of the Si membrane also make it ideal for stacking. A thin layer of polymer can be spun coated onto the coils to provide the necessary electrical insulation between the plates

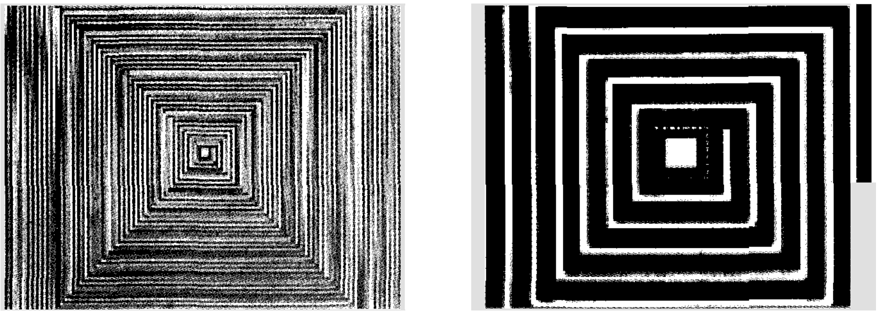

Figure 2. Micrographs of Cr coils..

3 Formulation

To analyze a micro-coil magnetically and mechanically, simplifying assumptions are made. A stack of identical micro-coils or pancakes with many turns is considered as a single multi-layer solenoid magnet. The number of turns of a double pancake is considered to be the number of layers of a solenoid, and twice the number of micro-coils in a pile is considered to be the number of turns for each layer. For example, a stack of 1000 double pancakes with 5000 turns on each side is considered as one solenoid magnet with 5000 layers and 2000 turns per layer.

The total magnetic field at the center of the resulting multi-layer magnet is the sum of the fields of each layer. The field of each layer is calculated from,

$$B = \mu_0 \frac{NI}{2a_1(\alpha - 1)} \ln \frac{\alpha + \sqrt{\alpha^2 + \beta^2}}{1 + \sqrt{1 + \beta^2}} \tag{1}$$

where B is the magnetic field in tesla, μ_O is the magnetic permeability in henry/m, N is the number of turns, I is the current in ampere, $\alpha = \frac{a_2}{a_1}$, $\beta = \frac{H}{2a_1}$, a_1, a_2 and H are inner radius, outer radius and height of a layer in meters, respectively. The stress at the inner radius of each layer is approximated from the equilibrium equation (by neglecting the gradient of radial stress),

$$\sigma = JBr \tag{2}$$

where σ is the stress in Pa, B is the magnetic field in tesla, J is the current density in A/m^2 and r is the radius in meter of the layer. The pulse duration is calculated from the heating of an adiabatic system,

$$\int J^2(t)dt = \int \frac{C_p(T)}{\rho(T,B)} dT \tag{3}$$

where C_p is the specific heat in J/m^{3}K, ρ is the resistivity in Ω•m, T_i and T_f are the initial and final temperatures of the wire in K, and τ is the pulse length in seconds. Assuming , i.e., for sine half wave, Eq. (3) reduces to

$$\frac{1}{2}\tau J^2 = \int_T^T \frac{C_p(T)}{\rho(T,B)} dT \tag{4}$$

The right hand side of Eq. (4) is called the "action integral" and only depends on the material properties of the wire.

4 Conductor Choice

To find an optimum conductor based on thermal, electrical and mechanical properties, two factors should be considered. One is the action integral which dictates the pulse length, and the other is the ultimate stress. Table 1 shows the action integral with $T_i = 4$ K and $T_f = 450$ K, and typical ultimate stress for selected metals. It is obvious from Table 1 that copper is a good compromise. Gold is the best candidate to obtain longer pulses, whereas higher fields may be achieved with tantalum.

Table 1. Action integral and typical ultimate stress for selected metals.

Metal	Action Integral x10^{16} A^2s/m^4	Ultimate Stress GPa
Copper (Cu)	7.62*	0.25
Aluminum (Al)	3.87*	0.09
Iron (Fe)	4.99	0.70
Tantalum (Ta)	1.40	0.90
Nickel (Ni)	5.84	0.32
Silver (Ag)	2.73	0.12
Gold (Au)	10.06	0.16
Beryllium (Be)	5.23	0.55

*Magnetoresistance has been considered.

Table 2. Parameters and calculation results for 50 and 20 T micro-coil systems.

Description	Unit	50 T	20 T
Inner radius (a_1)	μm	5	5
Outer radius (a_2)	μm	5000	5000
Distance between turns	μm	2	2
Wire width	μm	4	4
Wire height	μm	0.5	0.5
Substrate height	μm	6	6
Magnet height (H)	μm	8000	8000
Maximum field	T	50	20
Radial filling factor		0.67	0.67
Axial filling factor		0.125	0.125
Number of turns per pancake		832	832
Number of pancakes		1000	1000
Maximum current	A	0.228	0.091
Maximum current density	kA/mm^2	114.2	45.7
Action integral x10^{16} *	A^2s/m^2	7.63	7.63
Pulse duration	μs	11.68	73.20
Maximum stress	GPa	7.24	1.14

*Action integral is calculated based on properties of copper.

5 Results

Computations were made for a coil consisting of a stack of 1000 double pancakes to generate 50 and 20 T fields. Table 2 shows the parameters and results of this calculation. From Table 2 it can be perceived that the maximum stress for a micro-coil system generating 50 T is much higher than the ultimate stress of many metals. Even to generate 20 T with this system the maximum stress is beyond the ultimate stress of known conducting materials, e.g., copper. To reduce the stress significantly, a nonuniform distribution of current density is proposed. With this method the current density is lowered (by increasing the width) for each layer where the stress is higher than the maximum allowable stress.

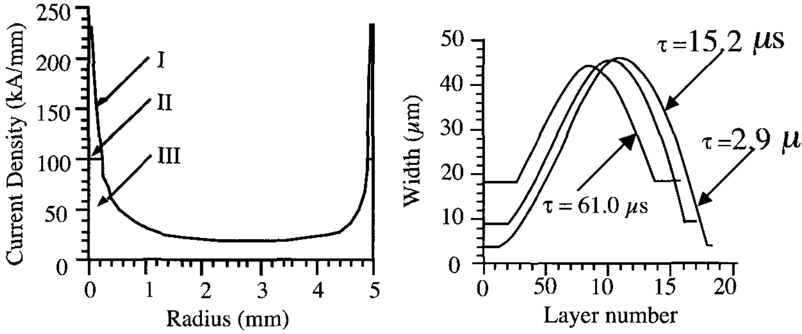

Figure 3. a) Distribution of the current density; b) distribution of the width of the layers.

Certainly, this action will reduce the magnetic field. For the example micro-coil system, assuming maximum stress of 0.4 GPa (i.e., for copper), a minimum width of 4 μm for the turns, and a current of 0.457 A, the magnetic field decreases from 100 T to 22.3 T and the number of layers for the magnet (number of turns for each pancake) is reduced to 182 layers. Fig. 3a shows the distribution of the current density (curve I) for this calculation. The pulse length for this system is calculated from the maximum current density and is about 3 μs. To increase the pulse length, the maximum current density needs to be reduced. By limiting the current density to 100 kA/mm^2 (Fig. 3a curve II), which requires a minimum width of 9.1 μm for the layers, the pulse length increases to 15.2 μs, however, the field reduces to 20.9 T. Limiting the current density to 50 kA/mm^2 (Fig, 3a curve III), or having a minimum width of 18.2 μm, the pulse length increases to 61 μs whereas the field decreases to 19.0 T. Fig. 3b shows the distribution of the width of the layers for these three cases.

6 Conclusions

Feasibility of micro-coils and their manufacturing was investigated and a scheme to fabricate a micro-coil based magnet using microelectronics processing technologies proposed. The use of an ultra thin Si membrane as the substrate circumvents the difficult problem of making electrical connections to the tiny coil, and makes it possible to have a high stacking density. Preliminary results from FIB milling of Si, deposition of Cu films on Si and the lithographic patterning of the coil have demonstrated the feasibility and potential of this scheme.

Calculations were presented for a micro-coil system to generate 50 and 20 T fields. The maximum stress is much higher than the ultimate stress of many metals if a 50 T field is desired. Adjusting the current density (by changing the width) of each layer reduced the maximum stress. The magnetic field decreased to 22.3 T for this nonuniform distribution of the current density.

The pulse length is determined by the heat capacity and the resistivity of the conductor. For this system, the pulse length is about 3 μs for a temperature rise of 4 K to 450 K. A higher pulse length may be achieved by decreasing the maximum current density or by increasing the minimum width of the turns at the expense of the magnetic field. Then, a pulse length of 15 μs (20.9 T) and 61 μs (19 T) can be achieved.

Future work will be done to compute the requirements for the power supplies of such micro-coils. Also, a detailed stress and field analysis should be done for each micro-coil. This will enable us to stack different micro-coils using different geometries in order to optimize the magnetic field.

References

1. See other contributions at this conference.
2. Hascicek, Y., Van Sciver, S., Schneider-Muntau, H-J., Godfrey, M., *HTS Thin Film Coils-Microcoil*, Internal Report, National High Magnetic Field Laboratory, Tallahassee, FL, (1993).

MICRO-MAGNETS

F. HERLACH, A. VOLODIN, C. VAN HAESENDONCK
Universiteit Leuven, Celestijnenlaan 200D, B-3001 Leuven
Laboratorium voor Vaste-Stoffysica en Magnetisme, Katholieke

Suggestions are made regarding the feasibility of building very small electromagnets for experimental applications. These structures would be made by lithographic techniques on a scale of microns. However, pulsed solenoid magnets with a bore on the order of a millimeter are also considered. These must be immersed in the cryogenic liquid used in the experiment, as the small bore does not allow for a separate cryostat. The magnets made by lithography could be single loops (e.g. to provide a field gradient), spirals, Helmholtz pairs, or stacks resembling a Bitter magnet. Superconducting magnets, resistive dc magnets and pulsed magnets (both non-destructive as well as self-destructing) are all considered.

1 Introduction

It is well known that higher fields can be obtained when the bore of a solenoid magnet is reduced; this motivates some researchers to miniaturize their experiments. Although techniques for the extreme miniaturization of both electronic circuits and mechanical devices have reached a high degree of sophistication, these have not yet been applied to the design of experiments in high magnetic fields, with the exception of two pioneering devices for magnetization measurements [1,2]. Most experiments require cryogenic temperatures, but there is a limit to the miniaturization of thermally insulated spaces in which cryogenic liquids such as liquid helium can be maintained. The only alternative is immersion of the magnet in the cryogenic liquid, together with the experiment. This is already feasible for magnets with a bore of the order of a few millimeters [3], but the ultimate miniature magnet will be smaller by orders of magnitude, manufactured by the same lithographic techniques that were used to make the sample assembly.

2 Design Considerations

Combining up to date electron beam lithography and lift-off techniques allows for preparation of high-quality, metal loop structures with a maximum thickness of about 100 nm and a width down to 20 nm. Hence, small, single-turn coils can be fabricated on oxidized Si wafers, where the field at the center will increase inversely proportional to the coil radius. Loops with a diameter between 1 and 5 μm and with a width of 200 nm are ideally suited to generate dc fields of the order of 1 mT in the inner part of the coil, when applying a current of a few mA [4]. This is used, for example, to calibrate the response of a magnetic force microscope (MFM) probe.

We intend to use similar single turn coils to generate short, high field pulses in a low temperature environment (liquid helium). E-beam lithography can be used to produce a mesoscopic sample near the center of the coil and the field dependence of the electrical transport properties can be measured. Alternatively, the tip of an atomic force microscope (AFM) can be positioned at the center of the coil with a magnetically active sample attached to the tip of the microscope. The response of the AFM cantilever resulting from the field pulse allows us to determine the sample magnetization [1]. In order to produce the maximum possible field, current pulses can be used which result in the destruction of the single turn coil, as elaborated below. For the AFM based experiments, several single shot experiments could be combined by fabricating an array of single turn coils. A current pulse with amplitude of about 10 A is required to produce a 6 T field at the center of a micrometer-sized coil. Relying on an optimized spiral shaped geometry should allow us to increase the field/current ratio to 6 T/A. Apart from mechanical stability considerations, the maximum current that can be sent through the coils strongly depends on the granular structure of the thin metal film evaporated into the lift-off profiles. In a first stage, a 100 nm thin Au film will be deposited on top of a 10 nm thick Ti layer to produce a homogeneous, low resistance metal wire. The use of hyper-conductive material such as In may considerably improve the maximum allowed current before breakdown. Alternatively, on a micrometer scale, plasma induced conduction can possibly give rise to a large current flow even after partial vaporization of the coil material. Another alternative is the use of superconducting material to obtain dc fields, but this would require further research on thin film superconductors such as granular materials.

A method to fabricate small helical coils is "microcontact printing" onto capillaries [5]. Presently, typical dimensions are on the order of 50 μm for the spacing of the turns, and 1 mm for the length of the coil. These coils have, of course, the advantage of high homogeneity.

3 Scaling of Pulsed Magnets

Pulsed magnets obtain the highest fields. These magnets are heated adiabatically during the pulse, therefore the pulse duration depends on the mass of the coil. For micro-magnets, this will result in very short pulse duration. This is determined by the action integral

$$\mathrm{J} = \int i^2 \mathrm{dt} = \int D\frac{c_p}{\rho}dT$$

where i is the current density, D the mass density, c_p the specific heat, ρ the resistivity, t time and T temperature. For heating copper from 77 K to 400 K, the order of magnitude of J is $10^{17}\,\mathrm{A^2m^{-4}s}$ (the same value applies to the temperature intervals 4 - 120 K and 27 - 150 K). The corresponding pulse duration is shown in the table that gives an overview of the order of magnitude of different parameters for a coil with square cross section where axial length, radial thickness and the bore diameter are each 1 micron. In the second row, the scaling with bore diameter b and magnetic field B is given for coils with the same proportions. The inductance is L, current is I and energy is W. The numerical values in the last four columns are calculated for a peak field of 100 T. This "magic number" represents the ultimate limit between destructive and non-destructive magnets. Immersion in a cryogenic liquid results in cooling with a time constant on the order of milliseconds. Depending on the coil configuration, this may substantially increase the possible pulse duration, but only if the duration is less than the time constant.

Table 1. Different Parameters of Pulsed Micromagnets

B/I	L	I	i	Δt	W
0.6 T/A	$2\times10^{-12}\times$H	170 A	2×10^{14} A/m^2	2×10^{14} A/m^2	3×10^{-8} J
b^{-1}	b	b•B	$b^{-1}B$	b^2B^{-2}	b^3B^{-4}

The necessary driving voltage is on the order of 100 V, resulting in very high electric fields; this could cause insulation problems. The inductance has been estimated for a single turn coil; in practice, this may be substantially smaller than the total circuit inductance. For pulsed micro-magnets, it will be difficult to build a discharge circuit with sufficiently low inductance to which the coil can be connected. One possibility is to use a charged cable (distributed inductance and capacitance) as a power supply, and ultimately a high-powered laser.

The peak field is limited by the mechanical strength of the coil structure. The scaling law for the mechanical performance does not depend on the absolute size; in its elementary form it contains only the ratio α between the outer and the inner diameter:

$$B_{max} = G\sqrt{2\mu_0\sigma_{max}}, G = \sqrt{\ln\alpha}$$

Here, σ_{max} is the tensile strength and G is the geometrical gain factor for an optimized current distribution which results in homogeneous stress. For a coil with constant current density, G is limited to √2; for homogeneous stress it is unlimited in principle, but the logarithmic increase becomes so flat that in practice one can hardly obtain $G = 2$ which corresponds to $\alpha = 50$. Of course, a large α is achieved more easily with a micro-coil. Strength is *a priori* the only advantage, unless it becomes possible to make very strong materials by evaporation techniques.

For self-destructing magnets with fields exceeding 100 T, the pulse duration is determined in the first place by the expansion of the coil due to the magnetic force. An estimate of the expansion is obtained either by integrating Newton's law or by the particle speed in the shock wave driven by the magnetic stress, whichever is faster. This particle speed is 1.7 km/s at 500 T for copper and scales roughly with $B^{3/2}$. As compared to traditional single-turn coils, which operate at energies exceeding 100 kJ, the advantage of the micro-coil is the very small energy, which results in minimal destructive effects. Depending on the inductance of the leads and power supply, it will be possible to achieve higher fields than the 300 T presently achieved with single-turn coils. The coil may be allowed to explode electrically (determined by the action integral) at the time when peak field is reached; this is an additional boundary condition. An interesting alternative is the use of a high-power picosecond laser beam to induce a current in a loop by generating hot electrons on the spot.

4 Conclusions

There are many possibilities for building micro-magnets of all sizes and shapes. It is likely that very high fields can be obtained eventually, but many problems with designing, manufacturing and energizing these magnets have to be solved. To make efficient use of these magnets, the extreme miniaturization of experiments is required, but this should be possible with modern technology.

Acknowledgements

This work was supported by the Fund for Scientific Research - Vlaanderen.

References

1. Naughton, M. J., et al., *Rev. Sci. Instrum.* **68** (1997) pp. 4061-5.
2. Aksyuk, V., et al., *Science* **280** (1998) pp. 720-2.
3. von Ortenberg, M., et al., in these proceedings.
4. Kong, L., Chou, S. Y., *Appl. Phys. Lett.* **70** (1997) pp. 2403-5.
5. Rogers, J. A., et al., *Appl. Phys. Lett.* **70** (1997) pp. 2464-6.

EARLY ATTEMPTS AT MINI (SUPERCONDUCTING) MAGNETS – ON THE WAY TO MICRO MAGNETS?

H. JONES
University of Oxford, Clarendon Laboratory, Oxford OX1 3PU, England

Using both Low Temperature Superconductors (LTS) and High Temperature Superconductors (HTS) some small magnets have been made at Oxford. The LTS magnet was a simple, split pair with an 8 mm bore giving some 4 tesla. The HTS magnet was a stack of ceramic-on-ceramic, machined "galaxy spirals" using BiSrCaCuO (2212). While these are hardly micro magnets, they do demonstrate how magnet technology becomes easier and infinitely cheaper if very small bores (and therefore magnets) can be used.

1 Introduction

For some years, much of the high field magnet community has been concentrating on big magnets for high fields. At the large international facilities there exist already, or are under development, hybrid magnets that can generate continuous fields of approaching 50 tesla. These require giant, superconducting outserts at the limit of the technology. There may be one or two dedicated helium liquefiers and the associated complex cryogenic engineering. The inserts are also state-of-the-art copper solenoids powered by tens of Megawatts of DC power that are water-cooled from a complex system of reservoirs, pumps and refrigeration able to extract the heat from such magnets. There are also a few laboratories with very high (>50 T) quasi-continuous fields; again, these facilities are large and costly. While these facilities are valuable, they are too costly to be at more than a handful of centers worldwide. At more localized centers, magnets are available that have more modest sizes, fields, pulse lengths, etc. These are magnets with bore sizes of the order of 10 to 20 mm, which still require quite substantial installations. It would be beneficial if magnet bore sizes could be smaller.

The bore size of magnet coils of whatever types, conventional, superconducting or pulsed, is very expensive real estate. For conventional or pulsed magnets the power or energy required goes as the cube of the bore. For superconducting magnets the amount, and therefore the cost, of superconductor needed is heavily dependent on the bore size. The ratio of outer diameter to bore diameter, α, is also an important parameter. For pulsed magnets, the mechanical strength of the coil, and therefore its highest field, depends on α [1]. If the bore size is very small, then it is much easier and cheaper to go to a high α coil. Clearly, minimizing the bore size and maximizing α can be highly desirable but it does mean that experimenters also have to reduce the physical size of that part of their experimental probes and samples accordingly. Sometimes, this can be quite difficult but the benefits are great.

2 A Mini LTS Magnet

For the past five years or so, a superconducting mini-magnet built in Oxford has been essential to the magneto-optical laser spectroscopy program being carried out in the Physics Department, Montana State University, under the direction of Prof. Rufus L. Cone. This magnet replaced an earlier and very much larger superconducting magnet and represented a *new philosophy*, where the magnet and crystal specimen were mounted in the same small diameter helium dewar, rather than the double dewar system used previously. The inner bore diameter was not only sufficient to allow tunable dye laser access to a rare earth ion crystal of mm dimensions, it was also possible to include an rf coil and sample rotation system for Zeeman ODNQR (Optically Detected Nuclear Quadrupole Resonance) studies as a function of field direction relative to crystal axes. This is an ongoing program at Montana State University; for the most recent publication see Hansen et al [2].

Figure 1. View of mini-magnet.

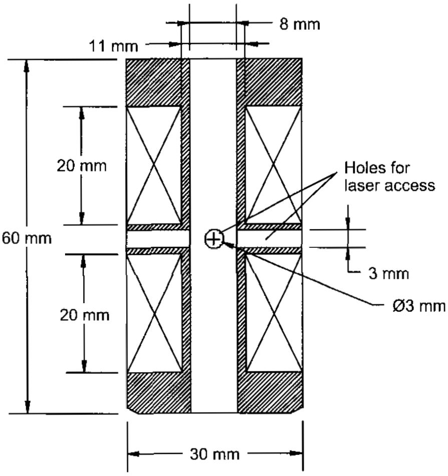

Figure 2. Section through mini-magnet.

A view of the magnet is shown in Fig. 1 and its dimensions are shown in Fig. 2. The magnet was wound from 0.33-mm diameter NbTi filamentary superconducting wire. The split in the winding permitted laser beam access through 3 mm diameter holes. The windings are interleaved with a preprg-epoxy glass cloth that was cured after winding. The magnet went straight to its short sample specification and gave 4.3 T with no training. It took two working days to test and produce, and cost only about £5 sterling for materials.

3 A Mini HTS Magnet

This was really an exploratory exercise to see if a very thick layer of Bi2212 High Tc

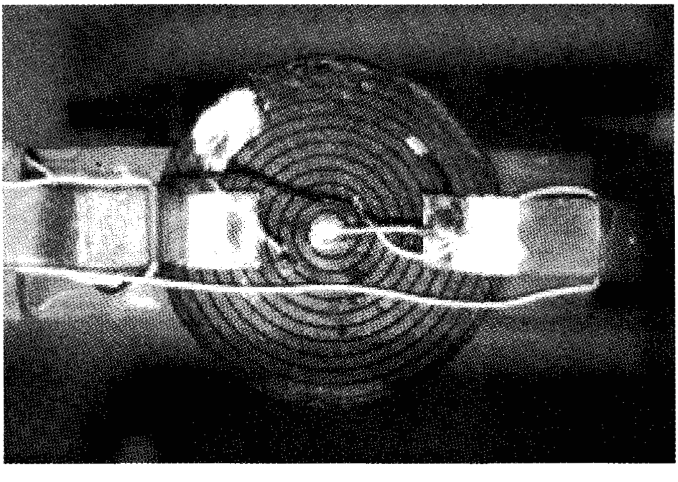

Figure 3. A view of HTA "galaxy spiral".

superconductor deposited on an MgO substrate, and then reacted, could be machined to give a continuous "Galaxy" spiral. A view of one such artefact is given in Fig. 3. The track is about 1 m long and 2 mm wide. The whole disc is 50 mm in diameter. The thickness of the track was not homogenous, being between 150 and 500 μm. Four such discs were stacked together alternating in spiral direction and joined electrically in series using ultrasonic soldering. These connections were rather resistive but the critical current for each disc was >3.5 amp at 4.2K. More detail can be found in Davies et al [3].

While this performance is not very impressive, it must be remembered that this was several years ago and this was a very primitive attempt at forming a "magnet" from bulk material. It does, however, point to a possible technique at forming "very thick film" magnet components that will carry amps. There are thin film technologies that lead to very high critical current densities but their actual critical currents are too low for practical magnet construction.

4 Conclusion

It is possible to produce magnets that are very small and can give useful fields for research. Not only can higher fields and mechanical strengths be achieved using this scaling down of bore sizes, but also considerable economic savings can be made. The increased sophistication of experimental techniques means that miniaturizing probe and sample assemblies is becoming easier. The next generation of mini magnets and maybe the development of micro magnets with bore sizes of approximately 1mm or less will have a significant impact on research.

Acknowledgements

It is a pleasure to acknowledge the considerable skills of Mr Tony Hickman, who had a major input into the work described. Dr M.J.M Leask provided the information on the experiments in Montana. The author is grateful to Mr Peter Richens for helping to produce this paper. The High Tc work was supported by EPSRC grant GR/F 83693.

References

1. Herlach, F., de Vos, G., Witters, J., *J. de Physique Colloque C1* (suppl.) 1 45 (1984) pp. 915-918.
2. Hansen, P. C., et al., *Phys Rev B*, 56 No. 13 (1997) p. 7918.
3. Davies, K., et al., *Applied Superconductivity*, 2 No 1 (1994) pp. 61-66.

HIGH TEMPERATURE SUPERCONDUCTING THIN FILM MAGNETS

Y. S. HASCICEK, Y. EYSSA, S. W. VAN SCIVER, H. J. SCHNEIDER-MUNTAU
National High Magnetic Field Laboratory, Florida State University,
Tallahassee, FL, USA

YBCO thin film double pancake units can be fabricated on a single wafer. It is possible to produce 5 tesla induction at 4.2 K in a background field of about 20 tesla by stacking these double pancake wafers. Small YBCO thin film flat coils can produce useful fields that can be very beneficial for MEMs. We have fabricated a proof-of-concept thin film coil from our YBCO thin films and tested it successfully.

1 Introduction

Although HTS conductor technology has come a long way, we are not even close to the potential of the materials in conductor form as far as its current carrying capacity and field dependence is concerned. Most of the present HTS conductor development techniques such as Powder-In-Tube (PIT) $Bi_2Sr_2Ca_1Cu_2O_x$ and $Bi_2Sr_2Ca_2Cu_3O_x$, result in low J_c conductors compared with the potential of the materials. Excellent current carrying capacity can be achieved in $YBa_2Cu_3O_{7-x}$ (YBCO) thin films. Therefore, using thin films in this unconventional manner gives us the opportunity to utilize the material in the highest J_c and most field tolerant state.

We propose to grow high quality YBCO thin films at both sides of polished dielectric substrates having central holes. The film at both sides of the substrate is then patterned by appropriate techniques to form a spiral pattern, basically forming an internally connected double pancake coil on one wafer. These wafers are then stacked together to form a high-temperature superconducting magnet.

Calculations show that it is possible to produce a magnetic induction of about 5 Tesla in the bore of such a magnet in a 20 T DC background field. The record field achieved by a similar size magnet by using PIT HTS conductors is about 1.5 Tesla at 4.2 K and in a 20 Tesla background field [1,2]. Presented are some examples of calculated fields by assuming moderate critical current densities (1.5×10^7 A/cm^2 at 4.2 K, and 5×10^6 A/cm^2 at 77 K) for YBCO thin films and our in-house laser patterning techniques for a miniature coil and sizable HTS magnet built by stacking the double pancakes on wafers: 1. Miniature coil: 1 mm OD, 0.5 mm ID, 0.0449 Tesla, made of 3 wafers, 2.4 mm high. 2. Insert coil: 60 mm OD, 20 mm ID, 2.094 Tesla, 20 wafers, 24 mm high. 3. High Field coil: 50 mm OD, 0.1 mm ID, 0.65 Tesla/wafer, 5.32 Tesla for 20 wafers, 7.21 Tesla for 40 wafers, 48 mm high.

2 Experiment

YBCO thin films were grown on <001> $LaAlO_3$ single crystal substrates by Pulsed Laser Deposition (PLD) using a Nd-YAG laser. SEM, EDS and XRD studies were done to verify that the film is, indeed, $YBa_2Cu_3O_{7-x}$ and has good topography at the surface. Small bridges were patterned to measure the critical current of the thin films. After measuring resistivity versus temperature to verify that the film has good T_c, and the transition is sharp, the critical current density of the bridges was measured by using a fast DC pulse technique and 4-wire arrangement under computer control.

We have built a proof of concept 26-turn one sided thin film coil and tested it at the National High Magnetic Field Laboratory. The size of this flat coil was about 12 mm by 12 mm. The YBCO thin film was patterned using a Nd-YAG pulsed laser with our Laser Direct Writing set up [3].

3 Results and Discussion

Fig. 1 shows a typical SEM micrograph of the surface of the YBCO thin film used for the HTS thin film coil. Direct laser writing setup (Fig. 2) was used to fabricate a 26-turn proof of concept YBCO thin film coil. Figs. 3 and 4 show the thin film coil and the laser-cut lines and turn widths. Fig. 5 shows the critical current density versus temperature of the short bridge fabricated from a similar YBCO thin film. Fig. 6 shows the J_c versus temperature of the 26 turn one-sided YBCO thin film coil as seen in Figure 3. A current density of 7.8 x 10^4 A/cm^2 and 3.7 x 10^4 A/cm^2 at 4.2 K were achieved for a short bridge and the 26-turn YBCO coil, respectively. The difference is probably due to the inhomogeneities, as seen in Fig.1, in the thin film quality in the longer path length of the coil. These thin films were, by no means, state of the art YBCO thin films and yet the current densities are better or comparable to the best of the conventional HTS conductors.

Since the upper critical magnetic field of YBCO thin films is excellent, these magnets can operate as insert magnets at very high magnetic fields. They can be used in the very high-resolution NMR spectrometers. They can also be used as miniature coils producing sizable magnetic fields in a very small volume that can be very beneficial in microelectronics applications. As flat coils they can also be used for Micro Electronic Machines (MEM).

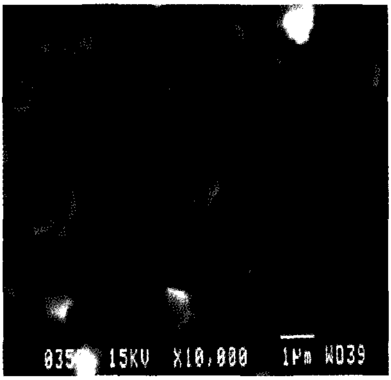

Figure 1. SEM micrograph of a typical YBCO thin film grown by in-house Pulsed Laser Deposition (PLD).

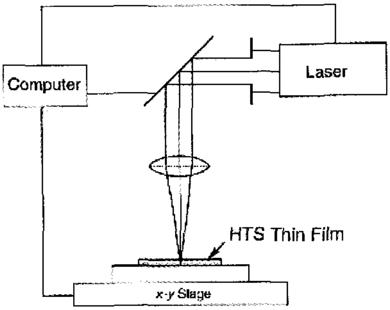

Figure 2. Schematic diagram of Direct Laser Patterning (DLP) set-up. It is fully automated.

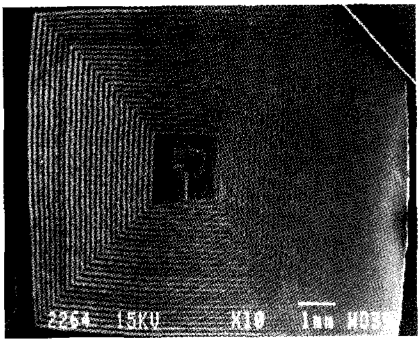

Figure 3. A square YBCO thin film coil fabricated at NHMFL. It is about 12 mm by 12 mm, and has 26 turns.

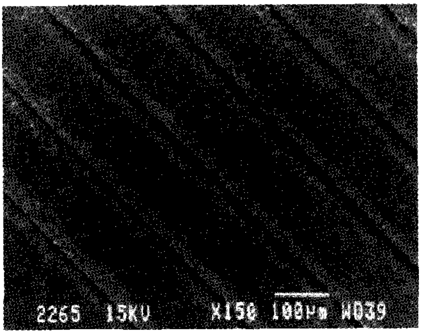

Figure 4. SEM micrograph of the laser cut width and turn width of the thin film coil as in Fig. 3.

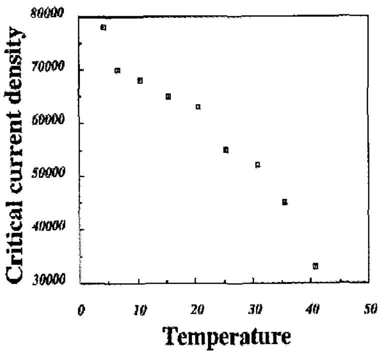

Figure 5. Critical current density (A/cm^2) versus temperature (K) curve for a typical short bridge fabricated from a similar YBCO film grown by PLD.

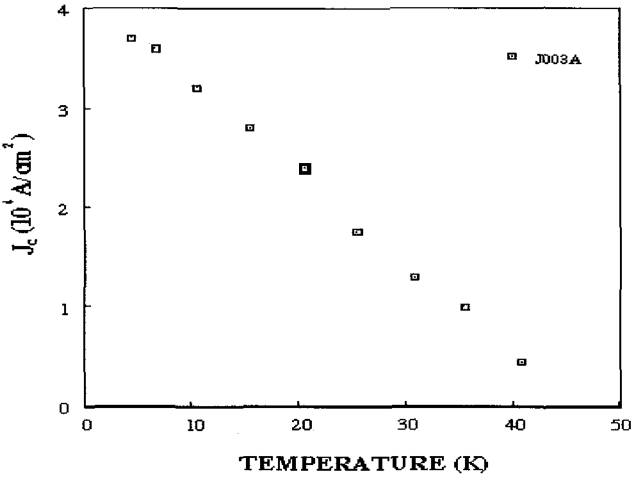

Figure 6. J_c versus temperature of the thin film coil as in Fig. 3.

4 Conclusions

We have fabricated a proof-of-concept thin film coil from our PLD YBCO thin films and tested it successfully. It is possible to produce 5 tesla induction at 4.2 K in the background fields of about 20 tesla using YBCO thin film technology. Small YBCO thin film flat coils can produce useful fields. These fields can be very advantageous for MEMs and other applications.

Acknowledgment

This work is based upon research conducted at the National High Magnetic Field Laboratory, which is supported by the State of Florida and the National Science Foundation, under Award No. DMR-9527035.

References

1. Kiyoshi, T., Inoue, K., Kosuge, M., Kitaguchi, H., Kumakura, H., Wada, H., Maeda, H., ICEC16/ ICMC Proceedings, Ed. by T. Haruyama, T. Mitsui, K Yamafuji, Elsevier Science (1997), pp. 1099-1102.
2. Weijers, H. W., Hazelton, D., Cowey, L., Hascicek, Y. S., Mutlu, I. H., Trociewitz, U. P., Van Sciver, S. W., *Advances in Cryogenics Eng.* **43**, (1998) p. 173.
3. Hascicek, Y. S., Kleinhammes, A., Testardi, L. R., *J. Materials Science Lett.* **11**, (1992) p. 1681.

PHYSICAL PROCESSES IN DYNAMIC MAGNETIC FIELDS TO 800 T

J. S. BROOKS, J. COTHERN
Physics Department & NHMFL, Florida State University, Tallahassee FL, USA

J. A. SIMMONS, M. J. HAFICH
Sandia National Laboratories, Albuquerque, NM, USA

W. LEWIS, S. GALLEGOS, D. DEVORE
Bechtel Nevada, Los Alamos, NM, USA

B. MARSHALL, M. GROVER, G. LEACH
Bechtel Nevada, STL, Santa Barbara, CA, USA

C. H. MIELKE, D. RICKEL, J. D. GOETTEE, D. CLARK, M. FOWLER, J. KING, L. TABAKA, J. DETWILER, E. C. CLARK
Los Alamos National Laboratory and NHMFL, Los Alamos, NM, USA

O. TATSENKO, V. PLATONOV, A. BYKOV
Institute of Experimental Physics, Nizhni Novgorod Region, Sarov, Russia

C. LANDEE, M. TURNBULL
Physics Department, Clark University, Worcester, MA, USA

The end of the Cold War has opened up new opportunities for university-based researchers to study basic condensed matter at the extremes of accessible magnetic fields. These fields, which can approach 1200 T, are produced on a microsecond time scale by explosively compressing the magnetic flux of an electromagnet. Here we describe several different types of experiments performed in such an environment on high T_c superconductors, linear chain magnets, and semiconductors. We argue that, although some results seem primitive, new and valuable information has been obtained for some systems in ultra-high magnetic fields. Therefore, these activities present a new frontier in materials science.

1 Introduction

A growing number of experimenters are attempting new measurements in explosively activated ultra-high magnetic fields [1]. Although these devices [2] are rarely available for experiments, there are many compelling reasons to make such attempts. Present interests include magneto-optics in semi-magnetic semiconductors [3], critical fields in high temperature superconductors, quantum limit effects in organic metals [4], and chemical bonds in special materials [5].

2 Methods

The physics motivating these studies is one of energy scale. When the magnetic energy, moment, or length is comparable with characteristic energies of the various systems of interest, one can expect new configurations of matter. For the systems above, these effects are expected in the range of 100 to 1000 T. When compared to a simple $S = 1/2$, $g = 2$ electron spin, 1000 T corresponds to 670 K, or 60 meV, or 14 THz, or 466 cm^{-1} or 21.5 μm (mid-infrared). For effects involving size, the corresponding magnetic length is $\sqrt{h/eB} = 2$ nm or 20 Å. Depending on the system studied, one can hope for anything from simple crossings in singlet and triplet energy levels to exotic electronic states in low-dimensional materials. Our own interests in magnetic flux compression based experiments have

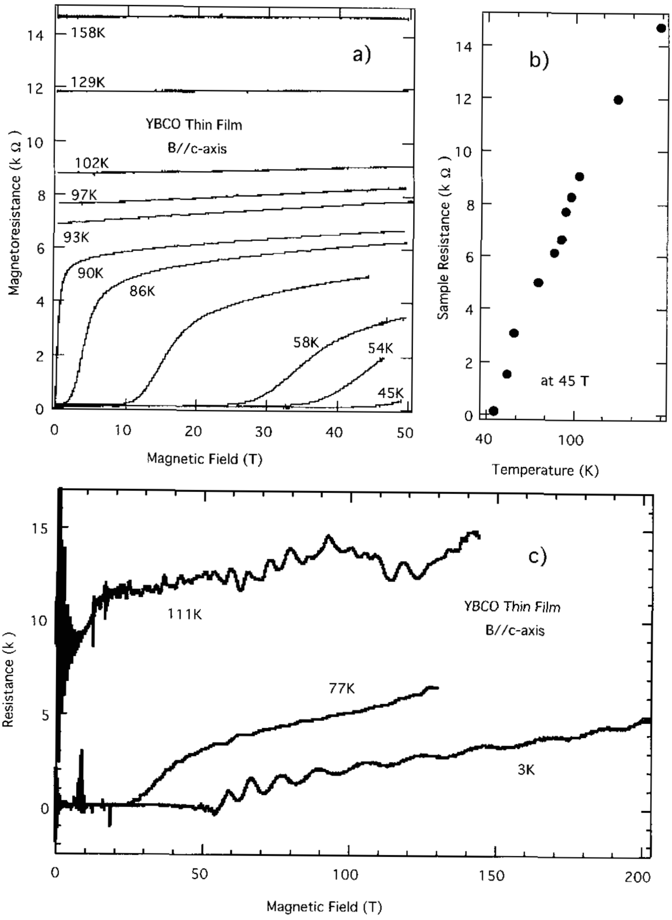

Figure 1. a) Magnetoresistance data for YBCO epitaxial thin film meander-line samples for different temperatures in pulsed magnetic fields. b) Normal-state resistance vs. temperature for YBCO from Fig. 1a. c) Magnetoresistance data for YBCO epitaxial thin film meander-line samples for different temperatures in flux compression fields.

centered on the temperature dependent critical field of high temperature superconductors ($YBa_2Cu_2O_7$ or "YBCO"), the breaking of gaps in spin-1 antiferromagnet chains, and low-dimensional conductors and semiconductor structures.

Our first studies [6,7,8] in this area involved the critical field of YBCO, which has a critical temperature over 90 K. By simple arguments, it should also have a critical field at low temperatures over 90 T. The critical field in YBCO should be very high, and we found it so. A comparison between measurements taken in non-destructive magnets with those in flux compression systems is shown in Fig. 1. Fig. 1a shows systematic transport results in a pulsed field of order 20 ms in duration for a thin, epitaxially grown YBCO film, with the field perpendicular to the conducting planes (B//c) both above and below the superconducting transition temperature. The special experiment configuration involves two meander line structures, one YBCO and one Nb placed back-to-back and connected in series. Hence, the induced emf that always accompanies dynamic field experiments is all but eliminated in the measurements. This applies to flux compression measurements made with the identical configuration, as shown in Fig. 1c. Here, the induced emf factors increase by about 1000, and proper subtraction of the emf signal is necessary to present the data. When the sample is superconducting below a finite critical field, it is straight forward to determine the emf contribution as seen for 3 K and 77 K. Otherwise, estimation is needed as in the normal state at 111 K. The data to 130 T is from a single section "strip line" generator, and the data to 200 T is from a double "bow-tie" generator [9]. The oscillations on this last curve are due to acoustic oscillations in one of the explosive elements. Although the data is noisy, the trends in the critical field with temperature, when compared with Fig. 1a, are clearly observable. Measurements for the field parallel to the conducting planes have also been addressed in the accompanying paper [10] and in previous microwave [11] and transport studies [12].

To assess advances in critical field measurements for YBCO thin films, we compiled the results of Fig. 1 with those involving AC or DC transport methods determining the critical field signature in YBCO for both field perpendicular (Fig. 2a) and in-plane (Fig. 2b). We present these data with the caveat that different researchers use varying criteria for the critical field - dissipative onset, inflection point, and full normal state resistance. As the field is so high, the data taken as a whole are starting to give us a consistent picture, uncertainties notwithstanding. We conclude from Fig. 2a and b that the normal state resistivity in YBCO at low temperatures is recovered at around 100 T for B//c-axis and about two or three times that for B//ab planes. Furthermore, the shape of the critical field curve begins to emerge in the low temperature limit. For B//c-axis, a scaling analysis [13] of the data of Fig. 1a along the lines of the Ullah-Dorsey [14] and Welp et al. [15] treatments yields an expression for the critical field which, applied over the entire temperature range, reasonably describes the results as well as those in the flux compression experiments. An application of the Maki [16]-Werthammer, Helfand, Hohenberg [17] (MWHH) treatment of the reduced critical field h* vs. reduced temperature t gives a reasonable fit to the B//c-axis data for dHc/dT = -1.9 T/K [18]. The values of spin independent (α) and spin dependent (λ_{so}) parameters are shown in Fig. 2c. This treatment is for a type II superconductor in the "dirty limit". For the B//ab-plane results, the picture is less clear as there are fewer data. Again, by applying the MWHH formalism with dHc/dT = -0.5 T/K [18] for this orientation, a reasonable correspondence is seen, although the parameter sizes needed for the fit may be at the limits of physical meaning. Thus, the measured, low temperature critical field in this direction may be too small to comfortably fit the MWHH convention. A possible explanation is that the Pauli limit is reached at around 250 T, as suggested by Dzurack et al. [10].

A second example of progress is in the magnetization of spin-1 Haldane gap systems [19]. Here, a small, highly compensated astatically wound pick-up coil detects the susceptibility of NENP (nickel bis(ethylenediamine)nitrite perchlorate), using the "strip-line" generator. The data, shown in Fig. 3, is the integrated signal (magnetization) with background emf ("db/dt") term subtracted, shown for two different samples. The expected

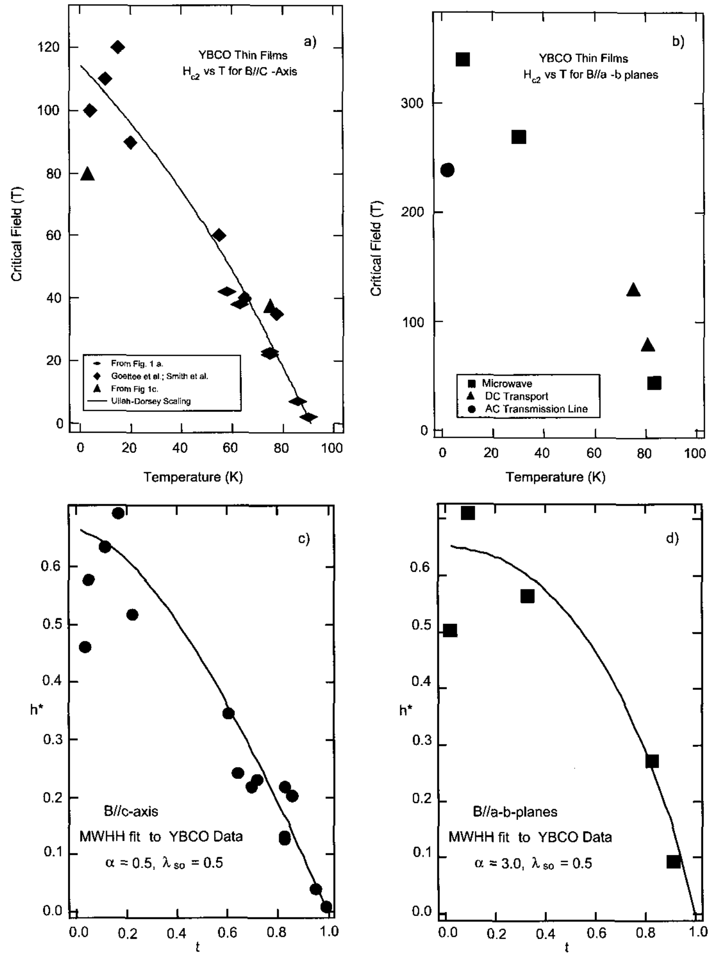

Figure 2. Synopsis of experiments in pulsed and flux compression magnetic fields. a) Compendium of pulsed field and flux compression field studies of YBCO for B//c-axis. Pulsed field results (from Fig. 1a) are based on inflection points in the R vs. B curves and the solid line is a fit of the critical field vs. temperature, which is a result of the scaling analysis. Diamonds are from Refs. [6, 7, 8, 25] and the triangles are from Fig. 1c. b) Results of flux compression studies of YBCO for B//a-b planes. Microwave results are from Ref. [11], DC transport is from Ref. [12], and the AC transport is from Ref. [10]. c) and d) Application of the MWHH formalism to the reduced field h* and reduced temperature t* to the in-plane and perpendicular critical field data.

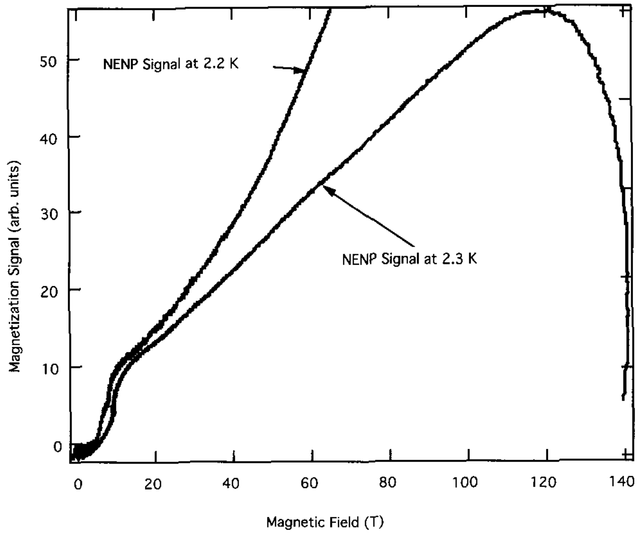

Figure 3. Magnetization signals from two NENP spin-1 Haldane gap materials. The gap is broken about 10 T. For the lower temperature trace, there was a premature termination of the signal due to technical problems. For the higher temperature trace the field is actually observed to begin to decrease before the shock wave terminates the experiment.

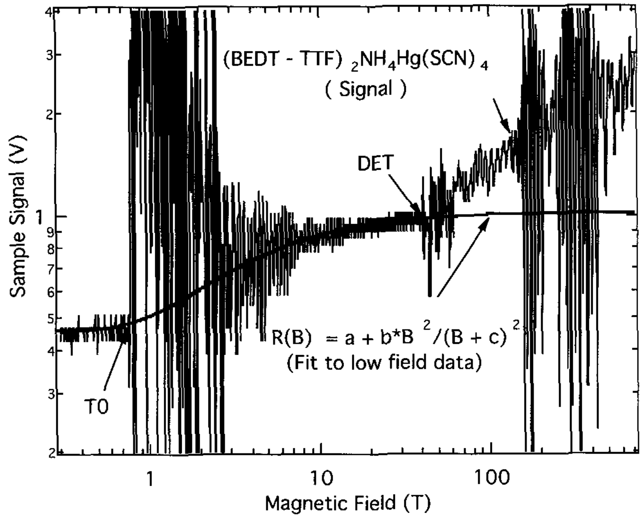

Figure 4. Raw magnetoresistance signal from a layered, organic metal at 2 K in the Dirac I - MC1 generator. T0 refers to the onset of the seed field and DET refers to the onset of the (explosive) flux compression. The solid line is a fit to the low field magnetoresistance taken from pulse field (non-destructive) data.

destruction of the spin-gap is seen at around 10 T, followed by an increase in magnetization, which should be linear as the susceptibility is now constant. In the first case, the signal saturated due to technical problems. In the second case, the sample survived even after peak field as seen in the reversal of the field direction. The data are very clean, only the background term seems to vary at the highest fields (and therefore the shortest time scales). Through these studies, we know that although the coils are compensated using radio frequencies in the lab, or by short pulse sources, the compensation is a function of the flux compression process, and the balance condition changes. This factor causes the signal to stray non-linearly as the field and/or the dB/dt term increases near the end of the process. Nevertheless, magnetization measurements are very practical and give good signal to noise in flux compression studies. The ability to use photolithography on a cylindrical surface (to make the compensated coils) might greatly enhance the exactness and stability of the balance condition.

The third example, where only primitive results have been obtained, involves organic conductors. This experiment was performed in the Dirac I series using a DC method in transmission line configuration [10] at low temperatures. When used in pulsed fields, this configuration gave excellent results [4,20] thus becoming a standard for such studies. However, in the environment of the MC1 generators in this series, some problems arose unrelated to the behavior in the high field limit. The result (raw signal) is shown in Fig. 4 for the layered organic metal ($(\text{BEDT-TTF})2\text{NH}_4\text{Hg(SCN)}_4$), where the resistance was measured in the least conducting direction. The sample resistance was about 500 ohms at zero field. From previous pulsed field measurements [21] the signal was expected to rise to about 1000 ohms at 50 T (solid line is a fit to the low field data), and to exhibit oscillations in the magnetoresistance (the Shubnikov de Haas effect). However, in flux compression measurements, there is an enormous induced voltage spike at zero field when the seed field is introduced (T0 in the graph when the capacitor bank is fired). This spike destroys many samples at this instant. The sample in Fig. 4 survived the surge and its magnetoresistance rose to the expected value as the seed field saturated at around 15 T. When the flux compression is initiated (DET in the graph where the explosion is initiated) there is further noise and the sample signal appears to increase again. In this range the field is increasing very quickly (600 T in 10 μs), the sample may be heating, and its average resistance, which increases with temperature, is observed to rise. Nevertheless, this average signal never exceeded the voltage compliance of the current source. We expect that the sample survived with an observable resistance until it was destroyed at peak field. This is a modest claim, but for 800 T this was state-of-the-art for this type of measurement on an organic metal.

In the Dirac II series, two approaches were taken to push accessibility for experimentation in very high magnetic fields. One team improved on the transmission line methods, on thermometry, and on sample mounting methods as described in the accompanying article [10]. Our team took a very different, simple approach to learn anything - no matter how primitive - but having good signal-to-noise. We were inspired by Faraday rotation measurements that are routinely made to aid in determining magnetic field. Fig. 5a is a schematic of a tiny Faraday device through which polarized light passes, is reflected and analyzed, all with optical fiber connections. For every 68 tesla the polarization rotates a total of 360 degrees, and the signal is insensitive to the type of electrical disturbances shown in Fig. 4. Our simple experimental setup is shown in Fig. 5b. We reflect light of 810 nm (1.52 eV) off of a small sample and collect it with a very fast 1.2 ns resolution detector filtered at 820 nm. Both Faraday and reflectivity devices sit below the transport cryostat in a liquid nitrogen flow, and the connecting optical fibers lead to a bunker 30 m away.

We were fortunate to have four shots in the Dirac II series. We observed two samples of a GaAs/AlGaAs multiple quantum well structure, one of a NbSe_2 single crystal (another low dimensional metal), and one control under no optical excitation, only “dark current”. Our results, including one of the Faraday traces, are shown in Fig. 5. We first address the results of the optical experiments.

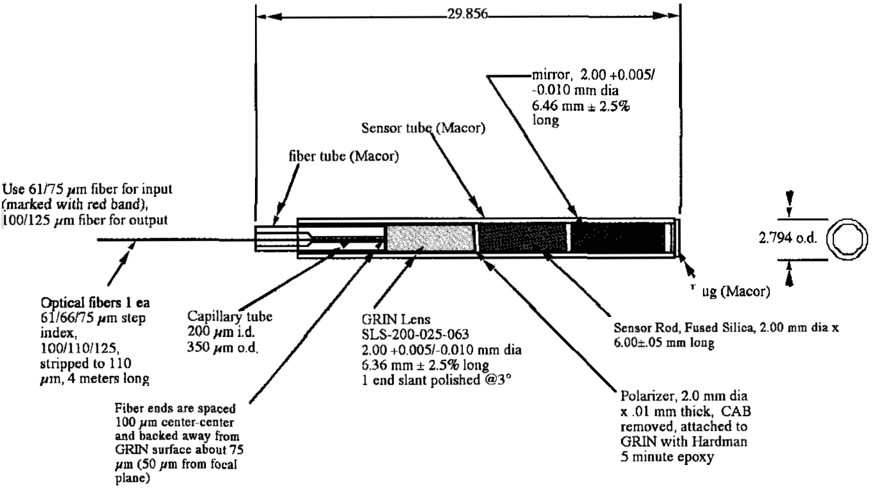

Figure 5a. Schematic of Faraday rotation device.

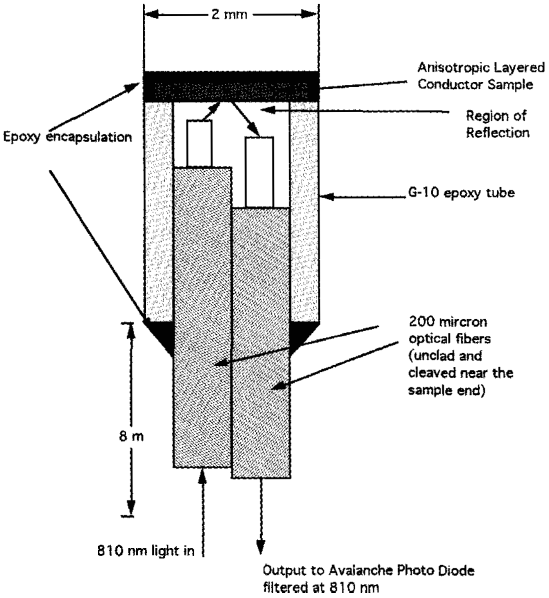

Figure 5b. Schematic of reflectivity device.

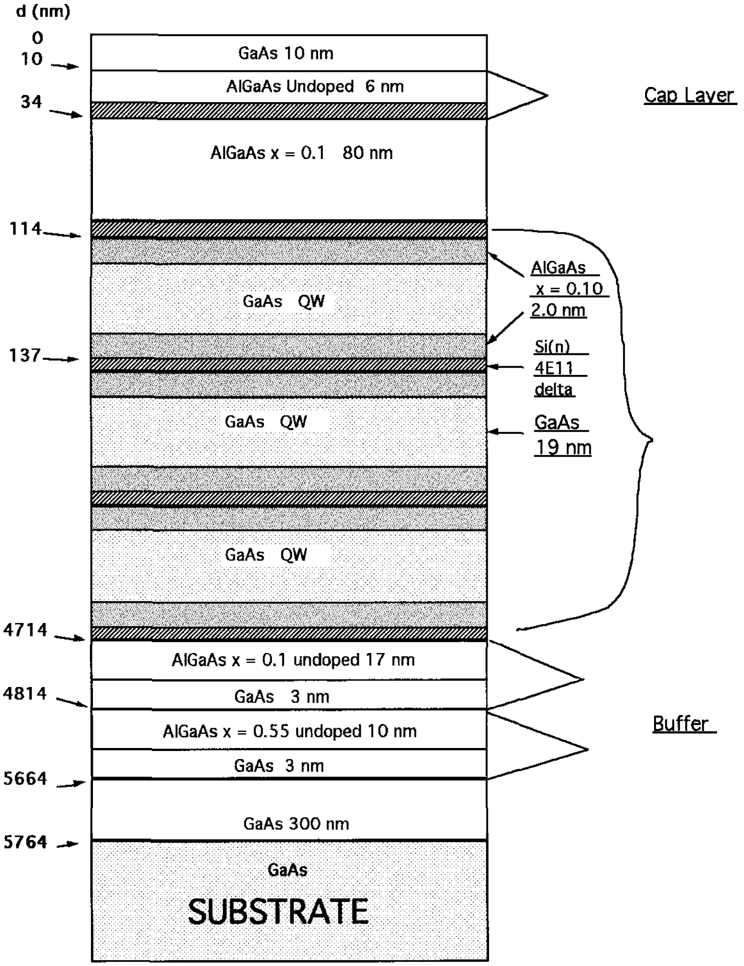

Figure 5c. Growth profile of GaAs/GaAlAs 200 layer quantum well. Light of 810 nm is incident on the top surface in the reflectivity experiments.

Above about 30 T we observe oscillations in reflectivity during both GaAs/GaAlAs experiments. The basic structure (Fig. 5c) of these samples was an alteration of 19 nm GaAs layers with 2.2 nm of Si doped Al$_x$Ga$_{1-x}$As with x = 0.18. The effective bandwidth of the layers is about 0.2 meV, and the electron carrier density is of order 4x10^{-11}/cm^2. The low temperature band gap for GaAs is 1.42 eV, and for Al$_x$Ga$_{1-x}$As where x = 0.1 it is greater than 1.5 eV [22]. Light at 810 nm (1.52 eV) is incident on the top surface, and the depth of the layered region is about 6.4 wavelengths to the substrate. There is the possibility that interference effects may influence the reflectance, particularly if the indices of refraction for the different components have magnetic field dependent effects, although no single layer is thicker than 3/8 of the wavelength. We do not think that the two-dimensional electron gas influenced the signal. The carrier concentration was very low, and the quantum limit is reached by 4 T in these samples. Extreme quantum limit (low fractional) states and/or metal-to-insulator behavior are possible due to the high fields reached, but the temperature is quite high for such processes to occur. We expect that since the incident light is on the very sensitive absorption edge of the GaAs and GaAlAs materials [22], even small variations in the band gap or other optical properties of the material can have large effects on the reflectivity. Furthermore, the optical properties of multiple quantum well structures are very rich: the AlGaAs "pulls up" the adsorption edge of the GaAs system ($\Delta E/\Delta x \approx$ 10 meV/%Al) and the layered structure introduces exciton resonances at and above the absorption edge with a period of about 0.1 eV [23]. Hence, any modulation of this complex absorption edge due to the magnetic field would affect the reflectivity. An electric field will modify the exciton features, and the magnetic field directly affects (increases) the binding energy of the excitons, which could shift the edge profile [23]. There is a position difference in the A and B features in the data for the two samples. This may be partly due to uncertainties in the magnetic field as derived from the B-dot coils and Faraday rotation. Strain may also be a factor due to the epoxy caps which surround the samples, and which may be different in the two shots. Clearly, this is a very rich area that deserves a more systematic investigation.

Next, we consider the 2H-NbSe$_2$ signal. This material has a charge density wave transition below 33 K and becomes a superconductor [24] below 7.2 K. Our measurements at 75 K are in the material's metallic state. The observed signal in Fig. 6 is intriguing in that the reflectance has structure (the frequency of the oscillatory structure is approximately 250 T) and, above 200 T, drops by about 50%. Quantum oscillations of 150 T are commonly observed in this material, but the Fermi surface is complicated and much larger frequencies (over 8000 T) are predicted. Therefore, the absolute quantum limit may not be reached by 800 T. Sample heating most likely causes the signal drop at high fields. Based on estimates for joule heating by a rapidly changing field, the 1.5 mm diameter sample possibly melted or vaporized above 200 T. A GaAs\GaAlAs sample with no excitation illumination was monitored in the control trace. The signal represented only the dark current up to the point of destruction, where the blast light was detected. We believe that there was no additional light produced by field changes, alone, in the sample configuration. All trials produced a sudden increase in light intensity near peak field due to the blast (or sun) light. This pulse width ranged from 1.6 μs to 75 ns in different trials. Hence, the final stage of these experiments, where the field is increasing some 100 T/μs or more, can end at various stages before or after the field has peaked.

3 Summary

There are many excellent experiments, which have worked very well for years, performed in the hostile environments described. These include streak camera spectroscopy, high-speed photography and x-ray structural studies, faraday rotation, and even the single turn loop whose signal is integrated to give us the magnetic field.

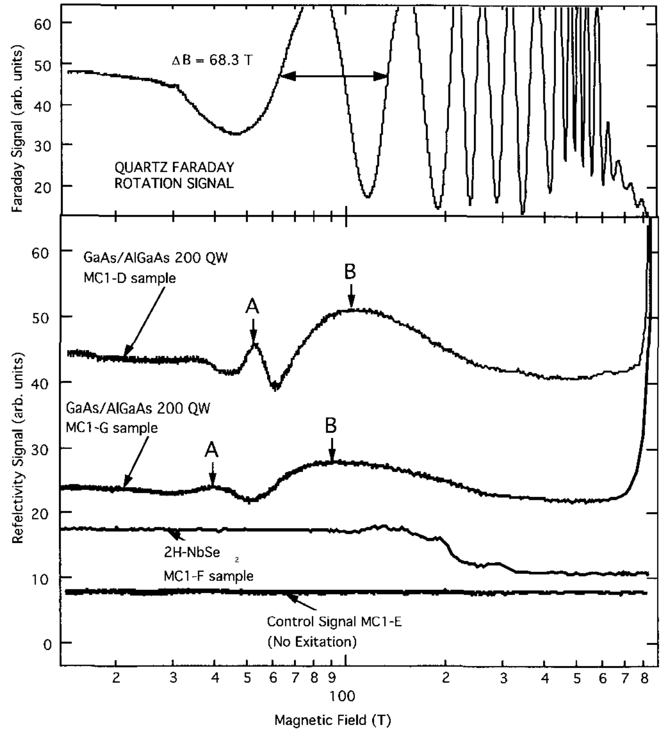

Figure 6. Optical data from Dirac II - MC1 experiments. Letters MC1-D, -E, -F, and -G refer to different MC1 experiments. All data had a 75 K starting temperature. Upper panel is signal from the Faraday rotation device. Lower panel is raw signals as received from GaAs/GaAlAs structures, $NbSe_2$ crystal, and control experiment. Labels A and B represent features in the data that were similar in runs D and G.

Albeit unsystematic, the critical field in a high temperature superconductor has been determined for both in-plane and perpendicular directions, for a variety of temperatures, and by at least three different groups above 100 T using transport methods on thin films. Although many caveats about flux motion and criteria for H_{c2} remain, the critical field of YBCO at low temperatures is very high and anisotropic. Furthermore, information about microscopic mechanisms controlling the critical field at low temperature and a comparison with theoretical considerations is emerging. This was unknown and unmeasured at low temperature before 1992.

The quest for reliable experimental methods in the flux compression environment has produced advances in cryogenics, and in AC and DC instrumentation for transport in less aggressive situations like pulsed field and single turn coil configurations. Experiments to date show that reasonable science in fields on the order of 1000 T can be done optically or by magnetization, by AC or DC transport, and that future studies on a growing variety of materials are within reach. The systematics and reproducibility required by the scientific method are emerging in this area. The time scale for the opportunity for a measurement is much longer than in other branches of science.

The bias of the first author is that the optical studies give superior signal to noise. Unfortunately, a direct application of light at 1 eV to study the beautiful transport and quantum limit behavior of the organic material (on the meV scale of energy) somewhere in the noise of Fig. 4 is a complete mismatch. There are two ways to achieve the physics proposed in the introduction while retaining the advantage of optical methods. One is to find the right system, as the LSU group is doing with Re_2Cl_8, to look for field-induced changes in the metal-metal quadrapole bond [5]. The other is to process semiconductor devices where the physics matches (in our case) the nature of low dimensional metals, but the energy scale is that of light which can propagate efficiently in optical fibers.

Acknowledgment

Funding: NSF-DMR-95-10427 (JSB); IHRP 500/5011 (JSB), DE-AC04-94AL85000 (JS-MH), NSF-DMR-95-27035 (NHMFL).

References

1. Solem, J. C. Sheppard, M. G., *Int. J. Quant. Chem.* **64** (1997) p. 619.
2. The explosive magnetic flux compression generators used by our group are of the 120 T or 220 T "strip line" types developed at Los Alamos, NM, USA, or of the 800 T to 1200 T "MC1" cylindrical type developed at Sarov (formerly Arzamas 16) Russia. The latter have been used in the Dirac I and II series. These devices, previously the domain of the defense industry in both countries, perform with an unusual degree of precision and reliability in terms of timing and magnetic fields obtained. The shock wave arrives later than the associated electromagnetic process, so data is obtained before the samples are destroyed.
3. Pavlovskii, A., et al., *JETP Lett.* **31** (1980) p. 622.
4. Brooks, J. S., et al., Los Alamos Preprint Report LA-UR 96-3472 and Proc. of Megagauss VII, Sarov Russia, 1996, to be published.
5. Maverick, A. S., Butler, L. G., *Int. J. Quant. Chem.* **64** (1997) p. 607.
6. Smith, J. L., et al., *Journal of Superconductivity* **7** (1994) p. 269.
7. Smith, J. L., et al., *J. Low Temp. Phys.* **95** (1994) p. 75.
8. Goettee, J. D., et al., *Physica B* **194-196** (1994) p. 1805.
9. Fowler, C. M., et al., *Physica B* **201** (1994) p. 33.
10. Dzurack, A. S., et al., *to be published.* (1998).
11. Bykov, A. I., et al., *Physica B* **211** (1995) p. 248.
12. Goettee, J. D., et al., *Preprint LA-UR-92-3100* (1992).
13. Brooks, J. S., Goettee, J. D., Valfells, S., *Unpublished* (1993).
14. Ullah, S., Dorsey, A. T., *Phys. Rev. B* **44** (1991) p. 262.
15. Welp, U., et al., *Phys. Rev. Lett.* **67** (1991) p. 3180.
16. Maki, K., *Physics* **1** (1964) p. 127.
17. Werthamer, N. R., Helfand, E., Hohenberg, P. C., *Phys. Rev.* **147** (1966) p. 295.
18. Welp, U., Kwok, W. K., Crabtree, G. W., Vandervoort, K. G., Liu, J. Z., *Phys. Rev. Lett.* **62** (1989) p. 1908.
19. Landee, C., et al., *Phys. Rev. B* **56** (1997) p. 147.
20. Kane, B. E., et al., *Rev. Sci. Instrum.* (1997) p. 1997.
21. Sandhu, P. S. et al., *Surf. Science* **361-362** (1996) p. 913.

22. Sze, S. M., Physics of Semiconductor Devices (Wiley, New York, second ed. 1981).
23. Kelly, M. J., Low-Dimensional Semiconductors (Clarendon Press, Oxford, 1996).
24. Corcoran, R., et al., *J. Phys. Condensed Matter* **6** (1994) p. 4479.
25. Stokka, S., Fossheim, K., *J. Phys. E: Sci. Instrum.* **15** (1982) p. 123.

MAGNETIC SYSTEMS IN MEGAGAUSS MAGNETIC FIELDS; RESULTS OF DIRAC AND KAPITSA EXPERIMENTS

O. M. TATSENKO, V. D. SELEMIR
RFNC-VNIIEF, SAROV, RUSSIA

The paper discusses the experimental series of Dirac-II and Kapitsa to explore material properties in ultra-high magnetic fields. A set of Dirac experiments was performed in June 1996 at Los Alamos National Laboratory. Scientists from six countries and eight Universities tested more than 60 samples in five explosive experiments using magnetocumulative generators of ultra-high magnetic fields. Test measurements were made using a 50 Tesla magnet of the NHMFL user facility ot LANL. The first scientific and practical workshop, Kapitsa, was performed in 1997 at the Russian Nuclear Federal Center (Sarov). More than 15 samples were tested during three shots. The Kapitsa series is planned to be performed annually. In the Kapitsa and Dirac experiments we explored magnetization of high-spin clusters $Mn_{12}Ac$, Mn_6, Fe_8, fulleren C_{60}, metamagnetic transitions in $ScCo_2$, valence transitions in $EuNi_2(Si_{1-x}Ge_x)_2$ and the transition semiconductor-metal in FeSi.

1 Introduction

Joint experiments to investigate material properties in megagauss fields began in 1993 with two teams, Los Alamos National Laboratory (LANL) and the Russian Federal Nuclear Center, All Russian Scientific Research Institute of Experimental Physics (VRFNC-VNIIEF). The results of this team collaboration are as follows:

- LANL obtained a magnetic field of 950 T and 1150 T in a 10 cm^3 volume.
- LANL measured the upper critical field HSTC at T = 4.2 – Hc2 = 340 T ● 40 T.
- The de Haas-van Alphen effect was measured at LANL in magnetic fields up to 200 T, and at VNIIEF in magnetic fields up to 500T.

This was awarded the "best work for the year" at the Russian Academy of Sciences. The collaboration was extended to multiple nations. A joint series of experiments was held at LANL (the Dirac experiments) and at VNIIEF (the Kapitsa series). Countries that participated in the Dirac series were: the USA, Russia, Japan, Germany, Brazil, Australia and Belgium. The countries that participated in the Kapitza series were: Russia, Germany and France. Samples were presented from Russia, Japan, Italy, France and Germany.

2 Discussion

In 1993, encouraged by M. Fauler and A. Pavlovskii for the first time in the world, we exploded at the Los Alamos firing point a device created at the Russian Federal Nuclear Center. This was an experiment using a 10 MG MC-1 generator [1]. The first two shots proved the reliability of the MC-1 generator operation. Using HE of various power, we measured magnetic fields of 1200 and 1300 T at a compression diameter of about 3 mm. The following three shots measured the upper critical field of high-temperature superconductors near zero temperature. The results of this activity proved the efficiency of international collaboration when performing unique experiments such as the study of megagauss magnetic fields.

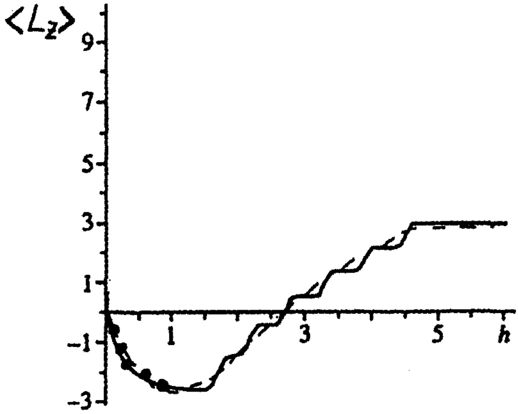

Figure 1. Orbital magnetic moment L_z dependence on magnetic field value *h*, where $h = \frac{B}{B\ddot{i}}$, $B\ddot{i} = 800$ T. Dashed curve - theoretical data T = 300 K. Solid curve - theoretical data at T = 4.2 K. The dots are experimental data at T = 2.3 K.

In 1996 four countries, the USA, Russia, Australia and Japan, took part in the Dirac series of experiments. We performed three shots using a 10 MG MC-1 generator, three shots using a 2 MG strip generator and some experiments using a pulsed 50 T magnet. Thus, the entire range of magnetic fields then available in the world was used for our studies. In this series of experiments we explored the wide spectrum of issues in the field of solid state physics, including magnetic transitions, quantum limit in 2-D organic metals and in 3-D electron gas and in half-metals (Bismuth films). A special method for measuring conductivity was developed based on strip microwave lines. For the first time in the world we performed measurements in the fields reaching 850 T at 2.3 K.

In this series we measured the Faraday effect in compounds with ions Eu^{3+} in fields to up to 700 T at 0.85 μm wavelength. Faraday rotation dependence for Eu^{3+}ions is given in Fig. 1. Faraday effect in the optical wavelength range is described by the equation $F = C \langle L_z \rangle + V_D H$, where $\langle L_z \rangle$ is the full orbital moment [2]. The first term is the paramagnetic contribution; the second term is the diamagnetic contribution. In fields up to 10^3 T, the diamagnetic term V_D does not depend on the magnetic field. Thus, linear dependence results from compensation of orbital and spin magnetic moments. A little increase of Faraday rotation is observed in fields higher than 500 T. This agrees with the predicted quantum jump and confirms a quantum character of jumps in rare-earth ions implemented in ultra-high magnetic fields [2]. Thus, we recorded the initial stage of quantum reorientation process of spin and orbital moments in Eu^{3+} ions from a ferrimagnetic phase to a ferromagnetic phase that appears in 800 T fields.

Recently, much attention has been paid to the study of semi-magnetic semiconductors having magnetic ions as impurity atoms. An example of these compounds may be the wide-gap semi-conductor $Cd_{1-x}Mn_xTe$ in which manganese replaces a cation in a lattice of crystal CdTe and is in a state of $Mn^{2+}$with $3d^5$ configuration. Presence of Mn results in interesting electric and optical phenomena appearing due to the spin-spin exchange interaction between s(p) zone electrons and localized moments of magnetic d-ions.

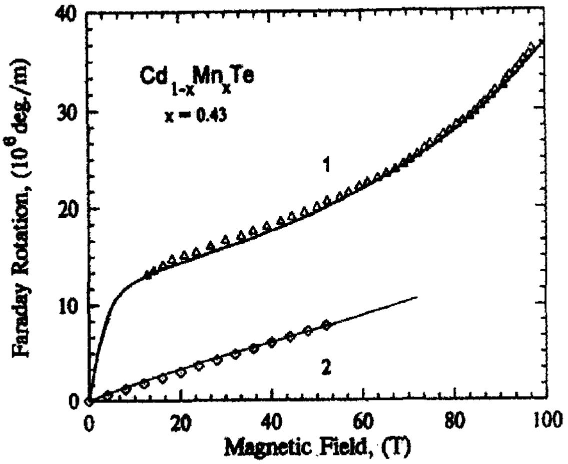

Figure 2. Faraday rotation dependence on magnetic fields. 1. Δ is experimental data at T = 4.2 K. Solid curve is theoretical data. 2. ◊ is experimental data at T = 300 K. Solid curve is theoretical data.

Faraday rotation was measured using samples of $Cd_{1-x}Mn_xTe$ with manganese concentration x = 0.43 and 0.1. We measured a surprising increase of polarization plane rotation angle in fields higher than 60 T. Based on theory, Faraday rotation dependence must have a maximum, and if an exchange term and Zeeman term are equal in the field ≈100 T, compensation of these contributions has to be observed. However, compensation of Faraday rotation is not only absent but it increases in fields > 50 T. This can be explained by dependence of the s(p)-d exchange on the magnetic field.

In 1997, Los Alamos performed the second series of Dirac experiments. Participants from seven countries came and measured about 60 samples. The results of the experiments were reported at the RHMF conference in Sidney.

In 1997, we performed a similar set of experiments at RFNC dedicated to the memory of A. Pavlovskii, who contributed much to the study of ultra-high magnetic fields. In four explosive experiments we studied magnetic phase transitions in molecular non-clusters $Mn_{12}Ac$, Mn_6 Fe_8, the transition semiconductor-metal in FeSi, the magneto-induced valence transition in $EuNi_2(Si_{1-x}Ge_x)_2$. Dr. Ortenberg measured the quantum limit in HgSe:Fe. The results of these experiments will be reported at this conference.

In the Kapitsa experiment, a 10 MG MC-1 generator created the magnetic fields. A helium cryostat provided sample cooling to 4.2 K. Inductive probes measured the magnetic field and magnetization values. Conductivity was measured by measuring the peak currents induced by a variable magnetic field and by a contact less inductance method. The induced peak currents contribute the magnetic moment $m_{ind} \sim \sigma(B)dB(t)/dt$ to the sample. Compensation coils measure the magnetic moment. If a sample does not have magnetic phase transitions, the changes in magnetization reflect the specifics of the magnetic field dependence of the sample conductivity. This method was used to measure the crossover field for various Landau levels with ion level Fe^{2+} in a semi-magnetic semiconductor HgSe:Fe. In low fields the probe sensitivity is low, the crossover structure is not measured. The expected crossover field of 0-Landau level occurs in the field at about 280 T. Within this range we observe a specific feature in the experiment that can be related to the last crossover of the 0-level. Sensitivity of this method is not high. In the future, we are planning to perform measurements using a contact-less high-frequency method.

The exploration of magnetic phase transitions is a tradition for us. It covers such classical materials as ferrimagnetics and antiferromagnetics and new materials such as nanostructural magnetics and high-spin metalo-organic clusters. In the Kapitsa series we measured metamagnetic transitions in $ScCo_2$, $EuNi_2(Si_{1-x}Ge_x)_2$, compounds and orientation transitions in high-spin nanoclusters Mn_6-radical and Fe_8. Earlier in Dirac 1 and Dirac 2 we studied magnetization of $Mn_{12}Ac$ nanoclusters, crossover of electron levels in ions Eu^{3+} and Sm^{3+}, magnetization of semimagnetic semiconductors $Cd_xMn_{1-x}Te$ and a spin-flip transition in MnF_2.

Metamagnetic transitions refer to the transitions of the first class and are easily measured by inductive probes. The signal induced in compensation coils is determined as

$$V(H) = dB/dt - K\ dH/dt = dM/dt + K dH/dt$$

where k is the decompensation coefficient. Since dH/dt is the field monotonous function, we can determine the value of a metamagnetic transition by the signal maximum $V(H)$. Earlier, this method was used to measure intermetallic rare-earth compounds Rco_2 [3]. In compounds the $ScCo_2$ d-subsystem is magnetostable; its main state is paramagnetic. Imposing an external magnetic field $H \sim 100$ T orders the orientation of magnetic moments of d-electrons and results in the appearance of a new ferromagnetic state of this subsystem. The principle possibility of these transitions in gap magnetics was predicted for the first time in [4]. This possibility is associated with some specifics of d-electron state density dependence on the energy close to Fermi level. In this work we measured metamagnetic transition in compounds $ScCo_2$ in a 130 T field at 4.2 K.

In a compound $EuNi_2(Si_{1-x}Ge_x)_2$ the state of valence instability appears between $Eu^{2+}(^4f_7)$ and $Eu^{3+}(^4f_6)$ configurations. The basic compound $EuNi_2Ge_2$ is antiferrmagnetic with a stable divalent Europium, whereas Europium in $EuNi_2Si_2$ is trivalent. The dependence of Eu-ion valence on the magnetic field results from a large difference in their magnetic moments. Metamagnetic transition in these compounds takes place in fields of ~100 T and depends on the Ge concentration. Magneto-induced metamagnetic transition is discovered in compounds with $x = 0.79 - 0.82$. We measured metamagnetic transition for x up to 0.5. The maximum of magnetization decreases as divalent Eu concentration decreases and moves into the region of high magnetic fields. The dependence of the metamagnetic transition field on x is non-linear.

Magnetic materials of mesoscopic sizes manifest new and very interesting properties, such as gigantic magnetostriction, magnetic resistance, magnetocaloric effect, bistability presence in a cluster scale, and macroscopic quantum tunneling of magnetization. In this respect molecular magnetic clusters including ions of transient metals are of great interest. These clusters can be considered as an ideal model of a nanodimensional single-domain particle. Typical field voltage values of exchange interaction in clusters are about 100 T, so the magnetization process of these clusters can be studied only in ultra-high magnetic fields. In the Kapitsa experiments we measured Mn_6 and Fe_8 clusters.

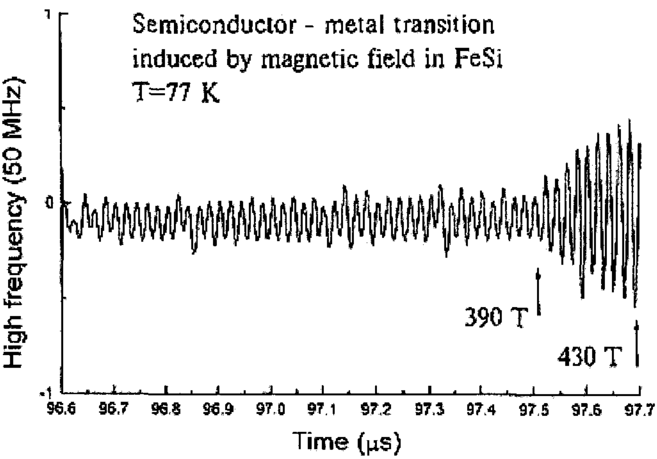

Figure 3. Semiconductor – metal transition induced by magnetic field in FeSi at T = 77 K.

For the first time we observed a fluid semiconductor to metal transition affected by the magnetic field. This compound is interesting because of its unusual spectroscopic, thermodynamic and magnetic properties. Some theoretical models were used to explain anomalies observed. The models take into consideration high electron correlations in narrow bands formed by iron d-electrons. Though effective electron masses obtained from band calculations are large, nevertheless they are significantly lower than experimental values, which is the evidence for mass renormalization due to inter-electron interactions. Recently a number of theoretical papers predicted metamagnetic transition in FeSi when the magnetic induction value was about 200 T, followed by a magnetic moment jump of about one boron magneton (μ_B). During the Kapitsa experiments we studied magnetic susceptibility and conductivity of single crystal EeSi in the ultra-high magnetic field. Fig. 3 shows a dependence of high frequency reflection signal at 77 K. At 77 K a fluid transition of semiconductor to metal was observed, and the FeSi conductivity increased in a field of 450 T approximately by two orders as compared to the zero field. At 4.2 K a magnetization jump was observed in a field of 350 ± 40 T. These results are the evidence for the presence of a jump-type transition singlet semiconductor-ferromagnetic metal in FeSi, which was predicted in the literature.

3 Summary

Measuring magnetic properties of materials in ultra-high magnetic fields is a very promising tool for molecular magnetic analysis. Some benefits are:

- Ultra-high magnetic fields allow full information about magnetization properties of many physically important systems to be obtained, such as metamagnetics, f-d magnetics with heavy rare earth, atomic and nano-scale magnetic clusters.
- Atomic and nano-scale clusters evidently show essential quantum behavior at the magnetization process in contrast to majority macroscopic materials.
- Jump anomalies in magnetic and magneto-optical effects, stipulated by field

induced phase transitions, open new possibilities for direct measurements of constants of exchange and spin-orbital interactions in solid states, clusters, high-spin molecules and ions.

Taking into account the specific significance of the investigations into magnetic nanocluster properties, we should mention that:

- Phase transitions, saving ferromagnetic properties in Mn12Ac compounds, are realized in fields between 180 - 750 T.
- The magnetization process in such clusters shows evident quantum nature.
- Constants values of exchange interaction for these compounds, usually used in the literature, are strongly overestimated.

References

1. Pavlovskii, A. I., Kolokolchikov, N. P., Tatsenko, O. M., Megagauss Physics and Techniques, (Ed. by P. Turchi, N.Y., Plenum Press. 1980).
2. Tatsenko, O. M., et al., *Physica B*, **246-247**, (1988) pp. 315-318.
3. Dubenko, I. S., et al., *Pis'ma Zh. Eksp. Teor. Fiz.* **64**, No.3, pp. 188-192.
4. Wohlfarth, E. P., Rhodes, P., *Phil. Mag.*, **7** (1962) p. 1817.

OVERVIEW OF THE 1997 DIRAC HIGH-MAGNETIC-FIELD-EXPERIMENT SERIES AT LOS ALAMOS

D. A. CLARK, L. J. CAMPBELL, K. C. FORMAN, C. M. FOWLER,
J. D. GOETTEE, C. H. MIELKE, D. G. RICKEL, AND B. R. MARSHALL*
Los Alamos National Laboratory, Los Alamos, NM, USA
**Bechtel Nevada Special Technologies Laboratory,*
Santa Barbara, CA, USA

During the summer of 1997, a series of high magnetic field experiments was conducted at Los Alamos National Laboratory. Four experiments utilizing Russian built MC-1 generators, which can reach fields as high as 10 Megagauss, and four smaller strip generator experiments at fields near 1.5 Megagauss were conducted. Experiments mounted on the devices included magnetoresistance of high temperature superconductors and semiconductors, optical reflectivity (conductivity) of semiconductors, magnetization of a magnetic cluster material and a semiconductor, Faraday rotation in a semiconductor and a magnetic cluster material, and transmission spectroscopy of molecules. Brief descriptions of the experimental setups, magnetic field measurement techniques, field results and various experiments are presented. Magnetic field data and other information on Dirac '97 can be found at http://www.lanl.gov/dirac.

1 Introduction

The second in the Dirac series of high magnetic field experiments, hosted by the National High Magnetic Field Laboratory and Los Alamos National Laboratory, was held at the Los Alamos Ancho Canyon facility in New Mexico during the summer of 1997. It provided the opportunity for more than 50 scientists representing 11 institutions from 6 countries to study the behavior of materials at magnetic fields very much higher than can be achieved under ordinary laboratory conditions. The primary field-producing device in the series was the Russian-built MC-1 flux compression generator [1,2]. The explosive-driven generator can produce magnetic fields exceeding 1000 T (10 MG) with a rate of change approaching 10^9 T/s. Smaller strip generators, which can produce fields as high as 150 T, were used for four experiments (Strip 4, 5, 6, 7). Several other experiments, mostly for test and calibration, were done in the capacitor-bank driven, 50 T pulsed electromagnet. Four MC-1 generators were fielded as primary devices in the series. Two (MC1D and MC1F) were dedicated to microwave transmission (magnetoresistivity) measurements and two (MC1E and MC1G) to magnetization and Faraday rotation experiments.

Two temperature regions were available on each MC-1 device, pumped liquid helium (LHe) at $T<2$ K and liquid nitrogen at about 75 K. Fiberglass, non-conducting, vacuum-jacketed cryostats, designed and fabricated at Los Alamos [3], were placed from the top into the vertically mounted generators. The cryostats had a long slender tail, less than 12 mm diameter and over 300 mm long, which fit into the center of the third cascade, placing the samples at magnetic center. A second sample holder was inserted from below and was cooled by liquid nitrogen (75 K) flowing downward from the cryostat outer jacket. Two inductive field measuring coils (B-dot coils) of 1 mm^2 area were mounted on the lower sample holder. The magnetic field was relatively uniform over a length of at least 40 mm. Larger B-dot probes were located between the first and second cascades and the second and third cascades. Figure 1 shows the MC-1 experimental configuration.

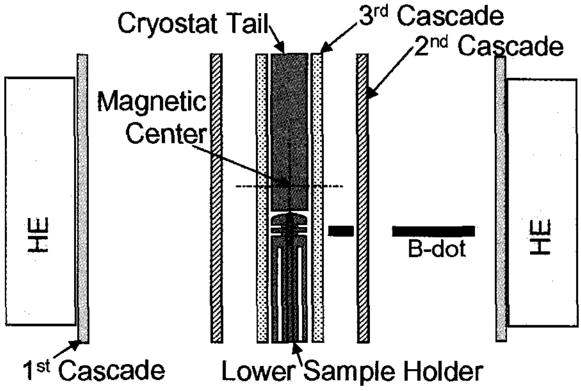

Figure 1. Schematic diagram of the MC-1 generator cross-section. Primary experiments were located on the upper sample holder in the cryostat tail and adjusted to magnetic center. B-dot coils were located in the two grooves in the lower sample holder and between the cascades. Quartz Faraday field measurement sensors were located in the lower sample holder below the B-dot coils or in the upper sample holder. A cylindrical charge of high explosives encloses the first cascade. The sketch is not to scale.

The primary field measurement technique was Faraday rotation. For the microwave experiments, shots D and E, the Faraday sensor was placed in the lower sample holder as close to magnetic center as possible. In the other experiments, the Faraday sensor was placed in the cryostat less than 10 mm above the samples under study.

Improvements in optical sensor fabrication, particularly the design of reflective sensors, were an important advancement for the Dirac 97 series. In the earlier series, most of the optical sensors were of "straight through" design, where the input fiber was on one end of the sensor and the output fiber on the other. For access, one of the fibers had to be bent 180 degrees within the small experimental diameter. Several of the optical sensors failed when the fibers broke during final cool down. In Dirac 97 the new sensors had both fibers on the same end and none were lost to broken fibers.

2 Experiments

Experiment title, institutions, sample material, technique, temperature, and shot number are given for most of the experiments.

- Magnetic field-induced reentrant superconductivity, UNSW, $YBa_2Cu_3O_{7-\delta}$ (YBCO), microwave transmission, T<2 K, MC1F [4].
- Quantum-limit phenomena at high electron densities, UNSW, GaAs/AlGaAs Parabolic Quantum Wells, microwave transmission, T<2 K, MC1D [5].
- Development of a GeAu thermometer, UNSW, GeAu sample, resistivity, T<2 K, MC1D [6].
- Reflectivity measurements on low dimensional, low electron density materials, NHMFL/FSU/LANL, GaAs/AlGaAs Parabolic Quantum Wells, 75 K, MC1D, MC1E, MC1F, MC1G [7].
- Zeeman-driven bond breaking in transition metals, LSU, ReCl and MoCl, absorption spectroscopy, T ~75 K, MC1E and MC1G [8].

- Optical absorption spectra of doped C60, UCSB, optical absorption ~320-560 nm, T ~75 K, MC1F.
- High-Field Verdet measurements of MnF2, VNIIEF, dual wavelength Faraday rotation 630 nm and 810 nm on one sample, T<2 K, MC1E and MC1G.
- Magnetization of Mn12AC magnetic cluster system, VNIIEF, Mn12AC, electrical magnetization measurement, T<4 K, MC1E and MC1F [9].
- Magnetization of C60, VNIIEF, electrical magnetization measurement, T<2 K, MC1E.
- Faraday rotation in diluted magnetic superconductors, VNIIEF, Cd1-xMnxTe, Faraday rotation at 810 nm, T ~4 K, Strip 4 [10].
- Magnetoresistance evidence for gap closure in the Kondo system SmB6, LANL, resistivity measurement, T ~4 K, Strip 5, 6, 7.

3 Field Measurements

Measurement of the fast rising magnetic field of the MC-1 generator is a difficult task. Inductive coils provide a robust signal but are susceptible to noise pickup, size change, heating, and have inductance that may influence results. Four B-dot probes were used in each MC-1 shot. Optical Faraday rotation sensors were used as the primary field measurement in the 1997 Dirac series. They are less susceptible to noise and mechanically quite sound and may survive longer than B-dot probes. All of the Faraday crystals returned good data. Figure 2 presents the Faraday data from MC1D along with B-dot 3 dB/dt and its time integral. The field values agree with each other quite well. For this shot, the B-dot probe and the Faraday sensor were located close together in the lower sample holder. Agreement is not as close in shots where the Faraday was in the upper sample holder and the B-dot in the lower sample holder. The sensors were evidently destroyed at approximately 72.8 μs. The change of slope (arrows) in the field plots occurs when the first cascade strikes the second and when the second strikes the third.

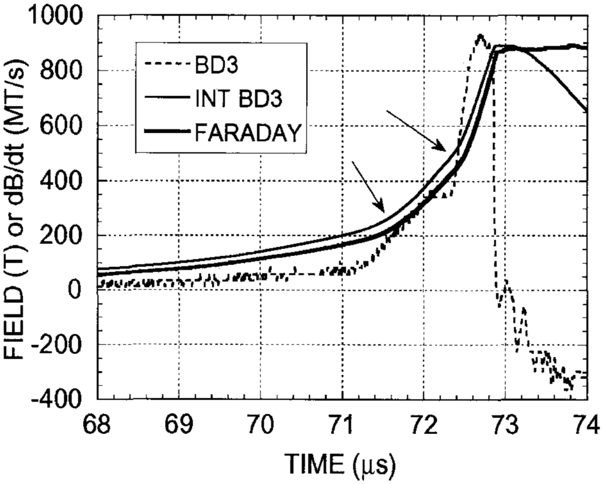

Figure 2. Comparison of Faraday (heavy solid line) and time integrated B-dot field measurement for MC1D. The dotted line is dB/dt from the B-dot probe.

Conclusion

The Dirac series of high magnetic field experiments was held at Los Alamos National Laboratory in the summer of 1997. Scientists from six countries performed over 12 major experiments. Some of the experiments were done at fields approaching 10 MG in Russian built MC-1 generators. Two temperature ranges, <2 K and 75 K were available for experiments.

The primary field measurement technique was Faraday rotation. Improvements in Faraday optical sensor fabrication, in particular, the design of reflective sensors, were an important advancement for the Dirac 97 series. All of the Faraday rotation field sensors returned good data to support the experiments fielded in each system. Details of the experiment series can be found at http:/www.lanl.gov/dirac.

Acknowledgements

Thanks to J. King, D. Torres, D. Herrera, W. Lewis, L. Tabaka, D. Bartram, O. Garcia, R. Owens, D. Devore, C. Gallegos, W. Zerwekh, J. Stokes, P. Friedman, and Y. Kim for the success of Dirac 97.

References

1. Pavlovski, A. I., “Ultrahigh magnetic fields cumulation,” *Megagauss Fields and Pulsed Power Systems*, Ed by V. M. Titov and G. A. Shvetsov, Nova Science (1990).
2. Fowler, C. M., Four decades in the megagauss world, *Physica B*, **246**, (1998) p. 158.
3. Rickel, D. G., Goettee, J. D., “Low temperature cryostat for experiments in megagauss fields,” Proc. 7th Inter. Conf. on Megagauss Magnetic Fields and Related Topics, Sarov, Russia, 5-10 August, 1996.
4. Dzurak, A. S., Kane, B. E., Clark, R. G., et al., Transport measurements of inplane critical fields in YBa2Cu3O7-delta to 300T, *Physical Review B-Condensed Matter* **57**, (1998) p. 14084.
5. Dzurak, A. S., Kane, B. E., Clark, R. G., et al., Low-temperature transport measurements of superconductors and semiconductors in magnetic-fields to 800 T, *Physica B* **246**, (1998) p. 40.
6. Lumpkin, N. E., Kane, B.E., et al., Dirac series experiments in 800 T fields: Innovations for transport measurements, *Physica B* **246**, (1998) p. 395.
7. Brooks, J. S., et al., Dirac-II series in 800 T fields: reflectivity measurements on low-dimensional, low electron-density materials, *Physica B* **246**, (1998) p. 50.
8. Maverick, A. W., Butler, L. G., et al., Zeeman-effect studies of the electronic absorption spectrum of octachlorodirhenate(2-) (Re==Re) in pulsed 50-Tesla magnetic fields, *Inorg. Chim. Acta* **243**, (1996) p. 309.
9. Platonov, V. V., Tatsenko, O. M., et al., “Nano-scale ferrimagnet Mn12AC in ultra-high magnetic field,” in preparation.
10. Platonov, V. V., Tatsenko, O. M., Bykov, A. I., et al., The faraday-effect in $Cd_{0.57}Mn_{0.43}Te$ in high magnetic-field, *Physica B* **246**, (1998) p. 319.

QUANTUM TRANSFORMATIONS OF Fe_8 MAGNETIC NANOCLUSTERS IN MEGAGAUSS MAGNETIC FIELDS

A. I. BYKOV, M. I. DOLOTENKO, A. V. FILIPPOV,
N. P. KOLOKOL'CHIKOV, V. V. PLATONOV,
O. M. TATSENKO
VNIIEF, Sarov, Russia

I. A. LUBASHEVSKY, A. A. MUKHIN, G. G. MUSAEV, V. I. PLIS,
A. I. POPOV, V. D. SELEMIR, A. K. ZVEZDIN
General Physics Institute, RAS, Russia

We have studied the magnetization of high-spin metal-organic clusters Fe_8 in megagauss magnetic fields at low and high temperatures. It is shown that in these mesoscopic clusters the transition from the ferrimagnetic to ferromagnetic states induced by the magnetic field is quantum in nature. At low temperatures, this transition experiences a sequence of jumps in magnetization rather than demonstrating classic, continuous behavior. These jumps are related to the intersections of the quantum energy levels of a Fe_8 cluster with increasing magnetic field. Such intersections should give rise to a change in the type of the cluster ground state, manifesting them as sharp jumps in magnetization.

1 Introduction

Molecular magnetism in high-spin organic clusters containing a large number of transition metal ions ($Mn_{12}Ac$, Mn_6Rad_4, Fe_6, Fe_8, Fe_{10}, *etc.*) has been a subject of considerable interest for years [1-10]. Magnetic materials of mesoscopic dimensions may exhibit novel and useful properties such as magnetic molecular bistability and macroscopic quantum tunneling [10]. Such clusters are perfect objects for studying the properties of nanoscale, single-domain particles (0-D~quantum objects) because their form is fixed and the interaction of the clusters with one another can be depressed by embedding them into an appropriate host medium.

Most large, metal clusters exhibit antiferromagnetic interactions between spins of the metal ions, so they may be treated as nanometric ferrimagnets. The typical exchange coupling fields are about 10^6 Oe in these clusters; therefore ultra-high magnetic fields must be used to study the details of their magnetization properties.

As the external field H increases it breaks down the ferrimagnetic order and, finally, leads to the ferromagnetic state. In macroscopic ferrimagnets, the transition from the ferrimagnetic to ferromagnetic states occurs as two second-order (continuous) phase transitions from the ferrimagnetic to canted phase, then from canted to ferromagnetic states.

However, Zvezdin and Popov have recently shown [8] that in $Mn_{12}Ac$ clusters the field-induced transformation of the magnetic structure should be essentially changed and is quantum in nature despite cluster mesoscopic dimensions. At low temperatures, the reorientation of magnetic moments due to the applied external field occurs as a sequence of quantum jumps, each leading to a sharp increase in cluster magnetization. At high temperatures the jumps become smoothed out and the dynamics of cluster magnetization is similar to classical behavior. These quantum jumps can be investigated experimentally by explosive compression of magnetic flux in the MC-1 generator [11].

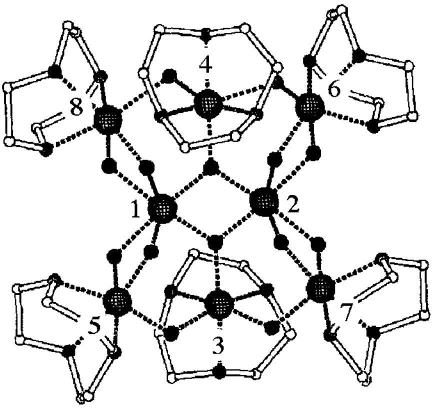

Figure 1. Structure of the Fe_8 cluster.

This work studies similar properties of other typical high-spin cluster Fe_8 under megagauss magnetic fields. Its general formula is $[(tacn)_6Fe_8O_2(OH)_{12}]$ and its structure is schematically shown in Fig. 1. The Fe_8 clusters may be considered as approximately possessing D_2 symmetry, and in weak magnetic fields their total spin is $S = 10$ at the base state. This spin value is caused by the antiferromagnetic exchange interactions between the Fe^{3+} ions, thus the Fe_8 clusters can also be treated as nanometric ferrimagnets.

2 Hamiltonian

Due to the structure of the Fe_8 cluster (Fig. 1), its magnetic properties are described by the Hamiltonian [9]:

$$\begin{aligned} H = {} & J_{12}(\vec{S}_1\vec{S}_2) + J_{13}(\vec{S}_1\vec{S}_3 + \vec{S}_2\vec{S}_3 + \vec{S}_2\vec{S}_4 + \vec{S}_1\vec{S}_4) \\ & + J_{15}(\vec{S}_1\vec{S}_5 + \vec{S}_1\vec{S}_8 + \vec{S}_2\vec{S}_7 + \vec{S}_2\vec{S}_6) + J_{35}(\vec{S}_3\vec{S}_5 + \vec{S}_3\vec{S}_7 + \vec{S}_4\vec{S}_6 + \vec{S}_4\vec{S}_8) \\ & + 2\mu_B H \textstyle\sum_{i=1}^{8} S_{iz}\ , \end{aligned} \tag{1}$$

where $S_i = 5/2$. The Hamiltonian (1) is actually amatrix acting in the spin space, which makes direct numerical analysis rather difficult. In order to study the energy level arrangement for this system, we account for the hierarchy of the exchange interaction constants [9]:

$$J_{13}{=}140\text{cm}^{-1}, J_{35}{=}48\text{cm}^{-1}, J_{12}{=}25\text{cm}^{-1}, J_{15}{=}17\text{cm}^{-1}. \tag{2}$$

We have then developed a certain perturbation technique that, at its low approximation, allows for the interaction of the Fe ions 1, 2, 3, 4 only. The other terms of the Hamiltonian (1) are taken into account to the second order. Thus we achieve the following expression characterizing the dependence of the essential energy levels on the magnetic field:

$$E_0(S,H) = E_0(S) - 2\mu_B S\,H - 20\mu_B H \tag{3}$$

Numerical values of $E_0(S)$ ($S = 0,1...10$) for the given magnitudes of, are presented in Table 1. Expression (3) shows that the lower energy levels corresponding to different values of S, and $M = -S - 10$ (M is the quantum magnetic number of the cluster as a whole) intersect one another as the magnetic field H increases. The values $\{H_S\}$ of the magnetic field at which the levels intersect are also presented in Table 1. Such intersections should give rise to a change in the type of the cluster ground state, manifesting themselves as sharp magnetization jumps demonstrated in the next section.

Table 1. The essential energy levels of the Fe_8 cluster and valuesof magnetic fields causing the changes in the type of the cluster ground state.

S	0	1	2	3	4	5	6	7	8	9	10
$E_0(S)$,cm^{-1}	-292	55	536	1153	1920	2808	3835	5000	6302	7745	9325
Hs,T	371	515	662	827	950	1099	1258	1393	1544	1698	

3 Fe_8 Cluster Magnetization

The dependence of cluster magnetization $M(T,H)$ on temperature T and magnetic field H is specified by the relationship:

$$M(T,H) = 2\mu_B \frac{\sum_{S=0}^{10} S \exp(-\frac{E_0(S) - 2\mu_B S H}{kT})}{\sum_{S=0}^{10} \exp(-\frac{E_0(S) - 2\mu_B S H}{kT})} + 20\mu_B \qquad (4)$$

Fig. 2 demonstrates the resulting dependence of the dimensionless magnetization on the magnetic field for the Fe_8 cluster. It is clearly seen that at low temperatures the field induced reorientation of magnetic moments leads to a sharp increase in cluster magnetization.

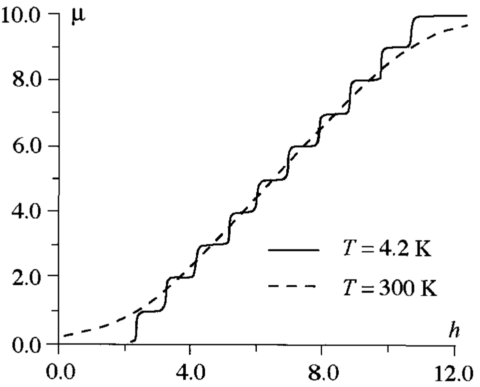

Figure 2. The dimensionless magnetization $\mu = M/2m_B$ of the Fe_8 cluster vs. the dimensionless magnetic field $h = 2\mu_B H/J_{13}$.

4 Conclusion

We have studied the field-induced reconstruction of the magnetic structure of the Fe_8 cluster. In particular, it is shown that the transition from the ferrimagnetic to ferromagnetic states occurs as a sequence of ten quantum jumps, with the amplitude of each jump equal to 1 . All of these jumps correspond to megagauss magnetic fields. The first three jumps can be studied experimentally with available, modern MC-1 generators [11], whereas fields exceeding 10 MGs are required to investigate the others.

Acknowledgment

The research described in this publication was made possible in part by the Russian Foundation for Basic Research, Grants 97-02-17972, 96-02-17576, and Grant 97-0-7.036 from the Russian State Education Department.

References

1. Gattecshi, D., Canecshi, A., Pardi, L., Sessoli, R., *Science* **265** (1994) pp. 1054.
2. Sessoli, R., Gattecshi, D., Canecshi, A., Novak H. A., *Nature* **356** (1993) pp. 141.
3. Kahn, O., Comments, *Cond. Mat. Phys.* **17** (1994) p.39.
4. Papaefthymiou, G. C., *Phys. Rev. B* **46** (1992) pp. 366.
5. Sessoli, R., Hin-Lien Tsai, Shake, A. R., *et al.*, *J. Am. Chem. Soc.* **115** (1993) pp. 1804.
6. Canecshi, A., Gattecshi, D., Sessoli, R., *J. Am. Chem. Soc.* **113** (1991) pp. 5872.
7. Villain, J., Hartman-Boutron, F., Sessoli, R., Rettory, A., *Europhys. Lett.* **27** pp. 159.
8. Zvezdin, A. K., Popov, A. I., *JETP* **109** (1996) pp. 2115.
9. Barra, A. L., Debrunner, P., Gatteschi, D., Schultz, C. H. E., Sessoli, R., *Europhys. Lett.* **35** (1996) pp. 133.
10. Kahn, O., Jay Martinez, C., *Science* **279** (1998) pp. 44.
11. Bykov, A. I., Dolotenko, M. I., Kolokol'chikov, N. P., Tatsenko, O. M., *Physica B* **216** (1996) pp. 215.

SPIN-FLIP TRANSITION AND FARADAY EFFECT IN MNF$_2$ IN MEGAGAUSS MAGNETIC FIELD

V. V. PLATONOV, O. M. TATSENKO
RFNC-VNIIEF, Sarov, Russia

D. A. CLARK, C. M. FOWLER, J. D. GOETTEE, D. G. RICKEL
Los Alamos National Laboratory, Los Alamos NM, USA

W. LEWIS, B. MARSHALL
Bechtel Corporation, Las Vegas NV, USA

A. A. MUKHIN, V. I. PLIS, A. I. POPOV, A. K. ZVEZDIN
General Physics Institute of the RAS, Moscow, Russia

Faraday effect in the antiferromagnet MnF$_2$ has been investigated in pulsed explosive fields up to 660 T at T = 2 K. The laser wavelength of 0.63 μm was used in the experiments. A change in the magnetic field dependence was observed at $H_{sf}\approx100$ T corresponding to the spin-flip transition. A feature of the magnetic field dependence of the Faraday rotation in this antiferromagnet is a lack of the saturation effect at $H>H_{sf}$ and up to 540 T. Theoretical analysis of the microscopic nature of Faraday rotation, including the diamagnetic, magneto-dipole and paramagnetic mechanisms, has been performed. The strong competition of these mechanisms is important to explain the extremely small value of the effect and its unusual magnetic field dependence.

1 Introduction

MnF$_2$ works well for studying the interrelation between the magneto-optical activity and orbital momentum of quantum systems. Mn^{2+} ions belong to the important class of ions having orbital momentum L = 0 in the ground state (e.g. Fe^{3+}, Mn^{2+}, Gd^{3+}, Eu^{3+}), as well as those with "frozen" orbital momentum (e.g. Cr^{3+}, Ni^{2+} in octahedron). The magneto-optical activity of these quantum systems is caused by the orbital momentum and spin-orbit coupling parameter of the excited states.

Measurements of the Faraday rotation in ultra-high magnetic fields provide opportunities to study this problem in more detail due to the competition of the ultra-high magnetic field with the "spin-orbit field" H_{SL} which is on the order of 10^6-10^7 Oe for the d- and f-ions.

Magneto-optics of the quantum system with zero ground state orbital momentum are interesting from a basic point of view as well as from a practical one; these systems are the typical ingredients of most magneto-optical materials.

2 Experiment

Faraday rotation in a MnF$_2$ single crystal was measured in pulse explosive fields to 660 T at T = 2 K. The cylindrical MnF$_2$ sample, 2.4 mm in diameter and 3 mm thick, was cut along the C$_4$-axis and placed in the helium cryostat. Measurements were made at the laser wavelength of 0.63 μm. Light passed through the polarizer, the sample and the analyzer, and was registered by two photoelectric multipliers. One multiplier registered the Faraday rotation and the other registered magneto absorption. The absorption of the sample was constant over the entire range of magnetic fields researched.

The high magnetic fields were produced by explosive compression of a magnetic flow in the generator MC-1 [1]. Induction pickup coils registered the magnetic field. The measurement error did not exceed 5 %.

Fig. 1 shows the magnetic field dependence of the Faraday rotation $\theta_F(H)$ for $\lambda = 0.63\ \mu m$. We note a bend in the magnetic field dependence $\theta_F(H)$ near 100 T, which corresponds to the spin-flip transition $H_{sf} = 2H_E$. Another feature of magnetic field dependence of the Faraday rotation in MnF_2 is a lack of saturation effect at $H>H_{sf}$ up to 540 T.

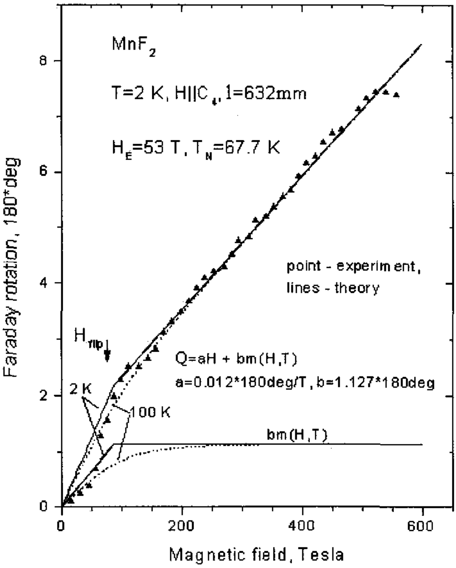

Figure 1. Magnetic field dependence of Faraday rotation. Dots denote experiment, lines denote theory, dotted lines show the field dependence of the second term bm(H,T).

3 *Magnetic Structure and Phase Transitions*

MnF_2 has a tetragonal crystal structure. Below the Neel temperature $T_N = 67.7$ K, the Mn^{2+} spins order antiferromagnetically and lie along the C_4 axis, making it possible to consider MnF_2 as a simple, uniaxial antiferromagnet.

The free energy of MnF_2 is given by

$$\Phi(\mathbf{M}_1,\mathbf{M}_2) = \Lambda \mathbf{M}_1\mathbf{M}_2 - (\mathbf{M}_1+\mathbf{M}_2)\mathbf{H} + F_A(\mathbf{M}_1,\mathbf{M}_2) - TS(\mathbf{M}_1,\mathbf{M}_2), \qquad (1)$$

where $\mathbf{M}_1$ and $\mathbf{M}_2$ are sublattice magnetizations, Λ is the intersublattice exchange constant,

$S(M_1,M_2)$ is the entropy and $F_A(M_1,M_2)$ is the magnetic anisotropy. In ultra-high magnetic fields, a contribution of the F_A term can be neglected and magnetic structure is determined by a competition of the exchange and the Zeeman energy. The relative total magnetization $m = (M_1+M_2)/2M_0$ is determined by

$$m = H/2H_E, \tag{2}$$

for $H< H_{flip}(T)$ and

$$m = B_J(\mu_0(H-H_E m)/T), \tag{3}$$

for $H> H_{flip}(T)$, where $H_{flip}(T)$ *is the field of the spin-flip transition*

$$H_{flip}(T) = 2H_E m_0(T), \tag{4}$$

and $m_0(T)$ is given by the equation

$$m_0 = B_J(\mu_0 H_E m_0/T), \tag{5}$$

B_J is the Brillouin function, $H_E = AM_0 \approx 57$ T is the exchange field, $\mu_0=5\mu_B$ is the Mn^{2+} magnetic momentum, $M_0 = \mu_0 N/2$, N is the number of the Mn^{2+} ions per cm^3.

4 Magnetic Field Dependence of the Faraday Rotation $\theta_F(H)$

There are three contributions to the Faraday rotation of the MnF_2

$$\theta_F = \theta_d + \theta_p + \theta_{matrix}, \tag{6}$$

where θ_d is the diamagnetic contribution of the allowed $^6S(3d^5) \rightarrow {}^6P(3d^4\,4P)$ electron transition of Mn^{2+}, having resonance frequency $h\omega_0 \approx 33000\ cm^{-1}$ [2]; θ_p is the paramagnetic contribution of the forbidden $^6S \rightarrow {}^4T_{1g}(G)$ electron transition, having resonance frequency $h\omega_1 = 19400$ at $T = 300$ K and line width $h\Gamma = 4000\text{-}5000\ cm^{-1}$ [2]; θ_{matrix} is the diamagnetic contribution of the MnF_2 matrix.

Faraday rotation θ_F can be expressed in the simple form

$$\theta_F(H,T) = aH + bm(H,T), \tag{7}$$

where a and b are constants and m(H,T) is the relative magnetization determined by Equations (2) and (3).

We have calculated the magnetic field dependence θ_F, and determined constants a = 0.012*180 deg/T and b = 1.127*180 deg by fitting the experimental data (Fig. 1).

5 Conclusion

1. Faraday rotation in magnets with S-ions, particularly MnF_2, is not saturated by increasing the external magnetic field to 500 T. This is explained by the joint action and competition of the effective spin-orbit field H_{SL} ($\approx$100 T), the exchange field ($\approx$53 T), and the external magnetic field up to 500 T.

2. The relatively large value of the Faraday rotation in MnF_2 at $\lambda = 0.63\ \mu m$ compared

to $KMnF_3$ [3] can be explained by decompensation of the different contributions to θ_F. In particular, we note that at wavelengths of 0.63 μm and larger (i.e. $\omega<\omega_1$) in MnF_2, the paramagnetic (θ_p) contribution according to (8)-(9) has the same sign as the diamagnetic (θ_d), while in $KMnF_3$ the former has the inverse sign at $\lambda = 0.63$ μm since $\omega<\omega_1$, here.

Acknowledgments

The authors thank James King, Dennis Herrera, David Torres, Cenobio Gallegos, Ronnie Owens, Donald Bartram, Leonard Tabaka, Katherine Foreman, William Zerwekh and Charles Mielke, and acknowledge the support of the United State Department of Energy, the International Science and Technology Center, Grants 238, the Russian Foundation of Basic Research, Grants 97-02-1797 and 96-02-17576.

References

1. Bykov, A. I., Dolotenko, M. I., Kolokol'chikov, N. P., Pavlovskii, A. I., Tatsenko, O. M., *Physica B*, **216** (1996) p. 215.
2. Stout, J. W., *J. Chem. Phys.*, **31** (1959) p. 709.
3. Mukhin, A. A., Platonov, V., Plis[1], V. I., Popov, A. I., Tatsenko, O. M., Zvezdin, A. K., *Physica B*, (1998) (in press).

NANO-SCALE FERRIMAGNET $Mn_{12}Ac$ IN MEGAGAUSS MAGNETIC FIELD

V. V. PLATONOV, O. M. TATSENKO, A. I. BYKOV
RFNC-VNIIEF, Sarov, Russia

D. A. CLARK, C. M. FOWLER, J. D. GOETTEE, D. G. RICKEL
Los Alamos National Laboratory, Los Alamos, NM, USA

A. K. ZVEZDIN, A. A. MUKHIN, I. A. LUBASHEVSKY
General Physics Institute, RAS, Russia

V. I. PLIS, A. I. POPOV,
Moscow Institute for Electronic Engineering, Moscow, Russia

B. BARBARA
CNRS - Laboratoire Louis Neel, France

A. CANESCHI, D. GATTESCHI, R. SESSOLI
Dept. of Chemistry of Firenze, Italy

The magnetization of the high-spin metallo-organic clusters $Mn_{12}Ac$ (crystal and powder) has been investigated experimentally and theoretically in magnetic fields up to 800 T at the temperature T = 2 K. It is shown that in these mesoscopic clusters the transition from ferrimagnet to ferromagnet states induced by the magnetic field is of quantum nature. In the field region of 400 - 800 T it undergoes a sequence of jumps in magnetization rather than demonstrating classic, continuous behavior. These jumps are related to the intersections of the quantum energy levels of the $Mn_{12}Ac$ cluster with increasing magnetic field. Such events should give rise to a change in the type of the cluster ground state, manifesting themselves in sharp magnetization jumps. Based on the experimental data, the constants of the exchange interaction between Mn ions are estimated.

1 Introduction

Molecular magnetism has been a subject of considerable interest for the last several years. The magnetic materials of mesoscopic dimensions may exhibit novel and useful properties such as giant magnetostriction, magnetoresistivity, the magnetocaloric effect, magnetic bistability in a cluster, and macroscopic quantum tunneling [1-3]. Molecular magnetic clusters containing a large number of coupled metal ions, e.g., Fe, Mn, Co, Ni are of great interest in this context. Besides, such clusters are the perfect objects for studying the properties of nanoscale single-domain particles (0-D quantum objects) because their form is fixed and their interaction with each other can be depressed by embedding them into an appropriate host medium.

Most of the large metal clusters exhibit antiferromagnet interaction between the spins of metal ions so they may be treated as nanometric ferrimagnets. Since the typical exchange coupling fields are about 10^6 Oe in these clusters, ultra-high magnetic fields should be used to study the properties of their magnetization in detail. This report describes the properties that $Mn_{12}Ac$, one of the most interesting high-spin clusters, exhibits under magnetic fields up to 800 T.

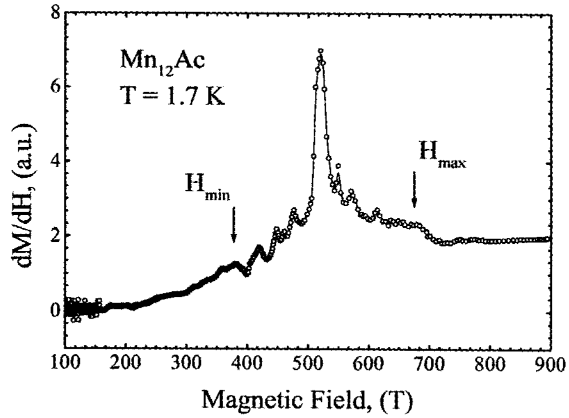

Figure 1. Derivative of the magnetization versus applied magnetic field for the $Mn_{12}Ac$ cluster, observed in a pulsed experiment at the 2 K in a field up to 800 T.

2 Experiment

The magnetization measurements were performed using an inductive method with well-balanced coils in pulsed magnetic fields up to 850 T in a series of experiments (the "Dirac Series") undertaken at Los Alamos National Laboratory in June, 1996. Orientated monocrystal $Mn_{12}Ac$ with approximate dimensions of 1x1x1 mm were glued to the glass plate and located on one of the inductive coils with diameter 1.6 mm and length 8 mm. The samples were cooled to 2 K in a plastic cryostat specially developed for these experiments.

Magnetic fields were created by the explosive compression of the magnetic flux in a MC-1 generator [4]. Field rise time of the pulse was 15 μs. These are single shot experiments and the measurement coils and samples are destroyed after each pulse. The signal, induced in the measurement coils, can be written as $U_1(t) = dM/dt + KdH/dt$, where the first component corresponds to the signal from the sample and the second one corresponds to the signal of the compensation coils. During the field pulse we recorded the signals U_1 from the compensation and magnetic field coils $U_2 = dH/dt$. These data allowed us to calculate the curves U_1/U_2 which, assuming a weak field value dependence from the decompensation signal K, are proportional to the differential susceptibility of the sample $dM/dH = (dM/dt)/(dH/dt)$. Magnetic field dependence from the signal dM/dH is shown in Fig. 1. The curves show these dynamics contain several clearly defined spikes. These spikes are due to sharp variations in the cluster magnetization that occur as the magnetic field increases and passes through a sequence of values $\{H_i\}_{i=1}^{i=9}$. In the next section we will discuss the nature of the spikes and relate the values $\{H_i\}$ to the exchange interaction constants.

3 Analysis and Discussion

The general formula of the compound $Mn_{12}Ac$ is $[Mn_{12}(CH_3COO)_{16}(H_2O)_4O_{12}] \cdot 2CH_3COOH \cdot 4H_2O$ and its structure is schematically shown in Fig. 2a. Twelve Mn ions of each unit cell form a mixed valence cluster with four inner Mn^{4+} ions (of spin $S=3/2$) surrounded by eight Mn^{3+} ions (of spin $S=2$) exhibiting the strong Jan-Teller distortions. The Mn ions interact with one another through the oxygen ions. The exchange interaction between the Mn ions of one cluster is illustrated in Fig. 2b and is described by the following Heisenberg Hamiltonian [5]

$$\begin{aligned} H = \mu H \sum_{i=1}^{12} S_{i(z)} &- 2J_1(S_1S_2 + S_3S_4 + S_5S_6 + S_7S_8) \\ &- 2J_2(S_2S_9 + S_4S_9 + S_4S_{10} + S_6S_{10} + S_6S_{11} + S_8S_{11} + S_8S_{12} + S_2S_{12}) \\ &- 2J_3(S_2S_4 + S_2S_6 + S_2S_8 + S_4S_8 + S_6S_8) \\ &- 2J_4(S_1S_9 + S_1S_{12} + S_3S_9 + S_3S_{10} + S_5S_{10} + S_5S_{11} + S_7S_{11} + S_7S_{12}), \end{aligned} \quad (1)$$

where S_i is the spin operator of the i^th^ ion, J_i are the constants of the exchange interaction, $(J_1<0)$, $H = \{0,0,H\}$ is the external magnetic field, and $\mu = g\mu_B$ $(g \sim 2)$. The energy of the single-axis anisotropy is significantly less than the exchange energy and to the first order can be neglected in studying the magnetic destruction under strong magnetic fields [3,5].

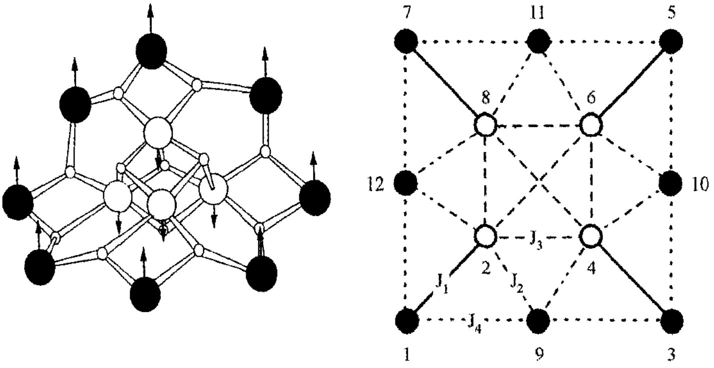

a b

Figure 2a. Schematic representation of the $Mn_{12}Ac$ cluster structure. The large black and white circles correspond to Mn^{3+} and Mn^{4+}, respectively, the small white circles are the oxygen ions. The water molecules and acid ligands are not shown; b - Illustration of the exchange bonds in the $Mn_{12}Ac$.

As the external field H increases it will tend to break down the ferrimagnetic order and, finally, will lead to the ferromagnetic state. It is well known that in macroscopic ferrimagnets this transition from the ferrimagnetic to ferromagnetic states occurs as two second order (continuous) phase transitions from the ferrimagnetic to the canted phase, then from the canted to ferrimagnetic states. At low temperatures, the reorientation of magnetic moments due to the applied external field H occurs as a sequence of quantum jumps with each leading to a sharp increase in the cluster magnetization $\mu(H)$. As shown in [5] to describe magnetization of the $Mn_{12}Ac$ clusters, we have only to take into account thirteen low energy levels;$_0$

$$E_i(H)=(\varepsilon_i\,(0) + \delta\varepsilon_i)|J_1| - 2(i+9)\mu_B H, \quad (2)$$

where $i=1,2,\ldots,13$, the constants $\{\varepsilon_i^0(0)\}$ are specified by the expression:

$$\varepsilon_i(0) = 3i\sum_{k=1}^{5}\delta_{ki} + 5(i-2)\sum_{k=6}^{9}\delta_{ki} + 7(i-4)\sum_{k=10}^{13}\delta_{ki} \qquad (3)$$

and the correction terms $\{\delta\varepsilon_i\}$ are given in Ref. [5].

In order to analyze the complex behavior of the field dependence of the cluster magnetization shown in Fig. 2b, let us assume the interaction constant J_3 to be positive, $J_3>0$. At fields $\{h_i\}$ the dependence of the $Mn_{12}Ac$ cluster magnetization on the magnetic field H should exhibits sharp jumps due to the changes in the type of the ground state, at least for low temperatures. The whole region of magnetic field where the jumps can occur involves three characteristic parts, each containing four equi-distant values of the critical fields h_i.

We point out that the distance between the critical fields inside one characteristic region is determined by the interaction parameter δ_3 only. Additionally, $\Delta h_{II} << \Delta h_{I}, \Delta h_{III}$. As follows from Fig. 1, the mean distance between the first four spikes is about $\Delta H_I^* = 33$ T. Then, setting $\Delta h_1 = 2\mu_B \Delta H_I^* / | J_1 |$ from (2) we get the estimate $J_3 \sim 5.75$ cm^{-1}. Using the critical fields corresponding to the first and the last spikes, H_1 and H_9, respectively, as well as the field H_5 matching the center point of the giant spike, we have found the following value of $J_1 \sim -70.0$ cm^{-1}, $J_2 \sim -32.0$ cm^{-1}, and $J_4 \sim -16.0$ cm^{-1}. For these values the distance between the center H_5 of the giant spike and the first critical field H_6 of region III is calculated to be 87 T, which gives a good approximation of the experimental value of 87 T.

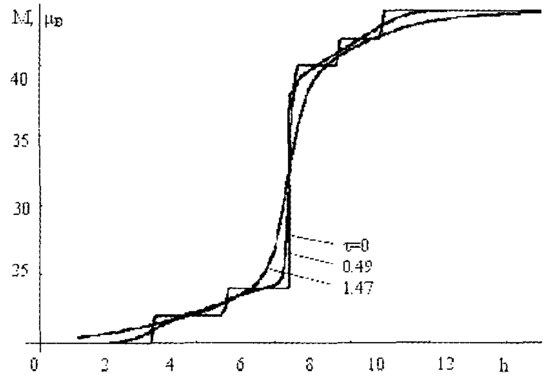

Figure 3. Theoretical dependence of the $Mn_{12}Ac$ cluster magnetization at temperature $\tau = \tau k_B T/| J_1 |$:*1* - $\tau = 0.2$; 2 - $\tau = 0.49$ (105K) and 3 - $\tau = 1.47$ (316 K). The curves have been obtained for $J_1 \sim -70.0$ cm^{-1}, $J_2 \sim -32.0$ cm^{-1}, $J_3 \sim$ 5.75 cm^{-1}, and $J_4 \sim$ -16 cm^{-1}. The temperature has been set equal to T = 4.2 K.

Fig. 3 shows these results in the dimensionless variables M/μ_B and $h = 2\mu_B H/|J_1|$. These theoretical curves demonstrate, in particular, that for the given parameters four individual spikes closely spaced in the second region merge into one large spike, as is the case for the experimental dependence.

4 Conclusion

We have studied the characteristic properties that the $Mn_{12}Ac$ clusters exhibit under magnetic fields up to 800 T. It has been found experimentally that the transition from the ferrimagnetic to ferromagnetic states in these mesoscopic clusters substantially demonstrates quantum behavior. The transition is manifested through a sequence of jumps in the cluster magnetization instead of by the classic, continuous transition.

The experimentally observed, spikewise singularities in the dynamics of the cluster magnetization have allowed us to estimates the exchange interaction constants. Based on these estimates, we have calculated the field dependence of the cluster differential magnetization which has been found to demonstrate the same characteristics as do the experimental curves describing the cluster magnetization dynamics. In particular, we have shown that there are three characteristic regions of the magnetic field, each containing four equidistant values of the field at which the magnetization jumps should occur. However, for the interaction constants found it has turned out that the jumps inside the middle region would merge into one large jump which we relate to the giant spike observed in the magnetization dynamics.

Acknowledgments

The authors thank James King, Dennis Herrera, David Torres, Cenobio Gallegos, Ronnie Owens, Donald Bartram, Leonard Tabaka, Katherine Foreman, William Zerwekh and Charles Mielke and acknowledge the support of the United States Department of Energy (USA), the International Science and Technology Center, Grant 238, the Russian Foundation of Basic Research, Grants 97-02-1797 and 96-02-17576.

References

1. Gatteschi, D. , Caneschi, A., Pardi, L., Sessoli, R., *Science*, **265**, (1994) p. 1054.
2. Sessoli, R., Gatteschi, D., Caneschi, A., Novak, H. A., *Nature*, **365**, (1993) p. 141.
3. Sessoli, R., Hin-Lien Tsai, Shake, A. R., et al., *J. Am. Chem. Soc*, **115**, (1993) p. 1804.
4. Bykov, A. I., Dolotenko, M. I., Kolokol'chikov, N. P., Tatsenko, O. M., *Physica B*, **216**, (1996) p. 215.
5. Zvezdin, K. , Popov, A. I. , *Sov. Phys.-JETP*, **82**, (1996) p. 1140.

INVESTIGATION OF LEVEL CROSSING EFFECT IN RARE-EARTH PARAMAGNETICS IN ULTRA-HIGH MAGNETIC FIELDS UP TO 500 T

V. V. PLATONOV, O. M. TATSENKO, I. M. MARKEVTSEV, M. P. MONAKHOV
Russian Federal Nuclear Center, All Russian Scientific Research Institute of Experimental Physics, (RFNC-VNIIEF), Sarov, Russia

Z. A. KAZEI, R. Z. LEVITIN, N. P. KOLMAKOVA, A. A. SIDORENKO
MSU Physical Faculty, Moscow, Russia

For the first time we have experimentally and theoretically investigated the effect of Pr and Yb ions crossing energy levels in the paramagnetic compounds $PrVO_4$ and $YbPO_4$ in an ultra-high magnetic field (up to 500 T) which was obtained by the explosion method. A wide maximum of the differential susceptibility dM/dH at the field $H_c \sim 280$ T, stipulated with crossover, is discovered in $YbPO_4$. Several maxima of the differential susceptibility are recorded in $PrVO_4$. The first maximum occurs at the field $H_c \sim 50$ T, the second one at a field of 100 T. The magnetocaloric effect, having a non-monotone dependence from the field and accompanied by significant cooling of the crystal close to the crossover, is calculated assuming adiabatic magnetization during the field pulsed.

1 Introduction

Thanks to great advances in the technique of generation of high and ultrahigh magnetic fields, a number of effects are presently accessible for experimental studies. Among these are crossover effects in rare earth (R) compounds, which consist of changing the ground energy level at an external magnetic field due to its crossing by some of the excited levels. In the tetragonal structure of R zircons, RXO_4 (X = V, P), a ground multiplet of $4f^n$ configuration of R ion, R^{3+}, is split by the crystal field and is characterized by a rich, weakly-degenerate spectrum with numerous energy level crossings at the magnetic field, giving rise to steps in the magnetization curves. The magnetocaloric effect is expected to be essential at the pulsed magnetic fields. Both heating and cooling of a sample are possible depending on the characteristics of the levels involved in the crossover.

2 Experiment

In this paper, energy level crossings and associated magnetic anomalies are investigated for paramagnetic $YbPO_4$ and $PrVO_4$. Magnetic measurements on the single-crystal $YbPO_4$ and $PrVO_4$ are performed at 4.2 K by an induction method in pulsed magnetic fields up to 450 T generated by an explosive method [1]. The duration of the pulsed field is about 15 μs. Measurement data are unitary. Pickup coils and samples are destroyed in a pulse, so a magnetic field signal cannot be fully compensated. Hence, a signal induced in pickup coils may be written as,

$$V(H) = V_1 + V_2 \sim dM/dt + KdH/dt, \tag{1}$$

where the first term corresponds to a sample signal and the second represents an uncompensated signal of coils. During a field pulse, the signals V_1 and V_2 from the pickup and field coils are recorded with a 0.002 μs interval (about 8000 points). This information

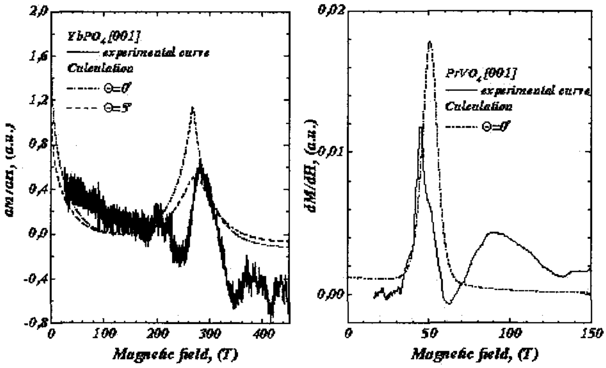

Figure 1. Differential susceptibilities d*M*/d*H* for a magnetic field orientation close to the tetragonal axis [001] (θ is a mis-orientation angle).

permits the calculation of the $V_1(H)/V_2(H)$ curves. They are proportional to the differential susceptibility of a sample d*M*/d*H* with precision of a constant K, assuming that the uncompensation signal weakly depends on the field. It also permits time averaging of a signal for decreasing the high frequency background fluctuations.

3 Results and Discussion

Figs. 1 show the experimental and calculated differential susceptibilities d*M*/d*H* for YbPO$_4$ and PrVO$_4$ in the magnetic field along the tetragonal axis [001]. A broad maximum of d*M*/d*H* at $H_c \approx 280$ T is connected with the energy level crossing of the Yb^{3+} ion. Its substantial width is apparently caused by a temperature change of the sample due to a magnetocaloric

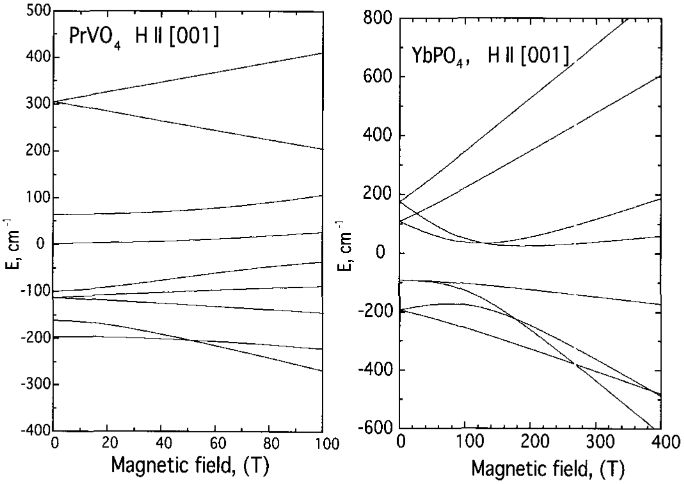

Figure 2. Zeeman effect for the Yb^{3+} ion in YbPO$_4$ for H||[001] (calculations) and for PrVO$_4$. The inset shows the gap in the spectrum near the crossover field when the J-mixing is taken into account.

effect in pulsed fields. For $PrVO_4$ a sharp susceptibility maximum at $H_C \approx 50$ T is caused by a crossover in the Pr^{3+} energy spectrum. The difference between the shapes of the anomalies in $YbPO_4$ and $PrVO_4$ is due to the different character of the energy level crossings in these two compounds (compare Figs. 2).

To calculate the Zeeman effect and magnetic characteristics, we use the crystal-field Hamiltonian plus a Zeeman term. The crystal field parameters were determined from a solution of the optimization problem with all the available experimental information: spectroscopic and EPR data [2,3] for $YbPO_4$ and spectroscopic and magnetic susceptibility data [4,5] for $PrVO_4$, plus our magnetic data. The H_C values for both compounds agree closely with the experiment within the accuracy of the field determination ±10% and a possible mis-orientation of a sample by $\leq 3^\circ$.

When calculating the magnetic characteristics, a "partial" magnetocaloric effect $dT = -(\partial M/\partial T)_H T \Delta H/C_H$ under the field change from H to H+ΔH is calculated, where C_H includes the lattice and magnetic heat capacities. These data allow calculating the sample temperature and the isothermal and adiabatic magnetization of $YbPO_4$ and $PrVO_4$ as a function of the magnetic field functions. In $YbPO_4$ the temperature has a nonmonotonic character, i.e. first the sample is heated by approximately 25 K and subsequently, near the crossover field, is cooled by 20 K. The magnetocaloric effect in $PrVO_4$ is characterized by cooling a sample up to the crossover field, and for $H > H_C$ it is rapidly heated.

4 Conclusion

In different R zircons and for various crystal directions one or two crossings may occur in intermediate fields, up to 40 T (e.g. in $DyPO_4$, $TbVO_4$), high, up to 100 T (e.g. in $ErPO_4$), or ultrahigh fields, up to 300-500 T (e.g. in $NdVO_4$, $TmVO_4$). Calculations of the appropriate isothermal and adiabatic magnetization curves and magnetocaloric effect show a great variety of anomalies and their sensitivity to the characteristics of the R ion.

Acknowledgments

The authors thank the support of the International Science and Technology Center, Grants 238.

References

1. Pavlovskii, A. I., Kolokol'chikov, N. P., Tatsenko, O. M., Megagauss Physics and Techniques, Ed. by P. Turchi, N.Y.: Plenum Press, (1980).
2. Becker, Hayhurst, T., Shalimoff, G., et al., *J. Chem. Phys.* **81** (1984) p. 2872.
3. Becker, Edelstein, N., Williams, G. M., Koningstein, J. A., Boatner, L. A., Abraham, M. M., *Phys. Rev. B* **45** (1992) p. 5027.
4. Bleaney, Harley, R. T., Ryan, J. F., Wells, M. R., Wiltshire, M. C. K., J. *Phys. C: Solid State Phys. B* **11** (1978) p. 3059.
5. Guo, Aldred, A. T., Chan, S.-K., *J. Phys. Chem. Solids B* **18** (1987) p. 229.

BAND CALCULATION STUDY OF METAMAGNETIC TRANSITIONS OF FeSi IN MEGAGAUSS FIELD

H. OHTA, T. ARIOKA
Department of Physics, Faculty of Science, Kobe University, Venture Business Laboratory, Kobe University, Japan

E. KULATOV
General Physics Institute, Russian Academy of Sciences, Russia
Venture Business Laboratory, Kobe University, Japan

S. HALILOV
Max-Plank Arbeitsgruppe "Elektronensysteme", Technische Universitaet, Abteilung Physik, Germany

L. VINOKUROVA
General Physics Institute, Russian Academy of Sciences, Russia

The band structure of FeSi was studied by the *ab initio* band calculations explicitly including the applied field. We found that the magnetization process of FeSi has at least two step-like transitions and saturates above 1200 T. Here, we also present the magnetic field dependence of the calculated optical conductivity spectrum in the megagauss field region.

1 Introduction

FeSi with a narrow semiconductor gap has been long investigated due to its anomalous magnetic behavior [1]. Recently, it was proposed that FeSi may be the first example of the *d* electron Kondo insulator, so the interest in FeSi is renewed [2].

Recent local density band calculations for FeSi showed essentially the same results, that the Fermi level is situated in the middle of a gap between sharp DOS peaks. These sharp DOS peaks near the Fermi level can be seen in other itinerant electron compounds. Using megagauss fields, the field-induced metamagnetic transition from the paramagnetic to the ferromagnetic state has been observed in itinerant electron compounds such as pyrite compounds $Co(Se,S)_2$ or Laves phase compounds YCo_2 [3]. Theoretical investigations indicate that the origin of these metamagnetic transitions come from the above-mentioned sharp DOS peaks [4]. Our previous *ab initio* band calculations including the explicitly applied field up to 240 T predicted that the first-order metamagnetic transition of FeSi would occur at around 180 T [5]. Here, we report the magnetization process of FeSi up to 1500 T and the magnetic field dependence of the optical conductivity.

2 Methods of Calculation

The electronic structure calculations for FeSi were made by using the *ab initio* full-potential linear muffin-tin orbitals method (FPLMTO) [6,7]. The crystal structure of FeSi belongs to the B20 structure that has no inversion center, and the interstitial region in FeSi occupies 44% of the unit cell volume. For such low symmetry and open structure, we used the FPLMTO-PW method in the previous calculation [5] that uses the plane wave expansions in the interstitial region for the representation of the charge and potentials. The charge density in the (110) plane deduced from the positron-lifetime study (Fig. 3 in [8]) is consistent with our previous result [5]. But here we use the FPLMTO-ASA method, which is the combined method of the atomic sphere approximation and full potential, to improve the speed of the calculation. Using FPLMTO-ASA, we can obtain the high field magnetization process.

For a given applied magnetic field, the potentials of majority and minority electrons are split by the field energy throughout the iterations until the total energy (and the spin magnetic moment, *m*) develops self-consistently. The charge and spin densities convergence was checked using the total energy, which was stable better than 0.1 μRy at the last iterations. Other parameters of the band calculation are identical to our previous work [5]. We smoothed the calculated optical conductivity with the linear inverse lifetime $\Gamma(\omega) = 0.1\,E$ eV.

3 Results and Discussion

Fig. 1 shows the calculated magnetization process for FeSi up to 1500 T. Up to 200 T the data coincides with our previous calculation [5]. The step-like increase exists around 180 T. Moreover, in higher field regions other step-like increases can be seen around 500 T. More detailed studies will confirm whether there are more transitions. Above 1200 T the magnetization process saturates where the magnetization value is 3.868 μ_B //Cell (1.013 μ_B /Fe, -0.046 μ_B //Si). This is the state similar to that previously suggested by Anisimov [9].

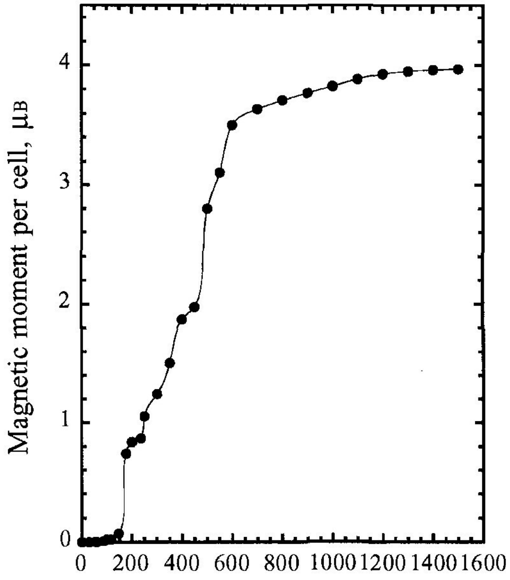

Figure 1. The high field magnetization process of FeSi.

Fig. 2 shows the magnetic field dependence of the optical conductivity spectrum. At 0 T the optical conductivity has 4 peaks at 0.16, 0.84, 2.0 and 6.0 eV. They coincide with our previous result, which is qualitatively consistent with the experimental optical conductivity data [10]. As the magnetic field is increased, the gap is destroyed and the optical conductivity becomes metallic. At higher magnetic fields of 500 T and 1000 T, the optical conductivity has an additional peak around 0.5 eV and the peak position of 2 eV at 0 T shifts to a higher energy. This is considered to be the renormalization of the d-band by the external magnetic field.

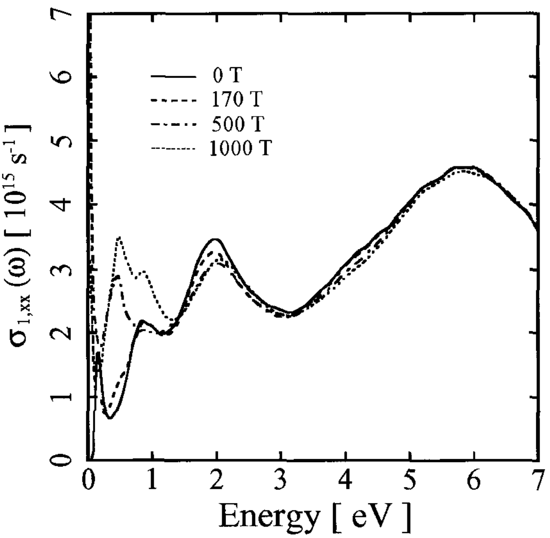

Figure 2. The magnetic field dependence of the optical conductivity: H = 0 T (solid line), H = 170 T (dashed line), H = 500 T (dashed and dotted line) and 1000 T (dotted line).

4 Conclusion

We calculated the magnetization process of FeSi up to 1500 T by the FPLMTO-ASA method. At least two metamagnetic transitions at 180 T and 500 T are suggested. The magnetic field dependence of the optical conductivity is also presented. The experiment to confirm our calculated results remains as a future problem.

Acknowledgments

The authors are grateful to Dr. S. Savrasov for providing us with the LMTO programs. The computations were done at the Information Processing Center of Kobe University. One of us (E.K.) acknowledges the financial support from the Photonics Materials Laboratory Project of the Venture Business Laboratory of Kobe University.

References

1. Jaccarino, V., Wertheim, G. K., Wernick, J. H., Walker, L. R., Arajs, S., *Phys. Rev.* **160** (1967) p. 476.
2. Aeppli, G., Fisk, Z., Comment. *Condens. Matter Phys.* **16** (1992) p. 155.
3. Adachi, K., Matsui, M., Omata, Y., Mollymoto, H., Motokawa, M., Date, M., *J. Phys. Soc. Jpn.* **47** (1979) p. 675.
4. Goto, T., Katori, H. A., Sakakibara, T., Mitamura, H., Fukamichi, K., Murata, K., *J. Appl. Phys.* **76** (1994) p. 6682.
5. Kulatov, E., Ohta, H., Arioka, T., Halilov, S., Vinokurova, L., *J. Phys.: Condens. Matter,* **9** (1997) p. 9043.

---

6. O. K. Andersen, Phys. Rev. B. **12** (1975) p. 3060.
7. S. Y. Savrasov, Phys. Rev. B. **54** (1996) p. 16470.
8. A. Bharathi, Y. Hariharan. A. Mani and C.S. Sundar, Phys. Rev. B. **55** (1997) R13385.
9. V. I. Anisimov, S. Y. Ezhov, I. S. Elfimov, I. V. Solovyev and T. M. Rice, Phys. Rev. Lett. **76**. (1996) p. 1735.
10. H. Ohta, S. Kimura, E. Kulatov, S. V. Halilov, T. Nanba, M. Motokawa, M. Sato and K. Nagasaka, J. Phys. Soc. Jpn. **63** (1994) p. 4206.

ISENTROPIC COMPRESSION OF ARGON AND KRYPTON USING AN MC-1 FLUX COMPRESSION GENERATOR

L. VEESER, C. EKDAHL, H. OONA, P. RODRIGUEZ, G. SCHMITT, J. SOLEM, AND S. YOUNGER
Los Alamos National Laboratory (LANL), Los Alamos, NM, USA

S. BAKER, C. HUDSON, W. LEWIS, B. MARSHALL, AND W. TURLEY
Bechtel Nevada Corp., Las Vegas, NV

A. BYKOV, G. BORISKOV, M. DOLOTENKO, N. EGOROV, N. KOLOKOL'CHIKOV, M. KOZLOV, Y. KUROPATKIN, AND A. VOLKOV
All Russian Federal Nuclear Center (VNIIEF), Sarov, Russia

LANL and VNIIEF are performing a set of joint experiments to explore the conductivity and possible metalization of argon and krypton compressed to up to five times normal solid density. The experiments use a magnetic field of several megagauss, generated by a Russian MC-1 generator [1], to compress a metallic tube containing solidified argon or krypton. A probe in the center of the tube measures the electrical conductivity to the walls, and a 70-MeV betatron serves as an x-ray source for three radiographic measurements of the compression. Several of these experiments for argon compressed to around 4 to 5 times solid density indicate a conductivity in the range of 10 to 100 Ω^{-1} cm^{-1}, well below that of a metal. For krypton preliminary results show a conductivity of order 1000 or more, indicating likely metalization of the compressed sample.

1 Introduction

We are studying argon and krypton under isentropic compression sufficient to cause them to become electrically conductive. The noble gases undergo phase transformations at high compression, but at the pressures of interest here they remain monatomic; thus molecular structure does not complicate the interpretation. When the density increases, the band gap becomes smaller, and as it becomes comparable with kT, electrons are increasingly able to move through the sample. In this experiment we measure the bulk conductivity of the sample, simultaneously radiographing it to determine its density near peak compression.

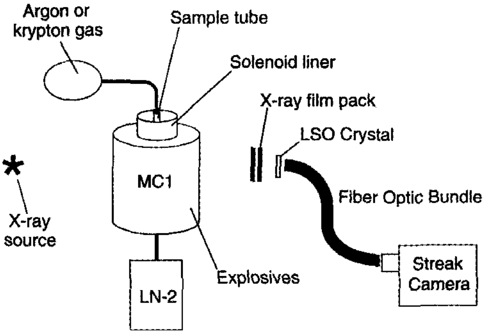

Figure 1. Schematic of the isentropic compression experiment.

2 Experiment

The experiment has been described previously [2] and is shown schematically in Fig. 1. Briefly, liquid nitrogen freezes a sample of argon or krypton inside a conducting tube on the axis of an MC-1 flux compression generator. An axial magnetic seed field is compressed, reaching about 500 T, compressing the tube and the sample to about half their original diameter. Smaller seed fields give higher compression because the implosion is faster. A probe on the axis of the sample sends current from a small capacitor bank through the sample to the tube walls, while in parallel the current flows through a 1 Ω reference resistor. The sample and probe are shown in Fig. 2. As the sample becomes conductive, the voltage across the resistor drops, giving a measurement of the sample conductivity. Details of the conductivity measurement will be published elsewhere [3]. Three x-ray pulses from a 70-MeV betatron traverse the sample radially at times near minimum sample volume. A thin crystal converts the transmitted x-rays to visible light, and a streak camera records the images to determine the sample diameter at the x-ray pulse times. Hydrodynamic calculations determine most of the density information, and the three x-ray images, as well as data from a film pack, provide calibration points for the calculations.

3 Results

We ran several series of MC-1 shots at the betatron to develop the techniques and collect data. One series included a Kr-Ar pair of 5 Mbar shots in the fall of 1997, several shots with completely insulated probes to study the insulators in the summer of 1998, and a series of 4 Mbar experiments in the fall of 1998. In addition, argon conductivity was measured a number of times earlier. In 1996 we did a series at higher compressions, but since we are not sure that there were not shocks during the implosions, those data are not reported here. After the 1997 shots we spent some effort reducing the electrical noise on the conductivity signals and improving the electronic imaging. We have just begun analysis on the most recent data, taken this past August, and the 1997 data required considerable data analysis and corrections. As this analysis is not yet completely finished, this paper is a progress report on our experiment.

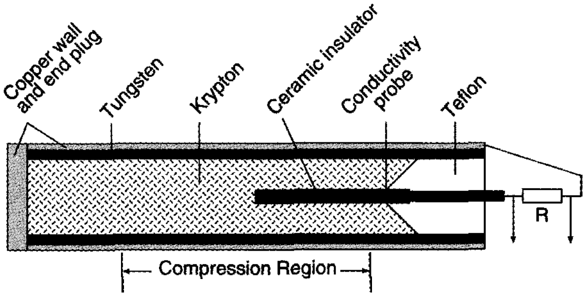

Figure 2. Sample tube and conductivity probe.

Table I shows a summary of the data, other than the insulator studies. The conductivity data marked ‡ are preliminary data and not yet fully analyzed. Conductivity data marked * were taken with a tungsten probe in a ceramic sleeve. The tungsten was ground to a fine tip, about 12 μm in diameter, and ceramic adhesive filled the region around the tip. Subsequently we determined that the adhesive was considerably less insulating than the ceramic tubing, causing an error in the probe calibration factor, which increases the apparent value of the measured conductivity. This problem has not yet been resolved, and the values marked * should be considered upper limits.

The results for argon at compressions between 4 and 5 times normal solid density indicate a measured conductivity of order 10 to 100. This has been explained as resulting from compressions that do not quite completely close the band gap [4], thus allowing electrons to "hop" from one atom to the next. For krypton, however, the conductivity is considerably larger, although the temperatures are estimated to be only 800 to 1000 K. At 5 times solid density the conductivity appears to be 1000 or more. When compressed 4 times, the sample is apparently on the verge of becoming conductive, as one of two such experiments gave a conductivity of about 1000 while the other was around 10.

Table I. Summary of the isentropic compression shots.

** Maximum pressures are estimated from EOS calculations, not measured.

Shot Name	Sample	B0 (kOe)	Pmax (Mbar)	Calc. Max. Compression	Measured Compression	Conductivity $(\Omega\ \mathrm{cm})^{-1}$
010894	Ar	175	2.8**	4.4	5.2±0.2	Not measured
220895	Ar	139	6.0**	5.9	4.9±0.2	8
281097	Ar	143	5.7**	5.8	4.3±0.3	170*
120898	Ar	165	3.5**	4.8	4.9±0.5‡	5‡
031197	Kr	142	5.8**	5.7	4.1±0.3	8,000*
070898	Kr	168	3.5**	4.7	3.9‡	1,100‡
110898	Kr	168	3.5**	4.7	4.5‡	5‡

* Upper limit, analysis in progress.

‡ Approximate value, analysis in progress

The krypton data are still under analysis. Although we do not know that the krypton is melted here, its conductivity may be similar to a liquid metal.

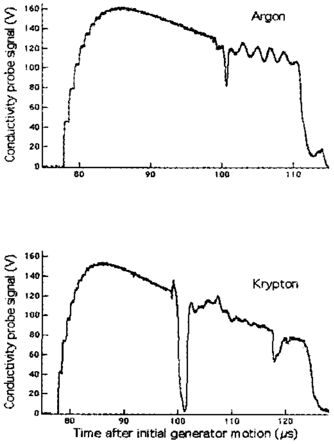

Figure 3. Conductivity voltage data for argon and krypton vs. time in microseconds. The voltage is measured across a reference resistor in parallel with the sample. The drops in signals around 100 μs indicate shunting of current through the samples at conductivity onset. When the samples decompress the voltage returns to its previous value. The ringing noise seen here was improved in later experiments. Krypton partially recompresses at 118 μs.

4 Conclusions

For isentropic compressions of around 5.0, solid argon becomes only slightly conducting, while frozen krypton acquires conductivity similar to a liquid metal.

References

1. Pavlovskii, A. I, et al., "Magnetic Fields Cumulation," in Megagauss Fields and Pulsed Power Systems, Ed by V. .M. Titov and G. A. Shvetsov, (Nova Science Publishers, New York, 1990), p. 1-14.
2. Veeser, L. R., et al., "Isentropic Compression of Argon," 11th IEEE Pulsed Power Conf., (Baltimore MD, 1997) proceedings to be published by IEEE.
3. Ekdahl, C.A., et al., "Measuring the Conductivity of Metallized Krypton," to be published.
4. Bauer, R., Windl, W., Collins, L., Kress, J., Kwon, I., "Electrical Conductivity of Compressed Argon," 11th IEEE Pulsed Power Conf., (Baltimore MD, 1997) proceedings to be published by IEEE.

HIGH SENSITIVITY MEGAGAUSS SPECTROSCOPY

N. PUHLMANN, I. STOLPE, H.-U. MÜLLER, O. PORTUGALL,
M. VON ORTENBERG
Humboldt-University Berlin, Institute of Physics (MGT), Berlin, Germany

This paper describes unique experimental techniques developed for minimizing disturbances due to transient electromagnetic fields during a capacitor discharge into a small single turn coil, generating magnetic fields above the megagauss limit. Results of cyclotron resonance measurements are presented as example of the capability of the experimental set-up to resolve transmission changes smaller than one percent.

1 Introduction

The combination of very high magnetic fields as a variable parameter with monochromatic infrared radiation as a fixed energy probe is established as one of the most powerful tools in solid-state research. Extremely strong magnetic fields are greatly appreciated, especially in semiconductor physics, as new and interesting phenomena are expected due to strong quantizing effects on spin systems and on the orbital motion of quasi-free charge carriers. Magnetic fields exceeding the megagauss limit ($B = 100$ T) are presently obtained by either the flux compression [1] or the single-turn coil technique [2]. Both methods are connected with several inconvenient experimental conditions, namely a tremendous shock wave, tiny space for the cryostat and the sample holder, short time duration of the field pulse and the presence of strong transient electromagnetic fields. The latter two aspects lead definitely to a considerable decrease in the signal-to-noise ratio, thus particularly complicating the detection of very weak resonance structures. The purpose of this paper is to demonstrate experimental techniques allowing the resolution of transmission changes smaller than one percent in megagauss cyclotron resonance (CR) experiments.

2 Experimental Set-up

Fig. 1 shows a schematic view of the experimental set-up including the single-turn coil megagauss generator, the control and data transfer systems, and the optical equipment required for performing CR experiments. The capacitor bank consists of 20 capacitors having a maximum charging voltage of 60 kV and a total capacitance of 125 μF. Rail gap switches are used for discharging the capacitor bank into the single-turn coil. The

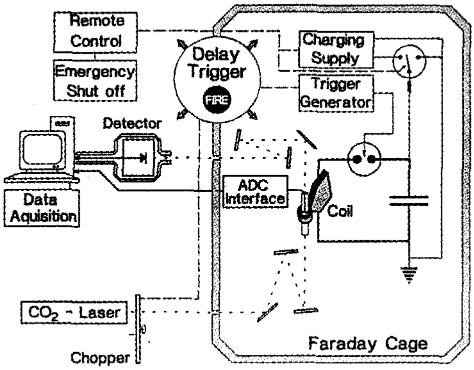

Figure 1. Schematic of the experimental set-up for megagauss cyclotron resonance experiments using the single turn coil technique.

rail gaps are triggered by a 70 kV trigger pulse with a rise time under 10 ns. The trigger pulse is inevitably accompanied by a strong, high frequency electromagnetic field that seriously disturbs the physical measurements to be made. Therefore, the megagauss generator was encapsulated by a grounded Faraday cage. All signal and remote control lines penetrating the cage are based on optical fibers and pneumatic tubes. The technical details of the interaction between the discharge unit and the supplementary components are described more precisely elsewhere [3]. CR-experiments are in Faraday geometry with the magnetic field oriented perpendicular to the sample surface performed without additional polarization of the CO_2 laser radiation on the order of 100 meV. The radiation is focused by using mirror optics on a sample having dimensions 1.5 x 1.5 mm^2. A fast HgCdTe detector located outside the Faraday cage is used to detect transmitted radiation intensity. Preceding experiments show that additional detector shielding is required to avoid unacceptable noise levels.

3 Results

Raw data of both the applied magnetic field and the transmission of 10.6 μm radiation through an epitaxially grown EuS/PbS multilayer at lowered temperature are plotted in the upper part of Fig. 2. The magnetic field was generated by a 155 kJ capacitor discharge into a coil with 15 mm inner diameter, and features a peak value of 148 T and a pulse length of 6 μs. A calibrated pick-up coil with one winding and a diameter of about 2 mm is used to probe the time derivative of the enclosed flux.

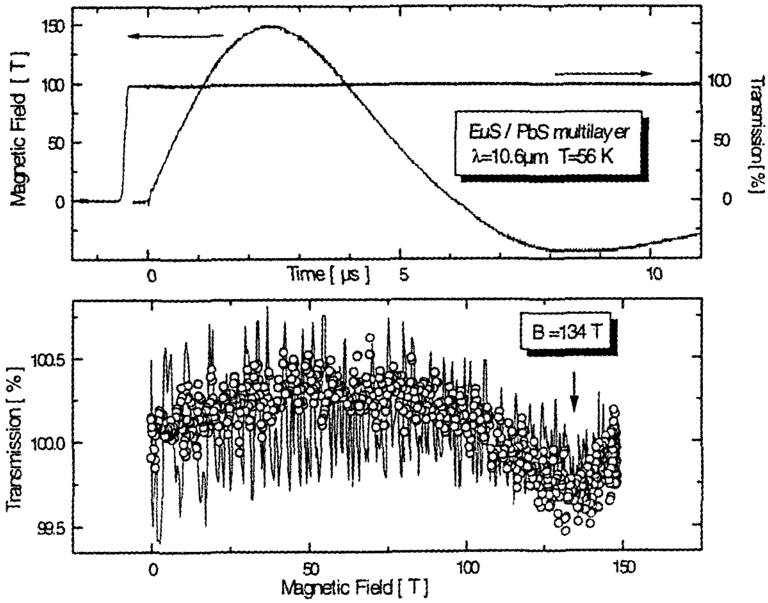

Figure 2. Cyclotron resonance observed on a EuS / PbS - multilayer at T = 56 K using CO_2 laser radiation ($\lambda = 10.6\ \mu m$). Both the magnetic field trace and the transmitted intensity are plotted vs. time in the upper part. The lower part shows the up (lines) and down (circles) sweep of the transmission vs. magnetic field.

The maximum field slope of about 100 T/μs yields an induced voltage of several hundred volts, which is subsequently integrated before being digitized and stored by the ADC interface. As shown in the upper part of Fig. 2, this method attenuates the trigger noise thus making the digitized signal a more reliable representation of the real field pulse. A more detailed description of the experimental techniques used for measuring the magnetic field was given previously [4]. To avoid heating, the sample is exposed to the laser radiation only slightly longer than the magnetic pulse length. No distinct changes of the transmitted radiation intensity normalized with respect to $B = 0$ can be observed in the transmission curve plotted versus time in the upper part of Fig. 2. However, if one plots the transmission versus the magnetic field, as shown in the lower part of Fig. 2, a resonance structure having a transmission minimum at 134 T is observed. The resonance positions in up and down sweep agree with each other and do not exhibit any hysteresis. Despite a rigorous shielding of the optical receiver module, the detector signal, in contrast to the field trace, could not be kept completely clear of electromagnetic trigger noise during the first half microsecond of the experiment. Therefore the up sweep exhibits a poorer signal-to-noise ratio than the down sweep. Nevertheless, the resonance structure, having a depth of about only 0.5%, is clearly resolved in both up and down sweep. A comparable level of accuracy in megagauss cyclotron resonance experiments has, to the best of our knowledge, not yet been reported in the literature. Unique experimental data on the valence band structure of cubic p-type GaN have been obtained very recently [5] using the methods described in this paper.

Acknowledgments

The authors are grateful to W.D. Dobrowolski for providing the EuS/PbS-sample. Special thanks are due to H. Scholz for the realization of highly sensitive electronic devices used in our experiments.

References

1. See for example: Shvetsov, G. A., *Physica B* **155,** (1989) p. 33, Pavlovskii, A. I., 1994 *Proc. 5th Int. Conf. on Megagauss Magnetic Field Generation and Related Topics* (Novosibirsk 1989) (New York: Nova Science), Miura, N., Nojiri, H., Imanaka, Y., 1995 *Proc. 22nd Int. Conf. on the Physics of Semiconductors* **2**, Ed. by D. J. Lockwood (Singapore: World Scientific) p. 1111.
2. Herlach, F., McBroom, R., Erber, T., *IEEE Trans. Nucl. Sci.* **18,** (1971) p. 809, Nakao, K., Herlach, F., Goto, T., Takeyama, S., Sakakibara, T., Miura, N., *J. Phys. E: Sci. Instrum.* **18** (1985) p. 1018.
3. Müller, H-U., Scholz, H., Puhlmann, N., Portugall, O., Barczewski, M., Stolpe, I., von Ortenberg, M., *Physica B* **246/247,** (1998) p. 356.
4. Puhlmann, N., Portugall, O., Müller, H-U., Barczewski, M., Stolpe, I., von Ortenberg, M., *J. Phys. D: Appl. Phys* **30** , (1997) p. 1861.
5. Puhlmann, N., Stolpe, I., Portugall, O., Müller, H-U., von Ortenberg, M., Schikora, D., As, D. J., Schöttker, B., Lischka, K., Megagauss Cyclotron Resonance in Cubic GaN-layers, invited paper at the *24th Int. Conf. on the Physics of Semiconductors,* Jerusalem, August 2-7, 1998.

EIGENSTATES OF BLOCH ELECTRONS IN A HIGH MAGNETIC FIELD: OPTICAL PROPERTIES

V. YA. DEMIKHOVSKII, A. A. PEROV AND D. V. KHOMITSKY
Nizhny Novgorod State University, Nizhny Novgorod, Russia

In this present paper we study quantum states of Bloch electrons in 3-D crystals with face-centered cubic lattices subjected to a uniform magnetic field. We observe the possibility of constructing a set of magnetic translations when the field is taken along one of the main cubic axes. The equation for eigenstates and eigenvalues is found and its spectrum is calculated. We also present the investigation of electron quantum states in lateral semiconductor superlattices subjected to a high magnetic field applied perpendecular to a 2-D electron gas plane. The resulting electronic structure is used to study the magneto-optical absorbtion. The absorbtion coefficient as a function of frequency for circular polarized waves is calculated for both allowed and forbidden transitions between magnetic subbands attached to different Landau levels.

1 Introduction

Since the early works of Landau in 1930, the problem of an electron in a crystal lattice under a uniform magnetic field has been extensively studied. These studies have led to deep insights in the physics of electrons in solids. The point is that the effects of the potential $V(\mathbf{r})$ and the field H are quite different in nature because the former causes the formation of energy bands while the latter quantizes the electron motion and tends to form narrow levels. In 1976, Hofstadter [1] numerically calculated the spectrum of the Harper model [2] and discovered its fractal structure. However, only 2-D electrons in a simple square lattice were the object of his research. Presently, super-high magnetic fields up to 28 MG (VNIIEF, Sarov) are achieved. Taking this into consideration, the observation of a non-trivial Bloch electron spectrum is possible. Thus, the generalization of the Harper model is required. We shall study quantum states of Bloch electrons in real 3-D crystals with non-simple lattice structure.

2 Electron States and Spectrum in the Face-Centered Cubic (FCC) Lattice in a Magnetic Field

We consider the case of the face-centered cubic (FCC) lattice. After Harper [2], we use a tight-binding approximation. Zak [3] showed that it is possible to classify all wavefunctions of Bloch electrons in a magnetic field if the field is along one of the basis directions of the lattice. In our case, the x, y, and z directions are chosen along the ribs of the cubic elementary cell having size a. The sights which make the cubic lattice face-centered have $(a/2,a/2,0)$, $(a/2,0,a/2)$, $(0.a/2,a/2)$, etc., coordinates. The magnetic field $\mathbf{H}$ is taken along the z - direction, and the vector potential is taken in Landau gauge $\mathbf{A} = (0,Hx,0)$. The important fact is that the $\mathbf{H}$ -direction in our case is not a shortest basis direction of the FCC lattice. However, we assume it is possible to construct a tightly bound wavefunction and to find translations ("magnetic translations") which give us the Bloch-type expression for the wavefunction being translated. The wavefunction is written as:

$$\psi_k(r) = \sum_n e^{-2\pi i \frac{p}{q} \frac{y - ma/2}{a/2} n} e^{ika_n} g_n \psi_0(r - a_n) \qquad (1)$$

Here, the sum is taken over all lattice sights with radius-vectors $\mathbf{a}_n$,. g_n is the amplitude of the n-th basis wavefunction ψ_0 which may be characterized by three whole numbers, for example, n, m and s.

Then, the magnetic translation is written in the form: $a_m = (qa/2, \tilde{m}a/2, \tilde{s}a/2)$ where $\tilde{m}$ and $\tilde{s}$ are any translations in y and z directions in the FCC lattice. According to the form of magnetic translations, the magnetic Brilloun zone will be q times narrowed in k_x direction.

We then substitude the wavefunction from (1) into the Schrodinger equation. The magnetic field has a non-trivial influence on the transfer integral between the chosen sight and the sight $((n \pm 1)a/2, (m \pm 1)a/2, sa/2)$. This transfer integral is:

$$\int exp\left(\pm 2\pi i \frac{p}{q} \frac{y}{a/2} \right) \psi_0 (r - a_n) \left(V_{cryst} - V_{isol} \right) \psi_0 (r - \tilde{a}_n) d\tau \ ,$$

where $\mathbf{a}_n = ((n \pm 1)a/2, (m \pm 1)a/2, sa/2)$. As a mean-value approximation we take $y = ma/2 \pm a/4$ as it goes from the lattice geometry. Thus, in the equation for g_n an additional phase $\pi p/q$ in the cosine has appeared. We underline that this phase is the direct result of the influence of a magnetic field. However, all our calculations are made for the case of a weak magnetic field. This means that the magnetic length is much greater than lattice period a.

After the ordinary calculations of the tight-binding approach, we get the system of linear and periodic equations for the amplitudes g_n:

$$g_{n+1} e^{i\frac{k_x a}{2}} \left(2\cos\left(\frac{k_y a}{2} + 2\pi \frac{p}{q} n + \pi \frac{p}{q} \right) + \right.$$
$$\left. + 2\cos\frac{k_z a}{2} \right) + g_{n-1} e^{-i\frac{k_x a}{2}} \left(2\cos\left(\frac{k_y a}{2} + 2\pi \frac{p}{q} n - \pi \frac{p}{q} \right) \right) +$$
$$4\cos\left(\frac{k_y a}{2} + 2\pi \frac{p}{q} n \right) \cos\frac{k_z a}{2} g_n = \varepsilon g_n .$$

Here $g_{n+q} = g_n$. The non-dimensional energy is a periodic function of magnetic flux: $\varepsilon_{p/q} = \varepsilon_{p/q=2}$. We may study the band structure in the presence of a magnetic field with different values of k_z.

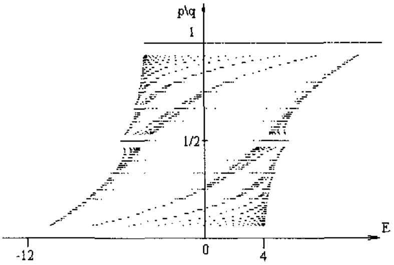

Figure 1. The energy band structure for $k_z = 0$.

The energy band structure for $k_z = 0$ is plotted in Fig.1. We observe some differences from the famous "Hofstadter butterfly" [1]. First, the structure is non-symmetric in energy with respect to $\varepsilon = 0$. Then, in weak magnetic fields when $p/q << 1$, we observe two series of Landau levels with different oscillator frequences, at the top and at the bottom of the energy band. If we consider other values of k_z in the Brillouin zone, we will observe energy bands with another structure than the one plotted in Fig. 1.

3 Magneto-Optical Properties of 2-D Lateral Superlattices

The investigations of electron quantum states in lateral superlattices in the presence of a magnetic field have been carried out in a series of theoretical and experimental papers. The wizardry of modern semiconductor technology makes it possible to fabricate such structures with electron mean free path larger than a period of the lattice [4,5]. The most perspective objects for the investigation of Bloch electron states in the presence of a magnetic field are 2-D quantum dot and antidot arrays tailored by electronic lythography methods [4]. In such artificial systems with periods of *80-300 nm* as the main parameter, the number of magnetic flux quanta per unit cell can be widely varied up to values much greater than unity. Moreover, by governing the gate voltage, it is possible to change the amplitude and the sign of periodic potential. Recent progress includes the experimental realization of the internal structures of the Landau bands [5]. In our mind, one possibility of experimental observation of the electron state structure deals with the measurements of the electromagnetic wave absorption.

4 Eigenstate Problem

The two-dimensional electron Hamiltonian of a square lattice in a magnetic field is written as:

$$H_0 = \frac{1}{2m^*}(\hat{p} + |e|A_0/c)^2 + V(x,y), \tag{2}$$

where the periodic potential has the shape $V(x,y)=V_0\cos^2(\pi x/a)\cos^2(\pi y/a)$. In Eq. (2) $A_0 = (0, Hx, 0)$ is a vector potential, m^* is the electron effective mass. The eigenfunction of the Hamiltonian (2) which satisfies the generalized Bloch conditions is decomposed on Landau functions $\varphi_N(x)$ along the x - direction and plane waves along the y - direction [6,7].

In our calculations of the electron quantum states we use typical values of lattice

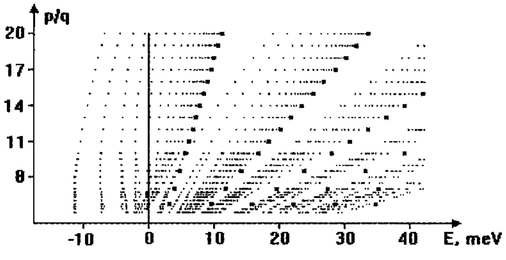

Figure 2. Allowed energy bands E as a function of p/p.

parameters $V_0 = -20$ meV, $a = 80$ nm. [5]. Fig. 2 shows how the energy spectrum calculated at $\mathbf{k} = 0$ varies with the magnetic field. We can see that each Landau level at the range $p/q > 8$ splits into p sublevels. When the wave vector changes in the magnetic Brillouin zone (MBZ) each sublevel is broadened into a magnetic subband.

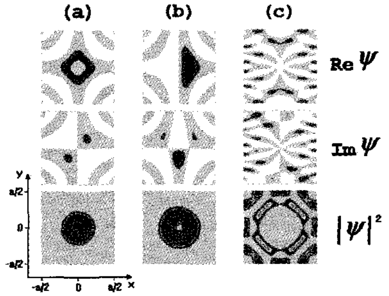

Figure 3. Schematic plot of the wavefunctions for different Landau subbands.

Fig. 3a,b,c illustrate the space behavior of electron wave functions and the electron density for three different Landau subbands $(N_0, n_0) = (0,1)\,(1,1)\,(1,10)$ under the fixed quasimomentum $\mathbf{k} = 0$. Here the value of the magnetic field corresponds to the number of magnetic flux quanta per unit cell $p/q = 15/1$. The highest values of ψ - functions are marked by a dark color. In this figure, we show only positive values of the real and imaginary parts of wave functions. As one can see, the wave functions $\psi^{(0,1)}_{(k=0)}(x.y)$ (Fig. 3a) and $\psi^{(0,10)}_{(k=0)}(x.y)$ (Fig. 3c) are transformed with respect to the symmetric representation **A** of the Hamiltonian point group C_2. The function $\psi^{(1,1)}_{(k=0)}(x.y)$ (Fig. 2b) is transformed through the asymmetric irreducible representation **B**.

5 Absorption Coefficient For Landau Intersubband Transitions

The calculations of the electron energy spectrum and wave functions make it possible to find the selection rules for Landau intersubband transitions and determine the structure of the absorption spectrum. We considered the cases of linearly polarized [8] and circularly polarized [9] electromagnetic waves (EMW) with xy - plane polarization. It was found [8] that in dipole approximation at the center of MBZ the allowed transitions between Landau subbands are $f = i + (2j + 1)$, where f and i are the final and initial subband numbers, j is an integer.

The absorption coefficient and matrix elements for direct intersubband Landau transitions in the case of circular polarized EMW have been calculated analytically in [9] at high magnetic field approximation where the Landau functions are strongly localized in the magnetic cell along the x - direction.

$$V_0 \ll \hbar\omega_c, \quad l_H \ll a$$

For 2-D electron concentrations of the order of 10^{11} cm^{-2} there is a set of occupied magnetic subbands splitted from Landau level $N = 0$ $(p/q = 15/1)$. Fig. 4 gives the plot of $\alpha(\nu)$ for the left polarized EMW in the case of nine occupied subbands $(0,1)\ldots(0,9)$. We can see the absorption lines corresponding to the transitions between magnetic subbands of Landau levels $N=0$ and $N=1$. The peaks labeled by arrows correspond to the transitions $(0,1)\ldots(0,9)\rightarrow(1,1)$ and the lines marked by "+" conform to $(0,1)\rightarrow(1,n)$ transitions. The frequencies of such transitions belong to the FIR range. The structure of the absorption spectrum here is similar to the situation of a linear polarized electromagnetic wave [8]. At low frequencies the absorption lines correspond to the transitions between Landau subbands of zero level. Here the first peak conforms to the transition between magnetic subbands (0,9) and (0,10). Therefore, we have the phenomenon of cyclotron resonance on Landau subbands attached to the same magnetic level [8,9].

The results of numerical calculations of the absorption coefficient for the right circularly polarized EMW are shown in Fig. 5. One can see that the absorption spectrum is

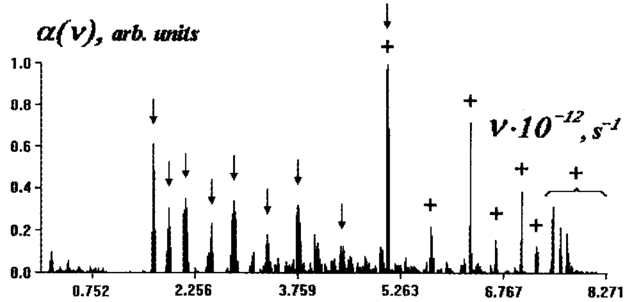

Figure 4. Absorption coefficient α for left polarized radiation as a function of frequency ν.

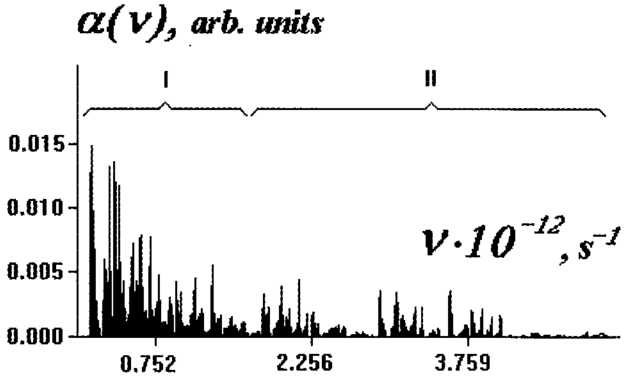

Figure 5. Absorption coefficient α for right polarized radiation as a function of frequency ν.

changed drastically compared to the case of the left polarization in both low frequency and high frequency intervals. First, it should be mentioned that transition probability from nine occupied subbands of zero Landau level to the magnetic subbands attached to the first level is small in intensity (range II in Fig. 5). In the absence of a periodic potential the transitions between Landau levels $N = 0$ and $N = 1$ are completely forbidden, but in the presence of the lattice potential such transitions become allowed due to the contribution of the second Landau state to the electron wave functions (3) of the magnetic subbands $(0,n)$.

5 Summary

Electron states and spectrum in a face-centered cubic lattice in a magnetic field are investigated here. A set of magnetic translations is constructed for the case of the magnetic field parallel to one of the main cubic axes. In a tight-binding approximation, an equation for eigenstates and eigenvalues is found. Its spectrum is calculated, being the generalization of a Hofstadter "butterfly" for a face-centered cubic lattice. It was shown also that absorption spectra for the left and right polarization are quite different in structure. The frequencies of transitions between magnetic subbands attached to the neighboring Landau levels belong to the FIR range and the frequencies corresponding to the transitions between Landau subbands of the same level belongs to the microwave range. In our opinion, the experimental investigation of absorption spectra in 2-D superlattices with the parameters shown above could give fundamental information about Bloch electron states in a uniform magnetic field.

Acknowledgment

This research was made possible thanks to financial support from the Russian Foundation for Basic Research (Grant No. 98-02-16412).

References

1. Hofstadter, D.R., *Phys. Rev. B* **14**, (1976) p. 2239.
2. Harper, P. G., *Proc. Phys. Soc.* (London) A **68**, (1955) p. 874.
3. Zak, J., *Phys. Rev. A* **134**, (1964) p. 1602; *Phys. Rev. A* **134**, (1964) p. 1607.
4. Weiss, D., Grambow, D., von Klitzing, K., et al., *Appl. Phys. Lett.* **58**, (25) (1991) p. 2960.
5. Schlösser, T., Ensslin, K., Kotthaus, J. P., et al., *Semicond. Sci. Technol.* **11**, (1996) p. 1582.
6. Demikhovskii, V. Ya., Perov, A. A., *Fiz. Tverd. Tela (Sov.Phys.:* Solid State Physics) **40**, No. 6, (1998) p. 1134.
7. Demikhovskii, V. Ya., Perov, A. A., Proceedings of the VIIth International Conference on Megagauss Magnetic Field Generation and Related Topics "Megagauss-VII", RUSSIA, Sarov, 1997.
8. Demikhovskii, V. Ya., Perov, A. A., *Zh. Exper. i Teor. Fiz.* **11** (1998).
9. Demikhovskii, V. Ya., Perov, A. A., *Phys. Low-Dim. Struct.* **7/8**, (1998) p. 135.

CYCLOTRON RESONANCE MEASUREMENT OF BEDT-TTF SALT UNDER HIGH MAGNETIC FIELD

H. OHTA, Y. OSHIMA, K. AKIOKA
Department of Physics, Faculty of Science, Kobe University, Japan

S. OKUBO
The Graduate School of Science and Technology, Kobe University, Japan

K. KANODA
Department of Applied Physics, Faculty of Engeering, Tokyo University, Japan

Cyclotron resonances of α-$(BEDT\text{-}TTF)_2MHg(SCN)_4$ have been observed below and above the density transition temperature T_D = 10 K in the millimeter and submillimeter wave region using pulsed magnetic fields up to 25 T. Fermi surfaces of low and high temperature phases are discussed.

1 Introduction

The two-dimensional organic conductor α-$(BEDT\text{-}TTF)_2KHg(SCN)_4$ is a very interesting system which shows a density wave transition at around T_D = 8 K [1]. We will call the phase below T_D in low field as DW phase and the high temperature phase as HT phase in this paper. The band calculation [2] shows that there is a two-dimensional hole closed orbit (α-orbit) and one-dimensional electron open orbit (ã-orbit) in this system at $T > T_D$. However, the Fermi surface of the system below T_D is still under discussion [3,4] in spite of many Shubnikov-de Haas (SdH) and de Haas-van Alphen (dHvA) measurements below T_D. There are also cyclotron resonance (CR) measurements below T_D [5-7]. However, there are few dHvA measurements above the kink field H_K = 23 T, where a change of the quantum oscillation occurs, and they suggest a change of the effective mass above H_K [8,9]. Recently, it has been suggested that a phase boundary exists between HT phase and high field phase (M phase) above H_K at low temperature [10,11]. Therefore, the comparison of

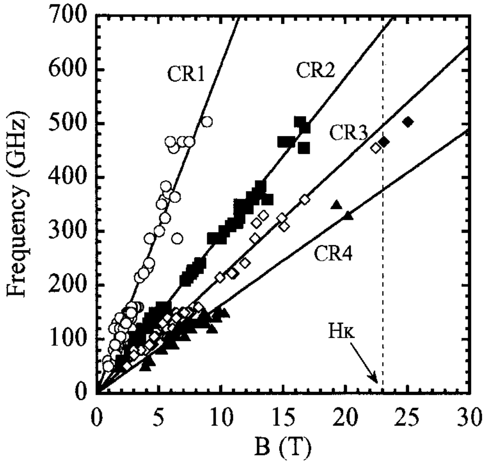

Figure 1. Frequency-field diagram of observed cyclotron resonances of α-(BEDT-$TTF)_2MHg(SCN)_4$ at 1.8 K. The field is applied perpendicular to ac-plane. Two solid lozenges are preliminary data shown in Fig. 3.

the CR in DW, HT and M phases is an interesting problem. However, no CR measurements have been performed in HT and M phases. Our final goal is to reveal CR of α-(BEDT-TTF)$_2$KHg(SCN)$_4$ in all three phases. Our extended results in DW and HT phases and our preliminary result for M phase are presented in this paper.

2 Experiment

The CR measurements were performed using our submillimeter wave ESR system [12,13] that can provide frequencies from 40 to 503 GHz using Gunn oscillators and backward traveling wave oscillators. A new cryostat equipped with a pulsed magnetic field up to 25 T [13] is used for the measurement at 1.8 K. Temperature dependence measurements are performed from 1.8 K to 30 K.

3 Results and Discussion

First, we will discuss our results for DW phase. Fig. 1 shows the frequency-field diagram of α-(BEDT-TTF)$_2$KHg(SCN)$_4$ observed at 1.8 K for B perpendicular to the conducting ac-plane. Both the frequency and field regions are extended compared to our previous result [7]. The obtained effective masses are 0.46 m_e, 0.96 m_e, 1.30 m_e and 1.71 m_e for CR1, CR2, CR3 and CR4, respectively. These results are consistent with our previous results except for the refinement of the effective mass of CR4 due to the increase of the number of data points.

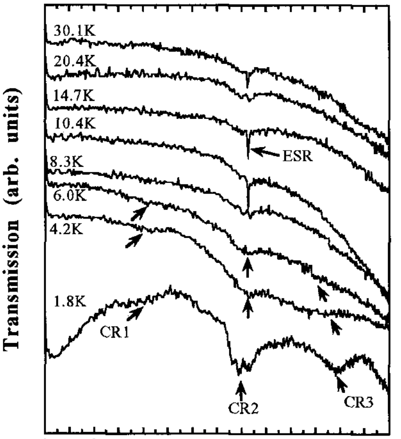

Figure 2. The temperature dependence of the transmission spectra of α-(BEDT-TTF)$_2$MHg(SCN)$_4$ observed at 232.3 GHz. The field is applied perpendicular to ac-plane. CR1 and CR3 disappear at around T_D = 8 K, while CR2 can be observed up to 30.1 K.

Now we will discuss the HT phase. Fig. 2 shows the temperature dependence of CR for B perpendicular to the ac-plane. CR1 and CR3 disappear as the temperature is increased and only CR2 seems to exist above T_D. Although more detailed discussion is required, we would like to point out that CR2 may be the CR coming from the closed α-orbit in the HT phase. Finally, we would like to comment on the CR for M phase.

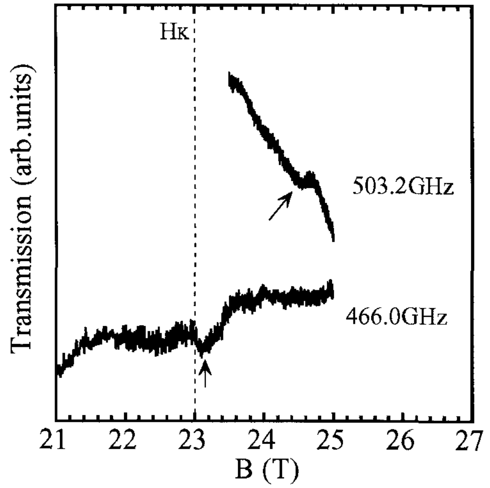

Figure 3. CR measurement of α-(BEDT-TTF)$_2$MHg(SCN)$_4$ just above the kink field H_K = 23 T at 1.8 K. The field is applied perpendicular to ac-plane.

Fig. 3 gives our preliminary CR measurements just above H_K. The weak signals indicated by arrows are observed resonances. These data are represented by solid lozenges in Fig. 1. The results seem to suggest that the effective mass of CR3 does not change much above H_K. However, we need more experiments in wider frequency and field regions to extract the final conclusion for the M phase. As we are expanding the energy of our capacitor bank from 23.5 kJ to 100 kJ, measurements up 40 or 45 T will be possible in the near future.

4 Conclusion

The CR measurements of α-(BEDT-TTF)$_2$KHg(SCN)$_4$ have been performed in DW, HT and M phases. The effective masses in DW phase are determined to be 0.46 m_e, 0.96 m_e, 1.30 m_e and 1.71 m_e by the measurements in extended frequency and field region. The result of the temperature dependence measurement suggests that CR2 may be coming from the closed α-orbit in the HT phase.

Acknowledgments

The authors are grateful to Dr. S. Uji of NRIM for the stimulating discussion. The authors are also grateful to Dr. K. Miyagawa of Tokyo University for cooperation in sample preparation. Author H. O. would like to acknowledge the support and the encouragement by Professor M. Motokawa of Tohoku University. This work was supported by Grant-in-Aid for Scientific Research from the Ministry of Education, Science, Sports and Culture, Japan.

References

1. Sasaki, T., Sato, H., Toyota, N., *Synth. Met.* **42**, (1991) p. 2211.
2. Mori, H., Tanaka, S., Oshima, M., Saito, G., Mori, T., *Bull. Chem. Soc. Jpn.* **63**, (1990) p. 2183.
3. Kartsovnik, M. V., Kovalev, A. E., Kusch, N. D., *J. Phys. I* (France) **3**, (1993) p. 1187.
4. Uji, S., Terashima, T., Aoki, H., Brooks, J. S., Tokumoto, M., Kinoshita, N., Tanaka, Y., Anzai, H., *Phys. Rev. B*, **86**, (1997) p. 2057.

5. Singleton, J., Pratt, F.L., Doporto, M., Janssen, T.J.B.M., Kurmoo, M., Perenboom, J.A.A.J., Hayes, W., Day, P., *Phys. Rev. Lett.* **68**, (1992) p. 2500.
6. Demishev, S. V., Semeno, A. V., Sluchanko, N. E., Samarin, N. A., Voskoboinikov, I. B., Glushkov, V. V., Singleton, J., Blundell, S. J., Hill, S. O., Hayes, W., Kartsovnik, M. V., Kovalev, A. E., Kurmoo, M., Day, P., Kushch, N. D., *Phys. Rev. B,* **53**, (1996) p. 12794.
7. Akioka, K., Ohta, H., Kimura, S., Okubo, S., Kanoda, K., Motokawa, M., *Physica B,* **246-247**, (1998) p. 311.
8. Harrison, N., House, A., Deckers, I., Caulfield, J., Singleton, J., Herlach, F., Hayes, W., Kurmoo, M., Day, P., *Phys. Rev. B,* **52**, (1995) p. 5584.
9. Uji, S., Chaparala, M., Seger, L., Szabo, T., Brooks, J. S., Tokumoto, M., Kinoshita, N., Kinoshita, T., Tanaka, Y., Anzai, H., *Synth. Met.* **86**, (1997) p. 2065.
10. Kartsovnik, M., Laukin, V. N., *J. Phys. I* (France) **6**, (1996) p. 1753.
11. Sasaki, T., Lebed, A., Fukase, T., Toyota, N., *Synth. Met.* **86**, (1997) p. 2063.
12. Motokawa, M., Ohta, H., Makita, N., *Int. J. Infrared & MMW,* **12**, (1991) p. 149.
13. Nakagawa, N., Yamada, T., Akioka, K., Okubo, S., Kimura, S., Ohta, H., Int. J. Infrared & MMW **19**, (1998) p. 167.

MAGNETO-RESISTANCE OF $La_{0,67}Ca_{0,33}MnO_3$ FILMS IN PULSED HIGH MAGNETIC FIELDS

S. BALEVIČIUS, B. VENGALIS, F. ANISIMOVAS, J. NOVICKIJ, R. TOLUTIS, O. KIPRIJANOVIČ

Semiconductor Physics Institute, 2600 Vilnius, Lithuania

J. NOVICKIJ

Vilnius Gediminas Technical University, Vilnius, Lithuania

L. ALTGILBERS

US Army Space and Missile Defense Command, Huntsville, AL, USA

The objective of this effort is to investigate the magneto-resistance of La-Ca-MnO for the purpose of developing high amplitude pulse magnetic field sensors and magnetic switches. The dynamics of the electrical resistance of these films was investigated in high magnetic fields at various temperatures. The results of experimental investigations of GMR in polycrystalline La-Ca-MnO under the action of microsecond-duration magnetic fields, with amplitudes up to 45 T, at various temperatures are presented.

1 Introduction

The phenomenon of giant (up to 10^6 %) magneto-resistance (GMR) in La-Ca-MnO materials has been actively investigated in recent years [1,2] due to both growing scientific interest and potential practical importance. The magnetic fields needed to generate large magneto-resistance are too high for the majority of conventional applications. However, the GMR phenomenon can be the basis of devices operating under strong magnetic field conditions. A search of the literature shows that, up until now, attention has focused on investigating GMR in dc magnetic fields with induction not higher than 12 - 15 T. The behavior of GMR in strong-pulsed magnetic fields has not been investigated. The data obtained from such studies would be helpful in developing megagauss magnetic field sensors and magnetically triggered switches used in various magnetic field compression devices [3,4].

2 Experimental Procedures

The samples used for these investigations were prepared in the form of thin $La_{0,67}Ca_{0,33}MnO_3$ films deposited by laser ablation onto MgO substrates. A 28.5 mm diameter disk made from a mixture of compressed La_2O_3, $CaCO_3$ and MnO_2 powder was used as the substrate. In order to make the target uniform and mono-phase, it was annealed at 1200^0 C in air for 20-30 hrs. After this, the target material was ground. This cycle was repeated three times. As a result, mono-phase material with a cubic perovskite structure (a = 3.867 Å) was fabricated. Laser ablation was performed using a Nd^{3+}YAG laser whose light wavelength was 532 nm. The duration of the laser pulse was 8 ns, repetition rate 12.5 Hz, and energy 50 mJ. During deposition, the substrate temperature was 750-770 ^{0}C. The thickness of the resulting film was 0.1-0.2 microns. The dependence of the resistance on temperature was measured by using the two-probe method (Fig. 1). The peak of this curve occurred at 170 K (Fig. 2).

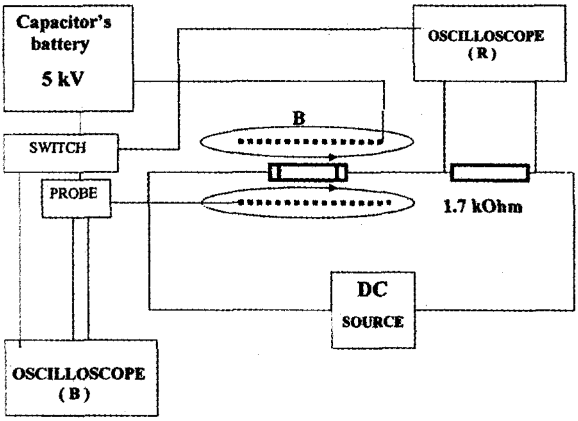

Figure 1. Test setup for resistivity measurements.

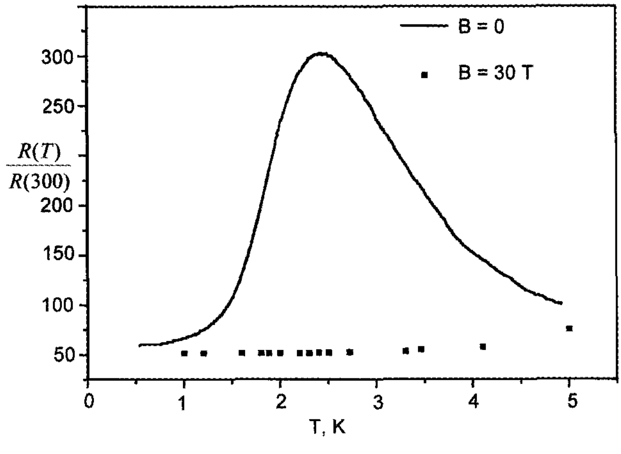

Figure 2. Resistivity vs. temperature dependence of the La-Ca-MnO film.

The samples used in these investigations were made in the shape of strips having two Ag electrodes. The length and width of each sample was 8 mm and 1 mm, respectively. Discharging a capacitor battery through a helix created strong magnetic field pulses. These pulses had a sinusoidal shape and were 1 millisecond in duration. The magnetic field was calculated by measuring the inductance of the helix and the current flowing in it by the shunt method (resistance probe method). Calculations show that the maximum magnetic field was about 45 T. In order to investigate the electrical response of the strip to the magnetic field, its resistance was measured. The sample was placed inside the helix, so that the current flowing through it was parallel to the axis of the solenoid. The temperature of the sample was changed from 77 K to 300 K by slow heating. The value of the resistance at zero magnetic field served as an indicator of sample temperature.

3 Results and Discussions

Typical electrical response to magnetic pulse action at three different sample temperatures is shown in Fig. 3. The dotted curve corresponds to the magnetic field and the solid curve corresponds to the change in sample resistance. It is shown that the shape of the electrical response pulse is similar to the shape of the magnetic field at temperatures close to the 300 K (see Fig. 3a). However, this shape changes with a decrease in the temperature of the sample (Fig. 3 b,c). At low temperatures, the rise time of the response pulse is significantly shorter (by more than half) than the duration of the magnetic field pulse, while the decay time is much longer than that of the magnetic field pulse.

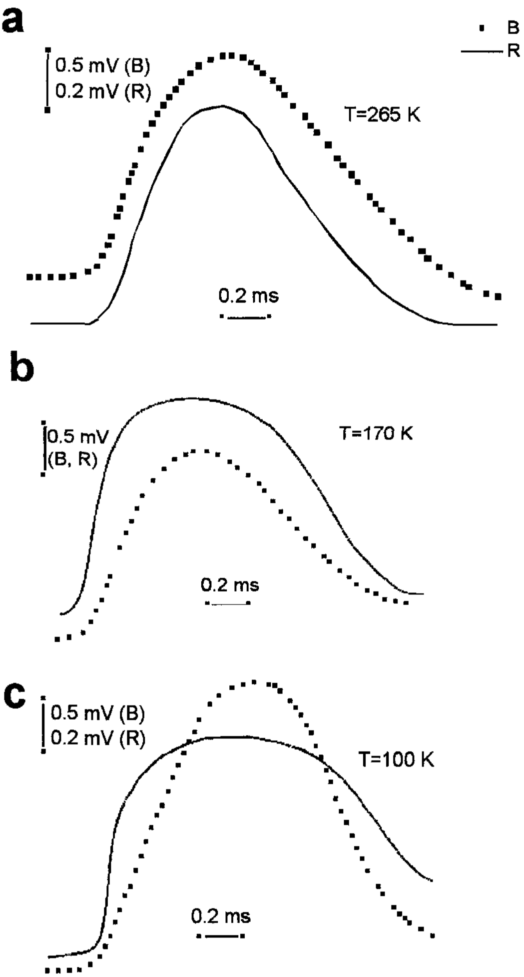

Figure 3. Magnetic field (dotted line) and electrical response (solid line) pulses.

This phenomenon can be understood as follows: The increase in the amplitude of the response pulse with an increase of the magnetic inductance (B) is due to the decrease in the sample resistance. For sufficiently high values of B and low temperatures, all charge carriers, which were trapped in magnetically activated states, are excited to the conductive band. For this reason, the semiconductor is in a degenerate state with high conductivity and any further increase of B does not change the resistance of the sample. As a result, the time needed to create this state is much shorter than the first half of the magnetic pulse and the response pulse is "sharper" compared to the magnetic pulse. This "sharpening" does not appear at high temperatures because, even at a magnetic field of B=30 T, the semiconductor material is not fully transitioned into the degenerate state (see Fig. 2) and an increase in the value of B induces changes in the response pulse amplitude. As the sample temperature decreases, the decay time increases as the result of the increase in the time needed for the magnetic domains, which are responsible for creating magnetically activated traps, to become disordered. At low temperatures, this disordering process is slow and a high conductivity state is maintained for a certain period of time, even if the magnetic field induction B decreases to zero.

The dependence of the ratio R_0/R_B on magnetic field inductance B at various sample temperatures was measured using the pulse method and the results are presented in (Fig. 4 a,b). R_0 and R_B are the resistance at zero magnetic field and at a magnetic field with inductance B, respectively. The highest value of $R_0/R_B = 200$ (B=30 T) was obtained at a temperature of 170 K temperature at which the curve $R_0 = f(T)$ has a peak value. The $R_0/R_B = f(B)$ curves were plotted so that the values of R_B correspond to the time intervals of the first half of the magnetic field pulse. As can be seen in Fig. 4, it is typical that the $R_0/R_B = f(B)$ curves consists of two regions. The first region begins from zero magnetic field and lasts up to a certain value of magnetic inductance B_c. Within this region the $R_0/R_B = f(B)$ curve measured at 170 K has a negative slope and satisfies the $R_0/R_B = C_1$ arctanh(B/B_1) law. For $B > B_c$, a second region appears, where the curve has a positive slope. In this case, $R_0/R_B = C_2$ tanh$[(B-B_C)/B_2]$. The time interval of the magnetic fields in this second region increases as the temperature of the sample decreases. Thus, at low temperatures, the largest part of the R_0/R_B vs B curve is covered by the second region, while at temperatures close to 300 K, the first region lasts up to 20 T. For such cases, the ratio R_0/R_B depends on B according to $R_0/R_B = C_3$ sinh(B/B_3) and $R_0/R_B = C_4$ arcsinh$[(B-B_C)/B_4]$ for the first and second regions, respectively.

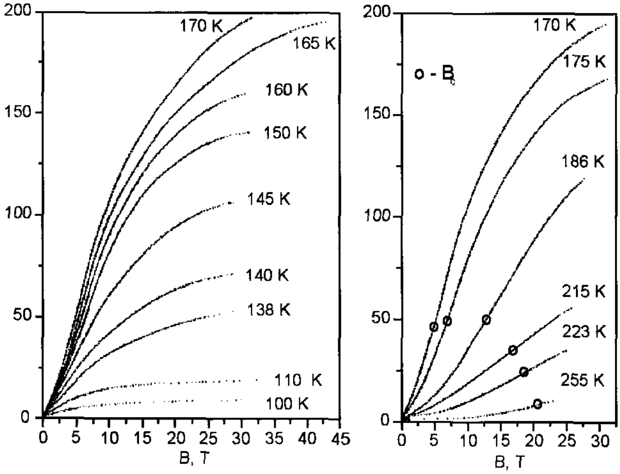

Figure 4. The ratio of resistances vs. magnetic field dependence at different temperatures.

The behavior of $R_0/R_B = f(B)$ can be understood if one assumes that the magnetic field induced transition from a high resistance semiconductor state to a low resistance degenerative state does not appear simultaneously throughout the whole volume of the film, but instead takes place in definite regions of the sample [5]. An increase in B leads to an increase of the number and size of such regions. For low values of B, the high conductivity regions are randomly distributed in the film but are not connected to each other in long clusters. Such states exist up to B_c, at which point the first long clusters connecting both electrodes of the sample appear. For $B > B_c$, the increase in B causes an increase in the size and number of long clusters. In other words, the regions occupied by the high Resistance State became smaller. Such a mechanism of magnetic field induced transition from a high resistance state to a low resistance state can be described using the percolation theory [6] on the basis of which a similar dependence of R_0/R_B vs B can be obtained.

4 Conclusions

It has been demonstrated that magneto-resistance changes can be used to measure high amplitude pulsed magnetic fields. As a result of these measurements, it may be possible to shift the operation of these devices to higher temperatures (room temperature). Additionally, it may be possible to develop a high temperature semiconducting bulk magnetic switch that could be used to switch high currents and form deeply modulated current waveforms.

References

1. Parkin, S. S., Li, Z. G. and Smith, D. J. *Appl.Phys.Lett.* **58** 2710 (1991); Levy, P. M., *Science* **156** (1992) p. 972.
2. Coffey, K. R., Hylton, T. L., Parker, M. A., and Howard, J. K., *Appl. Phys. Lett.*. **63** (1993) p. 1579.
3. Khan, M., Solid State Opening Switches, *Opening Switches* ed by A. Guenther, M. Kristiansen, and T. Martin, Plenum Press, New York, (1987) pp. 273 - 285.
4. Vitkovitsky, I., *High Power Switching*, Van Nostrand Reinhold Co., New York (1987) pp. 254 -279.
5. Nagaev, E. L., *Physica C* **222** (1994) p. 324.
6. Essam, J. W., *Rep. Prog. Phys.* **43** (1980) p. 53.

MAGNETIZATION OF AN S=1/2 AND 1 FERRIMAGNETIC CHAIN NiCu(pba)(D_2O)$_3$2D_2O IN HIGH MAGNETIC FIELDS

M. HAGIWARA[1,2], Y. NARUMI[3,2], K. TATANI[2], K. KINDO[2,3], K. MINAMI[4]

[1]*The Institute of Physical and Chemical Research (RIKEN), Japan*
[2]*KYOKUGEN, Osaka University, Japan*
[3]*CREST, Japan Science and Technology Corporation (JST), Japan*
[4]*Graduate School of Mathematics, Nagoya University, Japan*

We report the results of high field magnetization measurements on a powder sample of NiCu (pba)(D_2O)$_3$2D_2O (pba = 1,3-propylenebis(oxamato), $C_7H_6N_2O_6$) which is regarded as a ferrimagnetic chain composed of spins S = ½ and 1. From a fit of the susceptibility of this compound to numerical calculations (exact diagonalization for ten sites), we evaluated the exchange constant J/k_B = 121 K. In the magnetization measurements at 10 K up to 50 T, we observed a magnetization plateau of about 1.1 μ_B/(formula unit) corresponding to about one-third of the saturated magnetization. The increase of the magnetization at low magnetic fields is discussed and compared with some calculations.

1 Introduction

Spin systems with low dimensionality and small spin values have attracted much attention as quantum fluctuation plays an important role in the systems and they occasionally show some novel features. Recently, a spin alternating chain system composed of S = ½ and 1 has been studied [1-4]. The Hamiltonian for the S = ½ and 1 ferrimagnetic chain is given by,

$$\mathcal{H} = J\sum_{i=1}^{L}\left[S_i\cdot s_i + s_i\cdot S_{i+1}\right] - g_S\mu_B H\cdot\sum_{i=1}^{L} S_i - g_s\mu_B H\cdot\sum_{i=1}^{L} s_i \qquad (1)$$

where J (>0) is the nearest neighbor exchange constant, g_S and g_s the g values of S = 1 and S = ½ magnetic moments, μ_B the Bohr magneton, H the external magnetic field, S_i, S_{i+1} the S = 1 spin operators and s_i the S = ½ spin operator. Analytical and numerical studies using this Hamiltonian show some remarkable things written as follows. One of the excitation branches exists at about 1.77 J above the ground state, while J is deduced from the conventional spin wave theory. The spin correlation length between sublattice moments is extremely short and below unit cell length. The full magnetization curve is calculated [3] up to the saturated magnetization, which is different from that in manganese ferrimagnet [5] regarded as a classical ferrimagnet. In our previous paper, we reported the results of magnetic susceptibility measurements on the title compound. In this paper, we report the results of high field magnetization measurements up to 50 T and the comparison between magnetization at low magnetic fields and some calculations.

2 Experimental Results and Discussion

Syntheses of powder samples of NiCu(pba)(D_2O)$_3$2D_2O (pba = 1,3-propylenebis(oxamato), $C_7H_6N_2O_6$) were reported in [4]. This compound crystallizes in the orthorhombic system and belongs to the *Pnma* space group [6]. Alternating Ni and Cu bimetallic chains bridged by oxamato groups run along the *b*-axis. Susceptibility and magnetization at low magnetic fields up to 7 T were measured with a SQUID magnetometer (Quantum design's MPMS-XL7L) at KYOKUGEN in Osaka University and high field magnetization measurements were performed by using a pulse magnet at the same place.

In the inset of Fig. 1, we plot the temperature dependence of susceptibility times temperature χ*T of a powder sample of NiCu(pba)(D_2O)$_3$2D_2O. The χ*T decreases gradually with decreasing temperature from about 200 K and reaches the minimum around 70 K. Then, it increases steeply down to about 10 K and decreases rapidly upon cooling further. This rounded minimum of χ^*T is characteristic of a ferrimagnetic chain. The solid line in the inset is the result of a fit to the susceptibility calculated for the Hamiltonian (1) (exact diagonalization method for ten sites). From this fit, we evaluated the exchange constant J/k_B = 121 K and the g values of Ni and Cu as 2.22 and 2.09, respectively. High field magnetization process of a powder sample of this compound at 10 K up to about 50 T is shown in Fig. 1. Here, we measured the magnetization above the long range ordering temperature (~7 K). A magnetization plateau about 1.1 μ_B per formula unit appears up to about 50 T and this corresponds to about one-third of the saturated magnetization. Unfortunately, further increase of the magnetization, in which we are interested, was not observed in this experiment.

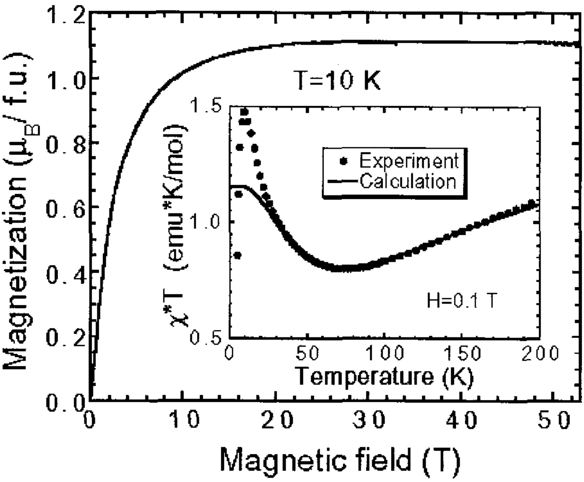

Figure 1. Magnetization curve of a powder sample of NiCu(pba)$(D_2O)_3 2D_2O$ up to about 50 T at 10 K. Inset: Temperature dependence of the susceptibility times temperature χ^*T calculated for the Hamiltonian (1) (exact diagonalization method for ten spins).

In order to precisely measure the magnetization at low fields, we measured the magnetization at low fields under static magnetic fields up to 7 T. The experimental result is shown in Fig. 2, together with some numerical calculations (k_BT/J = 0.08) for a designated number of spins. In the calculations we use the same parameter values as the exchange constant and the it{g} values of S = 1 and S = ½ magnetic moments obtained from the fit of the susceptibility. The temperature k_BT/J = 0.08 (J/k_B = 121 K) corresponds to the measuring temperature 10 K. The calculated magnetization increases with increasing number of spins. The magnetization for N = 2 (S = ½ and 1 ferrimagnetic dimer) is close to the S = ½ paramagnetic magnetization with it{g} = 2.35 (2.22*2-2.09) (S = ½ Brillouin function). Therefore, the magnetization has a ferromagnetic character with increasing the number of spins, which is consistent with one of the theoretical findings [1], namely, gapless excitation with a ferromagnetic character. Accordingly, the magnetization of this compound is shown to exhibit the steep increase at low magnetic fields compared to the paramagnetic magnetization.

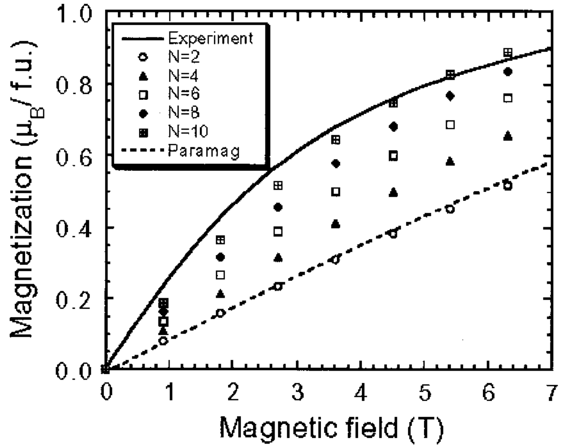

Figure 2. Magnetization curve of a powder sample of NiCu(pba)$(D_2O)_3 2D_2O$ at 10 K below 7 T measured with a SQUID magnetometer (solid line) and the magnetization curve calculated by an exact diagonalization method for the designated number of spins. The broken line shows the paramagnetic magnetization with $g = 2.35$ (S = ½ Brillouin function).

3 Conclusion

We have performed the magnetization measurements on powder samples of NiCu(pba)$(D_2O)_3 2D_2O$ regarded as the S = ½ and 1 ferrimagnetic chain. We have observed a magnetization plateau that is about one-third of the saturated magnetization. From the comparison with some numerical calculations, it has been found that the magnetization at low magnetic fields of this compound increases steeply compared to the paramagnetic magnetization and has a ferromagnetic character.

Acknowledgments

This work was carried out under the Visiting Researcher's Program of KYOKUGEN in Osaka University. This study was supported in part by a Grant-in-Aid for Scientific Research from the Japanese Ministry of Education, Science, Sports and Culture.

References

1. Pati, S. K., Ramasesha, S., Sen, D., *Phys Rev. B.* **55**, (1997) p. 8894.
2. Brehmer, S., Mikeska, H.-J., Yamamoto, S., *J. Phys.: Condens. Matter.* **9**, (1997) p. 3921.
3. Kuramoto, T., J. *Phys. Soc. Jpn.* **67**, (1998) p. 1762.
4. Hagiwara, M., Minami, J., Narumi, Y., Tatani, K., Kindo, K., *J. Phys. Soc. Jpn.* **67**, (1998) p. 2209.
5. Matsuura, M., Okuda, Y., Morotomi, M., Mollymoto, H., Date, M., *J. Phys. Soc. Jpn.* **46** (1979) p. 1031.
6. Pei, Y., Verdaguer, M., Kahn, O., Sletten, J., Renard, J. P., *Inorg. Chem.* **26**, (1987) p. 138.

MAGNETIZATION AND MAGNETORESISTANCE MEASUREMENTS UP TO 60 T AT 70 mK

Y. NARUMI[1,2], N. TAKAMOTO[2], K. KINDO[2,1],
T. C. KOBAYASHI[2,1]
1) CREST, Japan Science and Technology Corporation (JST), Japan
2) KYOKUGEN, Osaka University, Japan

N. SHIMIZU, F. IGA, S. HIURA, T. TAKABATAKE
Department of Quantum Matter, ADSM, Hiroshima University, Japan

M. VERDAGUER
Laboratoire de Chimie des Métaux de Transition, Université P. et M. Curie, France

High field magnetization and magnetoresistance measurements have been performed from 60 T down to 70 mK. A new magnet having an inner diameter of 18 mm and pulse duration of about 7 msec can generate fields up to 70 T and our plastic dilution refrigerator made of FRP can lower the temperature to 50 mK. The combination of this new magnet and a plastic dilution refrigerator allows us to carry out the experiment mentioned above.

1 Introduction

In combined extreme conditions (megagauss magnetic field, milliKelvin temperature), fascinating physical phenomena are expected. A pulsed magnetic field represents many challenges in realizing both high magnetic fields and extreme low temperatures, though pulse magnets are inevitable to obtain magnetic fields higher than 40 T. The extreme low temperatures below 100 mK are usually generated by using a dilution refrigerator. In pulsed magnetic fields, destruction of metallic cryostats, noise and heating derived from eddy currents are serious problems. To avoid eddy currents, metallic parts must be located outside the pulse magnet and the magnet must have a long pulse duration. We have carried out magnetization and magnetoresistance measurements in high magnetic fields and at milliKelvin temperatures using a combination of a plastic dilution refrigerator (Taiyo Toyo Sanso Co., Ltd.) and our newly developed pulse magnet. In this report, the details of the experimental system are presented in addition to experimental results of the magnetization of a Haldane compound TMNIN and the magnetoresistance of a Kondo insulator YbB_{12}.

2 Plastic Dilution Refrigerator

A schematic view of the mixing chamber is shown in Fig. 1. Most parts below the mixing chamber are under the influence of pulsed magnetic fields and are mainly constructed of fiber reinforced plastic (FRP) except for a pick-up coil and a Cu wire sheet used as a substitute for a 2 K shield. This Cu wire sheet is made of many fine wires glued in parallel to a sheet such that the heat travels in one direction and eddy currents are hardly induced. The compactness of the cryostat outer diameter, which is 15 mm, is also due to this Cu wire sheet. Our dilution refrigerator can reach temperatures below 70 mK in continuous mode and 50 mK in one shot mode. The cooling power is 30 μW at 100 mK.

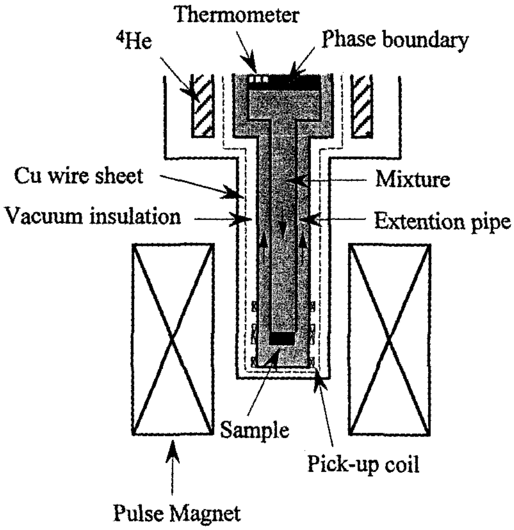

Figure 1. Schematic view of the dilution refrigerator and the pulse magnet around the mixing chamber. The three arrows in the mixture represent the flow of ^{3}He.

The mixing chamber temperature is monitored by a Ruthenium Oxide thermometer (RO-600A2 S/N 1813) which is located near the ^{3}He-^{4}He phase boundary outside of the pulse magnet. Samples are mounted at the end of the mixing chamber extension pipe below the phase boundary by about 200 mm as shown in Fig.1. The temperature gradient in the extension pipe has to be accounted for, although ^{4}He in the mixture must be superfluid. Then the temperature difference between RO-600A2 and the sample position was confirmed to be less than 20 mK in zero magnetic field.

Immediately after magnetic fields of about 60 T are generated, the exothermic effect is found to be negligible - about 2 mK in the case of an insulator sample. Furthermore, in order to obtain background signals, we must move the insert that contains the mixing chamber, the heat exchanger and the 1K pot, upward by about 20 mm. The mixing chamber temperature temporarily rises by 100 mK, however the temperature returns to its initial level in about 40 minutes. Because it takes about 30 minutes to cool the pulse magnet when magnetic fields of about 60 T are generated, we can measure the magnetization once every 40 minutes.

3 Magnetic Field Generation

Magnetic fields are generated by using a 9-layer Cu-Ag wire pulse magnet. These layers are reinforced by an outer back-up ring made of maraging steel, thus avoiding an outward deformation of the magnet. The magnet has a pulse duration of about 7 msec and a bore diameter of 18 mm. This wide bore easily accommodates the dilution refrigerator.

4 Magnetization and Magnetoresistance Measurement

Magnetization is measured by a standard pick-up coil. The pick-up coil, which consists of 40-80-40 turns of 0.08 mm Φ Cu-Sn wire, is set in the vacuum thermal insulation as shown in Fig. 1. Samples are filled inside a cylindrical Teflon tube. Resistance measurements are made by a standard DC four-wire method.

5 Results and Discussion

High field magnetization measurements have been performed on the Haldane compound $(CH_3)_4N[Ni(NO_2)_3]$ known as TMNIN [1,2]. The temperature dependence of the magnetization and the corresponding field derivative *dM/dH* are shown in Fig. 2(a). Because no hysteresis loop is observed within experimental accuracy, we may say that the sample temperature does not change during the sweep of the pulsed magnetic field.

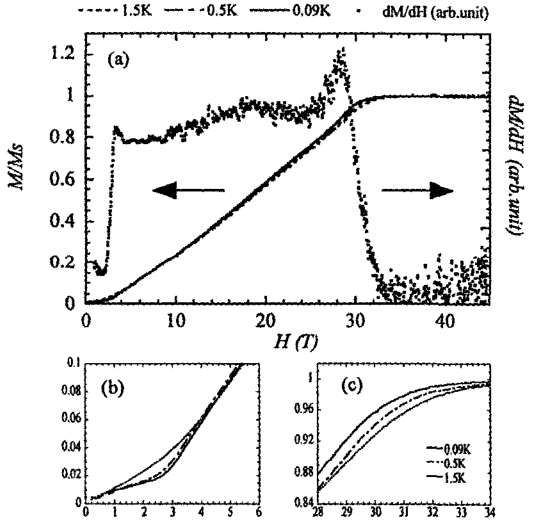

Figure 2. High field magnetization processes on a powder sample of the Haldane compound TMNIN. Figure 2(a) shows the temperature dependence of the magnetizations M at T=1.5, 0.5, 0.09 K and the corresponding field derivative of the magnetization *dM/dH* at T = 0.09 K. Figure 2(a) and (b) show the detail of the magnetization around the critical field and the saturation field.

Around H_c = 2.5 T, sudden rises in the magnetizations which originate from the Haldane gap quenching are observed and the magnetization increases almost linearly to saturate around H_s = 30 T. The gradient of the magnetization tends slightly to increase and the H_s becomes lower as the temperature decreases as shown in Fig. 2 (c). Alternately, though the magnetization below H_c decreases with decreasing temperature as shown in Fig. 2 (b), the change is smaller than that of H_s. The difference may be due to a paramagnetic impurity as well as the thermal excitation beyond the Haldane gap.

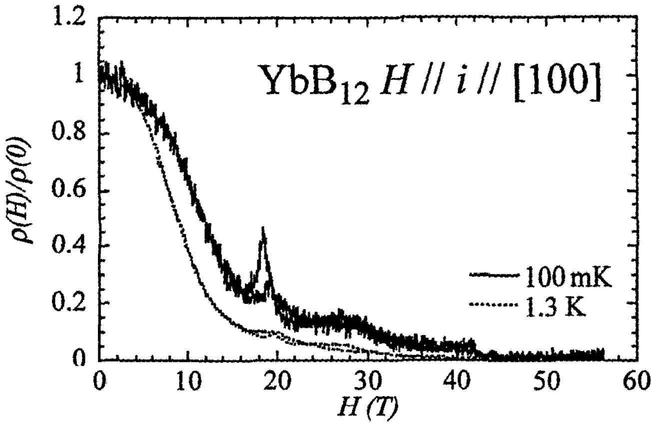

Figure 3. Magnetoresistance of the Kondo insulator YbB_{12} with H // i // [100]. The solid line shows the magnetoresistance at 100 mK by using a dilution refrigerator and the dotted line shows the magnetoresistance at 1.3 K by using a ^{4}He cryostat for comparison.

Figure 3 shows the result of the magnetoresistance measurements of the Kondo insulator YbB_{12} [3-5] with the H // i // [100] at 100 mK, together with the result at 1.3 K which was measured in a ^{4}He cryostat. Large negative magnetoresistances have been observed, and around 45 T an insulator-metal transition derived from closing a band gap has occurred at both temperatures. We have detected a sharp peak around 20 T, especially at 100 mK, which may indicate the existence of a narrow band of about 100 mK near the Fermi surface.

In summary, a combination of a plastic dilution refrigerator and a newly developed pulse magnet enabled us to measure magnetizations and magnetoresistances down to 70 mK and up to 60 T.

Acknowledgment

This study was partially supported by a Grand-in-Aid for Scientific Research from the Japanese Ministry of Education, Science, Sports and Culture.

References

1 Takeuchi, T., et al., *J. Phys. Soc. Jpn.* **61** (1992) p. 3262.
2 Granroth, G. E., et al., *Phys. B* **211** (1995) p. 208.
3 Kasaya, M., et al., *J. Magn. Magn. Mat.* **31-34** (1983) p. 437.
4 Sugiyama, K., et al., *J. Phys. Soc. Jpn.* **57** (1988) p. 3946.
5 Iga, F., et al., *J. Magn. Magn. Mat.* **177-181** (1998) p. 337.

MAGNETIZATION CURVES AND MAGNETIC PHASE TRANSITIONS OF NEW ISING FERRIMAGNETS

A. S. LAGUTIN, G. E. FEDOROV
Institute of Molecular Physics of the Russian Research Center "Kurchatov Institute", Moscow, Russia

J. VANACKEN, F. HERLACH
Laboratorium voor Vaste-Stoffysica en Magnetisme, Katholieke Universiteit Leuven, Celestijnenlaan, Leuven, Belgium

The magnetization of $Dy_xY_{3-x}Fe_5O_{12}$ single crystals (x = 0.3; 0.62; 0.9) was measured in pulsed magnetic fields up to 50 T at low temperatures. Several jumps of the magnetic moment were observed at **H**//[100], [110] and [111]. A theoretical model for the quantitative description of the phenomena was developed, based on the assumption of quasi -Ising ordering of rare earth ions.

1 Introduction

The present work is aimed at obtaining information about the magnetization and field induced phase transitions in $Dy_xY_{3-x}Fe_5O_{12}$ compounds at $T \leq 50$ K. Single crystals of dysprosium-yttrium ferrite-garnets without compensation point (x = 0.3; 0.62; 0.9) were studied at H // [100], [110] and [111]. The magnetization M(H) and the differential magnetic susceptibility dM/dt were measured in pulsed magnetic fields up to 40 T at the RRC "Kurchatov Institute" [1] and up to 50 T at the Katholieke Universiteit Leuven [2].

2 Experimental Results

The magnetization curves of $Dy_xY_{3-x}Fe_5O_{12}$ single crystals (x = 0.3; 0.62) for one of the orientations of the external magnetic field at different temperatures are presented in Figs. 1-2. It is evident that in all *M(H)* and *dM/dt (H)* curves there are three distinct ranges at T = 4.2 K which are typical for ferrimagnets. In the first range ($H < H_1$ = 7-13 T), M and *dM/dt* depend slightly on the external field. Significant changes of the magnetization M

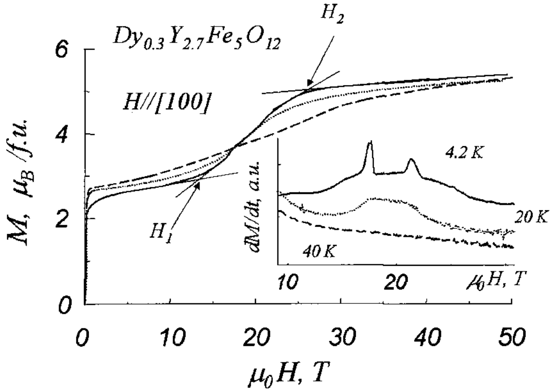

Figure 1. Magnetization curves of a $Dy_{0.3}Y_{2.7}Fe_5O_{12}$ single crystal for three orientations of the external magnetic field at different temperatures and H // [100]. Solid lines are T = 4.2 K; dotted lines are T = 20 K, dashed lines are T = 40 K. The insert shows variations of dM/dt during the increase of the field.

take place above $H = H_1$ up to the field $H_2 = 25$-32 T; in this interval, jumps of M occur. Finally, at $H > H_2$ the $M(H)$ and $dM/dt(H)$ curves change slightly with increasing external field. Similar features are observed at higher temperatures but with a significant smoothing of the curves. Ferri- and ferromagnetic states of the garnets are observed in the field ranges $H < H_1$ and $H > H_2$. The magnetic reversal of some of the nonequivalent moments M^i_{Dy} (I = 1...6) occurs in the range H_l $H < H_2$, accompanied by a reorientation of $\mathbf{M}_{Fe}$. The field range $\Delta H = H_2 - H_1$ tends to zero with decreasing Dy^{3+} concentration and increasing temperature.

The value $H_{eff} = (H_1 + H_2)/2 = 20 \pm 1$ T is practically constant for all compounds, temperatures and directions of the external magnetic field. Thus, H_{eff} ought to be

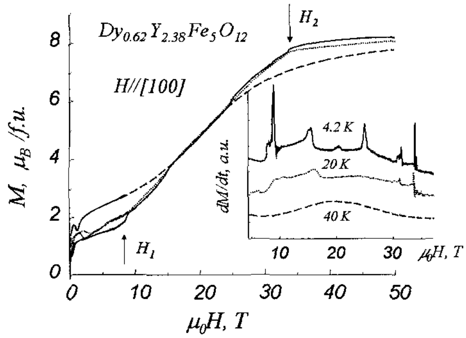

Figure 2. Magnetization curves of a $Dy_{0.62}Y_{2.38}Fe_5O_{12}$ single crystal for H // [100] at different temperatures. Solid lines are T = 4.2 K; dotted lines are T = 20 K, dashed lines are T = 40 K. The insert shows variations of dM/dt during the increase of the field

considered as effective field of the 3d-4f-exchange interaction [3-5]. Due to the fact that all magnetization curves indicate the presence of magnetic ions with a very large anisotropy, for the description of experimental results a model based on the assumption of quasi-Ising ordering of Dy^{3+} ions was selected. The model allows both reversals and slight rotations of the rare earth moments M^i_{Dy} (I = 1...6).

3 Discussion

One iron sub-lattice and six rare-earth sub-lattices were considered in the model. The magnetic anisotropy of the iron matrix was not taken into account. It was assumed that local axes of anisotropy of the RE ions (Ising axes) are oriented along directions of type [110]. The thermodynamic potential (TP) of one molecule of a $Dy_xY_{3-x}Fe_5O_{12}$ garnet can then be written as

$$\Phi = -\mathbf{M}_{Fe} \cdot \mathbf{H} - \frac{1}{T} \cdot \frac{x}{6} \sum_{i=1}^{6} \ln 2ch(\frac{\Delta_i}{T}) \qquad (1)$$

where Δ_i is the energy splitting of the lowest doublet of the Dy^{3+} ion in presence of exchange and Zeeman interactions:

$$\Delta^{(i)} = \left(\sum_{\alpha} g^{2}_{\alpha\alpha} \cdot (\lambda \cdot \mathrm{M}_{Fe\alpha}^{(i)} + \mathrm{H}_{\alpha}^{(i)})^{2} \mu_{B}^{2}\right)^{1/2} \qquad (2)$$

Here $M^{i}_{Fe\alpha}$ and H^{i}_{α} are the projections of $\boldsymbol{M}_{Fe}$ and $\boldsymbol{H}$ on the local axes of coordinates of the Dy^{3+} ion at the i^{th} nonequivalent site, $\alpha = j, k, l$. The parameters $g_{\alpha\alpha}$ are diagonal components of the g-tensor of the Dy^{3+} ion ($g_{xx} >> g_{yy}$, g_{zz}), and λ is a constant of the 3d-4f exchange interaction.

Due to fact that each of the six RE sub-lattices is independent and has 2 states, one should consider up to 2^6 different magnetic states of the rare earth subsystem. The equilibrium condition was determined by minimizing of the TP with allowance for all magnetic phases, distinguished by the signs of the projections of $\boldsymbol{M}^{i}_{Dy}$ ($i = 1...6$) on the local Ising axes and orientation of the $\boldsymbol{M}_{Fe}$. Some of the calculated $M(H)$ and $\chi(H)$ curves of a $Dy_xY_{3-x}Fe_5O_{12}$ single crystal are shown in Fig. 3. Comparison of the numerical and the experimental results indicates that the quasi-Ising model is adequate for the description of the magnetic properties of $Dy_xY_{3-x}Fe_5O_{12}$ in high magnetic fields at low temperatures. It is evident that the model correctly predicts the general character of the magnetization curves.

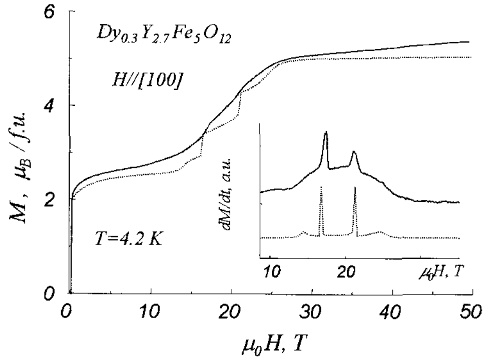

Figure 3. Magnetization curves of a $Dy_{0.3}Y_{2.7}Fe_5O_{12}$ single crystal at T = 4.2 K and H / / [100]; the insert shows variations of dM/dt during increase of the field: the solid line is the experiment and the dotted line is the theory. The theoretical curves are calculated in the framework of the quasi-Ising model ($g_{xx} = 10$, $g_{yy} = 3$, $g_{zz} = 0$).

4 Conclusions

Experiments have shown that magnetic reversal of the rare earth subsystem of dysprosium-yttrium ferrite-garnet involves several phase transitions, depending on the Dy content, orientation of the external magnetic field and temperature. The magnitude of the 3d-4f-exchange field $H_{ex} = 20$ T has been determined. A theoretical model based on the assumption of quasi Ising ordering of Dy^{3+}ions has been developed, taking into account the existence of several non-zero g-tensor components of the Dy ion.

References

1. Ozhogin, V. I., Gurtovoi, K. G., Lagutin, A. S., Reliable Solenoid for long pulses and magnetic study up to 50 T. In: High Field Magnetism, Ed. by M. Date, London, North-Holland, (1983) p. 267.
2. Herlach, F., Bogaerts, R., Deckers, I., Heremans, G., Li, L., Pitsi, G., Vanacken, J., Van Bocksta, L., Van Esch, A., *Physica B*, **201** (1994) p. 542.
3. Krupicka, S., Physik der Ferrite and der verwandten magnetischen Oxyde, Akademie der Wissenschaften, Prag, (1973).
4. Clark, A., Callen, E., *J. Appl. Phys.***39** (1968) p. 5972.
5. Zvezdin, A. K., Matveev, V. M., Mukhin, A. A., Popov, A. I., Rare-earth ions in magnetically ordered crystals, Science Publishing Co. (1985) (in Russian).

HIGH FIELD MAGNETIZATION PROCESSES OF *S*=1 ANTIFERROMAGNETIC CHAINS WITH BOND ALTERNATION

M. HAGIWARA[1,2], Y. NARUMI[3,2], K. KINDO[2,3], R. SATO[4],
H. NAKANO[5], M. KOHNO[5] AND M. TAKAHASHI[5]

[1] *The Institute of Physical and Chemical Research (RIKEN)*
[2] *KYOKUGEN, Osaka University, Japan*
[3] *CREST, Japan Science and Technology Corporation (JST)*
[4] *Department of Physics, Osaka University, Japan*
[5] *Institute for Solid State Physics, University of Tokyo, Japan*

High field magnetization measurements have been performed on some Ni bond alternating chain compounds, which are prototypical examples of the S=1 Heisenberg antiferromagnetic chain with bond alternation (HACBA). We compare the experimental results with those of some numerical calculations. From the comparison, we estimate the bond alternating ratio $\alpha \approx 0.3$ for $Ni_2(C_7H_{19}N_3)_2N_3(C_2O_4)(ClO_4)\times 0.5H_2O$ and $\alpha = 0.6$ for $Ni(C_9H_{24}N_4)N_3(ClO_4)$. We have observed a 1/2-plateau in the magnetization of the former compound and the nearly gapless behavior in the latter one. In the latter case, we have verified by experiment the gapless point of the $S = 1$ HACBA which is predicted by Affleck and Haldane.

1 Introduction

Recently, there has been a considerable interest in quantum spin systems, since Haldane [1] predicted in terms of a field theoretical method that an energy gap is open in the excitation spectrum for a Heisenberg antiferromagnetic chain (HAC) with integer spins, while gapless for HAC with half-odd-integer spins. Affleck and Haldane [2] applied Haldane's studies to bond alternating chains (HACBA) and conjectured that the gapless point exists in the HACBA with certain bond alternating ratios. Subsequent numerical studies [3] for the $S = 1$ HACBA confirmed this conjecture and the bond alternating ratio α_c was obtained as about 0.6 using the Hamiltonian defined by,

$$H = \sum_{i=1}^{N/2} J \boldsymbol{S}_{2i-1} \cdot \boldsymbol{S}_{2i} + \alpha J \boldsymbol{S}_{2i} \cdot \boldsymbol{S}_{2i+1} \tag{1}$$

where J is the exchange constant, α the bond alternating ratio, and $\boldsymbol{S}_{2i-1}$, $\boldsymbol{S}_{2i}$, $\boldsymbol{S}_{2i+1}$ the $S = 1$ spin operators. In the mid 90's, nickel bond alternating chain compounds, which are regarded as the $S = 1$ HACBAs, were synthesized and preliminary magnetic studies were performed. Under these circumstances, experimental studies of the $S = 1$ HACBA were reported quite recently [4,5]. In reference [5], high field magnetization was measured under the magnetic field up to 57 T. In this paper, we extend the measurement up to 67 T and report the results of experimental and numerical studies for some $S = 1$ HACBA compounds.

2 Experiment

Nickel bond alternating compounds used in this study are $Ni_2(C_7H_{19}N_3)_2N_3(C_2O_4)(ClO_4)\times 0.5H_2O$ and $Ni(C_9H_{24}N_4)N_3(ClO_4)$. Syntheses of these compounds were reported in the previous papers [4,5]. Both compounds crystallize in the triclinic system, space group $P\bar{1}$. The former compound consists of Ni chains bridged by oxalato groups and azido groups, alternately. Ni atoms in the latter compound are linked only by the azido group, but two kinds of alternating azido groups are present in the chain. Susceptibility measurements were done with a SQUID magnetometer (Quantum design's MPMS2) at RIKEN and high field magnetization measurements were performed by using a pulse magnet at KYOKUGEN in Osaka University.

Susceptibility of a single crystal sample of $Ni_2(C_7H_{19}N_3)_2N_3(C_2O_4)(ClO_4) \times 0.5H_2O$ along the chain direction shows a hump around 40 K. Below this temperature, the susceptibility steeply decreases upon further cooling. The high field magnetization process of this compound is shown in Fig. 1. No magnetization appears up to 17 T and increases almost linearly with increasing field up to about 43 T. Then, a plateau appears up to 55 T and the magnetization increases again.

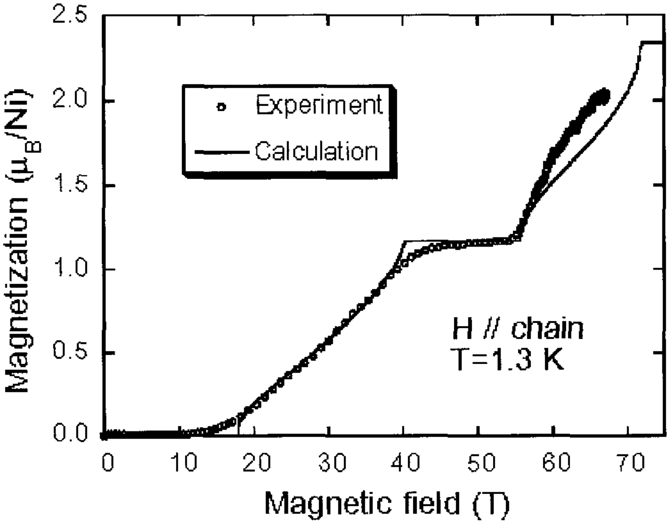

Figure 1. The magnetization curve at 1.3 K of a single crystal sample of $Ni_2(C_7H_{19}N_3)_2N_3(C_2O_4)(ClO_4) \times 0.5H_2O$ along the chain direction. The solid line represents the magnetization curve calculated by a PWFRG method (T = 0 K).

The temperature dependence of the susceptibility of a powder sample of $Ni(C_9H_{24}N_4)N_3(ClO_4)$ is quite similar to that of the $S = 1/2$ HAC which has the gapless excitation spectrum. A round maximum is seen around 120 K and the susceptibility decreases gradually down to about 10 K with decreasing temperature further. Then, the susceptibility decreases abruptly. Magnetization process of this powder sample at 1.4 K up to about 50 T is shown in Fig. 2. The magnetization increases with a concave curvature when the magnetic field is increased. No energy gap was observed with the experimental accuracy.

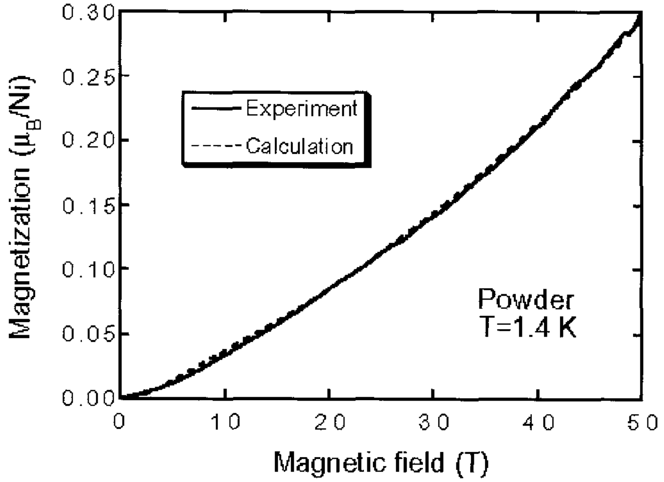

Figure 2. The magnetization curve of a powder sample of $Ni(C_9H_{24}N_4)N_3(ClO_4)$ at 1.4 K (solid line) and the magnetization curve calculated by a PWFRG method ($T = 0$ K) (broken line).

3 Discussion

Here, we compare the experiments with some numerical calculations. The solid line in Fig. 1 represents the magnetization curve at zero Kelvin calculated by the product wave-function renormalization-group (PWFRG) method [6] for the Hamiltonian (1) including the single ion anisotropy term DS_{iz}^2 and the Zeeman term $g\mu_B S_{iz} H$. The agreement between the experiment and the calculation is fairly good, except for the phase boundaries and the high field region above 60 T. From this fit, $\alpha = 0.25$, $J/k_B = 44.2$ K, $D/J = 0.08$ and $g = 2.34$ are evaluated and they are close to those obtained from the fit of the susceptibility ($\alpha = 0.3$, $J/k_B = 42.8$ K, $D/J = 0.07$ and $g = 2.29$) [7]. Accordingly, the compound $Ni_2(C_7H_{19}N_3)_2N_3(C_2O_4)(ClO_4)\times 0.5H_2O$ is regarded as the $S = 1$ HACBA with the bond alternating ratio $\alpha \approx 0.3$. The susceptibility of $Ni(C_9H_{24}N_4)N_3(ClO_4)$ is compared with the susceptibility calculated by a quantum Monte Carlo method (loop algorithm) [8] (96 sites) for the Hamiltonian (1) for various bond alternating ratios. The agreement between the experiment and the calculation is satisfactory over the whole temperature region when $\alpha = 0.6$. From this comparison, the exchange constant and the g value of Ni^{2+} are obtained as $J/k_B = 110$ K and $g = 2.46$. The broken line in Fig. 2 is a numerical result of the magnetization at zero Kelvin calculated by the PWFRG method for the Hamiltonian (1) including the Zeeman term with $J/k_B = 115$ K and $g = 2.46$. The calculation is in good agreement with the experiment. Thus, the compound $Ni(C_9H_{24}N_4)N_3(ClO_4)$ is considered to be the $S = 1$ HACBA with the bond alternating ratio $\alpha \approx 0.6$. The existence of the gapless point in the $S = 1$ HACBA is confirmed by experiment and the bond alternating ratio for the gapless point is expected to exist around 0.6.

4 Conclusion

We have performed the susceptibility and the high field magnetization measurements on some nickel bond alternating compounds which are regarded as the $S = 1$ HACBA's. In $Ni_2(C_7H_{19}N_3)_2N_3(C_2O_4)(ClO_4)\times 0.5H_2O$, we firstly observed a 1/2 plateau of the magnetization in the $S = 1$ HACBA. The compound $Ni(C_9H_{24}N_4)N_3(ClO_4)$ shows the gapless behavior in the susceptibility and the magnetization, and the results are in good agreement with the numerical calculation for the $S = 1$ HACBA with $\alpha = 0.6$.

Acknowledgments

This work was done under the Visiting Researcher's Program of KYOKUGEN in Osaka University. This study was supported in part by a Grand-in-Aid for Scientific Research from the Japanese Ministry of Education, Science, Sports and Culture.

References

1. Haldane, F. D. M., *Phys. Rev. Lett.* **50**, (1983) p. 1153.
2. Affleck, I., Haldane, F. D. M., *Phys. Rev. B* **36**, (1987) p. 5291.
3. Kato, Y., Tanaka, A., *J. Phys. Soc. Jpn.* **63**, (1994) p. 1277.
   Yamamoto, S., *Phys. Rev. B* **52**, (1995) p. 10170.
4. Hagiwara, M., Narumi, Y., Kindo, K., Kohno, M., Nakano, H., Sato, R., Takahashi, M., *Phys. Rev. Lett.* **80**, (1998) p. 1312.
5. Narumi, Y., Hagiwara, M., Sato, R., Kindo, K., Nakano, H., Takahashi, M., *Physica B* **246-247**, (1998) p. 509.
6. Nishino, T., and Okunishi, K., *J. Phys. Soc. Jpn.* **64**, (1995) p. 4085.
7. Nakano, H., Hagiwara, M., Chihara, T., Takahashi, M., *J. Phys. Soc. Jpn.* **66**, (1997) p. 2997.
8. Kohno, M., Takahashi, M., Hagiwara, M., *Phys. Rev. B* **57**, (1998) p. 1046.

COMPRESSION OF METALS UNDER INTENSE SHOCK WAVES

R. F. TRUNIN
RFNC – VNIIEF, Sarov, Russia

This paper presents analysis of results obtained by studying shock compression of metals by absolute methods, carried out in laboratory environments and at underground nuclear explosions. Maximum pressures were in the first case, 2.5 TPa and in the second case, 10 TPa. The data obtained complement each other. It is shown that at pressures of terapascals, averaging occurs of the individual properties of adiabats of various metals groups. This is manifested as leveling of their slopes.

1 Introduction

The research of shock parameters of metals and primarily of their shock compressibility was initially related to the problem of designing nuclear weapons. In the USA, experiments of that kind were started in 1945. Two years later, the compressibility of uranium under pressures up to 50 GPa was first measured in Russia. Up to now, work has been done on obtaining new positions of compression curves (Hugoniots) for the materials that had already been studied, and on widening the investigated pressure range. This is due to the fact that, currently, knowing the shock properties of various materials can solve many scientific and technical problems. These are the problems of high-velocity impacts; particularly spacecraft protection, meteorite protection, the inner composition of the Earth and of other planets, verification of theoretical models of material behavior under extreme loading conditions, synthesis of novel materials, high pressure chemistry and more.

In 1995, resulting from the work related to the pressure increase, laboratory shock generators driven by high explosives were built and used in Russia to generate pressures higher than 2500 GPa in heavy metals. These pressures were approximately a factor of two higher than those produced earlier in our country, and a factor of five (for the same materials) higher than pressures produced at research centers in other countries. Even higher pressures, up to 10000 GPa (10 TPa), were generated in underground nuclear tests. Both the figures - 2500 and 10000 GPa - were measured by so-called absolute investigation techniques, when kinematic and thermodynamic parameters of material compression were independent of additional assumptions and were determined only by the accuracy of the experiment, itself.

By now, a huge amount of experimental data on the shock compressibility of various materials has been accumulated. Here, we will dwell upon the results of 'solid' element investigations, and only those elements whose compressibility has been studied both under laboratory and test-site conditions will be considered in more detail. These elements are iron (ST-3), aluminum, copper, lead, cadmium and molybdenum.

2 Laboratory Devices

Let us briefly dwell upon the designs of measuring devices applied in shock compressibility studies and test-site experiments. Their operation is based on using high explosives, the energy of which generates shock pressures from units up to 2500 GPa in a tested sample.

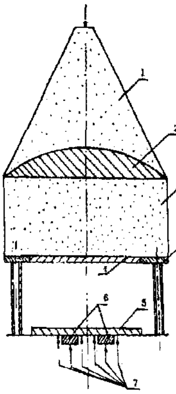

Figure 1. Measuring device with an accelerated aluminum impactor. 1-lens-shaped HE charge; 2 -planowave lens; 3 - main HE charge; 4 - impactor; 5 - reference-metal shield; 6 - tested sample; 7 - shorting-pin detectors.

There are several types of laboratory devices (Fig. 1). They are based on acceleration of metal plates by explosion products. Impact of these metal plates against the investigated samples causes shock compression pressures of up to 200 GPa.

Generators having spherical geometry [1] produced the highest pressures, ranging up to 2500 GPa, (Fig. 2). A HE charge detonation is triggered simultaneously over the entire outer surface. The explosion products of the spherically convergent detonation wave, expanding through the small air gap, accelerate the steel hemispherical impactor ('shell') to the center (the radius decreases).

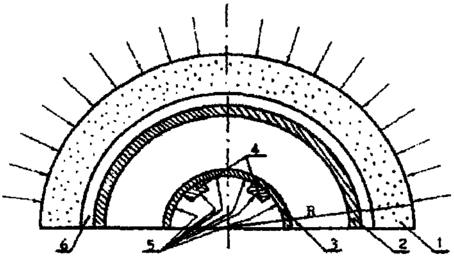

Figure 2. Measuring device with a spherically accelerated impactor shell. 1 - HE charge, initiated simultaneously over the whole surface; 2 - impactor-shell (Fe); 3 - shield (Fe); 4 - tested samples; 5 - shorting-pin detectors; 6 - air gap.

In the available devices, the shell velocity, which continuously increases as it converges towards the center, varies from 6.2 km/s (pressures in iron of ~270 GPa are close to those generated in accelerating systems -'guns') up to 22.7 km/s corresponding to pressure of 1.8 TPa in iron.

3 Test Site Measurement Set-Up

We will consider [2] the measurement setup for testing a relatively high-power charge (its energy release is more than 100 kilotons). When the nuclear charge, placed in a special chamber made in a rock is exploded, the explosion energy propagating as radiation energy and kinetic energy of the evaporated charge (the temperature of the explosion is 10^6 -10^8 degrees) affects the rock of the chamber walls, evaporating it. The intense heat wave generated in the rock and motion of the rock vapor is promptly converted into shock waves. In the rock close to the chamber walls, the shock waves generate pressures from units up to tens of TPa, depending on the explosion energy. In the metallic samples affected by those shock waves, equal or even higher pressures are produced.

The set-up for *compressibility measurements under test-site conditions is shown* in Fig. 3 (a,b). Fig. 3(a) shows versions of absolute compressibility measurements for iron in the terapascal pressure range by an impedance-matching technique. The device is comprised of a damping, low-density foam spacer ($\rho_0 \approx 0.03$ g/cm^3), a steel (St-3) impactor and a steel target. There is an air gap between the rock and device.

Fig. 3b shows the scheme of wave velocity measurements in the set comprised of three samples of various materials placed one behind the other. The first sample (shield) is a standard, located downstream, the equation of state of which is known. The tested samples are placed behind it. The velocities of shock waves are measured during their consecutive travels though the samples.

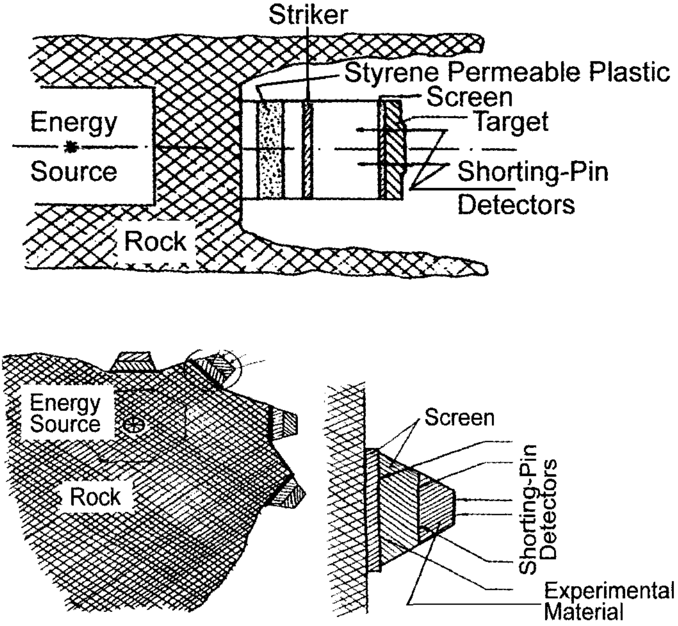

Figure 3. Variants of experiment set-up during underground nuclear explosion for measuring the velocity of the impactor flight and that of a shock in the target.

4 Experimental Compressibility Data Obtained by Absolute Methods

By now shock compressibility in various ranges of pressures has been determined for sixty metal elements of the periodic table of elements, i.e., for the majority of metals.

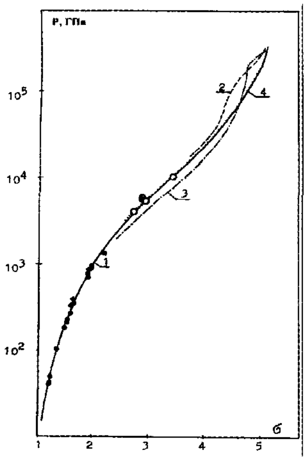

Figure 4. Interpolation Hugoniot plot for iron. • - laboratory measurements; O,⊗ - measurements during underground explosions; O - absolute measurements. 2,3,4 - calculations by SCF, MHFS and TFQC, respectively.

Under laboratory conditions, the pressures were as follows: for iron - 1.8 TPa, tantalum - 2.5 TPa, titanium - 1.3 TPa, molybdenum - 2.1 TPa. More than 11 metals were studied under pressure of up to 1.0 TPa and the remainder, depending on their initial density, were studied in the pressure range from 60 GPa (Li) up to 500 GPa (W).

Let us consider in detail the measurements of metal compressibility in underground nuclear tests.

1.1 Iron

Let us return to the discussion of the set-up and results of measurements performed during underground explosions. First, let us dwell upon measurements of iron compressibility by the deceleration technique. The layout of experimental versions is given in Fig. 3a. The impactor flight was recorded with electrical shorting-pin detectors. The iron data obtained in underground nuclear experiments are given in P-ρ coordinates (Fig. 4). The general conclusion that can be made on the basis of the considered results is that there is a good agreement among all the results.

1.2 Copper, lead, cadmium and molybdenum

The calculation of iron (the shield in the impedance - matching technique) Hugoniot by absolute methods allowed us to determine compression parameters of copper, lead, cadmium and molybdenum, for which the relations among their wave velocities and between each of them and that of iron had been determined earlier.

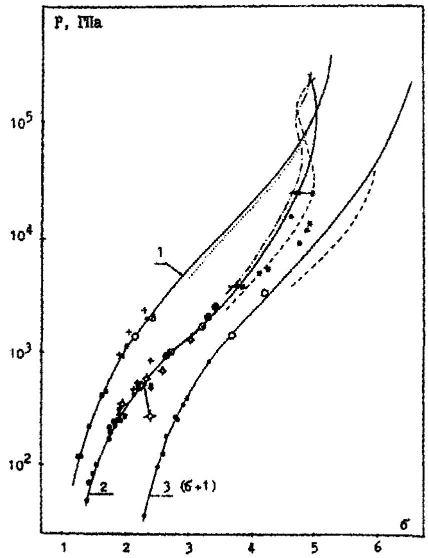

Figure 5. Interpolation Hugoniots of (1) molybdenum, (2) aluminum, (3) cadmium. • - laboratory measurements; O,⊙,⊕,+,Δ,* - test-site measurements; O,⊙ - absolute measurements.

Figure 5 compares the data obtained in laboratories and parameters measured by foreign research in underground tests. One can see quite a satisfactory agreement between the laboratory and the test-site measurements for all of the metals. In the range of high shock parameters for lead and cadmium, there is a good agreement between the data obtained in Russia and those obtained in the USA. For molybdenum and copper, some results obtained by Americans differ from the averaged P(ρ) relation and exceed the permissible experimental errors.

The laboratory devices designed in 1996 allowed us to solve this problem. In particular, through a hemispherical system, the data on molybdenum compressibility at pressures of 2.0 TPa were obtained, i.e. the data that agreed with those obtained in [7]. However, the other parameters such as D and U velocities, density, and energy happened to be different, so the new point on the Hugoniot curve of molybdenum did not coincide with that from [7] but corresponded to the linear D(U) relation. This was the first case used to verify the results of test-site measurements by a laboratory experiment performed at terapascal pressures.

Shock waves affect different physical processes of the tested metals, such as lattice compression by thermal excitation of nuclei and electrons, melting, excitation and collection of electrons. Ionization of atoms occurs at high pressures. The completion of these processes means the establishment of some 'averaged' metal states when individual features of crystals do not manifest themselves. This averaging relevant to the loss of individual features by elements apparently comes to an end (depending on the metal from the periodic table) at pressures of 1-2 TPa; after that, their D-U curves are characterized

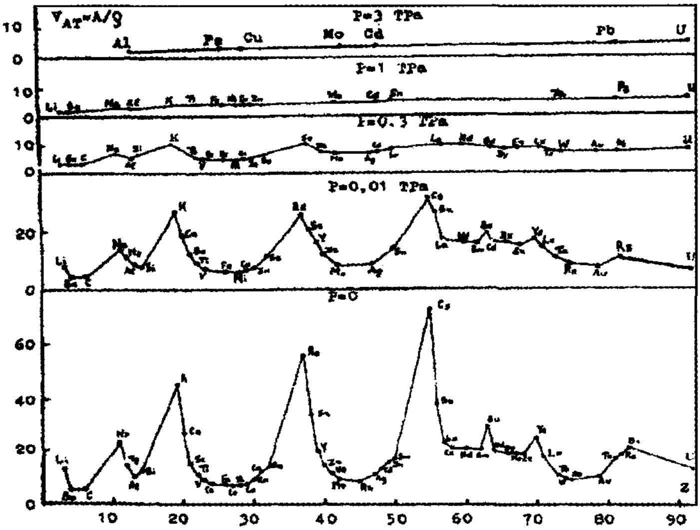

Figure 6. The diagram of atomic volume changes versus pressure of elements.

with almost constant slopes. Fig. 6 shows the changes of atomic volumes of elements depending on pressures. Under standard conditions (P=0) there is a pronounced periodic dependence of element atomic volumes (Vat) on the atomic number Z that corresponds to the consecutive filling of atom energy levels with electrons.

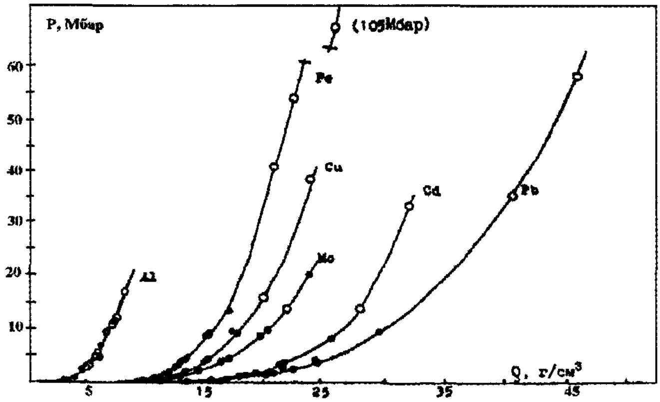

Figure 7. Absolute measurements: • - laboratory measurements; O - underground explosion data

'Loose' structures of alkaline and alkaline-earth elements are characterized by loosely-bonded electrons in s-levels and depicted by the higher section of the diagram corresponding to the maximum atomic volumes. 'Densely-packed' structures, with a great number of electrons filling d-levels, correspond to the minimum atomic volumes and are peculiar to transition metals.

When pressures increase, atomic volumes of elements equalize. In this case, the maximum volume change takes place in elements with loose structures at pressures of 3000 GPa. The V(Z) periodicity is not obvious and at $P > 1$ TPa it practically disappears, i.e., the elements 'lose' their individual features.

Let us note that the average experimental slope of Hugoniots of the metals, studied under underground explosion conditions, is $D_u \approx 1.25 \pm 0.04$ (from 1.15 to 1.35). It approximately corresponds to the value of the Hugoniot slope calculated by the modified Thomas-Fermi (TFQC) model [10] (taking into account nuclei interaction by [11]) determined at pressures of more than units and tens of TPa when this model is assumed to be valid. Fig. 7 shows the data on the metal compressibility obtained by the absolute technique. Lead is the most compressible material in the group of heavy metals. Cadmium, molybdenum, copper and iron follow it.

To complete the consideration of results on compressibility of metals using strong shock waves caused by chemical and nuclear explosions, we note that peaceful nuclear explosions result in higher parameters. These results are up to hundreds of TPa by comparative measurements of the compressibility of substances, when the equation of state of one of the substances is known. Such measurements were performed. Though the accuracy of determining compressibility in them is, in our opinion, still insufficient for strict quantitative determinations, these results are good illustrations of possibilities to perform in principle measurements using shock waves from nuclear explosions.

References

1. Al'tshuler, L. V., Trunin, R. F., et al. *Uspekhi Fiz. Nauk.* **166** (5) (1956) p. 575.
2. Trunin, R. F., *Uspekhi Fiz.Nauk.* **164** (110,1215 (1994).
3. Sin'ko, G.V, *Teplofiz.Vys.Temp.* **2** (6), (1983) p. 1041.
4. Nikiforov, A. F., Novikov, V. G., Uvarov, V. B., Mathematical modeling. *Physical and chemical substance properties. M.,* Nauka, 162 (1989).
5. Kalitkin, N. N., Kuz'mina, L.V., Prepr. Ins. of Appl. Math. Akad. Nauk SSSR, **35** (1977) p. 54.
6. Kopishev, V. P., Chisl.metodi.mekhan.sploshn.sredi. **8**(6), (1977) p. 54.
7. Ragan, III, C. E., Silbert, M. G., Diven, B. C., *J. Appl. Phys.* **48**(7), (1977) p. 2860.
8. Mitchell, A. C., Nellis, W. J., et al., *J. Appl. Phys.* **69**(5), (1991) p. 2981.

FUSION IN MAGNETICALLY COMPRESSED TARGETS

V. N. MOKHOV
Russian Federal Nuclear Center (RFNC-VNIIEF),
All-Russian Scientific Research Institute of Experimental Physics, Sarov, Russia

A comparative analysis is presented of the positive and negative features of systems using magnetic compression of the thermonuclear fusion target (MAGO/MTF) aimed at solving the controlled thermonuclear fusion (CTF) problem. The niche for the MAGO/MTF system, among the other CTF systems, in the parameter space of the energy delivered to the target, and its input time to the target, is shown. This approach was investigated at RFNC-VNIIEF for more than 15 years using the unique technique of applying explosive magnetic generators (EMG) as the energy source to preheat fusion plasma, and accelerate a liner to compress the preheated fusion plasma to the parameters required for ignition. EMG based systems produce already fusion neutrons, and their relatively low cost and record energy yield enable full scale experiments to study the possibility of achieving ignition threshold without constructing expensive stationary installations. A short review of the milestone results on the road to solving the CTF problem in the MAGO/MTF system is given.

1 Discussion

Present studies on pulsed thermonuclear fusion are generally based on rapid compression of small DT gas masses using a liner. Areas of such studies can be distinguished depending on the driver type used to drive the liner and compress the thermonuclear target. Most widespread are experiments using powerful lasers (LTF) and beams of accelerated charged particles: electrons (electron thermonuclear fusion) or ions (ion thermonuclear fusion, ITF). In recent years, the systems in which the liner is driven by super-high magnetic fields (magnetic implosion, MAGO) increasingly attracted attention. There are a number of other suggestions for achieving thermonuclear ignition, and a large number of papers are devoted to Hohlraum base systems.

Soft x-rays for Hohlraum can be produced with powerful lasers and charged particle beams as well as with magnetic fields. Ref. [1] drives the liner, fabricated from a large number of thin wires and known as a “squirrel cage” with strong magnetic fields, using the stationary facility HBFA-Z. Ref. [2] shows both, theoretically and computationally, the possibility of producing megajoule quantities of soft x-rays with EMG.

The above major CTF activity areas are not a random chaotic set of different methods to solve the CTF problem. Each area occupies its own region in the *(E,t)* parameter plane, where E is driver energy and t is time of energy supply to the target. If multi-layer thermonuclear targets with sufficient energy accumulation in the central region with DT gas are used, it can be shown [3] that the energy required for thermonuclear ignition should meet the approximate condition

$$E \geq At^k,$$

where the exponent k, depending on the energy cumulation degree in a layered system, is close to 1. A is on the order of 0.1, if E is taken in megajoules and t in nanoseconds. Fig. 1

shows the ignition region and marks off approximate regions of E and t values for LTF, ITF and target magnetic implosion systems MAGO. The gas-dynamical thermonuclear fusion (GDTF) system is also shown where a multi-layered thermonuclear target is imploded through liner acceleration by chemical explosive (HE).

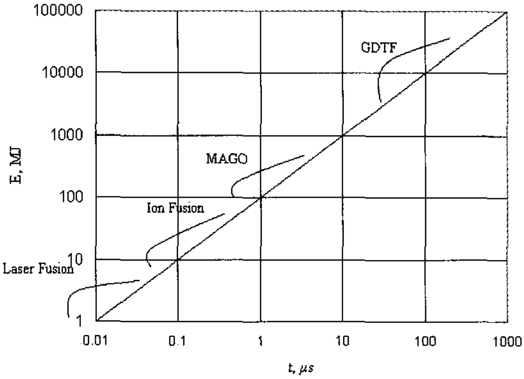

Figure 1. Parameter ranges of E, driver energy, and t, time of the energy supply to the thermonuclear target, at which thermonuclear ignition is reached.

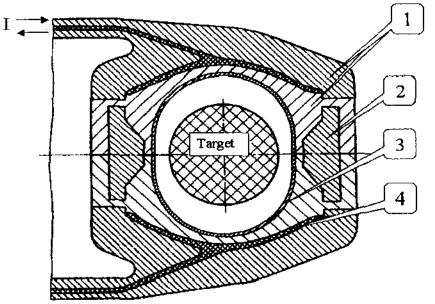

Figure 2. MAGO system physical scheme with spherical layered thermonuclear target: 1-conductors, 2-concentrator, 3-inner shell, 4-insulator.

As seen in Fig. 1, the ITF systems require energy several tens of times, and MAGO systems several hundreds of times as high as LTF systems do. However, the costs of stationary, nonconsumable power facilities for ITF (accelerators) and MAGO (magnetic energy storage or capacitors) are also reduced by the same orders of magnitude. Thus, the costs of making stationary facilities for ITF and MAGO prove to be about the same as those for LTF and possibly even lower.

This paper discusses, in detail, various types of systems with magnetic field driven liners that immediately implode the thermonuclear target, i.e. various types of magnetic implosion systems MAGO. The MAGO systems have additional attractive features, as the experimental studies (up to full-scale thermonuclear target ignition experiments) do not require construction of an expensive stationary facility. Such a facility would be required only at the construction stage of the power plant. Instead, the experiments can use expendable explosive magnetic generators (EMG) whose development and fabrication technology has been well mastered at RFNC-VNIIEF. Therefore, the costs of such studies can be relatively low. Currently, we have EMG capable of generating ~200 MJ of magnetic energy. Design studies have been made for EMG systems in which magnetic energy up to a GJ can be generated.

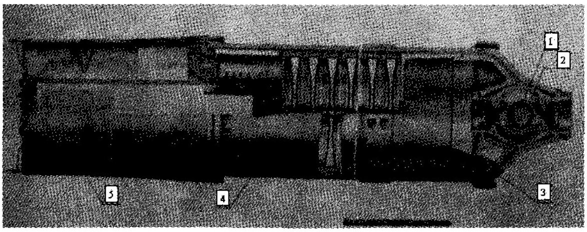

Figure 3. General view of the MAGO system with disk EMG used to accelerate imploding liner: 1 - liner, 2 - fusion target, 3 - opening switch, 4 - DEMG, 5 - helical EMG based pre-amplifier.

Historically, the first thermonuclear target magnetic implosion system was suggested and computationally modeled in 1972 [4,5] based on a liner imploding a spherical solid thermonuclear target with DT gas in the central area. Fig. 2 presents a schematic view of a potential ponderomotive unit type designed for implosion of a spherical thermonuclear target. Fig. 3 shows the MAGO system as a whole with the disk EMG and the ponderomotive unit. Feasibility of spherical thermonuclear target implosion under action of an axially symmetric magnetic field was demonstrated computationally (Fig. 4) and experimentally on models (Fig. 5) [5,6]. With a fair symmetry of the spherical target compression, thermonuclear ignition can be achieved by EMG magnetic energy on the order of 100 - 500 MJ. Computational thermonuclear energy release per event up to several tens of GJ can be obtained. A disadvantage of the systems is a high requirement for symmetry of the target spherical compression. The requirement is somewhat lower in the GDTF systems but it remains on the verge of modern technical abilities.

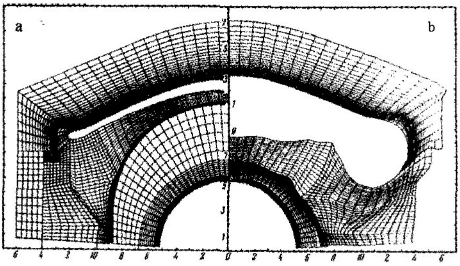

Figure 4. Initial (a) and final (b) geometry in 2-D computation for the model experiment demonstrating the feasibility to obtain spherical shape of the liner at its approach to the thermonuclear target.

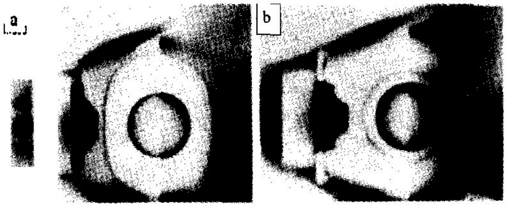

Figure 5. X-ray image at initial and final times in the model experiment with geometry of the ponderomotive unit selected by the 2-D computation in Fig. 4.

Cylindrical systems were considered [7] where energy is cumulated with one or more "magnetic pads". Fig. 6 shows the layout of the magnetic pad ponderomotive unit system. According to computations, at perfect compression symmetry, the imploding liner energy should be more than 25 MJ/cm of cylinder length for the system to achieve thermonuclear ignition. In the magnetic pad system this occurs at an EMG energy higher than 100 MJ. However, one must solve highly complicated problems relating to energy losses during the magnetic pad operation and the thermonuclear target compression asymmetry.

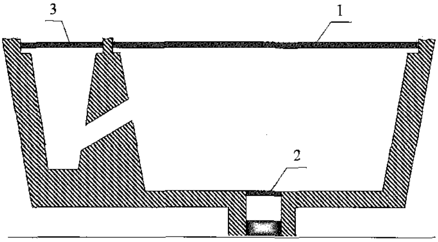

Figure 6. (above) Design of the ponderomotive unit with magnetic puff: 1-external massive liner, 2-second liner, 3-liner energizing the magnetic puff.

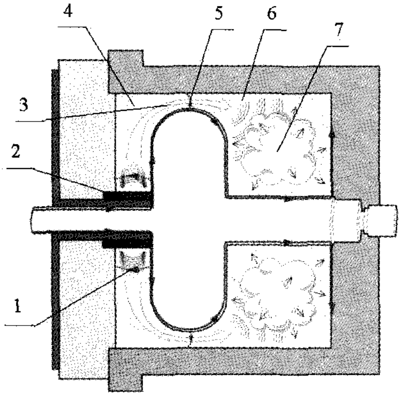

Figure 7. Design of the gaseous ponderomotive unit where magnetized DT gas is preheated: 1-region of the initial discharge, 2-insulator, 3-nozzle, 4-chamber of plasma acceleration, 5-discharge at the nozzle, 6-chamber where the fusion plasma stagnates, 7-fusion plasma.

As previously stated, in all systems based on DT gas implosion by a liner, the most complicated problem is to achieve the high compression required for thermonuclear ignition, hence, the high symmetry needed for target compression. In 1981, based on the availability of relatively high energies in the MAGO systems, a new thermonuclear target design was proposed [8] in which magnetized low-density (initial density around 10^{-6} g/cm^3) DT plasma heated to 0.2 - 0.5 KeV is produced in the first phase (Fig. 7). The liner spherically or cylindrically compresses the plasma in the second phase (Figs. 8, 9). The computational DT gas ignition in the system is reached at relatively low compression (no more than by 10 times in radius) with the minimum size of the DT gas region on the order of one centimeter at ignition. The required compression symmetry is then at the level already reached by modern experimental engineering.

Early MAGO experiments to generate magnetized plasma with neutron production were conducted at RFNC-VNIIEF in 1981. The maximum neutron yield from heated plasma (without further compression) is ~5×10^{13} neutrons per pulse. Stability of the obtained results was verified, and the dependence of the chamber operation on the chamber parameters (DT gas initial density, magnitude of currents supplied into the chamber, nozzle width, chamber sizes, etc.) was found. The experimental data agreed well with the computations (Figs. 10-12).

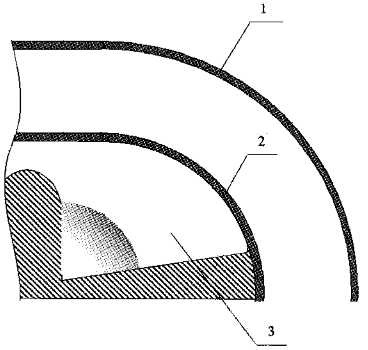

Fig. 8. Scheme of preheated DT plasma in a quasi-spherical compression: 1-high-energy liner, 2-chamber external wall, 3- second chamber.

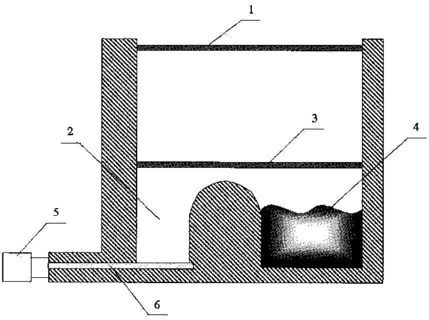

Figure 9. Scheme of preheated DT plasma cylindrical compression: 1-high energy liner, 2-first chamber, 3-chamber external wall, 4-second chamber, 5-energy source, 6-insulator.

In 1987 the feasibility of accelerating a cylindrical imploding liner (for implosion of a thermonuclear target of ~100 g in mass) to 25 km/s velocity was shown experimentally. Somewhat later, a ~1 g liner was accelerated to 45 km/s [9].

In 1987, jointly with the Kurchatov Institute affiliate branch under the leadership of E. P. Velikhov, the feasibility of a thermonuclear power plant based on MAGO thermonuclear targets was investigated. The target energy release is maintained within a steel chamber. An immovable storage inductor positioned outside the steel chamber is used for the driver.

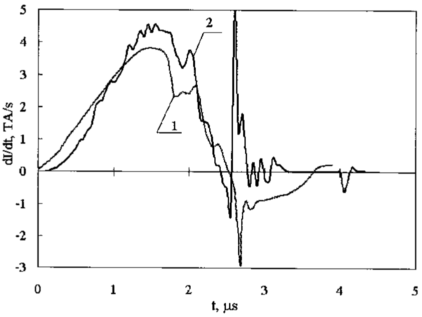

Figure 10. Computational and experimental time dependence of current derivative (with respect to time) in the MAGO chamber at the DT gas preheating phase: 1 - experimental, 2 -numerically modeled.

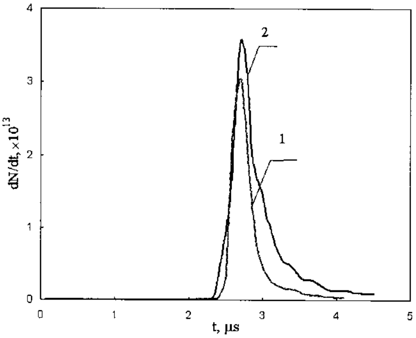

Figure 11. Computational and experimental dependence of derivative (with respect to time) of neutron yield from the MAGO chamber at the preheating phase: 1 - experimental, 2 -numerically modeled.

It was shown that good efficiency from the power plant could be achieved at the target thermonuclear energy release of one GJ or more. Under the leadership of S. B. Kormer, a study of the feasibility of implosion containment in steel chambers was initiated. Experiments using explosions of 100 kg (25 MJ) of chemical explosive were successfully conducted [10].

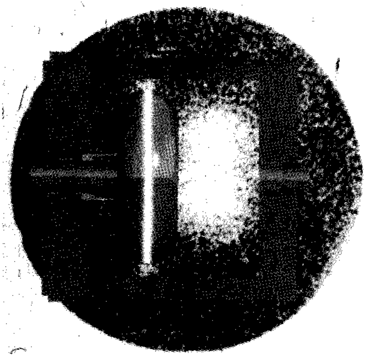

Figure 12. Time-integral pinhole image of the neutron generation region in the MAGO chamber at the preheating phase.

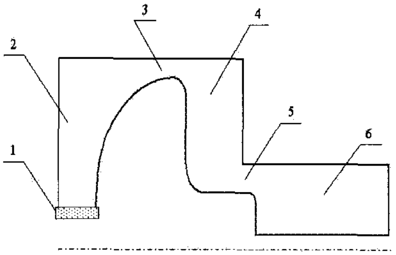

Figure 13. Physical scheme of a 3-chamber ponderomotive unit with two nozzles for fusion plasma preheating: 1-insulator, 2-first chamber of plasma acceleration, 3-first nozzle, 4-second chamber, 5-second nozzle, 6-fusion plasma stagnation chamber.

Since 1991, the work has been conducted by collaboration between RFNC-VNIIEF and LANL (USA). In 1983, LANL scientists theoretically investigated the feasibility of thermonuclear ignition by implosion of low-density magnetized DT plasma independently from RFNC-VNIIEF [11]. Such systems were called MTF (Magnetized Target Fusion). The MAGO system, using implosion of low-density magnetized heated plasma, was given the name MAGO/MTF. The principal goal of the effort is to study high-temperature plasma generated in MAGO/MTF, system preparation for experiments with further compression of heated plasma, and achievement of the thermonuclear ignition, if possible. The efforts will be discussed below in more detail.

In physical processes and parameters of thermonuclear plasma, the MAGO/MTF system occupies an intermediate position between the design of systems with high-density thermonuclear target base inertial thermonuclear fusion (laser and ion fusion) and that of stationary systems (TOKAMAKs). As previously stated, MAGO/MTF activities involve no high expenditures to construct large stationary facilities. There are a number of other advantages compared to the LTF, GDTF type systems, for example. MAGO/MTF requires lower compressions and involves less stringent requirements for compression symmetry. Compared to TOKAMAKs, by virtue of the pulsed character of the MAGO/MTF system operation, not all instabilities of magnetized low-density plasma are dreadful - only those are which can provide dangerous values of perturbation growth within microseconds. A drawback of MAGO/MTF is its high sensitivity to heavy chemical element impurities that can appear in DT plasma. The main objective of the joint VNIIEF-LANL works was to study this issue.

In the first phase of MAGO chamber operation, plasma heating, the main impurity sources can be material washing off from the chamber walls and insulator vaporization. A serious hazard comes from impurities from the chamber walls (the insulator vapor effect can be avoided, see below). The early joint experiments conducted at LANL were devoted to this issue. The measured maximum energy losses due to x-ray of heated plasma show that the heavy element impurity quantity in the plasma is quite small.

The second objective is to solve the problem of insulator vapors. Judging by a number of indirect evidences, insulator vaporization occurs in most experiments and the vapors invade the second section of the MAGO chamber. The RFNC-VNIIEF experiment conducted in 1997 showed that when there was no insulator vaporization (when the voltage across the insulator was quite small), DT plasma could exist in the MAGO chamber longer than 10 microseconds. We considered several ways to avoid insulator vapor invading the MAGO chamber ignition section where the DT gas compression is anticipated.

The simple way is the application of a three-chamber ponderomotive unit with two nozzles (Fig. 13). According to computations, in the third section of the chamber pure DT plasma, free of insulator vapors, can be produced at quite a high preheating (≥ 0.5 KeV).

This option seems preferable, as the conditions of the insulator and first chamber operation are experimentally verified, and setting up new experiments requires no complex technological developments. Therefore, the experimental studies began from there. This is consistent with potential use of the three-chamber system proposed by RFNC-VNIIEF in 1983 in order to attain a number of additional advantages from heated DT gas compression.

Parallel to the MAGO chamber refinement, theoretical, computational and experimental studies of issues relating to liner acceleration for DT gas implosion continue. A series of experiments at the LANL stationary facility, Pegasus, were conducted to study solid liner flight stability and liner interaction with end walls, to select the most promising liner material [12]. There was good agreement with computations by developed 2-D techniques, taking into account material strength and plasticity. This allows use of the techniques to select a compression system. The feasibility to accelerate liners without cumulative jet formation, where the liner glides against the end walls, is shown.

The first experiment, HEL-1, [13] was conducted jointly with LANL to verify the full-scale imploding liner. In the experiment, the liner velocity was about 10 km/s and the kinetic energy of the liner was 20 MJ.

According to the existing program, the following is required to commence full-scale experiments to study feasibility of thermonuclear ignition in the MAGO/MTF system:

- complete the verification of preheating DT plasma with quite low heavy element impurities,
- complete the refinement of the liner acceleration system to implode plasma, and
- design of the entire experimental system and verification of its serviceability.

2 Conclusions

MAGO/MTF systems for solving the controlled thermonuclear fusion problem can have certain advantages over alternative driver systems. Facility costs for MAGO/MTF systems are relatively inexpensive, and the EMG technology used in the system is well mastered. MAGO/MTF requires lower compressions and less stringent compression symmetry requirements than some systems (although compression symmetry requirements are still high) and it tolerates instabilities of magnetized low-density plasma that do not provide dangerous values of perturbation growth within microseconds. However, MAGO/MTF is highly sensitive to heavy element impurities that can appear in DT plasma during heating and from insulator vaporization. Feasibility studies of thermonuclear ignition in the system are planned.

References

1. Sanford, T. W., Allshouse, G. O., Marder, B. M., et al., X-Ray Power Increase from Symmetrized Wire-arrray Z-pinch Implosions, Proceedings of 11th International Conference On High Power Particle Beams, Prague, Czech Republic, 1996, p. 146.
2. Buyko, A. M., Burenkov, O. M., Garanin, S. F., et al., Changing mass liner system for soft X-ray generation, Zababakhin Science Conference, Cheljabinsk-70, 1995.
3. High energy-density physics. Proceedings of RFNC-VNIIEF, Ed. by V. N. Mokhov, R. F. Trunin et al., Sarov, Russia, 1997.
4. Khariton, Yu. B., Mokhov, V. N., Yuakubov, V. B., et al., On operation of magnetically imploded thermonuclear targets, UFN, **120** (1976) p. 706.
5. Mokhov, V. N., Chernyshev, V. K., Yuakubov, V. B., et al., On feasibility of controlled thermonuclear fusion problem solution basing on magnetogasdynamical energy cumulation, Dokl. AN SSSR **247** (1979) p. 83-86.
6. Degnan, J. H., Lehr, F. M., Beason, D. J., et al., Electromagnetic Implosion of Spherical Liner, *Phys. Rev. Lett.* **74** (1995) p. 98.
7. Buyko, A. M., Garanin, S. F., Mokhov, V. N., et al., On possibility of low-dense magnetized DT-plasma ignition threshold achievement in MAGO system, Digest of Technical Papers, Spring Workshop on Basic Science Using Pulsed Power, Santa Barbara, Cal., 1995.
8. Buyko, A. M., Volkov, G. I., Chernyshev, V. K., et al., Investigation of thermonuclear magnetized plasma generation in the magnetic implosion system MAGO, Proceedings of 9th IEEE International Pulsed Power Conference, Albuquerque, N.M., 1993. **1**, p. 156.
9. Buyko, A. M., Chernyshev, V. K., Demidov, V. A., et al. Investigation of the dynamic of a cylindrical exploding liner accelerated by magnetic field in the megagauss range, Proceedings of 5th International Conference on Megagauss fields and Pulsed Power Systems, Nona Science Publishers, New York, 1989.
10. Abakumov, A. I., Vyskubenko, B. A., Koksharov, V. V., Solovjev, V. P., et al, Confinment of 1 ton TNT equivalent explosion in a big size explosion chamber, 3rd Zababakhin Science Conference, Cheljabinsk-70, 1995.
11. Lindemuth, I. R., Kirkpatrik, R. C., Parameter space for magnetized fuel target in inertial confinement fusion, Nuclear Fusion 23 (1983) pp. 263-284.
12. Buyko, A. M., Garanin, S. F., Mokhov, V. N., et al., 2D instability simulation of magnetically driven cylindrical aluminum and aluminum alloy liners, in these Proceedings
13. Chernyshev, V. K., Mokhov, V. N., Buzin, V. N., et al., Study of High Energy Liner Compression in HEL-1 Experiment, Proceedings of 9th IEEE International Pulsed Power Conference, Baltimore, Md., 1997, p. 566.

MAGNETIZED TARGET FUSION (MTF): A LOW-COST FUSION DEVELOPMENT PATH

I. R. LINDEMUTH, R. E. SIEMON, R. C. KIRKPATRICK, R. E. REINOVSKY
Los Alamos National Laboratory, Los Alamos, NM, USA

Simple transport-based scaling laws are derived to show that a density and time regime intermediate between conventional magnetic confinement and conventional inertial confinement offers attractive reductions in system size and energy when compared to magnetic confinement, and attractive reductions in heating power and intensity when compared to inertial confinement. This intermediate parameter space appears to be readily accessible by existing and near-term pulsed power technologies. Hence, the technology of the Megagauss conferences opens up an attractive path to controlled thermonuclear fusion.

1 Introduction

In the more than three decades of the Megagauss conferences, remarkable progress has been made in magnetic flux compression technology for generating ultrahigh magnetic fields and intense, multimegampere electrical currents. One of the initial motivations for the development of this technology has been controlled thermonuclear fusion. However, it is only in light of recent developments that the technology of the Megagauss conferences can be considered to provide a complementary approach to the two conventional fusion approaches: magnetic confinement (MFE, or magnetic fusion energy), as now embodied primarily in tokamaks, and inertial confinement fusion (ICF), as now embodied primarily in laser driven targets. With proponents proposing or building two multi-billion dollar, multi-year next-generation facilities (ITER, or International Toroidal Experimental Reactor, for MFE, and NIF, or National Ignition Facility, for ICF), the conventional approaches have reached a funding crossroads. In this paper, we present arguments why controlled fusion may now be possible at substantially lower cost than the mainline approaches.

The plasma conditions that are required to achieve controlled thermonuclear fusion are well known. In general, these conditions are stated as an ion temperature, T_i, greater than 4 keV and either a number-density/confinement-time product, $n\tau$, greater than 10^{14} s·cm^{-3} (the "Lawson criterion" for MFE) or an areal density, ρR, greater than 0.4 g·cm^{-2}. The inability of any approach to obtain all of the required conditions simultaneously has frustrated fusion researchers. After forty years of increasing knowledge about plasma behavior, there is no guarantee that next-generation machines, after a major capital investment, will finally achieve the long sought goal.

More than four decades of plasma research has shown that plasma "transport" presents the major impediment to achieving fusion conditions. As shown recently by Siemon et al. [1], the required energy and physical size of both MFE and ICF systems can be estimated with knowledge of the applicable diffusion coefficient that determines plasma transport. The beginning point for such estimates is a diffusion equation that is integrated over a volume and Gauss's theorem applied:

$$-\frac{\partial Q}{\partial t} = -\nabla \cdot (D\nabla Q) \Rightarrow \frac{QV}{\tau} SD\nabla Q \qquad (1)$$

where Q can be a plasma quantity such as density, temperature, or magnetic field, D is the diffusion coefficient, τ is the characteristic transport time, V is the volume, S is the surface enclosing the volume, and, in the right-hand equation, Q and ∇ Q are "average" quantities. The average gradient, the volume, and the surface can be related to a characteristic dimension, a, as:

$$\nabla Q = -\frac{Q}{\alpha a}\,;\ \mathrm{V}=\varepsilon a^3;\ \frac{\mathrm{V}}{\mathrm{S}}\ \gamma a \tag{2}$$

where α, ε, and γ are geometric factors.

We now make the observation that for minimum system size, the fusion burn time and the characteristic plasma heating time must be comparable to the transport characteristic time, i.e.,

$$\tau \approx \tau_{burn} \approx \tau_{heat},\ \tau_{burn} = \frac{L}{n} \tag{3}$$

where L is the Lawson criterion and n is the plasma ion density. Combining Eq. 1 - 3, we arrive at an estimate for the minimum fusion system size:

$$a^2 = \frac{\mathrm{D}L}{\alpha\gamma n} \tag{4}$$

Once the size is determined, the corresponding minimum plasma mass, minimum thermal energy, and minimum heating power, respectively, required for the fusion fuel follow:

$$M = nm_i\varepsilon a^3\,;\quad E_p = 3nkT\varepsilon a^3\,;\ Ph = \frac{E_p n}{L} \tag{5}$$

where m_i is the average ion mass, k is the Boltzmann constant, and T is the plasma temperature.

Equations 4 and 5 give minimum required plasma parameters in terms of the transport diffusion coefficient, the plasma temperature, the Lawson criterion, the plasma density, and geometry dependent quantities. Various plasma transport diffusion coefficients can be found in the literature. For example, Gross [2] gives ion and electron thermal conductivities, which can be related to a diffusion coefficient by $\mathrm{D} = K/(3nk)$, where K is the appropriate thermal conductivity. As shown by Gross, the thermal conductivity perpendicular to a magnetic field can be substantially reduced when compared to the thermal conductivity without a magnetic field. This provides the basic motivation for magnetic confinement. However, as Gross and other authors discuss, many early attempts to confine plasmas magnetically encountered Bohm diffusion, a process that decreased inversely with the magnetic field, rather than inversely with the square of the magnetic field as predicted by "classical" diffusion theory.

2 Conventional Approaches to Fusion

From Gross, we derive the following expressions for three plasma diffusion coefficients:

$$D^{o} = 5.99 \times 10^{10} \frac{T^{5/2}}{n \ln \Lambda}$$

$$D^{c} = 4.53 \times 10^{13} \frac{\beta \ln \Lambda}{T^{3/2}} \tag{6}$$

$$D^{B} = 6.48 \times 10^{9} \frac{\beta^{1/2} T^{1/2}}{n^{1/2}}$$

where D^{o} is the electron-dominated thermal diffusion in the absence of a magnetic field, D^{c} is the ion-dominated "classical" thermal diffusion across a magnetic field, and D^{B} represents Bohm behavior. In Eq. 6, the diffusion coefficients have units of $cm^{2} \cdot s^{-1}$ for temperature in Kelvin degrees and plasma density in cm^{-3}. In Eq. 6, we have introduced dimensionless quantities β (the ratio of plasma pressure to magnetic pressure) and the "Coulomb logarithm."

We now explore the implications of Eq. 6. For simplicity, in all of our subsequent analysis, we will use a plasma temperature $T = 1.16 \times 10^{8}$ K (10 keV), a Lawson criterion, L, of 3×10^{14} $s \cdot cm^{-3}$, and a pressure ratio $\beta = 1$. We will also ignore the slow variation in the Coulomb logarithm, taking its value to be a constant with value 10. And we will assume that the temperature gradient scale factor $\alpha = 1$. We note that each of the diffusion coefficients in Eq. 6 scales differently with plasma density, n, and we note that the classical diffusion across the magnetic field is independent of n at fixed β.

First consider the case of steady state behavior without a magnetic field. At T = 10 keV, the plasma pressure is given by p(in atm) = $3.2 \times 10^{-14} n$. Structural integrity of a steady-state system generally limits the plasma pressure to the 1-10 atm range, e.g., $n = 10^{14} cm^{-3}$. Using spherical geometry ($\varepsilon = 4.189$, $\gamma = 0.333$) and substituting D^{o} from Eq. 6 into Eq. 4, we find that the minimum required system size is 2.79×10^{8} cm, approximately 20% of the diameter of the earth. Furthermore, Eq. 4 and 5 lead to a required plasma thermal energy of 4.39×10^{25} J, an amount exceeding the energy received by the earth from the sun in some 300 days. Hence, we conclude that a steady state, unmagnetized fusion system is impossible on earth.

At $10^{14} cm^{-3}$, the Bohm diffusion coefficient of Eq. 6 is substantially smaller than the unmagnetized case. However, even a Bohm-like reduction in thermal conduction does not lead to a practical steady-state fusion system. Eq. 4 and 5 give a characteristic dimension of 79 m and a required thermal energy of 1 TJ.

For toroidal geometry (e.g., tokamaks) with a major radius 3.5 times larger than the minor radius ($\varepsilon = 69.1$, $\gamma = 0.5$), D^{c} of Equation 6 leads to a "classical" steady-state magnetized plasma system size of approximately 46.7 cm. However, extensive research on toroidal geometries have, to date, found scaling approximately 30 times larger than classical, i.e., a diffusion coefficient of 10^{4} $cm^{2}s^{-1}$. This value leads to a system size of 245 cm, which is to be compared to the ITER design minor radius of 171 cm. According to Eq. 5, the required thermal energy is 487 MJ and the required heating power is 163 MW, numbers that are, again, comparable to ITER. It is the large volume and large heating requirements that lead to ITER's multi-billion dollar construction costs.

Whereas a steady state, unmagnetized fusion system is impossible, ICF is based upon a pulsed system. According to Lindl [3], to match the NIF laser with target requirements, the target "hot spot" density will be about $3 \times 10^{25} cm^{-3}$ (based upon an initial target radius of 0.087 cm, a radial convergence of 36, and a final areal density, ΔR, of about 0.3 $g \cdot cm^{-3}$).

Note that this density is more than 11 orders of magnitude higher than the MFE steady-state density. For this density, the estimates above lead to a characteristic size of 9.4 μm (compared to 24 μm for NIF) and a heating power of 50 TW (compared to the peak NIF laser power of 500 TW).

The plasma heating mechanism in ICF is compressional pdV heating. Eq. 4 and 5 permit an estimate of the required implosion velocity. The heating intensity is the heating power, P_h, divided by the surface area, S. The corresponding implosion velocity is given by dividing the intensity by the plasma pressure:

$$v_i = \frac{P_h / S}{2nkT} = \frac{3\gamma}{2L} an \qquad (7)$$

Since D^o of Eq. 6 is inversely proportional to n, a (in Eq. 4) is inversely proportional to n. Hence, the implosion velocity, v_i, is independent of n. In evaluating Eq. 7, we find that the required implosion velocity for ICF is 46.6 cm-μs^{-1}, which is comparable to the NIF target velocity of 41 cm·μs^{-1} [3]. It is this high velocity, with the corresponding high power and intensity requirements that leads to the multi-billion-dollar cost of NIF.

3 Magnetized Target Fusion

The simple estimates give accurate parameters for MFE, where the fusion fuel is magnetized, and for ICF, where the fuel is unmagnetized. The same procedures can be applied to plasmas having megagauss magnetic fields. At 10 MG and $\beta = 1$, the plasma density is 1.24×10^{20}cm^{-3}, a value more-or-less the geometric mean of the densities for MFE and ICF. At this density, the burn time, for $L = 3 \times 10^{14}$ s·cm^{-3}, is 2.4 μs.

For 1.24×10^{20}cm^{-3}, D^c of Eq. 6 (classical transport) applied to cylinders with a length-to-diameter ratio of 3.3 ($\varepsilon = 20.73$, $\gamma = 0.5$) leads to minimum required system size, mass, thermal energy, and heating power of 0.042 cm, 0.8 μg, 3.37 kJ, and 1.13 GW, respectively. The more pessimistic Bohm coefficient, D^B of Eq. 6, leads to 0.17 cm, 57 μg, 65 kJ, and 27 GW. In this intermediate density regime, the system sizes and energies are substantially lower than required for MFE while simultaneously the required power is more than three orders of magnitude less than required for ICF.

To this point, our analysis of the intermediate density regime has been general and has not addressed a specific heating mechanism. However, if compressional heating is considered, then Eq. 7 gives an implosion velocity of 0.013 cm·μs^{-1} for classical diffusion and 0.05 cm·μs^{-1} for Bohm diffusion.

Our analysis shows that next-generation facilities for MFE and ICF will marginally reach the minimum conditions required even after a major capital investment. On the other hand, as evidenced by a number of papers in these proceedings, the time scale, energy, and implosion velocity required at the intermediate density have already been substantially exceeded by imploding liners. Hence, accessing the intermediate density regime by compressing magnetized plasma by a magnetically driven liner appears particularly attractive. We refer to this approach as Magnetized Target Fusion (MTF), with the word "target" implying that the fuel is heated by implosion in a manner similar to that of ICF. In Russia, this approach is known as MAGO (see papers in these proceedings).

4 Conclusion

The simple estimates presented in this paper provide the motivation for MTF. Similar results using other plasma transport models have previously been reported [1]. More complete, fully time-dependent numerical simulations of magnetized targets can be found in the literature [4,5]. These more complete models lead to the same conclusion: operating in the intermediate density regime has many potential advantages over the more conventional approaches. In fact, the parameter space in which magnetized targets are apt to work is far more extensive than the parameter space of the more conventional approaches.

The most obvious advantage of MTF is a potential cost reduction. As shown in this paper, the MFE constraint of steady-state operation and the ICF constraint of pulsed operation without magnetic fields lead to the requirements for expensive facilities. On the other hand, existing Disk Explosive Magnetic Generators (DEMG) and the Los Alamos Atlas capacitor bank already under construction (see papers in these proceedings), and perhaps the Air Force Research Laboratory Shiva-Star capacitor bank, appear more than adequate to enable MTF to achieve the long-sought goal of "scientific break-even."

A number of researchers around the world have recognized the attractiveness of the intermediate density regime. In October 1997, the First International Workshop on Magnetized Target Fusion was held in Pleasanton, Ca. in conjunction with an IAEA Technical Committee Meeting on Innovative Approaches to Fusion Energy. At the combined meetings, MTF-related papers were presented by authors from the US, Russia, Canada, France, and New Zealand. A collection of presentations at these meetings is available from the authors of this paper. The presentations emphasized the point that various combinations of plasma formation systems and implosion systems appear feasible (see papers in these proceedings).

We believe the technology of the Megagaus conferences opens up this attractive and unexplored path to controlled fusion. MTF is clearly still a research topic, and substantial fusion yield has not yet been demonstrated. Although some physics uncertainties exist, no insurmountable obstacles have been identified. The basic driver technology required for demonstration of MTF clearly exists. MTF is certainly an "orthogonal," complementary alternate to MFE and ICF. Because MTF is qualitatively different from MFE and ICF-different time, length, and density scales-MTF fusion reactors will have different characteristics and trade-offs, increasing the chances that a practical fusion power scheme can be found.

References

1. Siemon, R., Lindemuth, I., Schoenberg, K., Why Magnetized Target Fusion Offers a Low-Cost Development Path for Fusion Energy, accepted for publication in *Comments on Plasma Physics and Controlled Fusion* (1998).
2. Gross, R. A., *Fusion Energy.*
3. Lindl, J., Development of the Indirect-Drive Approach to Inertial Confinement Fusion and the Target Physics Basis for Ignition and Gain, Lawrence Livermore National Laboratory report UCRL-JC-119015 (1995).
4. Lindemuth, I., Kirkpatrick, R., Parameter Space for Magnetized Fuel Targets in Inertial Confinement Fusion, *Nuclear Fusion* **23**, (1983) p. 263.
5. Kirkpatrick, R. and Lindemuth, I., Ignition and Burn in Inertially Confined Magnetized Fuel, *Fusion Technology* **20**, (1991) p. 834.

INITIAL EXPERIMENTS WITH THE PLASMA CHAMBERS MAGO, HAVING NO CENTRAL CURRENT-CARRYING POST IN THE PLASMA HEATING COMPARTMENT

A. A. BAZANOV, N. I. POZDOV

Russian Federal Nuclear Center - All-Russia Research Institute of Experimental Physics, Sarov, Russia

In all the experiments performed to date, the MAGO chambers had a central current-carrying post used for the introduction of the initial magnetic field into the chamber. The results of the first experiments on the capacitor bank facility CASCADE in which the initial magnetic field was not introduced into MAGO chamber, and the central current-carrying post was removed from the plasma heating compartment, are presented in the report. The experiments demonstrated the feasibility of obtaining high-temperature plasma in such chambers with neutron emission duration of 1-1.5 μs. The results may be very useful analyzing the mechanisms of the plasma preliminary heating in MAGO chambers and for testing the applied calculation techniques.

1 Introduction

MAGO chambers are designed to create magnetized hydrogenic plasma that may become a suitable object for subsequent quasi-adiabatic compression up to the formation of thermonuclear ignition [1]. Fig. 1 demonstrates the operation of MAGO chamber.

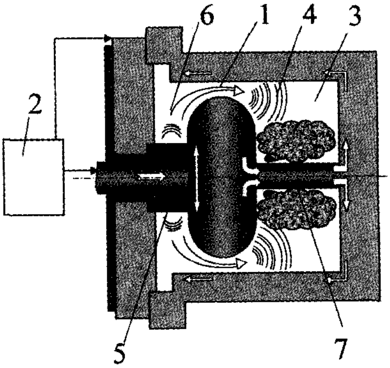

Figure 1. MAGO chamber operation.

Plasma magnetization is carried out by the slow introduction of an azimuthal magnetic field into an initially neutral gas. Breakdown and gas ionization occur initially in the nozzle 1 region at the moment that the powering system 2 switches over to fast introduction of electromagnetic energy into the chamber. As a result, the ionizing shock wave 4 begins propagating in the second compartment 3 of the chamber. About 0.5-1 μs later, a breakdown occurs near the insulator 5 in the first compartment 6 of the chamber. Plasma that was formed in the first compartment is accelerated towards the ring nozzle 1. The plasma that exits the nozzle has a relatively low density and high velocity. When this plasma collides with plasma that was formed in the second compartment by a primary ionizing shock wave, the kinetic energy is converted to thermal energy. A small fraction of plasma reaches a temperature of several keV, leading to generation of a neutron pulse.

Further on, in accordance with calculations, one may expect that the plasma temperature will equalize so that the main plasma mass will have an average temperature of 100-300 eV. This plasma is of interest for quasi-adiabatic compression.

The introduction of a magnetic field serves to suppress the thermal conductivity of plasma. In order to introduce the initial magnetic field, a central, current-carrying post 7 installed in the plasma heating compartment is used. It is possible to expect that, though playing a positive role in the phase of magnetized plasma formation, this post may become an obstacle in the subsequent effective compression of the plasma. In the reported experiments an attempt has been made to investigate whether the mechanism of high-temperature plasma formation would be disturbed if the initial magnetic field is not introduced through the central current-carrying post and the post itself is removed from the plasma heating compartment.

2 Facility

The capacitor bank facility "CASCADE" was used in the experiments [2]. Fig. 2 presents a scheme of its performance. The electrical circuit parameters are C = 205-410 μF, L = 10 nH, U_0 = 44kV.

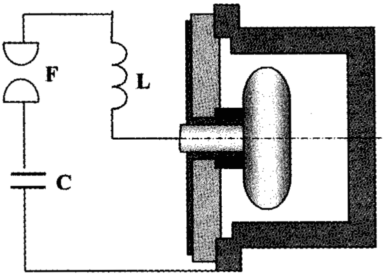

Figure 2. CASCADE capacitor bank facility performance schematic.

3 Experimental Results

In the first experiments the central, current-carrying post was not removed from the plasma heating compartment though the initial magnetic field was not introduced into the plasma chamber. Those experiments showed that the absence of initial magnetic field in plasma almost did not influence the magnitude of the integral neutron yield and did not change the typical neutron radiation duration of the "MAGO" chamber (0.5 - 1 μs).

The conditions under which four such experiments were performed and the neutron yield recorded are presented in Table 1.

Table 1. Experimental Data with Central Post

Shot	C, μF	I_{max},MA	Deuterium pressure, torr	Neutron yield
1.	205	2.2	3.8	$3 \cdot 10^8$
2.	246	2.4	4	$3 \cdot 10^8$
3.	246	2.5	6	$6 \cdot 10^8$
4.	410	3	5	$1.5 \cdot 10^9$

Figures 3 and 4, below, show the neutron pulse oscillograms obtained for the first two experiments presented in Table 1.

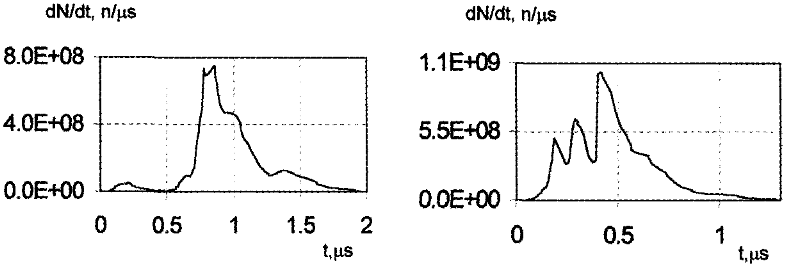

Figure 3, 4. Neutron pulse oscillograms for the first two experiments in Table 1.

In Fig. 5, one can see a record of neutron pulse and discharge current from one of the experiments performed without a central conductor under conditions identical to those in experiment 2 in Table 1. The record shows that a neutron pulse has 2 μs duration at the base. Its shape has much in common with the pulse shape presented in Fig. 4. The recorded value of the integral neutron yield was ~ $2 \cdot 10^8$.

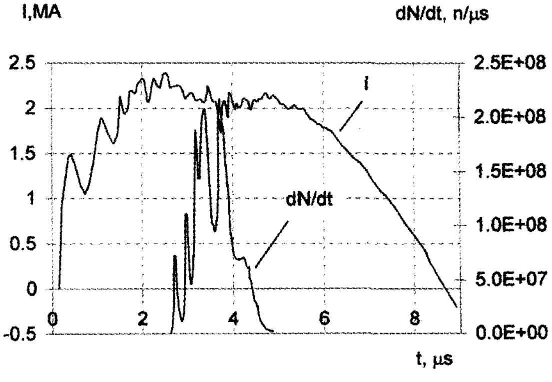

Figure 5. Neutron pulse and discharge current - no central conductor.

Fig. 6 presents for comparison the shapes of neutron and x-ray pulse obtained in a similar experiment. In this experiment the x-radiation of the second compartment plasma passed through a 0.3 μm thick chromium filter. The oscillogram demonstrates that the x-ray quite exactly repeats the shape of the neutron pulse.

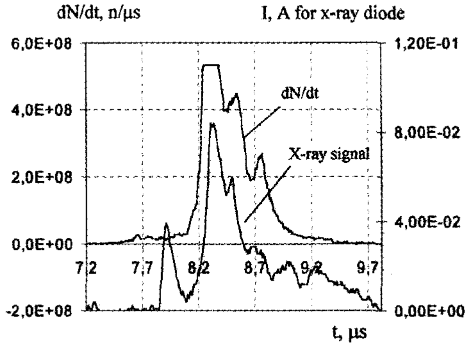

Figure 6. Comparison of x-ray and neutron pulse shapes.

Thus, one may conclude that the absence of initial magnetic field and removal of the central current-carrying post from the second compartment of the chamber do not influence significantly the process of formation of a low-density high-temperature plasma responsible for neutron production. Even if it were so, we have a way to estimate the efficiency of thermal conductivity suppression in the plasma by an initial magnetic field by simply comparing results with and without an initial magnetic field.

4 Conclusions

Thus, one may conclude that an absence of initial magnetic field and a removal of the central current-carrying post from the second compartment of the chamber does not significantly influence the formation of a low-density, high-temperature plasma responsible for neutron production. If it did, however, we can estimate the efficiency of thermal conductivity suppression in the plasma by an initial magnetic field by simply comparing results with an initial magnetic field and without it.

References

1. Lindemuth, I. R., Ekdahl, C. A., Kirkpatrick, R. C., Chernyshev, V. K., Mokhov, V. N., Garanin, S. F., et al., Magnetic-compression/magnetized-target fusion (MAGO/MTF): a marriage of inertial and magnetic confinement. Proceedings of the 16th International Conference of Fusion Energy, Montreal, 7-11 October 1996, **2**.
2. Bazanov, A. A., et al., Some results of experiments on obtaining high temperature plasma on laboratory model of plasma chamber "MAGO," 11th IEEE International Pulsed Power Conference, Baltimore, Maryland, June 29-July 2, 1997.

NUMERICAL SIMULATION OF MAGO/MTF CHAMBER OPERATION AND COMPARISON OF COMPUTED DATA WITH SOME EXPERIMENTS

A. A. BAZANOV, S. F. GARANIN, S. D. KUZNETSOV, V. I. MAMYSHEV, V. N. MOKHOV, A. N. SUBBOTIN, V. B. YAKUBOV

Russian Federal Nuclear Center - All-Russian Scientific Research Institute of Experimental Physics, Sarov, Russia

Numerical simulation of plasma flow in the azimuthal magnetic field in the magnetic implosion chamber (MAGO) is discussed. The different schemes on Eulerian grid and solution techniques are briefly described for 2-D magnetic gas dynamics in the one-component fluid approximation. Computed data of some KASKAD experiments are presented and compared with experimental data.

1 Introduction

One branch of high-temperature plasma generation uses the MAGO chamber [1-4]. Figure 1 presents the plasma chamber layout.

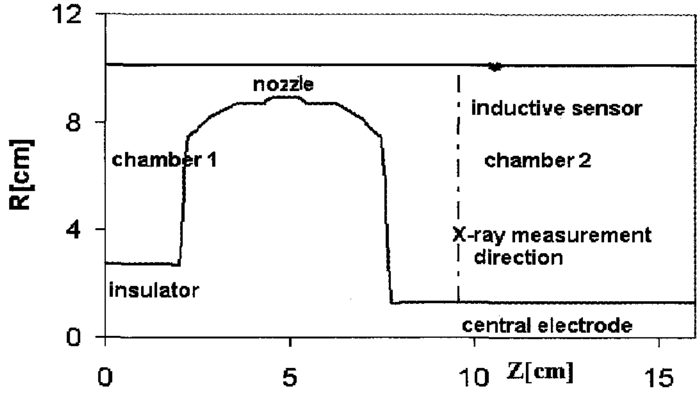

Figure 1. Chamber with central electrode.

The inner space of the chamber is filled with DD gas having 3-15 mm Hg initial pressure. The initial magnetic field is first induced in the chamber, and then the current at the chamber entrance rises. The current rise-rate and amplitude depend on the magnetic energy source. During rapid current growth, volumetric discharge in gas occurs in the first chamber compartment where the insulator is located, and in the nozzle. Under pressure from the increasing magnetic field, the low-temperature plasma begins to flow from the first compartment to the second through the relatively narrow nozzle. The plasma flow becomes supersonic at the nozzle exit and a shock wave is generated at the entrance to the second compartment. It is in this wave that the kinetic energy of the plasma flow is converted to the thermal energy of ions.

This paper considers a model of 2-D magnetic gas dynamics with one nonzero magnetic field component for computational simulation of the above processes. Description of the initial phase of discharge formation over the insulator surface and in the nozzle region is beyond the scope of this model. The presentation discusses the computations conducted under the assumption that at the start of the computation, the discharges have already formed and only the process of their further evolution is considered. The model does consider several physical processes that can noticeably influence gas heating in the chamber, for example:

- gas interaction with chamber walls (wall vaporization and material washout),
- influence of small-scale turbulence and Hall effect on the gas flow in the nozzle,
- processes responsible for interaction of the insulator surface with gas (H-pinched discharge, insulator heating and vaporization).

The comparisons of computed and experimental data discussed in the presentation allow that for some modes of MAGO chamber operation, the effect of the above processes is not significant for the final plasma characteristics.

2 Setting up the Problem and Computational Model

The chamber processes were computed within 2-D magnetic gas dynamics in the one-component fluid model with one magnetic field component $H\phi \neq 0$ and in the two-temperature approximation (ion and electron temperature). The magnetohydrodynamical (MHD) equation system is presented in [5]. The differential MHD equation system was approximated on a rectangular Eulerian grid with computational cell sizes constant in r and z, as in [6]. The method of splitting by processes and inside each process by directions r and z was used to solve the resulting differential equation system. The flow sweep in directions r and z [7] combined with the method of simple iterations was used to solve the differential equations approximating the magnetic field diffusion equation. The MHD equation system is complemented with boundary conditions that are of quite a natural form for a typical chamber geometry (Figure 1):

- electron and ion temperatures at the chamber boundaries are zero,
- the tangential component of the electric field is zero: at the chamber entrance the boundary magnetic field is given by $H(t)=0.2*I(t)/R$, where current I(t) at the chamber entrance can be estimated from the equations describing the electromagnetic energy source,
- the velocity vector component normal to the chamber walls is zero on all the chamber walls, excluding the boundary at the chamber entrance in the first compartment. The velocity at the boundary is estimated from the equations of motion based on the conditions Pe=0, Pi=0 and the boundary magnetic field value H(t). For the electromagnetic energy source, the KASKAD facility is composed of several sections, i.e., capacitor banks connected in parallel to the load (MAGO chamber). If the time difference in section connection due to the spread of discharger actuation in time and the cable transmission line effect are not accounted for, then the equation of the electromagnetic energy source can be written as $(Lc + Lk \bullet n) \bullet dI/dt + Rc \bullet I(t) = Uc(t) - Uk(t)$, $Uc(t)=Uc(0) - \int I(t)dt/C$, where Lc, Rc, C, Uc, I are inductance, resistance, capacity, voltage and current, respectively, in

one section, Lk is the header inductance, Uk is the voltage across the chamber entrance, the current at the chamber entrance is nI+Io, Io is the pre-energization current and n is the number of the sections.

3 Computed Data and Comparison with Experiment

The computations were conducted for two MAGO chamber types: chambers 20 cm in diameter with a central rod in the second compartment, and one with no central rod. The KASKAD facility parameters for the first chamber type are: n=12, Lc=47 nH, Lk=9.5 nH, C=41 μF, Rc=0.032 Ω, Uc=48 kV. The pre-energization current in the chamber is 0.5 MA. The initial pressure of DD gas in the chamber is 6 mm Hg. Figure 2 shows the experimental and computed dependence of the current at the chamber entrance (without pre-energization current) and neutron yield intensity.

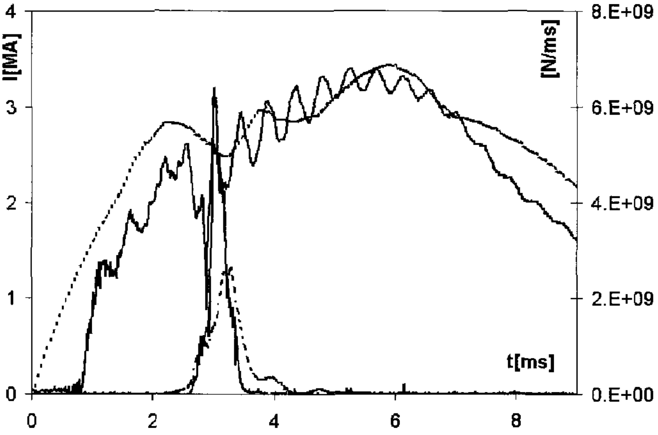

Figure 2. Entrance current and neutron yield.

On the whole, behavior of the presented curves is similar in nature. There are some differences, however. In particular, the experimental current has a pronounced minimum at the time corresponding to the peak neutron yield intensity, while in the computation the minimum is less pronounced. The time of neutron appearance in the computation essentially coincides with the experiment, though the intensity in the experiment proved higher. Plasma internal energy in the computation was 0.081 MJ, or ~1 MJ/g if scaled per gram, which corresponds to the average temperature ~70 eV in the chamber. At maximum neutron yield intensity, the ion temperature reaches ~5 keV in the neutron-generating region of the plasma. An attempt was made in the computations to estimate the diode response in the approximation of DD plasma bremsstrahlung spectrum and absence of radiation and absorption in the lines. To illustrate this, Figure 3 presents the computed diode signals found in the computations for pure DD gas and DD gas mixed with oxygen of 10^{-3} concentration in particle quantity, and also gives the experimental signal. The computations accounted for the additions in the corona approximation by using interpolation formulas [8].

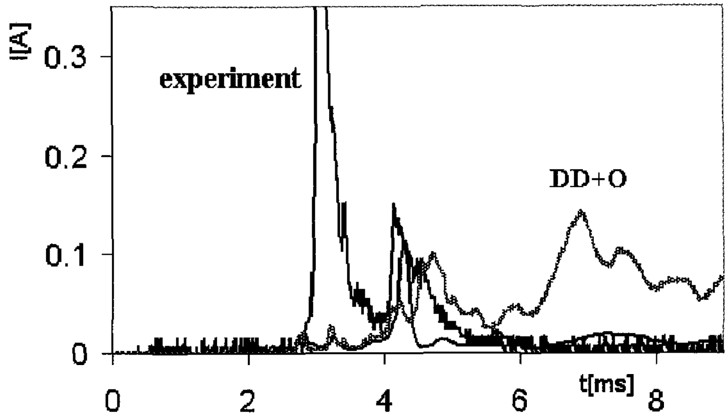

Figure 3. Diode signal.

It can be seen that the computation accounting for the additions provides data very similar to the experiment, though it is not impossible that this fact can be accidental.

4 Conclusion

The data discussed show that the 2-D one-component fluid MHD model is applicable to describe the MAGO plasma magnetic implosion. The computed electrotechnical parameters agree well with the experiment and the computed integral neutron yield is close to the experimental value. The degree of the addition effect on plasma energy as well as the process of impurity generation in the chamber require further theoretical and experimental study. As the computations show, even a relatively small quantity of foreign substance in DD gas can considerably reduce average plasma temperature, though it will not reduce the neutron yield.

References

1. Khariton, Yu. B., et al., *Usp. Fiz. Nauk.* **120**, (1976) p. 706 [*Sov. Phys. Usp.* **19**, (1976), p. 1032].
2. Morhov, V. N., et al., *Sov. Phys. Dokl.* **24**, (1979) p. 557.
3. Lindemuth, I. R., Kirkpatrick, R. C., *Nucl. Fusion* **23**, (1983) p. 263.
4. Kirkpatrick, R. C., Lindemuth, I. R., Ward, M. S., *Fusion Technol.* **27**, (1995) p. 201.
5. Braginsky, S. I., Transport phenomena in plasma. Voprosy Teorii Plasmy, No. 1, (1963) pp.183-272.
6. Nokh, V. F., Combined Eulerian-Lagrangian method for computing time-dependent 2D problems. In: Computational Methods in Hydrodynamics. Moscow, Mir Publishers, (1967).
7. Degtyarev, L. M., Favorsky, A. P., Flow version of the sweep method. ZhVM i MF 8, No. 4, (1968) pp.679-684.
8. Post, D. E., Jencen, R. V., Atomic data and nuclear data table 20. (1977) pp. 397-439.

THE ROLE OF DRIFTS IN MAGNETIZED PLASMA OF THE MAGO SYSTEM

S. F. GARANIN

All-Russian Research Institute of Experimental Physics,
Sarov, Russia

In the MAGO system, plasma cooling due to the classical electron and ion thermal conduction is nonessential, owing to severe plasma magnetization. Drift flows of heat, particles and magnetic flux are more important. Their values are estimated during the preliminary heating stage, as well as during the subsequent implosion and ignition stages. The influence these flows have on plasma cooling can be significant and should not be neglected, especially during the subsequent implosion stage. Increasing plasma density or system size can reduce their impact. For electron and ion components, these flows can be taken into account as a form of the Hall and Leduc-Righi effects and heat transportation by current.

1 Introduction

The MAGO (MAGnitnoye Obzhatie, or magnetic compression in Russia) or MTF (Magnetized Target Fusion in USA) system is an alternative to the main approaches for achieving controlled thermonuclear fusion, i.e. magnetic confinement fusion energy and inertial confinement fusion. MAGO consists of a thermonuclear target located at the center of a cylindrically symmetrical chamber, which is compressed by a liner that is imploded by a magnetic field. Preheated magnetized DT plasma can be one of the possible thermonuclear targets.

DT plasma with the following parameters [1] has been recently obtained in the MAGO chamber in a coaxial cylindrical volume of 8 cm in height, $R \sim 10$ cm in outer radius and 1.2 cm in inner radius: average density $n = 8\times10^{17}$ cm^{-3}, average temperature $T = 250$ eV, characteristic current in plasma $I \sim 4$ MA, characteristic magnetic field in plasma $B \sim 0.16$ MG, characteristic $\beta \sim 0.6$. This allows us to consider the plasma suitable for ignition at its quasi-spherical compression [1-4]. At adiabatic compression of the plasma to radius $R \sim 1.7$ cm and characteristic height ~1.4 cm (under action of magnetic and thermal pressure the internal metal rod radius decreases from 1.2 cm to about 0.8 cm) the plasma will have a density of $n = 2\times10^{20}$ cm^{-3}, characteristic temperature $T = 10$ keV, characteristic current $I \sim 70$ MA in the plasma, characteristic magnetic field $B \sim 10$ MG in the plasma, characteristic $\beta \sim 2$, total magnetic and thermal energy of the plasma $E \sim 10$ MJ. If the velocity of the plasma compression is $v \sim 10^6$ cm/s, the characteristic time of its compression will be $\tau \sim 9\times10^{-7}$ s and the Lawson criterion, $n\tau \sim 2\times10^{14}$ cm^{-3}s, will be met.

For the compression to be adiabatic, it is necessary that various losses be small. By virtue of a high plasma magnetization degree ($\omega_{ci}\tau \sim 400$), the classic electron and ion thermal conduction is insignificant and can be neglected. Losses due to drift of charged particles in the magnetic field leading to heat and magnetic flux transport are more important. These losses and relevant flows contain no collision frequencies thus they are collisionless. When considering thermonuclear energy release processes, the issue of α particle confinement in the magnetic field is also important, so that their energy is released in the fuel, increasing its temperature and gaining its reactivity or heating portions of cold fuel.

2 Role of Collisionless Losses in MAGO Plasma

A simplest example of collisionless drift losses is heat transport by the current. In the MAGO chamber, currents flow from one metal electrode to the other. Low-temperature electrons escaping from the cathode are moving with the current and substitute hot electrons of the plasma by themselves, thereby cooling it. By an order of magnitude, the current velocity of the electrons is $i \sim I/e\pi R^2 n$ and the effect of their transport on the plasma cooling can be estimated by the ratio of displacement of the electrons at their current transport to the system characteristic sizes

$$\frac{u\tau}{l} \sim \frac{I\tau}{e\pi R^2 nl} \sim \frac{I\tau}{eN}\,, \tag{1}$$

where N is the total number of particles in the chamber. During plasma compression the number of the particles is conserved. Given that the quasi-spherical compression occurs at a constant velocity, the duration of the characteristic inductance drop is shorter than time τ of the plasma compression and the current grows faster than $1/\tau$. Hence, the highest compression stage is the most dangerous for plasma cooling with current transport. When we substitute the above plasma parameters of this stage into formula (1), we obtain $\frac{u\tau}{l} \sim 0.3$. Thus, under these conditions, the effect of plasma cooling by current can be noticeable but not fatal.

It is easy to estimate the charged particle drift effect on plasma cooling. By order of magnitude the drift velocities are

$$u \sim \frac{r_{e,i}}{R}\, v_{Te,i} \sim \frac{cT}{eBR} \sim \beta\, \frac{I}{4\pi neR^2}\,. \tag{2}$$

They differ from the current velocity only by a factor of $\beta/4$. As during the quasi-spherical compression β grows, then, similarly to cooling by current transport, the highest compression states are the most dangerous for plasma cooling. At this state, $\beta/4 \sim 0.5$ and the role of the particle drifts can also be assessed as noticeable (~ 0.1) but not fatal. The effect of the magnetic flux transport by current (Hall effect) on the plasma state is of the same order of magnitude. Formula (2) shows that the losses due to drifts in the case of a system with $l \sim R$ give losses literally coinciding with those at Bohm diffusion, but have no small numerical factor (1/16) appearing in the Bohm diffusion coefficient.

It should be noted that in a 2-D plasma MHD description, all the drifts can be taken into account as Hall and Leduc-Righi effects, and heat transportation by current [5].

3 α Particle Confinement in Magnetic Field

The rate of α particle deceleration in plasma is determined by formula [6]:

$$\nu(\mathrm{s}^{-1}) \sim 1.6 \cdot 10^{-9}\, n(\mathrm{cm}^{-3})\lambda / T(eV)^{3/2}\,,$$

where λ is the Coulomb logarithm. As the time that α particles stay in DT plasma is limited with their drift, $\tau \sim l/u$ ($u \sim \dfrac{2c\varepsilon}{3zeBr}$ is the drift velocity of the charged particle with charge ze and energy ε in magnetic field B, decreasing over radius as $1/r$), the fraction of the energy deposited by the particle in the plasma can be estimated as $\nu l/u$. For α particle good confinement, it is desirable that this fraction be large. In our case for the above plasma parameters, this fraction is ~ 0.3 and depends on parameters $\sim Inl/T^{3/2}$. Thus, to improve the α particle confinement it is necessary to increase the plasma density, size, or current in the plasma.

If the problem is with energy transferring from hot to colder layers, then the α particles will be able to perform this function, as the particles' energy release increases with decreasing plasma temperature. Here, one should keep in mind that the drift of the α particles occurs along the Z-axis therefore, after the subsequent implosion, the hot and cold fuel regions must also be located along the Z-axis.

4 Conclusions

Collision-less charged particle drift effects result in plasma energy losses of the order of magnitude literally coinciding with Bohm diffusion, but have no small numerical factor (1/16) appearing in the Bohm diffusion coefficient. For MAGO plasma, the charged particle drifts are most dangerous for the highest compression stage. Even for this stage, their effect on plasma cooling is noticeable but not fatal. In a 2-D plasma MHD description, all the drifts can be taken into account as Hall and Leduc-Righi effects, and heat transportation by current.

For expected MAGO plasma parameters α particle confinement is not very good now. The fraction of the energy deposited by the particle in the plasma is ~0.3 and depends on parameters $Inl / T^{3/2}$. Thus, to improve the α particle confinement it is necessary to increase the plasma density, size, or current in the plasma.

Acknowledgements

The author is grateful to Drs. V. N. Mokhov and V. B. Yakubov for their useful discussions and interest in his study.

References

1. Lindemuth, I. R., Reinovsky, R. E., et al., Target plasma formation for Magnetic Compression/Magnetized Target Fusion (MAGO/MTF). *Phys. Rev. Lett*, **75** 10 (1995) pp. 1953-1956.
2. Buyko, A. M., Chernyshev, V. K., et al., Investigations of thermonuclear magnetized plasma generation in the magnetic implosion system MAGO. *Third Zababakhin Scientific Talks*, Kyshtym, Russia, January (1992). *Digest of Technical Papers: Proc. IX IEEE International Pulsed Power Conf.*, Ed. by K. Prestwich and W. Baker, Institute of Electrical and Electronics Engineers, New York, **1**, (1993) pp. 156-162.
3. Buyko, A. M., Garanin, S. F., Mokhov, V. N., Yakubov, V. B., Possibility of low-dense magnetized DT plasma ignition threshold achievement in a MAGO system. *Laser and Particle Beams*, **15** No. 1 (1997) pp. 127-132.
4. Garanin, S. F., MAGO system. *IEEE Trans. Plasma Sci.*, **26** No. 4, (1998).
5. Braginsky, S. I., Transport processes in a plasma. *Reviews of Plasma Physics.* **1** (Consultants Bureau, New York, 1965) p. 205.
6. Trubnikov, B. A., Particle interactions in a fully ionized plasma. *Reviews of Plasma Physics.* **1** (Consultants Bureau, New York, 1965) p. 105.

CHARACTERIZATION OF A TARGET PLASMA FOR MTF

F. J. WYSOCKI, J. M. TACCETTI, G. IDZOREK, H. OONA,
R. C. KIRKPATRICK, I. R. LINDEMUTH, P. T. SHEEHEY
Los Alamos National Laboratory, Los Alamos, NM, USA

Y. C. F. THIO
Massey University, Palmerston North, New Zealand

Magnetized Target Fusion (MTF) target plasmas are being characterized at the Los Alamos National Laboratory Colt facility. The goal of this project is to demonstrate plasma conditions meeting the requirements for an MTF initial target plasma. In the experiments discussed, a z-directed current is driven through a polyethylene fiber that explodes, producing a plasma which is subsequently contained in a 2 cm radius by 2 cm high cylindrical metal wall. Technical limitations prevented the use of a cryogenically frozen deuterium fiber, as originally planned. Therefore, a polyethylene fiber was used to study plasma dynamics and to look for evidence that an exploding-fiber plasma would eventually become quiescent as the plasma expands and contacts the containing metal wall; *i.e.*, becomes wall-confined and wall-stabilized.

1 Introduction

Magnetized Target Fusion (MTF) is an approach to fusion where preheated, magnetized plasma is adiabatically compressed to fusion conditions [1,2]. Successful MTF requires a suitable initial target plasma with an embedded magnetic field of at least 5 T in a closed-field-line topology, a density of roughly 10^{18} cm^{-3}, and a temperature of at least 50 eV but preferably closer to 300 eV. The plasma must be free of impurities that would raise radiation losses. The goal of experiments performed at Los Alamos National Laboratory is to demonstrate plasma conditions meeting the minimum requirements for MTF initial target plasma.

The experimental approach was based on two-dimensional magneto-hydro-dynamic simulations [3] indicating that suitable plasma could be formed by driving roughly 1-2 MA of z-directed current through a 2 cm long by 200 μm diameter, 89 μg, frozen deuterium fiber along the axis. The calculations show that the initial plasma expands rapidly due to instability driven heating and turbulence, and begins to fill a conducting metal containment region 2 cm in radius in several hundred nanoseconds. As the unstable plasma contacts the conducting metal wall, image currents begin stabilizing the plasma. After roughly a microsecond, the plasma attains a fairly quiescent state with smooth radial profiles. These simulations indicate the plasma could heat up to 350 eV density-averaged temperature by 2 μs, with a peak current of 1.8 MA flowing through the plasma, satisfying the requirements for an MTF target plasma.

Although much effort was devoted to producing the desired cryogenically frozen deuterium fiber, technical limitations prevented its successful extrusion into the inter-electrode load region. A polyethylene fiber was used as a substitute for the deuterium fiber. This allowed for a study of plasma dynamics and an evaluation of the premise that exploding-fiber plasma would eventually become quiescent in a conducting boundary. Experiments with a static gas fill of hydrogen or deuterium are described elsewhere [4].

2 Experimental Design and Results

These experiments are performed at Los Alamos National Laboratory using the Colt facility. The capacitor bank is a two-stage Shiva Marx module marxed to a maximum of 120 kV and 36 μF capacitance. The system inductance to the vacuum insulator is roughly

60-65 nH, the stored energy at maximum voltage is 0.25 MJ, and the current rise-time is ≈ 2.5 μs. The geometry of the electrodes is shown in Fig. 1, along with the positions of the 12 B-dot probes used to determine current-flow. Viewing access is through 10 rectangular holes each 4.8 mm high by 7.7 mm wide, centered vertically on the midplane of the containment region as indicated in Fig. 1. The polyethylene fiber consists of threads. Each thread is 38 μm in diameter and 23 μg per 2 cm of length. Discharges with 1 or 4 threads (92 μg) were performed.

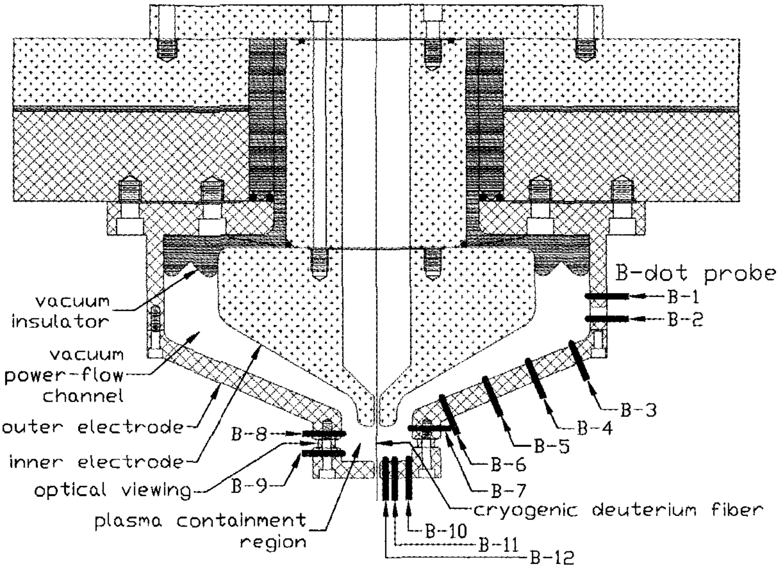

Figure 1. A cross-sectional view of the target-plasma generator, which includes the primary parallel-plate power-feed, region of conversion to coaxial-feed, electrical insulators, and inner and outer coaxial electrodes. The polyethylene fiber hangs in the position indicated by "cryogenic deuterium fiber". The plasma containment region measures 2 cm in radius by 2 cm high.

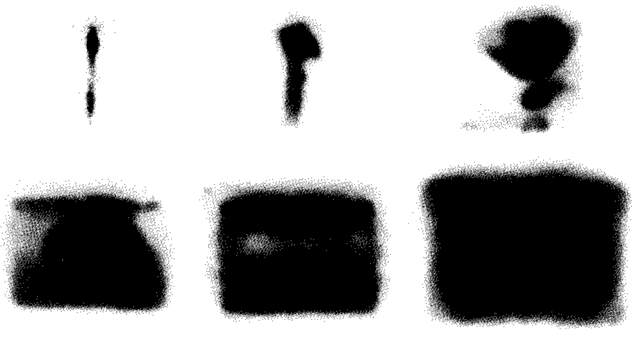

Figure 2. Optical framing camera pictures taken at t = 0.10, 0.32, 0.54 μs (top row) and t = 0.76, 0.97, 1.18 μs (bottom row) for a discharge with 1 polyethylene thread.

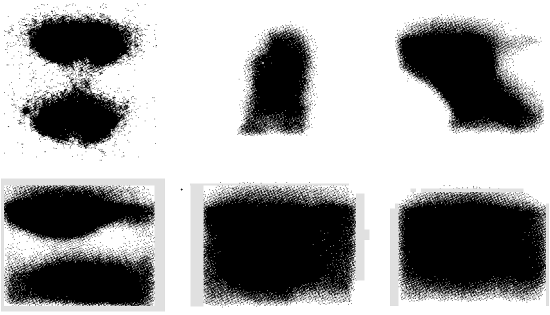

Figure 3. Optical framing camera pictures taken at t = 0.30, 0.53, 0.75 μs (top row) and t = 0.98, 1.20, 1.41 μs (bottom row) for a discharge with 4 polyethylene threads.

Discharges were performed with marxed output voltage ranging from 35 kV to 69 kV, corresponding to peak drive current ranging from 0.7 MA to 1.5 MA. Current flowing through the exploding fiber plasma tracks the drive current until the vacuum power flow channel breaks down. This breakdown occurs at a location between B-6 and B-7, at roughly 0.75 μs. As a result, the maximum current flowing in the fiber plasma has been limited to a maximum of 0.3 MA. As shown in Figs. 2 and 3, the qualitative plasma dynamics is roughly as expected. Instability dominated plasma expansion leads to a fairly uniform plasma distribution. In Fig. 2, the instability remained fairly axisymmetric ("sausage"). Fig. 3 shows evidence of a non-axisymmetric "kink" instability dominating in the third frame, but still evolving toward a fairly uniform distribution in later frames. Fig. 4 shows typical x-ray pulses produced. There are always two or more narrow pulses followed by a final pulse that is wider and usually more energetic then the previous pulses. Fig. 5 indicates a qualitative measure of the time evolution of the plasma temperature. The main feature is that the plasma cools rapidly during the 0.75 to 2 μs period, leaving a cold plasma by 2.5 μs. This cooling time may be too short for an MTF application.

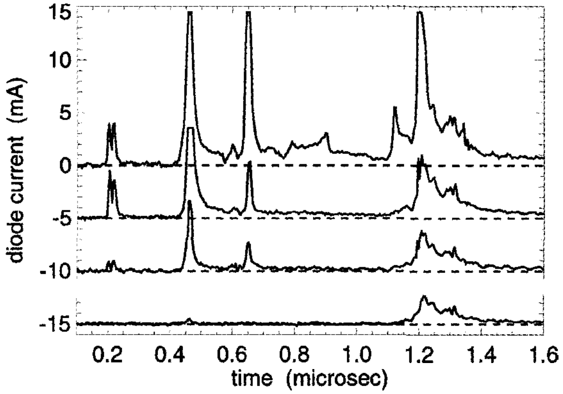

Figure 4. Signals from four filtered silicon diodes showing several narrow x-ray pulses, and one final pulse that is wider and more energetic. Top signal (baseline at 0): filter is 323 μg/cm^2 of kimfol ($C_{16}H_{14}O_3$) plus 10 μg/cm^2 of aluminum. Next signal (baseline at –5): filter is 452 μg/cm^2 of nickel. Third signal (baseline at –10): filter is 1,028 μg/cm^2 of aluminum. Bottom signal (baseline at –15): filter is 1,143 μg/cm^2 of titanium.

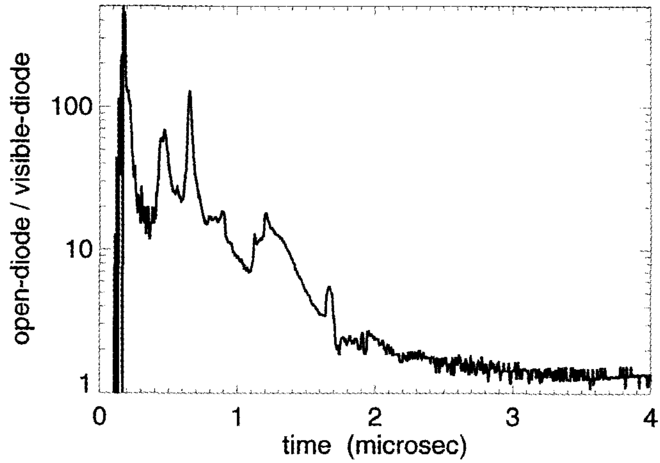

Figure 5. Ratio of the signal from a bare silicon diode divided by the signal from a diode with a thick polystyrene filter which only passes visible light. As this ratio approaches one, the plasma is cooling to a few eV.

3 Conclusions

Experiments were done to evaluate the prospects of using an exploding fiber approach to create a suitable MTF target plasma. The data shows the plasma dynamics is dominated by instability-driven expansion, as expected, for roughly the first microsecond. As the plasma contacts the containment wall, the optical framing images and the lack of narrow x-ray pulses indicate the plasma becomes quiescent. This would imply a wall-confined and wall-stabilized plasma that could be imploded. However, the ratio of x-ray emission to visible emission indicates a plasma cooling time of roughly 1 μs, which is shorter than expected and may be too short for an MTF application. At this time, the exact reasons for this rapid cooling have not been determined.

References

1. Lindemuth, I. R., Kirkpatrick, R. C., *Nuclear Fusion* **23** 263 (1983).
2. Kirkpatrick, R. C., et al., *Fusion Technology* **27** 201 (1995).
3. Sheehey, P. T., et al., *Physics of Fluids B* **4** 3698 (1992).
4. Wysocki, F. J., et al., *Digest of Technical Papers for the 11th IEEE International Pulsed Power Conference*, Baltimore, Maryland, June 29 - July 2, 1997, Ed. by G. Cooperstein and I. Vitkovitsky, p. 1393.

MODELING OF PRESENT AND PROPOSED MAGNETIZED TARGET FUSION EXPERIMENTS

P. SHEEHEY, R. FAEHL, R. KIRKPATRICK, I. LINDEMUTH

Los Alamos National Laboratory, Los Alamos, USA

During Magnetized Target Fusion (MTF), also known as Magnitoye Obzhatiye (MAGO) in Russia, preheated and magnetized target plasma is hydrodynamically compressed to fusion conditions. Because the magnetic field suppresses losses by electron thermal conduction in the fuel during the target implosion heating process, compression may take longer than traditional inertial confinement fusion. Hence, "liner-on-plasma" compressions, magnetically driven using relatively inexpensive electrical pulsed power, may be practical. A candidate target plasma, MAGO, was originated in Russia and is now under joint development by the All-Russian Scientific Research Institute of Experimental Physics (VNIIEF) and Los Alamos National Laboratory (LANL). Other possible target plasmas now under investigation at LANL include wall-supported, deuterium-fiber-initiated Z-pinches and compact toroids. Such target plasmas are undergoing detailed computational modeling. Also undergoing computational modeling are liner-on-plasma compressions of such target plasmas to fusion conditions. Experimental and computational investigation of liner implosions suitable for MTF continues. Results will be presented.

1 Introduction

Magnetized Target Fusion is an approach to controlled fusion that is intermediate between magnetic confinement and inertial confinement fusion (ICF) in time and density scales. Bigger targets and much lower initial target densities than in ICF can be used, reducing radiative energy losses. Reduced losses permit near-adiabatic compression of the fuel to ignition temperatures, even at low (e.g. 1 cm/μsec) implosion velocities. In MTF, the convergence ratio ($r_{\text{initial}}/r_{\text{final}}$) of the pusher in quasi-spherical geometries may potentially be less than 10, depending upon the initial temperature of the fuel and the adiabacity of the implosion. Therefore, "liner-on-plasma" compressions that are magnetically driven using relatively inexpensive electrical pulsed power may be practical [1-4].

An MTF system requires two elements: (1) a preheated and magnetized initial "target" plasma, and (2) a target implosion driver. Because the reduced energy losses in MTF relax the power and intensity requirements for an implosion driver, an optimal driver source for a liner-on-plasma implosion might be relatively inexpensive electrical pulsed power. This could utilize either fixed pulsed-power facilities such as Los Alamos' Pegasus or Atlas, or explosive-flux-compression generators, such as Los Alamos' Procyon or the Russian 200-MJ-class disk flux compression generators [3,4]. Such energy-rich sources might allow a demonstration of fusion ignition via MTF, without a major capital investment in driver technology. The success of magnetized target fusion will depend upon a number of issues. The initial target plasma must meet minimum temperature (~50 eV, preferably 100 - 300 eV), density (between 10^{-3} and 10^{-6} g/cm^3), and magnetic field (>50 kG) requirements, and must have a lifetime, adjacent to the supporting wall, greater than the implosion time (typically several μsec for a pulsed-power-driven implosion). Plasma-wall interaction must not create dynamical effects or introduce excessive impurities; these might lead to rapid cooling of the plasma. The target plasma must readily integrate with drivers for compression to fusion conditions. As it implodes the liner must remain sufficiently intact that it can effectively compress the target plasma.

LANL and VNIIEF have pursued MAGO/MTF research in recent years, as reported at this conference [3-8] and elsewhere [9,10]. Los Alamos is presently investigating three candidate target plasmas: the Russian-originated, explosive-pulsed-power-driven MAGO plasma formation scheme, the high-density Z-pinch, and the elongated compact toroid Field Reversed Configuration (FRC). MAGO work includes ongoing, joint US-Russian efforts aimed at determining the suitability of the plasma created for MTF compression. A partially wall-supported deuterium-fiber-initiated Z-pinch experiment at LANL has been investigated for MTF applications. Los Alamos is now beginning experimental and theoretical investigation of FRC plasma for MTF compression. Related experimental and computational work aims to evaluate explosive-flux-compression generators and existing pulsed power facilities as MTF liner drivers. Liner-on-plasma compressions of such target plasmas are being computationally modeled.

2 Mago Target Plasmas

The Russian-originated MAGO plasma formation experiments are the subjects of US-Russian collaboration involving LANL and VNIIEF [5-7,9,10]. MAGO is a unique discharge in two cylindrical chambers joined by an annular nozzle. Los Alamos 2-D resistive magnetohydrodynamic (MHD) computations show substantial agreement with the early dynamics of the discharge as evidenced by inductive probes, plasma interferometry, and neutron pulse timing. For times later than about 4 μsec, the computations predict a relatively stable and uniform wall-confined Z-pinch plasma in the right-hand section of the chamber, with parameters such as density, temperature and magnetic field very well suited to an MTF target plasma (e.g. 10^{18} cm^{-3}, 100 - 300 eV, 200 kG). However, if wall or insulator constituents contaminate the plasma, enhanced radiative cooling and mass dilution could drop the high late-time plasma temperatures rapidly. Hence, measuring late-time temperature and composition of the MAGO is a major focus of continuing experiments. Recently, the International Science and Technology Center has supported MAGO experiments in smaller chambers of 6 cm radius. Los Alamos simulations predict that 100 eV temperatures could be produced in such discharges with MAGO (4 MA) peak currents, but that a recent joint LANL-VNIIEF shot with 2.5 MA peak current probably reached less than 50 eV.

3 Fiber-Initiated Z-Pinch Target Plasmas

Another possible magnetized target plasma configuration, on which there is extensive experience at Los Alamos National Laboratory, is the deuterium-fiber-initiated Z-pinch [7, 10]. 2-D MHD modeling of a fiber Z-pinch plasma contained inside a conducting wall of 2 cm radius predicts that, after an instability-driven expansion, the plasma settles into a dense, hot, Kadomtsev-stable state, also having the desired MTF target plasma parameters. An experiment was built to investigate such plasmas, but deuterium fiber shots have not been executed due to problems with producing and inserting a deuterium fiber. Polyethylene fiber shots have been done, but simulations of polyethylene-fiber-initiated plasmas predict that, although similar densities and temperatures may be produced, the interesting Kadomtsev-stable state may not occur. Further effects, not yet modeled, include three-dimensional effects and plasma-wall material interactions. Late time MAGO plasmas and deuterium-fiber plasmas appear similar in some respects. They both have similarly stable pinches involving wall-support of plasma, although the MAGO plasma truncates the inner portion of the pinch with its central conductor.

4 FRC Target Plasmas

A new effort at Los Alamos aims to develop Field Reversed Configuration (FRC) plasmas for MTF targets. One potential advantage of such plasmas over MAGO/Z-pinch, direct current coupled plasmas is that FRCs, once formed, have current decoupled from the walls, removing that potential source of contaminants. FRCs can also be translated from a formation chamber to a liner compression chamber. Plans are to start with an FRC in the 10^{17} cm^{-3} density range, which is on the low end of the density desired for MTF. An FRC target plasma experiment is being designed and modeled at Los Alamos, and initial liner compression experiments designed for an FRC are to take place on the Shiva-Star pulsed power facility at the Air Force Research Laboratory.

5 High Energy Liners and Liner-On-Plasma Compression

A joint LANL-VNIIEF experiment (high-energy liner "HEL-1") executed in August of 1996 put approximately 100 MA through a cylindrical aluminum liner 24 cm in radius, 4 mm thick and 10 cm long. The liner was imploding at 7 mm/μsec and contained approximately 20 MJ of kinetic energy by the time it reached the 5.5-cm radius of the central measuring (diagnostic) unit (CMU) [7,8]. Such a liner approaches the energy and velocity regime required to drive an MTF target such as MAGO to fusion conditions. Los Alamos Eulerian 2-D MHD computations, including the effects of material strength, resistive field diffusion, glide-plane-liner interactions, and possible non-linear instability development, gave results in substantial agreement with experimental measurements. One interesting feature noted is that, although early current loading starts the liner with a substantial inward bowing which might seed long-wavelength Rayleigh-Taylor instability growth, the ultimate shape of the liner as it meets the CMU shows a pronounced outward bowing due to strong end effects. Mass thinning along the glide planes results in liner "glide plane run-ahead" and magnetic flux penetration along these areas.

Liner-on-plasma MTF experiments employing HEL-1-like explosive pulsed power drivers, or fixed pulsed power facilities such as LANL's Atlas, are now being computationally modeled.

6 Conclusions

Magnetized Target Fusion (MTF) is an approach to controlled fusion that potentially avoids the difficulties of the traditional magnetic and inertial confinement approaches. It appears possible to investigate the critical issues for MTF at low cost, relative to traditional fusion programs, utilizing pulsed power drivers much less expensive than ICF drivers, and plasma configurations much less expensive than those needed for full magnetic confinement. If inexpensive electrical pulsed power could be used as the implosion driver, smaller, more economically viable fusion reactors might be possible. Because of MTF's qualitative differences from the inertial or magnetic confinement approaches to fusion, MTF reactors will have different characteristics and trade-offs, enhancing the prospects for practical fusion power. Computational and experimental research into MTF is proceeding at Los Alamos, VNIIEF, and other laboratories.

References

1. Lindemuth, I., Kirkpatrick, R., *Nuclear Fusion,* **23** (1983) p. 263.
2. Mokhov, V., et al., *Sov. Phys. Dokl.,* **24** (1979) p. 557.
3. Chernyshev V., et al., in *Megagauss Fields And Pulsed Power Systems* Ed. by V. Titov and G. Shvetsov, Nova Science Publishers, NY (1990) p. 347.
4. Pavlovskii, P. et al., ibid. p. 361.
5. Chernyshev, V., et al, in *Megagauss Magnetic Field Generation and Pulsed Power Applications, Part 1,* Ed. by M. Cowan and R. Spielman, Nova Science Publishers, NY (1995) p. 557.
6. Lindemuth, I., et al., ibid. p. 361.
7. Sheehey, P., et al., *MegaGauss-VII Proceedings,* Sarov, Russia (1996).
8. Reinovsky, R., et al., ibid.
9. Lindemuth, I., Chernyshev, V., Mokhov, V., et al., *Phys. Rev. Let.* **75** (10). (1995) p. 1953.
10. Sheehy, P., et al., *Fusion Technology,* **30** (1996) p. 1355.

MEASUREMENTS OF DENSE PLASMA PARAMETERS BY THE INTERACTION OF PLASMA WITH STRONG MAGNETIC FIELD

**V. B. MINTSEV, S. V. DUDIN, V. K. GRYAZNOV, A. E. USHNURTSEV,
N. S. SHILKIN, V. E. FORTOV**
*Institute for Chemical Physics Research RAS, Chenogolovka,
Russia*

Experiments on measurements of the electron concentration and electrical conductivity in weakly non-ideal dense helium plasma were carried out by the interaction of plasma with a strong magnetic field. Explosively driven shock tubes were used for plasma generation. To obtain a strong magnetic field a solenoid was wound over the tube. To avoid plasma heating by the electrical field eddy current, a high level of conductivity was generated behind the reflected shock wave. Electron concentration was defined by measurements of Hall voltage. The four-point probe method was used to measure electrical conductivity. Experimental data are compared with the calculations.

1 Introduction

Direct measurements of the electron concentration and electrical conductivity of strongly coupled plasma generated behind powerful shock waves are very important in understanding physical processes at high energy density. Analysis of available experimental data on thermodynamical, transport, and optical properties of non-ideal plasma [1] shows that the highest uncertainty in these parameters occurs in the range of plasma partial ionization. In the present work, measurements of Hall effect parameters of shock-compressed helium have been made to determine electron concentration through interaction with the magnetic field.

2 Experimental Set-up

Linear explosively driven shock tubes [2] were used in these experiments (Fig. 1). Shock waves with velocities ~10 km/s in helium at initial pressure of 0.3 MPa were generated by expansion of the driver gas (detonation products). A solenoid, inside of which the ~5 T magnetic field was generated, was wound on the body of the shock tube. Experiments on flow visualization were carried out using VFU high-speed streak and frame cameras. It was shown that at a distance of 5-10 cm from the charge, enough stable flow was formed. So this facility generates enough of a homogeneous plasma slug behind incident and reflected shock waves with characteristic size of some centimeters and lifetime of microseconds to carry out the necessary measurements.

Helium behind the incident shock wave has a very low electrical conductivity comparable with that of expanded detonation products. Magnetic fields freely penetrate into the plasma and a flow is formed with Reynolds number $Re_m = \mu_0 \sigma U D < 1$. Here σ is the plasma electric conductivity, U is the particle velocity of its movement, and D is the characteristic size. Significant ionization starts when the flow runs into the obstacle. This circumstance allows diminishing eddy currents behind the incident shock wave and realization of the regime of a "frizzed" magnetic field behind the reflected shock wave.

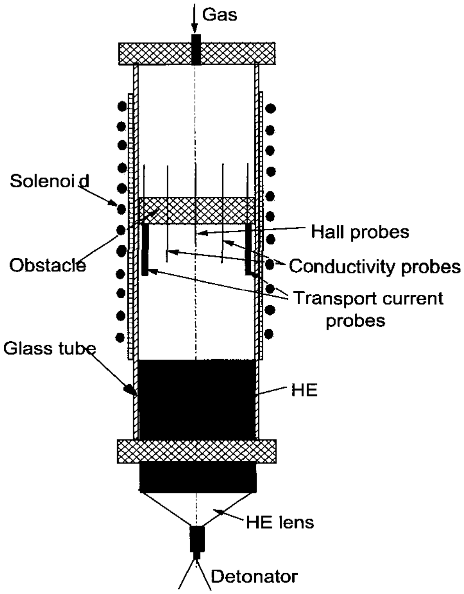

Figure 1. Scheme of the explosively driven shock tube.

To investigate the Hall effect the well-known method advanced by Van der Pauw [3] was applied, with coefficient R_H obtained from a change in resistance R by imposing homogeneous magnetic field $\boldsymbol{B}$ perpendicularly to a flat-parallel pattern of thickness d. $R_H = Rd/|\boldsymbol{B}|$. R is defined as a ratio of Hall voltage U_{Hall} to the current I_{pl} through the plasma. Knowing R_{HP}, one can determine the concentration of carriers as $N_e = r_H/R_H e$, where r_H is a Hall-factor.

To measure electrical conductivity of helium behind the reflected shock wave, we have used the well-known four-probe method [4]. Two additional electrodes for Hall voltage measurements were inserted perpendicular to those for conductivity measurements. The probes have different lengths for fixing the moments of the shock wave's arrival.

3 Measurements

The electrical scheme of the measurements is presented in Fig. 2. The solenoid circuit to produce the magnetic field was supplied by the capacitor bank with $C_s = 1$ mF and $U = 10$ kV. Small capacitor ($C_l = 100$ μF, $U = 3$ kV) was used to generate the plasma current. Rogovski coils were used to measure currents in these circuits. The discharge time for the circuits was approximately the same, ~200 μs. The high explosive is initiated at the moment of the current maximum. To diminish the influence of the parasitic inductance, shunts R_w and R_l were placed on the obstacle inside the shock tube. Electrical signals from the probes penetrate the impulse transformers, which are necessary for decoupling the ground. Oscilloscope TLS 216 was used to register all signals.

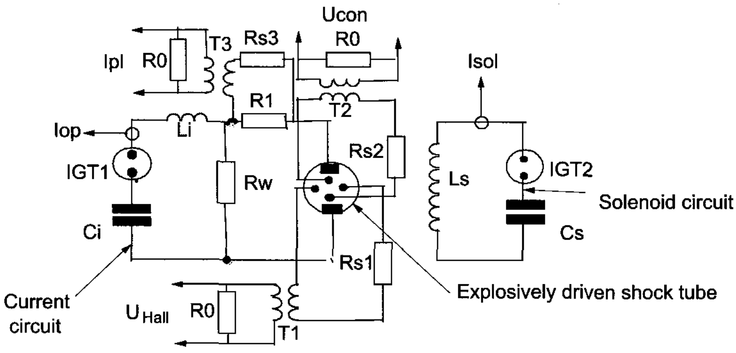

Figure 2. Electrical scheme of the experiment.

Typical waveforms of the signals from the shunt I_{pl}, electrical conductivity probes U_{con} and Hall probes U_{Hall} are shown on Fig. 3. Currents begin to penetrate the plasma at moment t_0 when the shock wave runs into the current electrodes. At moments t_1 and t_2, the shock wave reaches the conductivity and Hall electrodes, correspondingly. An incident shock wave runs into the obstacle at moment t_3. At moment t_4 a reflected shock wave reaches the boundary plasma detonation products. The flow starts to mix intensively and loses its known parameters. The electrical scheme was tuned by measuring parameters only behind the reflected shock wave in these experiments. The slow decrease of the signals is seen in accordance with the increase in plasma thickness.

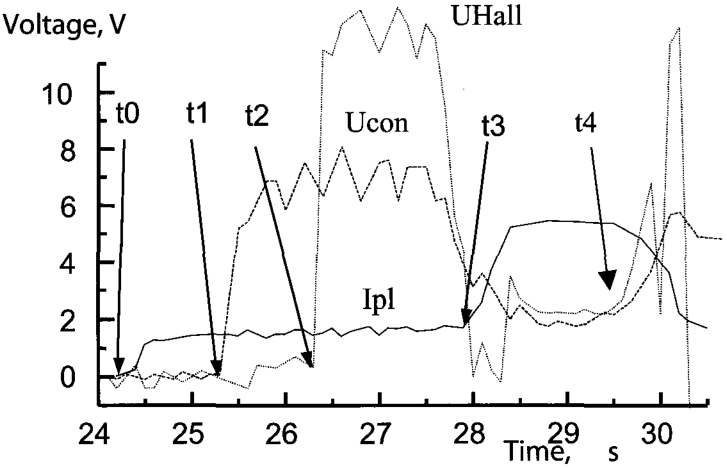

Figure 3. Typical waveforms of signals.

For comparison with the experiment, special calculations were done in frames of the Debye approximation in the grand canonical ensemble for thermodynamic properties, and modified Zeeman's theory for electrical conductivity [1]. The measured values of electrical conductivity (16 $\mathrm{Ohm^{-1}cm^{-1}}$) and electron concentration (3×10^{18} $\mathrm{cm^{-1}}$) agree well with the calculated values.

4 Conclusions

The suggested method looks promising for measuring the electron concentration of weakly ionized explosively driven plasma with strong interparticle interactions.

References

1. Fortov, V., Yakubov, I., Physics of Nonideal Plasma (Hemisphere, 1990).
2. Mintsev, V. B., Fortov, V. E., Explosively driven shock tubes, *Teplofizika Visokih Temperatur*, in Russian, 20, N4, (1982) p.745.
3. Zeeger, K., Physics of Semiconductors. Moscow, Mir, (1977).
4. Mintsev, V. B., Gryaznov, V. K., Fortov, V. E., Electrical conductivity of high temperature nonideal plasma, *Zh. Eksperim. Teor. Fiz.*, in Russian, **79**, No 1, (1980) p.116.

THE STABILITY OF QUASI-ADIABATIC PLASMA COMPRESSION BY A LONGITUDINAL MAGNETIC FIELD

V. F. YERMOLOVICH, A. I. IVANOVSKY, V. I. KARELIN, A. P. ORLOV, V. D. SELEMIR

Russian Federal Nuclear Center - VNIIEF, Sarov, Russia

The problem of magnetized plasma stability during quasi-adiabatic compression by a longitudinal magnetic field is considered. Under certain conditions, the compression stability is increased as the duration of the magnetic field pulse increases. Thus, radial compression without breaking symmetry can increase 20-30 times.

1 Introduction

The purpose of this work is to compare stability of plasma compression by a longitudinal magnetic field B_z at various amplifications. The maximum growth increment has Rayleigh-Taylor instability, at which magnetic field lines do not bend. At compression with a rate much smaller than the magneto-sonic wave velocity ϑ_{ms} the process has adiabatic character. Thus, the pressure is transferred from the border to the center by a magneto-sonic wave, which does not appreciably distort the density and pressure of the plasma, but because of large accelerations they can have an effect on compression stability. Three different cases of amplification of B_z are: I) in solenoid with linear rising current, II) compression by a previously accelerated cylindrical shell and, III) compression in Z-Θ-pinch geometry.

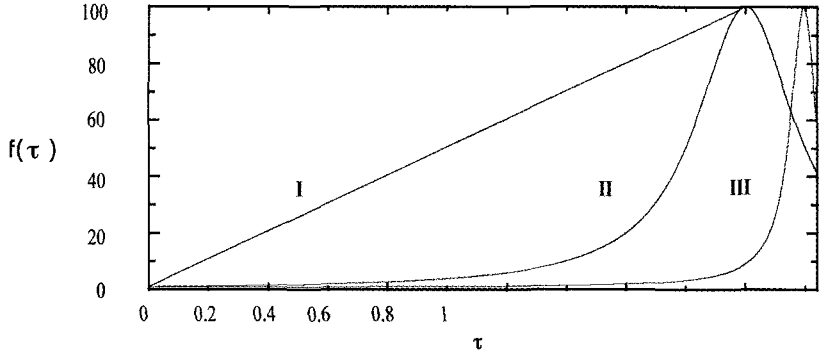

Figure 1. Dependence of external magnetic field intensity on time.

2 Problem Statement and Numerical Results

A plasma cylinder of radius R_0 with homogeneous pressure P_0 and density ρ_0 in a homogeneous axial magnetic field B_z in vacuum is examined. At $t = 0$ the external magnetic field begins to increase with rise time t_m as $B_z(t/t_m) = B_0 \cdot f(t/t_m)$ under dependencies I)-III) (Fig. 1) and to compress the plasma with some entrapped magnetic flux. For an ideal plasma, its parameters can be determined by solving Equation (1) for $\gamma = 5/3$.

Figure 2 represents dimensionless coordinates $R' = R(t)/R_0$ and acceleration $g' = g \cdot t_m^2/R_0$ of the plasma boundary for case II) calculated in 1-D radial magneto-hydrodynamic (MHD) approximation for ideal, perfectly conducting poasma with adiabatic constant $\gamma = 5/3$.

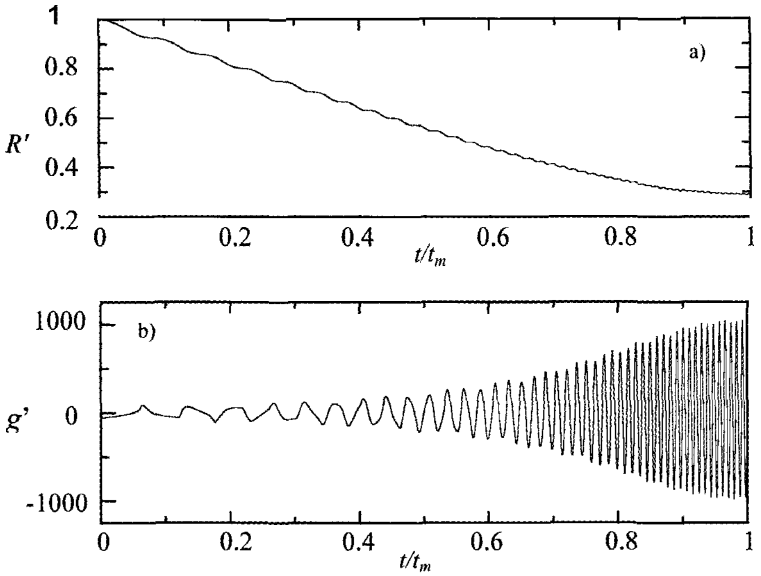

Figure 2. Radius and acceleration dependences of plasma border on time.

Oscillations connected to magneto-sonic wave excitation exist in a background of adiabatic compression. Especially sharp, they are displayed in acceleration dependence on time. The spatial distribution analysis shows that at Alfven velocity $\vartheta_A \geq 10\times R_0/t_m$ magneto-sonic waves insignificantly deform adiabatic structures of density and pressure. Neglecting these distortions, it is possible to simplify MHD equations to

$$\begin{cases} \ddot{R}' = \vartheta_{\mathrm{A}}'^2[(1-\beta)\cdot R'^{-3} + \beta\cdot R'^{-2\gamma+1} - R' f^2(\tau)], \\ \rho' = R'^{-2}, p = R'^{-2\gamma}, H = \sqrt{1-\beta}\cdot R'^{-2}, u = \dfrac{dR'}{d\tau} \end{cases} \tag{1}$$

where $\tau = t/t_m$, $\vartheta_A' = \vartheta_A \times t_m/R_0$, $\rho' = \rho/\rho_0$, $p = P/P_0$, $H = B/B_0$ are dimensionless time, Alfven velocity, density, plasma pressure and magnetic field intensity; $\beta = 8\pi P_0/B_0^2$ is the plasma parameter, $f(\tau)$ is the amplification of an external magnetic field. The comparative analysis of the numerical solutions of MHD and system (1) equations for a wide range of parameter variations has shown their qualitative coincidence. The peak values of accelerations differ no more than a factor of 1.5.

To solve the system of equations (1), the first equation is linearized. For this purpose we expand R' as

$$R'(\tau) = r_0(\tau) + r_1(\tau), \qquad |r_1| << r_0 \tag{2}$$

where $r_0(\tau)$ is a solution for equations (1) at $\vartheta_A' \longrightarrow \infty$ (adiabatic solution). As result of the limiting cases $\beta = 1$and $\beta = 0$, the equation for the plasma border coordinate becomes simpler:

$$\ddot{R}' + 2\alpha_1 \vartheta_A'^2 f^2(\tau)\cdot R' = 2\alpha_1 \vartheta_A'^2 f^2(\tau)\ r_0\ , \tag{3}$$

where $\alpha_1 = \gamma$ at $\beta = 1$, $\alpha_1 = 2$ at $\beta = 0$, $r_0 = f^{-1/\alpha 1}$. The asymptotic behavior of equation (3) for $\vartheta_A' \rightarrow \infty$ for acceleration $g(\tau) = \ddot{R}'(\tau)$is:

$$\begin{cases} g(\tau) = \ddot{r}_0 + \sqrt{2a_1}\vartheta_A \dot{r}_0 f^{\frac{3}{2}} \sin(\sqrt{2a_1}\vartheta_A \int\limits_0^\tau f(\tau')d\tau'), \text{ for case I, II} \\ g(\tau) = \ddot{r}_0 + \dfrac{\ddddot{r}_0}{2a_1\vartheta_A'^2} f^{\frac{3}{2}} \cos(\sqrt{2a_1}\vartheta_A \int\limits_0^\tau f(\tau')d\tau'), \text{ for case III,} \end{cases} \tag{4}$$

where $\dot{r}_0(0), \ddot{r}_0(\tau), \ddddot{r}_0(0)$ are the corresponding derivatives of the adiabatic radius.

From the asymptotic approximations of equations (4), it follows that:

- for cases I), II) the acceleration of the plasma boundary is determined by a rapid oscillation, for case III) - by an adiabatic component;

- for cases I), II) the amplitude of the rapidly oscillating part of acceleration g_m increases linearly as $\vartheta_{\square}' \sim t_m$, and for case III) - g_m decreases inversely proportional to the square of ϑ_A' and the solution approaches the adiabatic state.

These features determine the compression stability.

The growth of disturbances at a linear stage is estimated from

$$\Gamma = \exp(\int\limits_0^1 \sqrt{\frac{m \cdot (|g(\tau)| - g(\tau))}{2 \cdot R'(\tau)}} d\tau), \tag{5}$$

We consider that the cylindrical symmetry is broken at $\Gamma = \Gamma_m = 100$ [1].

The development of a Rayleigh-Taylor instability even on the first harmonic ($m = 1$) in the background of the rapidly oscillating component of acceleration in cases I) and II) breaks cylindrical symmetry of plasma at a radial compression of $\delta \leq 2$-3. The stability decreases as compression time increases.

For case III) the stability is determined by the adiabatic component of $g(\tau)$. In the case of a magnetized plasma ($\beta = 0$), application of small shear $B_\varphi = (0.01\text{-}0.03)\times B_0$ limits the instability growth at large m. In Fig. 3, the dependences $\Gamma(m)$ are given at maximum amplification of an external magnetic field $f_{max} = 247$ (continuous curve $B_\varphi = 0$, dotted curve $B_\varphi = 0.03$). The infringement of the compression symmetry at $B_\varphi = 0.03$ isobserved at $m \approx 10$-13.

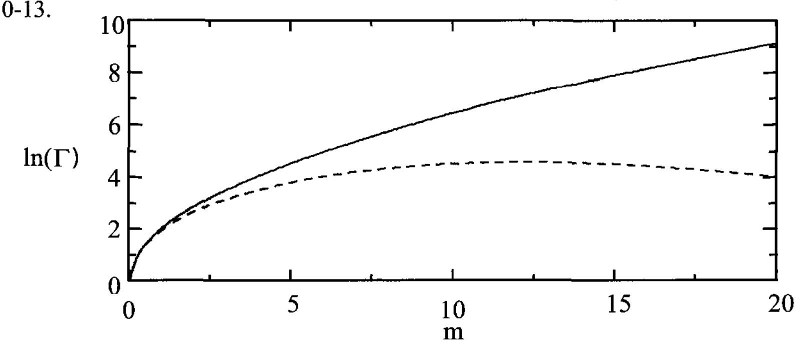

Figure 3. Γ dependence of harmonic number.

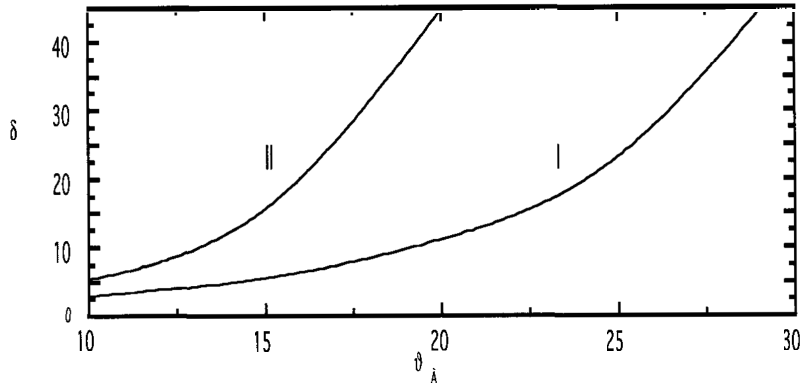

Figure 4. Maximum compression dependence of the Alfven velocity.

The dependence of the maximum compression δ from ϑ_A' for $B_\varphi/B_0 = 0.02$ (a) and 0.03 (b) are given in Fig. 4. As the solution approaches the adiabatic state (with increased ϑ_A) the radial compression increases, as well.

3 Summary

The value of $\delta_L \cong 22$ for magnetic flux compression by an imploding annular plasma liner is currently achieved [2], a theoretical maximum compression value is $\delta_L \cong 30$ [3. Thus, one can see that maximum value of plasma compression δ is limited by δ_L. So, in Z-Θ pinch configuration, radial compression values of $\delta \leq 20\text{-}30$ are possible.

References

1 Bud'ko, A. B., Velikovich, A. L., Kleev, A. I., et al., *Zh. Exper. Theor. Fiz.*, (1989) **95** No. 2, p. 496.
2 Felber, F. S., Malley, M. M., Wessel, F. J. et al., *Phys. Fluids*, (1988) **31** No. 7, p. 2053.
3 Golberg, S. M., Liberman, M. A., Velikovich, A. L., *Plasma Physics and Controlled Fusion*, (1990) **32** No. 5, p. 319.

PERPENDICULAR SHOCK WAVE STRUCTURE IN COLD COLLISIONLESS PLASMA CONSISTING OF TWO ION SPECIES

O. M. BURENKOV, S. F. GARANIN

All-Russian Scientific Research Institute of Experimental
Physics, Sarov, Russia

Perpendicular collisionless shock waves (CSW), in plasma consisting of two species of ions with initial zero β, are considered in 1-D stationary problem formulation. CSW is assumed composed of a narrow resistive front caused by anomalous resistance and heat conduction, followed by a stationary structure in which formation of self-consistent interaction of ion flows plays the principal role. CSW structure is determined for various Alfven-Mach numbers below critical value, for which the existence of such a solution is possible, and relative fractions of electron and ion heatings are found. It is shown that in two-flow CSW with Alfven-Mach numbers higher than some value, ions, having small velocity deviations from main flows and moving across fields of the obtained solution, experience parametric resonance and in this sense CSW may be considered unstable for these Alfven-Mach numbers.

1 Introduction

For perpendicular CSWs [1] in magnetized plasma at Alfven-Mach numbers below some critical value, the principal mechanism responsible for their structure is anomalous resistance due to current instability development. For an initially cold plasma of one ion species the CSW is a resistive front (having an effective electron heat conduction effect) following that there is plasma with heated electrons and weakly heated ions, as anomalous resistance Joule heating mainly goes into electron heating. The critical Alfven-Mach number for a purely resistive wave (for electron gas adiabatic exponent $\gamma = 5/3$) is $M_* = 2.76$ and taking into account electron heat conduction $M_{**} = 3.46$ [2].

In the case of a multi-component plasma in which different ion species have different charge-to-mass ratio z_i / m_i, a multi-velocity flow will be formed downstream the front. A CSW in a plasma with two ion species and with zero resistance, allowing for electron dispersion, was studied by one of us [3]. In the more realistic case of plasma with anomalous resistance and zero electron dispersion, a stationary solution may exist following the resistive front in which different ion species will make Larmor gyration in self-consistent fields. The multi-velocity flow arising in the solution should be unstable with respect to beam instabilities, however, as CSW numerical computations in the hybrid model show [4], this solution has a fairly lengthy existence.

2 Stationary Equations

We will consider a perpendicular CSW structure in the coordinate system where the front is at rest, the magnetic field is directed along the z-axis and the wave propagates along the x-axis. The structure of the stationary wave in plasma with two ion components will be determined with Maxwell's equations, continuity equations for the ion and electron components, taking into account the condition of quasi-neutrality, $n_e = n_1 + n_2$, the equation of motion for ion components, the equation of motion for electron component which is assumed to be without inertia, and the equation for electron energy with taking into account heat conduction and Joule heating.

The characteristic spatial scale corresponding to the ion gyration is $\sim \frac{c}{\omega_{pi}}$ for $M \sim 1$, $m_1 \sim m_2$. Simultaneously, the anomalous resistance estimates (and electron thermal conductivity coefficient corresponding to the resistance) give a CSW resistive front width much less than $\frac{c}{\omega_{pi}}$. The wave can then be represented as being composed of a narrow resistive front at which one can neglect the ion gyration and assume $u_{iy} = 0$ (u_{iy} is the ion velocity component) and of subsequent structure in which one can neglect plasma resistance and heat conduction during many periods of ion gyration.

The state of plasma immediately downstream the resistive front can be determined from the laws of conservation and the condition $u_{iy} = 0$. The following CSW structure downstream from the resistive front can be found using this plasma initial state and integrating the stationary equations, accounting for the adiabatic electron pressure variation downstream the resistive front. The structure will be periodic, as all values can be expressed from the laws of conservation as functions of one physical parameter varying within limited ranges.

The description of the ion motion downstream the resistive front assumed that the ions had zero temperature. The question of what will happen to the ions having a small energy deviation from the main beam is interesting. The equations of motion for the ions describe small oscillations with periodically varying parameters. Depending on conditions, the equations can yield solutions of either limited amplitude or of an increasing one (parametric resonance). In the former case, one can find by how many times "temperature" increases on the average downstream from the resistive front, i. e. what the energy smearing is for each of the beams. The latter case indicates existence of beam instability, even in one dimension, for which one can estimate the instability increment.

3 Calculation Results

Two ion species differing in mass by a factor of 1.5 (as applied, e.g., to DT plasma) and of equal initial concentration were considered. In that case, the computations showed that the critical Alfven-Mach number for a purely resistive wave is $M_* = 2.637$ and taking into account electron heat conduction it is $M_{**} = 3.128$.

Fig. 1 depicts the profiles of ion densities, magnetic field and ion velocities u_{ix} and u_{iy} for $M = M_{**} = 3.128$, obtained from numerical integration of the stationary equations. The following units are used to represent the data: n_0= density, B_0 = magnetic field, c_A = velocity, average mass m = $(m_1 + m_2)/2$ = ion mass, $\frac{c}{\omega_{pi}}$ = coordinate, where ω_{pi} is initial ion plasma frequency defined with average ion mass. In the figure subscript 1 denotes the light component. We can see that the ion species gyration around common center downstream from the resistive shock front results in large-amplitude oscillations of the ion densities and velocities, whereas the magnetic field oscillates only slightly.

Studying behavior of particles with a small velocity deviation from the main beam showed that at small Alfven-Mach numbers M, their motion was stable and with increasing M, first heavier and then lighter particles entered into the parametric resonance. The critical numbers of the transition are $M_{2*} = 2.278$ and $M_{1*} = 2.605$ for heavy and light particles, respectively. Thus, two-flow CSW can be unstable because of development of the parametric resonance that leads to thermal smearing of initially cold ions.

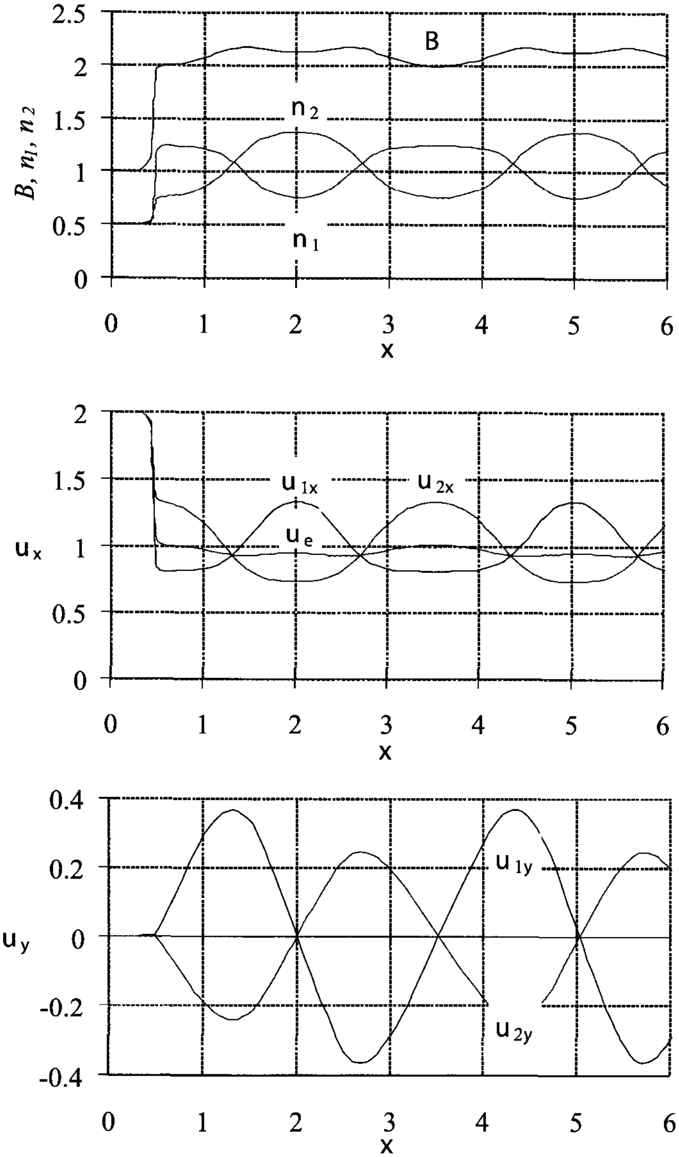

Figure 1. Profiles of ion densities (n_i), magnetic field (B), ion and electron velocities (u_{ix},u_{ex}) and ion velocities (u_{iy}) in the computation with M = 3.128.

Consideration of two-component plasma states downstream from the CSW front for various Mach numbers ($M = 1.5 \div 3.128$) showed that the fraction of electron heating in the plasma heat energy is major and even increases somewhat with increasing M.

4 Summary

We have shown that, in a plasma with two ion species, a sub-critical CSW consists of a narrow resistive front and, downstream of the front, a steady periodic two-stream structure (each stream corresponding to one ion species). In a plasma with two ion species whose charge-to-mass ratio = 1.5 and whose initial densities are the same, the critical Alfven Mach number for purely resistive wave is $M_* = 2.637$, and, allowing for electron heat conduction, it is equal to $M_{**} = 3.128$. A two-stream CSW that forms at Alfven Mach number above a certain value is unstable because of the onset of parametric-resonance instability, which gives rise to a thermal spread of the initially cold ions.

Acknowledgement

The research described in this publication was made possible in part by Award No. RP2-158 of the U.S. Civilian Research and Development Foundation for the Independent States of the Former Soviet Union (CRDF).

References

1. Biskamp, D. *Nucl. Fusion*, **13**, (1973) p. 719.
2. Velikovich, A. L., Liberman, M. A., Fizika udarnykh voln v gazakh i plazme (Physics of Shock Waves in Gases and Plasmas), Moscow: Nauka, (1987).
3. Garanin, S. F., Vopr. At. Nauki Tekhn. Ser. Teor. Prikl. Fiz., No. 2, (1985) p. 12.
4. Garanin, S. F., Golubev, A. I., Ismailova, N. A. International Congress on Plasma Physics. Praha. June 1998.

PLASMA HEATING AND EXPANSION IN ELECTRICAL EXPLOSION OF A CONDUCTOR IN STRONG MAGNETIC FIELD

Y. E. ADAMIAN, V. M. VASILEVSKIY, S. N. KOLGATIN, G. A. SHNEERSON

Saint-Petersburg Technical University, Russia

The possibility of plasma acceleration in an exploding wire and its intensive heating in the presence of a strong axial magnetic field was shown in [1,2]. In [3] the simple model of plane stationary plasma flow through the magnetic field was solved. It was shown that when the initial velocity of the media is higher than the adiabatic velocity of sound, the velocity increases as the coordinate grows. Next, the model of stationary plasma flow crosswise to the axial magnetic field in a cylindrical geometry was developed. Experiments on wire explosions in an axial field of $B_z = 50$ T confirmed that a high temperature peripheral area is formed due to induced azimuthal currents. The measured plasma conductivity is 200 - 400 $(\mathrm{Ohm{\text -}m})^{-1}$

1 Stationary Plasma Flow

The solution of the model problem of plane plasma flow through an orthogonal magnetic field was presented in [3]. Media elements move along the X-axis at speed $u_x(x)$; all distinctive parameters (density ρ, velocity u, pressure p, temperature T) are constant in time. At the point $x = 0$, the given boundary values of these parameters are ρ_0, u_0, p_0 T_0. Numerical calculations executed for boundary conditions $P(0) = U(0) = 1$ show that a type of solution is defined by the value of parameter $\theta_0=\rho_0 u_0 2/P_0$ (Fig. 1). Here, $\chi = x/x_0$ and $U = u/u_0$ are the non-dimensional coordinate and speed.

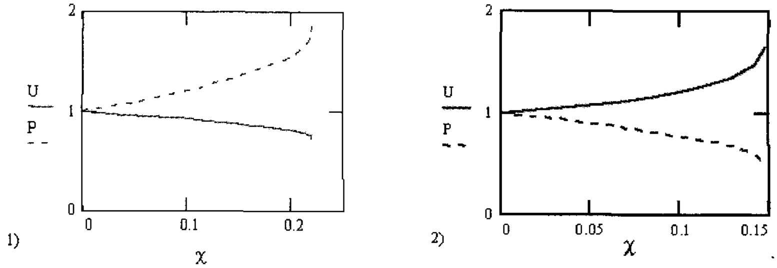

Figure 1. 1 - $\theta_0 = 2$, 2 - $\theta_0 = 1$.

If the initial velocity of the media is higher than the adiabatic velocity of sound at the boundary (in this case, $\theta_0 < \gamma$, where γ is the adiabatic index), the velocity decreases as x increases, but pressure grows. In the case $\theta_0 > \gamma$ velocity grows up to local adiabatic sound speed. This is confirmed by examples shown in Fig. 1 for $\gamma = 5/3$. In the first case (1), the accepted value $\theta_0 = 2$, in the second case (2), $\theta_0 = 1$. In (2), the inexactitude committed in [3] is corrected.

Plasma velocity and temperature increase along the length x_0 in time is given by:

$$\tau_0 \approx \frac{x_0}{u_0} \approx \frac{\rho_0}{B^2\sigma\theta_0} \qquad (1)$$

This value, having an accuracy of multiplier $1/\theta_0$, is known in magnetic hydrodynamics as the time of inducting deceleration. For $\theta_0 < 1$, the plasma velocity decreases in time on the order of τ_0. However, for $\theta_0 > 1$, this parameter becomes opposite in value. Now τ_0 becomes the time scale of the plasma heating and acceleration as it moves across the field.

In the case of cylindrical, stationary plasma flow perpendicular to the axial magnetic field, the geometry is analogous to the exploding wire in a longitudinal magnetic field. In this case, the answer can be found by solving a system of ordinary differential equations:

$$u\frac{d\rho}{dr}=\frac{\rho}{r}\frac{d(ru)}{dr} \quad \rho u\frac{du}{dr}=\frac{dP}{dr}-\delta Bz \quad \rho u\frac{d\varepsilon}{dr}=\frac{P}{r}\frac{d(ru)}{dr}+\delta^2\sigma$$

where ε - partial internal energy of plasma, ρ - density, u - radial speed, σ - conductivity, B_z - magnetic field value, $P=(\gamma-1)\rho\varepsilon$ - the ideal gas pressure, γ - adiabatic index. The azimuthal current density can be calculated as $\delta = uB_z\sigma$.

After some transformations one can obtain the expression for the radial velocity derivative:

$$\frac{du}{dr}=\gamma\left(\frac{B^2\sigma}{\rho}-\frac{u}{\theta}\right)\Big/\left(\frac{\gamma}{\theta}-1\right) \tag{2}$$

where θ is the local value of the parameter $\rho u^2/P$. It follows from (2) that if the parameter θ takes the value equal to γ at some radius, the velocity derivative becomes unlimited.

The system solution under plasma parameters typical for exploding wire plasma with not very high energy enclosing velocity (the boundary plasma temperature = 5 eV, density = 5 kg/m^3) has shown that if the boundary speed is less than adiabatic $C=\sqrt{\gamma\cdot P/\rho}$, there is no increase in velocity and decrease in density with radius. This situation is analogous to plane geometry. If the speed is more than C, there is an increase in velocity in the boundary area. In this situation, if field induction $B_z = 0$, radius r moving to infinity corresponds to density tending to zero.

Under the action of a longitudinal magnetic field, the velocity increase becomes non-monotone and when the velocity begins to decrease it is accompanied by the plasma's internal energy growth (Fig. 2a).

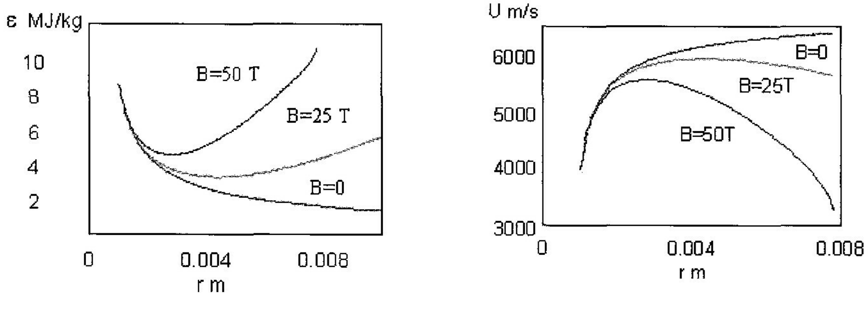

a) b)

Figure 2. Calculated profiles of plasma internal energy (a) and speed (b) for the case of stationary radial flow in cylindrical coordinate system in axial magnetic field. The plasma conductivity is $\sigma = 100\ (\Omega\text{-m})^{-1}$

the boundary area. Its growth is stopped at some radius, and then the velocity begins to decrease. The radius value that corresponds to equation $\theta = \gamma$ decreases with magnetic field growth. The approach to this radius is accompanied by a sharp internal plasma energy rise.

2 Experimental Results

The experimental study of wire explosion in magnetic fields was made under the following conditions: magnetic field-50 T, wire diameter-0.2 mm, capacitor bank parameters-10 kV, 4 mF, circuit inductivity-300 nH, pressure-10^{-5} Torr. Oscillograms of voltage and current are given in Fig. 3a.

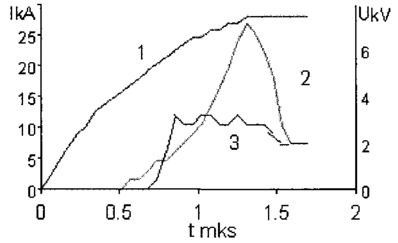

Figure 3a. Voltage and current oscillograms for the wire explosion. 1-current, voltage: 2-Bz = 0, 3-Bz = 50 T

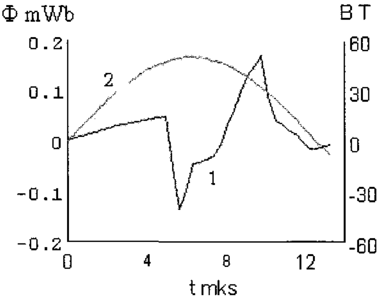

Figure 3b. Diamagnetic signal oscillogram (curve 1). Curve 2-induction of axial field Bz

Under the action of an axial field, the voltage drop of the wire plasma is decreased comparatively to an explosion without a field. This points to the fact that plasma conductivity rises.

The diamagnetic measurements made for the explosion in axial field resulted in the value of magnetic flux removed from plasma $\Delta\Phi$ (Fig. 3b). The oscillogram shows the sharp flux change at the moment of wire explosion. The slowly changing part of the signal is due to altering of B_z. The value of $\Delta\Phi$ is affected by plasma velocity and conductivity.

An electron-optic scanning camera was used to measure the plasma speed. The high-speed photographs (Fig. 4) have shown that in the presence of an axial magnetic field the rapidly expanding bright area is formed around the wire kernel (expansion speed is about 15 km/s).

It follows from the diamagnetic measurements that this area has a conductivity of about 200-400 $(\text{Ohm}\times\text{m})^{-1}$. This is about ten times less than Spitzer value. Under this condition, the azimuthal current density is $(1.5\text{-}3)\times10^{8}$ A/m^2, which is substantially higher than the axial current density ($\sim10^{7}$ A/m^2). The azimuthal current flow can produce the strong additional peripheral plasma heating.

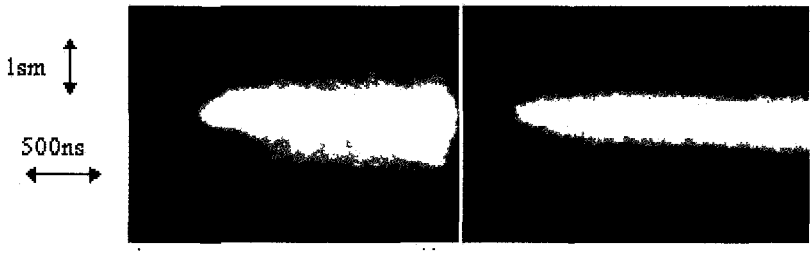

a) b)

Figure 4. High speed photographs of exploding wire: a) B_z=50 T, b) B_z=0

3 Acknowledgments

This work was supported by the Russian Fund for Basic Research, grant # 96-02-19185a.

4 References

1. Shneerson G.A. Letters to *J. Tech. Phys.* (*Pisma v Zurnal Technicheskoi Fiziki*) in Russian, **23**, No. 11, (1997), pp. 10–16.
2. Kolgatin, S. N., Shneerson, G. A. *J. Tech. Phys.* (*Zurnal Technicheskoi Fiziki*) in Russian, (1997), **67**, No. 1, pp. 12-19.
3. Adamyan, Yu. E., Vasilevsky, V.M., Kolgatin, S. N., Shneerson, G. A., Forming of high speed radial plasma flow due to its heating by induced azimuthal current in electrical explosion of wires in extra high magnetic field, Proceedings of the 12th International Conference on High-power Particle Beams, Haifa, Israel, 1998.

INTERACTION OF BOUNDARY MATERIAL WITH MAGNETIZED PLASMA

J. H. DEGNAN, G. F. KIUTTU, B. B. KREH, R .E. PETERKIN, JR, N. F. RODERICK, E. L. RUDEN, K. F. STEPHENS II, AND P. J. TURCHI
Air Force Research Laboratory, Directed Energy Directorate, Kirtland AFB, New Mexico, USA

S. K. COFFEY AND M. H. FRESE
NumerEx, Albuquerque, NM, USA

D. G. GALE AND J. D. GRAHAM
Maxwell Technologies, Inc, Albuquerque, NM, USA

D. MORGAN AND D. PLATTS
Los Alamos National Laboratory, USA

A proposed effort to study the interaction of imploding liner material with magnetized plasma is discussed. The experiments include forming magnetized plasmas within cylindrical or quasi-spherical metal shells 8 - 10 cm in diameter. The subsequent implosion of the metal shells (imploding liners) compresses the magnetized plasmas. The use of time-and-space-resolved spectroscopy is used to observe high atomic number boundary material mixing with the initial, low atomic number plasma. Magnetic pressure from a 10 - 15 megampere axial current discharge through the shells will drive the metal shell implosions. A variant of these proposed experiments, known as plasma working fluid compression, has been done. Triplets of sequential radiographs of such working-fluid compression experiments indicate that megabar fluid pressures were achieved. Our intended theoretical work will include 2-D MHD simulations of boundary material formation and mix during compression. Preliminary calculations as well as diagnostic schemes and issues will be discussed.

1 Proposed Experiments

Our proposed experiments include compression of magnetized, pre-heated deuterium plasma, also known as magnetized target fusion (MTF) [1,2], and spectroscopic observation of the high atomic number contaminants penetrating into the plasma from the boundaries. In the variant illustrated in Fig. 1, we modify our previously used working-fluid compression hardware designs [3,4,5], which employ a quasi-spherical imploding liner [6], driven by magnetic pressure from a 12 megamp axial discharge. Our 1300 μF Shiva Star capacitor bank [7] is used to drive such discharges. In the illustrated variant, the pre-compression plasma is injected by a coaxial plasma gun discharge through a circular array of injection orifices. The same auxiliary capacitor bank used to inject unmagnetized working fluid [3] will drive this injected discharge. The auxiliary bank consists of 3 Shiva Star-type modules. The injection discharge energy, current, and current rise time will be similar to that for working fluid injection, which is typically 350 kilojoules, ~1 megampere, ~3 μs. These discharge parameters are also appropriate for several other variants of pre-compression plasma formation. Such variants include compact torus formation using a magnetized coaxial plasma gun or a theta pinch gun [8], and *in situ* formation schemes such as discharges through cryogenic deuterium wire(s) or through a deuterium gas puff inside the metal liner. The theta pinch and *in situ* schemes may enable lower initial contamination. Suitable parameters of the pre-compression plasma [1,2] are ~10^{17} - 10^{18} ions/cm^3, ~100 eV temperature and initial magnetic field ~5 Tesla (in the illustrated case, azimuthal). The magnetic field reduces thermal conduction losses from the plasma to the boundaries, which is the essential feature of MTF [1,2].

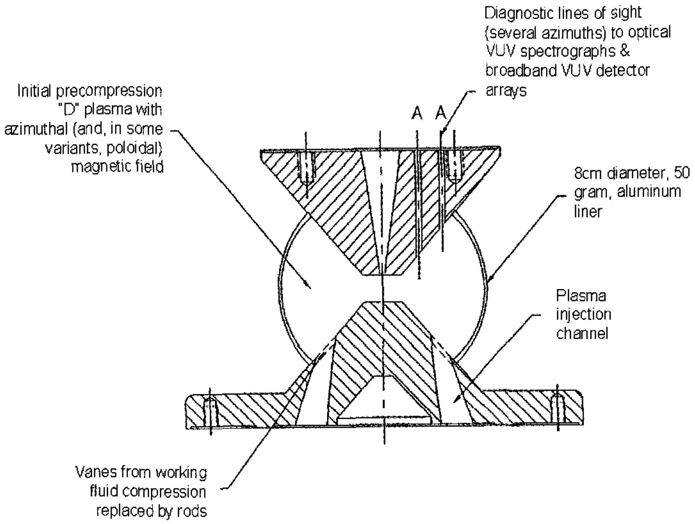

Figure 1. Illustration of quasi-spherical metal shell (imploding liner) with electrodes, cylindrical array of holes for magnetized plasma injection, and lines of sight for vacuum ultra-violet or soft X-ray diagnostics at several radii.

2 Previous Related Experiments

In previous experiments on working fluid compression, we produced an initial hydrogen plasma with density ~10^{20} (atoms plus ions)/cm^3, and initial temperature ~1 eV [3,4,5]. This is the correct energy density, ~10^{20} eV/cm^3, for MTF experiments. Since isotropic

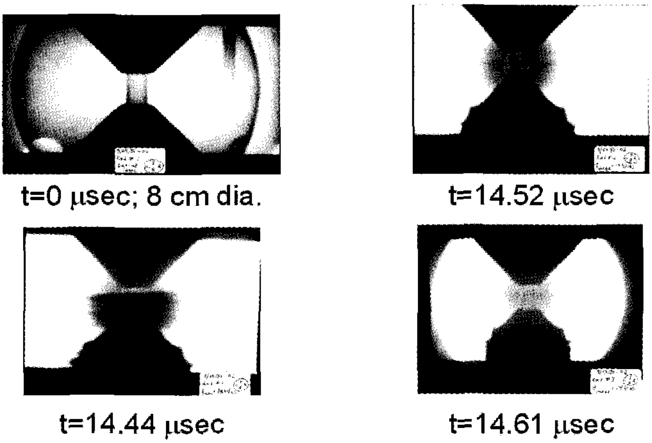
t=0 µsec; 8 cm dia.

t=14.52 µsec

t=14.44 µsec

t=14.61 µsec

Figure 2. Radiographs of imploding liner compressing unmagnetized hydrogen plasma, which then compresses central target shell. Done at energy levels and experiment complexity levels comparable to those of our proposed experiments on magnetized plasma compression

pressure was desired, we labored to demagnetize the initial plasma by using thin metal vanes to form the injection orifices. Radiographs of a quasi-spherical imploding liner that is compressing hydrogen working fluid are shown in Fig. 2. These radiographs were taken through the 0.6 cm aluminum outer conductor for the implosion discharge, using 300 - 450 kv, 10 - 30 nanosecond, several kiloamp pulsers and armored film packs. We show an initial condition radiograph and several dynamic radiographs taken late in the 15 µs implosion. A central target, consisting of a 0.33 cm radius copper shell, was used to provide a simple diagnostic of the fluid compression. The shell thickness was tapered (0.15 - 0.38 mm) to provide a more dynamic range of sensitivity. We obtained enough radiographic data from virtually identical shots (including three from the same shot) to see triplets of successive radiographs late in the implosion. From such triplets that show the compression of the central copper shell, we can obtain average fluid pressure over the interval of the radiographs. This pressure reaches the megabar range prior to liner contact with the central target. Our ability to perform these experiments inspires confidence in the prospect for experimenting on MTF.

Two-dimensional magnetohydrodynamic simulations, using the code Mach2 [9], agree with these experimental results on approximate maximum fluid pressure. However, simulations that we have done to date only agree with experiment on the time dependence of that pressure assuming that there is a small gap between the central target and the electrode. This gap is on the order of cumulative machining tolerances of approximately 1 mm. The experimental and simulated fluid pressure vs. time is shown in Fig. 3. Before taking this agreement seriously, several simulations testing the sensitivity of the calculations to the gap size must be made. We must also computationally explore the effects of non-uniformity in the initial fluid density, which might also explain the observed fluid pressure vs. time. Such simulations [10] indicate that the effective specific heat ratio, gamma, is 1.4 for this working fluid.

Auxiliary experiments without working fluid, but with a central target and with magnetic probes inside the imploding liner, confirmed a negligible magnetic field interior to the liner [5]. Thus, the pressure compressing the central target is presumably due to fluid pressure and not magnetic pressure.

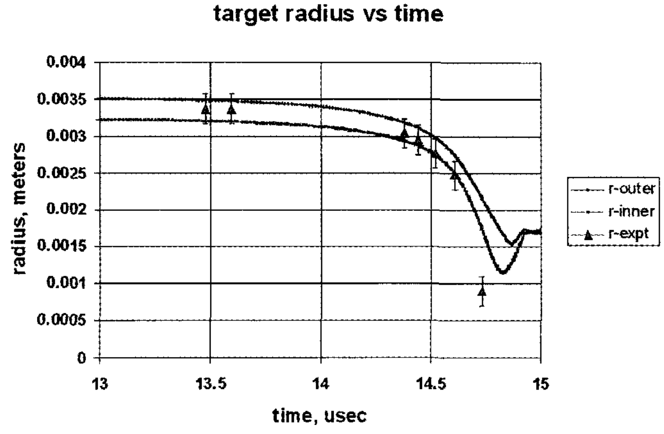

Figure 3. Experimental and simulated outer radius of central target vs. time. This indicates plasma compression to megabar range prior to contact between liner and target. See text for comments on simulation.

Other work related to our imploding solid liners and working fluid compression includes that of Turchi et al. [11], Sherwood et al. [12], Golovoznin, Khurtmullaev et al. [13], Mokhov [14] and Chernyshev et al. [15,16]. The earliest work [11–14] involves concepts and experiments with cylindrical or quasi-spherical imploding liners, with 1 to few mm/μs implosion velocities, to compress magnetized plasmas. More recent work by Chernyshev, Mokhov et al. [14] includes very good progress toward making suitable pre-compression plasma for MTF, as well as development of high-energy, high-current pulsers and imploding liners in their MAGO program. Our proposed MTF work is primarily oriented toward contaminant measurement.

3 Diagnostics of Contaminants in Proposed Experiments

For compressed, pure deuterium plasma, we expect the vacuum ultraviolet and soft X-ray spectrum to be only bremsstrahlung. If high atomic number contaminants are present, we also expect to see recombination and line spectral features. With arrays of filtered Si diode detectors and reasonable collimation geometry for spatial resolution, we expect to see signals large enough to use spectrum deconvolution, enabling us to see the presence of recombination edges.

For example, for a 10^{18} cm^{-3}, 50 eV pure deuterium plasma, the bremsstrahlung power is ~10^5 W/cm^3. For a Si detector area of 0.25 cm^2, diagnostic hole diameter of 0.25 cm, and detector distance of 30 cm, the unfiltered (50 ohm) signal is ~1.8 volts per cm of observation depth. This depth is typically ~3 cm, corresponding to ~5 volt unfiltered signal. We can expect filtered signals to be a factor of 10 to 100 times smaller. These signals will grow during compression. Therefore, it is reasonable to obtain usable signals and spatially resolved (via collimation), time-resolved, deconvolved spectra. From such observed spectral shapes we could distinguish between free-free, free-bound and bound-bound transitions, thus observing evidence of material with higher atomic number. From the location and size of the free-bound (recombination) step(s) in the spectrum, we can determine the approximate atomic number and density of materials with higher atomic number. Seeing this as a function of time, at two or more radii, the penetration rate of higher atomic number material into the magnetized plasma may be estimated.

Examples of recombination edges from our data in higher energy Z-pinch plasmas [17] and from contaminants in tokamak plasmas [18] are shown in Fig. 4. In our Z-pinch-like experiments, we used arrays of X-ray photo-diodes with the same deconvolution algorithm as used with the much more sensitive Si diode array in MTF experiments.

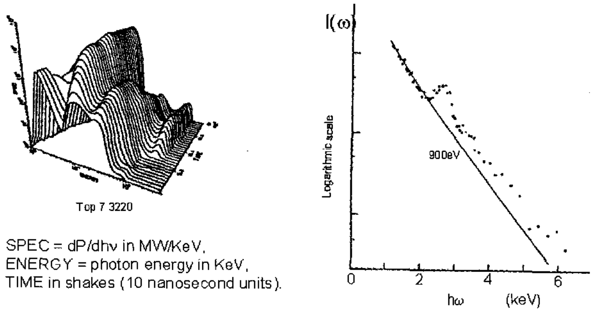

Figure 4. Examples of experimental spectra showing recombination spectral features. Allows observation and measurement of contaminants propagating into deuterium plasma. The left plot shows time resolved, deconvolved photon spectra from higher energy aluminum Z-pinch plasmas. The right plot shows photon spectra from a Tokamak plasma, with acceptably low impurity.

4 Conclusions

We have briefly discussed a proposed experimental effort to produce a magnetized plasma, compress it via implosion of a metal shell to magnetized target fusion (MTF) conditions, and to use vacuum ultraviolet diagnostics to observe the interaction of boundary material (from the metal shell) with the magnetized plasma. We have presented radiographic data from a similar experiment series in which we used magnetized pressure driven imploding metal shells (imploding liners) to compress an un-magnetized hydrogen plasma working fluid, with initial pressure ~100 bar, to ~ megabar pressure. We have also referenced related 2-D MHD simulations. These achieved related experiments and simulations give us some confidence that the proposed experiments are feasible.

Acknowledgements

The Air Force Office of Scientific Research supported this work. We would like to acknowledge the support and interest of Dr. W. L. Baker, Dr. B. Godfrey, Dr C. Hogge, and Dr. R. Kelley. We also thank J.J.Havranek, T.W.Hussey, F.M.Lehr, D.E.Lileikis, U.Shumlak, and others for past, related work and support.

References

1. Lindemuth, I. and Kirkpatrick, R., *Nucl. Fusion* **23** (1983) p. 263.
2. Lindemuth, I. et al, *Phys.Rev.Let.***75** (1995) p. 1953.
3. Lehr, F. M. et al, *J. Applied Physics* **75** (1994) p. 3769.
4. Lehr, F. M. et al, in *Digest of Technical Papers, Ninth International IEEE Pulsed Power Conference*, 21-23 June 1993, ed. by K. R .Prestwich and W. L. Baker, IEEE Catalog Number 93CH3350-6, LIBRARY OF CONGRESS 93-79733 p. 176.
5. Degnan, J. H. et al, presented at Megagauss-7 Conference, Sarov, Russia, Aug 96 (to be in Megagauss-7 Proceedings).
6. Degnan, J. H. et al, *Phys. Rev. Lett.* **74** (1995) p. 98.
7. Reinovsky, R. E., Baker, W.L., Chen, Y.G, Holmes, J. and Lopez, E.A., in *Digest of Technical Papers: Fourth IEEE International Pulsed Power Conference*, 6-8 June 1983, Albuquerque, NM, ed. by M. F. Rose and T. H. Martin (The Institute of Electrical and Electronic Engineers, New York, 1983), p. 196.
8. Schoenberg, K. F., Siemon, R. E., et al, LA-UR-98-2413.
9. Peterkin, Jr., R. E., Frese, M. H. and Sovinec, C. R., *J. Comp. Phys.* **140** (1998) p. 148.
10. Hussey, T. W., et al, in *Sixth International Conference on Megagauss Magnetic Field Generation and Related Topics*, ed. by M. Cowan and R. Spielman (Nova Science Publishers, Inc, Commack, NY, 1994) p.101.
11. Turchi, P. J., et al, in *Megagauss Physics and Technology*, Second International Conference on Megagauss Magnetic Field Generation and related Topics, ed. by P.J.Turchi (Plenum Press, New York, NY, 1980) p. 375.
12. Sherwood, A. R., et al, in *Megagauss Physics and Technology*, Second International Conference on Megagauss Magnetic Field Generation and related Topics, edited by P.J.Turchi (Plenum Press, New York, NY, 1980) p. 391.
13. Goloviznin, V. M., Khurtmullaev, R. Kh., et al, in *Megagauss Physics and Technology*, Second International Conference on Megagauss Magnetic Field Generation and related Topics, ed. by P.J.Turchi (Plenum Press, New York, NY, 1980) p. 415.
14. Mokhov, V., et al, *Sov. Phys. Dokl.* **24** (1979) p. 557.

15. Chernyshev, V. K., and Mokhov, V. N., in *Digest of Technical Papers: 8th IEEE International Pulsed Power Conference*, pp. 395-410.
16. Chernyshev, V. K., et al, in *Sixth International Conference on Megagauss Magnetic Field Generation and Related Topics*, ed. by M. Cowan and R. Spielman (Nova Science Publishers, Inc, Commack,NY, 1994) p. 815.
17. Degnan, J. H., Baker, W. L. and Turchi, P. J., in AIP Conference Proceedings 195, "Dense Z-Pinches", Second International Conference, Laguna Beach, CA, eds. N. R. Pereira, J. Davis, N. Rostocker, American Institute of Physics, NY (1989) p. 34.
18. Rice, J. E., et al, (1978), in *Principles of Diagnostics*, I. H. Hutchinson, Cambridge University Press, 1987, p. 176.

IMPLODING LINERS FOR CONTROLLED FUSION: SOME LESSONS LEARNED

P. J. TURCHI
The Ohio State University, Columbus, USA

There has been a recent rebirth of interest in the use of imploding liners to attain conditions for controlled thermonuclear fusion. Much of the latest interest has involved compression of plasmas in which magnetic fields provide thermal insulation from colder boundaries, rather than mechanical support of the plasma. This Magnetized Target Fusion" (MTF) vs. magnetic-confinement fusion benefits from the rapid and efficient compression of the plasma by liner implosion. Such implosions have been demonstrated in both theta-pinch and z-pinch forms, using cylindrical and quasi-spherical shells driven by fast capacitor banks. It has been almost thirty years since the last major effort on imploding liners for fusion, which was prompted by work in the Soviet Union and extended by the development of reversible, liquid-metal liner systems at the Naval Research Laboratory, Washington, DC. Here, we briefly review lessons learned and technical issues affecting both reactor embodiments and laboratory development of liner/plasma compression.

1 Introduction

In 1971, the Naval Research Laboratory began an experimental and theoretical study of imploding liners for controlled thermonuclear fusion that was inspired by the program of "theta-pinch with liner" under E. P. Velikov at the IAE Kurchatov, Moscow, USSR. This study, following the Soviet example, was originally organized to use solid-density liners, driven electromagnetically by energy initially stored in rotating machines (e.g., homopolar generators). Such an approach sought to avoid the use of high explosives, traditionally the route to obtaining megagauss fields. It was realized at the earliest stages of the project that energies of a few hundred megajoules would be required for a "scientific breakeven" demonstration.

2 Discussion

After successful demonstration of the use of electromagnetic implosion of large-radius, metal liners to generate megagauss magnetic fields, the consequences of dealing with the returning blast of high-energy debris from the implosion became evident. This recognition led to the notion that control of the liner material is important not merely for the eventual fusion reactor, but also for the intermediate steps during which many experiments would be required for plasma development. Thus, the NRL program became focused on the development of liner implosion technology providing controlled re-capture of the liner returning from peak compression. This development was successfully accomplished. The lack of an appropriate plasma (following a few false starts) eventually led to the end of the NRL program. This occurred even though the liner implosion reactor embodiment had been judged most desirable by the "Science Court" process convened by the Department of Energy to review alternative fusion concepts.

Technical details of the liner implosion technology developed by NRL and of the reactor concepts are discussed in previous proceedings of the Megagauss Conference. In particular, the proceedings of the second conference has a review of the NRL Linus program [1], and the design of a liner implosion reactor at 0.5 MG is described in the proceedings of the third conference [2]. Elements of the reactor concept included: 1) use of a field-reversed configuration for the target plasma, 2) use of the liner as the first-wall and reactor blanket, and 3) recovery of the alpha-particle energy for a D-T system in the work done on the re-expanding liner by the plasma. The last feature allowed operation of the reactor at modest nuclear-energy gains ($Q \equiv 2$), as its operation required less energy circulation back from the thermodynamic power system.

3 Summary

The lessons learned may be summarized as:

1. Responsibility for liner energy does not end with launching the liner.
2. Uncontrolled liner motion has substantial negative consequences for development of the target plasma in the actual situation of the imploding liner (i.e., beyond separate laboratory plasma experiments).
3. The reactor embodiment is critical for maintaining support for the project. However, agencies that deal with plasma must be shown progress in terms of plasma results. This is true even if the other concepts are not acceptable or attractive for reactors.

References

1. Turchi P. J., Review of the NRL Liner Implosion Program. In *Megagauss Physics and Technology*, ed. by P. J. Turchi. (Plenum Press, New York, 1980).
2. Turchi, P. J., Design of a Stabilized Imploding Liner Fusion Reactor at 0.5 Megagauss. In *Megagauss Physics, Techniques*, ed. by V. M. Titov and G. A. Shvetsov, Nauka, Moscow (1984).

RAILGUN, LAUNCHERS, AND RELATED TOPICS

HYPERVELOCITY RAILGUN: THE OPTIMAL SOLUTIONS

V. E. OSTASHEV, E. F. LEBEDEV, V. E. FORTOV
High Energy Density Research Center, Moscow, Russia

The paper describes the concept of a multistage plasma armature railgun (PARG). A conventional multistage PARG can be disabled to operate principally as an electromagnetic (EM) launcher. In order to create a multistage PARG one must create acceleration in each rail gun (RG) section, initiating the PA from a new metal foil adjacent to the back of the projectile; to ignite discharge moving with projectile velocity, to stabilize the PA at the initial phase of acceleration in each section while $d(mv) < 0$; to decrease the duration of this phase at the expense of a quickly growing RG current; to form specific time dependence of the energy supply for each RG section both for igniting the discharge, and accelerating the plasma without changing energy sources; and to alternatively feed the energy supply. Presented is the computer evaluation of the acceleration of a 2 g projectile from its initial velocity of 5 km/s over an acceleration distance of 2.5 m, with a permissible operating current of up to 1 MA. The proposed pulse-forming network (PFN) creates a powerful impulse for initiating PA from a metal foil, and also forms a quickly growing RG current. This PFN can transfer up to 45% of its initial energy into RG. The calculated results have shown that, under these circumstances, a muzzle velocity of 10-12 km/s may be achieved in PARG.

1 Introduction

An electric contact between an RG armature and electrodes evolves during an increase of an armature velocity from a solid to hybrid and then to plasma [1]. The PA is a final stage of armature evolution; consequently a PARG is an extreme rail accelerator.

A hypervelocity acceleration of a projectile in RG may be achieved only in the EM component. If this is the case, the extent of the magnetic field in an RG barrel must be changed proportionally with the velocity of the projectile ($m^{-1}dW_m/dv \sim v$, where W_m is the energy of magnetic field in the RG barrel). However, this operating regime of a PARG is absolutely unstable [2,3]. Thus, the duration of EM regime is restricted to $\Delta t_{EM} < \rho_p/\sigma_p B^2 \sim 1/\sigma_R v$, because of the restricted ability of the electroconductive tail of PA (σ_p, ρ_p) to conduct EM energy to a projectile. This regime evolves to the stable magneto plasma dynamic one (not an EM) in which a magnetic force F_m accelerates plasma flow $\dot{m}$ (kg/s) which, in turn, is decelerated at the back surface of the projectile, accelerating it to the velocity $\approx F_m/\dot{m}$.

There are some verified features of the EM component of a PARG [4]. The analysis of real volt-ampere characteristics of an investigated PARG revealed that the EM operating component was rarely achieved. So the latent possibilities of a PARG to accelerate massive projectiles are not fully realized and the actual muzzle velocity of 6-8 km/s is not a maximum [5].

The use of the multistage RG scheme enables optimization of acceleration in each stage depending on the projectile velocity and physical state of an armature to surpass the muzzle velocity achieved.

2 Results

From the simple equation $d(mv) \approx (F_m - F_f)dt$ of an accelerated mass motion under the action of a magnetic F_m and a friction F_f forces (F_f is an ascending function of velocity) two observations follow.

First, a PA armature is decelerated and destroyed at the beginning of each new section while $F_m < F_f(v)$, that is while the RG current $I < v_0(m_{PA}/L_1 h)^{0.5}$ (v_0 is the initial velocity, m_{PA} is the mass of PA, L_1 is the inductance of RG electrodes per unit length). Thus, a conventional multistage PARG can be disabled to operate principally as an EM launcher.

Second, as the velocity increases, the accelerating force and efficiency of an energy conversion into a RG decreases ($vdv/dx \approx (F_m - F_f)/m$). Nor is the stability of the EM component of a conventional PARG increased as the barrel length increases ($\sigma_p v \Delta t_{EM} \sim 1$). Thus, only 2-3 stages of a multistage PARG are optimal.

In order to ignite the discharge moving with the projectile velocity it is necessary to initiate acceleration in each new RG section, initiating PA from a new metal foil adjacent to the back of the projectile. When the velocity increases, the power of ignition also increases. A PFN with a special ignition circuit creates a powerful ignition impulse [6] (Fig. 1).

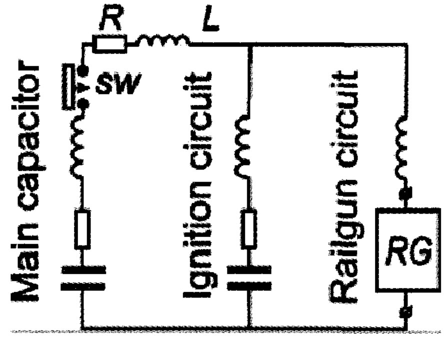

Figure 1. PFN with a special ignition circuit.

Stabilization of the PA armature at the initial phase of acceleration in each new section, during ignition and while the RG current $I < v_0(m_{PA}/L_1 h)^{0.5}$, may be ensured with the use of a massive projectile behind the main [7] (Fig. 2). Quick RG current growth decreases during this phase.

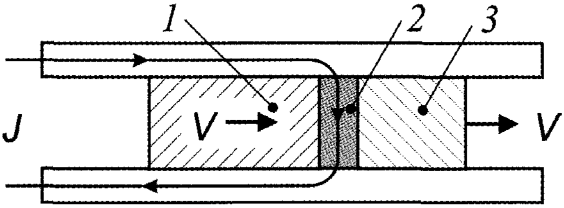

Figure 2. Formation of plasma armature. 1 – massive stabilizer; 2 – plasma armature; 3 – projectile.

Hereafter, the energy supply to the RG is responsible for the evolution of the PA as well as for the EM component of acceleration. Time dependence of power for each RG section is defined by the parameters of PFN, forming power without switching [8]. The use of different energy supply feed increases the stability reserve of the EM component of acceleration [9] (Fig. 3).

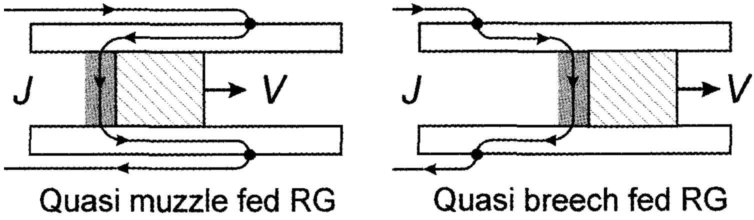

Figure 3. Current feeding to RG armature during acceleration process. Arrows point in the direction of RG current flow and projectile motion.

Fig. 4 shows a computer evaluation of launching a 2.5 m long, 2 g projectile during the second stage of PARG. The initial energy of the PFN was 1.4 MJ (6 kV). The breech velocity of the projectile was 5 km/s. The calculated results have shown that, under these circumstances, a muzzle velocity of 10-12 km/s may be achieved in PARG.

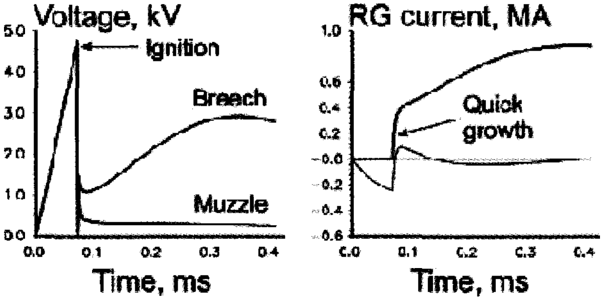

Figure 4. Computer evaluation, second stage of PARG.

3 Conclusion

The problems inherent in EM launching are discussed. It was shown that conventional multistage rail guns could be disabled to operate as an EM accelerator. Optimal solutions were selected that led to an increase of the reserve in stability of the EM component of acceleration in a plasma armature railgun. These are: creating acceleration in each new rail gun section; initiating the PA from a new metal foil adjacent to the back of the projectile; stabilizing PA at the initial phase of acceleration in each section while $d(mv) < 0$; decreasing the duration of this phase at the expense of a quickly growing RG current; forming specific time dependence of the energy supply for each RG section, both for igniting the discharge and accelerating the plasma without changing energy sources; and using an alternate energy supply.

The calculated results have shown that, under these circumstances, the muzzle velocity of 10-12 km/s may be achieved in a plasma armature rail gun with 2-3 stages.

Acknowledgment

We are sincerely grateful to our colleagues A. Ul'yanov and B. Yankovskii for fruitful discussions.

References

1. Ostashev, V. E., Zubkov, A. A., Lebedev, Ye. F., Ul'yanov, A. V., Formation and Evolution of a Current-Plasma Armature in a Magnetoplasma Accelerator of Macrobodies, *High Temperature*, **32**, (1), (1994) p. 15.
2. Protasov, Yu. S., Tchuvashev, S. N., Ostashev, V. E., Fortov, V. E., Forms of existence of plasmadynamic discharges into coaxial and rail electrode systems, *Megagauss fields and pulsed power systems,* Ed. by V. M. Titov and G. A. Shvetsov. N.Y.: Nova Science Publishers Inc., (1990) p. 789.
3. Ardelyan, N. V., Chuvashev, S. N., Yangulova,T. N., Ostashev, V. E., The Effect of Magnetogasdynamic Shunting of Magnetic-Current Structures with Current Layer. Nonlinear Stage. *High Temperature*, **34**, (3), (1996) p. 468.
4. Ostashev, V. E., Ul'yanov, A. V., Chuvashev, S. N., Operating modes of a Magnetoplasma Accelerator of Macrobodies, *High Temperature*, **34**, (1), (1996) p. 142.
5. Ostashev, V. E., Fortov, V. E., Summary of HEDRC-IVTAN Railgun Investigations, *IEEE Trans. on Magnetics*, **33**, (1), (1997) p. 589.
6. Ostashev, V. E., Startsev, S. A., Ul'yanov, A. V., Yankovskii, B. D., Initiation of electric current in the high-velocity armature of a railgun, *High Temperature*, **33**, (3), (1995) p. 842.
7. Lebedev, A. D., Zheleznyi, V. B., Plekhanov, A. V., Effects on the armature acceleration dynamics in electromagnetic rail accelerators, *High Velocity Acceleration of Macrobodies: Theory, Practice and Perspectives*, Ed. by A. S. Anshakov and A. I. Fedorchenko. N.Y.: Nova Science Publishers Inc., (1995) p. 17.
8. Ostashev, V. E., Lebedev, Ye. F., Ul'yanov, A. V., Yankovskii, B. D., Optimization of the Power Supply Mode of Railguns, *High Temperature*, **32**, (6), (1994) p. 842.
9. Fat'yanov, O. V., Ostashev, V. E., Lopyrev, A. N., Ul'yanov, A. V., Electromagnetic Configuration of Railguns, *High Temperature*, **31**, (3), (1993) p. 418.

CRYOGENIC LAUNCHER EXPERIMENTS: THE QUEST FOR A VERY HIGH EFFICIENCY

B. M. NOVAC, M. C. ENACHE
Department of Electronic and Electrical Engineering, Loughborough University, Leicestershire, UK, on leave from the National Institute for Laser, Plasma and Radiation Physics, Bucharest-Magurele, Romania

P. SENIOR, I. R. SMITH, K. GREGORY
Department of Electronic and Electrical Engineering, Loughborough University, Leicestershire, UK

This paper describes the latest phase of a combined experimental and practical program aimed at demonstrating that more than 50% of the available electrostatic energy stored in a capacitor bank can be converted into the kinetic energy of a launcher projectile. A 2-dimensional model of the launcher is used, and numerical results are presented showing different ways by which the overall efficiency can be optimised. Experiments using cryogenic cooling and various monitoring techniques are described.

1 Introduction

The paper presents highlights from an ongoing Loughborough University electromagnetic launcher research program aimed at experimentally demonstrating the possibility of obtaining very high overall electrostatic to kinetic energy conversion efficiency. The work continues that which is recorded in previous papers in the series [1,2] and demonstrates the theoretical and experimental achievements of the latest phase, in which cryogenic cooling has enabled computer-guided experiments to yield efficiency exceeding 50%.

The first section explains the basis for the 2-dimensional modelling of the launcher; the second describes various experimental techniques and presents typical results. Theoretical predictions are compared with experimental data in the third section, concluding with views concerning the most profitable way ahead.

2 2-Dimensional Launcher Modelling

Fig. 1 presents the arrangement of a single-turn coaxial electromagnetic launcher in which the energy stored in the capacitor C is discharged into the launch coil when switch S is closed. A full study of the launcher characteristics requires specification in terms of the appropriate set of magnetohydrodynamic equations. Nevertheless, it is possible to obtain an acceptably accurate assessment of the launcher characteristics by solving the electromagnetic equations for the system at each stage of a numerical solution and coupling the results obtained from this to the equations for the rest of the system. In all practical situations, one can neglect the displacement current in the Maxwell equations, leading to a quasi-static solution in which all that is necessary is to determine the current distributions in the coil and projectile.

Following the calculation of the current and magnetic field distributions during a time step of the numerical solution of the launcher equation, the mechanical equations of motion of the projectile determine its position at the end of the corresponding time step. A detailed analysis of a single-turn launcher energised from a capacitor bank is given elsewhere [3].

3 Experimental Arrangement and Results

The following data applies to the experimental arrangement [2] that was used in the present phase of the program:

Capacitor bank - $C = 56.6\ \mu F$, $V_0 = 30$ kV
Closing switch - 5-detonator, low-inductance switch

Mylar foil was used to form a liquid nitrogen reservoir around the projectile. With the reservoir full, temperatures below 240 K (-43 °C) were measured prior to a launch.

Optical sensors, using battery-operated laser diodes and fast opto-electronic converters coupled via long optical fibres, detected the projectile velocity. The position of the laser rays above the reservoir was such that nitrogen vapour could not disturb the measurements. However, the depth of the nitrogen determined the projectile temperature. This posed problems since the competing electromagnetic and drag forces shown in Fig. 1 signify only limited axial displacement "windows" exist between the projectile and the coil for which very high efficiencies are achieved.

A major problem caused by the low-temperature working environment was that the very thin layer of glue used to position the 0.52 mm thick laser-cut projectile became brittle. This can be overcome by using the *electrostatic* force between the coil and the projectile before the projectile is launched, but this technique implies a much-enhanced dielectric between the coil and the projectile (reducing the accelerating force) and the corresponding difficulty of grounding the projectile.

The best result achieved in the final phase of the research is given in Table 1 together with the best results reported in the earlier phases [1,2].

Table 1. Best experimental results from each phase of the experimental program.

	projectile							
Prog phase	Mat'l..	Size mm	Mass g	Initial c-p separation mm	Capacitor voltage kV	power source resist. mΩ	final vel. Mm/s	% Eff.
1	Cu	76/100/1.6	4.601	0.25	30	10	357	11.5
2	Al	76/100/0.5	5.803	0.22	29.4	7	1642	31.9
3	Al	180/200/0.5	8.102	0.22	28.8	3	1665	47.8
4	Al	180/200/0.52	8.182	0.20	30.0	2.5	1789	51.4

Figs. 5 and 6 show the filamentary current and temperature distributions at the first peak of current, inside both the drive coil and the projectile. This is at an early stage of the launch, when the magnetic coupling is strong, and Fig. 3 shows that the current and the temperature distributions are concentrated near the adjacent faces of the coil and the projectile. Both the current and the temperature distributions are readjusted as the launch proceeds and the magnetic coupling falls, with both the coil and the projectile distributions eventually being greater at the adjacent faces than in the interior. This may lead to possible melting along the surfaces of the projectile.

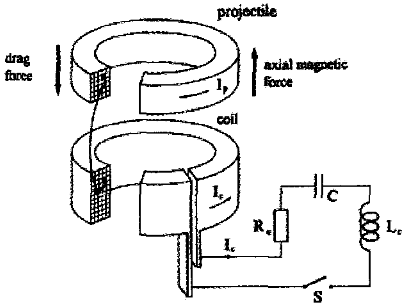

Figure 1. Single turn launcher filaments and magnetic interaction for modelling are shown.

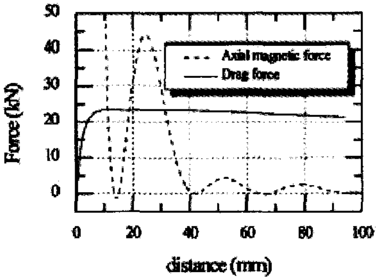

Figure 2. Axial magnetic force and drag force along the launch trajectory.

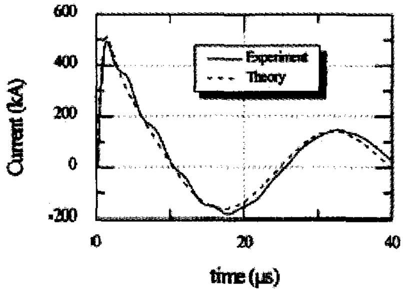

Figure 3. Experimental and predicted variations of coil current.

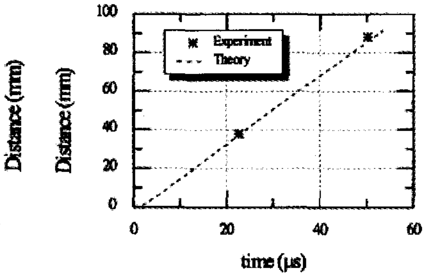

Figure 4. Projectile displacement from initial position (computed and two laser beam measurements.

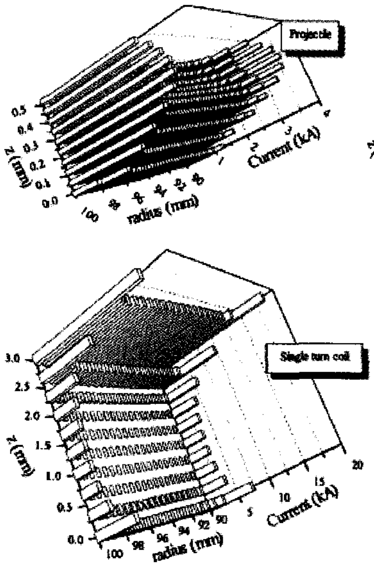

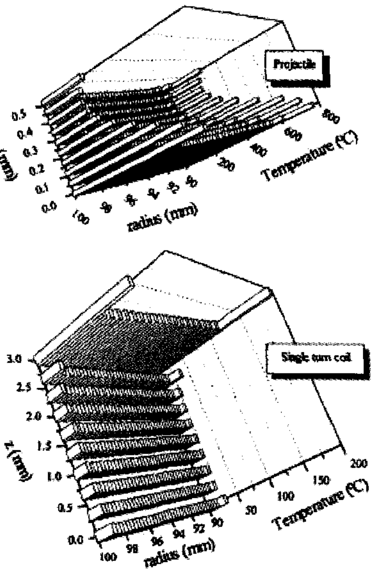

Figure 5. Current distributions at first peak current current (cross-sections as in Figure 1).

Figure 6. Temperature distribution at first peak current (cross sections as in Figure 1).

Conclusions

A detailed program aimed to show that more than 50% of the initial electrostatic energy of an electromagnetic launcher can be converted into the kinetic energy of the projectile has been successfully completed. A 2-dimensional numerical code developed to guide the experimental program and to analyse the results provided very close predictions of the actual performance, despite the 3-dimensional deformation of the projectile that was clearly evident.

To obtain even higher efficiencies, it will be necessary to lower the projectile temperature further and to use an electrostatic method of maintaining the initial position of the coil.

References

1. Novac, B. M., Smith, I. R., Senior, P., Gregory, K., Enache, M. C., High-Velocity Induction Launcher, *Megagauss VII*, Russia, (1996).
2. Novac, B. M., Smith, I. R., Senior, P., Can the Efficiency of an Electrostatic to Kinetic Energy Conversion Process Exceed 50%?, *11th International Pulsed Power Conference*, Baltimore, (1997), pp 1139-1142.
3. Novac, B. M., Tudorache, V. G., Smith, I. R., Gregory, K., Two Dimensional Filamentary Modelling,, *Romanian Journal of Physics*, To be Published.

THEORETICAL AND EXPERIMENTAL INVESTIGATION OF MAGNETIC-IMPULSE PLATE ACCELERATION

A. V. BABKIN, S. V. FEDOROV, S. V. LADOV
Bauman Moscow State Technical University, Moscow, Russia

V. A. GRIGORYAN, V. A. KRUZHKOV, A. V. SHERBAKOV
Niistali, Moscow, Russia

Results are presented of acceleration of metal plates by the magnetic field of a plane inductor experiencing a current impulse from a capacitor bank. Two models of acceleration by magnetic fields have been used. The first model is based on the application of finite relation of the transient process theory and the conservation laws. The second model is considered as a problem of perfectly conductive plate acceleration by an unsteady axis-symmetric magnetic field, taking into account the possible influence of a conductive surface nearby. Calculation results are in good agreement with test data, where a 0.5 kg aluminum plate obtained a velocity of 170 to 180 m/s with 22.5 kJ of energy. Calculations defined the existence of optimum acceleration energetic device parameters from the viewpoint of maximum velocity, considerable influence of conductive surface position on velocity and the ratio of plate diameter to inductor diameter.

1 Introduction

One possible method of projecting objects is electromagnetically, based on the principle that metallic plates can be launched by the pulsed magnetic field of a flat inductor included in the circuit of an electrical power source - a capacitor bank [1,2]. To optimise such energy plants, design models of electromagnetic launching devices are needed. Creating these models is the object of this paper.

2 Physical-Mathematical Models of the Plate Electromagnetic Launching

The simplest process model is built in analogy with the calculation procedures of magnetic-pulsed stamping parameters. The model is based on the use of Newton's second law, co-relations of the energy conservation law, theories of transient processes in electrical circuits, calculation of equivalent inductance and active resistance of a double-circuit system (circuit of the electric power source inductively connected to a launched conducting plate) [3,4]. Input data were geometrical parameters of the inductor and the launched plate, mass of the plate, electrotechnical parameters of the electrical circuit and the electric power source, and electrophysical characteristics of the plate and inductor materials.

The resulting plate launching velocity was defined at the current impulse maximum moment t_m=T/4=$\pi/(2\omega)$ from the integral equation solution

$$\int_0^{\bar{V}_M} \frac{d\bar{V}}{1-\bar{V}^2} = \frac{\pi}{4h_0\omega}\sqrt{\frac{2W_{mo}}{m}},$$

where $\bar{V}_m = V\sqrt{m/(2W_{mo})}$ is the non-dimensional velocity of the plate of mass m, W_{mo} is the magnetic energy of the inductor-plate system, is an initial gap between the inductor coils and the plate, ω is the current discharge frequency in the electrical circuit. Value W_{mo} was defined from the full energy of the capacitor bank with provision for active losses in the circuit, losses of magnetic energy on the circuit's own inductance and on the unused rear inductor.

A more correct and informative second model is realised within the framework of the problem of a perfectly conducting plate launched by the inductor's axis-symmetrical magnetic field. Here, one must provide for the possible influence upon the process of a perfectly conducting surface located near the inductor. This model is built on the basis of the Biot-Savart-Laplace law to calculate magnetic field spatial distributions, Kirchhof's laws, electromagnetic induction of Faraday and Ohm to calculate the transient process in the power source's electrical circuit, and Newton's second law to calculate motion of the launched plate under the action of magnetic pressure forces on the plate surfaces.

In calculating the magnetic field spatial distribution, the assumption of perfect conductivity was extended to the material of the inductor coils. The problem was reduced to numerical determination of surface currents in perfectly conducting elements based on the Biot-Savart-Laplace law, with provision for boundary conditions on the surfaces of these elements. These boundary conditions were expressed by the relation for the magnetic field induction normal component $B_n = 0$ and the relation for the tangent component B_τ following from the full current law, taking into account that on each inductor coil the same full current, J, should flow:

$$\oint_L B_\tau dl = \mu_0 J$$

where L is the outline of the coil cross-section, μ_0 is the magnetic constant. The following use of the superposition principle allowed definition of the resulting magnetic field in each point in space. The possibility of locating a perfectly conducting surface behind the inductor in this model was taken into account by using the "mirror display" principle [5]. Accordingly, when calculating the magnetic field induction the surface currents in the inductor and the plate were taken into account, as well as similar currents symmetrical to them but opposite in direction with respect to the surface.

The magnetic pressure on the plate surface was determined based on the distribution of the magnetic field induction, thus the entire force acting on the plate was calculated. The inductor-plate system equivalent inductance in the electrical circuit equation was also determined.

As a result, the plate electromagnetic launching process was described by an ordinary differential equation system (the electrical circuit equation, the law of voltage changing on the capacitor, the law of acceleration of the launched plate), the numerical integration of which allowed us to obtain the solution.

3 Calculations Results and Experimental Check-Up

Calculations of plates' electromagnetic launchings were carried out as applied to an experimental plant with the capacitor bank capacity of $C = 1800$ μF, initial voltage $U =$ 5kV, power $W_0 = 22.5$ kJ. When launching a 0.52 kg aluminium plate by an inductor with external diameter $D = 208$ mm, internal diameter $d = 68$ mm, coil number $n = 20$, initial gap between the coil plane and the plate $h_0 = 2$ mm, the experimentally fixed velocity was 175 m/s.

The calculation results presented in Fig. 1 - Fig. 4 present possibilities about the degree of correlation between calculations and experiments for the above models, and about the character of the power plant and inductor parameters' influences on the launching velocity.

The influence of capacitor bank parameters on the launching velocity calculated according to the simplest model is shown in Fig. 1. Calculations were carried out under maintained bank energy by changing its voltage and capacity. The maximum velocity, V_m = 183 m/s, is achieved at voltage U = 6460 V. However, the parameters realized in the experimental plant turn out to be sufficiently close to optimum under the given energy and given inductor, and the calculated launching velocity at these parameters is close to the one recorded experimentally.

Dynamics of plate launching and processes in the discharge circuit, calculated by means of a two-dimensional model, is shown in Fig. 2. Substantial deformation of the current pulse J is the result of the circuit total inductance increase due to the plate movement. The launched plate achieves velocity $V \approx$ 190 m/s on a relatively small acceleration base x. The plate launching velocity via the ratio of the plate diameter D_p and the external diameter of the inductor D at fixed plate mass is shown in Fig. 3. As seen, the velocity decreases considerably when the plate diameter decreases. The influence of the proximity of the conducting surface, which is placed behind the inductor, on the efficiency of plate electromagnetic launching is shown in Fig. 4. At small gaps h_s between the inductor and the surface, the velocity obtained by the plate decreases substantially.

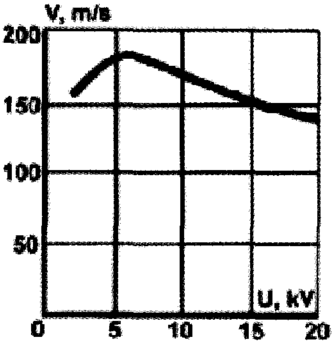

Figure 1. Influence of capacitor bank parameters on launching velocity for W_0 = const.

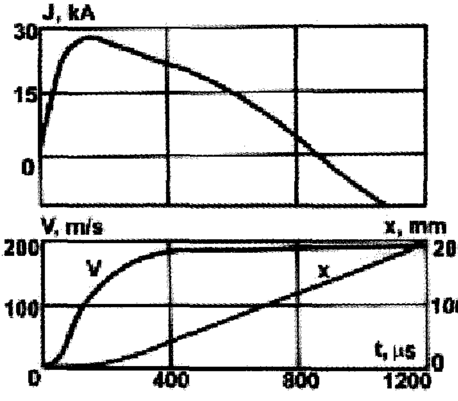

Figure 2. Dynamics of plate launching and processes in the discharge circuit.

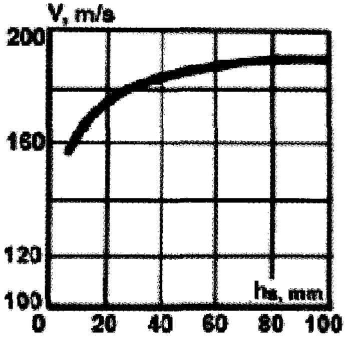

Figure 3. The plate launching velocity via the ratio of the plate and inductor diameters.

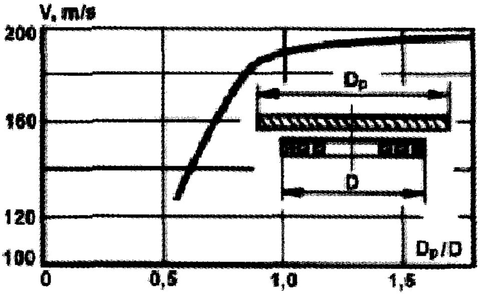

Figure 4. Influence of the conducting surface proximity on plate electromagnetic launching efficiency.

4 Conclusions

The presented physical-mathematical models of a metal plate electromagnetic launching allow calculation of the parameters of this process, and predicted results are in good correlation with the experimental data. The calculated optimization of the electromagnetic launching system, which is the aim of such models, can be carried out on the basis of their further improvement.

References

1. Ogorkievich, R., Future tank armors revealed. *Janes International Defense Review.* (1997) N 5.
2. Ernst, H. J., Sterzelmeier, K., Reactive armor mechanisms against KE- threat: High explosives and electromagnetic forces. *Proc. 17th Int. Symp. on Ballistics.* Midrand, South Africa. (1998).
3. Bely, I. V., Fertic, S. M., Chimenko, L. T., Guide to metal magnet-pulsed processing. Charkov: Charkov University Press. (1977) in Russian.
4. Knopfel, H., Ultrahigh pulsed magnetic fields. Moscow: *Mir.* (1972) in Russian.
5. Landow, L. D., Lifshic, E. M., Electrodynamics of continua. Moscow: *Science.* (1982) in Russian.

BEHAVIOR OF METALLIC SHAPED-CHARGE JETS UNDER THE ACTION OF A CURRENT PULSE

G. A. SHVETSOV, A. D. MATROSOV
Lavrentyev Institute of Hydrodynamics, Novosibirsk, Russia

A. V. BABKIN, S. V. LADOV, S. V. FEDOROV
Bauman Moscow State Technical University, Moscow, Russia

The paper reports results of experimental and numerical studies of the disruption of metallic shaped-charge jets (SCJ) through which a pulsed electric current is passed. The action of an electric current leads to a significant change in the jet "structure" and a decrease in the time required for jet disruption that, in turn, decreases the cavern depth in the target. Numerical simulation of the disruption of SCJ due to axial current was performed for the following three disruption mechanisms: a) development of the MHD instability of the SCJ, b) volume disruption, and c) joint manifestation of these mechanisms. The experimental data on the final depth of caverns in the target are compared with results of numerical simulation.

1 Introduction

Recent papers [1-3] were devoted to the effect of a pulsed electric current on metallic shaped-charge jets (SCJ). It has been shown experimentally and theoretically that SCJ are unstable when electric current is passed through them. The development of current instability and a decrease in the time of disruption of SCJ can lead to a severalfold decrease in the depth of SCJ penetration into a target, which is of great practical interest. The mechanisms of SCJ disruption by a pulsed current have not yet been completely understood.

This paper reports results of experimental and numerical studies of the effect on the penetration depth of the three possible mechanisms: a) volume disruption, b) development of magnetohydrodynamic (MHD) instability of SCJ, and c) joint manifestation of volume disruption and MHD instability.

2 Experimental Results

Diagrams of the experiments are given in Figs. 1a and b [1,2]. The experiments were performed with 50 and 100 mm diameter SC using steel and aluminum targets. The effect of electric current on the SCJ was additionally determined from the depth of jet penetration into the target.

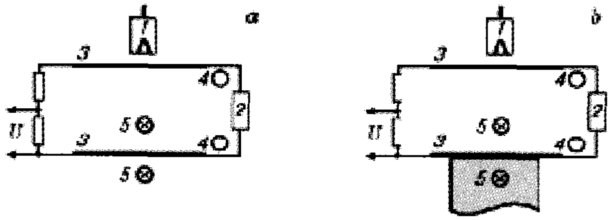

Figure 1. Experiment diagrams, where 1 is the shaped charge (SC), 2 is the source of electromagnetic energy, 3 - the electrodes, 4 - the inductive probes for measuring current and the derivative of the discharge current, 5 - the sites of flash radiography, and 6 is the target.

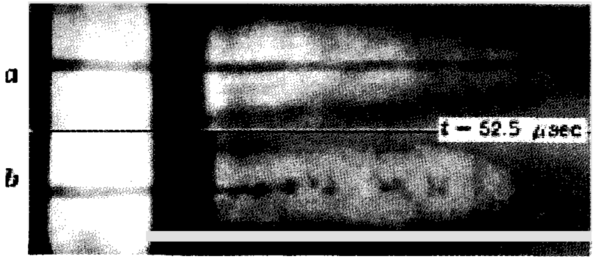

Figures 2a and b show X-ray photographs of two experiments performed with a 50-mm-diameter SC by the scheme shown in Fig. 1b: (a) refers to the experiment without a current and (b) to the experiment with a current (450 kA). It can be seen that in the experiment with a current, the jet broke up into individual fragments.

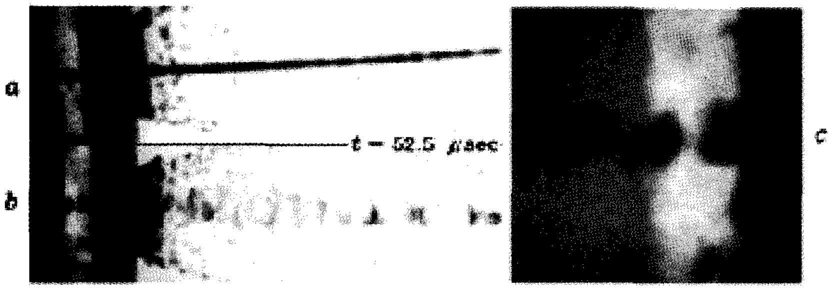

Figures 3a and b show pairs of X-ray photographs of a jet with and without a current, taken at the same times. The experiments were performed with a 50 mm diameter SC by the scheme shown in Fig. 1a. Figure 3c scales up a section of the SCJ of Fig. 3b in front of the lower electrode. The X-ray photographs clearly show the appearance and development of necks.

After passage through the lower electrode, the jet breaks into individual fragments with axial dimensions roughly equal to 1-3 jet diameters. The fragments are extended in the radial direction, reaching 5-10 jet diameters at the same cross-sections as in experiments without a current. X-ray photographs of jets from 100 mm diameter SC are given in Figs. 4a and b, where (a) refers to the experiment without a current and (b) to the experiment with a current. It is evident that the patterns of disruption of SCJ from 50 mm and 100 mm diameter discharges are the same.

It follows from the X-ray photographs that, after the jet passes the lower electrode, development of MHD instability and volume disruption of the SCJ material are observed. The number of necks in the jet without a current agrees well with the number of fragments in the experiments with a current.

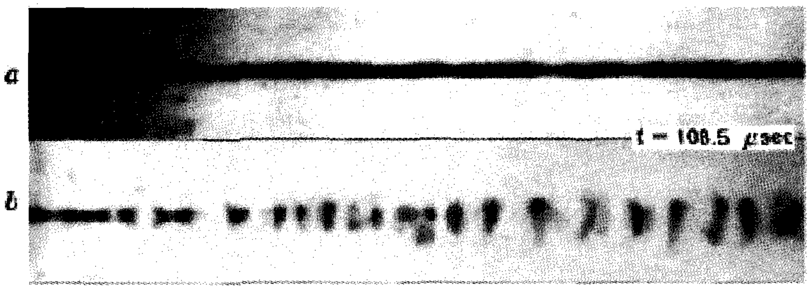

Figure 4. X-ray photographs of jets from 100 mm diameter SC, (a) refers to the experiment without a current and (b) to the experiment with a current.

Figures 2-4 clearly show the "disc formation" of SCJ fragments after disruption.

3 Numerical Simulation of the Action of an Electric Current on a Shaped-Charge Jet

The quasi-two-dimensional, nonstationary problem of the dynamic deformation of a conducting, high-gradient, thermally unhardened rod including time dependence of the total current through the jet was solved. The MHD and volume disruption models are presented in [3].

Thermal loss of strength was taken into account by the dependence of the current yield point σ_T on the temperature, $\sigma_T = \sigma_T\,(T_{mel} - T_0)(T_{mel} - T_0)$, where T_0 and T_{mel} are the initial temperature and the melting point, respectively. This model is adequate for the process of stretching of SCJ elements. For the cases of a purely mechanical process (in the absence of current) of the natural development of surface disturbances on a deformed SCJ, the model gives results that are practically identical to those obtained using more complex models [4].

Figure 5. Results of calculations of the natural deformation of one element of the middle part of the SCJ from a 50 mm SC, and deformation of the same element subjected to a 400 kA current of 5 μsec duration.

Calculations show that not only does an electric current accelerate the development of natural instability of a SCJ, leading to a more rapid break up of the jet into individual fragments, at a sufficient strength it can also cause the disc formation phenomenon. This is shown in Fig. 5, which gives the results of calculations of the natural deformation of one element of the middle part of the SCJ from a 50 mm SC, and deformation of the same element subjected to a 400 kA current of 5 μsec duration.

Calculations also show that the MHD instability and volume disruption are manifested at the same current-pulse parameters. Results of calculations of cavern depths in steel and aluminum targets using the models presented here are given in Tables 1 and 2. The experiments were performed by the schemes given in Fig. 1b.

Table 1. Steel Target Results

Experiment		Vol. Destruct.		MHD Inst. (Δ)		MHD Inst. (cavern)		MHD Inst.+ Vol. Destruct.	
No.	h, mm	h, mm	Δh, %	h, mm	Δh, %	h, mm	Δh, %	h, mm	Δh, %
98	79	82	+4	160	+103	54	-32	82	+4
101	91	132	+45	200	+120	65	-29	98	+8
103	147	184	+25	200	+36	100	-32	200	+36
102	160	200	+25	200	+25	131	-18	200	+25
116	195	200	+3	200	+3	150	-23	200	+3
contr.	205±10	-	-	-	-	-	-	-	-

Table 2. Aluminum Target Results

Experiment		Vol. Destruct.		MHD Inst. Vol. Destruct.		MHD Inst. (cavern)	
No.	h, mm	h, mm	Δh, %	h, mm	Δh, %	h, mm	Δh, %
52	257	353	+37	330	+28	257	0
53	130	353	+172	335	+158	158	+21
54	92	164	+78	144	+57	90	-2
56	93	176	+89	156	+68	91	-2
contr.	365±10	-	-	-	-	-	-

It follows from Tables 1 and 2 that, for a steel target, simultaneous allowance for the two mechanisms of SCJ disruption, i.e., development of MHD instability and volume disruption, gives the best agreement between the experimental and calculated depths of SCJ penetration into the target.

For an aluminum target, the best agreement between the experimental and calculated depths of SCJ penetration into the target is achieved on the assumption that only MHD instability is developed, provided that the current flows in the jet in the cavern.

4 Conclusions

The experiments performed showed that passage of a current through SCJ leads to development of necking MHD instability and volume disruption of the SCJ when the SCJ elements leave the electrode system.

Comparison of the experimental and calculated depths of SCJ penetration into the target shows that for steel targets, the best agreement is obtained when both disruption mechanisms are taken into account. In experiments with an aluminum target, the best agreement between the experimental and calculated SCJ penetration depths is obtained using the model of development of necking MHD instability provided that the current also passes through the SCJ when the jet moves inside the cavern.

References

1. Shvetsov, G. A., Matrosov, A. D., Pavlovskii, A. I., Current Instability of Shaped-Charge Jets, *Proc. 10-th Pulsed Power Conf.*, USA, Albuquerque (1995) pp. 1136 - 1141.
2. Shvetsov, A. G., Matrosov, A. D., “Experimental study of the current instability of shaped-charge jets,” Proc. 7th Intern. Conf. on Generation of Megagauss Magnetic Fields and Related Topics, Sarov (1996) (in press).
3. Babkin, A. V., Kruzhkov, V. A., Ladov, S. V., Marinin, V. M., Fedorov, S. V., “The behavior of metallic shaped-charge jets under the effect of a current impulse”, Proc. 7th Intern. Conf. on Generation of Megagauss Magnetic Fields and Related Experiments, Sarov (1996) (in press).
4. Chou, P. C., Carleone, J., The stability of shaped-charge jets *J. Appl. Phys.* **48** (10) (1977) pp. 4187 - 4194.

FEATURES OF METAL SHAPED CHARGE JET DEFORMATION IN LONGITUDINAL LOW-FREQUENCY MAGNETIC FIELD

S. V. FEDOROV, A. V. BABKIN, S. V. LADOV
Bauman Moscow State Technical University, Moscow, Russia

V. M. MARININ
Niistali, Moscow, Russia

The influences of a longitudinal axis-symmetric magnetic field on a metal, shaped charge jet stretching are considered. Magnetic fields were varied in time to allow for diffusion into the jet material. Theoretical investigations have shown that jet stretching with a diffused magnetic field is accompanied by magnetic field compression inside the jet, resulting in the appearance of radially stretching electromagnetic forces. As the plastic instability on the jet develops, the localization of these forces occurs at the neck region, which stabilizes jet stretching and results in increasing its effective length and penetration. The ratio of mechanical to electromagnetic forces in a jet at different external magnetic field intensity levels has been found. Laboratory test data are presented in which long, multi-looped solenoids were used instead of jet motion. The maximum increase in penetration depth of up to 10% is observed when changing the magnetic field induction from 1 to 10 T.

1 Introduction

At the detonation of a cylindrical, high explosive charge within a cavity lined by a thin, metal shell, a high velocity shaped-charge jet (SCJ) forms and stretches in free flight. This inertial stretching stage, at which jet elements are elongated uniformly, is followed by a necking stage. Necks develop as a consequence of plastic instability of the SCJ, resulting in the jet breaking up into separate non-deforming elements [1-4]. The length of the elements formed after the break-up defines the efficiency of SCJ armour-piercing effects.

In this report we have studied the influence of the longitudinal homogeneous magnetic field upon the process of the SCJ deformation in free flight.

2 Theoretical Studies

In studying the process of external magnetic field diffusion into the SCJ material, the distribution of the azimuthal induction currents volume density within the jet cross-sectional radius was considered as linear $j(r,t)=b(t)r$. On the basis of the electromagnetic induction law, the ordinary differential equation to determine $b(t)$ is

$$\frac{db}{dt}+2b\left(\frac{2\eta}{\mu_0 R^2}-\dot{\varepsilon}_z\right)=\frac{2}{\mu_0 R^2}\left(\dot{\varepsilon}_z B_e-\frac{dB_e}{dt}\right) ,$$

where ε_z is the jet element axial strain rate, B_e is the external magnetic field induction, μ_0 is the magnetic constant, η is the jet material specific resistance, R is the cross-section external radius, decreasing with time according to the differential ratio $dR/dt=-0.5\varepsilon_z R$.

As the calculations have shown, under a uniform SCJ elongation the process of magnetic field diffusion is defined by the non-dimensional parameter $\kappa=\varepsilon_{zb}\tau$, where ε_{zb} is the axial strain rate at the moment of the external field action beginning, $\tau=\mu_0 R^2{}_b/4\eta$ is the diffusion time constant.

Fig. 1 illustrates the changing magnetic induction on the SCJ element axis, where a constant magnetic field is achieved at $B_e=B_0$. At time t_e the field induction in the jet is equal to the external field induction, but then exceeds it. For the diffusion time t_e the approximation $t_e=1.05\tau/\kappa^{0.42}$ was obtained. At later stages of SCJ uniform deformation, the time t_e decreases proportionally to $n^{0.16}$, where n is the SCJ element elongation

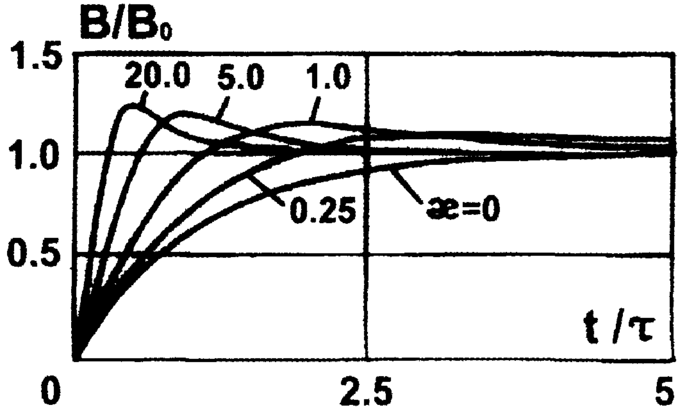

Figure 1. Magnetic field diffusion into stretching jet element.

coefficient. For example, a typical time t_e value for a middle element such as a copper SCJ, created by a laboratory shaped charge with diameter d_0 =50 mm, forms at about 15 μs after the inception of the necking stage.

The magnetic field compression effect in deforming SCJ leads to the appearance of radial tensile electromagnetic forces. These forces can stabilize the SCJ stretching process at the necking stage by localization in the regions of neck generation [5].

The model of an incompressible, rigid-plastic rod with variable cross-section was

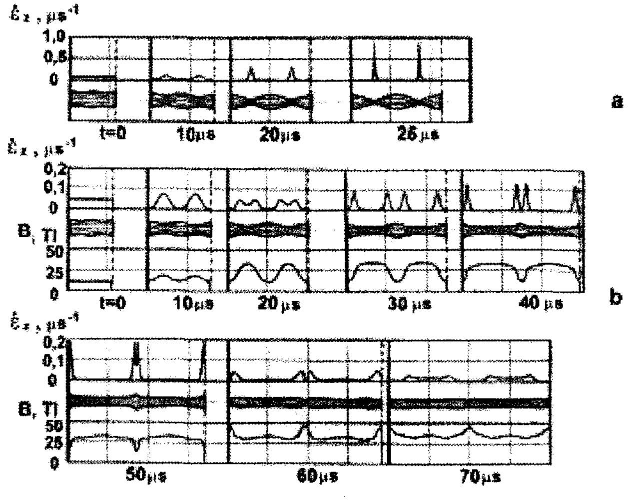

Figure 2. Perturbances' evolution on the necking stage of jet element stretching: a -natural stretching; b - stretching in magnetic field of B_0=10 T (under assumption of perfect jet material conductivity)

used to study plastic instability development in SCJ, based on the hypothesis of flat sections [6]. The initial rod parameters depended on the initial SCJ stretching necking stage. It was expected that at this moment in the SCJ material the magnetic field is created with the induction B_0, complying with the intensity of the external field in which the jet is deformed. Calculations showed that during deformation in a magnetic field, the initial perturbations on a perfectly conducting SCJ surface are suppressed and the jet stretching process has a stable nature (Fig. 2).

With final jet material conductivity (equivalent to copper) a full suppression of perturbations was absent, but their development was decelerated. The increase of the elongation of a SCJ element up to the break-up point, as a function of the acting magnetic field induction is illustrated in Fig. 3. Calculations were performed for middle jet elements created by shaped charges of 50 mm and 100 mm diameters at different values of the jet material yield strength Y.

It was found that the magnetic field stabilizing action noticeably reveals itself if the magnetic pressure $p_m=B^2{}_0/2\mu_0$ corresponding to this field intensity is comparable with the SCJ material yield strength Y. The scale factor influence is essential. With SCJ, geometric size increments increase the stabilization efficiency of the jet stretching process in increasing magnetic fields.

3 Experimental Results

Experiments to study the magnetic field influence on SCJ, in which a laboratory shaped charge of diameter $d_0 = 50$ mm was used, were carried out with the set-up shown in *Fig. 4*. A longitudinal magnetic field was created by the lengthened multiturn solenoid (3) placed between the shaped charge (2) and the steel target (1). A high-speed switch (4) that initiated the capacitor bank (5) discharge on the solenoid operated ahead of the charge initiation in order to increase the magnetic field. Parameters of the electrical circuit were such that the field in the solenoid changed only slightly during the SCJ formation.

The experimental results are presented in Table 1. At the magnetic field parameters realised, a strong effect was not achieved. However, the penetration depth in practically all of the experiments exceeds the maximum values obtained under comparable conditions without electromagnetic field. The increase is small (within 10%), although it is certain that a positive magnetic field influence on SCJ is observed.

Table 1. Experimental Results

N	Magnetic field induction, B_0, T	Penetration depth L/d_0
1	0	4.9
2	0	5.0
3	0	4.7
4	0	5.1
5	2.6	5.5
6	5.4	5.3
7	6.3	5.1
8	10.5	5.0
9	10.5	5.2

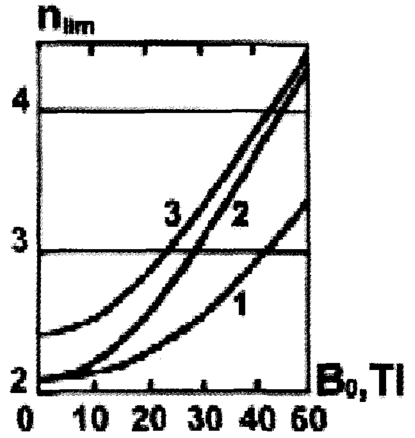

Figure 3. Magnetic field influence on the jet element limit elongation: 1 - d_0=50 mm, Y=475 MPa; 2 - d_0=100 mm, Y=475 MPa; 3 - d_0=50 mm, Y=237 MPa.

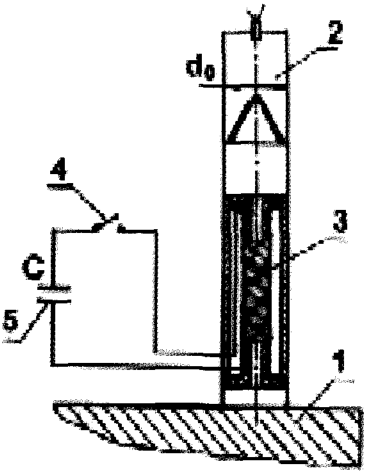

Figure 4. Experimental scheme.

Conclusions

Experiments have shown that a low-frequency, longitudinal magnetic field diffusing into shaped charge material jet before the jet breaks up on separate elements renders a stabilizing action on the jet stretching process.

References

1. Walters, W. P., Zukas, J. A., Fundamentals of shaped charges. New York: Wiley-*Interscience*, (1989).
2. Chou, P. C., Carleone, J., The stability of shaped charge jets. *J. Appl. Phys.* (1977) **48,** no. 10, pp. 4187-4194.
3. Romero, L. A., The instability of rapidly stretching plastic jets. *J. Appl. Phys.* (1989) **65,** no. 8, pp. 3006-3016.
4. Babkin, A. V., Ladov, S. V., Marinin, V. M., Fedorov, S. V., Features of shaped-charge jets inertial stretching in free flight. *Journal of Applied Mechanics and Technical Physics.* (1997) **38, no.2,** pp. 3-9 (in Russian).
5. Babkin, A. V., Marinin, V. M., Fedorov, S. V., Influence of longitudinal low-frequency magnetic field on shaped-charge jet stretching. *Defense technology.* (1993) **9** pp. 40-46 (in Russian).
6. Fedorov, S. V., Babkin, A. V., Ladov, S. V., Development of magnetic-hydrodynamic instability on shaped-charge jet being subjected electrodynamic action. *Defense Technology.* (1998) **1** pp. 49-56 (in Russian).

EXPLOSIVE ULTRA-HIGH PULSED POWER GENERATORS

ANALYSIS OF THE DISK EXPLOSIVE MAGNETIC GENERATOR OPERATION IN THE HEL-1 EXPERIMENT

V. K. CHERNYSHEV, V. N. MOKHOV, V. N. BUSIN, O. M. BURENKOV,
A. M. BUYKO, V. V. VAKHRUSHEV, B. E. GRINEVICH, YU. I. GORBACHEV,
A. I. KUZAEV, A. I. KUCHEROV, V. I. MAMYSHEV, YU. I. MATSEV,
A. A. PETRUKHIN, A. I. PISCHUROV, A. I. STARTSEV, V. B. YAKUBOV
VNIIEF, Sarov, Russia

A. G. ANDERSON, C. A. EKDAHL, D. CLARK, I. R. LINDEMUTH,
R. E. REINOVSKY, R. FAEHL, S. M. YOUNGER
Los-Alamos National Laboratory, New Mexico, USA

This report discusses the analysis of a powerful disk electromagnetic generator on a condensed liner.

1 Introduction

At the end of the eighties, experiments were carried out at VNIIEF to measure generator output parameters and to accelerate condensed aluminum and copper liners by a magnetic field, generated by operation of a 5-module disk explosive magnetic generator. The diameter of the generator was 1 m. It could store a larger quantity of magnetic energy than any other generator [1]. During the experiments, differences between the generator's operation and its design conditions were observed. Analogous experiments were performed in 1996: experiment HEL-1p, to determine the generator output parameters when driving a stretched (not compact) inductive load, and joint VNIIEF-LANL experiment HEL-1, in which an energy greater than 20 MJ was transmitted to the aluminum liner [2,3]. Compared to the preceding experiments, the above-mentioned experiments had some differences in setup that could influence the quality of the generator operation.

2 Experimental Results and Calculations

The load inductance values were 1.6 nH and 2.2 nH, respectively, in the experiments of 1988 and in the HEL-1p shot. Unlike the experiments of 1988, a stretched load was used in the HEL-1p shot that increased magnetic flux diffusion through the load walls. Besides, configuration of the load in HEL-1p implied that during high current flows, the load will expand and its inductance will increase. The currents of 10.5 MA and 9.1 MA were supplied to the generators in the experiment of 1988 and in the HEL-1p shot, respectively. The value of the current in the load for both generators is presented in Fig. 1.

A computational simulation of the experiments and comparison between computational and experimental data was made. The technique of computational simulation of the experiment is described in detail in [4].

The peculiarities of computational modeling of the experiments were as follows:

- all of the parameters of the transmission line (TL) and the load design diagram were used,
- additional losses of magnetic flux were simulated in two ways: by introduction of L_{eff} or by introduction of Ω_{eff} (ohmic losses),
- computations of the wall velocity were performed including elastic-plastic properties of the real walls having some finite thickness.

Our prediction for the nominal values of the current pulse's main characteristics in the HEL-1p experiment was:

$$\dot{I}_{max} \cong 15\ \text{MA}/\mu\text{s}, \quad I_{max} \cong 170\ \text{MA}.$$

That prediction, which took into account the specific design of the experimental device and accidentally agreed with experimental data, included a relatively big error (±20%) and fortunately agreed with the experimental data. Because the peculiarities of the HEL-1p experiment had not been studied in detail at that time, it was necessary to analyze them first on the basis of 1-D computations and later on the basis of 2-D computations.

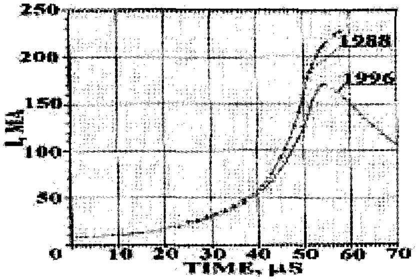

Figure1. Current-time dependence in the experiments with constant inductive load.

In the HEL-1p experiment, according to preliminary estimates, the value of the final inductance could have exceeded ~5 nH (at $t_* \approx 55$ μs). That was the primary reason that the current was less than ~230 MA in a similar experiment in which a compact load with inductance of $L_l \cong 1.6$ nH was used (instead of a long, coaxial transmission line), and the inductance of the DEMG transmission line was ~ 0.8 nH. The basic components of that inductance are:

- up to 0.8 nH - due to the TL wall expansion under the effect of magnetic pressure;
- up to 0.5 nH - "input" inductance caused mainly by the process of the device assembly;
- up to 0.5 nH - remnant inductance of DEMG cavities due to design differences in the DEMG modules tested in 1988 and in 1996.

The results of the HEL-1p experiment showed that in order to fully describe the results in the computations, it was necessary to take into account some additional magnetic flux losses.

It should be mentioned that a relatively large spread (±20%) in the results of the output computations of the HEL-1p experiment was due to the fact that the computations of the load inductance had a relative error several times higher than that of the liner experiment, for example. This occurs because the computation results are greatly influenced by the relative error caused by simulation of the TL real wall expansion rate. The absolute value of this error for wall thickness of 14-18 mm is ~10%. These results were obtained in 1-D computations including elastic-plastic characteristics of steel used as the wall material (yield strength is $\sigma_e \sim 25$ kg/mm^2). In the computations, the walls of the transmission line shifted under the effect of magnetic pressure. The maximum shift corresponded to the value of $I_{max} \cong 180$ MA ($t = 53.5$ μs). By that time, the walls of the TL shifted 0.6-0.8 mm and that corresponded to the increment of the TL inductance by 0.5-0.7 nH in the experiment.

Fig. 2 presents the current-time dependencies of the experiments on condensed liner acceleration performed before 1988, and of the HEL-1 experiment. One can see in Fig. 2 that in the HEL-1 shot, the current in the liner is higher than the current in the experiments of 1988.

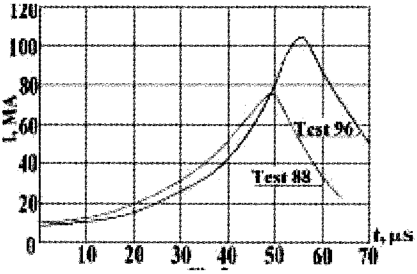

Figure 2. Current-time dependence in the experiments with liners.

Comparison between the computed and the experimental data show a satisfactory agreement. In the HEL-1 shot, the DEMG-PU system's operation was close to a lower estimate made before the experiment. There were some losses of magnetic flux in the system additional to those in our model DISK-l. These losses can be better accounted for if additional resistance $\Omega_{eff} \cong 0.13$ mΩ, not the value of $L_{eff} \cong 1.4$ nH, is introduced into the DEMG-PU current circuit.

The same estimate gives the best description of the results of two experiments having the same DEMG and inductive load; the experiments of 1988 and the HEL-1p shot.

However, the above-mentioned magnetic flux losses were smaller in the experiment under consideration than in the analogous liner experiments of 1988. According to computations made for the DEMG-PU system in that experiment, the maximum current of ~ 84 MA could correspond to the value of $\Omega_{eff} \cong 0.13$ mΩ, which was ~20% higher than the experimental value of the maximum current.

Thus, one can conclude that the pre-experimental measures taken to improve electrical contacts between current-carrying elements of the DEMG-PU current circuit were very useful, although they did not solve all problems.

Comparison of the experimental and computed data on the shift of the coaxial TL's wall by magnetic pressure showed satisfactory agreement.

Summary

To summarize, the analysis of generator operation in the 1988 and 1996 experiments on a rigid load shows a drop in the results of experiments done in 1996 compared to the results of the experiments carried out at the end of the 1980s.

In our opinion, that drop resulted from:

- a smaller value for the powering current: 8.9 MA instead of 10-10.5 MA;
- a higher final inductance: 5 nH instead of 3.6 nH;
- a larger value for the magnetic flux losses connected with diffusion through the walls, owing to a bigger load surface area.

Comparison of the experimental results and of the computations shows that a better agreement between them can be observed if additional effective resistance $\Omega_{eff} \cong 0.13$ mΩ is introduced into the computation.

References

1. Chernyshev, V. K., Grinevich, B. E., Vakhrushev, V. V., Mamyshev, V. I., Scaling image of 90MJ explosive magnetic generator. In megagauss fields and pulse power system. (Nova Science Publishers. New York.1990) p. 347.

2. Reinovsky, R. E., Anderson, B. G., Clark, D. A., et al., HEL-1: A DEMG based demonstration of solid liner implosion at 100MA, 11th IEEE Internanional Pulsed Power Conference, (Baltimore, Maryland, USA, 1997).
3. Chernyshev, V. K., Mokhov, V. N., Buzin, V. N., et al., Study of high – energy liner compression in HEL-1 experiment, 11th IEEE Internanional Pulsed Power Conference (Baltimore, Maryland, USA, 1997).
4. Buyko, A. M., Danov, V. M., Mamyshev, V., I., Yakubov, V. B., Technique for numerical simulation of the disk explosive magnetic generator with electroexplosive opening switch and

1.3 MV VOLTAGE PULSE FORMATION ON 13 Ω RESISTOR WITH MCG-160

A. S. KRAVCHENKO, A. S. BORISKIN, YU. V. VILKOV, V. D. SELEMIR, YE. M. DIMANT, A. S. YURYZHEV, D. I. ZENKOV, A. A. TKACHUK, YE. N. KIRSHANOVA, M. B. KOZLOV, T. BOUET
VNIIEF, Sarov, Russia

Described is a power source, based on MCG-160 with transformer energy output, allowing formation of high-power energy pulses (more than 100 GW) having a current rise time of approximately 1 μs on a load of 10 Ω effective resistance. The experimental results of the given magnetocumulative generator on the liquid resistor load are presented. Load connection to the source is provided by two serially connected gas-filled dischargers having triggering levels of (300 - 400 kV) each. A 1.3 MV voltage pulse is obtained on a resistive load of 13 Ω as a result of exploding electrical conductors. Voltage pulse parameters correspond to calculations. Experimental results show the possibility of 1 MV and higher voltage pulse formation with current rise times of ~100 ns.

1 Introduction

The application of magnetocumulative generators (MCG) [1] allows the creation of high-power energy devices that, having relatively small sizes, could provide ultimate parameters, for example, for plasma heating up to high temperatures, or for directed radiation flux formation. Since these are high impedance loads (from one to hundreds of Ohms), they should be effectively matched to the magnetocumulative generator. The power source for this purpose usually consists of an energy storage capacitor for initial magnetic field generation, the MCG, a voltage step-up transformer unit, storage contour, current breakdown unit and peaking discharger. In this paper we describe a magnetocumulative energy source with breaking unit made of electrically exploding conductors (EEC). Experimental and calculated results of its operation into the resistor with an active impedance of approximately 10 Ω are presented.

2 Magnetocumulative Generator

The appearance of MCG-160 type generator [2] with its transformer located on the output is presented in Fig. 1. Generator inductance decreases from 6.6 μH to 6 μH at the central tube fly apart under the influence of HE-charge detonation products from 64 mm to 104 mm diameter, where two metal semi-rings are located.

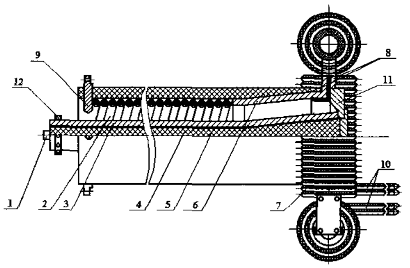

Figure 1. 1 - detonator, 2 - multi-sectional helix (stator), 3 - metal tube (armature), 4 - HE-charge, 5 - plexiglas tube, 6 - conical coaxial area, 7 - transformer unit, 8 - MCG output, 9 - explosion close switch, 10 - transformer unit output, 11 - conical flange, 12 - fastening clamp.

During the next 20 μs, when the central tube broadens to 161 mm in diameter, i.e. up to helix coils, generator inductance decreases up to 4 μH. Copper tubing 1391 mm long is used as an armature in the generator. Its external diameter is 64 mm and internal diameter is 56 mm for 860 mm of its length. Further, for 500 mm of its length, the tube broadens to 134 mm in diameter. The tube is supplied with two cast cylindrical and one conical HE-charges made of TNT-RDX (50/50). The total HE-charge mass is 7.2 kg.

3 Transformer Unit

A step-up transformer is used to coordinate magnetocumulative generator operation with the high-impedance load. An equivalent electrical circuit for the transformer is shown in Fig. 2. Constructively, the transformer unit consists of four cylindrical cable transformer blocks connected in parallel at the generator output [3]. A block is made of two parallel windings. Each winding has 16 turns. Cable shields in the windings are placed on the element and connected to the MCG output. Thus, a primary winding of the transformer unit with an inductive value of approximately 30 nH is created. A solenoid made of high-voltage cable is the secondary winding of the transformer unit. Here we have a transformer unit with the inductance of the secondary circuit equal to 28 μH and whose mutual inductance value is 0.8 μH.

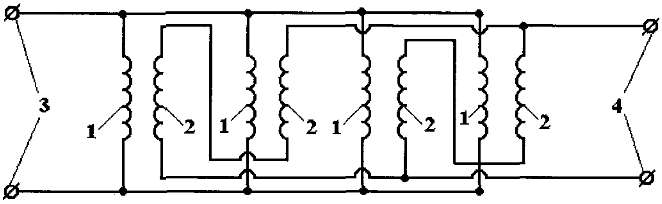

Figure 2. 1 - primary winding of a separate block, 2 - secondary winding of a separate block, 3 - low-inductive input, 4 - high-voltage output.

4 Peaking Unit and Load

A liquid resistor is used as a load for the MCG. Constructively, the liquid resistor is connected to the breakdown unit, made of EEC, which is part of the storage contour, and peaking dischargers. The liquid resistor consists of two similar blocks; each block length is 690 mm. A part of the liquid resistor with 7% table salt solution in water and gas-filled discharger with adjustable inter-electrode gap is located in each block on the axis. The resistor is made in the form of a cylinder with 110 mm internal diameter and 500 mm length. The active impedance value of one resistor, measured at ~9°C temperature, was 6.5 Ω. The breakdown unit is located coaxially with the liquid resistor. The breaking unit belongs to a separate block and consists of 13 copper wires, each having a cross-section of 0.375 mm2 and length of 2.25 m. Each conductor is folded into a helix with internal winding diameter of 50 mm and length of 500 mm.

5 Experiment and Results

The peaking unit and load were located behind the protective shield at a distance of ~8 m from the generator. Liquid resistors were located vertically one above the other, and their central part was grounded on the bunker. Uncontrollable gas-filled dischargers were mounted on high-voltage ends of the resistors. The inter-electrode volume was filled with a mixture of nitrogen and SF_6 (80% and 20% respectively) to 0.4 MPa pressure. The central part of the breaking unit was connected to the central part of the resistor and grounded. The maximum value of the initial current, created by a storage capacitor bank in the generator contour, was ~220 kA. During the MCG operation, a 535 kA current was obtained at the secondary circuit of the transformer unit. Measurement of time-dependent currents and voltages in the upper and lower halves of the load after triggering peaking dischargers (breakdown voltage is ~400 kV), was made using two Rogovsky coils, liquid resistors and divider. Voltage and current pulses in the load, synchronized with a time reference mark formed on 342 μs, are presented in Fig. 3.

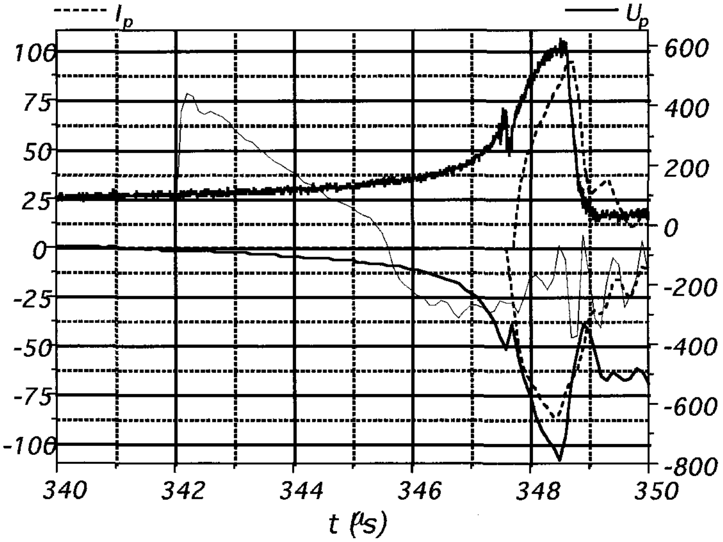

Figure 3. Voltage and current pulses on liquid resistors load, synchronized with the help of a time reference mark, formed on 342 μs.

To investigate further applications of this scheme for current pulse formation into a load with shorter fronts, we performed calculations where the breakdown of the two dischargers was at 1 MV. It follows that at a load of 13 Ω, it is possible to obtain current a pulse whose amplitude increases to 80% of its maximum value within 100 ns.

6 Conclusion

Current pulses having 90 kA amplitudes and 750 ns fronts (60 kA was obtained at 250 ns) were obtained in a load that consisted of a liquid resistor with an active impedance of 13 Ω. The voltage at the resistor was more than 1.3 MV, which corresponded to a maximum power of 120 GW. Experimental results and additional calculations show the possibility of voltage pulse formation higher than 1 MV and current rise times of ~100 ns.

References

1. Knopfel, G., Pulsed High Magnetic Fields. North-Holland Publishing Company, Amsterdam, London (1970).
2. Boriskin, A. S., Gusev, N. I, Zolotov, V. A., et al., Transportable Lightning Stroke Simulators Based on Magnetic Cumulative Generators, Electrical Technology- Pergamon, UK, *No* 4. (1995) pp. 19-25.
3. Bukharov, V. F., Vasyukov, V. A., Gurin, V. E., et al., Magnetocumulative Generators with Transformer Energy Output., PMTF, Russia, *No*1, (1982) pp. 4-10.

TRANSFORMER EXPLOSIVE MAGNETIC GENERATOR

A. JA. KARTELEV, V. K. CHERNYSHEV
VNIIEF, Sarov, Russia

This report presents the design and operational principles of the transformer explosive magnetic generator (EMG). The elements and properties of a pulse transformer and the disk EMG are integrated. The transformer is matched to capacitor power sources and low impedance loads, and produces currents having amplitudes of tens of megamperes with energy amplification factors up to 12.

1 Introduction

Circuits with a pulse current transformer connected between the capacitor bank and a single turn solenoid are often used to obtain high magnetic fields [1]. However, these circuits have a number of limitations: costs to fabricate transformers are high, and ohmic and inductive losses in the transformer are significant. Another method to obtain high magnetic fields with 2.3 MG intensity and 2 MJ of energy is the use of EMGs of the single turn "bar" [2] or "disk" [3] variety. Disadvantages of bar or disk EMGs are low inductance and high initial current, so these EMGs can operate only when combined with a helical explosive magnetic current preamplifier. The design and operation of a two stage current amplifier, also known as a transformer EMG, proposed by the authors in 1985 [4], are presented here.

2 Transformer EMG Design

A current transformer generator contains an internal primary multiple turn winding and an external secondary single turn winding, formed from oblate concentric cylinders (Fig. 1). The primary winding is constructed of one layer of copper enameled wire over the core. Depending on the transformer power, the number of turns in the transformer primary winding varies from 50-200 and the wire diameter varies from 1-5 mm. The primary winding leads are connected to a capacitor bank. The transformer core is made of electrical steel Э330. When the magnetic fields exceed the core material saturation inductance, a non-magnetic core is used. The secondary winding is made of sheet aluminum or copper 1-2 mm thick and is connected to a single turn solenoid made of tungsten alloy. The load is placed opposite to the primary leads and has 0.1-2 nH inductance. The primary and secondary windings of the current transformer – generator are separated from each other with an air gap determined by the supply conditions and required values of the current amplification factor. The high explosive charge is mounted on the outer surface of the secondary winding and the HE charge ignition system is placed on the side of the primary winding.

3 Operation Principle of a Current Transformer Generator

When switching the current transformer – generator to a capacitor bank, current begins to flow in the primary and secondary windings:

$$I_1 = (U_0/\omega(L_1 - M/(L_2 + L_H)))\sin(\omega t),$$

$$I_2 = -MI_1/(L_2 + L_H),$$

where U_0 is capacitor bank voltage; ω is primary loop frequency; L_1, L_2 and L_H are inductances of primary and secondary windings and load; and M is the mutual inductance between the primary and secondary windings.

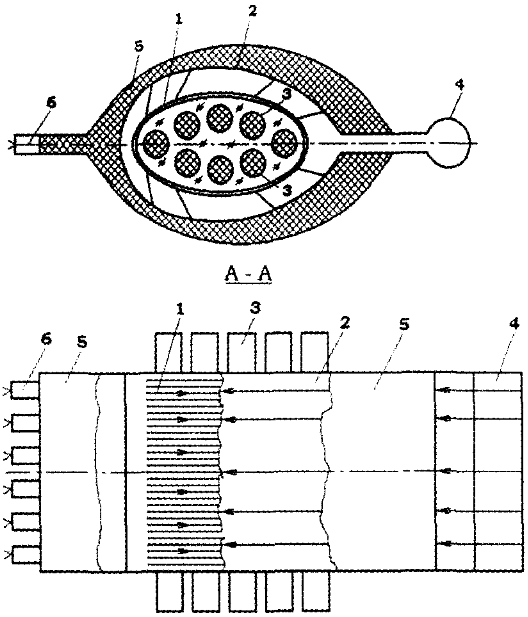

Figure 1. Scheme of a cylindrical type current transformer generator: 1 - primary multiturn winding, 2 - secondary single turn winding; 3 - core; 4 - load (a single turn solenoid); 5 - a sheet of explosives; 6 - system of explosive charge initiation.

Magnetic flux $\Phi_{gap} = L_2 I_2 (1 - K^2_{cpl})$ is introduced into the interwinding space of the transformer, where K_{cpl} is the magnetic link factor between the windings.

At the moment of maximum secondary current, the high explosive charge is initiated from the electric fuse, and the secondary winding starts moving toward the winding and load, under the effect of the HE products pressure. First, the secondary winding contacts the turns of the interwinding magnetic flux Φ_{gap} from penetrating into the primary winding. Then, the secondary winding, as a conducting piston, slides along the surface of the primary winding with the velocity of the detonation wave and presses out magnetic flux Φ_{gap} from the interwinding space of the transformer into the load. Significant current growth I_{2MC} is observed in the transformer load. Current amplification factor I_{2MC}/I_{2TR} is proportional to the ratio of cross-sectional areas of the interwinding space and the load, i.e., the larger the current transformer, the more effective the current amplification magnetocumulative stage, *and the higher the generator output power.*

4 Transformer EMG Testing Results

The experimental sample of the transformer EMG was fabricated at the VNIIEF experimental plant (Fig. 2). The windings of the experimental transformer generator had the form of oblate toruses. The diameter and height of the transformer at the secondary winding were 250 mm and 35 mm, respectively. The number of turns in the primary winding was 120 and the wire diameter was 1 mm. The secondary winding was made of 1 mm thick sheet aluminum, and the core was made of fabric based laminate. The 6 mm thick plastic high explosive charge was mounted on the outer surface of the secondary winding.

Eight detonators were installed on a 30 mm diameter circle in the center of the charge. Their function is to initiate the HE charge and produce a detonation wave spreading from the primary winding leads to the current transformer generator load.

When supplying a current of $I_1 = 1.4$ kA ("cold" mode), the following current values were obtained in the transformer EMG load with 0.13 nH inductance. At the stage of transformation when $I_{2TR} = I_L \sim 117$ kA and at the stage of the cumulation (compression of interwinding space) which was 10 μs long, the current was $I_{2MC} \sim 2.4$ MA. The resulting current amplification factor was $K_{I\Sigma} = 1710$, i.e. 14 times higher than the ratio of the transformer turns number $n_1/n_2 = 120$. The current transformer generator power was 36 MW, and the ratio of current transformer generator output magnetic energy to input energy was $L_L I_L^2 / L_1 I_1^2 \sim 12$, instead of 0.3 - 0.6 as in the known current transformers.

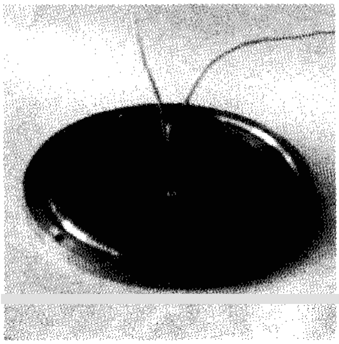

Figure 2. Photograph of primary and secondary winding of a toroidal current transformer generator of 250 mm diameter.

5 Conclusion

The proposed current transformer generator has the following advantages compared with known current transformers:

- 5-15 times higher current amplification factor and 25-250 times higher output magnetic energy;
- close to 5-15 times the energy transition factor from the power source to the transformer load, precisely the electric energy generation factor;
- the possibility of formation, due to transformation and magnetocumulative stages of current amplification, of different shaped current pulses: rectangular, linearly growing and staged.

All of this is achieved without any significant design changes to the transformer and its operation mode, and with minimal material and financial expenses for the EMG fabrication.

References

1. Karasik, V. R., Physics and Techniques of High Magnetic Fields. M.: *Nauka*, (1964).
2. Knoepfel, H., Ultrahigh Pulsed Magnetic Fields. M. *Mir*, (1972).
3. Chernyshev, V. K., Protasov, M. S., Shevtsov, V. A., The first disk explosive magnetic generators, Ultrahigh magnetic fields. Physics, techniques, application, M.: *Nauka*, (1984) pp. 23- 25.
4. Chernyshev, V. K., Kartelev, A. Ja., Two-stage explosive magnetic generator. A. S. No. 1384169 (USSR).

HIGH-VOLTAGE POWER SOURCE ON THE BASIS OF MAGNETOCUMULATIVE GENERATOR OF THE TYPE EMG-80

A. S. BORISKIN, YE. M. DIMANT, V. D. SELEMIR, A. A. SOLOV'YEV
VNIIEF, Sarov, Russia

Some mathematical models and results of mathematical simulations of voltage source operation (high-voltage generator) consisting of a magneto-cumulative generator (MCG) and voltage multiplier are presented in this paper. A voltage multiplier is a device in which all voltages resulting from electric explosions of the conductors in separate inductive storage capacitors, connected in parallel to the MCG, are summed with the help of special switching. For numerical studies we chose the MCG with the EMG-80-type transfomer. It is in serial production, has a significant power capacity of 200 kJ and has a small volume of ~0.25 m^3. Adaptability of this model for the analysis was confirmed with the experimental results. Calculations showed the possibility of obtaining megavolt voltage levels.

1 Introduction

Currently, there is a switching system proven in practice [1] that can provide summation of all the voltages produced by electrically exploding conductors (EEC) of the individual energy storages connected in parallel to one energy source, the magnetic-cumulation generator. The technological challenge and new problem areas facing designers of these powerful switching systems for high-voltage generation suggest the need for comprehensive numerical studies. With a suitable energy source available, the design and development can be expedited. Therefore, the numerical experiment was performed with a commercially available magnetic-cumulation generator (MCG) using a transformer such as EMG-80 [2].

2 Numerical Model

A numerical model was developed to look at the efficiency of high-voltage sources. Its circuit diagram is shown in Fig. 1. The model source includes N+1 inductive energy storages (inductors 1) and N additional inductors (inductors 2) to be formed by switching shots between inductors 1. Note in particular that this source has all of its inductors enclosed although they are one general circuit. In the circuit diagram, the inductance of this general circuit is identified as L_8. In calculations the L_8 inductance is found from segment additivity assumption, i.e. $L_8 = L_3 + L_4 + L^*$. Mathematically, calculations of the circuit that simulates the high-voltage source are confined to solving two sets of equations in sequence. The first to be solved is the set of equations that characterize currents until the time the conductors are exploded. The calculations to simulate MCG operation use some analytical expressions [3]. The relationship for R_5 with time is taken from [4]. When R_5 equals $20\times R_5^{(0)}$, all switches are making a shot. The calculation is then continued using the other set of equations that has been written for (4N+6) unknown currents I_o, I_1 (i=1÷4N+5), and the capacitor voltage U_c, with the assumption that a fixed value of the EEC resistance is achieved.

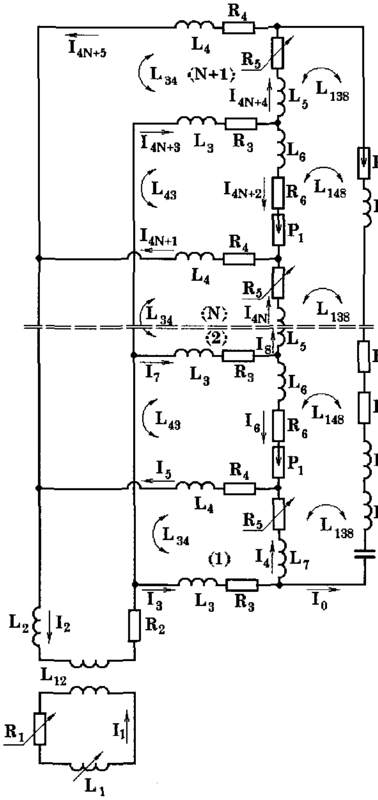

Figure 1. High-voltage source electric circuit. R_1, L_1 -resistance and inductance; L_{12} -mutual inductance of the transformer unit at MCG output; L_2, R_2 -the inductance and resistance of the transformer secondary winding and connection line to the branch-out point of EEC-carrying circuits; L_3, L_4, R_3, R_4 -inductances and resistances of the individual line segments which together with EEC form the inductive storage systems (inductors 1); $L_{13} = L_3+L_4+L_7-2L_{34}$ -inductance of inductor 1; L_7, R_5 -inductance and resistance of exploding wires; $L_{34} = \kappa_2\sqrt{L_3L_4}$ -mutual inductance (κ_2-coupling factor); $L_{14} = L_3+L_4-L_6-2L_{43}$ -inductance of the added circuit (inductor 2) formed by the switch shot between two neighboring inductors 1 at electric explosion; L_6, R_6 -inductance and resistance of the switch-carrying circuit segment; $L_{43} = \kappa_5\sqrt{L_3L_4}$ -mutual inductance not accounted until after forming the added inductor 2 (κ_5 -coupling factor); L_8 -inductance of general enclosing circuit; L_{11}, R_8, C -load quantities (inductance, resistance, capacitance); R_7 -resistance of the connection line between load and outer inductors 1; L_{10} -inductance of the line between load and general circuit; $L_{138} = \kappa_6\sqrt{L_{13}L_8}$ -mutual inductance of the general circuit with inductor 1 (κ_6 -coupling factor); $L_{148} = \kappa_7\sqrt{L_{14}L_8}$ -mutual inductance of the general circuit with inductor 2 (κ_7- coupling factor); P_1 -spark gap between two EEC; P_2 -sharpening spark gap.

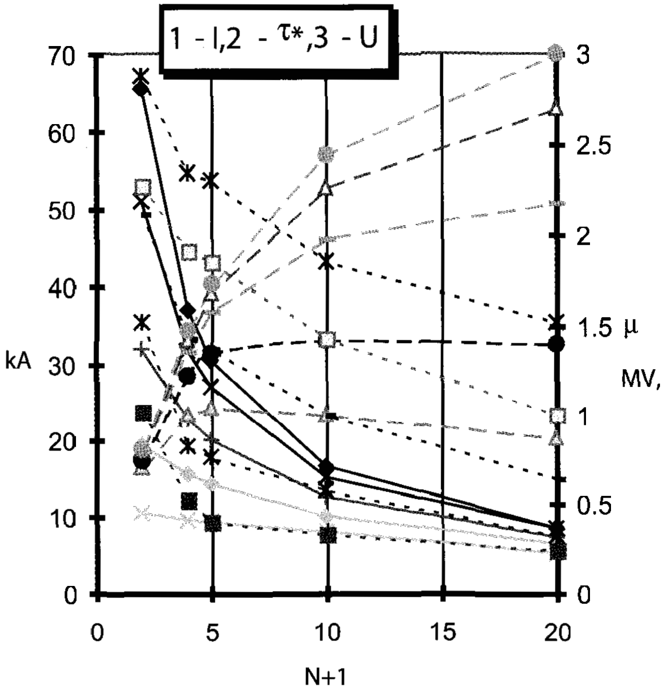

Figure 2. Numerical output data of the source: voltage, current and current risetime to 90% (τ*) as a function of L*. (1)- L* = 5 μH, (2)- L* = 10 μH; (3)- L* = 25 μH; (4)- L* = 50 μH; (5)- L* = 100 μH.

2 Conclusion

We obtained 2.2 MV in experiments with MCG-80 with the transformer unit on the output, and voltage multiplier consisting of seven inductive energy storage devices. This corresponded to a seven-fold voltage increase compared to the single voltage. Good agreement of the experimental results with the calculated ones confirmed the appropriate application of this model. It was only numerically that the operation of these voltage multipliers was considered in terms of the number of inductors used (Fig. 2).

For all of the inductors in the calculations, the EEC (1 m long, $S_1 = 0.078$ mm^2 for each conductor, total number $\Sigma = 20$), had an initial resistance of $R^{(0)}_{5\Sigma} = 0.01254\ \Omega$, a fixed mass of $M_{5\Sigma} = 15.25$ g and an inductance of $L_{7\Sigma} = 0.08\ \mu$H, respectively, and the resulting inductance for the total of inductors 1 was invariably 6.94 μH. Moreover, the EEC inductance (L_7) in an individual inductor 1 was defined as $(N+1)L_{7\Sigma}$ ($L_6 = 0.4\ \mu$H). The secondary winding inductance L_2 and resistance of the transformer unit together with the line from this to the initial branch-out point of EEC-containing circuits R_2 would be generally 14.68 μH and 0.05 Ω, respectively. A numerical simulation of a voltage source operating into a load with resistance $R_8 = 30\ \Omega$ and inductance $L^* = 0.31\ \mu H$ has shown that the voltage at spark gap switching will be 470 kV. However, after 0.09 μs there will be a maximum current of $I_0 = 32.3$ kA in the load, and the voltage will rise to 0.98 MV (Fig. 3). Numerical simulations have proven the possibility of generating voltages on a megavolt scale.

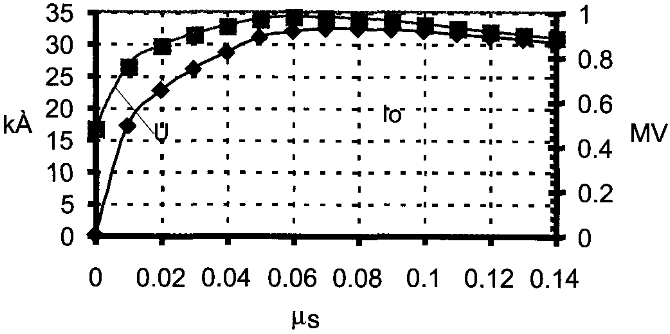

Figure 3. Calculated current and voltage curves. ($N+1 = 4$, $L_8 = 9.1\ \mu H$, $L_{13} = 8.96\ \mu H$, $L_{14} = 8.93\ \mu H$, $R_{5\Sigma}^{(0)} = 0.033\ \Omega$, $L_7 = 0.18\ \mu H$, $M_5 = 0.91$ g)

References

1. Boriskin, A. S. et al., Linear and Circular Multiloop Voltage Multiplier. In: *Megagauss Magnetic Field Generation and Pulsed Power Application.* Nova Science Publishers, N.Y. (1994) pp. 697-712.
2. Boriskin, A. S., et al., Transportable Lightning Stroke Simulators Based on Magnetic Cumulative Generators, *Electrical Technology* - Pergamon, UK - No. 4 (1995) pp. 19-25.
3. Berdyshev, A. V., Malyshev, I. I., Nakhmanson, G. S., et al., On the Feasibility of Explosive Magnetic Generators as Transmitters of Emergency Information, In: Megagauss and Megaampere Pulse Technology and Applicacation, VNIIEF, Sarov (1997) pp. 1021-1030.
4. Pavlovskii, A. I., Kravchenko, A. S., Selemir, V. D., et al., EMG Magnetic Energy for Superpower Electromagnetic Microwave Pulse Generation, In: *Megagauss Magnetic Field Generation and Pulsed Power Application.* Nova Science Publishers, N.Y. (1994) pp. 961-968.

AUTONOMOUS MAGNETOEXPLOSIVE GENERATOR OF MEGAVOLT, 100 NS PULSES

V. YE. GURIN, V. N. KATAEV, P. V. KOROLEV, V. I. KARGIN,
G. F. MAKARTSEV, V. N. NUDIKOV, A. S. PIKAR, N. F. POPKOV,
A. F. SARATOV
All-Russian Scientific Research Institute of Experimental Physics (VNIIEF), Sarov, Russia

Here we present the results of the work carried out at different stages aimed at the development of autonomous magnetocumulative generators having 100 ns megavolt pulses. This generator is meant to replace the PIRIT-01 stationary facility by a magnetocumulative energy source. Using a generator with permanent magnets as a source of initial energy and multiplying this energy by a cascade of magnetoexplosive generators allows 100 kJ of energy accumulation in a contour. The generator that has a permanent magnet does not need an additional energy source for its operation. It is convenient to operate and is always available for service. Shortening the MC generator current pulse up to 1 μs is implemented using a high-voltage explosive driven opening switch. In the first sharpening cascade, the voltage increases up to 500 kV. Further shortening of the current pulse duration up to 100 ns and the voltage rise up to 1 MV are performed using plasma opening switches according to the two-stage formation scheme. Such a scheme allows the decrease of electric field strength on the insulator surface and the use of magnetic insulation in the high-voltage section of the facility.

1 Introduction

The purpose of our work was to develop a design of a small-dimension variant of the electromagnetic pulse generator having parameters similar to the stationary facility PIRIT-01. The PIRIT-01 pulse facility provides 100 ns megavolt pulse with 250 kA current amplitude when discharging onto a vacuum or plasma diode. Implemented in the facility is a circuit using a plasma opening switch to accumulate inductive energy and sharpen electromagnet pulses.

The stored energy of a capacitor bank is converted into magnetic energy of the discharge current over a microsecond. The energy is then transmitted into the load. To form a pulse, the simplest design and easiest to use plasma-erosion opening switch with six plasma injectors is used. The plasma-erosion opening switch operation is based on a property of the high current plasma discharge to increase its resistance quickly when the current reaches its critical magnitude:

$$\sqrt{M_i/m_eZ}\,n_iZeV_i2\pi Rl\ ,$$

where M_i, m_e are ion and electron mass, Z *is* ion charge, n_i is plasma density, V_i is plasma flow rate, and $2\pi R$ is flow area.

At the PIRIT-01 facility, a 1.4 MV voltage pulse is generated using 500 kilovolts of shape voltage at the five-stage Marx generator on the plasma opening switch, i.e., an increase of voltage and power occurs. A circuit with an inductive storage has proven to be sufficient. This facility is now successfully employed as an electron beam accelerator and x-ray pulse generator. However, to enlarge the range of the generator application we had to create a small transportable analog.

2 Experiment

To solve the set problem we used a well-refined technology of magnetocumulative energy generators, high-voltage explosive-driven plasma opening switches combined with the technology of stationary inductive storage devices and plasma-erosion switches. While developing the generator it was necessary to solve a number of problems. MC-generators have too low internal resistance (10^{-3} Ohm) and have several tens of microseconds operation time. The PIRIT-01 facility has 10 Ohm of internal resistance and a 100 ns operation time, i.e., the difference constitutes several orders of magnitude. Though explosive driven opening switches reduce pulse duration up to a microsecond, their resistance is more than one order lower than required. As far as plasma erosion opening switches are concerned, at power pulse duration on the order of one microsecond, the plasma discharge is shifted up to 0.5 m. This process leads to the fact that plasma penetrates into the load area and, if a vacuum diode is installed, it fills its volume. All the above- mentioned items and a number of additional problems had to be studied before starting to develop the high voltage generator.

At the PIRIT-01 installation plasma diode operation modes were optimized, the plasma-erosion opening switch was investigated, electrode shapes and the form and number of plasma injectors were defined, and facility power modes and those of the injectors were studied. Also, the insulator was designed and optimum techniques to measure currents and voltages were developed. The plasma erosion opening switch steadily operated from 200 - 300 kA and provided current switching up to 50 kA in the vacuum diode at 1.4 MV break voltage. With the plasma diode, it was possible to increase the current switched onto the load up to 250 kA. We performed a number of experiments (Fig. 1) with explosive driven MC-generators at currents up to 10 MA, with pulse sharpening by the explosive driven plasma opening switch of up to 1 μs and secondary pulse sharpening by the plasma erosion opening switch of up to 100 ns. [2].

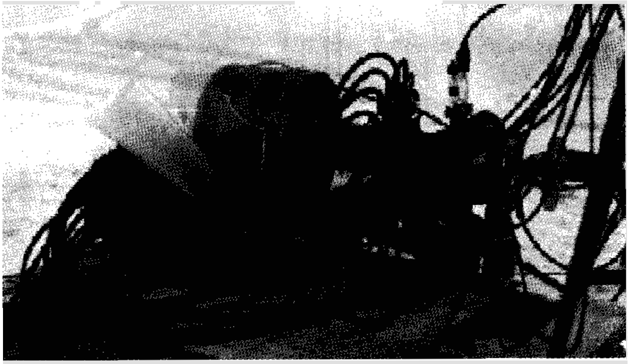

Figure 1. General view of the magnetoexplosive generator with a two-stage forming device.

The experiments demonstrated the possibility to sharpen the MC-generator current pulse in a two-stage formation circuit. In the same experiments on the plasma filled diode, we obtained a number of interesting data on the behavior of the plasma erosion opening switch discharge. In particular, an operation mode was found at which there was a series of pulses generated instead of one monopulse. The experiments were conducted on the available MC-generators with EM mass exceeding 10 kg and with simple, explosive-driven opening switches that were not very suitable for our purpose. However, these first experiments gave promising results and allowed us to answer a number of questions. First, there exists a significant difference between the form of the PIRIT-01 facility current pulse and that of current generated by the explosive-driven opening switch. Numerical calculations do not explain how the plasma discharge would behave, though they do not predict anything negative. The experiments show that the erosion opening switch operates at a more abruptly rising current pulse.

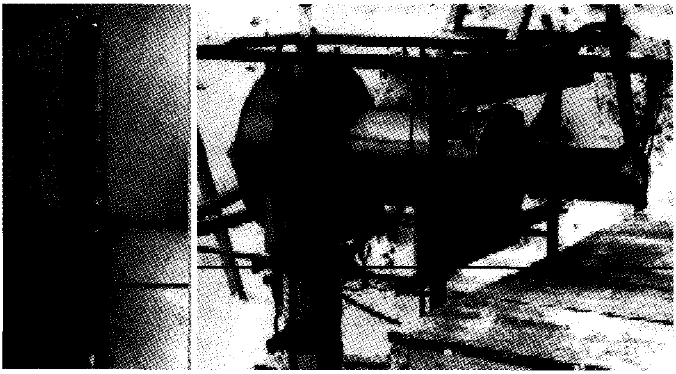

Figure 2. Explosive-driven helical plasma opening switch (a) and magnetoexplosive megavolt microsecond electron accelerator (b).

Earlier, we developed another type of high-ohmic opening switch for an explosive-driven megavolt microsecond duration electron beam accelerator [3]. Fig. 2 shows a general view of the explosive driven helical plasma opening switch (a) and a megavolt electron beam accelerator (b) made on its basis.

The plasma discharge burns by helix in this opening switch. As a result, it is possible to raise its internal resistance significantly. In the series of experiments on various designs of helical opening switches, voltage pulses of microsecond duration having amplitudes from 1 up to 1.5 MV and currents from 250 up to 140 kA were obtained.

In this paper we had the task to develop a generator with simpler electric parameters, though with significantly lower weight, smaller dimensions and, importantly, with shorter pulse duration. It was necessary to develop a device weighing less than 100 kg that reduced electromagnet pulse duration up to 100 ns. The generator should not need any additional energy sources for its operation and should always be available for service. The structural diagram of such an autonomous small-dimension generator of megavolt 100 ns pulses is analogous to the operation scheme [2] and is shown in Fig. 3.

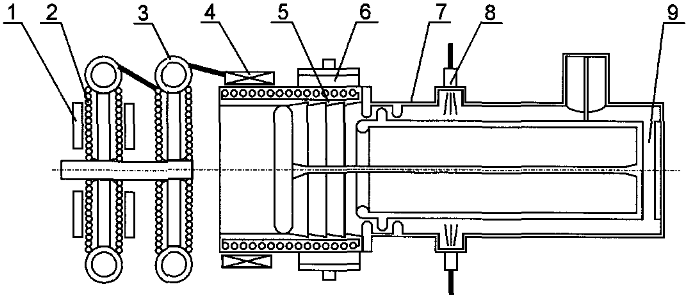

Figure 3. General structural diagram of a megavolt 100 ns generator.

For the first stage, we developed a MC-generator design with a magnetic field formed by permanent magnets (1) with 2 J initial calculated energy and 600 J output energy. Basic physical operation principles of the permanent-magnet generator are given in one of the reports in this conference [4]. Energy is then increased in a MC-amplifier up to 250 kJ. In this process, the sum of the weights of the permanent magnet generator and HE charges and MC-amplifier charge does not exceed 1 kg. Both generators are implemented according to the standard circuit with a current carrying wire as a multiturn flat helix (2). With the help of a 4-turn matching transformer (3) the generators are connected to the load.

The generators operate in quite an intense mode where the voltage between the turns is up to 30 kV, when strong radial and axial shifts occur. This required detailed numerical calculations of the operation, design optimization and a detailed choice of generator spirals turns distribution by sections. The current pulse is transmitted from the output stage onto the primary winding of the high-voltage transformer (4) and supplies the first formation stage of inductive storage. The explosive-driven helical opening switch (5) of the first formation stage is assembled with a charge (6) having dimensions $\varnothing 300 \times \varnothing 250 \times 90$ mm^3, with an external surface initiation system. This opening switch has been manufactured according to the same technology that has been used for other opening switches [3], but differs from them in its design implementation. At the current contour break of the first sharpening stage, the current pulse with calculated amplitude of 400 kA powers the vacuum inductive storage (7). In the second stage, the plasma-erosion opening switch (8) must sharpen a pulse up to 100 ns and generate 1.5 MV. Then, through plasma drift, the break area is shifted into the diode space (9). This provides better conditions for interrupting and allows the transfer of up to 80% of the stored current into the load.

The external device diameter equals 350 mm. The common length is 1000 mm. The facility is implemented by two variants. In the first variant, all of the units are assembled in one device. In the second variant, the eliminated section consisting of the MC generator explosive-driven opening switch is separated from the non-eliminated vacuum storage by a high-voltage cable line. The equivalent schematic diagram of the megavolt generator is given in Fig. 4.

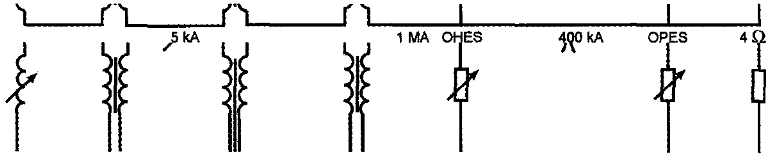

Figure 4. Equivalent schematic diagram of the megavolt 100 ns generator.

The MC generator energy is supplied through the transformer into the inductive storage having 500 nH inductance. A storage current of 1 MA is switched by the explosive-driven helical plasma opening switch with an operation time of about 1 μs. Along the high-voltage line at 400 kV and through the high-voltage discharge, a 400 kA current pulse is transmitted into the second sharpening stage storage with total inductance of about 500 nH. After current contour breaking on the plasma-erosion opening switch the voltage should be on the 1.5 MV level.

The megavolt 100 ns generator may be used to generate relativistic electron beams with currents up to 300 kA, and to generate x- and microwave radiation. The generator is made according to the transportable variant with ∅350×1000 mm overall dimensions, the weight of the entire device does not to exceed 100 kg.

References

1. Popkov, N. F., Kargin, V. I., Ryaslov, E. A., Pikar, A. S., Plasma X-Ray Radiation Source, *Journal of X-Ray Science and Technology* 5, (1995) pp. 289-294.
2. Pavlovskii, A. I., Popkov, N. F., Pikar, A. S., Ryaslov, E. A., Kargin, V. I., Two-stage System for Short Current MC Generator Pulse Formation. In: Megagauss Fields and Power Systems, Ed. by V. M. Titov and G. A. Shvetsov, New York: Nova Science Publishers, (1990) pp. 393-397.
3. Pavlovskii, A. I., Popkov, N. F., Pikar, A. S., Kargin, V. I., Ryaslov, E. A., Experimental Studies of Electron Beam Explosive High-Power Generator, Proceedings of the 10th International Conference on High Power Particle Beams, San Diego, California, (June 20-24, 1994).
4. Gurin, V. E., Kargin, V. I., Pikar, A. S., Popkov, N. F., Ryaslov, E. A., Calculation of Autonomous Magnetocumulative Generator with the Permanent Magnet, Megagauss VII (1998).

HIGH VOLTAGE PULSED MCG-BASED ENERGY SOURCE

E. V. CHERNYKH, V. E. FORTOV, K. V. GORBACHEV, E. V. NESTEROV, S. A. ROSCHUPKIN, V. A. STROGANOV

High Energy Density Research Centre, Russian Academy of Sciences,
IVTAN, Moscow, Russia

Design of a compact high-voltage generator capable of producing a voltage pulse with a peak value of 450 kV and a length of 200 ns on a load of 2 Ohm is proposed. A transformer-type and inductive storage and a current breaker based on an electro-explosive opening switch (EEOS) is used to generate a voltage pulse. A two-stage MCG with axial priming in the last stage is a source of energy for the device described.

1 Introduction

To generate REB with energy >500 kV and current >100 kA, the optimum circuit based on MCG must include transformer inductive storage and EEOS. The design of sectionalized MCG is combined. The first stage uses the face priming of an explosive charge, and the last one uses axial priming. This way, the operation time of the last stage as well as effective operation time of the MCG itself is reduced. The current in an EEOS circuit begins simultaneously with the start of the last stage compression of the MCG.

Simulations using numerical methods and engineering electro-technical models of non-linear circuit elements allowed optimization of the design. Calculation techniques and elements of design, as well as initial and output system parameters are discussed in the report.

Presently, the creation of compact power sources for high-current accelerators is connected to MCG usage. Despite significant progress in creating capacitors having high specific characteristics, their capacitive storage cannot compete with MCG when the energy of the pulse formed is higher than a few kJ.

Long term experience at HEDRC in the development of and experimental research with high current REB generators based on MCG, as well as printed data, resulted in the design of a self-contained high voltage source (SCHVS) with the following parameters:

Resistance of a load	2 Ohm
Inductance of a load	100 nH
Peak voltage Um	450 kV
Duration on height 0.8 Um	200 ns
Voltage rise time 0.1 - 0.9 Um	≤50 ns
Maximum power	80 GW
Pulse energy	~20 kJ

2 Preliminary Choice of the Characteristics of a Self-Contained High Voltage Pulsed Source Based on MCG

It is worth mentioning that for compact SCHVS based on MCG, the use of an inductive intermediate storage of energy (ISE) to shape the high voltage pulse has no alternative, as is choosing electrically exploded wires (EEW) as a circuit current breaker. To match the MCG to high-inductive storage, one should use a pulse transformer (PT) (Fig. 1). It is easy to show that energy losses will be minimized when the transformer combines properties of both matching element and inductive storage. This is known as transformer inductive storage of energy (TISE). Simultaneously, $L_s = L_2(1 - k_c^2)$, where L_2 is the inductance of a secondary winding of the transformer, k_c is the coupling coefficient of PT windings.

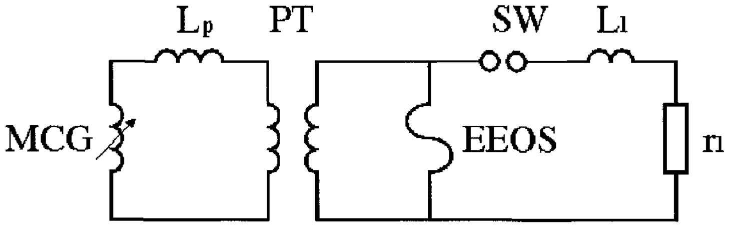

Figure 1. Circuit diagram of SCHVS with a transformer inductive storage.

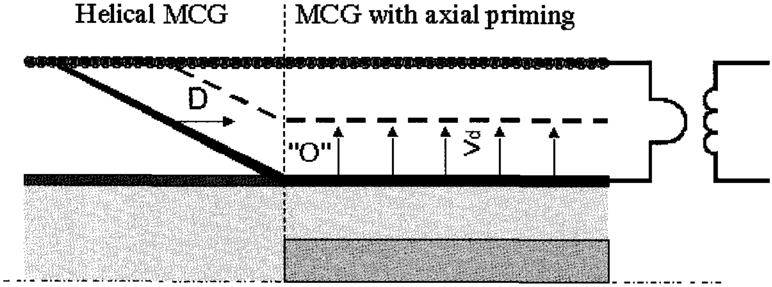

Figure 2. Circuit diagram of MCG with axial priming in the last section.

To diminish the effective operating time of MCG t_{ef} the axial priming of HE in the last MCG section (Figure 2) is used. The first stages of such an MCG operate as in a normal spiral MCG with face initiation HE. When a detonation wave approaches the point "O" corresponding to the boundary of the last section, simultaneous priming of HE along the axes occurs and a smooth, cylindrical detonation wave falls on the armature surface. This process allows sharp reduction of the operating time of the last cascade and effective operating time of the entire MCG.

3 Mathematical Modeling

By taking the optimum approach explained above as a zero approximation, we have conducted many alternative computations of the circuit design offered. The design procedure for the first four sections of the MCG design as discussed is borrowed from [4]. The design of the fast-run last MCG section was carried out using data given in [5]. Calculations have proven the necessity of using two spiral MCG with axial priming in the last sections. The most characteristic initial and output parameters of the circuit are given below:

Peak MCG current	2.6 MA
MCG operating time before the beginning of EEW stage	66 μs
Initial inductance of a pair of MCG	40 mH
Inductance of a primary PT winding	0.14 mH
Inductance of a secondary PT winding	5 mH
Diameter of EEW wires	0.15 mm
Length of EEW wires	600 mm
Number of EEW wires	60
Effective MCG operating time	3.8 μs
Maximum EEW current	0.297 MA
Discharger operation voltage	400 kV
Peak voltage across a load	436 kV
Maximum current in a load	0.209 MA
Peak power in a load	88.1 GW
Voltage pulse duration at height 0.8 U_m $t^{0.8}$	215 ns
Voltage rise-time from 0.1 U_m up to 0.9 U_m	50 ns

4 SCHVS Design

Installation includes the following units: CS with an explosive commutator for creating an initial magnetic field to energize the MCG; two spiral MCG, with windings connected in series and having systems with axially-primed HE charges in the last section of a spiral; a rolled type (RT) pulse transformer storage; a unit for generating a high voltage pulse, including the case with EEW as a package of copper wires and sharpening discharger.

The spiral MCG consists of a multi-entry spiral and an armature tube with a charge of HE. The spiral has 4 sections. The first section is wound with a 2.5 mm diameter insulated wire having two entries. The number of entries is doubled in each section for the three following sections, and tripled in the final one. The armature is made of a copper pipe with outer diameter of 40 mm and wall thickness of 2 mm.

5 Conclusions

The main problems associated with using MCG to generate short, high-voltage pulses are unduly long MCG operating times and the difficulty of matching MCG to the relatively high resistive load. Application of the transformer as an intermediate inductive storage device as well as axial priming used in the last stage of MCG solve both of these problems and create a super-compact pulsed power generator based on MCG.

References

1. Azarkevitch, E. I., Kotov, Yu. A., Raschet electrovzrivnogo cascada dvoukhkascadnogo prerivatelya toka (Design of electroexplosive stage of a two-staged current breaker). Book of abstracts of joint meeting of sections of scientific councils of AS USSR (in Russian). Tomsk (1986) p. 111.
2. Boriskin, A. S., Brodsky, A. Ya., Eksperimentalnie issledovaniya po generatsii elektronnogo puchka na vzrivnom elektrofizicheskom stende (Experimental study of electron beam generation at the explosive electro-physical installation) MG-VII, Book of Abstracts (in Russian) p.132.
3. ERI report (All-union electrophysics research institute). A generator "Stream" (in Russian).
4. Pavlovskii, A. I., Lyudaev, R. Z., et al., Mnogosektsionniy generator MK-2 (A multisectional generator MC-2). In *Superhigh magnetic fields. Physics. Technics. Application.* Nauka Publ. (in Russian) (1984) p. 312.
5. Zharinov, E. I., Demidov, V. A., Chernishov, V. K., Predelnie vozmozhnosti koaksialnikh VMG s osevim initsiirovaniem zaryada (Ultimate abilities of coaxial MCGs with an axial priming of a charge) in Russian. ibid. p. 298.

THE OUTPUT CHARACTERISTICS OF A TWO-STAGED EXPLOSIVE MAGNETIC COMPRESSION GENERATOR WITH HIGH INDUCTIVE LOAD

X. G. GONG, C. W. SUN, W. P. XIE, Q. Z. SUN, Z. F. LIU
Southwest Institute of Fluid Physics, Chengdu, Sichuan, P. R. China

The design and experimental studies of a two-staged explosive magnetic flux compression generator (MFCG) with high inductance load are described in this paper. The first stage of the generator consists of a cylindrical helix and amplifies the current and energy, the second stage carries out impedance transformation to an inductive load of 5-6 μH where an output current of 50-70 kA and an electromagnetic energy of 10-15 kJ is obtained. The pulsed voltage across the load could reach 40-60 kV.

1 Introduction

The explosive magnetic flux compression generator (MFCG) is a type of pulsed source that transforms the chemical energy of explosives into electromagnetic energy. The MFCG consists of a stator of larger inductance and an explosive driven armature that reduces the inductance of the stator, compressing the magnetic flux initially trapped in the circuit so that the current and energy passing through the load can be amplified. Typically, the load inductance is of the order of several to tens of nanohenries although the initial inductance of the stator is much larger. Therefore, the amplification of current or energy for MFCGs having a small inductance load is very high, making them useful for special purposes. In fact, many practical loads such as charged particle accelerators, lasers and other pulsed power devices have larger inductance. The development of MFCGs having a high impedance load has been carried out since the late 1997s.

Many authors have experimented on MFCGs with high impedance loads. Zherlitsn [1], Lyudaev [2] and Freeman [3] proposed the axially initiated helical generator in order to decrease its operation period and current rise time. They achieved a higher output voltage range of 120-470 kV across the inductive loads in their experiments. The transformers to couple the magnetic flux of the stator helix into the load circuits were adopted by Zherlitsn [1], Freeman [4] and Pavlovskii [5,6], consequently higher output impedance and very high voltage up to 1.5 MV were obtained. Fortov [7] and Leontyev [8] combined the above two ways of enhancing generator output impedance by not only increasing the current rate by decreasing the runtime, but by also enhancing the output impedance of the generator with a dynamic transformer. They developed the two-stage MFCGs that achieved an output electromagnetic energy of 3-6 kJ for a load of 5 μH. Although their device was compact in structure, the output current and energy were lower.

MFCGs with high impedance load have also been developed at the Southwest Institute of Fluid Physics, China. The Model 8-4 device was a single stage, conical helix MFCG that achieved the output energy of 1 kJ for a load of 5 μH, across which the voltage was 60-70 kV. On the basis of Fortov and Leontyev's work, the two-staged Model 8-5-II device was developed in 1997. In this model, amplification of input current and energy was performed by the first stage using a cylindrical helix stator, and the impedance conditioning was conducted by the second stage using a conical helix. An output current of 50-75 kA over an inductive load of 5-6 μH was obtained, and the corresponding electromagnetic energy reached 10-15 kJ. The output pulsed voltage across the load was 40-60 kV. The calculation of a circuit model agrees well with the measured current histories.

2 Design Parameters of the MFCG MODEL 8-5-II

As described above, the MFCG Model 8-5-II was a two-staged generator with a central copper tube as the armature, whose schematic is shown in Fig. 1. The explosion of powdered RDX in the tube was initiated at the left edge with a detonator, then the explosively expanding tube wall progressively hit the cylindrical helix (the first stage), then the conical one (the second stage). The input coupling for both stages was the same, i.e., by the transformer method. The total mass of this model was 8 kg.

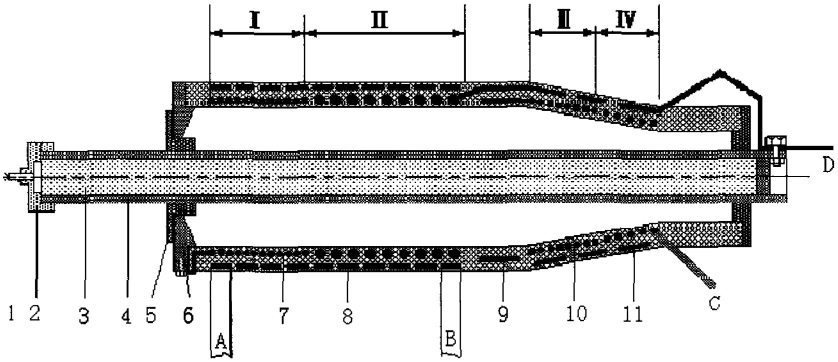

Figure 1. Model 8-5-II MFCG Device. 1-detonator; 2-booster gear; 3-RDX power explosive; 4-T2y copper center tube; 5-PTFE insulation flank; 6-disk crowbar; 7-first stage inner coil; 8-first stage outer coil; 9-crowbar for second stage; 10-second stage inner coil; 11-second stage outer coil; A, B-initial current input ends; C, D-connections to the load.

A capacitor bank of 1.01 mF with charging voltage $V_0 = 1.5$-2 kV provided the initial current $I_0 = 3.5$-4.3 kA to the first stage outer coil, and the input energy $E_0 = 0.47$-0.71 kJ. The central tube (armature) was made of T2y copper and had outer and inner diameters of 6.26 and 5.73 cm, respectively. Its length was 0.6 m. RDX explosive powder having density 1.04-1.08 g-cm^{-3} was inside the tube and its mass was about 1.6 kg. The coil parameters for both stages are listed in Table 1. The diameter of the first inner helix was 12.5 cm and the half-conical angle of the second inner helix was 8.5^0, and their diameters at two edges were 12.35 and 8.4 cm, respectively.

Table 1 Model 8-5-II device coils parameters

	Stage		1st stage cylindrical helix		2nd stage conical helix	
Inner coil	Coil		L2		L4	
	Section		1	2	3	4
	Conductor diameter (cm)		0.1	0.178	0.16	0.16
	Wire diameter (cm)		0.175	0.25	0.269	0.269
	Wire number		1	2	1	1
	Pitch (cm)		0.2	1.0	0.2791	0.3588
	Turns		50.75	11	25	16
	Length (cm)		10.2	11	6.72	6.12
	Inductance (μH)	Without central tube	269.2		103.7	
		With central tube	219.5		73.0	
Outer coil	Coil		L1		L3	
	Wire conductor (cm)		0.2×0.5		0.2×1.5	
	Wire number		1		2	
	Turns		40		3	
	Inductance (μH)	Without central tube	96.2		1.10	
		With central tube	78.8		0.84	

3 Experimental Results and Model Computations

A series of experiments was conducted to check the performance of model 8-5-II with an inductive load of 5-6 μH, and to compare calculations with experimental data. The experimental circuit including the initial energy source (C), the MFCG and the inductive load (L_H) is shown in Fig. 2

The current through the coils of both stages and its derivatives were measured with Rogovski coils and magnetic probes, respectively. The summary of the experimental data for eight shots of this model is listed in Table 2, and typical current forms are shown in Fig. 3-5.

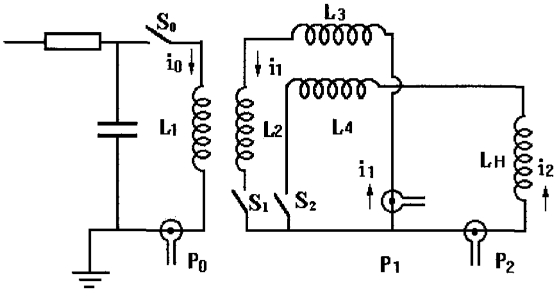

Figure 2. Circuit for the experiments of model 8-5-II with inductive load

Table 2. Inductive load experimental results for model 8-5-II device.

No	L_H /μH	Initial source	Input parameters			Second stage			V_{LH} /kV	$\frac{E_2}{E_0}$	$\frac{\phi_2}{\phi_0}$
		E_c /kJ	I_0 /kA	E_0 /kJ	ϕ_0 /Wb	I_2 /kA	E_2 /kJ	ϕ_2 /Wb			
1	5.28	2.0	3.6	0.52	0.29	57.6	8.8	0.30	46	16.8	1.03
2	5.34	2.0	4.0	0.64	0.32	74.5	14.8	0.40	57	23	1.25
3	5.93	2.0	4.3	0.71	0.33	60.1	10.7	0.37	53	15	1.12
4	5.93	1.3	3.5	0.48	0.28	55.9	9.3	0.33	42	19.2	1.18
5	5.93	1.3	3.5	0.47	0.28	58.2	10	0.35	42	21	1.25
6	5.93	1.3	3.5	0.49	0.27	73.5	16	0.44	62	1.03	1.63
7*	5.93	1.5	3.9	0.59	0.31	66.1	13	0.39	48	22	1.27
8*	5.93	1.3	3.6	0.52	0.29	60.5	10.9	0.36		21	1.24

It is noted that the maximum current derivative in the first stage was (2.38±0.40)X 10^{10}A-s^{-1}, and that in the second stage it was (0.88±0.14)X10^{10}A-s^{-1} among the eight shots. The output current through the inductive load of 5~6 μH was greater than 55 kA, and the maximum was near 75 kA. The electromagnetic energy $E_2 = \frac{1}{2} L_H I_2^2$ stored in the load was greater than 8.8 kJ, and the maximum was greater than 15 kJ. The energy amplification factor ($E_2/E_0 = \frac{1}{2} L_H I_2^2 / \frac{1}{2} L_0 I_0^2$) exceeds 15, and the maximum is 33. The voltage $V_{LH} = L_H dI_2 / dt$ across the load exceeds 40 kV, and the maximum is 62 kV. Due to the initial flux of the two-stage input by the transformer coupling during MFCG operation, the magnetic flux is compensated and the factor $\Phi_2/\Phi_0 = L_H I_2 / L_0 I_0$ exceeds 1.

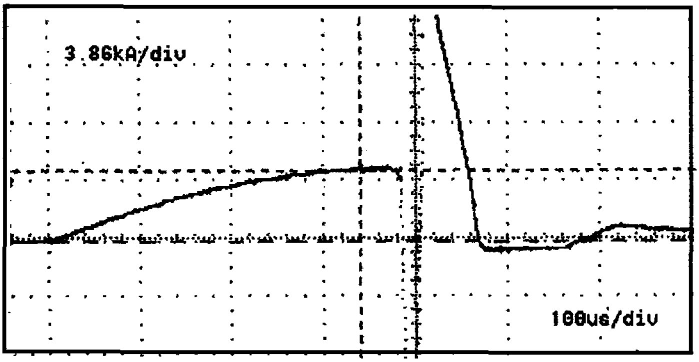

Figure 3. Input current I_0 waveform in experiment 6.

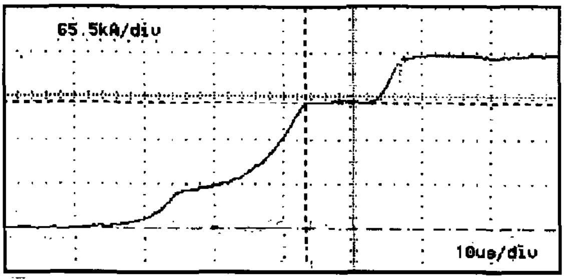

Figure 4. First stage current I_1 waveform in experiment 6

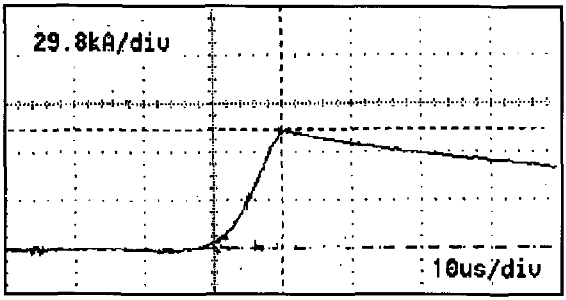

Figure 5. Second stage current I_2 waveform in experiment 6.

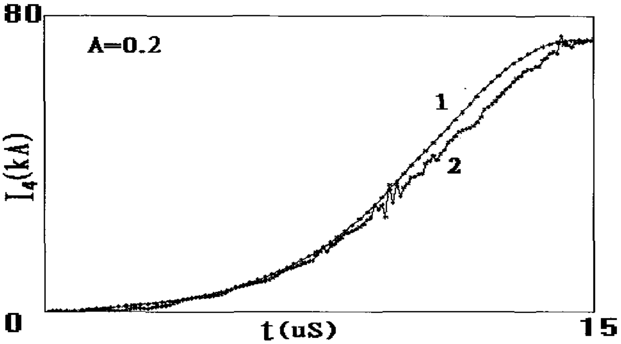

Figure 6. Comparisons between experiment and computation for second stage current I2 in experiment 6. 1 - computational curve, 2 - experimental curve.

The 8-5-II-type MFCG is a generator with trapped flux that gains not only current and energy, but also amplifies the magnetic flux. Fortov, Mintsev et al. [7] had proposed a five-loop circuit computational model for this generator, where the circuit flux can be regarded as ohmic resistance R_f = -AdL / dt and A, the coefficient of flux loss, is constant. In our work, A for model 8-5-II is assumed to be 0.2, and model computational results are well in agreement with the experiments. They are shown in Fig. 6.

4 Conclusions

The Model 8-5-II MFCG device is a compact explosive magnetic flux compression generator with a high impedance load. It consists of a cylindrical and conical helix. The initial flux for two stages uses the coupling input. The first stage completes the current and energy amplifications, the second stage performs the impedance transformation. The device, for which the total mass is only 8 kg, can run under a large inductive load of 5-6 μH. We conclude the following through several tens of experimental trials:

1) This device can produce a pulse current of 50-70 kA and store electromagnetic energy of 10-15 kJ in the large inductive load of 5-6 μH, producing a pulse voltage of 40-60 kV across the load.
2) The best input parameters for the device are: $i_0 = 3.5$ kA, $E_0 \cong 0.48$ kJ, $\Phi_0 \cong 0.28$ Wb.
3) The results calculated by the model agree well with the experimental curves.

References

1. Zherlitsin, A. G. et al., High Voltage Pulse Generation Using an Explosive Magnetic Generator with Axis Initiation. In: Titov, V. M., Shvetsov, G. A., Megagauss Fields and Pulsed Power Systems. New York: Nova Science Publishers (1990) p. 607.
2. Lyudaev, R. Z. et al., Investigation of Helical Magnetocumulative Generators with Axial Initiation. In: Chernyshev, V. K., Selemir, V. D., Plyashkevich, L. N., Megagauss and Megaampere Pulse Technology and Applications. Sarov (Arzamas-16), VNIIEF (1996).
3. Freeman, B. L. et al., Testing the Mark 101 Magnetic Flux Compression Generator. In: Fowler, C. M., Caird, R. S., Erickson, D. J., Megagauss Technology and Pulsed Power Application. (New York and London, Plenum Press, 1987) p. 441.
4. Freeman, B. L., et al., Magnetic Flux Compression Generator Power Electron Bean Experiments. In, Fowler, C. M., Caird, R. S., Erickson, D. J., Megaguass Technology and Pulsed Power Application. (New York and London: Plenum Press, 1987) p. 729.
5. Pavlvskii, A. I. et al., Magnetic Cumulation Generator as Power Source to Accelate Intense Electron Fluxes, In: Titov. V. M., Shvetsov, G. A., Megagauss Fields and Pulsed Power System. (New York: Nova Science Publishers, 1990) p. 449.
6. Pavlovskii, A. I. et al., EMG Magnetic Energy for Super Power Electromagnetic Microwave Pulse Generation. In: Cowan, M., Spielman, R. B., Megagauss Magnetic Field Generation and Pulsed Power Applications. (New York: Nova Science Publishers, Inc., 1994) p. 961.
7. Fortov, V. E., et al., Testing of Compact Magnetocumulatative Generators. In: Cowan, M., Spielman, R. B., Megagauss Magnetic Field Generation and Pulsed power Applications. (New York: Nova Science Publishers, Inc., 1994) p. 947.
8. Leontyev, A. A., et al., Two-stage Magnetic Flux Compressors with Flux Trapping. In: Chernyshev, V. K., Selemir, V. D., Plyashkevich, L. N., Megagauss and Megaampere Pulse Technology and Applications. Sarov (Arzamas-16), VNIIEF (1996).

ON THE DEVELOPMENT OF MCG WITH ARMATURE, ASSEMBLED FROM SEPARATE TUBES

L. N. PLYASHKEVICH
All Russian Scientific Research Institute of Experimental Physics (VNIIEF), Russia

The new direction in MCG technique is the application of a set of metal tubes with HE-charge inside as an armature. The tubes can be parallel to each other and initiated from one of the ends. In another variant, the tubes are located on the circuit radii, and they form a solid metal disk at their initiation from the center or periphery. Developing pilot constructions of MCGs with such an armature is necessary as the first step. This could be the analogue of the fast plain MCG, one plane of which is replaced with the block of parallel tubes, and a coaxial MCG. One can see three possible constructions that could have advantages over the existing MCGs. First is the MCG with radial tubes. Another is the application of the armature having a block of parallel tubes. The operation time of such a block is determined by the tube length and could be very small, about several microseconds. The third direction is connected with the development of large-scale helical energy preamplifiers. Using, among other things, an armature assembled from separate tubes, it is possible to decrease the quantity of HE-charge to tolerance limits (3-4 times less compared to traditional MCGs).

1 Introduction

An application of multitube armature in a magnetic cumulation generator (MCG) is shown in [1,2], where parallel tubes located from each other at a distance equal to the tube external diameter are considered (Fig. 1a). The tubes are initiated simultaneously from their ends with an explosive lens. The tube walls fly apart and touch each other, forming a continuous common surface perpendicular to the tubes. This common surface moves along the tubes with the rate of the HE-charge detonation velocity; its unevenness is comparatively small.

In another type of armature [3], the tube disposition on circumference radii (Fig. 1b) is used. At initiation from the circumference center, their walls form a continuous metal disc (quasi-disc) with an external diameter that increases in time and can experience magnetic cumulation. This disc can also be used to compress a solenoidal magnetic field. In this case, its side surface must be continuous during MCG operation.

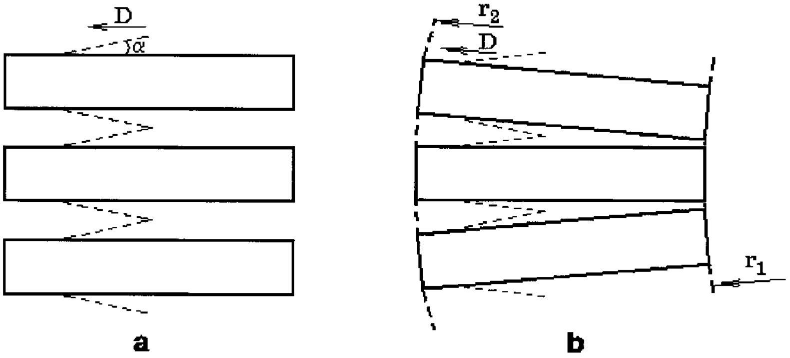

Figure 1. Scheme of a multitube armature. a - parallel located tubes; b - radial located tubes. D - the detonation velocity. r_1, r_2 - inner and outer radii of quasi-disc.

Experimental gas-dynamic investigations for studying the multitube armature are necessary. We demonstrated, for example, that generating cumulative jets at wall collisions do not create obstacles for MCG operation.

Many MCG types can be formed based on the proposed armature. However, MCGs represent a rather well developed field of technique. In these cases, novelties have the right to life if they give some essential advantages.

A multitube armature involves radical changes in MCG. Some prospects of such MCGs are currently evident. However, it is necessary to create and to investigate experimentally some pilot MCG designs to study their peculiarities and possibilities. It is more preferable to elaborate these MCGs as the analogues of the existing types. Initially, two analogues are sufficient. They are the fast flat MCG [4] and the usual coaxial MCG. These generators are simple to make and the use of multitube armatures in these generators is obvious.

In an ordinary flat MCG, the movable plate (armature) flies to the immovable plate. In the case of the multitube armature, the parallel tube set is located perpendicular to the immovable plate that is a very short distance from the tube ends, since the load inductance of a flat MCG is small. Therefore, it is very important to ensure the total decrease of the MCG working volume at the detonation end. We can use the technical decision for multidisc MCGs here [5,6]. Either a metal cone glideplane on the end of every tube, or tubes with cone broadening on the end are used. Both methods are also used in ordinary coaxial MCGs having a single tube.

The operation of a coaxial MCG with a multitube armature is similar to an MCG having axial initiation of a HE-charge. That is why it is preferable to construct the coaxial inner conductor of a multitube MCG as a solid metal rod with cone broadening at the end. A multitube armature facilitates the creation of large diameter coaxial MCGs, since massive and cumbersome end-output designs are unnecessary. By controlling the tube number in the armature cross-section, we can possibly increase the generator efficiency.

2 MCG Variants

From prospective MCG schemes, three variants are considered briefly here that allow us to realize their advantages compared to traditional MCGs.

2.1 MCG with Tube Radial Location

A set of quasi-discs can be located on the axis of a coaxial MCG perpendicular to the axis. The tubes are directed along disc radii. These tubes are initiated from the axis; the tube walls of neighboring discs, when flying, touch each other. Thus, we will have a device that is similar to both an MCG with axial initiation and a multidisc MCG.

Compared to the first MCG, this device will operate faster since its working volume will increase with the detonation velocity. The advantages compared to a multidisk generator are not evident. For example, we can increase the generator rapidity by increasing the number of discs. In the case of a multitube armature, since a quasi-disc is transparent for an axial current, unlike a multidisc MCG, the generator's inner resistance does not increase with the disc number.

Quasi-discs do not require high precision manufacturing and are not detailed; therefore the entire generator can be mounted directly at the shot location. We can also easily increase the generator sizes to improve the output energy to some hundreds of megajoules.

2.2 MCG with a Set of Parallel Tubes

This is the most interesting MCG. The operation time of this generator may be very short (about several microseconds). Filling up the generator working volume with multitube packets, we can increase the MCG size without increasing its operation time. This unique possibility of the proposed technology will allow us to improve the output power.

The packet consists of a plate explosive lens of about 1 cm thickness and a set of tubes located perpendicular to the lens. This packet has a round form in analogy with a multidisc MCG. A rectangular packet form is also possible.

There are technical difficulties in the creation of such MCGs (more complicated explosive system, problem of the output electrical strength, etc.). However, these MCGs have tempting prospects.

2.3 Helical MCG

It is useful to employ the multitube technique to create large helical energy preamplifiers. Currently, the output energy of the largest helical MCG does not exceed 30 MJ. High voltage and mechanical strength problems are the main difficulties in large helical MCGs [1].

If we decrease the current regime (and output energy and inner magnetic field), these difficulties will also decrease. These MCGs can be interesting for some applications, if their sizes are rather large.

For example, a 4 m long helix generator with a 1 m helix diameter, for a fast helical MCG [7] with 240 mm diameter, would have an output energy of ~ 120 MJ (initial energy ~ 1.2 MJ). Its operation time of ~ 500 μs is still acceptable.

However, the HE-charge occupies ~ 20% of the inner volume in a traditional MCG. In the MCG considered here, the HE-charge is 1.5 tons. A very large amount of mass is used with little efficiency. The multitube armature does not decrease the HE-charge; however this is possible in a piston of a helical MCG that has holes. Magnetic flux losses in these holes are noticeable if the section containing holes in the piston area is large enough. For a multitube armature, simply eliminating some tubes would create the piston holes. We hope that the HE mass could be decreased 3-5 times at permissible flux losses.

For a multitube armature, we can possibly use a helix with a rectangular cross-section. This allows us to more easily manufacture a large helix, since it can be assembled *in situ* before the experiment. These helix energy preamplifiers can be used to feed the above-mentioned coaxial MCGs. This will allow us to create devices with output energy of hundreds of megajoules at a high output power.

3 Summary

The application prospects of a set of metal tubes as an armature are considered. On this basis, some analogues of the existing MCG types can be developed.

References

1. Pavlovskii, A. I., Plyashkevich, L. N., Shuvalov, A. M., Boriskin, A. S., Dimant, Ye. M., Vinogradov, A. V., Some New Possibilities of Helical MCG Design, in: *Megagauss Magnetic Field Generation and Pulsed Power Applications,* (Ed. by M. Cowan and R.B. Spielman, N.Y., Nova Sci. Publ., 1994) pp. 637-644.
2. Plyashkevich, L. N., Some Possibilities of MCGs with Multielement Armature, Consisted of Separate Tubes, in: *Megagauss and Megaampere Pulse Technology and Applications.* (Ed. by V. K. Chernyshev, V. D. Selemir, and L. N. Plyashkevich, Sarov: VNIIEF, 1997) pp. 314-318.
3. Plyashkevich, L. N., Demidov, V. A., Selemir, V. D., New Type of Facilities for Magnetic Flux Explosive Compression, in: *Digest of Technical Papers, 11th IEEE International Pulsed Power Conference,* Baltimore, 1997. (Ed. by G. Cooperstein and I. Vitkovitsky) pp. 1482-1485.
4. Erickson, D. J., Caird, R. S., Fowler, C. M., Freeman, B. L., Garn, W. B., Goforth, J. H., A Megavolt Pulse Transformer Powered by a Fast Plate Generator, in: *Ultrahigh Magnetic Fields. Physics. Techniques. Applications.* (Ed. by V. M. Titov and G. A. Shvetsov, Moscow: Nauka, 1984) pp. 333-341.

5. Demidov, V. A., Kraev, A. I., Mamyshev, V. I., Shevtsov, V. A., Shpagin, V. I., Three - Module Disk Explosive Magnetic Generator, in: *Megagauss Field and Pulsed Power Systems,* (Ed. by V. M. Titov and G. A. Shvetsov, N.Y., Nova Sci. Publ., 1990) pp. 557-583.
6. Reinovsky, R. E., Lindemuth, I. R., March, S. P., Future Explosive Pulse-Power Technology for High-Energy Plasma Physics Experiments, in: *Digest of Tecnical Papers, 8th IEEE International Pulsed Power Conference,* San Diego, 1991, (Ed. by K. Prestwich and R. White) pp. 415-418.
7. Demidov, V. A., Zharinov, Ye. I., Kazakov, S. A., Chernyshev, V. K., Fast helical explosive-magnetic generators, *Ref.4*, in Russian, pp. 330-332.

TWO-STAGED MAGNETOCUMULATIVE GENERATORS FOR HIGH IMPEDANCE LOADS

A. E. USHNURTSEV, S. V. DUDIN, V. B. MINTSEV, V. E. FORTOV
Institute of Problems of Chemical Physics, RAS, Chernogolovka, Russia

V. E. OSTASHEV, A. A. ULYANOV, E. F. LEBEDEV
High Energy Density Research Center, Moscow, Russia

A. A. LEONTYEV, A .V. SHURUPOV
The Department of High Temperature Institute, RAS, Shatura, Russia

Two-staged magnetocumulative generators (MCG) with flux trapping for high impedance loads are considered. With an initial energy of several kilojoules, these generators have supplied energies up to 15 kJ into a 5 μH inductive load in about 15 μs. The total energy was amplified about 20 times. To get the open circuit voltage of the second stage under 60 kV, the working helix of the booster stage has a special set of pitches and increases the energy for ~30 μs. The second stage peaks the output electric pulse in the load. We also consider the possibilities of the MCGs designed for lightning action simulation on a grounded installation. In many cases, testing objects for lightning endurance is made at their locations. Compact, transportable, explosively driven MCG seems to be the most convenient equipment for this purpose.

1 Introduction

Efficient MCG work on high impedance vircator systems is described in [1-3]. To get higher RF power output and energy, the MCG output energy must increase. Besides, progress in modern technology claims that the high quality and reliability of electrical power supplies results from their lightning protection. Recently, advances in pulsed power technology raised interest in investigating devices to produce powerful electrical impulses with parameters simulating another type of high impedance load-lightning.

Here, we describe our advances with a two-staged MCG with flux trapping [4-6]. With initial energy of several hundred joules, the MCG could produce energy pulses of about 17 kJ for 15 μs into a high-impedance load (5 μH). We describe MCG experiments switched on a grounded stake.

2 Magnetocumulative Generator Design

Schemes of the two-staged generator are presented in Figs. 1-2. The MCG consists of inner solenoid L_{2B}, outer solenoid L_{2L}, and inner solenoid L_{3C}. The initial current in L_{2B} is supplied by discharging a capacitor bank. When the secondary circuit is switched on, magnetic flux is trapped and pushed out into the L_{3L} load.

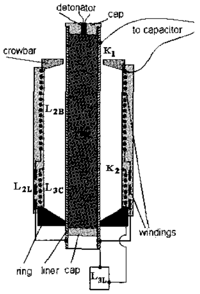

Figure 1. MCG scheme

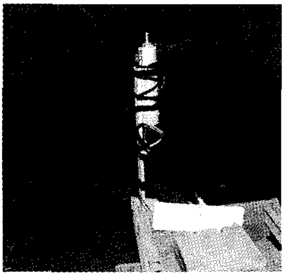

Figure 2. MCG snapshot

Recently, the necessity of good turn-to-turn insulation, insulation between armature and inner helices, insulation between inner and outer helices, and special booster helix design was shown to avoid a large open-circuit voltage in the second stage between the armature and the beginning of the L_{3C} working helix [9]. Thus, the booster stage has a diameter of 100 mm and length of about 290 mm. It has three spiral sections with lengths of 110 mm, 75 mm, and 105 mm, and pitches of 2 mm, 4 mm, and 12 mm, respectively. Cylindrical MCGs second stage is 80 mm long, with a 100 mm outer diameter and 2.5 mm pitch. The copper armature has a 50 mm outer diameter and 2 mm wall thickness. The mass of HE is about 1 kg.

3 Experimental Results and Discussion

Preliminary MCG designs were tested with a 5 μH inductive load. A capacitor, $C_0 = 100$ μF, was used to produce the initial magnetic flux in the booster coil. Results of typical experiments are shown in Table 1. The L_{2L} inductance was calculated for the time at which the second stage started.

Typical currents and their derivatives in the primary and secondary circuits are presented in Figs. 3-6. The booster generator increased the energy up to 27.4 kJ (Table 1, col. N1). The maximum energy amplification $\psi_{1,2}$ was 36.8 times (Table 1, col. N3). The second cascade had a run time of about 15 μs with output energy of 12-17 kJ. The total amplification coefficient of energy $\psi_{1,3}$ was about 20. Thus, the MCGs designed have shown promise for high impedance loads. The generator has good efficiency.

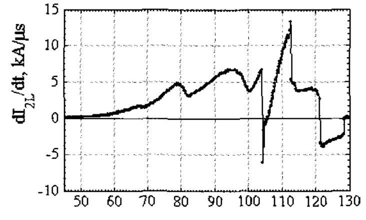

Figure 3. Current derivative vs. time of booster MCG

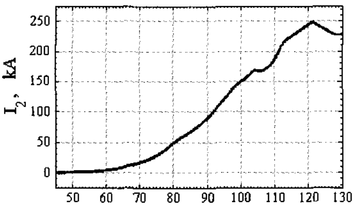

Figure 4. Current vs. time of boosterMCG

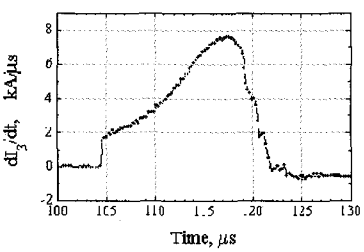

Figure 5. Current derivative vs. time of the second stage

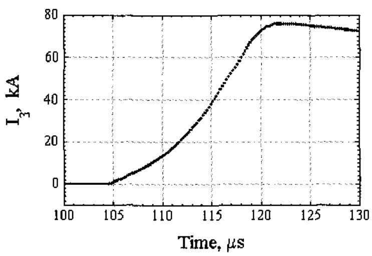

Figure 6. Current vs. time of the second stage

Table 1. Results of some typical experiments.

Exp. N	1	2	3	4	5	6	7
L_{2B}, μH	291.5	163.1	198.4	182.6	209.2	200.4	199.2
L_{2L}, μH	0.99	1.0	0.65	0.77	1.27	1.37	1.16
L_{3C}, μH	73.3	63.5	73.46	83.4	106.8	99.8	93.0
L_{3L}, μH	5.19	5.1	5.0	4.96	5.05	4.94	5.35
E_1, J	798	850	695.6	746.5	567.7	634.7	629.3
I_{2B}, kA	234.5	217.5	281	228.5	133.6	134	171
E_{2B}, kJ	27.38	23.84	25.6	20.1	11.35	12.28	16.96
I_{3C}, kA	81.16	72.1	69.9	74.6	82.35	73.49	76.75
E_{3C}, kj	17.1	13.25	12.25	13.8	17.1	13.34	15.76
$\psi_{1,2}$	34.2	28	36.8	26.9	20.0	19.33	27
$\psi_{2,3}$	0.62	0.56	0.48	0.69	1.51	1.09	0.93
$\psi_{1,3}$	21.2	15.6	17.7	18.6	30.2	21	25.1

4 MCG for Lightning Simulation

We have also considered the possibility of short-pulsed MCGs for the lightning simulation. The load in these experiments was a 5 m long metal stake placed in the ground (Figs. 7, 8). The resistance of the load contour was 19 ohm and its inductance was about 20 μH. Before explosions, special experiments were performed with the Marx generator and exploding wires opening switch. Currents of up to 10 kA with rise times of hundreds of nanoseconds were obtained in the load (Fig. 9).

Figure 7. Grounded metal stake.

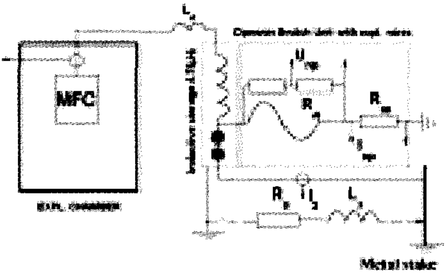

Figure 8. Experiment scheme.

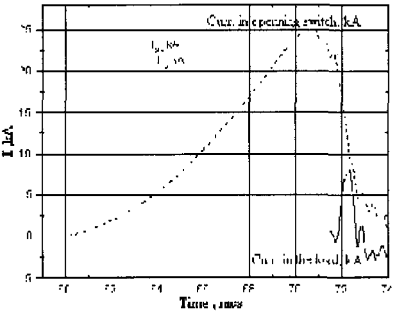

Figure 9. Current vs. time on the outdoor load.

5 Conclusions

Thus, the MCGs designed have shown promise for high impedance loads. The generator has good efficiency. Besides, it has been shown that the values of the load resistance at high impulse currents are less than those at the stationary conditions.

References

1. Azarkevich, E. I., Didenko, A. N., Dolgopolov P. V., et al., *Russian Physiks Dokladi*, **319** (1991) p. 352.
2. Azarkevich, E. I., Didenko, A. N., Zherlitsin, A. G., et al., *High Temperatures*, **32** (1994) p. 127.
3. Azarkevich, E. I., Didenko, A. N., Zherlitsin, A. G., et al., Generation of Microwave Radiation with the Aid of High Explosive, *Preprint, Chernogolovka*, (1992) in Russian.
4. Mintsev, V. B., Ushnurtsev, A. E., Fortov, V. E., *High Temperatures*, **31** (1993) p. 469.
5. Karpushin, Yu. V., Mintsev, V. B., Ushnurtsev, A. E., et al., *High Temperatures*, **31** (1993) p. 662.
6. Leont'ev, A. A., Mintsev, V. B., Ushnurtsev, A. E., Fortov, V.E., Shurupov, A.V., In: *Megagauss-YII*, Sarov (1997) p. 335.

CLASSIFICATION OF HELICAL FLUX-COMPRESSION GENERATORS

B. M. NOVAC[1], I. R. SMITH[2]
2)*Department of Electronic and Electrical Engineering, Loughborough University, Loughborough, Leicestershire, UK*
1)*On leave from the National Institute for Laser, Plasma and Radiation Physics, Bucharest, Romania*

Magnetic flux compression experiments were probably first performed in the early 1940s as part of Project Y, the Los Alamos atomic bomb project [1]. Fifty years later, it is now possible to begin a classification of the various devices that are known collectively as either flux-compression generators (FCGs) or magnetocumulative generators (MCGs). This paper suggests the main characteristics on which a grouping can be based, with emphasis given to the commonly available helical generator. After indicating the fundamental limitations of generator performance, this paper mentions various aspects on which a proposed classification can be based and gives values for the most important parameters of the different aspects.

1 Introduction

The main development of flux-compression techniques began in the early 1950s in Russia and the US, followed by the UK, France, EURATOM (in Italy) and China in the 1960s. Research groups in Japan, Poland, Germany and Romania have since joined what can be termed the Megagauss Club, as summarized in Table 1.

Table 1. The Megagauss Club: maximum magnetic field, energy and current achieved with flux-compression generators (data as of September 1998).

	Magnetic field density MG(10^2T)	Energy MJ	Current MA	Program start	References
Russia (USSR)	17/25*	100	>300	1952	[2], [3], [4]
USA	10^+/14*	50	320	1950	[5], [6], [7], [8]
France	10/11.7*	8.5	24	1961	[9], [10]
Japan	5.5	-	-	1970	[11], [12]
EURATOM (Italy)	5.4/7*	2	16	1961	[13], [14]
UK	5	10	20	1956	[15], [16]
Romania	5/7.5*	0.5	12	1979	[17], [18], [19]
Poland	3.5	-	0.8	1973	[20], [21]
P R China	-	-	2(?)	1967	[22]
Germany	-	-	1.2(?)	1975	[23]

* obtained rarely - data not available, ? much higher figures probably obtained, $^+$ inferred from X-rays pictures and a numerical simulation code

2 Generator Classification

There are two basic flux-compression devices. The first are (a) implosive systems, in which the magnetic field energy is concentrated towards the centre to provide an ultrahigh magnetic field (MG) (known as MK-1). The second is (b) the conventional flux-compression generator, in which high energies (MJ) and high current (MA) are produced in an external load (MK-2). Characteristic parameters for both are given in Table 2, together with the maximum values that have been achieved.

Table 2. Characteristic values for parameters and peak values obtained from MK1 and MK2 generators.

Class	**Final Characteristics**	**Driving Force**		
		Explosive (solid, liquid, gas)		**Electro-magnetic**
		metallic liners	dielectric-metallic shock-wave transition	metallic liners
I (MK-1)	$B_f = B_0\left(\lambda\frac{S_0}{S_f}\right)$	$\lambda \approx 0.8$ $\frac{S_0}{S_f} \approx 200$ $B_{max} \approx 1700T$	$\lambda \approx 0.056$ $\frac{S_0}{S_f} \approx 1600$ $B_{max} \approx 350T$	$\lambda \approx 0.6$ $\frac{S_0}{S_f} \approx 440$ $B_{max} \approx 550T$
II (MK-2)	$I_f = I_0\left(\lambda\frac{L_0}{L_f}\right)$ $W_f = W_0\left(\lambda^2\frac{L_0}{L_f}\right)$	$\lambda \approx 0.2 \div 0.8$ $\frac{L_0}{L_f} \approx 5 \div 16000$ $I_{max} \approx 320MA$ $W_{max} \approx 100MJ$	? $I_{max} \approx 0.027MA$ $W_{max} \approx 0.20MJ$	—

B - magnetic induction, I - electrical current, W - magnetic energy, L – inductance, S - cross sectional area, λ - magnetic flux conservation factor. (Subscripts 0 and f are for initial and final parameters.)

It is possible to consider four features of these generators that vary from one design to another:

a) geometric form

class I (or MK-1, Russian classification) - cylindrical (imploding/exploding)
class II (or MK-2, Russian classification) - cylindrical-coaxial (imploding/ exploding), helical, disk, Archimedes spiral, plate, bellows, spherical (both micro and large scale)

Most of these devices can have shaped geometry designed to increase the dL/dt rate (see (c)).

b) explosive charge initiation

surface plane initiated (PWG), line initiated (LWG), axial initiated (axial detonators) - cylindrical imploding (CWG or multipoint detonators), spherical imploding (multi point detonator/PWGs, exploding wire mesh techniques), spherical exploding (nuclear).

WG stands for explosive (shock) wave generators sometime termed explosive "lenses".

c) **inductance rate-of-change (dL/dt)**

time constant: plate, bellows, cylindrical-coaxial, single-pitch helical

time variable: all generators including all above shaped (or multiple section variable/pitch for the helical generator)

As shown in [24], the maximum energy multiplication k is related to the action Λ and the chemical to electromagnetic efficiency η by $\Lambda=\eta k$. If dL/dt = constant then $\Lambda \leq 1$ as was first demonstrated in [25], and only if dL/dt is variable can Λ exceed unity [24].

d) **compression time** - **slow**: tens to hundreds of microseconds
- **fast**: less than ten microseconds

3 Classification of Various Types of Helical Flux Compression Generators (HFCG)

A particular Class II (MK-2) generator, probably that most frequently used in practice, is the helical generator. Its basic design is described by the following characteristics.

classical design:

- helical coil (usually multisectional), cylindrical/coaxial coil-armature system (no shaping)
- fast crowbarring - direct feed (return current through armature).

Depending on the specific application, numerous variations of the basic design have been produced. A summary of the most important types is given below:

a) **fast pulse** - Two-end initiation, as in Sandia generators [26] or by inductive coupling and late crowbarring – FLUXAR system [24], [27].

b) **high efficiency** - dL/dt optimisation [28], or shaping or by using special nested (Matrioshka) designs [29], [30]. Because Λ is limited the energy multiplication cannot be too high.

c) **high voltage** - Inductive feed with axial initiation [31] or Marxing [32].

d) **high current** - By shaping the helical coil and/or the armature [33], [34], or by using tilted turns[16], - By parallel 'battery' coupling [32] or by choosing a low value inductive/resistive load.

e) **high energy** - dL/dt optimisation (scaling), to maintain a constant internal high electric field [35] and by using high value inductive/resistive loads.

f) **high energy/current multiplication** - A high value can only be obtained by an inductive coupling chain. With Λ limited by present technology, i.e. by the maximum internal electric field that can be sustained [24], very high values of k from a *single* generator are only possible if the efficiency is low. One of the largest values of k(10^3) reported in the literature was obtained with only about 4% of the energy stored in the explosive charge converted into electrical output [35]. Therefore the need is clear for inductively coupled generator chain systems, using aircore transformers [36], autotransformers [37], or dynamic transformers (flux trapping technique or FLUXAR system: see [24] and references therein).

4 Classification of Classical Design HFCGs

Many laboratories have produced classical design HFCGs. Table 3 summarizes the principal parameters of the four types of HFCGs. The range of some parameter values overlaps to some extent.

Table 3. Principal parameters of classical design HFCGs

	Large	Medium	Mini	Micro
Length (mm)	1000-2500...	500-1500	100-500	<100
Diameter (mm)	250-500...	100-250	40-100	<40
Total Mass (kg)	200-2000...	10-200	0.2-10	<0.2
Explosive Mass (kg)	20-200...	1-20	0.05-1	<0.05
Current (MA)	10-50...	1-10	0.1-5	<0.1
Energy (MJ)	10-100...	0.2-10	0.1-0.5	<0.1
Compression time (μs)	100-300...	50-200	10-50	<10

Table 4 gives an indication of the difficulties encountered in the mathematical modelling and design of the four types of generators.

Table 4. Numerical modelling and design problems for classical design HFCGs

Class	Design problems	Main tasks for numerical modelling	Overall design difficulty (1-5 scale)
Large	• cost • magnetic forces! • Insulation	• coil and armature 2-dim movement -radial and axial (magnetohydrodynamics) • contact delays	3-4
Medium	• explosive mass • insulation/voltage breakdown • magnetic forces • energy efficiency	• electric field • 1-dim (radial) coil dynamics • resistance	1-2
Mini	• energy efficiency • nonlinear diffusion • armature cracks • 2π clocking	• electric field • resistance	2-3
Micro	• manufacture • armature cracks • 2π clocking • voltage breakdown • maximum current	• electric field • resistance • exotic losses (contact point delay, microjets, etc)	4-5

5 Application of Classical Design HFCGs

The wide range of applications for which HFCGs have been used is summarized in Table 5:

Table 5. Applications of HFCGs

Large	Medium	Mini	Micro
• Fusion, Laser, X-rays generators	• Most applications including emg launchers; lightning simulators; microwave and radiowave emitters; X-ray, laser, neutron, electron and ion beam sources; proof of principle experiments; large detonating systems	• Rocket borne applications, proof-of-principle experiments, inductively coupled systems, special detonator array systems.	• Special applications (radar jamming, aviation, spacecraft technology, artillery, special autonomous detonators for nuclear weapons, etc).

6 Conclusion

This paper represents an early attempt to classify the very diverse range of helical FCGs and their applications on the basis of a set of operating features.

References

1. Hawkins, D., Manhattan District History, Project Y, The Los Alamos Project. **1** Inception until August 1945, Report *LAMS-2532* **1**(1946) pp. 141,143,194,201,228,232.
2. Pavlovskii, A. I., Magnetic cumulation. A memoir for Andrei Sakharov. *Megagauss Magnetic Field Generation and Pulsed Power Applications*, ed. by M Cowan and R B Spielman (New York, Nova), (1994) pp. 9-22.
3. Pavlovskii, A. I., et al., Cascade magnetocumulative generator of 20 MG range magnetic fields. *Megagauss Magnetic Field Generation and Pulsed Power Applications*, ed. by M. Cowan and R B Spielman (New York, Nova), (1994) pp. 141-148.
4. Chernyshev, V. K. "Scaling image of 90 MJ explosive magnetic generators. *Megagauss Fields and Pulsed Power Systems*, ed. by V. M. Titov and G. A. Shvetsov (New York, Nova), (1990) pp. 347-350.
5. Fowler, C. M., Garn, W. B., and Caird, R. S., Production of very high magnetic fields by implosion. *J. Appl. Phys.* **31** (1960) pp. 588-594.
6. Hawke, R. S., et al., Method of isentropically compressing materials to several megabars. *J. Appl. Phys.* **43** (1972) pp. 2734-2741.
7. Schearer, J. M., et al., Explosive-driven magnetic-field compression generators. *J Appl Phys* **38** (1968) pp. 2102-2116.
8. Cnare, E., Cowan, M., Explosive generators for low-cost pulsed power. *5th IEEE Pulsed-Power Conf*, (Arlington, USA), (1985) pp.194-199.
9. Besancon, J. E., Contribution a l'etude de la compression de champ magnetique intense par implosion d'un tube metallique. Doctoral thesis. Universite Paris-Sud, Centre d'Orsay, Paris (1971).

10. Vedel, J., et al., Commutation ultra-rapide de courants intenses superieures au mega-amperes. *Rev Gen d'Elec* **80** no 11(1971) pp. 873-877.
11. Miura, N., Nojin, H., Recent advances in megagauss physics. *Physica B* **216** (1996) pp. 153-157.
12. Yokoi, H., et al., Development of a small-size bellows-type megagauss generator. *Megagauss and Megaampere Pulse Technology and Applications, Megagauss Conference*, Ed. by Y. K. Chernyshev, V. D. Seelimir and L. N. Plyashkevich (VNIEF,Sarov), (1997) pp. 138-143.
13. Knoepfel, H., Very high electromagnetic energy density research at Frascati up to the seventies and beyond. *Megagauss Technology and Pulsed Power Applications* ed. by C. M. Fowler, R. S. Caird and D. J. Erickson (New York and London, Plenum), (1987) pp. 7-18.
14. Knoepfel, H., et al., Generation and switching of magnetic energies in the megajoule range by explosive systems. *Rev. Sci. Instr.* **40** (1969) pp 60-67.
15. Speight, C. S., Theoretical and experimental field limitations in cylindrical flux compression experiments. *AWRE Report* no 0-71/67 (1967).
16. Stewardson, H. R., (1994) Private Communication.
17. Novac, B. M., Serban. A., Development of a high initial field megagauss generator. *Megagauss Magnetic Field Generation and Pulsed Power Applications* ed. by M. Cowan and R. B. Spielman (New York, Nova) (1994) pp. 133-139.
18. Novac, B. M., Zoita, V., Zambreanu. V, et al., A pulsed power source for plasma focus single-shot experiments. *8th IEEE Pulsed-Power Conf,* (San Diego, USA), (1991) pp. 434-437.
19. Ursu, I., et al., Pulsed power from helical generators. *Megagauss Fields and Pulsed Power Systems* ed. by V. M. Titov and G. S. Shvetsov (New York, Nova), (1990) pp. 347-350.
20. Farynskii, A., et al., Generation of intense magnetic fields with up to 350 T induction by the method of explosively-produced compression. *J. Tech. Phys.* **22** (1981) pp. 379-390.
21. Farynskii, A., (1985) Private communication.
22. Gong Xiaggen, et al., A compact magnetic flux compression generator driven by explosives. *Megagauss Magnetic Field Generation and Pulsed Power Application* ed. by M. Cowan and R. B. Spielman (New York, Nova), (1994) pp. 417-424.
23. Scholles, H., Inaugural dissertation zur Erlangung des Doktorgrades, Universitat Dusseldorf, Germany (1982).
24. Novac, B. M., et al., 2D modelling of inductively coupled helical flux-compression generators - FLUXAR systems. *Lasers and Particle Beams* **15** no 3, (1997) pp. 397-412.
25. Cummings, D. B., Morley, M. J., Electrical pulses from helical and coaxial flux-compression generators. *Megagauss Magnetic Field Generation by Explosives and Related Experiments* EUR 2750e, ed. by H. Knoepfel and F. Herlach (Brussels, EURATOM), (1966) pp. 451-471.
26. Crawford, J. C., Damerow, R. A., Explosively driven high-energy generators. *J. Appl. Phys.* **39** (1968) pp. 5224-5231.
27. Shvetsov, G. A., Matrosov, A. D., Explosive magnetocumulative generator with outer excitation. *Ultrahigh Magnetic Fields: Physics, Techniques, Applications* ed. by V.M. Titov and G. A. Shvetsov (Moscow, Nauka), (1984) pp. 263-264.
28. Morin, J., Vedel, J., Generateurs de courants intenses par conversion d'energie explosive en energie electrique. *C. R. Acad. Sci.,* Paris **272** B (1971) pp. 1232-1235.
29. Long, J., Rosen, L., Zucker, O., (1989) Power conditioning enhanced efficiency explosive generator. Private communication to B. M. Novac.
30. Basmanov, V. F., et al., Resistive 100 MJ mcg with radial line - Matreshka - 640. *Megagauss Magnetic Field Generation and Pulsed Power Applications* ed. by M. Cowan and R. B. Spielman (New York, Nova), (1994) pp. 455-458.
31. Caird, R. S., Fowler, C. M., Conceptual design for a short-pulse explosive-driven generator. *Megagauss Technology and Pulsed Power Applications* ed. by C. M. Fowler, R. S. Caird and D. J. Erickson (New York and London, Plenum), pp. 425-431.

32. Pavlovskii, A. I., et al., Magnetic cumulation generator parameters and means to improve them. *Megagauss Physics and Technology*, ed. by P. J. Turchi (New York and London, Plenum) (1980) pp. 557-583.
33. Pavlovskii, A. I. et al., A multiwire helical magnetic cumulation generator. *Megagauss Physics and Technology*, ed. by P. J. Turchi (New York and London, Plenum), (1980) pp. 585-593.
34. Boriskin, A. S., et al., Helical conical mcg of contrast pulses. *Megagauss Magnetic Field Technology and Pulsed Power Applications,* ed. by M. Cowan and R. B. Spielman (New York, Nova) (1980) pp. 475-480.
35. Chernyshev, V. K., et al., High-inductance explosive magnetic generators with high energy multiplication. *Megagauss Physics and Technology,* ed. by P. J. Turchi (New York and London) (1980) pp. 641-649.
36. Pavlovskii, A. I., et al., Transformer energy output magnetic cumulation generators. *Megagauss Physics and Technology,* ed. by P. J. Turchi (New York and London) (1980) pp. 611-626.
37. Cummings, D. B. Cascading explosive generators with autotransformer coupling. *J. Appl. Phys.* **40** (1969) pp. 4146-4150.

AUTONOMOUS ENERGY SOURCE ON THE BASIS OF HELICAL MCG WITH SIMULTANEOUS HE-CHARGE INITIATION ON THE AXIS

A. S. KRAVCHENKO, YU. V. VILKOV, A. S. YURYZHEV,
M. M. SAITKULOV, I. M. BRUSNIGIN
VNIIEF, Sarov, Russia

The description of a helical magnetocumulative generator with simultaneous HE-charge initiation on the axis, powered from a helical MCG with transformer energy bending is given in this paper. Experimental results, obtained when testing this generator with an inductive load are presented. The experimental results are compared to the numerical simulation of the generator. Numerical calculations show that at the initial energy of 1 kJ, the formation of a voltage pulse of approximately 1 MV on an active load of 10 Ω can be achieved. It requires that the generator have a fuse made from electrically exploded copper wires located in an arc-suppressing medium.

1 Introduction

One way to obtain short (≤1 μs) energy pulses is to store energy in an inductive load during the operation of an MCG and allowing its fast release and transmission to the load using, for example, explosive open switches [1]. But much energy is lost with this method. The lower the power of the energy source, the more energy is lost. Thus, in this case it is very useful to use fast MCGs. The helical AMCG is one of such generators with simultaneous axial initiation of a HE-charge [2]. Investigation results presented in [3] show that helical magnetocumulative generators with simultaneous initiation of cylindrical HE-charge on the axis (HAMCG) have high specific power operating under a load with relatively high inductance value. In one of the experiments with the helical AMCG having a helix internal diameter of 115 mm and 320 mm length of working volume, we obtained a magnetic energy pulse of ~ 90 GW power in an inductive load of ~5 μH at ~ 350 kV. The generator contour deformation time was ~ 10 μs and the specific generator power was ~ 10 GW/kg. The current amplification coefficient of the investigated HAMCG is limited by the residual inductance value and does not exceed four [3].

2 Description of Calculated Model

This paper analyzes the calculated results of the operating parameters of the helical AMCG on a load, which includes inductive storage and a current contour breakdown unit. Calculations were performed using similar methods to those described in [3]. These methods were compared with the results of many experiments. We will give two examples to illustrate this. One of the investigated HAMCG had the following geometrical dimensions: generator operating volume length $l = 320$ mm; average helix radius $r_S =$ 62.5 mm, internal helix radius on insulation $r_{SW} = 57.5$ mm, quantity of helix coils $\omega =$ 30; initial external radius of the central tube $r_0 = 34.5$ mm; external radius of HE-charge cylinder $r_{HE} = 33.5$ mm. The initial inductance value of this generator was $L_0 \approx 26$ μH and its load inductance was $L_H \approx 5$ μH. The initial current value in the generator was $I_0 = 83.5$ kA. Calculated and experimental curves of the current derivative in the load are presented in Figure 1a. For the second example, we took the generator powered on the mode of flux capture. Its main geometrical dimensions are: $l = 330$ mm, $r_S = 62.5$ mm, $r_{SW} = 57.5$ mm, $\omega = 31$, $r_0 = 37$ mm, $r_{HE} = 33.5$ mm. The initial inductance value of this generator was $L_0 \approx$ 23 μH and the load inductance was $L_H \approx 5$ μH. The value of the initial magnetic flux in the generator was $\Phi = 1.7$ Wb. Calculated and experimental curves of the current derivative in the load are presented in Figure 1b. In the calculations, we didn't consider magnetic flux losses on the active impedance in the generator contour since they are relatively small in this case, compared to flux losses in inter-coil space and insulation of helix wire.

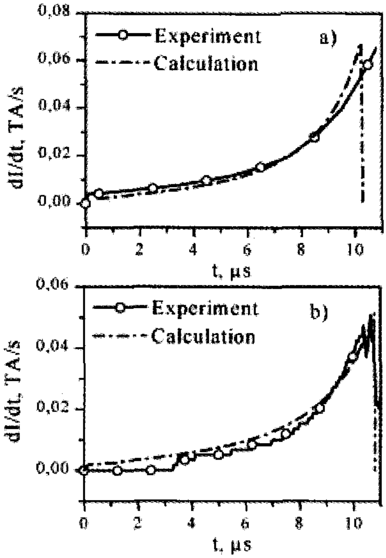

It was assumed that the breakdown unit of the current contour consists of copper conductors, the specific impedance of which was described with semi-empirical dependences obtained from the experiments on the electrical explosion of conductors [4]. A special magnetocumulative generator with transformer energy output described in [5] was chosen as a source of the initial field for the HAMCG-inductive storage-current contour breakdown unit. Operating parameters of this generator were determined using the method described in [6].

3 Calculated Results

In calculations we investigated HAMCG having an operating volume length of $l = 320$ mm and average helix radius $r_s = 62.5$ mm. The initial inductance value of such a generator was $L_0 \approx 26$ µH, and load inductance (inductive storage and current contour breakdown unit) was $L_H \approx 5$ µH. We performed numerical investigations of the operating characteristics of the helical AMCG on a load, which includes inductive storage and a current contour breakdown unit, at different variants of initial field creation in the generator. It was discovered that the breakdown unit, made of fuses, allows creation of voltage pulses higher than 1 MV at a maximum possible value of electrical field strength of 200-300 kV/mm on the generator output. Here, maximum electrical power in the breakdown unit significantly (2.5-3 times) exceeds the power, produced by the generator in a load with optimum inductance value without energy pulse peaking, and reaches ~ 0.25 TW. The highest power and voltage could be obtained at creation of the initial field in HAMCG using an energy source with an effective operation time comparable to the operating time of the power generator being investigated. A helical generator with transformer energy output [5] could be used as a power source for the HAMCG under investigation. Increasing the effective time of the initial field creation leads to a significant decrease in the power and voltage of the output pulse. Creation of the initial field using an external solenoid (so-called scheme with flux capturing) allows the creation of high-voltage pulses up to ~ 3 MV at an output power of ~ 200 GW. However, current levels of the electric strength of the output of such a helical AMCG (~350 kV with a load connection to the middle of the helix [3]) allows the breaking unit, made of fuses, to handle 90-100 GW pulses at 600-700 kV, and using the mode of flux capturing – 70-80 GW and 800-1100 kV, respectively. Increasing the generator electrical strength at the expense of ~1.5 times increase in HAMCG size will allow creation of energy pulses with a maximum power of 100 GW on a load with ~ 10 Ω impedance. Calculated results of operating parameters of the helical AMCG on the load, which includes inductive storage and the current contour breaking unit, show that HAMC generators could be used to create autonomous magnetocumulative power sources for high-power electromagnetic pulse generation (see Fig. 2).

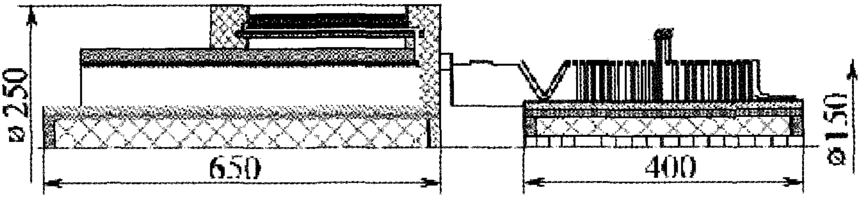

Figure 2. HAMC generator used to create an autonomous magnetocumulative power source for electromagnetic pulse generation.

4 Summary

Satisfactory coincidence of parameters of HAMCG operation and the initial field generator, obtained in the calculations, with experimental results shows that the results considered in this paper have sufficient reliability.

References

1. Bakulin, Yu. D., Kuropatenko, V. F., Luchinsky, A. V., Magnetohydrodynamical Calculation of Fuses, *JTPh.* (1976) **46**, No. 9. pp. 1963-1969.
2. Shearer, J. W., Abraham, F. F., Aplin, C. M. et al., Explosive-driven magnetic-field compression generators, *J. Appl. Phys.* (1968) **39**, No. 4. pp. 2102-2116.
3. Lyudaev, R. Z., Kravchenko, A. S., Yuryzhev, A. S., Vilkov, Yu. V., Saitkulov, M. M., Investigation of Helical Magnetocumulative Generators with Simultaneous Initiation of Cylindrical HE-Charge on the Axis, Megagauss and Megaampere Pulsed Technology and Application. Ed. by V. K. Chernyshev, V. D. Selemir, L. N. Plyashkevich. Sarov, VNIIEF, (1997) pp. 310-314.
4. Pavlovskii, A. I., Lyudaev, R. Z., Kravchenko, A. S., Zolotov, V. A., Yuryzhev, A. S., Magnetic Cumulation Generator Power Increase. Megagauss Fields and Pulsed Power Systems. Ed. by V. M. Titov and G. A. Shvetsov, N.Y.: Nova Science Publishers. 1990. pp. 385-392.
5. Kravchenko, A. S., Boriskin, A. S., Vilkov, Yu. V., Dimant, E. M., Karpov, A. I., Nazarenko, S. T., Pavlov, V. S., Kozlov. M. B., Experimental Investigation of Operation of Helical Magnetocumulative Generator with Transformer Energy Output. In the proceedings of this conference.
6. Kravchenko, A. S., Vilkov, Yu. V., Numerical Simulation of Operation of Helical Magnetocumulative Generators with High Energy Amplification Coefficient. In the proceedings of this conference.

EXPERIMENTAL INVESTIGATION OF OPERATION OF HELICAL GENERATOR WITH TRANSFORMER ENERGY OUTPUT

A. S. KRAVCHENKO, A. S. BORISKIN, YU. V. VILKOV, YE. M. DIMANT, A. I. KARPOV, S. T. NAZARENKO, V. S. PAVLOV, M. B. KOZLOV
All-Russian Scientific Research Institute of Experimental Physics (VNIIEF), Sarov, Russia

The experimental results of perfecting a small (helix diameter of 120 mm) compact helical generator with transformer energy output are presented in this report. The transformer unit is located coaxially with the generator. The influence of the initial magnetic energy on the generator energy amplification coefficient is investigated. Generator performance and numerical calculations of the generator contour deformation are compared without considering liner braking in the helix magnetic field.

1 Introduction

Helical magnetocumulative generators, investigated by different scientific groups [1,2] are the basis for creating high-power autonomous energy sources since they have high enough (50-100 J/cm^3 [3]) specific characteristics relative to initial generator volume, a high-energy amplification coefficient of ~1000 and wide possibilities for current and voltage pulse formation at the generator output. Experimental results obtained while testing the small helical generator with transformer energy output at different initial energy levels are presented and compared with the results of numerical calculations.

2 Generator Design and Experimental Results

The generator consists of a stator, central tube and transformer unit, located coaxially with the generator. The stator is wound with profiled copper wire with 0.25 mm thick film insulation. The internal diameter of the stator is 120 mm and it consists of 5 sections. The first section is 96 mm long and is wound with one profiled wire. Its minimum pitch is 2.5 mm and its maximum pitch is 3.85 mm. The second section is 88 mm long and has 2 levels of wire, and the third section is 80 mm long and has 4 levels. The fourth section is 72 mm long and has 8 levels, and the fifth section is 112 mm long and has 16 levels of this wire. The fifth section has conical narrowing on the last 32 mm with an angle of 80°30′ at the cone base. The external diameter of the central copper tube is 57 mm; its internal diameter is 53 mm. The tube was filled with 48 mm diameter HE in a plexiglass shell. The HE detonation rate was $D = 7.6$ km/s and HE density was $\rho = 1.65$ g/cm^3. The primary winding of the transformer unit was located coaxially with the stator and consisted of one turn of 218 mm diameter and 260 mm length. The secondary winding of the transformer unit was made with 7 mm diameter copper wire with 1.5 mm thick polyethylene insulation. The secondary winding had 25 turns; the average diameter of the winding was 233 mm. The generator inductance was measured as $L_g = 106$ μH and the inductance of the secondary circuit of the transformer unit was 80 μH. Mutual inductance at the end of the contour deformation was 1.96 μH, and the load inductance was 22 μH.

The first experiment was performed at a relatively low level of initial current, 3.5 kA. A current pulse of 2.7 MA was recorded in the primary circuit of the transformer unit. The magnetic energy reached 150 kJ. A current pulse of 70 kA was obtained in the load, which had an inductance value of 22 μH. The maximum value of the voltage pulse on the load exceeded 100 kV. The energy amplification coefficient in the generator contour was approximately 240. The current derivative in the generator contour is shown in Fig. 1a. The calculated curve of the current derivative in the generator contour, obtained according to the method described in [4], is also presented in Fig. 1. The maximum magnetic field is reached at the end of the fifth section deformation and is $H_m = 38$ MA/m. The maximum electrical field is obtained at the end of the deformation of the first section of the stator helix and is $E_m = 4.8$ MV/m. The second experiment was performed at a significantly higher initial energy. The maximum current in the generator contour was 3.8 MA and the magnetic energy was 300 kJ. Comparison of the current derivative in the generator obtained in this experiment and the calculated one (Fig. 1b) shows that a significant deviation of the experimental curve from the calculated one is observed at the fourth section deformation. The strength of the electrical field at the end of the deformation of the first section of the helix exceeded 11 MV/m. The current derivative obtained experimentally corresponds, however, to the calculated one during the operation of the first three sections. It is therefore possible to assume that a sharp decrease in the current derivative at the end of the fourth section's operation could be caused by liner braking in the relatively high magnetic field on the last coils in the fourth section. To clarify the reasons for this sudden decrease in the energy coefficient, we decreased the initial energy value in the third experiment to 1.3 kJ and increased the liner kinetic energy in the fourth experiment, increasing the HE-charge diameter and liner thickness. HE-charge parameters in the fourth experiment were as follows: detonation velocity $D = 8.15$ km/s, density $\rho = 1.7$ g/cm^3 and 65 mm diameter. The liner external diameter was 75 mm. Besides, the insulation thickness of the copper wires in the fourth and fifth generator stator sections was increased to 0.25 mm. Experimental and calculated dependences of the current derivative in the generator contour are shown in Figs. 2a and 2b, respectively. Some parameters of the investigated generators, and main experimental results, are presented in Table 1.

Table 1. Generator Parameters Experimental Results

N	L_0, μH	I_0, kA	L_e, nH	I_g, MA	K	H_m, MA/m	E_m, V/m
1	104	3.5	42	2.7	240	38	4.8
2	104	7.5	42	3.8	100		
3	104	5	42	3.6	210	50	7.8
4	80	7.5	42	3.9	140	60	12.5

L_0 is the initial value of the generator inductance, I_0 the initial current value, L_e the final effective value of the generator inductance, I_g the maximum current in the generator contour, H_m the maximum strength of the magnetic field in the generator contour, E_m the maximum strength of the electrical field in compressed contour of the generator, and K the energy amplification coefficient.

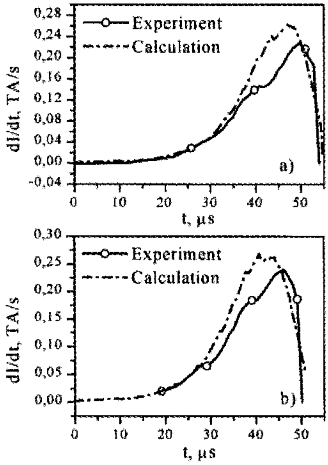

Figure 1.

Good agreement of the calculated current derivative with the experimental one obtained in the third and fourth experiments shows that, with 0.25 mm film insulation, the maximum value of the electrical field E_m = 12.5 MV/m achieved in the fourth experiment does not influence the current rise character in the generator. The maximum value of the magnetic field H_m = 50-60 MA/m obtained in the third and fourth experiments also does not influence the current rise in the transformer unit. The transformer unit, located coaxially with the helical generator, reduces the dimensions of the entire unit and allows operation of the magnetocumulative generator with a wide range of loads.

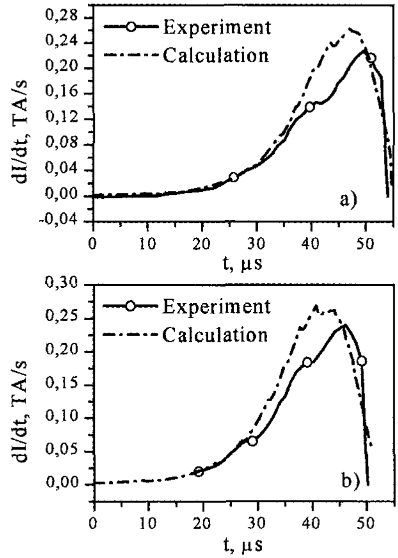

Figure 2.

3 Summary

Investigations showed that, in high-inductive helical generators, the maximum value of the magnetic field strength in the generator helix reaches 60 MA/m, and maximum value of the electrical field exceeds 12 MV/m, and the process of current rise in the generator contour does not differ from the calculated one. The transformer unit, located coaxially with the helical stator, significantly reduces the dimensions of the generator and allows effective transmission of the energy created in the generator contour to a wide range of loads. Experimental results certify the possibility of creating high-power autonomous energy sources with high specific characteristics based on magnetocumulative generators.

References

1. Pavlovskii, A. I., Lyudaev, R. Z., Plyashkevich, L. N., et al., in Megagauss Physics and Technology, Ed. by P. J. Turchi. N.Y. and London. Plenum Press, (1979) pp. 585-593.
2. Chernyshev, V. K., Zharinow, Ye. I., Demidov, V. A., Kazakov, S. A., ibid. pp. 641-649.
3. Ludaev, R. Z., Kravchenko, A. S., Yurizhev, A. S., Vilkov, Yu. V., Saitkulov, M. M., Investigation of Helical Magnetocumulative Generators with Simultaneous Initiation of Cylindrical HE-charge along the axis. Megagauss and Megaampere Pulsed Technology and Applications. Ed. by V. K. Chernychev, V. D. Selemir, L. N. Plyashkevich. Sarov, VNIIEF. (1997) pp. 310-314.
4. Kravchenko, A. S., Vilkov, Yu. V., Numerical Simulation of Helical Magnetocumulative Generators Operation with High Energy Amplification Coefficient. In the proceedings of this conference.

COMPACT HELICAL MAGNETOCUMULATIVE GENERATOR FOR THE FORMATION OF POWERFUL HIGH-VOLTAGE ENERGY PULSES

A. S. KRAVCHENKO, V. D. SELEMIR, A. S. BORISKIN, YU. V. VILKOV, YE. M. DIMANT, A. B. YERMAKOV

All-Russian Scientific Research Institute of Experimental Physics (VNIIEF), Sarov, Russia

The description of a helical generator with a 240 mm diameter internal helix and transformer energy output is presented. The generator is planned for ~100 GW high-power energy-pulse formation at maximum voltage on a load of ~1 MV. An experimental sample of the generator was tested in a purely inductive load of 44 μH. At relatively low operation levels, when the maximum inductance of the magnetic field in the generator did not exceed 80 T, a 140 kA current pulse at 250 kV was obtained. Numerical calculations show that when operating at such levels it is possible to obtain a voltage pulse of ~3 MV at the fuse consisting of electrically exploded copper conductors in an arc-suppressing medium.

1 Introduction

Application of magnetocumulative generators as sources of power and high-power electromagnetic energy pulses impose definite limitations on mass and size characteristics of such sources. We believe that, according to these characteristics, a helical generator with high-energy amplification coefficient [1,2], having a transformer unit and located coaxially with the stator and armature of the generator [3], is most promising for forming high-power, high-voltage energy pulses. Such generators have high specific energy and power characteristics and allow effective transmission of power (developed by the generator) to loads with relatively high (~1 Ω) impedance at the expense of inductive coupling of the generator and load contours. Use of a fuse unit made of electrically exploded wires in the load contour in an arc-suppressing medium allows an increase in the voltage pulse, developed on the output of the transformer unit, by more than one order of magnitude and respectively, increases the permissible load impedance [4]. The maximum power delivered to the load is comparable with the maximum electrical power developed by the generator on the input at the transformer unit.

2 Description of the Generator Design

The generator design is presented in Fig. 1. The generator has a length of 1000 mm and a maximum diameter of 500 mm. The generator consists of three parts: stator, in the form of a multi-sectional cylindrical helix; liner, in the form of a cylindrical copper tube located coaxially with the stator; and the transformer unit where the primary and secondary windings are located coaxially with the stator and the liner. The multi-sectional helix, 800 mm in length, consists of 20 sections. The length of each section is 40 mm. The internal diameter of the stator is 240 mm. Helix sections were wound with copper wires, insulated by polyethylene terephthalate film, 20 μm thick. The total thickness is 0.25 mm. Characteristics of the winding of the stator helix sections are presented in Table 1. The 19th and 20th sections had conical narrowing toward the load direction with an 80°30′ base angle of the cone. The liner was made of copper tubing with 114 mm external diameter and 4 mm wall thickness. The tube was filled with HE of 96 mm diameter in a 4 mm thick Plexiglas shell. HE density was $\rho = 1.65$ g/cm3, detonation rate $D = 7.6$ km/s. The primary winding of the transformer unit is a one-turn solenoid consisting of 64 parallel, insulated wires each 6.5 mm in diameter. The average diameter of the winding is 466 mm and the winding pitch is 520 mm. The secondary winding of the transformer unit was made with flexible, high-voltage copper wire in Teflon insulation. The diameter of the cable conductor is 10 mm; the diameter with insulation is 20 mm. The measured value of the generator inductance was 250 μH, and the inductance value of the secondary transformer

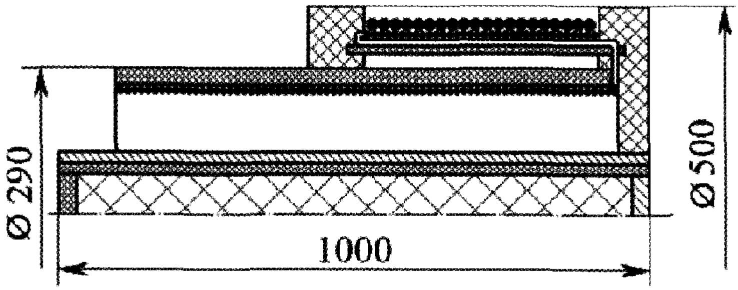

Figure 1. Generator Design. See text for details.

unit was 190 μH. Mutual inductance between the primary and secondary windings of the transformer unit was 4.8 μH.

Table 1. Characteristics of Stator Helix Section Windings.

Section No.	1,2	3	4	5,6	7	8	9,10	11	12	13,14	15	16	17,18	19,20
Wire Diameter, mm	4.5	5.7	6.5	4.5	5.7	6.5	4.5	5.7	6.5	4.5	5.7	6.5	4.5	6.5
No. of Wires	1	1	1	2	2	2	4	4	4	8	8	8	16	16
Turn Spacing, mm	4.5	5.7	6.5	9	11.4	13	18	22.8	26	36	45.6	52	72	122
Angle α	0	0	0	0	0	0	0	0	0	0	0	0	0	9°30′

3 Experimental Results of Compact Generator

Generator testing was performed on a load having 44 μH inductance. A small condenser battery with energy storage of 10 kJ (U = 16 kV, C = 84 μF) was used as a source of initial magnetic field for testing the generator. The first experiment was performed at a relatively low level of the initial magnetic field. The value of the initial current was 5 kA, and the initial energy in the generator magnetic field was 3.1 kJ. The value of the magnetic energy at the end of the generator contour deformation was 1.25 MJ, and the energy amplification coefficient was 400. The current derivative in the load contour is presented in Fig. 2. The calculated curve of the current derivative obtained with the method described in [5] is also presented in Fig. 2. Maximum current value in the generator contour was 5.1MA, maximum value of current derivative was 2.5×10^{11}A/s. A current pulse of 140 kA was obtained in the load with an inductance of 44 μH. The maximum value of the current derivative in the load was 6.6×10^{10}A/s, and the maximum voltage on the generator output was 290 kV. The magnetic field strength increases monotonically from section to section and reaches its maximum of 66 MA/m at the end of the deformation of the generator contour. Monotonous strength rise of the magnetic field is characteristic for a helical generator with a high-energy amplification coefficient. The maximum strength of the electric field E_m = 6.5 MV/m is obtained at the end of the deformation of the 16th helix section.

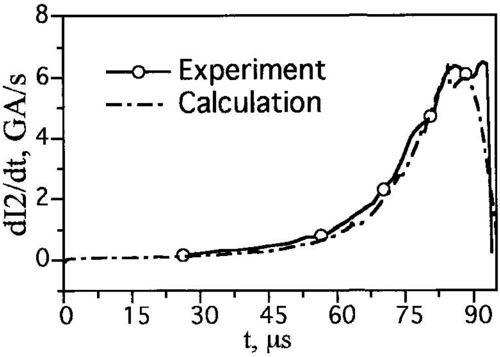

Figure 2. Current derivative in the load contour.

The good coincidence of experimental values of the current derivative in the load with calculated values [5] shows that there are no breakdowns between helix coils and between the coils and tube at the obtained strength values of the electric and magnetic fields. Liner braking in the magnetic field of the generator helix is negligible. The maximum strengths of magnetic and electric fields obtained by investigating helical magnetocumulative generators, exceed 80 MA/m [2] and 12 MV/m [3]. Hence, we can hope to increase the output characteristics of the described generator by increasing the initial magnetic field energy. To determine the boundary characteristics of the described generator, it is necessary to perform additional experiments. It is interesting to mention that, according to the calculations performed, the tested generator at the given energy level allows the formation of voltage pulses with amplitudes greater than 3 MV at the fuse unit which is made of electrically exploded wires in an arc-suppressing medium. For the calculations, we used experimentally obtained [4] dependencies of the resistance of electrically exploded copper conductors in Teflon insulation at an input energy of almost similar energy input times and current density values as in exploding conductors. Comparable levels (2.5 MV) of voltages were obtained. Maximum power in the fuse unit was 0.3 TW. This shows that one quarter of this power could be passed on to the load. In this case, the value of the active resistance of the load will be equal to the value of active resistance of the fuse unit.

4 Conclusion

We proposed and experimentally checked the construction of a compact helical magnetocumulative generator with transformer. Experimental results confirmed its high generation characteristics: output power of the high-voltage transformer unit is 40 GW; voltage pulse amplitude is 290 kV; the energy amplification coefficient in the generator contour is ~400. Operating this generator on the fuse unit made of electrically exploded conductors could cause the voltage amplitude at the fuse unit to exceed 3 MV. Electric and magnetic fields measured in the generator contour are lower than those obtained in some other experiments. This shows that it is possible to increase the output characteristics of the developed generator by increasing the initial magnetic field energy.

References

1. Pavlovsky, A. I., Ludayev, R. Z., Magnetic Cumulation, Questions of Modern Experimental and Theoretical Physics. L.: Nauka, (1984) pp. 253-255.
2. Demidov, V. A., Zharinov, E. I., Kazakov, S. A., Chernishev, V. K., Fast Helical Magnetocumulative Generators, Ultra-High Magnetic Fields, Ed. by V. M. Titov, G. A. Shvetsov. M. Nauka, 1984. pp. 330-332.

3. Kravchenko, A. S., Boriskin, A. S., Vilkov, Yu. V., Dimant, E. M., Karpov, A. I., Nazarenko, S. T., Pavlov, V. S., Kozlov, M. B., Experimental Investigations of Operation of Helical Magnetocumulative Generator with Energy Transformer Bending.
4. Pavlovskii, A. I., Lyudaev, R. Z., Kravchenko, A. S., Zolotov, V. A., Yuryzhev, A. S., Magnetic Cumulation Generator Power Increase, Megagauss Fields and Pulsed Power Systems. Ed. by V. M. Titov and G. A. Shvetsov, N.Y.: Nova Science Publishers. 1990. pp. 385-392.
5. Kravchenko, A. S., Vilkov, Yu. V., Numerical Simulation of Operation of Helical Magnetocumulative Generators with High Energy Amplification Coefficient. In the proceedings of this conference.

ONE APPROACH TO SELECTING THE MAIN PARAMETERS OF THE EMG HELICAL COIL

V. K. CHERNYSHEV AND B. T. YEGORYCHEV
VNIIEF, Sarov, Russia

This report considers the criteria that have been used when designing the EMG helical coil. It also presents the test results of the helical EMG working under the inductive load of 25 nH.

1 Introduction

It is shown [1] that the generator's final current depends on index F~1+(R/dL/dt), where R is an active resistance of the helical EMG conducting contour and dL/dt is the speed of the helical generator inductance extraction. The smaller the correlation of R/dL/dt, the better the helical generator should operate. Thus, the utmost attention has been given to this index in the design of the helical generator.

2 Design

The EMG under consideration has a multi-section helical coil. The helical coil inductance has been inversely computed for every section of the coil [2]. The last section has been computed first, then the next to last, and so on. The entire helical coil has been computed in sequence. The inductance of every new section has been set approximately twice as high as the inductance of the previously computed section in order to provide current duplication to compensate for losses. This has proceeded from the requirement that the current in the generator should increase by an order of two at the extraction of each section inductance. This simplifies the construction and lets us assess the operation of each section separately.

In order to increase dL/dt in the generator, the pitch of the helical coil turns has been intentionally reduced to a minimum. Limiting factors have been taken into account, such as the permissible value of the voltage on the helical coil turns in relation to the dynamic contact point, and the connected probability of electrical breakdowns of the turns' insulation. Another factor is the probable pocketing of magnetic flux due to the turns' pitch reduction.

The number of the conductor starts in each section of the helical coil has been computed proceeding from a given permissible linear current density. In order to preserve the minimal value of R, the linear current density in the helical coil conductors should be no more than 0.6 MA/cm in this case, and the specific integral of current action should be no more than $1 \bullet 10^9$ A^2 s-cm^{-4}. Computations to compare the coils are being done to define the coil parameters when the linear current density is no more than 0.8 and 1.0 MA/cm. The influence of the skin-layer thickness on the value of R has also been taken into account.

A helical EMG has been fabricated to experimentally check the computations. The design and specifications of the EMG correspond to the computed data. The generator sketch, a scheme of the power supply, and the measurements of the basic parameters are presented in Fig. 1.

The generator has a helical coil with a diameter of 160 mm and length of 560 mm. The copper central armature has an outer diameter of 78 mm and wall thickness of 6.5 mm. The total length of the generator is 725 mm and its outer diameter is 190 mm. The generator's initial inductance is 49.2 μH and the total inductance is 25 nH.

In the experiment, the initial generator current has been chosen as 2.3 kA. The final current of 2.15 MA has been obtained in the inductive load. Current derivative and current in the load are given, correspondingly, in Fig. 3 and 4. The voltage on the helical coil turns has been measured by the voltage dividers R1-R7, ρ (Fig. 1). Dependence of the voltage value on the time in the helix coil turns is presented in Fig. 2.

As expected, a duplication of current in each section, if compared with the preceding one, has been observed in the experiment with a "cold" mode (see Table 1):

Table 1

Section N	Section 1	Section 2	Section 3	Section 4	Section 5	Section 6
Current, kA	79.66	137.8	260.2	664.5	1202.4	2020.1

A performance of the analogous experiment under a "hot" mode is of interest in order to examine to what extent the principle of current duplication by each section can be confirmed.

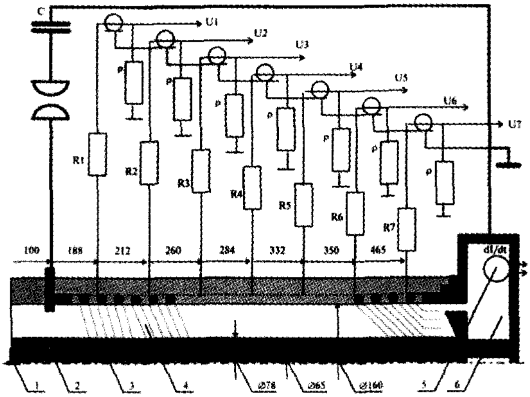

Figure 1. Helical generator diagram. 1 - electrodetonator; 2 - explosives; 3 - armature; 4 - helical coil; 5 - probes; 6 - load; C - capacitor bank.

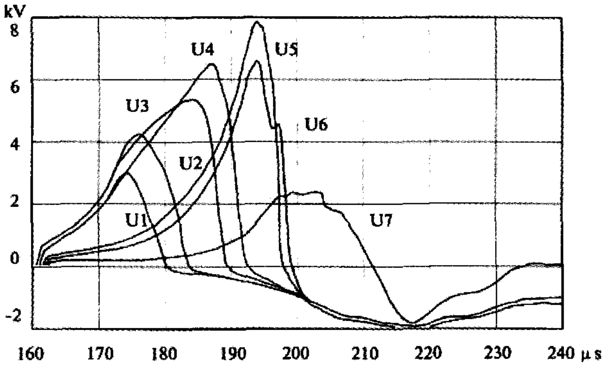

Figure 2. Voltage in the helical coil turns.

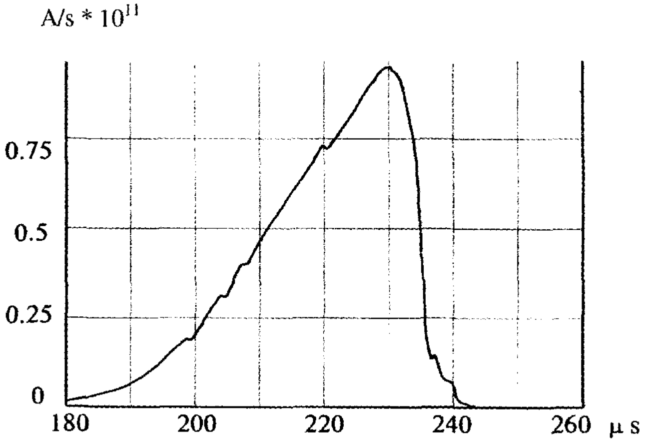

Figure 3. Helical generator current derivative.

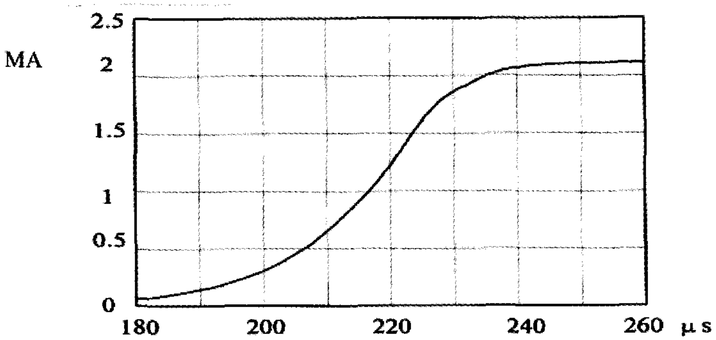

Figure 4. Helical generator load current.

3 Conclusion

The experimental values of voltage distribution in the helical coil and the current values in the helical EMG sections have been obtained. As expected, a duplication of current in every new section, if compared with the preceding one, has been observed in the experiment in accordance with the proposed method of designing a helix.

References

1. Shearer, J. W., Abraham, F. F., Aplin, C. M., Benham, B. P., Faulkner, J. E., Ford, F. C., Hill, M. M., McDonald, C. A., Stephens, W. H., Steinberg, D. J., Wilson, J. R., Explosive-Driven Magnetic-Field Compression generator. Journal of Applied Physics 39, 4 (1968) pp. 2102-2109.
2. Kalantarov, P. L., Tseitlin, L. A., Computations of the inductance: Reference book. (Leningrad, "Energy" Publishing House, 1970).

HELICAL EMG EFFECTIVE RESISTANCE

V. K. CHERNYSHEV, E. I. ZHARINOV, V. N. BUSIN, B. E. GRINEVICH, O. V. SOKOLOVA, G. N. SMIRNOVA, K. N. KLIMUSHKIN
Russian Federal Nuclear Center- VNIIEF, Sarov, Russia

The efficiency of explosive-magnetic system operation depends on the magnetic flux losses produced under circuit deformation. Losses primarily arise from circuit ohmic resistance and flux pocketing due to the disturbed continuity of helix wires deformation. This is because of technological faults in fabrication and potential electric breakdowns resulting from the voltage overload in the generator circuit. Since it is rather difficult to identify each type of loss mentioned, all soles are expressed as the effective resistance of the circuit, R_{eff}. The EMG-160 multi-sectional helical generator with a 760 mm long helix having an inner diameter of 160 mm is considered as an example. EMG-160 initial conductance was 34 μH and the final inductance was 25 nH. The effective resistance of the circuit was calculated for this experiment. The method of determining the effective resistance allows estimation of EMG efficiency at all stages of generator operation.

1 Introduction

The efficiency of the helical explosive magnetic generator (EMG) operation depends on magnetic flux losses in the process of contour deformation [1,2]. Losses mainly result from contour resistance and flux "pocketing" (cut-off) resulting from discontinuity of the helix turns extraction caused by technological inaccuracy when fabricating the construction, and from possible electrical breakdowns which occur because of the shift and bridging of the turns under magnetic field effects [3].

A picture typical of magnetic flux "pocketing" in the EMG, caused by the geometrical imperfection of the construction, is presented in Fig. 1.

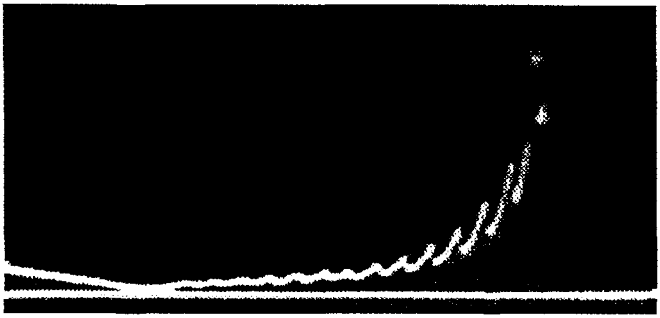

Figure 1. Magnetic flux "pocketing" in the EMG.

The current derivative oscillogram shows a distinctly transient $\dot{I}(t)$ increase, in which the number of "jumps" corresponds to the number of helix turns.

In [4], J. W. Shearer proposed a method of estimating the operation efficiency of the helical EMGs through F, the construction imperfection factor. Taking into account electrical breakdowns, we propose another method of estimating the EMG operation efficiency: through the value of the contour's effective resistance.

To include the flux "pocketing" into the magnetic cumulation equation, let us suppose that at every helix turn the "cut-off" inductance, due to geometrical bridging and electrical breakdowns, will be $\Delta L_{cut.}$ The time interval during which the "cut-off" of the inductance occurs between two adjacent turns is Δt.

In differential form, at Δt→0 we get: $\frac{\Delta L_{cut}}{\Delta t} \rightarrow \dot{L}_{cut}$

The value of $\dot{L}_{cut}$ represents an average value of the cut off inductance speed in the interval of the helix turns winding pitch. Taking into account the active resistance of the contour and the "cuts-off", the magnetic cumulation equation may be written as:

$$\frac{d\Phi}{dt} + IR + I\dot{L}_{cut} = \frac{d\Phi}{dt} + I(R + \dot{L}_{cut}) = 0 \qquad (1)$$

where Φ is flux, I is current, R is contour resistance.

As it is rather difficult to single out each of the above-mentioned types of losses in the experiment, we propose to formally express all losses through the effective resistance of the contour, which also includes the cuts-off, i.e. $R_{eff}=R+\dot{L}_{cut}$.

In this case equation (1) will be:

$$\frac{d\Phi}{dt} + IR_{eff} = 0 \qquad (2)$$

and its solution: $$I = Io\left(\frac{Lo}{L}\right) \cdot exp\left\{-\int_0^t \frac{R_{eff}}{L} dt\right\} \qquad (3)$$

The value of the effective resistance is determined to be:

$$R_{eff} = -\frac{d\Phi}{dt} \cdot \frac{1}{I} = -\frac{\dot{\Phi}}{I} \qquad (4)$$

Expression (4) makes it possible to estimate the efficiency of EMG at all the stages of its operation, due to experimental data.

2 Experiment

The estimate of the operation efficiency dependence on the effective resistance at different values of the initial current was made using a sectionalized helical EMG-160 with helix turns of an inner diameter of 160 mm and the length of 760 mm. The generator's initial inductance was 34 μH and the final inductance was 25 nH. If there were no flux losses, i.e. $R_{eff} = 0$, then according to (3), the larger the value of the initial current, the higher the final current would be.

The first explosive experiment with such a generator was performed at the high initial current of 30 kA. The experimental curves of the current derivative and current in that experiment are presented in Fig. 2.

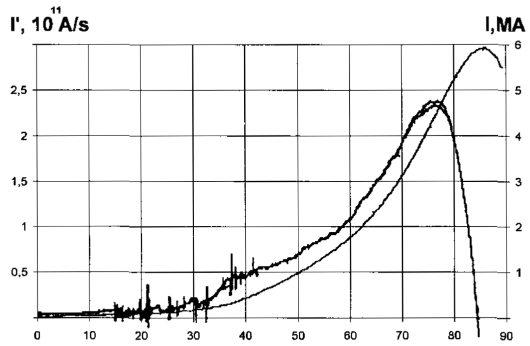

Figure 2. Experimental curves of current derivative and current.

The plots show that at the initial current of 30 kA, the final current in the load was 6MA. The energy amplification coefficient did not exceed $K_E \cong 30$. The behavior of the current derivative may draw one's attention. A peculiarity of the oscillogram is a slow increase of current derivative in the first part of the process and appearance of "overshoots" up to approximately 45 μs from the beginning of EMG operation.

Using formula (4) and the experimental data, we built up the dependence of the effective resistance on the contour deformation time (Fig. 3).

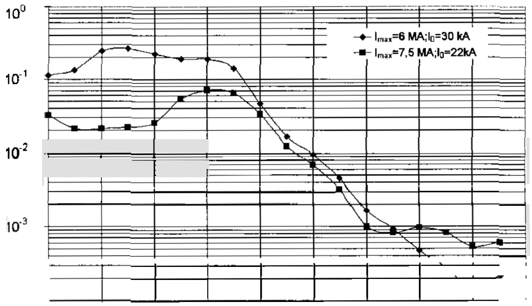

Figure 3. Effective resistance on contour deformation time.

If the initial resistance of the generator does not exceed ~ 0.05 Ohm, then the maximum value of effective resistance in the experiment could grow up to 0.3 Ohm at the initial stage of EMG operation.

The appearance of "overshoots" on the current derivative and, correspondingly, the increase of effective resistance denotes the presence of electrical breakdowns in the generator.

In order to avoid the breakdowns, it was necessary to reduce the current used to power up to the value at which the voltage in the helix could be no higher than the electric strength of the generator. According to our estimates this power-up current of powering should be reduced not less than a factor of 1.3 - 1.4. Therefore, the power-up current was reduced up to 22 kA in the next experiment. The experimental results are presented in Fig. 4.

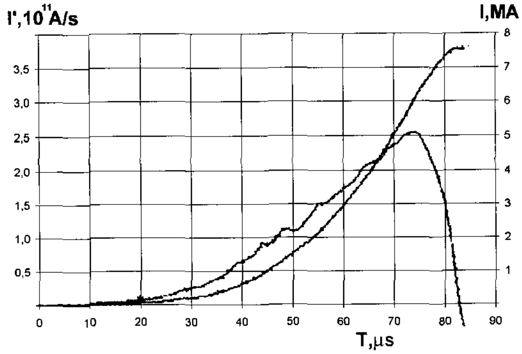

Figure 4. Experimental results.

We succeeded in raising the final current in the experiment to 7.5 MA, the energy amplification coefficient to $K_E = 85$, i.e. almost by a factor of 3 in comparison with the preceding experiment. R_{eff} (t) dependence is shown in Fig. 3. The curve shows that the maximum value of the resistance did not exceed 0.07 Ohm, and this maximum was close to the initial value of the resistance measured in the generator before the experiment.

The experiments with EMG-160, performed at even smaller initial currents of 15 - 16 kA, showed that the energy amplification coefficient was rather stable - an average of 80 over all of the experiments.

3 Conclusion

In order to avoid electrical breakdowns in the process of operating EMG-160 with an initial inductance of 34 μH and load inductance of 25 nH, the optimal power-up current should be no more than 22 kA.

References

1. Knoepfel H., Ultra-high pulsed magnetic fields, *Mir*, Moscow (1972) p. 221.
2. Chernyshev, V. K., Zharinov, E. I., Kazakov, S. A., Busin, V. N., Vaneev, V. E., Korotkov, M. I., Magnetic Flux Cutoffs in Helical Explosive Magnetic Generators, MG-IV, Megagauss Technology and Pulsed Power Applications. Plenum Press, New York and London (1986) pp. 455-469.
3. Zharinov, E. I., Mikhailov, O. D., Chernyshev, V. K., The effect of the axial shift of turns on the appearance of breakdowns in helical EMG, *PMTF*, **1** (1985) pp. 3-6.
4. Shearer, J. W., Abraham, F. F., Aplin, C. M., et al., Explosive-Driven Magnetic-Field Compression Generators, *Journal of Applied Physics*, **39** (4) (1968) p. 2102.

INVESTIGATION OF MAGNETO-PLASMA COMPRESSOR OPERATION POWERED FROM A HELICAL FLUX COMPRESSION GENERATOR

S. N. GOLOSOV, YU. V. VLASOV, V. A. DEMIDOV, S. A. KAZAKOV
VNIIEF, Sarov, Russia

A mathematical model for a helical flux compression generator (FCG) with a plasma-dynamical load in the form of a magnetoplasma compressor (MPC) is presented. The problem of electrically matching the MPC with an FCG is solved analytically. The mathematical model enables one to calculate the output parameters of the FCG-MPC system for given initial conditions. A comparison is made between the calculated results and the experiment.

1 Introduction

The creation of artificial plasma formations with a high output of light energy radiation is an effective means for solving many important scientific and applied problems. As mentioned in [1], FCG-MPC systems can be applied to these purposes.

2 Mathematical Model

The construction of a FCG-MPC system is briefly described in [2]. A system of simple algebraic equations is presented here for the simulation of helical FCG and MPC joint operation.

The system's electrical parameters can be described by expressions (1-6).

$$L(t) = L_0\, exp(-st) \tag{1}$$

$$I(t) = I_0\, exp\left\{ st - \frac{\gamma\left[d + (20+d)\, exp(st)\right]}{s\beta d L_0} \right\} \tag{2}$$

$$R(t) = \frac{\gamma I(t)^2}{\beta\left[I(t)^2 + exp(-t)\right]} \tag{3}$$

$$W(t) = W_m - \frac{I(t)^2 dL_0\left[s\beta dL_0 + 2\gamma(20+d)\, exp(st)\right]}{4\gamma(20+d)^2\, exp(st)^2} \tag{4}$$

(5)

$$W_m = \frac{I_0^2 dL_0\left[s\beta dL_0 + 2\gamma(20+d)\right]}{4\gamma(20+d)^2\, exp(st)^2}\, exp\left(-4\gamma\frac{10+d}{s\beta dL_0}\right) \tag{6}$$

where: $L(t)$ -inductance of an electrical contour, [μH]; L_0 -FCG initial inductance, [μH]; s, γ, β -constants; t -current time of a discharge, [μs]; $I(t)$-MPC discharge current, [MA]; $R(t)$ -MPC discharge resistance, [Ω];, $W(t)$ -maximum and current joule energy, released in MPC discharge, [MJ]; I_0 -initial current, [MA]; L' -linear inductance of MPC electrodes, [nH/cm]; η -MPC kinetic efficiency; $\bar{A}$-average nuclear weight of a material of plasma generating insulator; d -FCG helix diameter, [cm]; r_1, r_2 -internal and external radius of the MPC electrodes, [cm].

The maximum current I_m, electromotive force U_m of an electrical contour and time of achievement of the maximum current t_m are determined by expressions (7-9)

$$I_m = I_0 \frac{s\beta d L_0}{\gamma(20+d)} exp\left(-\frac{\gamma + s\beta L_0}{s\beta L_0}\right) \tag{7}$$

$$U_m = I_m \frac{\gamma(20+d)}{\beta d} \tag{8}$$

$$t_m = \frac{1}{s} ln\left[\frac{s\beta d L_0}{\gamma(20+d)}\right] \tag{9}$$

Gas-dynamic parameters of MPC plasma flow can be determined through the average mass velocity V(t), [km/s] and average density ρ(t), [kg/m^3] (10).

$$V(t) = \frac{10^3 L' I(t)^2}{\beta\left[I(t)^2 + exp(-t)\right]} \qquad \rho(t) = 0.26 \frac{\beta^2 I(t)^2}{(r_1 + r_2)^2 L'} \tag{10}$$

The parameters of the shock-compressed plasma and gas are determined by Roentgen-Hugonio ratios for shock waves [1]. The maximum energy of radiation E_m and effective brightness temperature of shock-compressed plasma T_m, equal to the temperature of a black body with the same level of radiation energy loss, could be estimated by expressions (11,12)

$$E_m = \theta\eta W_m \cdot \left(\frac{\alpha+1}{\alpha}\right)^2 \qquad T_m = 28.9 \cdot \left[\frac{\theta\alpha(L')^2 I_m^2}{\eta r_1 t_m}\right]^{\frac{1}{4}} \tag{11}$$

$$\theta = \left[1 + \sqrt{\frac{\rho(t_m)}{\rho_g}}\right]^{-2} \qquad \alpha = 1 + \sqrt{\frac{\rho_g}{\rho(t_m)}} \tag{12}$$

where: ρ_g - density of gas media on which the braking a plasma flow takes place, [kg/m^3]; E_m - [MJ]; T_m -[eV].

3 Calculation Results and Their Analysis

Calculations using the suggested mathematical model and their comparisons with test results were made of several FCG and MPC designs. There is satisfactory agreement between experimental and calculated data. As an example, calculated and experimental values of the current and shock wave velocity of plasma flow for two FCG and MPC designs with helix diameters of 50 mm and 100 mm are shown in Fig. 1. Values $E_m = 1$ kJ, $T_m = 5.5$ eV for the FCG design with the 50 mm diameter, and $E_m = 61$ kJ, $T_m = 8$ eV for the FCG design with the 100 mm diameter are obtained.

Analysis of the obtained functions shows that energy-power characteristics largely depend on parameters β, s and γ. However, the range of changes in β, s and γ is limited by peculiarities of the design. For example, the constant s is limited by the given electrical strength and FCG dimensions, β is limited by MPC dimensions, etc. The model offered allows optimizing the FCG-MPC system while designing the device.

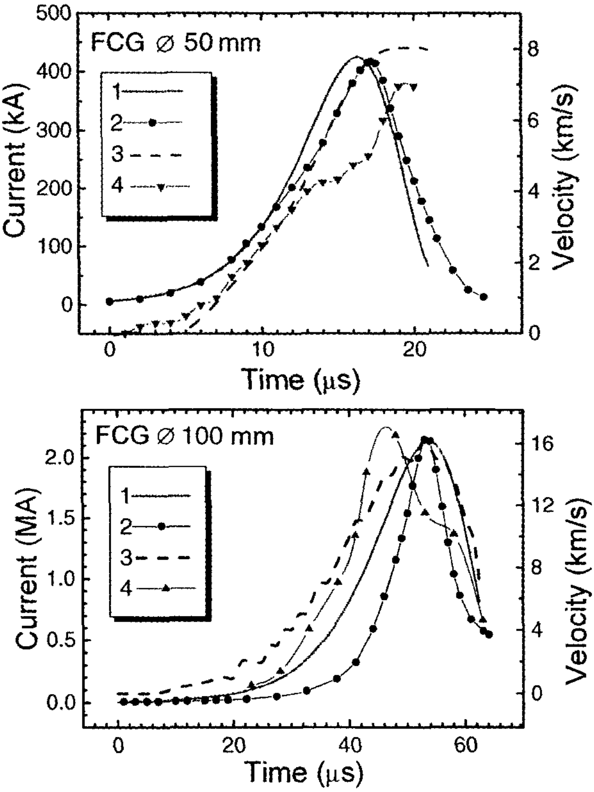

Figure 1. Calculated and experimental values of current and shock wave velocity of plasma flow for two MPC designs and FCG having helix diameter of 50 mm and 100 mm. 1 - calculated current values, 2 - experimental current values, 3 - calculated velocity values, 4 - experimental velocity values.

4 Conclusions

The problem of electrotechnical matching of MPC with helical FCG is solved analytically. Comparing the calculating results to the experiment shows that the mathematical model can calculation the output parameters of the FCG-MPC system at given initial conditions and can optimize this calculation.

References

1. Radiation Plasma-Dynamics. Vol. 1. Ed. by Yu. S. Protasov, Moscow: Energoatomizdat (1991) pp. 48-86.
2. Vlasov, Yu. V., Golosov, S. N., Demidov, V. A., Kazakov, S. A., Calculation Simulation of the Explosive Magnetic Generator-Magnetoplasma Compressor System. In: Megagauss and Megampere Pulse Technology and Applications, Ed by V. K. Chernyshev, V. D. Selemir and L. N. Plyashkevich. Sarov, VNIIEF, (1997) pp. 500-504.

HELICAL EXPLOSIVE FLUX COMPRESSION GENERATOR RESEARCH AT THE AIR FORCE RESEARCH LABORATORY

M. LEHR, D. CHAMA, J. DEGNAN, G. KIUTTU
Directed Energy Directorate, Air Force Research Laboratory, Kirtland AFB, NM, USA

T. CAVAZOS, D. GALE, P. PELLITIER, W. SOMMARS
Maxwell Technologies, Inc., Albuquerque, NM, USA

S. COFFEY
Numerex, Inc., Albuquerque, NM, USA

L. BAMERT, K. BELL
Applied Research Associates, Inc., Albuquerque, NM, USA

The inherently high energy density of explosives make them an obvious choice for pulsed power systems requiring high peak power and energy in compact packages. Ongoing research at the Air Force Research Laboratory's Directed Energy Directorate into helical explosive flux compression generators is discussed. These generators provide the initial pulsed power drive for a high voltage, long pulse system, which is the subject of a companion paper. The helical generator research described here centers on experiments utilizing two distinct generator designs based on 7.6 cm and 15.2 cm diameter aluminum armatures, respectively. Experiments using several different stator coil winding schemes with these armatures are described.

1 Introduction

High explosives provide extremely high energy density (~4 MJ/kg) and discharge times that are suitable for many pulsed power systems (often with further conditioning). Helical explosive flux compression generators (FCGs) generally provide high current and energy gain. However, they are low impedance current sources and require power conditioning to match the generator to high voltage, high impedance loads. Additionally, while the discharge time of helical FCGs is of the order of microseconds to tens of microseconds, many loads require fast rise times and somewhat shorter, high fidelity pulses. Thus the pulse conditioning system often must provide both temporal and impedance matching between the FCG and the load.

Several computer codes are used and more are in development to support the Air Force Research Laboratory (AFRL) explosive pulsed power program. These include circuit codes such as Microcap and circuit-based, generator-specific design and modeling codes such as CAGEN [1]. CAGEN models helical and coaxial explosive flux compression generators as circuit elements containing conducting armatures driven by high explosives. Being primarily a modeling code, CAGEN requires some empirical feedback.

Material interface tracking and explosive detonation capability has been incorporated into MACH2, a 2 ½-dimensional magnetohydrodynamic code [2]. MACH2, and MACH3, the fully three-dimensional version under development, are well suited to detailed studies of areas such as armature expansion and stator/armature interactions.

2 Experiments

The AFRL explosive pulsed power facility is located in a remote canyon and can accommodate experiments of up to 1000 lb of high explosives. The experimental facility includes a 200 kJ, 10 kV capacitor bank for providing seed flux for FCGs. A shed located on the pad houses a Beckman and Whitely 189 high-speed framing camera used for optical diagnosis of explosive events. Electrical and optical signals are fed to a screen room located in the explosive facility.

Explosive pulsed power experiments began at the Air Force Research Laboratory in the summer of 1995 with joint pulsed magnetohydrodynamic experiments with Sandia National Laboratory. These experiments, described in [3], spurred the development of explosive experiment infrastructure at the AFRL. Early explosive flux compression generator experiments centered on the use of simple helical explosive generators. These experiments drove further development of explosive experiment infrastructure and diagnostic techniques, and provided benchmarking data for design and analysis codes. These experiments are detailed in [4].

The next experiments were performed using 7.6 cm armature-based generators. These generators were wound with various bifurcated winding schemes to limit current density, thus limiting conductor surface magnetic flux density. These generators used aluminum armatures with hand packed C4 explosive systems. The experiments were primarily designed to provide empirical benchmarking data for the CAGEN generator modeling code. Due to space limitations, these experiments will be described in a future publication.

The most recent experiments were done using 15.2 cm armature-based generators, i.e., twice the armature and stator diameter of the 7.6 cm generators. The primary goal of these experiments was to attain the ultimate required output current and magnetic flux to the load. Numerous changes were made to the 15.2 cm armature based generators (relative to the 7.6 cm generators) more or less simultaneously. While such changes would ideally be made incrementally to better assess their effect on generator performance, this was impossible due to schedule and cost constraints. The major changes include: Cold cast PBXN-110 explosive in place of hand loaded C4, greater aluminum armature wall thickness, concrete tamping (inertial confinement) of the stator winding, two parallel generator windings, 550 nH load inductance (*vs.* 250 nH), and low mass crowbar tabs.

The PBXN-110 explosive is energetically similar to C4. Cold casting the explosive provides much more uniform density than hand packed C4. Voids and other density variations in C4 could lead to erratic armature behavior and jetting.

The thicker armatures resulted from a scale-up of the 7.6 cm armatures. The wall thickness of the 15.2 cm armatures was determined to keep the Gurney expansion angle [5] the same as in the 7.6 cm case. The resulting armature thickness was 0.95 cm, 1.5 times the thickness of the 7.6 cm armatures. This increased the magnetic flux diffusion time relative to the seed flux loading time, as detailed below. This is important, as any flux diffusing into the armature cannot be compressed, thus contributing to the overall flux loss in the generator.

The diffusion time for the 15.2 cm armature, t_d', is related to the diffusion time for the 7.6 cm armature, t_d, by

$$t_d'/t_d = (d_r'/d_r)^2 = (1.5)^2 = 2.25, \qquad (1)$$

where d_r', d_r are the wall thickness of the 15.2 and 7.6 cm armatures, respectively. The seed current loading time for the 15.2 cm armature based generator, t_s', is related to that for the 7.6 cm armature based generator, t_s, by

$$t_s'/t_s = (L_g'/L_g)^{0.5} = (2)^{0.5} = 1.4, \qquad (2)$$

where L_g', the initial inductance of the 15.2 cm generator, is approximately twice L_g, the inductance of the 7.6 cm generator. Thus, the increase in the magnetic diffusion time is approximately 1.6 times greater than the flux seeding time for this increase in armature dimensions.

These generators had two windings in parallel (displaced 180 degrees in azimuth) to take advantage of inherent feed and load symmetry. The low-mass crowbar tabs were designed to provide substantial crowbar switch action at the generator input while minimizing perturbation of the expanding armature.

Numerous stator winding schemes were examined within the general framework outlined above, including multiple bifurcations of the windings, increases in wire diameter toward the load end of the explosive generator, and expanded stator pitch (i.e., stator turns not close-packed).

The bifurcations and changes in stator wire diameter created high current joints within the FCG, i.e., connections that, toward the end of the generator burn, are carrying megamperes of current. It was suspected that molten copper, and perhaps vapor and plasma as well, was being ejected from the joints into the volume of the generator, where it could contribute to stator-to-armature breakdown. An FCG was built with clear windows covering critical current joints so the joints could be imaged with the high-speed framing camera during generator operation. Analysis of the photographs indicated that light, and thus likely some material, was issuing from the current joints. Steps are being taken to eliminate or delay the onset of material ejection from the current joints.

The best FCG performance obtained thus far in this program is a current of greater than 1.6 MA in the load. This represents a current gain of approximately 160 and an output flux of 0.9 Wb.

References

1. Chase, J. B., Chato, D., Peterson, G., Pincosy, P., CAGEN: A Modern, PC-based Computer Modeling Tool For Explosive MCG Generators and Attached Loads. *Proceedings of the Eleventh IEEE International Pulsed Power Conference.* (1997) pp. 1005-1009.
2. Frese, M. H., Mission Research Corporation Report AMRC-R-874.
3. Agee, F. J., Lehr, F. M., Vigil, M., Kaye, R., Gaudet, J., Shiffler, D., Explosively-Driven Magnetohydrodynamic (MHD) Generator Studies. *Proceedings of the Tenth IEEE International Pulsed Power Conference* (1995) pp. 1068-1071.
4. Lehr, M., Baca, G., Chama, D., Hackett, K., Kiuttu, J., Shiffler, D., Graham, J., Sommars, W., Coffey, S., Englert, T., Explosive Pulsed Power Experiments at the Phillips Laboratory. *Proceedings of the Eleventh IEEE International Pulsed Power Conference*, (1997) pp. 579-584.
5. Kennedy, J. E., Explosive Output for Driving Metals. *Proceedings of the Twelfth Annual Symposium on the Behavior and Utilization of Explosives in Engineering Design* (1972) pp. 109-124.

SIMULATION, DESIGN AND CONSTRUCTION OF A PULSED POWER SUPPLY FOR HIGH POWER MICROWAVES USING EXPLOSIVELY DRIVEN MAGNETIC FLUX COMPRESSION

M. KRISTIANSEN, J. DICKENS, M. GIESSELMANN,
E. KRISTIANSEN
Pulsed Power Laboratory, Texas Tech University, Lubbock, Texas

T. HURTIG
FOA (Defense Research Establishment), Grindsjoen, Sweden

This paper describes a coaxial pulsed power system intended to drive a high power microwave diode. The system consists of several sections. The first section is a 52 μF high-energy capacitor followed by a triggered spark gap. In the final design, an explosively driven magnetic flux compressor will replace the capacitor. The output of the triggered spark gap is fed into a coaxial energy storage inductor, which is terminated by an exploding wire fuse. The fuse is designed to explode at the peak value of the current in the energy storage inductor. After the explosion of the fuse, the current in the inductor is commutated into the load. The voltage at the load is the product of the commutated current and the load impedance. On the output of the fuse, a spark gap is mounted which is set to a breakdown voltage of approximately 200 kV. The spark gap connects the output of the fuse to a short transmission line and the load. For initial tests, the load consisted of a 15 Ω water resistor. After the initial tests, a microwave diode with a virtual cathode oscillator was connected at the output.

1 Circuit Simulation

Before building a hardware prototype, the system was simulated using the PSpice circuit simulation environment, Release 8.0. For this purpose, custom parts and associated models have been generated for the explosive flux compression generator, the exploding wire fuse, the spark gap, and the microwave diode. Fig. 1 shows the top level of the simulation circuit for the system that was used for this paper. The model for the fuse calculates the temperature rise of the fuse wires, which are made of copper, due to energy deposition as a function of current and temperature. The model uses the dependence of the resistance on the temperature and specific heat capacity of the fuse wires to calculate the instance of current interruption. The results of the system simulation are shown in Fig. 2. The current in the fuse at the time of current interruption is around 100 kA. After the fuse wires begin to vaporize, the model provides for an exponential increase of the fuse resistance up to a large maximum value, which is equivalent to a completely open circuit. The explosion of the fuse causes a large voltage rise across the energy storage inductor, which leads to the breakdown of the peaking spark gap. In the experimental system, the spark gap is pre-ionized using UV radiation to eliminate the statistical time lag in the breakdown characteristic of the gap. As can be seen from Fig. 2, the momentary power across the load resistor is close to 25 GW.

2 Experimental Setup

Fig. 3 is a drawing of the experimental setup that was constructed in order to test the power conditioning scheme outlined above. The complete setup was constructed in a coaxial system in order to eliminate electrical noise radiation from the experiment, and because this geometry is suitable for the final application. In this experimental setup, the fuse is located in a coaxial tube that is attached at a right angle to the main system. This facilitates the replacement of the fuse after each shot. In the final design of the power conditioning system, the fuse is placed in the center of the storage inductor.

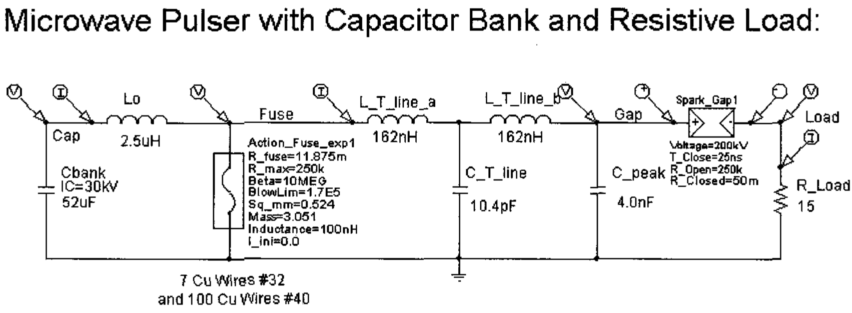

Figure 1. Top level of PSpice Simulation for Power Conditioning System.

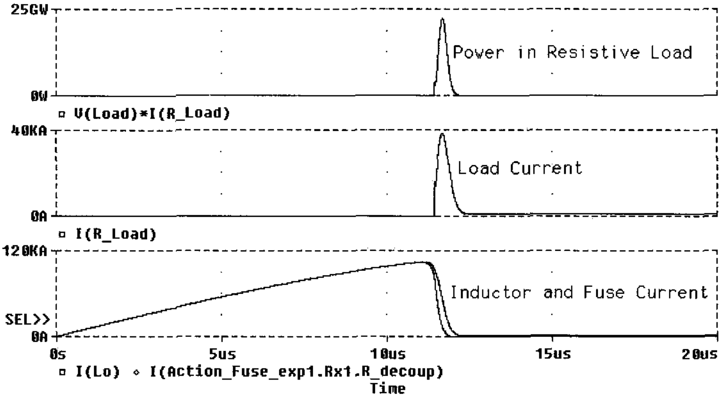

Figure 2. Simulation Results from PSpice Model

After initial test firings of the power conditioning system, it was found that the current fall-time of the fuse could be significantly lowered if the coaxial tube containing the fuse wires is filled with fine-grained sand. The sand quickly absorbs the energy generated by the plasma from the exploding wire, thereby reducing the recovery time and the hold-off voltage after recovery. This is important because the faster current fall-time will lead to a proportionally higher voltage across the inductor. Without the sand filling, the current fall time was significantly slower than in the simulation, and several re-strikes were registered after fuse recovery. Fig. 4 shows a photograph of the pulse conditioning system shown schematically in Fig. 3, as seen from the load side. The picture shows the load resistor inside the last coaxial section. The inner conductor is extended beyond the end of the load resistor to provide room for mounting a current sensor. For diagnostic purposes, both commercially available Pearson current monitors as well as shielded Rogowski coils have been mounted at the input side of the inductor section, at the load side and at the end of the fuse section. The locations of the current sensors are shown in Fig. 3.

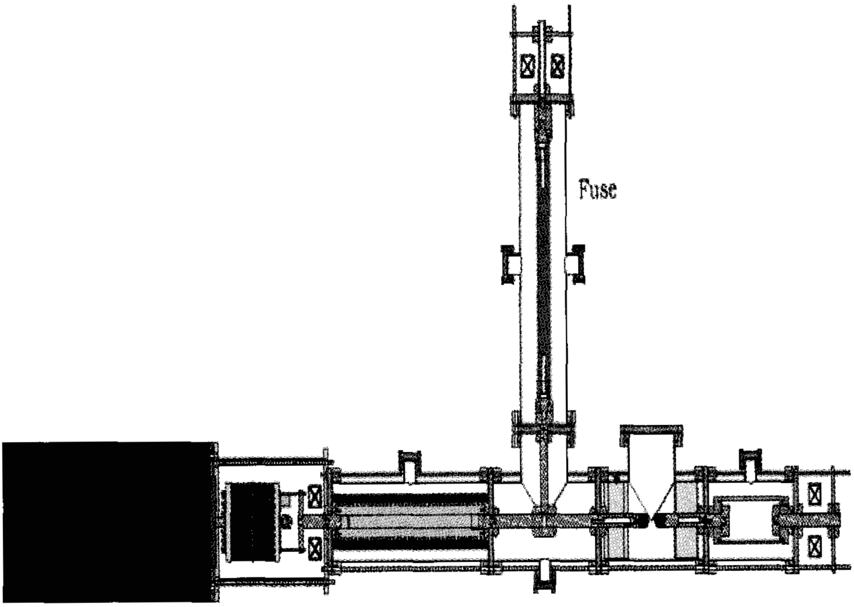

Figure 3. Drawing of the overall Coaxial Pulse Conditioning System

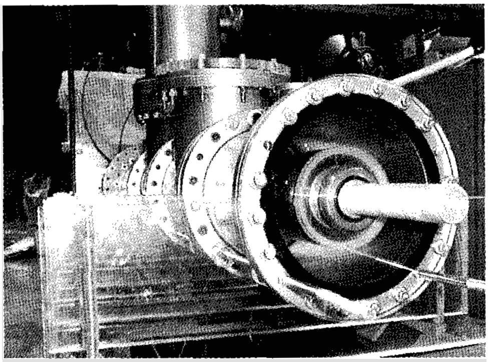

Figure 4. Picture of the experimental setup of the Pulse Forming System

3 Results

Fig. 5 shows an oscilloscope trace of the current in the fuse. The current was measured using a Pearson 110A wide-band current monitor. The trace in Fig. 5 shows an approximate fall time of 2.5 μs of the fuse current after the start of the current interruption. This agrees closely with the fuse parameters used in the simulation from the literature [1,2,3]. The rising edge of the current is not a perfect sinusoid. The fuse is heated to vaporize at the top of the waveform, so the discharge is damped.

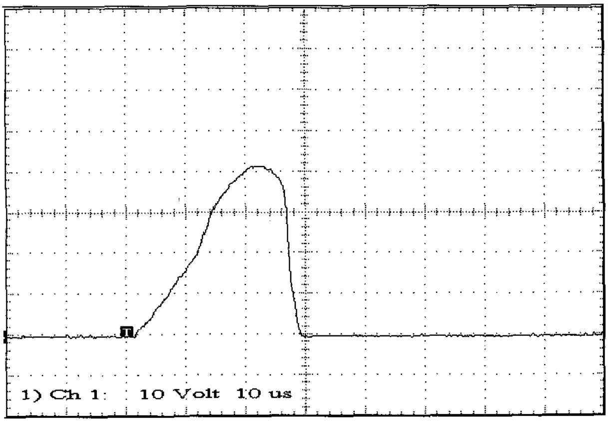

Figure 5. Oscilloscope trace of the fuse current obtained from a Pearson current monitor. 8 kA/div, 10μs/div.

4 Conclusions

A coaxial pulse forming system to generate high voltage pulses for High Power Microwave applications has been designed, modeled, and tested. The inner diameter of the outside tube of the coaxial structure was 6 inches. The most critical design parameters are the material of the fuse wires, the number of wires in the fuse, their length and diameter as well as the filling material for arc suppression.

Acknowledgment

This work was primarily funded by the Explosive-Driven Power Generation MURI program under the Director of Defense Research & Engineering (DDR&E) and managed by the Air Force Office of Scientific Research (AFOSR). Additional funding was provided by FOA.

References

1. Burtsev, V. A., Kalinin, N. V., Luchinski, A. V., Electric explosion of conductors and its application in electro-physical installations. *M. Atomizdat* (1990) pp.289.
2. Andrezen, A. B., Burtsev, V. A., Vodovozov, V. M., Drozdov, A. A., The investigation of commutating properties of electric exploding foils in arc-quenching media. *Oh. Techn. Fiz.*, **50** (1980) pp. 2283-2294.
3. Energy storage, compression and switching, Ed. by W. H. Bostick, V. Nardi, O. S. F. Zucker, (Plenum Press, New York, 1975).

GENERATING MICROWAVE RADIATION PULSES WITH MCG

A. G. ZHERLITSYN, G. G. KANAEV, G. V. MELNIKOV, V. I. TSVETKOV
Nuclear Physics Institute of Tomsk Polytechnic University, Tomsk, Russia

A. E. USHNURTSEV, S. V. DUDIN, V. B. MINTSEV,
V. E. FORTOV
Institute of Problems of Chemical Physics, RAS, Chernogolovka, Russia

Transformer schemes matching magnetocumulative generators (MCG) with high impedance loads, like vircator, look promising for achieving long pulse duration of 1 μs. An analysis of expected parameters is made here. The necessary MCG and transformer parameters are discussed and the experimental set-up is described. The shots with the MCG simulator were carried out first. At simulator voltage 40 kV and reserved energy 12 kJ, the voltage pulse with amplitude to 600 kV and 320 ns duration is generated on a triode with a virtual cathode. Microwave radiation of 300-400 MW and 200-300 ns duration is generated within a 10 cm wavelength range.

1 Introduction

Investigating processes to effectively transform chemical explosive energy into electromagnetic radiation is of scientific and practical interest. In papers [1,2] generation of high-energy microwave radiation using chemical explosives was demonstrated. In both cases, magnetocumulative generators (MCG) were applied to transform explosion energy into electromagnetic energy. However, further investigations revealed a number of nontrivial problems connected with matching the magnetic flux compressor with the microwave radiation generator (MWG). It was shown that, for effective conversion of energy accumulated in the magnetic flux compressor to microwave radiation energy, one must introduce an additional facility between the MFC and MWG to form a high voltage pulse as a power supply with certain parameters for the MWG.

2 Experimental Set-up

In paper [2] the schematic presented in Fig. 1a to generate high voltage pulses was used. According to the schematic, the voltage pulse is created using an inductive energy accumulator consisting of a compact inductance, electroexploding opening switch (EES) and a sharpening spark gap (SG). However, using the scheme limits the duration and size of the formed voltage pulse on the load, as these parameters are proportional to the value of its inductance. This is why an accumulator with inductively connected coils was made. The scheme of this voltage generator is presented in Fig. 1b.

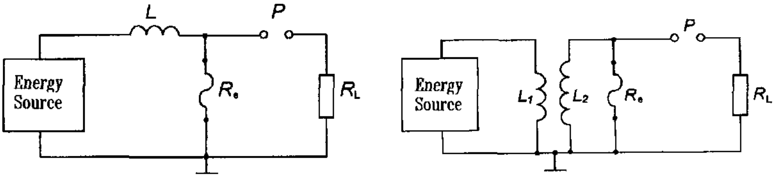

a. b.

Figure 1. Schemes of voltage generators. L - inductive store, R_e – opening switch, P –spark gap, R_H - vircator, L_1-L_2 - transformer inductive store

As follows from the scheme, the pulse generator consists of two circuits. One, MCG - L_1, supplies the current for the inductive accumulator from the beginning of the experiment to the initial moment that the switch R_e breaks. The second, L_2 - R_L forms a voltage pulse with required parameters at the break of EES and action of SG. Until the moment that the switch R_e breaks (the regime of shorting), the maximum values of currents in the circuits, the current increase time to a maximum value at which the EES explosion occurs, are all determined by the parameters of the initial energy source (MCG) and by the inductance, $L_{1sh} = L(1-k^2)$. This is the inductance of the first circuit coil at the moment the second coil shorts, by the coupling coefficient k between coils and by the coefficient $n = \sqrt{L_2/L_1}$. A voltage pulse of duration $t \sim L_{2sh}/R_H$ occurs at breaking switch R_e and by the action of SG switching the inductance current, $L_{2sh} = L_2(1-k^2)$. Here, L_{2sh} is the inductance of the second coil when the first is shorted.

Therefore, separating the circuit bringing energy into the inductive accumulator from the circuit putting energy out to the load permits optimization of an initial source of energy (MCG) and EES to form voltage pulses having the necessary amplitude and duration on the load.

A program to numerically simulate experiments was developed to form the voltage pulses on the load. This permitted us to diminish the body of investigations with MCG. However, numerical experiments for generating MW radiation using vircator do not give authentic results, so it is necessary to conduct experiments on the real set-up, employing the MCG. This makes the investigations more expensive and time consuming. Under these circumstances, we created an experimental stand containing the MCG with an explosion chamber, an imitation MCG, and the facility for high voltage pulse formation and MW generator (vircator-like triode with a virtual cathode). The imitation MCG permits us to form current pulses with parameters similar to those of MCG current pulses. The current pulse generator (CPG) is used as an imitation MCG. Commutation of CPG with the first coil is carried out by a controlled spark gap as in [3], where current on the magnetic flux compressors (MCG) was applied. However, further investigations revealed a number of nontrivial problems connected with matching the magnetic flux compressor with the microwave radiation generator (MWG). Thus, for effective conversion of energy accumulated in the magnetic flux compressor into microwave radiation energy, there must be some additional facility permitting formation of a pulse commuting between the MCG and MWG. This was executed with a multichannel discharge on the surface of a solid dielectric.

The facility for high voltage pulse formation involving the MW generator consists of four main units: an inductive accumulator, a commutation block, a vacuum insulator, and a triode with a virtual cathode (VK). The inductive accumulator is made of two inductively connected coils with copper foils wound coaxially. The commutation block includes EES and a two-electrode sharpening gas spark gap. EES represents a collection of copper wires in parallel, connected and stretched on an insulator cage. The switch is placed in a nitrogen atmosphere under pressure. A vacuum insulator is fabricated traditionally: alternating dielectric and metal rings with a forced distribution of potential along the insulator. On the insulator axis some high voltage electrode is disposed, in the outlet tip of which the anode is attached in the vacuum chamber of triode with VC. The triode with VC contains an anode grid and exploding-emitting cathode, which are placed in the vacuum chamber. The MW radiation power is extracted through the dielectric window. Fig. 2 shows the experimental results of MW radiation generation obtained using the MCG imitator. The experiments were conducted at the following accumulator parameters: $L_1 = 1.36$ μH, $L_2 = 21.4$ μH, $k = 0.7$, and the voltage on CPG was 45 kV. The energy entered into EES for time $t \approx 3\times10^{-6}$ s and the maximum value of current in EES was 22 kA. At these parameters the voltage pulse in the triode with VC reached 500 kV, the current in the anode-cathode gap was 14 kA, and the pulse duration was no less than 300 ns. This permitted us to generate MW pulses of 300-400 MW and 200-300 ns duration within a ten-centimeter wavelength range. Presently, new experiments are being prepared at this installation to generate high power pulses using MCG described in [4].

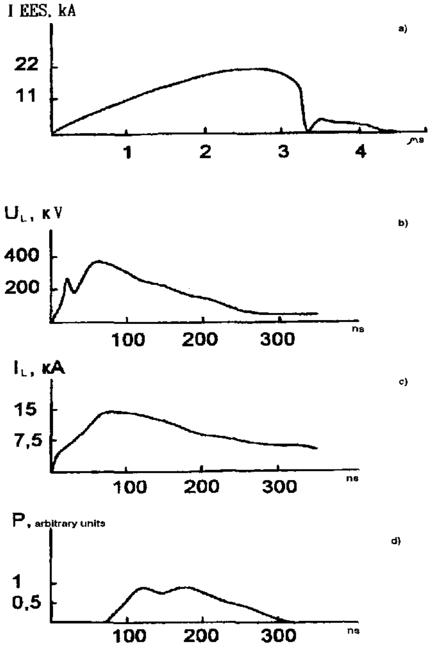

Figure 2. Typical waveforms of the signals from: a) current in EES, b) voltage and c) current in vircator, d) microwave power.

3 Conclusions

The installation for investigation of energy conversion processes was designed and built. Chemical explosive energy was converted into electromagnetic radiation energy using the MCG and the imitation MCG. This permits us to perform quick and cheap experiments on MW generation. The uniqueness of the design is the use of an inductive energy accumulator consisting of two inductively connected coils, one of them controlling the time energy is let into EES, and the other controlling the voltage pulse amplitude and duration on the load. This application makes it possible to generate MW radiation pulses in triode with VC and with high power levels.

References

1. Brodski, A. Ya., Vdovin, V. A., Korzhenovski, A. V., et al., *Russian Physics Dokladi*, **314** (1990) p. 846.
2. Azerkevich, E. I., Didenko, A. N., Dolgopolov, P. V., et al., *Russian Physics Dokladi*, **319** (1991) p. 352.
3. Grigoriev, A. V., Dashuk, P. N., Makarov, S. N., et al., *PTE*, **4** (1976) p. 151.
4. Leontyev, A. A., Mintsev, V. B., Ushnurtsev, A. E., Fortov, V. E., Shurupov A. V., Two-staged magnetic flux compressors with flux trapping. In: Meggauss -VII, Sarov (1997) p. 334.

CONSIDERATIONS OF AN AUTONOMOUS COMPACT SOURCE FOR HIGH POWER MICROWAVE APPLICATIONS

B. M. NOVAC AND I. R. SMITH
Department of Electronic and Electrical Engineering, Loughborough University, Loughborough, Leicestershire, UK.

The fast-rising, high voltage output step necessary for the use of explosively driven flux compressors as light and compact autonomous single-shot power supplies for high-power microwave applications requires special attention to be paid to the conditioning and matching elements of the overall system. The paper addresses various schemes by which this may be achieved. Based on proven techniques a practical approach using a high-voltage transformer is described in detail. It is also shown that future developments in long conduction plasma opening switches and fast-pulse compressors will lead the way to much more compact and higher performance systems, with characteristics that could also match the requirements of high power lasers and ion beam generators.

1 Introduction

There are fundamentally two situations in which explosively driven flux-compression generators are used as energy sources. The first is when possibly tens of megajoules are needed for proof-of-principle experiments (nuclear fusion research, X-ray simulators, etc), the second is when single-shot, rocket- borne experiments are performed at remote sites or even in outer space.

This paper addresses technical considerations relevant to the design of a light, compact energy source for high-power microwave generator applications that arise in the second of these situations. For example, in the magnetically insulated line oscillator [1], an autonomous high power source is required to provide a very fast-rising half-MV step to a load having a resistance of some ohms, and to maintain the voltage as constant as possible for at least some hundreds of nanoseconds. The basic scheme for achieving this is shown in Fig. 1. The paper concentrates on the high-energy part of the system rather than on the initial energy source. In view of the limited space available here, only one solution is considered in detail.

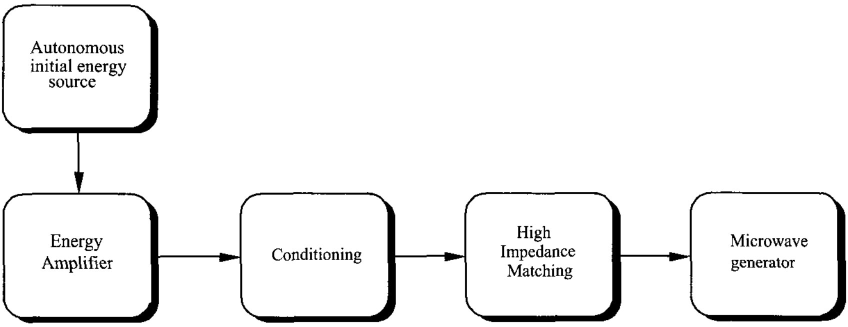

Fig. 1 Schematic of the autonomous compact source for high-power microwave application.

2 High Power Systems

The most suitable of the various techniques used in high-energy pulsed power for the generation of fast-rising, *long-duration* high-voltage pulses on high impedance loads appear to be either a Plasma Opening Switch (POS) [2] or a High Voltage Transformer (HVT) [3]. Both of these high-impedance matching elements need a pre-conditioned input pulse in order for the POS to function properly or for the HVT to provide the required voltage output.

The authors considered two different kinds of conditioning arrangements. The first was based on an Explosively Formed Fuse (EFF) [4] and the second on a Fast-Pulse Helical Flux Compression Generator (F-H-FCG) [5]. By combining the two matching elements with the two possible conditioning arrangements, four different high power systems become possible, as presented in Figs. 2 - 9, together with their predicted output voltage pulse. The main parameters used in the numerical modelling are given in Table 1. For all systems, the Autonomous Initial Energy Source (AIES) can be considered as one of the solutions presented in literature using battery powered capacitors [6] or explosively driven shock wave sources [7].

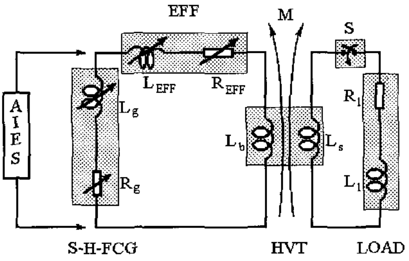

Figure 2. System I: electrical scheme.

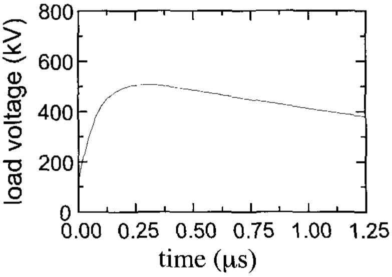

Figure 3. System I: load voltage.

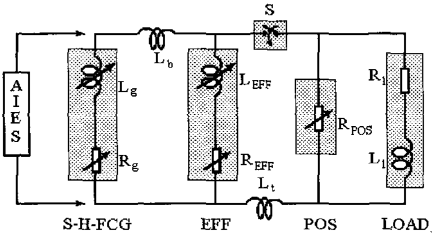

Figure 4. System II: electrical scheme.

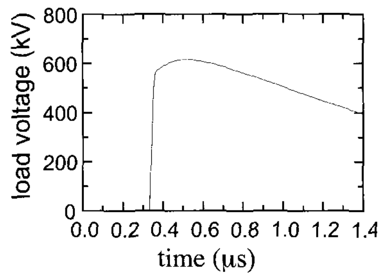

Figure 5. System II: load voltage.

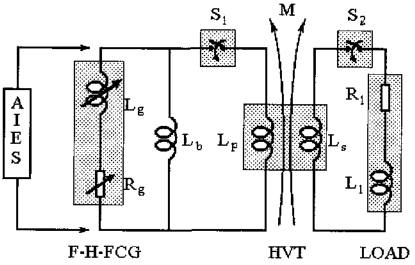

Figure 6. System III: electrical scheme.

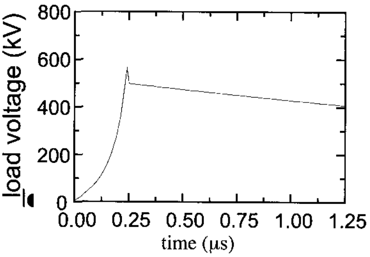

Figure 7. System III: load voltage.

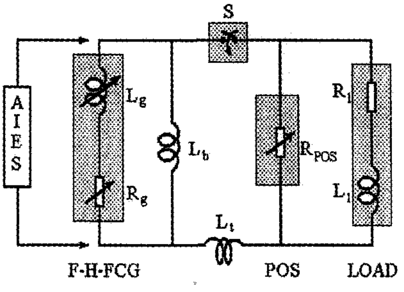

Figure 8. System IV: electrical scheme.

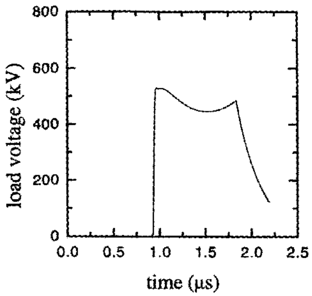

Figure 9. System IV: load voltage.

3 Design Procedure for System I

The slow helical flux compression generator (S-H-FCG) will have a classical design [8] well documented in [9]. Its use in the present system designs is straightforward, as the action of the S-H-FCG *is always decoupled* from that of the other system components. Its role is simply to amplify the energy from the initial source and to compress the final flux into a *static* ballast load L_b. The S-H-FCG is assumed to have the following conservative design characteristics [9]: energy multiplication $k = 100$, flux conservation $\lambda = 30\%$, global (chemical to electromagnetic) energy efficiency $\eta = 4\%$, explosive charge initial density and heat of detonation $\rho = 1.8$ g/cm^3 and $q = 4.5$ MJ/kg, maximum linear current density $\Delta \leq 0.2$MA/cm, expansion (coil/armature diameter) ratio $(d_c/d_a) \approx 2$.

It follows from this data that, for the S-H-FCG, the ratio of the initial inductance to the final (ballast) inductance $L_g(t = 0)/L_b = k/\lambda^2 = 1100$, the ratio of the total explosive mass to the total (maximum) delivered energy is $M_{ex}/W_m = 1/\eta q = 5.6$ kg/MJ, and that a first estimate of the armature diameter is $d_a = I_m/\pi\Delta$ where I_m is the maximum current. The length λ of the device depends on the maximum allowable internal voltage; λ can only be determined by using either a zero [9] or a 2-dimensional helical coil numerical design code [10].

Table 1. Systems Components & Parameters

Component	***System I***	***System II***	***System III***	***System IV***
1. S-H-FCG	Yes	Yes	No	No
$L_g(0)$ (μH)	100	400	-	-
ℓ(mm)	500	1000	-	-
d_a (mm)	140	120	-	-
d_c (mm)	300	250	-	-
M_{ex} (kg)	14	20	-	-
I_m (MA)	6	2.5	-	-
W_m (MJ)	2.5	3.8	-	-
2. F-H-FCG	No	No	Yes	Yes
dLg/dt (Ω)	-	-	-1.4	-0.6
I_m (MA)	-	-	2.5	0.9
W_m (MJ)	-	-	0.6	0.65
3. EFF	Yes	Yes	No	No
geometry	plane	cylindrical	-	-
dimensions (mm)	400x280	80x960		
	(W x L)	(D x L)	-	-
no of grooves	35	120	-	-
max voltage (kV)	200	800	-	-
Energy dissipated (MJ)	0.84	1.7	-	-
4. HVT	Yes	No	Yes	No
k_v	3	-	8	-
N	4	-	10	-
ω(mm)	400	-	150	-
t (mm)	1.2	-	0.7	-
r (mm)	95	-	230	-
L_p (μH)	See L_b	-	0.7	
L_s (μH)	1.3	-	62	-
M (μH)	0.3	-	5.6	-
5. Ballast inductor L_b (μH)	0.1	0.35	0.7	1.9
6. Transmission line L_t (μH)	No	1.5	No	1
7. AIES Energy requirement (KJ)	30	400	220	400

W, D and L for exploding forward fuses are width, diameter and length and dLg/dt is the time rate of change of inductance for a "fast" helical generator.

Following Stewardson et al., [11] a conservative set of design data for a standard EFF [4] Teflon made groove (6.5 mm wide, 1.5 mm die and 13 mm deep) is as follows: voltage across 6.5 kV, linear current density 0.15 MA/cm, deposited energy 0.6 kJ/cm width.

The design methodology for an air core cylindrical high voltage transformer HVT is presented elsewhere [12]. It has an N turn secondary winding of internal radius r inside a single-turn primary winding, both of width ω. The transformer geometry is completely defined by an interwinding Mylar insulation thickness of t and a primary-secondary insulation thickness of Nt. However accurate the calculations, the actual coupling coefficient k_c between the primary and secondary windings will be lower than that predicted. A value of $k_c = 0.85$ was assumed here. If the actual voltage multiplication factor is k_v and the primary inductance is L_p, the secondary inductance is $L_s=(k_v/k_c)^2L_p$ and the mutual inductance $M = k_v L_p$.

The parameters of the load, a magnetically insulated line oscillator, will be considered to be time independent with a resistance of 5 Ω and an inductance of 100 nH [1]. The voltage pulse required should have a rise time of less than 100 ns, amplitude of about 0.5 MV and duration of 1 μs. As presented in Fig. 3, these are generated by the power supply, with the main characteristics presented in Table 1.

This system clearly provides the most robust solution within the constraints of existing technology since it employs already established techniques, and the overall system development is straightforward. The entire system, as presented in Fig. 1, will weigh less than 200 kg and occupy only 1.5 m^3.

System IV will provide an increasingly attractive alternative as technology advances. Potentially, it can generate much higher voltage pulses with an extremely short rise time, while being lighter and far more compact than other systems. To take full advantage of the outstanding characteristics it offers requires the development of (i) a vacuum based F-H-FCG capable of withstanding internal voltages of some hundreds of kV and (ii) a long conduction time POS. It is important to note that these two requirements are universally related, and that the greater the conduction time that can be obtained from a POS the lower will be the internal voltage stress in the F-H-FCG.

Although the high power source design was considered for microwave applications, this future solution will also be useful for driving high power lasers or ion beam accelerators.

Acknowledgement

The ideas contained in this paper arose following discussions the authors held on their previous work on flux compressors with representatives of the US Army, Navy and Air Force. They are grateful for the funding from the European Office for Aerospace Research and Development that made these discussions possible.

References

1. Lemke R W., Clarke, M. C., Theory and simulation of high-power microwave generation in a magnetically insulated transmission line oscillator, *J Appl Phys.* **62**, (1987) pp. 3436-3470.
2. Weber, B. V. et al., Plasma erosion opening switch research at NRL, *IEEE Transactions on Plasma Science,* **PS-15**, No 6, (1987) pp. 635-648.
3. Martin, J. C., Smith, I. D., Improvements in or relating to high-voltage pulse-generating transformers and circuits, UK Patent, No 1, 114713, (1968).
4. Goforth, J. H., Williams, A. H., Marsh, S. P., Multi-megampere current interruption from explosive deformation of conductors, *5th IEEE International Pulsed Power Conference,* Ed. by P. J. Turchi, and M. F. Rose, (1985) pp. 200-203.
5. Caird, R. S., Fowler, C. M., Conceptual design for a short-pulse explosive-driven generator, *Megagauss Technology and Pulsed Power Applications,* Ed. by C. M. Fowler, R. S. Caird and D. J. Erikson, Plenum Press, NY and London, (1987) pp. 425-431.
6. Vorthman, J. E., et al., Battery-powered flux compression generator system, *Megagauss Fields and Pulsed Power Systems*, Ed. by C. M. Fowler, R. S. Caird and D. J. Erikson, Plenum Press, NY and London, (1990) pp. 437-440.
7. Demidov, V. A., et al., Helical cascade FCG powered by piezogenerator, *11th IEEE International Pulsed Power Conference,* **II**, Baltimore, USA, (1997) pp. 1476-1489.
8. Novac, B. M., Smith, I. R., Classification of helical flux-compression generators, *VIIIth International Conference on Megagauss Magnetic Field Generation & Related Topics.*
9. Novac, B. M., et al., Design, construction and testing of explosive-driven helical generators, *J Phys D Appl Phys,* **28**, (1985) pp. 807-823.
10. Novac, B. M., et al., Simple 2-dimensional model for flux-compression generators, *Lasers and Particle Beams*, **15**, No. 3, (1997) pp. 397-412.

11. Stewardson, H. R., et al., Fuse conditioning of the output of a capacitor bank to drive a PEOS, *10^{th} International Pulsed Power Conference*, **2**, Ed. by W. Baker and G. Cooperstein, Albuquerque, USA, (1995) pp. 1115-1120.
12. Stewardson, H. R., Novac, B. M., Smith, I. R. Fast exploding-foil switch techniques for capacitor bank and flux compressor output conditioning, *J Phys D: Appl Phys*, **28**, (1995) pp. 2619-2630.

COMPACT EXPLOSIVE DRIVEN SOURCES OF MICROWAVES: TEST RESULTS

L. ALTGILBERS, I. MERRITT, M. BROWN
Advanced Technology Directorate, U.S. Army Space and Missile Defense Command, Huntsville, Al, USA

J. HENDERSON
Survivability & Electronic Analysis Directorate, Army Research Laboratory, White Sands Missile Range, NM, USA

D. HOLDER
Weapon Science Directorate, U.S. Army Aviation and Missile Defense Command, Huntsville, AL, USA

A. VERMA
Defense Threat Reduction Agency, Albuquerque Office, Albuquerque, NM, USA

M. J. HOEBERLING, R. F. HOEBERLING
Explosive Pulsed Power, Inc., Los Alamos, NM, USA

G. CARP
Scientific Application International Corporation, McClean, VA, USA

W. FENNER
Allied Signal Technical Services Corporation, Albuquerque, NM, USA

C. M. FOWLER
Los Alamos National Laboratory, Los Alamos, NM, USA

J. PINA
Consultant, Annandale, VA, USA

M. LEWIS
Pentagon Medical Center, The Pentagon, Washington, DC, USA

In 1994, a paper [1] was published by A.B. Prishchepenko, in which he described several different designs of compact explosive driven sources of microwaves. He called these devices "electromagnetic ammunition" (EMA). In 1997, a joint test of the EMA was conducted in Nalchik, Russia at the High Mountain Geophysical Institute (VGI). In addition, a parallel test of one version of the EMA (i.e., the Explosive Magnetic Generator of Frequency) was conducted at the Energetic Materials Research and Testing Center in Soccoro, New Mexico. The results of both tests are presented in this paper.

1 Introduction

A. B. Prishchepenko tested his first device in 1983 and has continued testing since then [2,3]. Although all the EMA are based on the conversion of chemical energy into microwave energy, he developed various designs that use different methods for energy conversion. Most of the EMA require a low value capacitive load (10 - 1000 pF) to generate microwaves. The EMA tested in Nalchik were:

- Ferromagnetic Generator of Frequency (FMGF) (Fig. 1)
- Explosive Magnetic Generator of Frequency (EMGF) (Fig. 2)
- Implosive Magnetic Generator of Frequency (IMGF) (Fig. 3)
- Cylindrical Shock Wave Source (CSWS) (Fig. 4)
- The EMA tested at Soccoro was the EMGF (Fig. 5)

In this paper, a brief description of each device tested is presented, followed by a description and results of the tests and conclusions. The results and conclusions are based only on the devices tested. No conclusions can be drawn about other versions or designs of the EMA.

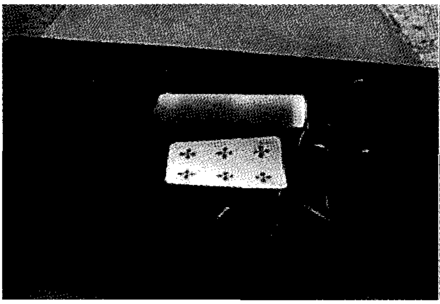

Figure 1. FMGF tested in Russia.

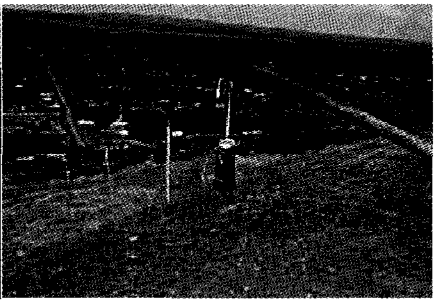

Figure 2. EMGF tested in Russia.

Figure 3. IMGF tested in Russia.

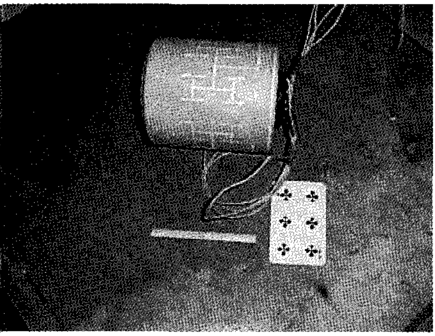

Figure 4. CSWS tested in Russia.

Figure 5. FCG device tested at Socorro.

2 Description of the EMA Tested

The FMGF consists of a detonator, explosive charge, magnetic material, output coil, and capacitive load [3]. When the explosive is detonated, it sends a shock wave into the magnetic material and demagnetizes it. The rapid change in magnetic field induces a current in the output coil. The capacitor causes the current to ring, thus generating microwaves. From the available literature, it is unclear how the microwaves are radiated. The FMGF are reported to be low energy sources.

The EMGF consists of a detonator, seed source, spiral magnetocumulative generator (MCG), and capacitive load [4-5]. The seed source, consisting of either permanent or electromagnets, is used to create the initial magnetic field in the MCG. If electromagnets are used, then a battery, capacitor, or ferromagnetic generator (FMG) is used to power the electromagnet. When the magnetic field in the MCG reaches its peak value, the explosive is detonated. This drives the liner outward, shorting out each succeeding coil of the spiral generator, thus converting chemical energy into electrical energy. The capacitive load causes the current to ring. As each turn is shorted out, the inductance of the LRC-circuit decreases and the frequency of the ringing current increases. As in the case of the FMGF, how the microwaves are radiated is not addressed.

The working principle of the IMGF is similar to that of the EMGF except that the liner uniformly implodes [3,6]. Unlike the EMGF, the coils of the spiral are all shorted out at the same time, which means that the frequency of the ringing current does not change.

The CSWS is different in that magnetic compression takes place within a monocrystalline or a powdered material, rather than air [7]. This reduces formation of Rayleigh-Taylor instabilities and improves device predictability. The CSWS consists of a detonator, seed source, MCG, solenoid, and working body, which may have been CsI. The MCG generates a current in the solenoid that induces a magnetic field within the working body. When this magnetic field is at its peak value, a second explosive charge is detonated and drives the solenoid inward. The imploding solenoid impacts on the surface of the working body and generates a shock wave that propagates radially inward. Researchers found in the early 1980s that, under extreme shock pressures, some dielectrics, such as CsI, become electrically conducting within the shock front. As this electrically conducting shock front propagates into the crystal, it compresses the magnetic field and induced current flows through the shock wave and acts like a magnetic dipole radiator. Of the 4 EMA described, the CSWS is reported to generate the highest microwave powers.

Other versions of the EMA and their descriptions can be found in References [3,8,9].

3 Description of the Tests in Russia

The tests at VGI took place between June 14 - 21, 1997. A total of 16 devices were tested: 3 FMGF, 3 EMGF, 5 IMGF, and 5 CSWS. The EMA were suspended by string from a metal pole2. They were connected to three 30 m long buried cables that ran from the firing point to the bunker. The first cable connected the seed source (capacitor) to the EMA, the second carried the fire pulse to the detonator, and the third the signal from a Rogowski coil.

The test instrumentation included 2 Tektronix TDS 684B and 2 Tektronix TDS 784A oscilloscopes, 3 D-dot sensors for the FMGF and EMGF tests, 4 Vivaldi antennas (two with X-band detectors and two without detectors), 96 Vivaldi antennas with 50 μJ fuses (witness plates), a dipole antenna built from indigenous materials, and locally procured cables. The Vivaldi antennas were not originally intended to detect energy recorded by the oscilloscopes. They were improvised in the field, since antennas intended for this purpose did not reach the test site. Twelve spectrometers (6 "Sirius" and 6 Kharkov spectrometers) traditionally used by Prishchepenko in testing the EMA were also used to measure the microwave output. Since these spectrometers were not available for evaluation, their data could not be properly analyzed. Therefore, only the microwave and Rogowski measurements made with the US equipment are discussed.

The capacitor was charged to 40-50 kV and then discharged when a pre-selected voltage was attained. At this voltage, the fire pulse was sent to the detonator. The oscilloscopes then recorded the microwave and Rogowski signals.

4 Description of the Tests at Soccoro

The Soccoro tests were to provide additional opportunity to measure the radio frequency and microwave emissions from small flux compression generators (FCGs) using detectors built by Los Alamos National Laboratory and to test the modified Vivaldi antennas used in the Russian tests. The units tested used the same load circuit as the Russian devices. The capacitive loads used in the Soccoro tests were the same Russian-made 1 nF high voltage capacitors used in previous Russian EMGF tests. The FCG devices tested at Socorro (Fig. 5) were modified versions of a US designed generator manufactured by Explosive Pulse Power, Inc. and were not meant to directly replicate the EMGFs tested in Russia. Information from previous publications (1-4) was used to modify the winding patterns to be similar to the Russian EMGF. All of the FCGs tested used permanent magnets for the seed source.

The diagnostics used to detect the radiated signals were the Automated Microwave Instrument (AMI), an array of 15 Vivaldi antennas with integrated 50 μJ fuses, and several TEM horn antennas. AMI is a third generation microwave spectrometer developed by Los Alamos National Laboratory for explosive tests. The exterior is a fully shielded screen box with 110 dB isolation. AMI uses fourteen antenna/waveguide/crystal detector channels to record time resolved microwave pulses from 2.6 to 110 GHz. Twelve of the channels were simultaneously digitally recorded inside AMI and remotely read out via a fiberoptic data link. The main controller that also triggers the detonator externally triggered the recording channels. The full frequency band at highest sensitivity was used throughout the tests. The Vivaldi array was arranged in five radial lines with three antennas in each line at different distances. Each of the antennas has positive gain from 1 to 5 GHz. One of the TEM horns used a ridged guide antenna and crystal detector to monitor the band of 0.5 - 8 GHz. The horns used individual coaxial cables that ran back into a bunker where the signals were recorded by RTD 720 digitizers. The other active TEM detector used a Vivaldi antenna with a crystal detector and duplicated the system used in Russia.

5 Russia Test Results

Due to the large amount of data recorded, only the most significant results are presented in this paper. Since four types of EMA were tested, the results of each type of device tested are discussed in turn. General conclusions about the tests are also presented.

Since the Vivaldi antennas connected to the oscilloscopes had not been calibrated in this configuration, background measurements were taken to ascertain their characteristics. The witness plate antennas were designed to operate in the frequency band from 2.5 - 10 GHz when the fuses were attached. However, background measurements revealed that when the fuses were removed and the antennas were connected to the oscilloscopes, they detected very low amplitude signals in the frequency band from 5 MHz to 2.5 GHz.

Three FMGFs were tested. It was originally intended that the oscilloscopes be triggered by the RF signal radiated by the FMGF. However, it was learned during the first shot that not enough energy was radiated to trigger the oscilloscopes. Therefore, it was decided to trigger the oscilloscopes with the Rogowski signal, which was measured by a dedicated Russian oscilloscope. The Rogowski signal was split-off from these oscilloscopes. None of the Rogowski waveforms recorded by the US oscilloscopes looked like those recorded by the Russian oscilloscope. It is believed that this is due to grounding and impedance mismatch problems associated with splitting the signal to the Tektronix oscilloscopes from the Russian oscilloscopes. The fast Fourier transform (FFT) of the Rogowski signal revealed that its frequency content was less than 100 MHz. No RF energy was detected. The small amplitude signals that were measured are thought to be background noise.

Three EMGFs were tested. Due to the triggering problems encountered in the FMGF tests, the modified triggering scheme in Fig. 8 was used. Figs. 6 and 7 show the Rogowski signal for one of the EMGF shots. The "fish" shaped waveform for the EMGF is similar to that described in [5]. Closer examination of the peaks of the oscillations shows what appears to be the "meandering" reported by Prishchepenko [5]. However, analysis reveals that the observed "meandering" is probably digitization noise.

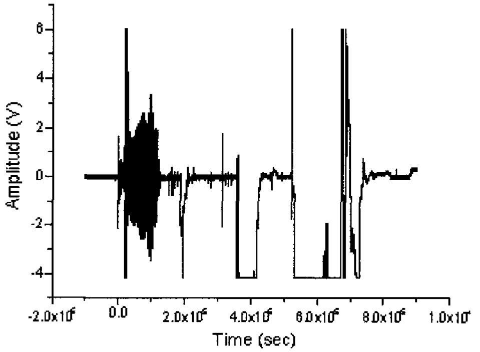

Figure 6. Rogowski signal from the EMGF.

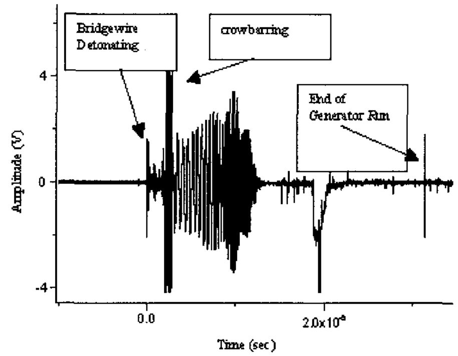

Figure 7. Enhanced view of the Rogowski signal from the EMGF.

Some inferences can be made about the Rogowski measurements, but they are subject to uncertainties due insufficient EMGF design information. The first pulse is probably caused by the detonation of the bridge wire in the detonator, and is followed by a pulse that drives the oscilloscope off scale. This latter pulse is probably the liner crowbarring with the first turn of coil in the MCG. The following train of pulses tends to increase in amplitude, but then dampens out due to unexplained high resistance that builds in the device. The ringing only lasted about 13 μsec of the 30 μsec run time of the EMGF. The frequency of the ringing current increased throughout the run of the EMGF, which is typical of explosive type MCGs, due to the decrease in the inductance of the generator as the coils are shorted out. The FFT of the Rogowski signal shows that the frequency content of the current is less than 50 MHz.

Close examination of the Rogowski signals and of the RF signals reveals that the radiated signals arrived at the sensors before the Rogowski signal by 50 - 150 ns. One hundred nanoseconds of time correspond to a 30 m difference in effective cable length path, which is the approximate length of the Rogowski cable. Therefore, the signals detected by the antennas were probably radiated by the EMGF and not cross talk between the channels of the oscilloscope.

The radiated and the Rogowski waveforms are very similar. While a "fish" RF waveform was expected, the close similarity was not expected. The FFT of the radiated signal shows that most of the energy was in a frequency band less than 25 MHz.

Five IMGFs were tested. The Rogowski signal consisted of two successive damped sinusoids. The first damped sine wave is probably the detonator and the second the implosive MCG. A dip at about 35 μsec appears to be the liner colliding with the coil of the MCG. There is no frequency change in the ringing current, which is typical of implosive MCGs. The FFT of the Rogowski signal contains frequencies out to about 50 MHz. The radiated RF signals detected by the Vivaldi antennas are damped sinusoids. The FFT of the signal reveals that most of the energy was in a frequency band less than 25 MHz.

Five CSWSs were tested. Based on the available literature, it was expected that the CSWS would generate a single nanosecond pulse. However, both the Russian spectrometers and the US oscilloscopes detected multiple pulses. The sensors and oscilloscopes, due to their limited bandwidth (1 GHz in the case of the Tektronix oscilloscopes), used in the Nalchik tests could not detect nanosecond pulses. The FFT of the Rogowski signal shows that the frequency of the ringing current was less than 10 MHz. The FFT of the detected RF signal reveals that most of the energy was in a frequency band less than 5 MHz. A bright flash accompanied the detonation of the CSWS. This was not observed in the FMGF, EMGF, and IMGF, and it is probably due to photo luminescence caused by the shock wave in the working body (CsI).

6 Soccoro Test Results

Four FCGs were tested and each had a stator inside diameter of 28 mm. One was a baseline unit with an inductive load that was a reference for a standard US design. The generator behaved satisfactorily and had an energy gain of approximately seven. The other three were tested with a 1 nF capacitor load. One of the units had a stator winding length of 26 mm and the other two were 127 mm long. The diagnostics and FCGs all triggered satisfactorily throughout the test series. In all of the tests, the TEM antennas were able to detect the transient pulse due to the firing of the detonator and then monitor the full FCG run time interval for radiated signals. AMI was triggered with the same pulse. The time resolved waveform from the test of the shorter FCG tested into a capacitive load is shown in Fig. 8. The "fish" shaped oscillation envelope is evident. The FFT (Fig. 9) indicates the major portion of the radiated energy to be in the frequency band from 20 to 40 MHz. The two longer FCGs with capacitive loads produced no significant high frequency radiation during the generator run. No microwave radiation was detected in any of the twelve AMI channels for any of the four tests.

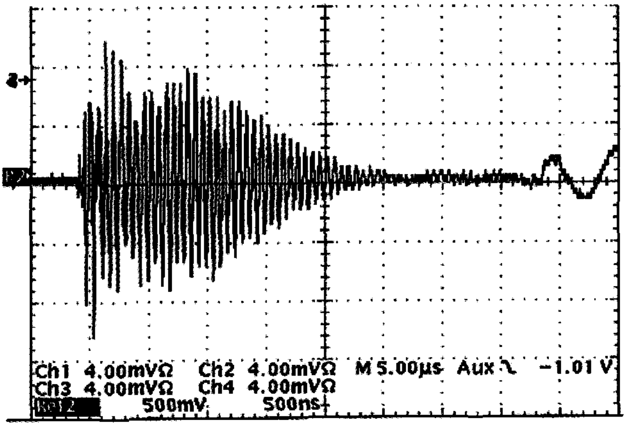

Figure 8. RF signal from the US FCG.

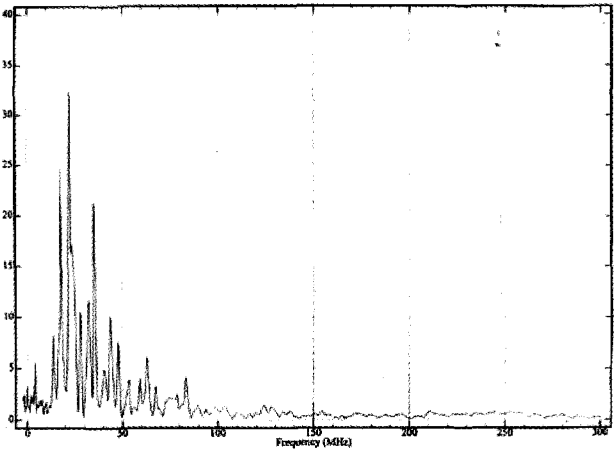

Figure 9. FFT of the RF signal from the US FCG.

7 Conclusions

Results from the tests conducted in Russia:

- The EMGF use an explosive type MCG, the Rogowski signal had the published “fish” waveform, and the frequency of the radiated RF energy did chirp.
- The IMGF use an implosive type MCG and the frequency of the radiated RF energy did not chirp.
- The CSWS use an implosive type MCG and there was a working body.

- None of the devices radiated significant energy in frequency band from 5 MHz to 2.5 GHz.

Results from the Soccoro tests:

- The test results agreed with the calculated radiation frequencies for the capacitive load used; that is, most of the energy radiated was in a frequency band < 50 MHz.
- No significant energy at frequencies > 100 MHz was observed by the TEM horns.
- AMI, which was set at full sensitivity, recorded no signals in the frequency band from 2.4 GHz to 110 GHz.

Acknowledgements

The authors would like to thank Dr. G. Lu and his staff at the Defense Special Weapons Agency – Field Command, Dr. M. Kristiansen and Dr. J. Dickens at Texas Tech University, and Mr. P. Tracy of Teledyne Brown Engineering for their technical support and recommendations in preparing the U.S. team for the tests in Russia. The authors would also like to thank all of the Energetic Materials Research and Testing Center personnel for their technical support and recommendations throughout the Soccoro test effort. Doug Olsen, Fred Sandstrom and Per-Anders Persson also made significant contributions to the success of the tests.

References

1. Prishchepenko, A. B., Kiseljov, V. V., Kudimov, I. S., Radio Frequency Weapon at the Future Battlefield, EUROEM, in Proceedings of EUROEM 94, Bordeaux (1994).
2. Prishchepenko, A. B., Zhitnikov, V. P., EM Weapon (EMW) in Air Defense or Some Aspects of Application of EM Radiation in the High-Frequency Band as a Striking Force, Air Defense Hearld, No. 7, (1993) pp. 51 - 55.
3. Prishchepenko, A. B., Zhitnikov, V. P., Microwave Ammunitions: SUMM CRIQUE, in Proceedings of AMREM 96, Albuquerque (1996).
4. Prishchepenko, A. B., Devices Built Around Permanent Magnets for Generating an Initial Current in Helical Explosive Magnetic Generators, *Instruments and Experimentation Techniques*, **38**(4), Part 2, (1995) pp. 515 - 520.
5. Prishchepenko, A. B., Shchelkachev, M. V., Operating Regime of an Explosive Magnetic Field Compression Generator with a Capacitive Load with a Consideration of Magnetic Flux Losses, *Journal of Applied Mechanics and Technical Physics*, **32**(6), (1991) pp. 848 - 854.
6. Prishchepenko, A. B., Shchelkachev, V. M., The Work of the Implosive type Generator with Capacitive Load, *Electricity*, No. 7, (1997) pp. 54 - 57.
7. Barmin, A. A., Prishchepenko, A. B., Compression of a Magnetic Field in a Single Cyrstal by a Strong Converging Ionizing Shock Wave, in *Megagauss Magnetic Field Generation and Pulsed Power Applications* (Ed. by M. Cowan and R. B. Spielman), Nova Science Publ., New York, (1994) pp. 35 - 40.
8. Prishchepenko, A. B., Tretjakov, D. V., Shchelkachev, M. V., Energy Balance by Explosive Piezoelectric Generator of Frequency Work, *Electrical Technology*, No. 1, (1997) pp. 141 - 145.
9. Prishchepenko, A. B., Electromagnetic Munitions, 96UM0427 Moscow Soldat Udachi, No. 3, (1996) pp. 45 - 46.

EXPLOSIVE DEVICE FOR GENERATION OF PULSED FLUXES OF SOFT X-RAY RADIATION

V. D. SELEMIR, V. A. DEMIDOV, A. V. IVANOVSKY,
V. F. YERMOLOVICH, V. G. KORNILOV, V. I. CHELPANOV,
S. A. KAZAKOV, Y. V. VLASOV, A. P. ORLOV
VNIIEF, Sarov, Russia

The concept and realization of the explosive electrophysical device EMIR to generate soft x-ray radiation pulses are described. EMIR is based on the development of VNIIEF technologies in high-power flux compression generators, and on transforming systems based on lines with distributed parameters and current opening switches. Vacuum lines with magnetic insulation or water coaxial lines are considered for transmission of the energy pulses to the load. Transformation of magnetic energy to kinetic energy, thermalization and soft x-ray radiation are performed in a z-pinch with a double liner system.

1 Introduction

The progress, achieved during the last few years in the develoment of electrophysical devices with inductive energy storage, and generation of soft x-ray radiation (SXR) in z-pinch type devices [1] opens prospects of creating of energy systems for investigations in the field of high-energy density physics and simulation of thermonuclear compression processes. The explosive device EMIR is based on the development ofVNIIEF technologies in high-power flux compression generators, and on transforming systems based on lines with distributed parameters and current opening switches. Vacuum lines with magnetic insulation or water coaxial lines are considered for transmission of the energy pulses to the load. Transformation of the magnetic energy to kinetic energy, thermalization and soft x-ray radiation are performed in a z-pinch with a double liner system. Hydrodynamical equations were solved to determine SXR parameters in combination with the radiation transfer equation in 2-D geometry. Equations of state were used in the approximation of Tomas-Fermi. Bremstrahlung absorption, photoionization, and absorption in the lines were taken into account.

2 Conception and Methods of Device Realization

The progress achieved during the last few years in the development of electrophysical devices with inductive energy storage, and generation of soft x-ray radiation (SXR) in z-pinch type devices [1] opens prospects of creating energy systems for investigations in the field of high-energy density physics and simulation of thermonuclear compression processes.

The explosive device EMIR for generation of soft x-ray radiation pulses is based on the development of VNIIEF technologies. It is designed on the module principle. A block scheme is presented in Figure 1.

Multi-element disk FCG (DFCG) 2 is the power base of the device. It is powered with preamplifier 1. A current pulse from DFCG is transmitted through cable line 3 to device 4 to increase voltage and reduce the forefront. The transformed pulse is transmitted by line 5 to the summator 6, combining all EMIR modules for energy pulse formation on the load 7.

DFCG contains 20 serially connected elements with HE-charges 240 mm in diameter. According to the calculations, with an initial powering of ~7 MA, DFCG provides a ~40 MA current with a characteristic rise time less than 4 μs in the 20 nH load [2].

The transforming system of the EMIR device is based on the linear inductive accelerator (LIA) scheme with inductors on the short-circuit lines with distributed parameters [3,4]. The key element of this scheme is an opening switch. Its operating time should be less than the run time of the electromagnetic wave along the short-circuit line and the final resistance R_k should be greater than the line wave resistance ρ_0. Plasma-erosion opening switches meet these requirements [5].

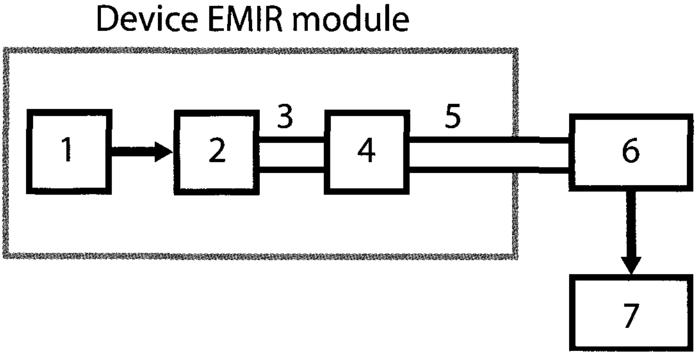

Figure 1. Block scheme of the device EMIR. 1 - helical FCG, 2 - disk FCG, 3 - cable line, 4 - transforming device, 5 - transmission line, 6 - summator, 7 - load.

Homogeneous radial lines with an external diameter of D = 300 cm and an internal diameter of d = 100 cm are used in the EMIR transformer. The base transformer module will consist of 5 inductors with full inductance of ≤20 nH. DFCG provides the initial current I_0 = 8 MA in the short-circuit inductor line. The value of the output voltage of one inductor is ~2 MV for $R_k \cong 2\ \Omega$, $\rho_0 \cong 0.67\ \Omega$ and a transmission line resistance $\rho_L \cong 1\ \Omega$. The voltage pulse, formed by 5 inductors on the load $Z_0 = 5\rho_L \cong 5\ \Omega$ will reach ~10 MV. Pulse duration in the transformer with a water insulator of 3 m in diameter will be ~120 ns.

Vacuum or water transmission lines are proposed for energy transmission from the transformer to the summator and the load.

To connect the vacuum transmission line to the inductors on the short-circuit lines with water as dielectric, it is necessary to create insulators that separate vacuum volume and deionized water. The electric field intensity on the insulator surface will be ~10 MV/m. The confinement of such fields is a rather complicated technical problem today.

With the application of a water transmission line, the crucial problem is to create an output insulator having surface electric strength of 10-20 MV/m. However, small pulse duration (~120 ns) and magnetic self-insulation gives hope of realizing such construction.

Energy pulses, formed by the base modules, are transported to the radial (biconical) line with the load in the center. Depending on the experimental conditions, the number of the base modules could be changed. Consequently, the wave resistance of the summator line must be changed, as well. It should be equal to Z_0/n, where Z_0 is the transmission line wave resistance and n is the module number. In particular, at the considered parameters of the base modules, the realization of the wave resistance of the summator line of ~0.1 Ω requires the parallel operation of 48 modules.

3 Estimation of SXR Characteristics

Principal scheme of the device forming SXR is presented in Figure 2.

☐

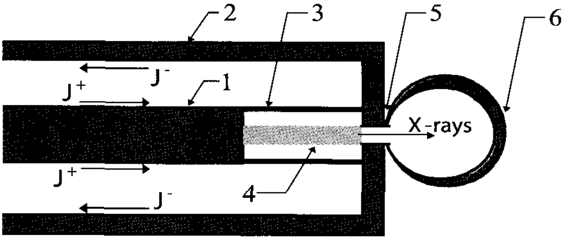

Figure 2. Scheme of the plasma element, forming SXR. 1 - supplying current conductor, 2 - reverse current conductor, 3 - external liner, 4 - internal liner, 5 - radiation output window, 6 - spherical cavity.

The energy supply system, consisting of direct 1 and reverse 2 current conductors powers the external liner 3. The kinetic energy of the external liner, acquired at the interaction with the magnetic field, is transmitted to the internal liner 4 as the result of a discharge. As in the result of the internal liner collapse, SXR is generated and emitted through the window 5 to the spherical cavity 6 with the thermonuclear target.

The external liner is made of heavy metal (e.g. tungsten) and the internal liner is made of light material to provide great radiation runs along the axis. Linear masses m of the liners are equal. The scheme is approved on the Angara-5 device [6] at electromagnetic energy of ~1 MJ.

Liner parameters at the start of thermalization were determined from a semi-empirical model [7]. For the conditions of this experiment we obtained:

$$m r_0^2 \approx 0.1 \cdot \frac{\mu_0}{4\pi} \frac{U_0^2 t_0^2}{R_0^2} \approx 0.1 (\mathrm{g} \cdot \mathrm{cm}); \quad \frac{r_0}{\vartheta_0 t_0} \approx 0.23; \quad \Delta r \approx 0.05 r_0 ,$$

where r_0 - initial radius of the external liner, ϑ_0, Δr - liner velocity and width at the moment of thermalization beginning. Numerical estimations correspond to the voltage pulse of $U_0 = 10$ MV, wave resistance $R_0 = 0.1\ \Omega$, and pulse duration $t_0 = 100$ ns.

Hydrodynamical equations were solved to determine SXR parameters in combination with the radiation transfer equation in 2-D geometry. Equations of state were used in the approximation of Tomas-Fermi [8]. Bremstrahlung absorption, photoionization, and absorption in the lines [9] were taken into account.

Numerical investigations showed that the maximum intensity coming into the SXR cavity are reached at $\vartheta_0 \cong 7 \cdot 10^7$ cm/s, position of the internal boundary of the liner $r_{in} \cong 0.2 r_0$, liner system length $l > 1.5$ cm (at $m \cong 0.035$ g/cm, $r_0 \cong 1.7$ cm). Maximum SXR intensity in the cavity having volume $V = 1$ cm^3 is ~0.5 MJ/ns, maximum radiation temperature is ~0.3 keV.

The calculation energy balance gives: supplied electromagnetic energy $W_k = 85$ MJ; liner kinetic energy $E_k \cong 17$ MJ; energy of the radiation, coming into the cavity $E_V \cong 1.7$ MJ ($E_V \cong 0.02 W_k$).

4 Conclusions

The concept and realization of the EMIR explosive electrophysical device to generate soft x-ray pulses is described. Estimations of SXR characteristics are made, and numerical investigations showed that the maximum SXR intensity in the 1 cm^3 cavity is ~0.5 MJ/ns and the maximum radiation temperature is ~0.3 keV.

References

1. Spielman, R. B., et al., PBFA-Z: A 20 MA Z-Pinch Driver For Plasma Radiation Source, in: Proceedings of the 11th International Conference on High Power Particle Beams. BEAMS'96, **1**, pp.150-153.
2. Demidov, V. A., Kazakov, S. A., Kravchenko, A. S., et al., High-Power Energy Sources Based on the FCG Parallel and Serial Connection, in: Digest of Technical Papers 11th IEEE International Pulsed Power Conference. Ed. by G. Cooperstein, I. Vitkovitsky. Baltimore, Maryland. (1997) pp. 1459-1464.
3. Itshoki, Ya. S., Pulsed Devices. Moscow: Soviet Radio, (1959).
4. Bossamykin, V. S., Gordeev, V. S., Pavlovskii, A.I., New Schemes for High-Voltage Pulsed Generators Based on Stepped Transmission Lines, in: Proceedings of the 9th International Conference on High-Power Particle Beams, Washington, May 25-29, (1992) **1**, pp.511-516.
5. Babkin, A. L., Chelpanov, V. I., Kornilov, V. G., et al., Electron Accelerator Powered by Inductive Storage Based on Induction Plasma Injectors, in: Proceedings of the 9th IEEE International Pulsed Power Conference, Albuquerque (1993) pp. 908-909.
6. Dyabilin, K. S., Lebedev, M. E., Fortov, V. E., Smirnov, V. P., et al., Investigation of Thermalphysic Substance Properties at Effect of High-Power Pulse of Soft X-ray Radiation of Z-pinch Plasma. TVT, (1996) **34**, No.3, p.479.
7. Katzenstein, J., Optimum coupling of imploding loads to pulse generators. *J.Appl.Phys.* (1981) **52**(2), p.676.
8. Yeliseev, G. M., Klinishov, G. E., Equations of State of Solid Bodies and its Spline Approximation. Preprint IPM AS USSR, (1982) No.173.
9. Degtyarenko, N. N., Yeliseev, G. M., About Fractal and Spline-Spectrum of Cross-Sections of Photons Absorption in Plasma, in: Fractals in Applied Physics, Ed. by A. Ye. Dubinov, Arzamas-16: VNIIEF (1995).

SHOCK COMPRESSION OF MAGNETIC FIELDS IN CsI

P. TRACY
Teledyne Brown Engineering, Huntsville, AL

L. L. ALTGILBERS, I. MERRITT, M. BROWN
Advanced Technology Directorate, Missile Defense and Space Technology Center
Huntsville, AL

Traditional magnetocumulative generators (MCGs) convert chemical energy from high explosives into electromagnetic energy by means of metallic conductors that compress magnetic fields in air. However, considerable energy is lost due to diffusion, compressibility of the conductors, and Rayleigh-Taylor and other instabilities. A technique based on the compression of magnetic fields within a solid medium such as CsI was developed to reduce these losses. This technique was applied to the development of the Cylindrical Shock Wave Source (CSWS) [1], which consists of a magnetocumulative generator (MCG), solenoid, and CsI monocrystal. The MCG provides current to the solenoid. When this current reaches peak value, the solenoid is implosively driven into the crystal creating a shock wave within it. Under sufficiently high pressures, CsI becomes electrically conducting. Therefore, the converging electrically conducting shock wave compresses the magnetic field induced in the crystal by the solenoidal current. To model the pressure and temperature changes within the CsI, a semi-empirical model has been developed based on the Hugoniot equations. To verify this model, it was applied to other materials and the results compared to published data. It was found that the model agreed well with experimental data. One objective for developing this semi-empirical model is to begin to formulate an explanation of how this device radiates microwave energy as reported in [2].

1 Introduction

When certain semiconductor and insulator materials are exposed to high static and/or dynamic pressures, they transition from a non-conducting state into a conducting state in which their electrical conductivity increases by six to eight orders of magnitude. Some substances that exhibit this property include powdered silicon, germanium, gray tin, silicon oxide, germanium iodide, and cesium iodide (CsI). Using this property, experiments demonstrated [3] that it is possible to create highly conducting shock fronts within these materials that can be used to compress magnetic fields in a manner similar to that of conventional MCGs. These types of MCGs are called *shock wave magnetocumulative generators* (SWMCG) or *semiconductor magnetocumulative generators*. The advantages of the SWMCG over conventional MCGs are [3]:

- More efficient transfer of chemical energy from the explosive to the shock wave.
- Highly efficient magnetic field compression due to low diffusion losses.
- Increased initial magnetic field in the generator because the energy is concentrated.
- Fast startup time, since it is practically independent of the time it takes to create the initial magnetic field in a conventional MCG.
- Reduced losses due to instabilities.

A drawing of an SWMCG is presented in Fig. 1. Either permanent magnets or electromagnets may be used to create the initial magnetic field within the working medium. D_s is the velocity at which the shock wave moves through the semiconductor and D_1 is the velocity at which the shock wave moves through the explosives. A conductive layer is formed within the shock front in the semiconductor material, which moves transverse to the magnetic field, exciting an EMF in this layer. Since this conductive layer and the other circuit elements form a closed circuit, the magnetic field is captured and compressed. The magnetic field distribution, direction of motion of the shock wave and direction of the current in a representative geometry are shown in Fig. 1.

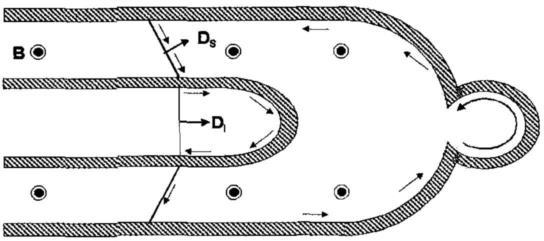

Figure 1. Shock wave source. When the explosive in the inner cassette is detonated, a shock wave is generated within the working body. At high shock pressures, the working body becomes electrically conducting and the propagating shock compresses the magnetic field created by either external permanent or electromagnets. An electric current is induced, which flows along a closed loop consisting of metal conductors and the shock front.

In 1994, A. B. Prishchepenko reported that, under certain circumstances, the SWMCG could produce microwave and millimeter wave radiation. He referred to this as the *Cylindrical Shock Wave Source* (CSWS) (Fig. 2) [2]. The purpose of this paper is to present a semi-empirical model for calculating the energy radiated by the CSWS. During the derivation of the model, a simpler form of the Hugoniot equations was derived and compared to experimental data.

2 Electrodynamics of the CSWS

The converging shock wave is assumed to be a magnetic dipole [4]. The vector and scalar potentials of a magnetic dipole are defined by the equations:

$$\vec{A} = \frac{\mu_0}{4\pi c^2 R}\ddot{\vec{m}} \tag{1}$$

and

$$\varphi = -\frac{\mu_0}{4\pi}\nabla \cdot \frac{\vec{m}}{R}, \tag{2}$$

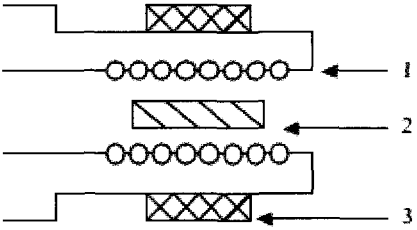

Figure 2. Cylindrical shock wave source: 1 - input coil, 2 - working body, and 3 - explosive charge.

where μ_0 is the permeability of free space, c is the speed of light, R is the distance from the dipole to a field point, and $\vec{m}$ is the dipole moment. The electric and magnetic fields of the magnetic dipole are:

$$\vec{E} = -\nabla\varphi - \frac{\partial\vec{A}}{\partial t} \tag{3}$$

$$\vec{B} = -c^2\nabla\times\vec{A} \tag{4}$$

Retaining only the far field terms, these equations become:

$$\vec{E} = \frac{\mu_0}{4\pi cR}(\hat{R}_0\times\ddot{\vec{m}}) \tag{5}$$

$$\vec{B} = \frac{\mu_0}{4\pi c^2 R}\left[\hat{R}_0\times(\hat{R}_0\times\ddot{\vec{m}})\right] \tag{6}$$

where $\vec{R}_0$ is a unit vector in the direction of $\vec{R}$.

The magnetic dipole moment can be expressed in terms of the compressed magnetic field within the crystal by using the approximation:

$$m = \frac{1}{\mu_0}\int B_d dV = \frac{1}{\mu_0}\int B_d\frac{dV}{dt}dt, \tag{7}$$

where V is the volume containing the dipole field and the subscript d is used to distinguish the radiated magnetic field from the magnetic field due to the dipole. The first and second time derivatives of Eq. (7) are:

$$\dot{m} = \frac{B_d}{\mu_0}\dot{V} \tag{8}$$

and

$$\ddot{m} = \frac{1}{\mu_0}(\dot{B}_d\dot{V} + B_d\ddot{V})\,. \tag{9}$$

The total power radiated by the magnetic dipole is:

$$P = \frac{\mu_0\ddot{m}^2}{6\pi c^3} = \frac{1}{6\pi c^3\mu_0}(\dot{B}_d\,\dot{V} + \dot{B}_d\ddot{V})^2. \tag{10}$$

Thus, it is necessary to account for the time dependent behavior of the magnetic field in the compression region and the volume containing the field.

3 Magnetic Field Compression

As the shock front propagates into the crystal, the temperature increases. This causes electrons to be elevated from their valence band into a conduction band, increasing the electrical conductivity of the crystal. When the conductivity becomes sufficiently high, the magnetic field is compressed by the shock wave.

A measure of the onset of the magnetic compression is the magnetic Reynold's number:

$$R_M = \frac{U\tau}{L}, \tag{11}$$

where U is the velocity of the shock wave, τ is the characteristic time for the diffusion of the magnetic field into the conducting medium, and L is a characteristic length for the problem under consideration. The magnetic Reynold's number can be expressed in terms of the cylindrical geometry and the electrical conductivity:

$$R_M = r_0\left[1 - \frac{r(t)}{r_0}\right]\mu_0 \sigma U, \tag{12}$$

where r_0 is the initial radius of the cylindrical crystal, σ is the electrical conductivity, and r(t) is the time dependent radial distance from the axis of the cylinder to the imploding shock front. The condition for the onset of magnetic compression is $R_M > 1$. If $R_M \to \infty$ the field is frozen into the shock wave.

An empirical expression for temperature dependence of the electrical conductivity is given in [5] as:

$$\ln\frac{\sigma}{\sigma_0} = 4.7\sqrt{\frac{T}{T_0}} - 6.64, \frac{T}{T_0} \leq 2 \tag{13}$$

$$\sigma = \sigma_{0.}\frac{T}{T_0} > 2,$$

where $T_0 = 10^4\ K$ and $\sigma_0 = 8.89 \times 10^6$ mho/m. Thus, the degree of magnetic compression depends on the temperature generated by the passage of the shock front.

As the shock wave propagates radially into the crystal, compressing the magnetic field, magnetic flux must be conserved, assuming that σ changes sharply, so that a good approximation is:

$$\frac{dB_d}{dr} = -\frac{r_0 B_d}{A} = -\frac{r_0 B_d}{\pi r^2}, \tag{14}$$

where A is the cross sectional area of the cylindrical crystal and the field is directed along its axis. The initial radius, r_0, was introduced as a characteristic dimension and the negative sign indicates that the magnetic field increases as the radius of the shock front decreases. Integrating Eq. (14) yields:

$$B_d = \xi e^{\frac{r_0}{\pi r}}, \tag{15}$$

where ξ is the integration constant. Assuming that $B_d = B_0$, when $r = r_0$, yields:

$$B_d = B_0 e^{\frac{1}{\pi}(\frac{r_0}{r} - 1)} = 0.73 B_0 e^{0.32\frac{r_0}{r}}. \tag{16}$$

So far, this analysis has addressed the relationships between the shock front, electrical conductivity, magnetic field, and radiated energy. In a more detailed analysis, these relationships can be expected to be a great deal more complex than presented here.

4 Equation of State for CsI

A significant amount of data on shock conditions in CsI has been published. For example, [5] provides an empirical expression for the Hugoniot curve as:

$$p\,(\mathrm{Mbar}) = 143 e^{-10.6(\frac{V}{V_0})}, \tag{17}$$

where V_0 = 57.6 cm^3/mole for CsI. A comparison of the plot of this equation with experimental data is shown in Fig. 3; the agreement is quite good.

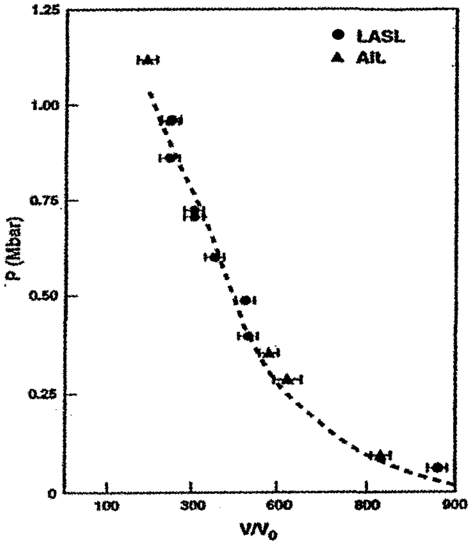

Figure 3. Comparison of calculated (dashed line) Pressure vs. Volume curves to experimental data.

An empirical expression for the temperature at the shock front is:

$$T(K)=\begin{cases}1.10\times10^{4}(1-e^{-1.28\times10^{-3}P}), p\leq0.5\text{Mbar}\\ 1.10\times10^{4}(1-e^{-1.28\times10^{-3}P})+3.50\times10^{3}(1-e^{-7.50\times10^{-3}(p-0.5)}), p>0.5\text{Mbar}.\end{cases} \tag{18}$$

where P is in Mbars. A comparison of the plot of this equation with experimental data is shown in Fig. 4. Again, the agreement is good.

At the shock front, the conservation of mass and momentum equations yield [6]:

$$P=\rho_0U^2(1-\frac{V}{V_0}), \tag{19}$$

where Eq. (19) neglects the initial pressure in the material. Given the velocity of the shock wave in the CsI, the temperature in the shock front can be determined. Knowing the temperature, Eq. (13) can be used to determine the electrical conductivity of the shock wave.

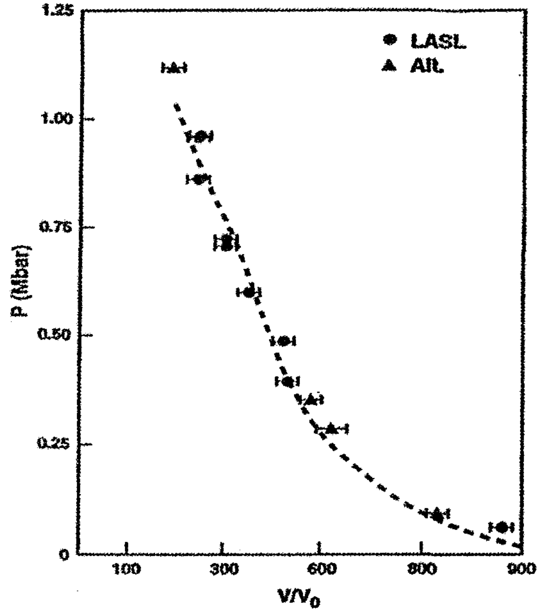

Figure 4. Comparison of calculated (dashed line) temperature vs. pressure curves to experimental data.

5 Shock Wave Propagation

Intuitively, it is expected that the compression wave induced in the crystal reaches a maximum velocity. As the velocity increases, the electrical conductivity increases rapidly beyond an onset pressure. This compresses the magnetic field. As the compressed field increases, the magnetic pressure that retards the converging shock wave increases and causes the velocity of the shock wave to decrease from its peak value. This process continues until the magnetic pressure is equal to the shock pressure and the compression stops.

Mathematically, this motion can be described by the equation:

$$r = r_0 e^{-at^n}, \tag{20}$$

where a and n are constants whose values must be determined. Differentiating this equation yields an expression for the velocity of the shock wave:

$$U = -anr_0 t^{n-1} e^{-at^n}, \tag{21}$$

where the velocity is zero at t = 0, but increases to a maximum value at time:

$$t_M = \left(\frac{n-1}{an}\right)^{\frac{1}{n}} \tag{22}$$

then decreases continuously for t > t_M. The minus sign in Eq. (21) indicates that the velocity is directed towards the axis of the cylinder.

Eq. (20) is a reasonably good match to the available data in [5] for the position of the shock front as a function of time when n = 2, a = $15.5/t_0^2$ sec^{-2} and t_0 = 5.43 µsec. Using these values, the maximum velocity occurs at $t_M = 0.18t_0$ = 0.975 µsec. In the experiments described in [5], the initial radius of the CsI crystal was 1.5 cm. Using Eq. (20), the distance to the shock front at t = t_m is r = 0.908 cm and the velocity at this time is U_M = 9.33 km/sec. Using Eqs. (17) and (19), $V = 0.385V_0$ and $\rho = \rho_0/0.385$ = 11.7 g/cm^3, where ρ_0 = 4.51 g/cm^3. Therefore, the pressure and temperature in the shock wave are calculated to be 241.5 GPa (2.415 Mbars) and 14,242 K, respectively. Knowing the temperature, the electrical conductivity is calculated to be 3.08 x 10^6 mho/m and the magnetic Reynold's number at this time would be R_M = 214.

Using the above data, the magnetic field at the maximum time is calculated to be $B_d = 1.24B_0$, which is in approximate agreement with the experimental value of $1.4B_0$. For an initial magnetic field of 4 T, the magnetic pressure at the maximum time is calculated to be $P_B = B_d^2/2\mu_0$ = 9.76 MPa and $\beta = P/P_B = 2.47 \times 10^4$.

The point at which β = 1, when the dynamic pressure of the shock wave equals the magnetic pressure, occurs when B_d = 780 T, r = 0.0859 cm, and t = 2.33 µsec. In performing these calculations, it was assumed that the dissipative losses are negligible. The radiated RF power is calculated to be P = 0.14 W.

It has been reported [2] that the radiated power of the CSWS is 1 GW. Calculating the values at which this power level can be achieved, one obtains r = 0.0258 cm, t = 2.28 µsec, and $B_d = 8.84 \times 10^7 B_0 = 3.54 \times 10^8$ T. That is, the shock wave must propagate a distance of 0.581 mm beyond the point where the dynamic pressure equals the magnetic pressure, which is where the shock wave should stop and move radially outward. The magnetic pressure at this point would be 5 x 10^{22} Pa. The velocity of the shock at the point where β = 1 is 2.12 km/sec. The question arises: can the shock wave penetrate a distance of Δr = 0.581 mm beyond this point due to its inertia or some other effect? To answer these questions, we must determine whether or not the CSWS radiates a 1 nsec, 1 GW pulse. This requires additional experiments.

6 Conclusions

Semi-empirical models were developed that could be used to estimate the power radiated by a converging conducting shock front, and pressure and temperature changes in CsI. The pressure and temperature model was applied to CsI and other materials, and there is good agreement between the model and published data. The model provides simpler relationships than those in [4] for calculating the pressure and temperature changes in materials subjected to high pressures. Using this model, the conditions required for the CSWS to radiate a 1 GW pulse were estimated. While the material presented in this paper does not answer the questions about the basic physics of the CSWS, it does provide a starting point for estimating operating conditions, designing experiments and developing an improved understanding of CSWS functioning.

References

1. Barmin, A. A., Prishchepenko, A. B., "Compression of a Magnetic Field in a Single Crystal", in *Megagauss Magnetic Field Generation and Pulsed Power Applications*, Ed. by M. Cowan and R. B. Spielman, Nova Science Publ., New York, (1994) pp. 35-40.
2. Prishchepenko, A. B., "Microwave Ammunitions: SUMM CRIQUE", Proceedings of the EUROEM Conference (1994).
3. Bichenkov, E. I., Gilev, S. D., Trubachev, A. M., Proceedings of the 3rd International Conference on Megagauss Magnetic Field Generation and Related Topics, Ed. by V. M. Titov and G. A. Shvetsov, Nauka, (1984) pp. 88-93.
4. Barmin, A. A., et al., Losses of Electromagnetic Energy in Compression of a Magnetic Field by a Shock of the Second Kind, Izo. Akademii Nauk SSSR, *Mekhanika Zhidkosti I Gaza*, No. 6, (1988) pp. 166-170.
5. Radousky, R., Mitchell, A.C., Nellis, W.J., Shock Temperature and Melting in CsI, *Phys. Rev. B*, **31** (3), (1985) pp. 1457-1462.
6. Zeldovich, Ya. B., Raizer, Yu .P., *Physics of Shock Waves and High-Temperature Hydrodynamics Phenomena*, Vol. 2, Academic Press, New York (1966).

EXPLOSIVE MHD GENERATORS

E. F. LEBEDEV, V. E. OSTASHEV AND V. E. FORTOV
High Energy Density Research Center of RAS, IVTAN, Moscow, Russia

Explosive driven MHD generators (EMHD) occupy an intermediate position between destroyed Explosive Flux Compression Generators and solid-propellant- pulsed MHD generators. Studies revealed the negative consequences of destroying a plasma liner through Rayleigh-Taylor instability. The real efficiency of conversion of condensed HE charge chemical energy reaches ~10% if the magnetic field in a MHD channel is approximately 8-10 T. Accommodation of 20-30 linear MHD channels into a toroidal magnet seems to be optimal for EMHD generator design. This device may operate repeatedly with a frequency of up to 6.5×10^3pps.

1 Introduction

Active development of EMHD generators was conducted in the United States and Russia for more than twenty years. One working section of this type of generators is a plasma liner generated in the head of the flow, formed when a condensed HE charge is detonated (Fig. 1).

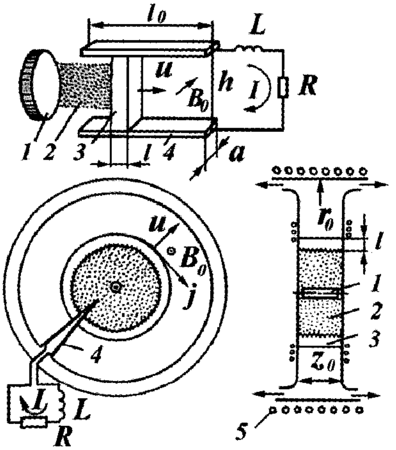

Figure 1. The schemes of EMHD generators. *1* – charge of HE; *2* – flow of gas of detonation products; *3* – plasma liner; *4* – electrodes; *5* – magnet coils; B_0 – magnetic field, *u* – velocity of liner, *I* – current of generator.

Results of the complex studies of EMHD generators are collected in a book [1] published in Russia. It presents data obtained at the Institute for High Temperatures at the Russian Academy of Sciences from 1970-1995. Linear (EG-5, EG-6 and EG-10) and radial (T-2, T-4 and R-1) models of generators were studied (Fig. 2). Superconducting magnets were used in models EG-5 and R-1.

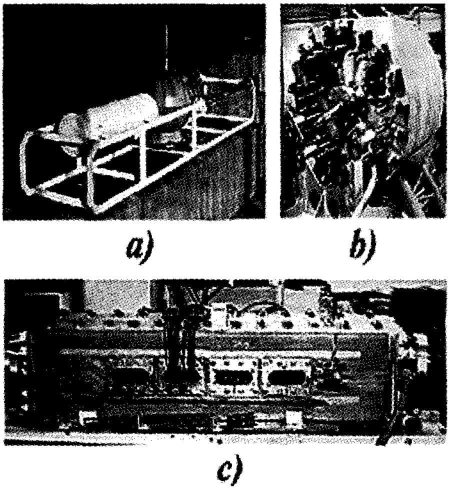

Figure 2. Some experimental EMHD generator models developed in IVTAN. *a* – EG-5; *b* – T-4; *c* – EG-10

Unlike the pioneer investigations of the American authors [2-10], who emphasized the energetic parameters of generators, [1] also presents the studies of explosive flow structures as well as gas dynamic and electric parameters. This has allowed the study of physical processes that limit the efficiency of conversion of chemical energy of the condensed HE charge in EMHD generators.

2 Energy Conversion in an EMHD Generator

A low conductivity gas produced by the detonation products contains the major part of the energy of the explosive flow. However, only a thin plasma liner localized at the front of this flow ($l << l_0$) directly interacts with the transverse magnetic field B_0 in the MHD channel.

Due to deceleration of the plasma liner in the magnetic field, a dynamic gas compression wave is formed that spreads upwards in the flow. This wave consists of gas from the detonation products interacting with the magnetic field. The thinner the plasma liner, the more quickly its parameters are reconstructed in the magnetic field and the more effectively the gas interacts with the magnetic field (Fig. 3).

Only a part of the detonation product flow, covered by the compression wave, is involved in the interaction with the magnetic field. It uses no more than ~20% of its energy working against the electromagnetic force. Evaluations and experimental results have shown that the correlation $(B/u)^2/2\mu_0\rho_{dg} \approx 1$ is a condition of optimum conversion of explosive flow energy in the MHD channel (ρ_{dg} is the gas density of detonation products in the head of the flow).

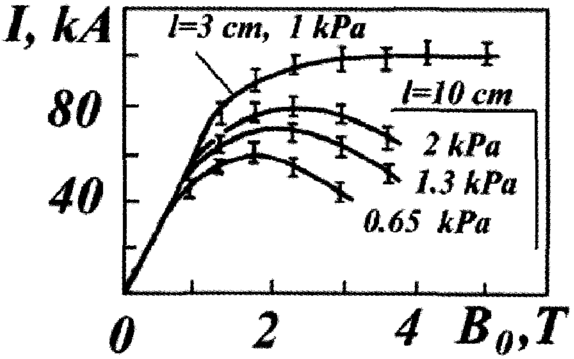

Figure 3. Current in a linear EMHD generator depends on the width of the plasma liner as well as the initial pressure of a gas into the MHD channel.

3 Rayleigh-Taylor Instability

With deceleration of the plasma liner, the Rayleigh-Taylor instability destroys the contact surface of the plasma and the denser gas of the detonation products. The nonlinear stage of instability is characterized by formation of the gas streams of detonation products that penetrate into the plasma of the shock-heated gas (Fig. 4). During strong MHD interaction, destruction of the shock wave front of the expanding the flow in cylindrical channels was observed. One full interruption of induced circular current in a plasma liner occurred in a disc.

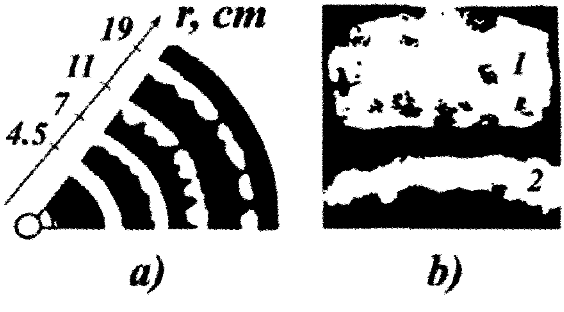

a) b)

Figure 4. Registration of Rayleigh-Taylor instability in radial generators. *a* – instability evolution in the disc generator T-2; *b* – fragment of plasma in the cylindrical generator T-4: *1* – view of the plasma front; *2* – view along the channel axis.

As a consequence of turbulent mixing of plasma and gas of the detonation, both a reduction of efficient plasma liner conductivity and an increase of its average density products were observed. Liner conductivity was increased to 300-500 S/m at the expense of increased joule heating when raising the magnetic induction to 5-6 T, and a contribution of cesium seed in the HE charge (up to 10^3 S/m). Ionization of the cesium seed occurred under turbulent mixing of the gas of the detonation products and the plasma of the liner. Increasing the liner density ρ_l reduces the relative level of MHD interaction (characterized by the parameter $(B_0/u)^2/2\mu_0\rho_l$). This prevents disintegration of the plasma liner in a strong magnetic field and raises the efficiency of energy conversion in an EMHD generator.

4 Limiting Energy Features of EMHD Generators

The most attainable energy parameters of EMHD generators are decided by evaluating their competitiveness with other types of pulsed generators. Parameters reached in experiments with linear generators are given in Table 1.

Table 1: Parameters of linear EMHD generators

Generators s	Channel's dim., cm	B_0, T	N_R, MW	Q_R, kJ	m_{HE}, g	η_Σ, %
[3]	2.5×2.5×46	1.7	2.8	0.15	7.5	0.2
[3]	2.5×10×46	2.3	2.3	0.75	15	1
[2]	15×20×100	2.8	280	36	400	1.6
EG-5 [1]	1.7×5×50	1.35	1	0.02	10	0.03
EG-6 [1]	10×10×70	2.5	100	5	100	1
[5]	∅15×80	3.5	100-200	18	100	4.3
EG-10 [1]	5×10×100	6.5	50	12	40	4.80

N_R, Q_R – pulsed power and energy in generator load, m_{HE} – mass of HE charge η_Σ – efficiency of chemical energy conversion of HE charge

At 2-3 T, maximum power and energy in the electrical load were obtained in the generator with the largest MHD channel volume [2]. Maximum energy conversion efficiency of ~5% was obtained with the highest magnetic field induction (EG-10, [1]). Double-sided expansion of one HE charge in two MHD channels was obtained in the generator [5]. This result demonstrated a potential to optimize explosive flow.

Parameters of generators with cylindrical MHD channels are given in Table 2. Both pulsed magnets (PM) and superconducting magnets (SCM) were used in these generators. As a rule, the cylindrical HE charges were initiated simultaneously on their longitudinal axes.

Table 2. Parameters of radial EMHD generators

Generators	Channel's dim		B_0, T	m_{HE}, g	I_{pl}, kA	I_{ind}, kA	Magnet	η_Σ, %
	r_0, cm	z_0, cm						
T-2 [1]	22	2	2.5	10	6	–	PM	0.8
T-4 [1]	36	10	2.2	35	17	–	PM	0.8
R-1 [1]	26	100	2.6	700	78	–	SCM	0.3
T-4* [1]	36	5.4	1.4	18	12	–	PM	2
[10]	24	6	2	10	5	0,1	PM	~0
[10]	15	33	3	420	10	4	SCM	~0
[6, 8]	15	33	3	300	100	20	SCM	~0.01
[7]	30	6,5	0,5	300	90	80	PM	0.1
[7]	15	33	3	420	200	200	SCM	0.6

I_{pl} – current in plasma (metallic) liner; I_{ind} – current induced in external inductor

The conductive method of energy extraction in the electrical load (see Fig. 1) was used in [1], the inductive method was used in papers [6-8,10]. In the first case, a higher level of energy conversion efficiency (η_Σ=1-2%) was ensured. Relatively high values of current in experiments [6-7] resulted from replacing the plasma liner with a thin metallic cylinder.

Cylindrical flow with a front velocity up to 10 km/s was created in the T-4 generator, which had a plasma liner thickness of ~2 cm and average conductivity of ~2×10^3 S/m. This has led to a relatively high-energy conversion efficiency of up to 2% under a moderate magnetic field of ~2 T. The negative role of longitudinal MHD effects was revealed in experiments with the 1 m long R-1 generator. It resulted from the difference of the magnetic field in the center of a cylindrical MHD channel (4 T) to that of its exterior channel (2 T).

A sound analysis of results on the study of energy conversion efficiency in EMHD generators shows that the linear type of these generators has been studied more carefully than the radial types (Fig. 5). Energy conversion efficiency can be carried up to 7-8% in linear generators. The $\eta_\Sigma(W_0/W_{HE})$ dependence indicates that the potential of the radial type generators has not yet been realized.

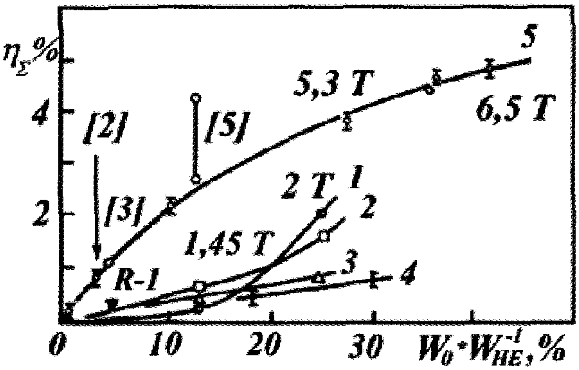

Figure 5. Efficiency of chemical energy conversion of HE charges W_{HE} in MHD generators of radial (*1-4*) and linear (*5*) types. (W_0 – magnetic energy into MHD channel).

Reference [11] has shown that parameters of EMHD generators are reproduced even if a shock wave flow is formed in the residual gas of the detonation products from the preceeding pulse.

5 Conclusion

Through experience in developing linear EMHD generators as well as creating superconducting magnets, a prospective generator scheme can be offered (Fig. 6).

There are 30 MHD channels with dimensions of 10x10x100 cm^3 and the magnetic field induction is 6.5 T. The mass of the HE charge in each channel is 100 g. The charge reloading frequency is up to 5 Hz. The outputs of the channels are attached to a pumped receiver so that a pressure of 50-100 Torr is produced at the beginning of a new pulse.

At a conversion efficiency of ~7%, ~30 kJ of energy is generated in each channel during a ~120 μs pulse. If the generator load is general, under the synchronous start of all MHD channels the peak voltage on the load will be from 1 to 30 kV and the output current will be from 12 to 0.4 MA, depending on how the channels are connected. If the channels are started consistently, 30 pulses are generated with frequencies up to 6.5×10^3 pps. Such a series of pulses may be reproduced through the HE charge reloading frequency.

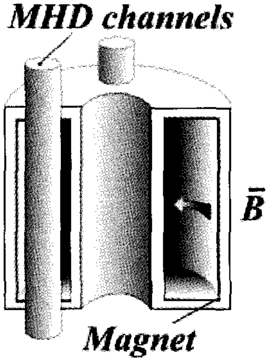

Figure 6. The scheme of a multi channel EMHD generator with a superconducting magnet

References

1. Pulse MHD conversation of chemical energy to electrical, Ed. by A. Sheindlin and V. Fortov. Moscow. Energoatomizdat, (1997).
2. Jones, M. S., Webster, P. W., Webb, F. N. et al., Large scale explosively driven MHD generator experiments, Proc. 7th Symp. on Eng. Aspects of MHD. Pittsburg, (1965) p. 965.
3. Jones, M. S., Experimental observation of peak current limit in explosive driven MHD generators, Proc. 13th Symp. on Eng. Aspects of MHD. USA Stanford University, (1973) Late paper session. p. 1.
4. Teno, I., Sonju, O. R., Development of explosively driven MHD generator for shot pulse aircraft high power, Techn. Rep. AFAPL-TR-74-48. (June 1974) p. 451.
5. Bangerter, C. D., Hopkins, B. D., Brogan, T. R., Explosively driven MHD power generation, Proc. 6th Intern. Conf. on MHD Electrical Power Generation. Washington, **4,** (June 1975) p. 155.
6. Chare, E. C., Brooks, W. R., Cowan, M., Proc. 2nd IEEE Intern. Pulsed Power Conf. Lubbock. TX. USA. (June 1979) Dig. Techn. Pap., Ed. by A. Guenther and M. Kristiansen. p. 343.
7. Cowan, M., Chare, E. C., Leisker, W. B., et al., Pulsed energy conversation with a superconducting magnet, *Cryogenics*. (December 1976) p. 699.
8. Wright, T. R., Baker, L., Cowan, M., Freeman, I. R., Magnetic flux compression by expanding plasma armatures. Proc. 2nd Intern. Conf. on Megagauss Magn. Fields Generation and Related Topics. Washington. D.C. USA., Ed. by P. Turchi. N.Y., London: Plenum Press, (1980) p. 241.
9. Gill, S. P., Directed energy power source could generate EW-Technology revolution, *Defense Electronics*. **16**, No. 4. (Apr. 1984) p. 116.
10. Jones, M. S., Bangerter, C. D., Hopkins, B. D. et al., Techn. Rep. No. 669. MHD Research Inc., (1969).
11. Kondratenko, M. M., Lebedev, E. F., Ostashev, V. E., *Simulation on frequency mode of* explosively driven MHD generator, Proc. 3rd Intern. Conf. on Megagauss Magn. Fields Generation and Related Topics. Novosibirsk. USSR., Ed. by V. Titov and G. Shvetsov. Moscow. Nauka, (1984) p. 254.

OPTIMIZING THE RANCHERO COAXIAL FLUX COMPRESSION GENERATOR

D. G. TASKER, J. H. GOFORTH, W. L. ATCHISON, C. M. FOWLER, D. H. HERRERA, J. C. KING, I. R. LINDEMUTH, E. A. LOPEZ, E. C. MARTINEZ, H. OONA, R. E. REINOVSKY, J. STOKES, L. J. TABAKA, D.T. TORRES

University of California, Los Alamos National Laboratory, Los Alamos, New Mexico, USA

P. J. MILLER

Naval Air Warfare Center, Weapons Division, China Lake, California, USA

Ranchero is an explosively driven magnetic flux-compression generator that has been developed over the last four years as a versatile power source for high energy density physics experiments. It is coaxial and comprises a 15 cm diameter armature and a 30 cm diameter stator, each made of aluminum. The length may be varied to suit the demands of each experiment. Thus far, lengths of 0.43 m and 1.4 m have been used. The armature is filled and driven by a high-performance cast explosive, and the ultimate performance of the device is limited by the smoothness of the armature expansion. The armature explosive is initiated on axis by PETN hemispheres spaced at intervals of between 18 mm and 24.5 mm. Each is simultaneously detonated by a slapper detonator system. Armature expansion calculations predicted ripples less than 0.2 mm, which was confirmed in early experiments. Yet, ripples approaching tens of millimeters were observed in some more recent experiments. We will discuss the possible origins of these large ripples and the methods we have used to correct them.

1 Introduction

The Ranchero system has been described in detail previously [1,2]. A single module with an end output configuration has been developed to provide the electrical energy to be used for imploding liner tests. The module is 0.43 m long and expands the armature by a factor of two to reach the 30 cm OD stator. The experiments are conducted in the range of 30-48 MA currents. The modules are filled with high explosive PBXN-110 charges, 43 cm long. We have performed tests and related 1-D MHD calculations at the 48 MA current level with small loads. From these results, we determine that we can deliver currents of approximately 50 MA to loads of 8 nH with the 1.4 m modules.

The Ranchero armature is a 6 mm thick aluminum cylinder with an outer diameter of 15.2 cm, and the total length can be varied from 140 to 43 cm, dependent on the electrical requirements of the load. Two slapper detonator cables, placed back-to-back, initiate detonation of the explosive charges within the armature, each with 56 discrete points (total of 112 points) placed 24.5 mm apart. Current gain in this device is limited by the residual inductance that remains after the armature has reached the stator. In a 43 cm generator with 0.5 mm insulation the residual inductance is 1.11 nH, at least 0.7 nH of which is due to insulation and diffusion. This means that, at worst, we achieve an overall gap of 0.8 mm. Clearly, this gap, and therefore the residual inductance, strongly depend on the smoothness (ripple) of the armature surface [3]. Consequently, it is important to achieve the smoothest possible outer surface.

Using a 2-D hydrodynamic code, MESA-2D, the thickness of a poly-methyl-methacrylate (PMMA) smoothing layer was adjusted to achieve the smoothest armature expansion. Ripples of less than 0.2 mm were predicted which was confirmed by experiment. However, ripples approaching tens of millimeters were observed in a significant number of experiments. Figure 1 shows a high-speed photograph of one such experiment, where ripples of ~10 mm were observed in the expanding aluminum armature.

2 Origins of Ripple

We hypothesized various possible causes of the large ripple, including the quality of the explosive; its age; the manufacture of the slapper system; the type of PETN booster; the electrical system that powers the slappers; and point failure. A database was assembled for tens of experiments to identify the possible culprit, but no clear pattern of failure was detected. The slapper system was tested repeatedly - without the surrounding PBXN-110 - with many variations in electrical drive, yet with no obvious failures, so this was quickly eliminated as a culprit.

Figure 1. Photograph of armature ripple.

3 Calculations of Armature Expansion

In the initiation system for Ranchero, a series of electrically energized Kapton flyers (slappers) are used to initiate PETN hemispheres by impact. The subsequent detonation of the hemispheres transfers shock waves into the main PBXN-110 explosive filling. One concern was that the shock waves transferred to the explosive were barely adequate to initiate prompt detonation, thereby leading to the random failure of experiments. The MESA-2D code could not model the growth of a reaction in the explosive to full-detonation [1]. Hence, we resorted to the use of the DYNA-2D code, which has a well-calibrated reaction and growth routine for PBXN-110 [4].

The problem was modeled axisymmetrically about the z-axis with a 4-point spherical initiation system. The right and left boundaries were constrained to fixed z-positions, thus representing an infinitely long system, Fig. 2. The coaxial cylinders were filled with PBXN-110 throughout. We modeled both the 24.5 mm (and its 7.0 mm PMMA smoother) and 18 mm center-to-center spacing (and 3.2 mm smoother), with the same outside radius. The questions addressed were: whether the PBXN-110 ignited promptly on the outside of the PMMA, i.e., what was the run distance to detonation; what was the ripple on outside surface of the aluminum shell at the maximum radius (compared to MESA-2D predictions). We also studied the effect of deliberately preventing a PETN sphere from igniting (i.e., turning it off), and the effect of reducing the PETN pressing density from 1650 to 1550 kg/m^3.

4 Computational Results

The results of the DYNA-2D calculations, shown in Fig. 3, confirmed the MESA-2D results, i.e., that ~0.2 mm ripples would be expected for the 18 mm spacing. Calculations of the ripple when a point was "turned-off," for the 24.5 mm spacing, were especially interesting. Here the predicted ripple was ~10 mm, in good agreement with experimental results (in the bad experiments). This confirmed that a likely cause of the bad ripple was point-failure. Neither the MESA nor DYNA-2D codes predicted that the pressing density of the PETN cups would have any effect on the initiation of the PBXN-110.

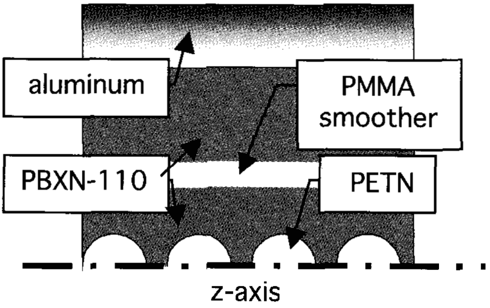

Figure 2. Initiation system schematic.

5 Explosive

We realized that one slapper design might allow the migration of the explosive ingredients to the PETN booster cups. The migration of certain materials is known to "poison" PETN, i.e., sufficiently contaminate the surface such that the PETN will not detonate. PBXN-110 is an explosive with a bimodal mixture of 88% by weight HMX (66% coarse - 279 μm mean particle size, 22% fine - 39 μm) in a 12% HTPB polyurethane binder [5]. Isodecyl pelargonate (IDP) is added to the HTPB binder to initiate its curing and has a history of migration problems. Consequently, the slapper cable was redesigned to minimize the possibility of IDP migration and tested by firing the Ranchero armature without the stator, as described in the next section.

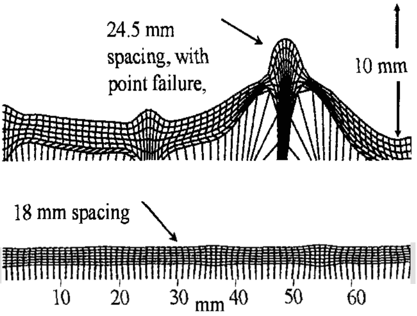

Figure 3. Calculated ripple showing single point failure (top) and optimized expansion.

6 Camera Experiments

High-speed camera experiments were performed in which two separate armatures were fired end-to-end in the same experiment, one with the standard PETN booster and one with a two-component pressing (PETN and LX-10 [6]). The observed ripple was significantly reduced in both armatures, i.e.; the results confirmed that IDP migration was responsible for the poisoning of the PETN pellets. The conventional PETN (1550 kg/m^3) pressing had ripples of ~1 mm, whereas the two-component pressing had ripples of <0.2 mm. This was clear evidence that the low density (1550 kg/m^3) PETN was not providing the necessary stimulus to promptly detonate PBXN-110. Both of the codes had failed to predict this poor initiation of the PBXN-110 by the 1550 kg/m^3 PETN.

7 Summary and Conclusions

The results of a series of experiments and computer calculations suggest that there are two independent causes of large ripple in the armature expansion. There is substantial evidence that we must design the combined slapper and explosive system to prevent IDP migration and the consequent point failures. These point failures are responsible for ripples of ~10 mm or more. There is also clear evidence that the reduction of the PETN booster density from 1650 to 1550 kg/m^3 causes a smaller ripple of ~1 mm, probably because of inadequate initiation of the PBXN-110 explosive – although the computer analyses failed to predict this. We expect to verify these findings and fixes with camera tests to be performed in the coming weeks.

Acknowledgments

LANL report LAUR-98-4566. This work was supported by the US Department of Energy.

References

1 Goforth, J. H., et al., *Ranchero: A High Current Flux Compression Generator System For Heavy Liner Experiments,* Seventh Conference on the Generation of Megagauss Magnetic Fields, 1996.

2 Goforth, J. H., et al., *The Ranchero Explosive Pulsed Power System*, Eleventh IEEE Int. Pulsed Power Conference, Baltimore, MD, (1997) p. 573.

3 Lee, E. L. and Tarver, C. M., *Phys. Fluids*, **23**, (1980) p. 2362.

4 Miller, P. J. and Sutherland, G. T., *Reaction Rate Modeling of PBXN-110,* Shock Compression of Condensed Matter – 1995, 413, Seattle, WA, Aug 1995. *AIP Conference Procs.* p. 370.

5 Lemar, E. R., Forbes, J. W., and Sutherland, G. T, *Detonation Wave Velocity and Curvature of IRX-4 and PBXN-110,* Shock Compression of Condensed Matter – 1995, p. 791, *ibid.*

6 LX-10: HMX, Viton A (95:5 by weight)

ENERGY CONVERSION EFFICIENCY OF MCG-BASED LIGHTNING SIMULATORS

E. V. CHERNYKH, V. E. FORTOV, K. V. GORBACHEV, I. P. KUJEKIN, E. V. NESTEROV, V. A. STROGANOV
High Energy Density Research Center, Russian Academy of Sciences, Moscow, Russia

YU. A. KARPOUSHIN, A. V. SHOURUPOV
Shatura Department of HTI, RAS, Moscow, Russia

The problem of HE mass gain minimization is extremely important due to environmental and safety considerations of MCG application to mobile simulators of lightning current (MSLC). There are several methods of increasing the efficiency of MSLC with an electrical explosive opening switch (EEOS) in the circuit of the secondary winding of a conventional transformer (CT) with inductance L_2. One may use the battery of fast-run MCGs of a small diameter, or increase both the magnitude of L_2 and the energy of power supply bank of capacitors, or use larger diameter wires with solid insulation. Results of experiments using spiral-coaxial MCG, 36 mm in diameter, have produced an acceptable efficiency of 12%. When the wires were insulated with polyethylene, energy absorption was high. Analysis of alternatives to open switches (OS) in the MCG circuit has shown their competitiveness. They allow reduction of the optimum L_2 magnitude, use of a modular device design, and shaping of the waveform and of the lightning current pulse duration during its droop by introducing one additional MCG module into the circuit.

1 Introduction

Special attention is paid to trials of lightning protection systems used for objects equipped with interlinked computer networks and electronic devices under actual operating conditions, when the full complex behavior of functional links and ultimate parameters of electromagnetic test pulses is occurring. Reported herein are results of efforts to create an electrophysical basis of mobile simulators of lightning current (MSLC) design based on MCG.

When MCGs are used, one must consider environmental and operational safety of the trials. From our point of view, the commercial application of MSLCs based on MCGs is possible only when MCG is tightly encapsulated inside a protective compression chamber. This is why effective conversion of HE chemical energy in electromagnetic energy delivered to the MSLC load is of the highest importance.

2 Canonical Scheme of MSLC

The most complicated problem is to secure the desired duration of current decay down to half of the peak value. For known MSLC [1] with the canonical scheme (MCG, CT and EEOS in a circuit of CT secondary winding), this problem was solved by introducing an additional inductor into the circuit with inductance L_s. As a result, for commercial MCG C-160, the efficiency of HE chemical energy in electromagnetic energy delivered to the load conversion was less than 1%. MCG underwent irregular working conditions, drawing less current than its share of the load when a rather small energy gain factor (from MCG circuit to a load) $k_t = 0.09$ occurred due to the large ratio $L_s/L_2 = 3.6$.

Considering the outcomes of the MSLC optimization trials conducted, we can suggest the following measures to increase efficiency of the canonical scheme:

1. Replace a single, powerful universal MCG C-160 (diameter of a spiral of 160 mm, HE mass 10 kg) with a battery of transformer MCGs of a smaller diameter having approximately the same efficiency [2].
2. As one cannot simultaneously satisfy conditions for both peak efficiency and large energy gain factors w_a for MCG, it is necessary to reduce the energy produced by MCG to the energy accumulated in capacitive storage for initial MCG supply ratio.
3. One can ensure that k_t be 30-40% by redistribution of L_s and L_2 values to obtain acceptable magnitudes for both L_2 and the voltage applied to the secondary winding.
4. To alleviate the overvoltage of secondary CT windings, one must connect them in series.

Based on our calculations, the MCG with a spiral-coaxial solenoid of diameter 36 mm (C-36) and a two-fold extended armature tube was chosen as a highly effective amplifier-generator. The spiral of the generator consists of separate sections. The generator can be conditionally divided into an amplifying stage (3 sections having identical lengths of lc = 40 mm with spiral pitches of 5, 10, 20 mm), and a generating stage (2 spiral sections 40 mm long each with pitches of 40 and 80 mm and a cylindrical coaxial, 80 mm long). The first section was wound using a wire with 2.4 mm in overall diameter (including insulation) in two starts. As a result of the conducted experiments, a peak current of 2.5-3.1 MA through the CT primary winding with L_1 = 8-10 nH and resistance r_1 = 0.3 mOhm was measured. With a supplied initial energy of 1.5 kJ, the magnetic energy gain factor was w_a = 17. With an energy of 70 grams of HE filled into an armature tube, the magnetic energy conversion efficiency was 7%, while the overall efficiency allowing for heat released in the load was 12%. One important outcome of these experiments is that the transformer was not destroyed by detonation products and could be reused.

A high-energy absorber is necessary for MSLC, as OS should dissipate large amounts of energy. The most productive absorber is a dense medium in which the wires are placed. To ensure similar conditions across electrical explosions when researching braking properties of EEOS, a secondary battery circuit for the transformer generators (C-36) was used in the LCR-circuit. A basic criterion for simulation [3] is "the reduced velocity of wires heating" j^2d (j = current density, d = wire diameter). Fig. 1 shows the relative EEOS resistance R/R_0 as a function of specific energy input w into the conductor. The wire with a solid sheath has greater ability to absorb energy at a moderate increment of resistance and maximum relative resistance growth compared with an electrical explosion in air.

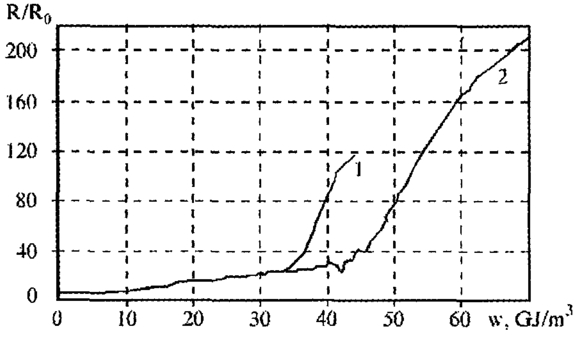

Figure 1. The relative wire resistance growth during electrical explosion as a function of specific energy input per unit of volume. $j^2d = 5*10\ 9\ A^2m^3$, charging voltage U_0=15 kV of the capacitor C_0 = 25 mF, inductance L_0 = 15 mH, d = 0.21 mm. 1-wires in Polythene, 2- wire with a free surface.

3 Alternate MSLC Schemes

When OS is introduced into MCG circuit, a time constant of current droop in a load with resistance r_l and inductance L_l is $\tau = [(L_l+L_2)/r_l+L1/R]$. For canonical scheme $\tau = [L_l+L_2(1-k_c^2)]/r_l$, which results in both reducing the optimum L_2 value and further raising k_r, since the reverse energy transfer to the MCG circuit is prevented when connecting a high-impedance load. The given circuit with modules connected in series specifies higher requirements for stability and reproducibility of output parameters of MCG, because of the possible discrepancy in EEOS operation for each module. The calculations done for various values of MCG efficiency in every module indicate that the change in peak values of the current pulse is insignificant, while the spread in MCG efficiency mainly influences the speed of current growth. Evidently, the scatter in MCG efficiency for the given circuit must be restricted by 15-20% compared to 8-10 kJ/ton for capacitor banks.

Performance of explosive current breakers (EOS) is indifferent to the discrepancy in MCG efficiency. This gives preference to their application in MSLC modules operating in parallel. The mass energy density of MSLCs based on MCG is evaluated as 140 kJ/ton.

The MSLC circuit for rL-loads, where the current breaker is introduced into the MCG circuit, gives an opportunity to detach the processes of formation of both leading and trailing edges of simulated lightening current pulse one from another. For this purpose, every module of the battery is proposed to consist of two MCGs: a fast-run generator and a generator with operation time close to the given duration of current drop through the load. Each MCG is powered by its own capacitor bank, charged by a voltage of differing polarity. According to the circuit in Fig. 2, the current breaker OSW ensures both, shaping the leading edge and connecting MCG-2.

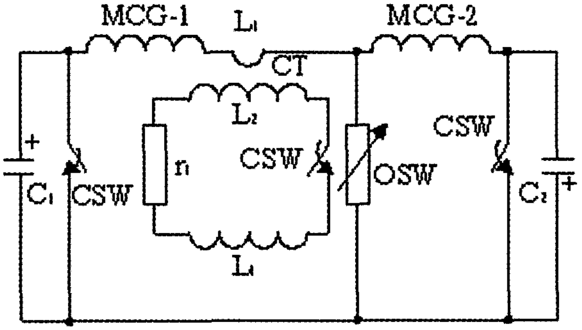

Figure 2. The equivalent electrical circuit of MSLC with an active shaping of load current droop.

Concerning the shape of the current droop, for hyperbolic output inductance behavior of L_g (t) of MCG-2, the current increases linearly, and the current through the load is constant and equal to the peak current during the MCG operation. Variations are possible if one uses exponential laws for L_g (t). Initially, the current decay is explained by the fact that as the rate of energy dissipation in the load decreases, the current gain factor for such MCG increases.

4 Conclusion

Accumulated experience in MCG studies and the method of matching them to high-impedance loads with the help of MSLC created on this basis, allows us to experiment on objects under conditions inaccessible to any other pulsed sources, and to do this with high commercial efficiency.

Acknowledgment

This work is supported by the Russian Foundation for Fundamental Research.

References

1. Boriskin, A. S., Gusev, N. I., Kravchenko, A. S., et al., Transportable MCG-based lighting simulators. *Megagauss Magnetic Field Generation and Pulsed Power Applications. MG-YI.* (1994) p. 923.
2. Pavlovskii, A. I., et al., MCG parameters and means to improve them. *Megagauss Physics and Technology.* (Plenum Press, N.Y.) (1980) p. 557.
3. Azarkevitch, E. I., Kotov, Yu. A., Design of electroexplosive stage of a two-staged current breaker. Book of abstracts of joined meeting of sections of scientific councils of AS USSR. *Tomsk,* (1986) p. 111.

STABILITY OF MAGNETICALLY IMPLODED LINERS FOR HIGH ENERGY DENSITY EXPERIMENTS

R. REINOVSKY, W. ANDERSON, W. ATCHISON,
R. BARTSCH, D. CLARK, C. EKDAHL, R. FAEHL,
J. GOFORTH, R. KEINIGS, I. LINDEMUTH, D. MORGAN,
G. RODRIGUEZ, J. SHLACHTER, D. TASKER
Los Alamos National Laboratory, Los Alamos, NM, USA

Magnetically imploded cylindrical metal shells (z-pinch liners) are attractive drivers for a wide variety of hydrodynamics and material-properties experiments. The ultimate utility of liners requires the acceleration of near-solid density shells to velocities exceeding 20 km/sec while retaining good azimuthal symmetry and axial uniformity. Two pulsed power systems (Ranchero and Atlas), currently operational or under development at Los Alamos, provide electrical energy adequate to accelerate ~50 g liners to 1- 2 MJ/cm kinetic energy. As in all z-pinches, the outer surface of a magnetically imploded liner is unstable to magnetohydrodynamic Rayleigh-Taylor (MHD-RT) modes during acceleration. Therefore, initially small imperfections can grow large-scale distortion making liners unusable for many experiments. On the other hand, material strength in the liner should, from first principles, reduce the growth rate of RT modes, and strength can render some combinations of wavelength and amplitude analytically stable. The growth of instabilities in both soft aluminum liners and in high strength aluminum alloy liners has been studied analytically, computationally, and experimentally at liner kinetic energies up to 100 KJ/cm on the Pegasus capacitor bank using driving currents up to 12 MA.

1 Introduction

Perhaps the most challenging application of high velocity imploding liners is the delivery of strong shocks (up to 100 Mbar) to a central target. Such applications require both high velocity (>20 km/sec) and large kinetic energies (1-50 MJ/cm). Furthermore, such applications require that the liner arrive at the central target at near solid density, retaining good azimuthal symmetry and axial uniformity. Previously, [1] the authors have discussed some of the aspects of accelerating liners to appropriate conditions, concluding that while overall dynamics are tractable, and appropriate power systems have been demonstrated, *it is the behavior of the liners under extreme acceleration that may ultimately limit their* usefulness. During the compression of such a cylindrical liner, a variety of dynamic processes can result in distortion. The inner free surface of the liner can wrinkle as a result of the compressive motion - a phenomenon known as Bell-Plesset effect [2]. Interactions between the liner and the electrodes (glide-planes) can initiate perturbations that propagate into the central region of the liner at (or above) the speed of sound. Perhaps most significantly, the outer surface of the liner (the interface between the liner and the driving magnetic field) is magnetohydrodynamically unstable in the same way that an interface between fluids of differing density is subject to unstable growth of a small perturbation.

2 Material Strength in Solid Liners

While the growth of the MHD-RT instability in a plasma shell or column has been explored extensively and is generally understood, the detailed behavior of a solid or near-solid liner is relatively unexplored. The behavior of a solid liner is complicated because, unlike a plasma column, the solid liner initially retains material strength. Analytically, material strength, like surface tension, reduces the growth rate of perturbations. For sufficiently short wavelengths, the growth rate is zero for a given acceleration, resulting in a "stable" implosion. The material parameters of yield strength (Y_0) and sheer modulus (G) characterize the effects of material strength; it is convenient to compare both with the magnetic drive pressure. For cases where the drive pressure exceeds both yield strength and sheer modulus for most of the implosion, material strength effects are likely to be insignificant. For practical cases, as the case of a high purity aluminum liner approximately 1mm thick imploded with 5-30 MA currents, the drive pressure is larger than Y_0 and smaller than G for most of a 10 μs implosion.

The situation is further complicated in two respects. First, ohmic heating from the multi-megampere drive current (up to 100 MA in [1]) raises the temperature of the liner, reducing its strength. In the extreme, ohmic heating can melt the liner, resulting in virtually complete loss of material strength. Second, in a cylindrical liner, the drive current flows initially on the outer (unstable) surface of the liner and diffuses toward the inner surface, resulting in non-uniform heating through the thickness of the liner. Non-uniform heating results in spatial variations in strength through the thickness of the liner. In general, the strongly accelerated, magnetically imploded solid density liner is a complicated situation.

Conceptually, we can investigate the stability of a magnetically imploded liner by considering several cases. In the first case, the drive is modest and the current does not significantly heat the liner. The liner does not melt and retains much of its ambient strength for all times of interest. In the second case, the drive is increased so that the outer surface of the liner melts early in the implosion process. With melting, the liner conductivity decreases significantly, allowing the current to diffuse rapidly into the bulk of the liner. Thus, for much of the implosion, the liner consists of an unmelted, inner layer that retains material strength and a melted, weak, outer layer. Furthermore, the proportion of solid-to-liquid material is constantly changing. The limit of the second case is where the driving current density is sufficiently high that the entire thickness of the liner melts at some point during the implosion. After melting, the classic fluid instability analysis provides a good description of the liner's behavior. The third case is intermediate between the first two. In the third case, the melting of the outer layer is delayed so that a significant fraction thickness of the liner is unmelted and displaying material strength during much of the implosion. However, the effect of strength is steadily decreasing as more of the liner heats and the entire liner melts before the end of the event

3 Experimental Observations

To compare the three cases, a series of experiments was conducted using a high purity aluminum liner with an axial height of 20 mm and inner radius of 24 to 25 mm. The liner was imploded with currents ranging from 4-12 MA delivered by an 860 μF laboratory capacitor bank with a short-circuit quarter period of about 8 μs. In each case, multi-view radiographs taken transverse to the cylindrical axis are the primary diagnostic. For some experiments, exterior, transverse visible light imaging, magnetic probe and impact probe measurements inside the liner augmented the radiographs. On a few experiments, VISAR measurements of the inner surface velocity were taken.

For the first case, the liner initial wall thickness is 0.4 mm and the peak drive current is 4.2 MA. The implosion time is about 16 μs. Figure 1 shows a series of radiographs taken from two consecutive experiments. The liner implodes smoothly with little evidence of perturbation growth on the outer surface. The inner surface of the liner reaches 3-4 km/sec and one-dimensional MHD calculations show the liner to be largely unmelted through the entire implosion.

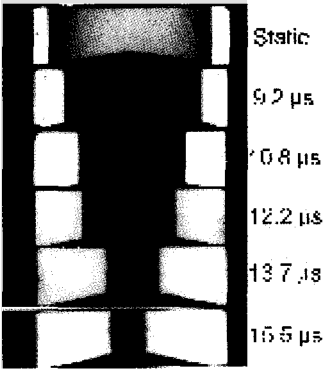

Figure 1. Drive Current 4.2 MA

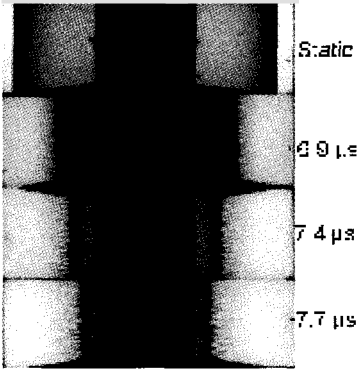

Figure 2. Drive Current 12 MA

For the second case, the liner wall thickness was increased to 1.15 mm and the peak drive current increased to 12 MA. The implosion took just over 8 µs. Figure 2 shows a sequence of radiographs timed to capture the last microsecond of the implosion. One-dimensional MHD calculations show that the outer surface of the liner melts at about 4 µs. By the time the last radiograph was taken (7.7 µs) the outer 45% of the liner material had melted. Because of convergence effects, the melted material formed a layer about 1.3 mm thick. The radiographs show that after the outer surface melts, small wavelength perturbations with 0.5 to 1.0 mm wavelength appear and grow to amplitude of 1-2 mm. The perturbations appear to be limited to the outer (melted) part of the liner and do not appear to distort the solid, inner part.

For the third case, a 0.4 mm liner was imploded with an intermediate value drive current of 6.4 MA. The implosion time was just over 10 µs. The peak acceleration was about 10^9 m/s^2 and the peak drive pressure was just over 10 GPa. One-dimensional MHD calculations show that the outer surface of the liner melts at just under 6.0 µs and the inner surface melts just after 7.5 µs. The overall character of the liner in this case is intermediate between the behaviors shown in Figs. 1 and 2.

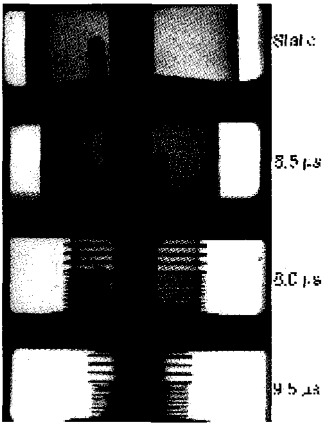

Figure 3. Drive Current 6.4 MA

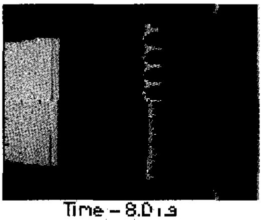

Time - 8.0 µs

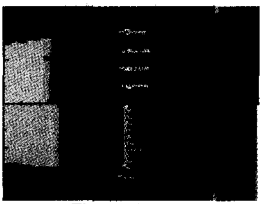

Time = 8.6 µs

Figure 4. 2-D MHD calculations

The parameters for this third case are chosen such that the liner remains unmelted for much of the implosion and then melts throughout its thickness in a relatively short time. This may be the most challenging set of parameters to simulate. Experiments were conducted in which a set of small amplitude perturbations was machined into the outer surface of the liner and the growth of those perturbations was monitored radiographically. For the radiographs shown in Fig. 3, the initial perturbation was 50 μm in peak-to-peak amplitude with wavelengths of 0.75 mm and 2.0 mm. The radiographs show the perturbation during the linear growth phase (when the perturbation retains its sinusoidal shape), the non-linear spike-and-bubble phase, and when the perturbation has grown to such amplitude that the magnetic field is breaking through and completely disrupting the liner. The growth of the perturbation was simulated with a 2-D Eulerian MHD code using analytic fits to material strength properties [3]. The results are shown in Fig. 4.

Several analytic treatments of perturbation growth have been published. Recently, Rayevski [4] has offered an analytic formulation that predicts threshold acceleration for unstable growth as a function of initial amplitude and wavelength. Since the acceleration of the interface changes as a function of time, a time-dependent threshold amplitude can be calculated for each initial perturbation wavelength. In Fig. 5 we have plotted (1) the time-dependent amplitude of the (growing) perturbation from a 2-D MHD calculation, (2) the amplitude measured from radiographs at two times, and (3) the time (acceleration) dependent amplitude threshold for perturbation growth predicted by the analytic elastic-plastic stability model. The figure shows that the radiographically measured perturbation amplitudes are in good agreement with those predicted in the calculation. Furthermore, when the perturbation amplitude is below the threshold, as is the case for several microseconds after the beginning of the current pulse, the perturbation does not grow. As the critical amplitude threshold drops below the initially imposed value (as the acceleration increases), the perturbation begins to grow. The figure also shows the time of outer-surface melt and inner-surface melt. When the entire liner is melted, the perturbation appears to grow as predicted by fluid models.

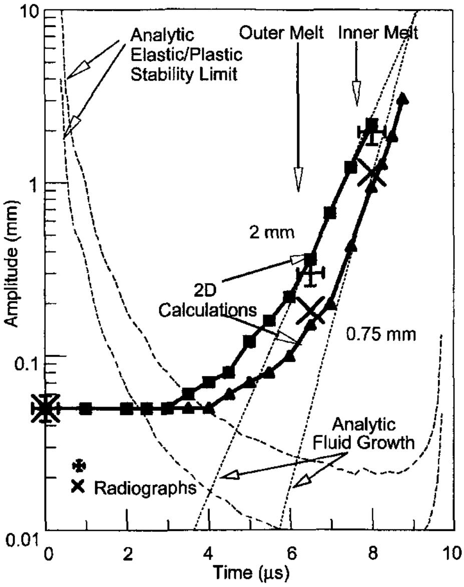

Figure 5. Intermediate Drive

4 Liner Fabrication Criteria

The concept of a threshold amplitude/wavelength for given material properties and acceleration provides a specification to which a liner must be fabricated to implode successfully. Several kinds of departures from perfectly cylindrical liners can occur in the fabrication process. The short wavelength, small amplitude variations resulting from tooling on the inner and outer surfaces (surface finish) can be reduced to a fraction of a micro-inch (<0.02 μm) by using costly, high-precision processes including single crystal diamond tooling and air-bearing machines. If acceptable, however, conventional processes are much more economical. The larger amplitude, long wavelength variation in overall wall thickness, "waviness", is governed more by machine tolerances than by tooling processes. In Fig. 6, we plot the threshold for perturbation growth in amplitude/wavelength space for one material (high conductivity aluminum), for several values of acceleration typical of the peak and average accelerations observed on "low voltage" (LV) Pegasus experiments, and projected for the future Atlas experiments at higher acceleration. The figure shows that for higher accelerations the area of perturbation space where stable operation can be expected is reduced. More significantly, the plot shows that for accelerations considered, the short wavelength, small amplitude perturbations characteristic of surface finish are likely not to be a limiting criteria as long as the outer surface retains material strength. On the other hand, the long wavelength "waviness" may lead to significant perturbation growth and the material strength of 1100 aluminum will not be adequate to stabilize this effect.

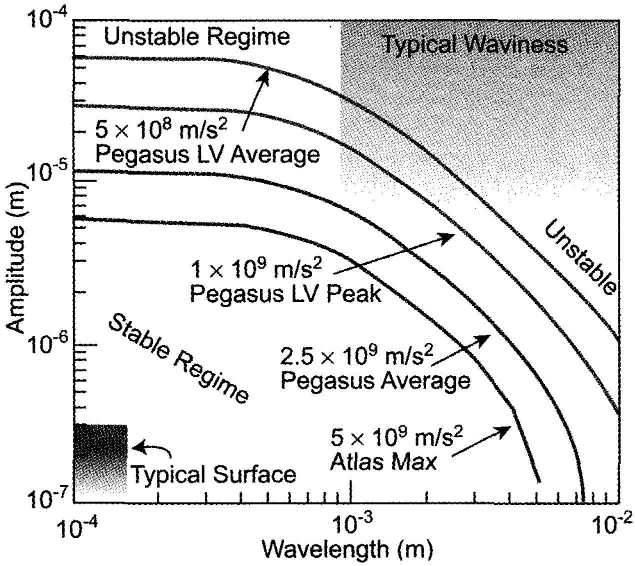

Figure 6. Stability Boundaries

One experiment was conducted to directly compare two surface finishes – one made by very high quality diamond tooling, and one using conventional technique. (~1 μm rms). Imploded by an almost 8 MA driving current, the outer surface of the liner was calculated to melt at 7 μs. The first radiograph, about two microseconds later, showed little evidence of perturbation growth for either the fine or coarse surface finish. This result is consistent with the predictions in Fig. 6. After melting, the short wavelengths begin to grow with a rate characteristic of their wavelength, ultimately becoming discernable at 9.6 μs. By

10.8 μs the substantially larger initial amplitude of the coarse surface manifested itself in substantially larger perturbations late in the implosion.

5 Conclusion

The behavior of an unmelted, solid density liner may be significantly influenced by material strength. Simulations track unstable behavior through a broad range of linear and non-linear amplitudes. Experimental measurements compare favorably with both simulations and analytic formulations for perturbation growth.

References

1. Reinovsky, R., Ekdahl, C., Development of Imploding Liners with Kinetic Energies Above 100 MJ, *Proceedings, Megagauss VIII,* Sarov, Russian Republic, VNIIEF (1998).
2. Plesset, M. S., On the Stability of Fluid Flows with Spherical Symmetry, *J. Appl. Phys.,* **25** (1954) pp. 96-98.
3. Steinberg, D. J., Cochran, S. G., Guinan, M. W., A Constitutive Model for Metals Applicable at High Strain Rate, *J. Appl. Phys.* **51** (1980).
4. Rayevsky, V., et al., Hydrodynamic Instability in Strong Media, VNIIEF, (Published by Univ. of California UCRL-CR-126710, 1997).

INSTABILITY GROWTH OF MAGNETICALLY IMPLODED CYLINDRICAL ALUMINUM AND HIGH-STRENGTH ALUMINUM ALLOY LINERS

A. M. BUYKO, O. M. BURENKOV, S. F. GARANIN, YU. N. GORBACHEV,
B. E. GRINEVICH, V. V. ZMUSHKO, G. G. IVANOVA, A. I. KUZYAYEV,
V. N. MOKHOV, P. N. NIZOVTSEV, A. A. PETRUKHIN, A. I. PISHCHUROV,
V. P. SOLOVYEV, V. N. SOFRONOV, V .K. CHERNYSHEV, V .B. YAKUBOV
Russian Federal Nuclear Center - All-Russian Scientific Research Institute of Experimental Physics, Sarov, Russia

B. G. ANDERSON, W. E. ANDERSON, W. L. ATCHISON, R. R. BARTSCH,
W. BROSTIE, J. COCHRANE, C. A. EKDAHL, R. FAEHL, I. R. LINDEMUTH,
D. V. MORGAN, H. OONA, R. E. REINOVSKY, J. STOKES, L. C. TABAKA,
S. M. YOUNGER
Los Alamos National Laboratory, Los Alamos, New Mexico, USA

Experimental data which considerably complements earlier results [1] is given for the initial perturbation growth of liners made of high-purity soft aluminum (A995, 99.995% Al) and high-strength aluminum alloys with major magnesium (AMg6) or zinc (B95) additives. Preliminary data analysis and comparison with VNIIEF and LANL numerical simulation allows us to revise parameter estimations of dynamic strength and conductivity of the materials used for designing magnetically driven liners.

1 Introduction

Perturbation growth of magnetically driven liners, which depends on liner strength and conductivity, can be a limiting factor for liner utility [1,2]. Therefore, the joint Pegasus-2 capacitor bank experiments RUS1 and RUS2 compared the initial perturbation growth of liners fabricated from materials of considerably different quasi-static yield strengths and specific electric resistance: $Y_{0.2} \approx (0.15\text{-}1.5\text{-}6)$ kbar and $\eta_0 \approx (2.65\text{-}7.1\text{-}4.2)$ μΩcm for A995-AMg6-B95, respectively. Similar LS series experiments [1] studied type Al1100 aluminum liners in which $Y_{0.2} \approx 0.3$ kbar and $\eta_0 \approx 2.92$ μΩcm.

2 Setting Up the Experiments and Experimental Data

The experimental cylindrical liners had identical radii of 24 mm, height of 20 mm and average thickness of 0.5 mm. In the RUS1 experiment the liner was fabricated from aluminum A995 and alloy AMg6 with welding in the plane of symmetry. Axially symmetric sinusoidal type perturbations of $\lambda_0 = 2$ mm wavelength and $A_0 \approx 2$ μm amplitude (from "hump" to "hollow") were applied to the outer surface of either liner material. In the experiment RUS2 the liner was fabricated from alloy B95 and had similar initial perturbations ($A_0 \approx 9$ μm) only on one half of its height. Due to turning, the liner also had perturbations whose characteristic λ_1 and A_1 was less by an order of magnitude (roughness). The liners were driven by ~ 6.5 MA currents with ~ 7 μs rise time.

Major diagnostics used were liner photography and radiography (LANL); systems of inductive, optical (LANL, VNIIEF) and electro-contact (VNIIEF) probes under the liners, i.e. on the end walls and in central measurement units (CMU) of 13 mm (RUS1) and 5 mm (RUS2) radii. Data on liner surface light emission was obtained, magnetic field penetration under the liners was measured, and the RUS1 experiment measured the longitudinal and angular time difference of the liner impact on CMU.

The data was analyzed in detail, including "density reconstruction" by radiograms and comparison with 1-D and 2-D computations, allowing us to provide a non-contradictory experimental pattern of liner behavior approximating the main computations. In particular, angular asymmetry of the weld light emission was observed in the liner, testifying some angular asymmetry of the current driving the liner (RUS1). The time differences (more than 40 ns) of actuation of the electrocontact probes nearest in CMU height ($\Delta Z = 1$ mm) located under the "hollows" and "humps" of the A995 liner initial perturbations are close to that predicted by 2-D computations (more than 30 ns). Comparison of currents under the liners with computed currents (Fig. 1) would allow us to computationally describe liner conductivity more adequately [2].

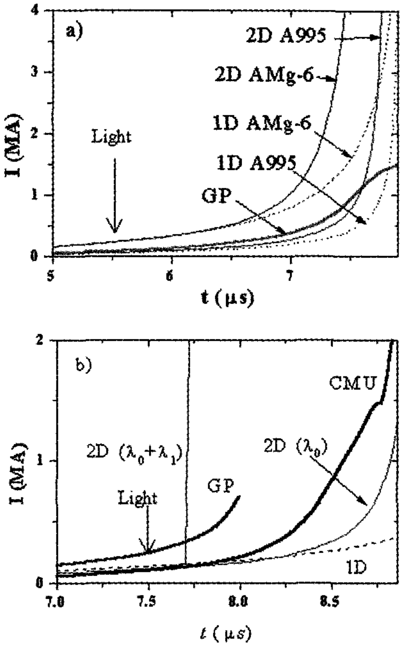

Figure 1. Currents under the liners on end walls (GP) and at central measurement unit (CMU) from experiments RUS-1 (a) and RUS-2 (b) compared with 1-D and 2-D MHD computations [2]. The vertical arrows point the start of the intensive light emission under the liners.

The X-ray images (Fig. 2) provide detailed information about the liner motion and perturbation growth. The A995 liner radiogram at time 7.26 μs provides a perturbation amplitude estimate of A ~ 0.9 mm. On the A995 liner radiograms at time 7.71 μs, and on those of the AMg6 liner at time 7.26 μs (RUS1), very thin solid state areas are still observed on one of the antipodal liner areas because of angular asymmetry. The perturbation amplitude can be estimated as A ~ 1.7 mm, while on the other there are already no similar liner areas. The instability "bubbles" have already broken through the liners, however, traces of the perturbation amplitude which was close to 1.7 mm can be seen, which results in the estimate: $A_{max} \approx 1.7$ mm. The B95 liner radiograms at 7.24 μs and 7.63 μs (RUS2) provide very rough perturbation amplitude estimates (~ 0.3 mm and ~ 0.7 mm) because of severely developed small-scale perturbations of ~ 0.2 mm wavelength, probably due to the liner turning.

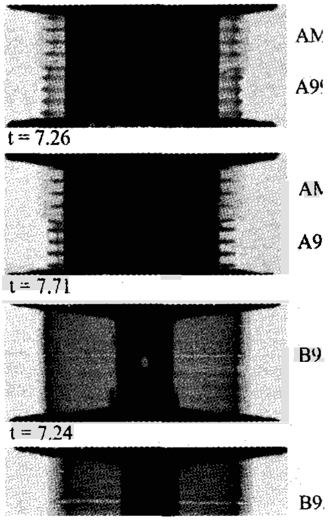

Figure 2. X-ray images of the liners in experiments RUS-1 (a) and RUS-2 (b). Time is in microseconds.

The experimental behavior of the A995 liner resembles that of the Al1100 liners in similar LS experiments [1] and was predicted by LANL and VNIIEF computations with the Steinberg elastic-plastic model for Al1100. The experimental growth of the AMg6 liner perturbation amplitude was predicted by the VNIIEF computations with elastic-plastic model [2]. The LANL AMg6 and B95 alloys liner computations with the Steinberg elastic-plastic models can provide computational data close to experimental data, if yield strengths in the models and specific resistances of the liquid phase are reduced. In similar VNIIEF computations it is sufficient to reduce the yield strengths of the alloys [2]. The computations corresponding to the experimental data in liner perturbation growth achieve about identical maximum yield strength of ~ 2 kbar in all the three materials studied [2]. In most computations there are no dense "clouds" which were pronouncedly observed under the AMg6 and B95 liners. Estimations by "density reconstructions" from the first radiograms give cloud densities ranging from ~ 0.3-0.8 g/cm^3 and maximum liner density ~ 1.8 g/cm^3. The origin of the clouds may be related to the turbulent conditions of the magnetically driven liner instability evolution; other mechanisms are also possible [2].

3 Conclusion

New experimental data for aluminum and aluminum alloys is obtained. In particular, it was shown that quasi-static yield strengths of the materials studied were not responsible for their dynamic strength. Some of the aluminum alloy dynamic strength and conductivity models used require considerable improvement. This type of experiment can constitute a new method for estimating material dynamic strength and conductivity.

References

1. Reinovsky, R. E., Stability of magnetically imploded liners for high energy density experiments. Presentation at this Conference.
2. Buyko, A. M., Garanin, S. F., Zmushko, V. V., et al., 2-D computations of magnetically driven cylindrical aluminum and aluminum alloy liner instability. Presentation at this Conference.

STUDIES OF SOLID LINER INSTABILITY DURING MAGNETIC IMPLOSION

W. ATCHISON, R. FAEHL, R. REINOVSKY
Los Alamos National Laboratory, Los Alamos, NM, USA

A variety of potential applications exist for solid cylindrical liners driven by high-energy pulsed-power systems. These applications include studies of shock formation and propagation, equation of state, constituitive properties of materials under megabar pressures and high strain rates, and the production of megagauss magnetic fields through flux compression. These applications require well-characterized, reproducible behavior of the liners under strong acceleration by the **J** x **B** forces. We have conducted a series of experiments in which sinusoidal perturbations were machined on the outside edge of thick (400-600 μm) aluminum (Al-1100 alloy) liners. Our experiments have conclusively demonstrated that the initial perturbation wavelength remains the dominant scale length, even for amplitudes that are a factor of 5-10 greater than the initial liner thickness. Scale length mixing or evolution seems absent from liners in which strength is still present.

1 Introduction

One major concern in solid liner driven experiments is the unstable growth of perturbations arising from the fabrication process or liner/electrodes interactions. Often an analogy is drawn to fluid behavior with use of the term Magneto Rayleigh-Taylor instability [1,2]. In these experiments, magnetic field still provides the driving force to accelerate the liner but the liner, itself, is not a fluid until late in the experiment. Thus, the liners retain strength in an elastic-plastic state during much of the implosion. In our experiments sinusoidal perturbations were machined into the outer surface of the liner to seed unstable behavior. We observed instability growth and found good agreement between the data and 2-D MHD calculations. The growth and nonlinear phases exhibit slightly different dynamics than classical Rayleigh-Taylor instability. The late phase seems unique, evolving into coherent, disk-like structures at the same scale-length as the initial perturbations. Even as the drive parameters are increased, the presence of a single dominant scale length is observed. This allows us to track the development of the perturbations well into the late non-linear stages.

Solid liner instability has been addressed experimentally [3,4] and theoretically [5,6,7]. Earlier experiments conducted by Barnes, et al. [3,4] were generically similar to the present ones, except that explosives provided the acceleration. The expected growth behavior was observed but so were wavelength and amplitude dependent thresholds. These thresholds were correlated with simple theories that included both yield strength and shear modulus. More sophisticated analysis of solid liner acceleration instabilities by Robinson and Swegle [7,8] provided a more detailed treatment of the processes but did not generate any new data. Further analysis by Bakhrak, et al. [9] attempted to provide an analytic technique to estimate growth thresholds based on material parameters.

2 Data/Simulation Comparisons

We present here the comparison between numerical simulations with series of pulsed power experiments designed to investigate the quantitative evolution of unstable solid liners. Our emphasis has been on the effects of strength and field diffusion. Two key diagnostics were examined. The first was high quality radiography that enabled us to see the onset and amplitude growth of the initial perturbations. The high quality of these radiograms has permitted quantitative analysis of the liner shape and detailed correlation with 2-D MHD simulations. The second was a series of field probes on axis, allowing us to measure the diffusion of magnetic field through the liner.

The experiments were performed on the PEGASUS-II capacitor bank. For this series of experiments, a wide variety of liners and drive conditions were used. The basic liner was soft aluminum 400 μm thick with an inner radius of 2.5 cm. Variants of this liner were used to explore the effects of strength and resistivity. The electrodes were made of copper and had a slope of 8°. An aluminum rod with a 1.0 cm OD was placed on the axis, connecting the two electrodes to permit the measurement of field diffusion and eventual rupture and release of flux to the inside region. A B-dot probe was inserted into the region outside the center conductor, but inside the liner, to measure this signature.

The outer surface of the liner was divided at the mid-plane. Each half had along the z-axis a different machined surface and, in one instance, two different materials were welded together. These liners were imploded radially with a nearly sinusoidal drive current whose period was approximately 8 μsec.

Table 1. Liner Stability to Date

	Peak			Side 1		Side 2	
Liner	Current	Strength	Resist.	Amp	λ(mm)	Amp	λ(mm)
LS - 4	4.6	Soft	Low	-	-	50.0 μ	2.0
LS - 5	6.3	Soft	Low	25.0 μ	2.0	25.0 μ	.75
LS - 6	6.3	Soft	Low	12.5 μ	2.0	12.5 μ	.50
LS – 7*	10.1	Soft	Low	-	-	-	-
LS - 8*	10.1	Soft	Low	10.0 μ	6.0	10.0 μ	1.2
R – 1'	6.5	H/S	M/L	12.5 μ	2.0	12.5 μ	2.0
R – 2'	6.6	Hard	High	4.0 μ	2.0	-	-

(*) - $R_o = 3.5$ cm thick = 0.6 mm (·) - $R_o = 2.5$ cm thick = 0.5 mm

Each experiment used three pulsed sources, which were placed at different azimuths around the liner chamber and fired at three different times. The resulting radiograms were processed to provide the amplitude of the perturbation at specific times for comparison with the 2-D MHD numerical simulations. The data and calculations were compared to threshold estimates based on a formulation developed by Rayevsky [8].

The radiographs show the mass distribution but do not provide adequate information about the electrical condition of the liner. To infer such information, we placed a B-dot probe inside the liner but external to the CMU. The onset of magnetic field into this interior region provides a clear signature of the electrical "rupture" of the liner. The measured B-dot signals showed several phases. The first was a low-level slow rise we associated with simple diffusion through solid material. The next stage was a slight increase in slope associated with melting and gradual increase in resistivity through heating, followed finally by the abrupt release of the magnetic field in the interior region, interpreted as physical rupture of the liner. The data also suggest that no more than 40-50% of the field penetrates into the inner region. The bulk of the current is still carried by the liner material even though much of the current path is relatively tenuous, hot plasma. The calculated results depend on accurate knowledge of the resistivity of the aluminum as it transitions from solid to liquid to plasma. The poor agreement between the data and calculations during the rupture process indicates that our knowledge of resistivities is incomplete in the region of moderate temperatures near solid/liquid and liquid vapor phase changes as well as in the strongly coupled plasma regime.

3 Conclusions

There are several significant conclusions that can be drawn from the series of experiments LS-4, LS-5, and LS-6 performed on the PEGASUS II capacitor bank. First, we found that longer wavelengths begin to grow sooner. However, the shorter wavelengths may grow faster once growth begins. Several competing mechanisms appear to be present. There is strong computational evidence that heterogeneous resistivity profiles, caused by additional heating due to non-uniform diffusion, enhances melt preferentially in the bubble region. Conversely, spikes retain strength at time of rupture. There is competition between magnetic diffusion, resistivity, and elastic-plastic flow. The last effect seems to be dominant for the 2.0-mm wavelength; the others are more critical for the 0.5-mm wavelength. Axial flow appears to be the strongest effect during liner rupture and disc formation. We are studying these processes to derive a more integrated model for the liner stability, and continue to make progress.

References

1. Harris, E. G., Rayleigh-Taylor Instabilities of a Collapsing Cylindrical Shell in a Magnetic Field, *Phys.Fluids,* **5** (1962) pp. 1057-1062.
2. Harris, E. G., Dienes, J. K., Taylor Instability in a Viscous Fluid, *Phys. Fluids,* **9**, (1966) pp. 2518-2519.
3. Barnes, J. F., Blewett, P. J., McQueen R. G., Meyer, K. A., Venable, D., Taylor Instability in Solids, *J. App. Phys.,* **45** (1974) pp. 727-732.
4. Barnes, J. F., Janney, D. H., London, R. K., Meyer, K. A., Sharp, D. H., Further Experimentation on Taylor Instability in Solids, J. App. Phys., **51(9)** (1980) pp. 4678-4679.
5. Drucker, D. C., *Mechanics Today,* **5** (1980) Oxford, Pergamon, pp. 37-47.
6. Lebedev, A. I., Nisovtsev, P. N., Rayevsky, V. A., Rayleigh-Taylor Instability in Solids, *The 4th International Workshop on the Physic of Compressible Turbulent Mixing,* Cambridge, England, 29 March - 1 April 1993.
7. Swegle, J. W., Robinson, A. C., Acceleration Instability in elastic-plastic solids. I. Numerical simulations of plate acceleration, *Journal of Applied Physics,* **66** (1989) pp. 2838-2858; Robinson, A. C., Swegle, J. W., Acceleration Instability in elastic-plastic solids. II. Analytic techniques, *J. Applied Physics,* **66** (1989) pp. 2859-2872.
8. Robinson, A. C., Swegle, J. W., Acceleration Instability in Elastic-Plastic Solids. II. Analytic Techniques, *F. Applied Physics*, **66** (1989), pp. 2859-2872.
9. Bakhrakh, S. M. et al., Hydrodynamic Instability in Strong Media, Review of Open VNIIEF Publications, UCRL-CR-126710, Lawrence Livermore National Laboratory, 1997.

HYDRODYNAMIC LINER EXPERIMENTS USING THE RANCHERO FLUX COMPRESSION GENERATOR SYSTEM

J. H. GOFORTH, W. L. ATCHISON, C. M. FOWLER, D. H. HERRERA, J. C. KING, E. A. LOPEZ, H. OONA, R. E. REINOVSKY, J. L. STOKES, L. J. TABAKA, D. G. TASKER, D. T. TORRES, F. C. SENA, J. A. MCGUIRE, I. R. LINDEMUTH, R. J. FAEHL, R. K. KEINIGS, O. F. GARCIA

Los Alamos National Laboratory, New Mexico, USA

B. BROSTE

Bechtel, Las Vegas, Nevada, USA

At Los Alamos, we investigate solid density materials under extreme conditions of high pressure or strain. To further these studies, we develop pulsed power techniques for driving high energy imploding liners. We have developed the Ranchero explosive-driven magnetic flux compression generator (FCG) system to perform such experiments at very high energy, in remote locations. Our first charter is to support the development of the Atlas capacitor bank [1] which, when completed in 2001, will deliver up to 30 MA to hydrodynamic liners. The basic unit of the Ranchero system is a 1.4 m long coaxial FCG that is simultaneously initiated along its axis and has an armature expansion ratio of 2:1. We performed initial system tests using 43 cm long [2,3] coaxial modules and are finalizing the design and development of our 1.4 m detonation system. This development, which met with unexpected difficulties, is the subject of another paper in this conference [4]. The 43-cm module combined with the 2.4 MJ capacitor bank at our high explosive pulsed power facility has the capability of delivering ~40 MA to a load of ~5 nH. Coupled with a fuse opening switch (FOS), the system will generate a good approximation of Atlas waveforms with 5 nH in the load and transmission lines. This allows us to begin preliminary Atlas related tests before the 1.4 m module is completed. Herein is described our efforts to develop the capability and the design of our first imploding liner experiment.

1 Ranchero Development Tests

Early development tests examined a variety of module parameters [2,3]. More recently, experiments have focused on investigating features needed to power Atlas-like loads. Our final examination of the generator, alone, used the same end output configuration tested earlier for Atlas work and added the inductance of an Atlas power flow system. The current generated in this test is given in Fig. 1. With our 12 mF capacitor bank charged to 19 KV, we can deliver 4.5 MA initial current to the ~56 nH generator. With a load of 4.5 nH plus ~0.5 nH hook-up inductance, the generator developed 39 MA. Earlier tests indicate that we have ~1.3 nH residual inductance in the FCG. Including this with the 5 nH load gives us an energy of 4.8 MJ. Because of its overall similarity, we consider this test as a baseline for modeling future experiments. In particular, we used the current (I) and dI/dt data from this shot to establish an FCG model for use in self-consistent calculations involving time-varying circuit elements. To establish the model, we derived an inductance curve from our Raven 1-D MHD code and then used the data to establish a companion resistance function. Within the limits of reproducibility, these two curves specify a model for the module for all similar applications, even if neither one is completely accurate. The subsequent step in using the 43 cm module to power liner loads was to develop a FOS to isolate the liner from the high current associated with initializing the FCG field and early flux compression.

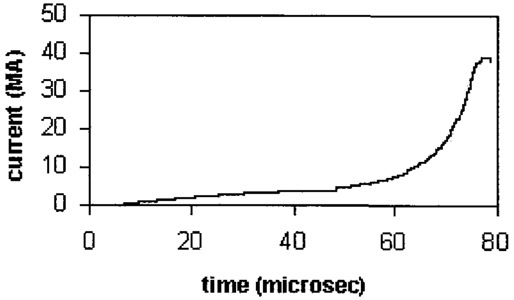

Figure 1. Current delivered to a 5 nH static inductance load.

2 Fuse Development

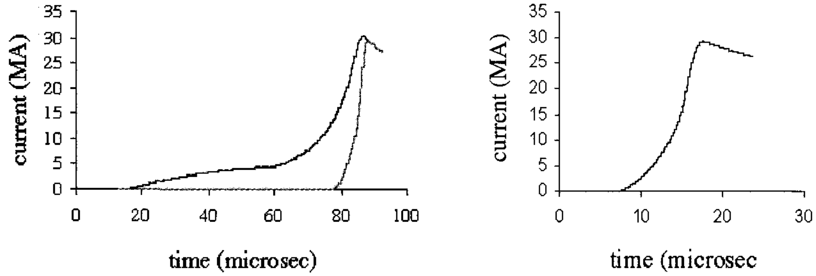

Figure 2. FCG and load currents on fuse development test. The right-hand curve is expanded and on arbitrary time scale.

We have chosen FOS parameters for a variety of high explosive pulsed power systems in the past using our CONFUSE computer code [5,6]. With the generator model obtained as described above, we applied the code to choose fuse dimensions for the first system test. Our first experiment was designed conservatively, avoiding any fuse performance limits that would lead to fuse failure and not test the rest of the system. In the system, we have ~2 nH inductance in the fuse hardware and an additional 3 nH in the transmission line and dummy load that mocks up an imploding liner test. Experimental results are shown in Fig. 2. Load isolation switches in the system were closed relatively early to avoid high voltage problems that could arise from overestimating fuse opening time. However, the fuse performed much as expected and the load pulse of 29 MA resulted. This current is enough to perform preliminary Atlas tests and can be improved substantially by optimizing the fuse design and closing switch time. The fuse for the test shown in Fig. 2 was 50 μm thick, 2.7 m wide, and 0.3 m long; CONFUSE suggests that a fuse 50 μm thick, 3.5 m wide, and 20 cm long would provide some improvement. A careful comparison of the results to CONFUSE predictions left some unanswered questions that may be related to either the fuse or generator models. Therefore, we will conduct our first liner test with a fuse of the same dimensions as those used for this test, after which we will further compare results.

3 Liner Design And Preliminary Experiment

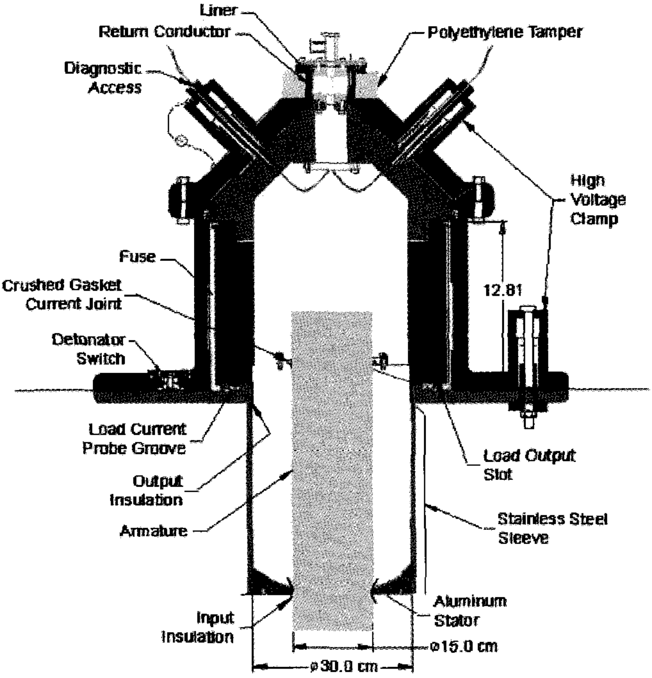

Figure 3. Liner test system

The system for our first liner test is shown in Fig. 3. The conical transmission line section emulates an Atlas transmission line. Two high voltage clamps allow us to assemble the load with access to both ends of the liner and then install that sub-assembly onto the pulsed power section. These clamps further allow diagnostic access to the inside of the assembly via small optical fibers. At 30 MA, the linear current density in the return current path outside the liner approaches 1 MA/cm. Because of this high current density and the close coupling between the current in the liner and return path, there are no cutouts allowed in the return conductor. At 5 mm thick, it is made as thin as possible to allow maximum penetration of x-rays to diagnose the liner. The only operational change between the FOS test and the first liner test is to close the load isolation switches 2 μs later than on the test in Fig. 2. This will remove some of the low current foot from the curve, but should not run the sizeable risk of overvolting the transmission lines. The curves should be very similar to those in Fig. 2, with two exceptions. The liner load inductance has increased above our 5 nH goal, and the liner dynamics will further decrease the peak current. We expect to see peak generator current of ~26 MA, and a liner current between 20 and 25 MA on the first test. The experiment will use a 3 mm thick aluminum liner, twice the thickness of our eventual goal. This liner will move more slowly (~0.7 cm/μs) than liners planned for future tests, but will be easier to diagnose initially where many variables are being measured.

4 Conclusions

We have developed a system for driving hydrodynamic liners at currents approaching 30 MA. Our 43 cm module will deliver currents of interest and, when fully developed, the 1.4 m module will allow similar currents with more total system inductance. With these systems we can perform interesting physics experiments and support the Atlas development effort.

References

1. Keinigs, R. K., Atchison, W. L., Faehl, R. J., Thomas, V. A., Mclenithan, K. D., Trainor, R. J., One-and Two-Dimensional Simulations of Liner Performance at Atlas Parameters. *J. Appl. Phys.* (to be published).
2. Goforth, J. H., et al., Ranchero, A High Flux Compression Generator System for heavy Liner Experiments, Seventh International Conference on Megagauss Magnetic Field Generation and Related Topics, August 5-10, 1996 Sarov (Arzamas-16), Russia.
3. Goforth, J. H., et al., The Ranchero Explosive Pulsed Power System, *Proceedings of the Eleventh IEEE International Pulsed Power Conference*, Ed. by Cooperstein and Vitkovitsky, Baltimore, Maryland (1997), p. 573.
4. Tasker, D. G., et al., Optimizing the Ranchero Coaxial Flux Compression Generator, P. Miller, Naval Air Warfare Center, Weapons Division, China Lake, California.
5. Goforth, J. H., et al., Performance of the Laguna Pulsed Power System, *Proceedings of the Sixth IEEE Pulsed Power Conference,* Ed. by Turchi and Bernstein, Arlington, Virginia (1987) p. 445.
5. Reinovsky, R. E., Lindemuth, I. R., Goforth, J. H., Caird, R. S., and Fowler, C M., High Power Switching and Pulse Shaping, *Proceedings of the Megagauss Fifth Conference,* Ed. by Titov and Shvetsov, Nova Science Publishers, Inc. (1990) p. 453.

LINER STABILITY EXPERIMENTS AT PEGASUS: DIAGNOSTICS AND EXPERIMENTAL RESULTS

D. A. CLARK, D. V. MORGAN AND G. RODRIGUEZ
Los Alamos National Laboratory, Los Alamos, NM, USA

A series of experiments to compare imploding liner performance with magneto-hydrodynamic (MHD) modeling was performed at the Los Alamos National Laboratory Pegasus II pulsed power machine. Liner instability growth originating from initial perturbations machined into the liner was observed with high resolution. The experiments used three major diagnostics: radiography, Velocity Interferometer for a Surface of Any Reflector (VISAR), and fiber optic impact pins. For radiography, three flash x-ray units were mounted radially to record liner shape at three different times during implosion. In two experiments, liner velocity and radial position were measured continuously with VISAR for the entire distance traveled. Optical impact pins provided a high-resolution measure of liner symmetry and shape near the end of travel. Liner performance compared well with model predictions.

1 Introduction

Nine liner stability (LS) experiments were conducted at the Los Alamos National Laboratory Pegasus facility. The experiments' purpose was to measure performance of imploding liners under different initial conditions and compare the results to predictions. A good understanding of instability growth would provide valuable input for liner specifications and fabrication for future high-energy liner experiments.

Several different liner types were used. Some were completely smooth with no initial perturbations. Others were initially perturbed with sinusoidal grooves of a single wavelength machined on the outside of the entire liner length; others had grooves of different wavelengths and amplitudes on each half of a single liner. Different surface qualities were also used. Major liner performance diagnostics used were radial x-rays, VISAR, and fiber optic impact pins. Each diagnostic provided a unique view of the liner and performance crosscheck with the other diagnostics. All three diagnostic systems were mounted on LS-8 and LS-9. The LS-9 liner was initially smooth while the LS-8 liner had 10 μm peak-to-peak amplitude sinusoidal perturbations machined on the outer surface. Perturbation wavelength on the half with the VISAR was 1.2 mm. The other half had 6 mm wavelength perturbations. The Pegasus capacitor bank drove both liners under nearly identical conditions of 78 kV charge voltage and 10.1 MA peak current.

2 Radiography

Over the past several years, the P-22 radiography team developed a family of portable flash x-ray sources for dynamic radiography (Platts-flashes) [1]. These sources were designed to meet the experimental requirements of the High Energy Density Physics program. They are compact, shielded against extreme electromagnetic pulse (EMP) environments, battery powered, and fiber optically controlled. The x-ray tubes are inexpensive and can be disassembled to change the anode material in order to modify the spot size and x-ray spectral characteristics. These units have been tested and fielded extensively.

Three Platts-flash x-ray sources at Pegasus are aligned radially with the liner, with lines-of-sight at 120° intervals to provide dynamic x-ray images of the implosion. They are fired sequentially to obtain radiographs of the liner at three different times during the implosion. The radial Platts-flash x-ray systems are specially equipped to operate in the extreme EMP environment of the 4 MJ Pegasus discharge without accidental misfires. Figure 1 is the third radiograph taken on LS-8. It shows that the original 10 μm amplitude perturbations of 1.2 mm and 6 mm wavelength (left and right halves) have grown to large amplitude. Fiber optic pins in their supporting tubes are seen at the lower right of the image.

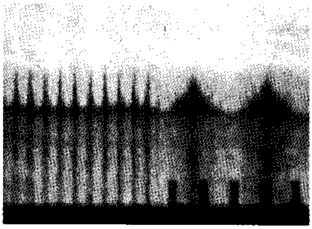

Figure 1. Flash x-ray radiograph of the LS-8 liner 10.10 μs after current start. Initially, the perturbations machined into the liner outer surface were 6.0 mm and 1.2 mm wavelength with 10 μm peak-to-peak amplitude.

3 VISAR

VISAR is proven for its ability to accurately measure the velocity and position of highly accelerated surfaces [2,3]. VISAR is an invaluable diagnostic tool for liner stability experiments as it provides a continuous, highly precise measurement of the liner free surface velocity and radius from start to final target implosion. Inclusion of this diagnostic in Pegasus imploding cylindrical liner experiments permitted experimental validation of MHD computer models predicting liner performance. VISAR measurements on imploding liners helped characterize instability growth and shock breakthrough signatures, determined melt time and target-shock pressure. VISAR operates by measuring the optical Doppler shift of single-frequency laser light reflected off the liner surface. Doppler shift is proportional to surface velocity and produces fringes in a fringe counting interferometer. Fringes are recorded electronically in quadrature, and then analyzed to extract velocity and position information. Figure 2 displays VISAR results for the LS-8 and LS-9 experiments.

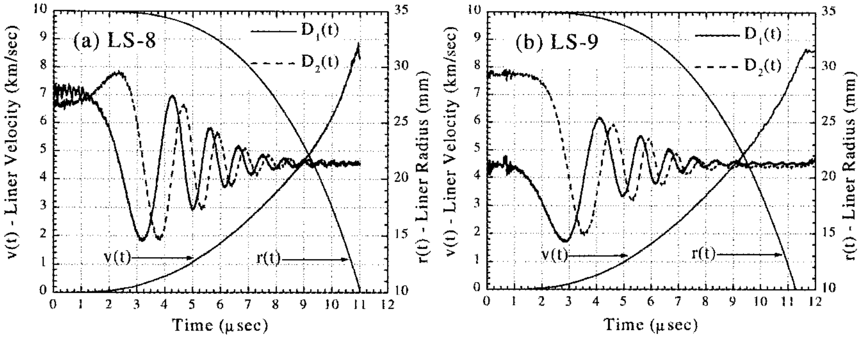

Figure 2. VISAR recorded quadrature fringe data D$_1$(t) and D$_2$(t), retrieved velocity profile v(t), and liner radius r(t), versus time for liner stability experiments: (a) LS-8 and (b) LS-9. Peak liner velocities of 8.8 km/sec and 8.26 km/sec are recorded for LS-8 and LS-9 respectively.

The VISAR data are in excellent agreement with the radiographic and optical impact pin data also used to track liner motion. Future integration of VISAR on imploding liner experiments will extend VISAR capabilities to include particle velocity measurements using shock wave profiling techniques.

4 Fiber Optic Impact Pins

Fiber optic impact pins have been used in place of electrical contact pins in many types of experiments for detecting shock arrival times since the mid 1980's [4]. A pin consists of an optical fiber placed in a stainless steel hypodermic tube and mounted so that it is struck on the end by the moving material. Shock heating of the fiber material produces light, which travels along the fiber to a photodetector. A digitizer or oscilloscope records the detector output. A sharp increase in the light signal occurs when the pin is struck. Occasionally, when the pins are mounted to protrude from the target, a second shock is seen when the moving material strikes the target material holding the pin.

Optical fibers are small and quite flexible. They are used in the target cylinder of the Liner Stability experiments to measure velocity, and axial and azimuthal symmetry of the liner as it nears the end of travel. Optical pins are also used in the glide plane to measure implosion velocity. Figure 3 compares radiographic data from the inner surface of the liner with pin data from LS-8. The original 10 μm amplitude has grown to approximately 1.5 mm.

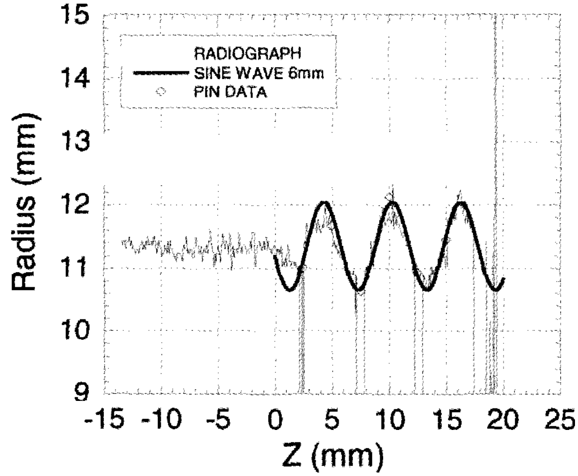

Figure 3. Comparison of optical pin data and x-ray data. The light solid line is a photo density scan along the inner surface of the liner from the radiograph in Figure 1. The large negative excursions occur when the scan picks up the optical pins. The heavy line is a 6 mm wavelength sinusoid fit to the pin data. The x-ray data and pin data both have the same wavelength as the original perturbation machined into the liner.

5 Summary

A series of experiments observing liner stability issues was conducted at Pegasus. Instability growth due to perturbations and surface finish characteristics machined into the liners was observed and compared to calculation. Three major diagnostics: radiography, VISAR, and fiber optic impact pins, observed instability growth and agreed with each other and MHD calculations very well [5].

References

1. Platts, D. et al., *Proc.10th Int. Pulsed Power Conf.*, Albuquerque, NM (1995) p. 892.
2. Hemsing, W. F., *Rev. Sci. Instrum.* (1979) **50** p. 73.
3. Asay, J. R., in *High Pressure and Shock Compression of Solids,* ed. by J. R. Asay and M. Shahinpoor (Springer-Verlag, New York, 1993).
4. Veeser, L. R., et al., SPIE **838** Fiber Optic and Laser Sensors V, (1987) pp. 60-68.
5. MHD calculations with respect to liner stability experiments are discussed elsewhere in these proceedings.

IMPLODING LINER MATERIAL STRENGTH MEASUREMENTS AT HIGH-STRAIN AND HIGH-STRAIN RATE

R. BARTSCH, H. LEE, D. HOLTKAMP, B. WRIGHT, J. STOKES, D. MORGAN, W. ANDERSON
Los Alamos National Laboratory, New Mexico, USA

W. BROSTE
Bechtel Nevada Corporation, Las Vegas, Nevada, USA

Imploding, cylindrical liners provide a unique, shockless means of simultaneously accessing high-strain and high-strain-rate to measure strength of materials in plastic flow. Radial convergence in the liner geometry results in the liner thickening as the circumference decreases. Strains of up to ~1.25 and strain rates of up to ~10^6 sec^{-1} can be readily achieved in a material sample placed inside an aluminum driver liner, using the Pegasus II capacitor bank. This can provide yield strength data at conditions where none presently exists. The heating from work done against the yield strength is measured with multichannel pyrometry of infrared radiation emitted by the material sample. The temperature data as a function of liner position can be unfolded to give the yield strength along the strain, strain-rate trajectory. Proper design of the liner and sample configuration ensures that the current diffused into the sample adds negligible heating. An important issue in this type of temperature measurement is shielding the pickup optics from other radiation sources. Recent data on 6061-T6 Aluminum are compared with an existing model for strain and strain-rate heating. Liner configuration and pyrometry diagnostic is also discussed.

1 Introduction

Liner implosion hydrodynamic experiments using pulsed power typically have high purity aluminum as the current carrying element, frequently in combination with another metal as an impactor, or sample, on the inner surface [1]. In addition to ohmic heating from the drive current, cylindrical convergence results in heating of the liner and sample layer due to plastic deformation from strain and strain-rate effects.

This additional heating can change the state of the material, e.g. melt, and alter the stability of the liner system [2,3]. Moreover, viscous forces that oppose strain and lead to heating can alter the dynamics of the liner's radial motion. A typical, moderate energy experiment on Pegasus has a liner velocity at maximum convergence (impact with a target) of ~ $4\mathrm{mm}\cdot\mu\mathrm{sec}^{-1}$. Therefore, the energy density from radial motion is ~20 $\mathrm{kJ}\cdot\mathrm{cm}^{-3}$ for the aluminum layer(s). For a ~3:1 radial convergence, the strain and strain rate heating of the high purity aluminum portion of the liner system can reach ~500 $\mathrm{J}\text{-}\mathrm{cm}^{-3}$ with a temperature rise of 200 K. The present series of Pegasus experiments to evaluate strain and strain rate heating operate at strains up to 200% and strain-rates of nearly $2\mathrm{x}10^6$ sec^{-1}.

The Atlas facility, presently under construction at Los Alamos, will be able to drive liners at 15-20 $\mathrm{mm}\cdot\mu\mathrm{sec}^{-1}$ and radial convergences of more than 10:1. Under these conditions, strain-rates of well over 10^6 sec^{-1} and strains of 200 to 300% can be reached. If full work hardening is assumed at these levels of strain and strain rate, and the maximum yield strength of 480 MPa applies for high purity aluminum [4], the driver liner will nearly melt based on material strength effects alone. This added source of heating has strong and linked implications for the material-strength-dependent stability of the Atlas liner and diffusion of the drive current into the driver liner. The resistivity of the high purity aluminum can increase about four times when heated from room temperature to melt.

2 Pegasus Experiments and Analysis

Liner implosion experiments have been conducted on Pegasus to measure the strain and strain-rate heating of high strength, 6061-T6 aluminum and infer yield strength; and develop their-pyrometry diagnostic, key to the application of liner implosions to strain and strain-rate material strength measurements [2]. The liner for these experiments consists of 700 μm thick 1100 series aluminum driver liner, 2 cm high and with 1.75 cm inner radius, and an attached inner layer of 400 μm of 6061-T6 aluminum. For these experiments, the Pegasus capacitor bank drive system is operated at 42 kV, a peak current of ~6 MA, and a time-to-peak-current of ~7 μsec. Inner and outer liner radii as a function of time are shown in Fig. 1 for the second experiment in this series. The measured data are from side-on flash X-ray radiography and agree with the calculated trajectories. Impact with the 0.5 cm radius pyrometry structure, located on axis, occurs at 10 μsec.

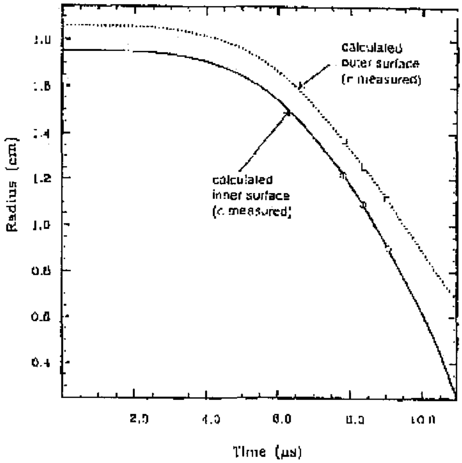

Figure 1. Calculated and measured liner position vs. time. Measured from side-on radiography.

In a cylindrically convergent system, the strain ε is related to the radius by $\varepsilon = K\ln(r(0)/r(t))$, where an approximate analytic derivation yields $K = 2/\sqrt{3}$, and a code calculation K ~1.33.

A simple, approximate connection can be made between the strength of the 6061-T6 aluminum sample and the observed strain and temperature due to the liner implosion. This is possible because work hardening from strain, for strains greater than a few percent, results in a nearly flat saturation of the plastic strength for this material. Also, recent data using a Hopkinson bar suggests that strain rate effects may also saturate well below the nominal range for these Pegasus shots [2,6]. Here, the material strength is constant at its maximum value, Y_{max} (tabulated by Steinberg), and the temperature rise is given by $\Delta T = (1 - \exp(-BY_{max}\,\varepsilon/c))/B$ where C_v is the specific heat at constant volume and B is the temperature softening factor. For 6061-T6 aluminum $B = 1/1623$ °C, $Y_{max} = 680$ $J{\cdot}cm^{-3}$ and C_v is 2.55 $J{\cdot}cm^{-3}$ °C. A temperature trajectory based on this model and the experimental r(t) is compared in Fig. 2 with the temperature measured by a four channel IR-pyrometer [5]. In this case, some background subtraction was done to reduce the effect of contaminating radiation. This arises from the interaction between the moving liner and the stationary conductors, glide planes, at top and bottom. From the liner configuration

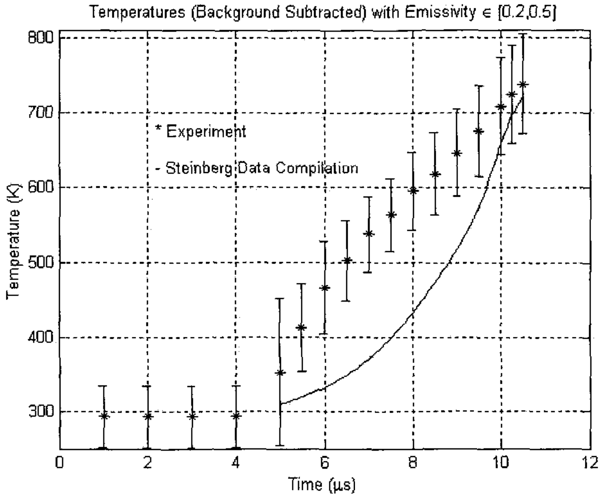

Figure 2. Measured inner surface temperature compared with analytic estimate based on fully work-hardened model. Strain for the analytic estimate is from the measured and calculated r(t). Error bars on measured temperature are due to uncertain emissivity on the sample surface that is in the range 0.2 to 0.5.

shown schematically in Fig. 3, it is apparent that this extraneous light will be eliminated as the liner collapses against the pyrometer structure at 0.5 cm radius. This may account for the improved agreement of the late time experimental data point with the simple model presented.

The temperature data in Fig. 2 illustrate key factors in IR-pyrometry measurements: (1) avoiding spurious radiation, and (2) knowledge of the emissivity in dynamic systems. A third experiment was fielded in this series, with low-density foam baffles to block radiation from the liner-electrode interface. This proved unsatisfactory, since the foam was heated to high temperature from the snowplow action by the imploding liner. The foam did, however, block the background radiation generated by shear-strain heating at the liner-electrode interface. A fourth experiment is in preparation with a two times higher liner and improved radiation absorption on the non-viewed surfaces of the liner system's interior.

Figure 3. Cross-section of liner assembly with pyrometer head located on-axis. The pyrometer optics (not shown) view the liner ID from along the axis via the 45°. 400 micron 6061-T6 Aluminum sample layer on the liner ID.

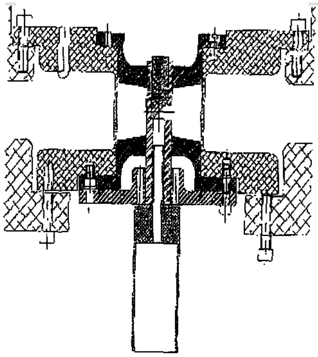

3 Conclusion

Future experiments will apply this liner based high-strain, high-strain-rate yield strength measurement technique to high density metals such as platinum, tungsten, and tantalum, which have application as impactor layers on Atlas. These experiments will provide strength data in a range of combined strain and strain rate not currently accessible by other means. Data from these experiments will also facilitate a comparison between two phenomenological strength models that have different parametric dependences on strain rates [7,8].

Acknowledgment

This work was performed under the auspices of the U.S. Department of Energy under contract No. W-7405-ENG-36.

References

1. Lee, H., Composite Liner to Maximize the Shock Pressure Beyond Megabars, Proceedings of the 7th International Megagauss Conference, Sarov, Russia, 1996.
2. Reinovsky, R. E., this conference.
3. Atchison, W. L., this conference.
4. Steinberg, D. J., Equation of State and Strength Properties of Selected Materials, UCRL-MA-106439 (Lawrence Livermore National Laboratory Report), Feb. 13, 1996.
5. Partouche, D., Holtkamp, D. B., Bartsch, R. R., Lee, H., Schmitt, G. G., to be published.
6. Gray, G. T., Blumentahl, W. R., unpublished.
7. Steinberg, D. J., Lund, C. M., *J. Appl. Phys.* **65** (1989) p. 1528.
8. Preston, D. L., Tonks, D. L., Wallace, D. C., PTW Materials Model, unpublished.

Z AND θ-CURRENT GEOMETRY FEATURES OF METALLIC TUBES COMPRESSION IN PULSED HIGH MAGNETIC FIELDS TO STUDY CONSTITUTIVE RELATIONS AT HIGH STRAIN RATE

Y. A. ALEXEEV AND M. N. KAZEEV
Nuclear Fusion Institute RRC, Kurchatov Institute, Moscow, Russia

J. PETIT
DGA/DCE/Centre d'Etudes de Gramat, France

The opportunities of tube compressions in pulsed high magnetic fields in Z and θ-current geometries in the strain rate range of 10^5-10^6 s^{-1}, in which few tests are available, are studied. The proposed experiments are based in TROB (Russia) and CYCLOPE (France) facilities used to study the behavior of structural materials. Advantages of the high strain rate tube compression in the Z geometry of current propagation are considered. The strain rate ranges accessible for the above mentioned field generators and tube thickness of approximately 1 mm have been determined. The experimental effects of high conductivity on tube compression are estimated.

1 Introduction

Pulsed power systems are often used to drive solid liner implosions for a variety of applications [1]. Solid liner drivers can be used to compress working fluids to generate shock waves and study material properties. In [2], the compression of metallic tubes in pulsed high magnetic fields to test the behavior modeling at high strain rate has been performed, using a middle-energy, capacitively driven facility. In this first configuration with θ-current geometry, a numerical simulation using the measured outer magnetic field has validated constitutive relations by comparing numerical closure of the sample tube with the experimental one recorded with a streak camera. This processing mode is limited. For the highest strain rates, the plastic work becomes too low compared to the electromagnetic (or kinetic) energy, and the influence of mechanical properties disappears in the tube motion. Whatever the strain rate, the temperature of the inner surface measured simultaneously with the velocity of the outer surface could be a good method to determine the plastic work and, consequently, the stress in the material. The z-current geometry offers a possibility in which both surfaces can be more accessible for diagnostics. This method can be easily used if Joule heating remains very low compared to plastic heating.

2 Tube Dimensions

Dynamics of tube compression does not depend on the configuration (Z or θ) of a magnetic field. The maximal strain rate $d\varepsilon/dt$ which is achieved during compression without final tube destruction, i.e. with the following final conditions: inner velocity $V_i = 0$ for inner radius $R_i = 0$, is:

$$d\varepsilon/dt \sim \sigma_S^{0.5} \rho^{-0.5} R_{no} \tag{1}$$

where σ_S is the elastic-plastic limit, ρ is the density and R_{no} the initial outer radius. Thus, under these conditions, Equation (1) shows that an increase of the outer tube radius reduces the maximal strain rate reached during the compression. However, even if the external radius increases, it is possible to reach $d\varepsilon/dt \geq 10^5$ s^{-1} when $\varepsilon = 1.5$, but this situation probably induces tube destruction.

To deform a tube with initial outside radius R_{no} and thickness Δ up to the required strain $d\varepsilon/dt$ for a given strain ε, it is necessary to transfer energy equal to the sum of kinetic energy, W_k, and plastic work, W_p:

$$W_k(J)=1.5\ 10^{-7}\pi\rho l\ (d\varepsilon/dt)^2\ R_{no}^4(1-s)^2 \exp(-2.88\ \varepsilon)\ \ln[1+s \exp(-1.44\ \varepsilon)\ /(1-s)] \qquad (2)$$

$$W_p(J) = -0.5\ 10^{-7}\pi\sigma_s\ R_{no}^2\ l\ [x \ln(x/(x-s)) + s \ln((x-s)/(1-x)) + \ln(1-s)] \qquad (3)$$

where l is the length in cm, R_{no} is in cm, $s = 1- (R_{io}/R_{no})^2$, σ_s is constant and in kbars, $x = (R_{n\cdot}/R_{no})^2$.

Parallel to this first analysis, numerical simulations were made with the specific code LINER in z-current configuration. The relation between the internal tube radius and the energy of the capacitor bank for copper (1 mm wall thickness) and aluminum (1.2 mm wall thickness) tubes is shown in Figure 1. Here, $d\varepsilon/dt = 10^5\ s^{-1}$ when $\varepsilon = 1.5$.

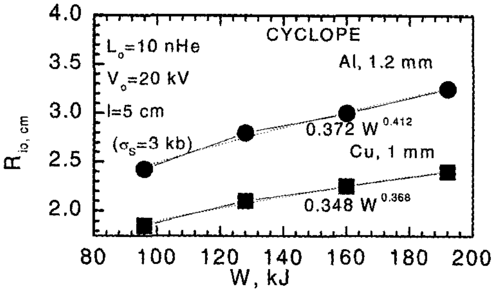

Figure 1. Relation between the inner tube radius for and aluminum tubes and the capacitor bank energy required to obtain $d\varepsilon/dt = 10^5 s^{-1}$ when $\varepsilon = 1.5$.

Higher strain rates can be reached when ε =1.5 at the CYCLOPE facility. For this purpose it is necessary to decrease the tube weight (either radius or wall thickness):
- for an aluminum tube with 1.2 mm thick wall, $d\varepsilon/dt \sim 10^5\ s^{-1}$ - $10^6\ s^{-1}$ when 3.3 cm $\geq R_{n0} \geq$ 1.1 cm;
-for a copper tube with 1.0 mm thick wall, $d\varepsilon/dt \sim 10^5\ s^{-1}$ - $6.10^5\ s^{-1}$ when 2.2 cm $\geq R_{n0} \geq$ 1.0 cm.

3 Temperature Distribution in a Tube

A temperature increase on an internal surface of the tube in these experiments is related to Joule heating and mechanical deformation of the material. Temperature increase due to tube deformation is approximately equal to $\Delta T_i^M \sim \sigma_s\varepsilon/c\rho$. Here c and ρ are the specific heat and density of the tube material, σ_s - plasticity strain and ε - equivalent deformation in a point R = Ri. When $\varepsilon = 1.5$, it is possible to expect $\Delta T_i \sim$ 100-250 °C. The value of temperature increase on the internal surface, due to Joule heating, depends upon the tube size, the magnetic field on its external surface, and also upon its compression mode. An increase in tube thickness or current frequency will induce a Joule heating decrease. For a given initial tube thickness, an increase of the strain rate (i.e. time decrease to reach $\varepsilon_s = 1.5$) has the same effect. This occurs because the higher the strain rate, the faster the thickness increases and, consequently, the later the magnetic field reaches the inner surface. In Figure 2, results of numerical simulations are reported. They show Joule heating of the internal surface of aluminum and copper tubes versus wall thickness Δ for the CYCLOPE facility in z-current configuration and for $d\varepsilon/dt = 10^5\ s^{-1}$ when $\varepsilon = 1.5$ is reached.

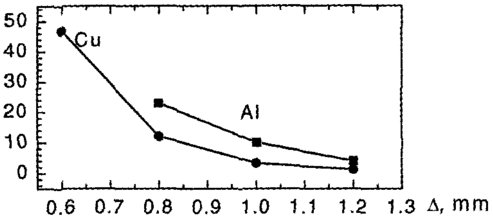

Figure 2. Joule heating of the internal surfaces of Al and Cu tubes vs. their thickness for $d\varepsilon/dt = 10^5\ s^{-1}$ when $\varepsilon = 1.5$ is reached in z-current configuration.

As expected, when the tube thickness is reduced the Joule heating of the internal surface is increased. For copper and aluminum tubes with 1-1.2 mm wall thickness, the temperature jump on the internal surface due to Joule heating approaches about 5 and 10 °C, respectively.

Numerical simulations with integral parameters of the CYCLOP facility were performed to assess possibilities of Z and θ configurations at a higher strain rate than $10^5\ s^{-1}$. Figure 3 shows results of these simulations. A strain rate close to $10^6\ s^{-1}$ was obtained in the booth configurations when $\varepsilon = 1.5$. The decrease of inductance in the z- configuration allowed higher maximal magnetic fields, consequently use of a thicker tube.

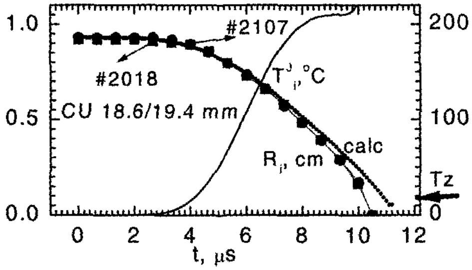

Figure 3. Inner tube radii and surface temperatures due to Joule heating with z- and θ-configuration for high strain rate () = 0.9 mm in z-configuration and) = 0.4 mm in θ-configuration).

Thus, the Joule heating of the inner surface is strongly decreased and the main temperature jump will be provided by the deformation.

4 Conclusion

1. The use of a z-current configuration in tube compression experiments by pulsed high magnetic fields appreciably expands opportunities of the CYCLOPE facility.
2. The range of strain rates at $\varepsilon = 1.5$ using the CYCLOPE facility in the z-current configuration with a tube thickness of about 1 mm is:

- $10^5\ s^{-1}$ - $6\cdot10^5\ s^{-1}$ for copper (Δ = 1 mm) when the outer tube radius varies from 2 to 1 cm. A strain rate up to $10^6\ s^{-1}$ can be obtained by decreasing the tube thickness or increasing the charging voltage;
- $10^5\ s^{-1}$ - $10^6\ s^{-1}$ for aluminum (Δ = 1.2 mm) when the outer tube radius varies from 2.5 to 1 cm;

3. For materials with high electroconductivity (Al, Cu), compression modes are available with strain rates from 1.5 10^5 s^{-1} to 10^6 s^{-1} and with Joule heating of an inner surface of the tube not higher than 10 °C.

References

1. Turchi, P. J., Cooper, A. L., Ford, R. D., Jenkins, D. J., Burton, R.L., Review of NRL Liner Implosion Program. *Megagauss Physics and Technology*, Ed. by P. J. Turchi, Plenum Press New York, (1980).
2. Petit, J., Alexeev, Yu. A., Ananiev, S. P., Kazeev, M. N., Compression of Metallic Tubes in Pulsed High Magnetic Fields to Test Behavior Modeling at High Strain Rate. *Megagauss Pulsed Technology and Applications*, Ed. by V. K. Chernyshev, Sarov, (1997).

MAGNETIC IMPLOSION FOR NOVEL STRENGTH MEASUREMENTS AT HIGH STRAIN RATES

H. LEE, D. L. PRESTON, R. R. BARTSCH, R. L. BOWERS,
D. HOLTKAMP, B. L. WRIGHT
Los Alamos National Laboratory, Los Alamos, NM, USA

Recently, Lee and Preston have proposed using magnetic implosions as a new method for measuring material strength in a regime of large strains and high strain rates inaccessible to previously established techniques. By its shockless nature, this method avoids the intrinsic difficulties associated with an earlier approach using high explosives. We illustrate how the stress-strain relation for an imploding liner can be obtained by measuring the velocity and temperature history of its inner surface. We discuss the physical requirements that led us to a composite liner design applicable to different test materials, and also compare the code-simulated prediction with the measured data for the high strain-rate experiments conducted recently at LANL. Finally, we present a novel diagnostic scheme that will enable us to remove the background in the pyrometric measurement through data reduction.

1 Introduction

The material strength models used for hydrodynamic code simulations of dynamic metal deformation must be fit to accurate flow stress data spanning the strains, strain rates, and temperatures characteristic of the deformation process. Hydraulic testing machines can access large strains, but the strain rates are limited to about $10\ s^{-1}$. The split Hopkinson pressure bar has been used for accurate strength measurements up to plastic strain rates of roughly $10^4\ s^{-1}$. However, there is at present no developed technique for measuring material strength to large plastic strains of order 100%, at rates above $10^4\ s^{-1}$. Data in this regime is essential for benchmarking and validating the existing material strength models and for the development of advanced models.

Over ten years ago Preston [1] proposed a novel technique for measuring the material strength of metals to strains of a few hundred percent at a rate beyond 10^6. The proposed experimental vehicle was a spherical shell of test metal imploded by high explosives. Initial attempts to make time-resolved pyrometric temperature measurements met with serious difficulty because of the appearance of hot spots at shock breakout and the additional shock loading to the convergence-induced stresses in the shell. Both effects complicated the data analysis significantly and compromised its value for model development.

Recently, two of us (HL and DLP) proposed a promising modification [2] of the original approach by using z-pinch to implode a cylindrical liner. The use of magnetic implosion is a significant improvement because it induces no shocks in the test material. Analysis indicated that a maximum plastic strain of about 200% and strain rates exceeding $10^6\ s^{-1}$ could be attained using the pulsed power facility Pegasus at Los Alamos. An experimental effort was initiated after its technical feasibility was affirmed by a detailed theoretical investigation.

2 Physics Issues and Constraints in Liner Design

Let $r(t)$ be the inner liner radius as a function of time. Neglecting material compression, the strain and strain rate are given by (dot stands for time derivative):

$$\varepsilon(t) = (2/\sqrt{3})\ \ln[r(0)/r(t)] \tag{1}$$

and

$$\dot{\varepsilon}(t) = -(2/\sqrt{3})\dot{r}(t)/r(t)] \tag{2}$$

It has been shown [1] that the rr-component of the stress deviator tensor, $S_{rr}(t)$, of the liner can be solved numerically from the following differential equation,

$$\dot{S}_{rr} - \frac{2\dot{r}}{\sqrt{3}r}\left(\frac{B}{\rho C_v T} - \gamma S_{rr}\right) = \frac{B\dot{T}}{\gamma T}, \tag{3}$$

provided that r(t) and the absolute temperature $T(t)$ are measured. In Eq. (3) B, γ, C_v and Δ are, respectively, the bulk modulus, Grüneisen parameter, constant-volume heat capacity and density of the liner material. With the strain history $\varepsilon(t)$ given by Eq. (1), we obtain the stress-strain (S_{rr}- s) curve that can be compared with the calculated results obtained from different strength models. We can also compare the measured and computed $T(t)$ directly to discriminate among various models.

From Eq. (1) we see that high strain can be achieved only if we have a large convergence ratio, $r(0)\ /\ r_f >> 1$, where r_f is the final radius at $t = t_f$. To achieve high strain rate, Eq. (2) implies that we must also make the final velocity v_f large and r_f small. Diagnostic requirement sets the lower limit $r_f = 0.5$ cm. Thus, we need $v_f \geq 4$ mm/μs for $\dot{\varepsilon}$ to exceed $10^6\ s^{-1}$. Now the task is how to maximize v_f using the equation of motion, subject to the requirement that the ohmic heating in the inner liner layer be kept negligibly small compared to the plastic strain heating. This requirement is equivalent to minimizing the liner mass per unit length, m, under the condition $T_p >> t_f$, where T_p is the current penetration time across the liner. In an earlier theoretical investigation on the liner design that maximizes the shock pressure via impact velocity, Lee [3] has established a general conclusion that a composite liner using aluminum as the outer layer, when optimized, will give the best performance. The underlying chain of physical reasoning [3,4] is too lengthy to be given here; but it is also applicable to the liner optimization for the high strain rate experiments.

3 Liner Design and Modeling for the Experiment

The composite liner optimally designed for our experiments on Pegasus consisted of two layers, with the outer one (0.7 mm thick) made of 1100 series aluminum and the inner one made of test material. As a start, we chose 6061-T6 aluminum (0.4 mm thick) as the test material to boost the pyrometer signal level, since its high strength would give a much higher strain heating than soft aluminum. The liner was 2 cm long with an inner radius of 1.75 cm. The drive current used in liner design has an approximate sinusoidal waveform with a peak value of 5.8 MA at 7.6 μs. In Fig. 1 we show the calculated time-dependent strain and strain rate in the innermost layer, using the Steinberg-Guinan (SG) model. The two curves reach about 200% and $2\times10^6\ s^{-1}$, respectively, when the implosion ends at 9.9 μs. For a detailed description of the experimental setup, we refer the readers to a companion paper [5].

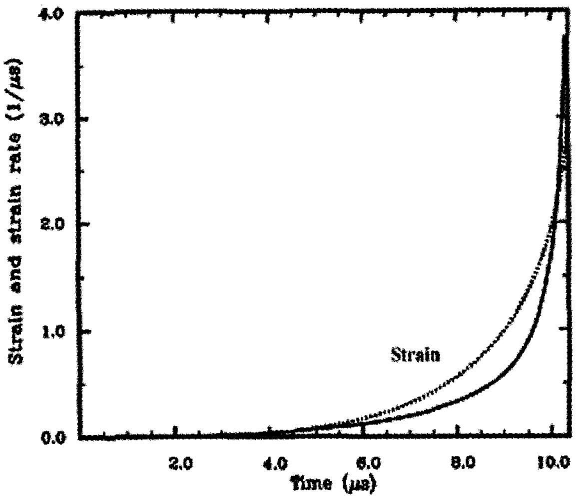

Figure 1. Predicted time-dependent plastic strain (dotted curve) and strain rate in the innermost liner layer.

4 Experimental Results

The first two experiments were successfully carried out in June and October of 1997, using identical liner specifications and drive conditions to ascertain the reproducibility of the pyrometer data. The temperature history inferred from pyrometer data for the second shot is compared with the code-simulated result in Fig. 2. We notice that the final temperature is about 200 ± 60 K higher than the result calculated from the SG model. Furthermore, the temperature history exhibits a large and sudden jump at 4.5 μs, suggesting the onset of a large background. A careful examination of the 2-D simulation has convinced us that this background radiation came from the end areas of the liner, where extra heat is generated by shear strain as the electrodes cut through the moving liner. The peak temperature in these areas increases rapidly by more than 350 K at a time coincident with the sudden jump observed in the data.

We have found an effective solution to reduce the background radiation by increasing the liner length from the usual 2 cm to its allowable limit of 4 cm. The large improvement can be explained as follows. To enhance the signal and reduce the background, we have blackened the inner liner surface except the portion within the field of view of the mirror that reflects the light to the detector. However, for the 2 cm liner, the radiation coming from certain parts of the liner-electrode (L-E) interface can reach the detector by just one reflection from the shiny portion of the liner. The 4 cm liner configuration changes the geometry so that no radiation from the L-E interface reaches the detector without reflecting at least once from the blackened surface. Thus, the background radiation that can reach the detector is substantially reduced since the reflectivity of the blackened surface is about 0.1. The 4 cm liner will be field tested in our next experiment.

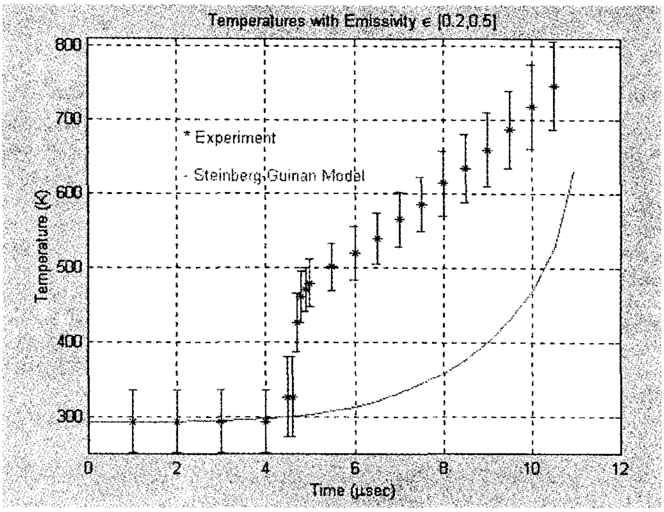

Figure 2. Calculated temperature history of the inner liner surface compared with the one deduced from pyrometer data.

5 Conclusions

Our experiments are the first attempts to establish the feasibility of a recent proposal to use magnetic implosions for measuring material strength where large strains and high strain rates make previously established techniques impractical. While the preliminary result indicates a rather large background radiation coming from the liner-electrode interface, the problem can be eliminated in principle by a new liner design. We are reasonably hopeful that there is no intrinsic technical showstopper to this new approach.

References

1. Preston, D. L., IMP2 Proposal, LANL Memorandum X-4:86-190U (1986).
2. Lee, H., Preston, D. L., Using Pulsed Power for High Strain Rate Strength Measurements, *Conference Record-Abstract of IEEE International Conference on Plasma Science*, Raleigh, NC, June 1998.
3. Lee, H. Composite Liner Design to Maximize the Shock Pressure beyond Megabars, *Proceedings of VIIIth MEGAGAUSS International Conference,* Aug. 5 - 10, Sarov, Russia (1996).
4. Lee, H., et al., Megabar Experiments on Pegasus II, *Proceedings of 11th IEEE International Pulsed Power Conference*, Baltimore, MD (1997) p. 336.
5. Bartsch, R. R., et al., Imploding Liner Material Strength Measurement at High-Strain and High Strain Rate, Proceedings of this conference.

AN EVALUATION OF THE LOS ALAMOS PRECISION AUTOMATED TURNING SYSTEM (PATS) AS A PRODUCTION TOOL FOR ATLAS LINERS

W. ANDERSON, R. DAY, D. HATCH, R. GORE, D. MACHEN, J. BARTOS, M. SALAZAR, P. HANNAH
Los Alamos National Laboratory, Los Alamos, NM, USA

The PATS is proposed as a possible means for efficient production of precision liners for Atlas [1]. The Los Alamos National Laboratory's High Energy Density Physics (HEDP) program supported an evaluation of this prospect over the last two years. The machine operations have been carefully mapped out, the status of the controllers and on-machine gauging evaluated, and dynamic error addressed. The PATS has been used to generate diamond turned liners with dimensions similar to those proposed for Atlas. In the mean time, Atlas liner criteria have become even more stringent. This paper will evaluate the known status of the PATS in view of current liner designs for Atlas.

1 Introduction

Atlas liners are 75 mm diameter aluminum cylinders with extremely demanding dimensional tolerances. The most exacting dimensional specification is that the waviness on the cylinder wall, over its 60 mm length, must be less than ±10 nm for spatial wavelengths of 10 mm. It is anticipated that hundreds of these liners will be needed annually; therefore an inexpensive and very accurate means of producing and inspecting these liners is sought. The PATS appears to have the appropriate set of resident technologies for liner production, so its capabilities were carefully evaluated.

2 Description of the PATS

PATS is a very accurate lathe developed for the nuclear weapons complex [2] that incorporates state-of-the-art machining and controller technology. It has two independent spindle and slideway systems so that two totally different parts can be machined simultaneously. Each spindle/slideway system also has independent inspection stations so a part can be measured after it is machined.

A laser interferometer was used to determine the accuracy of the machining slideways. The measurement results, taken over a volume that would encompass a part 600 mm in diameter and 300 mm long are summarized in Table 1. These data show that the PATS is accurate enough to make the ATLAS liners except for the radial horizontal straightness, which should be less than ±0.01 μm. This straightness measurement was made for a length of 300 mm, however, and the ±0.01 μm criteria only applies to a length of 60 mm. The data indicated that there might be 60 mm long regions of the slideways that are sufficiently straight to produce the liners. Therefore, a liner was produced and inspected to determine if the PATS could produce a liner of sufficient quality.

Table 1. Summary of PATS Slideways Accuracy

ERROR NAME	ERROR
Radial horizontal straightness	± 0.15 μm
Radial positioning	± 0.23 μm
Longitudinal straightness	± 0.13 μm
Longitudinal positioning	± 2.25 μm
Horizontal squareness	0.06 arc seconds

3 Production and Inspection of Liner on the PATS

The most cost effective method of producing the ATLAS liners is to have them both machined and inspected on the same machine. Therefore, an evaluation of the on-machine measuring features of the PATS was incorporated into the liner production test. A slightly shorter version of the ATLAS liner (45 mm long) was machined using a single crystal diamond-cutting tool. This tool was used because diamond produces a far superior surface finish than any other tool materials, and the residual stresses induced into the liner by the diamond are much lower than for other tool materials.

It was determined that the most accurate method for measuring the wall thickness variation was to place the measuring stylus on the opposite side of the spindle from the cutting tool, The machining slideway is then used to move the measuring stylus along the part, and any deflection of the stylus reflects twice the amount of error in the part [3]. Fig. 1 shows the wall thickness variation that was measured along the cylindrical axis.

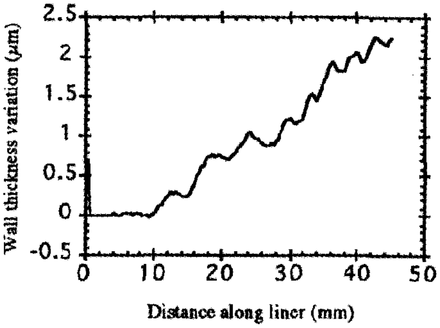

Figure 1. Wall thickness variation of an ATLAS liner that was machined and measured on the PATS.

The plot in Fig. 1 reveals two primary errors. The first is the increasing slope from 10 mm to 45 mm. This slope indicates that the spindle axis was not parallel to the machining axis. This error is easily corrected by either an alignment adjustment or by changing the part program to cut a compensating taper. The second error is the waviness along the line. These waves have an amplitude of ± 0.18 μm with a spatial wavelength of about 5 mm. Simulations indicate that surface perturbations of this size can adversely effect the implosion dynamics [4].

Surface finish data was also taken with the PATS and compared to that taken with an optical profilometer. The PATS data showed an average surface roughness of 16.7 nm; the data from the optical profilometer showed an average surface roughness of 16.7 nm. These measurements are in excellent agreement.

The above experiments concluded that PATS has inherent slideway straightness errors that must be corrected if stable ATLAS liners are to be produced. The simplest correction to make is a software correction that causes the machining tool to move along an inverted profile to the one shown in Fig. 1; thus, the errors in the slideways will be cancelled. The part error data shown in Fig. 1 was acquired as a function of time and then related to position on the part because the tracing velocity was known. This is a good technique for determining error magnitudes; however, when making part corrections the position where the errors are occurring is very important. Therefore, part error data must be acquired by the machine tool controller to assure that accurate position information is obtained. The PATS controller had hardware capable of taking this data but the software required some modification to accomplish the data acquisition. A project was initiated to demonstrate that the PATS controller could be used as a data acquisition system to obtain continuous part error data.

4 Recording Inspection Data with the PATS Controller

The acquisition of controlling data is a unique feature of the PATS controller. After the appropriate software changes were made, a cylinder was traced and its form errors were recorded with the controller. These data appear in Fig. 2. A recording oscilloscope was used to simultaneously record the data offline so a comparison could be made to determine of errors occurred in the controller's data acquisition system. Both sets of data compared very favorably. Since it has been demonstrated that inspection can be successfully recorded with the controller, the next project will be to perform part correction.

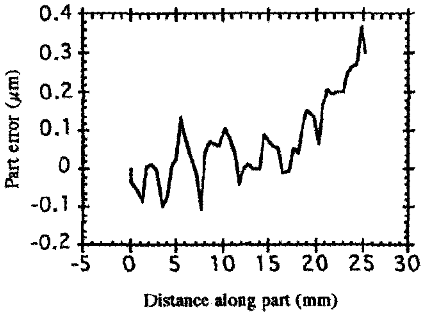

Figure 2. Part error data collected with the PATS controller.

5 Conclusions

The allowable dimensional errors on the Atlas liners are extremely small and it is anticipated that hundreds of these liners may be required per year. Potentially, the fastest and most accurate method for inspecting the liners is to inspect them on the machine on which they were made, providing that the accuracy of this method can be assured. The PATS is an ultra-precision lathe that has the unique feature of having independent measuring stations and the ability to record inspection data for parts with the controller. A test Atlas liner was machined and inspected on the PATS but it was determined that the inherent accuracy of the PATS was not sufficient to produce an acceptable liner without writing a correction program. Writing the correction program is the next step in determining if the PATS can produce these parts or if another machine must be developed to accomplish this task.

Acknowledgments

This work was supported by the Department of Energy under contract W-7405-ENG-36. This support is gratefully acknowledged.

References

1. Anderson, W., et al., Fabrication and Characterization of Aluminum Heavy Liners for the Pulse Power Systems of the High Energy Density Physics Program at Los Alamos, MEGAGAUSS-VII, Sarov, Russia, (August, 1996).
2. Rhorer, R., Hobson, W., Jarosz, J., Precision Engineering Aspects of the PATS Project, Proceedings of the American Society for Precision Engineering Annual Meeting, (September, 1990), p. 204-207.
3. ANSI Standard B5.57M, Methods for Performance Evaluation of CNC Lathes and Turning Centers, (1997).
4. Keinigs, R. K., et al., One-and-Two-Dimensional Simulations of Liner Performance at Atlas Parameters, These proceedings.

FABRICATION PROCESS FOR MACHINED AND SHRINK-FITTED IMPACTOR-TYPE LINERS FOR THE LOS ALAMOS HEDP PROGRAM

B. RANDOLPH
Materials Science and Technology Division, Los Alamos National Laboratory, University of California, USA

Composite liners have been fabricated for the Los Alamos liner-driven High Energy Density Physics (HEDP) experiments using impactors formed by physical vapor deposition, and by machining and shrink fitting. Chemical vapor deposition has been proposed for some ATLAS liner applications. This paper describes the processes used to fabricate machined and shrink-fitted impactors; these processes have been used for copper impactors in 1100 aluminum liners and for 6061 T-6 aluminum impactors in 1100 aluminum liners. The most successful processes have been largely empirically developed and rely upon a combination of shrink-fitting and light press fitting. The processes used to date will be described along with some considerations for future composite liners for the HEDP Program.

1 Introduction

Fabrication processes for machined and shrink-fitted impactor-type liners have been developed for the HEDP utilizing computer-numerical-controlled (CNC) machining capabilities. At present we have fabricated five machined impactor-type liners for experiments on the Pegasus pulse power facility: two for RT Mix experiments with copper impactors, and three for High-Strain-Rate experiments with 6061 T-6 aluminum impactors [1,2]. The liners were machined on a Hardinge Super-Precision CNC Chucker lathe having a multi-tool removable turret system that is capable of repeatability to within 20 micro-inches (.00002"). The lathe is equipped with a 5C-threaded, precision-bearing nose spindle that is capable of producing finishes down to 4 micro-inches rms (Rq). The spindle receives hardened, precision-ground collets or machinable soft collets for specialized workpieces. Adaptable faceplates will also mount on the spindle. The faceplate fixtures can be removed and replaced on the spindle without losing parallelism and concentricity between features, which is very important to the process described in this paper.

2 Liner Fabrication Process (Roughing Stages)

Liners are fabricated on the Hardinge Chucker in three stages. The first two are roughing stages, and the third is a finishing stage. At the first stage, the liner is rough-machined to within .010" on all dimensions (except the cylinder wall portion, which is left heavy for strength during drilling operations). After the first stage has been completed, drilling operations are performed on a CNC mill. Second stage operations are then performed: all dimensions are machined to within .003" except the current joint on the small flange end, which is finish-machined. The .003" of material left on the liner allows for finish machining at the third stage with Polycrystalline Diamond (PCD) cutting tools, providing 5- to 10-micro-inch-rms surface finishes, as specified.

During these first two stages, a machinable soft collet and closer system from Hardinge is used to hold workpieces, and a roughing turret equipped with special, hand-made, high-speed grooving tools is used for heavy roughing operations and chip control. Finish machining for these stages is done with ceramic-coated (KC-730) inserts from Kennametal.

3 Impactor Sleeve Fabrication Process

An impactor sleeve is made as a cylindrical tube that has a flange on one end. The outside diameter is left oversize and the inside diameter is made undersize, leaving material for finish machining. The sleeve is put onto a brass mandrel and the outside diameter is finish-machined, using a PCD insert tool, to a 6-micro-inch surface finish and to a tolerance of 20 - 40 micro-inches (.00002" - .00004") less than the mating bore of the liner. This allows for smooth insertion into the liner mating bore. At the flange end of the impactor sleeve, the last .100" of cylinder height is made .0002" larger in diameter, enabling a light press fit at the small-flange end of the liner when the sleeve is inserted.

4 Preparation of Liner to Receive Impactor Sleeve

At this point the small-flange end of the liner is held in a specially made soft collet, Fig. 1. The collet pocket is bored .0005" smaller in diameter than the small flange of the liner. Three clamping pins are left in the soft collet so that very little clamping pressure is exerted on the liner flange when it is being clamped, which prevents the liner from distorting. The face, outside diameter, and counter bore of the large-flange end are then finished to specification. The finished large-flange end is then placed on a Hardinge faceplate to which an aluminum fixture plate is permanently attached.

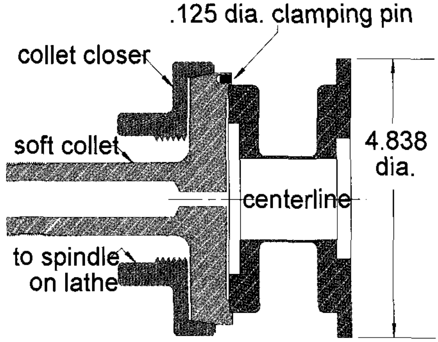

Figure 1. Soft collet holding High-Strain-Rate Liner.

The liner is fastened to the aluminum fixture plate via four holes that are already in the liner. This faceplate fixture can be removed and reinstalled at any time without losing concentricity of liner features.

The 1100 aluminum liner bore is then finish-machined to a 6-micro-inch surface finish for smooth insertion of the impactor sleeve. The last .100" of liner bore is finished .0002" smaller in diameter. This provides a light press fit at the large-flange end of the liner when the impactor sleeve is fully inserted.

5 Insertion of Impactor Sleeve into Liner

The faceplate fixture with liner attached is removed from the threaded nose spindle, and the liner bore is cleaned with ethanol and then allowed to thermally equilibrate at room temperature. The impactor sleeve is also cleaned with ethanol and cooled by rapid evaporation of ethanol, stimulated by a clean, dry, compressed-air shower. Thermal contraction slightly reduces the diameter of the impactor. The cleaned and cooled impactor sleeve is then very carefully inserted into the liner mating bore, Fig. 2. The two mating parts are designed to provide a light press fit at both ends of the impactor sleeve at thermal equilibrium but are not intentionally strained over the active length of the composite liner. The press fit at the impactor ends is believed to ensure coupling of spindle torque to the impactor sleeve while the inside diameter is being finished.

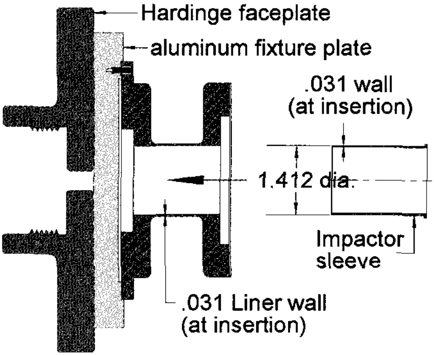

Figure 2. Impactor Insertion (High-Strain-Rate Liner)

6 Completion of Composite Liner (Third Stage)

The faceplate fixture, with the now-composite liner attached, is put back onto the threaded nose spindle of the Hardinge Chucker lathe, and a finishing turret is placed onto the lathe. All outside and inside contours can then be finished with PCD tooling, including the inside diameter of the inserted 6061 T-6 aluminum impactor. This method of fixturing allows all critical dimensions to be machined in the same setup, thereby preventing loss of parallelism or concentricity between features. All CNC programs, tool settings, soft collets, and fixtures are saved and can be used for future liner fabrication.

7 Composite Liners Fabricated by Coating Processes

For completeness, it is noted that impactors of some composite liner designs can also be fabricated by coating processes, especially when the impactor is thinner than those used with the liners described here. Physical-vapor-deposited platinum impactors were used in the Pegasus Megabar experiments [3]. Chemical-vapor-deposited tungsten impactors are being considered for composite liners that will be used to drive future hydrodynamic experiments at the Atlas facility (now under construction at Los Alamos).

8 Summary

Composite liners have been fabricated for Pegasus with machined metal impactors as thin as .008" wall thickness. The machining and fabrication methods described here ensure concentricity between the liner and impactor, do not physically distort the composite liner, and provide sufficient interfacial force to allow finish machining operations on the impactor. We expect to be able to extend the fabrication method to even thinner impactors, perhaps less than .004" thick, and to use different materials for impactors. Coating technologies have also been used to fabricate composite liner for Pegasus experiments. Both machined and coated impactors are candidates for the fabrication of composite liners to be used at the Atlas facility.

Acknowledgments

I would like to thank Wallace Anderson (HEDP Project Leader) and Ginette Andreatta (MST-7 Group Office) for their help and support in completing this paper. I would also like to thank Mike Salazar for helping make the accompanying poster.

References

1 Sheppard, M. G., Atchison, W. L., Anderson, W. E., Bartlett, R. J., et al., "Raleigh-Taylor Mix Experiment on Pegasus," Proceedings of the 11th IEEE International Pulse Power Conference (1997) pp. 1399–1404.

2 R.R. Bartsch, H. Lee, D. Holtkamp, B. Wright, et al., "Imploding Liner Material Strength Measurements at High Strain and High Strain Rate," VIIIth International Conference on Megagauss Field Generation and Related Topics, October 18–23, 1998, Tallahassee, FL (to be published).

3 H. Lee, R. R. Bartsch, R. L. Bowers, W. E. Anderson, et al., "Megabar Liner Experiments on Pegasus II," Proceedings of the 11th IEEE International Pulse Power Conference (1997) pp. 366–371.

FABRICATION OF HIGH ENERGY DENSITY PHYSICS LOADS

M. A. SALAZAR, W. ANDERSON, E. ARMIJO, F. GARCIA
Los Alamos National Laboratory, USA.

The Los Alamos High Energy Density Physics (HEDP) program requires a variety of loads for solid liner driven experiments. The Polymers and Coatings Group of the Los Alamos Materials Science Division fabricate most of the HEDP experimental loads and their associated liners. This paper describes some of the design and fabrication methods used to construct complex composite loads. The types of loads that are described utilize variations of an acrylic container with adhesive bonded joints to contain combinations of liquid Gallium, polymer foams, machined metal structures, and various gases at pressures to 5 atm.

1 Introduction

The LANL Pegasus II Pulse Power Facility is used to drive solid phase cylindrical liners for cylindrical hydrodynamic experiments with good symmetry. The Pegasus Precision Liner, as used in HEDP experiments (5 MA, 40 kV), produces a 300 kbar shock in cylindrically convergent geometry [1]. Lawrence Livermore National Laboratory/USA, AWE/United Kingdom, CEA/France, and VNIIEF/Russia have also used the facility. The types of loads that are described here are typically mounted by the glide planes of a Pegasus liner and have been used in Pegasus experiments such as the LLNL Microspall series of experiments and the Los Alamos Disrupted Hydrodynamics (DH) series of experiments [2,3].

2 Adhesive Bonded Joints

It is important to keep excess assembly adhesive from being pushed into active working volumes of adhesively bonded liner driven loads. It is often important to generate optically transparent joints for diagnostic purposes and to have joints that are capable of handling gas pressure. To achieve these objectives, a unique family of adhesive joints has been designed. The design of these joints (Fig. 1) is self-aligning. Excess adhesive and air is squeezed out of holes and vents as the parts are assembled. The mating parts are made with a slightly diverging taper that reduces clearance to almost zero as the joint begins to close. This feature forces the adhesive to flow toward the vents and keeps adhesive from flowing into undesirable areas. When done carefully, no air is trapped in the joint and adhesive is not displaced to the interior. We use an ultraviolet (UV) light curing acrylic adhesive that is a good optical, x-ray, and chemical match to acrylic components. Other types of adhesives are used as needed.

Subassemblies are joined using several different means to fix various components. UV light cured adhesive is of great advantage in many of these operations. One can assemble, adjust and clean parts before the curing process.

Pegasus experiment PH-1 was designed by AWE/UK. The acrylic pieces used in the load assembly were fabricated by conventional machining. Computer Numerical Control (CNC) machining and CNC air bearing machining are also used to provide the precision plastic parts needed for the type of load shown in Fig. 2. Acrylic cylindrical shells, half shells and end caps are assembled to create abrupt radial steps in the walls of a hollow acrylic cavity.

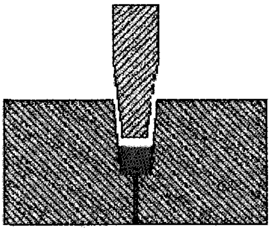

Figure 1. Self aligned joint

Conventional machining, CNC machining and CNC wire Electron Discharge Machining (EDM) are used to create assembly fixture parts such as that shown in Fig. 3 which was used to position the half shells of the DH-1 experiment for bonding. Special and unique fixtures are often indispensable for the assembly of unusual load designs. Many of these tools are used only once and it is thanks to our rapid machine capabilities that these unique tools are possible.

Fixtures can be simple. In Fig. 4 a rubber band holds an acrylic half cylinder to an acrylic full cylinder for adhesive bonding.

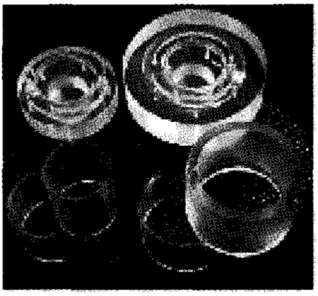
Figure 2 Acrylic cylindrical shells

Components of the LLNL designed Pegasus experiment LLNL-1 were manufactured and assembled in the same manner as those of DH-1 except that the acrylic assembly contains an Aluminum hollow cylinder. Straight wires of Stainless Steel, Cu and Ta were heat shrunk into high aspect ratio holes drilled through the Al cylinder wall, parallel to the cylinder axis. Ends of the mm diameter wires can be seen in Fig. 5. The Al cylinder also has a gold marker stripe electroplated onto the interior surface.

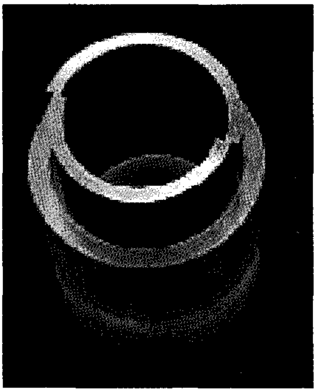
Figure 3 Wire EDM machined alignment fixture.

The photo Fig. 5 shows a finished LLNL-1 liner driven experiment insert. Both interior and exterior acrylic end cap surfaces are optically clear and flat, generated by a CNC air-bearing lathe with single point diamond tooling to achieve optical finishes of 1-2 micro inches RMS. The acrylic assembly is bonded gas tight and is filled with a few atmospheres of inert gas for the Pegasus liner driven hydrodynamic experiment.

3 Gallium Filling Operations

Liquid gallium has been used in Pegasus liner driven experiments as a dense metal with no strength. Gallium is one of the few materials that expand when solidified. Parts must be maintained at a temperature well above the Ga melting point of 29.8 °C. Preheated parts and a hand type heat gun are used to maintain the proper temperature when filling.

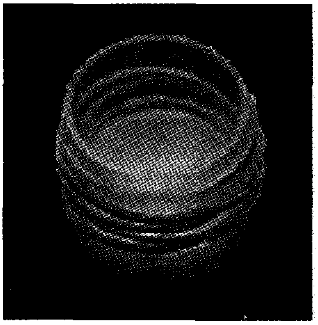
Figure 4. Rubber band Assembly

Gallium filling operations are conducted in vacuum. The preheated part to be filled with gallium is placed into a vacuum chamber, Fig. 6. A syringe with a long hypodermic tube is inserted through a custom vacuum tight fitting into the fill cavity in the plastic part. The chamber is evacuated and warm, liquid gallium is slowly injected by syringe to completely fill the cavity. Gallium has a very high surface tension and does not readily wet the plastic.

After filling the cavity of the experiment load with liquid gallium, liquid UV curing adhesive is floated on top of the gallium in the cavity fill hole and then cured with UV

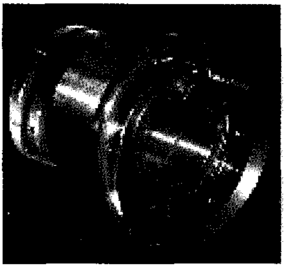

Figure 5. Finished load

Figure 6 Gallium fill apparatus

light. UV curing the floated adhesive is the first stage of sealing the gallium cavity. The entire part is then placed into a UV light-curing station for 2 hours and then is heat cured for at least 12 hours at 50 °C. We have found through experimentation that this prolonged heat cure is necessary to achieve full cure and therefore structural integrity. Gallium filled Pegasus loads are maintained at a temperature above the gallium melting point until they have been used in an experiment, for many months in some cases.

4 Pegasus Gas Fill System

The gas fill system is simple, utilizing the vacuum of the experimental chamber to evacuate the load. Components of the fill system include valve manifold, pressure transducer, digital read out, Conflat port feed through, polyurethane tubing, target, and a gas supply with a regulator.

The electronic pressure transducer readouts are not Electro Magnetic Pulse (EMP) hardened and must be removed from the experimental area prior to shot time. The timing of the shot must be anticipated and the monotonic drop in gas pressure must be accounted for when filling the target with gas.

5 Conclusion

We have developed composite multi-chamber loads, which can be filled with liquids and sealed, in our assembly laboratories. Some loads can be also be filled with gasses at the experiment site. We have developed gas and liquid tight, optically clear, fillet free, structural adhesive joints for pulse power experiments and also for laser driven experiments.

The Los Alamos Polymers and Coatings Group research, design and manufacturing capabilities in the areas of precision machining, electroplating, physical vapor deposition, chemical vapor deposition, polymer synthesis-fabrication, and target assembly processes, allow complex and complete target assemblies to be manufactured and characterized in our facilities. The integrated internal knowledge of these capabilities often allows the group to suggest experiment design improvements.

Acknowledgement

This work is supported by the U.S. Department of Energy under contract number W7405-ENG36 LA-UR-98-1326

References

1 Shlacter, J. S., et al., Pegasus II Experiments and Plans for the Atlas Pulsed Power Facility, Proc. 11th IEEE International Pulsed Power Conference, (1997).

2 Chandler, E. A., et al., Use of the Pegasus z-pinch machine to study inertial instabilities in aluminum: a preliminary report, D W 6th International Conference on the Physics of Compressible Turbulent Mixing, Marseilles, France, (June 18-20, 1997) (UCRL-JC-127667) [Published in Proceedings book].

3 Obst, A. W., et al., Performance of the Multi-Pulse X-ray Imaging System for the Pulsed Power Hydrodynamic Experiments at LANL, 85 Proc. 11th IEEE International Pulsed Power Conference, (1997).

CAGEN: A MODERN, PC BASED COMPUTER MODELING TOOL FOR EXPLOSIVE MCG GENERATORS AND ATTACHED LOADS

J. B. CHASE, D. CHATO, G. PETERSON, P. PINCOSY
CARE'N CO., Tracy, CA, USA

G. F. KIUTTU
AFRL, Phillips Research Site, Kirtland AFB, USA

We will describe the PC based computer program CAGEN. CAGEN models the performance of many varieties of Magneto-Cumulative-Generators (MCG) or Magnetic Flux Compression Generators (FCG) that are energized with High Explosive (HE). CAGEN models helical wound or coaxial types, which have HE on the interior. Any materials and any HE types may be used. The cylindrical radius of the windings (or outer conductor) and the radius of the armature may vary with axial position. Variable winding width, thickness, and pitch can be represented, and divided windings are allowed. The MHD equations are used to advance the diffusion of magnetic field into the conductors in order to compute resistance, melting, and contact effects. Magnetic pressure effects are included. The MCG model is treated as part of a lumped circuit, which includes the priming circuit, an opening fuse switch, an inline storage inductance, a transformer or a voltage dividing fuse, peaking-circuit, and several interesting load models. A typical problem will complete in a few seconds to a few minutes. Graphical input, run control, and analysis of results is provided by MathGraf, which is a CARE'N CO. application.

1 Introduction

For decades, HE driven MCGs have been used for experiments that required enormous delivered electrical energy (Megajoules) at modestly high electrical power (Terawatts) or at least high energy/power for the size/weight allowed for the source. There is a very large literature base [1] on such applications and the device technology associated with them. The simulation and modeling of these interesting devices and the circuits to which they have been attached is not nearly so advanced as the technology itself. Large axisymmetric (2-D) hydro-codes have had the MHD approximations to Maxwell's equations incorporated and have been applied to the truly axi-symmetric devices called coaxial MCGs. The simulation results have been, at times, remarkably good [2]. Most interesting applications of MCGs utilize the helical wound MCG because of the high gain offered. These devices are not axisymmetric, although they have some characteristics that are axisymmetric. At this writing, there are no 3-D simulations of this device, although several organizations are actively pursuing this goal. There can be no 2-D simulations of these 3-D constructions, only models. However, 2-D models of these "almost" symmetric helical wound MCGs have appeared in several publications [3]. CAGEN is such a code - with a difference.

2 Description of CAGEN

1.1 The Circuit

The evolution through time of the parameters determining the dynamic state of the generator and the other components of the circuit is computed by integrating the simple difference equation representing each state, starting from their initial values. The difference equations are the voltage loop equations. Although some components are not dynamic, most change with their temperature and configuration. Each component is represented in Fortran by an individual subroutine. Consequently, model changes are quite modular. All time scales are supported by sub-cycling each activity at a rate needed to resolve the fastest time scale. For example, the loop equations are cycled fast enough to resolve the shortest resonance available.

2.2 *The Generator*

The generator is conceptually sliced into disks of variable thickness placed perpendicular to the pseudo-symmetry axis. All hydrodynamics parallel to the axis are ignored. However, all of the important dynamics are included. The HE region is assumed to be surrounded by a metal, electrically conductive layer, and both are assumed to be exactly axisymmetric. The HE expands the metal armature according to a tabulated acceleration profile obtained by various methods including the Gurney relation. The outer winding region, the stator, is encountered by the outward moving armature forming a first contact point which moves smoothly from left to right. "Turn splitting" is allowed, and windings may have circular or rectangular cross section. The diameters of the armature and stator may vary with position along the axis.

2.3 *Inductance and Resistance*

The inductance of the generator is evaluated at every moment from tables and analytic fits from Grover [4]. The resistance is much more complicated. Our solution is one of the unique features in CAGEN. Within each axial zone (the disks), the armature and the stator are sub-zoned from their surfaces into their interior. The MHD equations are solved over these sub-zones to determine the fully dynamic configuration of the penetrating magnetic field and the current distribution. The circuit resistance is determined from the field distribution. Heating of each sub-zone is computed and the conductivity is adjusted appropriately. The shape of the conductors and the proximity of the nearby conductors are accounted for. A "contact" resistance is computed from the loss of magnetic flux contained within the conductors as the contact point moves along.

2.4 *The Opening Switch*

There are three opening switch systems available: a Bulk Electrically Exploded Fuse (BEEF), a Bulk Explosively Formed Fuse (BEFF), and an MHD modeled Electrically Exploded Fuse (MHDEEF). The BEEF incorporates no hydrodynamics but includes such effects directly in the "EOS" for the resistivity table that is a function of Joule heating specific energy. The EOS can be provided from an experiment. The BEFF uses a resistance versus timetable for its function, while the MHDEEF computes the explosion of the foil in 1-D dynamical detail.

2.5 *The Transformer*

The transformers modeled are an air-core tape wound auto-transformer and a wire wound air-core type. The inductances are computed from Grover tables or are specified by the user.

2.6 *The Closing Switch*

The closing switch operates discontinuously when one of two conditions is met: the voltage across the switch exceeds the breakdown value provided, or the time exceeds that which is provided. The rise time of the current through the load is determined by the explicit components specified.

2.7 The Load

The load models available include an unvarying resistance and inductance, a Bulk Electrically Exploded Fuse (BEEF), a Bulk Explosively Formed Fuse (BEFF), a resistance derived from an electrically exploding foil modeled with a 1-D MHD solver (MHDEEF), and a resistance computed from the Child-Langmuir equation.

3 Benchmark Calculations

Very few adjustable parameters are available in CAGEN for the MCG model. The most prominent is a multiplier on the contact resistance where the exact physics is dubious. Other less obvious parameters are associated with the material specifications such as the resistivity and heat capacity. The inductance is quite accurate except where either strong 3-D effects are at play, or when structures exist not modeled in the code. Sometimes the inductance must be modified to compensate. However, the purpose of a model code is to initially guess at the performance of an MCG and then to be benchmarked against some appropriate experiment. The following is an example benchmark comparison.

1.1 The Minigen

The mini-generator [5] was approximately 2 inches in diameter. It had no turns splitting and was wound with constant diameter copper wire at a constant pitch. This example represents a system of quite high flux that displays very high internal resistive flux loss. Fig. 1 shows the current comparison between model and experiment. The contact resistance factor was set to 1.0. It is clear that some additional loss mechanism is at work in this experiment. This experiment was particularly interesting because of the careful measurement of both the terminal voltage and the voltage between two nearly adjacent turns near the terminal end of the MCG. Fig. 2 shows the turn-to-turn voltage (shown converted to E field) and Fig. 3 is the terminal voltage. The time has been shifted to make the currents match.

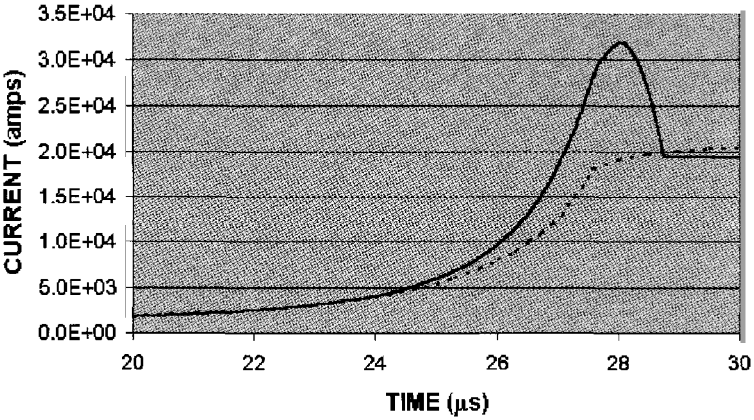

Figure 1. CAGEN calculation compared to the measured current (dotted line) for the mini-generator.

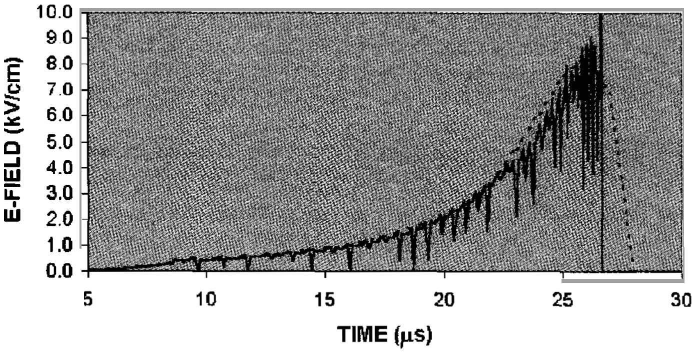

Figure 2. CAGEN calculation compared to the measured 2-turn electric field (heavy line) for the mini-generator.

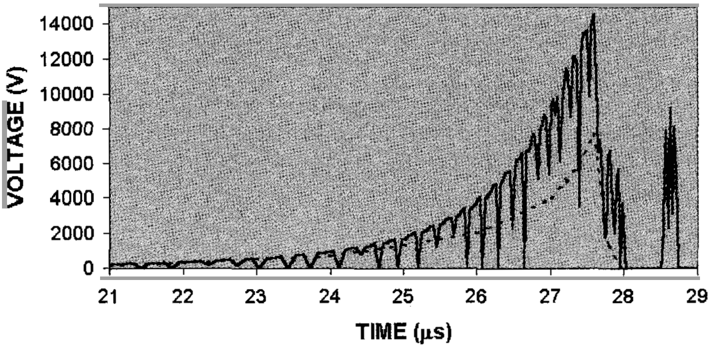

Figure 3. CAGEN calculation (dotted line) of the terminal voltage compared to the measured value for the mini-generator.

4 The Full Circuit

When the generator model is being solved in concert with the full circuit, an integrated, tightly coupled, self-consistent solution is obtained. As an example, Figures 4 and 5 show some of the dynamic parameters for an MCG driving the primary loop of a tape wound transformer in series with an electrically exploded fuse. In Fig. 4, the heavy line is the decreasing inductance of the generator, and the small dashed line is the generator resistance. The resistance curve clearly shows the collision of the armature with the stator windings at the point when the inductance is at about half value. This is where the contact resistance begins to take effect, since only then can flux be lost behind the contact point. Later, the generator resistance falls with decreasing generator length and at each winding splitting point. The thin solid line is the current flowing in the primary loop while the heavy dashed line is the resistance of the fuse. The fuse is sized to transition to a vapor at the point where the inductance of the generator is near zero. Thus, the full voltage generated across the fuse is seen by the primary of the transformer. The voltage across the self-closing break down switch becomes very high before it shorts, placing the load onto the transformer and shorting out the fuse. That is why the fuse does not re-strike. Fig. 5 shows the two other currents: the peaking circuit current and the load current. Before the closing switch closes, current flows into and out of the peaking capacitor, producing a net residual charge. When the switch closes, the initial rapid rise in the current through the load is due to energy flowing from the capacitor, while the second peak is due to the magnetic energy stored in the transformer.

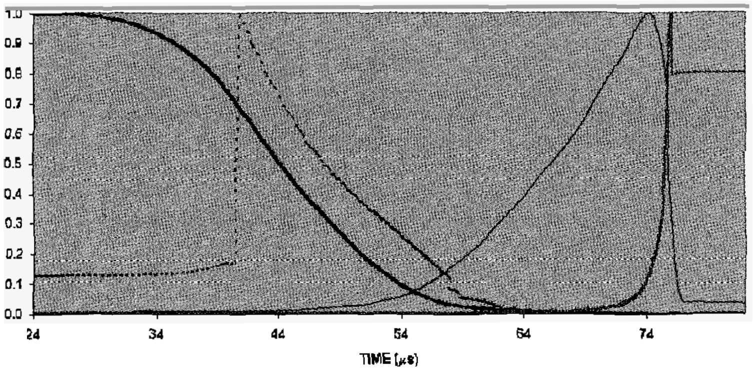

Figure 4. CAGEN circuit values showing generator inductance (heavy line decreasing from the left), generator resistance (dashed line abruptly increasing from the left), current (thin line increasing from middle), and the fuse resistance (line abruptly increasing on the right).

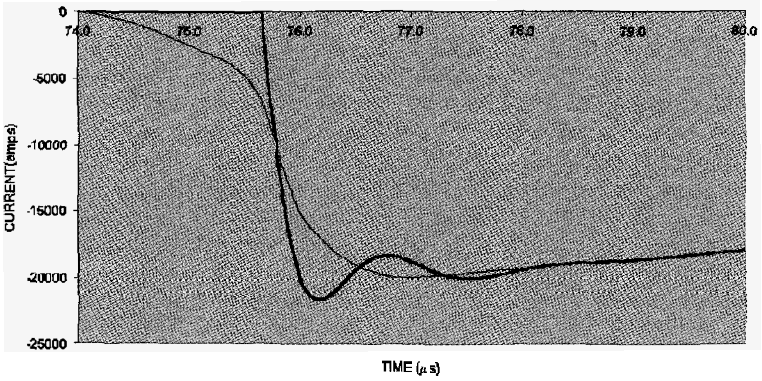

Figure 5. CAGEN secondary currents for the same circuit showing the peaking circuit current (thin line) and the load current (heavy line).

5 The Input to Cagen

Input is via a graphically assisted menu system. It is intended to be very nearly self-documented. As development continues, features will enhance and perfect the ease of building a new problem and repeating an existing problem while exploring the effects of some parameter. When all pages used to determine all of the parameters have been entered, the problem can be run by typing "crun". Progress is reported via a separate window. When the problem is done, in a few seconds to minutes, CAGEN stops in the analysis state and waits for plotting instructions.

6 Conclusions

CAGEN is a very competent model code that can be used to design MCGs and the attached application circuit. The code is still under development with improvements driven by current applications. Written in Fortran, it is very portable, and currently operates on the PC-Pentium platform. MathGraf provides the graphical input engine. The output phase depends upon MathGraf's forte: very fast interactive Math-Graphics.

References

1. See the proceedings of the International Megagauss Technology and Pulsed Power conference series, and the IEEE Pulsed Power conference series.
2. Tipton, R. E., A 2-D Language MHD Code, Megagauss Technology and Pulsed Power Applications, Ed. by C. M. Fowler, R. S. Caird, D. J. Erickson, Plenum Press, 1987, P. 299.
3. Chase, J. B., CIRC: A Specialized Circuit Analysis Computer Simulation Program for a High Explosive Generator Model. ibid., p. 397. Cowan, M. Kaye, R. J., Finite-Element Circuit Model of Helical Explosive Generators, Ultra High Magnetic Field Physics, Technology and Applications, Ed. by V. M. Titov, G. A. Shvetsov, Moscow, *Nauka*, 1984, p. 240. McGlaun, J. M., et al., COMAG-III: A 2-D MHD Code for Helical CMF Generators, Megagauss Physics and Technology, Ed. by P. J. Turchi, Plenum Press, 1979, P. 193. Novac, B., Smith, I. R., Cenache, M., Stewardson, H., Simple 2-Dimensional Model for Helical Flux Compression Generators, Seventh International Conference on Megagauss Magnetic Field Generation and Related Topics, August, 1996.
4. Grover, F. W., Inductance Calculations, Instrument Society of America, 1981.
5. Pincosy, P. A., et al., Testing and Performance of a High Gain Flux-Compression Generator, Megagauss Fields and Pulsed Power Systems, Nova Science, 1990, p. 411.

AN INTEGRATED SOFTWARE PACKAGE FOR THE DESIGN OF HIGH PERFORMANCE PULSED MAGNETS

J. VANACKEN, LI LIANG, L. TRAPPENIERS, K. ROSSEEL,
W. BOON, F. HERLACH
Laboratorium voor Vaste-Stoffysica en Magnetisme, Katholieke Universiteit Leuven,
Leuven, Belgium

The different aspects of pulsed magnet design have been combined in a single, user-friendly package by means of a VISUAL BASIC shell. At the basis are four FORTRAN codes, which calculate the field distribution and basic coil parameters, the discharge of a capacitor bank into the coil, and the stress distribution at the mid-plane of the coil including winding pre-stress, thermal expansion and plastic deformation. Stress and strain are calculated both at peak field and after the pulse.

1 Introduction

The design of a pulsed magnet is governed by the following constraints: (i) the coil must be matched to the power supply (here we use a capacitor bank) to generate the desired field, (ii) the pulse duration should be adjusted to avoid overheating in order not to damage the insulation, (iii) the coil structure should be sufficiently strong to contain the magnetic forces without undue deformation. While the stresses in wires and reinforcements must not exceed the Ultimate Tensile Stress limit (UTS), plastic cycling must be limited in order to obtain a longer service life of the coil. This paper describes a software package that allows the design of pulsed magnets that reliably generate high fields in the 50-100 T range.

2 Methodology for the Design

The software package brings together four FORTRAN codes [1] in a user-friendly VISUAL BASIC shell. The input to the shell program is the configuration of the coil structure (layer by layer) and of the capacitor bank. The latter can be omitted if only the deformation is calculated. Four components, compiled from fast FORTRAN codes, calculate the *electrical properties* of the proposed coil, simulate the *discharge* including *coil heating*, calculate the stress at *peak field* and *after the down sweep*. The latter gives information on the residual stress and the extent of plastic deformation. Each program component offers the possibility to visualize the results such that adjusting electrical and structural parameters can iterate the design process.

1.1 Configuring the Coil Layer Structure

The design of the coil involves many degrees of freedom as illustrated in the design menu on Fig. 1. The bore diameter, coil length and the desired maximum field are the three basic input parameters. The coil is defined by alternating layers of conductor and reinforcement. The thickness of the reinforcement materials can be changed continuously, and using the "separate" check box, a separation (e.g., a Teflon layer) can be added. The present version of the program allows the use of 2 types of conductor and 2 types of reinforcement in each coil; these can be selected from an extensive library of materials. All physical properties of the materials, which are needed for the calculation, are stored in a user-definable database.

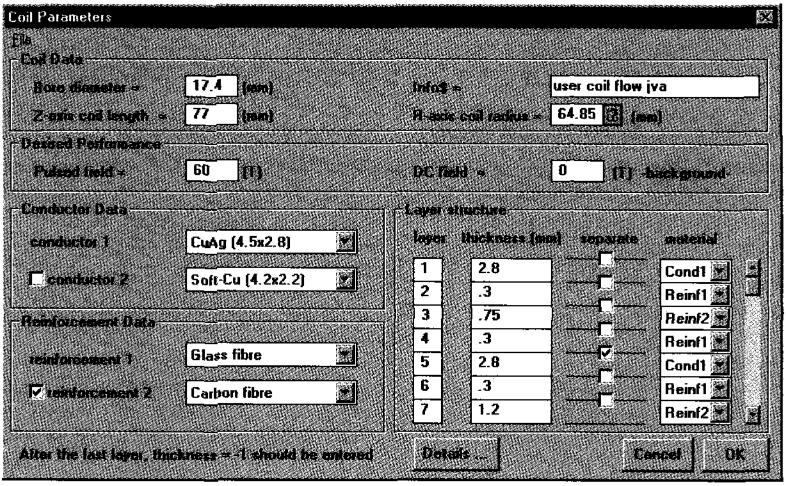

Coil Data

Bore diameter = 17.4 (mm)

Z-axis coil length = 77 (mm)

Info$ = user coil flow jva

R-axis coil radius = 64.85 (mm)

Desired Performance

Pulsed field = 60 (T)

DC field = 0 (T) -background-

Conductor Data

conductor 1: CuAg (4.5x2.8)

☐ conductor 2: Soft-Cu (4.2x2.2)

Reinforcement Data

reinforcement 1: Glass fibre

☑ reinforcement 2: Carbon fibre

Layer structure

layer	thickness (mm)	separate	material
1	2.8	☐	Cond1
2	.3	☐	Reinf1
3	.75	☐	Reinf2
4	.3	☐	Reinf1
5	2.8	☑	Cond1
6	.3	☐	Reinf1
7	1.2	☐	Reinf2

After the last layer, thickness = -1 should be entered

Figure 1. The coil design parameter window.

As an example, we describe the design of a coil which (i) generates a peak field of $B_{max} \sim 60$ T with (ii) an energy of $E \sim 250$ kJ, (iii) a bore diameter of 17 mm and (iv) a pulse duration of 20 ms. To reduce the deformation and thus increase the service life, this design uses a strong CuAg micro-composite wire [2] combined with carbon fiber reinforcement. This has a high modulus of elasticity that is a better match to the stiff CuAg wire; the modulus of elasticity of glass fibre is about one half of that of carbon fiber. The shortcoming of carbon fiber is its electrical conductivity. As shown in Fig. 1, this problem was solved in our example coil by sandwiching each carbon layer between 2 thin insulating glass fiber layers. Combining materials and adjusting the thickness of each reinforcement layer distribute the stress efficiently throughout the coil structure. Details of this example coil (serial number Mel83) are described by Li [3].

1.2 Calculations and Graphical Output

The modelling is initiated by the calculation of the essential coil properties: (i) the coil *inductance,* (ii) the coil *resistance* at T = 300 K and T = 77 K, (iii) the *current versus field* (I/B) factor and (iv) the field *homogeneity*. The calculated inductance and resistance match those measured after construction of the coil within 10 %. With this data, the energy can be estimated which will be stored in the magnet at peak field. The next step is the *stress calculation* to determine the allowable *peak field* and the *stability* of the coil. By increasing the field in small increments, the hoop stress, radial stress and axial stress are calculated in the mid-plane of the coil. During this calculation, it is checked if the reinforcement layers will be stressed beyond their yield point (3 GPa for C-fiber, 2.6 GPa for glass fiber).

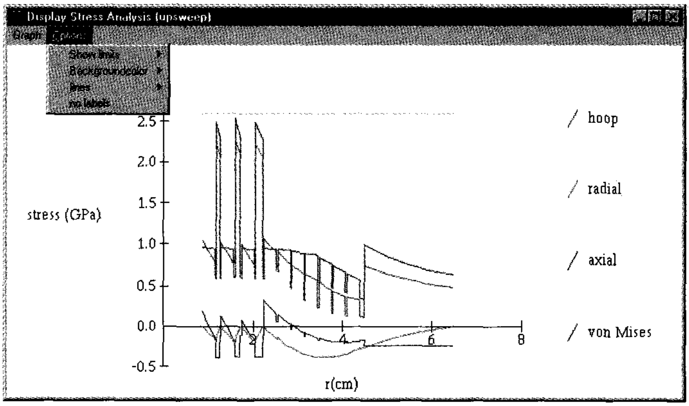

Figure 2. The visualized information of the stress at peak field calculation

Fig. 2 shows the stresses at peak field (at B = 60 T). It can be seen that the reinforcement layers are taking up large stresses, almost up to 2.5 GPa. The criterion for material failure is not simply when any of these stresses exceed a critical limit, it is rather an appropriate combination of these; the combination used in this code is the von Mises stress. Since the von Mises stress in the first three layers (which consist of C-fiber) is always below 3 GPa, and in the other layers (glass fiber) always below 2.6 GPa, Mel 83 is expected to survive the forces encountered in a 60 T pulse. The next step is usually to check if the existing capacitor bank is able to generate the desired field. This can be done by going to another menu of the PMDS shell. The result of this calculation is visualised in Fig. 3. Besides the pulse shape, the program also calculates the local heating inside the coil, always in the mid-plane where both the stress and the heating are highest. Both graphical outputs allow the designer to determine if the desired field can be reached without overheating. As can be seen in Fig. 3, even the initial sharp peak in dB/dt is predicted. This is due to the skin effect, which is incorporated in the code.

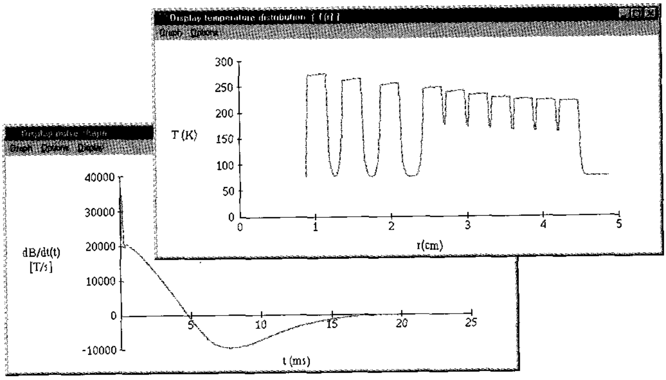

Figure 3. The predicted dB/dt versus time (below) and the predicted coil heating T(r).

3 Conclusions

During a period of several years, we have developed a useful tool for the design of pulsed field magnets. This is the basis of the code described in this paper, which allows determination of all-important parameters and the performance of the coils (inductance, resistance, B/I ratio, stresses and elongation, heating, pulse shape). The procedure has been successfully used for the design of user coils, which provide fields up to 60 T with a service life of up to 1000 pulses.

Acknowledgments

J. V. is a post-doctoral fellow of the FWO; L. T. is a research fellow of the IWT.

References

1. Deformation analysis of pulsed magnets with internal and external reinforcement, Li, L., Herlach, F., *Meas. Sci. Technol.* **6** (1995) p. 1035.
2. Showa Electric Wire & Cable Co., Japan.
3. Li, L., Ph. D. thesis K. U. Leuven 1998.

NUMERICAL SIMULATION OF OPERATION OF MAGNETOCUMULATIVE GENERATORS WITH HIGH ENERGY GAIN

A. S. KRAVCHENKO, YU. V. VILKOV
VNIIEF, Sarov, Russia

One-dimensional numerical calculations of helical magnetocumulative generators (MCG) are presented in this report. During the creation of this calculation method, it was noted that magnetic flux density does not exceed 100 T in helical MCGs operating in the regimes of energy amplifiers and generators. Liner braking can be neglected in such a field. This substantially simplifies the description of such MCG operation. Current losses in these generators are determined by intercepting magnetic flux located in the conductor material and inter-coil insulation. We believe that exactly these losses drive the process of current rise in the generator. In helical MCGs where inductance decreases relatively smoothly and there is an absence of electrical breakdowns during generator operation, geometrical parameters of the helix and central tube accurately determine the flux value, remaining beyond the contact point. Calculation results are compared with the experiment. For flux skin-layer values less than the radius of the stator conductors the method shows good agreement between calculations and experimental results.

1 Introduction

High specific characteristics of MCGs make them irreplaceable in high energy-density physics experiments. Due to the fact that the level of MCG development allows us to perfect energy sources, simulating MCG operation processes could significantly decrease the energy content of these generators.

2 Description of Calculation Model

Very often, magnetic flux density does not increase beyond 100 T in helical magnetocumulative generators (HMCG) operating in the regimes of amplifiers and energy generators. The pressure of such a field can in first approximation be neglected. This significantly simplifies the description of the HMCG operation. Thus, the following equation could be written for the HMCG operation into an inductive load

$$(L_G + L_L)\cdot\frac{dI}{dt} + \left(\frac{dL_G}{dt} + R\right)\cdot I = 0 \tag{1}$$

where L_G - generator inductance, L_L - load inductance, R - coefficient that describes the active generator impedance and magnetic flux losses in HMCG contour. Active helix impedance can be determined as the sum of the impedance of each section to the alternating current with the frequency $f = \frac{dI}{dt}\Big/\pi I$. Estimations [2] show that the central tube can increase the generator active impedance by approximately 1.5-2 times in comparison with the stator impedance. The magnetic flux, which is insulated in the helix coils and in the conducting material of the solenoid and central tube and is located outside of the contact point does not take part in the process of flux compression. The value of the magnetic flux determines the current rise process in the generator. Considering the helix generator operation in electro-technical approximation, the process of flux intercepting, which is in the conductor material and intercoil insulation, can be included into the equation describing the operation of an ideal generator as an additional factor $\frac{dL_S}{dt}\cdot I$

[2]. We believe that, in most cases, exactly these losses determine the *R* coefficient value in Equation (1). Equation (1) can then be written as:

$$(L_G+L_L)\cdot\frac{dI}{dt}+\left(\frac{dL_G}{dt}+\frac{dL_S}{dt}\right)\cdot I\approx 0\ . \qquad (2)$$

Thus, in the first approximation, Equation (2) describes the current rise process in a helical generator with a contact point moving along the insulated helix coils, as in the case of HMCG operation in an inductive load. Accounting for the effect of the central tube, the inductance value of a multi-section helical generator can be presented as:

$$L_G=(L_1+L_{12}+...+L_{1n})\left(1-\frac{V_{1T}}{V_{1C}}\right)+...+(L_{n1}+L_{n2}+...+L_n)\left(1-\frac{V_{nT}}{V_{nC}}\right), \qquad (3)$$

where L_i - inductance of the *i*-st section, L_{ij} - mutual inductance between the *i*-st and *j*-st sections, V_{iC} - i-st section volume, V_{iT} - volume occupied by the central tube under the *i*-stsection. Inductance of the *i*-nd section and the mutual inductance value between the *i*-st and *j*-st solenoid sections could be calculated using the formulas presented in [3]. In the helical MCGs with relatively smooth inductance output and absence of electrical breakdowns during generator operation, the value of the flux remaining behind the contact point is determined with good precision by the geometrical parameters of the helix and central tube.

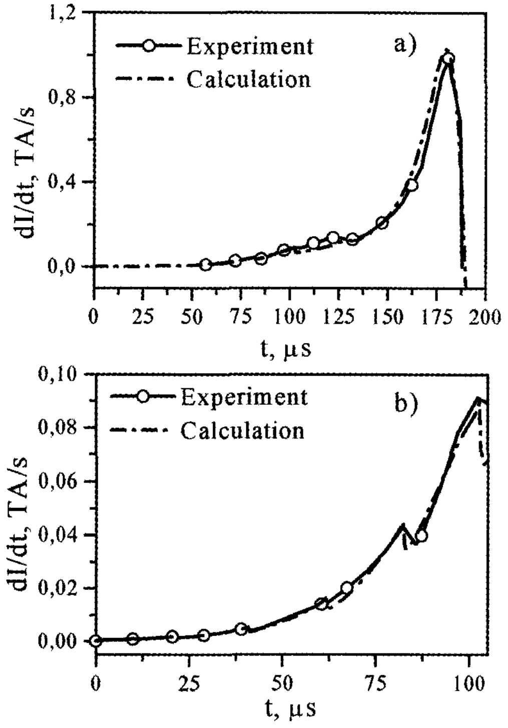

Figures 1 a) and b). Generator experiment *vs* calculations.

3 Comparison of Some Experimental Data with Calculations

One of the examples presented in this paper describes the results of the generator experiment, the helix of which consists of seven sections [1]. The helix diameter is 161 mm, external diameter of the central tube is 80 mm and length of each section is 156 mm. The generator worked with an inductive load of 8 nH. The calculated and experimental curves of the current derivative in the load are presented in Figure 1a. Figure 1b shows precisely the same curves at the operation period of the first five helix sections.

For comparison we took the experimental results of the Mark VIII generator [4]. Figure 2a shows calculated and experimental curves of the current derivative for the operation of this generator into a load of 160 nH. Figure 2b shows calculated and experimental curves of the current derivative at the operation of this generator into a load of 750 nH. The decrease of current derivative at the sections joints is connected with a sudden (2 times) increase of the coil pitch of the helix wire.

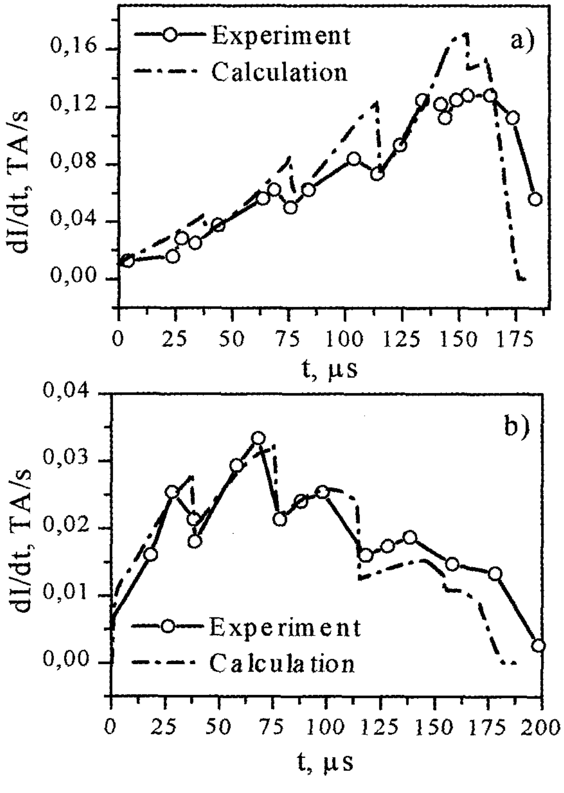

Figures 2 a) and b). Experimental results of the Mark VIII Generator *vs* calculations.

4 Conclusion

The presented method of one-dimensional numerical calculations of helical magnetocumulative generators gives good agreement of calculated and experimental results at an energy level of ~15 MJ.

References

1. Pavlovsky, A. I., Ludayev, R. Z., Magnetic Cumulation, *Issues of Modern Experimental and Theoretical Physics. L.*: Nauka, (1984) pp. 206-270.
2. Cowan, M., Kaye, R. J., Finite-Element Circuit Model of Helical Explosive Generators, Ultrahigh Magnetic Fields. Physics. Techniques. Applications, Ed. by V. M. Titov and G. A. Shvetsov. Moscow: Nauka, (1984) pp. 240-245.
3. Kalantarov, P. L., Tseytlin, L. A., *Raschyot Induktivnostey. L.*: Energia, (1970).
4. Degnan, J. H., Baker, W. L., Fowler, C. M., et al., Test of 10 Megajoule Electrical Output Magneto-Cumulative Generator, Ultrahigh Magnetic Fields. Physics. Techniques. Applications, Ed. by V. M. Titov and G. A. Shvetsov. Moscow: Nauka. (1984) pp. 352-358.

A FIELD-THEORY APPROACH TO MODELING HELICAL FCGs

C. M. FORTGANG
LANSCE-9, Los Alamos National Laboratory, New Mexico, USA

Often helical flux-compressor generator (FCG) design codes are essentially circuit codes utilizing known equations for parameterizing circuit elements such as armature and stator inductance. We present an analytical model based more on first principles. The stator inductance is calculated using a definition of inductance in terms of the magnetic vector-potential. The calculation accounts for winding-pitch and bifurcations, and works for any ratio of length to diameter. The armature current is calculated self-consistently and not assumed to simply 'mirror' the stator current. Resistive losses and magnetic diffusion losses are calculated less rigorously but we are working on better methods. Model details and comparison with experiment are presented.

1 Introduction

Modeling helical flux compression generators is not a new enterprise; many papers on this subject can be found in Megagauss conference proceedings [1-6]. We present a model and computer code that calculates generator inductance from first principles using magnetic vector potential. The calculation does not assume the stator pitch angle is small or that azimuthal currents flowing on the armature surface 'mirror' those flowing on the stator. The armature currents are calculated self-consistently. The stator and armature can be of arbitrary aspect ratio and the stator can have an arbitrary number of sections and parallel wires. Any spacing between wires is allowed and accounted for.

The model is presently linear. One consequence of this assumption is that heating effects are not calculated. Losses due to resistance and magnetic diffusion are included but not calculated with the same rigor as the generator inductance.

Here we discuss the most important features of the model, then compare the computer code results with experiments using two very different helical flux-compressors.

2 Stator Self-Inductance

By using Stokes Theorem, stator self-inductance can be expressed in terms of the magnetic vector potential, A.

$$L = \frac{\Phi}{I} = \int \frac{B \bullet dS}{I} = \oint \frac{A \bullet dl}{I} \tag{1}$$

The magnetic vector potential at any point in space, from a system of wires with known current densities, is given by

$$A(x,y,z) = \frac{\mu_o}{4\pi} \int_{Vol} \frac{J(x',y',z')\,dx'\,dy'\,dz'}{|r - r'|} \tag{2}$$

Consider n parallel wires, with pitch angle θ, on a cylinder of radius a, carrying a total current I. From Eq. (2) the vector potential from this set of wires, at any point in space, is

$$A_x(x,y,z) = \frac{\mu_o}{4\pi}\sum_j^n \int_{\phi_{j\,\mathrm{init}}}^{\phi_{j\,\mathrm{final}}} \frac{-\mathrm{I}\cos\theta \sin\phi_j\, a\,(1+\tan^2\theta)^{1/2}\,\mathrm{d}\phi_j}{\mathrm{n}\sqrt{(\mathrm{x}-\mathrm{a}\cos\phi_j)^2+(\mathrm{y}-\mathrm{a}\sin\phi_j)^2+(z-(z_{0i}+a\tan\theta\,(\phi_j-\phi_{j\,init})))^2}} \quad (3)$$

$$A_y(x,y,z) = \frac{\mu_o}{4\pi}\sum_j^n \int_{\phi_{j\,init}}^{\phi_{j\,\mathrm{final}}} \frac{\mathrm{I}\cos\theta \cos\phi_j\, a\,(1+\tan^2\theta)^{1/2}\,\mathrm{d}\phi_j}{\mathrm{n}\sqrt{(\mathrm{x}-\mathrm{a}\cos\phi_j)^2+(\mathrm{y}-\mathrm{a}\sin\phi_j)^2+(z-(z_{0i}+a\tan\theta\,(\phi_j-\phi_{j\,init})))^2}}$$

$$A_z(x,y,z) = \frac{\mu_o}{4\pi}\sum_j^n \int_{\phi_{j\,init}}^{\phi_{j\,\mathrm{final}}} \frac{\mathrm{I}\sin\theta\;\, a\,(1+\tan^2\theta)^{1/2}\,\mathrm{d}\phi_j}{\mathrm{n}\sqrt{(\mathrm{x}-\mathrm{a}\cos\phi_j)^2+(\mathrm{y}-\mathrm{a}\sin\phi_j)^2+(z-(z_{0i}+a\tan\theta\,(\phi_j-\phi_{j\,init})))^2}}$$

The integration variable φ monotonically increases with the number of wire turns. Z_{0i} is the initial z-position of the n wires. All wires in each section begin at the same z-position but have different initial values of φ, usually evenly spaced from mπ to (m+1)π. If the stator has bifurcations, thus multiple sections with different pitch angles, then there is an additional summation over sections.

The unit vector dl that points along a wire which lies on a cylinder of radius a, with pitch angle θ is given in either cylindrical or Cartesian coordinates by

$$\mathrm{dl} = \mathrm{a}\tan\theta\,\mathrm{d}\phi\,\hat{\mathrm{z}} + \mathrm{a}\,\mathrm{d}\phi\,\hat{\varphi} = \mathrm{a}\,\mathrm{d}\phi\,(\tan\theta\,\hat{\mathrm{z}} - \sin\varphi\,\hat{\mathrm{x}} + \cos\phi\,\hat{\mathrm{y}}) \quad (4)$$

With expressions for the components of **A** at any point in space, and the unit vector dl that defines the direction of a stator wire, we can use eq. (1) to calculate the stator self-inductance.

$$\oint A \bullet dl = \oint_{stator} (-A_x(r_{wire})\sin\phi + A_y(r_{wire})\cos\phi + A_z(r_{wire})\tan\theta\,)\,a\,d\phi \quad (5)$$

The vector $\mathbf{r}_{\mathrm{wire}}$ depends on the integration variable φ as follows

$$\mathbf{r}_{\mathrm{wire}} = (\mathrm{a}-\varepsilon)\cos\phi\,\hat{\mathrm{x}} + (\mathrm{a}-\varepsilon)\sin\phi\,\hat{\mathrm{y}} + (\mathrm{a}-\varepsilon)\tan\theta\,(\phi-\phi_{\mathrm{init}})\,\hat{\mathrm{z}} \quad (6)$$

The line integral is performed around the stator on the inside surface of the wire (a-ε). The exact value of ε is unimportant as the stator self-inductance depends weakly on the exact current distribution in the wire. We usually let ε = Δ-δ, where Δ and δ are the wire radius and a nominal skin depth, respectively. If there are multiple parallel wires in a section then the line integral follows one of those wires, usually the center one. Note that Eq. (5) is a double integral; each component of the vector potential at every point along the stator involves an integral over all current carrying conductors making up the stator. The implicit double integral provides the usual N^2 dependence of inductance on wire turns.

As the armature expands and stator turns are shorted out, the stator self-inductance is re-calculated as described above using a time-dependent initial starting position for the remaining turns. The numerical code calculating the stator-self inductance gives excellent agreement with analytic formulas for less complicated geometries.

3 Armature Mutual Inductance

The presence of the armature decreases the generator inductance. Azimuthal currents on the armature surface exclude flux from the armature interior. We calculate these currents self-consistently, without making the usual assumption that, as a function of z, the armature line-current density is equal and opposite of the stator line-current density. The expanding armature is broken into a series of rings, each with its own radius and current. Once the armature shorts to the stator, its effective length decreases, but the number of rings used to model the remainder of the armature is kept constant, thus maintaining spatial resolution at the end of the generator run when the armature is quite short.

The flux linking each armature ring is attributed to the stator current, the current of all the other rings, and the current in the ring itself. Stator flux linking a ring is calculated by integrating the stator vector-potential around the ring (Eq. (1). This line integral is done at a fixed z (the middle of the ring), thus only involving the x and y components of the stator vector-potential given in Eq. (3). Flux linking a ring due to the other rings is equivalent to a calculation of mutual inductance. Reference [7] describes how to calculate mutual inductance between coaxial circular filaments. We use the same procedure but include a second integration in z to include the effect of finite ring width. The self-flux of a ring is obtained similarly, but the z-location of the two rings coincides. After all three of these calculations are performed we write the flux linking the ith ring as

$$\Phi_i = \Phi_i^{stator} + M_{i,j} \, Jring_j \tag{7}$$

Here $M_{i,j}$ is the mutual inductance matrix and Jring is the vector representing the unknown values of the ring currents. Note that because we are dealing with rings, not filaments, $M_{i,j}$ and $Jring_j$ have units of H·m and A·m^{-1}, respectively. We now assert that the armature currents exclude all flux from the interior of each ring. After setting the LHS of Eq. (7) to zero and inverting the matrix $M_{i,j,}$ we can solve for the ring currents

$$Jring_j = -M_{i,j}^{-1} \; \Phi_i^{stator} \tag{8}$$

Using Eq. (2) we can now calculate the vector potential at any point in space due to the armature

$$Aarm_x(x,y,z) = \sum_i^{Nrings} \frac{\mu_o}{4\pi} \int_{zstart_i}^{zend_i} \left(\int_0^{2\pi} \frac{-Jring_i \, sin\phi \, b_i \, d\phi}{\sqrt{(x - b_i \, cos\phi)^2 + (y - b_i \, sin\phi)^2 + (z - zring_i)^2}} \right) dz \tag{9}$$

A similar expression can be found for the y-component. The vector b_i represents the radius of the rings and varies in time according to the expansion angle of the armature and detonation velocity of the high explosive [8]. The z-component of the armature vector potential is zero because the armature currents that contribute to flux compression are purely azimuthal. Finally, we calculate the mutual inductance between the armature and stator by doing the following line integral around the stator,

$$M = \frac{\oint_{stator} Aarm\,(x,\, y,\, z) \bullet d\text{l}}{I} \tag{10}$$

The results of this approach were checked against known solutions for simple cases of coaxial solenoids and excellent agreement was found.

4 Stator Resistive Losses

Ohmic losses in the stator are calculated similar to that found in references [4,9]. A time-dependent effective 'skin depth' (δ) is calculated based on a characteristic time constant τ

$$\tau(t) = \frac{I}{\partial I / \partial t}, \qquad \delta(t) = \sqrt{\frac{\tau(t)}{\sigma \pi \mu_0}} \qquad \text{where } \sigma \text{ is the wire conductivity} \tag{11}$$

$$R_{\text{stator}}(t) = \sum_{i}^{\#\text{ of Sections}} \int_{\phi_i^{\text{init}}(t)}^{\phi_i^{\text{final}}(t)} \frac{a(1+\tan^2\theta_i)^{1/2}\,d\phi}{n_i \pi\, r_w \delta_i(t)\sigma} \tag{12}$$

Here, r_w is the wire radius, θ_i is the pitch angle of section i, and n_i is the number of wires in parallel for section i.

5 Armature Resistive Losses

Armature resistive losses take into account both the circuit current I, flowing in the axial direction, and inductive current flowing in the azimuthal direction around each armature ring.

$$R_{\text{armature}}(t) = \sum_{i}^{\#\text{ of Rings}} \left(1+\left[\frac{\text{Jring}_i(t)}{I/2\pi b_i(t)}\right]^2\right)\frac{\Delta z_i(t)}{\sigma\, 2\pi\, b_i(t)\,\delta(t)} \tag{13}$$

Ring length and radius are time-dependent and given by Δz and b, respectively.

6 Magnetic Diffusion Losses

Magnetic flux loss is not due solely to resistive losses. Inside the conductors composing the armature and stator, at any time t exists magnetic energy (not available for flux compression) roughly equivalent to the integrated power, or energy, lost from joule heating. Only use of the problem geometry in solving the magnetic diffusion equation can give the exact relationship between lost magnetic energy due to flux diffusion and that due to resistive heating. However, it has been shown that for a wide range of geometries and time-dependent current profiles, flux losses due to these two mechanisms are nearly equal [10]. Presently, we estimate diffusion losses by assuming they are equal to armature and stator resistive losses. We are currently working on a model that explicitly calculates flux loss due to both joule heating and magnetic diffusion. This model solves the magnetic diffusion equation using an approximate geometry, and will introduce non-linear effects due to conductor heating.

7 The Circuit Equations

As with many flux compressor codes, a circuit model is solved to predict the generator performance. The most important terms in the circuit model have been discussed. The most general circuit we use for a FCG is shown below.

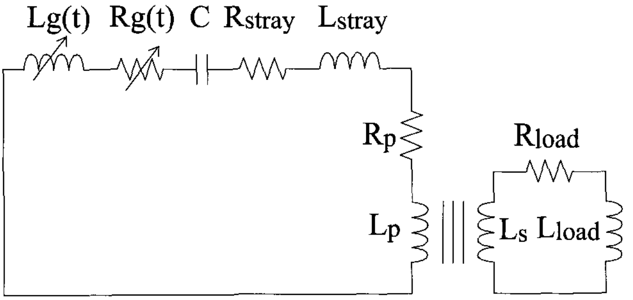

Figure 1. Circuit schematic for a helical flux compressor generator.

Many of the helical FCGs built at Los Alamos involve the use of an air-core transformer [11]. The primary, secondary, and mutual inductance are measured and used as circuit parameters in the model. The following two coupled-circuit equations are solved to obtain the results.

$$\int_0^t \frac{I_p}{C}\,dt + (L_p + L_g(t) + L_{stray})\dot{I}_p + I_p(R_g(t) + R_{stray} + R_p) + I_p\dot{L}_g(t) + M\dot{I}_s = 0 \qquad (14)$$

$$M\dot{I}_p + (L_s + L_{load})\dot{I}_s + I_s R_{load} = 0 \qquad (15)$$

Here I_p and I_s refer to the primary and secondary currents, respectively.

8 Comparison with Experiments

The MARK 9 generator [12] provides a benchmark as results and all-important parameters needed to model the device have been published. The stator ID is 35.6 cm and the armature OD is 17.3 cm. The overall length is 112 cm with 4 sections having 5, 10, 20, and 40 parallel wires, respectively. Other specifications can be found in the reference. Figures 2 and 3 show a comparison of the experimental data (taken from the graphs in the reference) and the simulation.

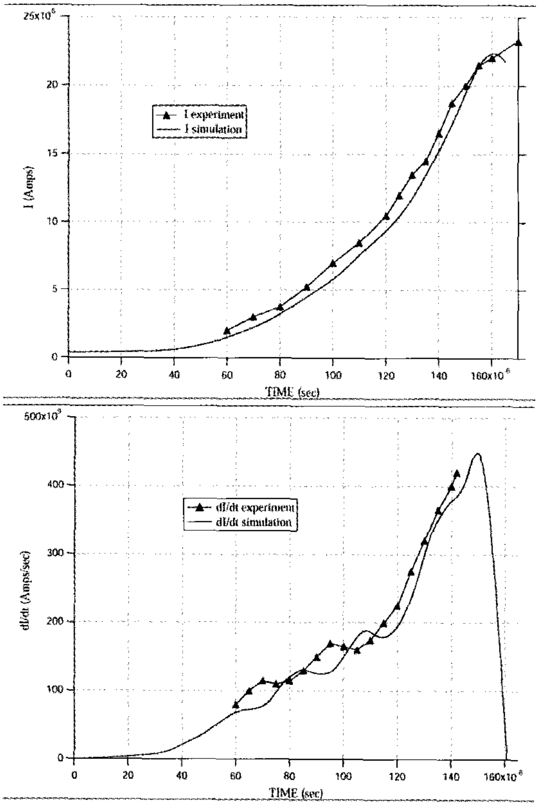

Figures 2 and 3. A comparison of experiment and simulation of I and dI/dt for the Mark 9 generator with a 56 nH load.

The simulation uses all parameters as listed in the original publication but includes an additional 1 mΩ of load resistance. Without this additional resistance, the agreement with experiment is still excellent until the last 15% of the generator run where the simulation diverges from the experimental data and peaks at 39 MA and 1x 10^{12} A/sec. Though the agreement as shown in Figures 2 and 3 appears excellent, the simulation's sensitivity to a small amount of stray resistance means that this result cannot validate the model.

Using our computer model, we have recently designed and tested a small generator. This 24 cm long generator has a stator radius of a 6.3 cm and an armature radius of 2.8 cm, and drives a 75 nH, 28 mΩ load. The stator has 4 sections with 1, 2, 4, and 8 parallel wires, respectively. Comparisons between the model and experiment are shown in Figures 4 and 5.

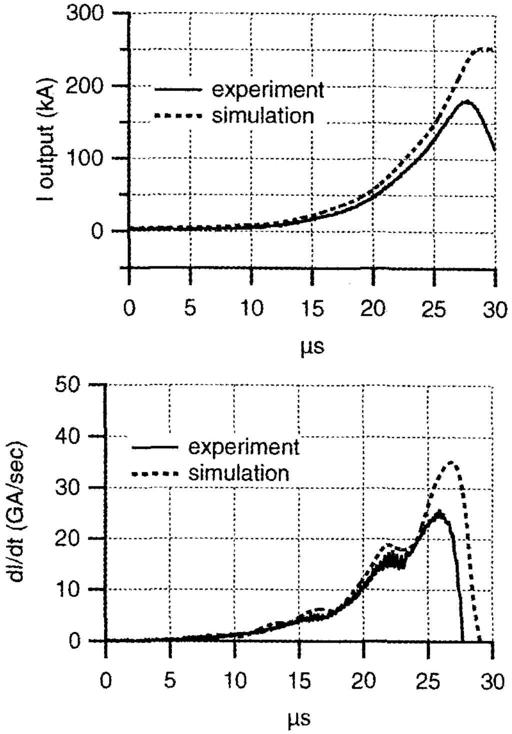

Figures 4 and 5. A comparison of theory and experiment for the LANL small generator.

Only measured load parameters are used for the simulation. Simulation results are insensitive to any stray resistance due to the relatively high (28 mΩ) load resistance. Thus, in contrast to the Mark 9 device, the small generator makes a better test for the model.

In fact, we assert that a good test of a generator model is to have it predict the performance of a generator driving a higher impedance load than normally optimum thus minimizing any anomalous loss that is either unknown or difficult to measure. It is possible, even likely, to have good agreement between theory and experiment with a high impedance load, and poor agreement with a low (or optimum) impedance load. One conclusion drawn from such a circumstance is that major effects included in the model are correct but smaller effects that play an important role with a low-impedance load either are not included or are not calculated accurately.

References

1. McGlaun, J., Thompson, S., Freeman, J., Proceedings of Second Inter. Conf. On Megagauss Magnetic Field Generation and Related Topics, Ed. by P. Turchi, Washington, DC, June 1979, p. 193.
2. Jones, M., *ibid.* p. 249.
3. Tucker, T. *ibid.* p. 265.
4. Freeman, J., McGlaun, J., Thompson, S., Cnare, E., *ibid.* p. 205.
5. Chase, J., Proceedings of Fourth Inter. Conf. On Megagauss Magnetic Field Generation and Related Topics, Ed. by Fowler, Caird, and Erickson, Santa Fe, NM, July 1986, p. 397.
6. Abe, D., Chase, J., *ibid.* p. 411.
7. Smythe, W., *Static and Dynamic Electricity*, (Hemisphere Publ. Co., New York, 1989)
8. Kennedy, J., Gurney Energy of Explosives: Estimation of the Velocity and Impulse to Driven Metal, Sandia National Laboratory, internal report SC-RR-70-790, 1970.
9. Pincosy, P., Abe, D., Chase, J., Proceedings of Megagauss Fields and Pulsed Power Systems (MG V), Ed. by V. Titov and G. Shetsov, Novosibirsk, USSR, July 1989, p. 441.
10. Knoepfel, H., *Pulsed High Magnetic Fields* (North-Holland, Amsterdam, 1970.)
11. Fortgang, C., Erickson, A., Goettee, J., A High-Voltage Pulse Transformer for Explosive Pulsed-Power Devices, in these proceedings.
12. Fowler, C. M., Caird, R., Proceedings of the Seventh IEEE Pulsed Power Conference, Ed. by R. White and B. Bernstein, Monterey, CA, June 1989, p. 475.

NUMERICAL SIMULATION OF MAGNETIC FLUX COMPRESSION IN HELICAL-CONE MAGNETOEXPLOSIVE GENERATORS

YU. N. DERYUGIN, P. V. KOROLEV, V. I. KARGIN, A. S. PIKAR, N. F. POPKOV, E. A. RYASLOV
All-Russia Scientific Research Institute of Experimental Physics (VNIIEF), Sarov, Russia

We present the results of calculations of the physical processes of magnetic flux compression in a magnetocumulative generator with a large diameter spiral. The generator considered is a modification of the one developed for the multimegajoule energy source and intended for the PIRIT-EMG stationary electrophysical facility, pumping a pulsed energy of 80 MJ. The development of the magnetocumulative generator required calculating its output parameters and optimizing the generator dimensions, choosing the form and calculating the shape and thickness, insulation type and electric strength of the spiral wire. The authors developed a program package to simulate the helical-cone generator operation and numerically investigate the physical processes occurring at magnetic flux compression. To calculate the liner scatter dynamics, Eulerian equations were solved for counter-running sliding detonation waves. The system of equations is integrated using a finite-difference method for 2-D stationary grids adapting to the peculiarities of the flow. The liner collision with spiral coils as well as the destruction of the insulation is considered in 2-D through a model of nonviscous gas without heat conductivity. The magnetic flux compression is calculated using the analytical solutions of dynamic tasks and a 1-D non-linear diffusion of the magnetic field in conductors. Moreover, using a sufficiently simple algorithm, we managed to account for the basic losses of the magnetic flux related to diffusion, cuts-off at section and wire joints, and the losses related to spiral and liner misalignment.

1 Introduction

For the project of the multimegajoule stationary electrophysical facility PIRIT-EMG [1] aimed at generating high-power soft x-ray radiation fluxes, a spiral-coaxial magnetoexplosive generator of comparatively low cost and high enough specific characteristics is used as a basic source of energy. The 48 MA EMG-720 that pumps the inductive storage with energy of up to 25-30 MJ was previously developed. The next step in our activities is to develop a generator having energies up to 80 MJ and that reduces current pulse duration to 5 μs. Such possibilities were initially assigned to the EMG-720 design and can be realized with minor modifications.

2 Calculation Technique

In this report, the results of numerical simulations of the magnetic flux compression in a modified EMG-720D generator are presented and the basic physical processes related to its operation are investigated. Calculations of EMG-720 [2] generator operation previously performed using the technique presented in paper [3] give a higher value of expected final current (80 MA) as compared to the experimental result (48 MA). This divergence is primarily due to the fact that the magnetic flux losses related to non-linear diffusion of magnetic field in the spiral segment of the generator were not correctly accounted for in the program.

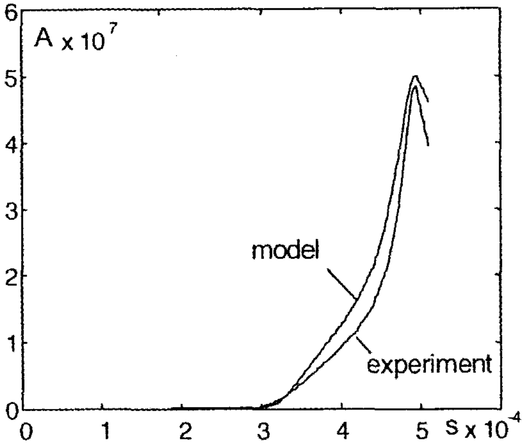

Figure 1. Comparison of the calculated current with the experimental one.

As these inaccuracies are insufficient to develop a generator, the authors developed a calculation technique based on a stricter account of magnetic pulse losses over the entire operation process. The essence of the technique is that Eulerian equations are solved for sliding detonation waves in order to calculate the liner scatter dynamics. The system of equations is integrated using a finite-difference method for 2-D stationary grids adapting to the flow peculiarities. Then, these data are used to define the initial velocity of the liner scatter and to calculate the magnetic flux compression in the generator using comparatively simple analytical formulas for inductances and quasi-linear diffusion of magnetic field in conductors. After getting the zero approximation of the generator current, the task of magnetic non-linear field diffusion in conductors for all points along the generator length is solved. The values obtained for the skin depth of non-linear diffusion are used to find the losses of magnetic flux and to calculate the generator current in the first approximation. The process of diffusion calculation and current estimation is repeated until the difference for the current at the next stage of iteration is less than a given value. In addition, by taking advantage of a sufficiently simple algorithm one can accurately account for the basic magnetic flux losses connected with diffusion at the section joint cut-offs.

The calculation of generator current is based on the law of magnetic flux preservation in the contour covering the generator volume together with the skin, the cavities formed at the section joints and the loops between the coils, i.e. at each time step, the magnetic field losses are found and then subtracted from the total flux. Next, in order to find the current, the remaining flux is divided by the contour inductance $I = \Phi/L$.

3 Calculation Results

The value of the generator final current is most affected by the flux losses in the skin and by the flux cut-offs. At the magnetic field increase there occurs a considerable deformation of the current contour that leads to the losses resulting from the magnetic flux cut-offs in the formed loops. Moreover, the current conducting surface movement leads to the growth of the contour final inductance that, in turn, sets a limit on the final current. Though the law of liner movement under the influence of HE affects current-time dependence, it manifests itself in the final value of this current, however slightly.

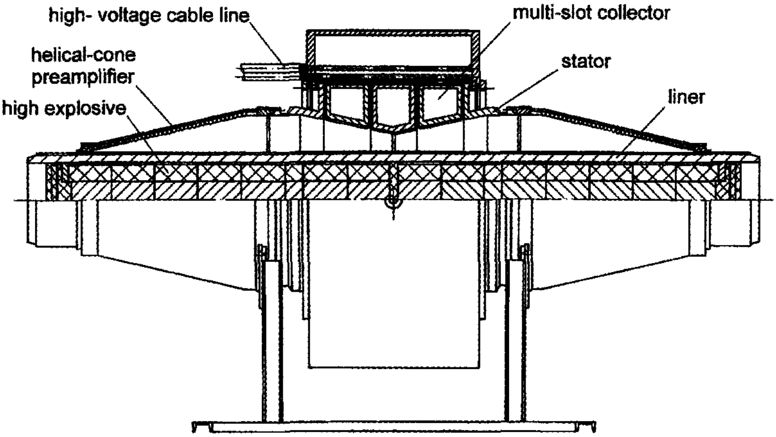

Figure 2. Design scheme of EMG-720D generator.

Testing the calculation technique by comparison with the experiment (Fig. 1) demonstrated close coincidence of the results. It is explained by the fact that we calculated the flux losses related to non-linear magnetic field diffusion in conductors as well as the flux cut-offs at the section joints.

We calculated the magnetic flux compression for the modified EMG-720D generator, shown in Fig. 2. The generator consists of two helical-cone preamplifiers with a total inductance of 110 μH, operating for the total coaxial section to which a distant cable line is connected. The total inductance of the line and the load is 20 nH. The generator overall dimensions are 720 mm in diameter and 3000 mm long. The aluminum liner wall thickness is 35 mm, just as it is in the experimental generator. The HE Ø300x750 with the internal filling is exploded simultaneously on two sides ensuring the convergence of detonation waves towards the center. The generator operates for 500 μs, of which powering requires 300 μs, the preamplifier operation takes 150 μs, and 50 μs is covered by operation of the coaxial section during which the basic energy amplification occurrs.

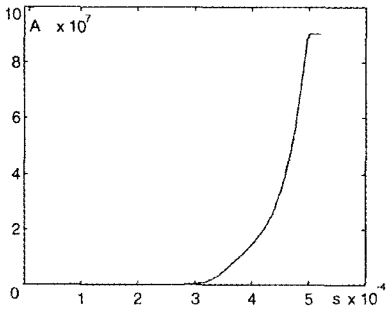

Figure 3. Calculated current of EMG-720D generator operating with 20 nH inductive load at 95 kA initial current.

Fig. 3 shows the generator current in a 20 nH inductor at 95 kA initial powering. The energy generated by the generator is 80 MJ.

4 Conclusion

The calculation technique developed makes it possible to accurately simulate the magnetic flux compression in helical-cone generators possessing a comparatively high coefficient of current and energy increase. The technique was perfected and tested using the experimental data from the EMG-720 generator previously developed.

We demonstrated that modifying the EMG-720 can increase its energy 3-4 times and solve the task of supplying the PIRIT-EMG power complex with a comparatively cheap energy source.

References

1. Popkov, N. F., Pikar, A.S., et al., "EMG-PIRIT" Experimental Complex for Investigations of High Energy Plasma Formations. In: 9th IEEE Pulsed Power Conference, Albuquerque, New Mexico, 1993.
2. Deryugin, Yu. N., Zelenskii, D. I., et al., Numerical Simulation of Explosive Magnetic Cumulative Generator EMG-720. In: 11-th International Conference on High Power Particle Beams, **1**, Prague, 1996, p. 158-161.
3. Pavlovskii, A. I., Lyudaev, R. Z., Boyko, B. A., et al., Numerical Model for Helical Magnetic Cumulation Generators. In: Megagauss Fields and Pulsed Power System. (Ed. by V. M. Titov and G. A. Shvetsov. Nova Science Publishers, NY, 1990) p. 233.

SEMI-EMPIRICAL MODEL FOR THE RESISTANCE OF SPIRAL MAGNETOCUMULATIVE GENERATORS

L. ALTGILBERS, I. MERRITT, M. BROWN
Advanced Technology Directorate, Missile Defense and Space Technology Center, U.S. Army Space and Missile Defense Command, Huntsville, AL, USA

P. TRACY
Teledyne Brown Engineering, Huntsville, AL, USA

The Explosive Magnetic Generator of Frequency (EMGF), developed by A. B. Prishchepenko at the Institute of Chemistry and Mechanics in Moscow, consists of a spiral magnetocumulative generator (MCG) with a small capacitive load. Based on published experimental results [1], the EMGF is reported to generate a "fish" shaped electric current waveform in which the amplitude of the oscillating current first increases and then decreases until it dampens out. This waveform was confirmed in experiments performed in June 1997 at the High Mountain Geophysical Institute in Russia and at Socorro in New Mexico [2]. Examination of the test data revealed that the current oscillations dampened out about one-third of the way through the operating time of the EMGF. It is unclear why this happened, so an investigation of the resistance changes in the EMGF was undertaken. As a result, a semi-empirical resistance model was developed for the EMGF. To verify this model, it was applied to three other types of spiral MCGs with different types of loads. It was found that this model works quite well for all four generators considered. In addition, it was found that an empirical constant derived for the EMGF by fitting the model to published data for the EMGF is applicable to the other three MCGs considered. The physical meaning of this constant is unclear at this time, but establishment of its physical significance may provide insight into how the EMGF works.

1 Introduction

The principal operating components of the EMGF (Fig. 1) are a seed source, spiral MCG, and a small capacitive load (10-1000 pF) [1]. The circuit diagram (Fig. 1) approximates the EMGF as a simple lumped parameter LRC-circuit and its current rings at a predictable frequency. In experiments conducted in June 1997, it was found that the current oscillations dampen out about one-third of the way through the operating time of the MCG (Fig. 2). This suggests that the dynamic resistance of the EMGF first decreases and then increases to a rather high value. A resistance model was developed to describe the resistance changes taking place within the EMGF.

To verify this model, it was applied to three other spiral MCGs [4]: 1) MARK IX, 2) EF-3, and 3) FLEXY I. These generators were selected since experimental data is available on them in the literature. Of the four devices considered, only the EMGF had a capacitive load.

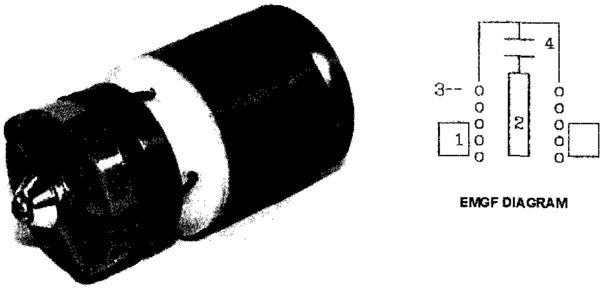

Figure 1. Explosive Magnetic Generator of Frequency. The numbered components are 1 - external magnets, 2 - liner filled with explosives, 3 - spiral coil, and 4 - capacitive load.

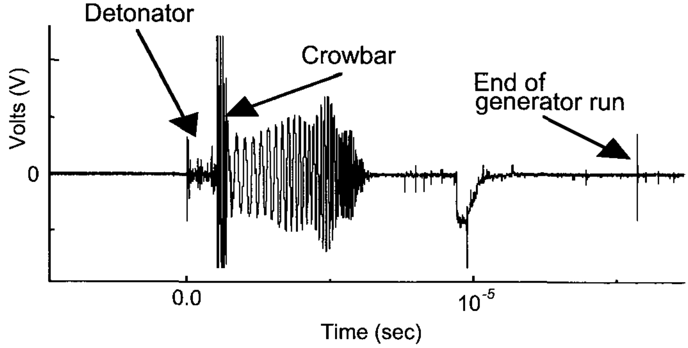

Figure 2. Rogowski signal for the EMGF.

2 Circuit Model

In the circuit diagram of the EMGF, it is assumed that the inductance and resistance are time dependent. Summing the potentials around the circuit yields:

$$L\frac{d^2I}{dt^2}+\left(2\frac{dL}{dt}-R\right)\frac{dI}{dt}+\left(\frac{d^2L}{dt^2}+\frac{dR}{dt}+\frac{1}{C}\right)I=0 \tag{1}$$

where I is the current, R the resistance, L the inductance, and C the capacitance. We assume that the time behavior of the resistance and inductance is the same and can be represented by:

$$L = L_0 e^{-\frac{t}{\tau}},\ R = R_0 e^{-\frac{t}{\tau}}, \tag{2}$$

where τ is a characteristic time that depends on the dimensions of the device, the type of explosives used, and other physical characteristics of the device. The general solution of Eq. (1) is:

$$I = z^{2-\nu}\left[AJ_\nu(\lambda z)+BY_\nu(\lambda z)\right], \tag{3}$$

where $z^2 = e^{\frac{t}{\tau}}$ and J(x) and Y(x) are Bessel functions of the first and second kind, respectively, of order ν and argument x. The order and argument of the Bessel functions in Eq. (3) are: $\nu = \frac{R_0}{L_0}\tau$ and $\lambda = \frac{2\tau}{\sqrt{L_0 C}}$. The constants A and B are determined from the initial conditions.

Employing the identity:

$$J_\nu(\lambda)Y_{\nu-1}(\lambda) - Y_\nu(\lambda)J_{\nu-1}(\lambda) = \frac{2}{\pi\lambda} , \tag{4}$$

and assuming that the arguments of the Bessel functions are large ($\lambda \geq 10$), Eq. (3) becomes:

$$I = I_0 z^{\frac{3}{2}-\nu} \cos[\lambda(1-z)]. \tag{5}$$

The measured output of the EMGF reported in the literature is: $I_0 = 20$ A, $L_0 = 50$ μH, C = 1 nF, $\tau = 3.5$ μsec, and $\nu = 0.72$. Using these values, the initial value of the resistance is calculated to be $R_0 = 10.3$ Ω. For $\nu = 0.72$, the amplitude of the current, defined by Eq. (5) will increase continuously in time. Therefore, Eq. (5) does not represent a physically acceptable solution and the experimental results indicate that ν should be a function of time. Empirically, very good agreement can be attained between Eq. (5) and the experimental results if the value of ν is taken to be:

$$\nu = \begin{cases} \frac{R_0\tau}{L_0}, t \leq t_0 \\ \frac{R_0\tau}{L_0} e^{T_A(t-t_0)}, t > t_0 \end{cases} \tag{6}$$

where $t_0 = 6$ μsec and the factor $T_A = 1.8 \times 10^5$ was obtained by fitting the resistance model to the published curves for the EMGF. Fig. 3 compares the plots of the envelope of the output current of the EMGF calculated by using Eq. (5) to that published in [3].

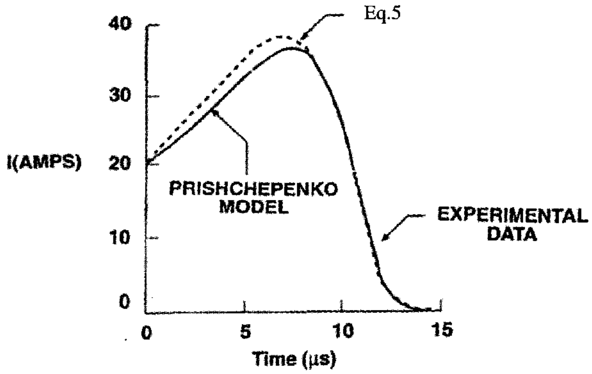

Figure 3. Comparison of measured and calculated plots of the envelope of the output current of the EMGF coil current versus time. The plot labeled Eq. 5 is based on the resistance model for the EMGF proposed in this paper.

3 Verification of the Circuit Model

In order to verify the model, the semi-empirical resistance model was applied to three other MCGs: the MARK IX developed at Los Alamos National Laboratory, the EF-3 developed at the Institute of Atomic Physics in Romania, and the FLEXY I developed at Loughborough University [3].

Unlike the EMGF, these three devices were tested without a capacitive load; nevertheless, our analysis shows that the proposed semi-empirical resistance model provides an excellent representation of the output of all three generators. The basic circuit equation for all three generators is:

$$\frac{d(LI)}{dt} + IR = 0 \tag{7}$$

Solving and incorporating the semi-empirical resistance model, the solution is:

$$I = \begin{cases} I_0 \exp\left[\frac{t}{\tau}\left(1 - \frac{R_0 \tau}{L_0}\right)\right], t \le t_0 \\ I_0 \exp\left[\frac{t}{\tau}\left(1 - \frac{R\tau}{L_0}\exp(T_A(t - t_0))\right)\right], t > t_0 \end{cases} \tag{8}$$

where the initial values will be different for each device and are given in Table 1. Substituting Eq. (8) into Eq. (7), the resistance model for the three generators is:

$$R = \begin{cases} R_0 exp[-\frac{t}{\tau}], 0 \le t \le t_0 \\ R_0(1 + T_A t)exp\left[-\left(\frac{t}{\tau} - T_A(t - t_0)\right)\right] \end{cases} \tag{9}$$

Using the parameters in Table 1 and Eq. (8), it can be seen in Figs. 4 - 6 that there is good agreement between the predicted and measured values of current as a function of time, and that the common factor T_A is applicable to all four generators. The factor T_A corresponds to an inverse characteristic time. Even though the specific physical significance of this factor is not yet understood, the fact that the same value can be used to represent the current output for four different spiral generators with different loads is interesting and dictates further analysis.

Table 1. Parameters of the EMGF, EF-3, MARK IX, and FLEXY I.

	EMGF	EF-3	MARK IX	FLEXY I
I_0 (KA)	0.020	5.0	413.0	48.0
L_0 (μH)	50.0	650.0	6.0	35.0
τ (μsec)	3.5	31.7	39.7	30.0
t_0 (μsec)	6.0	200.0	150.0	133.0
R_0 (Ω)	10.3	0.0285	.000238	0.00205

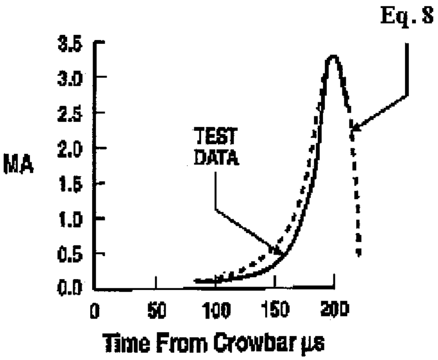

Figure 4. Comparison of the measured and calculated current generated by the EF-3. The plot labeled Eq. 8 was calculated using this equation and the resistance model proposed in this paper.

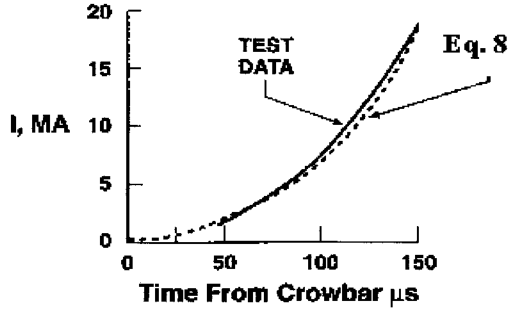

Figure 5. Comparison of the measured and calculated current generated by the MARK IX. The plot labeled Eq. 8 was calculated using this equation and the resistance model proposed in this paper.

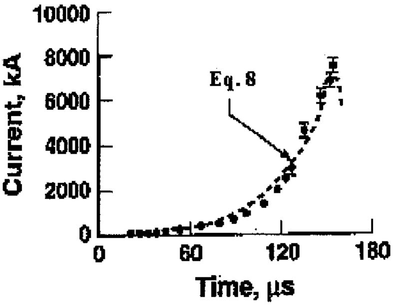

Figure 6. Comparison of the measured and calculated current generated by the FLEXY I. The plot labeled Eq. 8 was calculated using this equation and the resistance model proposed in this paper.

4 Conclusions

During the process of developing a resistance model for the EMGF, the factor T_A was discovered. When this model was applied to other MCGs, it was found that the value of this factor remains the same. In order to understand the physical significance of this factor, we looked at some of the common features of all four generators. These include that all: 1) are spiral generators, 2) have a finite distance between the armature and spiral coil, and 3) are gas filled (air in the EMGF, EF-3, and FLEXY I, and SF_6 in the MARK IX). Further study is required and is currently under way to understand the significance of T_A and the physics of what is occurring within the four generators, which includes studying the effects of geometry and plasma chemistry taking place between the armature and stator during compression.

Acknowledgments

The authors acknowledge Dr. C.M. "Max" Fowler and Dr. R. Hoeberling at Los Alamos National Laboratory and Dr. S.T. Wu of the University of Alabama in Huntsville for reviewing this paper and making valuable comments.

References

1. Prishchepenko, A. B., Zhitnikov, V. P., Microwave Ammunitions: SUMM CRIQUE, Proceedings of the AMREM Conference, Albuquerque, NM, May 1996, in publication.
2. Altgilbers, L. L., Merritt, I., Brown, M., Henderson, J., Verma, A., Hoeberling, M. J., Hoeberling, R. F., Carp, G., Holder, D., Fenner, W., Fowler, C. M., Pina, J., Lewis, M., Compact Explosive Driven Microwave Sources: Test Results, Megagauss VIII, 1998.
3. Prishchepenko, A. B., Devices Built Around Permanent Magnets for Generating an Initial Current in Helical Explosive Magnetic Generators, Instruments and Experimentation Techniques, **38** (4), Part 2, (1995), pp. 515 - 520.
4. Novac, B. M., Smith, I. R., Stewardson, H. R., Senior, P., Vadhev, V. V., Enache, M. C., Designs, Construction, and Testing of an Explosive-Driven Helical Generator, *J. Phys. D, Appl. Phys.*, **38** (4), (1995), pp. 807 - 823.

VOLTAGE DISTRIBUTION OVER EMG HELIX WIRES

V. R. CHERNYSHEV, E. I. ZHARINOV, V. N. BUZIN, B. E. GRINEVICH, K. N. KLIMUSHKIN, I. D. KUDELKIN, A. A. BAZANOV, O. V. SOKOLOVA, M. M. GUBIN, S. V. PAK, A. N. SKOBELEV

Russian Federal Nuclear Center- VNIIEF, Sarov, Russia

The efficiency of EMG operation depends on the magnetic flux losses produced under circuit deformation. Voltage overloads in the circuit generator resulting in electrical breakdowns are among the potential reasons for these losses. A sectionalized EMG with a 100 mm inner diameter of its helix turns is considered as an example. The initial inductance of this generator is 17 μH and the final inductance is 20 nH. The maximum voltage was found on the helix turns at about 130 mm from the beginning of the helix when the cone base was about 60 mm from the beginning of the helix (the cone was about 74 mm long). The electric strength of the EMG insulation, measured under laboratory conditions, was 30 kV. With this insulation, the value of power-up current for the system figure of merit F = 0.8 and the detonation rate of 8.1 km/s should not exceed 30 kA in order to avoid electric breakdowns. The method presented here allows estimation of the voltages evolving during generator operation and choice of the power-up current value, assuring the absence of electric breakdowns in the EMG.

1 Introduction

The effectiveness of the explosive magnetic generator (EMG) operation depends on the losses of magnetic flux during the deformation of a circuit. One of the probable reasons for the losses is an overvoltage in the generator circuit, leading to electrical breakdowns. Thus, when designing the helical EMGs, it is very important to correctly compute the voltages arising in the process of the EMG's operation and to choose the thickness of the helical coil insulation. If the insulation thickness is insufficient, electrical breakdowns may occur. If the insulation is too thick, the EMG output parameters will decrease due to the increase of transient resistance between the wires and the exploding armature. This paper studies the distribution of voltage over the EMG helical coil length.

2 Discussion

When the turns of the helical coil are deformed by the cone expanding under the effect of explosion products of the central armature, a one-sided compression of magnetic flux takes place (Fig. 1).

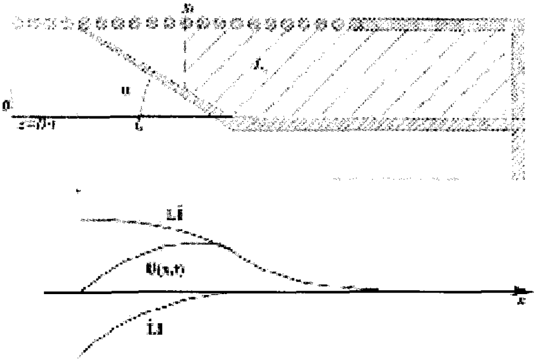

Figure 1. One-sided compression of magnetic flux.

If one neglects the voltage drop over the circuit's active resistance, then for any moment in time the voltage distribution in the coil will be:

$$\mathrm{U(x,t)} = \frac{d\Phi}{dt} = \frac{d(LI)}{dt} = \frac{dL(x,t)}{dt} I + L(x,t)\frac{dI}{dt} \tag{1}$$

where x is a coordinate of the point under consideration, where the voltage is determined (beginning of the coil corresponds to the value of x = 0).

The value of the voltage in the coil at point x_i is determined by two components: $L(x,t)\cdot\dot{I}$ and $\dot{L}(x,t)\cdot I$.

Component $L(x,t)\cdot\dot{I}$ depends on the rate of current increase in the circuit $\dot{I}$ and on the value of the inductance *L(x,t)*. This part of the circuit is shaded in Fig. 1.

As $\dot{I}$ is a positive quantity during the circuit deformation, the voltage component $\dot{L}(x,t)\cdot I$ is also positive.

Component $\dot{L}(x,t)\cdot I$ is determined by the rate of inductance *L(x,t)* decrease and the value of discharge current *I* in the circuit.

Voltage component $\dot{L}(x,t)\cdot I$ is a negative quantity. A qualitative picture of the voltage component's distribution and of the coil turns' resultant voltage is presented in Fig. 1.

If time "t" is expressed through coordinate "z" (the distance from the coil's beginning to the point of the armature cone contact with the coil at time t, z = D· t), then formula (1) will be:

$$\mathrm{U(x,z)} = \frac{dL(x,z)}{dz}\cdot\frac{dz}{dt}\cdot I + L(x,z)\frac{dI}{dt} = \frac{dL(x,z)}{dz}\cdot D\cdot I + L(x,z)\cdot\frac{dI}{dt} \tag{2}$$

where D is a detonation rate.

The current may be determined through the EMG's figure of merit F [1] as

$$I = I_0\left(\frac{L_0}{L(z)}\right)^F \tag{3}$$

The current derivative is
$$\frac{dI}{dt} = -\frac{I_0 FD}{L(z)}\left(\frac{L_0}{L(z)}\right)^F \frac{dL(z)}{dz} \tag{4}$$

The expression (2) may be written as

$$\mathrm{U(x,z)} = I_0\cdot\left(\frac{L_0}{L(z)}\right)^F\cdot D\left\{\frac{dL(x,z)}{dz} - F\cdot\frac{L(x,z)}{L(z)}\cdot\frac{dL(z))}{dz}\right\} \tag{5}$$

It follows from formula (5) that the voltage is proportional to the initial current and to the rate of the explosion's detonation; it also depends on a degree of contour compression $K_{compr} = \frac{L_0}{L(z)}$ and a figure of merit F.

To determine the maximum voltage arising in the process of EMG operation, it is necessary to plot a series of curves U(z) for a large number of "x" points. To plot the curves, one should know the inductance values at "x" points and those values of inductance at the same "x" points but with variables "z".

The EMG inductance was computed according to the model proposed in [2].

$$L(x,t) = \mu_0 \int_{x_k(t)}^{l} [\pi(R^2 - r^2(x,t))/h^2(x) + \frac{1}{2\pi} \ln(R/r(x,t))]dx \qquad (6)$$

where R is the radius of the coil turns; h(x) is the distribution of the turn's pitch along the helix; r(x,t) is the profile of the expanding armature outer boundary at time t; l is the coil length.

The expending armature profile was computed by

$$r(x,t) = \max(R-(x-t \times D) \times tg(\alpha), r_0),$$

where (x>t×D) . α is the armature expansion angle; D is the explosive charge detonation rate; r_0 is the original outer radius of the armature.

The accuracy of the EMG inductance computations was checked by inductance measurements using an EMG mock-up with an inner coil diameter of 100 mm. The length of that multi-section coil was 600 mm. The initial inductance of the EMG with an aluminum central armature, having an outer diameter of 60.2 mm, was 17 μH. That EMG provided a current pulse of up to 5 MA at an inductance of 15 nH.

When making measurements using a mock-up, the armature expansion was simulated by a truncated cone with the angle equal to the armature expansion angle (cone length is l_c = 74 mm). By shifting the cone on the armature along the coil (z changes), a z-dependence was determined at the given points x_i. The difference between the computation results and the measurement results does not exceed 10%

In order to determine the maximum voltage arising in the process of EMG operation, the dependence of voltage distribution U(x,z) along the coil length was calculated by formula (5); the locations of contact points z ranged from 0 to 420 mm. This dependence is shown in Fig. 2. The computations were made with F = 0.8 and I_0 = 30 kA.

Fig. 2 shows that each dependence has a maximum voltage, the value of which is different for different z. The EMG's maximum voltage arises when the distance from the contact point is somewhat less than the cone length.

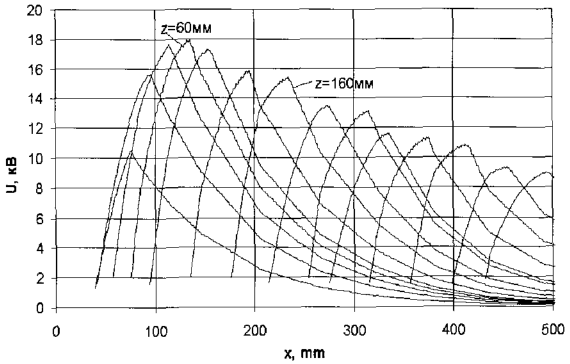

Figure 2. Maximum voltage for each dependence.

To estimate the maximum voltages arising in the process of EMG operation, we have plotted, according to formula (5), the dependence of $U_{max}(z)$ along the coil length with the contact point z location from 0 to 420 mm. One can see that the voltage reaches its maximum when the contact point is located at a distance of about 60 mm from the beginning of the coil. For the explosives with D = 8.1 km/s at the initial current of 30 kA, the maximum computed voltage arising in this EMG does not exceed 18 kV.

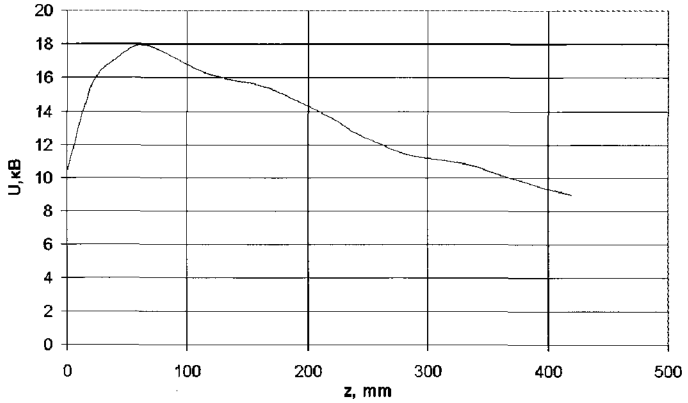

Figure 3. Voltage maximum at 60 mm.

This paper does not consider the problems of the electrical field intensity near the contact point and of the probability of the electrical breakdowns between the turns nearest to the contact point.

References

1. Shearer J. W., Abraham F. F, Aplin, C. M., et al., Explosive-Driven Magnetic-Field Compression Generators. *J. Appl. Physics,* **39** No. 4 (1968) pp. 2102-2115.
2. Pavlovskii, A. I., Ludayev, R. Z., et al., Multisection generator MC-2 //Ultra-high magnetic field. Physics. Technology. Application. MG-III, Moscow, *Nauka* (1984) pp. 312-320.

CALCULATION OF THE AUTONOMOUS MC-GENERATOR WITH A PERMANENT MAGNET

V. E. GURIN, V. I. KARGIN, A. S. PIKAR, N. F. POPKOV, E. A. RYASLOV
All-Russian Scientific Research Institute of Experimental Physics (VNIIEF), Sarov, Russia

Numerical calculations of an autonomous magnetocumulative generator with permanent magnets based on barium oxide are presented. Application of barium oxide magnets allows creation of a closed magnetic circuit with four acting gaps and provides magnetic flux compression with axial geometry. A generator using a permanent magnet does not require an additional energy source thus it is convenient to operate and always ready for activation. Numerical calculation results are discussed here and compared with tests of trial samples. A numerical simulation describes the capture of the magnetic flux, its compression by a copper expanding liner, energy losses to cut the flux and non-liner diffusion of magnetic field in conductors. The optimized autonomous generator design using the MKM-48 permanent magnet is shown. Energy is released from the generator by a low-inductive matching transformer. The generator using permanent magnets and having an explosive charge mass of several tens of grams provides 30 J of magnetic energy, sufficient to drive cascade energy amplifiers of submegajoule range.

1 Introduction

A source of initial energy with several tens of joules is required to power cascade amplifiers. As a rule, a capacitor bank or an accumulator with a high-voltage converter is used for this purpose. However, the most convenient to operate may be a generator using permanent magnets, which does not demand other energy sources. Earlier, preliminary experiments were performed with these generators that demonstrated good results and high reliability. Further upgrading of the construction required detailed numerical calculations and improvement of dimensions in order to increase the final energy output of the generator.

2 The Generator MKM-48 Design

The generator involves a central tube 1, coaxially arranged bus-bars 2 passing into a hollow cylinder (barrel) 3, and a load fabricated as four cylindrical turns 4. The magnetic circuit (Fig. 1, A-A cross-section) consists of four air gaps and four magnets 8. Arrows point to the primary magnetic field intensity in the gaps, H_0.To obtain such a field, permanent magnets were made as triangle prisms arranged in pairs and previously magnetized. The cylindrical turns connection 4 with the barrel and a central tube 1 is made through flat flanges 5 and 6. A radial slot is filled with insulator 7.

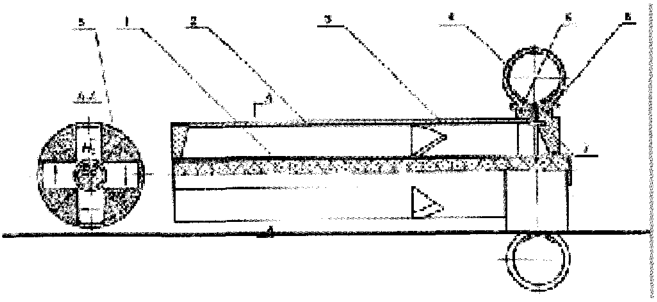

Figure 1. MKM-48 generator layout. See text for details.

Geometric MKM-48 generator dimensions:

Central tube wall thickness	— 1 mm;
Bus-bar length	— 200 mm;
Bus-bar width	— 4 mm;
Inner barrel diameter	— 48 mm;
Barrel length	— 40 mm;
Radial slot width	— 1 mm;
Inner turns diameter	— 8 mm;
Turns length	— 68 mm;
Distance between turns axes and generator axis	— 44 mm.

3 Calculation Results

Numerical simulation describes the capture of magnetic flux in the volume between bus-bars and the liner, compression of this flux at explosion of an explosive charge and liner movement, flux losses as a result of magnetic field diffusion in conductors, energy transformation and its transfer into the inductive load. The use of barium oxide magnets allows us to ignore magnetic system material conductivity, and to consider the generator analogous to a generator powered with initial current. The current calculation algorithm in the generator is based on detecting skin magnetic flux losses in conductors, registering magnetic flux losses in structural cavities on the junctions of separate generator assemblies and the transformer as well as losses in parasitic transformer inductivities.

To refine the structure, experiments were performed at the operation of a 0.35 nH inductive load generator whose bus-bars are 10 mm wide. Experimental results are given in Fig. 2. It should be noted that due to the presence of several slopes at junctions of the transformer bus-bars and barrel in the generator structure, as well as due to significant parasitic transformer inductivity, a scant load energy of 16 J was reached.

As calculations show, the generator's bus-bar width decreases to 4 mm and the magnetic system length increases from 160 mm up to 200 mm, allowing the load energy to rise to 30 J. The MKM-48 generator current calculation curve is given in Fig. 3. The generator current reaches a maximum of 370 kA

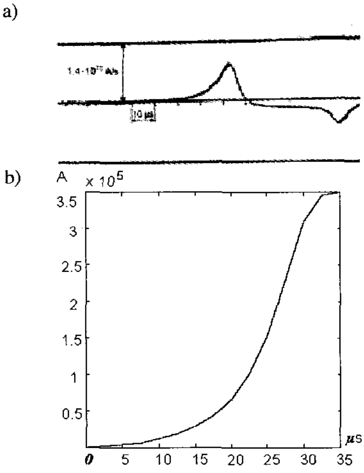

Figure 2. a) generator current derivative; b) generator current.

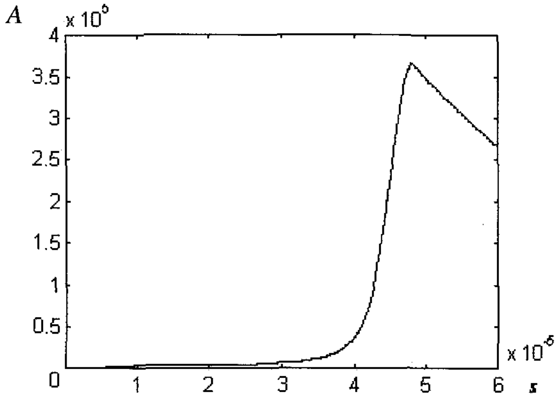

Figure 3. MKM-48 generator current calculation curve.

4 Conclusion

The generator with permanent magnets does not need an additional energy source for its operation and is always ready for operation. The output generator energy of 30 J is enough to power a cascade system that allows creation of small-dimension, autonomous energy sources in the submegajoule range.

2-D HYDRODYNAMIC FLOWS CALCULATION AT ISENTROPIC SUBSTANCE COMPRESSION WITH ULTRA-HIGH MAGNETIC FIELD PRESSURE

V. V. ASEEVA, G. V. BORISKOV, A. I. PANOV
Russian Federal Nuclear Center, All Russian Scientific Research Institute of Experimental Physics (RFNC-VNIIEF), Sarov, Russia

Valuable information on thermodynamic and electrical properties of easily compressed crystalline substances can be obtained by placing them inside a metal tube on which a pulse of ultra-high magnetic field pressure is applied. In such experiments it is important to know the characteristics of longitudinal substance motion due to the non-uniform distribution of magnetic field pressure. For this purpose we carried out one-dimensional (along the axial coordinate) and two-dimensional hydrodynamic calculations for solid argon. A numerical magnetohydrodynamic (MHD) model of the compression device based on the MC-1 generator, and results of compression tube x-ray image processing were used for setting the motion velocity of the tube's inner surface. Calculations showed the absence of jets and supersonic flows that are able to cause the premature destruction of the experimental unit. The length of uniformly compressed argon section was found to be sufficient to determine sample density on the x-ray compression tube image.

1 Introduction

In experiments on isentropic compression of substances assisted by an ultra-high magnetic field [1], it is often important to know the main features of the longitudinal motion of a substance resulting from the non-uniform distribution of the magnetic pressure along the outer surface of the sample tube. To accomplish the required calculations, the velocity or radius of the compression chamber (tube) inner surface must be defined as a function of the axial coordinate and time.

2 Problem Statement

The profile of the tube including the substance, considered at any time during the compression process, consists of the following specific segments: domain of the uniformly compressed sample, where the velocity of the tube's inner surface does not depend on the axial coordinate and can be taken as function of time from appropriate one-dimensional MHD calculations; domain of the uncompressed sample, where the velocity of the tube's inner surface is equal to zero; and transitional domain. It is natural to require that the velocity function of the last segment is smooth (without breaks and humps) from zero up to the value specified for uniform compression domain. This requirement is met, for instance, by a cubic polynomial with properly selected factors or by the function of the following type: $A+B \exp[(C + Dz - z_2)/(E + Fz - z_2)]$, with parameters selected from the above condition for a smooth joining. (The results weakly depend on the concrete type of the approximating function.) At compression, the boundaries Zi ($i = 1; 2$) of transitional domain travel along the tube axis with time. It is logical to assume that the difference $Zi(t) - Zi(0)$ is proportional to the degree of deviation of a uniformly compressed segment's radius $R(t)$ from its initial value $R(0)$. dZi/dt must be zero when this deviation is equal to zero. One of the simplest dependencies possessing the above properties has the form: $Zi(t) - Zi(0) = Ci\,(R(0) - R(t))^2$. Proportionality coefficients can be determined from results of experiments that give transitional domain sizes at the specific moment of compression. Without loss of available information, the values of $Zi(0)$ can be taken as equal to each other and coinciding with the middle of the transitional domain. If the law of inner surface motion is known for the compression chamber (its edges are considered to be immovable), then the axial distributions of substance density, temperature, pressure and velocity can be found from the solution of the system of one-dimensional or (for accounting the radial distributions) two-dimensional equations of mass, impulse and energy balance together with the specified equation of state (EOS) for the substance being studied. Calculations of this type were done for crystalline argon with an initial temperature of 77.36 K. Argon was compressed isentropically by the magnetic field of the MC–1 generator [2]. The generator initial field is 140 kG. The length and initial inner diameter of the compression chamber are 180 mm and 7 mm, respectively. The form and sizes of the tube, which are needed to evaluate constants *Ci*, were determined using an x-ray image made at the moment of maximum compression of the sample. The "cold" part of the argon EOS was taken in the form of a polynomial of the 5th power from variable $\delta^{1/3}$, where $\delta = \rho/\rho_{00}$ (ρ_{00} - argon density at zero pressure and temperature). Its coefficients were determined from the condition of passing a sought curve through metallization points, calculated in [3], and also from the conditions of smooth joining with the curve [4] and with the curve of the quantum statistical model [5] at the boundaries of applicability for the expressions from [4] and [5].

3 Calculation Results

Results of calculations are presented in Figs. 1-3. Fig. 1 illustrates the axial distribution of the argon pressure, averaged in the radial direction, at the moment of maximum compression. Length of the uniformly compressed sample is ~ 7 mm. This is sufficient to determine average argon density at this segment using an x-ray image of the tube being compressed. A similar profile for the temperature of the investigated substance is given in Fig. 2. The axial distribution of mass velocity and sound velocity for argon at the moment of maximum compression of a sample is reproduced in Fig. 3. One can see that there were no supersonic currents able to cause premature destruction of the experimental device anywhere inside the compression chamber. Calculations taking into account radial gradients of density, temperature and velocity have shown the absence of jets, thus confirming results derived with the help of 1-D codes.

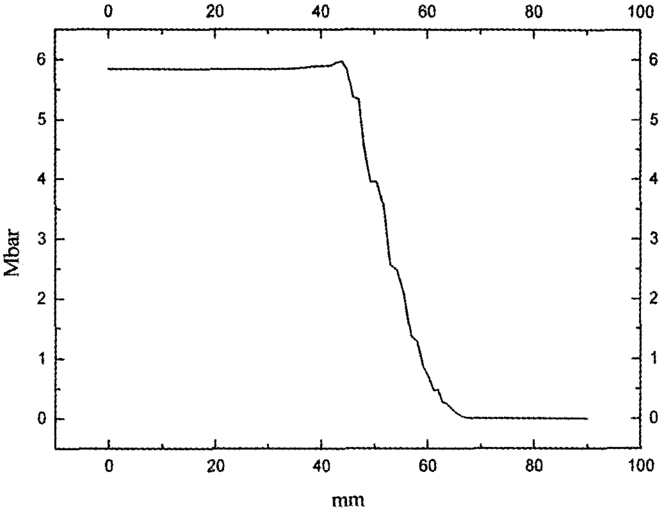

Figure 1. Axial distribution of argon pressure at maximum compression.

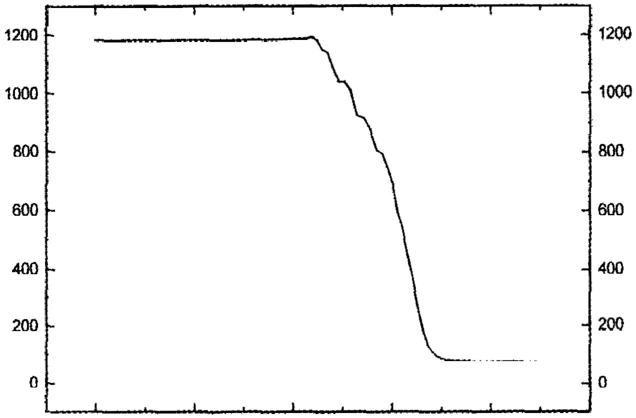

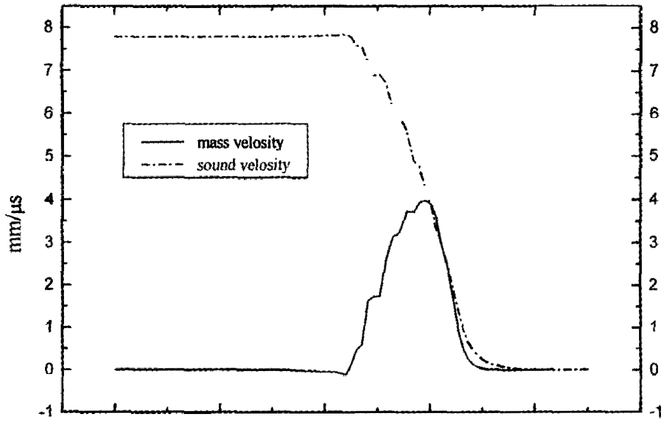

The calculation technique described to get axial flow parameters for an easily compressed sample can be combined with radial MHD calculations of tube motion and motion of cascades for an MC-generator. This allows us to describe two-dimensional currents in the entire compression device without resorting to simulations of the boundary motions of the investigated spatial region.

References

1. Dolotenko, M. I., Bykov, A. I., Kolokol'chikov, N. P., Boriskov, G. V., Yegorov, N. I., Aseeva, V. V., Tatsenko, O. M., Younger, S. M., Ekdahl, C., Compression of Argon up to megabar pressure: transition to a conducting phase. Megagauss And Megaampere Pulse Technology And Applications, Ed by V. K. Chernyshov, V. D. Selemir, L. N. Plyashkevich. Sarov, VNIIEF, 1997.
2. Sakharov, A. D., Lyudaev, R. Z., Smirnov, E. I., et al., Magnetic Cumulation, *Dokl. Akad. Nauk*, **165** (1965), pp. 65 - 68.
3. Kwon, I., Kollins, L. A., Kress, J. D., Troulier, N., First-principles study of solid Ar and Kr under high compression, *Phys. Rev. B*, **52** (1995), pp. 15165 - 15169.
4. Adamskaya, I. A., Grigoriev, F. V., Mikhailova, O. L., Mochalov, M. A., Sokolova, A. I., Urlin, V. D., Quasi-isentropic compression of liquid argon up to 600 kbar, *Zh. Eksp. Teor. Fiz.*, **93** (1987) pp. 647 - 651.
5. Kalitkin, N. N., Kuz'mina, L. V., Curves of cold compression under high preassures, *Fiz. Tv. Tela*, **13** (1971) pp. 2314 - 2318.

EXPLOSIVE AXIAL MAGNETIC FLUX COMPRESSION GENERATOR ARMATURE MATERIAL STRENGTH AND COMPRESSION EFFECTS

E. L. RUDEN, G. F. KIUTTU, R. E. PETERKIN, JR.
Air Force Research Laboratory, Kirtland Air Force Base, NM, USA

J. B. CHASE
CARE'N Co.

The expansion of the armature of an axial magnetic flux compression generator results in an increase in the armature's electrical resistivity and possible melting due to compression and plastic work heating. If melting occurs, further flux compression is impaired by a greatly enhanced Rayleigh-Taylor instability. Even without melting, the expansion process can become unstable, with the armature fragmenting by plastic instability. These processes result in decreased performance. To complement more detailed modeling via multi-dimensional codes, terms are derived suitable for use in a code that couples a zero dimensional model of the armature to a lumped circuit. For computational simplicity, only armature properties averaged over the armature thickness as functions of axial position and time are modeled. Further simplifications resulting in analytic approximations are presented to provide some preliminary indication of the significance of material effects.

1 Introduction

We consider the temperature evolution and mechanical stability of a cylindrical tube of ductile material loaded with high explosive and detonated at one end. Bounds on the shock heating of the tube, an estimate of the subsequent plastic work heating as the tube wall flares outward into a cone, and the radius for onset of plastic instability, are derived using the Steinberg (EOS) and material strength model [1,2]. The purpose is to provide self-contained expressions for shock heating and plastic work as tractable parts of the larger problem of armature thermodynamics and to provide expressions for the heating rate due to these processes for numerical simulations of flux compression generators.

2 Shock Heating

The EOS in the Steinberg model relating pressure P to density ρ and internal energy per unit mass relative to that at standard conditions ($P = 0$, temperature $T = T_s = 300\ K$) E is [1],

$$P(\mu,E)=\begin{cases}\dfrac{\rho_0 C_0^2\mu[1+(1-\frac{\gamma_0}{2})\mu-\frac{b}{2}\mu^2}{[1-(S_1-1)\mu-S_2(\mu^2/(\mu+1))-S_3(\mu^3/(\mu+1)^2)]^2}+(\gamma_0+b\mu)\rho_0 E & \text{for } \mu>0\\ \rho_0 C_0^2\mu+\rho_0\gamma_0 E & \text{for } \mu\leq 0\end{cases} \tag{1}$$

Here, $\mu = \rho/\rho_0 - 1$ and C_0 (sound speed), ρ_0 (standard density), γ_0, b, S_1, S_2, and S_3 are available phenomenological parameters [2].

To find an expression for T, we start with the fact that for any given μ, $T = (E - E_C)/C$, where C is specific heat (assumed constant) and $E_C = E$ at compression μ and $T = 0$ [1]. Subtracting both sides of this equation, solved for the special case of the adiabat from standard conditions were $T = T_0(\mu)$ and $E = E_0(\mu)$, from the respective sides of the general case, results in,

$$T = T_0(\mu) + (E - E_0(\mu)) / C \tag{2}$$

For this, $T_0(\mu)$ may be found from the adiabatic relationship [3],

$$T_0 = T_s \exp\left[-\int_{V_0}^{V} \frac{\gamma(V')}{V'} dV'\right] \qquad \gamma(V) = V\left(\frac{\partial P}{\partial U}\right)_V \tag{3}$$

where V is volume with V_0 its standard value, U is internal energy, and γ is the Grüneisen ratio [2,3]. Changing variables via $V = V_0/(\mu + 1)$ and $U = \rho_0 V_0 E$, using (1) for P, and integrating,

$$T_0(\mu) = \begin{cases} T_s(\mu+1)^b \exp\left(\frac{(\gamma_0 - b)\mu}{\mu+1}\right) & \text{for } \mu>0 \\ T_s \exp\left(\frac{\gamma_0 \mu}{\mu+1}\right) & \text{for } \mu\leq 0 \end{cases} \tag{4}$$

$E_0(\mu)$, meanwhile, may be found from (1) since $dU = -PdV$ along an adiabat. This results in the following differential equation and its solution [4],

$$\frac{dE}{d\mu} = \frac{P(\mu, E)}{\rho_0(\mu + 1)^2} \qquad E_0(\mu) = \frac{T_0(\mu)}{\rho_0} \int_0^{\mu} \frac{P(\mu', 0)}{(\mu' + 1)^2 T_0(\mu')} d\mu' \tag{5}$$

This expression may be approximated to within 2% in the specified ranges by,

$$E_0(\mu) \approx \begin{cases} \frac{C_0^2 T_0(\mu)}{T_S} \sum_{i=2}^{4} a_i \mu^i & \text{for } 0<\mu<0.35 \\ \frac{C_0^2 T_0(\mu)}{T_S} \sum_{i=2}^{5} b_i \mu^i & \text{for } -0.20<\mu\leq 0 \end{cases}$$

$$a_2 = ½ \qquad a_3 = \frac{1}{6}\left(4S_1 - 6 - 3\gamma_0\right)$$

$$a_4 = 800 \exp\left(\frac{(b-\gamma_0)}{5}\right)\left(\frac{4}{5}\right)^b \frac{40 - 4\gamma_0 - b}{(25S_1 + 5S_2 + S_3 - 125)^2} - \left(2S_1 - 3 - \frac{3}{2}\gamma_0\right) - 4$$

$$b_2 = \frac{1}{2} \qquad b_3 = -\frac{1}{3}\left(2 + \gamma_0\right) \qquad b_4 = \frac{1}{8}(6 + 6\gamma_0 + \gamma_0^2)$$

$$b_5 = \left(\frac{4}{245} - 8192 \exp\left(\frac{\gamma_0}{7}\right) + 8134 + 1078\gamma_0 + 49\gamma_0^2\right) \tag{6}$$

The coefficients are determined by Taylor expansion of the integrand of (5), except for a_4 and b_5. For greater accuracy, the latter are chosen to make the integrand error zero at $\mu' = -1/8$ and $1/4$.

If we assume the external pressure rises instantaneously from 0 to a constant P_1 at a planar surface of an initially stationary solid with standard conditions, the resultant shock can be described by the Hugoniot relations [5], expressed as,

$$v_s^2 = \frac{(\mu_1+1)P_1}{\mu_1\rho_0} \qquad K_1 \equiv \frac{v_1^2}{2} = E_1 = \frac{\mu_1 P_1}{2\rho_0(\mu_1+1)} \qquad \mu_1 = \frac{\rho_1}{\rho_0}-1 \tag{7}$$

ρ_1, v_1, P_1, E_1, and K_1 are density, velocity, P, E, and kinetic energy per unit mass behind the shock, respectively, and v_s is shock speed. Substituting E_1 in Eq. 7 into Eq. 1, with $P = P_1$, and solving for P_1 gives us our Hugoniot function,

$$P_1 = \frac{\rho_0 C_0^2 \mu_1(\mu_1+1)}{\left[1-(S_1-1)\mu_1 - S_2\frac{\mu_1^2}{\mu_1+1} - S_3\frac{\mu_1^3}{(\mu_1+1)^2}\right]^2} \tag{8}$$

For the modest compressions discussed here, we may neglect the S_2 and S_3 terms [6]. Eq. 8, then, reduces to a quadratic in μ_1 with (meaningful) solution,

$$\mu_1 = \frac{\sqrt{4\Pi S_1+1}-2\Pi(S_1-1)-1}{2-2\Pi(S_1-1)^2} \qquad \Pi = \frac{P_1}{\rho_0 C_0^2} \tag{9}$$

Plugging this into Eqs. 7 gives,

$$v_s^2 = \Pi C_0^2/\alpha_1 \qquad K_1 \equiv \frac{v_1^2}{2} = E_1 = \alpha_1 \Pi C_0^2/2 \tag{10}$$

$$\alpha_1 = \frac{\mu_1}{\mu_1+1} = \frac{\sqrt{4\Pi S_1+1}-2\Pi(S_1-1)-1}{\sqrt{4\Pi S_1+1}-2\Pi S_1(S_1-1)+1} \tag{11}$$

The temperature behind the shock is, from Eq. 2,

$$T_1 = T_0(\mu_1) + (E_1 - E_0(\mu_1))/C \tag{12}$$

$E_1 - E_0(\mu_1)$ is the irreversible contribution to the energy behind the shock and is, therefore, a *lower bound* on the final energy E_f after P falls off and waves dissipate. However, the initial shock unloads at the liner OD, sending a continuous adiabatic rarefaction wave inward. Some energy is transmitted back into the driver gas, and some reflects as a second outward shock. These and subsequent shocks and rarefactions continue to increase heat and smooth the pressure profile, respectively. An *upper bound* on E_f is E_1. Given a final $\mu = \mu_f = -\gamma_0 E_f/C_0^2$, from Eq. 1 ($P = 0$), we may use Eq. 2 to find bounds on the final T,

$$T_f = T_0(-\gamma_0 E_f/C_0^2) + \frac{E_f - E_0(-\gamma_0 E_f/C_0^2)}{C} \qquad E_1 - E_0(\mu_1) \le E_f \le E_1 \tag{13}$$

The shock transit time is short compared to the time it takes the shell to expand by many thicknesses, so then E_f may be added to contributions from other sources.

3 Plastic Work

The Levy-Mises (L-M) relation for rigid plastic flow is [7],

$$\mathbf{D} \equiv \frac{1}{2}(\nabla\mathbf{v}+\nabla\mathbf{v}^{\mathrm{T}})-\frac{1}{3}(\nabla\cdot\mathbf{v})\mathbf{I}=\frac{3}{2}\frac{d\varepsilon}{dt}\frac{\mathbf{S}}{Y} \qquad \varepsilon=\frac{2}{\sqrt{6}}\int\sqrt{\mathbf{D}\cdot\mathbf{D}}\,dt \tag{14}$$

where Y is the uniaxial yield strength, $\mathbf{S}$ is the deviatoric stress tensor ($\mathbf{S}\cdot\mathbf{I}=0$), $\mathbf{D}$ is the deviatoric strain rate tensor, and ε is the equivalent plastic strain. Incompressibility ($\nabla\cdot\mathbf{v}=0$) is assumed in this model and section. The Steinberg model's strain rate independent material strength equation [1] is,

$$Y=Y_0 f(\varepsilon)\frac{G(P,T)}{G_0} \qquad f(\varepsilon)=\begin{cases}[1+\beta(\varepsilon+\varepsilon_i)]^n & \text{for } \varepsilon<\varepsilon_c\\ Y_{\max}/Y_0 & \text{for } \varepsilon\geq\varepsilon_c\end{cases} \tag{15}$$

where $G(P,T)$ and G_0 are the pressure and temperature dependent shear modulus and its initial value, respectively, β, n, $Y_{\max}$, Y_0, and ε_i are phenomenological parameters tabulated for several materials [2], and,

$$\varepsilon_c=[(Y_{\max}/Y_0)^{1/n}-1]/\beta\text{-}\varepsilon_i \tag{16}$$

The work rate [7] per unit mass is, using Eq. 14 and Eq. 15,

$$\frac{dE_P}{dt}=\frac{\mathbf{S}\cdot\mathbf{D}}{\rho_0}=\frac{Y}{\rho_0}\frac{d\varepsilon}{dt}=\begin{cases}\dfrac{Y_0 G(P,T)}{\rho_0 G_0}[1+\beta(\varepsilon+\varepsilon_i)]^n\dfrac{d\varepsilon}{dt} & \text{for } \varepsilon<\varepsilon_c\\[2ex] \dfrac{Y_{\max}G(P,T)}{\rho_0 Y_0 G_0}\dfrac{d\varepsilon}{dt} & \text{for } \varepsilon\geq\varepsilon_c\end{cases} \tag{17}$$

where ρ_0 is the standard mass density of the material (assumed constant here).

Given an axisymmetric thin walled shell of radius $R=R(z,t)$ expanding at radial velocity $V=V(z,t)$, nonzero components of $\mathbf{D}$ and ε are, from Eqs. 14,

$$(D_{rr},D_{\theta\theta},D_{zz})=(-1,1,0)\frac{V}{R} \qquad D_{rz}=D_{zr}=\frac{1}{2}\frac{\partial V}{\partial z} \tag{18}$$

$$\varepsilon=\frac{2}{\sqrt{3}}\int\left[\left(\frac{V}{R}\right)^2+\left(\frac{1}{2}\frac{\partial V}{\partial z}\right)^2\right]^{\frac{1}{2}}dt \tag{19}$$

Differentiating Eq. 19 and plugging into Eq. 17 gives us,

$$\frac{dE_p}{dt}=\begin{cases}\dfrac{2Y_0 G(P,T)}{\sqrt{3}\rho_0 G_0}[1+\beta(\varepsilon+\varepsilon_i)]^n\left[\left(\dfrac{V}{R}\right)^2+\left(\dfrac{1}{2}\dfrac{\partial V}{\partial z}\right)^2\right]^{\frac{1}{2}} & \text{for } \varepsilon<\varepsilon_c\\[3ex] \dfrac{2Y_{\max}G(P,T)}{\sqrt{3}\rho_0 Y_0 G_0}\left[\left(\dfrac{V}{R}\right)^2+\left(\dfrac{1}{2}\dfrac{\partial V}{\partial z}\right)^2\right]^{\frac{1}{2}} & \text{for } \varepsilon\geq\varepsilon_c\end{cases} \tag{20}$$

We now consider an initially round cylindrical shell of uniform thickness filled with high explosives and detonated from the center of one end. A reasonable estimate of the plastic heating over a specified interval may be made by using the following approximations for V and, from Eq. 19, ε,

$$V = V_r \Theta(C_x t - z) \qquad \varepsilon = \frac{2}{\sqrt{3}} \ln \frac{R}{R_0} + \frac{V_r}{\sqrt{3} C_x} \quad \text{for } t > \frac{z}{C_x} \tag{21}$$

Here V_r and C_x are the radial expansion velocity and the axial explosive detonation velocity, respectively, and both are assumed constant. $\Theta(z)$ is the Step Function. In other words, we assume the armature is stationary until a purely axial shock front passes, at which time the *armature is instantaneously accelerated to radial velocity* V_r, *flaring out into a conical shape.* If we further assume a constant G, then from Eq. 20, for $\varepsilon < \varepsilon_c$ and $\varepsilon \geq \varepsilon_c$, respectively,

$$E_p = \begin{cases} \dfrac{Y_0}{\rho_0 \beta (n+1)} \left([1+\beta(\varepsilon+\varepsilon_i)]^{n+1} - [1+\beta\varepsilon_i]^{n+1} \right) \\ \dfrac{Y_0}{\rho_0 \beta (n+1)} \left([1+\beta(\varepsilon_c+\varepsilon_i)]^{n+1} - [1+\beta\varepsilon_i]^{n+1} \right) + \dfrac{Y_{\max}}{\rho_0 Y_0} (\varepsilon - \varepsilon_c) \end{cases} \tag{22}$$

One may add E_p to the E_f term in Eq. 13 as boundaries to the final temperature due to the combined effects of shock and plastic work heating. For a simpler estimate of the temperature increment due to E_p, however, one may use $\Delta T_p \approx E_p/C$.

In the above, azimuthal symmetry is assumed. It is worth noting, however, that expansion beyond a critical point is unstable, and after a period of subsequent instability growth, the liner will fail. A band of ductile material being stretched will undergo plastic instability when the relative increase in the yield strength dY/Y due to work hardening over a time interval dt falls below the relative decrease in the band's cross sectional area dA/A. In the incompressible limit, this occurs when [8] $Y = dY/d\varepsilon$. From Eq. 15, this condition is met when ε reaches the following value, which corresponds to the given radius, based on Eq. 21,

$$\varepsilon_p = \begin{cases} n - \dfrac{1}{\beta} - \varepsilon_i & \text{for } n - \dfrac{1}{\beta} - \varepsilon_i < \varepsilon_c \\ \varepsilon_c & \text{for } n - \dfrac{1}{\beta} - \varepsilon_i \geq \varepsilon_c \end{cases} \qquad R_p = R_0 \exp\left[\frac{\sqrt{3}}{2} \varepsilon_p - \frac{V_r}{2 C_x} \right] \tag{23}$$

If this expression yields $R_p < R_0$, then expansion is unstable from the onset and $R_p = R_0$ may be used instead.

4 Conclusion

We conclude with a tabulation of results (table1) for four metals for the case of an armature which expands at $V_r = 0.26\ C_x$ after shock passage. ΔT_p is calculated at radius $R = 2R_0$ ($\varepsilon = 0.95$, from Eq. 21). We use for P_1 *one half* the pressure behind an RDX explosive induced shock normally incident to the various metal surfaces. This approximates the pressure of an oblique shock [9]. Figure 10.8 of Knoepfel [6] provides P_1 for Cu and Al directly. The (v_1, P_1) plot needed to infer P_1 for RDX an Ag from this figure is obtained by solving for v_1 in Eq. 10. T_1 and the bounds on T_f are found from Eq. 12 and Eq. 13, respectively. $\Delta T_p \approx E_p/C$, and R_p/R_0 are found from Eq. 22 and Eq. 23, respectively. Silver's high R_p and electrical conductivity make it an intriguing, albeit expensive, option.

Table 1. Results for four metals.

	Al 6061-T6	Al 1100-0	Cu OFHC (1/2 hard)	Ag
C_0 (cm/μs)	0.524	0.539	0.394	0.327
S_1	1.40	1.339	1.489	1.55
S_2,S_3,ε_i	0	0	0	0
γ_0	1.97	1.97	2.02	2.4
b	0.48	0.48	0.47	0.56
Y_0 (MPa)	290	40	120	50
Y_{max} (MPa)	680	480	640	660
β	125	400	36	28
n	0.10	0.27	0.45	0.8
ρ_0 (kg/m^3)	2703	2707	8930	10,490
C (J/kgK)	885	884	383	233
P_l (GPa)	20	20	27.5	27.5
T_l (K)	543	531	473	590
T_f min (K)	422	414	379	453
T_f max (K)	920	911	790	1049
ΔT_p (K)	169	63	117	134
R_p/R_0	1	1.11	1.27	1.70

References

1. Steinberg, D. J., Cochran, S. G., Guinan, M., W., *J. Appl. Phys.* **51** (1980), p. 1498.
2. Steinberg, D. J., Equation of state and strength properties of selected materials (rev.), Tech. Report UCRL-MA-106439, change 1, LLNL, 1996.
3. Walsh, J. M., Rice, M. H., McQueen, R. G., Yarger, F. L., *Physical Review*, **108** (1957), p.196.
4. Boyce, W. E., DiPrima, R. C., *Elementary Differential Equations*, John Wiley & Sons, New York, third edition, 1997.
5. Zel'dovich, Y. B., Raizer, Y. P., *Physics of Shock Waves and High-Temperature Hydrodynamic Phenomena*, American Elsevier, New York, 1966.
6. Knoepfel, H., *Pulsed High Magnetic Fields*, Americal Elsevier, New York, 1970.
7. Kahn, A. S., Huang, S., *Continuum Theory of Plasticity*, John Wiley & Sons, Inc., New York, 1995.
8. Chakrabarty, J., *Theory of Plasticity*, McGraw-Hill, New York, 1987.
9. Duvall, G. E., Fowles, G. R., in *High Pressure Physics and Chemistry*, Ed. by R. S. Bradley, Academic Press, New York (1963), pp. 191-209.

ON FEASIBILITY OF RAYLEIGH-TAYLOR INSTABILITY MAGNETIC STABILIZATION OF LINER IMPLOSIONS

S. F. GARANIN, S. D. KUZNETSOV, V. N. MOKHOV, L. V. YAKUBOVA, V. B. YAKUBOV
All-Russian Scientific Research Institute of Experimental Physics, Sarov, Russia

C. EKDAHL
Los Alamos National Laboratory, New Mexico

The feasibility of Rayleigh-Taylor (RT) instability stabilization during liner implosion using azimuthal and poloidal magnetic fields is theoretically studied. The possibility is shown to considerably reduce growth increments of small perturbations with an arbitrary direction of the wave vector for most rapidly growing harmonics (of wavelength on the order of liner thickness).

1 Introduction

Ref. [1] has solved the problem of RT instability when the acceleration is provided by magnetic rather than gas-dynamical pressure. It is shown that for the perturbations whose wave vector is parallel to the magnetic field, a decrease in increment γ compared to the classic one, $\gamma_{RT} = \sqrt{kg}$ takes place (k is wave number, g is acceleration). The expression for the increment obtained in [1] can be written as

$$\gamma = \sqrt{\mathrm{kg}} \cdot \sqrt{F(\vec{\mathrm{q}}, \vec{\mathrm{H}})} \text{ if } F \geq 0; \quad \gamma \equiv 0, \text{if } F < 0 \qquad (1)$$

$$F = \sqrt{\mathrm{A}^2 + 1 - 2\mathrm{q_H}^2/\mathrm{q}} - \mathrm{A}, \mathrm{A} = \mathrm{q_H}^2 \mathrm{cthq}/\mathrm{q}, \mathrm{q_H} = \Delta\vec{\mathrm{k}} \cdot \vec{\mathrm{H}}/\mathrm{H} = \mathrm{q}\cos\theta\ . \qquad (2)$$

As the wavelength becomes shorter, the stabilizing effect of the Maxwellian tension of magnetic lines of force becomes stronger. In this case, the growth of short-wave perturbations ($\lambda < 4\pi\Delta$, where Δ is liner thickness) is suppressed completely ($\gamma = 0$). However, if the perturbation wave vector is directed to the magnetic field at an angle θ, when θ increases to $\theta = \pi/2$ the magnetic stabilization effect attenuates to zero ($\gamma = \gamma_{RT}$). The results obtained in [1] mean the following, as applied to the magnetic implosion of cylindrical liners. Usually, cylindrical liners are driven by the azimuthal magnetic field (z pinch geometry). Here the magnetic field suppresses the growth of $\vec{k} = \vec{k}_\varphi$ perturbations, however $\vec{k} = \vec{k}_z$ (i.e. azimuthally symmetric) perturbations grow exactly in the same manner as those of the classic RT instability. For thin walled liners ($R/\Delta \geq 10$), the growth of the perturbations can result in liner failure at its convergence to small relative radii. From this viewpoint it seems interesting to study the possibility of attaining magnetic stabilization for perturbations of an arbitrary direction of the vector $\vec{k}$. Below, we consider the cases where this is possible.

2 Liner Implosion under Action of Rapidly Rotating Magnetic Field

Consider the case where the azimuthal field near the liner surface varies with time as $\sin\Omega t$ and the axial field as $\cos\Omega t$. We assume identical amplitudes of both fields. Assume frequency Ω is quite high in order to neglect a variation in field and liner perturbation amplitudes per period. In order to obtain a period-averaged increment under the above assumptions, it is necessary to average the perturbation of magnetic pressure that is proportional to $\cos^2\theta$ over time, then compute the increment similar to [1]. The result is obtained by substituting q_H^2 for $q^2/2$ in (2). Effective increment vs. q is plotted in Fig. 1. As Fig. 1 shows, in the case of fast rotation of the driving magnetic field vector, the time-averaged increment decreases by 20% in the long-wave region (q<<1) and reaches zero in the region q > 1 ($\lambda < 2\pi\Delta$).

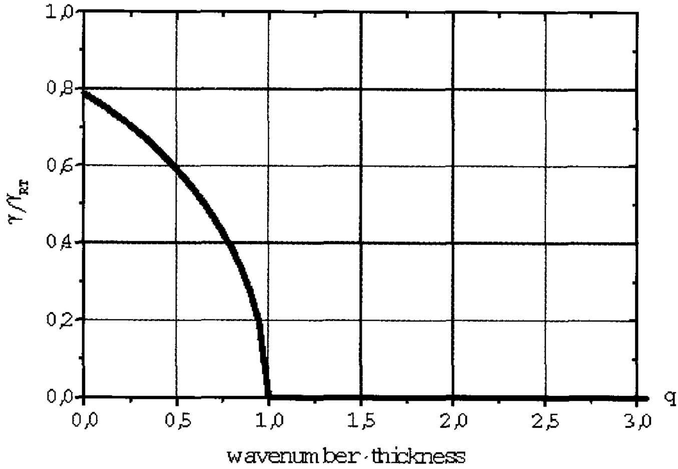

Figure 1. Multiplier to function $\sqrt{kg}$ versus wavenumber.

3 Liner Implosion under Action of the Magnetic Field Rotating Through an Angle Close to 90°

This case corresponds to a situation where the total driving magnetic field is principally poloidal at the beginning of the implosion and principally azimuthal at the end. This case can be affected if the liner is placed inside a solenoid where the same current running through the liner is passed through the solenoid. The solenoid coil density can be made quite high, so that the axial component of the magnetic field near the liner at its initial position is higher (or much higher) than the azimuthal component. By the implosion's end, when the liner radius decreases by several times, the field ratio H_z/H_φ near the liner decreases. This occurs principally due to the increase in H_φ ($H_\varphi \sim 1/R$) then secondarily due to the decrease in H_z (at invariable current). The decrease in H_z relates to the liner entrance into the space between current-conducting electrodes. As a result, H_φ can become the principal field by the implosion’s end.

For the type of system under discussion, zero-dimensional numerical computations were conducted which approximately describe the liner implosion under action of the superposed axial (poloidal) and azimuthal fields and the perturbation growth. The current pulse and liner parameters were chosen orienting to Pegasus-II liner experiments [2]. The initial-to-final liner radius ratio was taken equal to 4. The initial time field ratio $C = H_z/H_\varphi$ varied from 1 to 3. The liner length h also varied. The growing small perturbation harmonics were characterized by the parameter q_z ($q_z = 2\pi\,\Delta_0/\lambda_z, \lambda_z$, -“longitudinal” wavelength, Δ_0 - initial liner thickness) and azimuthal number of the harmonic $m(e^{im\varphi})$. Fig. 2 presents results of one of the computations showing variation in the exponent of $e^{E_1}\left(E_1 = \int \gamma\,dt\right)$ accumulated during the liner implosion vs. q_z and number m. For comparison, the curves $E_2(q_z, m)$ are also given without taking into account the stabilizing action of magnetic field $\left(E_2 = \int \gamma_{RT}\,dt\right)$. Fig. 2 shows that in the liner implosion conditions under discussion, as in case 1, a considerable decrease in the perturbation growth degree at any direction of vector $\vec{k}$ is possible.

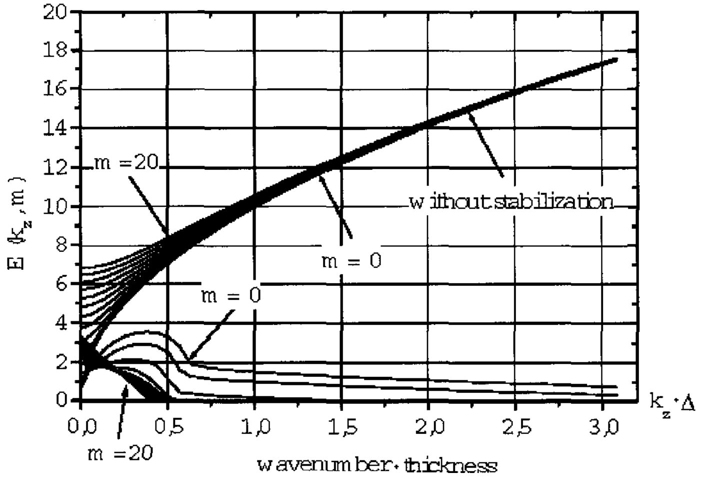

Figure 2. Integrated in time increment of perturbation growth versus wavenumber for various azimuthal numbers. $I_{max} = 2.6\ MA$, $t_{1/4} = 8\ \mu s$, $R_0 = 2.4\ cm$, $R_{min} = 0.6\ cm$, $h = 2.4\ cm$, C $= 2$, $\Delta_0 = 0.04\ cm$, $\rho_0 = 2.7\ g/cm^3$.

4 Liner Implosion Under Action of the Azimuthal Field, Given the Axial Field Inside the Liner

In this case the formula for F (see (2)) is follows:

$$F = -(\alpha_\varphi + \alpha_z)\cdot cthq + \sqrt{((\alpha_\varphi + \alpha_z)\cdot cthq)^2 + (1 + 2\alpha_z)(1 - 2\alpha_\varphi)}, \qquad (3)$$

where

$$\alpha_\varphi = \frac{P_\varphi}{P_\varphi - P_z}\frac{q_\varphi^2}{q}; \quad \alpha_z = \frac{P_z}{P_\varphi - P_z}\frac{q_z^2}{q}; \quad P_\varphi = H_\varphi^2/8\pi; P_z = H_z^2/8\pi .$$

Analysis of formula (3) allows inference of the following:

- The increment γ at any direction of the vector $\vec{k}$ is smaller than γ_{PT}.

- The most rapidly growing perturbations are those with the vector $\vec{k}$ directed along the z axis. This relates to the fact that the stabilizing field H_z must be less than H_φ.

-The perturbation growth stabilization effect is higher in the long-wave region (q<<1) than in the short-wave (q>>1). If $H_z \rightarrow H_\varphi$, then the stabilization effect becomes more isotropic and more severe. However, in practice it is not beneficial to use these conditions, as magnetic pressures P_φ and P_z are not summed up, as in Section 2, but are subtracted and the liner acceleration decreases.

5 Discussion

Three options of cylindrical liner implosion are considered, using the azimuthal and axial (poloidal) magnetic field that possesses the property to reduce the small perturbation growth increment, compared to the classical RT instability at any direction of the perturbation wave vector. Option 2 seems most acceptable for practical use. Option 1 requires variation times in fields H_z and H_φ, that are much shorter than the liner implosion time, while Option 3 is not beneficial in terms of energy. Also, note that the estimated data presented for Option 2 pertains to the middle of the liner (near the plane of symmetry). Near the liner edges where the liner contacts the gliding planes, the axial field is reduced and the stabilization effect becomes attenuated. To avoid liner destruction by non-stabilized perturbations near the gliding planes, it is necessary to use a larger angle of inclination of the gliding surfaces instead of the usual 6° - 8°. This issue needs further study.

References

1. Harris, E. G., Rayleigh–Taylor Instabilities of a Collapsing Cylindrical Shell in a Magnetic Field, *Physics of Fluids*, **5**, No. 9, (1962) pp. 1057 - 1062.
2. Hockaday, M. P., Chrien, R. E., Bartsch, R., Cochrane, J., Ladish, J., Oona, H., Parker, J. V., Platts, D., Stokes, J., Veeser, L., Sorenson, D., Walton, R., Bowers, R. L., Lee, H., Scannapieco, A., Anderson, W., Liner Target Interaction Experiments on Pegasus II. IEEE Pulsed Power Conference, (1995).

2-D INSTABILITY SIMULATION OF MAGNETICALLY DRIVEN CYLINDRICAL ALUMINUM AND ALUMINUM ALLOY LINERS

A. M. BUYKO, S. F. GARANIN, V. V. ZMUSHKO, V. N. MOKHOV,
P. N. NIZOVTSEV, V. P. SOLOVYEV, V. B. YAKUBOV
Russian Federal Nuclear Center - All-Russian Scientific Research Institute of Experimental Physics, Sarov, Russia

The Rayleigh-Taylor (RT) type instability evolution in magnetically driven metal liners depends on their strength (S) and Joule heating (J), see e.g., [1]. Simulation of this (SJ-RT) instability made use of two 2-D numerical codes: MIMOZA [2] and DRAKON [3]. Necessary conductivity and dynamic strength assumptions were made for three materials studied in liner experiments [4]. Elastic-plastic medium approximation [5] and viscous-elastic-plastic model [6] were used. Three aluminum materials whose quasi-static yield strengths differ by a factor of up to 40 exhibited essentially identical ultimate dynamic yield strength of ~2 kbar in the calculations. Data is obtained for more adequate computational description of aluminum and aluminum alloy dynamic strength and conductivity.

1 Introduction

Instability of accelerated metal plates [6] is numerically simulated with various physical models of medium strength, among which are the elastic-plastic, viscous-elastic-plastic and relaxation models. Also, the techniques have been used since 1995 for computing instability of liners driven by current pulses from explosive magnetic generators and from capacitor banks [1].

2 Setting Up Computations and Computed Data

The program system MIMOZA [2] provides the possibility of computations on Lagrangian, Eulerian and combined Eulerian-Lagrangian regular meshes. Different materials can be segregated with Lagrangian lines. Magnetic gas dynamics are computed with an explicit two-step difference scheme. In the Lagrangian technique, DRAKON [3], the magnetic field diffusion was not computed, but the Joule heating of the liner computational cells was taken into account by 1-D MHD computations. Most computations described the material shear strength with the Steinberg elastic-plastic model [5] in which the yield strength Y grows with growing strain and pressure and drops with growing temperature. For alloy AMg6, an elastic-plastic model with viscosity [6] was used. In the computations, the equation of state and conductivity of the liners was described with model [7] developed for aluminum. The materials differed in specially selected conductivity parameters α of solely condensed states: $\frac{\sigma_0}{\sigma}=\frac{\rho_0}{\rho}(1+\alpha\cdot q)$, where ρ is density, q is specific Joule heating, σ_0 and α are parameters. Fig. 1 presents upper and lower estimates of aluminum conductivity and only lower estimates for the alloys. Liner geometries, initial perturbations of the liners' outer surface, and currents in the liners corresponded to the experiments [4]. The liner fragments, 2 mm in height and equal to the initial axially symmetric perturbation wavelength, were computed.

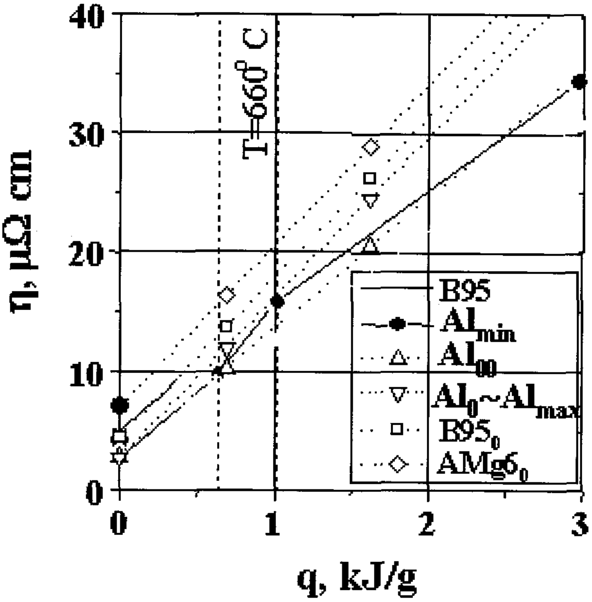

Figure 1. Estimated specific resistance of aluminum and aluminum alloys at normal density (dotted line) by VNIIEF data.

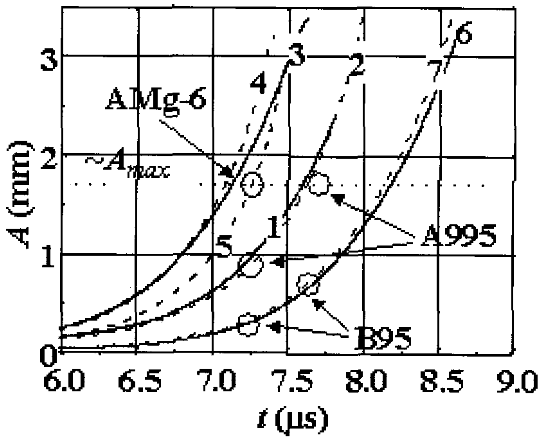

Figure 2. Perturbation amplitudes A(t) computed with MIMOZA (solid line) and DRAKON (dotted line) techniques: 1, 2 - Al1100 model; 5 - viscous-elastic-plastic model; 3-4, 6 - 7 - Al6061 model with Y0 = 1 - 1.5 kbar, and comparison with experimental results.

Fig. 2 compares the computed liner perturbation amplitudes A with the experimental data [4]. The elastic-plastic model of alloy AMg6 describes the experiment well. Both techniques with identical values of the initial yield strength Y_0 of elastic-plastic models provide results close to the experiment. The A995 liner is well described with the Al1100 model, however the description of the aluminum alloy liners required several times the reduction in Y_0 compared to that in [5]. Fig. 3 presents computed distributions of Joule heating in the liners and computed X-ray images of the liners; the latter agree essentially with experiments in [4]. Report [4] presents agreement of the experimental currents in the liners with 1-D and 2-D MHD computations discussed above. The 2-D computations achieve the ultimate yield strength of ~2 kbar, about identical for all the three materials studied, including A995 and B95 differing in the quasi-static yield strength by a factor of ~40. In the 2-D MHD computations under discussion there are no low-density "clouds" observed above the AMg6 and B95 liners during the experiments. Any clouds might have been related to the small-scale perturbation growth and to local electric explosions, which can arise in the computations at a more adequate initial perturbation and conductivity simulation.

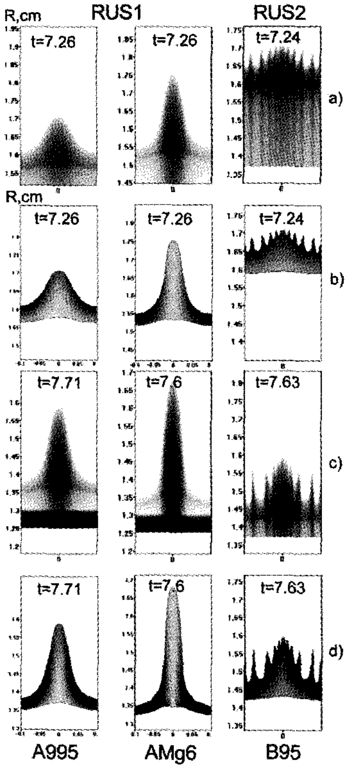

Figure 3. Computational radiograms (a, c) and Joule heating (b, d) of liners corresponding to the first (a, b) and second (c, d) radiograms in experiments RUS1 (A995, AMg6) and RUS2 [4].

3 Conclusion

The above 2-D computations with two techniques satisfactorily describe the major experimental data for the initial perturbation growth in aluminum A995 and alloy AMg6 and B95 liners [4]. The computations achieve about identical ultimate yield strength of ~2 kbar in all three materials. However, it was necessary to considerably modify notorious parameters of elastic-plastic models [5] for the alloys. This testifies for the need to improve the models describing dynamic hardening of the materials (for example, by introducing the dependence of material dynamic hardening on the strain rate). The data can also be used to better describe the conductivity of aluminum and aluminum alloy.

References

1. Buyko, A. M., Delov, V. I., Zmushko, V. V., et al. Numerical study of perturbation growth in liner systems taking into account liner elastic-plastic properties. Presentation, Workshop, Los Alamos, USA, July 5-9, (1996).
2. Sofronov, I. D., Afanasyeva, E. A., Vinokurov, O. A., Voropinov, A. I., Zmushko, V. V. et al., Program system MIMOZA for solving multidimensional continuum mechanics problems on ELBRUS-2 computer, VANT, *Ser. Mat. Modelir. Fiz. Protsessov*, (1990), No.2, pp. 3-9.
3. Abakumov, A. I., Nizovtsev, P. N., Pevnitsky, A. V., Solovyev, V. P., Program system DRAKON for computing elastic-plastic flows at shock-wave loading in 2D and 3D approximations. Proc.International Conference. 4-th Zababakhin Scientific Talks. October 16-20, (1995), Snezhinsk, Chelyabinsk region, Russia.
4. Buyko, A. M., Burenkov, O. M., Chernyshev, V. K. et al., Instability growth of magnetically imploded cylindrical aluminum and high-strength aluminum alloy liners. (Results of early joint LANL/VNIIEF Pegasus-2 experiments). Presentation at this Conference.
5. Steinberg, Daniel J., Equation of State and Strength Properties of Selected Materials, (1991).
6. Lebedev, A. I, Nizovtsev, P. N., Rayevsky, V. A., Solovyev, V. P., Rayleigh-Taylor instability in strong media. Experimental study. 5th International Workshop on the Physics of Compressible Turbulent Mixing, New York, Stony Brook, (July 1995).
7. Buyko, A. M., Garanin, S. F., Demidov, V. A., et al., Investigation of the dynamics of a cylindrical exploding liner accelerated by a magnetic field in the megagauss range. Megagauss fields and pulsed power systems (MG-V) (1989) p.743.

EXPLORING WAYS TO IMPROVE Z-PINCH CALCULATIONS

W. MATUSKA, J. AUBREY, R. BOWERS, H. LEE, D. PETERSON
Los Alamos National Laboratory, Los Alamos, NM, USA

C. DEENEY, M. DERZON, T. NASH
Sandia National Laboratory, Albuquerque, NM, USA

Recent two-dimensional radiation magnetohydrodynamic (2-D RMHD) calculations of radiating Z-pinches agree well with integral data (current waveform, yield and power). The agreement between these calculations and detailed data, such as time-resolved X-ray images, is generally not as good. Improved physics models of Z-pinches, which better match detailed data, are needed to have true predictive capability. Furthermore, a better understanding of small-scale features may be crucial in designing and evaluating application experiments that use central targets. To address these problems, we first determine which integral data are most sensitive to the details in the models. This information is then used to investigate aspects of the pinch to which the data is sensitive, using non-standard techniques. For example, the pinch is calculated in (x,y) coordinates to investigate how a non-symmetric implosion affects the simulated data and whether the simulated data can be made to match the X-ray images as well as the integral data.

1 Introduction

In order to have confidence in predictive capability, one must get the correct answers for the correct reasons. In other words, the physics that dominates a natural phenomenon must be included in the calculation, whereas physics that plays a minor role can often be eliminated unless a high degree of accuracy is needed. Above all, parameters should not be adjusted to compensate for a dominant aspect of the physics that has been ignored. The preceding statement is largely self-evident; however, determining which physical processes are dominant and which play a minor role is sometimes non-trivial.

Traditionally, axially symmetric 2-D RMHD codes have been used to calculate radiating Z-pinches by imposing random density perturbations in the r-z plane on the initial geometry. These calculations can then be made to match integral data [1-3]. On the other hand, these calculations consistently disagree with time resolved X-ray images [4,5]. Intuitively, these differences appear to be related to the fact that axially symmetric codes force exact mass convergence on axis, a situation that does not actually occur due to small variations in initial dimensions and masses, non-uniform current flow, and other irregularities. In fact, data images show the maximum intensities to lie at varying distances off axis along the pinch.

Rather than attempting to go directly to 3-D models, we have modified an existing Eulerian code to calculate a radiating Z-pinch in (x,y) coordinates. In addition to being simpler than a 3-D code, understanding the relative contributions in (x,y) coordinates as well as in axially symmetric coordinates should help us to understand issues that need to be addressed by 3-D codes. This will enable us to come closer to true predictive capability. Others [6-9] are also investigating non-symmetric implosions.

2 Traditional Calculations

Traditional calculations employ a 2-D axially symmetric Eulerian code with MHD and three-temperature radiation diffusion. Using the amplitude of an initial random density perturbation as one free parameter ("knob"), the integral data can be matched self consistently for the known drive circuitry. X-ray images have been calculated from these 2-D Eulerian simulations at times corresponding to the data images from experiments. Spectra are calculated by solving the transfer equation, at a fixed time, along 3-D rays traced through the 2-D mesh. These rays have the same orientation as the experimental line-of-sight (LOS) and have a rectangular spacing that approximates the resolution of the X-ray camera. This spacing is also approximately equal to the Eulerian zone size. These spectra are then convolved with the camera response function to obtain the calculated 2-D image.

Data and calculated images of bare pinches compare similarly in the Pegasus, Saturn and Z-machine regimes. At time of maximum power, data and calculations show a series of bright spots along the symmetry axis, with the calculated spacing agreeing reasonably well with the data. This spacing is determined by the axial, long wavelength instabilities. The existence of these instabilities has been verified with visible light images on Pegasus.

Major differences exist between the calculated X-ray images and data, as seen by the comparison of line-outs from a Saturn shot in Fig. 1. Since the camera is not absolutely calibrated, the intensity scale is arbitrary; thus we compare the relative magnitude of calculated and measured features. On-axis hot spots in the data (Fig. 1) are only about 30% more intense than the valleys between them. The corresponding difference in the calculated intensity between hot spot and valley is about an order of magnitude. In the data, the off axis intensities are very similar at these two axial positions, while the calculated intensities at these positions are very different from each other. These comparisons suggest that the mass does not actually stagnate exactly on axis as it does in the axially symmetric 2-D calculations, but converges in an irregular (i.e. 3-D) manner about the axis.

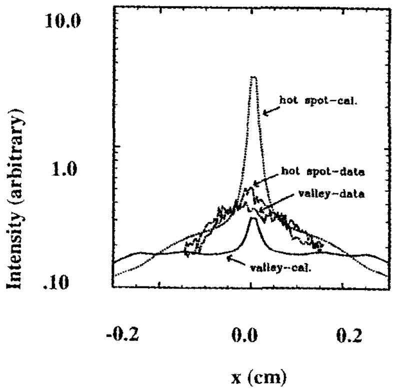

Figure 1. Line-outs from X-ray images perpendicular to the pinch axis.

Calculated densities vary axially by more than three orders of magnitude, with most of the mass collecting in the hot spots. The data suggests that the axial variation in density may be much less. In fact, this blurring effect may be the dominating mechanism for many important quantities (X-ray images, XRD measurements, spectra and power), while the axial instabilities could be secondary.

3 Different Approach

We begin our investigation of axial convergence by modifying a one-temperature radiation diffusion hydrodynamics Eulerian code in (x,y) coordinates to include the magnetic force between current elements oriented perpendicular to the plane. The Biot-Sevart law describes the magnetic force acting between the elements

$$\vec{F}_i = -\frac{\mu_o}{4\pi}\sum_j I_i I_j \iint \hat{r}_{ij} \frac{dl_i \cdot dl_j}{r_{ij}^2} \tag{1}$$

The total current is decomposed into elements I_i passing through the i^{th} element (height assumed to be 1.0 cm). Each element (represented by a zone) is attracted by the currents in all other zones at distance r_{ij} to calculate the force F_i at each time step. As a first approximation, the current in each zone is chosen to be proportional to the mass in the zone. For non-uniform current flow, the current varies by a specified function of angle about the center of mass, which is calculated at each time step. The zonal currents are normalized such that their sum equals the specified total current at each time step. Equation (1) lends itself to any other irregularity in mass or current that one wishes to specify. Forces due to irregularities in the return conductor may also be taken into account. Resistive heating is approximated using a constant resistivity in all zones. This could be changed to tabular resistivities.

The drive current is specified as a function of time rather than solving for the current waveform self-consistent with the rest of the calculation. This was motivated by a parameter study using a self-consistent circuit to study r-z instability development for a variety of length scales. The current waveform and energy generated by the pinch was found to vary weakly with the instability model. However, the peak power was quite sensitive to the model used.

Cylindrical convergence calculations in Eulerian (x,y)-coordinates are not made without difficulties. Convergence is not exact, and the tight pinch exhibited by unperturbed calculations with axially symmetric codes cannot be reproduced. Therefore, we only intend to show the effects of azimuthal variations in (x,y) coordinates relative to an (x,y) calculation with no intentional variations.

4 Results

An (x,y)-coordinate calculation with uniform current flow is compared with a similar calculation with non-uniform flow. These calculations are based on parameters for the Z-machine shot Z-26, which had a 4.1 mg tungsten wire array of 2.0 cm radius and 2.0 cm height. In the calculations, the mass of the wire array was uniformly distributed in a 0.1 cm annulus about the 2.0 cm initial radius. The maximum current was 16.1 MA. The function that defined the non-uniformity in current was randomly generated and varied from 4.2% above the nominal current to 3.5% below.

The power and energy generated (Fig. 2a) differ for these two calculations, with the power curves showing the greater amount of variation. The non-uniform current flow reduces the peak power. A comparison of temperature contours from the two calculations (Fig. 2b) show that the high temperature spike in the uniform calculation is greatly reduced in the non-uniform calculation. In this example, the reduced spike has actually divided into two components. (Note the non-circular contours for the uniform calculation, a difficulty mentioned above.)

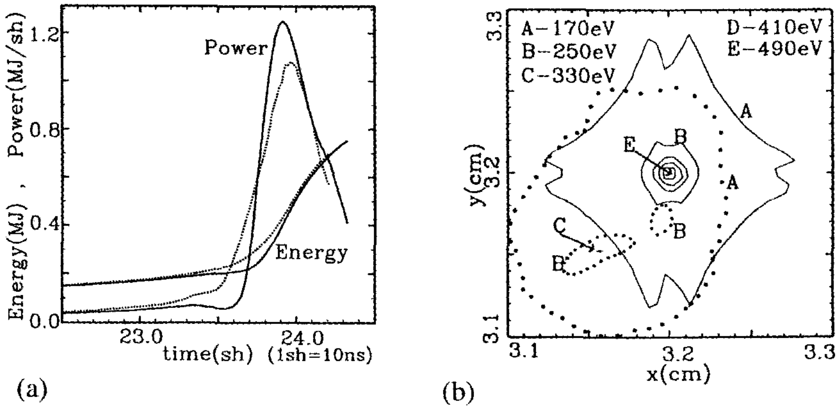

(a)

(b)

Figure 2. For uniform (solid) and non-uniform (dotted) current flow, compare (a) power and energy, (b) temperature contours.

5 Summary

Time-resolved X-ray images and other data suggest that Z-pinches may not implode in a manner consistent with traditional axially symmetric calculations that use an initial random density perturbation as a free parameter. Even though this model can be made to match integral data for a wide variety of Z-pinches, it has only a limited value as a predictive tool. It appears that one or more important piece of physics is not included in this model. The density perturbation "knob" is used to compensate for this omission in a manner that is not consistent with the detailed data. There are many candidates for this missing physics. The data shows the pinch to be non-symmetric and suggests that the density variation in the axial direction is not nearly as great as that calculated with the traditional model. These two observations make calculations in (x,y) coordinates a good candidate for investigation. Other candidates should also be considered, in turn.

We have shown that irregularities in (x,y) coordinates alter the pinch in a manner that is consistent with the differences in Fig. 1, hence these irregularities will probably need to be considered in order to calculate the detailed data correctly, such as in Fig. 1. The present (x,y) model must be improved to include a more realistic current distribution and to produce circular contours in the uniform case. This (x,y) method is, of course, also susceptible to "knobs." However, if this or any other model depends largely on the dominant physics where the associated physical quantities are accurately known, then the need for "knobs" will be greatly reduced or eliminated. Such a model will correctly calculate detailed data, which is a necessary part of true predictive capability.

References

1. Peterson, D. L., et al., *Phys. Plasmas* **3** (1996) p. 368.
2. Matuska, W., et al., *Phys. Plasmas* **3** (1996) p.1415.
3. Peterson, D. L., et al., *Phys. Plasmas* **5** (1998) p. 3302.
4. Matuska, W., et al., *10th IEEE Inter. Pulsed Power Conf.*, (1995) p. 1041.
5. Matuska, W., et al., *11th IEEE Inter. Pulsed Power Conf.*, (1997) p. 826.
6. Marder, B. M., et al., *Phys. Plasmas* **5** (1998) p. 2997.
7. Peterkin, R. E., et al., *IEEE Trans. Plasma Sci.*, **27**, no.1 (1999) p. 118.
8. Sanford, T. W. L., et al., *Phys. Plasmas* **6** (1999) p. 2030.
9. Chittenden, J. P., et al., Plasma Formation and Implosion Structure in Wire Array Z-pinches, *Phys. Rev. Lett.* (in press).

THE APPLICATION OF 2-D SIMULATIONS TO Z-PINCH EXPERIMENT DESIGN AND ANALYSIS

D. L. PETERSON, R. L. BOWERS, W. MATUSKA
Los Alamos National Laboratory, USA

G. A. CHANDLER, C. DEENEY, M. S. DERZON, M. K. MATZEN, R. C. MOCK, T. J. NASH, T. W. L. SANFORD, R. B. SPIELMAN, K. W. STRUVE
Sandia National Laboratories, Albuquerque, USA

The successful 2-D simulations of cylindrical wire array z-pinch experiments (reproducing such features as the measured experimental current drive, radiation pulse shape, peak power and total radiated energy) can lead to a better understanding of the underlying physics in z-pinch implosions. There now exists the opportunity to use such simulations in the analysis of experimental data and in the design of new experiments. Examples include the explanation of the power-to- length results in reduced length pinches and the prediction of the current best power and pulse width that occurred in a "nested" wire array experiment. Further examples discussed here are those of "dynamic hohlraum" experiments in which the tungsten plasma implodes onto a central cylindrical foam target. The utility of the 2-D simulations in designing experiments is illustrated along with examples of the simulation predictive capability.

1 Introduction

Two-dimensional simulations of hollow z-pinches have been successful in reproducing important experimental results on a variety of machines, loads, currents and timescales [1]. The following series of experiments illustrates the utility of such simulations in experiment design, analysis and interpretation. First considered are two experiments, one with a single cylindrical tungsten wire array, and another employing a second tungsten array (at smaller initial radius) nested within the first array. Second, dynamic hohlraum (DH) experiments are discussed. The DH experiments used the single or nested array configurations described previously to create a tungsten plasma shell that strikes an on-axis target cylinder of CH foam. This target cylinder may have a gold coating [2].

2 Experiments Without a Central Target

Two-dimensional simulations of experiments for pinches 2-cm and 1-cm long provided an explanation for the result that the energies radiated in both cases were nearly the same, and that the 1-cm pinches had higher-than-expected powers [3]. Also, simulations by Douglas, et al., indicated, and experiments subsequently confirmed, that reduced pulse widths could be obtained by the use of nested tungsten wire arrays [4]. Two 1-cm long experiments, Z-104 with a single array, and Z-215 with nested arrays, were conducted and employed as the baseline loads for later DH experiments. The side-on (radial) radiation powers along with the results from 2-D simulations are shown in Fig. 1. An example of a difference between simulation and experiment can be seen in Fig. 1(b), which shows a radiation pulse associated with the collision of the nested arrays while the measured result does not. Nonetheless, these simulations gave good overall agreement with measured currents, timings, peak powers, pulse widths and shapes as well as with total radiated energy.

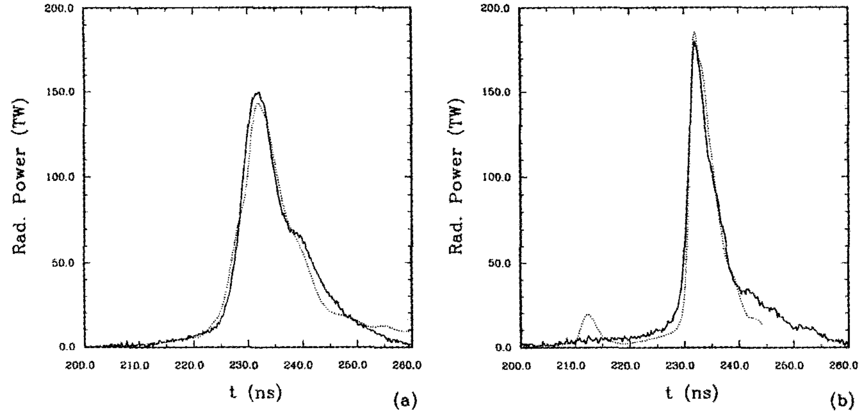

Figure 1. Measured side-on radiation power (solid) and 2-D simulation (Dotted for: (a) Z-104 (single array) and (b) Z-215 (Nested arrays).

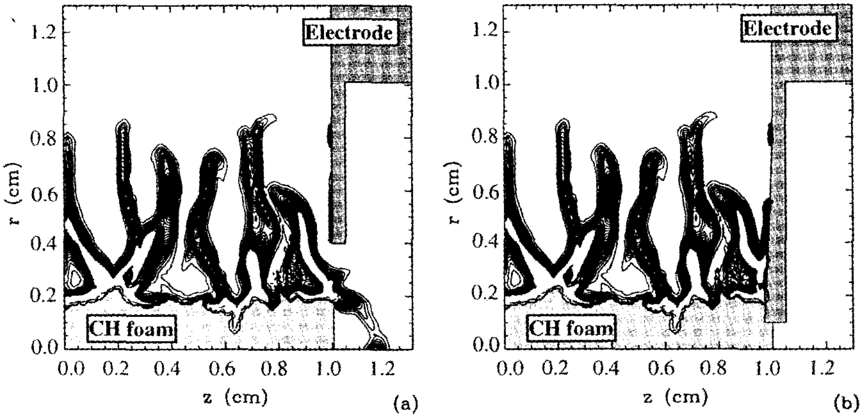

Figure 2. 2-D simulation tungsten density contours impacting the CH foam target: (a) Z-112 with a large aperture and (b) Z-216 with the redesigned aperture and electrode.

3 DH Experiments

The DH experiment Z-112 gave promising, if somewhat puzzling, results. Using the Z-104 simulation as a starting point, the 2-D simulation of Z-104 indicated that the large on-axis electrode aperture could be expected to allow the tungsten plasma to blow past the end of the CH obscuring the end-on view of the foam, as illustrated in Fig. 2(a). This conclusion was consistent with end-on images of the foam, which showed an early-time bright spot on-axis. Subsequently, the simulations were employed to redesign the electrode, including a 3° inward slope and smaller aperture size as shown in Fig. 2(b). Experiment Z-216, employing these changes, showed improved performance without any indication of tungsten obscuration of the view of the foam.

As can be seen by comparing Figs. 1a and 1b, we should be able to expect improved performance for DH targets driven by plasmas from nested arrays as the rise time is shorter and the peak power is higher for these loads. The simulations indicated that instability growth at the time of impact on the DH target in the nested array load would be considerably less than that for the single array and this would create a more uniform hohlraum with higher radiation temperatures. Two DH experiments, Z-258 (6 mg/cc CH coated with 0.6 μm of Au), and Z-255 (uncoated 6 mg/cc CH) are compared here to the predictions created by including these DH targets into the simulation used to match Z-215.

The on-axis power during the DH time period (after the plasma has struck the DH target but before the combined tungsten and target final pinch on-axis: about t = 225 to 237 ns in Fig. 3) is shown for Z-258 and the 2-D simulation in Fig. 3(a). Uncertainties exist in both the simulation and experimental powers at the final pinch time (after t = 240 ns in Fig. 3) due to material jetting through the on-axis aperture. The side-on radiation pulse shape and timing is compared with that of the simulation in Fig. 3(b). No reliable determination has been made for the absolute scale of this power, so the results have been normalized to show a value of 1.0 for the first peak (as the plasma strikes the foam) as the dynamic hohlraum is created. Reasonable agreement in pulsewidth, shape and timing can be seen, as well as in pulse width and shape in the final peak.

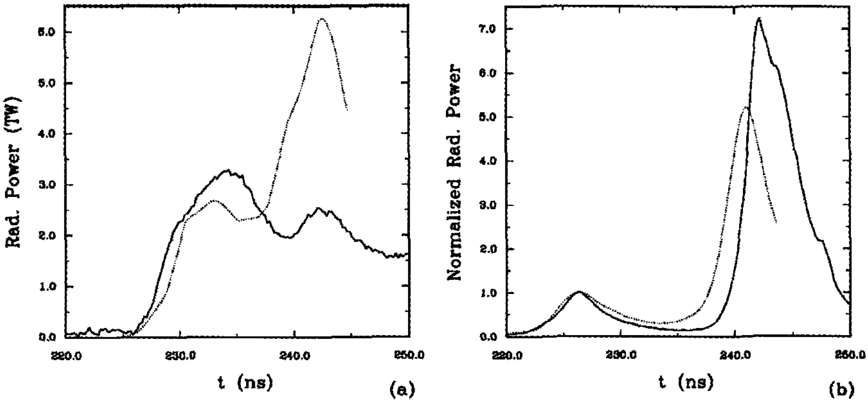

Figure 3. Radiation powers, measured (solid) and 2-D simulation (dotted), for Z-258 (Au coated CH): (a) absolute end-on and (b) normalized side-on.

Side-on data was saturated for Z-255, but a comparison of end-on data is shown in Fig. 4. As seen in Fig. 4(a), the simulation does indicate a small increase in end-on power for the uncoated foam target but the experimental value increased by much more. In Fig. 4(b), the normalized first peaks of the end-on power are seen to be similar in shape and duration, suggesting that the simulation may have properly modeled timing and perhaps some development of the DH, though underestimating the peak power and total energy during this time.

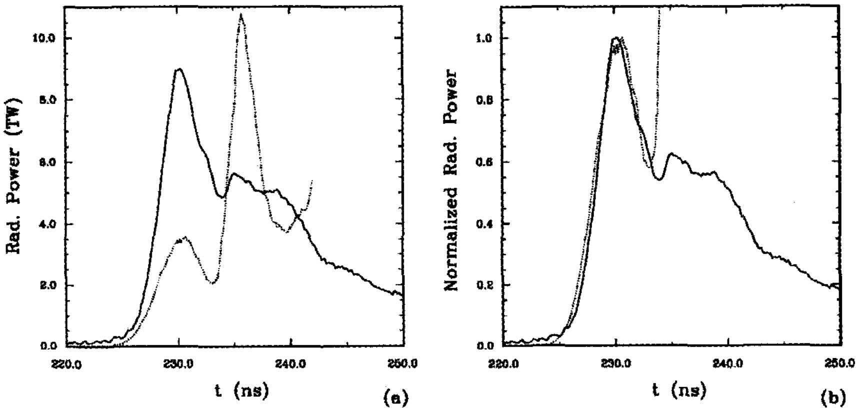

Figure 4. End-on radiation power for Z-255 (uncoated CH), experimental (solid) and 2-D simulation (dotted): (a) absolute scale and (b) normalized.

4 Conclusions

The examples shown here indicate the usefulness of 2-D simulations in interpreting and understanding experimental data, and enhancing results by using the 2-D code as a design tool. Such codes allow some predictive capability (as seen in the improvement of nested vs. single wire arrays) though in other cases, the codes may only indicate trends (as seen in the comparison of end-on powers for coated vs. uncoated foam DH experiments). Though much room for improvement remains, the combination of experiments and simulations has been fruitful in improving results and in understanding the underlying z-pinch physics.

Acknowledgments

This work was supported by the US Department of Energy.

References

1. Peterson, et al, *Phys. Plasmas* **5**, (1998) pp. 3302 and references therein.
2. Brownell, et al, *Phys. Plasmas* **5**, (1998) pp. 2071.
3. Deeney, et al, *Phys. Plasmas* **5**, (1998) pp. 2605.
4. Deeney, et al, *Phys. Rev. Lett.* **81**, (1998) pp. 4883.

PLASMADYNAMIC SWITCHING AT MEGAGAUSS MAGNETIC FIELD LEVELS

P. J. TURCHI
The Ohio State University, Columbus, Ohio, USA
Present Address: Air Force Research Laboratory, Kirtland AFB, NM, USA

The Plasma Flow Switch consists of coaxial electrodes connected by a high-density plasma discharge and driven by a high current source. Vacuum conditions exist initially upstream and downstream of the discharge, which accelerates axially due to electromagnetic forces. In typical arrangements, the discharge attains speeds of about 70 km/s in about 3 microseconds. During this time, most of the system energy is stored as magnetic energy in the vacuum between the discharge and the upstream, high-voltage insulator. Motion of the discharge off the end of the center electrode releases this stored energy to a load in about 100 nsec. The velocity of very low-density plasma trailing the main discharge governs this type of release. Experimentally, this plasma can flow to the load at speeds in excess of 2000 km/s, corresponding to super-Alfvenic expansion. Scaling relationships for PFS operation are considered, including the effects of high magnetic fields on electrode boundary layers. Applications of the PFS to liner implosions and controlled fusion are described.

1 Introduction

The Plasma Flow Switch (PFS) was developed [1] to match multi-megajoule, microsecond pulses to sub-microsecond loads, such as large-radius plasma implosions [2,3]. It represents a form of inductive storage and switching system specialized to the environment of very high energies and currents typical of low impedance capacitor banks and magnetic-flux compression generators. As such, it offers an alternative to high energy, high voltage pulseline technology based on Marx generators. This alternative may provide relatively low cost opportunities for evaluation of very high power, pulsed plasma technologies.

The Plasma Flow Switch has been used successfully on the Shiva Star capacitor bank at stored energy and peak currents of 6 MJ and 12 MA, respectively. In experiments on Shiva Star, the PFS delivered power to plasma implosion loads, resulting in upwards of one megajoule of soft X-radiation [3]. A separate series of experiments [4] provided ultrahigh speed plasma flows (>2000 km/s) of both aluminum and tungsten plasmas, corresponding to peak voltages across the switch of half a megavolt. Switch operation generated a megajoule of ion kinetic energy, resulting in fully stripped aluminum plasma at electron temperatures of 30 keV. Development of plasma flow switching has also proceeded on the Pegasus capacitor bank [5] and the Procyon explosively driven magnetic-flux compression generator system [6].

This paper discusses scaling of PFS operation with magnetic field level, potential difficulties in using megagauss-level fields, and possible application of PFS techniques on present or near-term systems such as Shiva Star and Atlas [7].

2 Review of Plasma Flow Switch Operation

The Plasma Flow Switch basically consists of coaxial electrodes in vacuum, connected by well-localized annular plasma. In its original experimental embodiment, vaporization and ionization of an array of wires in vacuum provides this plasma; an additional dielectric foil stretched between the electrodes limits the early axial motion of plasma downstream of the main discharge. The use of this arrangement, compared to a gas pre-fill (as in the Mather-type, dense-plasma-focus apparatus), permits maintenance of vacuum conditions near the insulator surface, upstream of the discharge. Electromagnetic energy enters through this surface to fill the coaxial inductive store formed by the electrodes and the annular plasma discharge. Baffles prevent line-of-sight transfer of radiation energy from the discharge to the insulator surface, an essential feature in preserving the high-voltage strength of the insulator interface. With all the inertia of the plasma present initially (vs. accumulated by sweeping up a prefill), the dynamic impedance of the discharge remains low during the early part of the current rise. Thus, electromagnetic energy storage in the vacuum between the insulator and the discharge can occur at relatively low voltage.

The Lorentz force accelerates the plasma axially near the inner conductor surface to speeds greatly exceeding thermal speeds of plasmas. This allows rapid growth of an effective gap when the propagating plasma discharge passes over the downstream corner of the inner conductor. The term "effective" emphasizes the fact that low-density plasma fills the region upstream of the plasma discharge, including the vicinity of the electrode corner. Electromagnetic energy accumulated in this upstream region flows through the annular gap at the end of the center conductor to a downstream load region. The speed of the highly magnetized, low-density plasma flow limits release of energy to the load (hence the name *Plasma Flow Switch* for this device).

Plasma flow speeds scale with the Alfven sound speed,

$$v_{Ao} = B_o / (\rho_o \mu_o)^{1/2} \tag{1}$$

where B_o is the magnetic field in the coaxial inductive store, which contains plasma whose mass density, ρ_o, is much less than that in the propagating plasma discharge (the *plasma armature*).

The density of plasma upstream of the plasma armature depends on several processes. These include Rayleigh-Taylor instability of the accelerated plasma discharge, and expansion of surface plasma into the inter-electrode space. 2-D numerical simulations [8] of plasma armature dynamics suggest that instability does not leave major portions of the armature mass behind as the plasma accelerates, but these calculations may not accurately follow relatively low-density plasma. Guidelines for PFS operation include maintaining a positive rate-of-rise of current as the armature travels the length of the inner conductor, so that the Lorentz force would hold surface plasmas in place. While this may prevent gross hydrodynamic expansion, statistical mechanics demand that some plasma extends away from the surface, scaled by the density there. As a benchmark, experiments [4] with peak fields on the inner conductor of 29 T indicated a residual plasma mass-density of 10^{-4}

kg/m^3, which is less than values in the plasma armature by factors of about a thousand. In successful experiments, v_{Ao} thus exceeds a few thousand km/s. The flow upstream of the propagating discharge, which travels at about 70 km/s, behaves sub-sonically until released toward the load region.

The annular gap off the end of the center conductor represents the minimum cross-sectional area (i.e., the "throat") for the magnetized plasma flow. For sufficiently low values of magnetic pressure in the downstream load region compared to the magnetic energy density in the coaxial inductive store, choking occurs at the throat. Therefore, the flow speed equals the local Alfven sound speed, u^*:

$$u^* = B^* / (\rho^* \mu_o)^{1/2} \tag{2a}$$

$$= (2/3)^{1/2}\, v_{Ao} \tag{2b}$$

where we have connected conditions at the throat to values in the coaxial store (i.e., stagnation conditions) using the frozen-field approximation in a high magnetic Reynolds number, zero-beta, steady plasma flow. The Poynting vector ExB/λ at the throat then provides the rate of transfer of electromagnetic energy from the inductive store:

$$P^* = E^*\, B^*\, A^* / \mu_o \tag{3a}$$

$$= u^* B^{*2} A^* / \mu_o \tag{3b}$$

$$= (2/3)^{5/2}\, B_o^{\ 3} A^* / \mu_o (\rho_o \mu_o)^{1/2} \tag{3c}$$

where A^* is the area of the annular gap (normal to the flow direction). For unsteady flow, a factor of $(2/3)^{1/2}$ should multiply the right-hand-sides of Eqs. 2b and 3c. In either idealized limit, the cubic dependence of the output power on B_o provides the interest in high values of operating magnetic field.

If no impediment exists to the flow of magnetized plasma downstream of the throat, plasma may attain an ultimate speed of $(2)^{1/2} v_{Ao}$, (or $2v_{Ao}$, for the unsteady limit). For implosion loads, however, the liner surface presents a relatively slow-moving boundary condition for this plasma flow. If the magnetic pressure in the load region builds sufficiently, the throat can un-choke. Throughout the flow field, the local plasma speed becomes less than the local Alfven speed (i.e., the flow is subsonic), which reduces differences in magnetic pressure, (corresponding to current flow). If the ratio of implosion speed to Alfven speed approaches zero, the magnetic pressure at the liner surface follows the stagnation pressure in the inductive store (multiplied by the inverse-square of relative radii to account for cylindrical geometry). Thus, in the case of a PFS delivering power to a liner implosion load, a transient of supersonic wave flow (with choking at the throat) precedes un-choking and application of the full current to the liner surface. If the implosion speed increases sufficiently, the throat may re-choke and the current at the liner surface will be less than that in the inductive store. The effective gap changes during energy transfer to the load, so conditions of choking will depend on the rate of increase of the gap compared to that of the liner implosion speed. Inefficient current delivery to the load results from magnetic pressure differences required by the dynamics of the magnetized plasma flow. Electrical breakdown of an already ionized plasma and electron-beam effects in an environment with very low impedance and high magnetic field do not participate in the plasma flow switch.

3 Effects of High Magnetic Fields

Several phenomena can significantly affect PFS performance compared to the idealized picture presented in the previous section. These primarily relate to conditions near the corner of the inner electrode where the gap must open to release the accumulated magnetic energy. The dynamics and thermodynamics of plasma in this region require numerical simulation, severely challenging even state-of-the-art computer codes. Some qualitative discussion may provide useful insights for expected scaling of behavior with high magnetic fields.

Recent studies [8] of the plasma layer along the inner conductor suggest that complex processes control the effective gap of the PFS. Briefly, the relative cold electrode allows plasma from the discharge to collect at higher mass density near the electrode surface. This "boundary layer" does not accelerate to the same high speed as the "freestream" portion of the main discharge, but can attain axial speeds much higher than thermal values. Material from this layer can extend off the end of the center conductor, interfering with the creation of a low-density gap between the corner and the main discharge plasma. The duration and extent of such interference increase with the boundary layer thickness, which tends to grow as the discharge accelerates along the electrode surface. Use of an annular slot just upstream of the end of the inner conductor to capture the boundary layer appears to improve PFS performance on Pegasus II, both experimentally and in numerical simulations [8]. Experiments on Shiva Star, which operated at higher currents than Pegasus II, did not use such a boundary-layer trap, and numerical simulations indicate that the boundary-layer structure resulted in thinner layers in the gap in these experiments. Plasma heating at higher current density can support shorter gradient scales for heat conduction to the cold electrode boundary, which would imply thinner layers of high mass-density. Thus, higher operating magnetic fields might improve PFS performance.

To estimate the dependence on magnetic field of a plasma boundary layer based on thermal effects, we can use an idealized model. In a steady balance of resistive heating and heat conduction near the electrode, we have:

$$\frac{\partial}{\partial x}\kappa(T)\frac{\partial}{\partial x}T = -\eta(T)j^2 \tag{4}$$

where the thermal conductivity, κ, and the electrical resistivity, η, are both functions of temperature; x is the distance normal to the electrode. The current density, j, depends on the magnetic field driving the plasma armature, and attaches to the electrode surface with a characteristic distance, Δ_a, in the stream-wise direction obtained by setting the magnetic Reynolds number equal to unity:

$$\Delta_a = \eta / \mu_o u_g \tag{5}$$

where u_g is the axial speed of the plasma armature. In terms of this distance and the magnetic field, the current density is:

$$j \cong B / \mu_o \Delta_a$$

$$= u_g B / \eta \tag{6}$$

If the thermal conductivity and electrical resistivity have simple power-law forms:

$$\kappa(T) = K_h T^K \tag{7a}$$

and

$$\eta(T) = K_R / T^N \tag{7b}$$

where K = 5/2 and N = 3/2 in the case of a classical plasma and both K_h and K_R are constants, we may write Eqn. 4 in term of dimensionless variables, $\Theta = T / T_c$ and $\alpha = x / x_c$:

$$\frac{d}{d\alpha} \Theta^K \frac{d}{d\alpha} \Theta = - \Theta^N [x_c^2 u_g^2 B^2 / K_h K_R T_c^{(1+K-N)}] \tag{8}$$

where T_c is a characteristic temperature (say, the value in the freestream plasma), and x_c is a characteristic thickness of the temperature distribution. We may specify this thickness by setting the collection of terms in the brackets equal to unity, so:

$$x_c = (K_h K_R)^{1/2} T_c^{(1+K-N)/2} / u_g B \tag{9}$$

This suggests that the thickness of the thermal boundary layer, in which the plasma temperature accommodates to the cold electrode and the plasma density increases to maintain pressure equilibrium, decreases with higher magnetic field. The plasma pressure, however, scales as the square of the magnetic field, so the product of density, ρ_{bl}, and thickness of material, $\delta_{bl} \cong x_c$, spilled from this layer over the electrode corner, will increase with B.

The strictest condition for proper operation of the PFS would demand that the spillage from the plasma boundary-layer accelerates radially to the local Alfven speed of the low-density flow:

$$(B_l^2 / 2\mu_o)\, \delta t / \rho_{bl} \delta_{bl} = B_l / (\rho_l \mu_o)^{1/2}, \tag{10}$$

where δt is the time during which the spilled material may impede the flow of low-density magnetized plasma to the load region. Higher values of the operating magnetic field do not affect this limitation on switching time if the mass density of the residual plasma following the armature does not scale with the density in the armature. Alternatively, if the mass density of the trailing plasma scales with that in the armature so it increases with magnetic pressure, δt will decrease with higher magnetic fields. We may, therefore, expect some improvement of PFS operation at higher field levels, but only if the magnetized plasma flow speed becomes limited by increases in the residual plasma density upstream of the plasma armature.

Processes within the main plasma discharge certainly provide a response of the plasma to the cold electrode boundary, leading to gradient scale lengths that interact with the basic plasma dynamics. The electrode surface, itself, also responds to enormous heat loads associated with the high current discharge. In the simplest process, the conductor surface temperature increases because of the skin-current heating. The temperature increase of the electrode material depends on the magnetic energy density in the vacuum:

$$\Delta T = s\,(B^2 / 2\mu_o) / C_v \tag{11}$$

where s is a surface heating factor [9] based on the time-variation of the vacuum field, and C_v is the specific heat per unit volume for the electrode material. Before skin-current heating can bring the surface to significant fractions of the boiling temperature (at a vapor-pressure of one atmosphere), however, the electrode would already have suffered structural difficulties precluding the use of such a high magnetic field. For example, skin heating can raise the surface temperature of copper electrodes from room temperature to 2500 K, if the operating magnetic field exceeds 1.4 MG, (with s = 1.27). At the magnetic pressure associated with this field, the surface would move about 0.4 mm in a two microsecond pulse, which is more than the skin-depth in copper for this pulse time. Thus, such motion could significantly disrupt the current path in the metal surface, especially if joints, welds or surface cracks are present, leading to failure of the apparatus during the current pulse. This failure may manifest itself by the release of material into the vacuum region through which electromagnetic power flows, preventing energy transfer to the coaxial inductive store or, subsequently, to the load. Thus, concern with disruption of the electrode surface may limit the maximum operating magnetic field for a plasma flow switch.

Energy transfer by the discharge to the electrode surface can create plasma of high mass-density near the surface and represents a much more intricate process than skin-current heating. For example, if the inner conductor is the cathode, (as it is in all PFS experiments to date), electron emission can cool the surface. Indeed, models of cathodes at high current density often assume adiabatic conditions at the surface. Evaporation of the surface at the resulting temperature then contributes material to the local plasma. A simple approach to estimating this contribution invokes experimental data for cathode mass-loss per unit of charge transfer in pulsed, high-current arcs. Values range upwards from ten to a hundred micrograms per coulomb (for simple, solid electrodes). The total mass produced in the course of plasma armature motion along the inner depends only on the time-integral of the current pulse. For current supplied by a capacitor bank, this equals the product of bank capacitance and the drop in bank voltage during the pulse. Much of this mass will remain near the surface and not propagate with the plasma armature, especially as the amplitude of the current rises and the Lorentz force presses plasma against the surface. However, mass generated just upstream of the end of the inner conductor may have the opportunity to accelerate with the armature and spill off the corner.

Mass flow enters the discharge from the surface at a rate:

$$dm_s/dt = M_c\,(2\pi r_1 B_1 / \mu_o) \tag{12}$$

where r_1 is the radius of the inner conductor, B_1 is the magnetic field there, and M_c is the mass-loss per coulomb. To accelerate this mass flow to the speed of the armature, u_g, requires the action of magnetic pressure as the mass travels a distance δ_s from the surface:

$$(B_1^2 / 2\mu_o)\, 2\pi r_1 \delta_s = u_g\, dm_s /dt \tag{13}$$

We may then estimate the thickness of the layer of surface material as:

$$\delta_s = 2M_c u_g / B_1 \tag{14}$$

The average mass density, ρ_s, in this layer also depends on the magnetic field approximately as:

$$\rho_s u_g^2 = B_1^2 /2\mu_o \tag{15}$$

To push the surface layer quickly away from the gap at the corner requires the lowest value of the product of mass density and thickness:

$$\rho_s \delta_s = M_c B_1 / \mu_o u_g \tag{16}$$

Application of the condition of Eqn. 10 to this product would demand a time, δt_s:

$$\delta t_s = 2M_c / u_g\, (\rho_1 \mu_o)^{1/2} \tag{17}$$

During this time, the surface material may impede power flow to the load region. With $u_g = 70$ km/s and $\rho_1 \cong 10^{-4}$ kg/m^3 [4], δt_s ranges from 25 to 250 ns for values of M_c from 10 to 100 μg/C. Such times correspond to observed values for PFS current delivery times. Other mechanisms, including simple filling of the region between the corner and the load by the magnetized plasma flow, however, may yield similar times. Note that, for fixed ρ_1, δt_s does not depend on the value of magnetic field, so no advantage accrues to operating at megagauss levels. Again, however, if the residual plasma density increases with magnetic pressure, acceleration to the Alfven speed becomes easier because this speed does not increase with B, and δt_s decreases with operation at higher magnetic fields.

4 Applications of the Plasma Flow Switch

The plasma flow switch was originally developed to drive liner implosions, particularly the sub-microsecond multi-megampere, multi-megajoule, large-radius plasma shells for the Shiva EM implosion X-ray source [2]. For this type of load, magnetic flux can remain in the magnetized plasma flow and energy will still transfer to the load as work performed on the outer surface of the liner. Transfer of current and energy to a diode-type load demands that magnetic flux separate from the high conductivity plasma flow. For the density and magnetic-field levels of the PFS, such separation will not occur. To drive a vacuum diode, the load must instead connect between the vacuum inductive store and the plasma armature using, for example, a plurality of post-hole convolutes and closing switches. Initially, the current through the plasma armature equals that in the inductive store. Current transfers to the load as the PFS releases magnetic flux downstream of the convolutes and closing-switches to the diode load actuate. The voltage rate-of-rise across the diode follows the 20-200 ns rise times of the PFS. Such rise times are quite adequate for some loads, including wire-arrays and various particle-beam sources.

Experiments on the Atlas pulser [7], under development at Los Alamos National Laboratory, require implosion of solid-density shells that separate the state of the inner surface of the liner from that of the electrically heated outer surface. Energy-density needs of these experiments call for fields at megagauss-levels on the outer surface of the liner. With an expected rise-time exceeding 4 μs for the current pulse from Atlas, the problem of motion of the conductors leading to the megagauss region intrudes into the design of the apparatus. The PFS may find application here by reducing the rise time of current near the liner surface, thereby limiting the penetration of thermal changes in the liner. It could also allow most of the power feed near the liner to operate at somewhat lower field levels.

A new possibility for the PFS arises in the context of controlled fusion concepts based on so-called advanced fuels (e.g., D-He^3, p-Li^6, p-B^{11}). These fuels require much higher temperatures to attain useful reaction-rate parameters [10] than "conventional" D-T reactions, (>100 keV vs. 20 keV). The ultrahigh speeds demonstrated with residual aluminum plasmas and tungsten plasmas (>2000 km/s) suggest that the PFS can provide pulsed, multi-megajoule flows with particle energies of tens of keV for the nuclei of advanced fuels. Capture of such flow by distension of a solenoidal magnetic field into a field-reversed configuration [11] would permit adiabatic compression of plasma to the 100 keV temperatures for optimum fusion gain. For a PFS diameter of 10-20 cm, as in previous multi-megajoule experiments, liner implosion techniques can operate with significant volumes in demonstration tests of alternative fusion concepts using advanced fuels. Reactor notions include the use of a stabilized liner implosion system [12] to extract work directly from the charged-particle output of the advanced fuel reactions. For D-He^3, the liner also acts as a shield against high-energy neutron products that occur as side-reactions. Direct-conversion of charged-particle energy by reversible liner motion may offset the lower efficiency (reaction-energy vs. reactant energies) of advanced fuels compared with D-T. Combination of imploding liner technology with the PFS and advanced fuels thus offers a route to obtaining copious amounts of high temperature plasma for controlled fusion research, in a direction toward attractive reactor designs.

Acknowledgments

Over the last several years, the author has had many pleasant discussions of plasma flow switching with R. L. Bowers and N. F. Roderick.

References

1. Turchi, P. J., et al., Review of Plasma Flow Switch Development, *IEEE Trans. on Plasma Science*, PS-15, **6**, (1987) p. 747.
2. Turchi, P. J., Baker, W. L., Generation of High Energy Plasmas by Electromagnetic Implosion, *J. Appl. Phys.* **44**, (1973) p. 4936.
3. Baker, W. L., et al., Current Delivery and Radiation Yield in Plasma Flow Switch Driven Implosions, *Journal of Fusion Technology*, **27** (March 1995).
4. Turchi, P. J., et al., Generation of High Energy X-Radiation Using a Plasma Flow Switch, *J. Appl.Phys.* **69** (4), (Feb. 1991) p. 1999.
5. Cochrane, J. C., et al., Plasma Flow Switch Experiments on the Pegasus Facility, Proc. of Eighth IEEE Pulsed Power Conference, IEEE Publication No. 91CH3052-8 (1991). p. 618.
6. Goforth, J. H., et al., Design of an Explosive Pulsed Power System for Driving 16 MA Plasma Flow Switch Experiments, in Megagauss Physics and Pulsed Power Systems, Ed. by V. M. Titov and G. A. Shvetsov, Nova Science, NY (1990). p. 651.
7. Parsons, W. M., et al., The Atlas Project - A New Pulsed Power Facility for High Energy Density Physics Experiments, *IEEE Trans. on Plasma Science*, **25**, 2, (1997) p. 205.
8. Bowers, R. L., et al., Current Switching Efficiency of Plasma Flow Switches in Inductive-Store Pulsed Power Experiments, to appear in IEEE Trans. on Plasma Science, Special Issue on Pulsed Power (Oct., 1998).
9. Knoepfel, H., Pulsed High Magnetic Fields, North-Holland Pub., Amsterdam (1970). Chapter 4, Table 4.II.
10. Cox, Jr., L.T., Thermonuclear Cross Section and Reaction Rate Parameter Data Compilation, USAF Phillips Laboratory Report AL-TRÑ90-053, (July, 1991). Present address: Air Force Research Laboratory, AFRL/PR, Edwards AFB, CA 93523-5000.
11. Tuszewski, M., Field Reversed Configurations, *Nuclear Fusion*, **28**, 11, (1988) p. 2033.
12. Turchi, P. J., A Compact-Toroid Fusion Reactor Design at 0.5 Megagauss, Based on Stabilized Liner Implosion Techniques, in Ultrahigh Magnetic Fields, Ed. by V. M. Titov and G. A. Shvetsov, Nauka, Moscow (1984). p. 184. Stabilized liner implosion technology is also discussed in P. J. Turchi, et al., Review of the NRL Liner Implosion Program, in Megagauss Physics and Technology, Ed by P. J. Turchi, Plenum, NY (1980) p. 375.

MACH2 SIMULATIONS OF THE DECADE PLASMA OPENING SWITCH USING A TEFLON PLASMA

D. KEEFER, R. RHODES
University of Tennessee Space Institute, Tullahoma, TN, USA

The MACH2 computer code has been used at the University of Tennessee Space Institute (UTSI) for the past several years to model the DECADE plasma opening switch (POS) using plasma properties from a doubly ionized carbon model (C^{++}). Our recent simulations use thermodynamic properties for an equilibrium Teflon (C_2F_4) plasma calculated at UTSI using a locally developed Saha code. We have found that including a model for the desorption of gas from the walls of the switch strongly affects the way the switch opens.

1 Introduction

The DECADE nuclear effects simulator at the Arnold Engineering Development Center (AEDC) uses a plasma opening switch (POS) to create a high voltage pulse to drive an x-ray diode. The intent of this study is to provide an understanding of the physical processes occurring in DECADE so that a rational approach may be taken to improve its performance.

The time history of measured currents and voltages and other observed phenomena are used to verify the applicability of the model. The process of opening is characterized by a thinning of the plasma followed by a rapid rise in voltage across the load. Time dependent measurements of current and voltage have been made at various locations in the switch that can be compared to the calculations from the model. Experimental data show that the magnetic field propagates first on the anode. Model calculations have not been able to explain these results.

2 Theory

A continuum flow model using the fluid mechanical equations for mass momentum and energy and Ohm's law for the magnetic field is used to describe the processes that are involved in a POS. Convection of the magnetic field is important when the plasma electron density is relatively high and the magnetic field is frozen into the plasma. The Lorenz forces move the plasma resulting in "snowplowing" the injected plasma into a thin layer that is accelerated toward the load. In the DM1 configuration magnetic diffusion seems to have little effect on the computed results. The diffusion of magnetic field is small compared to convection and Hall propagation, and the ohmic heating is totally overwhelmed by the *pdv* work resulting from shock heating as the magnetically accelerated gas interacts with the stagnant residual gas in the MITL. Fruchtman [1] first showed the importance of the Hall field on the propagation of the magnetic field in those regions where the electron density is small. He demonstrated how the Hall effect could greatly enhance or retard the magnetic field penetration depending on the direction of current flow. We have previously shown the importance of the Hall effect in the calculated performance of a POS [2].

For axisymmetric geometry and no axial or radial magnetic field components the equation for Hall propagation is:

$$\partial B_\theta/\partial t = B_\theta /m_0 e N_e \, [(2/r + \partial ln N_e/\partial r) \, \partial B_\theta/\partial z - 2/r \, \partial ln N_e/\partial z \, \partial r B_\theta/\partial r]$$

In a radially uniform electron density field with a negative inner electrode the Hall effect will propagate the magnetic field on the cathode ahead of the anode. A density gradient at the walls where the electron concentration falls away from the wall will enhance propagation on the anode and retard it on the cathode. Some interferometer measurements presented at a DECADE modeling review meeting in 1998 indicate a detectable plasma layer on the MITL about a millimeter thick. This effect could explain the experimental observation that magnetic field propagates first along the anode.

3 Model

The MACH2 computer code [3] solves the time dependent mass continuity, momentum, energy, and magnetic field equations for an ionized gas in the DECADE POS subject to a set of boundary and initial conditions. The necessary thermodynamic and transport properties are computed in the code. All of the calculations described here were made with the following assumptions.

1) A slip wall boundary condition is used for all solid surfaces.
2) Numerical viscosity used to stabilize the algorithm.
3) Thermal diffusion is neglected.
4) Radiation losses are neglected or treated as a heuristic energy loss.
5) Electrons and heavy particles have the same temperature.
6) Electrical conductivity is calculated from a Spitzer model.
7) The Hall effect is included in the calculation.
8) A resistive load in the model simulates the actual diode load in DM1.

Cable gun plasma generators are modeled assuming an axisymetric distribution around the POS with a sinusoidal temporal variation of velocity from 10 to 20 km/s directed toward the axis and a constant density distribution. The assumed value for the density controls the total mass injected prior to the start of the current to the POS. The baseline density is obtained by finding a value that gives the experimental opening time. An equation of state (EOS) for the injected plasma was calculated at UTSI from the Saha equation and tabulated energy levels for a CF_2 mixture as a function of temperature and pressure. The level of ionization varies from 1 to 4 electrons per ion. This EOS has been used with MACH2 calculations of a cable gun [3]. Recent experiments at UTSI show a significant loss of the center electrode of a cable gun indicating that the injected plasma may be as much as half copper. The best EOS to use is an open issue both because of the uncertainty in the composition and questions about possible significant deviations from equilibrium.

An adsorbed wall layer of molecules is assumed to be desorbed at a rate proportional to the power being dissipated in the layer, characterized by J^2 at the wall multiplied by a constant wall resistance.

Radiation loss and losses to the wall are not included. However, we have put an arbitrary upper limit on the temperature (equivalent to having an unspecified energy loss mechanism) for all of the runs described here.

An RLC circuit model, coupled to the calculated port voltage, is used to represent the actual DECADE power supply. Circuit parameters were chosen to match the experimental current waveform. The port voltage is calculated from the surface integral of the resistive voltage drops and the volume integral of time rate of change of magnetic flux. B-dot probe results are the compared with value of rB_θ at selected grid locations chosen to match the experimental locations.

4 Calculated Results

Without a model for wall desorption from the MITL, the simulation predicts that the magnetic field propagates along the cathode ahead of the anode. In the low, uniform electron density in the MITL the Hall propagation has a 1/r dependence that results in faster propagation where the radius is smallest (Fig. 1). When the desorption model is included, near the cathode the negative radial gradient of the electron density reduces propagation velocity and near the anode the positive radial gradient of electron density increases the propagation velocity. For this case, the simulation predicts that the magnetic field propagates along the anode ahead of the cathode. Also, the switch voltage decreases because the overall increase in electron density in the MITL reduces the rate at which the B field fills the MITL. The calculated results do not completely match the experiments since the shape of the calculated B-dot currents differ from the experimental values (Fig. 2). However, these differences are comparable to the experimental variation among individual experiments, and the simulation does agree qualitatively with the sequence of the B-dot measurements. At later times in the simulations, there appears to be a large amount of thermally induced motion of the gas in the MOTL resulting in density gradients changing with time. This causes a very uneven propagation of the magnetic field in the final stages of the opening that is not apparent in the data.

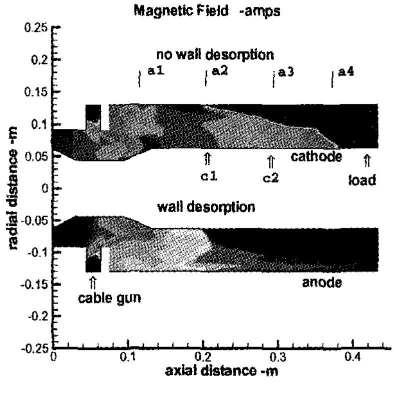

Figure 1. Magnetic field contours just prior to "opening" show propagation that occurs first on the cathode when there is no wall desorption and the gas density is uniform (upper plot), and first on the anode when an electron density gradient is formed on the MITL wall as a result of the desorption of 10^{-10} kg/m^2 of gas (lower plot).

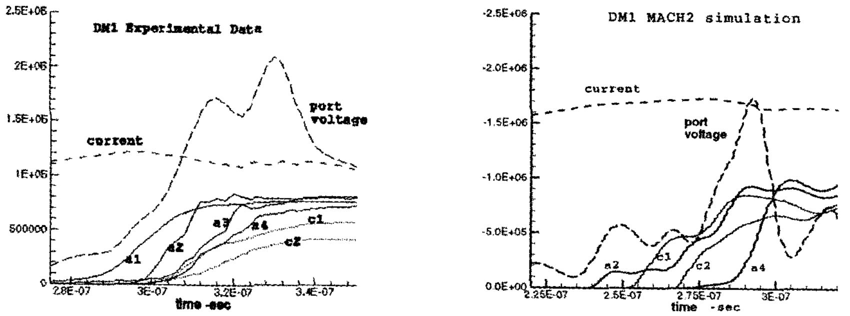

Figure 2. Currents and voltages from DM1

The calculated results do not completely match the experiments since the shape of the calculated B-dot currents differ from the experimental values (Fig. 2). In the calculations there appears to be convection of gas into the MITL and a large amount of motion of the gas in the MITL. This results in a reduced rate of propagation of magnetic field, that in turn reduces the port voltage, and in density gradients that cause a very uneven propagation of the magnetic field in the final stages of the opening. This effect is not apparent in the data. When the Hall effect is augmented by a wall desorption model the main features of a POS are at least qualitatively predicted by MACH2.

5 Conclusions

An MHD computer code such as MACH2 can be used to model basic features of a plasma opening switch (POS) during the conduction phase and can be extended to the initial part of the opening phase if the Hall effect is included and augmented by a wall desorption model. When the current is applied to a POS, the gas and resulting magnetic field motion are coupled and the Lorentz force at first compresses, then stretches and thins the injected plasma. When the plasma has thinned sufficiently, the Hall effect decouples the magnetic field from the gas and allows the rapid propagation of magnetic field into the MITL, which is seen in the experimental data. The simulation indicates that desorption of less than a mono-layer of gas from the wall of the MITL is sufficient to establish an electron density gradient near the walls that enhances the Hall propagation of magnetic field on the anode and retards it on the cathode.

References

1. Fruchtman, A, *Phys. Fluids B* 3 (8) (August, 1991).
2. Conference Record, 1996 IEEE ICOPS, Boston, (June, 1996).
3. MACH2: A Reference Manual, AFRL, Philips Research Site (1998).
4. Conference Record, 1996 IEEE ICOPS, Boston, June, 1996. Peterkin.

SHOCK-WAVE DRIVEN FLUX COMPRESSION TECHNIQUE

E. I. BICHENKOV
Lavrentyev Institute of Hydrodynamics, Novosibirsk, Russia

Presented is a review of papers on high magnetic fields generation by magnetic flux compression in materials transferred from non-conducting to conducting state under shock wave action. The physical models of shock-wave flux compression and restrictions due to material properties and some peculiarities of the transition to conducting state are analyzed. The spatial and electrodynamic structure of the current waves generated in the samples of the material is considered, and the magnitude of the current and magnetic momentum is derived as a function of the material properties and the geometry of the compressed samples. The effects accompanying the current wave propagation in non-homogeneous materials and generated electromagnetic radiation are investigated. The possibilities of utilizing the effects mentioned are discussed. Limitations of magnetic field generation by the structure of the current waves are considered.

1 Introduction

Magnetic fields in the megagauss range have been produced by small and relatively simple shock-wave generators, independently proposed by our group and the K. Nagayama group [1-3]. The advantages and some prospects of this type of MCGs have been described in our paper [4]. The analyses of these generator performances have been produced under the assumption that the magnetic field behind the shock wave is equal to the field ahead of the wave. We show that this assumption is valid for the ideal shock of zero width [5]. When the front of the wave has a finite thickness, a certain current can be located inside this front and some new effects can occur.

2 Field Compression by the Current-Carrying Waves

We describe the shock-induced current wave by the parameter $b = (B_f/B_0)$, where B_f is the field behind and B_0 is the field ahead the shock. Considering only entrainment of the flux with conducting material, and neglecting the field diffusion, we derive the equation for flux φ in the compression region of MCG:

$$d\varphi = ds\frac{b\varphi}{ns} \tag{1}$$

All quantities here are related to their initial values, $n=\rho_f/\rho_0$ is the compressibility of the material. For constant parameters n and b, the flux, field, and magnetic energy in compression region S are the functions of $s=S/S_0$.

$$\Phi = \Phi_0 s^{b/n}, \quad B = B_0^{\left(b/n - 1\right)}, \quad U_m = U_{m0} s^{\left(2b/n - 1\right)} \tag{2}$$

For current-free wave b=1, and

$$\Phi = \Phi_0 s^{1/n}, \quad B = B_0 s^{\left(1/n - 1\right)}, \quad U_m = U_{m0} s^{\left(2/n - 1\right)} \tag{3}$$

When the compression region is entirely contracted ($S \rightarrow 0$), flux goes to zero, magnetic field increases infinitely, but magnetic energy can be finite if $n < 2$.

The highest current is captured by the shock front, when $b = n$,

$$\Phi = B_0 s, \quad B = B_0, \quad U_m = U_{m0} s$$

and the current inside the wave entirely shields the flow of the electromagnetic energy produced by the conductor's motion and locks it behind the wave. Ahead of the wave there is no energy flow. The field remains equal to its initial value and field compression does not occur. This example shows that the current captured in the wave front can be extraordinarily important.

3 The Wave Front Structure and the Captured Current, When Dielectric-Conductor Transition Occurs

The details of the electron-ion density relaxation aftershock has been investigated in [5], and an equation for the magnetic field in the material was derived:

$$\frac{dB}{d\zeta} = s\left(\frac{B(\zeta)}{r(\zeta)} - \frac{B_f}{n}\right) \tag{4}$$

Here, $\zeta = (z - Dt)$, $r = \rho(\zeta)/\rho_0$ is the compression of the material. The stationary wave propagation involves that $B_f = n$. This means that the wave can be considered as a current generator having linear density $c/(4\pi)*(n - 1)*B_0$. When the thickness of the shock wave is zero, all current is located in the diffusion zone ahead the wave, which has a thickness of $c/(4\pi\sigma)*(c/D)$. If the shock wave has a structure, part of this current is captured in the front of the wave. This part is determined by the front thickness l, the location of the possible jump of the conductivity x_s, the value of the conductivity s and compressibility of the material n.

Problems involving the shock-induced dielectric-conductor transitions are more complicated. Taking (4) as a base, changing the spatial variable ζ to compression r as new main variable, and choosing for its approximation

$$r(\zeta) = \frac{n+1}{2} + \frac{n-1}{2} th\left(\frac{\zeta}{l}\right) \tag{5}$$

we reduce the problem to the equation

$$\frac{dy}{dx} = \frac{ls}{2}\frac{1}{1+(n-1)x}\frac{y-x}{x(1-x)} + \frac{ls}{2n}\frac{1-y_f}{x(1-x)} \tag{6}$$

Here, the new variables x and y are introduced instead of density r and field b: $r = 1+(n-1)x, b = 1+(n-1)y$. This exposes the relative augmentation of density and magnetic field in the shock wave. The figure y_f gives the magnetic field behind the shock wave, coinciding with the current captured in the wave.

The approximation (5) describes, to a certain degree, the well-known solution to the problem of the shock wave thickness [7]. Discussing problems allows introduction of the explicit value of the wave thickness into equations and is convenient for analytical estimations and numerical calculations.

The results of the numerical calculations of the equation (6) for $s = 1$, array of the captured currents $y_f = \{0.1, 0.2, \ldots, 1\}$ and wave thickness $l = 0.125$, and $l = 1$ are shown in Fig. 1. The equation (6) was integrated from the point $\{x = 1, y = y_f\}$ to some moment of the compression x_s, when $y(x_s) = 0$. At this point the magnetic field is equal to its initial value. This allows us to consider the calculated point x_s as the position, where the dielectric-conductor transition occurs. The described calculations can be produced for different values of the parameters in equation (6), and current y_f can be determined as a function of these parameters and the position of the phase transition. However, the analytical approach is preferable.

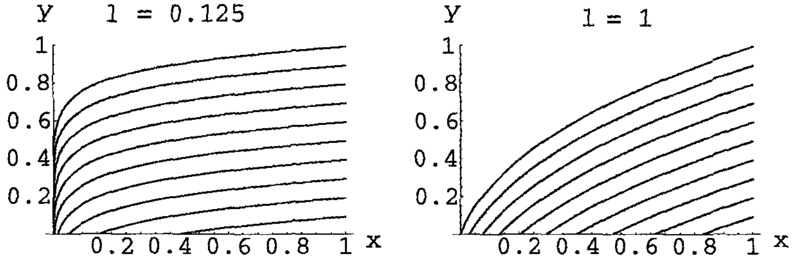

Figure 1. Field compression vs. density compression for two wave front thicknesses and array of the captured current.

Equation (6) may be integrated by quadratures. This results in the $y(x_s) = 0$ condition as an integral equation that can be reduced to

$$\frac{dy_f}{dx_s} = -\frac{l}{2n}\frac{1+(n-1)y_f}{1+(n-1)x_s}\left(\frac{1-y_f}{x_s} - \frac{ny_f}{1-x_s}\right) \tag{7}$$

The solution of (7) for initial condition $\{x_s=1, y_f=0\}$ gives the current captured into front y_f as a function of l, n, and x_s. Its asymptotic expansion is as follows:

$$y_f = \frac{l}{n}\frac{(1-x_s)}{l+2n} + \frac{l(1-x_s)^2}{l+4n}\left(\frac{n-1}{n^2} + \frac{2l(n-1)}{n(l+2n)^2} + \frac{2}{l+2n}\right) \tag{8}$$

This series simplifies to

$$y_f = \frac{1}{n}(1-x_s)\left(1+\left(1-\frac{1}{n}\right)(1-x_s)\right) - \frac{2}{l}(1-x_s)\left(1-\frac{1}{n}(1-x_s)\right) \tag{9}$$

when $l \to \infty$, and to

$$y_f = l\left(\frac{1-x_s}{2n} + \frac{1}{2n^2}\left(1-\frac{1}{2n}\right)(1-x_s)^2\right) \tag{10}$$

when $l \to 0$. It is easy to see from this estimation that a thin wave carries very little current proportional to the wave thickness and "distance" between the position of the phase transition and the end of the wave. When the material's compressibility increases, the current decreases as ~ $1/n^2$. For a thick wave, the generated current goes to the limit value

(9), depending exclusively on the location of the phase transition inside the wave front and compressibility.

4 Some New Problems of the Physics of Shock Waves

Shock wave propagation in a magnetic field results in the emergence of a shock-induced current wave in conducting materials or in materials with shock-induced transition from non-conducting to conducting state. The current circuit must be closed. This means that a system of currents having the same magnitude but opposite in direction must arise on the conducting surfaces of the compressed samples. We name them anti-currents. The distribution of the anti-currents, their density and location depends on shock-wave position, the shape of the conducting surfaces, and conductivity of the materials. Thus, we pose a new class of problems in the physics of shock waves. The following section explains the problems of electrodynamics for the anti-current distribution accompanying the solution of a hydrodynamic problem. To clarify this declaration let us consider two simple problems and discuss some results.

5 Creation of Current Pairs when a Shock Wave is Crossing the Boundary of the Material

Let us consider the entry of a flat shock wave into conducting semi-space. The analytical solution of this problem was described in [8], and its essence is to consider the conducting surface as a thin layer consisting of a current - anti-current pair embedded into one another. The coming wave throws the current and carries it with the wave. The anti-current remains at the surface and diffuses slowly into the conducting material behind the wave. If the initial state of the material is non-conducting, and when $l \to 0$, all current concentrates inside the wave front but its magnitude may be negligible. The presence of the electric field at the wave front results in emission of electromagnetic energy ahead of the front, due to magnetic field compression from the shock wave.

The evolution of the magnetic field distribution for this problem is shown in Fig. 2. It is easy to see that the diffusion current zone ahead of the wave is formed when the wave travels the distance $4l_d$ in the material. During this time, the non-stationary component of the electromagnetic energy occurs. Its evolution is shown in Fig. 3.

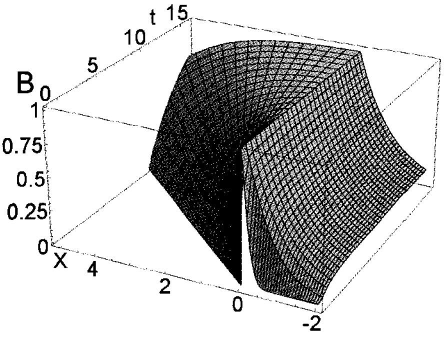

Figure 2. Space-time distribution of the relative increase of the magnetic field.

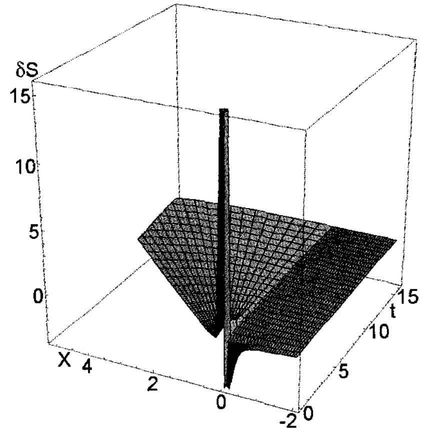

Figure 3. Space-time distribution of radiation intensity.

6 Breakdown of the Current Waves at the Boundary of the Materials

The break down of the shock wave at a boundary of materials with different compression properties is a classical problem of shock wave physics. This breakdown in magnetic field for conductors or for materials with phase transition from non-conducting to conducting state is accompanied by the breakdown of consequent current waves. The current - anti-current pair will be created and propagate from every boundary.

7 Magnetic Momentum of the Current - Anti-Current Pairs; the Possible Emission of Electromagnetic Energy

The system current - anti-current forms a closed current circuit with the magnetic momentum

$$m(t)=\frac{I(t)S(t)}{c} \tag{11}$$

The time dependent momentum emits electromagnetic radiation

$$\frac{dU}{dt}=\frac{2}{3c^3}\left(\ddot{m}(t)\right)^2 \tag{12}$$

Analyses of the performance of MCGs with homogeneous magnetic fields in the compression region shows that magnetic momentum of the generated currents differs only by a constant multiplier from the full magnetic flux in the compression region and in the material. This means that when high-conducting materials are used, the magnetic momentum may be about constant and radiation in the outer space may be very low.

Sometimes, shock wave compression can be accompanied by the generation of rarefaction waves. If this is the case, not only will a new current pair occur, but also the material can be mechanically destroyed. This can act as an opening switch of the anti-current concentrated at the outer surface of the compressed sample and produce a power pulse of radiation. This phenomenon may be the nature of the high flow of electromagnetic radiation, mentioned in the papers, describing the shock-wave compression of the cylinder made of *CsI* [9].

References

1. Bichenkov, E. I., Skorobogatykh, N. G., Trubachev, A. M., Magnetocumulative generator. Certificate of Invention No762706 (USSR, 1978).
2. Bichenkov, E. I., Gilev, S. D., Trubachev, A. M., MC-generators utilizing the transition of the semiconductor to conducting state. In Russian. *PMTF* **5** (1980) p. 125-129.
3. Nagayama, K., New Method of Magnetic Flux Compression by Means of the Propagation of Shock Induced Metallic Transition in Semiconductor. *Appl. Phys. Lett.* **38** (2) (1981) pp. 109-116.
4. Bichenkov, E. I., Gilev, S. D., Ryabchun, A. M., Trubachev, A. M., The Shock-wave Cumulation of the Magnetic Field. The Limits of the method. Megagauss and Megaampere Pulse Technology and Applications. Ed. by V. K. Chernyshev, V. D. Selemir, L. N. Plyashkevich. *Sarov.* VNIIEF (1997) Part 1 pp. 118-126.
5. Bichenkov, E. I., Structure of a Shock Induced Stationary Current Wave in a Conducting Material with a Transverse Magnetic Field. Combustion, Explosion, and Shock Waves. (Russian FGV) **33** (4) (1997) pp. 491-503.
6. Bichenkov, E. I., Gilev, S. D., Trubachev, A. M., Shock-wave MC-generators. Ultra High Magnetic Fields. Physics. Techniques. Applications. Ed. by V.M. Titov, G.A. Shvetsov. Moskow: *Nauka.* In Russian (1984) p. 88-93.
7. Zeldovich, Ya. B., Raizer, Yu. P., Physics of Shock-Waves and of High Temperature Hydrodynamics Phenomena. Moskow: *Nauka.* in Russian (1966).
8. Bichenkov, E. I., The Electromagnetic Field and Current Waves Generated by the Shock Wave Coming in Conducting Sample with Transverse Magnetic Field. *PMTF.* In Russian (1997) **38** (2) pp.19-25.
9. Barmin, A. A., Melnic, O. A., Prishchepenko, A. B., Filippova, O. L., Shakbazov, A. Sh., Shchelkachev, M. V., Losses of Electro-magnetic Energy During Compression of Magnetic Field by the Jump of the Second Kind. in Russian. *MZhG.* **6** (1988) pp.881-887.

ELECTRICAL CONDUCTIVITY OF THE DETONATION PRODUCTS

P. I. ZUBKOV
Lavrentyev Institute of Hydrodynamics,
Sibirian Branch of the Russian Academy of Sciences, Novosibirsk, Russia

Estimations of upper and lower length boundaries of free electron path for such explosives as PETN, RDX, NMX are presented. Electron concentrations necessary to determine the observed electroconductivity were obtained. Electroconductivity of trotyl detonation products was studied. Dissipating and adsorbing electrons on macroscopic particles of condensed carbon explain its anomalous behavior. For both cases, the necessary concentrations are supplied by thermal ionization facilitated by high densities and pressures.

1 Introduction

Upon detonation of condensed explosives, a detonative plasma arises with electroconductivity σ = (0.1-10) $\mathrm{Ohm^{-1}cm^{-1}}$ behind the shock front of an initiating shock wave. Presently, there is no common mechanism of conductivity. Current vehicles and the nature of their appearance are unknown.

The following was experimentally [4,5] discovered. Detonation products of explosives such as PETN, RDX, NMX have an area (<1 mm) of non-equilibrium conductivity coinciding with the zone of chemical reaction and the equilibrium zone.

In the non-equilibrium zone behind the initiating shock wave for a width of ≈ 1 mm the electroconductivity increases and achieves its highest value of about 0.5 $\mathrm{Ohm^{-1}cm^{-1}}$ and then decreases to equilibrium. In thick charges (∅ > 20 mm) the equilibrium conductivity is sometimes less than the highest one and decreases in rarefaction waves. Its value is about 0.1 $\mathrm{Ohm^{-1}cm^{-1}}$.

The electroconductivity in detonation products of explosives with high negative oxygen balance shows the opposite behavior. For instance, in trotyl, electroconductivity increases to its highest value of about 5 $\mathrm{Ohm^{-1}cm^{-1}}$ in 10^{-7} s. The electroconductivity decrease is exponential [5] with a characteristic distance from the detonation front of about 1 cm. This size does not correlate with the chemical reaction zone ≈ 1mm [6] and is not determined by rarefaction waves.

Type of vehicles, the nature of their rise, average time between collisions or their free mean path are the basic problems of studying conductivity mechanisms. The present paper is devoted to these problems.

The differences in electroconductivity behavior in equilibrium products in PETN, RDX, HMX and trotyl demand different models for their explanation. For equilibrium products, the electroconductivity value $\sigma \approx 0.1$ $\mathrm{Ohm^{-1}cm^{-1}}$ will be explained, as well as for trotyl's electroconductivty value $\sigma \approx 5$ $\mathrm{Ohm^{-1}cm^{-1}}$ and its exponential decrease.

2 Conductivity of Equilibrium Detonation Products

Presented are estimates of characteristic magnitudes. A detonation density of $\rho_0 = 2$ g/cm^3 and a temperature T = 3.5×10^3 K$^\circ$ is assumed. The number of particles per volume unit is n = 3×10^{22} cm^{-3}, the distance between particles $a \approx n^{-1/3} = 3\times10^{-8}$ cm. The distance coincides with characteristic size of the particles, themselves.

As will be shown further, electron concentration in equilibrium products does not surpass 10^{17} cm^{-3}. At this density, the degeneration temperature [7] $T_0 \approx 4.5\times10^{-11} n^{2/3} = 10$ $K << T$, electrons are not degenerated and submitted to the Boltzman statistics. The heat velocity of electrons is V ≈ 5×10^7 cm/s and the corresponding length of the electron wave is $\lambda \approx 2\times10^{-7}$ cm.

The length of the electron wave surpasses the particle size and distance between particles by an order of magnitude. At these conditions, the classic view on elastic dissipation of electrons on molecules with gas-kinetic section ≈ 10^{-15} cm^2 is not correct. A quantum-mechanical investigation of their interaction with molecules of the detonation products is necessary.

Here, we introduce the electron free path length l. According to [8], an electron wavelength cannot be greater than or of the same order of magnitude as a free mean path length due to its physical properties. For free electrons $l >> \lambda = 2\times10^{-7}$ cm. This condition allows considering the electron motion to be quasi-classic.

The evaluation of l from above follows from experimental results on spark-over of equilibrium detonation products. According to [9,10], their electric strength $E = 10^6$ V/cm. Molecules of detonation products in free states have the ionization potential ≈ 12-15 eV. Considering a medium influence, its decrease $\Delta I \approx e^2/a = 5$ eV. Therefore, we will take I_e = 7 - 10 eV as the effective ionization potential. Consequently, we obtain $l_i \approx {}^{I_e}\!/_{eE} = 10^{-5}$ cm for the electron free mean path length with respect to ionization.

Usually, $l < l_i$. Thus, for equilibrium detonation products we have 2×10^{-7} cm $<< l <$ 10^{-5} cm. This evaluation is enough for our use; it allows the explanation of the observed electroconductivity of equilibrium detonation products without considering thin effects.

Proceeding from values of electron density n and temperature T, it is possible to show that electrons are independent and their collisions are rare. For these conditions, electroconductivity is given by the Drude-Sommerfeld expression $\sigma = {}^{ne^2 l}\!/_{mv}$. It follows from the expression that an electron concentration n necessary to provide electroconductivity $\sigma = 0.1$ Ohm^{-1}cm^{-1} is within the limits 10^{17} cm^{-3} $>> n >$ 10^{15} cm^{-3}.

Evaluation of the electron density in equilibrium detonation products can be obtained from the Saha formula. Interaction of neighboring particles in a dense medium is usually considered by introducing the effective ionization potential. For equilibrium detonation products, the Saha formula gives $n = 10^{17} - 10^{14}$ cm^{-3}. In [1], the value $n = 10^{16} - 10^{13}$ cm^{-3} is obtained.

The given evaluations show that electroconductivity of equilibrium detonation products of the same type as PETN, RDX and HMX can be electronic. Electrons arise as the result of thermal ionization with a density high enough to provide the observed electroconductivity and their interaction with product molecules obeys the quantum-mechanical regularities.

3 Conductivity Behind the Detonation Front in Trotyl

Characteristic values for products of a trotyl detonation are: density ~ 2 g/cm^3, temperature ~ 3.5×10^3 K°. The concentration of trotyl molecules at this density is about 0.5×10^{22} cm^{-3}, every molecule has 7 carbon atoms, their concentration is about 3.7×10^{22} cm^{-3}. Condensed carbon is 20% of charge weight [11], which corresponds to a concentration of free carbon atoms of $n_0 \approx 2\times10^{22}$ cm^{-3}.

The number of all particles in detonation products is $n_a \approx 5\times10^{22}$ cm^{-3}, the distance between particles $a \sim n_a^{-1/3} = 3\times10^{-8}$ cm coincides with the characteristic molecule size.

The average size of diamond particles resulting from trotyl detonation is about (4-5)×10^{-7} cm [11]. For these estimations, we consider the size of condensed carbon particles to coincide with the average size of diamond particles, and their density n_k to coincide with the density of solid phase nuclei. Under these assumptions, $n_k \sim (10^{19} - 10^{18})$ cm^{-3}. The average distance between particle centers is $d \sim n_k^{-1/3} < 10^{-6}$ cm. The distance between particles is $d - 2r$ which decreases with particle size growth.

The effective potential of carbon atom ionization, considering its decrease in dense detonation products, is I_e = 6-7 eV. Evaluation of electron density according to the Saha formula gives $n = (10^{17}\text{-}10^{16})$ cm^{-3}.

Let us introduce the free path length l_a of an electron in non-condensed detonation products. For free electrons, $l_a \gg \lambda = 2\times10^{-7}$ cm.

On one hand, at the size of condensed particles of carbon, $r \sim 10^{-7}$ cm $\sim \lambda$, the distance between them becomes of the order of l_a or less. On the other hand, the "quantum" electron for molecules becomes "classical" for particles of condensed carbon. Under these conditions, carbon particles are centers of electron dissipation and absorption. As far as $r \sim \lambda$, we consider the probability of absorption to be small. The electron free path length l will be determined by dissipation on an intermediate section of carbon particles and their density $l \approx 1/n_k \pi r^2$.

For electroconductivity, we obtain the expression $\sigma \approx ne^2/n_k m v \pi r^2$, where e is the electron charge and m is the electron mass. For $r \sim 10^{-7}$ cm, it follows from the expression that 10 Ohm^{-1}cm^{-1} $\geq \sigma \geq$ 0.1 Ohm^{-1} cm^{-1}.

Without considering processes in the chemical reaction zone (~ 1mm), we assume that electrons disappear through absorption by condensed particles. Other processes influencing electron density we consider as unimportant.

A free electron's velocity many times surpasses the velocity of ions and molecules that, due to inertia, do not manage to follow its motion. An electron absorbed by a condensed particle becomes "immobile"; it is localized by the particle and its mobility practically equals zero.

The practically immobile particle absorbs an electron and creates an electric field around itself $E \approx e/r2 \sim 10^7$ V/cm. The Debye radius of screening at an electron density of $n \sim 10^{17}$ cm^{-3} results in $\sim 10^{-6}$ cm, on the same order as the distance between condensed particles. A charged condensed particle will be not screened. The particle will acquire an ion current. The characteristic time of neutralizing the particle is $\tau \sim 1/4\pi\sigma_i$, where σ_i is the ionic (C+) electroconductivity. Estimation of the neutralization time gives $\tau \sim 10^{-9}$ s, which is considerably less than the characteristic detonation times and allows holding particles of condensed phase to be neutral at every moment in time.

During time Δt in a unit of volume $\Delta n \approx nv\beta t/l$ of electrons, collisions with particles of condensed carbon occur. For absorption probability β, disappearing electrons will be determined by the ratio $\Delta n \approx -nv\beta\Delta t/l$. In the coordinate system connected with the detonation front, we have $\Delta n/\Delta x \approx -nv\beta/ul$, where u is the velocity of detonation products and x is the coordinate. Electron density decreases according to the exponential law with characteristic size $x_0 \sim ul/v\beta$. Electroconductivity will decrease according to the same law, as the dependence on particle size r is weak.

Therefore, the above estimates show that electroconductivity of trotyl detonation products has the non-contradictory explanation in assuming dissipation and absorption of electrons on macroscopic particles of condensed carbon.

If the proposed model is correct, then it allows the estimation of electron absorption probability $\beta \approx ul/x_0v \sim (10^{-8} - 10^{-7})$. The probability turns out to be very low.

Electroconductivity in the detonation wave of lead azide was measured in [1]. It is of the same order of magnitude as the detonation in trotyl. In this case, electrons probably increase as the result of thermal ionization of lead atoms with low ionization potential (for free state $I = 7.4$ eV). Dissipation and absorption of electrons occurs on macroscopic particles of condensed lead.

4 Conclusions

Electronic conduction in detonation waves is possible. The necessary concentration of electrons is provided by thermal ionization, ignited by high pressures. Interaction between electrons and the molecules of detonation products are quantum-mechanical in nature.

Free carbon is the main supplier of electrons in trotyl detonations. Electron dissipation and absorption occurs on particles of condensed carbon that are larger than the electron wavelength. This explains the exponential conduction decline seen. It is possible that free carbon atoms are responsible for the behavior of conduction during the detonation of HMX, RDX and PETN.

References

1. Brish, A. A., Tarassov, M. S., Tsukerman, V. A., Electroconductivity of explosion products of condensed explosives. *JETP*, (1959) **37**, No. 6 (12), pp 1543-1549.
2. Ershov, A. P., Zubkov, P. I., Luk'yanchikov, L. A., Electrophysical characteristics of detonation plasma and fast explosion breakers of current. *AMTP*, (1977) No. 6, pp. 19-23.
3. Antipenko, A. G., Yakushev, V. V., Nature of electroconductivity of detonation products of condensed explosives // Detonation. Proceedings of V International Symposium on combustion and explosion. Odessa, 1977. Chernogolovka, (1977) pp. 93-96.
4. Ershov, A. P., Ionization at detonation of condensed explosives. PCE, (1975) **11**, 6, pp.938-945.
5. Dremin, A. N., Savrov, S. D., et al., Detonation waves in condensed media. Moscow, "Nauka", (1970).
6. Landau, L. D., Livshits, E. M., Statistical physics. Moscow, "Nauka", (1964) p. 568.
7. Efros, A. L., Localizing electrons in non-ordered systems. UPN, (1978) **126**, pp. 41-65.
8. Korol'kov, V. L., Mel'nikov, L. A., Tsyplenko A. P., Spark-over of detonation products. *JTP*, (1974) **44**, No. 12, pp. 2537-2538.
9. Zubkov, P. I., Luk'yanchikov, L. A., Rjabinin, Yu. V., Electric strength of detonation products of condensed explosives. *AMTP*, (1978) No. 3, pp. 44-47.
10. Titov, V. M., Anisichkin, V. F., Mal'kov, I. Yu., Investigation of synthesis process of ultradisperse diamond in detonation waves. *PCE*, (1989) **35**, No. 3, pp 117-126.

ANALYSIS OF THE SPATIAL VARIATION AND TIME DEPENDENCE OF THE CURRENT DISTRIBUTION IN A SINGLE-TURN COIL FOR MEGAGAUSS FIELDS

H.-U. MUELLER, O. PORTUGALL, M. VON ORTENBERG
Humboldt-University, Institute of Physics, Berlin, Germany

Due to the semi-destructive character of the single-turn coil, this technique is especially useful for reproducible experiments in megagauss fields. Theoretically, geometry, the skin effect, and resistivity changes due to inhomogeneous Joule heating determine the current distribution within the coil. To calculate the current and temperature distribution, the cross section of the coil is divided into small rectangular filaments according to Nakao et al. The dimensions of these sections have to be comparable or smaller than the skin depth in order to get realistic results. These results show that the time dependence of the magnetic field values on the coil axis are different for different distances from the coil center. This result implies that the zero in the magnetic field at a given position on the coil axis does not necessarily agree with the zero of the total current. This effect has been observed for the first time experimentally with our equipment using a twin pick-up system for special analysis of the spatial distribution of the magnetic field on the coil axis.

1 Introduction

One of the most effective methods for megagauss magnetic field generation is the *single-turn coil* technique as introduced as a scientific instrument by [1] and subsequently extremely successfully applied by [2]. In Berlin, at the Humboldt University, a *single-turn coil* was installed which deviated in particular construction principles such as coil orientation, strip-line technique for current leads, and general light-weight construction [3,4]. We performed a realistic, overall simulation to completely understand the discharge and field generation process in this device.

2 Capacitor Bank

The capacitor bank consists of twice 5 modules integrating two 6.25 µF/60 kV capacitors and 1 rail-gap switch with a total series inductance of 25 nH. Note that the series inductivities of the strip line (2.3 nH) have to be included as well as the collector inductance of 8.4 nH for realistic simulation as shown in Fig. 1.

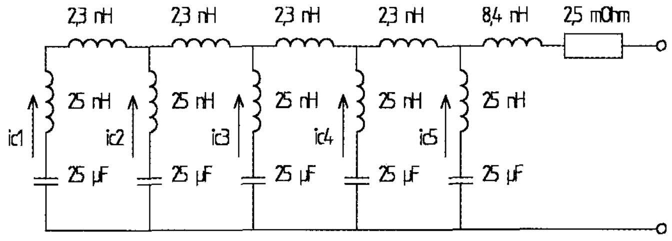

Figure 1. Effective schematic of the capacitor/switch/strip-line circuit.

3 Single-Turn Coil

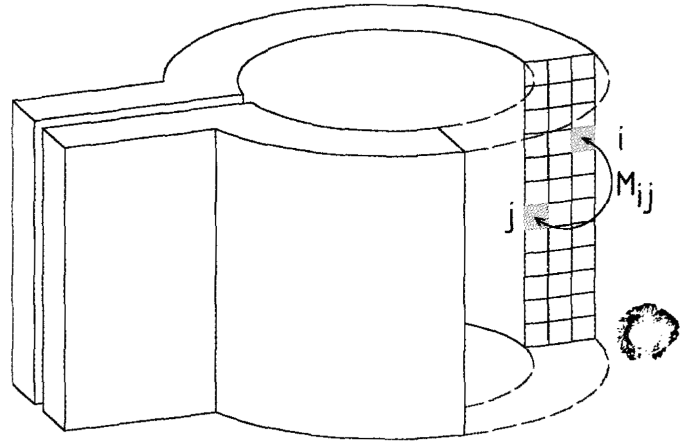

Figure 2. Finite element division of the *single-turn coil.*

Due to the time- and spatially dependent current variation within the single-turn coil, it is the most complicated segment to simulate. In Fig. 2 we show the finite element division into 9 layers, each having 36 ring elements for the mathematical approach. The geometrical dimensions of the copper coil are ID = 12 mm, OD = 18 mm, L = 12 mm. This geometry is kept fixed over the entire pulse, which is realistic only for low-voltage shots up to 10 kV. Nevertheless, under this assumption, the behavior of the coil has been calculated up to 50 kV charging voltage to study the effects of coil heating and current distribution as separate effects as distinguished from coil expansion.

The mutual inductance between two coaxial loops with radii R_i and R_j and distance d_{ij} is given by

$$M_{ij} = \mu_0 \sqrt{R_i R_j} \left[\left(\frac{2}{k} - k \right) K(k^2) - \frac{2}{k} E(k^2) \right] \quad i \neq j$$

with,

$$k = \sqrt{\frac{4 R_i R_j}{(R_i + R_j)^2 + d_{ij}^2}}$$

$E(k^2)$ and $K(k^2)$ are the complete elliptic Integrals. To calculate the self-inductance of the i-th loop, the quadratic cross section of the loop is approximated by a round wire with a diameter 2b equal to the side of the square.

$$M_{ii} = \mu_0 R_i \left(\ln \frac{R_i}{b} + 0.32944 \right).$$

Applying this more realistic approximation, we differ from [3,4]. Special care had to be taken with respect to the convergence of the solution of the set of differential equations.

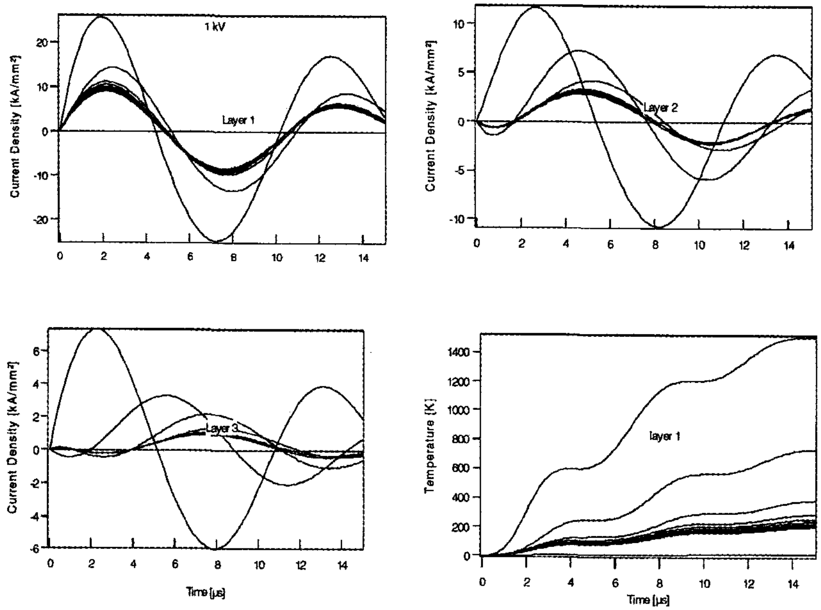

Figure 3. Time dependence of the simulated current density and temperature

The temperature dependence of the resistivity of Cu is simplified by

$$\rho(T) = \rho_{300}(1 + \alpha T)$$

with $\alpha = 2.5 * 10^{-3} K^{-1}, \rho_{300} = 1.7 * 10^{-8} \Omega m$, and a specific heat capacity of $c_v = 4 * 10^{-6} Joule K^{-1} m^{-3}$. Part of the results of the simulation is shown in Fig. 3 for the time dependence of the current density and temperature.

4 Results

The results can be summarized as follows:

1) Despite the exclusion of any expansion effects of the coil, the inductance of the coil changes drastically due to the variation of the current density (15% for U_{load} = 50 kV). The initial inductance is lowest.
2) The time variation of the magnetic field varies with axial displacement from the coil center as shown in Fig. 4.

The time variation of the magnetic field in the coil center differs from that of the total current; especially, the zeroes in both functions occur at different times.

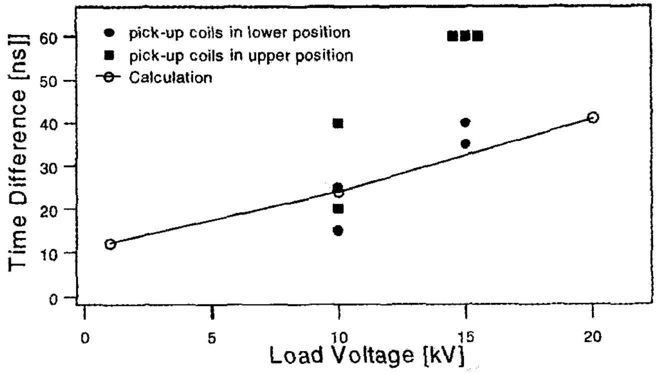

Figure 4. Comparison of simulation and double pick-up coil experiment.

References

1. Herlach, F., Mc Brom, R., *J.Phys.E:Sci. Instum.* **6** (1973) p. 652.
2. Miura, N., Herlach, F., *Springer Topics in Applied Physics* **57** (1985) p. 274.
3. Nakao, K., Herlach, F., Goto, T., Takeyama, T., Sakakibara, T., Miura, N., *J. Phys. E: Sci. Instum.* **18** (1985) p. 1018.
4. Miura, N., Nakao, K., Technical Report of ISSP, Ser. A, No. 2125 (1989) Institute for Solid State Physics, University of Tokyo.

CURRENT PULSE SHARPENING BY FERROMAGNETIC OPENING SWITCH

G. A. SHNEERSON, I. P. EFIMOV, S. I. KRIVOSHEEV,
YU. N. BOTCHAROV

Saint Petersburg State Technical University, Russia

A controlled system for megampere current pulse sharpening using a ferromagnetic opening switch (FOS) is developed. Control is achieved by an orthogonal magnetic field that is produced by an external source. The system is non-destructive and is especially effective for low inductance solenoids. It produces sharpening multiplicity of 5 - 10 times. FOS can also be used in combination with an electro-explosive opening switch.

1 Introduction

Switching is the main problem in using inductive and inductive-capacitive energy storage systems in devices built to generate megampere currents. Switching is difficult for low inductance loads, in small volume solenoids.

The convention is to use an explosive foil as the current opening switch for low-inductance circuits having megampere currents. In this device, replacing a conductor after each discharge is required. Detonation time essentially depends on the current change law in the commutation stage.

The alternative to this convention is offered through the FOS, shown in Fig. 1. The magnetic field in the ferromagnetic core has orthogonal components, one formed by the main current and the second formed by the control current. Switching results from the control current breaking away, which is due to the core transition from the saturated state into a state in which its inductance is much higher.

2 Procedure

For fast switching current in inductive and inductive-capacitive energy storage systems, circuits are used in which a sharp increase of the transient impedance in one of the circuit element occurs. This process may be realized in different ways, including a jump in the inductance of the circuit (Fig. 1) from its initial value L_1' to the final L_1''. The load current and current i_l will then be determined by the expressions [1]:

$$i_2'' = i_0'(K-1)\left(\frac{L_2}{L_1'}+K\left(1+\frac{L_2}{L_0}\right)\right)^{-1}, \quad i_1'' = i_0'\cdot\left(1+\frac{L_2}{L_1'}+\frac{L_2}{L_0}\right)\left(\frac{L_2}{L_1'}+K\left(1+\frac{L_2}{L_0}\right)\right)^{-1} \qquad (1)$$

where i_0' is the initial current value i_0, is the current in the inductive load, $K = L_1''/L_1'$ is the ratio of inductance variation.

Generation of high magnetic fields in single-turn low-inductance solenoids requires forming a current pulse in the megampere range with a rise time of the order of 10^{-6} s and less. Here, one may use the inductance-capacitance storage to shorten the current pulse front [2]. In the experiments mentioned, the condition is usually satisfied where L_0 is the inductance of the energy source.

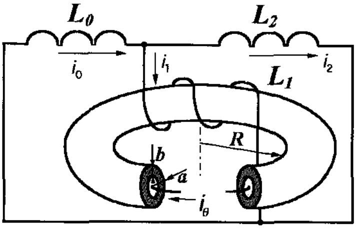

Figure 1. The circuit for current switching into inductive load.

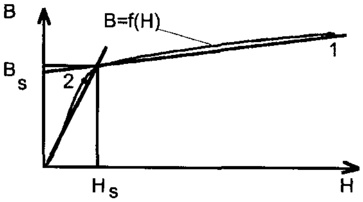

Figure 2. The approximation of the magnetization curve.

The possibility of using the jump in magnetization of the coil core L_1 under external action for switching purposes is considered. In the initial state, the core should be deeply saturated. At the required moment, the material of the core should transit into the unsaturated state that is accompanied by the sharp increase in the inductance up to the value and transition of the current into the load L_2. The process should be performed so that the inductance jump and the time of its realization are determined by the external action and not by the current in the storage circuit. For this purpose, it is proposed to use a system with orthogonal fields [3].

A coil having a toroidal core, the winding of which experiences current flow i_1 producing toroidal field with induction B_θ is used in the proposed device as the inductance L_1. The circuit with current i_θ is situated at the core axis. The induction of the toroidal field of current i_1 is orthogonal to the poloidal field induction B_φ produced by the current . The inductance L_1 may vary in a wide range with the aid of the control current i_θ. This may be shown, for example, when the core material is isotropic and the induction dependence on the magnetic field intensity has the form $\vec{B} = \mu(H)\vec{H}$. The magnetic permeability in this formula depends on the intensity module $H=(H_\varphi^2+H_\theta^2)^{1/2}$. The initial state conditions $H_\phi >> H_S$ and $H_\theta \geq H_S$ hold (point 1 in Fig. 2). Here, H_S is the threshold intensity that corresponds to the intersection point of the two sections of the broken line approximating the magnetization curve. In the initial state, the core is deeply saturated due to the action of the poloidal field H_φ. After switching off the current i_θ the field H_ϕ becomes zero and the state of the system is characterized by point 2. The inductance L_1 sharply increases. The currents i_0, i_1, and i_2 in the circuit elements of the inductive storage vary correspondingly.

For an approximate description of the FOS magnetic circuit, the magnetization curve may be substituted by a line (Fig. 2).

$$B(H)=\begin{cases}\mu H & , B \le B_S \\ \mu_{eff} H & , B \ge B_S\end{cases}, \tag{2}$$

where: $$\mu_{eff} = \frac{B_S + (H - H_S)\mu_0}{H} = \mu_0\left[1 + \frac{B_S}{\mu_0 H}\left(1 - \frac{\mu_0}{\mu}\right)\right]$$

As a calculation model, we examine the system of the hollow toroid satisfying the condition $b<a<<R$ (Fig.1) at the saturated state $H \approx H_\varphi = i_\theta / 2\pi a$. Under the conditions $\mu >> \mu_0$ and $H_\varphi >> H_\theta$ at the initial state we have $\mu_{eff} = \mu'_{eff} \approx \mu_0(1+p) = \mu_0(1 + l_\varphi B_S / \mu_0 i_\theta)$, where $p = B_S / \mu_0 H_\varphi$. In this formula $l_\varphi = 2\pi a$ is the length of the poloidal field line and H_φ is its intensity. In further estimations we adopt the value 1.5 T for B_S.

If the condition $w_1 i''_1 < B_S l_\theta / \mu = i_{1s}$ holds true, the core will not be saturated after switching (w_1 is the turn number). The current i''_1 may be found from formula (1), which is conveniently rewritten in the following form:

$$i''_1 = i'_0 \frac{\alpha}{K + \beta} < i_{1s} / w_1, \tag{3}$$

where $\alpha = (1 + L_2/L'_1 + L_2/L_0)/(1 + L_2/L_0)$ and $\beta = (L_2/L'_1)/(1 + L_2/L_0)$ are dimensionless numbers determined by inductance ratios. Then equation (3) yields the condition limiting the value of the switched current:

$$w_1 i'_0 \le \frac{i_{1s}}{\alpha}(K + \beta) \tag{4}$$

The magnetization current is relatively small. Nevertheless, condition (4) may be satisfied even for large switched currents if the ratio $\mu / \mu'_{eff} = K$ is sufficiently large.

Using formula (2) we obtain general expressions for K, the admissible switch current, and the load current:

$$K = \frac{L''_1}{L'_1} = \frac{\mu_0/\mu}{1 + p\cdot(1 - \mu_0/\mu)};$$

$$i'_0 = \frac{l_\theta B_S}{\mu}\left(1 + \frac{\mu}{\mu_0}\left(1 + p + \frac{L_2 l_\theta}{\mu_0 S[1+p]} + \frac{p L_2 l_\theta}{\mu_0 S[1+p]}\right)^{-1}\right);$$

$$i''_2 = \frac{l_\theta B_S}{\mu_0}\cdot\left(1 + p + \frac{L_2 l_\theta}{\mu_0 S[1+p]} + \frac{p L_2 l_\theta}{\mu_0 S[1+p]}\right)^{-1}. \tag{5}$$

Fig. 3 represents the curves illustrating the given relationships as functions of the dimensionless parameter p.

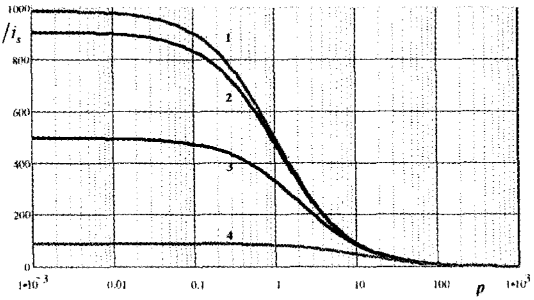

Figure 3. Dependence i_2/i_s (lines) and K (points) from size of the parameter p. For L_2/L_1^0: 1 - 0.01, 2 - 0.1; 3 - 1; 4 - 10.

In the real condition $\mu'_{eff} > \mu_0$, which corresponds to the conditions of low saturation: $p > 1$ (the right section of Fig. 3). The condition $p << 1$ corresponds to the conditions of high saturation (the left-hand section of Fig. 3). This condition may be used to generate megaampere currents in the low inductance load. In this case, the length l_θ should be sufficiently large and the section of the solenoid should be chosen so that the ratio L_2/L_1' would not be high. For a considerably large length of the solenoid section and low load inductance, the FOS can provide controlled switching of the megaampere current into the load of the inductive storage.

For example, we consider switching the current in the real inductance-capaci-tance storage with the following characteristics: $C_0 = 10$ µF, $L_0 = 200$ nH, $U_0 = 100$ kV. The result of switching a current impulse with an amplitude of 400 kA and rise time of about 0.3 µs is formed from a current impulse having an amplitude of 600 kA and rise time of about 2.5 µs on a load $L_2 = 5$ nH (Fig. 4).

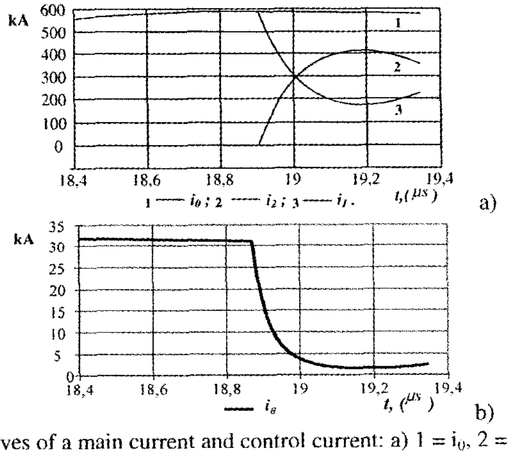

Figure 4. Curves of a main current and control current: a) 1 = i_0, 2 = i_2, 3 = i, b) i_θ

3 Conclusions

- The controlled change of the inductance in the system with orthogonal fields may be used for current switching into the load of an inductive storage system.
- The FOS allows switching currents in the megaampere range in systems with a low-inductance load (of the order of 10^{-9} H).

References

1. Shneerson, G. A., Field and transients in Superhigh Pulse Current Devices. (Nova Science Publishers, Inc. New York. 1997).
2. Burtsev, V. A., Kalinin, N. V., Luchinsky, A. V., Electrtrichesky vzriv provodnicov. Energoatomizdat. Moscow (1990).
3. Dorogco, L. I., Libkind, M. S. Reactors with transversal magnetization. Energy. Moscow (1977).

OPENING MECHANISMS IN AN EXPLOSIVELY FORMED FUSE OPENING SWITCH

D. KEEFER[1], M. H. FRESE[2], L. D. MERKLE,
R. E. PETERKIN, JR., N. F. RODERICK[3],
K. F. STEPHENS II[4]
Air Force Research Laboratory: Phillips Research Site, AFRL/DEHE, Kirtland AFB, NM USA
Permanent addresses: [1] University of Tennessee Space Institute, Tullahoma, TN;
[2] NumerEx, Albuquerque, NM; [3] University of New Mexico, Albuquerque, NM;
[4] University of North Texas, Denton, TX

MACH2 is a general purpose MHD code that has been used to simulate the evolution of an explosively formed fuse consisting of a thin cylindrical aluminum shell that is driven into a Teflon die by an explosion. The simulations included the initiation and propagation of the explosive detonation wave and tracked the extrusion of the fuse into the Teflon die. The code predicted that the fuse resistance increased by approximately three orders of magnitude due to the lengthening and thinning of the fuse material and the rise of temperature caused by the ohmic heating. Comparisons with recent experimental measurements performed at Los Alamos National Laboratory indicate that the predicted resistance is approximately one order of magnitude too small and suggest that the fuse must undergo a transition to a plasma in order to reach the observed switch voltage. Additional simulations of a short fuse segment were performed to investigate this transition and to evaluate the effect of spent explosive resistivity on the maximum electric field obtained. These simulations revealed a rapid expansion and heating of the vaporized fuse material that allows current to diffuse into the spent explosion products and limit the maximum value of electric field obtained.

1 Introduction

MACH2 is a general purpose MHD code that previously has been used to simulate a wide variety of pulsed power plasma devices [1]. Recent extensions to the code permit accurate tracking of moving material interfaces that enables simulation of explosively formed fuses (EFF). The explosively formed fuse was developed at Los Alamos National Laboratory (LANL) and has been used as an opening switch for a variety of pulsed power devices [2].

The fuse consists of a thin aluminum cylinder surrounding an explosive material that is detonated simultaneously along its axis. The pressure from the explosion extrudes the aluminum fuse into slots machined in a surrounding Teflon die. This rapid stretching, thinning and heating of the fuse material raises its resistance and transfers pulse energy into an inductor or load. Lindemuth [3] has given a model for fuse behavior, and Goforth [2] presents results of hydrodynamic code simulations for the fuse deformation.

Time accurate simulations of the fuse deformation are difficult because of the non-linear interplay of hydrodynamics, material properties, and ohmic heating. MACH2 is capable of simulating all of these processes from initial explosion to final extrusion and separation of the aluminum with arc formation. For the present simulation, it is important to accurately track the magnetic field as the fuse deforms to determine the ohmic heat input to the fuse and to obtain the inductance change induced by the fuse motion. Two different types of simulation will be presented here. The first is a 2-D simulation of the deformation of the fuse into the Teflon die and the second is an idealized 2-D simulation of a cylindrical fuse segment as it transitions into an arc.

2 Simulation Models

The first simulation is for a fuse assembly that was tested at LANL using input current from a capacitor bank. A schematic of the assembly is shown in Fig. 1. The center cylinder and the cylindrical annulus between the fuse and output conductor are filled with explosive. The simulation domain consists of one of the periodic structures from the centerline to just beyond the outer radius of the slot in the Teflon die. Fig. 2 shows the deformed fuse at a time of 8.5 μs after detonation. The Teflon finger has deformed into a mushroom shape and the aluminum fuse is heated by the current flowing in the fuse. The gray scale within the aluminum boundary shows the ohmic power dissipated in the aluminum, which maximizes near the thinnest part of the fuse. The maximum power dissipation is approximately 1×10^{16} W/m^3, which is approximately a factor of ten too small to produce the voltage rise observed in experiments at LANL. This suggests that the voltage rise is produced by a separation of the aluminum fuse and subsequent arc formation.

The second MACH2 simulation explores the transition to arc plasma. Modeled is a thin, cylindrical fuse segment having the same inner diameter as the actual device. It is supported by a Teflon backing and pressurized by explosion products having the same temperature and density as predicted by the previous simulation. The fuse segment is initially 50 μm thick in the center and 100 μm thick at the ends to produce the 2-D effects of ohmic heating. The segment carries a constant current of 2.5 MA. The computational domain is shown in Fig. 3. Ohmic heating causes the center to heat and expand, increasing its resistivity until it separates into a plasma arc. This effect is seen in Figures 4 and 5. In Fig. 4, the fuse is beginning to expand and heat at 2.4 μs. The peak temperature is approximately 0.7 eV and the fuse is still intact but more resistive, increasing the heating rate. In Fig. 5 the fuse has expanded so much at 4.0 μs that the current density and heating rate is reduced, but the gap is now filled with a low-density plasma arc at a peak temperature of approximately 3 eV. The magnetic field has diffused out of the aluminum into the explosion products through which current is flowing. The effect of explosion product resistivity on the electric field generated by the plasma was assessed using simulations. Plasma resistivity was modeled using a simple electron-neutral collision cross section. Results are shown in Fig. 6. The peak electric field occurs at about 3.5 μs, increasing as the explosion products become more resistive. For a fuse length of 0.44 m, this electric field is comparable to that measured in the LANL experiments.

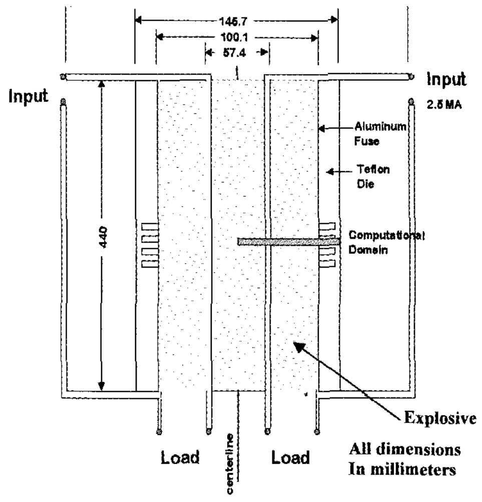

Figure 1. Fuse schematic

3 Summary and Conclusions

The general-purpose MHD code MACH2 has been used to simulate an explosively formed fuse opening switch. The simulation was successful in simulating the large deformations in a thin aluminum fuse driven into a Teflon die by explosion pressure and, simultaneously, calculating the electromagnetic field produced by the fuse current. However, the simulation failed for times greater than 10 microseconds and subsequent studies indicated that the aluminum fuse did not thin sufficiently to "fuse" within this time.

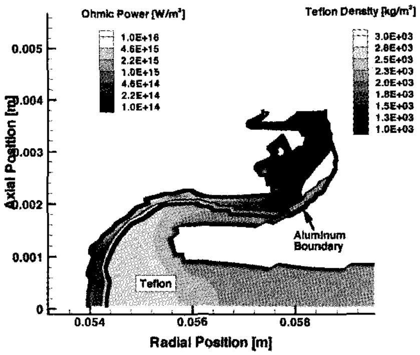

Figure 2. Deformed fuse segment.

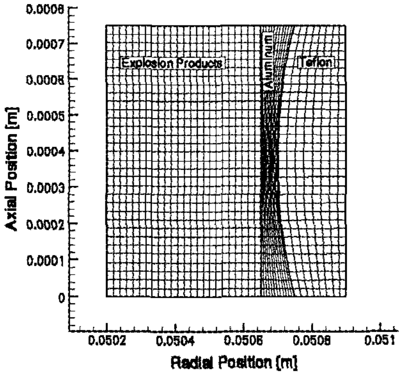

Figure 3. Computational domain

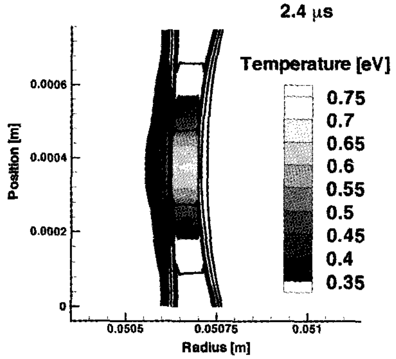

Figure 4. Temperature and aluminum contour lines - 2.4 μs.

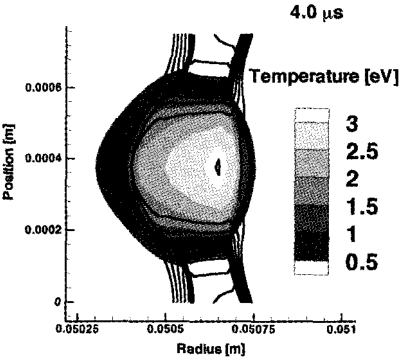

Figure 5. Temperature and aluminum contour lines - 4.0 μs.

Additional simulations were performed on a simple model of a short cylindrical fuse segment to provide better understanding of the physical processes involved in "fusing" where the nonlinear ohmic heating process dominates the physics. These simulations were successful in following the process from an initially solid aluminum conductor through expansion and heating that transformed the solid aluminum into an aluminum plasma. They indicated that ohmic heating did not become the dominant process for this fuse geometry and current until the fuse thickness was reduced below 100 micrometers. The minimum thickness in the EFF simulations at 10 microseconds was 80 - 100 micrometers, and the simulation would have to continue for approximately 13 microseconds to observe "fusing."

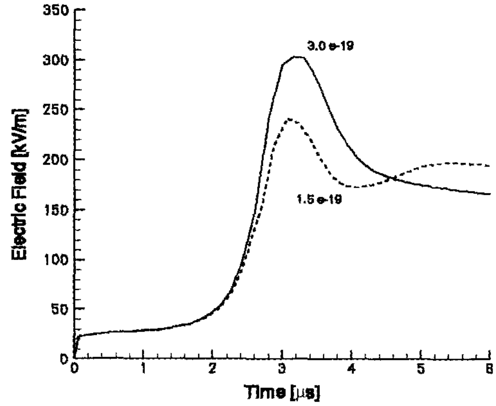

Figure 6. Electric field for two different resistance models.

These simulations also showed that the field diffused out of the aluminum and into the hot explosion products as the aluminum temperature and resistivity increased. The simulations indicated that the peak voltage attained by the switch depended on the resistivity of the explosion products. This result suggests that higher peak opening voltages might be obtained by using explosives with higher resistance explosion products. The simple fuse simulations indicate that little significant ohmic heating occurs until the aluminum fuse thins to less than 100 micrometers. Therefore, the initial fuse thickness could be reduced to lessen the deformation required before "fusing" occurs.

References

1. Frese, M. H., *MACH2:* A Two-Dimensional Magnetohydrodynamic Simulation Code for Complex Experimental Configurations, AMRC-R-874, (1987).
2. Goforth, J. H., Anderson, B. G., Bartram, D. E., Findley, C. E., Garcia, O. F., Heltne, G. J., Herrera, D. H., Herrera, T. J., King, J. C., Lindemuth, I. R., Lopez, E. A., Marsh, S. P., Martinez, E. C., Thompson, M. C., Oona, H., Stokes, J. L.,Torres, D. T., Veeser, L. R., Yapuncich, M. L., and Zerwekh, W. D., Explosively Formed Fuse Opening Switches For Multi-Megajoule Applications, 10th IEEE International Pulsed Power Conference (1995).
3. Lindemuth, I. R., Reinovsky, R. E. and Goforth, J. H., Exploding Metallic Fuse Modeling at Los Alamos, LA-UR-89-2921 (1989).

HIGH VOLTAGE APPLICATIONS OF EXPLOSIVELY FORMED FUSES

D. G. TASKER, J. H. GOFORTH, C. M. FOWLER, D. H. HERRERA,
J. C. KING, E. A. LOPEZ, E. C. MARTINEZ, H. OONA, S. P. MARSH,
R. E. REINOVSKY, J. STOKES, L. J. TABAKA, D. T. TORRES, F. C. SENA

University of California, Los Alamos National Laboratory, USA

G. KIUTTU, J. DEGNAN

Air Force Research Laboratory, Kirtland AFB, USA

At Los Alamos, we have primarily applied Explosively Formed Fuse (EFF) techniques to high current systems. In these systems, the EFF has interrupted currents from 19-25 MA, thus diverting the current to low inductance loads. The transferred current magnitude is determined by the ratio of storage inductance to load inductance and, with dynamic loads, the current has ranged from 12-20 MA. In a system with 18 MJ stored energy, the switch operates at a power of up to 6 TW. We are now investigating the use of the EFF technique to apply high voltages to high impedance loads in systems that are more compact. In these systems we are exploring circuits with EFF lengths from 43-100 cm, which have storage inductances large enough to apply 300-500 kV across high impedance loads. Experimental results and design considerations are presented. Using cylindrical EFF switches of 10 cm diameter and 43 cm length, currents of approximately 3 MA were interrupted producing ~200 kV. This indicates the switch had an effective resistance of ~100 mΩ where 150-200 mΩ was expected. To understand the lower performance, several parameters were studied including electrical conduction through the explosive products; current density; explosive initiation; insulator type and conductor thickness. The results show a number of interesting features, most notably that the primary mechanism of switch operation is mechanical and not electrical fusing of the conductor. Switches opening on a 1-10 μs time scale with resistances starting at 50 μΩ and increasing to perhaps 1 Ω now seem possible to construct using explosive charges as small as a few pounds.

1 Introduction

Previous studies [1] suggest that electrical fusing following mechanical deformation performs a primary role in EFF operation. The parametric studies reported here show that electrical fusing performs a secondary role, and the mechanism of switch operation is hydrodynamic deformation of the conductor.

In the course of development of the switch for high voltage applications there was a noticeable and unexpected degradation in switch performance. Using cylindrical EFF switches of 10 cm diameter and 43 cm length, currents of approximately 3 MA were interrupted, producing ~200 kV. This indicates the switch had an effective resistance of ~100 mΩ where 150-250 mΩ was expected. To understand the lower performance and to optimize the performance of the full-scale experiments, several parameters were studied in a series of small-scale experiments. Eventually, it was learned that the switch performance in the 10 cm diameter EFF was limited by explosive initiation problems peculiar to the 10 cm assembly. These problems were corrected after the small-scale tests were performed.

2 Small-Scale Planar Experiments

Planar, rather than cylindrical, assemblies were fired for simplicity and economy. These experiments were designed to match the electrical and physical conditions of the full-scale switches. The anvil patterns were identical, and the current densities were matched to ~80 kA/cm, see Fig. 1. The effects of varying the following parameters were studied: the explosive; the aluminum thickness; the current density; the addition of Teflon between the explosive and the aluminum; the type of die plastic; the cavity-depth in the plastic die; the surface finish of the plastic; and the load inductance. Due to space limitations, only the more interesting effects are reported.

3 Baseline Experiment

In the baseline small-scale assembly, the 6061-T6 aluminum conductor was 812 μm thick, 63.5 mm wide and 127 mm long. Typically, the current in the conductor was between 550 kA and 600 kA. The PBX-9501 explosive had a thickness of 12.7 mm and was initiated by a P40, ~100 mm diameter plane wave lens. There was no insulation between the explosive and the aluminum. The Teflon switch die was 165.1 mm square, with nine 1.50 mm-wide anvils and ten 6.00-mm spaces making ten patterns; the cavity depths were 12.7 mm. A capacitor discharge circuit was used with circuit parameters of 170 nH, 3 nF, and 2.9 mΩ. A typical current profile is shown in Fig. 2. In these experiments, the switch was timed to interrupt current at peak current from the bank. At the beginning of switch operation the aluminum conductor was compressed into the Teflon cavities, which reduces the switch inductance. Accordingly, there is a compression of flux and the current increases as shown in the inset of Fig. 2. The time of first flux compression (first motion) is a useful diagnostic, as it pinpoints the exact time that the explosive shock wave reaches the free surface of the aluminum conductor.

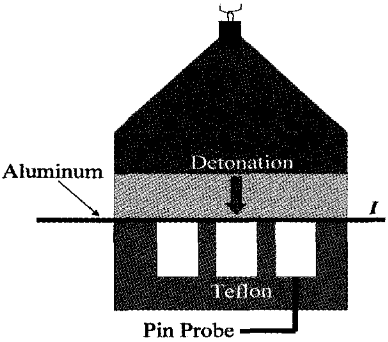

Figure 1 Schematic of small-scale assembly.

4 Joule Heating

To quantify the effects of electrical fusing in the aluminum, two experiments were fired in which the current density was reduced. In these experiments the currents were 126 and 105 kA, so the Joule heating rate (proportional to I^2) was reduced by factors of 19 and 27 from the standard experiment (~550 kA). If Joule heating contributed to the fuse action, then there would be a corresponding degradation in performance of the switch. In fact, switch performance was improved. The resistances were 540 mΩ and 580 mΩ respectively, compared to ~250 mΩ for the standard switch and current density. From these results we conclude that switch action is primarily by mechanical deformation rather than electrical fusing; and because the resistance had increased, that switch performance is ultimately limited by breakdown in the explosive product gases. We did note that the rate of resistance rise was slower in these shots, which suggests that electrical fusing does perform a secondary role in switch action.

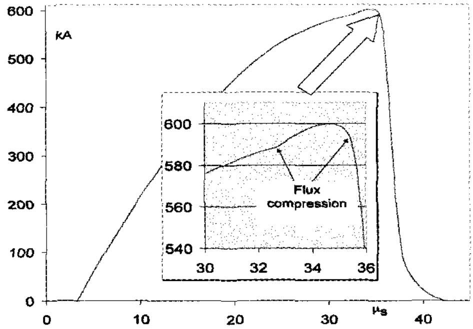

Figure 2. Switch current showing flux compression and current termination.

5 Effects of Varying Aluminum Thickness

If the aluminum thickness is reduced below the standard 813 μm, calculations show that the initial velocity, when explosively projected into the Teflon cavity, stays close to ~4.1 km/s because the PBX-9501 explosive to metal mass ratio is high [2]. As the velocity is approximately constant, the predominant effect of thickness might be expected to increase Joule heating as the current density increases. Experiments were performed using pure aluminum conductors of 254 μm and 508 μm thickness, and the resulting voltage data was compared with the standard experiment (813 μm), Fig. 3. The data are plotted from the time of first motion. Two curves are plotted for the standard experiment: one at the full current (550 kA); and one at low current (105 kA) - multiplied by five to reveal the structure. The results show the peak voltages are roughly equal, yet there is a double-hump structure that varies with thickness. The delay to the first hump increases linearly with thickness. The 813 μm data show the delay is independent of the current density, thus electrical fusing is again not responsible for the structure, and the effects are hydrodynamic. As shown by the pin data discussed below, impact with the Teflon cavity floor occurs at 2.20 μs after first motion in the standard (813 μm) thickness, as indicated by the dashed line.

Hydrodynamic calculations of aluminum deformation confirmed that the initial velocities were identical, and that the times of impact with the cavity floor were similar; impact occurs at ~2.0 μs for the 254 μm thickness compared with 2.2 μs for the thickest sample. However, there was a significant thinning of the aluminum jet prior to impact. The calculations show maximum thinning of the aluminum occurs at ~1 μs and ~2 μs after first motion for the 254 μm and 508 μm thicknesses, i.e., both before impact, but does not occur in the 813 μm thickness until after impact. These calculations agree with the data of Fig. 3. The calculations also show that for the two thinnest samples, the aluminum thickens again after impact as the aluminum piles up into the cavity floor. We conclude that mechanical fusing of the aluminum causes the first hump. The 813 μm thickness appears to be optimal for providing a broad, flat-topped structure.

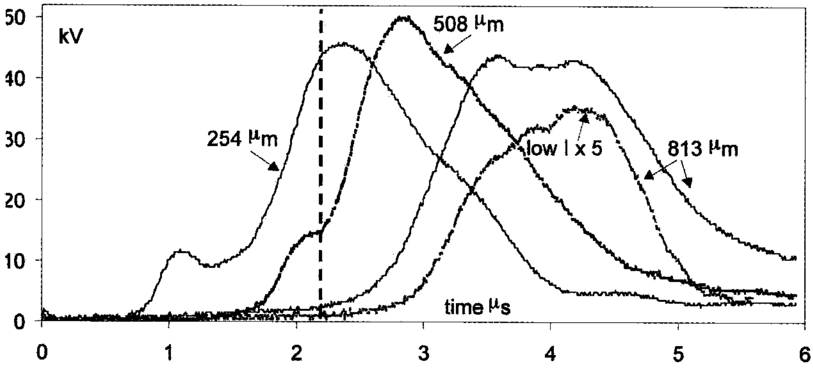

Figure 3. Results for three aluminum thicknesses.

6 Timing – Voltage Pin Diagnostics

To verify the calculations of switch performance published in [1], a voltage pin probe was added to the test as shown in Fig. 1. The probe was inserted so that the active element was flush with the floor of the switch cavity and insulated with a 125-μm Kapton layer. Consequently, no voltage appeared on the probe until impact of the aluminum jet with the cavity floor. The results of the small-scale experiment are shown in Fig. 4, plotted from time of first motion. Impact occurred at 2.20 μs, in good agreement with the predictions of [1]. The switch acted as a voltage divider, thus reducing the pin data by a factor of 4.5. At impact, the switch voltage had risen to ~1 kV.

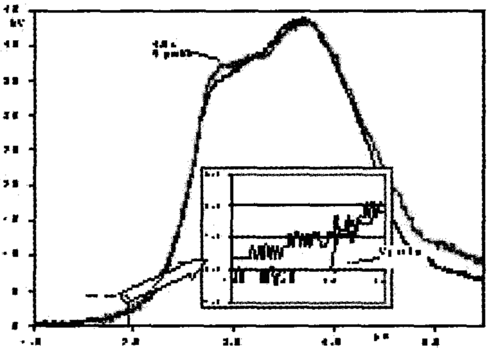

Figure 4. Voltage probe and pin data; inset shows impact on pin.

7 Inductance Effects

The voltage across the switch at the time of switch opening and peak current is given by:

$$V = IR = -L\frac{dI}{dt}$$

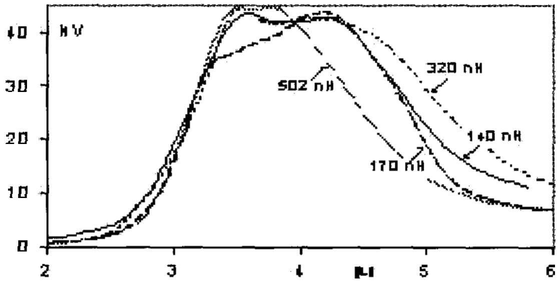

Figure 5. Load inductance effects.

If R were constant the output voltage would be independent of inductance, but if dI/dt were constant the voltage would be proportional to inductance. Also, as flux is conserved and increases with inductance for a given current, the integral of voltage with time should increase with inductance. Fig. 5 shows the output voltages for inductances of 140 to 502 nH for the same peak currents in the standard configuration. These are each plotted from the time of first motion. The waveforms are remarkably similar. The rising edges of the waveforms are almost identical both in amplitude, slope and timing. Differences are only evident after the initial peak. This implies that the initial resistance of the switch is constant and that dI/dt decreases as the inductance increases. Moreover, the fact that the voltage integral does not increase with inductance implies that breakdown is occurring after the initial peak.

8 Die Plastic

In one series of small-scale experiments the effects of substituting polyethylene for Teflon as the die plastic were studied. Polyethylene is known to be an inferior insulator to Teflon [3] at high pressures and was not expected to perform as well. In fact, the polyethylene exceeded the performance of Teflon, producing a voltage of 65 kV compared to ~45 kV for Teflon. However, there was no double-hump structure as seen in the Teflon, which implies that aluminum thinning did not occur prior to cavity floor impact.

9 Mass-Balanced, Insulated Experiment

To study the contribution of conduction in the explosive gas products, layers of 381-μm thick Teflon and 508-μm thick aluminum were substituted for the single layer of 813-μm thick aluminum. The masses were thus matched between the combined layers and the single layer of aluminum so the velocity of the aluminum would be the same. The Teflon was placed between the explosive and the aluminum to insulate the aluminum from the gas products. The results showed a significant degradation in performance with a peak switch resistance of 129 mΩ compared to ~250 mΩ for the standard experiment, and there were signs of breakdown in the dI/dt record. We speculate that this breakdown occurred along the surface of the Teflon between adjacent anvils.

10 Summary and Conclusions

From the results of an extensive series of experiments and hydrodynamic calculations, we conclude that EFF switch action is primarily by mechanical deformation rather than electrical fusing of the aluminum; and that switch performance is ultimately limited by breakdown in the explosive product gases and along plastic surfaces. The hydrodynamic calculations were tested by experimental measurement of the time of cavity floor impact, with good agreement. The time and magnitude of the initial voltage rise was found to depend on aluminum thickness, and that the 813 μm aluminum thickness is optimum for a flat top. The initial voltage rise is independent of load inductance. Preliminary tests show that polyethylene may perform better than Teflon, but more work is needed to optimize its performance.

Acknowledgments

LANL report LAUR-88-4484. This work was supported by the US Department of Defense.

References

1. Goforth, J. H., Marsh, S. P., Explosively Formed Fuse Opening Switches. *Proceedings of Megagauss Fields and Pulsed Power Systems (Megagauss V)* (1989) p. 515.
2. Jones, G. E., et al., Ballistics Calculations of R. W. Gurney. *Am. J. Phys.*, **48** (4) April 1980, p. 264.
3. Champion, A. R., Effect of Shock Compression of the Electrical Resistivity of Three Polymers. *JAP* **43**(5) p. 2216.

HIGH EFFICIENCY CLOSING SWITCHES FOR MEGAMP PULSED CURRENTS

P. SENIOR, I. SMITH
Department of Electronic & Electrical Engineering, Loughborough University, Loughborough, Leicestershire, UK

A closing switch is essentially an insulating gap between two electrodes that is bridged by one or more plasma channels followed, in some cases, by a metal-to-metal contact. The gap may be a vacuum or contain a gas, liquid or solid dielectric. If it exploits the contact plane between two such media, it is known as a surface switch or edge plane gap. The closure mechanism is usually divided into the resistive and inductive phases and the various implementations of the switch technologies exhibit different balances between the two. Some switches are essentially single shot mechanisms, and some do not handle current reversal very well. In developing a high-efficiency, single-turn electromagnetic launcher with current rising to near 1 MA in 1 μs, a number of the above technologies were evaluated in principle, with the most promising being investigated experimentally. Those described also have the potential to handle much higher currents.

1 Introduction

One aspect of a broad program of research into electromagnetic launchers has been an investigation of the maximum possible conversion efficiency between initial stored electrostatic and final kinetic energy. The launcher coil and projectile both resemble flat washers, with masses and dimensions chosen to optimally match them to the driving capacitor bank. With a projected 1 μs rise time flat, wide, minimum length transmission lines were implemented. Minimum safe insulator thickness and maximum line width served to keep down inductance and transient skin depth resistive dissipation. Losses due to nonlinear diffusion may be avoided if the ratio of current to conductor-width is kept below 0.1 MA per cm throughout the circuit. Finally, with anticipated peak currents of between 0.5 and 1 MA, it was essential that the closing switch presented low inductance and dissipation, thus necessitating minimal disturbance to the line geometry. It was evident that the resultant forces would be extremely destructive, leading to a launch interval measured in hours rather than seconds.

2 Dielectrics and Interfaces

The basic element of a closing switch is the plasma channel with inductive and resistive phases each having its own time constant. Historically, efficient switches were needed to discharge Blumlein line generators over tens or hundreds of nanoseconds. It is difficult to impedance match with other energy sources, but guidelines are available in [1] (page 291) for fast capacitor banks. In general, gas gap plasma channels have resistive time constants that are between one and two orders of magnitude higher than those in liquid and solid dielectric gaps of a similar voltage stand-off [2]. They permit repetitive triggering, and those that only pass current efficiently in one direction have their uses, but not in the present application.

Liquid gaps are often exploited to eliminate interfaces in designs where the same medium can be used for energy storage as well as switching. Such a switch was not a candidate, and appears rarely in the literature although invaluable information may be found scattered through [1] and in Chapter 6 of [3]. A solid dielectric offers minimal separation, with fast inductive and resistive phases, as discussed in the relevant sections of [1] and [3]. Multichannel operation is obtained from careful electrode design and maximising the trigger voltage rate-of-change. Surface discharges have been widely used both as switches and light sources as mentioned in [1] and [3] and specifically in [4].

Metal to metal switches offer resistances on the order of micro-ohms, and may be closed when there is no voltage across the gap. Reference [3] has a relevant background section, and specific applications were investigated [5].

3 Candidate Switches

Three forms of solid dielectric gap had been used prior to the launcher program: the single channel, gravity triggered 'nail' or 'thumb-tack' switch, detonator-driven metal-to-metal units, and a multichannel Blumlein line-triggered AWRE design [6]. The detonator switches were the most expensive per closure. Development started with a nail switch, briefly examined the surface switch technology, and obtained the best results with multiple detonators. Future work will exploit the economy of an updated AWRE-type unit. The nail switch used an anvil falling through a 1 m long, plastic guide tube, safely isolating the trigger circuit. Synchronisation with other events was not an issue. As a single channel backed up by metal-to-metal contact, the switch introduced some 6nH but only 1.2 mΩ into the circuit. The nail switch has an unsurpassed sub-nanosecond closure time because the field can reach 8 MV/cm at the tip. In view of its speed of operation, a nail switch was used to drive the trigger strap of the surface switch in Figure 1. The number of switch channels increased with the trigger voltage rate-of-change, and produced a respectable 2.7 mΩ from 10 kV. The resistance of the plasma channels would also have been reduced at 30 kV, but the field across the surface may have required a gas other than air, as well pressurisation. A modified design could also have reduced the inductance from 10.4 nH down to approximately 2 nH. With careful choice of materials and control of surface current density, repetitive triggering would be possible in other applications.

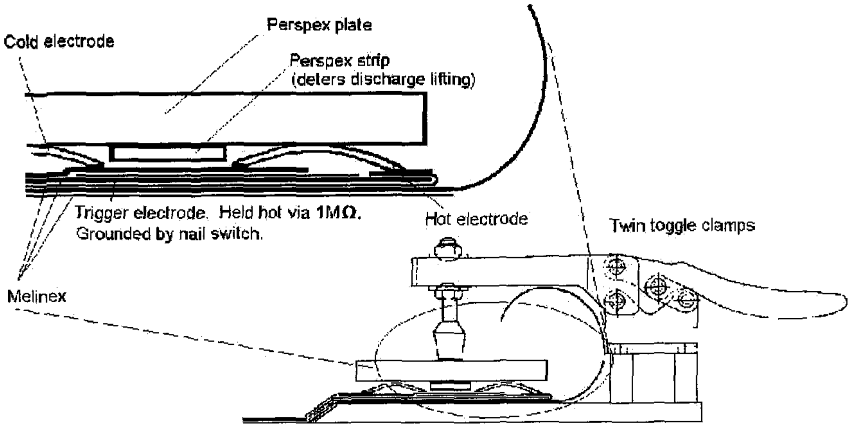

Figure 1. Surface Switch

The ultimate low dissipation possible for the switch in Figure 2 was only limited by the number of detonators that could be fired by a single circuit, and their cost. Initial estimates for three detonators was 400 μV, but a more sophisticated analysis of the circuit later showed the figure was about half this value, with an inductance of some 2 nH. This switch was used when launcher efficiencies of 47% were achieved, and may be scaled for much higher currents.

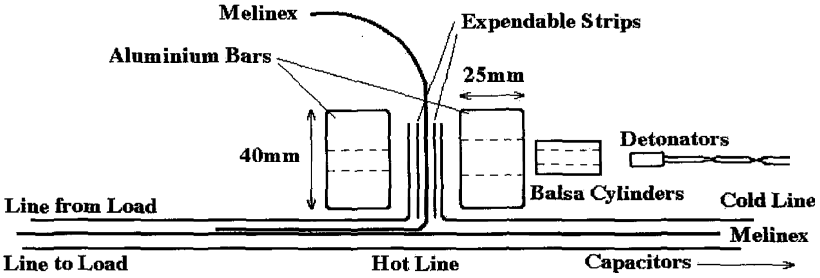

Figure 2. Detonator-driven metal-to-metal switch.

Future development of the switch in Figure 3 will reduce trigger circuit size by using a fast-charged water Blumlein. If it achieves the performance recorded by AWRE, it will introduce only 100 μΩ and 1 nH into the circuit. The pulse injected into the trigger strap simultaneously produces hundreds of intrinsic breaks in the insulation on a sub-nanosecond timescale, evenly along its length, by virtue of a carefully chosen taper. Once the energy of the bank begins to flow, 30% of the breaks become major current carriers. Eight such switches have been fired simultaneously in discharging a 2 MJ bank [6], and may thus be scaled for higher currents.

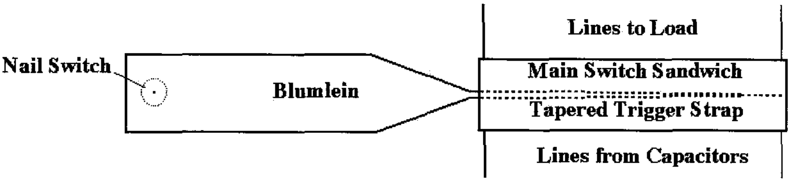

Figure 3. Multichannel solid dielectric switch.

4 Conclusions

In approaching 1 MA, the three switches examined were well within their current limits. As peak values and duration increases, careful consideration would have to be given to the mechanical impulse imparted to components throughout any circuit. Useful guidelines specific to transmission lines may be found in [6].

References

1. Martin, T. H., et al., J.C. Martin on pulsed power (Plenum Press, New York & London, 1996).
2. Schaefer, G. et al., Gas discharge closing switches (Plenum Press, New York & London, 1990).
3. Vitkovitsky, I., High power switching (Van Norstrand Reinhold Co., New York, 1987).
4. Etlicher, B., et al., Low inductance triggered multichannel surface switch for inductive energy storage generator, 10th IEEE International Pulsed Power Conference, Albuquerque, New Mexico, (1995) pp. 243-248.
5. Parker, J.V. et al., An improved, explosively actuated closing switch for pulsed power applications, 9th IEEE International Pulsed Power Conference, Albuquerque, New Mexico (1993) pp. 922.
6. Bealing, R., Carpenter, P.G., A compact 2MJ capacitor bank, AWRE Report No. O 2/76, March 1976.

FIRST RESULTS OF MULTI-RADIOGRAPHY IN THE EXPERIMENTS WITH MC-1 GENERATOR

G. V. BORISKOV, A. I. BYKOV, M. I. DOLOTENKO, N. I. YEGOROV, N. P. KOLOKOL'CHIKOV, YU. P. KUROPATKIN, N. B. LUKYANOV, V. D. MIRONENKO, V. N. PAVLOV, V. I. TIMAREVA

Russian Federal Nuclear Center, All-Russian Scientific Research Institute of Experimental Physics (RFNC-VNIIEF), Sarov, Russia

The possibility of recording several frames on one X-ray film is investigated. This will help to reduce the number of experiments needed to obtain information on the dynamics of liner compression of cascade MC-1 generators. We developed the method to gain information on the dimensions of cylindrical structural components moving with velocities up to several km/s. We exposed the film with two or three bremsstrahlung pulses of an ironless betatron, programmable in time. The possibility of obtaining several coaxial images of a tungsten tube on one and the same film, compressed by ultra-high magnetic field pressure, is shown. Spatial resolution was good enough to determine the tube dimensions at each moment in time.

1 Introduction

The method of pulsed radiography is widely used in the study of fast processes, particularly in experiments using a magnetocumulative generator (MCG) of the MC-1 type [1,2]. The data is obtained by X-raying the experimental assembly with the short pulse of a betatron bremsstrahlung. When an X-ray film records the shadow imaging, (r-t) diagrams of the processes are built based on the series of experiments radiographing the assembly at various times. The method has high spatial resolution and sensitivity, however it requires the use of many MCG, making it very expensive. Also, we get additional errors when synchronizing the results from several shots.

Our team has developed multipulse (two or three pulses) operation conditions of a betatron [3], which allows the distance between pulses to be varied within a large range. This multipulse mode and radiation intensity distribution over pulses allows fewer shots. However, the issue remains on how to record images. Electron devices of multi-frame or continuous recording are in the process of being designed (it is already clear that they are very expensive). This paper describes the method of (r-t) diagram building in the experiment using a recorder based on X-ray film, and presents the first experimental data on multi-radiography of an isentropically compressed material.

2 Radiography System

The schematic of the radiography experiment is given in Fig. 1. This method has been tested in experiments on isentropic compression of frozen gases. Fig. 1 shows a coaxial structure of an isentropic compression assembly consisting of a two-cascade MC-1 generator, two steel cryostat tubes, a two-layer (copper and tungsten) compression tube and a sample (frozen argon). The goal of the experiment is to measure the diameter of a compressed sample two or three times during a compression process.

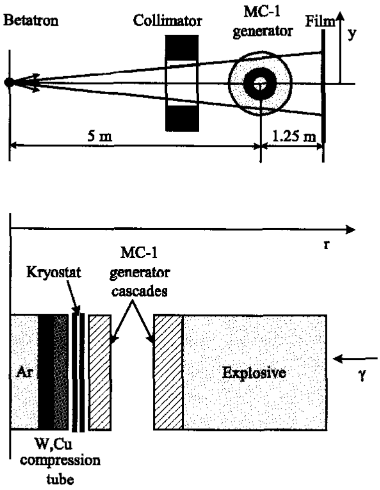

Figure 1. Radiography system (top picture). Cross-section of an isentropic compression assembly before an explosion (bottom picture).

3 Mathematical Model of the Method

A mathematical model involves calculation of an object radiation response *J'*, i.e. attenuation of the direct radiation flux. The goal of modeling is to determine the optimum mode of X-raying, i.e. to distribute radiation intensity in pulses and determine the time interval between pulses. Changes in an object's size with time *F(y,t)* and radiation intensity *J"(t)* are calculated by:

$$J' = \int_a^b F(y,t)\, J''(t)\, dt$$

System radiation response J is calculated by taking into account the function A:

$$J = J' \otimes A$$

We consider the mode to be optimal when it allows two sample interfaces to be resolved in one picture.

Using the interface trajectories of the structural components discovered with the help of the numerical model, function A, which was discovered experimentally, and varying betatron radiation characteristics, we showed that it is possible to get a picture showing at least two sufficiently clear sample interfaces. Fig. 2 presents one of the simulation results as a calculated picture densitogram, where local densitogram minima correspond to these interfaces.

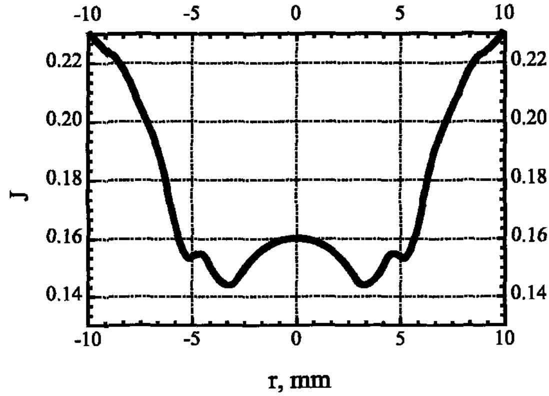

Figure 2. Portion of calculated densitogram. The local minima correspond to two interfaces - compressed argon-tungsten.

4 Experimental Results

Fig. 3 shows radiograms of the initial assembly and of the experiment, obtained in the X-raying mode close to optimum. Fig. 4 shows densitograms of these pictures. The experimental densitogram agrees well with the simulation results. It allowed argon compression at two different times and the sample interface average velocity to be determined. These data also agree well with the compression unit model.

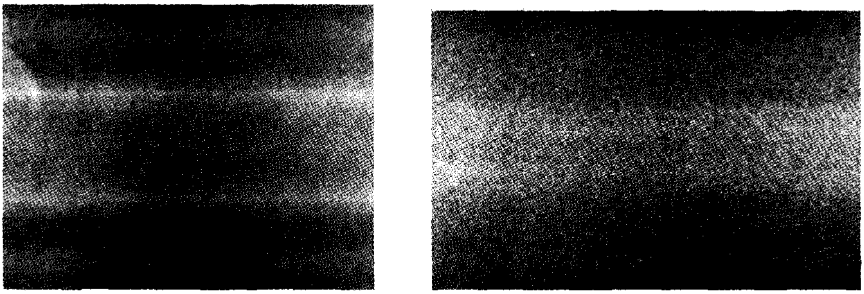

Figure 3. Radiograms of inital assembly (left), and during experiment (right).

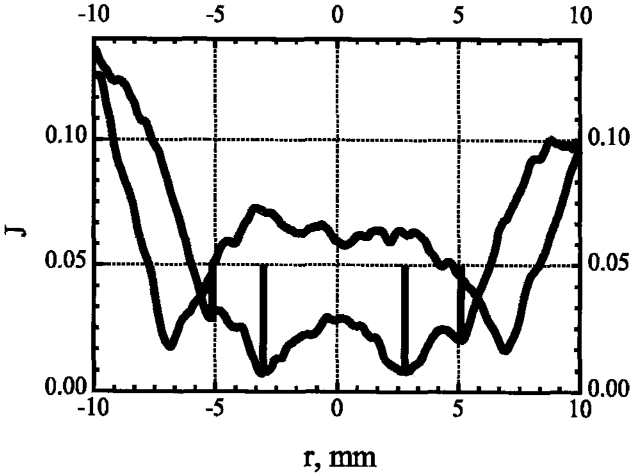

Figure 4. Densitograms of pictures from Fig. 3. Vertical lines denote Ar-W interface.

5 Conclusions

Using an example of the unit for isentropical compression of frozen gases, which is difficult to X-ray and model, we demonstrated multi-radiography by recording several locations of the structural components of explosive devices on a single film. This process does not complicate the experiment, but decreases a number of necessary experiments.

References

1. Pavlovskii, A. I. et al., Issledovanie dinamiki ckhlopyvaniya obolochki magnitokumulyativnogo generatora. *Sverkhsil'nye magnitnye polya*, Moscow, Nauka, (1984) p. 14.
2. Bykov, A. I. et al., Equation of state study using the method of isentropic compression by ultrahigh magnetic field pressure in cascade MC-1 generators. *Megagauss field and pulsed power systems, MG-V.* Nova Science Publishers: New York (1990) p. 155.
3. Kuropatkin, Yu. P., et al., Characteristics of the installation for flash radiography based on the uncored betatron BIM-M. 11th IEEE Pulsed Power Conference. Digest of technical papers, Ed. by G. Cooperstein and I. Vitkovitsky (1997) p. 1663.

EXPERIMENTAL INSTALLATION FOR ELECTRODYNAMIC COMPRESSION

B. E. FRIDMAN, N. N. KUSTOV, A. G. LEX, PH. G. RUTBERG
Institute of Problems of Electrophysics of RAS, Saint Petersburg, Russia

An experimental installation to create high pressure and study material phase transformations has been built at the Institute of Problems of Electrophysics, RAS. Pressure is produced inside a cylindrical metal conductor using the pinch effect by passing a large pulse current up to 10 MA and creating a megagauss magnetic field on the conductor's surface. The E7-25 capacitive energy storage system is the source of the current pulse for the installation. The experimental installation design features are described. Large axial forces are shown to act on the discharge chamber when the heavy current pulse passes through the chamber's elements. These forces exceed possible limits, determined by construction strength. The design of the installation provides the creation of initial squeezing forces for contact connections in the discharge chamber and the absorption of kinetic energy of the discharge chamber's moving parts after the current pulse passes. The installation test results are presented.

1 Introduction

Pulse compression methods are used to study phase transformations of materials as well as in the technology of hyper-firm materials production. As a rule, one uses the explosion of brisant explosive substances for pulse compression, and the duration of the pressure pulse is one to several microseconds. The substance's crystal phase output ratio can be increased if one increases the pulse duration up to 40-100 μs [1]. However, it is practically impossible to create pressures of such duration by using an explosive substance.

The technique of heavy current pulses and strong magnetic fields creates high compression. It has been suggested [2] that high current pulses can be used to synthesize artificial diamonds. In this method the specimen containing carbon is heated by current flowing through its axis, and is compressed by its own magnetic field (pinch-effect). The compression of matter is also possible when a current pulse passes through the cylindrical liner from a material with high conductivity (copper, aluminum). Here, the substance being investigated is placed inside the liner or inside a steel ampoule also placed inside the liner. A facility is, therefore, required where stored capacitive energy is discharged onto a cylindrical sample of the material to be investigated to achieve this type of compression.
It is necessary to create a magnetic field more than 100 T on the liner's surface to produce pressures of several gigapascals. A natural limit restricts the pressures to be produced. This limit is determined by temperature, when overheating would possibly lead to the explosion of the liner's metal in high magnetic fields.

Estimations of the allowable modes of pulse compression, at which the researched material does not overheat, was made by computing the nonlinear diffusion of strong magnetic fields in a metal tube [3,4]. These calculations show that required pulse compression modes can be realized only at reasonably large liner sizes and at large discharge current values (about 6-10 MA). Such an installation was designed and manufactured at the Institute of Problems of Electrophysics. It was assembled with the E7-25 capacitive energy storage device [5] and an electrodynamic test bench connected to the capacitor bank.

2 Design of the Electrodynamic Test Bench

The cross-section of the test bench's discharge chamber is shown in Fig. 1. The investigated specimen 1 is fixed between two electrodes 2 and 3. The internal surface of the discharge chamber 4 is coated with a copper shell 5. The current to the internal surface of discharge chamber is fed through a demountable contact connection with the top copper bus. The bottom electrode 3 is fastened to the bottom ground bus. Both buses are connected to the terminal of the energy storage systemE7-25. The test bench is designed for a current of up to $I_{max} = 10$ MA and a current integral of $J = 5\times10^9$ A^{2}xs.

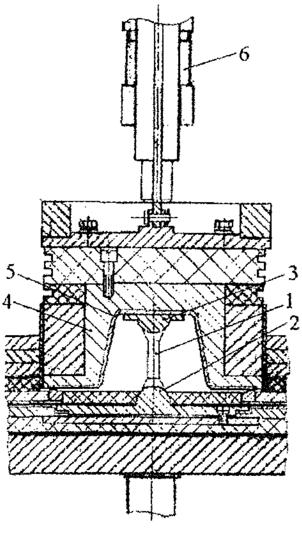

Figure 1. Cross-section of the discharge chamber

The test bench is bulky and contains a large quantity of metal. The total weight of the test-bench is 3 tons; the total mass of the discharge chamber and connected moveable elements is 125 kg. The length of the contact surfaces in the connection between the buses and capacitor bank terminal is 2000 mm. This length is defined by limiting the current pulse density for demountable contacts, which in our experience should not exceed 50 kA/cm.

The current passes through two flat copper buses divided by 1 mm thick polymer film insulation. The large repulsive forces act on the buses when the current pulse passes. If the current is 10 MA, then the total force acting on the bus is 530 tons and the momentum of this force is 2800 kgxmxs^{-1}. The copper buses are fixed between bulky steel plates to provide strength and stiffness. Ten bulky bolts clamp these plates. The cross-sectional area and length of the bolts are chosen so that their elastic deformation could absorb the momentum.

Large electrodynamic forces act on the electrodes and surface of the discharge chamber when the current pulse passes (up to 2600 tons at 10 MA). The discharge chamber 4 begins to move upwards under the action of these forces. Two hydraulic buffers 6 absorb the kinetic energy of the chamber movement. The braking distance of chamber 4 must not exceed 100 mm; the braking force is not more than 15 tons. The application of hydraulic buffers has reduced the vertical forces acting on the construction by two orders of magnitude.

Initially, during test bench operations, there was a problem with providing a good contact between electrodes and sample, as well as between top bus and discharge chamber. High quality contact can only be obtained by creating a rather large contact pressure. It is impossible to create such pressure on the electrodes and simultaneously on the contact connection between the chamber and top bus, as this deformation system is static and undefined. Moreover, the contact pressure mechanism will be inevitably broken after the current pulse has passed.

Thus, the mechanism for clamping the contact surfaces was built into the structure of the test bench. This mechanism is mounted on the test bench columns. Before the pulse, it was clamped to the chamber and the sample with screws. Now, the clamping forces are transferred to the discharge chamber and the sample through one or two steel pins. Plastic deformation of the sample (liner) causes contact pressure between the electrodes and the sample, as well as between the top bus and the discharge chamber, under the action of clamping forces. After the current pulse, the chamber moves upwards and breaks the steel pins. Hydraulic buffers provide braking and stopping of the chamber.

3 Testing of the Installation

The electrodynamic installation was tested with a 6 MA pulse current. 8 modules of the E7-25 energy storage system were used with a total capacitance of $C = 17.367$ mF, which were charged up to 14 kV initial voltage. The stored energy was 1.7 MJ; the initial charge was 245 Q. The 25 mm diameter copper sample has fully evaporated. The oscillograms of current, I, in the sample and voltage, U, between the test-bench's buses are presented in Fig. 2. In this experiment, an energy of $W \approx 1$ MJ, was dissipated in the discharge chamber, the current integral $J = 1.8\times10^9$ A^{2}s and charge $Q > 500$ Q passed through electrodes and sample. The steel pins of the mechanism to initially clamp the contacts were broken after the pulse. The discharge chamber was lifted approximately 50 mm and was stopped by hydraulic buffers. A large erosion of electrodes was observed in this experiment. It is necessary to note that the spherical electrodes worked well with currents under 0.3 MA/cm^2.

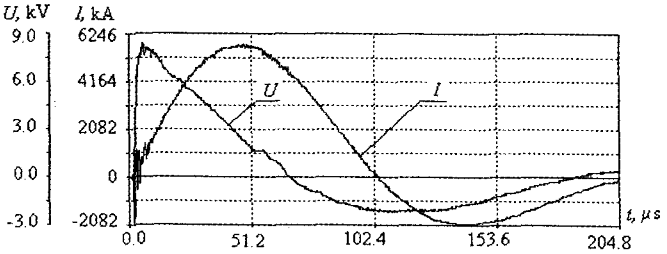

Figure 2. Current I and voltage U oscillograms in the short-circuit test

Acknowledgment

The installation was created with financial support from the Russian Foundation for Fundamental Research, projects N 94-02-03372 and N 96-02-16009.

References

1. Batsanov, S. S., Bolchovitinov, L. G., Martynov, A. I., About Saving Meta-Stabilised Phases of High Pressure at Shock Compression. *Letters in the Journal of Technical Physics,* (in Russian) (1990) **2**, pp. 53-54.
2. Bushman, A. V., Vorob'ev, V. S., Rakhel, A. D., Fortov, V. E., About Possibility of Electro Discharge Synthesis of Artificial Diamonds. *Doklady Academii Nauk,* (in Russian) (1990) **315**, No. 5, pp. 1124-1126.
3. Fridman, B. E., Rutberg, Ph.G., About the Use of Large Pulse Currents in Experiments of Dynamic Compression of Solid Bodies, *Journal of Technical Physics*, (1996) **66**, No. 2, pp. 123-131.
4. Fridman, B. E., Rutberg, Ph. G., About Creation of High Pressure by 10 MA and more than 60 μs Long Pulse Current for the Substances' Phase Conversion Study, *Proceedings of 7th International Conference on Megagauss Magnetic Field Generation and Related Topics*, (1997) Sarov, **2**, pp. 601-606.
5. Emelin, P. Yu., Rutberg, Ph. G., Fridman, B. E., E7-25 Capacitor Energy Storag,. *Instruments for Experimental Techniques*, (1993) **36** No. 5, pp. 730-733.

GENERATION OF HIGH-POWER SHOCK WAVES ON PIRIT-2 FACILITY

M. V. ZHERNOKLETOV, V. I. KARGIN, D. V. KOTELNIKOV,
A. V. MELKOZEROV, A. L. MIKHAILOV, A. Y. NAGOVITSIN,
N. F. POPKOV, E. A. RYASLOV

All-Russian Scientific Research Institute of Experimental Physics (VNIIEF), Sarov, Russia

Results of the first experiments performed on radiation flux hydrodynamics carried out at the PIRIT-2 facility are presented here. A Z-pinch was used as a radiation source. The soft X-radiation energy flux density was $0.5\ 10^{11}$ W/cm^2. The photochronograph method and a laser interferometer velocity meter were used to record shock wave velocities. Transparent matter with dynamic rigidity parameters similar to those of the sample was placed and the mass velocity recorded by the LDVM method.

1 Introduction

A strong shock wave is produced in a sample to study the matter state equation using the dynamic method. Such a wave can be obtained by different methods: using an explosive through a striker possessing a high velocity, and through laser or X-radiation. When X-radiation intensity is 10^{12} W/cm^2 in the sample, a strong shock wave is formed and shock pressures up to 1 Mbar are created [1,2].

2 Description of the PIRIT-2 Facility

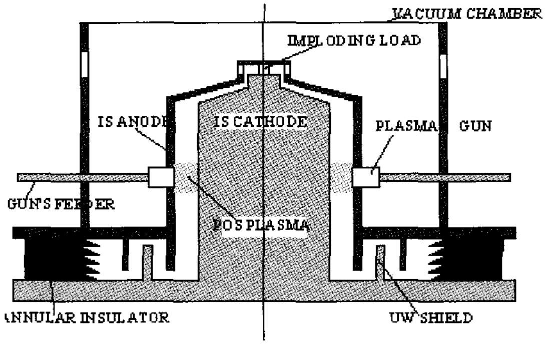

Figure 1. Design of the vacuum chamber at the PIRIT-2 facility.

The PIRIT-2 facility assemblies were advanced to perform radiation flux hydrodynamics experiments to study material flows arising under the influence of strong X-radiation fluxes [3]. Advances included a plasma opening switch, a plasma load, a vacuum chamber and a diagnostic system. A 30 cm long inductive storage (IS) is made using a 40 cm diameter vacuum coaxial line and a 5 cm gap. A plasma opening switch (POS) section is installed at the anode break, similar to those used in the PIRIT-2 facility. The plasma opening switch operates at a magnetic field intensity of 30 kA/cm.

The IS section located behind the plasma gun switch is meant for plasma motion during the time when the switch is in the conductive state. The section length is 30 cm. The gap between conic line electrodes slowly changes from 5 cm in the IS to 1 cm on a 10 cm diameter. Line inductance upstream from the load is 10 nH.

At the line output are current and magnetic field probes. Plasma load electrodes (Fig. 2) are connected to the conic line, transferring IS current to Z-pinch plasma, gas imploding sheath, thin wire array etc. The end load electrode is attached to the line anode through 12 bars that are 3 cm long and 0.5 cm in diameter. These bars provide X-radiation output in the radial direction onto the samples and diagnostic

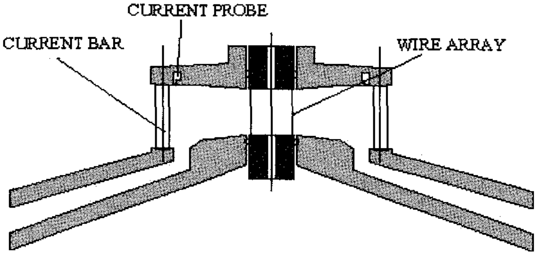

Figure 2. Plasma imploding load.

The wire array is 2 cm long and 2.5 cm in diameter. After the wires have been exploded, a cylindrical plasma sheath is formed that is imploded to the axis by a powerful IS current pulse provided by the POS. Current rise time in the load is 120 ns and the working current approaches 4.5 MA. X-radiation pulse duration is 20-30 ns at 2-5 10^{10} W/ cm^2 flux power, 2 cm from the Z-pinch [4].

3 Experimental Techniques

The sample studied is installed at the axis of the plasma load at the minimum distance from Z-pinch. When loading with an X-radiation strong flux, a strong shock wave is formed in the sample, collapsing it with pressures up to the megabar range. Two methods are used to record shock wave states in the sample: a photochronograph and a laser Doppler velocity meter (LDVM).

In a step form type of sample, the shock wave velocity can be recorded at the known base of the sample by the photochronograph method. The laser Doppler method is used to record both mass velocity and shock wave velocity. Both of the methods are presented in Fig. 3. In the photochronograph method, radiation flux from the Z-pinch is collected by a lens and transmitted by a light guide onto the photochronograph, where the time that it takes the shock wave to arrive at the step sample boundaries is recorded.

The shock wave velocity is determined in the same way as the laser method. There, an interference image resulting from the original laser beams, and those reflected from the sample is recorded. The interference picture will depend on the reflected beam frequency Doppler shift, which is proportional to the sample velocity.

The laser Doppler method can record the matter mass velocity in the investigated sample. Transparent matter with dynamic rigidity parameters similar to those of the sampleis placed on the sample boundary. The laser beam is focused on the sample-window interface and the interferometer records interface velocity, i.e. mass velocity

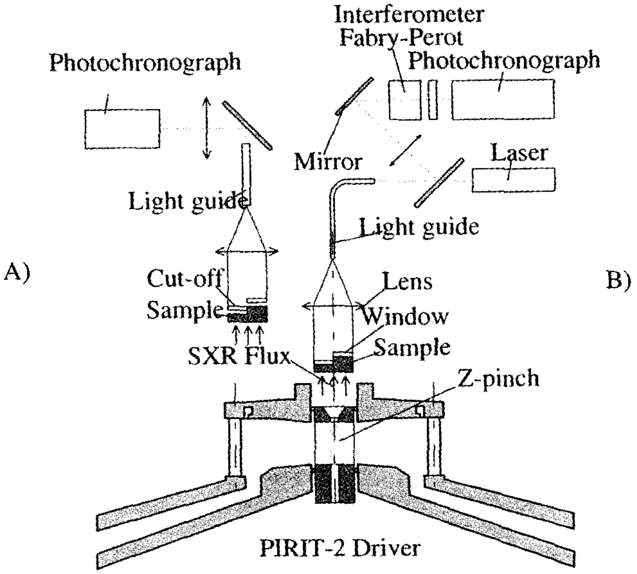

Figure 3. Technique of sample shock wave parameters measurement, a)-photochronograph method and b)-laser method

A 10 W narrow-strip argon laser is used to produce a basic laser signal. The laser Doppler velocity meter also records phase transition and spalling strength of the samples investigated. The time resolution for the LDVM method is 10^{-9} s and the measured velocity limit is from 100 - 10^6 m/s. Such a wide range of measured velocities allows measuring a sample mechanical impulse affected by an X-radiation flux.

One-dimensional calculations of soft X-radiation energy absorption in SiO_2 and graphite samples were performed for different variants of the spectrum, duration, and SXR intensity and shock wave pressure profiles arising during this process. According to the calculation, at 0.2 keV plasma radiation temperature the peak pressure in the graphite approaches 300 kbar (Fig. 4). In the 1 mm thick sample, peak pressures in the shock wave front equal to 100 kbar were obtained. The shock wave velocity is 2 km/s.

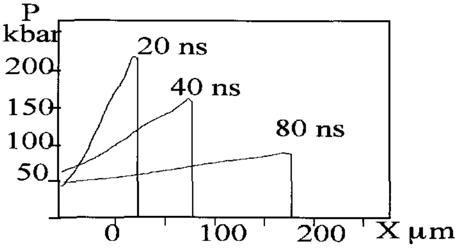

Figure 4. Pressure profile dependency in graphite.

4 Conclusion

This paper presents results of the first experiments performed on radiation flux hydrodynamics carried out at the PIRIT-2 facility. A Z-pinch was used as a radiation source. The soft X-radiation energy flux density was 0.5 10 ^{11} W/cm^2. The photochronograph method and the laser interferometer velocity meter were used to record shock wave velocities. At the mass velocity recording by LDVM, transparent matter with dynamic rigidity parameters similar to those of the sample was placed.

References

1 Branitskij, A. V., et al., Excitation of intense shock waves by soft X-radiation, *Proceeding of 11th International Conference on High Power Particles Beams*, Prague, June 1996 pp. 292-295.
2 Ramirez, J. J., The X-1 Z-Pinch Driver, in *IEEE trans. on Plasma Science*, **25**, No. 2, (1997).
3 Pavlovskii, A. I., Popkov, N. F., Ryaslov, E. A., et al., Powerful pulsed energy sources for plasma physics investigations, *Megagauss magnetic field generation and pulsed power application*, Ed. by M. Cowan and R. B. Spielman, N.Y.: Nova Science Publishers (1994) pp. 429-435.
4 Pavlovskii, A. I., Popkov, N. F., Ryaslov, E. A. et al., Characteristic optimization of pulsed energy sources with plasma switches, *Megagauss magnetic field generation and pulsed power application*, pp. 757-761.

STEEL AND GRAPHITE HEATING BY MEGAAMPERE CURRENT PULSES

B. E. FRIDMAN, A. G. LEX, I. P. MAKAREVICH,
Ph. G. RUTBERG
Institute of Problems of Electrophysics of RAS, St.-Petersburg, Russia

A. D. RAKHEL
High Energy Density Research Center, Incorporated Institute of High Temperatures of RAS,
Moscow. Russia

Many properties of metals and graphite are investigated by the exploding wires technique. For typical conditions of exploding thin wires of 0.1-1.0 mm, the pressure is no more than 0.1 GPa. Application of electrical currents greater than 1 MA in amplitude allows us to reach gigapascal pressures, more typical for the megagauss field generation devices. In this case, the energy of a pulse is fairly high and it becomes possible to use relatively large samples of up to 1 cm in diameter. This gives an advantage in scope measurements during the process. Here, we present the results on steel and graphite heating by electrical current pulses of large amplitude, and duration of up to 100 μs. Cylindrical rods of 0.6-1 cm diameter and 3-8 cm in length were used. Electrical current was passed through the sample and the voltage drop across it was measured. The shadow graph method was used to observe the course of the sample heating. The information on electrical specific resistance as a function of specific energy and current integral was defined from these data. This information was obtained for solid, liquid and mixed (solid and liquid) phases for steel. Some preliminary results of pulse heating of graphite are also presented.

1 Introduction

The processes of pulse heating and electrical explosion of conductors define the limiting values of magnetic induction and current density of the generation of ultra-high magnetic fields. The analysis of these processes can be executed on the basis of dependencies determining the state equation of a material and its electrical resistance. Sometimes [1] the dependencies, obtained through static measurements, are used for analysis of strong magnetic field diffusion in a metal. It does not correspond to the real characteristics of materials under pulse loading conditions. The necessary information regarding pulse heating can be obtained from the experiments in pulse heating and electrically exploding conductors. However, such experiments are usually performed with thin wires and small currents of tens of kiloamperes [2,3]. The created pressure does not exceed some tenths of one gigapascal, and that does not correspond to conditions to generate strong magnetic fields.

It is possible to increase the pressure up to several gigapascals by performing the experiments on pulse heating with massive cylindrical conductors approximately 10 mm in diameter, using currents up to several megaamperes. The installation for electrodynamic compression [4] allows performance of such experiments. The first results of pulse heating of steel and graphite, obtained on this installation, are presented here.

2 Pulse Heating of Steel

The experiments were executed with 10 mm diameter samples made from low-carbon steel (St3). To measure its specific resistance, two rings made from copper wire were fixed onto a central, cylindrical section of the sample where homogeneous loading conditions exist. Coaxial cable leads were soldered to the rings to measure the voltage drop on the sample's central section. The distance between the rings ranged from 21 to 38 mm depending on experimental conditions.

Almost all experiments were carried out in two stages. At the first stage, the test was made with a small current of up to 350 kA. The inductance coefficient L was determined from the current, I, and voltage drop, U_r, across the sample. Also,

$$L = M + L_0 ,$$

where M is the coefficient of mutual induction between the current I and measuring loop, and L_0 is the own inductance of the sample's area between rings.

The electrical explosion of a sample occurs at the second stage of the experiment. The coefficient L, determined early in the first stage, was used for processing oscillograms of the second stage. Thus, it was possible to calculate the active component of the voltage drop over the sample's central section.

This method is valid in the absence of a skin effect in the sample. The calculation of the current distribution has shown that there is a weak pronounced skin effect in a "cold" steel sample. That is why measurements of resistance R and specific resistance ρ in the first stage experiments overestimate values by 2.0–2.5 times. Heating equalizes the current density j throughout the sample's cross-section.

Resistance of the sample's section between contact rings was determined by

$$R_a = \begin{cases} \dfrac{U_a}{I} = \dfrac{U_r - L\dfrac{dI}{dt}}{I}, & if\ |I| \geq 200\,kA, \\ 0, & if\ |I| < 200\,kA, \end{cases}$$

where U_r is the signal of the voltage drop over the sample's central section after median filtration on 7 points, dI/dt was calculated from current signal I after smoothing on 43 points, L is the coefficient determined in the first stage.

Fig. 1, 2 represent typical oscillograms of current, I, and voltage drop, U_r, over the sample's central section. In some experiments (Fig. 1) a break in the contact between rings and sample was observed. The contact was then restored through roughly 20 μs. We explain this break by sample compression. It is possible to explain the restoration of contact by thermal expansion of the sample. Therefore, in subsequent experiments, we did not use the wire contact rings and applied wire pieces that were attached to the sample's surface by argon-arc welding. Thus it was possible to avoid temporarily breaking contact.

In Fig. 3 and Fig. 4 the graph of specific resistance ρ as a function of current integral $\xi=\int^{t} j^2 \cdot dt$ are presented. Here, $j = I/S$ is current density, S is the area of the "cold" sample's cross-section. The dashed line in Fig. 4 shows the dependence $\rho(\xi)$ obtained experimentally when the contact wire rings were used (Fig. 1). This graph corresponds with the others except in the time interval when the contact between the wire rings and the sample was broken.

$$\rho(w)=\begin{cases} \rho_0+\beta_1 \cdot w, & 0 \le w \le w_1, \\ \rho_1+\beta_2 \cdot (w-w_1), & w_1 \le w \le w_2, \\ \rho_2+\beta_3 \cdot (w-w_2), & w_2 \le w, \end{cases}$$

where ρ_0 is the "cold" specific resistance, $\rho_1=\rho_0+\beta_1 \cdot w_1$, $\rho_2=\rho_1+\beta_2 \cdot (w_2-w_1)$, w_1 is the change of internal energy of steel when it begins to melt. This approximation was used earlier to calculate the initial stage of the wire explosion [5]. We confirmed this approximation in our experiments when the field induction on the conductor's surface reached 65 T, and we have obtained the coefficients β_1, β_2, β_3, w_1, w_2 for pressures up to 3 GPa. A similar piece-wise linear approximation can be used to determine the function $\rho(\xi)$, and is probably more convenient for calculating the nonlinear diffusion of a pulsed magnetic field in steel.

In Fig. 5, frames of high-speed photography obtained in the experiment (Fig. 2) are presented. The frames were made by the shadow graph method. They show that the sample is heated more intensively in the vicinity of the conic edge. It is possible to explain this phenomenon by inhomogeneity of current distribution in the sample's conic edge. The central part of sample, where the voltage U_r was measured, was heated homogeneously.

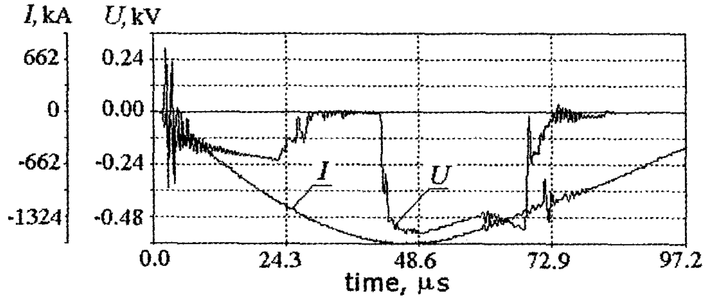

Figure 1. Current I and voltage U oscillograms of steel heating. Measurement of voltage produced with help of wire rings.

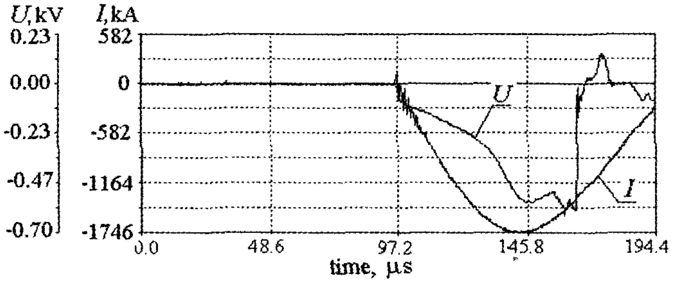

Figure 2. Current I and voltage U oscillograms of steel heating. Measurement of voltage U produced with help of wires, joined to sample by weld.

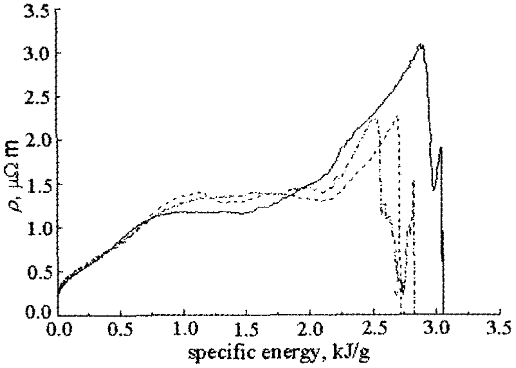

Figure 3. Specific resistance ρ vs. specific energy dissipated in steel.

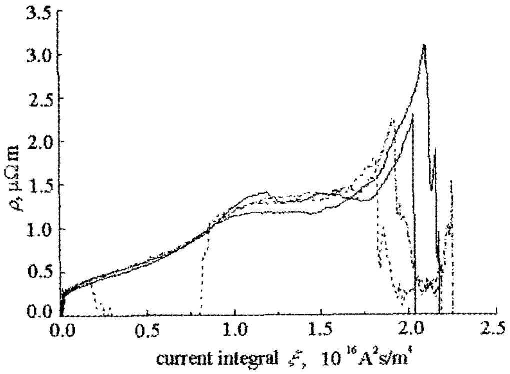

Figure 4. Specific resistance ρ vs. current integral $\xi = \int_0^t j^2 \cdot dt$ for steel samples. Dash-line correspondes to the oscillograms on Fig. 1.

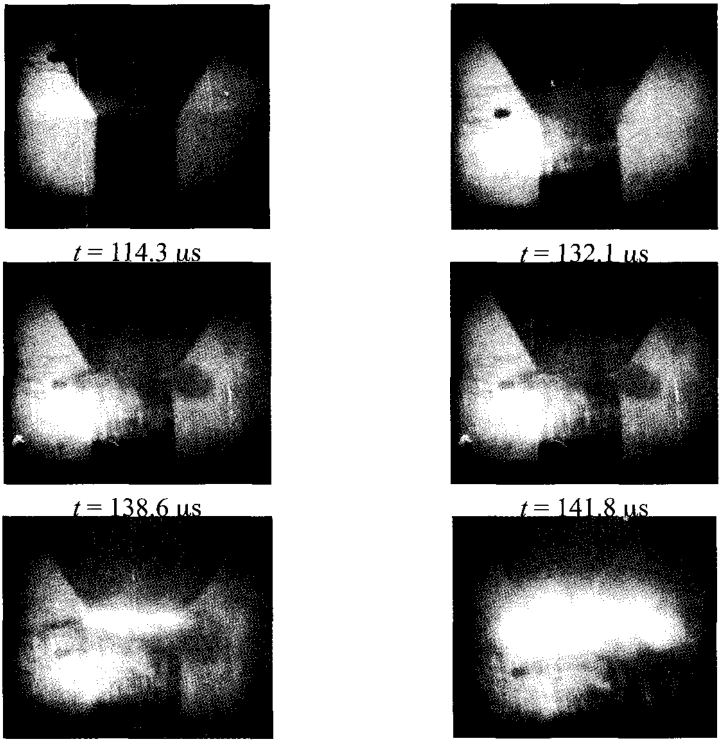

t = 114.3 μs

t = 132.1 μs

t = 138.6 μs

t = 141.8 μs

t = 143.4 μs

t = 145.1 μs

Figure 5. High-speed photography frames of the initial stage of the steel sample's electric explosion. The photographs were made through a blue filter. The time instants in captions under each frame correspond the oscillograms on Fig. 2.

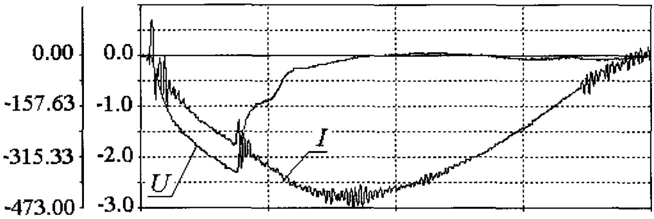

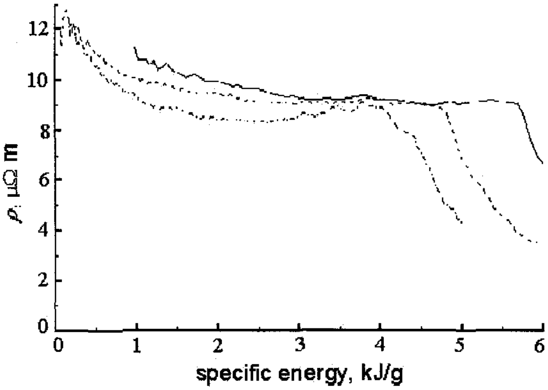

Figure 7. Specific resistance ρ vs. specific energy, dissipated in graphite

3 Pulse Heating of Graphite

Cylindrical, pyrolytic graphite rods of 5.8x30 mm with density $\gamma = 1.73$ g/cm^3 and initial specific resistance ρ_0=11$\mu\Omega$•m were used in the pulse heating of graphite experiments. These samples are characterized by a high initial full resistance of about 13 mΩ, explaining why the inductive component of the voltage drop over the sample and measuring loop is small. Consequently, this voltage component was not accounted for in processing the oscillograms.

The typical oscillograms of a current, *I*, and the voltage drop on a graphite sample, *U*, are shown in Fig. 6. Fig. 7 represents the dependence of specific resistance ρ on specific energy, dissipated in graphite. A step-like reduction of the voltage drop on the sample was observed when specific energy was approximately 4-5 kJ/g. The change of specific resistance from 11 down to 9 μΩ xm is part of the process of heating the graphite before this step reduction.

4 Conclusions

The first experiments at the installation for electrodynamic compression showed the peculiarities of the pulsed heating and compression of the low-carbon steel and graphite cylindrical samples by the large pulsed current. The piece-wise linear dependence of the steel's specific resistance on the specific energy dissipated in the sample was confirmed in the range of specific energy up to 3 kJ/g, current integral up to $2 \cdot 10^{10}$ A^{2}s/m^4 and pressure up to 3 Gpa. It was found that the resistance changes of pyrolytic graphite are insignificant in the range of specific energy up to 6 kJ/g.

Acknowledgment

This work was made possible by financial support from the Russian Foundation for Fundamental Research, projects N 96-02-16009.

References

1. Knoepfel, H., Pulsed High Magnetic Fields. North-Holland Publishing Company, Amsterdam – London, (1979).
2. Seydel, U., Fucke, W., Sub-Microsecond Pulse Measurements of High Temperature Electrical Resistivity of the 3d-Transition Metals Fe, Co, and Ni, *Z. Naturforsch.Teil A* **32** (1977) pp. 994-1002.
3. Pottlacher, G., Jager, H., Neger, T., Thermophysical Measurements on Liquid Iron and Nickel. High Temperatures – High Pressures, (1987) **19** pp. 19-27.
4. Fridman, B. E., Kustov, N. N., Lex, A. G., Rutberg, Ph.G., Experimental installation for electrodynamic compression. These proceedings.
5. Burtsev, V. A., Kalinin, N. V., Luchinsky, A. V., Electrical Explosion of Conductors and Its Application in Electrophysical Installations. (in Russian) Moskow, Energoatomizdat, (1990) p. 23.

A HIGH-VOLTAGE PULSE TRANSFORMER FOR EXPLOSIVE PULSED-POWER DEVICES

C. FORTGANG, A. ERICKSON, J. GOETTEE
Los Alamos National Laboratory, New Mexico, USA

It is often necessary to use a high-voltage pulse transformer for impedance matching an explosive generator to a higher impedance load. Also, a particular application may require high voltage rather than the high current which flux compressor generators (FCGs) normally deliver when driving suitable low impedance loads. We have designed and built air-core transformers with measured coupling coefficients in the range of 0.88 to 0.94, for use with FCGs. The turns ratio for these transformers vary from 10 to 40. We have used these transformers in FCG shots and have measured 250 kV and 250 kA on the secondary, simultaneously and without breakdown. So far, the FCG and not the transformer have limited the voltage. Experiments to determine a voltage limit are ongoing. Our design and results are presented.

1 Introduction

Because explosively driven flux compressors work best into low-impedance loads, a step-up transformer is necessary to drive high-impedance loads such as an electron-beam diode. Transformers designed and tested for such an application have been previously reported [1-4]. These transformers have all been of the tape-wound type. They are cylindrical in shape, where primary and secondary are wound azimuthally around the cylinder axis, creating mostly a B_z field. A sketch of such a transformer is shown in Figure 1.

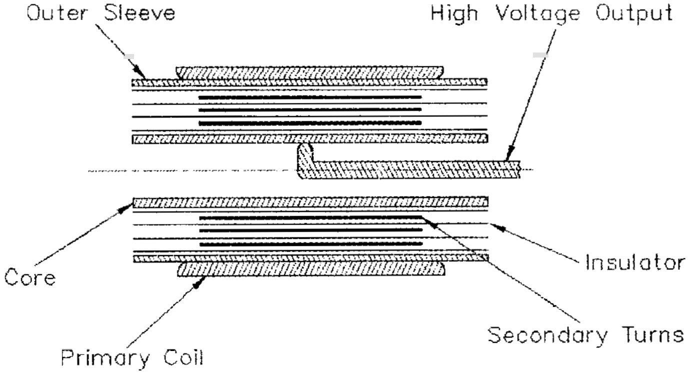

Figure 1. A tape-wound transformer with a solenoid geometry, from Ref. [1].

We report on another type of transformer that is also cylindrical in shape but where the primary and secondary windings are coaxial. That is, the currents are primarily in the z-direction, creating mostly a B_ϕ field. A simplified sketch is shown in Figure 2.

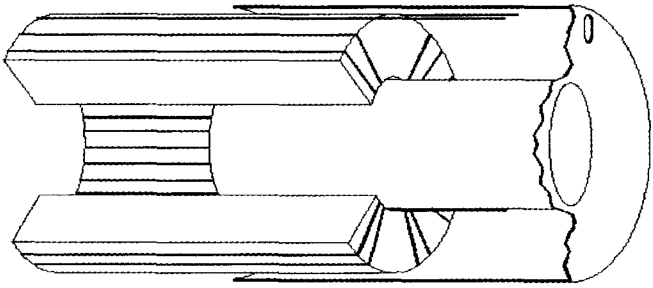

Figure 2. A cut-away view of a coaxial transformer with a single turn primary. Primary and secondary are offset for clarity.

The primary is a single turn coax made of aluminum. The multi-turn secondary is wound on a polyethylene core, which slips inside the primary. The secondary is comprised of 2 parallel windings, each wound 180^0 around the transformer circumference. Therefore, the high-voltage secondary output-terminals are separated by about 80% of the transformer outer diameter. In practice, each of the secondary windings is comprised of several individual insulated wires and is brought out through insulated holes in the primary. We use the maximum number of parallel wires that will fit around the ID of the secondary, without overlapping the wires.

We believe the coaxial design has some important advantages over the tape-wound design. First, it has an inherently higher coupling constant. The spacing between primary and secondary is the same for every secondary turn and does not progressively increase with the number of secondary turns, as in the tape-wound design. Second, the windings do not have edges that enhance the electric field and increase the possibility of breakdown. Therefore, voltage-grading techniques [1,5] are unnecessary. Third, we found that the wire-wound coaxial transformer is easier to fabricate and is more robust than the tape-wound transformer [6]

2 Calculation of Inductance and Coupling

The calculation of primary and secondary inductance is approximate but very simple. End effects are not accounted for. The primary and secondary are treated as ideal coaxes. This is not an approximation for the primary because it is constructed with metal pipe, but the secondary consists of many parallel wires. By using the maximum number of wires possible, the coax assumption is better justified. Given these assumptions the primary, secondary, mutual inductance, and coupling coefficient are:

$$L_p = \frac{\mu_0}{2\pi}\left(\ln\frac{c}{a} + \mu_r \ln\frac{d}{c} + \ln\frac{b}{d}\right)\Delta z \qquad L_s = \frac{\mu_0}{2\pi} N^2 \left(\mu_r \ln\frac{d}{c}\right)\Delta z$$

$$M = \frac{\mu_0}{2\pi} N \left(\mu_r \ln\frac{d}{c}\right)\Delta z \qquad k = \frac{M}{\sqrt{L_p L_s}} \tag{1}$$

where a, b, c, d, and Δz are the primary inner and outer radii, the secondary inner and outer radii, and the transformer length, respectively. In these equations we allow for a secondary magnetic core with relative permeability μ_r, but for our air core transformers $\mu_r = 1$. Note that in the limit $\mu_r >> 1$, these equations yield $L_s/L_p = N^2$, the usual result.

3 Design and Test of a Transformer

The insulation thickness is given by (c-a) and (b-d) on the inner and outer radii, respectively. A minimal amount of insulation is used to maximize coupling. To wind the secondary, we use the inner conductor of Reynolds type-C coax cable, which has an insulation thickness of 0.03". In addition, we add 20 layers of 0.002" thick kapton sheet around the OD and ID of the secondary.

When designing any transformer it is important to have the secondary impedance much greater than the load impedance. If ω is a characteristic frequency for the pulse, then we require

$$L_s >> L_{load} \quad \textit{and} \quad \omega L_s >> R_{load} \tag{2}$$

When transformed to the primary, this condition is equivalent to

$$\omega L_p >> X(Z_{load}) \approx \frac{Z_{load}}{N^2} \tag{3}$$

Another design consideration arises if there is a closing switch in the secondary circuit. Under that condition, for the generator to run efficiently (i.e. drive a low-impedance when the switch is open) we require that:

$$L_p << L_{generator} \tag{4}$$

It is often the case that Equations (3) and (4) cannot be simultaneously satisfied. Under these less than ideal conditions, the designer should use a FCG code that includes a transformer model [7] to optimize performance.

We have designed 2 types of coaxial transformers as described above. We have built and tested 3 transformers of the first type. We have finished design of the second type and will assemble and test it in the near future. For the first type, with which we have more experience, the secondary has 11 turns and an inductance of 5.4 μH. It is desirable to have a larger secondary inductance but physical constraints on the size of the transformer limit this. We measured the coupling coefficient to be 0.94. The coupling coefficient is measured by discharging a HV, 55 μF capacitor bank into the transformer primary with the secondary shorted. Under these conditions, we measure both the primary and secondary currents and calculate the coupling coefficient.

The primary inductance for this transformer is about 52 nH, and leakage inductance is given by:

$$L_{leakage}=(1-k^2)Lp=6nH \tag{5}$$

To maximize transformer performance, it is important to keep stray inductance between the FCG and the transformer primary to a value much smaller than the transformer leakage inductance. We do this by keeping connections to a minimum length and using the usual low-inductance design principles.

4 Experimental Results

The first test used an explosive plate-generator to drive the transformer with a secondary load of a few microhenries. Data from this shot is shown in Figures 3 and 4. Note that there is an offset in the time scales for the two figures. The plate generator was driven with a capacitor bank.

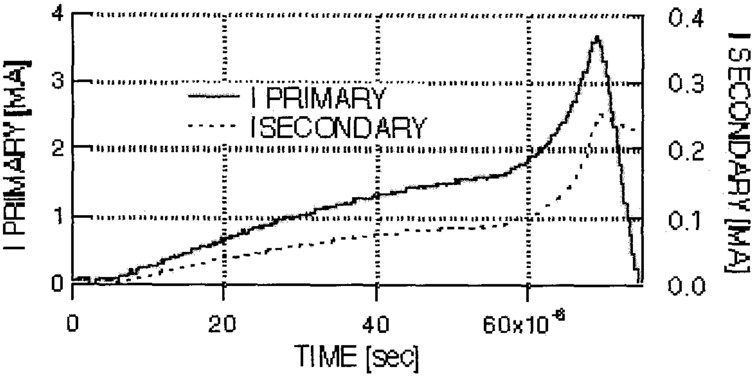

Figure 3. Primary and secondary current. Peak primary current is 3.7 MA.

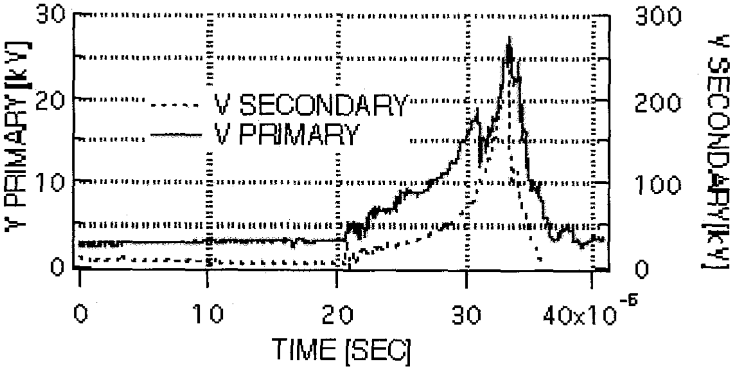

Figure 4. Primary and secondary voltage. Peak secondary voltage is 263 kV.

In this test, the transformer delivered about 100 kJ to the load. Similar data has been obtained on 3 other transformers. We are presently building a new transformer that will be driven with up to 8 MA of primary current and will be tested up to 500 kV on the secondary. This transformer will be tested using a large capacitor bank and is designed for multiple-pulse operation.

5 Summary

We have successfully tested air-core pulse transformers for use with FCGs. These transformers are coaxial, have a high coupling coefficient and have delivered about 100 kJ to a load. We are continuing to test these transformers to explore their voltage and energy limits.

References

1. Erickson, D., Caird, R., Fowler, C., Freeman, B., Garn, W., Goforth, J., Proceedings of the Third International Conference on Megagauss Magnetic Field Generation and Related Topics, Ed. by V. Titov and G. Shvetsov, Novosibirsk, Russia (1983) p. 333.
2. Fowler, C., Caird, R., Erickson, D., Freeman, B., Garn, W., Proceedings of the Second International Conference on Megagauss Magnetic Field Generation and Related Topics, Ed. by P. Turchi, Washington DC (1979) p. 275.
3. Sarjeant, W., Rohwein, G., Proceedings of the Fourth IEEE Pulsed Power Conference, Ed. by M. Rose and T. Martin, Albuquerque, NM, (1983) p. 631.
4. Freeman, B., Bostick, W., Proceedings of the Fourth International Conference on Megagauss Magnetic Field Generation and Related Topics, Ed. by C. Fowler, R. Caird, and D. Erickson, Santa Fe, NM (1986) p. 583.
5. Rohwein, G., Sandia Nat. Lab. Report SAND-80-0451C (1980).
6. Erickson, A., Los Alamos Nat. Lab., private communication.
7. Fortgang, C., A Field Theory Approach to Modeling Helical FCGs, in these proceedings.

1 MV, 20 NS PULSE GENERATOR FOR HIGH-CURRENT MAGNETRON

V. I. KARGIN, A. S. PIKAR, N. F. POPKOV, E. A. RYASLOV
All-Russian Scientific Research Institute of Experimental Physics (VNIIEF), Sarov, Russia

E. B. ABUBAKIROV, N. F. KOVALEV, M. I. FUCHS
IPF RAN (IAP RAS), Nizhny Novgorod, Russia

This paper gives the results of investigations aimed at developing small, high-current generators for relativistic magnetrons. A generator, having 120 kJ of stored energy and two sharpening cascades, forms a megavolt 100 kA current pulse with 10-20 ns duration. To decrease the generator's size, magnetic insulation is applied in a high-voltage section of the facility and load. The generation of megavolt pulses is highly promising for physics research because of their high specific characteristics.

1 Introduction

Nowadays, the relativistic magnetron is one of the most powerful and effective generators of radio frequency radiation in the centimeter range among relativistic high frequency electronics devices. Experiments with relativistic magnetrons, which were performed in Russia and the USA, demonstrated their usefulness at megawatt power levels in pulses of the order of tens of nanoseconds. 10 GW of radiation power at a frequency of 2.9 GHz has been obtained [1]. The energy flux density at such power levels achieves 10^{10}-10^{11} W/m^2. Further increase of radio frequency radiation power is limited by the electric strength at the irradiator surface. These limitations can be reduced through the increase of electrical strength for pulse durations in the sub-nanosecond range. If a small, 10^{11} W radio frequency radiation generator is required the use of a magnetocumulative generator (MCG) as both a primary energy source and a current pulse shaper is most expedient. A magnetocumulative generator possesses higher energy density than a capacitor storage system. The pulse power supply system of a magnetron should meet the following requirements: load voltage 1-1.5 MV, load current 100 kA, current pulse front duration 20 ns. When using MCG, it is necessary to reduce the current pulse duration of the inductive storage from 100 μs to 20 ns. To reduce the current pulse front to 1 μs, it is appropriate to take advantage of explosive switches [2] and, for its further reduction, plasma opening switches (POS) [3]. POS operation is based on the property of a high-current discharge in a plasma to increase its resistance sharply when the current reaches the critical value [4]. Because of the fact that the increase in power is followed by significant voltage increase, the generators based on POS are used in accelerator engineering aimed at generating electron beams and X-ray bremsstrahlung pulses [5,6]. This work presents the results of a two-stage breakage of an inductive storage circuit with the aid of plasma switches. This method allows shaping a 1 ns pulse of an inductive storage system to a 100 kA amplitude current pulse with a 20 ns front duration.

2 Facility Design

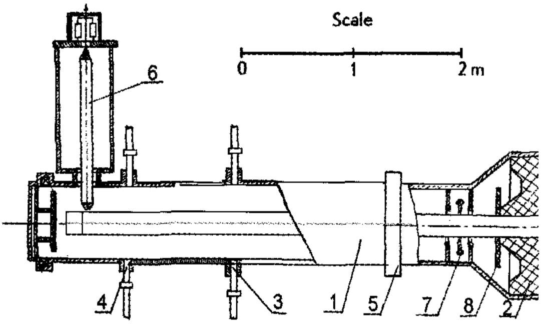

Figure 1. Structural scheme of the facility. See text for details.

The structural design of the device to investigate the shaping of a short current pulse is given in Fig. 1. The Marx generator (VG) was used as primary energy storage. The generator inductance is 0.7 μH, the stored energy is 40 kJ at 100 kV charging voltage. The Marx generator output was connected to the coaxial vacuum inductive storage 1. The vacuum portion of the storage device is separated from the oil collector by polyethylene insulator 2, with a diameter of 450 mm. The amplitude of the discharge current in the line is 160 kA, while the discharge current period is 4 μs. The system of injectors consisting of six plasma guns (3,4) is located at a distance of 1200 mm and 2150 mm, respectively, from the insulator. The vacuum line is coaxial. It consists of a number of sections, connected by adapting rings, where the inductive current probes (5) are located. The external coaxial diameter is 214 mm, the internal diameter is 40 mm. At the end of the line a high-voltage divider (6) is located. To prevent the insulator from being illuminated by plasma POS and to protect it against evaporation products, it is shielded by a set of metal washers (7) and a dielectric disk (8).

After the Marx generator and current generators (CG1 and CG2), which power the plasma guns, have been charged, generator CG1 is triggered. After a delay time t_1, the CG2 generator is triggered and plasma is injected into the inductive storage gaps (d_1 and d_2). After a delay time t_2, which is necessary to fill gap d_1 with plasma and create the necessary density, the Marx generator fires and the inductive storage contour is closed via POS1. When a critical current is reached, a sharp increase of plasma resistance takes place and energy is transferred into the next contour, which is closed via POS2. After POS2 operation the energy is transferred into the load.

3 Experimental Results

The experiments on current pulse shaping, performed by the authors with the aid of POS, allowed them to sharpen the generator current pulse from 1 μs to 50 ns [7]. Based on the plasma trace left on the cathode, they concluded that when the magnetic field strength was 10 kA/cm and powering time was 1 μs, the POS1 plasma was shifted towards the load by 40-50 cm. The POS plasma shift under the 1/c [JB] force at 1 kA/cm^2 current density in the opening switch and 100 kA current becomes considerable if the duration of the inductive storage pulses is on the order of microseconds. The acceleration obtains the value of 10^{13} cm/s^2 and the plasma removal covers tens of centimeters, while the velocity is as high as (5-7)$\cdot 10^7$ cm/s. As this factor is undesirable when working with the magnetron, additional research was done.

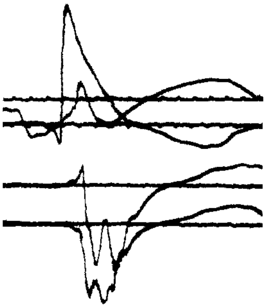

Figure 2. Signals from the first and second and from the second and third magnetic probe. The time marks are 100 ns.

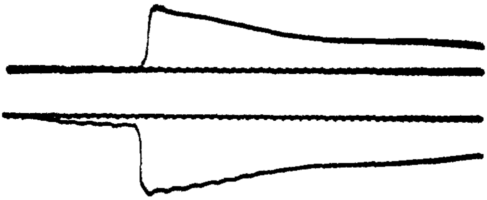

Figure 3. Current signals in two load points, 100 ns marks.

Magnetic probes installed on the cathode were used to define the POS current layer plasma drift. The first was installed under the injectors, the other two at 10 and 20 cm distances towards the load. The signals, obtained with the aid of magnetic probes, are presented in Fig. 2. The breakage occurs when the current sheath (and the plasma) is shifted 20 cm towards the load. In further experiments with the inductive load two sections long, it was noted that the signal of the first current detector and the load current differs in the form of a pedestal of 10% from the total amplitude, which started 200-300 ns before the main pulse (Fig. 3). It supports the fact that the POS current layer has a precursor carrying 10% of the POS current and is shifted by more than 1.5 m. Moreover, the pedestal amplitude grows as the VG operation delay increases. Thus, in further experiments, the load was installed 93 cm from the block of injectors to fully exclude the appearance of the prolonged pre-pulse in the load. The scheme of pulse shaping with the aid of a one-stage POS made it possible to reduce the current rise time in the load to 50 ns and to obtain 1.3 MV. Compared to the initial pulse, the reduction of the front was significant. One additional POS stage was applied two sections after the first POS to further sharpen the current pulse. The storage current, POS1 current, load current and difference current IPOS - IL were recorded for the experiments.

The following parameters were varied: delay parameter t_2 of switching on VG as related to CG1, delay of CG2 switching on t_2, and charging voltage of CG2 at the fixed switching-off voltages of VG (75 kV) and CG1 (50 kV). The oscillograms obtained are shown in Fig.4. Each POS was tested for values similar to those from the two-stage version, i.e. t_1=2.2 μs, t_2=1.5 μs. A current rise time in the load of 20 ns was obtained for the following parameters of the facility: U_{VG}=75 kV, U_{CG1}=50 kV, U_{CG2}=40 kV, t_1=2.2 μs, t_2=1.5 μs; in this case the voltage on the load was as high as 1.5 MV. The current derivative increased two times as compared to the one-stage version and achieved the value of $7.5 \cdot 10^{12}$ A/s. The second stage powering time was 100 ns. Within this time period the plasma precursor does not reach the load at 465 mm distance. Thus, the current pulse in the load does not possess a prepulse.

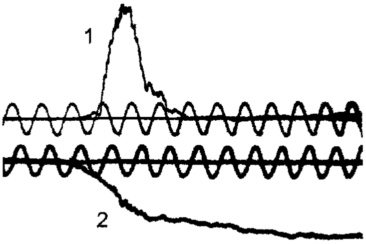

Figure 4. 1-voltage, 2-current in the load of a two-stage scheme of current pulse sharpening, 100 MHz marks.

4 Conclusion

The investigations demonstrated that the current pulse front of an inductive storage system could be reduced from 1 μs to 20 ns. The voltage is increased up to 1.5 MV and the prepulse is eliminated. As a result of this progress, a relativistic magnetron can now be used as a load.

References

1. Didenko, A. N., et al., Proceedings of the Third International Topical Conference of High Power Electron and Ion Beams. Novosibirsk, July 3-6,1979, p. 683.
2. Pavlovskii, A. I., et al., 5-th International Conference on Megagauss Magnetic Field Generation and Related Topics, July 3-7, 1988, Novosibirsk, USSR. p. 503.
3. Meger, R. A. et al., *Appl. Phys. Lett.*, **42**, (1983) p. 943.
4. Ottinger, P. F., et al., *J. Appl. Phys.*, **56** (3), (1984) p. 774.
5. Sincerny, P., Ashby, S., Childers, K., et al., "The DECADE high power generator." Proceedings of the Ninth IEEE Pulsed Power Conference, (1994) pp. 880-883.
6. Popkov, N. F., Ryaslov, E. A., Kargin, V. I., Pikar', A. S., et al. "A 10 TW pulsed facility 'PIRIT' for investigation of short-wave radiation generation." Journal of X-ray science and technology, 5, May 1995, pp. 284-288.
7. Popkov, N. F., et al., 11-th International Conference on High Power Particle Beams, Prague, Czech Republic, June 10-14, 1996.

Z: A FAST PULSED POWER GENERATOR FOR ULTRA-HIGH MAGNETIC FIELD GENERATION

R. B. SPIELMAN, W. A. STYGAR, K. W. STRUVE, J. R. ASAY, C. A. HALL, M. A. BERNARD, J. E. BAILEY, D. H. MCDANIEL
Sandia National Laboratories, Albuquerque, NM, USA

Advances in fast, pulsed-power technologies have resulted in the development of very high current drivers that have current rise times ~100 ns. The largest such pulsed power driver today is the new *Z* accelerator located at Sandia National Laboratories in Albuquerque, New Mexico. *Z* can deliver more than 20 MA with a time-to-peak of 105 ns to low inductance (~1 nH) loads. Such large drivers are capable of directly generating magnetic fields approaching 3 kT in small, 1 cm^3 volumes. In addition to direct field generation, *Z* can be used to compress an applied, axial seed field with a plasma. Flux compression schemes are not new and are, in fact, the basis of all explosive flux-compression generators, but we propose the use of plasma armatures rather than solid, conducting armatures. We present experimental results from the *Z* accelerator in which magnetic fields of ~2 kT are generated and measured with several diagnostics. Issues such as energy loss in solid conductors and dynamic response of current-carrying conductors to very large magnetic fields are reviewed in context with *Z* experiments. We describe planned flux-compression experiments that are expected to create the highest-magnitude uniform-field volumes yet attained in the laboratory.

1 Introduction

The generation of ultra-high magnetic fields necessarily leads to low impedance, pulsed current drivers [1,2]. Current densities above ~10 MA/cm (magnetic fields > 1 kT) have dynamical time constants < 100 ns. The rapid development of pulsed power technologies [3,4] has enabled the routine generation of magnetic fields above 1 kT. We describe the pulsed power design and performance of Sandia's *Z* accelerator as well as results from experiments in which peak currents of 15-20 MA are delivered to various low inductance loads generating magnetic fields of order 1 kT.

2 Accelerator Description

Z's pulsed power design [4] is based on Sandia National Laboratories Marx-generator and water-pulse-forming technology developed over the last 30 years (see Figure 1). *Z* contains 36 nearly identical modules. Each module contains a Marx generator with sixty 1.3 μF capacitors charged to a voltage of 90 kV. The Marx generators store a total of 11.4 MJ and each delivers its energy to a water-dielectric coaxial capacitor in 1 μs. The coaxial capacitor reaches a peak voltage of 5 MV. A low-jitter, laser-triggered gas switch is used to couple the energy into a second, lower-inductance coaxial water capacitor in 200 ns. Self-breaking water switches are used to transfer the energy into a 4.32 Ω constant-impedance water transmission line. The electrical pulse at this point has a voltage of 2.5 MV and a pulse width of 105 ns FWHM. The total power generated in the accelerator is 60 TW.

The water transmission lines are a bi-plate, constant-impedance, constant anode/cathode gap designed to optimize the energy efficiency of the transmission lines and to maximize the coupling of the energy in the water transmission lines to an inductive load. The impedance of each of the 36 bi-plate lines is 4.32 Ω. The transmission line gap is fixed at 14 cm. We accurately measure the voltage and current, hence the power and energy, in each water transmission line.

The insulator stack is the boundary between the water dielectric and the vacuum that is necessary to drive the z-pinch load. The insulators, nearly 4 m in diameter, are made from Rexolite™ (high-density cross-linked polystyrene). The voltages and currents were measured at each of the insulator stacks, giving a very accurate measure of the power and energy through the insulator stack.

The MITLs consist of four separate, conical-disk feeds coupled together at the vacuum convolute. The upper two MITLs are 2 Ω impedance and the lower two MITLs are 2.75 Ω impedance. The MITLs operate successfully at a peak electric field of 2 MV/cm with vacuum gaps as small as 1 cm. We placed current monitors at two radial locations and 3-6 azimuthal positions in each of the four MITL anodes to better study vacuum power flow.

A critical point in the vacuum power flow is the double posthole convolute that couples the four, conical-disk MITLs. This is done in order to combine the current from each level and deliver the summed currents to a single z-pinch load. The baseline convolute on *Z* is a 12-posthole design with 1.0-1.5 cm diameter posts and post-to-cathode gaps of 1-2 cm. A drawing of the convolute is given in Fig. 3.

3 Load Design

The generation of magnetic fields with these large pulsed power drivers can be direct, in which current flows in a conductor (typically a coaxial arrangement) or indirect, in which a seed magnetic field is inserted then compressed by the main current. Each configuration has advantages and disadvantages. The primary problem with directly driven systems is the non-uniformity of the magnetic field. In a coaxial geometry, the azimuthal magnetic field falls off as 1/r. The peak field is on the inner conductor and may be unusable for most experiments. In flux compression schemes, the B_z magnetic field is uniform over the volume being compressed but the fact that the conducting plasma shell is moving and radiating strongly can compromise many potential experiments. We describe two such load designs for the *Z* accelerator.

The actual load to which current is delivered is relatively small. The driver energy or, equivalently, the load inductance limits the load dimensions. Our directly driven load is coaxial with a 6 mm diameter inner conductor and a 12 mm inner diameter for the outer conductor. The length is 1 cm (see Fig. 2). The inductance of this load is 1.38 nH. All materials for this experiment were 304L stainless steel. We examined the hydrodynamic motion of the inner conductor due to the magnetic forces. With a peak current of ~ 20 MA and a diameter of 6 mm the motion of the inner conductor is small in 100 ns. Increases in magnetic field (reductions in conductor diameter) are possible if higher density materials are used for the conductors.

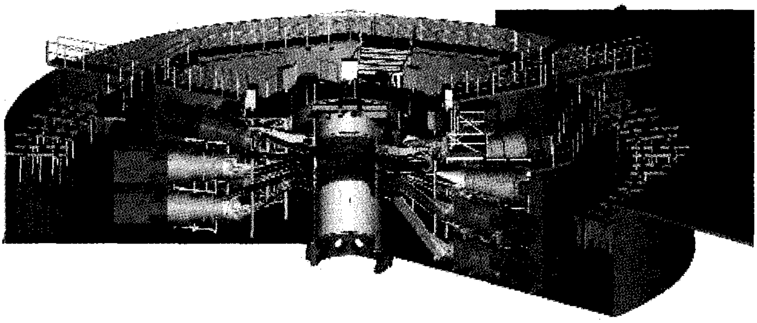

Figure 1. Schematic of the Z accelerator showing the pulsed power layout. The diameter of the outer oil tank is 33.5 m.

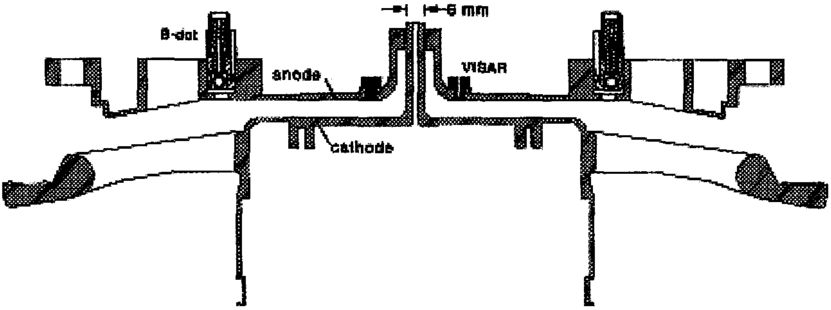

Figure 2. Drawing of a coaxial load in which azimuthal magnetic field is generated in the volume surrounding the inner conductor. The locations of the B-dot current monitors and the VISAR probes are shown.

4 Magnetic Field and Current Diagnostics

One of the greatest challenges of high magnetic field experiments is the measurement of the magnetic field itself. We describe two methods that are used to infer the magnitude of the magnetic field on Z. First, we use B-dot current probes [5]. On Z, we used four of these current monitors located 6.0 cm from the load. The current density is < 1 MA/cm at this position and the current monitors work well. Thus, we have a direct measurement of the magnetic field from which we infer the local current. Typically, we assume that this current flows through the load without losses. Second, we have used VISAR techniques [6] to measure the magnetic pressure on the conductor itself, near the load. This technique uses laser interferometry to directly measure the rear surface velocity of a small piece of the electrode. The magnitude of the driving magnetic field is then inferred from the velocity history of the electrode.

Our B-dot current monitors have 1 mm diameter loops aligned with the magnetic field. Copper sleeves surround the detector to minimize the diffusion of current in nearby conductors, thus minimizing changes in the detector sensitivity to the local fields. The B-dot current monitors are calibrated in a fixture in which a current pulser provides up to 10 kA to the load and NIST traceable resistance standards are used to compare with the measured B-dot signal. Typically, the calibration data provides a calibration accuracy of ~1%.

The VISAR pressure diagnostic uses reflected laser light from the rear surface of a well-characterized metallic sample (for example, copper or iron) located on the current path [7]. The VISAR sample is located 1.39 cm from the load axis. This radial location was chosen to keep the sample pressure below ~30 GPa and to minimize radial pressure gradients. The detector is sensitive to motion of the back surface of the sample through a Doppler shift in the reflected light. As the pressure builds up on the front of the sample, it is coupled to the back surface of the sample, causing rear surface motion. This motion is then measured. The particle velocity of the sample can be correlated to the applied pressure through well-characterized material properties. The measurement error of the pressure is now 5% but may be reduced to 1-2% in the near future.

We believe that spectroscopy may be used in the future to directly measure the time- and space-resolved magnetic field in the load. There are a number of issues involving plasma opacity and plasma motion that remain unresolved.

5 Data

We describe data from Z shot 315. This shot used the direct-drive load design described above. *Z* delivered a peak current of 19.3 MA, a peak average voltage of 3.5 MV, a peak power of 48.5 TW, and total energy of 2.92 MJ at the main insulator stack (measured with carefully calibrated B-dot and V-dot electrical monitors). This current flowed to the inner load region where it was measured by the local current diagnostics (see Figure 3). A small current loss caused the current measured at the insulator stack to be slightly higher than the actual load current. The B-dot data show that the current reaches a peak value of 16.7 ± 0.85 MA in 105 ns. At this current level, the peak magnetic field in the 6 mm diameter coaxial load was 1.1 ± 0.05 kT. With a load inductance of 1.38 nH, we find that the energy stored in the load is 192 kJ. These data are consistent with the overall energy balance in the vacuum section of *Z*.

On the same shot, the VISAR data show that a peak pressure of 31.4 ±1.5 GPa was developed at the surface of an iron sample (see Figure 4). At this pressure, the surface magnetic field acting on the VISAR sample was 280.9 ± 7 T. The current at a radius of 1.39 cm, consistent with this pressure and magnetic field, was 19.45 ± 0.5 MA. The VISAR data was of sufficiently high quality that detailed iron material properties were obtained. The time units in Figure 4 are relative.

We found that the current measured by the VISAR sample was slightly higher than that measured by the current monitors. We do not yet fully understand the discrepancy, but possibilities include the conductor skin depth at these higher current densities, or plasma shielding of the B-dot probes. Refinements in MHD calculations using the best equations of state and material resistivities may reduce this apparent difference.

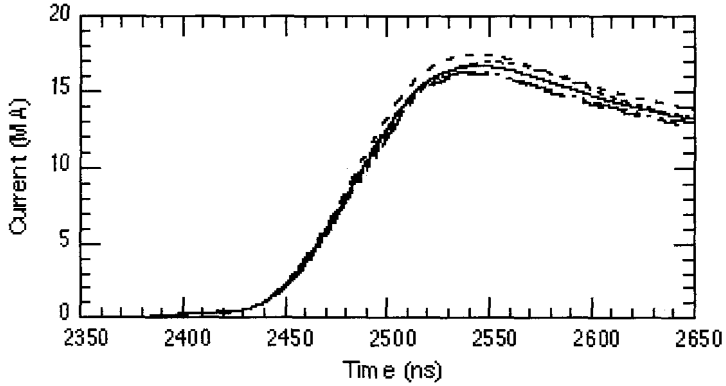

Figure 3. Current wave forms measured with four B-dot current monitors located 4.3 cm from the load. The heavy solid line is the average of the four data waveforms.

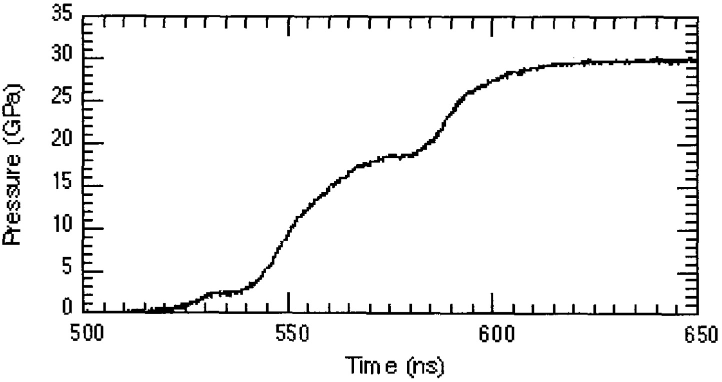

Figure 4. The pressure waveform measured with the VISAR diagnostic. The peak pressure measured by is 31.4 GPa. The structure in the data is due to the material properties of iron.

6 Conclusions

The development of 100 ns, 20 MA pulsed power drivers enables a large class of high magnetic field experiments. These experiments, at fields greater than 1 kT, permit the study of basic material properties at pressures and densities heretofore unavailable. The capabilities of this new class of pulsed power driver have not been explored in any level of detail. We expect that new experiments using Z and future drivers at higher magnetic fields will yield a wealth of new data and will result in changes in our fundamental understanding of materials at high pressure and density.

Acknowledgment

The United States Department of Energy under Contract DE-AC04-94AL85000 supported this work.

References

1. Spielman, R. B., Hussey, T. W., Hanson, D. L., Lopez, S. F., *Megagauss Fields and Pulsed Power Systems*, Edited by V. M. Titov and G. A. Shvetsov (NOVA Science Publishers, NY 1990) p. 43.
2. Spielman, R. B., Martin, T. H., McDaniel, D. H., Savage, M., Woodall, H., *Megagauss Magnetic Fields and Applications,* Edited by M. Cowan and R. B. Spielman (NOVA Science Publishers, NY 1995) pp. 437-444.
3. Bloomquist, D. D., Stinnett, R. W., McDaniel, D. H., Lee, J. R., Sharpe, A. W., Halbleib, J. A., Schlitt. L. G., Spence, P. W., Corcoran, P., *Proc. of the Sixth IEEE Pulsed Power Conf.*, Arlington, VA, Edited by P. J. Turchi and B. H. Bernstein (IEEE, New York, 1987) p. 310.
4. Spielman, R. B., Stygar, W. A., Seamen, J. F., Long, F., Ives, H., Garcia, R., Wagoner, T., Struve, K. W., Mostrom, M., Smith, I., Spence, P., Corcoran, P., *Proc. of the Eleventh IEEE Pulsed Power Conf.*, Baltimore, MD (1997) p. 709.
5. Stygar, W. A., Spielman, R. B., Ives, H., Moore, W. B. S., Seamen, J. F., Sharpe, A. W., Wagoner, T. C., Gilliland, T. L., Broyles, R. S., Mills, J. A., Dinwoodie, T. A., Slopek, J. S., Struve, K. W., Reynolds, P. G., *Proc. of the Eleventh IEEE Pulsed Power Conf.*, Baltimore, MD (1997) p. 1258.
6. Barker, L. M., Hollenbach, R. E., *J. Appl. Phys.* **45**, (1974) p. 4872.
7. Asay, J. R., Hall, C. A., Fleming, K. J., Trott, W. A., Holland, K. G., Bernard, M. A., Clark, B., Spielman, R. B., Stygar, W. A., "Z-Pinch Drivers for Shock Physics Research", these proceedings.

GENERATION OF MEGAGAUSS FIELDS BY ELCTROMAGNETIC FLUX COMPRESSION AND THE SINGLE-TURN COIL TECHNIQUE AT ISSP

N. MIURA, Y. H. MATSUDA, K. UCHIDA, S. TODO
Institute for Solid State Physics, University of Tokyo,
Roppongi, Minato-ku, Tokyo, Japan

We present the present state of the art of the generation of very high magnetic fields in the megagauss range at the Megagauss Laboratory (MGL) of the ISSP, and of the application of megagauss fields to solid-state experiments. Pulsed high magnetic fields up to several megagauss are produced either by electromagnetic flux compression or the single-turn coil technique. For the former technique, efforts have been devoted to increase the peak field by increasing the liner velocity and improving the symmetry of the liner deformation. So far, we have obtained a maximum field of 606 T. As regards the latter technique, we built a new system of vertical axis coils for inserting a liquid He cryostat from the top. The vertical system is convenient for transport and magnetization experiments at low temperatures, while a horizontal axis coil system is more suitable for optical experiments. An introduction is also given to the new facilities that we are constructing in the new campus at Kashiwa where the ISSP will be moving shortly.

1 Introduction

Generation of very high magnetic fields can be achieved only by destructive methods in the range above a certain threshold. Many attempts have been made to produce very high pulsed fields without destroying magnets. Up to now, however, the maximum field that can be produced non-destructively is limited to about 80 T. A megagauss field, a field higher than 100 T, is produced by several different destructive techniques such as explosive flux compression, electromagnetic flux compression, single turn coil technique, plasma focus or plasma pinch technique, laser technique, and others [1]. At the Megagauss Field Laboratory (MGL) of the ISSP (Institute for Solid State Physics), University of Tokyo, we have developed techniques for the electromagnetic flux compression and the single turn coil technique. These two are very convenient methods for application to solid-state physics. We have actually conducted a variety of experimental studies under megagauss fields generated by these two techniques.

In parallel with the study of solid-state physics in megagauss fields, we have recently achieved considerable advances in the techniques for generating higher fields. As regards the flux compression, we have obtained the highest record of 606 T by increasing the energy density using a smaller liner and by improving the symmetry of the liner implosion. For the single turn coil technique, we have newly constructed a coil system with a vertical axis in order to obtain very low temperatures by inserting a plastic cryostat for transport or magnetization experiments at low temperatures.

In this paper, we discuss the technical developments mentioned above. In addition, we present the outline of the new facilities that we are constructing at the Kashiwa new campus.

2 Electromagnetic Flux Compression

Figure 1 shows the primary coil design for electromagnetic flux compression employed at ISSP. It is made from steel and composed of two sections, the round coil and the flat electrode, which are bolted together. The coil is clamped by a press and firmly connected to collector plates to which 240 coaxial cables carry current from the capacitor bank. Inside we place a copper liner. Between the primary coil and the liner, we insert a phenolic pipe as insulation. The inside of the pipe is pumped to vacuum for the liner to be imploded. The main capacitor bank at the ISSP has a total energy of 5 MJ when we charge it to 40 kV. We normally use 4/5 of the whole capacitors, using just 4 MJ. A primary current of about 4 MA is supplied from the capacitor bank to the primary coil. This current provides an enormous magnetic pressure to rapidly squeeze the liner inward. To inject the seed field to be compressed, a sub-capacitor bank of 1.5 MJ (10 kV) is employed. The seed field is produced by a pair of Helmholtz type solenoids placed at both sides of the liner. Seed fields (long pulse fields) of 2-3 T are generated. Details of the technique are described in previous papers [2-4].

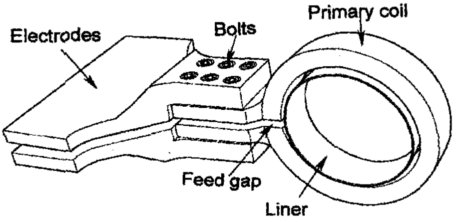

Figure 1. Coil system for electromagnetic flux compression.

By using a primary coil with an inner diameter of 160 mm, a wall thickness of 25 mm, and a length of 50 mm, and a liner with an outer diameter of 150 mm, a wall thickness of 1.5 mm and a length of 55 mm, and injecting a seed field of 2.3 T, we produced a maximum field of 550 T in 1992 [2-4].

It is well known that there is a limitation in the maximum field determined by the velocity of the liner. If the liner velocity is insufficient, the magnetic flux diffuses out during the compression process. There are two mechanisms in the diffusion. One is the electromagnetic diffusion determined by the finite conductivity of the liner. The other one is the diffusion with the particle speed of the shock wave generated by an enormous magnetic pressure [1]. Usually, the latter speed is much faster than the former, so that we need to compress the flux with a liner speed higher than the particle speed that depends on the generated field. When the field reaches the value at which the particle speed is nearly equal to the liner velocity, the flux starts diffusing out, and we observe the 'turn-around effect' [5]. Actually, if we plot the peak field produced by the flux compression as a function of the liner velocity, we find that the peak is larger as the velocity increases. Figure 2 shows such a plot for our series of previous experiments, together with the more recent ones. We can see that the data points fall near the line of the particle speed for copper. The experimental points should be always below the particle speed line. However, it is found that some points are above this line. The reason can be explained by the fact that the liner velocity cannot be measured accurately near the final stage of the compression. We measured the liner velocity by high speed framing photographs taken by an image converter camera. The motion of the inner wall of the liner is greatly enhanced as the inner diameter becomes small due to the effect of thickening of the liner wall. The framing pictures cannot monitor such a thickening effect accurately at the final stage, and underestimate the velocity, although the field diffusion is determined by the velocity at the final stage.

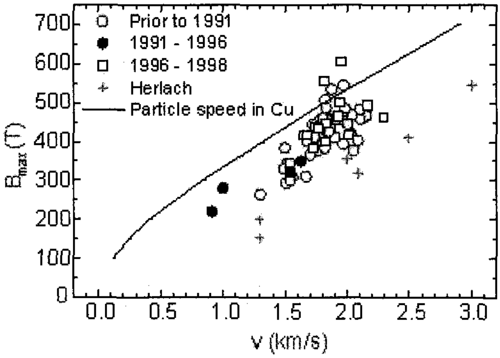

Figure 2. Peak field as a function of liner velocity. The velocity was estimated from framing pictures taken by an image converter camera (as shown in Fig. 3). The solid line denotes the particle speed of the shock wave in copper. The data denoted Herlach were taken from [5].

To generate higher fields, therefore, it is important to increase the liner velocity. For this purpose, it is preferable to input as much energy as possible and to reduce the size of the primary coil and the liner for the given amount of energy.

However, one serious problem in the electromagnetic flux compression is the existence of the feed gap in the primary coil. The magnetic field near the feed gap is weaker than the other part. As a result, the squeezing of the liner takes place in such a way that a protruded part is left behind from the circular cylinder on the side of the feed gap. An example of high-speed photographs of the liner is shown in Fig. 3. We can see the protruded part on the left side. This effect deteriorates the cylindrical symmetry of the liner causing fast destruction of the probe or the sample set at the center of the liner before the peak field due to the attack of the liner. Furthermore, a plasma jet is spouted out from the protruded part, and the jet also destroys the probe or sample. The asymmetry of the liner deformation is enhanced as the liner velocity is increased [4]. Therefore, it is important to reduce the feed gap effect as much as possible when we increase the input energy.

To solve this problem, we decreased the feed gap distance from the previous value of 4 mm to 2 mm, taking care of the insulation between the gap. Simultaneously, we decreased the length of the primary coil to 45 mm and that of the liner to 50 mm in order to increase the liner velocity. With such a change of the parameters, we obtained a maximum field of 606 T. The profiles of the magnetic field and the primary current are shown in Fig. 4. Themain condenser bank was used with energy of 4.0 MJ (5 mF, 40 kV) and the seed field was 2.3 T. The field was measured by a pick up probe placed at 2 mm off the center of the liner (to the feed gap side). The size of the pick up coil was 1.0 mm in diameter and 3 turns of thin Cu wire was wound.

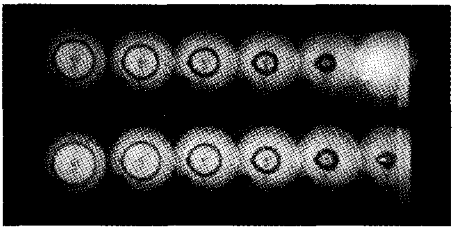

Figure 3. (left) An example of the framing photographs of the imploding liner. The photographs were taken by using an image converter camera. The time proceeds from left bottom to right top. The time interval between the frames was 2 μs. The feed gap was in the left side of the liner.

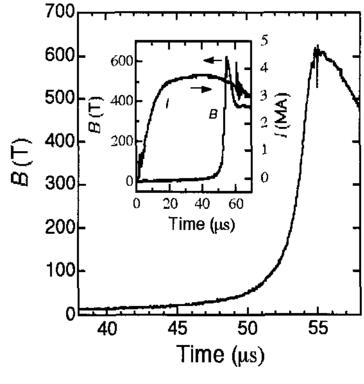

Figure 4. (right) Profiles of the magnetic field (B) produced by electromagnetic flux compression and the primary current (I). The inner diameter, the length, and the wall thickness of the primary coil were 160 mm, 45 mm, and 25 mm, and the outer diameter, the length, and the wall thickness of the liner were 150 mm, 50 mm, and 1.5 mm, respectively. The capacitance and the voltage of the capacitor bank were 5.0 mF and 40 kV, and the seed field was 2.3 T.

Attempts to increase the input energy to obtain even higher liner velocity that should lead to a higher peak field are in progress. Other than the increase of the liner velocity, another method of increasing the peak field is to use a liner made from materials that have slower particle speeds. Good candidates of the material for this purpose are platinum or tantalum. Considering the cost, we are trying to use a copper liner lined with a thin Ta sheet. The experiments are under way.

3 Single Turn Coil Technique

The single turn coil technique has a great advantage for application to solid-state experiments in a sense that the samples and cryostats are not destroyed at every shot although the coils are destroyed. We can repeat experiments on the same sample and measuring system by replacing only coils. Thus, the reliability of the measurement is very high. At MGL, we use a fast capacitor bank of 100 kJ (40 kV) to supply short pulse currents to the single turn coils. The peak field depends on the coil size. When we use a standard copper coil with an inner diameter of 10 mm, 10 mm length and of 3 mm wall thickness (10 x 10 x 3 mm), the peak field is 150 T. Using other sizes, the maximum field is 201 T with 6.0 x 7.2 x 2.8 mm, 184 T with 8.0 x 8.1 x 2.8 mm, 111 T with 14 x 14 x 3 mm, and 97 T with 16 x 16 x 3 mm. The details of the present system and its performance are described elsewhere [2,6].

In the present single turn coil system of MGL, coils are mounted with their axis oriented horizontally. With this orientation, the coil mounting is easier than the coil system with vertical axis since we can clamp the coil with a press that moves vertically. The horizontal coil arrangement is also very convenient for optical experiments because we can focus the incident light beam directly onto the sample by an optical system set beside the coil system. One disadvantage is that we must use a special cryostat to refrigerate the sample, as an ordinary cryostat cannot be inserted into the coil. Figure 5 shows the

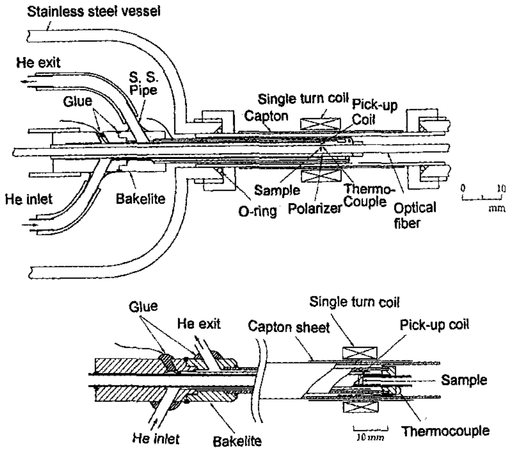

Figure 5. Cryostat and sample holder for the single turn coil system (horizontal axis).

cross-sectional view of the cryostat that we use for the single-turn coil system. The cryostat is made from phenolic tubes that are glued by stycast glue. The sample is cooled by a liquid helium flow back and forth through the gaps between the tubes. The outside of the tubes is kept in vacuum. The sample is mounted in the innermost tube. Near the sample, a thermocouple of Au·Fe-Chromel is set to measure the temperature. Changing the amount of helium flow controls the temperature. Lowest temperatures of about 7-10 K can be obtained. Essentially, a similar but slightly different system of the helium flow type cryostat is also used for the electromagnetic flux compression system.

For lowering the temperature further, we immerse samples directly in liquid helium in a cryostat. To use a liquid helium cryostat that can be inserted in the coil, we constructed a system with a vertical coil axis. The system was installed at the other side of the collector plates for the horizontal coil system and the same power supply is used for the two systems. When we use one of the systems, we shut off the other one, completely insulating the electrodes. In order to rotate the current direction, two vertical plates with a thickness of 35 mm and a height of 500 mm are firmly connected with the collector plates to which 120 coaxial cables are connected from the bottom. Because of the existence of the vertical plates, the residual inductance and the resistance of the vertical system were found to be larger than the horizontal system by 5.1 nH and 0.9 mΩ, respectively. Consequently, the peak field is a little lower than the horizontal system. Fig. 6 shows the field profiles produced by the horizontal and vertical coil systems. The peak field of 132 T was obtained with the vertical system, whilst that of the horizontal system was 150 T. The rise time to the peak was 2.8 μs as compared with 2.4 μs for the horizontal coil.

Combined with a plastic cryostat inserted in the coil, the vertical system can be conveniently used for low temperature experiments, particularly for transport and magnetization experiments. Liquid ^{3}He temperature would be also available with this system.

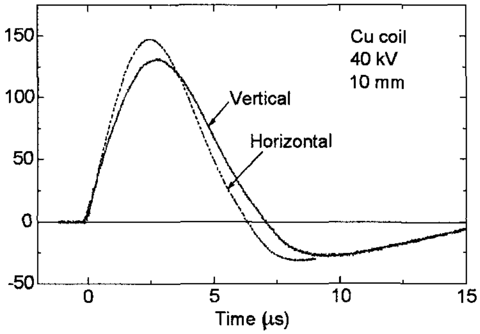

Figure 6. Waveform of the magnetic field pulses generated by the horizontal and vertical single coil systems. The coils were 10 mm in bore, 10 mm long and 3 mm in wall thickness. The 100 kJ 40 kV bank was employed.

4 New Megagauss Facilities at the Kashiwa Campus

The ISSP is planning to move to a new campus at Kashiwa in Chiba prefecture within the year 2000. Prior to this move, it has been decided that the MGL will move there in March 1999 as one of the advance groups. The new MGL building with a total area of 2,280 m^2 was completed in March 1998. The new facilities are being constructed for completion by March 1999. The new facilities consist of four capacitor banks; (1) Electromagnetic flux compression system with a 40 kV, 5 MJ bank (for implosion) and a 10 kV, 1.5 MJ bank (for seed fields), (2) Single turn coil system for horizontal coil axis with a 50 kV, 200 kJ bank, (3) Single turn coil system for vertical coils system with a 40 kV, 200 kJ bank, (4) Non-destructive long pulse field system with a 10 kV, 900 kJ bank. Four independent capacitor bank systems are constructed. The design of each condenser bank has taken into account the results of computer simulations and is based on the experience we have accumulated with the present system. The computer simulation of the field generation has been found to agree well with the experiment in the present system, both for electromagnetic flux compression and the single turn coil technique [7], so it should reliably predict the performance of the system.

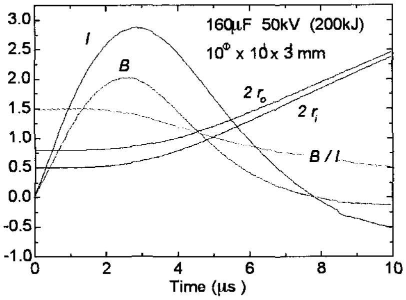

Figure 7. An example of the computer simulation for the single turn coil technique. The horizontal coils system with 200kJ (50kV) bank is used. The coils size is 10mm in bore, 10mm in length and 3mm in wall thickness. The peak field of 202T is expected.

For the electromagnetic flux compression, we decreased the residual inductance and resistivity by doubling the number of cables between the bank and the collector plates (480 cables). We can expect a significant increase of the liner velocity, and hopefully we will be able to generate a field up to 750 T. For the single turn coil systems, we increased the energy to 200 kJ as compared with 100 kJ of the present system. The vertical system consists of two 100 kJ (40 kV) banks, and they can be fired either as a single bank of 100 kJ, or simultaneously as a 200 kJ bank. This will be conveniently used for low temperature experiments. The horizontal system can be charged to 50 kV, and will be used mainly for magneto-optical experiments. These two single turn coil systems can produce a much higher field than the present system - more than 200 T in a bore of 10 mm and more than 150 T in a bore of 10 mm. An example of the results of the computer simulation is shown in Fig. 7 for the single turn coil system with a horizontal axis.

References

1. Miura, N., Herlach, F., in *Strong and Ultrastrong Magnetic Fields and Their Applications,* Ed. by F. Herlach (Springer-Verlag, 1985), Chap. 6, p. 247.
2. Miura. N., *Physica B,* **201** (1994) p. 40.
3. Miura, N., Nojiri, H., Takamasu, T., Goto, T., Uchida, K., Katori, H. A., Haruyama, T., Todo, T., in *Megagauss Magnetic Field Generation and Pulsed Power Applications (Proc. 6th Int. Conf. Megagauss Field Generation and Related Topics, Albuquerque, 1992*), Ed by M. Cowan and R. B. Spielman, (Nova Science Pub., Commack, New York, 1994) p. 125.
4. Nojiri, H., Takamasu, T., Todo, S., Uchida, K., Haruyama, T., Goto, T., Katori, H. A., Miura, N., *Physica B,* **201** (1994) p. 579.
5. Herlach, F., in *Megagauss Technology and Pulsed Power Applications*, Ed. by C. M. Fowler, R. S, Caird, D. J. Erickson, (Plenum Press, 1986) p. 39.
6. Nakao, K., Herlach, F., Goto, T., Takeyama, S., Sakakibara, T., Miura, N., *J. Phys. E, Sci. Inst.,* **18** (1985) p. 1018.
7. Miura, N., Nakao, K., *Jpn. J. Appl. Phys.*, **29** (1990) p. 1580.

THE ATLAS PULSED POWER SYSTEM; A DRIVER FOR PRODUCING MULTI-MEGAGAUSS FIELDS

J. C. COCHRANE, JR., R. R. BARTSCH, G. A. BENNETT, D. W. BOWMAN, H. A. DAVIS, C. A. EKDAHL, R. F. GRIBBLE, H. J. KIMERLY, K. E. NIELSEN, W. M. PARSONS, J. D. PAUL, D. W. SCUDDER, R. J. TRAINOR, M. C. THOMPSON, R. G. WATT

Los Alamos National Laboratory, Los Alamos, NM, USA

Atlas is a pulsed power machine designed for hydrodynamic experiments for the Los Alamos High Energy Density Physics Experimental program. It is presently under construction and should be operational in late 2000. Atlas will store 23 MJ at an erected voltage of 240 kV. This will produce a current of 30 MA into a static load and as much as 32 MA into a dynamic load. The current pulse will have a rise time of ~5 μs and will produce a magnetic field driving the impactor liner of several hundred Tesla at the target radius of one to two centimeters. The collision can produce shock pressures of ~15 megabars. Design of the pulsed power system will be presented along with data obtained from the Atlas prototype Marx module.

1 Introduction

The pulsed power system for Atlas is designed to provide a current pulse that will be used to implode "heavy" metallic liners in a Z-pinch configuration. The self-magnetic field on the surface of a liner carrying 30 MA at an initial radius of 4 cm is 1.5 MG rising to 6 MG at a radius of 1 cm. The J x B forces on a 40 g liner will cause it to implode in about 7 μs, reaching a velocity of about 16 mm/μs with a kinetic energy of 5 MJ. The optimum liner in simulations done to date is aluminum, 4 cm tall, 4 cm in radius with a mass of about 40 g. These parameters are chosen to give the fastest velocity while keeping the inner surface of the liner solid.

2 Circuit Description

To provide the current pulse to the load, a direct-drive capacitor bank is used, i.e., there is no pulse shaping switches between the capacitors and the load. There are no 'auxiliary' circuits such as crowbar switches. To control the current oscillations after the liner has imploded, resistive damping is used. Hydrodynamic experiments on Pegasus done at currents from 6 MA to 12 MA have shown good stability of the liner inner surface for implosion times of 8-9 μs. The combination of available energy, capacitor energy storage technology, and implosion time scale imply an optimum voltage of 240 kV. We achieve this voltage by switching in series four 60 kV, 60 kJ capacitors. The Atlas pulsed power system is composed of 96 of these Marx units connected in parallel. The Marx units are in oil tanks and are connected to an oil filled vertical tri-plate transmission line (VTL) via cables. The VTL connects to a disk line in the center of the machine. This solid dielectric-insulated disk line contains the conical power flow channel and the load. The circuit diagram of a Marx module is shown in Fig. 1.

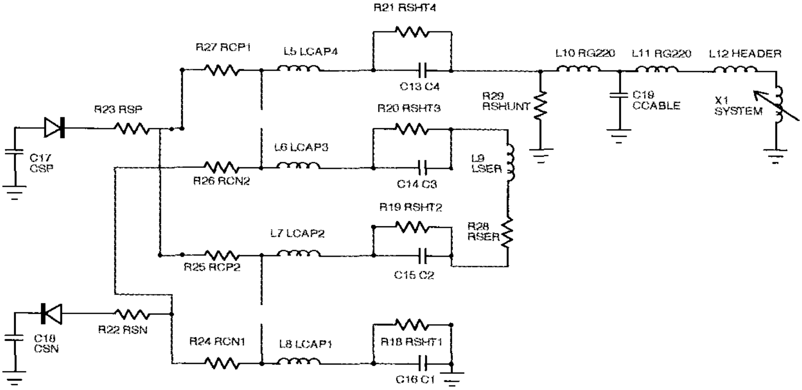

Figure 1. Marx module schematic: (Rsht1-Rsht4 = 20 MΩ; C1-C4 = 34 μF; Lcap1-Lcap4 = 60 nH; all other R's = 400 Ω; Rser = 1.5 mΩ; Rshunt = 5 Ω; total cable L = 100 nH; headerL ~ 10 nH; total equivalent system (without Marx) L = 12.3 nH).

The RC filter and diode at the input to the Marx is to protect the power supply and limit current in case of a short during charge. The Atlas system inductance budget is given in the following table.

Marx modules	2.6 nH
Cables	.94 nH
Header / LPS	.53 nH
VTL / transition	6.1 nH
Disk line	.76 nH
Power flow channel	3.9 nH
Load	1 nH
Total	**15.8 nH**

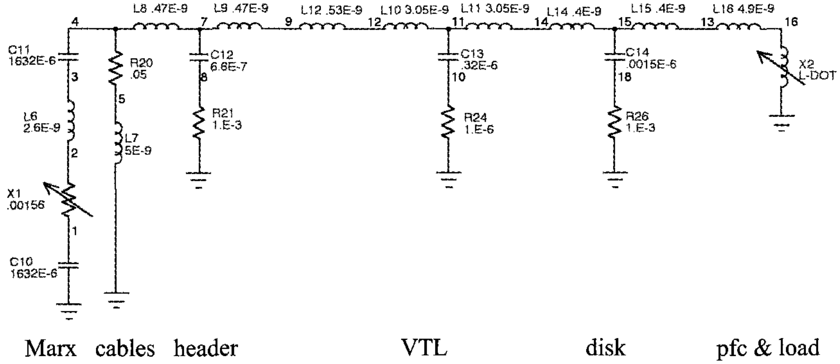

Figure 2. Atlas schematic

In Fig. 2, the series resistor is shown as a variable resistor. This is because the resistor is made of folded stainless steel and has a ΔT of ~80 C. This resistor also represents the varying resistance of the railgap switches. A static R of 1.8 mΩ gives an equivalent result to the actual time varying R.

Tests have been done on all of the Atlas Marx components. A prototype Marx has been constructed and tested for over 500 full voltage shots at an equivalent system current of 27 MA. A module of the Atlas distributed control system was used to control and acquire data from the Marx. No failures have occurred in the Marx, including 10 fault condition shots at ~600 kA/Marx.

The major Marx components are:

1. Capacitors; Maxwell 34 μF, 60 kV, I(fault) = 750 kA, ΔV = 69 kV/capacitor for rated lifetime, fiberglass case with electrodes on either end,
2. Trigger system; Maxwell charged cable system, measured jitter <5ns on Marx,
3. Switches; Maxwell railgaps, L = 20 nH/switch, Q = 5 C/shot, I (fault) = 750 kA, demonstrated maintenance interval = 160 shots, insulating gas, 85% Ar + 15% SF6,
4. Connecting cables; RG-220,
5. Series resistor; folded 304 SS in Kapton laminate, R (cold) = 150 mΩ/module,
6. Shunt resistor; CuSO4 solution in Tygon tubing, R = 5 Ω/module,
7. Isolation resistors; 170 kV, 165 kJ, 400 Ω.

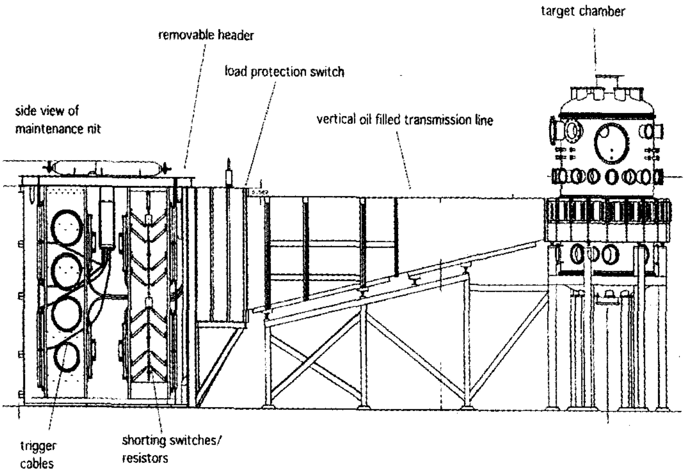

Figure 3. Side view of oil tank housing apparatus.

Fig. 3 shows a side view of one of the 12 oil tanks housing 8 Marx modules, the VTL, disk line, and target chamber. The Marx modules are arranged into groups of 4 forming what we call a maintenance unit (MU). A MU will be removed for switch maintenance and inspection on a rotating basis every 96 shots. Each MU has its own transmission line and load protection switch (LPS). The LPS shorts the MU output until just before firing.

3 Test Results

Figure 4 shows current from the prototype at 240 kV (285 kA) and 180 kV (213 kA). At each voltage, a simulation is fitted to the data using the varying resistance for the railgap switches and the SS series resistor. The model accurately predicts the current at different voltages. It is this model that is used to predict the current on the full Atlas system. The model predicts that at a voltage of 190 kV, 30 MA can be delivered to a load with ΔV on each capacitor = 69 kV. If the energy used to implode the load is not returned to the capacitors, by a liner bounce for example, the load will provide additional damping. A flashover of the load region when the Poynting vector reverses will effectively prevent this energy return. This flashover is observed on Pegasus. Under this assumption, the voltage can be raised to 220 kV with 32 MA delivered to the load and keep ΔV within specification. Raising the voltage higher to $\Delta V \sim$ 72-75 kV/capacitor will have a minimal effect on capacitor lifetime. This is an option since the Weibull analysis of capacitor life tests have shown that under a worst case assumption, 6 capacitor failures could be expected in 1000 system shots at full voltage.

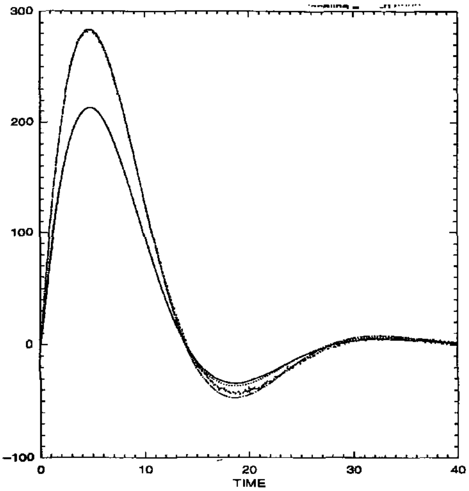

Figure 4. Current of prototype.

4 Conclusion

Preliminary tests of Atlas components have shown that a system reliability of 95% should be achievable using the load protection switch to protect the load from trigger pre-fires. This reliability is based on full voltage operation at 240 kV erected voltage. Shots taken at lower voltage will improve this reliability number. Atlas is presently in the final design and construction phase. Parts have been ordered for construction of a "first article" consisting of a complete MU with its VTL and a dummy load. The building that Atlas will occupy is being prepared for occupancy of the machine. Construction is planned to be complete by late 2000 or early 2001. A series of hydrodynamic and EOS experiments have been planned for Atlas in support of its role in stockpile stewardship. Interested parties are considering other experiments such as magnetized target fusion experiments.

Acknowledgments

Work performed under the auspices of the University of California for the USDOE, contract # W-7405-36 ENG.

MULTI-MODULE FLUX COMPRESSION ENERGY SOURCE “SPRUT”

V. A. DEMIDOV, V. D. SELEMIR, S. A. KAZAKOV, YU. V. VLASOV,
R. M. GARIPOV, A. P. ROMANOV
VNIIEF, Sarov, Russia

Powerful electromagnetic energy sources are required to study high-temperature plasmas on the basis of magnetic gas-dynamic cumulation systems, megabar pulsed pressure generation, obtaining soft x-ray radiation, and other experimental research. The “Sprut” energy complex, which stores several hundreds of megajoules of energy using flux compression generator modules connected in parallel, is presented. A multi-element disk flux compression generator (DFCG) is chosen as a basic module. Two versions of the modules are considered. These are the 20-element DFCG with HE-charges of 240 mm (DFCG-240) and 480 mm (DFCG-480) diameter. DFCGs are connected in parallel using special high-voltage low-inductance cables. Results on DFCG-240 experiments are presented.

1 Introduction

High energy density physics experiments require short current rise times. This necessitates storage of several hundreds of megajoules of energy, since large energy losses occur during peaking of current pulses.

Disk generators are the most powerful high-current energy source [1-3]. The highest currents and energies are obtained in 1-meter diameter generators. However, the effective operation of a large diameter DFCG is possible only at low inductive loads. Hence, to power real loads with high currents, it is useful to make comparatively small diameter batteries consisting of multi-element DFCG (modules) and connect them in parallel. This is the basic principle of the “Sprut” energy complex, which stores several hundreds of megajoules of energy.

2 The Scheme of Multi-Module Energy Source

The success of a multi-module power source lies in the technique used to connect the modules with a common load. Parallel connection of an FCG having a coaxial output must be implemented using special, high-voltage low-inductance cables [4]. Figure 1 shows parallel connection of a DFCG to a collector with a load located in its center, using cables. The important feature of this design is that it provides a symmetric current supply to the load at any number of modules.

We investigated two versions of modules of the system. These are the 20-element DFCG with HE charges of 240 mm (DFCG-240) and 480 mm (DFCG-480) in diameter. The choice of two disk modules, one twice the size of the other, makes it possible to upgrade the unit using only a small, cost-effective module. Moreover, it allows creation of many versions of a multi-module energy source.

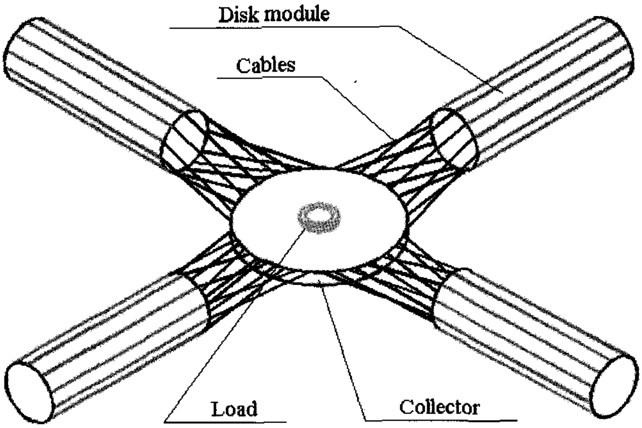

Figure 1. “Sprut” power unit design.

3 Calculation Results

Figure 2 gives a sketch of the DFCG half-element. A program for designing DFCG parameters has been developed. The program was tested based on the results of former experiments and previously calculated data [5]. The DFCG optimization was calculated over the parameters r, z, and δ.

Table 1 gives the calculated results of the 20-element DFCG-480 operation with different HE charges at the initial current of $I_0 = 10$ MA with various inductive loads (L_l). The mass of HE in DFCG-480 is ~ 300 kg.

Comparing the generator output characteristics using the charges from different HE: OMA (HMX: density $\rho = 1.82$ g/cm^3, detonation rate D = 8600 m/s) and a cheap cast mixture TG5/5 (TNT/RDX 50/50: $\rho = 1.65$ g/cm^3, D = 7550 m/s), one can see that the power of the unit with OMA is about 20% greater than the one with TG5/5.

The inductance value of the load $L_l = 20$ nH is chosen to determine the limiting output characteristics (magnetic field and power) of the disk generator. The DFCG-480 operation with a high-inductive load $L_l = 40$ nH is closest to a real operating mode using several generators connected in parallel.

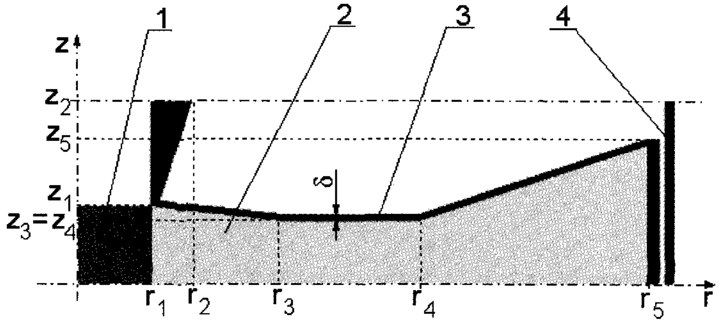

Figure 2. DFCG half-element sketch. 1- initiating system, 2 - HE charge, 3 - armature, 4 - reverse conductor.

Table 1. Calculation results for a 20-element DFCG-480

HE	L_0 nH	L_l nH	$(dI/dt)_{max}$ MA/μs	I_{max} MA	W_{max} MJ
OMA	387	20	17.4	149	222
OMA	407	40	8.8	89.2	159
TG5/5	387	20	14.2	142	202
TG5/5	407	40	7.6	87.5	153

From the results presented, one can see that the maximum current values do not greatly depend on the type of HE applied. The characteristic current rise time (“e” times at the final stage of the generator operation) changes from ~ 7.5 μs for the module with OMA and L_l = 20 nH up to ~ 10 μs for TG5/5 and L_l = 40 nH. The magnetic field in the point of the sliding contact is smoothly built up from ~ 0.5 MG up to ~ 0.9-1.3 MG, depending on the load magnitude.

Similar calculations were made for DFCG-240. For this module, the minimum characteristic current rise time is ~ 3.6 μs (for OMA and L_l = 10 nH) and the maximum characteristic time is ~ 5 μs (for TG5/5 and L_l = 20 nH). The maximum field values in the contact point and the character of its buildup are almost the same as in DFCG-480.

Calculations of the thermal effect of current on the cables have shown that short characteristic current rise times (5 and 10 μs) do not greatly influence the heating of the current-carrying cable elements. The magnitude of the radial shift of external conductor (shield) under the effect of magnetic field forces, with regard only to inertial confinement, is ~ 0.7-1.1 mm. This causes a 20-30% increase of their inductance per unit length.

With *n* DFCG-240 modules are connected in parallel, "Sprut," with a 20/*n* nH load, can provide a ~ 45*n* MA current and ~ 20*n* MJ magnetic energy. The application of DFCG-480 modules will make it possible to obtain a ~ 90*n* MA current and ~ 160*n* MJ magnetic energy with a 40/*n* nH load.

4 Experimental Results

The experimental improvement of the "Sprut" power complex was begun on the DFCG-240 module containing three disk elements. Previously in gas-dynamic experiments, the initiation system of disk HE-charges from the OMA mixture was checked. The symmetry and dispersion velocity of a copper armature in the magnetic flux compression cavity was also determined.

In electrodynamic experiments, the three-element DFCG-240 was powered by a helical generator 100 mm in diameter. For an initial current of ~ 5 MA, a pulse of ~ 50 MA amplitude with a characteristic rise time on a terminal phase of ~ 4 μs is obtained in the load of the disk generator. This corresponds well to calculations.

5 Conclusions

The "Sprut" complex uses disk flux compression generators connected in parallel and can produce energy of several hundred megajoules. Two versions of its modules are discussed. These are the 20-element DFCG with HE-charges of 240 mm and 480 mm in diameter. The parallel connection in the DFCGs is made using special, high-voltage low-inductance cables. Results on DFCG-240 experiments are presented.

References

1. Chernyshev, V. K., Protasov, M. S., Shevtsov, V. A., The First Disk Explosive Magnetic Generators, in: Ultra-High Magnetic Fields. Physics. Engineering. Applications. (Ed. by V. M. Titov and G. A. Shvetsov) Moscow: Nauka, (1984) pp. 23-25.
2. Demidov, V. A., Kraev, A. I., Mamyshev, V. I., et al., Three-Module Disk Explosive Magnetic Generator, in: Megagauss Fields and Pulsed Power Systems. (Ed. by V. M. Titov and G. A. Shvetsov). N.Y.: Nova Science Publishers, (1990) pp. 351-354.
3. Boriskin, A. S., Dymant, E. M., Lyudaev, R. Z., Pavlov, S. S., Pavlovskii, A. I., 100 TW CDMCG-1280. Casette MCG of Gigajoule Range with External Load, in: Megagauss Magnetic Field Generation and Pulsed Power Applications. (Ed. by M. Cowan and R. B. Spielman). N.Y.: Nova Science Publishers, (1994) pp. 459-465.
4. Pavlovskii, A. I., Lyudaev, R. Z. Kravchenko, A. S., et al., Formation and Transmission of Magnetic Cumulation Generators Electromagnetic Energy Pulses, in: Megagauss Physics and Technology. (Ed. by P. J. Turchy), N.Y.-L: Plenum Press, (1980) pp. 595-609.
5. Reinovsky, R. E., Lindemuth, I. R., Marsh, S. P., et al., Explosive Pulse Power for Fusion Applications, in: Megagauss Magnetic Field Generation and Pulsed Power Applications. (Ed. by M. Cowan and R. B. Spielman). N.Y.: Nova Science Publishers, Inc., (1994) pp. 671-678.
6. Demidov, V. A., Kazakov, S. A., Kravchenko, A. S., et al., High-Power Energy Sources Based on the FCG Parallel and Serial Connection, in: Digest of Technical Papers 11th IEEE International Pulsed Power Conference. (Ed. by G. Cooperstein and I. Vitkovitsky). Baltimore, Maryland, (1997) pp. 1459-1464.

CONVENTIONAL AND EXPLOSIVE PULSED POWER DEVELOPMENT AT TEXAS A&M UNIVERSITY

B. FREEMAN, T. FALESKI, I. HAMILTON, J. ROCK, T. PARISH
Texas A&M University, College Station, TX, USA

A new capability for performing conventional and explosive pulsed power programs is being developed at Texas A&M University (TAMU), through the Texas Engineering Experiment Station of the TAMU System. The primary machine being installed in this facility is a low inductance, ~460 kJ, 60 kV capacitor bank. Flexibility to support different loads is being designed into this system, as is the ability to disconnect experiments from the laboratory machine for testing at the explosive pulsed power test site. Initial experiments will be conducted using a plasma focus as the load, with this low inductance, high-current capacitor bank as a driver. We expect to realize peak currents of 3 to 4 MA in the plasma focus. Potential applications include pulsed neutron source studies, intense X-ray production development for possible commercial applications, and high-energy-density plasma science investigations. Other potential loads for this capacitor bank include magnetohydrodynamic plasma accelerators and systems that may be of interest to magnetized fusion energy experiments. The proposed site for the explosive pulsed power facility on the TAMU Riverside Campus has been experimentally qualified. We anticipate that with a fully developed facility that incorporates blast, shrapnel, and acoustic mitigation measures, experiments containing 22.7 kg of explosive will be reasonable. Presently, parts are available to assemble a power source for potential explosive generator development and application shots.

1 Introduction

With the end of the Cold War, many of the national laboratory and commercial plasma science and pulsed power efforts have been greatly curtailed or eliminated. However, the need for these experimental activities remains, though at a reduced scope. We are building a new capability at Texas A&M University (TAMU), through the Texas Engineering Experiment Station of the TAMU System, to provide a continuing resource for experimental research in these areas, in collaboration with other institutions. Both conventional and explosive pulsed power systems will be used within this capability. Initially, most of the faculty and staff for this effort will be drawn from the TAMU Nuclear Engineering Department although personnel from the entire TAMU College of Engineering will be encouraged to participate in the program. The facilities for the Plasma Science/Pulsed Power effort will be located on the TAMU Riverside Campus, about 11 km from the main campus. The laboratory for the conventional pulsed power effort is located about 1.6 km from the approved location for the explosive pulsed-power firing site

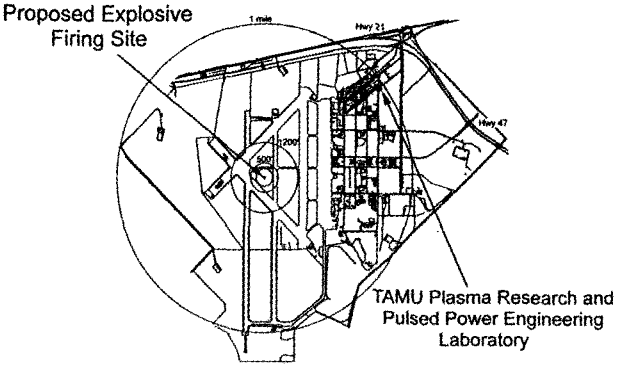

Figure 1: Pulsed Power Research Sites at Riverside Campus

2 Facilities

The new Plasma Science/Pulsed Power Laboratory will be initially housed in a renovated building containing about 150 m^2 of floor space (Figure 1). The primary machine that will be located within this structure will be a low inductance, high-voltage capacitor bank.

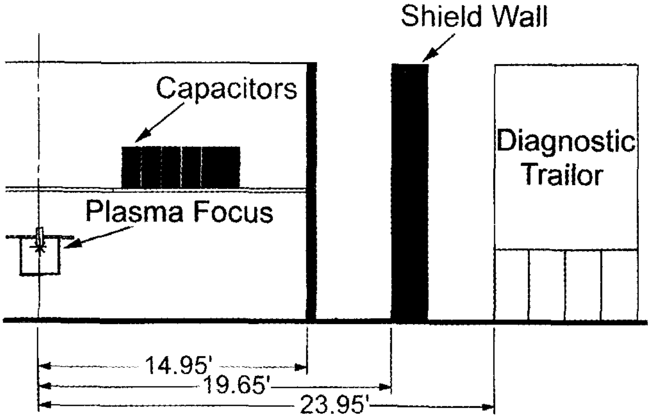

Figure 2: Relative Layout of Plasma Focus, Capacitor Bank, and Diagnostic Trailer

This pulsed power source will be housed in a 75 m^2 area including a mezzanine to support the capacitive storage above the experimental area. A 46 m^2 trailer will be co-located with this building to provide an electromagnetically shielded control and diagnostic enclosure (Figure 2).

The large capacitor bank will have a maximum charge voltage of 60 kV and will store about 460 kJ of energy. It will be organized into six modules, each containing 24, 1.85 uF capacitors (Figure 3). Each module will be fired through a single rail-gap switch. The output of the rail switches is fed into 72, Rg-17/14 cables that connect to a header ring. The bank's short circuit inductance will be about 16.7 nH to this common collector/connector ring. The associated short-circuit current at the connection ring will be about 7.6 MA. This approach enables several different loads to be accommodated without the necessity of re-cabling the machine.

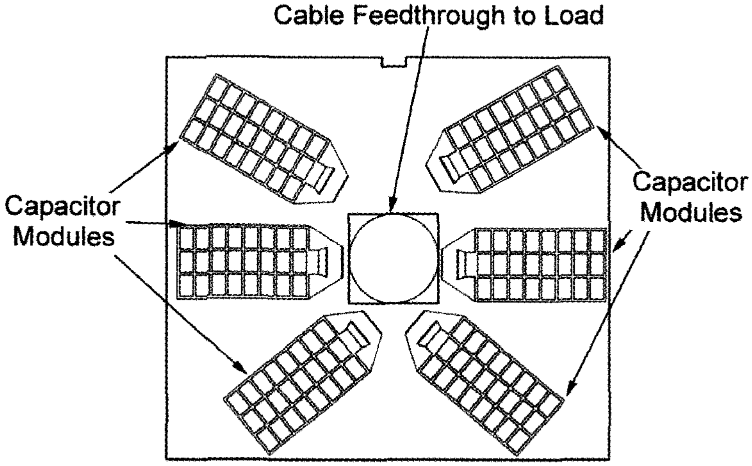

Figure 3: Capacitor Bank Layout in Building 6775

In addition to the Plasma Science/Pulsed Power Laboratory, a second location on the Riverside Campus has been selected and qualified for explosive pulsed power research. This site was experimentally qualified in a series of three explosive detonations of 0.45, 3.64, and 4.54 kg of pentolite. Subsequent to these tests, the TAMU Facilities Planning Committee approved this location for explosive pulsed power research. The control/recording facility will be enclosed in a heavy, steel blast shield. The area surrounding the firing pad will be bermed and sprayed with concrete to provide both debris and acoustic mitigation. Additional measures may be implemented, as needed. One such measure would use a double ring of concrete columns with staggered spacing to catch debris to a higher angle of ejection and to act as an acoustic scattering array to break up coherent shock fronts. A fully developed facility will be able to detonate experimental assemblies containing as much as 22.7 kg of explosive while still meeting the required debris and acoustic operational limits. Parts are available to assemble a prime power capacitor bank, which would store a modest 50 kJ of energy at 20 kV.

3 Near-Term Research

One of the first research issues will be to determine the deterioration mechanism for the new ATLAS rail-gap switch design. By understanding this mechanism, relatively minor modifications to these switches might be made that could enhance the present mean time between maintenance of 160 shots. Also, we expect to examine a trigger system redesign for this switch that will increase the trigger dV/dt from ≤10 kV/ns to 15-20 kV/ns. There are two advantages of such an improvement. First, the trigger stability and reliability of the rail switch will be improved. Alternatively, the ratio of the operating voltage to the self-break voltage might be increased to lessen prefire probability characteristics. Second, it may be possible to replace the Ar/SF_6 gas mixture in these switches with either synthetic air or an argon/air mixture. This would lower operating expenses and eliminate the operationally troublesome gas, SF_6.

Another area of research will involve the examination of the electrical characteristics of SF_6 gas under conditions similar to those encountered within a functioning explosive-driven flux compression generator. As a propagating-burn helical generator armature approaches the stator, the gas between the armature and stator is shocked and compressed, while the voltage potential progressively increases. A small shock tube experiment will be built and used to measure the electrical characteristics of SF_6 under these conditions.

Once the 60 kV capacitor bank is completed and operational, the first experiments will drive a plasma focus. Maximum currents of 3 to 4 MA should be achievable with a Mather-geometry focus. These experiments will examine the feasibility of using the plasma focus and the $^{11}B(p,\alpha)2\alpha$ fusion reaction for deep space propulsion applications. Diagnostics for this effort will include an X-ray spectrometer and various neutron measurements, along with the standard set of electrical measurements. A distinctive challenge of this research will be the requirement to operate the plasma focus at elevated temperatures, about 125 °C.

Other potential applications of a high-current plasma focus include pulsed neutron source studies, intense X-ray production development for possible simulator and commercial applications, and high-energy-density plasma science investigations. Other potential loads for this capacitor bank include magnetohydrodynamic plasma accelerators and systems that may be of interest to magnetized fusion energy experiments.

4 Summary

An ambitious effort is under way at Texas A&M University to offer the research community a broad-based plasma science and pulsed power capability. The main emphasis for this capability will be in high energy density plasma systems. To energize these systems, we anticipate using both conventional and explosive-driven power supplies. The first conventional power supply of this nature will be a ~460 kJ, 60 kV capacitor bank. The initial experiments with this bank will begin in February 1999.

THE HUMBOLDT HIGH MAGNETIC FIELD CENTER: MEGAGAUSS OPERATION AND RESULTS UP TO 300 TESLA

M. VON ORTENBERG, O. PORTUGALL, N. PUHLMANN,
H.-U. MUELLER, I. STOLPE, A. KIRSTE
Humboldt Universität, Berlin, Germany

The Humboldt High Magnetic Field Center operates different magnetic field generators providing DC fields up to 20 T, nondestructive pulsed fields up to 62.5 (78.5) T, and semidestructive pulsed fields up to 311 T using the single-turn coil technique over the full range from liquid Helium to room temperature. These fields are combined with sophisticated measuring techniques for the study of semiconductor structures and magnetic materials. Of special interest are the applications to c-GaN, HgSc:Fe, and $Tb_3Ga_5O_{12}$. The data obtained by magneto resonance and Faraday rotation are interpreted in direct connection with theoretical models.

1 Introduction

Intense magnetic fields in condensed matter physics provide not only excellent tools for probing both electronic energy levels and the dimensions of nanostructured potentials but they are also able to create new states of matter. To investigate these phenomena, the full range of magnetic fields up to multi-megagauss is necessary, as is the sophisticated peripheral equipment to provide the necessary low-temperature environment, and the high intensity monochromatic electromagnetic radiation.

2 Set-Up at the Humboldt High Magnetic Field Center

Three kinds of field generators are used: DC-superconducting solenoids up to 20 T, nondestructive pulsed fields up to 62.5 T with a pulse length of about 10 msec, and semi-destructive fields up to 311 T by the single-turn technique with a pulse length of about 5 µsec [1, 2]. These generators are standard for routine investigations, whereas the concept of *mini-coils* for nondestructive megagauss generation is still under development and results, so far, in a peak field of 78.5 T [3]. Pulsed magnetic fields provide for many investigations the same or even better experimental conditions than DC fields. Optical experiments take advantage of the increased stability of the radiation source over short pulse lengths that, on the other side, are sufficiently long to apply phase-sensitive modulation techniques [4]. For experiments beyond the domestic 300 T, the Humboldt High Magnetic Field Center participates in explosive flux-compression experiments through the DIRAC and KAPITZA series [5, 6]. Whereas megagauss field generation in Berlin is no longer a problem and the special, light weight strip-line system has been essentially understood and simulated [7], the measuring technique becomes more and more sophisticated to tackle even those problems, which are already demanding in DC fields [8].

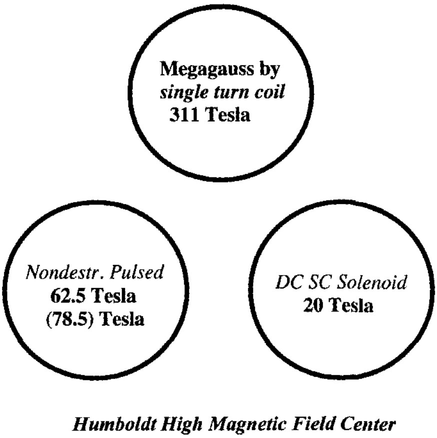

Figure 1. Field generators of the *Humboldt High Magnetic Field Center*

3 Megagauss Magneto-Optics

Any kind of optical experiment is most suitable for megagauss fields, since the interacting electromagnetic fields are focused onto the sample either by Gaussian imaging or dielectric wave-guides. In this way, any electrical conductive contacts with final loop for pick-up obscuring the actual signal are avoided. Resonant magneto-spectroscopy is most suitable to probe the Landau level structure of solids. By comparison to non-resonant spectroscopy (Shubnikov-de Haas and magneto-phonon effect), resonance spectroscopy provides information on the energy separation of the states involved as well as directly on the state functions by the transition matrix element. The Q-value of the cyclotron resonance is determined by the product of carrier mobility and resonance field $\mu \cdot B_{res}$, so that megagauss experiments are definitely required for low-mobility materials. For high-mobility materials, the resultant data in this high-field regime provide, by the detailed line shape, much additional information of the energy states involved. Thus, the magnetic field acts as a "zoom" with respect to the energy levels considered. In the following section we demonstrate the efficiency of this method by recent results on GaN and HgSe.

4 Landau Levels in Cubic GaN

The wide-gap material GaN is the most promising compound with respect to blue laser-diode and high temperature applications [9]. Whereas the natural crystal structure of GaN is of the *wurtzite* type, a *cubic* modification can also be obtained by *molecular beam epitaxy* on GaAs substrates, promising improved properties in technical applications compared to the natural *wurtzite* type. The low carrier mobility for p-type GaN of μ = 200 cm^2/Vsec permits cyclotron resonance measurements only in megagauss fields in connection with CO$_2$-laser radiation [10]. We have plotted the obtained data in Fig. 2. In the upper part, the magnetic field is recorded as a function of time, whereas the corresponding data of the total

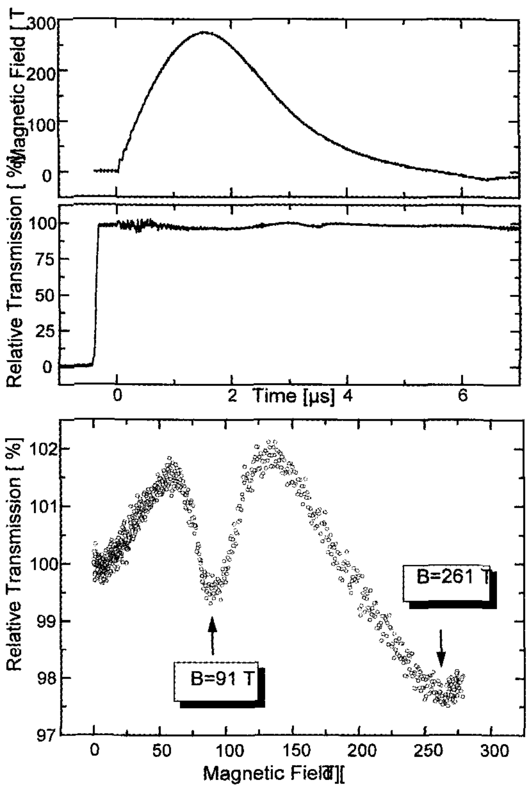

Figure 2. Cubic GaN in megagauss field. After [10]

transmission are shown in the middle. The actual quality of the data is so high that, after offset suppression and scale enlargement, the resonance structure is clearly demonstrated as shown in the lower part of the same figure as a function of the magnetic field. Frequency and temperature dependence of the observed resonance lines corroborate that the observed structures are due to hole resonances within the coupled system of valence bands. They are in good agreement with the theoretical results calculated in the Luttinger model [10]. The primary condition for the success of this investigation was not only the generation of megagauss fields but definitely also a very sophisticated measuring technique with optimal noise suppression. As a matter of fact, our equipment is able to resolve magneto resonance with only 0.5% transmission changes [11].

5 HgSe in High Magnetic Fields

The efficiency of megagauss cyclotron resonance experiments to investigate the energy band structure of HgSe:Fe has been repeatedly demonstrated [12, 13]. We also like to point out that interband magneto-optical transitions from the valence band to the conduction band are an excellent experimental tool as long as the radiation energy can excite carriers above the Fermi energy into empty states. For a zero-gap semiconductor like HgSe, this is possible as long as $\hbar\omega > E_{fermi}$. In Fig. 3 we have reproduced the corresponding data using 117 meV radiation for a MBE-grown sample [14]. The spectrum is dominated by the interband transitions, whereas the cyclotron resonance at about 30 Tesla can be hardly recognized due to the small carrier concentration. The resonance lines exhibit the typical sharp onset and the approximate $1/\sqrt{(E-E_n)}$ singularity of a one-dimensional combined density of states representing the carrier motion parallel to the external magnetic field. The resonance positions are in good agreement with the scheme of Landau levels calculated for $k_z=0$.

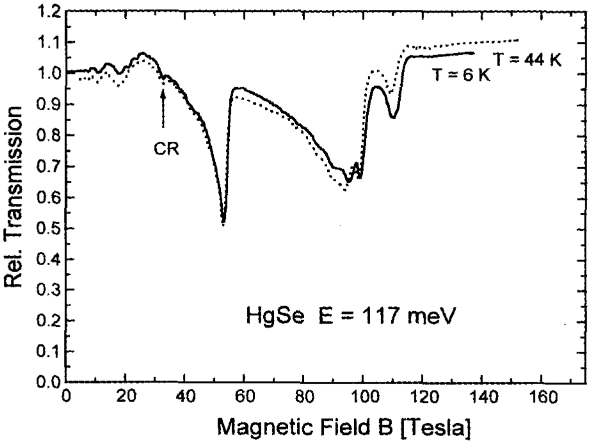

Figure 3. Interband resonances in pure HgSe. After [14]

In contrast to pure HgSe, the ternary compound HgSe:Fe has a Fe^{2+} donor degenerated with the conduction band states about 210 meV above the valence band edge. The iron donor gets ionized and populates the conduction band until the Fermi energy gets pinned to the donor level [15]. It should be noted that the coupled donor/conduction band system represents a non-conservative system with respect to the effective concentration of mobile charge carriers [16]. Especially as soon as the lowest Landau level of the conduction band crosses the donor level, all donor states get populated again so that the remaining concentration of free carriers is drastically decreased. Depending on the actual magnetic field dependence of the Fe^{2+} level, this effect should occur beyond 200 Tesla. In the framework of EUROMEGAGAUSS [17] and in cooperation with VNIIEF, Sarov, Russia, corresponding data applying the generator MC1 together with the eddy current spectroscopy [18] exhibit clearly a sharp peak-like decrease at 420 Tesla for samples with different Fe-concentration of $5 \cdot 10^{19}$ cm^{-3} and $8 \cdot 10^{18}$ cm^{-3} [19].

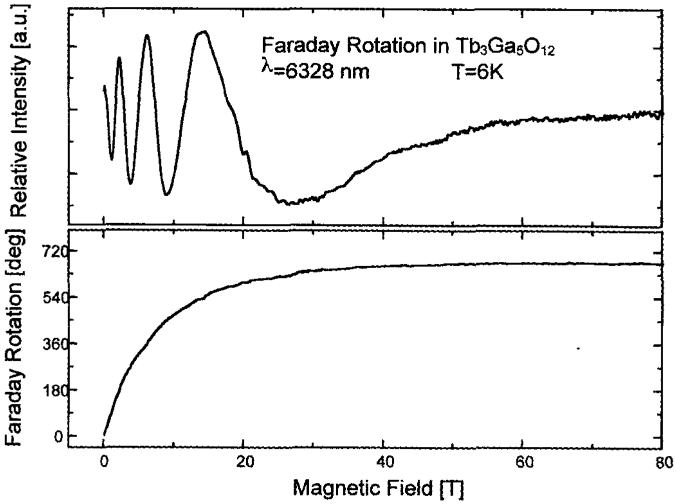

Figure 4. Faraday rotation of $Tb_3Ga_5O_{12}$. After [20]

6 Faraday Rotation in $Tb_3Ga_5O_{12}$

The Faraday effect is an optical off-resonance effect providing detailed information on the effective internal magnetization of the sample. In cooperation with VNIIEF, we have performed measurements of the Faraday effect on $Tb_3Ga_5O_{12}$ using 633 nm wavelength radiation in fields up to 150 Tesla as shown in Fig. 4 [20]. In the upper part of the figure is plotted the intensity modulation of the linearly polarized radiation passing the sample and analyzer. The evaluated magnetization is plotted in the lower part of Fig. 4. Due to the higher sensitivity of the Faraday rotation method compared to the explosive flux compression, both methods complement each other ideally to obtain detailed information over the entire field range.

7 Conclusions

Megagauss magnetospectroscopy is a very efficient tool for the investigation of both magnetic and semiconducting materials. Because of the necessary field generator in the form of a *single-turn coil*, extensive peripheral equipment setups are necessary to provide a broad spectrum of information of the samples to be investigated.

References

1. von Ortenberg, M., et al., *Physica B* **201** (1994) p. 572.
2. von Ortenberg, M., et al., *Proc.* MG VII, **1** Sarov (1997) p. 213.
3. Portugall, O., et al., *Physica B* **246** (1998) p. 54.
4. Machel, M., von Ortenberg, M., **Physica** *B* **211** (1995) p. 355.
5. Dzurak, A. S., et al., *Physica B* **246** (1998) p. 40.

6. KAPITZA Seminary I (1997) and II (1998) in Sarov, Russia.
7. Mueller, H-U., Portugall, O., von Ortenberg, M., this volume
8. Puhlmann, N., Stolpe, I., Mueller, H-U., Portugall, O., von Ortenberg, M., this volume.
9. Nakamura, S. et al., *J. Appl. Phys.* Part 2 **35** (1996) L 74.
10. Puhlmann, N., et al., Invited Paper at *ICPS 24*, Jerusalem (1998) in print.
11. Portugall, O., Miura, N., Bauer, G., Schoenfeld, R., von Ortenberg, M., *Physica B* **201** (1994) p. 280.
12. Portugall, O., Barczewski, M., von Ortenberg, M., Schikora, D., Widmer, T., Lischka, K., *J. Crystal Growth* **184/185** (1998) p. 1195.
13. Portugall, O., Barczewski, M., von Ortenberg, M., Schikora, D., Widmer, T., Lischka, K., this volume.
14. Portugall, O., von Ortenberg, M., von Truchsess, M., Becker, C., to be published.
15. Mycielski, A., MRS Symposia Proceedings. **89** (1987) p. 159.
16. Laue. I., Portugall. O., von Ortenberg, M., Dobrowolski, W., Springer Series in Solid State Sciences **101**, Ed by G. Landwehr (1992) p. 449.
17. EUROMEGAGAUSS foundation by Selemir, V., Zevzdin, A., von Ortenberg, M., Sarov, Russia., October 1998.
18. von Ortenberg, M., Springer Series in Solid-State Sciences **87**, Ed. by G. Landwehr, Springer Verlag (1988) p. 486.
19. von Ortenberg, M., Platonow, V., Tatsenko, O., Dobrowolski, W., to be published.
20. Platonow, V., Tatsenko, O., Zvezdin, A., Puhlmann, N., von Ortenberg, M., to be published.

THE EUROPEAN 100 T PROTOTYPE PROJECT

P. P. J. VAN ENGELEN (1,2), W. JOSS (1)

1) Grenoble High Magnetic Field Laboratory, Max-Planck-Institut für Festkörperforschung and Centre National de la Recherche Scientifique, Grenoble, France
2) Van der Waals-Zeeman Instituut, Universiteit van Amsterdam, Amsterdam, The Netherlands

Joint efforts of institutes in Europe towards the realization of pulsed high magnetic fields date back to 1988. The present 100 T Prototype Project, financed by the European Commission, started in 1996 and is the most recent activity of a partnership of seven European institutes. The objective of the project is to build and test prototype magnets that yield the technology for constructing and energizing a long pulse 100 T magnet. The prototypes are designed to generate 80-100 T in an 8-20 mm bore, and will be operated with 2-10 ms pulses. At a later stage, scaling up to 100 T / 0.1 s should occur. The project follows two parallel routes involving wire-wound coil systems and polyhelix systems. The wire-wound systems deal with four differently composed magnets that cover a broad range in platform fields and energizing methods. In the polyhelix approach one institute aims at using magnetic energy storage. The project also tracks the development of fast measuring techniques and instrumentation. This paper presents an overview of the project, emphasizing its organizational aspects.

1 Introduction

In 1988 a consortium was established including institutes in Amsterdam, Grenoble, Leuven, Oxford and Toulouse with the objective of developing conductors for 100 T magnets. The consortium was operating in two successive projects from 1989 to 1996 that were financed by the European Commission. Based on the expertise that was gained in the course of the work on strong conductors, a design study for 100 T magnets was started in 1993 together with two new partners located in Berlin and Parma. The cooperation is continued in the present project, started in 1996, that aims to build and test prototype magnets yielding the technology for constructing and energizing a long pulse 100 T magnet. The project is financed by the European Commission in the amount of 1.8 MECU and expires in 1999. The prototypes are designed to generate 80-100 T in an 8-20 mm bore, and will be operated with 2-10 ms pulses. At a later stage, scaling up to 100 T / 0.1 s should occur. The project follows two parallel routes involving wire-wound coil systems and polyhelix systems. The approach along these two routes is based on the expertise of the partners.

2 Partnership and Coordination

The organization of the project and its cooperation patterns are closely connected with the expertise and capabilities of each partner:

• high-strength, high conductivity wire	Oxford, Toulouse
• high-strength, high conductivity tube	Grenoble
• helices cut out of tubes	Grenoble, Parma

• coils with internal reinforcement	Leuven
• strong outer reinforcement of coils	Toulouse
• multi-section coils	Oxford
• energizing by a capacitor bank	Leuven, Oxford, Parma, Toulouse
• energizing by a generator	Grenoble
• energizing by a high-speed thyristor converter from the mains	Amsterdam
• experimental techniques	Berlin

The project is coordinated by the Grenoble High Magnetic Field Laboratory.

3 Wire-Wound Magnets

The partners in Amsterdam, Leuven, Oxford and Toulouse cooperate in the wire-wound approach. Apart from conventional conductor materials like Cu and CuAg alloy, Cu-stainless steel (ss) is applied. The latter is developed and produced in Oxford (ss mantle) [1] and Toulouse (ss filaments). The internal reinforcement of the coils consists of glass or carbon fiber. Monolithic coils as well as combined outer and inner coils [2] are manufactured. The monolithic coils operate by simultaneously energizing different subcoils, whereas the combined coils are sequentially energized such that the outer coil provides a platform field for the inner one.

The objectives of this route are to build and test four different high-field magnets covering a broad range in platform fields and energizing methods:

- an 80 T monolithic magnet using internal reinforcement (Leuven); testing in Leuven with a capacitor bank
- a 56 T inner coil (coilin) with internal reinforcement (Leuven), in a 24 T/90 mm bore outer coil (coilex) energized from the mains (Amsterdam); combined testing in Amsterdam
- a 36 T coilin with internal reinforcement (Leuven), in a 54 T/60 mm bore capacitor driven coilex (Toulouse); combined testing in Toulouse
- a 70 T multi-section coilin (Oxford), in a 10 T/240 mm bore superconducting magnet (Oxford); combined testing in Oxford

Capacitor banks drive the coilins. The optimum design for pulsed high-field wire-wound magnets is determined by the different methods of generating the platform field.

Two capacitor banks are modified. The capacitor bank in Toulouse is upgraded with high current and voltage reversal capability to 14.4 MJ/800 MW in order to energize high field large bore magnets such as the 54 T coilex, and in Leuven to 1 MJ/700 MW. A 100 kJ transportable capacitor bank is built in Toulouse for the purpose of testing the 56 T and 36 T coilins.

4 Polyhelix Magnets

The institutes in Grenoble and Parma are involved in the polyhelix route. Polyhelix magnets consist of isolated coaxial helices cut out of tubes. The current density along a helix may vary by introducing a variable pitch.

In Grenoble a large number of helices in the form of Stresses and Heating Optimized Tubular Solenoids (SHOTS) are used for the high-field magnet [3]. New mechanical machining techniques for the cutting process of the SHOTS are developed. The SHOTS high-field magnet is energized using of Kapitza's concept of magnetic energy storage: the energy of a large outer storage coil is partly transferred in a short time into the inner high-field SHOTS magnet. To achieve this, a high voltage and high current electrical circuit is developed and manufactured in cooperation with the Efremov Institute, St Petersburg. The system test is made at a high-power test station in Grenoble where the storage coil, manufactured by industry, can be charged up to 60 MJ using a flywheel generator. Calculations reveal that 80 T may be obtained with a flat top of a few tens ms [3].

The polyhelix approach in Grenoble aims to achieve:

- the verification of the SHOTS concept by testing a prototype SHOTS
- an 80 T/20 mm bore SHOTS magnet
- the high voltage and high current electrical circuit
- proof of workability of magnetic energy storage

The institute in Parma focuses on the use of only two small coaxial helices which are energized sequentially by capacitor banks. Spark gaps able to sustain the very large currents needed in this concept are developed.

The dual-helix approach in Parma aims to deliver:

- an 80 T/10 mm bore/0.3 ms magnet; both outer and inner helix 40 T
- a 100 T/10 mm bore/0.2 ms magnet; outer helix 40 T, inner helix 60 T

5 Experimental Techniques

The objectives of the institute in Berlin are to develop and test fast measuring techniques and instrumentation to be used for experiments in extreme conditions such as high fields with a short pulse, small sample-space and very low temperatures. The development is focused on microcryostats, sources and detectors for FIR and VIS light, analogue glass fiber communication, noise-protected transient recorders, and electromagnetic pulse protection.

Another objective at Berlin is the generation of fields far above 100 T, implying that the magnet is self-destructing. The aim is to achieve 300 T in a 5 mm bore during a 5 μs pulse [4]. In this microsecond domain the instrumentation has to meet even more stringent requirements. The experimental work concentrates on magnetospectroscopy and magnetization measurements of solids, notably semiconductor structures of reduced dimensionality.

6 Conclusions

The status of the European 100 T prototype project has been presented. Seven European institutes are developing the technologies for the construction of 80–100 T prototype magnets. The objectives, first results, partnerships and the coordination of the project were described.

References

1 Jones, H., van Cleemput, M., in High Magnetic Fields, Applications, Generation and Materials, Ed. by H.-J. Schneider-Muntau, World Scientific (1997), p. 499.

2 Herlach, F., Li, L., Harrison, N., van Bockstal, L., Louis, J.-M., Frings, P., Franse, J., van Cleemput, M., Jones, H., Dupouy, F., Askenazy, S., *IEEE Trans. Magn.* **32** (1996), p. 2507.

3 Aubert, G., Dubois, M., Joss, W., Kratz, R., Kuchinski, V., Proc. Megagauss and Megaampere Pulse Technology and Applications, Sarov, Russia, 1996 (Megagauss VII), Ed. by V.K. Chernyshev, V.D. Selemir, L.N. Playshkevich.

4 Portugall, O., Puhlmann, N., Stolpe, I., Barczewski, M., Müller, H.-U., von Ortenberg, M., Proc. Research in High Magnetic Fields, Sydney, Australia, 1997, publ. in *Physica B* **246/247** (1998), p. 54.

HIGH FIELD LABORATORY DRESDEN

R. KRATZ

Max-Planck-Institut für Physik komplexer Systeme, Dresden, Germany, and
Forschungszentrum Rossendorf, Dresden, Germany

Presented is a status report on the new High Field Laboratory Dresden. A 1 MJ capacitor bank driving standard 50 to 60 T coils, which is a smaller version of the magnet system, is constructed as a first step towards the final field of 100 T.

1 Introduction

The objectives of the new Highfield Laboratory Dresden are:

Field [T]	Bore [mm]	Pulse time [s]
100	24	0.01
70	24	0.1
60	50	1

A quick estimation shows that the necessary energy source must deliver about 50 MJ. Because of the specific geographic conditions at the planned site of the laboratory, the most promising technique is a capacitive energy storage system. Such an ambitious project needs to be prepared carefully; the first step will be to construct a smaller version of the capacitor bank. Thus, one can study modularization and circuit issues as well as proper safety designs. The general idea is to split the bank into several modules. Each module has its own protective elements and is separated from all other modules. One module's failure would not affect the other.

For a quick start, the first coils will be bought from the National High Magnetic Field Laboratory, Tallahassee. Coils will also be manufactured in Dresden. The infrastructure, such as a wire-drawing bench, is installed. The activation of a wire development program has begun.

Similar pulsed filed facilities are installed in Amsterdam, Frankfurt, Leuven, Los Alamos, Nijmegen, Osaka, Oxford, Tokyo, and Toulouse. We would like to thank the laboratories in Frankfurt, Grenoble, Leuven, Tallahassee and Vienna for their help and advice.

2 A 1 MJ Capacitor Bank

The 1 MJ capacitor bank is divided into four identical and independent 250 kJ modules connected in parallel (see Fig. 1). Each module has its own thyristor switch that detects reverse voltage, preventing any discharge into a faulty module due to a short circuit.

Switching 1, 2, 3 or all 4 modules in parallel, as seen by the high field coil, can modify the capacitance of the bank. The bank can be charged to full energy, which is 1 MJ at 10 kV, in about 40 seconds using two high voltage power supplies.

The circuit for one module is sketched in Fig. 2. It consists of three parallel sub-units, made from one capacitor with protection coil and fuse in series and a crowbar diode with discharge resistor in parallel.

After all thyristors are fired, the capacitors are discharged over the protection coil and the fuse into the highfield coil. The protection coil limits the maximum current to safe values if the highfield coil has a short circuit. After the current maximum the voltage is reversed over the capacitor terminals and the crowbar diode is conducting. The reverse voltage is limited by the discharge resistor, under normal conditions, to less than 30 % of the load voltage.

If the high field coil has a short circuit, then the reversal voltage can be 80% of the load voltage. The capacitors will not be destroyed, but their lifetime will be affected. The fuses do *not* react under this fault condition.

The fuses will blow only if there is a severe problem within the capacitor bank, itself (for instance, when one capacitor becomes shorted). The other two capacitors of the same module will then discharge into the shorted one. In this, case the fuse will react.

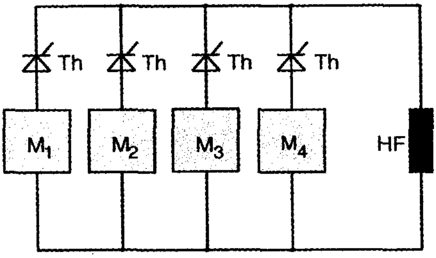

Figure 1. Division of the capacitor bank into four modules, M_1 to M_4. Ignition of the thyristors Th discharges all four modules into the high field coil HF.

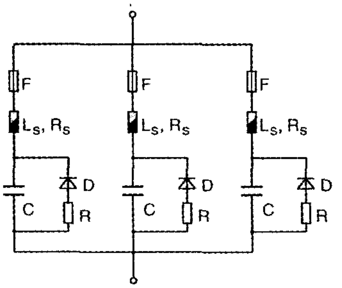

Figure 2. Principal circuit of one 250 kJ module. There are three capacitors with their individual protection elements: the protection coil L_s, R_s, a fuse F, a crowbar diode D and a discharge resistor R.

3 The Capacitors

The capacitors were purchased from Maxwell Energy Products, Inc. These are pulse capacitors with a high energy density of 0.76 J/l. High energy capacitors with metallic electrodes are well suited for large capacitor banks with discharge times in the millisecond range [1]. These exhibit a more predictable failure characteristic than traditional capacitors based on foil designs. Instead of developing a short circuit and dissipating the full bank energy, the metallic electrode capacitors only lose capacitance. The loss of capacitance over the lifetime of our chosen product is less than 5%. Monitoring capacitance determines when capacitors have to be replaced. Furthermore, the high energy density reduces the total weight and size of the capacitor bank. The single drawback is that the capacitors can only be charged with one polarity. Therefore, special circuitry is necessary to achieve both positive and negative field pulses.

Only 12 capacitors are necessary for the 1 MJ bank due to their high energy density. The reduced number of components is especially important for the big 50 MJ bank where space, weight, electrical wiring and reliability are concerns.

Some technical data for the capacitors are given in the following table:

Capacitance	1667	μF
Tolerance	± 10	%
Rated voltage	10.0	kV
Test voltage	11.0	kV
Rated energy	83.3	kJ
Rated voltage reversal	30	%
Max. voltage reversal	80	%
Rated peak current	60	kA
Max. peak current	120	kA
Design life at rated	10000	Cycles
DC Life	42	Hours
Reliability at rated life	90	%

4 Outlook

The setup of the 1 MJ bank is imminent. All the essential parts have been ordered. Upon delivery, the single components will be connected to the single modules. After a thorough test, the modules will be assembled to the final bank, which will be commissioned next year.

References

1. Larson, D. W., MacDougall, F. W., Yang, X. Y., Hardy, P. E., in The Ninth IEEE Pulsed Power Conference, Albuquerque, NM (1993).

THE TOULOUSE 14 MJ CAPACITOR BANK PULSE GENERATOR

S. ASKENAZY, L. BENDICHOU, G. COFFE, P. FERRE, J. M. LAGARRIGUE, J. P. LAURENT, F. LECOUTURIER, J. MARQUEZ, S. MARQUEZ, D. RICART
Service National des Champs Magnétiques Pulsés, CNRS - UPS - INSA, 31062 Toulouse Cedex, France

The 14.4 MJ pulsed capacitor bank generator will be operational in December 1998. We present the characteristics of the pulse generator in the first section and justify the choice of a high operation voltage, here 24 kV, necessary to operate the 14 MJ coils. The second section is a comment on the reliability of the pulsed bank.

1 Introduction

The Service National des Champs Magnétiques Pulsés (SNCMP) constructed a 1.25 MJ crowbarred pulsed capacitor bank 25 years ago. Seven magnet coils can be connected in turn to the bank. These magnets are conventional coils, *i.e.*, with a uniform winding distribution, externally reinforced with a cylinder of TA6Vli. The pulse duration is longer than that produced, at equal energy and magnetic field, by coils with optimized current distribution [1] or by coils with optimized internal reinforcement [2].

Our coils are immersed in liquid N_2 or preferably in liquid N_2 cooled to its triple point, 63 K, which improves their performance in terms of pulse duration and efficiency of conversion into magnetic energy.

The Toulouse team was the first to implement a thyristor switch, optically triggered, composed of a parallel connection of several packs of thyristors, each pack current-balanced by an inductance. These inductances also play the role of limiting the current when the bank is accidentally short-circuited. This often happens when a magnet is destroyed.

In 1987 we obtained 46 T in Ø1.4 cm (inner bore of 1.4 cm diameter) using a reliable, very thick coil made of copper wire (UDD-FIM, Delle) of rectangular 2.5×3.15 mm^2 cross section. This conventional coil designed for the 1.25 MJ pulse generator had a pulse duration close to 1 s. The same year, we achieved 61 T non-destructive in Ø1.4 cm with a coil of reinforced copper wire. Here, the pulse duration exceeded 0.2 s - a record in terms of long duration during the 90's. The reinforced wire was produced through the Alsthom/SNCMP collaboration supported by the French National Defense in view of a program on induction-based magnetic launchers. This microcomposite NbTi/Cu wire evolved from multifilament superconducting wire manufactured by Alsthom (GEC-Alsthom, Belfort) for the construction of the French superconducting Tokamak. Reliable and non-destructive means a lifetime of a few hundred shots at maximum magnetic field for the coils of the SNCMP, and a few thousand shots at 80% of the maximum field.

Applying the scaling laws to the duration of the pulse and the coil volume implies a ten times higher energy to build reliable coils geometrically scaled to the above-mentioned coils, that would be 45 T/4 s/Ø3 cm and 60 T/1 s/Ø3 cm for 14 MJ. Considering the progress achieved on nanocomposite conductors reinforced by continuous whiskers [3], we can predict 75 T/0.4 s/ Ø 1.5 cm and possibly 80 T, as well as insert coils of 10 ms/ Ø1.0 cm in 54 T/14 MJ outer coils [4, 5, 6] to yield a total field of 90 T.

The current in the solenoid that generates these pulsed fields is completely free of parasitic ripple because it stems from the discharge of a capacitor into a coil that is its electric dual. As a consequence, these long pulsed fields should allow measurements with a very low noise level and this down to temperatures as low as a few tens of mK. This is why, in 1989, we proposed a project to the CNRS, called *Operation 12 MJ,* conceived to power 10 coils, each dedicated as a function of its coil-supporting cryostat either to IR magneto optics or to the magnetic Kerr effect, or to transport or magnetization in the 10 mK range.

The *Operation 12 MJ* is a completely coherent program in three steps:
1st step- Acquisition of 600 capacitors for 22 kV having 20 kJ/unit (selected supplier: Heafely-Trench, St. Louis). Construction of a 3600 m^2 laboratory and subsequent installation of the mechanical and electrotechnical machine shops and the cryostat construction shop in this building. Acquisition of three hundred 4 kV/1200 A mean current thyristors and five hundred 4.4 kV/1000 A mean current diodes selected from the manufacturer's batches to have at $V_m/2$ a leakage current two orders of magnitude lower than the regular specifications (selected supplier: Powerex Europe, Le Mans). Mastering the fabrication process of the reinforced conductors.
2nd step- Construction of the 12 MJ pulse generator and connection to the 10 experimental stations that will house the pulsed magnets. Implantation of the wire drawing shop necessary for the R&D on reinforced macrocomposite and nanocomposite conductors, and the shop for the construction of coils.
3rd step- Transfer of the scientific equipment from the 1.25 MJ facility to the 12 MJ laboratory and interfacing the 10 experimental stations to function as a facility.

The 2nd step is well underway: the wire drawing shop produces reinforced conductors and the capacitor bank is nearly completed.

In reality we are constructing a $W = 14.4$ MJ pulsed bank. The state of progress of the construction allows us to affirm that the 14.4 MJ pulse generator will be completely operational in December 1998.

The machines for winding and rectifying the 14 MJ coils and for inserting them into their TA6Vli reinforcement cylinders are yet to be constructed. The principle of these machines is based on the small machines that we have built for the 1.25 MJ coils. The machine shop for the construction of 14 MJ coils is scheduled to be operational in June 2000.

2 Description of the 14.4 MJ Pulse Generator

The overall characteristics are as follows:
Capacity 50 mF. Charging voltage $V_m = 24$ kV maximum.
600 capacitors connected in parallel. Weight 100 tons.
Dielectric of capacitor composed of paper/castor oil.
Short-circuit tests via a 0.2 Ω resistor: 120 kA per capacitor.
Charging up to 24 kV with constant current. Duration of charge to 24 kV: 5 min.
Total number of solid-state power components for the switch and the crowbar: 240 thyristors and 400 diodes, respectively.
The pulsed bank in short-circuit has a current limited to 65 kA by an integrated set of inductances of 4.6 mH/73 m Ω with a total weight of 8 tons.
The pulse shape is of the resistive crowbar type.

The pulse generator is controlled by a programmable industrial controller and is installed in a 500 m^2 room located in the basement. Above it is the 300 m^2 experimental hall with its 10 protection boxes in which the magnets will be placed. The capacitor room is ventilated by four large air ducts at its corners allowing the pressure wave that could appear during the explosion of a capacitor to diffuse. The probability of an explosion is extremely weak, nevertheless we cannot exclude the eventuality of a breakdown of the dielectric of one of the six hundred capacitors during the charging phase of the bank. To limit possible damage, each capacitor is connected to the current line through a fuse. The very intense current wave volatilizing the fuse of a defective capacitor would provoke a destructive resonating surcharge on a network of interconnecting lines arranged as a comb over 500 m^2.

This effect should not occur on a small bank. We have verified this with a 720 kJ bank: 30 capacitors charged at 24 kV. The residual voltage after the explosion of a fuse is 23.7 kV, which means that 20 kJ have been dissipated. This number is very well compatible with the 15 kJ estimated to volatilize a fuse made of a 0.06 mm^2 cross section copper wire of length 100 cm, sufficient to prevent a plasma effect at 24 kV.

Consequently, the pulsed bank is composed of 10 autonomous 1.44 MJ units connected in parallel. These units described in Figure 1 are divided in two elementary groups of 30 capacitors. The two groups are weakly coupled by their two current-limiting self-inductances of 2 × 92 mH connected in series. Thus, if one capacitor is defective only the 29 others of its group will discharge into its fuse.

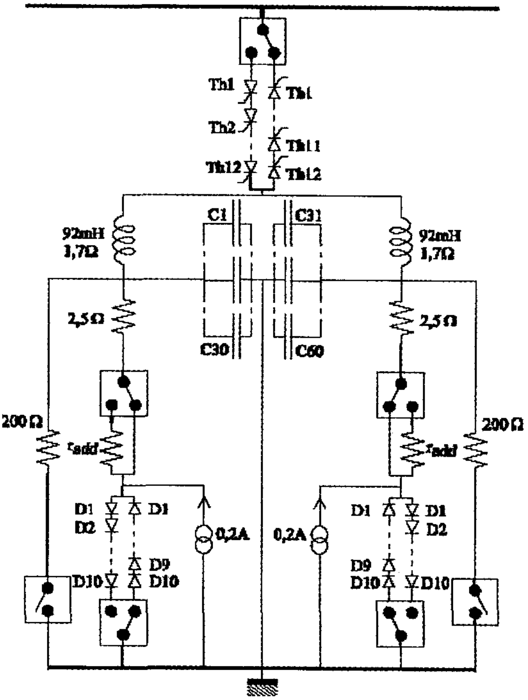

Figure 1. A 1.44 MJ unit.

Considering the working conditions of our pulse generator, the optimum voltage of our paper/castor oil energy storage capacitors, in terms of price/energy/reliability is $n \times 8$ kV. Why have we chosen 24 kV and not 8 kV, which would appear to be more reassuring? The 24 kV result from a compromise. Experience has shown that it is difficult to realize a winding with a reinforced conductor of cross-section $S > 15$ mm^2.

The product $SV_m \propto B_0 W^{2/3}$ is a characteristic of the coils. For a 60 T/14 MJ coil wound with Cu60 %/SS40 % wire we obtain $S < 15$ mm^2 if $V_m > 20$ kV. Clearly, to construct coils 32 kV or even 40 kV are more favorable than 24 kV. But for 32 kV we need, with respect to 24 kV, 1/3 times more components for the crowbar and the switch, fuses of 1.40 m instead of 1 m, increased insulation for the capacitor bank, the chargers and the coil-supporting cryostats. In conclusion, 24 kV seems to us the best compromise for a 14 MJ bank.

3 Remarks on the Lifetime of the Capacitor Bank

The power diodes and thyristors used for the crowbars and the switches, respectively, operate at conditions much lower than their ratings in the most extreme case, which is when the pulse generator is short-circuited. This means that their reliability is unlimited. Consequently, the expected number of shots at V_m, N, is exclusively limited by the lifetime of the capacitor bank. The ageing of the capacitors is a result of two factors: on the one hand the time accumulated under static charge, on the other hand the number of discharges that induce a fatigue which is all the more important if the discharge is rapid and the reversal voltage is high.

The lifetime under static charge obeys the power law $\tau_s \propto V^{-s}$. For our capacitors, $s \cong 22$. Lets call t_s the ageing time under the static voltage V_m, corresponding to the time t_{ch} necessary for the charger to accumulate in the capacitor bank the energy W at V_m. According to the power law $t_s = \Delta_s t_{ch} < t_{ch}$. Using $x = t/t_{ch}$ and $\theta = V(t)/V_m$: $\Delta_S = \int_0^1 \theta^s(x)\mathrm{d}x \leq 1$.

The expected number of charges at V_m, N_s, is written as $N_s = \tau_s/t_s$. The power P_{ch} of the charger is limited because its price is proportional to P_{ch}. t_{ch} and thus t_s are therefore conditioned by the type of charger and the characteristic time $\delta = 2W/P_{ch}$. For P_{ch} fixed, the charger that minimizes t_s is the charger at constant power where the current $i \propto t^{-1/2}$. Here $\Delta_{s,p} = 2/(s+2)$ and $t_{ch,p} = \delta/2$ so $t_{s,p} = \delta/24$. This type of power supply is difficult to realize because i must be infinite at $t = 0$. On the other hand, the constant current charger i_0 where $V \propto t$ is nearly as efficient. Indeed, here $\Delta_{s,i} = 1/(s+1)$ and $t_{ch,i} = \delta$ so $t_{s,i} = \delta/23 \cong t_{s,p}$. Charging the capacitor bank C using a constant-voltage power supply V_∞ with a load resistor R_{ch} in series is not recommended because $t_{s,v} \gg t_{s,i}$.

We constructed a constant-current charger for our 1.25 MJ bank 25 years ago using a motorized variac that delivered a linear ramp of AC voltage $V_{AC} \propto t$. For the 14 MJ bank, we are using double resonant converters that deliver a constant charging current. This relatively new generation of converters, pioneered by the Laboratoire d'Electrotechnique et d'Electronique Industrielle du CNRS [7], insures very soft switching conditions of its semiconductor components, guaranteeing a very high reliability and an efficiency above 94 %.

We have fixed t_{ch} at 5 min. The corresponding t_s is 13 s. For a shot at 0.8 V_m the charging time is reduced to 4 min and the effective duration of ageing for this shot is two orders of magnitude smaller than t_s. The experimenters have the option of keeping the bank charged for one minute before they fire a shot. Beyond one minute, the pulse generator is automatically discharged into the safety power resistors with a time constant of 0.5 s. This happens infrequently and, according to our 25 years of experience with the 1.25 MJ bank, the time between the end of the charge and the triggering of the field is essentially less than 10 s. Considering these 10 seconds added to $t_s = 13$ s and τ_s estimated at 4000 h, we deduce $N_s > 600{,}000$.

The aim of the energy storage capacitors is their use in a rapid discharge mode. This is why data about the dynamic lifetime N_d in number of pulses concern essentially half-sinusoidal pulses whose widths $2t_0$ lie between 1 μs and 100 μs. For our capacitors and this range of pulse widths the following power law $N_d \propto 0.95^{k\%} V^{-d} t_0^{1/2}$ is roughly verified for $d = 11$. Here k% represents, in percents, the rate of voltage inversion that very strongly reduces the lifetime N_d. To illustrate, the most extreme rate of inversion that will be accepted for the bank is 60 %. This allows us, for monolithic 75 T/0.4 s coils, to recover a non-negligible part of the Joule heat during the decrease of the magnetic field, but causes $N_d(60\ \%) = 0.05\ N_d\ (0)$.

For 0.4 s/60 % inversion we obtain N_d = 450,000 by applying the power law to the typical results measured at 10 μs. We deduce from $1/N = 1/N_d + 1/N_s$ and from this power law that $N(V_m)$ = 250,000. $N(V_m)$ should give, if N_d is realistic, a pessimistic estimate of the lifetime of the bank for an operation at 14.4 MJ. The application of the power laws for all shots lower than 0.8 V_m yields a lifetime $N(0.8\ V_m)$ that we can consider as unlimited. $N(V_m)$ = 250,000 and $N(0.8\ V_m)$ guarantees 50 years of service for the pulse generator.

Nevertheless, it seemed less than credible, in the absence of measurements at low frequencies, to extrapolate blindly, over six orders of magnitude from 1 μs to 1 s, the power law that yields N_d in the range 1 μs to 100 μs. This is why we set up a bank in 1996 to systematically test ageing of a sample of six capacitors connected in parallel. The elementary dielectric windings of these capacitors are identical to those of the 14 MJ bank.

The aging cycle is the following:

a) Charging to 1.025 V_m with t_{ch} = 5 min. Here, the charger is a constant-voltage source that supplies currents at all times into C through a load resistor such that $t_{ch}/R_{ch}C = 4$. This means that, scaled to V_m, $t_{s,v}$ = 131 s. This is nearly six times the static ageing time for a shot at V_m for the 14 MJ bank.

b) Pseudo-oscillating discharge with a period of 0.34 s and a first inversion rate of 70 %. This discharge is much more damaging for the capacitor than the pulse 0.4 s/60 % inversion during a 75 T shot.

The test capacitors underwent more than 150,000 aging cycles until October 1, 1998.

4 Conclusion

The 14 MJ pulsed capacitor bank will, in principle, be totally operational in December 1999. We are certain about its reliability for at least 30 years of operation. The year 2000 will be dedicated to connect the bank to the 10 experimental stations. We foresee for the end of 2000 six 60 T/0.3 s 3 MJ coils and one magnet coilin 32 T/coilex 48 T (8MJ) delivering 80 T in ∅1.5 cm. On each magnet a high-power snubber will give a linearly increasing dB/dt at the beginning of the shot instead of the classical step. These fields will be at the disposal of users as of January 2001. The construction of the 14 MJ/60T/1 s coils is planned to start in 2002, and we expect to have four magnets available for scientific experiments at the 2003 RHMF Symposium.

References

1. Askénazy, S., Van Bockstal, L., Herlach, F., Schneider-Muntau, H. J., *Meas. Sci. Technol.*, **4** (1993) p. 1058.
2. Askénazy, S., Van Bockstal, L., Dupouy, F., Herlach, F., *Meas. Sci. Technol.* **7** (1996), p. 680.
3. Askénazy, S., Lecouturier, F., Thilly, L., Coffe, G., *in these Proceedings.*
4. Askénazy, S., *Physica B,* **211** (1995) p. 56.
5. Askénazy, S., *Physica B* **216** (1996) p. 221.
6. Askénazy, S., *Physica B* **246-247** (1998) p. 67.
7. Cheron, Y., "Soft Switching in the Static Conversion of Electrical Energy". Ed. by Chapman et Hall, London (1992).

GENERATION OF HIGH MAGNETIC FIELDS IN THE MEGAGAUSS RANGE AT THE OSAKA FACILITY

K. KINDO
KYOKUGEN, Osaka University, Japan
CREST, Japan Science and Technology Corporation

A few pulsed magnets recently developed at Osaka University are presented. The basic magnet is a Cu-Ag wire wound type with a bore of 18 mm and 7 ms pulse duration. This magnet is externally reinforced by a maraging steel shell and can generate fields up to 71.3 T. Installing a small coil reinforced with a maraging steel shell into the basic magnet and connecting it in series has produced an 80 T-class magnet. This magnet has an inner diameter of 10.5 mm, pulse duration of 8 ms and can generate 80.3 T. Some magnetization measurements obtained with this 80 T-class magnet are reported. A new reinforced magnet, expected to generate fields in the megagauss range, is also described.

1 Background

In 1975, the High Magnetic Field Laboratory at Osaka University was founded by M. Date [1], who pioneered the generation of very high pulsed magnetic fields up to 80 T by means of polyhelix coils made from maraging steel [2]. A Foner-type maraging coil (nominal 40 T-class magnet) with a 60 mm bore and 150 mm outer diameter can produce a field up to 45 T. Further development of this type of coil has produced a nominal 60 T-class maraging steel coil magnet. This 60 T-class magnet consists of an outer 40 T-class magnet coil and an additional inner coil. The Foner-type inner coil has a 20 mm bore and a 50 mm outer diameter. A field of up to 63 T can be produced when these two coils are connected in series. Installing a third, small, wire-wound coil into the nominal, 60 T-class maraging steel coil magnet and connecting it in parallel produces an 80 T-class magnet. The nominal 40 T-class and nominal 60 T-class maraging steel coil magnets are useful, and have been used to make significant scientific contributions after the high field laboratory was reorganized as KYOKUGEN of Osaka University in 1987. The 80 T-class magnet has only been used for the magnetoresistance measurement of the high T_c superconductor at 77 K because its bore provides only 6 mm of room temperature space. Therefore, it was necessary to develop a new 80 T-class magnet with sufficient inner space to make scientific measurements under extremely high conditions. About four years ago, there was an effort to reevaluate the maraging steel coil type magnets with the goal of making a megagauss class magnet with the required bore size [3].

It has become clear through re-evaluation of the maraging steel coil type magnets that multi-layer coils are necessary to obtain megagauss fields. But the inefficiency of energy transfer and joule heating of the maraging steel coils becomes a serious design problem of multi-layer coils. Therefore, it is desirable to combine the efficiency of the wire wound coil and the strength of the maraging steel to produce a megagauss field. This combination is achieved through the concept that a magnet should consist of two parts: the conductive wire in which the current flows and the maraging steel, which withstands the electromagnetic force. In 1997, a magnet utilizing this concept produced a field of 80.3 T. The fabrication procedure for this 80 T-class magnet is reviewed below.

3 Basic Magnet

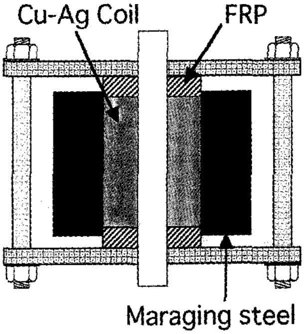

Figure 1. Vertical section view of the 70 T-class magnet.

The basic magnet consists of a wire-wound coil and maraging shell as shown in Figure 1. The maraging steel shell has an inner diameter of 60 mm, an outer diameter of 150 mm and a length of 150 mm. The maraging steel used is YAG-300™ made by Hitachi Metal Co., Ltd. This steel has a tensile strength of about 2160 MPa at room temperature. The maraging steel shell is used only to support the coil. The wire-wound coil has a bore of 18 mm, an outer diameter of 60 mm and a coil length of about 120 mm. The coil conductor is Cu-24wt%Ag 2 mm x 3 mm cross-section wire made by Showa Electric Wire & Cable Co., Ltd. with a tensile strength of 900 MPa. Wrapping with Kapton™ tape electrically insulates the wire. A 9-layer coil is produced by winding this wire around a silicone grease coated 18 mm diameter stainless steel mandrel, which is removed after completion of the coil. The radial thickness of the wire including the Kapton™ insulation is 2.3 mm; 9 layers of this wire produce a coil with an outer diameter of about 59.4 mm. Glass fiber is wound around the coil to make its outer diameter larger than 60 mm. The coil is then impregnated with Stycast™ 1266 epoxy resin under a pressure of 78 bar. After hardening the epoxy resin, the outer diameter of the coil is cut down to 60 mm and the coil is inserted into the maraging steel shell.

When cooled to liquid nitrogen temperature this basic coil can produce up to 71.3 T in its 18 mm diameter bore. The pulse duration is about 7 ms when a 7.5 mF capacitor bank powers the magnet. The coil life versus field produced was tested and the results obtained are as follows: 8 pulses at 69 T, in excess of 20 pulses at 65 T and about 150 pulses at 60 T. Prior to the use of Cu-Ag wire, this same magnet design produced fields of 60 T and 64 T using copper wire and Cu-Cr-Zr alloy wire, respectively. This improved performance confirms the importance of wire tensile strength in reaching high magnetic fields.

Two examples are given to demonstrate that an 18 mm diameter magnet bore is sufficient for experimental purposes. One example is measurements at very low temperatures. A plastic dilution refrigerator (PDR) can be installed into this 18 mm bore [4] and magnetization or magnetoresistance measurements can be made at temperatures down to 60 mK. Fig. 2 shows typical results from such a measurement.

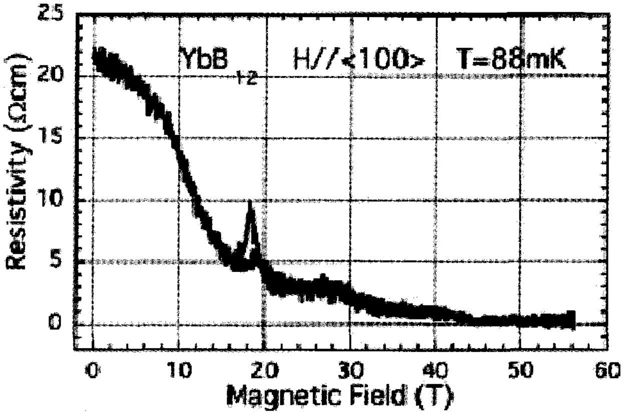

Figure 2. Magnetoresistance in YbB_{12} at 88 mK up to 60 T.

The PDR used has an outer diameter of 15 mm, a 4 mm sample space and was made by Taiyo Toyo Sanso Co., Ltd. The other example is a magnetization measurement made under high pressure using a Cu-Be piston cylinder cell pressurized to 12 kbar. Fig. 3 shows results from such a measurement [5]. The piston and cylinder pressure cell used has an outer diameter of 9 mm and a 3 mm sample space.

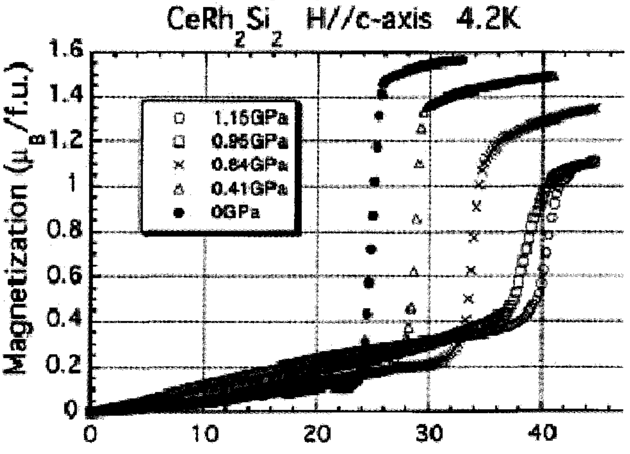

Figure 3. Magnetization curves in $CeRh_2Si_2$ at 4.2 K up to 12 kbar.

3 80 T-Class Magnet

Installing a small, single layer coil instead of a PDR or high-pressure cell into the basic magnet described previously produces an 80 T-class magnet. This arrangement is shown in Fig. 4.

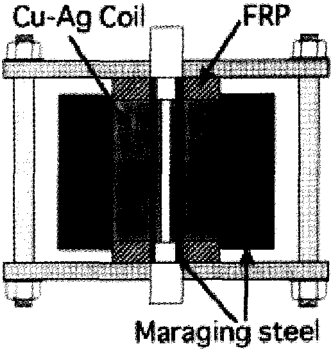

Figure 4. Vertical section view of the 80 T-class magnet.

This single layer coil is fabricated by winding the same wire used in the basic magnet around a 10.5 mm diameter silicon-grease coated stainless steel mandrel. An external maraging steel tube with an internal diameter of 16 mm and an outer diameter of 18 mm is placed over the wire for reinforcement. This 80 T-class magnet can generate fields to 80.3 T with pulse duration of 8 ms as shown in Fig. 5.

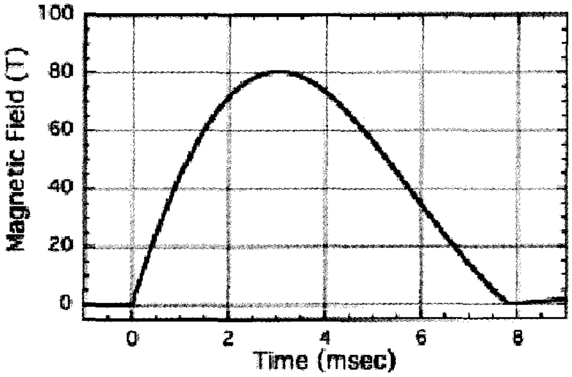

Figure 5. Pulse shape of the magnetic field generated by the 80 T-class magnet.

This field is achieved when the single layer inner coil is connected in series with the basic magnet, and a 10 mF capacitor bank powers the combined set of coils. The coil life versus field produced for this coil is 5 pulses at 75 T and more than 20 pulses at 70 T. The magnet bore provided by this coil configuration is sufficient for measurements at liquid helium temperatures. A magnetization measurement taken for this magnet is shown in Fig. 6.

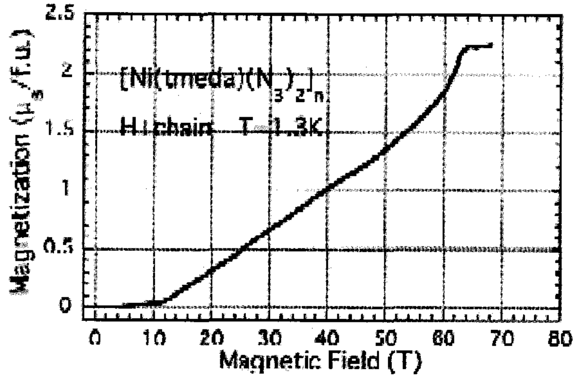

Figure 6. Magnetization of $[Ni(tmeda)(N_3)_2]_n$ at 1.3 K up to 70 T.

4 Magnets Under Development

Large bore magnets are often requested for many experiments. A large bore magnet has been constructed and tested to meet this requirement. This coil has a bore of 58 mm and an outer diameter of 100 mm. The coil is reinforced with an external maraging steel shell with an inner diameter of 100 mm and an outer diameter of 150 mm. The wire used in winding the coil is the same type used in the basic magnet. Fields up to 44.4 T can be produced with this magnet. Its bore size will enable experiments to be conducted with pressures up to approximately 1 Mbar.

A new 100 T-class magnet has also been fabricated and partially tested. The concept used is a full perimeter support of the wire forming the coil layer. A tightly fitted maraging steel casing provides this support. Experience gained with the basic magnet indicates that the tensile strength of the magnet wire is very important in attaining magnetic fields higher than 80 T. Wire materials, however, are not expected to be stronger than the currently available Cu-Ag. Therefore, a full perimeter support of the magnet wire configuration is proposed to increase the wire's effective tensile strength by allowing transfer of some of its electromagnetic load to the supporting maraging steel. The inner portion of the full perimeter support casing is fabricated by machining a groove that follows a helical path on the outside of a thick maraging steel tube. The helical path followed by the groove has a helix angle sufficient to leave a thick, axially supporting thread of maraging steel as shown in Fig. 7. The cross-section of the groove is 2.5 mm x 3.5 mm that produces a close fit with the Cu-Ag wire forming the coil. The Cu-Ag wire is wound into the groove to form the coil layer. This assembly is installed into another tightly fitted maraging steel tube to produce a configuration that completely surrounds the wire with supporting material. The inner 3 layers of the new 100 T-class magnet are fabricated using this full perimeter support concept. The outer 9 layers of the magnet are wound in a manner similar to the previously described basic magnet. This magnet has been tested to 40 T. Testing at higher fields has not been completed due to insufficient energy being available from the capacitor bank. Tests of this magnet at higher fields are expected.

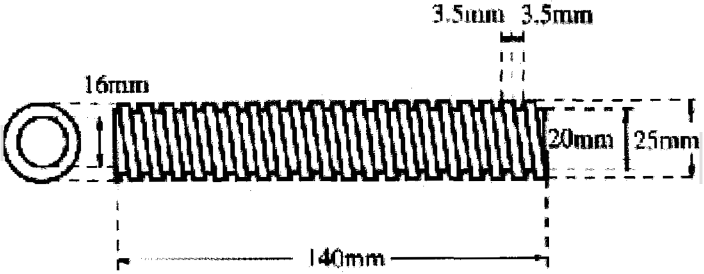

Figure 7. Inner portion of maraging steel full perimeter support casing used in the 100 T-class magnet.

Acknowledgments

This work was done partly under the Visiting Researcher's Program of the Advanced Science Research Center, Japan Atomic Energy Research Institute. This study was also supported in part by a Grant-in-Aid for Scientific Research from the Japanese Ministry of Education, Science, Sports and Culture.

References

1. Yamagishi, A., Date, M., in *High Field Magnetism*, Ed. by M. Date (North-Holland, Amsterdam, 1983) p. 289.
2. Yamagishi, A., Date, M., *Physica B* **155**, (1989) p. 91.
3. Kindo, K., *Physica B* **216**, (1996) p. 171.
4. Narumi, Y., Kobayashi, T. C., Kindo, K., presented at Megagauss VIII, published in this volume.
5. Hamamoto. T., et al., presented at PPHMF III.

THE NEW OXFORD HIGH FIELD FACILITY

H. JONES
University of Oxford, Clarendon Laboratory, Oxford, England

Following the retirement of our 75 year old, 2 MW motor - generator set we have abandoned dc water cooled magnets and are now concentrating our efforts on expanding our pulsed field facility and high field superconducting magnets - including high Tc coils. To this end we have successfully obtained funding for refurbishing the space that was occupied by the generator in order to accommodate the new facilities and equip it with state-of-the art high field magnets. The existing two storey space has been fitted with a floor that will enable a three station pulsed magnet laboratory (fields in excess of 60 T) to be located on the ground floor and rooms for experimental equipment, e.g. lasers (with access ports to connect with the magnets below) on the upper floor. In addition we will have a 21 T plus (in 40 mm bore) superconducting magnet that can be configured to give 19 T in a 110 mm bore for High Tc insert coil development. A report on the progress of the construction of this high field magnet suite will be given as well as a description of the technologies that are being used for high field generation in Oxford.

1 Introduction

All good things must come to an end and, in May 1997, an era at the Clarendon Laboratory ended when the 75 year old, 2 MW motor-generator set, which had powered the laboratory's water-cooled magnet stations for nearly 50 years, was broken up and removed for scrap. The demise of this old machine had been anticipated some dozen years earlier and a decision was made that the future for the UK's principal magnet laboratory lay in high field pulsed magnets and superconducting magnets. Consequently, a programme was established whereby the necessary technology for ultra-high pulsed field magnets could be developed. In 1993 The Oxford pulsed field laboratory was commissioned [1]. Every opportunity to equip the magnet laboratory with state-of-the-art superconducting magnets was taken. We built on the experience we had accumulated of mobile, multi-user superconducting magnets that we had pioneered in the early 70s [2,3]. Today, we can offer over 60 T routinely in pulsed magnets and 18 T using superconducting magnets. In this paper we will describe recent developments that will give us a considerable upgrade and expansion of our facilities.

2 The Space Problem

The pulsed field facility was so successful that its rather cramped single station set up was causing bottlenecks in research. The old generator occupied a large hall, two stories high. It was decided that once the machine had been scrapped, we would develop this space for the expansion of the magnet lab. An award from the Wolfson Foundation greatly facilitated and expedited this initiative and, at the time of writing, the refurbishment is nearing the completion of the first phase. The work involved the installation of a floor so that the magnet suite now is comprised of two stories. On the lower floor there will be 3 pulsed magnet cells and a central control room. One of the cells is smaller than the other two and is to be dedicated to testing and training new magnets.

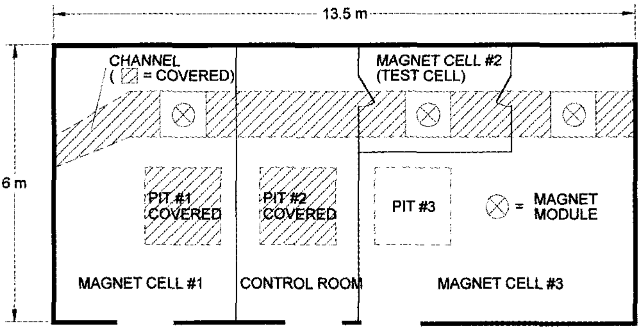

Figure 1: Layout of lower floor of high magnetic field suite.

One feature of the old generator hall has proved very useful in this new set-up. The floor contains a number of pits and channels that used to serve several purposes when the generator was there. We are taking advantage of these and will be installing the pulsed magnet modules below floor level. This makes for much greater safety and will allow us to be a little more adventurous in our coil designs. A plan schematic of the lower floor layout is presented in Fig. 1. On the upper floor, there will be two "laser" rooms. This loose naming comes about because the principal use of the space will be for lasers that are involved in experiments in the pulsed magnets. Strategically placed ports in the floor will allow optical access to the floor below and, therefore, to the magnet cells. Appropriate blast proof partitioning will create spaces for (a) the capacitor bank (with space for its future expansion) and (b) cabinets containing the electrical / electronic components associated with the system. Examples of these are:

- Pneumatic switches for bank section selection, and field reversal.
- The thyristor and ignitron switches
- The crowbar diode and resistances
- Some instrumentation such as a current transducer

In Table 1, the main parameters of the pulsed power supply are presented. More detail will be found in Siertsema and Jones [1].

Table 1. The main features of the capacitor bank.

Total bank energy	No. of capacitors	Voltage	Switches	Maximum Current
800 kJ	40	7 kV	Thyristor (single stack) or ignitron	30 kA

3 The Coil Technology

In general, the coils used in the Oxford facility are conservatively built. The aim is to have coils of long lifetimes rather than spectacularly high fields. Coils with lifetimes of many thousands of shots are quite routine. However, as stated above, the new facility, with its dedicated test cell and magnet modules below floor level, will enable us to explore less conservative coil constructions and this will lead ultimately to higher fields. The current conductor and coil technologies most favoured in Oxford have been widely reported [4,5,6] but can be summarised as follows:

- Most commonly used conductor: Cu / stainless steel macrocomposite manufactured in-house [7,8,9].
- Most coils use the Cu/ss wire but CuNb, Cu/BeCu, Glidcop, hard Cu and soft Cu also sometimes used [10,11].
- Coils are currently more than a single winding. 1, 2 and 3 section coils have been made sometimes all of the same conductor and sometimes mixing materials [11].
- All coils have an external shell of high strength fibre, usually carbon, for extra reinforcement (at 60 T the bursting pressure is 14,000 atm.)
- Multi section coils have additional internal fibre reinforcement at the section boundaries.
- Bore sizes of 20 or 12 mm are standard but we will be exploring smaller bore sizes in order to attain higher fields.
- All coils and reinforcements are vacuum impregnated with epoxy resin.

4 Superconducting Magnets

All steady dc fields are currently produced using superconducting magnets. Most of these are standard commercial magnets but we still produce our own when there are special features, such as an unusual geometry, required. There are several magnet systems producing in the region of 15-18 T in bores of 40 - 50 mm. Two of the systems are “mobile”. Different workers in various locations can use them on a pre-booked, rotational basis. These systems stay cold for weeks, if not months. Although this may seem to be obvious for deploying modern superconducting magnet systems, at one time it was sufficiently novel to be remarked on by the report of the Panel on High Magnetic Field Research and Facilities of the US National Academy of Sciences in 1979 [12] when we first applied the practice using the world’s first 15 tesla plus magnet [2,3]

It is currently possible to achieve >20 tesla using low temperature superconductors and we are fortunate to have attracted substantial funding for such a magnet to be supplied by Oxford Instruments Plc. It is hoped that we may be able to have up to 22 tesla in a 40 mm bore (21 T guaranteed). The most novel feature of the magnet, however, will be that its innermost section will be removable. This feature will allow us to access 18/19 T in a 110 mm bore and this is for our work on the development of high field magnet inserts using high temperature / high field superconductors [13]. Below we show the specification of this new magnet, which is due for delivery in March 1999.

4.1 Field Specifications For 40 mm Cold Bore Configuration

Guaranteed field at 4.2 K	19.0 T
Design field at 4.2 K	19.5 T
Guaranteed field at 2.2 K	21.0 T
Design field at 2.2 K	>21.5 T

4.2 Field Specifications For 110 mm Cold Bore Configuration

Guaranteed field at 4.2 K	16.0 T
Design field at 4.2 K	16.5 T
Guaranteed field at 2.2 K	18.0 T
Design field at 2.2 K	>18.5 T

4.3 Other Parameters

Nominal operating current	115 amps at 21 T
Outer diameter	425 mm
Inductance	365 Henries
Stored energy	2.25 MJ at 21 T
Homogeneity DSV	0.1 % in 10 mm

The magnet will be contained in a NMR style cryostat for low helium consumption but this does mean that we will need to break and remake a large diameter indium seal when we change bore configuration from 40 mm to 110 mm and vice versa.

5 High Tc Magnets

As mentioned above, we have a program for developing magnet coils using High Tc materials in their practical formats, usually dip coated or powder in tube tapes. We have developed successful windings working at 77 K, for iron circuits used in a Maglev demonstrator [13] At present we are concentrating on techniques for making pancakes using very thin silver alloy tape dip coated with Bi 2212. The work is supported by industry and is therefore commercially sensitive but we can say that progress has been good. Engineering current densities of over 100 A mm^{-2} have been achieved, in self fields of about 0.5 T, in small pancake coils we have wound using up to 10 m of tape. If we can achieve the level of superconductor current densities that have been exhibited in short samples of the tape, we will be well on the way to having the means to boost background fields of ~ 20 T (from low Tc coils) to 25 T and more using high Tc insert coils. The new 21 T superconducting magnet described above will play an important role in this.

6 Conclusion

High field magnet research in Oxford is entering a new era. Both pulsed fields and superconducting magnet fields are increasing significantly, as is the size of the magnet facility, thanks to the conversion of the old generator hall. The magnet development program is vigorous and healthy and should make a significant contribution to the next generation of high field magnets for research.

Acknowledgements

The work described in this paper has been supported by a variety of agencies. We are grateful to the Wolfson Foundation for funding the conversion of the generator hall. A consortium of the British Higher Education Funding Council, the Engineering and Physical Sciences Research Council, Oxford Instruments Plc and the University of Oxford is funding the new superconducting magnet under the Joint Research Equipment Initiative and we are grateful to all parties. The European Union has, over a long period, also supported much of the work described in this paper and we acknowledge its contribution with gratitude. Peter Richens and Mark Newson were very helpful in the production of this paper and are thanked accordingly. The "we" used throughout this paper pays tribute to members of the author's group and other colleagues who would be too numerous to mention by name but who have contributed much to the success, past, present and, hopefully, future of the Oxford high field facility.

References

1. Sierstsema, W. J., Jones, H., *IEEE Trans Mag* **30** (1994) pp. 1809-1812.
2. Hudson, P. A., Jones, H., *Cryogenics* **16** (1976) p. 593.
3. Jones, H., Hudson, P. A., Mains, E. F., Markiewicz, W.D., *Proc 9th International Magnet Technology Conference* (1985) Zurich, Ed by C. Marinucci and C. Weymuth.
4. Jones, H., et al., *IEEE Trans Mag*, **24** (1988) pp. 1055-1058.
5. Jones, H., Herlach, F., Lee, J. A., *Proc. 11th International Magnet Technology Conference*, Ed by T. Sakiguchi and S. Shimomoto, Elsevier (1990) p. 639.
6. Jones, H., *Megagauss Magnetic Field Generation and Pulsed Power*, Ed by M. Cowan and R. B. Spielman, Nova Science, New York (1994) pp. 109-116.
7. Van Cleemput, M. et al., *Physica B* **216** (1996) pp. 226-228.
8. Jones, H., Eyssa, Y., Schneider – Muntau, H-J., Van Cleemput, M., *IEEE Trans Mag.* **32** (1996) pp. 2466-2469.
9. Jones, H., Van Cleemput, M., *High Magnetic Fields: Applications, Generation and Materials*, Ed. H-J Schneider-Muntau, World Scientific (1997) pp. 499-509.
10. Jones, H., Schneider-Muntau, H-J., Herlach, F., *IEEE Trans Mag.* **30** (1994) pp. 1651-1656.
11. Jones, H., Van Cleemput, M., Hickman, A. L., Ryan, D. T., Saleh, P. M., *Physica B* **246-247** (1998) pp. 337-340.
12. See pages 79-82 of the report (1979). Available from Solid State Sciences Committee, National Research Council, 2101 Constitution Avenue, Washington DC.
13. Jones, H., Richens, P. E., Ryan, D. T., Goodall, R. M., *Physica B* **246-247** (1998) pp. 333-336.

AUTHORS INDEX

The VIIIth International Conference on Megagauss Magnetic Field Generation and Related Topics (Megagauss VIII) was held October 18-23, 1998, at the National High Magnetic Field Laboratory (NHMFL) in Tallahassee, Florida, USA. The conference was the eighth in a series that began in 1965 in Frascati, Italy. Other megagauss conferences have been held in Washington, DC; Novosibirsk, Russia; Santa Fe, New Mexico; Albuquerque, New Mexico, and Sarov, Russia.

The meeting was intended to combine technological and scientific aspects of the generation and use of megagauss fields. The conference presentations provided the latest results on the generation of magnetic fields at the megagauss level and higher and offered highlights of the research in these fields. Principal topics included megagauss field generation, production of non-destructive fields up to and beyond the megagauss level, handling terawatt range power at high energy density, and application of ultra-high fields in technology and science. Research topics encompassed solid state physics, nuclear fusion, atomic physics, biology, chemistry, and theory. Other techniques and applications of megagauss fields were reviewed as well. The session devoted to the Dirac series of experiments in explosively generated fields up to 1000 T demonstrated the feasibility, as well as the potential, of research in megagauss fields.

ISBN 981-256-016-5
9 789812 560162

www.worldscientific.com
5631 hc